.

NASA Program: Solar & Heliospheric Physics Supporting Research & Technology (SR&T) and Low Cost Access to Space (LCAS)

NASA Contract Number: NNH11CC42C

Contract Title: Understanding Heliospheric CMEs using a Robust, Event-Based MHD Model

Principal Investigator: Pete Riley, Predictive Science Inc., San Diego

ANNUAL REPORT

Covering the period MARCH 3, 2011 - MARCH 2, 2014

1. Overview

This report summarizes the technical progress made during all three years of the contract "Understanding Heliospheric CMEs using a Robust, Event-Based MHD Model," (Contract NNH11CC42C) between NASA and Predictive Science, and covers the period from March 3, 2011 to March 2, 2014. Under this contract, Predictive Science Inc. (PSI) has conducted numerical and data analysis related to issues concerning the eruption and evolution of coronal mass ejections (CMEs) and the development of a semi-empirical, event-based CME generator, resulting in 18 peer-reviewed publications and over 20 presentations by team members at scientific meetings and/or workshops. During this investigation our team focused on: (1) Development of a robust, semi-empirical model for generating CMEs in the solar corona; (2) Analysis of the relationship between magnetic clouds and interplanetary coronal mass ejections (ICMEs) in the solar wind; (3) Investigation of the probability of occurrence of extreme solar events; (4) The development of an ion-kinetic code for studying CME-driven shocks; (5) The development and testing of a heliospheric MHD code with the capability of being driven by a range of CME inputs; (6) Investigation of the Bastille-day event; (7) cone-model simulations of ICMEs; (8) Simulations of extreme ICMEs; (9) The coupling of our global MHD CME code with University of New Hampshire's energetic particle code (EPREM); and (9) Miscellaneous studies, in collaboration with other institutions, applying our CME models to study a variety of phenomena related to CME initiation and evolution. We also list the main presentations made and publications resulting from this effort. Appendix A provides copies of all significant peer-reviewed papers that resulted from this investigation.

2. Summary of Work

2.1. Development of a robust CME Generator

We began our first year of investigation by completing the development of a kinematically-initiated CME (KIC) model for solar eruptions. The underlying motivation for this approach was to bridge the gap between purely ad-hoc methods and fully self-consistent techniques. The former have the advantage that they are relatively easy to implement and can be adjusted (through various parameters) so as to produce an eruption with the desired properties. However, they suffer from the fact that as a superposition of two magnetic fields, the initial conditions are never physically realized by the Sun. Moreover, the actual explosive phase of the eruption is driven by the superposition process. Self-consistent methods, while of more fundamental scientific value, are considerably more challenging to implement, and sometimes produce results that do not match observations well. The KIC model was intended to pro-

vide a sufficient level of realism to an otherwise simple approach: An initially in-equilibrium solution was kinematically-evolved by winding up the footprints of field lines connecting two polarities of a bipole. Although the resulting structure was not dynamically-evolved to a non-equilibrium state, the field itself was well-defined.

In an effort to further develop the KIC CME generator, we realized that a more physically-defensible approach was to adopt the Titov-Demoullin flux rope (TDFR) prescription and insert an in-equilibrium flux rope in the solar corona. We began by developing a TDFR model within a Cartesian geometry. Our technique differs from other approaches in that the flux rope is allowed to relax to an equilibrium prior to eruption. Thus, the initial conditions are considerably more self-consistent than these "superposition" models, which produce ejecta simply by being out of equilibrium initially.

Following this, we began exploring the properties of the new TDFR model. We implemented the TDFR model in our global spherical model and conducted several tests investigating the stability of the structure within within a zero-beta approximation. We found that, in general, the flux rope was very stable; however, we were able to cause it to erupt under certain conditions.

During this second year of investigation, we focused our efforts on developing a robust CME generator using the "modified Titov-Demoullin" (mTD) flux rope method. Our goal is to use this approach to produce fast CMEs that would otherwise be difficult to initiate from first principles. While our previous calculations relied on a zero-beta approximation, in our first set of thermodynamic MHD simulations, we were also able to successfully generate a fast CME. The CME, which propagated through a quadrupolar magnetic field geometry generated a fast-mode shock wave by $\sim 2R_S$, but slowed substantially as it plowed through the ambient plasma above.

To understand why the CME appears to strongly decelerate in the model corona, we hypothesized that it might be due to the influence of the spatial grid resolution. We performed a series of zero beta simulations using the same model parameters, but varying the numerical grid in the radial direction, along which the main propagation takes place. While the results so far indicate that the resolution indeed plays an important role, they are unfortunately not yet conclusive. The reason for this is that we used different resolutions along the whole radial mesh, in particular at low heights. As a result, we found very different onset times and strengths of reconnection below the respective rising flux ropes, leading to very different acceleration profiles of the ropes; thus, making a proper comparison difficult.

We also tested whether a density cavitation, created at the onset of strong reconnection in the wake of the expanding CME, can be avoided using improved spatial grid resolution.

We found that the cavitation is delayed, but still occurs and therefore leads to numerical problems in many of our runs. This delay, we believe, is due to the fact that the current layer below the CME is captured by a higher-resolution grid for a longer period of time, which, in turn, delays the onset of reconnection. Although this is an improvement, it did not resolve the problem.

To address this, we implemented a density truncation routine, whereby, on each grid point, the mass density is prevented from falling below a certain value during the integration. These values are set to a certain fraction (typically 10^{-3}) of the initial density (i.e., after the system has been thermodynamically relaxed to a steady-state solar wind solution and before the mTD flux rope is inserted). Using this density truncation routine, we performed the first CME simulation in which the eruption is started from a fully relaxed and stable flux rope. After being inserted into the relaxed solar wind solution, the rope is further relaxed for 20 Alfven times (corresponding to eight hours of real time). While the rope itself achieves a magnetic equilibrium relatively quickly, the system must relax further to allow the relatively strong, wave-like perturbation caused by the insertion of the rope to travel out to sufficiently large heights prior to the eruption of the CME. The initiation is then accomplished by imposing photospheric converging flows toward the polarity inversion line along which the rope is located.

We also modified the boundary conditions so that the initial wave-like perturbation of the system (caused by the insertion of the rope into the global MHD solution) travels out of the simulation domain during the relaxation, so that the subsequent eruption provides a clear, unambiguous picture of the global impact that the CME has on the corona. In particular, we were able to follow the global MHD wave triggered by the eruption (a so-called EUV wave) and analyze its relationship to the CME driving it. For example, the simulation succinctly shows the de-coupling of the wave and the CME after the eruption has reached a certain height in the corona.

We also ran similar cases in which the eruption originated from a significantly stronger active region, with peak field strengths of about 1000 Gauss. Previously, attempts to simulate CMEs from such strong fields always led to numerical instabilities. Using our new "density cavitation limitation" method, the simulation remained stable for a longer period of time. However, eventually, it too terminated when the (flare) reconnection in the wake of the CME became too violent.

Figure 1 summarizes the main aspects of the mTD model prior to eruption. The top two panels show the configuration of the CME structure after insertion of the flux rope, while the bottom panels show the configuration after it has relaxed.

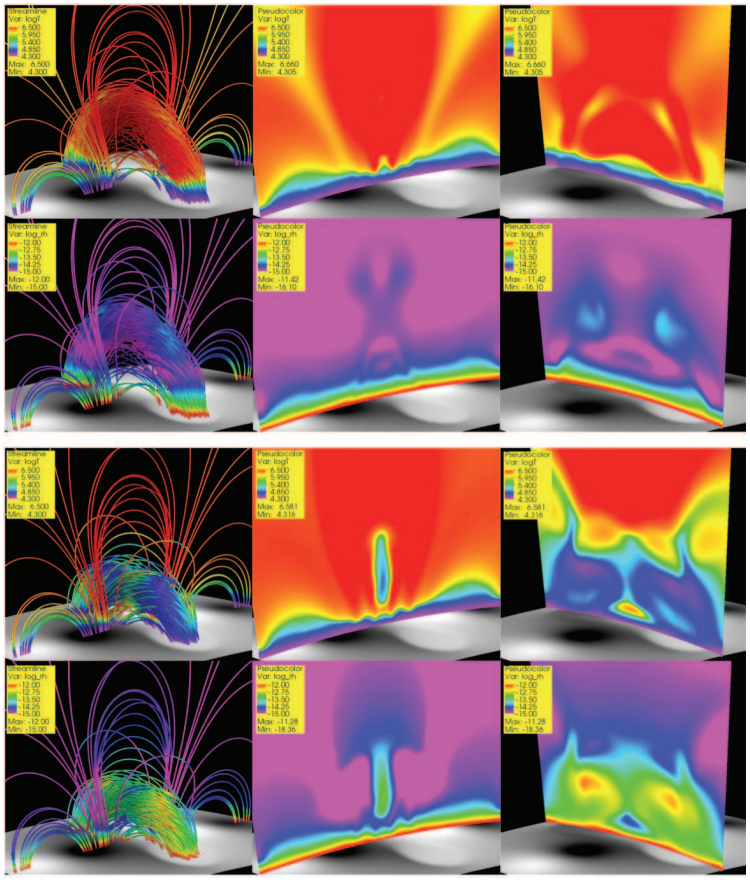

Fig. 1.—: *Insertion of the mTD flux rope. The top panels show the configuration after insertion, while the bottom panels show the configuration after relaxation. Alternating rows show Log(T) and log(Density).*

To resolve the issues of the density cavitation when strong fields are involved, we added the capability of arbitrarily enhancing the resistivity (and viscosity) in a specified localized region, while keeping the resistivity low in the rest of the simulation domain. In preliminary tests, the code now survives the critical time period of reconnection, so that we can, in principle, model CMEs from active regions with kilogauss fields. We note, however, that the current method of setting the enhanced resistivity within a specific region is achieved in an ad hoc fashion.

Using these techniques for ensuring numerical stability, we completed a CME simulation in which the eruption: (a) originates within a source region containing kilogauss fields and; (b) starts from a flux rope configuration that is in magnetic equilibrium. We consider these crucial steps towards realistic simulations of extreme CMEs. During the relaxation of the system we observed the accumulation of cold and dense plasma within the flux rope, which

strongly resembled actual prominences on the Sun. While we have yet to investigate how this 'prominence' forms in the simulation, and so cannot claim that the formation process is realistic, it is nevertheless a useful proxy for studying how the presence of dense material within the pre-eruption rope influences the final speed and morphology of the CME as seen in white-light observations.

We continued to increase the spatial resolution of the numerical grid in the radial direction with each subsequent simulation. Our main motivation was to check whether improved resolution helps to decrease, or even suppress, the relatively strong deceleration of the CME observed in earlier runs. This experiment was only partially successful: the deceleration is less pronounced than in earlier runs, but still persists and is significant. Thus, this remains an ongoing question. Alternatively, it may well be that impulsively accelerated fast CMEs, in contrast to gradually-accelerated slow and average speed CMEs, undergo a significant deceleration low in the corona (i.e., prior to their further deceleration high in the corona and solar wind). If so, it would suggest the need for even stronger model active region fields to produce CMEs with final (coronal) propagation speeds of 1500 km/s or more. Indeed, two out of the three fast CMEs reported by Temmer et al. (2010) showed a strong deceleration (a reduction in speed by a factor of approximately 2) at relatively low coronal heights.

We also explored an additional aspect of these simulations: the connection between CMEs and their related EUV signatures in the low corona, such as EUV waves and coronal dimming regions. The framework we use in our simulations allows us to explore the full non-linear response of the corona to an eruption, while also retaining configurations that are simple enough to allow clear comparisons between runs. For example, when comparing a fast CME run with large energy release to a weaker one produced from a similar region with lower field strength, we noticed important qualitative differences between both the initial speed of the EUV front and the points at which it no longer appeared to be driven by the CME shock. In both simulations, we also identified fine scale oscillations developing just behind the outward propagating front, reminiscent of features discovered recently by AIA observations. By studying such features in detail and contrasting them between runs, we hope to gain insight into how EUV waves are driven in the low corona, and why they might appear different depending on the nature of the CME itself. Concerning coronal dimming regions, we are now able to explore how the changing magnetic field due to a CME relates to regions of transient density depletion in the low corona (dimming). Although it is clear that some coronal mass will be lost during a CME eruption, why adjacent coronal regions sometimes display strong or asymmetric dimming regions is not yet fully understood, and suggested observational mechanisms need to be tested. By following how portions of nearby closed flux systems became effectively open in one of our quadrupolar active region runs, we developed a relatively simple picture for how such extended dimming regions might occur

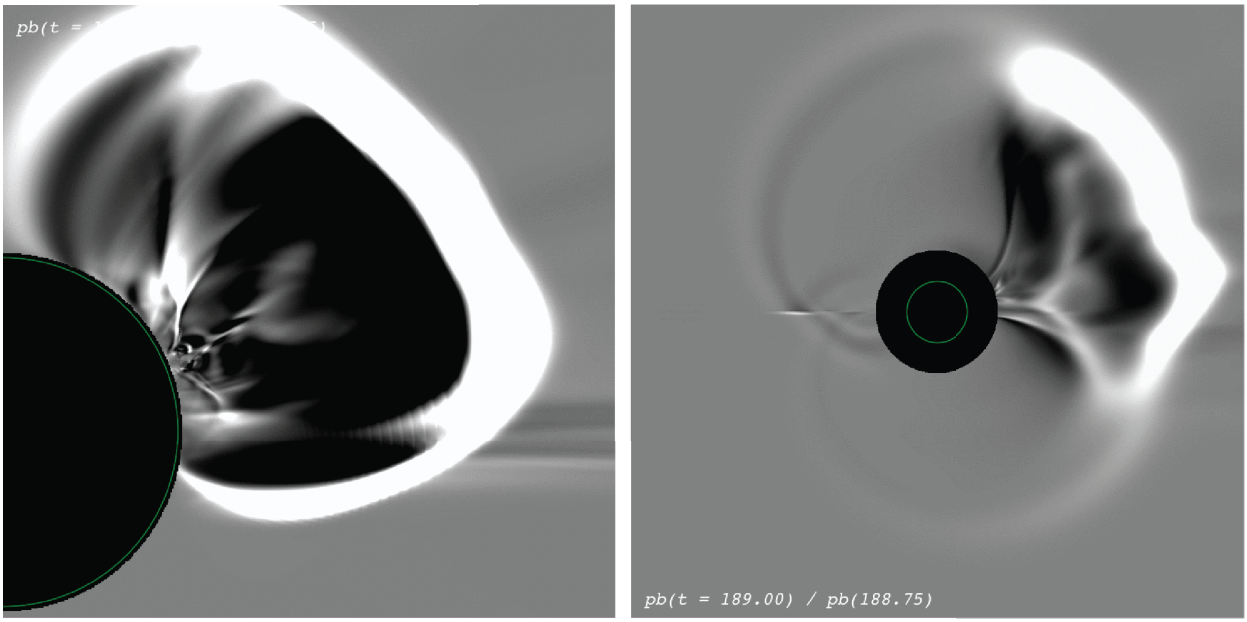

Fig. 2.—: *Evolution of a CME initiated using the mTD technique (left) close to the Sun and (right) higher in the corona.*

away from the flare site. We hope to explore this in more detail in forthcoming simulations with asymmetric initial configurations.

In collaboration with Kathy Reeves from CFA, we investigated plasma heating during the eruption of a CME. Recent studies have shown that, in addition to the material observed in post-flare loops, the plasma that escapes from the Sun as the CME is heated during the eruption. At present, it is unclear which is (are) the most important mechanism(s) for heating the CME plasma(e.g. Murphy et al. 2011). Our analysis suggests that heating of the plasma due to compression from the upward-directed flare reconnection jet below the erupting CME is significantly stronger than joule heating and may be the dominant mechanism. This result is consistent with earlier theoretical suggestions by Longcope et al. (2009), and, to the best of our knowledge, represents the first time it has been verified with simulations. Caution is required, however, when undertaking these simulations because both the strength of the reconnection jets and the amount of joule heating depend (at least to some extent) on the values of viscosity and resistivity in the simulations. Therefore, it is important to explore the parameter space by varying viscosity and resistivity and assessing their impact on the model results.

We also produced a series of synthetic polarization brightness images of the solar corona from several of our recent CME simulations, as well as corresponding running difference and running ratio images. These synthetic data will allow us to study various aspects

like the CME white-light morphology (which can be viewed from an arbitrary angle) and the evolution of large-scale CME-related features, such as global waves and shocks. We also developed a semi-automatic tool to generate height-time profiles from the images. A preliminary analysis of these profiles, in combination with the simulation data, suggests that the deceleration of our model CMEs reported earlier may be in fact related to unrealistically large reconnection jets in some of the runs. It appears that if reconnection occurs while the rising CME flux rope has not yet reached a sufficient height, a reconnection outflow, which is significantly faster than the CME velocity, can temporarily accelerate the CME to a speed that it would not otherwise reach. Following this short, but strong perturbation, the CME appears to "fall back" to the speed governed by the large-scale forces acting on the flux rope. This effect may be present in observed events (see, e.g., Fig. 8 in Temmer et al. (2010)). We plan to investigate this in more detail by repeating selected runs, where we attempt to damp the reconnection outflows by imposing a sufficiently large localized viscosity around the reconnection region.

Figure 2 shows a running-ratio polarization brightness image from one of the mTD simulations. The "coronagraph" FOV has been set to mimic observations, although in reality, of course, the model ran from the surface marked with the green line. Close to the Sun, the strong eruption has driven a wave, which has likely steepened into a shock by a few solar radii. Within the cavity defined as the region within the bright front, there is a considerable amount of structure. Further away from the Sun (right panel), one can see (albeit only faintly) that the eruption-driven wave has decoupled from the ejecta and has "interfered with itself" at the opposite side of the Sun. We are continuing to investigate these results.

Based on evidence that suggests quiescent prominences outside active regions may have a hollow core current profile, while active region filaments may instead be dominated by currents concentrated within the flux rope, we generalized the TDm model to account for these two possibilities. Until recently, the so-called "hollow core" current profiles in the model allowed specification of current densities concentrated in an annulus at the edge of the flux rope. With the new option, we can now prescribe a parabolic radial current profile within the flux rope. With these two options, we should have sufficient flexibility to build a wide range of pre-eruptive coronal configurations.

During our third year, we continued to refine the TDm model. While our previous efforts focused on generating faster eruptions by experimenting with different flux rope configurations, we began a complementary effort to investigate the effects of different large-scale coronal magnetic configurations on the solutions. This was motivated in part by observations that line-of-sight magnetic field strengths in the Kitt Peak magnetograms are significantly

weaker than those obtained by MDI. Moreover, magnetograms may be produced at significantly different times, with respect to the time of eruption. Initially, we focused on zero-beta solutions. Our tests thus far indicated that stronger fields will yield more powerful and faster eruptions.

In the TDm model, the electric currents are located at the surface of the flux rope, within a layer of finite thickness. Up until now, this layer had not been not force-free, leading to a violent reconfiguration of the flux rope when the analytical model is used as an initial condition in an MHD simulation. While the rope quickly found a new equilibrium state, which could then be employed as a pre-eruption configuration for CME modeling, this initial reconfiguration triggered a strong perturbation of the global configuration. We developed a new analytical version of the mTD model in which the current layer is approximately force-free, and we experimented with this new version to find the parameters that yield a solution best matching a fully force-free state.

We also constructed a new flux rope configuration using fields derived from MDI magnetograms. MDI fields appear to be significantly stronger, allowing us to construct a substantially more compact flux rope, containing stronger fields. We performed a variety of zero-beta test runs with the new flux rope and were able to generate notably more powerful eruptions. We also experimented with different converging-flow profiles, aimed at mimicking the temporal evolution of the active region, and ultimately triggering the eruption.

We defined and ran a series of test simulations for our new, force-free description of the TDm model. The simulations showed that numerical equilibria can be achieved for the new model version for different ambient magnetic fields and for flux ropes that are tilted with respect to the vertical direction. The latter are useful for asymmetric CME source regions, where one magnetic polarity is stronger than the other. The runs with tilted flux ropes revealed that current concentrations are present in a localized area surrounding the symmetry axis of the TDm current ring, which are not visible in non-tilted cases, since the symmetry axis is then located fully below the photospheric plane.

Based on evidence that suggests quiescent prominences outside active regions may have a hollow core current profile, while active region filaments may instead be dominated by currents concentrated within the flux rope, we generalized the TDm model to account for these two possibilities. Until recently, the so-called "hollow core" current profiles in the model allowed specification of current densities concentrated in an annulus at the edge of the flux rope. With the new option, we can now prescribe a parabolic radial current profile within the flux rope. With these two options, we should have sufficient flexibility to build a wide range of pre-eruptive coronal configurations.

We also generalized our global MHD code, MAS, to allow specification of a TDm flux rope at some arbitrary height above the surface. Previously, the simulation domain was required to begin at 1Rs. With this new capability, we are able to study eruptions from, say, 20Rs, which will avoid having the sometimes unnecessary expense of having to compute computationally intensive solutions, particularly if we are more interested in the heliospheric evolution of such structures. Ultimately, we plan to incorporate this into the heliospheric version of the MAS code, which will allow us to directly simulate flux-rope-like ejecta from 20Rs to say 1-5 AU. This model approach should complement our recently developed "spheromak" ejecta (see below), and provide an alternative, simple ICME generator, which includes magnetic structure.

2.2. On the Relationship between Magnetic Clouds and ICMEs

In-situ measurements of interplanetary coronal mass ejecta (ICMEs) display a wide range of properties. A distinct subset of them, "magnetic clouds" (MCs), are readily identifiable by a smooth rotation in an enhanced magnetic field, together with an unusually low solar wind proton temperature. In this part of the investigation, we analyzed Ulysses spacecraft measurements to systematically investigate five possible explanations for why some ICMEs are observed to be MCs and others are not: (1) An observational selection effect, that is, all ICMEs do in fact contain MCs, but the trajectory of the spacecraft through the ICME determines whether the MC is actually encountered; (2) Interactions of an erupting flux rope (FR) with itself or between neighboring FRs, which produce complex structures in which the coherent magnetic structure has been destroyed; (3) An evolutionary process, such as relaxation to a low plasma-β state that leads to the formation of a MC; (4) The existence of two (or more) intrinsic initiation mechanisms, some of which produce MCs and some that do not; or (5) MCs are just an easily identifiable limit on in an otherwise continuous spectrum of structures. We applied quantitative statistical models to assess these ideas. In particular, we used the Akaike Information Criterion (AIC) to rank the candidate models and a Gaussian Mixture Model (GMM) to uncover any intrinsic clustering of the data. Using a logistic regression, we found that plasma-beta, CME width, and the ratio O7/O6 are the most significant predictor variables for the presence of a MC. Moreover, the propensity for an event to be identified as a MC decreases with heliocentric distance. These results tend to refute ideas (2) and (3). GMM clustering analysis further identified three distinct groups of ICMEs; two of which match (at the 86% level) with events independently identified as MCs, and a third that matches with non-MCs (68% overlap). Thus, idea (5) is not supported. Choosing between ideas (1) and (4) is more challenging since they may effectively be indistinguishable from one another by a single in-situ spacecraft. This study

is described in more detail in the Appendix, where we also offer some suggestions on how future studies may address this.

2.3. On the Probability of Occurrence of Extreme Space Weather Events

By virtue of their rarity, extreme space weather events, such as the Carrington event of 1859, are difficult to study, their rates of occurrence are difficult to estimate, and prediction of a specific future event is virtually impossible. Additionally, events may be extreme relative to one parameter but normal relative to others. In portion of the study, we analyzed several measures of the severity of space weather events (flare intensity, CME speeds, *Dst*, and >30 MeV proton fluences as inferred from nitrate records) to estimate the probability of occurrence of extreme events. By showing that the frequency of occurrence scales as an inverse power of the severity of the event, and assuming that this relationship holds at higher magnitudes, we were able to estimate the probability that an event larger than some criteria will occur within a certain interval of time in the future. For example, the probability of another Carrington event (based on $Dst < -850$ nT) occurring within the next decade is ∼12%. We also identified and addressed several limitations with this approach. In particular, we assumed time stationarity and, thus, the effects of long-term space climate change were not considered. While this technique cannot be used to predict specific events, it may ultimately be useful for probabilistic forecasting. This work is described in more detail in the Appendix.

2.4. A Hybrid Model for ICMEs

During the previous year, we explored a novel approach to modeling CMEs using a hybrid code. In these so-called ion-kinetic techniques, the ions are treated as "macro-particles" while the electrons are treated as a fluid. Such models have never been applied globally to CMEs in the past because the the size of a CME in the solar wind far exceeds the spatial scales that can be captured by hybrid simulations. (Previous attempts, dating back 13 years, relied on "scaled down" models of ICMEs). However, we believe that by parallelizing the code, restricting the analysis to two dimensions, and using the fastest supercomputers available, we can simultaneously model both fine-scale, and global shock structure associated with fast CMEs. This will allow us to investigate: field-line draping, magnetic reconnection, back-streaming ions upstream of quasi-parallel shocks, and mirror-mode waves behind quasi-perpendicular shocks. Our preliminary results suggest a rich set of solutions, which are driven substantially by the incident angle of the IMF into which the CME propagates.

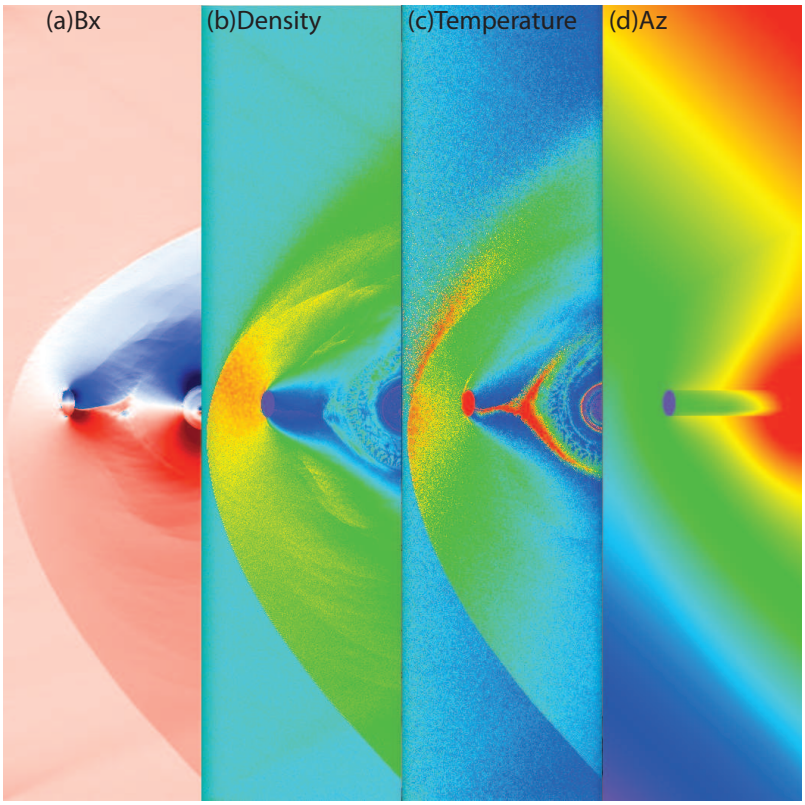

Fig. 3.—: *Hybrid CME solutions for a fast, elliptically-shaped CME propagating through the solar wind at* ~ 1 *AU. (a) The x-component of the magnetic field. (b) The plasma density. (c) The plasma temperature. (d) The z-component of the vector potential (contours of Az trace along field lines for these 2.5-D solutions).*

We successfully simulated several 2-D cases with a spatial scale of $1200 \times 4800 c/W_{pi}$ grid points. Although this is still smaller than the true scale size of ICMEs, it is 10 times larger (in each dimension) than we had previously been able to achieve. We also developed a parallel (OpenMP) version of the code, which allowed us to run these cases locally on 12-processor desktop computers. We are currently installing the code on NASA's Pleiades and Endeavor systems, with the hope of scaling to near-ICME sizes.

Figure 3 illustrates one of the solutions. In it, the ICME is treated as an immovable elliptical flux rope. (In future simulations, we may allow the flux rope to dynamically interact with the flow). Thus, the simulation is taking place in the rest frame of the flux rope. The solar wind flows from the left to the right with typical solar wind values. The interplanetary magnetic field is oriented at a 45° angle from the upper left to the lower right. This can be seen in the panel showing contours of the z-component of the vector potential, A_z, which, in 2.5-D acts as a fiduciary of the magnetic field. In an analogous way that bow shocks are set up

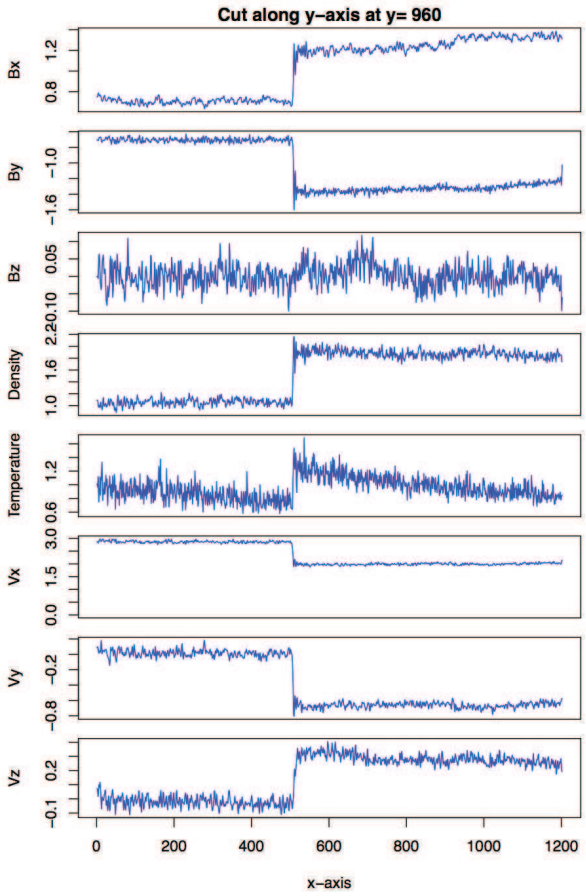

Fig. 4.—: *Traces through the simulation summarized in Figure 3. From top to bottom, the traces show: the three components of the magnetic field, plasma density and temperature, and the three components of the bulk plasma velocity. The shock crossing can be seen at* $\sim 500c/W_{pi}$.

at planets, a CME-driven shock forms ahead of the flux rope. The northern hemisphere is a quasi-parallel shock, while the southern hemisphere is a quasi-perpendicular shock. Although we are still investigating the richness of these solutions, we note the presence of upstream streaming of particles and ion-cyclotron waves, both of which would not be produced using the MHD formalism.

We believe that these model results will allow us to better interpret *in-situ* measurements, which, compared to the hybrid results, are significantly under-sampled. Figure 4 summarizes a trace through the quasi-perpendicular portion of the shock, and contains a rich set of ion-kinetic features that we are currently investigating.

2.5. Development of a Heliospheric MHD code for simulating ICMEs

During our second year of investigation, we developed a version of our fully-parallel, resistive MHD code suitable for inner heliospheric calculations. We have found it computationally efficient to separate the solar corona from the inner heliosphere, running the latter model with output from the former. The new code, MAS-H, retains all of the features of the coronal code, but in addition, can be run in either the inertial reference frame or the corotating frame. The model can also be run with boundary conditions based in either frame of reference and will translate accordingly, inserting fictitious forces, if necessary.

We tested the model by running several mTD solutions through the inner boundary, whilst at the same time, running the solution further out in the coronal model. Comparisons of the model results in this overlapping region of the inner heliosphere demonstrated that the two models had been joined seamlessly. Figure 5 illustrates one such solution. The left-most column summarizes the eruption of a mTD flux rope above an active region. Field lines associated with the flux rope are colored arbitrarily. Open background field lines are colored purple. In the middle panel, the flux rope evolution is shown in the upper corona. Note the kinks in the purple field lines marking the position of the shock wave propagating ahead of the ejecta. Finally, in the right-most panels, the flux rope is shown as it approaches 1 AU (3rd panel down).

During the third year, we tested MAS-H extensively using a range of inputs. Because it was developed very generally, MAS-H can accept a wide range of possible inputs. These tests included the use of a cone-model generator (see below), the output from a TDm flux rope, and even a self-consistent coronal solution. We studied one of the TDm simulations in detail, and, in particular, compared the model results at 1 AU with typical spacecraft measurements of ICMEs and magnetic clouds. The analysis revealed that: (i) the CME flux rope is transformed to a "blob"-like magnetic field structure; and (ii) this blob seems to strongly rotate out of the "plane" of CME propagation, so that upon arrival at 1 AU the axial field of the blob appears to be directed almost perpendicular to that plane. If such "blob" formation and subsequent rotation indeed occurs in observed events, this result would have significant implications for magnetic cloud and ICME models, which tacitly assume that the CME flux rope axis at 1 AU lies within the plane of propagation. Initial comparisons with observed events suggest that this model solutions are roughly consistent with some cases, but cannot obviously explain the propensity for rotations to be seen in the z-component of the magnetic field. Additionally, the extensive reconnection and reconfiguration of the field lines in the model leaves very few, if any, closed loops, which is in conflict with observations, which suggest - via the signature of counter streaming supra thermal electrons - the ubiquitous presence of closed fields within ICMEs. We have begun investigating potential

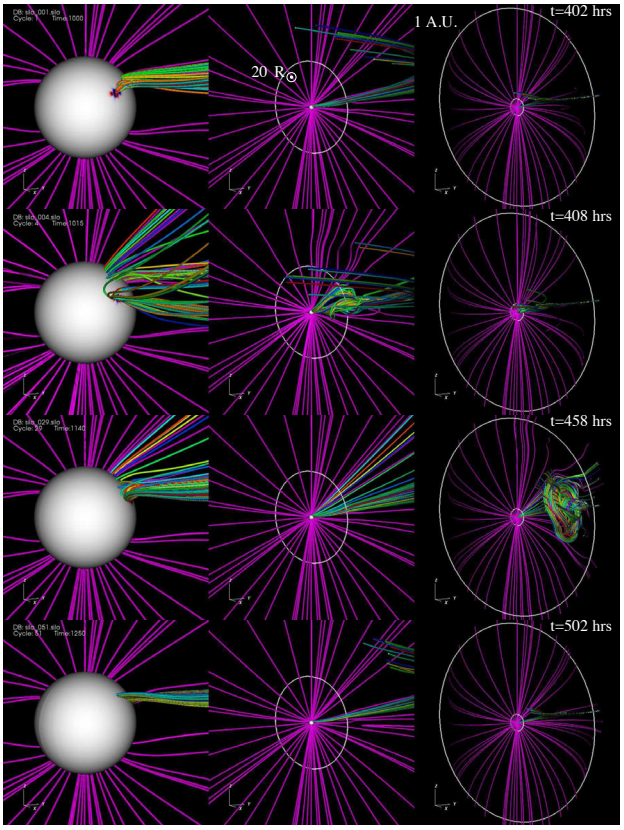

Fig. 5.—: *Evolution of a CME from the solar surface (left column), through the boundary between the two codes (middle column), and out to 1 AU (right column). In each panel, the purple lines trace open magnetic field lines, and the colored-field lines mark the location of the CME. The white circle in the middle panel indicates* $20R_S$*, which is the boundary between the coronal and heliospheric codes, while the white circle in the right panels marks 1 AU. The grey spherical surface in the left-most panels marks the location of the solar surface.*

effects that could cause such a rotation. The most promising candidate at present is the JxB force due to the interaction of the flux rope (blob) current and the open magnetic field into which it propagates. This force should lead to a rotation perpendicular to the plane of propagation. To test this, we performed a set of idealized test simulations, with the simplest, relevant configuration, namely a freely expanding three-dimensional current ring (flux rope) in cartesian geometry. We found that if the ring is placed into a magnetic-free environment, it continuously expands without any rotation. If, however, a uniform field running perpendicular to the symmetry axis of the ring is added, the ring indeed rotates out of its plane of propagation. We have begun writing up the results and anticipate submitting the manuscript for peer review.

2.6. Investigation of the Bastille-day event

We applied our modified Titov-Demoulin (mTD) model to the so-called Bastille-day event. A particularly difficult aspect of this event is that the pre-eruptive, non-potential magnetic field ran along a highly curved polarity inversion line. A limitation of our mTD model is that the analytical model flux rope has no writhe, that is, the flux rope axis is straight in projection on the solar disk, which renders a single mTD rope inappropriate for modeling eruptions that originate from highly curved inversion lines. To overcome this difficulty, we implemented a capability of inserting more than one mTD rope into a given source region potential field, while still preserving the original magnetogram. For the Bastille-day event, we placed three mTD ropes with carefully chosen, overlapping foot-points along the inversion line of the potential field and numerically relaxed the system. Remarkably, the three ropes merged at their common foot-points, creating a single, well-connected and curved flux rope that winds along the inversion line.

In a further refinement to the model of the Bastille-day event, we applied localized converging flows toward the main polarity inversion line (PIL) of the active region, which serve to slowly lift the pre-eruptive flux rope to a critical height at which point it becomes unstable and erupts. As a first test, we applied ad-hoc flows only within a relatively small area, located where the first observed flare signatures were visible. We obtained an eruption, however, only a fraction of the flux rope erupted. We then repeated the experiment by imposing additional converging flows at several other locations along the PIL and found that, in this case, the whole rope erupted, in better agreement with observations. This demonstrated that the choice of the imposed converging flow pattern plays a strong role in influencing how much of the pre-eruptive flux rope actually erupts, even though the rope appears to be a coherent entity.

Next, began development of a thermodynamic (full MHD) simulation for the Bastille Day Event. We experimented with the coronal heating parameters to find the most appropriate heating model for the configuration and computed a thermodynamic relaxation of the global configuration on a grid with good spatial resolution within the erupting active region and moderate resolution elsewhere. We found that while a relatively large number of grid points was used (251 x 200 x 310), the resolution outside the main active region was unable to produce a smooth calculation, resulting in numerical difficulties that required a relatively large viscosity to counteract. By increasing the spatial resolution, we were able to complete a thermodynamic MHD relaxation run of the Bastille Day event corona with improved spatial resolution and insert a pre-relaxed flux rope into the solution. While a significant amount of magnetic energy was still released as the system adjusted to the inserted, strong-field flux rope, the rope now retained its coherence much better. Moreover, the improved resolution

greatly improved the quality of synthetic satellite images in the sense that spurious oscillations and disturbances that we had previously seen in the images are now almost completely absent within the active region.

2.7. Cone Model Simulations of ICMEs

At the start of the third year of investigation, we developed a cone model CME generator for our recently completed global heliospheric MHD code. Our approach is based on the empirical formulation driven by white-light observations of ejecta close to the Sun, similar to Enlil. Additionally, we have developed a magnetic component to the ejecta based on a magnetic spheromak topology. Although the dynamics of the eruption are still primarily controlled by the plasma properties of the ejecta (speed and density primarily), initial tests suggest that even a modest magnetic field modifies the profiles of the disturbance at 1 AU. We will investigate these results in more detail, and, in particular, assess the effects of different field strengths within the ejecta.

2.8. Cone-Model Simulations of Extreme Events

For our initial case study of the cone-model CME generator, we are modeling the July 23, 2012 event, which was well observed in situ by STEREO A. We also derived a spheromak-like magnetic field solution that bore many similarities to global solutions produced using the coupled mTD model. To test the new code, we initiated six CMEs (without a magnetic field) from the inner boundary, each with a progressively faster initial speed (up to 4,000 km/s). The resulting solutions compare favorably with previous ICME calculations undertaken by our group and others. In particular, we find that fast ICMEs: (1) produce a strong shock ahead of the ejecta; (2) are significantly distorted by the ambient solar wind; (3) generate strong low density regions within them; (4) produce radial magnetic fields behind them; (5) broaden significantly in the transverse direction; and (6) compress the the upstream magnetic field significantly within a sheath region. For each solution, we computed deceleration profiles for the ejecta as it moved from 30Rs to 1 AU. In conjunction with the available, but limited STEREO measurements (magnetic field, bulk solar wind speed, and plasma parameters upstream and downstream, but not within the ejecta), we used these simulations to attempt to reconstruct the properties of the July 23, 2013 ICME, which has been likened to a modern day equivalent of the Carrington event.

The July 23, 2012 CME had an average transit speed from the Sun to 1 AU of 2780

km/s, and the speed of the leading portion at 1 AU was still over 2,000 km/s. We found that an ejecta with an initial speed of 3950 km/s produced the best match with the velocity profile at 1 AU. However, this may be an overestimate as there was evidence of a precursor CME that may have preconditioned the ambient solar wind. In that case, it may have been possible for an initially-slower ejecta to still maintain a speed in excess of 2,000 km/s at 1 AU.

As the study progressed, we continued to compute more realizations of the July 23, 2012 extreme ICME, each differing slightly from one another, but within the uncertainties for the initial conditions for this event, ultimately resulting in ~ 100 cases. These explored a variety of input parameters, including the shape, duration, amplitude, and speed of the main CME as well as whether or not a precursor CME was first launched. We found that the addition of the precursor event sufficiently preconditioned the ambient solar wind such that we could launch the main CME with speeds comparable to those observed by LASCO for this event. In contrast, previous modeling by other groups had required unrealistically large initial CME speeds to match the speeds observed at 1 AU. Although promising, our results point to the intrinsic non-uniqueness of these simulations: It is possible to reproduce ICME observations at STEREO-A using a variety of combinations of input parameters. We will attempt to identify other constraints that will limit the flexibility in the input parameters.

2.9. Coupling of Global MHD CME Code with University of New Hampshire's Energetic Particle Code

In preparation for two presentations at the Fall AGU, 2013, one of the promising model solutions for the July 23, 2012 CME was chosen to provide the background plasma and magnetic field parameters to accelerate protons using the EPREM code suite at the University of New Hampshire (UNH). We provided the ICME solutions as high-temporal snapshots of speed, density, and magnetic field, and using their fully parallelized energetic particle transport and acceleration algorithm EPREM, the UNH team were able to accelerate protons and produce particle spectra with properties that matched the essential features observed. The results suggest that the included particle acceleration mechanisms can more than adequately produce distributions like those observed. However, these 'coupled' simulations are limited in the sense that there is no feedback: the energetic particles are treated as test particles and the pressure is unbounded. For the July 23, 2012 event in particular, and, as pointed out by Russell et al. (2013), the intense flux of energetic particles may have substantially modified the plasma conditions. This level of coupling is significantly more challenging than the 'one-way' methodology currently employed. Nevertheless, it is likely to be a crucial

component of any robust and accurate model in the future. Thus, we are developing plans, in collaboration with UNH, to ultimately produce a coupled MHD/particle code that can self-consistently model the plasma, magnetic, and energetic particle properties of fast, and even extreme CMEs.

2.10. Miscellaneous other studies related to modeling CMEs

We conducted several other studies with colleagues from other institutions. Here, we briefly summarize three of them. Details of the remaining ones can be found in the Appendix.

Although sympathetic CMEs have been observed for many years, the mechanisms by which one eruption can trigger another remain poorly known. We have studied two possible mechanisms using 3-D MHD simulations that could account for sympathetic eruptions. The geometry consists of two flux ropes, embedded within a unipolar streamer (pseudostreamer) and a flux rope positioned next to it. By initiating the eruption of the flux rope next to the unipolar streamer, the two flux ropes within it can be incited to erupt. While this is only strictly applicable to the configuration modeled, we suggest that it may also apply in a range of magnetic configurations. We applied the results of the model to interpret the August 1, 2010 eruptions, and found that the model results, at least qualitatively, reproduced the main features of the observations. Moreover, it provided a natural explanation for the so-called twin filament eruptions. This work is described in more detail in the Appendix.

In collaboration with W.T. Thompson (Adnet Systems Inc.; NASA GSFC) and B. Kliem (MSSL/UCL, UK; Potsdam University, Germany; NRL), we performed a 3D reconstruction of an erupting prominence associated with a CME that took place on 9 April 2008 (the so-called "cartwheel CME"), using EUVI and COR data from STEREO. The 3D reconstruction allowed us to obtain a height-rotation profile of an erupting prominence/CME for the first time. Understanding the mechanisms that cause CME rotation is important, since a strong rotation already in the low corona will influence the final magnetic orientation of the CME (magnetic cloud) when it arrives at Earth. This orientation is one of the two main parameters that determines the geo-effectiveness of CMEs. This study is summarized in two papers reproduced in the Appendix.

Finally, we initiated a project (in collaboration with Dr. Rui Liu from the Space Weather Research Laboratory at the New Jersey Institute of Technology) to study an active-region filament with a "double-decker" configuration, that is, a filament composed of two bifurcated branches sharing the same ends. We triggered the eruption flare heating near one end of the filament and the eruption was driven by the kink instability. Below, a sigmoid structure

formed quickly in the gap between the two original branches. Again, this study is described in detail in the Appendix.

2.11. Presentations and Publications

The work performed as part of this investigation were presented at a number of conferences and workshops. These included:

1. P. Riley, "Modeling CMEs using the KIC model", CME Workshop, 2011 November, San Diego, CA.
2. P. Riley, "First steps in modeling extreme CMEs", CME Workshop, 2011 November, San Diego, CA.
3. P. Riley, "Summary of group's modeling effort both for CMEs and CIRs", Seminar at the Universidad National Autonoma de Mexico, 2011 August, Morelia, Mexico.
4. P. Riley, "Understanding the relationship between magnetic flux ropes and ICMEs through global MHD simulations", CAWSES Flux Rope Workshop, 2011 September, Alcala, Spain.
5. P. Riley, "Relationship between flux ropes and ICMEs", Fall AGU, San Francisco, CA.
6. P. Riley, "Global MHD modeling of CMEs", Fall AGU, San Francisco, CA.
7. T. Török, "Modeling sympathetic eruptions", Seminar at Potsdam University, 2011 May, Potsdam, NY.
8. T. Török, "Numerical Modeling of Fast CMEs", Hinode 6 meeting, held 2012, August 14-17 in St. Andrews, Scotland.
9. T. Török, "Sympathetic Eruptions on 2010 August 1", EGU General Assembly, 2012 April 22-27, Vienna, Austria.
10. T. Török, "What Determines CME Velocities?", ESWE Workshop, 2012 May 14-17, Boulder, CO.
11. T. Török, "The Slow Rise Phase in Solar Eruptions", SHINE Conference, 2012 June 25-29, Wailea Maui, HI (Invited).
12. T. Török, "Using Multi-wavelength Observations to Constrain CME Simulations", AGU Fall meeting, 2012 December 3-7, San Francisco, CA (Invited).

13. T. Török, "Harvey prize plenary talk on eruptions and their modeling", AAS meeting, 2013 June 4, Indianapolis.

14. V. Titov, "The impact of the magnetic topology of pseudo-streamers on the particle acceleration during eruptions", SHINE Workshop, 2013 June 26, Buford, Georgia.

15. T. Török, "Summary of our efforts to model the Bastille day fast CME event", Colloquium at the High Altitude Observatory (HAO), 2013 November 6, Boulder, CO.

16. T. Török, "Simulations of the Bastille Day event", Seminar Talk at George Mason University, 2013 November 27, Fairfax, VA.

17. P. Riley, T. Török, Z. Mikic, and M. Gorby, "Global MHD modeling of the July 23, 2012 extreme CME and the distribution of particles accelerated by it", Fall AGU, 2013 December, San Francisco, CA.

The following manuscripts were either accepted for publication, or published during the course of this investigation:

1. Riley, P., & Richardson, I. G. (2013). Using Statistical Multivariable Models to Understand the Relationship Between Interplanetary Coronal Mass Ejecta and Magnetic Flux Ropes. Solar Physics, 284(1), 217-233.

2. Riley, P. (2012). On the probability of occurrence of extreme space weather events. Space Weather, 10(2).

3. Török, T., Panasenco, O., Titov, V. S., Mikic, Z., Reeves, K. K., Velli, M., ... & De Toma, G. (2011). A model for magnetically coupled sympathetic eruptions. The Astrophysical Journal Letters, 739(2), L63.

4. Thompson, W. T., Kliem, B., & Török, T. (2012). 3D reconstruction of a rotating erupting prominence. Solar Physics, 276(1-2), 241-259.

5. Kliem, B., Török, T., & Thompson, W. T. (2012). A Parametric Study of Erupting Flux Rope Rotation. Solar Physics, 281(1), 137-166.

6. Török, T., Temmer, M., Valori, G., Veronig, A. M., van Driel-Gesztelyi, L., & Vrsnak, B. (2013). Initiation of Coronal Mass Ejections by Sunspot Rotation. Solar Physics, 286(2), 453-477.

7. Titov, V. S., Mikic, Z., Török, T., Linker, J. A., & Panasenco, O. (2012). 2010 August 1-2 Sympathetic Eruptions. I. Magnetic Topology of the Source-surface Background Field. The Astrophysical Journal, 759(1), 70.

8. Bernhard Kliem, Tibor Török, Viacheslav S. Titov, Roberto Lionello, Jon A. Linker, Rui Liu, Chang Liu, and Haimin Wang, Slow Rise and Partial Eruption of a Double-Decker Filament. II Modeling by a Double Flux Rope Equilibrium, submitted to Ap. J., 2012.

9. Gosain, S., Schmieder, B., Artzner, G., Bogachev, S., & Török, T. (2012). A multi-spacecraft view of a giant filament eruption during 2009 September 26/27. The Astrophysical Journal, 761(1), 25.

10. Liu, R., Liu, C., Török, T., Wang, Y., & Wang, H. (2012). Contracting and Erupting Components of Sigmoidal Active Regions. The Astrophysical Journal, 757(2), 150.

11. Liu, R., Kliem, B., Török, T., Liu, C., Titov, V. S., Lionello, R., ... & Wang, H. (2012). Slow rise and partial eruption of a double-decker filament. I. Observations and interpretation. The Astrophysical Journal, 756(1), 59.

12. Mikic, Z., Török, T., Titov, V., Linker, J. A., Lionello, R., Downs, C., & Riley, P. (2013, June). The challenge in making models of fast CMEs. In SOLAR WIND 13: Proceedings of the Thirteenth International Solar Wind Conference (Vol. 1539, No. 1, pp. 42-45). AIP Publishing.

13. Valori, G., Török, T., Temmer, M., Veronig, A. M., van Driel-Gesztelyi, L., & Vrsnak, B. (2013). Initiation of Coronal Mass Ejections by Sunspot Rotation. Proceedings of the International Astronomical Union, 8(S300), 201-208.

14. Török, T., Kliem, B., Berger, M. A., Linton, M. G., Demoulin, P., & van Driel-Gesztelyi, L. (2014). The Evolution of Writhe in Kink-Unstable Flux Ropes and Erupting Filaments. arXiv preprint arXiv:1403.1565.

15. Török, T., Leake, J. E., Titov, V. S., Archontis, V., Mikic, Z., Linton, M. G., ... & Kliem, B. (2014). Distribution of Electric Currents in Solar Active Regions. The Astrophysical Journal Letters, 782(1), L10.

16. Lionello, R., Downs, C., Linker, J. A., Török, T., Riley, P., & Mikic, Z. (2013). Magnetohydrodynamic Simulations of Interplanetary Coronal Mass Ejections. The Astrophysical Journal, 777(1), 76.

17. Leake, J. E., Linton, M. G., & Török, T. (2013). Simulations of Emerging Magnetic Flux. I. The Formation of Stable Coronal Flux Ropes. The Astrophysical Journal, 778(2), 99.

18. van Driel-Gesztelyi, L., D. Baker, T. Trk, E. Pariat, L. M. Green, D. R. Williams, J. Carlyle et al. "Magnetic reconnection driven by filament eruption in the 7 June 2011 event." Proceedings of the International Astronomical Union 8, no. S300 (2013): 502-503.

19. Gopalswamy, N., Nieves-Chinchilla, T., Hidalgo, M., Zhang, J., Riley, P., van Driel-Gesztelyi, L., & Mandrini, C. H. (2013). Preface-Flux-Rope Structure of Coronal Mass Ejections.

20. Yashiro, S., Gopalswamy, N., Mkel, P., & Akiyama, S. (2013). Post-eruption arcades and interplanetary coronal mass ejections. Solar Physics, 284(1), 5-15.

21. Gopalswamy, N., Mkel, P., Akiyama, S., Xie, H., Yashiro, S., & Reinard, A. A. (2013). The solar connection of enhanced heavy ion charge states in the interplanetary medium: implications for the flux-rope structure of CMEs. Solar Physics, 284(1), 17-46.

22. Xie, H., Gopalswamy, N., & Cyr, O. S. (2013). Near-sun flux-rope structure of CMEs. Solar Physics, 284(1), 47-58.

23. Mkel, P., Gopalswamy, N., Xie, H., Mohamed, A. A., Akiyama, S., & Yashiro, S. (2013). Coronal hole influence on the observed structure of interplanetary CMEs. Solar Physics, 284(1), 59-75.

24. Kim, R. S., Gopalswamy, N., Cho, K. S., Moon, Y. J., & Yashiro, S. (2013). Propagation Characteristics of CMEs Associated with Magnetic Clouds and Ejecta. Solar Physics, 284(1), 77-88.

25. Zhang, J., Hess, P., & Poomvises, W. (2013). A Comparative Study of Coronal Mass Ejections with and Without Magnetic Cloud Structure near the Earth: Are All Interplanetary CMEs Flux Ropes?. Solar Physics, 284(1), 89-104.

26. Cho, K. S., Park, S. H., Marubashi, K., Gopalswamy, N., Akiyama, S., Yashiro, S., ... & Lim, E. K. (2013). Comparison of helicity signs in interplanetary CMEs and their solar source regions. Solar Physics, 284(1), 105-127.

27. Al-Haddad, N., Nieves-Chinchilla, T., Savani, N. P., Mstl, C., Marubashi, K., Hidalgo, M. A., ... & Farrugia, C. J. (2013). Magnetic field configuration models and reconstruction methods for interplanetary coronal mass ejections. Solar Physics, 284(1), 129-149.

28. Hidalgo, M. A., Nieves-Chinchilla, T., & Blanco, J. J. (2013). On the Flux-Rope Topology of Ejecta Observed in the Period 19972006. Solar Physics, 284(1), 151-166.

29. Blanco, J. J., Cataln, E., Hidalgo, M. A., Medina, J., Garca, O., & Rodrguez-Pacheco, J. (2013). Observable Effects of Interplanetary Coronal Mass Ejections on Ground Level Neutron Monitor Count Rates. Solar Physics, 284(1), 167-178.

30. Vourlidas, A., Lynch, B. J., Howard, R. A., & Li, Y. (2013). How many CMEs have flux ropes? Deciphering the signatures of shocks, flux ropes, and prominences in coronagraph observations of CMEs. Solar Physics, 284(1), 179-201.

31. Isavnin, A., Vourlidas, A., & Kilpua, E. K. J. (2013). Three-dimensional evolution of erupted flux ropes from the Sun (220 R?) to 1 AU. Solar Physics, 284(1), 203-215.

32. Romashets, E., & Vandas, M. (2013). Modeling Irregularities in Solar Flux Ropes. Solar Physics, 284(1), 235-243.

33. Berdichevsky, D. B. (2013). On Fields and Mass Constraints for the Uniform Propagation of Magnetic-Flux Ropes Undergoing Isotropic Expansion. Solar Physics, 284(1), 245-259.

34. Osherovich, V., Fainberg, J., & Webb, A. (2013). Observational Evidence for a Double-Helix Structure in CMEs and Magnetic Clouds. Solar Physics, 284(1), 261-274.

35. Hu, Q., Farrugia, C. J., Osherovich, V. A., Mstl, C., Szabo, A., Ogilvie, K. W., & Lepping, R. P. (2013). Effect of Electron Pressure on the GradShafranov Reconstruction of Interplanetary Coronal Mass Ejections. Solar Physics, 284(1), 275-291.

36. Owens, M. J., & Crooker, N. U. (2007). Reconciling the electron counterstreaming and dropout occurrence rates with the heliospheric flux budget. Journal of Geophysical Research: Space Physics (19782012), 112(A6).

37. Crooker, N. U., & Horbury, T. S. (2006). Solar imprint on ICMEs, their magnetic connectivity, and heliospheric evolution. Space science reviews, 123(1-3), 93-109.

38. Crooker, N. U., & Webb, D. F. (2006). Remote sensing of the solar site of interchange reconnection associated with the May 1997 magnetic cloud. Journal of Geophysical Research: Space Physics (19782012), 111(A8).

39. Owens, M. J., Crooker, N. U., & Horbury, T. S. (2009, October). The expected imprint of flux rope geometry on suprathermal electrons in magnetic clouds. In Annales Geophysicae (Vol. 27, No. 10, pp. 4057-4067). Copernicus GmbH.

40. Crooker, N. U., & Owens, M. J. (2012). Interchange Reconnection: Remote Sensing of Solar Signature and Role in Heliospheric Magnetic Flux Budget. Space science reviews, 172(1-4), 201-208.

These papers are reproduced in the Appendix.

REFERENCES

Longcope, D. W., Guidoni, S. E., & Linton, M. G. 2009, Ap. J. Lett., 690, L18

Murphy, N. A., Raymond, J. C., & Korreck, K. E. 2011, Ap. J., 735, 17

Russell, C. T., Mewaldt, R. A., Luhmann, J. G., Mason, G. M., von Rosenvinge, T. T., Cohen, C. M. S., Leske, R. A., Gomez-Herrero, R., Klassen, A., Galvin, A. B., & Simunac, K. D. C. 2013, Ap. J., 770, 38

Temmer, M., Veronig, A. M., Kontar, E. P., Krucker, S., & Vršnak, B. 2010, Ap. J., 712, 1410

Appendix

The Astrophysical Journal Letters, 739:L63 (5pp), 2011 October 1 doi:10.1088/2041-8205/739/2/L63

A MODEL FOR MAGNETICALLY COUPLED SYMPATHETIC ERUPTIONS

T. Török[1], O. Panasenco[2], V. S. Titov[1], Z. Mikić[1], K. K. Reeves[3], M. Velli[4], J. A. Linker[1], and G. De Toma[5]
[1] Predictive Science, Inc., 9990 Mesa Rim Road, Suite 170, San Diego, CA 92121, USA
[2] Helio Research, La Crescenta, CA 91214, USA
[3] Harvard-Smithsonian Center for Astrophysics, 60 Garden Street, Cambridge, MA 02138, USA
[4] Jet Propulsion Laboratory, California Institute of Technology, Pasadena, CA 91109, USA
[5] HAO/NCAR, P.O. Box 3000, Boulder, CO 80307-3000, USA
Received 2011 July 20; accepted 2011 August 9; published 2011 September 14

ABSTRACT

Sympathetic eruptions on the Sun have been observed for several decades, but the mechanisms by which one eruption can trigger another remain poorly understood. We present a three-dimensional MHD simulation that suggests two possible magnetic trigger mechanisms for sympathetic eruptions. We consider a configuration that contains two coronal flux ropes located within a pseudo-streamer and one rope located next to it. A sequence of eruptions is initiated by triggering the eruption of the flux rope next to the streamer. The expansion of the rope leads to two consecutive reconnection events, each of which triggers the eruption of a flux rope by removing a sufficient amount of overlying flux. The simulation qualitatively reproduces important aspects of the global sympathetic event on 2010 August 1 and provides a scenario for the so-called twin filament eruptions. The suggested mechanisms are also applicable for sympathetic eruptions occurring in other magnetic configurations.

Key words: methods: numerical – Sun: corona – Sun: coronal mass ejections (CMEs) – Sun: filaments, prominences – Sun: flares – Sun: magnetic topology

Online-only material: animations, color figures

1. INTRODUCTION

Solar eruptions are observed as filament (or prominence) eruptions, flares, and coronal mass ejections (CMEs). It is now well established that these three phenomena are different observational manifestations of a *single eruption*, which is caused by the destabilization of a localized volume of the coronal magnetic field. The detailed mechanisms that trigger and drive eruptions are still under debate, and a large number of theoretical models have been developed (e.g., Forbes 2010).

Virtually all existing models consider single eruptions. The Sun, however, also produces *sympathetic eruptions*, which occur within a relatively short period of time—either in one, typically complex, active region (e.g., Liu et al. 2009) or in different source regions, which occasionally cover a full hemisphere (the so-called global eruptions; Zhukov & Veselovsky 2007). It has been debated whether the close temporal correlation between sympathetic eruptions is purely coincidental, or whether they are causally linked (e.g., Biesecker & Thompson 2000). Both statistical investigations (e.g., Moon et al. 2002; Wheatland & Craig 2006) and detailed case studies (e.g., Wang et al. 2001) indicate that physical connections between them exist.[6]

The exact nature of these connections has yet to be established. They have been attributed, for instance, to convective motions or destabilization by large-scale waves (e.g., Ramsey & Smith 1966; Bumba & Klvana 1993). At present, it seems most likely that the mechanisms by which one eruption can trigger another act in the corona and are of a magnetic nature. Perturbations traveling along field lines that connect source regions of eruptions (e.g., Jiang et al. 2008) and changes in the background field due to reconnection (e.g., Ding et al. 2006; Zuccarello et al. 2009) have been considered. In an analysis of a global sympathetic event (see Section 2), Schrijver & Title (2011) found evidence for connections between all involved source regions via structural features like separators and quasi-separatrix layers (QSLs; Priest & Forbes 1992; Démoulin et al. 1996), suggesting the importance of the structural properties of the large-scale coronal field in the genesis of sympathetic eruptions.

A magnetic configuration that appears to be prone to producing sympathetic eruptions is a unipolar streamer or pseudo-streamer (PS; e.g., Hundhausen 1972; Wang et al. 2007). A PS is morphologically similar to a helmet streamer, but divides open fields of like polarity and contains an even number (typically two) of closed flux lobes below its cusp. PSs are quite common in the corona (e.g., Eselevich et al. 1999; Riley & Luhmann 2011) and occasionally harbor two filaments. It seems that if one of these erupts, the other one follows shortly thereafter (the so-called twin filament eruptions; Panasenco & Velli 2010).

Here, we present a numerical simulation that suggests two possible magnetic trigger mechanisms for sympathetic eruptions. It was inspired by the global sympathetic event on 2010 August 1, which involved a twin filament eruption in a PS.

2. THE SYMPATHETIC ERUPTIONS ON 2010 AUGUST 1

A detailed account of the individual eruptions that occurred in this global event can be found in Schrijver & Title (2011). Here we focus on a subset of three consecutive filament eruptions, all of which evolved into a separate CME. Figures 1(a), (b), and (c) show, respectively, the eruptions as seen by *STEREO*/EUVI (Howard et al. 2008), the pre-eruptive filaments, and a synoptic magnetogram obtained from the *Solar and Heliospheric Observatory*/Michelson Doppler Imager (*SOHO*/MDI; Scherrer et al. 1995) data. The large filaments 2 and 3 were located along the inversion lines dividing an elongated positive polarity and two bracketing negative polarities; the small filament 1 was located at the edge of the southern negative polarity. A potential field source surface extrapolation

[6] We do not distinguish here between sympathetic flares and sympathetic CMEs, since both are part of the same eruption process.

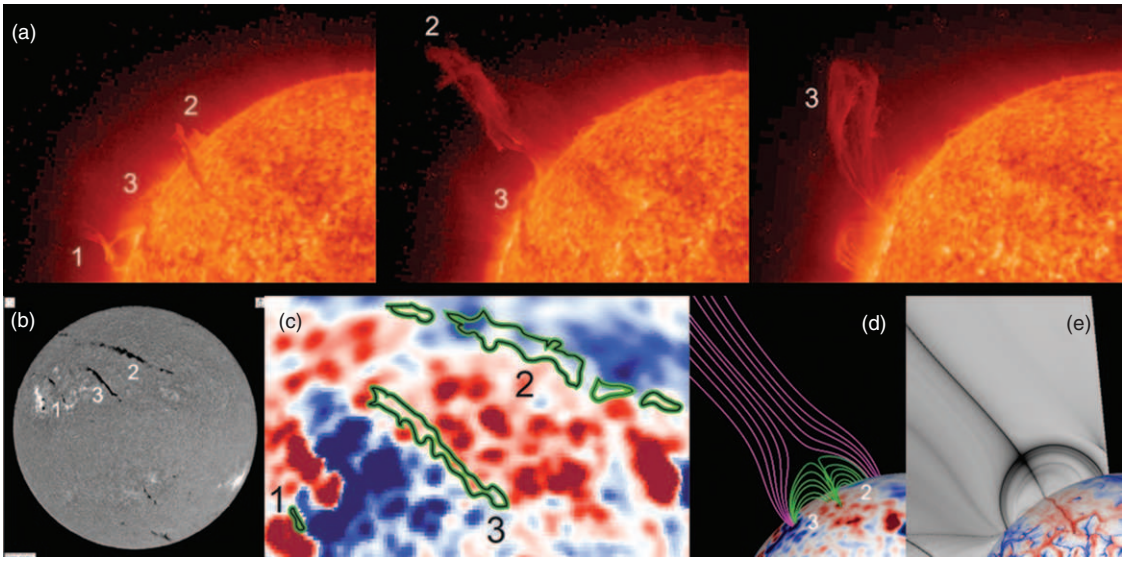

Figure 1. (a) *STEREO-Ahead*/EUVI 304 Å observations of three subsequent prominence eruptions (marked by their order of eruption) on 2010 August 1, shown at 02:56, 09:16, and 22:06 UT (from left to right). (b) Big Bear Observatory Hα observation on 2010 July 30, showing the corresponding pre-eruptive filaments. (c) Filament contours (drawn by eye) overlaid on a synoptic magnetogram for Carrington rotation 2099, with red (blue) showing positive (negative) radial fields. (d) Magnetic field lines from a corresponding PFSS extrapolation, revealing a pseudo-streamer. Green lines outline the lobes in which filaments 2 and 3 were located, pink lines show adjacent coronal holes. (e) Coronal distribution of Q (gray scale) and photospheric distribution of slog Q, where red (blue) outlines positive (negative) magnetic fluxes.

(A color version of this figure is available in the online journal.)

(PFSS; e.g., Schatten et al. 1969) for Carrington rotation 2099 reveals that filaments 2 and 3 were located in the lobes of a PS (Figure 1(d); see also Panasenco & Velli 2010).

Figure 1(e) shows a cut through the coronal distribution of the squashing factor Q (Titov et al. 2002) above filaments 2 and 3. The dark lines of high Q outline structural features and exhibit here a shape characteristic for a PS (compare with Figure 3(b) below). The photospheric distribution shows slog Q (Titov et al. 2011), depicting the footprints of (quasi-) separatrix surfaces. The structural skeleton of a PS consists of two separatrix surfaces, one vertical and one dome-like, which are both surrounded by a thin QSL (Masson et al. 2009) and intersect at a separator (Titov et al. 2011). It has been demonstrated that current sheet formation and reconnection occur preferably at such separators (e.g., Baum & Bratenahl 1980; Lau & Finn 1990).

The presence of the PS above filaments 2 and 3 suggests that the CME associated with filament eruption 1 may have triggered the subsequent eruptions by destabilizing the PS, presumably by inducing reconnection at its separator. We now describe an MHD simulation that enabled us to test this scenario using an idealized model.

3. NUMERICAL SIMULATION

The basic simulation setup is as in Török et al. (2011), where two instances of the coronal flux rope model by Titov & Démoulin (1999, hereafter TD) were used to simulate the interaction of two flux ropes in a PS. Here we add a TD configuration on each side of the PS (Figure 2(a)). The new configuration on the left is used to model the CME associated with filament eruption 1, while the new one on the right is merely used to obtain a (line-)symmetric initial configuration, which facilitates the construction of a numerical equilibrium. It does not significantly participate in the dynamic evolution described below. The flux ropes FR1-3 are intended to model filaments 1–3.

We integrate the zero β compressible ideal MHD equations, neglecting thermal pressure and gravity. The equations are normalized by the initial TD torus axis apex height, $R-d$ (see TD), the maximum initial magnetic field strength and Alfvén velocity, $\boldsymbol{B}_{0\max}$ and $v_{a0\max}$, and derived quantities. The Alfvén time is $\tau_a = (R-d)/v_{a0\max}$. We use a nonuniform Cartesian grid of size $[-25, 25] \times [-25, 25] \times [0, 50]$ with resolution $\simeq 0.04$ in the flux rope area. The initial density distribution is $\rho_0(\boldsymbol{x}) = |\boldsymbol{B}_0(\boldsymbol{x})|^{3/2}$, such that $v_a(\boldsymbol{x})$ decreases slowly with distance from the flux concentrations. For further numerical details we refer to Török & Kliem (2003).

The model parameters are chosen such that all flux ropes are initially stable with respect to the helical kink (Török et al. 2004) and torus instabilities (TI; Kliem & Török 2006). The ropes are placed along the y-direction, at $x = \pm 1.5$ and ± 5.5, and have identical parameters ($R = 2.75$, $a = 0.8$, $d = 1.75$, $L = 0.5$, $q = 4.64$; see TD). The signs of the sub-photospheric point charges, $\pm q$, are set according to the signs of the polarities surrounding filaments 1–3 (Figure 1(c)). The half-distance between the charges, L, is such that the TI can be triggered by a relatively weak perturbation (Schrijver et al. 2008). To obtain a numerically stable initial configuration that contains (semi-)open field above the PS lobes, the two charges associated with each flux rope are adjusted to $-0.55\,q/0.65\,q$ (for FR1 and FR4) and to $-0.34\,q/0.24\,q$ (for FR2 and FR3). The twist is chosen to be left-handed for all ropes to account for the observed dextral chirality of filaments 2 and 3 (Panasenco & Velli 2010).

We first relax the system for 85 τ_a and reset the time to zero. Then we trigger the eruption of FR1 by imposing localized converging flows at the bottom plane (as in Török et al. 2011), which slowly drive the polarities surrounding FR1 toward the local inversion line, yielding a quasi-static expansion of the rope's ambient field. The flows are imposed for 25 τ_a (including phases of linear increase (decrease) to a maximum velocity of $0.02\,v_{a0\max}$ (to zero), each lasting 5 τ_a).

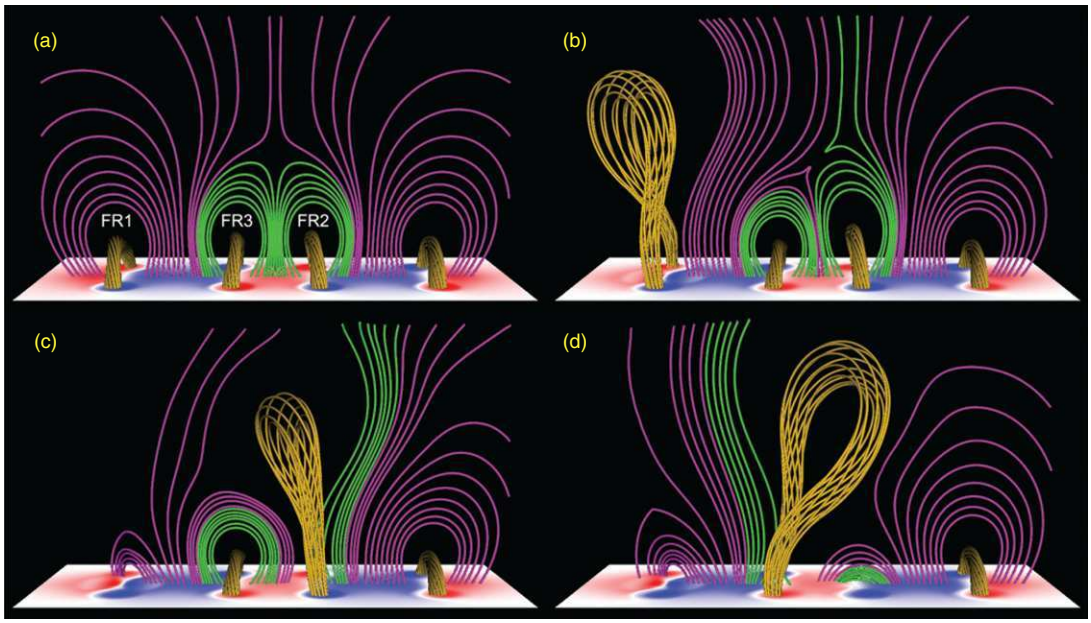

Figure 2. Snapshots from the simulation, showing magnetic field lines with fixed footpoints and the normal component of the magnetic field at the bottom plane, where red (blue) depicts positive (negative) fields. Orange lines belong to the flux ropes, green ones to the initial pseudo-streamer lobes, and pink ones to initially closed or (semi-)open overlying flux. Panel (a) shows the configuration after initial relaxation and panels (b)–(d) show the successive flux rope eruptions and ambient field evolution at $t = 85$, 126, and 181 τ_a, respectively. "Already erupted" flux ropes are omitted for clarity.

(An animation and a color version of this figure are available in the online journal.)

Though we solve the ideal MHD equations, extra diffusion is introduced by numerical differencing (as in every MHD code that models solar magnetic fields). This numerical diffusion is localized in regions where the current density is largest and leads to reconnection of magnetic field lines. Although it is much larger than the diffusion expected on the Sun, experience has shown that simulations produce solutions with physically expected behavior, as long as the numerical diffusion is sufficiently small. We therefore expect that our simulation indicates the true evolution of the system, but that the reconnection rates might differ from those present on the Sun.

4. RESULTS

Figures 2 and 3 summarize the main dynamics and reconnection occurring in the simulation. Figure 3(a) shows the initial configuration and Figures 2(a) and 3(b) show the system after relaxation, during which weak current layers form at the PS separatrix surfaces, but no noticeable reconnection occurs. Note the correspondence between the current layer pattern and the Q-distribution shown in Figure 1(e).

As the converging flows are applied, FR1 starts to rise slowly, in response to the quasi-static expansion of its ambient field. In contrast to other simulations, where such flows have been used to create a flux rope from a sheared arcade (e.g., Amari et al. 2000), here they do not lead to noticeable reconnection. The slow rise lasts until the rope reaches the critical height for TI onset at $t \approx 40\,\tau_a$, after which it rapidly accelerates upward driven by the instability (Török & Kliem 2007; Fan & Gibson 2007; Schrijver et al. 2008; Aulanier et al. 2010). FR1 attains a maximum velocity of $\approx 0.45\,v_{a0\max}$ at $t \approx 90\,\tau_a$ before it slowly decelerates. Figure 2(b) shows the system in the course of this eruption. The rise of the rope is slightly inclined, due to the asymmetry of its ambient field (e.g., Filippov et al. 2001). The rope rotates counterclockwise about its rise direction (as seen from above), due to the conversion of its twist into a writhe (e.g., Green et al. 2007).

The expansion of FR1's ambient field compresses the field between FR1 and the PS, particularly at larger heights where it is weak (see online animations). As a result, a tilted arc-shaped current layer forms around the PS separator (Figures 3(c) and 4). Further compression by the eruption steepens the current densities until reconnection (R1) between the open flux to the left of the PS and the closed flux in the right PS lobe sets in. The lobe flux then starts to open up, while the open flux starts to close down above the left PS lobe (Figures 2(b) and 3(c)). This successively decreases (increases) the magnetic tension above FR2 (FR3), so that FR2 rises slowly, while FR3 is slowly pushed downward. At $t \approx 95\,\tau_a$ FR2 reaches the critical height for TI onset and erupts, attaining a maximum velocity of $\approx 0.60\,v_{a0\max}$ at $t \approx 120\,\tau_a$. Figure 2(c) shows that FR2 also rises non-radially, but rotates less than FR1. The apparently smaller rotation of FR2 is due to the faster decay of its overlying field with height, which leads to a distribution of the total rotation over a larger height range than for FR1 (Török et al. 2010). By the time shown, FR1 has fully erupted, an elongated vertical current layer has formed in its wake (Figure 3(d)), and reconnection therein has produced cusp-shaped field lines below it. As FR2 erupts, it rapidly pushes the arc-shaped current layer to large heights (Figure 3(d)). While R1 still commences for some time, it does not anymore play a significant role in the following evolution.

A vertical current layer also forms below FR2. The subsequent reconnection (R2) initially involves the very same flux systems that took part in R1. The flux previously closed down by R1 opens up again, and the flux previously opened up by R1—and by the expansion of FR2—closes down to form cusp-shaped field lines below the current layer (Figure 3(e)). After these fluxes are exhausted, R2 continues, now involving the left PS lobe and the open flux to the right of the PS. While the former opens up, the latter closes down as part of the growing cusp (Figure 3(f)). Thus, R2 continuously removes closed flux above FR3. As before, this progressive weakening of magnetic tension leads to a slow rise of the rope, followed by its erup-

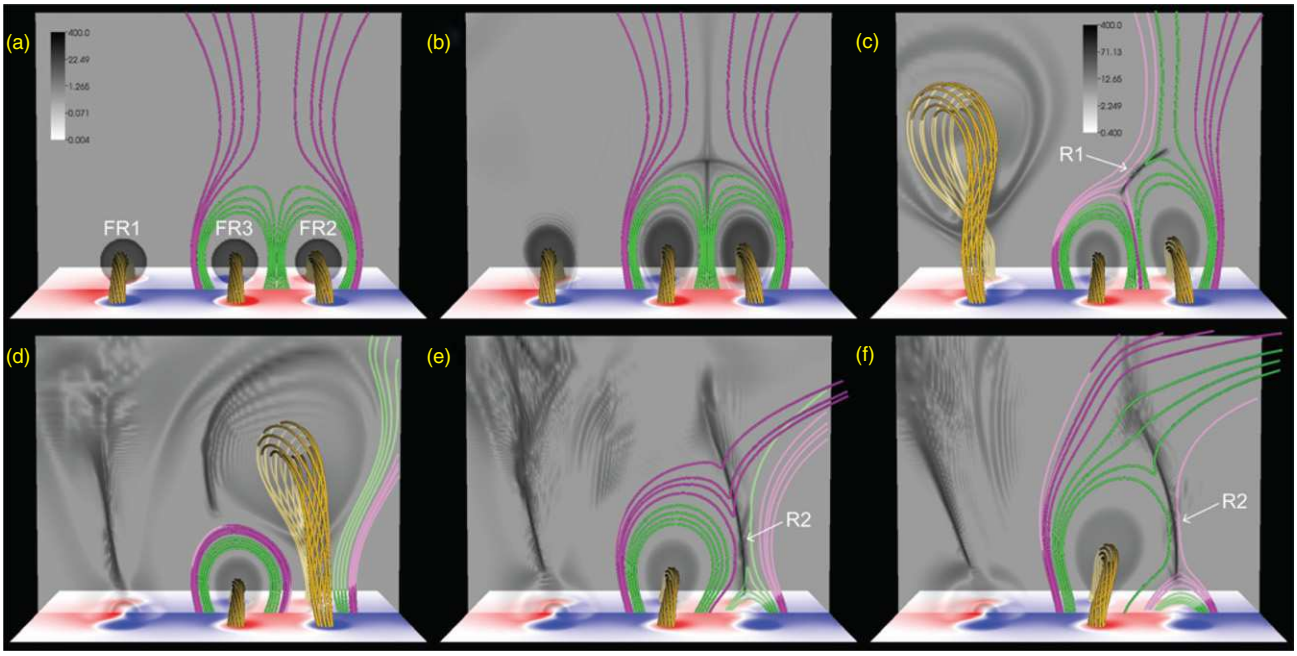

Figure 3. Illustration of the two reconnection phases that trigger the successive flux rope eruptions in the pseudo-streamer. Field lines are colored the same as in Figure 2. The transparent inverted gray scale in the central plane, $\{y = 0\}$, shows the logarithmic distribution of $|\mathbf{j}|/|\mathbf{B}|$, where $\mathbf{j}$ is the electric current density, outlining flux rope currents and thin current layers. Fainter field line segments are located behind the transparent layer. Panel (a) shows the initial configuration, panel (b) the system after relaxation, and panels (c)–(f) show the dynamic evolution, at $t = 85, 126, 142$, and $158\,\tau_a$, respectively. Panels (a) and (b) and (c)–(f) use a different scaling of $|\mathbf{j}|/|\mathbf{B}|$, respectively. Panel (c) shows reconnection R1, which triggers the eruption of FR2, and panels (e) and (f) show reconnection R2, which triggers the eruption of FR3. Panel (d) shows a state between the two reconnection phases.

(An animation and a color version of this figure are available in the online journal.)

tion (Figures 3(f) and 2(d)). The rapid acceleration of FR3 by the TI starts at $t \approx 138\,\tau_a$, yielding a maximum velocity of $\approx 0.35\,v_{a0\max}$ at $t \approx 175\,\tau_a$. The rope shows a significant rotation and an inclined rise which is now mainly directed toward the positive x-direction.

5. DISCUSSION

The eruptions of FR2 and FR3 are initiated by the removal of a sufficient amount of stabilizing flux above the flux ropes via reconnection. R1 is similar to quadrupolar "breakthrough" or "breakout" reconnection (Syrovatskii 1982; Antiochos et al. 1999). Here it is driven by a nearby CME rather than by an expanding arcade and, in contrast to the breakout model, a flux rope is present prior to eruption. R2, on the other hand, corresponds to standard flare reconnection in the wake of a CME. Here it removes flux from the adjacent PS lobe, thereby triggering the eruption of FR3. A similar mechanism for the initiation of a second eruption in a PS was suggested by Cheng et al. (2005), who, however, attributed it to reconnection inflows rather than to flux removal. We emphasize that R1 and R2 merely *trigger* the eruptions, which are *driven* by the TI and supported by the associated flare reconnection (e.g., Vršnak 2008). Thus, in the system studied here, both PS eruptions require the presence of a pre-eruptive flux rope. We further note that the reconnections do not have to commence for the whole time period until the TI sets in. It is sufficient if they remove enough flux for the subsequently slowly rising flux ropes to reach the critical height for TI onset.

R1 is driven by a perturbation of limited duration—the lateral expansion of a nearby CME—and is slow since it involves only weak fields, around a separator at a significant height in the corona. Therefore, its success in triggering an eruption depends on parameters like the distance of the CME from the PS and the amount of pre-eruptive flux within the PS lobes. Indeed, if we sufficiently increase these parameters in the simulation we find that R1 still commences, but does not last long enough to trigger an eruption. In contrast, R2 is driven by the rise of FR2 and involves strong fields. It is therefore faster and more efficient, which supports the finding by Panasenco & Velli (2010) that an eruption in one lobe of a PS is often followed by an eruption in the neighboring lobe.

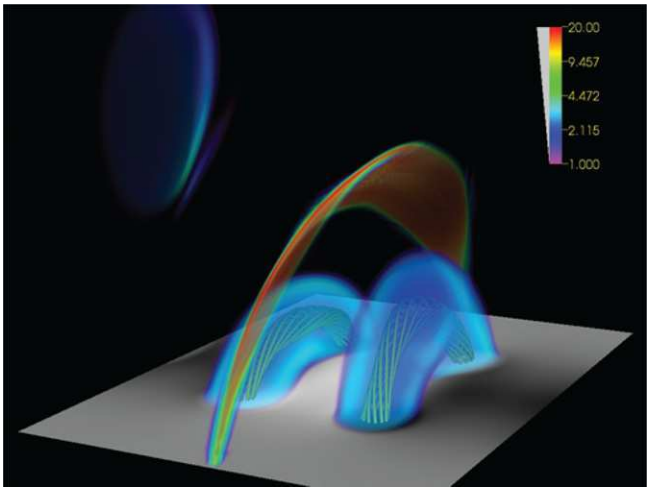

Figure 4. Volume rendering of $|\mathbf{j}|/|\mathbf{B}|$ in the pseudo-streamer area at the same time as in Figures 2(b) and 3(c), outlining the tilted arc-shaped current layer that forms around the separator.

(A color version of this figure is available in the online journal.)

Figure 2 shows that the simulation correctly reproduces the order of the eruptions shown in Figure 1(a) and yields a good match of their inclinations and rotations. Assuming that the first eruption indeed triggered the subsequent ones, it is surprising

that the filament located further away from it went off first. While filament 2 may simply have been closer to its stability limit than filament 3 (as indicated by its larger height; see Figure 1(a)), the simulation provides an alternative explanation: the perturbation of the separator yields an orientation of the current layer that leads to a removal of closed flux only in the right PS lobe (Figure 3(c)), thus enforcing the eruption of FR2. Hence, although we could not find observational signatures of R1 (presumably because the involved fields were too weak), the observed eruption sequence supports its occurrence. The time intervals between the simulated eruptions exhibit a ratio different to the observed ones. Matching the observed ratio requires a search for the appropriate model parameters and a more realistic modeling of reconnection, which are beyond the scope of this work.

FR2 reaches a velocity about 35% larger than that of FR1, which is in line with Liu (2007) and Fainshtein & Ivanov (2010), who found that CMEs associated with PSs are, on average, faster than those associated with helmet streamers. Liu (2007) suggested that this difference is due to the typically smaller amount of closed flux the former have to overcome. Indeed, FR1 has to pass through flux that is closed at all heights above it, while FR2 faces much less closed flux, a significant fraction of which is, moreover, removed by R1. FR3 remains significantly slower than FR2, most likely because it encounters more closed flux at eruption onset, and only partially opened flux later on (Figures 3(e) and (f)).

6. CONCLUSIONS

We present an MHD simulation of two successive flux rope eruptions in a PS, and we demonstrate how they can be triggered by a preceding nearby eruption. The simulation suggests a mechanism for twin filament eruptions and provides a scenario for a subset of the sympathetic eruptions on 2010 August 1. More realistic initial configurations and a more sophisticated treatment of reconnection are needed for a quantitative comparison with observations.

Our results support the conjecture that the trigger mechanisms of sympathetic eruptions can be related to the structural properties of the large-scale coronal field. However, while structural features are present in our model configuration, they do not connect the source region of the first eruption with the source regions of the subsequent ones. Moreover, the mere presence of such features in a source region is not a sufficient criterion for the occurrence of a sympathetic event, even if reconnection at structural features is triggered by a distant eruption. The conditions in the source region must be such that the resulting perturbation forces the region to cross the stability boundary.

The two trigger mechanisms presented here are independent and applicable also to other magnetic configurations. Triggering a sympathetic eruption by R1 requires the presence of a separator (or null point) above closed flux that stabilizes a pre-eruptive flux rope, which can be realized, in the simplest case, in a so-called fan-spine configuration (e.g., Antiochos 1998; Pariat et al. 2009; Török et al. 2009). Triggering a sympathetic eruption by R2 requires the presence of an adjacent closed flux system overlying a flux rope, which can exist, for example, in quadrupolar configurations.

We thank P. Démoulin, B. Kliem, and K. Schrijver for stimulating discussions. The contribution of T.T, V.S.T., Z.M., and J.A.L. was supported by NASA's HTP, LWS, and SR&T programs, CISM (an NSF Science and Technology Center), and a contract from Lockheed-Martin to Predictive Science, Inc. O.P. was supported by NASA grant NNX09AG27G, G.D.T. by NASA/SHP grant NNH09AK02I, and K.K.R. by contract SP02H1701R from Lockheed-Martin to SAO. M.V's. contribution was carried out at JPL (Caltech) under a contract with NASA. Computational resources were provided by NSF TACC in Austin and by NASA NAS at the Ames Research Center. This work was partially supported by the International Space Science Institute via International Team 174 on Solar Prominence Formation and Equilibrium.

REFERENCES

Amari, T., Luciani, J. F., Mikic, Z., & Linker, J. 2000, ApJ, 529, L49
Antiochos, S. K. 1998, ApJ, 502, L181
Antiochos, S. K., DeVore, C. R., & Klimchuk, J. A. 1999, ApJ, 510, 485
Aulanier, G., Török, T., Démoulin, P., & DeLuca, E. E. 2010, ApJ, 708, 314
Baum, P. J., & Bratenahl, A. 1980, Sol. Phys., 67, 245
Biesecker, D. A., & Thompson, B. J. 2000, J. Atmos. Sol.Terr. Phys., 62, 1449
Bumba, V., & Klvana, M. 1993, Ap&SS, 199, 45
Cheng, J., Fang, C., Chen, P., & Ding, M. 2005, Chin. J. Astron. Astrophys., 5, 265
Démoulin, P., Henoux, J. C., Priest, E. R., & Mandrini, C. H. 1996, A&A, 308, 643
Ding, J. Y., Hu, Y. Q., & Wang, J. X. 2006, Sol. Phys., 235, 223
Eselevich, V. G., Fainshtein, V. G., & Rudenko, G. V. 1999, Sol. Phys., 188, 277
Fainshtein, V. G., & Ivanov, E. V. 2010, Sun Geosphere, 5, 28
Fan, Y., & Gibson, S. E. 2007, ApJ, 668, 1232
Filippov, B. P., Gopalswamy, N., & Lozhechkin, A. V. 2001, Sol. Phys., 203, 119
Forbes, T. 2010, in Models of Coronal Mass Ejections and Flares, ed. C. J. Schrijver & G. L. Siscoe (Cambridge: Cambridge Univ. Press), 159
Green, L. M., Kliem, B., Török, T., van Driel-Gesztelyi, L., & Attrill, G. D. R. 2007, Sol. Phys., 246, 365
Howard, R. A., Moses, J. D., Vourlidas, A., et al. 2008, Space Sci. Rev., 136, 67
Hundhausen, A. J. 1972, Coronal Expansion and Solar Wind (Berlin: Springer)
Jiang, Y., Shen, Y., Yi, B., Yang, J., & Wang, J. 2008, ApJ, 677, 699
Kliem, B., & Török, T. 2006, Phys. Rev. Lett., 96, 255002
Lau, Y.-T., & Finn, J. M. 1990, ApJ, 350, 672
Liu, C., Lee, J., Karlický, M., et al. 2009, ApJ, 703, 757
Liu, Y. 2007, ApJ, 654, L171
Masson, S., Pariat, E., Aulanier, G., & Schrijver, C. J. 2009, ApJ, 700, 559
Moon, Y., Choe, G. S., Park, Y. D., et al. 2002, ApJ, 574, 434
Panasenco, O., & Velli, M. M. 2010, AGU Fall Meeting Abstracts, A1663
Pariat, E., Antiochos, S. K., & DeVore, C. R. 2009, ApJ, 691, 61
Priest, E. R., & Forbes, T. G. 1992, J. Geophys. Res., 97, 1521
Ramsey, H. E., & Smith, S. F. 1966, AJ, 71, 197
Riley, P., & Luhmann, J. G. 2011, Sol. Phys., submitted
Schatten, K. H., Wilcox, J. M., & Ness, N. F. 1969, Sol. Phys., 6, 442
Scherrer, P. H., Bogart, R. S., Bush, R. I., et al. 1995, Sol. Phys., 162, 129
Schrijver, C. J., Elmore, C., Kliem, B., Török, T., & Title, A. M. 2008, ApJ, 674, 586
Schrijver, C. J., & Title, A. M. 2011, J. Geophys. Res. (Space Phys.), 116, A04108
Syrovatskii, S. I. 1982, Sol. Phys., 76, 3
Titov, V. S., & Démoulin, P. 1999, A&A, 351, 707
Titov, V. S., Hornig, G., & Démoulin, P. 2002, J. Geophys. Res. (Space Phys.), 107, 1164
Titov, V. S., Mikić, Z., Linker, J. A., Lionello, R., & Antiochos, S. K. 2011, ApJ, 731, 111
Török, T., Aulanier, G., Schmieder, B., Reeves, K. K., & Golub, L. 2009, ApJ, 704, 485
Török, T., Berger, M. A., & Kliem, B. 2010, A&A, 516, A49
Török, T., Chandra, R., Pariat, E., et al. 2011, ApJ, 728, 65
Török, T., & Kliem, B. 2003, A&A, 406, 1043
Török, T., & Kliem, B. 2007, Astron. Nachr., 328, 743
Török, T., Kliem, B., & Titov, V. S. 2004, A&A, 413, L27
Vršnak, B. 2008, Ann. Geophys., 26, 3089
Wang, H., Chae, J., Yurchyshyn, V., et al. 2001, ApJ, 559, 1171
Wang, Y., Sheeley, N. R., Jr., & Rich, N. B. 2007, ApJ, 658, 1340
Wheatland, M. S., & Craig, I. J. D. 2006, Sol. Phys., 238, 73
Zhukov, A. N., & Veselovsky, I. S. 2007, ApJ, 664, L131
Zuccarello, F., Romano, P., Farnik, F., et al. 2009, A&A, 493, 629

Solar Phys (2012) 276:241–259
DOI 10.1007/s11207-011-9868-5

3D Reconstruction of a Rotating Erupting Prominence

W.T. Thompson · B. Kliem · T. Török

Received: 10 June 2011 / Accepted: 15 September 2011 / Published online: 8 November 2011

Abstract A bright prominence associated with a coronal mass ejection (CME) was seen erupting from the Sun on 9 April 2008. This prominence was tracked by both the *Solar Terrestrial Relations Observatory* (STEREO) EUVI and COR1 telescopes, and was seen to rotate about the line of sight as it erupted; therefore, the event has been nicknamed the "Cartwheel CME." The threads of the prominence in the core of the CME quite clearly indicate the structure of a weakly to moderately twisted flux rope throughout the field of view, up to heliocentric heights of 4 solar radii. Although the STEREO separation was 48°, it was possible to match some sharp features in the later part of the eruption as seen in the 304 Å line in EUVI and in the Hα-sensitive bandpass of COR1 by both STEREO *Ahead* and *Behind*. These features could then be traced out in three-dimensional space, and reprojected into a view in which the eruption is directed toward the observer. The reconstructed view shows that the alignment of the prominence to the vertical axis rotates as it rises up to a leading-edge height of ≈ 2.5 solar radii, and then remains approximately constant. The alignment at 2.5 solar radii differs by about 115° from the original filament orientation

Part of this work was done while B. Kliem visited the Space Science Division of the Naval Research Laboratory, Washington, DC 20375, USA.

W.T. Thompson (✉)
Adnet Systems Inc., NASA Goddard Space Flight Center, Code 671, Greenbelt, MD 20771, USA
e-mail: William.T.Thompson@nasa.gov

B. Kliem
Insitut für Physik und Astronomie, Universität Potsdam, Potsdam 14476, Germany

B. Kliem
Mullard Space Science Laboratory, University College London, Holmbury St. Mary, Dorking, Surrey RH5 6NT, UK

T. Török
LESIA, Observatoire de Paris, CNRS, UPMC, Université Paris Diderot, 5 place Jules Janssen, 92190 Meudon, France

Present address:
T. Török
Predictive Science, Inc., 9990 Mesa Rim Road, Ste. 170, San Diego, CA 92121, USA

inferred from Hα and EUV data, and the height profile of the rotation, obtained here for the first time, shows that two thirds of the total rotation are reached within ≈0.5 solar radii above the photosphere. These features are well reproduced by numerical simulations of an unstable moderately twisted flux rope embedded in external flux with a relatively strong shear field component.

Keywords Corona, active · Prominences, active · Coronal mass ejections · Initiation and propagation · Magnetic fields, corona

1. Introduction

The bandpass of the inner coronagraph (COR1) telescopes on the two *Solar Terrestrial Relations Observatory* (STEREO) spacecraft runs from 650 – 670 nm (Howard *et al.*, 2008). This range was selected to include the hydrogen Hα line at 656 nm, so as to be sensitive to erupting prominences associated with coronal mass ejections (CMEs). A particularly bright prominence eruption was observed by both COR1 telescopes on 9 April 2008. Although the relative contributions of Hα emissions and Thomson-scattered light cannot be derived from the COR1 observations alone, it is presumed that Hα is a significant contributor for the extremely bright parts of the prominence early in the eruption. This CME and prominence eruption was also observed by the STEREO *Extreme Ultraviolet Imager* (EUVI) telescopes (Howard *et al.*, 2008) before entering the COR1 field of view, as well as by TRACE at 171 Å (Handy *et al.*, 1999), and by the *Hinode* XRT telescope (Golub *et al.*, 2007) and EIS spectrometer (Culhane *et al.*, 2007). Landi *et al.* (2010) analyze this event, combining *Hinode*/XRT and EIS data, together with *Solar and Heliospheric Observatory* (SOHO)/UVCS/EIT/LASCO and STEREO/EUVI/COR1/COR2 images, to characterize the thermal properties of the ejected plasma, and constrain the heating rate. The post-CME current sheet following this event is analyzed by Savage *et al.* (2010) and Ko *et al.* (2010). Patsourakos and Vourlidas (2011) determine the geometrical parameters of the CME and post-CME current sheet in the field of view of the outer coronagraph (COR2) on STEREO. This event has become known as the "Cartwheel CME" because of the highly visible rotation around the line of sight seen during the initial stages of the eruption. Rotation about the vertical direction can also be observed through triangulation as the prominence material rises through the EUVI and COR1 height ranges. The plane-of-sky motions which give this event its "Cartwheel" name is actually a combination of the rotation about the vertical axis together with a deflection of the prominence in latitude and longitude during the initial rise phase. A rotation around the axis of the prominence, known as "roll effect" (Martin, 2003), may have contributed as well. Further rotation about the vertical direction is indicated by the CME orientation in the COR2 data. This paper presents an exploration of the rotation about the vertical direction in the EUVI and COR1 height ranges, using triangulation from the two STEREO viewpoints. The height profile of the rotation angle for the erupting prominence is obtained, which could not be done prior to the STEREO mission.

The separation of the two STEREO spacecraft at this time was 48°. Co-identification of features in both views is quite difficult with such a large separation. However, it was possible to match some sharp features in the later part of the eruption as seen by EUVI in the He II line at 304 Å. Features were also tracked in white light (with a possible Hα component) as seen by COR1, although not necessarily the same features seen at 304 Å.

The derived height profile of prominence rotation is compared with the orientation of the polarity inversion line of the radial field component (PIL) at various heights, to check

whether the rotation is simply the result of alignment with the PIL. The radial field component is obtained from a potential-field source-surface (PFSS) extrapolation. Additionally, the rotation and rise profiles of the prominence, as well as the STEREO images, are compared with the corresponding data obtained in a series of CME simulations in a companion paper (Kliem, Török, and Thompson, 2011; in the following Paper II), in order to explore a broader range of possible origins of the large total rotation observed. The comparisons suggest that the major part of the rotation was due to the presence of a shear field component of considerable strength in the source region (Isenberg and Forbes, 2007) and that the weak helical kink instability of a moderately twisted flux rope (Török, Kliem, and Titov, 2004) contributed as well. Field line plots of the best-matching case are included here to demonstrate the correspondence with the observed overall shape and helical threads of the rising prominence.

2. Data Analysis

2.1. Source Region

The eruption on 9 April 2008 occurred in the remnants of NOAA active region (AR) 10989, located about 23° behind the west limb as seen from Earth, and had an onset time near 09 UT. The filament had been visible nearly throughout the disk passage of the active region, which was in its decaying stage and spotless after 31 March. The filament erupted twice on 5 April 2008, reforming afterwards. These eruptions were visible on disk to EUVI on STEREO *Ahead*. Both eruptions appeared to propagate inclined from the radial direction toward higher southern latitudes, similar to the eruption on 9 April. The inclination made it difficult to discern rotational motions based on images from only a single viewpoint. However, a stereoscopic reconstruction of the second eruption revealed a considerable rotation of about 90° (Bi *et al.*, 2011). Interestingly, the rotation was in the clockwise direction, opposite to that of the eruption on 9 April.

As with most filaments, it is difficult to discern the magnetic connections at its ends. However, both eruptions on 5 April produced a dimming and endpoint brightenings in the EUV (Wang, Muglach, and Kliem, 2009) near the southeastern end of the filament, which were located in negative polarity, the polarity which dominated the southwestern side of the filament channel, so that the filament was dextral according to the classification of Martin (1998). This is further supported by the right-bearing orientation of the filament barbs (see Figure 1). Dextral filaments are embedded in field of left-handed chirality, as indicated by the typical skew of the overlying arcade of coronal loops (Martin, 1998). If the assumption of flux rope topology holds for the filament, then the filament itself is also threaded by left-handed field. Otherwise, it may have the opposite chirality (see Martin and McAllister, 1997; Ruzmaikin, Martin, and Hu, 2003; Muglach, Wang, and Kliem, 2009). If a filament in dominantly left-handed helical field rotates upon eruption, the direction of rotation is generally found to be in the counter-clockwise direction, as expected from helicity conservation (Rust and LaBonte, 2005; Green *et al.*, 2007).

Note that the dextral chirality of the filament is an exception to the usual hemispheric rule (Martin, Bilimoria, and Tracadas, 1994). However, Pevtsov, Balasubramaniam, and Rogers (2003) show that 16 – 25% of filaments do not follow the hemispheric rule, and that the rule is weaker for filaments in active regions.

On 5 April, the filament was oriented at an inclination of $\approx 24°$ to the east–west direction on the Sun and had a length of ≈ 135 Mm in the image shown in Figure 1 (top). However,

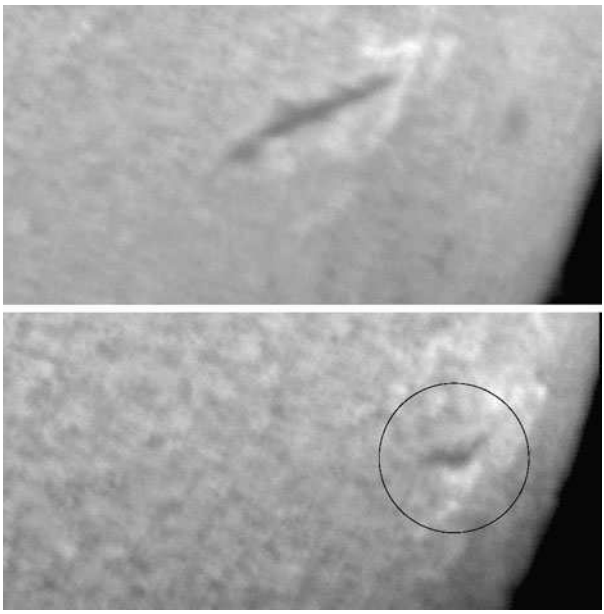

Figure 1 Hα image of the filament as seen on the disk on 5 April 2008, 01:51 UT, before the first eruption on that day, and on 6 April, 02:44 UT (circled), reformed after the two eruptions on 5 April (from the Yunnan Astronomical Observatory in Kunming, China).

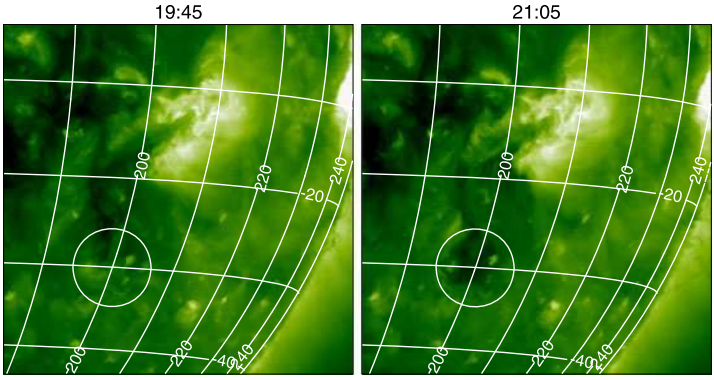

Figure 2 STEREO *Ahead* EUVI 195 Å images of AR 10989 before and after the second filament eruption on 5 April 2008, displaying an area of 640″ on a side. The image on the left at 19:45:30 UT shows the full extent of the filament on the south-eastern end at the onset of the eruption (up to the middle of the circle), and the image on the right at 21:05:30 UT (with the circle plotted at the same position) shows that a dimming has developed at this location. Therefore, the erupting flux should be rooted in this area. Comparison with Figure 1 shows that only the upper branch of the filament is visible in Hα. Overplotted grid lines represent Carrington longitude and latitude.

the dimmings and endpoint brightenings formed in the eruptions later on the same day suggest that the true extent of the flux in the filament channel was larger by about one third, ≈ 175 Mm, see Figure 2.

Due to foreshortening, the Hα images on the following day show the filament, its magnetic connections and barbs far less clearly, but it can be seen that the filament reformed in a similar location (Figure 1, bottom). The better perspective of the EUVI-*Ahead* images indicates that the main body of the reformed filament was nearly straight, oriented at a tilt

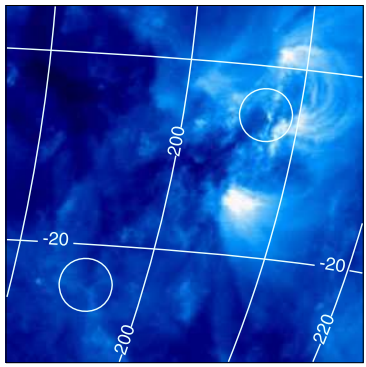

Figure 3 STEREO *Ahead* EUVI 171 Å image of the reformed filament on 6 April 2008, 15:01 UT. The area shown is 320″ on a side. The circles mark the ends of the filament material visible at this wavelength. Their distance is ≈175 Mm. The main body of the filament as seen in this line is oriented at an inclination of ≈26° to the east–west direction on the Sun.

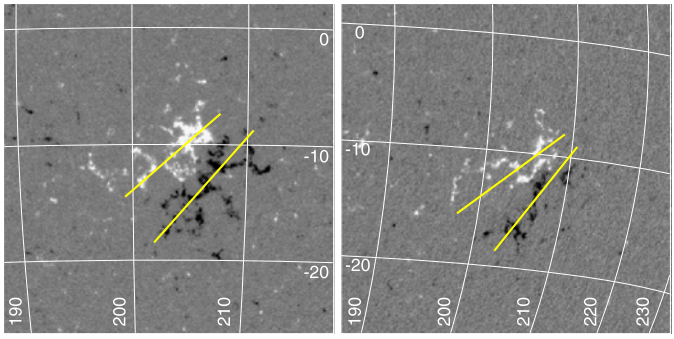

Figure 4 Magnetogram of AR 10989 on 31 March (left) and on 4 April 2008 (right) taken by SOHO/MDI. The overplotted bars indicate rough estimates of the distance between the center of each polarity (in a center-of-gravity sense), which is an important input parameter for the numerical modeling of the event in Paper II.

angle of ≈26° to the east–west direction, and extended across a similar length as on 5 April (Figure 3). This is most clear if the 171 Å and 304 Å images are viewed in animated format. As far as the increasing foreshortening allows a judgment, the filament appeared to keep its orientation and shape through the subsequent days until a new eruption launched the Cartwheel CME.

Since the numerical modeling in Paper II reveals a strong influence of the distance between the polarities in the source region on the rotation of the ejected flux rope, we attempt to estimate this parameter. Figure 4 shows magnetograms of the region from the SOHO *Michelson Doppler Imager* (MDI) on 31 March and 4 April 2008. The overplotted bars run through the middle of each polarity in a one-dimensional center-of-gravity sense, providing an indication of the distance between the main polarities. This value increases from ∼40 Mm to a range of ∼(40–75) Mm over the four-day time span. A range twice as wide may have been characteristic of the configuration after the similar time span to the eruption on 9 April. It appears impossible to estimate a single relevant value. We will adopt a distance of 90 Mm as a base value in most simulations in Paper II, but also study the influence of its variation. This base value lies in the middle of the estimated range, so it is consistent with the fact that much of the rotation occurred in the course of the radial ascent above the southeast edge of the remnant active region, which is characterized by a considerable distance between the polarities (see Section 2.3).

The magnetograms in Figure 4 show an overall displacement of the two polarities in the direction of the PIL. While the negative flux is more or less uniformly distributed along the filament channel, the positive flux is more concentrated near the northern end. This results in a net shear field component pointing along the filament channel in the southeastward direction. Coronal field lines that arch above the filament thus possess a skew corresponding to the upper part of a left-handed helix, in agreement with the implication made above that the filament was dextral.

We have also estimated the height of the prominence from data taken by the EUV Imaging Telescope (EIT) (Delaboudinière *et al.*, 1995) onboard SOHO on 8 April, when the prominence was close to the limb. The material seen at that time in the 304 Å line extended up to a height of $\approx 0.04\ R_{\odot}$ above the photosphere, and the absorbing material seen at 171 and 195 Å extended up to $\approx 0.033\ R_{\odot}$. From EUVI 304 Å data about an hour before the eruption, we estimate the height to lie in the range $\approx 0.05 - 0.06\ R_{\odot}$, so it is clear that the prominence experienced a slow rise before the eruption.

Motions along the prominence could be seen in the 171 Å channel of EUVI-*Ahead* on 9 April from about 08:20 UT onward. The first upward motions of prominence material along the CME path can be discerned by comparing the images at 08:48:30 and 08:51 UT. Landi *et al.* (2010) give a rather conservative estimate of the CME start time, 09:10 UT, but the 171 Å images, taken at 2.5 min cadence, show that most of the prominence body visible to EUVI-*Ahead* was already moving by 08:53:30 UT, the start time quoted in Savage *et al.* (2010). Since the event commenced in the absence of a strong perturbation (no signs of a significant brightening, of a jet, or of perturbations resulting from nearby activity were seen), it must have developed from a small perturbation when the configuration was near the boundary between stable and unstable states. In such cases the initial motion of the unstable flux is expected to behave exponentially, which requires some time to develop to a level that causes visible changes. Rapid changes in the vertical position were first seen between the EUVI-*Ahead* images at 08:48:30 and 08:51 UT. Therefore, the actual start time should lie before 08:51 UT.

A helmet streamer, best seen in the COR2-*Ahead* images, extended above AR 10989 in the plane-of-sky projection. In order to estimate the orientation of the heliospheric current sheet above the streamer, and whether it was magnetically connected with the PIL in the active region, we ran a PFSS extrapolation and a Wang–Sheeley–Arge model for Carrington Rotation 2068 at the Community Coordinated Modeling Center (CCMC), using a source-surface location at 2.5 solar radii for both models. Figure 5 shows the PIL and corresponding field lines originating at the 2.5 $R_{\odot}$ source surface of the PFSS model, which yields a nearly east–west orientation of the heliospheric current sheet at the longitude of radial CME propagation estimated in Section 2.3. The Wang–Sheeley–Arge model gives the same result. It is clearly seen that the field at large heights above the active region is dominated by the large-scale field of the Sun, which points essentially opposite to the shear field component in the active region at small heights.

A similar representation of the radial field component of the PFSS model at several representative heights is given in Figure 6. The PIL above AR 10989 is part of a magnetic structure which is distinct from the PIL at the base of the heliospheric current sheet, and which is seen as a separate ring in the low corona (*e.g.* at 1.15 $R_{\odot}$). With increasing height, the ring-shaped PIL disappears (between 1.2 and 1.3 solar radii), and the PIL associated with the heliospheric current sheet gradually approaches the equator at the estimated longitude of the CME.

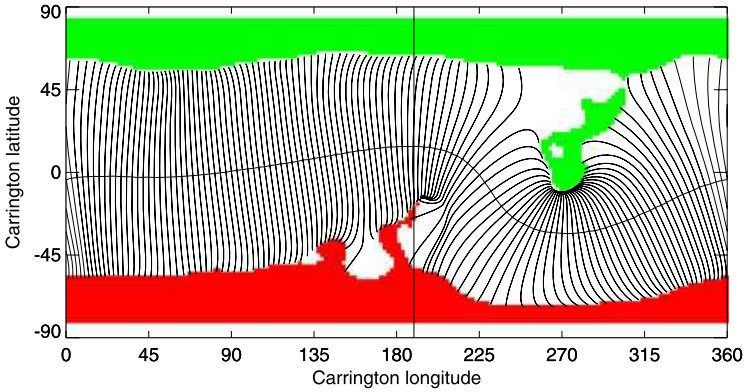

Figure 5 Location of the heliospheric current sheet for Carrington Rotation 2068 from a potential-field source-surface extrapolation. The current sheet runs nearly east–west above the estimated CME direction of propagation as indicated by the vertical bar. The green and red regions represent open field regions of negative and positive polarity, respectively.

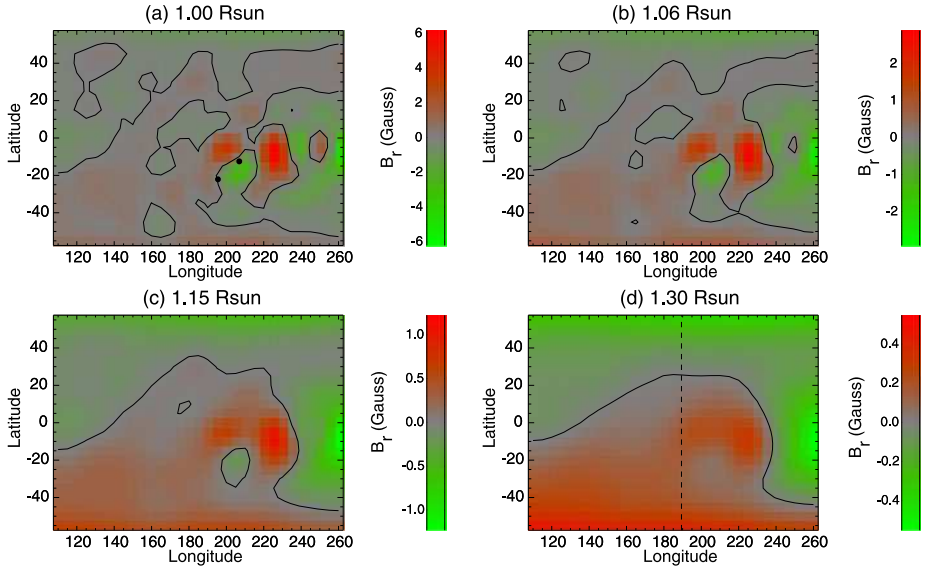

Figure 6 Polarity inversion line of the radial field component in the PFSS model, (a) in the photosphere, (b) at the estimated initial height of the prominence, (c) at the largest height that shows an orientation of the PIL above AR 10989 relatively clearly, and (d) at 1.3 $R_{\odot}$ where the PIL above AR 10989 is completely gone. Dots in panel (a) mark the end points of the prominence shown in Figure 3, and the vertical line in panel (d) marks the estimated longitude of the CME, as in Figure 5.

2.2. 3D Reconstruction

The SolarSoft routine `scc_measure` was used to measure the three-dimensional location of features in the STEREO EUVI and COR1 images. The action of this program is as follows: The user is presented with two side-by-side images, one from each of the two STEREO spacecraft. The images are selected so that they represent the same observation

time, with a slight offset to account for the difference in light travel time from the Sun. The user can zoom in on the region of interest in the two images, and adjust the color table and data range to optimize the appearance of the feature being measured. A point is selected on one image with the cursor. The program calculates the three-dimensional line of sight represented by this point, and then overplots the projection of this line onto the image from the other satellite. This is known as an epipolar line. Since both the EUVI and COR1 optics produce a gnomonic projection on the CCD detector, straight lines in space will always appear as straight lines in the image. The feature selected by the user in the first image must appear along the epipolar line drawn by the program in the second image. The correct location along this line is selected by the user, which leads to another line of sight calculation which intersects the original line of sight. The intersection of these two lines determines the three-dimensional (3D) location of the feature. In this investigation, we use this technique to find the 3D locations of multiple points along prominence threads.

The main difficulty in applying this technique to the prominence eruption is source confusion. On 9 April 2008, the two STEREO spacecraft were separated by 48° along the ecliptic plane. Thus, the appearance seen by STEREO *Ahead* was quite different from that seen by STEREO *Behind*. This made it very difficult to locate features which could be positively identified to be the same in both images. Another goal was to identify features which could be tracked through several frames. (However, no attempt was made to match identifications between EUVI and COR1.) In spite of these difficulties, it was possible to identify several features which could be identified in both views, and which could be tracked through several frames.

2.3. EUVI and COR Measurements

Figures 7 and 8 show the tracked features as seen in the 304 Å channel of EUVI-*Ahead*. The colored lines represent the filamentary features that were measured at each time step. Each line has a different color, and a dot at one end, to better show the relationship with the reprojected graphs along the right side. The different colors do not necessarily represent the same threads at each time step. The He II 304 Å channel was chosen as being most representative of the cool prominence material seen later in a combination of Hα and Thomson-scattered light by COR1. Although the eruption is clearly seen by *Ahead* at 9:06 UT, and by *Behind* at 9:36 UT, source confusion made it impossible to track features earlier than 10:06 UT. Initially, little sense could be made from an examination of these data viewed in 3D (*e.g.*, through an anaglyph representation). However, because the measurements are made in 3D, they can be reprojected to another viewpoint. By selecting the proper viewpoint, it is possible to see aspects of the data that are not evident in the frame in which the data are taken. The plots to the right in Figures 7 and 8 show the same data as in the images, but from a viewpoint at Stonyhurst longitude 98° west (relative to Earth), and 24° south. It is estimated that from this viewpoint, the CME is traveling straight toward the observer.

From this perspective, a certain organization can be perceived. The primary alignment in the 10:06 UT data is vertical, *i.e.* aligned north–south, with the upper prominence threads lying almost directly over the lower threads in the frame of the figure. However, in the later images the primary alignment is distinctly sloped, with the upper threads lying toward the east, and the lower ones toward the west. This is particularly well seen in the image at 10:46 UT in Figure 8, where the data display an overall slope of −50°. As one goes through the time steps, a counter-clockwise rotation can be perceived as one steps from 10:06 to 10:46 UT.

The prominence structure must have rotated through ≈65° from its original orientation to achieve the nearly north–south structure seen at 10:06 UT, followed by an additional ≈50°

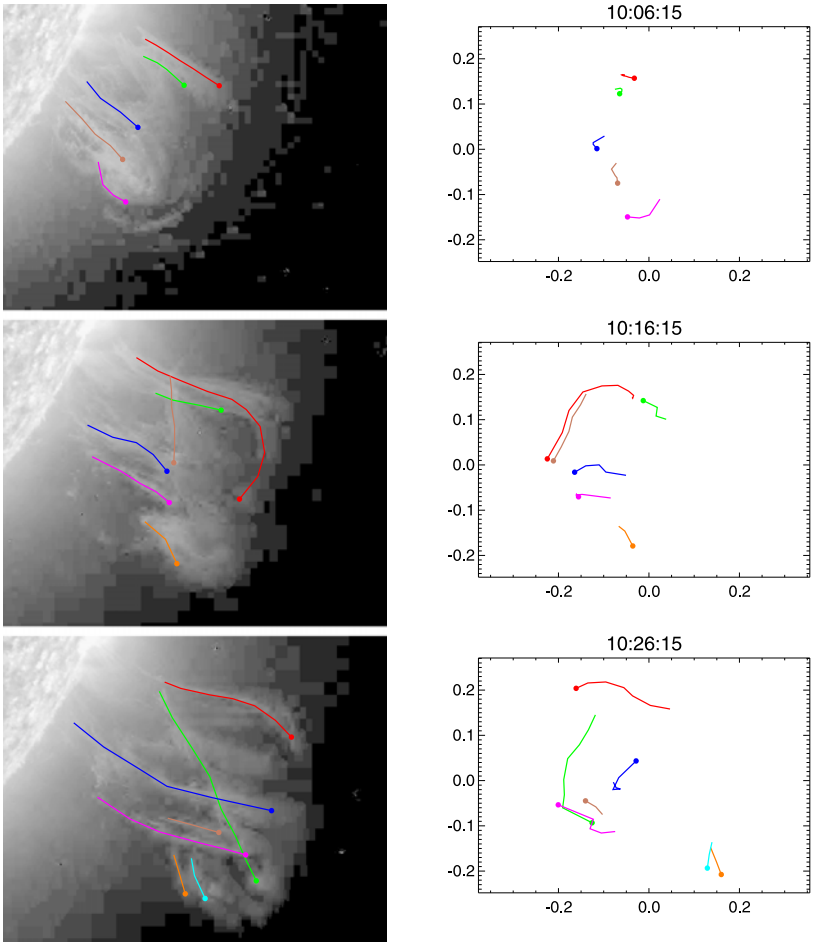

Figure 7 Images and plots of the prominence eruption from 10:06 to 10:26 UT, as seen in the 304 Å channel of the STEREO EUVI telescopes. Subsequent frames are shown in Figure 8. Along the left are shown the EUVI-*Ahead* images with the tracked features overplotted. The lower-right corner of each image is outside the EUVI field of view, causing the threads to appear truncated in height at 10:26 UT and subsequent times. The plots along the right show the same data reprojected to a viewpoint at Stonyhurst longitude 98° west (relative to Earth) and latitude 24° south. Axes are in units of solar radii.

to reach the maximum rotation at 10:46 UT. Thus, the full amount of rotation experienced by the prominence in the EUVI height range was on the order of 115°.

The EUV observations of the early part of the eruption also show a shift of the entire prominence structure southward, from about $-14°$ to $-24°$ latitude. Compared with the earlier Hα observations (Figure 1), the prominence must have also shifted $\sim 15°$ eastward in the early phase of the eruption. These initial motions were followed by radial propagation at the new latitude and longitude, $\approx$98W24S. This is consistent with the analysis of Savage *et al.* (2010) and Patsourakos and Vourlidas (2011). The latter authors fitted a croissant-shaped flux rope model to COR2 images from both STEREO satellites and found that the radial propagation of the CME projects back to a position $11° \pm 5°$ behind the limb, as seen from Earth, and $17° \pm 3°$ south. Savage *et al.* (2010) quote a heliographic position of 113°

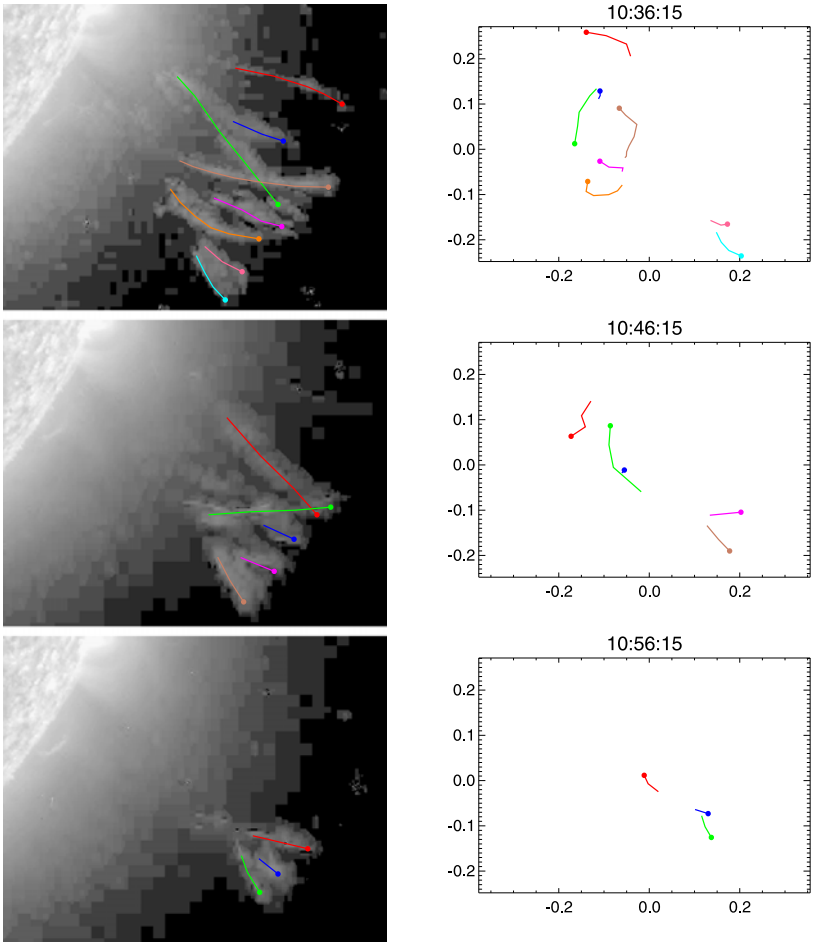

Figure 8 Continuation of Figure 7 for time steps 10:36 to 10:56 UT.

for the associated active region at the time of the eruption, and describe the initial motion of the prominence as being toward the observer. The measurements shown in Figures 7 and 8 were derived from the radial phase of the eruption.

The same analysis performed on EUVI was also performed on the COR1 images. At the location of the eruption, the COR1-*Ahead* occulter edge is at 1.37 solar radii, and the COR1-*Behind* edge is at 1.59 solar radii. The features seen by COR1 are a continuation to higher radial distances of the truncated 304 Å features seen by EUVI. There is a small region of overlap between EUVI and COR1 on both spacecraft, and the observations agree within this region. The COR1 results are shown in Figure 9. The prominence is seen to maintain the orientation seen in the final EUVI images. There is a slight indication of a shift back in the clockwise direction. However, the orientations for the final two time steps at 11:15 and 11:25 UT are based on only parts of the prominence legs, so the apparent reverse rotation may not truly represent the behavior of the loop as a whole.

Patsourakos and Vourlidas (2011) estimated the orientation of the CME flux rope from their croissant model fit at a leading-edge heliocentric distance of about 13 $R_{\odot}$. They found

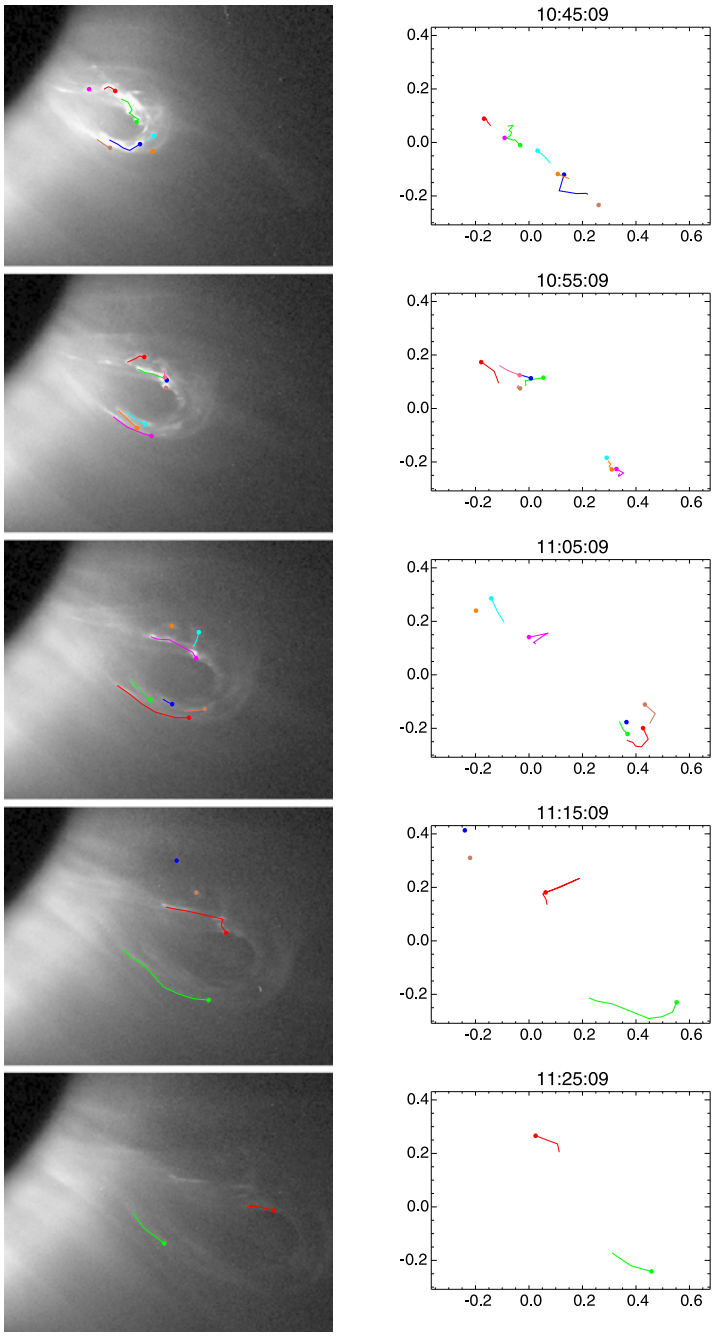

Figure 9 Images and plots of the prominence eruption from 10:45 to 11:25 UT, as seen in the COR1 telescopes. Along the left are shown the COR1-*Ahead* images with the tracked features overplotted. The plots along the right show the same data reprojected to a viewpoint at Stonyhurst longitude 98° west (relative to Earth) and latitude 24° south. Axes are in units of solar radii.

that the flux rope (croissant) axis was inclined to the east–west direction on the Sun by a tilt angle of $-4° \pm 7°$. This indicates a further counter-clockwise rotation to a total value of $150° \pm 7°$ from the original orientation estimated in Section 2.1. (The other possible interpretation of a clockwise rotation by $\approx -145°$ following the counter-clockwise rotation in the EUVI height range appears far less likely.) It should be noted that the croissant model does not include any writhe of its axis, so that the uncertainties may be higher; however, this is not expected to change the result by a large amount. The rotation angle at large heights represents a close alignment of the CME flux rope with the heliospheric current sheet (Figure 5), which corresponds to the suggestion in Yurchyshyn (2008) and Yurchyshyn, Abramenko, and Tripathi (2009).

To our knowledge, the rotation of the prominence by $\approx 115°$ in the corona and by $\approx 150°$ up to 13 $R_\odot$ belongs to the largest ever inferred in this height range. Yurchyshyn, Abramenko, and Tripathi (2009) report one case of rotation by $\approx 143°$ and six cases in the range $80° - 100°$ out of a sample of 101 halo CMEs observed by SOHO/LASCO, *i.e.*, up to a distance of 30 $R_\odot$. The largest rotation found at 1 AU is on the order of 160° (Dasso *et al.*, 2007; Harra *et al.*, 2007).

It is also of interest to note that the COR1 images resolve the basic structure of the dense prominence material in the core of the CME out to a heliocentric distance of four solar radii. The CME core has the structure of a weakly to moderately twisted flux rope: a single flux loop with threads that are systematically but only weakly to moderately inclined to the axis of the loop. These indications of twist prove to be the primary observational finding that sets a preference for a slightly kink-unstable flux rope above a kink-stable flux rope, which match the observed rise and rotation characteristics to a comparable degree in the numerical modeling of the event in Paper II. Only few observations have revealed a flux rope structure for an erupting prominence so clearly in this height range (see, *e.g.*, Plunkett *et al.*, 2000). The images also indicate a nearly self-similar evolution of the flux rope throughout the instrument's field of view of $(1.5 - 4)$ $R_\odot$. The outer coronagraph COR2 imaged the CME core as well but did not resolve the details of its structure.

2.4. Rotation and Rise Profile

Figure 10 summarizes the rotation of the erupting prominence as a function of time from both EUVI and COR1. The values plotted were obtained by averaging the orientations of the individual threads whose 3D positions could be reconstructed. The values obtained at 10:16 and 10:26 UT are considered to be less reliable than the others in the figure, since at these times the threads which could be located in 3D do not appear to be organized in a well defined structure, as, for example, flux rope legs (see the right panels in Figure 7). It was not possible to derive the 3D prominence orientation for times before 10:06 UT due to source confusion. However, the visible appearance of the prominence as seen from STEREO *Ahead* between 9 – 10 UT is consistent with considerable rotation throughout this time period, leading to the conclusion that most of the rotation occurred during the initial phase of the eruption.

We also used `scc_measure` to derive a time–height curve for the prominence eruption. This was done by matching points at the leading edge of the prominence in both images. Since these points in the two images are not guaranteed to represent exactly the same point in 3D space, the results can only be treated as an approximation. However, since the extent of the prominence material is relatively small, the approximation is quite valid. The resulting time–height curve for the top of the prominence is shown in Figure 11. The COR1 values appear to be a bit higher than one would expect from an extrapolation of the EUVI data. That

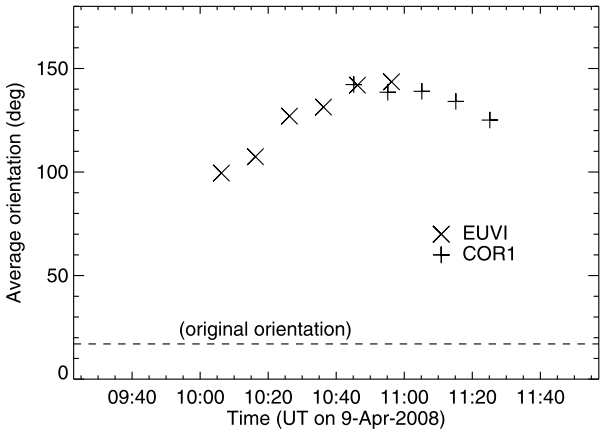

Figure 10 Orientation of the prominence body as a function of time. The dashed line represents the original orientation as estimated from the EUVI-*Ahead* 171 Å image on 6 April in Figure 3. The points at 10:16 and 10:26 UT are considered to be less reliable than the others – see text.

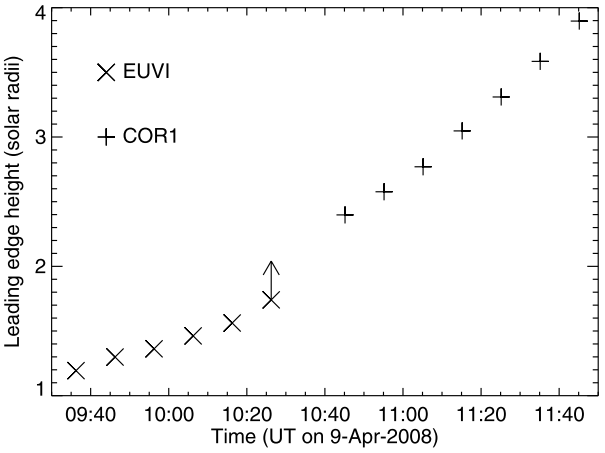

Figure 11 Heliocentric heights of the prominence leading edge *vs.* time. The value for 10:26 UT is shown as a lower limit, since the prominence is right at the edge of the EUVI-*Ahead* field of view at this time.

may represent a difference between the appearance of the prominence at 304 Å versus white light. In addition, the heights derived from EUVI data after 9:56 UT may systematically fall short of the true heights. It is possible that the traceable threads did not extend up to the true top of the structure in these images, since an upward extension of the loop-shaped structure in the image at 9:56 UT had faded by 10:06 UT. The estimated height at 10:26 UT is only a lower limit given by the edge of the EUVI-*Ahead* field of view.

A quadratic fit to the EUVI data gives an initial speed of 67 $\mathrm{km\,s^{-1}}$, accelerating to 173 $\mathrm{km\,s^{-1}}$ as the prominence leaves the EUVI field of view. A quadratic fit to the heights measured by COR1 gives a velocity starting at 206 $\mathrm{km\,s^{-1}}$, and accelerating to 379 $\mathrm{km\,s^{-1}}$ by the end of the COR1 data. There is some evidence from the COR1 quadratic fit that the acceleration strongly decreased when the leading edge of the prominence reached a heliocentric height of 3 solar radii. This is borne out by a linear fit to the COR1 data points above 3 solar radii, which gives a slightly lower velocity of 327 ± 9.2 $\mathrm{km\,s^{-1}}$. The combined EUVI and COR1 data in Figure 11 give the visual impression that much of the acceleration actually occurred up to ≈ 2.5 solar radii. The COR2 data give a speed close to 400 $\mathrm{km\,s^{-1}}$. All of these values refer to estimated positions of the apex point of the visible flux rope structure in the core of the CME.

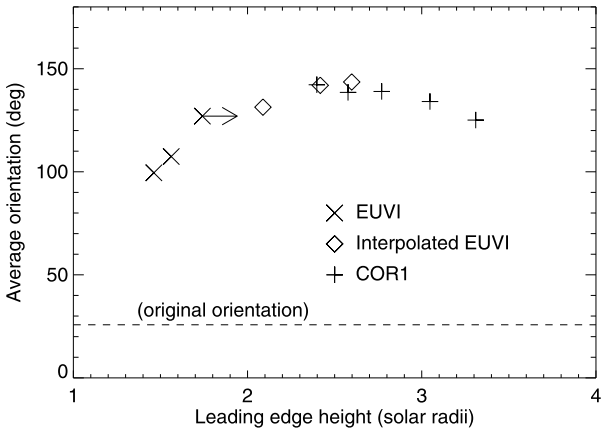

Figure 12 Prominence rotation *vs.* heliocentric height of its leading edge. The diamond symbols represent EUVI and COR1 height data from Figure 11 interpolated to the times of EUVI orientation measurements in Figure 10.

Landi *et al.* (2010) also derive a time–height profile for the leading edge of the prominence material, using a combination of STEREO *Ahead* and SOHO data. Their results are very close to those presented here, with the possible exception of the amount of acceleration. Landi *et al.* quote an acceleration of 59.6 m s^{-2}, while our results are more consistent with a smaller value of 37.9 ± 4.0 m s^{-2} over the time range covered by Figure 11. They also give the projected velocity of the CME leading edge in the plane of the sky of STEREO *Ahead*, which approaches 700 km s^{-1}, still rising, at a heliocentric height of 3 $R_{\odot}$.

Combining the information in Figures 10 and 11, we obtain the rotation of the prominence as a function of its leading-edge height; see Figure 12. (As there are only three time steps in common between the EUVI data sets, we have interpolated the EUVI and COR1 height data from Figure 11 to the times of the EUVI measurements in Figure 10 to better show the trend.) These data emphasize again that much of the rotation is acquired in the height range $h \lesssim R_{\odot}/2$, or ~ 2 initial footpoint separations, above the photosphere.

2.5. Comparison with the Orientation of the PIL

The comparison of the PFSS extrapolation with the orientation of the prominence at large distances from the Sun obtained in Patsourakos and Vourlidas (2011) shows that the prominence has approached a close alignment with the heliospheric current sheet (Section 2.3). An obvious question is whether such alignment could also lead to the rotation in the coronal height range studied here. We will see in Paper II that the rotation of erupting flux ropes and the change of the PIL orientation with height always point in opposite directions if the eruption originates in a simple bipolar region. However, Figure 6 shows that the topology of the field above AR 10989 is more complex. In particular, the field component along the filament channel, which influences the rotation of erupting flux (Isenberg and Forbes, 2007), changes sign with increasing height. In Figure 6, it is clearly seen that the relevant section of the PIL keeps a nearly constant orientation up to about 1.15 $R_{\odot}$, above which it starts to shrink noticeably, disappearing completely by 1.3 $R_{\odot}$. Thus, any rotation in the height range up to about 1.15 $R_{\odot}$ could not be caused by a changing PIL direction. In the height range $\approx (1.15-1.3)$ $R_{\odot}$ the prominence did not see a PIL with a well defined direction. Above 1.3 $R_{\odot}$, the prominence entered the large-scale field structure defined by the polar fields and the heliospheric current sheet. The PIL direction in this range is relatively similar to the direction of the photospheric PIL in the active region and the original orientation of

the prominence. Hence, throughout the height range of strong initial prominence rotation, $\sim(1-1.5)\ R_{\odot}$, the assumption of rotation by alignment with the relevant PIL is inconsistent with the structure of the field. The prominence actually rotated away from the PIL in this height range.

The situation changed when the initial prominence rotation began to level off at a large angle. The subsequent rotation up to the height considered in Patsourakos and Vourlidas (2011) is consistent with an alignment with the PIL in the heliospheric current sheet. From the orientation reached in the initial phase, it was favorable for the prominence to continue the rotation to align with the PIL nearly antiparallel to the original orientation.

These conclusions are robust against the limitations of the PFSS model, which reflects the magnetic structure in and around AR 10989 primarily at the time of central meridian passage, since the region did not show any strong magnetic changes in the time before the eruption on 9 April. The orientation of the PIL in the photosphere, as outlined by the prominence in the EUV, changed by about 20°, much smaller than the observed prominence rotation in the low corona. No signs were seen of any major flux emergence which might have altered the topology of the ring-shaped PIL seen at low coronal heights.

Generally, one expects a dominance of the Lorentz force in driving any rotation of erupting flux at low coronal heights, where the plasma beta is small. As summarized in the following section and detailed in Paper II, the Lorentz force due to both the tension of twisted field lines and the presence of a shear field component in the ambient field causes a rotation away from the PIL, along which the rising flux is originally oriented. As larger heights are reached, the currents and Lorentz forces in the erupting flux decrease, while the influence of the pressure gradient force increases with the increasing plasma beta in the ambient field. The alignment with the heliospheric current sheet then reaches an increasing importance in the dynamics of the eruption. The transition is expected to occur when the plasma beta approaches unity.

A difference between the PIL in AR 10989 and the large-scale PIL in the streamer should be noted. While the PILs are nearly parallel to each other, the field direction across them is reversed (Figure 6). The horizontal field component across the PIL in the streamer exerted a Lorentz force on the prominence legs according to the mechanism proposed in Isenberg and Forbes (2007), because the prominence was directed approximately along this field component (perpendicular to the PIL) after the initial rotation had leveled off, *i.e.*, in the whole COR1 height range. With the current flowing opposite to the axial field of the dextral prominence, the direction of this force on the legs of the prominence is such that the top part rotates in the clockwise direction. This might explain the slight backward rotation indicated by the COR1 data. If this were the dominant effect in the subsequent evolution, the initial rotation would be reversed until the prominence aligns with the heliospheric current sheet in the direction parallel to its original orientation. Since the transition to high-beta conditions occurs in the COR1–COR2 height range, it is unlikely that the Lorentz force could dominate the subsequent rotation. Consequently, antiparallel alignment with the PIL in the heliospheric current sheet due to the pressure gradient force, which drives such alignment on the shortest possible path, independent of the field direction, appears to be the most likely evolution in the COR2 height range.

3. Numerical Modeling

Paper II presents a parametric study of various effects which lead to, or influence, the rotation of ejected flux ropes in low-beta plasma. The initial flux rope twist, the strength of

the external shear field component, and the height profile of the overlying potential field are varied. The latter is related to the distance between the main polarities in the photosphere. Figure 13 shows field line plots from the numerical model that best fits the observations in their entirety (rise and rotation profiles and the STEREO images). In this model, a moderate initial twist of $\Phi = 3.5\pi$ triggers a weak helical kink instability, which lifts the initially force-free, toroidal flux rope into the torus-unstable range of heights and also contributes to the rotation. The ejection is primarily driven by the torus instability (Kliem and Török, 2006), so that the model belongs to the loss-of-equilibrium category (Priest and Forbes, 2002). The major part of the rotation in this run is due to the presence of an external shear field component (pointing along the prominence and polarity inversion line and due to sources outside the flux rope), as first suggested in Isenberg and Forbes (2007). The strength of the shear field at the initial flux rope apex is 2/3 of the external poloidal field which holds the rope in equilibrium. The value is consistent with a very rough estimate of this ratio from the structure of the active region. The ratio of the distances between the main polarities along and across the PIL is about 1/2 in the PFSS field, and the shear should slightly increase with the gradual change of the PIL direction in the time till the eruption.

The overall shapes of the flux rope in the considerable height range included in Figure 13, as well as the inclination of the still weakly twisted field lines to the axis of the rope at the largest height, match the observations reasonably well. (Note that the rope has acquired a large part of its total rotation already at the first time selected; see Figure 10.) Similar agreement is demonstrated in Paper II for the height–rotation and time–height profiles.

A model with subcritical initial twist, $\Phi = 2.5\pi$, which allows only for the development of the torus instability, reproduces the rise profile similarly well, while the match with the rotation profile is somewhat worse. The field lines at the strongly expanded stage of the final COR1 image in Figure 13 are rather straight and hardly show any indication of the observed twist. Moreover, this flux rope requires a considerable initial perturbation to reach the torus-unstable range of heights, which is not supported by the pre-eruption height estimate and the initial dynamics of the prominence described in Section 2 (see Paper II).

4. Summary and Conclusions

The images of the STEREO EUVI and COR1 telescopes resolve the basic structure of the erupting prominence in the core of the "Cartwheel CME" on 9 April 2008 out to heliocentric distances of 4 $R_\odot$. A single flux rope with indications of weak to moderate twist is revealed. The flux rope expands approximately self-similarly in the COR1 field of view of (1.5 – 4) $R_\odot$.

The true path of the prominence could be reconstructed from stereoscopic observations even when the angular separation between the STEREO spacecraft was as much as 48°. The reconstruction reveals that the dextral prominence rotated counter-clockwise by a large angle of $\approx 115°$ up to a heliocentric height of 2.5 $R_\odot$, where the rotation leveled off. A gentle backward rotation by $\approx 15°$ may have followed in the height range up to 3.3 $R_\odot$. Two thirds of the rotation were acquired within 0.5 $R_\odot$ from the photosphere. The coronal height profile of the rotation angle in a CME is thus derived for the first time. To our knowledge, this ranks as one of the largest rotations so far measured in the corona.

Taken jointly with recent results about the orientation of the CME at a heliocentric distance of ≈ 13 $R_\odot$, obtained from fitting a croissant-shaped flux rope model to stereoscopic images from COR2 (Patsourakos and Vourlidas, 2011), a further counter-clockwise rotation by $\approx 35°$ from the value at 2.5 $R_\odot$ is indicated. This aligned the erupted flux closely with

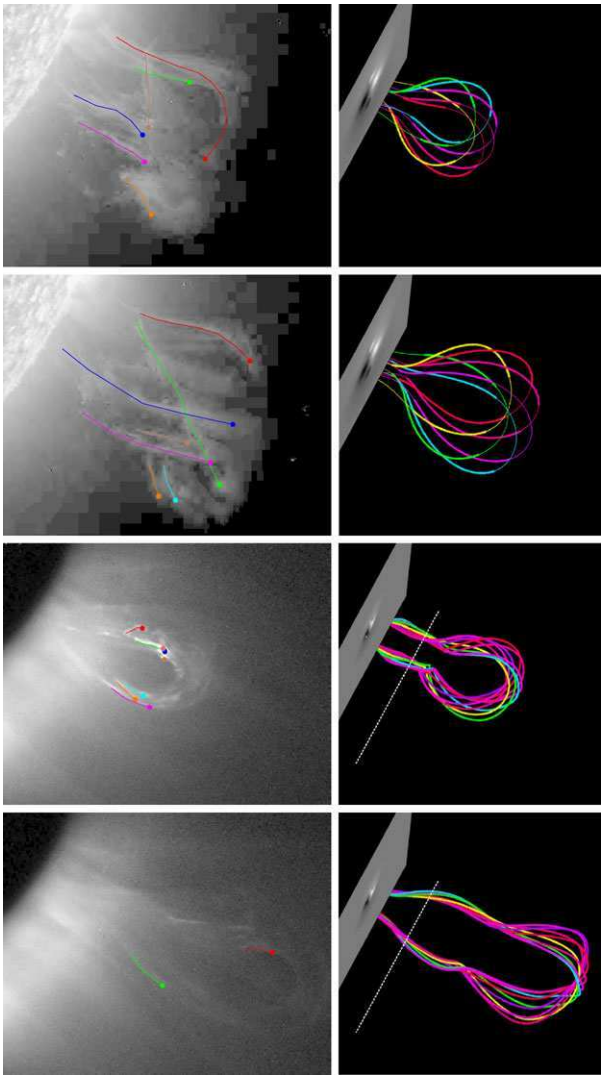

Figure 13 Shape of the erupting flux in the best-matching numerical model – a weakly kink-unstable flux rope of initial twist 3.5π – at various stages of the rise, compared with STEREO *Ahead* images at 10:16, 10:26, 10:55, and 11:25 UT. A set of field lines enclosing the magnetic axis of the simulated flux rope is plotted at the times the rope apex has reached the corresponding heights, $h = 7.3$, 9.6, 20, and 30 h_0 (h_0: initial apex height), which are obtained from the scaling of the footpoint distance, 3.3 h_0, to the value of 175 Mm estimated in Section 2.1. The observed and simulated flux ropes are displayed at the same perspective: the line connecting the footpoints of the rope makes an angle of 26° with the line of sight and the vertical axis in the simulation is tilted away from the observer by 8° (so that the magnetogram, $B_z(x, y, 0, t)$, is seen from the bottom side). The dotted line indicates the edge of the COR1 occulting disk. Since the visible threads in the EUVI images do not outline the complete shape of the flux rope, sections of the field lines in the corresponding simulation snapshots are highlighted for better visual correspondence. For each field line, 200 segments at the top and 150 segments at each bottom end are plotted with reduced line width. The segments are obtained from a numerical integration along the field line with adaptive step size and are all different, resulting in different lengths of the highlighted sections, analogous to the observations.

the heliospheric current sheet above the active region. However, the structure of the field within the first $\sim 0.5\ R_{\odot}$ above the original location of the prominence, obtained from a PFSS extrapolation, precludes alignment with the PIL as mechanism for the initial rotation.

The rotation and rise profiles of the prominence in the EUVI-COR1 height range are reproduced by a numerical model that follows the evolution of an unstable force-free flux rope. A parametric study of flux rope rotation in this model, detailed in Paper II, suggests that the main part of the rotation in this height range was caused by the shear field in the source volume. While the rotation and rise profiles can be modeled nearly equally well by a weakly kink-unstable flux rope of 3.5π initial twist and by a kink-stable flux rope of 2.5π initial twist, the indications of twist in the COR1 images and the absence of a strong initial perturbation in the EUVI-*Ahead* data favor the 3.5π model, suggesting that the helical kink instability did occur and contributed the remaining part of the rotation.

In summary, the large total rotation of the erupting flux rope in the Cartwheel CME is due to a combination of three effects. The internal Lorentz forces associated with the shear field and with the tension of twisted field lines caused a strong rotation in the inner corona. The resulting orientation relative to the heliospheric current sheet was favorable for the subsequent alignment with the sheet in the outer corona and inner solar wind to proceed with the same sense of rotation. Since the heliospheric current sheet had an orientation relatively near the original direction of the erupting flux, a very large final rotation angle was reached.

Acknowledgements We acknowledge the use of data provided by the Global High Resolution Hα Network, and by the SECCHI instruments on the STEREO spacecraft. Magnetic field extrapolations were supplied by the CCMC; special thanks to Lutz Rastaetter and Peter MacNeice for help with the CCMC data. We thank the anonymous referee for a constructive report which led to a deeper consideration of PIL orientation *vs.* height, and S. Patsourakos for information about his fitting of the CME orientation in the COR2 height range. WTT's work was supported by NASA Grant NNG06EB68C. BK's work was supported by the DFG, the STFC, and by NASA through Grant NNX08AG44G. TT's work was partially supported by the European Commission through the SOTERIA Network (EU FP7 Space Science Project No. 218816) and by the NASA HTP and LWS programs.

References

Bi, Y., Jiang, Y.C., Yang, L.H., Zheng, R.S.: 2011, *New Astron.* **16**, 276. doi:10.1016/j.newast.2010.11.009.

Culhane, J.L., Harra, L.K., James, A.M., Al-Janabi, K., Bradley, L.J., Chaudry, R.A., Rees, K., Tandy, J.A., Thomas, P., Whillock, M.C.R., Winter, B., Doschek, G.A., Korendyke, C.M., Brown, C.M., Myers, S., Mariska, J., Seely, J., Lang, J., Kent, B.J., Shaughnessy, B.M., Young, P.R., Simnett, G.M., Castelli, C.M., Mahmoud, S., Mapson-Menard, H., Probyn, B.J., Thomas, R.J., Davila, J., Dere, K., Windt, D., Shea, J., Hagood, R., Moye, R., Hara, H., Watanabe, T., Matsuzaki, K., Kosugi, T., Hansteen, V., Wikstol, Ø.: 2007, *Solar Phys.* **243**, 19. doi:10.1007/s01007-007-0293-1.

Dasso, S., Nakwacki, M.S., Démoulin, P., Mandrini, C.H.: 2007, *Solar Phys.* **244**, 115. doi:10.1007/s11207-007-9034-2.

Delaboudinière, J., Artzner, G.E., Brunaud, J., Gabriel, A.H., Hochedez, J.F., Millier, F., Song, X.Y., Au, B., Dere, K.P., Howard, R.A., Kreplin, R., Michels, D.J., Moses, J.D., Defise, J.M., Jamar, C., Rochus, P., Chauvineau, J.P., Marioge, J.P., Catura, R.C., Lemen, J.R., Shing, L., Stern, R.A., Gurman, J.B., Neupert, W.M., Maucherat, A., Clette, F., Cugnon, P., van Dessel, E.L.: 1995, *Solar Phys.* **162**, 291. doi:10.1007/BF00733432.

Golub, L., Deluca, E., Austin, G., Bookbinder, J., Caldwell, D., Cheimets, P., Cirtain, J., Cosmo, M., Reid, P., Sette, A., Weber, M., Sakao, T., Kano, R., Shibasaki, K., Hara, H., Tsuneta, S., Kumagai, K., Tamura, T., Shimojo, M., McCracken, J., Carpenter, J., Haight, H., Siler, R., Wright, E., Tucker, J., Rutledge, H., Barbera, M., Peres, G., Varisco, S.: 2007, *Solar Phys.* **243**, 63. doi:10.1007/s11207-007-0182-1.

Green, L.M., Kliem, B., Török, T., van Driel-Gesztelyi, L., Attrill, G.D.R.: 2007, *Solar Phys.* **246**, 365. doi:10.1007/s11207-007-9061-z.

Handy, B.N., Acton, L.W., Kankelborg, C.C., Wolfson, C.J., Akin, D.J., Bruner, M.E., Caravalho, R., Catura, R.C., Chevalier, R., Duncan, D.W., Edwards, C.G., Feinstein, C.N., Freeland, S.L., Friedlaender, F.M., Hoffmann, C.H., Hurlburt, N.E., Jurcevich, B.K., Katz, N.L., Kelly, G.A., Lemen, J.R., Levay, M., Lindgren, R.W., Mathur, D.P., Meyer, S.B., Morrison, S.J., Morrison, M.D., Nightingale, R.W., Pope, T.P., Rehse, R.A., Schrijver, C.J., Shine, R.A., Shing, L., Strong, K.T., Tarbell, T.D., Title, A.M., Torgerson, D.D., Golub, L., Bookbinder, J.A., Caldwell, D., Cheimets, P.N., Davis, W.N., Deluca, E.E., McMullen, R.A., Warren, H.P., Amato, D., Fisher, R., Maldonado, H., Parkinson, C.: 1999, *Solar Phys.* **187**, 229. doi:10.1023/A:1005166902804.

Harra, L.K., Crooker, N.U., Mandrini, C.H., van Driel-Gesztelyi, L., Dasso, S., Wang, J., Elliott, H., Attrill, G., Jackson, B.V., Bisi, M.M.: 2007, *Solar Phys.* **244**, 95. doi:10.1007/s11207-007-9002-x.

Howard, R.A., Moses, J.D., Vourlidas, A., Newmark, J.S., Socker, D.G., Plunkett, S.P., Korendyke, C.M., Cook, J.W., Hurley, A., Davila, J.M., Thompson, W.T., St. Cyr, O.C., Mentzell, E., Mehalick, K., Lemen, J.R., Wuelser, J.P., Duncan, D.W., Tarbell, T.D., Wolfson, C.J., Moore, A., Harrison, R.A., Waltham, N.R., Lang, J., Davis, C.J., Eyles, C.J., Mapson-Menard, H., Simnett, G.M., Halain, J.P., Defise, J.M., Mazy, E., Rochus, P., Mercier, R., Ravet, M.F., Delmotte, F., Auchere, F., Delaboudiniere, J.P., Bothmer, V., Deutsch, W., Wang, D., Rich, N., Cooper, S., Stephens, V., Maahs, G., Baugh, R., Mcmullin, D.: 2008, *Space Sci. Rev.* **136**, 67.

Isenberg, P.A., Forbes, T.G.: 2007, *Astrophys. J.* **670**, 1453.

Kliem, B., Török, T.: 2006, *Phys. Rev. Lett.* **96**, 255002.

Kliem, B., Török, T., Thompson, W.T.: 2011, *Solar Phys.* to be submitted (Paper II).

Ko, Y., Raymond, J.C., Vrsnak, B., Vujic, E.: 2010, *Astrophys. J.* **722**, 625. doi:10.1088/0004-637X/722/1/625.

Landi, E., Raymond, J.C., Miralles, M.P., Hara, H.: 2010, *Astrophys. J.* **711**, 75. doi:10.1088/0004-637X/711/1/75.

Martin, S.F.: 1998, *Solar Phys.* **182**, 107. doi:10.1023/A:1005026814076.

Martin, S.F.: 2003, *Adv. Space Res.* **32**, 1883. doi:10.1016/S0273-1177(03)90622-3.

Martin, S.F., McAllister, A.H.: 1997, In: Crooker, N., Joselyn, J.A., Feynman, J. (eds.) *Coronal Mass Ejections: Causes and Consequences*, *Geophys. Monogr. Ser.* **99**, AGU, Washington, 127.

Martin, S.F., Bilimoria, R., Tracadas, P.W.: 1994, In: Rutten, R.J., Schrijver, C.J. (eds.) *Solar Surface Magnetism*, 303.

Muglach, K., Wang, Y., Kliem, B.: 2009, *Astrophys. J.* **703**, 976. doi:10.1088/0004-637X/703/1/976.

Patsourakos, S., Vourlidas, A.: 2011, *Astron. Astrophys.* **525**, A27. doi:10.1051/0004-6361/201015048.

Pevtsov, A.A., Balasubramaniam, K.S., Rogers, J.W.: 2003, *Astrophys. J.* **595**, 500.

Plunkett, S.P., Vourlidas, A., Šimberová, S., Karlický, M., Kotrč, P., Heinzel, P., Kupryakov, Y.A., Guo, W.P., Wu, S.T.: 2000, *Solar Phys.* **194**, 371.

Priest, E.R., Forbes, T.G.: 2002, *Astron. Astrophys. Rev.* **10**, 313. doi:10.1007/s001590100013.

Rust, D.M., LaBonte, B.J.: 2005, *Astrophys. J.* **622**, 69.

Ruzmaikin, A., Martin, S., Hu, Q.: 2003, *J. Geophys. Res.* **108**, 1096. doi:10.1029/2002JA009588.

Savage, S.L., McKenzie, D.E., Reeves, K.K., Forbes, T.G., Longcope, D.W.: 2010, *Astrophys. J.* **722**, 329. doi:10.1088/0004-637X/722/1/329.

Török, T., Kliem, B., Titov, V.S.: 2004, *Astron. Astrophys.* **413**, 27.

Wang, Y., Muglach, K., Kliem, B.: 2009, *Astrophys. J.* **699**, 133. doi:10.1088/0004-637X/699/1/133.

Yurchyshyn, V.: 2008, *Astrophys. J.* **675**, 49. doi:10.1086/533413.

Yurchyshyn, V., Abramenko, V., Tripathi, D.: 2009, *Astrophys. J.* **705**, 426. doi:10.1088/0004-637X/705/1/426.

On the probability of occurrence of extreme space weather events

Pete Riley[1]

Received 16 September 2011; revised 18 November 2011; accepted 22 December 2011; published 23 February 2012.

[1] By virtue of their rarity, extreme space weather events, such as the Carrington event of 1859, are difficult to study, their rates of occurrence are difficult to estimate, and prediction of a specific future event is virtually impossible. Additionally, events may be extreme relative to one parameter but normal relative to others. In this study, we analyze several measures of the severity of space weather events (flare intensity, coronal mass ejection speeds, *Dst*, and >30 MeV proton fluences as inferred from nitrate records) to estimate the probability of occurrence of extreme events. By showing that the frequency of occurrence scales as an inverse power of the severity of the event, and assuming that this relationship holds at higher magnitudes, we are able to estimate the probability that an event larger than some criteria will occur within a certain interval of time in the future. For example, the probability of another Carrington event (based on $Dst < -850$ nT) occurring within the next decade is $\sim$12%. We also identify and address several limitations with this approach. In particular, we assume time stationarity, and thus, the effects of long-term space climate change are not considered. While this technique cannot be used to predict specific events, it may ultimately be useful for probabilistic forecasting.

Citation: Riley, P. (2012), On the probability of occurrence of extreme space weather events, *Space Weather*, *10*, S02012, doi:10.1029/2011SW000734.

1. Introduction

[2] In analogy with terrestrial weather, "space weather" is the state or condition of the space environment surrounding and within the Earth's magnetosphere. And, just as terrestrial events such as tornados and hurricanes can have devastating effects on Earth, severe space weather events can produce a host of consequences that impact society, including the disruption or loss of space-based assets, such as spacecraft [e.g., *Reeves et al.*, 1998], and terrestrial assets, such as electric power transmission networks [e.g., *Bolduc*, 2002]. As our society becomes progressively more dependent on technology, assessing the impact of, and ultimately predicting space weather events, and particularly the most extreme ones, will become ever more crucial. In this study, we seek to answer, or at least address the question: What is the probability of such an extreme event occurring within the next decade, or 100 years?

[3] "Extreme" means that which is far removed from the mean or average. But, while an event might be extreme with regard to one parameter, it might only be average relative to others. Moreover, there are an almost limitless number of parameters that can be used to describe the severity of a solar event. Beginning at the Sun and moving toward the Earth, these include, but are certainly not limited to: (1) soft and hard X-ray flares; (2) coronal mass ejection (CME) speed; (3) shock strength; (4) Solar Energetic Particle (SEP) fluxes, including Solar Proton Events (SPEs); (5) *Dst*, *Kp*, *aa*, and other geomagnetic indices; (6) the equatorward edge of the diffuse or discrete aurora; (7) sudden ionospheric disturbances (as inferred from Solar Flare Effects (SFEs); and (8) nitrate deposition in ice. As we move through these parameters, we shift from causes to consequences, and, from a societal point of view, it is those parameters affecting the near-Earth environment that have the most impact. The connection between different parameters also drops significantly as they become further removed from one another. A massive flare on the backside of the Sun, for example, will not likely leave a record in Earth's ice. Additionally, the relationship between parameters need not be linear. Fast CMEs, for example, may not drive an intense geomagnetic storm unless there is a strong negative interplanetary magnetic field (IMF) associated with it.

[4] The term "extreme" is also time scale-dependent. An event might be extreme on the time scale of a year, or decade, but only moderately severe on the scale of 100 years. Here, we invoke a working definition that "extreme" is something we have not experienced within the space era. That is, an event that we have not yet observed during the time our society has become dependent on technology, and which could result in significant adverse consequences affecting a significant fraction of the

[1]Predictive Science, San Diego, California, USA.

Earth's population. The Carrington event of 1859 [*Carrington*, 1859] is perhaps the largest known example of this.

[5] On the morning of 1 September 1859, as Richard C. Carrington was observing sunspots on the solar disk, a particularly large and complex active region destabilized, launching an extremely fast coronal mass ejection toward Earth. A large solar flare ensued, its optical brightness lasting some 5 min and equaling that of the background Sun. Extrapolating knowledge from less severe events observed during the space age, we can infer some of the likely properties of the so-called "Carrington" event. In soft X-rays, the flare has been estimated to be >X10 [*Cliver and Svalgaard*, 2004]. The ejecta propagated rapidly away from the Sun, generating a fast-mode wave ahead of it, which rapidly steepened into a fast-mode forward shock. The shock, traveling in excess of 2000 km s^{-1} [*Cliver et al.*, 1990] accelerated suprathermal ions in the ambient solar wind to high energies. As these accelerated particles streamed away from the shock, they excited plasma waves that pitch angle scattered the ions, further accelerating the particles. Some of these energetic ions escaped, traveling ahead of the shock. As they streamed through the heliosphere, they amplified the ambient resonant plasma waves, simultaneously undergoing pitch angle scattering by them. Propagating through an ever-weakening magnetic field, the particles were focused and decelerated. The first particles arrived at the Earth within an hour, although the peak intensity of the particle distribution arrived with the shock, some 17.6 h later [*Cliver and Svalgaard*, 2004]. The CME and its associated disturbance rammed into the Earth's magnetosphere, generating one of the largest magnetic storms in recorded history [*Tsurutani et al.*, 2003]. Meanwhile, the energetic particles entered the Earth's magnetospheric environment directly through the polar cap region. The most energetic particles penetrated to the stratosphere and produced nitrogen oxides (NO_x) via impacts with molecular nitrogen and oxygen. The lower-energy particles, on the other hand generated NO_x in the mesosphere and thermosphere. NO_x, acting as a catalyst, destroys ozone in the stratosphere, while HO_x rapidly destroys ozone in the mesosphere, and levels decreased substantially immediately following the arrival of the energetic particles. However, more remarkably, over a period of 4 months, vertical winds enhanced by the polar vortex transported the remaining NO_x from the middle and upper atmosphere into the stratosphere, leading to a second significant depletion in the main ozone layer. Ice core measurements indicated that most of the nitrates were deposited within weeks of production, suggesting that gravitational precipitation (i.e., snow) must have played a key role in its downward transport [*McCracken et al.*, 2001]. While this only partially substantiated description of the Carrington event of 1859 sounds plausible, it is not without controversy. The connection between ice core records and SPEs, for example, is currently under debate [*Wolff et al.*, 2008].

[6] Occurring after important advances in observing techniques and theory had occurred, but before the advent of many more, the 1859 storm holds the record as the largest space weather event in over 400 years [*McCracken et al.*, 2001]. Additionally, since the event occurred only ~150 years ago, it is a constant reminder that a similar event could reoccur any day. But how probable is such an event? With only one such case in the historical records, it cannot be readily predicted from simple "time to event" calculations.

[7] Several recent studies have begun to address the probability of extreme space weather events. *Ruzmaikin et al.* [2011] studied the power law distribution of coronal mass ejection (CME) speeds, which are an integral component of space weather phenomena. They found that, within the range of 700–2000 km s^{-1}, the speeds were distributed according to a power law with exponent, α = −3.4. They argued that the existence of such a self-similar distribution suggests a single physical process for their generation (at least within this speed range). Additionally, they noted that the time intervals between the events are not independent: Fast CMEs are produced in clusters (a result previously inferred from observations by *Feynman* [1997]).

[8] *Barnard et al.* [2011] inferred a rate for major SEP events of P_{SEP} = 5.2 per century, based on nitrate measurements from ice cores that contained 15 major events between 1700 and 1970 [*Shea et al.*, 2006]. Restricting their interval to the space era, however, which has thus far produced only one major event led to a probability of occurrence, P_{SEP} = 2.6 per century. *McCracken and Beer* [2007] also commented on this apparent decline using ground-level event (GLE) data. However, whether this represents an underlying trend, or merely the result of low-number statistics remains to be determined.

[9] A number of techniques can, in principle, be applied for estimating the likelihood of a rare event. These include: event trees, similarity judgments, "time to event," and extrapolation from more frequent events. Event trees rely on breaking up a chain of smaller events that lead to the catastrophic event being studied, with each smaller event being connected to another either by an "and" or "or" gate [*Wang and Roush*, 2000]. The probability of the main event is then determined by a combination of the probabilities of the smaller events. The inquiry into the Challenger accident represents perhaps the best known example of this type of analysis [*Stamatelatos*, 2002]. Unfortunately, for space weather applications we do not know the probabilities of the smaller events or their relationship to one another any better than for the main event. Similarity judgements [e.g., *Bordley*, 2011] extend the probability of known rare events to new situations, such as estimating the probability of an earthquake on the east coast based on more available data from earthquakes on the west coast, say. Again, however, for space weather situations, there are no obvious known events that can be linked to the one under study. "Time to event" techniques use the time between the occurrence of two or more rare events to

estimate the probability of an event happening. Unfortunately, for events that are rarely, if ever observed, estimating this time may not be possible. Even so, such calculations may provide a useful basic check on results obtained from other approaches.

[10] Extrapolation techniques, unlike event trees or similarity judgments, do not rely on knowing any underlying physical processes giving rise to the rare event, or the availability of two or more case studies. Instead, they rely on the assumption that the range over which the events are well observed can be reliably extended to regimes where they are rarely, if ever observed. In this study, we will argue that many space weather parameters exhibit a power law distribution that can be extrapolated to extreme regimes. With this assumption, it is straightforward to estimate probabilities.

[11] Finally, we note that there is a useful distinction worth making between predicting specific rare events and assessing the probability that one will occur within a certain period of time. For the types of space weather phenomena that concern us here, the former task is incredibly more complex and we will focus on probabilistic assessments from hereon.

2. Methodology

[12] Here we outline the basic tools we will employ to compute the probability of occurrence of an extreme space weather event. A set of events, x, is said to follow a power law distribution if the probability of occurrence, $p(x)$, obeys the following relationship:

$$p(x) = Cx^{-\alpha} \tag{1}$$

where the exponent, α, is some fixed value, and C is a constant determined from where the power law intercepts the y axis. Known as Zipf's law or the Pareto distribution, power law distributions, which relate the magnitude of an event to its frequency, appear remarkably frequently throughout all areas of science, including earthquake magnitudes [*Christensen et al.*, 2002] and solar flare size [*Lu and Hamilton*, 1991]. It is worth emphasizing that power laws fall off much less rapidly than the more often encountered Gaussian distribution. Thus, extreme events following a power law tend to occur far more frequently than we might intuitively expect [*Newman*, 2005].

[13] Following *McMorrow* [2009], a more useful quantity for our study, however, is the complementary cumulative distribution function (CCDF), $P(x)$, which is defined as the probability of an event of magnitude equal to or greater than some critical value x_{crit}:

$$P(x \geq x_{crit}) = \int_{x_{crit}}^{\infty} p(x')dx' \tag{2}$$

which, using equation (1) becomes

$$P(x \geq x_{crit}) = \frac{C}{\alpha - 1} x_{crit}^{-\alpha+1} \tag{3}$$

Thus, the CCDF also follows a power law with a reduced exponent ($\alpha - 1$).

[14] There are several advantages in using CCDFs over the original power law distributions. First, they avoid the problem noisy tails. Unless $p(x)$ is computed from bins of data that are logarithmically spaced, the ever-smaller number of events landing in the largest event bins drives the errors associated with those estimates up [*Newman*, 2005]. On the other hand, when the data are summed in a complementary manner as with the CCDF, the noise is minimized. In fact, the data need (and should) not be binned at all; the CCDF at some value x is just the sum of the number of events where $x \geq x_{crit}$. Second, computing the slope of the power law distribution (which is the single most important parameter describing the data) from a least squares fit is prone to systematic biases [*Goldstein et al.*, 2004]. Instead, the maximum likelihood estimate (MLE) is a significantly more accurate method for computing the slope:

$$\alpha - 1 = N \left[\sum_{i=1}^{N} \ln \frac{x_i}{x_{\min}} \right]^{-1}, \tag{4}$$

where x_i are the measured values of x, N is the number of events in the data set, and $x_{\min}$ is some appropriate minimum value of x, below which the power law relationship breaks down [*Newman*, 2005].

[15] A third advantage of the CCDF relates to its application. When considering extreme space weather events, we would usually like to know the probability of occurrence of some event of a particular strength or greater. That is, the consequences of an event larger than a certain threshold, such as the Carrington event, are what concern us from a societal view, rather than the probability of an event say between x and $x + \Delta x$.

[16] Given the probability of an event as large as or larger than x_{crit} it is simple to compute the number of events expected to occur during the period covered by the data set:

$$E(x \geq x_{crit}) = NP(x \geq x_{crit}), \tag{5}$$

where N is the total number of events in the data set. Moreover, again, assuming the events occur independently of one another, we can use the Poisson distribution to infer the probability of one or more events greater than x_{crit} occurring during some time Δt:

$$P(x \geq x_{crit}, t = \Delta t) = 1 - e^{-N\frac{\Delta t}{\tau}P(x \geq x_{crit})}, \tag{6}$$

where τ is the total time span of the data set. Equations (3)–(6) thus give us a robust method for computing the

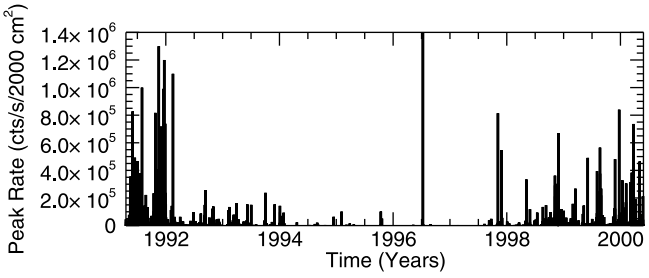

Figure 1. Hard X-ray data from the BATSE spacecraft covering the time period from April 1991 through May 2000. The data were obtained from ftp://umbra.nascom.nasa.gov/pub/batse.

probability that an event of severity exceeding x_{crit} will occur some time within the next Δt years, subject to several assumptions.

[17] The assumption that the data follow a power law, both within the regime where measurements are made and into the region of rare and, for the most part, unseen events must be carefully considered. Typically, the power law relationship must break down at both low- and high-frequency events. In the high-frequency portion of the spectrum, the curve usually flattens often due to the fact that smaller events are less easily measured or identified. At the low-frequency portion of the spectrum, several factors could play a role. First, the statistics of small numbers may lead to the curve deviating from what might otherwise be a straight line. Second, and particularly when the power law distribution falls off more rapidly than higher-frequency rates would suggest, the cutoff may be a real physical limitation. For example, there is undoubtedly a limit to the speed of CMEs, related to the maximum kinetic energy that can be derived from the finite magnetic fields within an active region. Even if arguments could be made to circumvent this, as an absolute limit, CMEs certainly cannot travel faster than the speed of light. Third, the distribution may be composed of distinct parts, each governed by different physical processes, such that the curve becomes either steeper or more shallow than the main portion that is measured. The initiation of coronal mass ejections, for example, may occur through flux cancelation, "break out," the kink instability, flux emergence, or some other mechanism [*Forbes*, 2000], each of which could produce CMEs with different distributions of speeds. Similarly, energetic particles are thought to be produced either through an impulsive mechanism or a gradual one [e.g., *Lin*, 2011].

[18] A second implicit assumption in our analysis is that of time stationarity; both during the time of the measured data, and over the time in the future over which we aim to extrapolate. For the Sun, this is clearly an approximation that requires careful assessment. On the scale of a decade or so, the solar activity cycle modulates many solar parameters [e.g., *Riley et al.*, 2000]. The largest 2% of geomagnetic storms (the so-called "super storms"), for example, tend to occur shortly after the maxima of the decadal-scale solar activity cycles, occurring most often near the equinoxes [*Bell et al.*, 1997]. Thus, the data used to construct the power law should have a duration at least as long as this. By extension, we must also recognize that any predictions made over say the next decade would necessarily be solar cycle-averaged predictions, and the actual probability of an extreme space weather event at some point in the cycle may be different.

[19] A final tool that will be useful for our analysis relies on the average time to the next event to compute a probability of occurrence. For Bernoulli distributions, that is, independent events that either happen or do not, with a constant probability of occurrence, it can be shown that the probability of occurrence is given by

$$P(x) = \frac{1}{1+\tau}, \tag{7}$$

where τ is the average time to the event. Thus, an event that occurs once every 100 years would have a probability, $P = 1/(1 + 100/10) = 0.09$, or 9% of occurring during the next decade.

3. Analysis of the Data Sets

[20] Although there is an almost endless list of candidates, we have chosen four space physics data sets from which to assess the likelihood of an extreme event with respect to those measurements: Peak rates from solar flares; the speeds of CMEs; the strength of geomagnetic storms, as determined from *Dst*; and nitrate spikes in ice cores, arguably capturing large SPEs. These choices encompass a range of "causes" and "consequences" along the chain from the solar surface to the polar ice. And, while their relationship has not been well established, flares and CMEs are clearly related to the same explosive release of magnetic energy in the corona [*Gosling et al.*, 1993]. Similarly, SPEs likely represent a subset of SEPs. Our final motivation for choosing this subset of parameters was to highlight both the power and the limitations in applying this power law extrapolation technique.

3.1. Solar Flares

[21] X-ray fluxes from solar flares represent a natural starting point for analyzing the probability of occurrence of extreme space weather events since it has been firmly established that they follow a power law distribution in peak photon flux over many orders of magnitude [*Lin et al.*, 1984; *Dennis*, 1985; *Lu and Hamilton*, 1991].

[22] For our analysis, we use the hard X-ray measurements from the BATSE instrument on board CGRO (ftp://umbra.nascom.nasa.gov/pub/batse/), which recorded solar flare data continually for almost a full decade. In Figure 1 we show the peak count rates (proportional to flux) of all 7236 BATSE X-ray flares observed from April 1991 through May 2000. We note several points. First, the time series is clearly nonstationary: During the

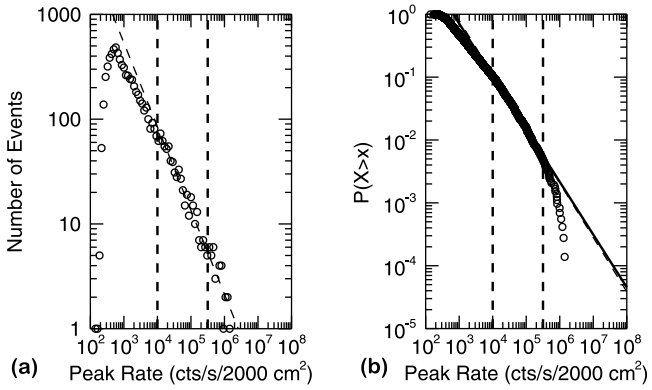

Figure 2. (a) Histogram of number of hard X-ray solar flares as a function of peak size, as measured by the BATSE instrument on board Compton Gamma Ray Observatory (100 bins were equally spaced in peak rate between 10^2 and 10^8 counts^{-}s per 2000 cm^2). (b) Complementary cumulative distribution function (CCDF) for the same events. The vertical dashed lines in both Figures 2a and 2b mark the interval over which the least squares fit (dashed line) to the data was produced. The solid straight line in Figure 2b is a MLE fit to the data above the lower threshold indicated by the left-most vertical dashed line.

approximately solar cycle duration of the data, the peak rate decreases to a minimum in mid/late 1996 and then rises, in phase with sunspot number. Second, the events are strongly biased toward low peak rates, with only a tiny fraction exceeding 10^5 counts/s/2000 cm^2.

[23] Figure 2a shows a histogram of the number of events as a function of peak rate. Several points are worth noting. First, the noise increases as the peak rate increases. These data were binned in intervals separated equally in linear, not logarithmic space, and thus the number of events at high values of peak rate becomes extremely small ($\rightarrow 0$). Although this could have been partially rectified by binning the data in logarithmic space, it serves to highlight one of the advantages of computing the CCDF: The noise does not increase with increasing peak rate since all of the data at a particular peak rate and above are summed to compute that value. Second, although the histogram shows a clear power law distribution over several orders of magnitude, at lower values ($<10^4$ counts/s/2000 cm^2) the slope becomes shallower. Furthermore, below a peak rate of $\sim 5 \times 10^2$ counts/s/2000 cm^2, the number of events drops quickly to zero.

[24] In Figure 2b we show the CCDF, i.e., the probability of an event occurring that exceeds some critical peak rate, as a function of peak rate. The noise is significantly reduced. Here, the change in slope is also apparent, as is the rollover at 10^2 s/2000 cm^2, which appears here as a flattening in the curve. We note that the slope of the event-frequency plot is ~ -1.8, in agreement with previous studies [*Lin et al.*, 1984; *Dennis*, 1985], while the slope (computed using MLE) for the CCDF is -0.84. Theoretically, we would expect the latter to be one less than the former, which, given the errors associated with computing the former, is relatively consistent. More importantly, however, for slopes where $(\alpha - 1) < 1$ (or $\alpha < 2$), the mean value of the peak rate becomes infinite [*Newman*, 2005]. Of course the BATSE data contains a finite number of samples, and the mean peak rate must therefore remain finite. In practical terms, this suggests that mean values computed from a number of subsets within the BATSE data set would not converge.

[25] The slope of the CCDF has two major issues for predicting future extreme events. First, there appears to be either two slopes or a general curve from a more shallow to steeper slope over the well-populated portion of the data (from 10^3 to 3×10^5 counts/s/2000 cm^2). We used the second portion of the distribution to fit a straight line (using both least squares (dashed) and MLE (solid). However, more significantly, the data drop sharply at higher peak rates, suggesting a saturation in flare peak rate at $\sim 2 \times 10^6$ counts/s/2000 cm^2. While the theoretical implications of this are interesting to consider, for our purposes, this proves to be a significant hinderance for estimating the probability of extreme events. Although it is possible that this is the result of errors stemming from low-number statistics (which we will argue is likely the case for another data set later), here, the deviation from the power law line begins while there are still a reasonably large number of events and the profile is smooth.

[26] The next issue we encounter lies in our choice of a critical peak rate from which to compute a probability of occurrence. For the 1859 event, we have only indirect evidence about the size of the solar flare observed by Lord Carrington. In fact, he is credited with the first observation of a solar flare. Unfortunately, Carrington observed it in white light and described it only in qualitative terms [*Carrington*, 1859]. And, although it must have been extremely strong to have been visible to the naked eye, *Cliver and Svalgaard* [2004] estimated that it was only among the top $\sim$100 flares of the last century and a half, undoubtedly exceeding X10.

[27] Ideally, we would like to use measurements of brightening in visible light, which is what Lord Carrington observed [*Carrington*, 1859]. However, so-called "white light" flares are too rare to generate accurate distributions. Hard X-ray emissions, on the other hand, have been regularly observed for decades. This emission, though, is produced by nonthermal electrons in the chromosphere, as opposed to the white light emission, which originates near the photosphere. *Watanabe et al.* [2010] found that the energy in white light emission was equivalent to the energy supplied by all electrons accelerated above 40 keV, suggesting that the electrons are responsible for the white light emission. However, beyond this, translating what Carrington qualitatively described into a robust peak flux rate in X-rays is challenging, if not impossible.

[28] Although we could apply equations (3)–(6) to estimate the probability of a large event occurring, given that

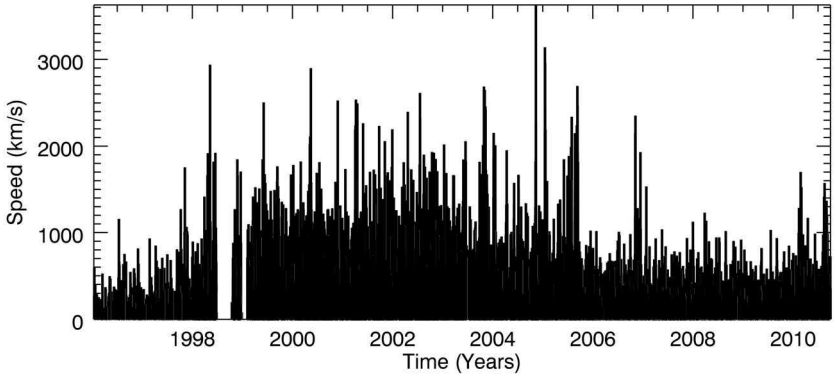

Figure 3. CME speeds derived from the LASCO instrument onboard the SOHO spacecraft from 1996 through 2010. The data were obtained from http://cdaw.gsfc.nasa.gov/CME_list/.

(1) we have no reliable "yardstick" for how big the Carrington event would have been in hard X-ray emission and (2) the power law relationship appears to break down at peak rates exceeding 2×10^6 counts/s/2000 cm^2, any probabilities derived would be dominated by uncertainty.

3.2. Speeds of Coronal Mass Ejections

[29] The strongest geomagnetic storms are produced by fast CMEs, and faster CMEs produce more severe effects [*Gosling et al.*, 1990]. Thus, a next logical stop in the Sun-to-Earth chain is to consider the distribution of CME speeds. For this, we have extracted speeds from the LASCO CME database (http://cdaw.gsfc.nasa.gov/CME_list/), which contains plane-of-sky speeds for 14,735 CMEs observed over the lifetime of the SOHO mission (1996–2010). For this study, we use the quadratic speeds, which are computed by fitting a second-order polynomial fit to the height-time measurements and estimating the speed at the time of the highest measurement possible. In Figure 3 we show CME speeds as a function of time. As with the X-ray flare data, we note the strong clustering at low speeds. Additionally, there is a trend for the number and speed of the fast CMEs to increase from 1996 (solar minimum) to 2002–2004 (2 years after solar maximum) returning to a relative minimum again in 2008–2009 [*Riley et al.*, 2006].

[30] *Cliver et al.* [1990] estimated that the 1859 event took 17.6 h to travel the distance from the Sun to Earth, suggesting an average speed of $\sim 1.5 \times 10^8$ km/(17.6 h $\times$ 3600 s/h) = 2400 km s^{-1}. In comparison, from the LASCO database, two of the fastest CMEs of solar cycle 23 (on 10 April 2001 and 24 September 2001) had travel times of $\sim$32.5 h. Since both of these events had observed plane-of-sky speeds of $\sim$2400 km s^{-1}, to a first approximation, we might estimate an initial speed of $\sim 2400 \times 32.5/17.6 =$ 4500 km s^{-1} for the 1859 CME. Since an initially faster CME will undoubtedly display a stronger declaration profile than this linear extrapolation presupposes, we could reasonably round our guess for the Carrington CME's initial speed to 5,000 km s^{-1}.

[31] In Figures 4a and 4b we show a histogram and CCDF of CME speeds. We note the relatively good power law distribution in speeds in Figure 4a as well as the rollover, marking the median speed of events, at $\sim$350 km s^{-1}. In agreement with the study by *Ruzmaikin et al.* [2011], we find power law spectra both in the histogram and CCDF over a relatively broad range between 700 km s^{-1} and 2,000 km s^{-1}. Using this slope (-3.2), for a critical CME speed, $v_{CME} \sim$ 5,000 km s^{-1}, this would suggest a probability of observing such an event, or greater, over the next decade as 85%. However, the fastest CME observed by LASCO in 15 years of operation was only 3500 km s^{-1}, and thus, we believe this estimate is not credible.

[32] We suggest that the reason for this artificially high probability is that above 2000 km s^{-1} there appears to be a well-defined "knee" in the distribution. Therefore, to address this, in Figure 5, we have replotted the CCDF for the highest speeds and computed a MLE fit to only the distribution above 2000 km s^{-1}. Thus, using the more restricted fit to the tail of the CME speed data, the same extreme event, (i.e., $v_{CME} >$ 5,000 km s^{-1}) would only have

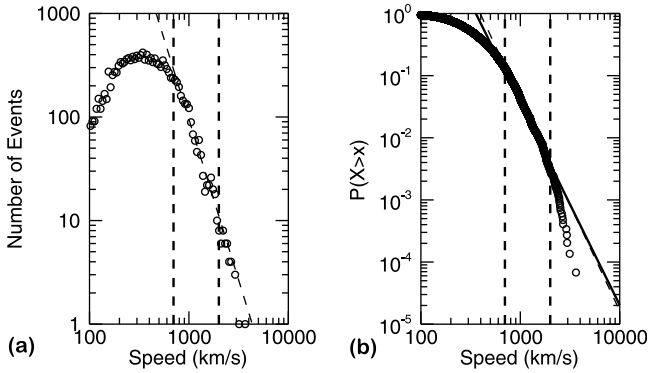

Figure 4. As Figure 2 except that the variable is the number of CMEs as a function of speed. In Figure 4a 100 bins were equally spaced in *Dst* between 10^2 and 10^4 km s^{-1}.

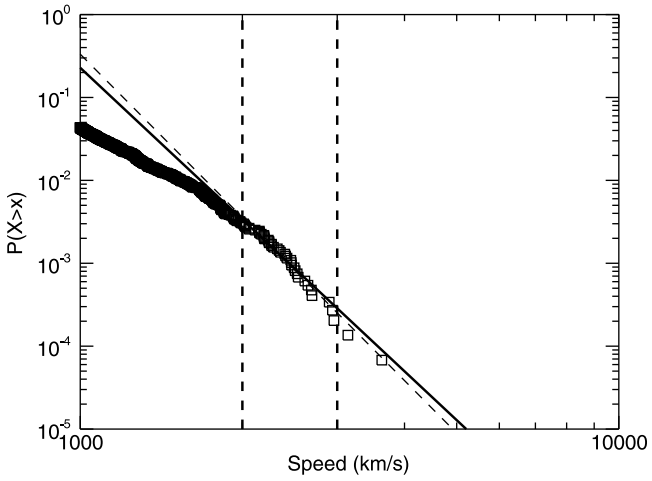

Figure 5. As Figure 4, showing a close-up of the CCDF for CME speeds between 1000 and 3500 km s^{-1}. The vertical dashed lines mark the interval over which the least-squares fit to the data was produced.

a probability of 12%, based on a revised slope of −6.1. (For reference, we note that the least squares fit to these data produced a slope of −6.5, the most significant difference of all four data sets, leading to a probability estimate of 8.5%).

3.3. Geomagnetic Storms

[33] In general terms, a geomagnetic storm is a disturbance in the Earth's magnetosphere driven by changes in the solar wind. Both high-speed streams as well as CMEs can drive such storms, with the latter typically leading to more significant effects. Different components in the solar wind produce different consequences in the magnetosphere. Fast-mode shocks and their following sheath, for example, compress the magnetosphere, while pronounced intervals of southward interplanetary magnetic field can transfer energy from the solar wind to the magnetosphere [*Kivelson and Russell*, 1995].

[34] Although there are a number of indices that capture various aspects of geomagnetic activity, large negative excursions of the "disturbance–storm time" index, or *Dst*, perhaps best describes the main phases of a magnetic storm [*Gonzalez et al.*, 1994]. Moreover, it is arguably the best "societal impact" parameter. Although anecdotal, we remark that while the 13 March 1989 event, with a peak $Dst < -600$ nT, caused the collapse of the Hydro-Québec power grid, and a resulting loss of electrical power to six million people [*Bolduc*, 2002], the so-called "Bastille Day" event of 14 July 2000 which was associated with a peak *Dst* of −300 nT, caused no power failures or other significant terrestrial effects. *Tsubouchi and Omura* [2007] used *Dst* measurements between 1957 and 2001 to estimate the probability of occurrence of intense geomagnetic storms, finding that a storm on the scale of the 1989 event was likely to occur every 60 years or so.

[35] A "storm" can be arbitrarily defined when the main phase falls below some value, typically −50 nT. Additionally, we can classify storms as moderate (-50 nT > *Dst* > -100 nT), intense (-100 nT > *Dst* > -250 nT), and severe (-250 nT > *Dst* > -600 nT). The Carrington event of 1859 was initially estimated to have a peak negative *Dst* of −1760 nT [*Lakhina et al.*, 2005], although this was later revised, and reduced by a factor of two to −850 nT [*Siscoe et al.*, 2006]. Since the beginning of the space age (1958), only one storm has exceeded −600 nT, the 1989 storm for which $Dst \sim -640$ nT [*Gonzalez et al.*, 1994].

[36] In Figure 6 we show a 46 year time series of *Dst*. Several points warrant comment. First, *Dst* is strongly asymmetric: storms reveal themselves as sharp negative excursions lasting a few days at most, and hence, on this scale, a single vertical line. This allows us to relax the need to track the sign of *Dst* since whenever |*Dst*| exceeds, say, 100 nT, it must be a negative quantity. Second, *Dst*'s envelope is clearly modulated on a time scale of ∼11 years, with minima (maxima) in the amplitude coinciding with solar minima (maxima).

[37] To generate an event-based data set, we arbitrarily define a "significant" magnetic storm to be one for which |*Dst*| exceeds 100 nT. In principle, we could define an

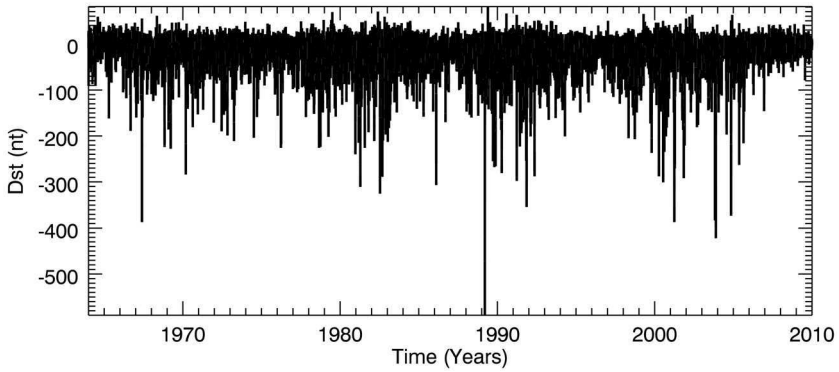

Figure 6. Time series of *Dst* from 1964 through early 2010. The data were obtained from NASA's COHOWEB.

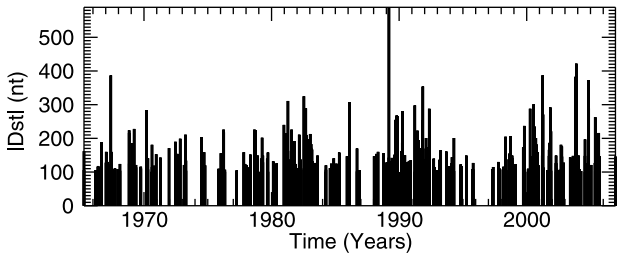

Figure 7. Geomagnetic storms (identified as intervals where $Dst < -100$ nT) as a function of time from 1964 through early 2010.

"event" as the hourly value of *Dst* and compute our probabilities based on that. However, this might impact the results in two negative ways. First, we are not concerned with the slope of the CCDF for small values of *Dst*. Therefore, this portion of the parameter space is not relevant for computing the slope. Second, we are interested in predicting the probability of events, where one event is when *Dst* exceeds a threshold for some period of hours or days. Thus, we would rather identify a contiguous range of data that all exceeds some criteria as a single event, rather than a set of events. In Figure 7, we show the occurrence of these significant storms as a function of time. Again, their density distribution changes in phase with the solar cycle. We note that only one event exceeds 600 nT, and, moreover, only two events exceed 400 nT. Another potentially important trend is the tendency for the strongest storms to become stronger over the last four solar cycle maxima. Whereas the top 5 storms around 1970 lay between 200 and 300 nT, by 2005, the five most intense storms lay between 350 and 450 nT. If such a trend is real it suggests a basic nonstationarity in the data on the same scale as the duration of the data set, and that predictions of future events may underestimate their true probability.

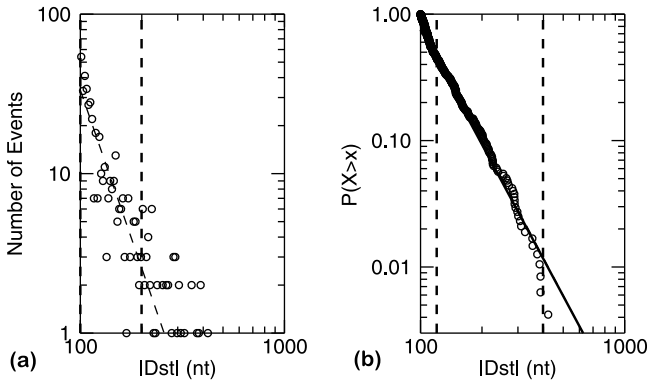

Figure 8. As Figure 2 except that the variable is the number of geomagnetic storms as a function of storm size, as measured by *Dst*. In Figure 8a, 100 bins were equally spaced in *Dst* between $|Dst| = 100$ and $|Dst| = 10^{2.7}$.

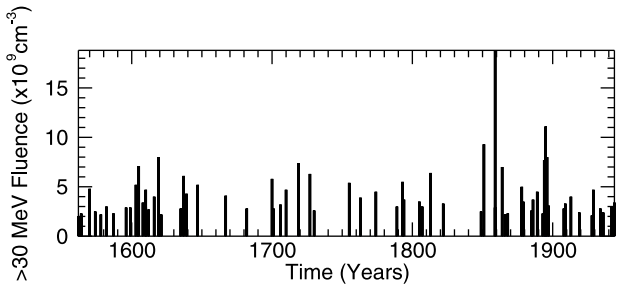

Figure 9. Time series of >30 MeV proton fluences inferred from nitrate records from 1562 through 1944. The data were obtained from *McCracken et al.* [2001].

[38] In Figure 8a, we show a histogram of events as a function of the severity of the storm. The data appear to follow a power law distribution, as indicated by the least squares fit to the data. In Figure 8b the power law relationship of the CCDF is considerably better: Only the last 3 points (which are made up of only 1, 2, and 3 events, respectively) deviate. The slope of the MLE fit is −3.2. Again, we note the clear advantage in using the CCDF as computed here, rather than a histogram approach. The histogram was computed using 100 bins equally spaced in linear *Dst* space, while the CCDF on the left was created by cumulatively summing points from the right. Therefore, the CCDF contains all original 746 geomagnetic storms that were identified in the data set, whereas the histogram contains only 100 points.

[39] Using equation (3), we compute the probability of an event of magnitude equal to, or greater than a threshold value of $Dst_{crit} = -850$ nT to be 0.001. And, using equations (5) and (6) we estimate the probability of such an event occurring over the next decade to be 12%. If we require an event to exceed a threshold of −1700 nT, the probability of it occurring over the next decade reduces to 1.5%.

3.4. Extreme Space Weather Events From Nitrate Records

[40] Finally, in the chain of space weather parameters from the Sun to the Earth, we arrive at space weather records potentially contained within ice cores. The value of these data lies in their long time span, going back more than 400 years; however, they are not without caveats. First, while the nitrate spikes are generally believed by space physicists to be a record of large, historical space weather events [*McCracken et al.*, 2001], ice core chemists are skeptical [*Wolff et al.*, 2008]. They posit that no viable mechanism exists by which Solar Proton Events could be imprinted within the ice, suggesting instead that high concentrations of sea salt provide a simpler and more consistent explanation for the deposition of aerosol nitrates. Second, there are only 70 events spanning the 450 years for which we have data. The largest event in the data set, with a fluence of 18.8×10^9 cm^{-1}, occurred in 1859. That is, the largest event in the last 400 years was the Carrington event. More importantly, however, with such a

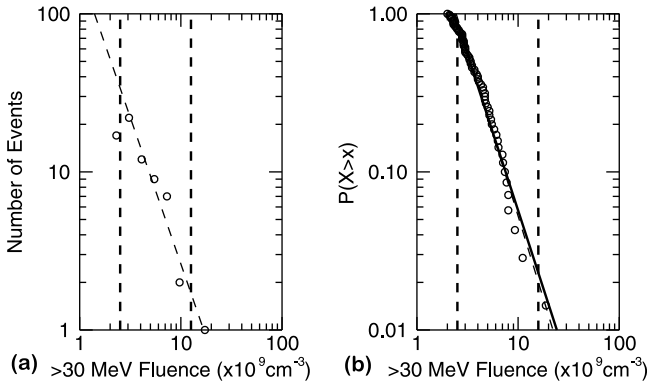

Figure 10. As Figure 2 except that the variable is the number of large proton events as a function of proton fluences (>30 MeV). In Figure 10a, 9 bins were equally spaced between $10^{0.3}$ and $10^{1.3} \times 10^9$ cm^{-3}.

limited number of events, the statistics of the fit and the resulting probability estimates will be more prone to error.

[41] Figure 9 shows all >30 MeV proton events with fluences exceeding 10^9 pr cm^{-2} as a function of time between 1562 and 1944. Although it is not possible to show rigorously, because of the limited sample size, there is no obvious trend in the distribution of event sizes or temporal clustering to suggest that the time series is obviously nontime stationary. Of note is that the Carrington event is substantially larger than the other events in the data set, with the second largest event producing a fluence of only 59% of the value of the 1859 event.

[42] Figure 10a shows a histogram of events versus event size and Figure 10b shows the CCDF as a function of event size. Comparison of the two distributions emphasizes the strength of the CCDF approach. Whereas 70 events contributed to the plot on the right, the plot on the left was made up of only 9 bins, a number large enough to see a trend in the data, but small enough that a sufficient number of points would fall into most of the bins. The MLE fit to the line in Figure 10b gives a slope of -2.0. Using equations (3)–(6) we estimate the probability of an event of, or exceeding 18.8×10^9 cm^{-1} occurring over the next decade to be 3.0%.

4. Summary and Discussion

[43] In this study, we have applied a power law probabilistic analysis to assess the likelihood of a space weather event on the scale of, or larger than the Carrington event of 1859. Based on *Dst* variations over the last 45 years or so, we inferred a probability of ~12% that an event with $|Dst| >$ 850 nT would occur over the next decade. By requiring a more significant threshold of 1700 nT, the estimate reduced to 1.1%. Similar analysis of CME speeds also yielded a probability of 12%. For nitrate records, for which the Carrington event is believed to be contained within, a probability estimate of 3.0% was found. We also investigated hard X-ray flare data, but, because of several significant limitations, we were unable to obtain a reliable estimate.

[44] Although it is tempting to ascribe extra significance to the matching probabilities we obtained from *Dst* and CME speeds (12%), we stress that this may be more of a coincidence than any underlying truth. It is possible, for example, that the CME responsible for the Carrington event was only traveling at 4,500 km s^{-1} and that $Dst \sim -1000$ nT, in which case the probabilities would have become 21% and 7.3%, respectively. Nevertheless, based on our initial estimates for *Dst* and CME speed, a probability of ~12% remains our best estimate.

[45] Our analysis has relied on several important assumptions, the most significant of which is that the data are time stationary. On the shortest time scales of a decade or so, the solar cycle drives important variations in most, if not all of the quantities we studied here. Over longer time scales, there is ample evidence for nonstationarity. *Solanki et al.* [2004], for example, argued that compared to activity over the last 11,000 years, the last 70 years have been a time of exceptional activity. *Steinhilber et al.* [2008] also found that solar activity now is stronger than 85% of the time over the last 9,300 years. Nonstationarity can also be seen 'directly' in ancient proxy sunspot number catalogues [*Wittmann and Xu*, 1987]. If the time series were not stationary in the past, they are no more likely to be stationary in the future. With a consensus beginning to emerge between various reconstructions of the heliospheric field on the time scale of several centuries [*Svalgaard and Cliver*, 2010; *Lockwood and Owens*, 2011], it may be possible to predict the future large-scale behavior of solar activity. *Abreu et al.* [2008], for example, estimated that the current grand maximum is only likely to persist for another 15–36 years. Similarly, *Lockwood et al.* [2009] argued that solar activity rose during the first half of the 20th century, peaking in years 1955 and 1986, and subsequently declined, with the grand maximum ending within the next 20 years or so. *Lockwood et al.* [2009] further estimated that there is a 10% probability that activity on the Sun will decrease producing grand minimum conditions during the next 40 years. Obviously, if such conditions do ensue, probabilistic forecasts based more active solar conditions may be less accurate. However, not necessarily for society's benefit: During periods of very low activity, for example, radiation from galactic cosmic rays (GCRs) will be higher, posing larger risks for passengers and airline crew, as well as avionics. And, while SEP events themselves may decrease, the consequences from the ones that are produced may be more severe [e.g., *Barnard et al.*, 2011].

[46] A related but distinct effect is clustering. CMEs have been shown to occur in groups [*Feynman*, 1997; *Ruzmaikin et al.*, 2011], which, to some degree, violates the assumption of time stationarity. Moreover, from a physical perspective, the clustering of events may lead to interactions between them as one CME overtakes another ahead of it. This may destroy or dampen a previously extreme event, or, conversely, lead to a nonlinear amplification, promoting a large event to an extreme one.

[47] A second important assumption for our analysis is that the power law relationship extends beyond the measurements, that is, that events more extreme than have been observed continue to fall along a straight line in log-log space. We argued that the flare data (Figure 2) deviates significantly from the power law relationship that holds for lower peak rates, and, thus, cannot be reliably extrapolated beyond observed events. In contrast, the remaining quantities could, arguably, be considered to lie on power law lines up to the most severe observed case. Moreover, the solar proton events, which are the only measurements that captured an extreme event (the Carrington event), displayed power law characteristics at all fluences.

[48] Each of the parameters we chose to analyze in this study displayed unique strengths and weaknesses for the purpose of computing a probability estimate of extreme space weather events. The nitrate record, which is the only one that actually purports to have captured the Carrington event is limited to a small number of events, making statistical inferences the most dubious. However, issues have been raised about whether the ice core record is actually measuring events from space [*Wolff et al.*, 2008]. In contrast, the hard X-ray data from CGRO's BATSE instrument are abundant, but the resulting power law distribution is not of a single slope, making extrapolation dubious. CME speeds, as determined from the SOHO/LASCO database, appear to show two distinct power law distributions, joined at a "knee." While this may be hinting at the possibility of two classes of CMEs ("fast" and "very fast"), it is also possible that the fastest events are merely an asymptotic falloff. We currently lack the understanding of CME initiation and acceleration to be able to place robust limits on initial CME speeds. Finally, analysis of *Dst* perhaps yields the best estimate for the prediction of the likelihood of an extreme event. It is global in scope, contains a large number of events, spans four solar cycles, and appears to follow a single power law distribution. However, even here, we must reiterate one of the primary assumptions of this analysis; that the power law can be reliably extrapolated beyond known events. However, here, we also have indirect estimates of *Dst* during the Carrington event that provide at least a qualitative check on our results.

[49] It is also not surprising that the probabilities we have estimated for another Carrington event occurring within the next decade based on *Dst* and nitrate records do not match: In addition to the aforementioned controversy about whether the nitrates records even capture space weather events, they are predictions of different consequences.

[50] Our choice of data sets and the probabilities determined should not be construed as definitive, in any way. The parameters were chosen to illustrate a range of distributions, features, and limitations. Instead, we could have analyzed soft X-ray data from GOES [e.g., *Feldman et al.*, 1997], the Solar Proton Event (SPE) list maintained by NOAA (http://www.swpc.noaa.gov/ftpdir/indices/SPE.txt), or the equatorward edge of the auroral oval [e.g., *Newell and Meng*, 1988]. For each data set, we would have identified similar, but unique artifacts and derived similar, but distinct probabilities.

[51] The choice of the best parameter from which to compute these probabilistic predictions depends on several factors. First, they should be closely related to the effect one is trying to predict. SPEs, for example, would be an appropriate parameter for estimating radiation doses of astronauts, while localized measurements of the horizontal component of the magnetic field might be more suited for ground induced currents (GICs) and their effects on the power grid. Second, the parameter should be distributed according to a power law. Although solar flares are perhaps the best known example of a power law distribution in space physics, we showed that at least the peak rate from BATSE measurements is not ideal. Third, one should not be able to present a credible argument that the power law relationship breaks down before the critical value to be predicted. It may be that the best parameter is not something that is usually studied. For example, it is well known that geomagnetic activity is sensitive to the speed of the CME, but also the magnitude and sense of B_z, i.e., the dawn-dusk electric field across the magnetosphere. Therefore, an alternative, and arguably better parameter that could be studied and predicted would be 'events' where the average solar wind electric field drops below some threshold for some minimum period of time, provided that these 'electric field events' follow a power law distribution.

[52] Risk analysis involves balancing the probability of a particular event occurring with the consequences of that event. While we have focused on the first part of this relationship, others have speculated on the consequences that an event at least as large as the Carrington event could have on society [*Schieb*, 2011]. Unfortunately, the predicted effects are at least as poorly known as the probability of occurrence, thus limiting the ability of decision makers to use these results to guide policy. Nevertheless, it may be worth putting the probabilities computed here into perspective. Consider, for example, the probability that an asteroid (of sufficient size that it would cause substantial damage to a localized region of the globe) will hit the Earth in the next decade. It has been estimated that objects as large as, or larger than 50 m hit the Earth roughly once every thousand years [*Chapman*, 1994]. The Tunguska event of 1908, for example, was about this size, and would have been capable of destroying a large metropolitan area [*Longo*, 2007]. Of course, the average effect of such an event is considerably lower since there is a much larger probability of it hitting an ocean where the death toll could easily be zero. On the other hand, a space weather event will always be global in nature (although its effects would be amplified in certain areas). While global satellite monitoring can now rule out potential impacts in the near future, using equation (7), we can estimate the probability of such an impact over the next decade to be $\sim$1%, which is an order of magnitude smaller than our estimate for a Carrington event based on *Dst* and CME

speed considerations. The two scenarios become comparable from a risk analysis perspective if the consequences of a Carrington event are even one tenth those of a meteor impact. If financial resources are limited, such knowledge could be used to allocate funds more effectively. Moreover, if better mitigation strategies exist for one scenario than another, they could be more aggressively pursued. For example, if major, prolonged power outages, which could, in turn, result in food and water shortages, potentially over many months, are realistic consequences of a Carrington event [*Schieb*, 2011], effort should be expended into building infrastructure that can withstand such an event. In contrast, there appears little that can be done, at least in the near term, to mitigate a meteor impact, beyond effective evacuation measures.

[53] Computing probabilities for extreme space weather events may ultimately be useful in shaping policy decisions. One of the problems with extreme events is that prior to their occurrence, their perceived risk is effectively zero, yet following it, the risk rises to nearly 100%. Thus, it is important to develop objective estimates for these probabilities, which can serve as a starting point for risk analysis, even if the errors associated with them are larger than we might like. Thus, if the results presented here are further substantiated, are there measures that could, or should be enacted to minimize damage from an extreme solar event?

[54] In closing, we reiterate that our primary aim in this study was to introduce a technique for estimating the probability of occurrence of extreme space weather events. Additionally, our analysis has shown that a relatively rich subset of space physics data can be approximated by power law distributions. Our results allowed us to answer a basic question, at least in an approximate way: How likely are such events? The answer of course depends on what you mean by "event" and how severe you define "extreme" to be. Nevertheless, our results overall suggest that the likelihood of another Carrington event occurring within the next decade is ~12%.

[55] **Acknowledgments.** The author gratefully acknowledges the support of NSF's FESD and NASA's SR&T program, under which this work was performed. He would also like to thank both referees for providing valuable suggestions that improved the quality of the manuscript.

References

Abreu, J. A., J. Beer, F. Steinhilber, S. M. Tobias, and N. O. Weiss (2008), For how long will the current grand maximum of solar activity persist?, *Geophys. Res. Lett.*, *35*, L20109, doi:10.1029/2008GL035442.

Barnard, L., M. Lockwood, M. A. Hapgood, M. J. Owens, C. J. Davis, and F. Steinhilber (2011), Predicting space climate change, *Geophys. Res. Lett.*, *38*, L16103, doi:10.1029/2011GL048489.

Bell, J. T., M. S. Gussenhoven, and E. G. Mullen (1997), Super storms, *J. Geophys. Res.*, *102*, 14,189–14,198, doi:10.1029/96JA03759.

Bolduc, L. (2002), GIC observations and studies in the Hydro-Québec power system, *J. Atmos. Sol. Terr. Phys.*, *64*, 1793–1802, doi:10.1016/S1364-6826(02)00128-1.

Bordley, R. F. (2011), Using Bayes' rule to update an event's probabilities based on the outcomes of partially similar events, *Decis. Anal.*, *8*, 117–127, doi:10.1287/deca.1110.0204.

Carrington, R. C. (1859), Description of a singular appearance seen in the Sun on September 1, 1859, *Mon. Not. R. Astron. Soc.*, *20*, 13–15.

Chapman, C. R. (1994), Impacts on the Earth by asteroids and comets: Assessing the hazard, *Nature*, *367*, 33–40, doi:10.1038/367033a0.

Christensen, K., L. Danon, T. Scanlon, and P. Bak (2002), Unified scaling law for earthquakes, *Proc. Natl. Acad. Sci. U. S. A.*, *99*, suppl. 1, 2509–2513.

Cliver, E. W., and L. Svalgaard (2004), The 1859 solar-terrestrial disturbance and the current limits of extreme space weather activity, *Sol. Phys.*, *224*, 407–422, doi:10.1007/s11207-005-4980-z.

Cliver, E. W., J. Feynman, and H. B. Garrett (1990), An estimate of the maximum speed of the solar wind, 1938–1989, *J. Geophys. Res.*, *95*, 17,103–17,112, doi:10.1029/JA095iA10p17103.

Dennis, B. R. (1985), Solar hard X-ray bursts, *Sol. Phys.*, *100*, 465–490, doi:10.1007/BF00158441.

Feldman, U., G. A. Doschek, and J. A. Klimchuk (1997), The occurrence rate of soft X-ray flares as a function of solar activity, *Astrophys. J.*, *474*(1), 511.

Feynman, J. (1997), Evolving magnetic structures and their relationship to coronal mass ejections, in *Coronal Mass Ejections*, *Geophys. Monogr. Ser.*, vol. 99, edited by N. U. Crooker, J. A. Joselyn, and J. Feynman, pp. 49–55, AGU, Washington, D. C.

Forbes, T. G. (2000), A review on the genesis of coronal mass ejections, *J. Geophys. Res.*, *105*, 23,153–23,166, doi:10.1029/2000JA000005.

Goldstein, M. L., S. A. Morris, and G. G. Yen (2004), Problems with fitting to the power-law distribution, *Eur. Phys. J. B*, *41*, 255–258, doi:10.1140/epjb/e2004-00316-5.

Gonzalez, W. D., J. A. Joselyn, Y. Kamide, H. W. Kroehl, G. Rostoker, B. T. Tsurutani, and V. M. Vasyliunas (1994), What is a geomagnetic storm?, *J. Geophys. Res.*, *99*, 5771–5792, doi:10.1029/93JA02867.

Gosling, J. T., S. J. Bame, D. J. McComas, and J. L. Phillips (1990), Coronal mass ejections and large geomagnetic storms, *Geophys. Res. Lett.*, *17*, 901–904, doi:10.1029/GL017i007p00901.

Gosling, J. T., S. J. Bame, D. J. McComas, J. L. Phillips, V. J. Pizzo, B. E. Goldstein, and M. Neugebauer (1993), Latitudinal variation of solar wind corotating stream interaction regions: Ulysses, *Geophys. Res. Lett.*, *20*(24), 2789–2792, doi:10.1029/93GL03116.

Kivelson, M. G., and C. T. Russell (1995), *Introduction to Space Physics*, 568 pp., Cambridge Univ. Press, Cambridge, U. K.

Lakhina, G. S., S. Alex, B. T. Tsurutani, and W. D. Gonzalez (2005), Research on historical records of geomagnetic storms, in *Coronal and Stellar Mass Ejections*, *IAU Symp. Colloq. Proc. Ser.*, vol. 226, edited by K. Dere, J. Wang, and Y. Yan, pp. 3–15, Cambridge Univ. Press, Cambridge, U. K., doi:10.1017/S1743921305000074.

Lin, R. P. (2011), Energy release and particle acceleration in flares: Summary and future prospects, *Space Sci. Rev.*, *159*, 421–445, doi:10.1007/s11214-011-9801-0.

Lin, R. P., R. A. Schwartz, S. R. Kane, R. M. Pelling, and K. C. Hurley (1984), Solar hard X-ray microflares, *Astrophys. J.*, *283*, 421–425, doi:10.1086/162321.

Lockwood, M., and M. J. Owens (2011), Centennial changes in the heliospheric magnetic field and open solar flux: The consensus view from geomagnetic data and cosmogenic isotopes and its implications, *J. Geophys. Res.*, *116*, A04109, doi:10.1029/2010JA016220.

Lockwood, M., A. P. Rouillard, and I. D. Finch (2009), The rise and fall of open solar flux during the current grand solar maximum, *Astrophys. J.*, *700*, 937–944, doi:10.1088/0004-637X/700/2/937.

Longo, G. (2007), *Comet/Asteroid Impacts and Human Society: An Interdisciplinary Approach*, 546 pp., Springer, Berlin.

Lu, E. T., and R. J. Hamilton (1991), Avalanches and the distribution of solar flares, *Astrophys. J.*, *380*, L89–L92.

McCracken, K. G., and J. Beer (2007), Long-term changes in the cosmic ray intensity at Earth, 1428–2005, *J. Geophys. Res.*, *112*, A10101, doi:10.1029/2006JA012117.

McCracken, K. G., G. A. M. Dreschhoff, E. J. Zeller, D. F. Smart, and M. A. Shea (2001), Solar cosmic ray events for the period 1561–1994: 1. Identification in polar ice, 1561–1950, *J. Geophys. Res.*, *106*, 21,585–21,598, doi:10.1029/2000JA000237.

McMorrow, D. (2009), Rare events, *Rep. JSR-09-108*, Off. of the Secr. of Def., Washington, D. C.

Newell, P. T., and C.-I. Meng (1988), Categorization of dispersion curves in the equatorward edge of the diffuse aurora, *Planet. Space Sci.*, *36*, 1031–1038, doi:10.1016/0032-0633(88)90041-4.

Newman, M. (2005), Power laws, Pareto distributions and Zipf's law, *Contemp. Phys.*, *46*, 323–351.

Reeves, G. D., et al. (1998), The relativistic electron response at geosynchronous orbit during the January 1997 magnetic storm, *J. Geophys. Res.*, *103*, 17,559–17,570, doi:10.1029/97JA03236.

Riley, P., J. A. Linker, Z. Mikic, and R. Lionello (2000), Solar cycle variations and the large-scale structure of the heliosphere: MHD simulations, paper presented at The Sun and Space Weather, IAU Joint Discussion 7, Int. Astron. Union, Manchester, U. K.

Riley, P., C. Schatzman, H. V. Cane, I. G. Richardson, and N. Gopalswamy (2006), On the rates of coronal mass ejections: Remote solar and in situ observations, *Astrophys. J.*, *647*, 648–653, doi:10.1086/505383.

Ruzmaikin, A., J. Feynman, and I. Jun (2011), Distribution of extreme solar energetic proton fluxes, *J. Atmos. Sol. Terr. Phys.*, *73*, 300–307, doi:10.1016/j.jastp.2009.12.016.

Schieb, P.-A. (2011), Geomagnetic storms, *Technical Report*, Off. of Risk Manage. and Anal., Dept. of Homeland Security, Washington, D. C.

Shea, M. A., D. F. Smart, K. G. McCracken, G. A. M. Dreschhoff, and H. E. Spence (2006), Solar proton events for 450 years: The Carrington event in perspective, *Adv. Space Res.*, *38*, 232–238, doi:10.1016/j.asr.2005.02.100.

Siscoe, G., N. U. Crooker, and C. R. Clauer (2006), *Dst* of the Carrington storm of 1859, *Adv. Space Res.*, *38*, 173–179, doi:10.1016/j.asr.2005.02.102.

Solanki, S. K., I. G. Usoskin, B. Kromer, M. Schüssler, and J. Beer (2004), Unusual activity of the Sun during recent decades compared to the previous 11,000 years, *Nature*, *431*, 1084–1087, doi:10.1038/nature02995.

Stamatelatos, M. (2002), Fault tree handbook with aerospace applications, *Technical Report*, Off. of Safety and Mission Assurance, NASA, Washington, D. C.

Steinhilber, F., J. A. Abreu, and J. Beer (2008), Solar modulation during the Holocene, *Astrophys. Space Sci. Trans.*, *4*, 1–6, doi:10.5194/astra-4-1-2008.

Svalgaard, L., and E. W. Cliver (2010), Heliospheric magnetic field 1835–2009, *J. Geophys. Res.*, *115*, A09111, doi:10.1029/2009JA015069.

Tsubouchi, K., and Y. Omura (2007), Long-term occurrence probabilities of intense geomagnetic storm events, *Space Weather*, *51*, S12003, doi:10.1029/2007SW000329.

Tsurutani, B. T., W. D. Gonzalez, G. S. Lakhina, and S. Alex (2003), The extreme magnetic storm of 1–2 September 1859, *J. Geophys. Res.*, *108*(A7), 1268, doi:10.1029/2002JA009504.

Wang, J., and M. Roush (2000), *What Every Engineer Should Know About Risk Engineering and Management*, *What Every Eng. Should Know*, vol. 36, 251 pp., Marcel Dekker, New York.

Watanabe, K., S. Krucker, H. Hudson, T. Shimizu, S. Masuda, and K. Ichimoto (2010), G-band and hard X-ray emissions of the 2006 December 14 flare observed by Hinode/SOT and Rhessi, *Astrophys. J.*, *715*, 651–655, doi:10.1088/0004-637X/715/1/651.

Wittmann, A. D., and Z. T. Xu (1987), A catalogue of sunspot observations from 165 BC to AD 1684, *Astron. Astrophys. Suppl. Ser.*, *70*, 83–94.

Wolff, E. W., A. E. Jones, S. J.-B. Bauguitte, and R. A. Salmon (2008), The interpretation of spikes and trends in concentration of nitrate in polar ice cores, based on evidence from snow and atmospheric measurements, *Atmos. Chem. Phys.*, *8*(18), 5627–5634, doi:10.5194/acp-8-5627-2008.

P. Riley, Predictive Science, 9990 Mesa Rim Rd., Ste. 170, San Diego, CA 92121, USA. (pete@predsci.com)

Nature of Prominences and their role in Space Weather
Proceedings IAU Symposium No. 300, 2013
B. Schmieder, J.-M. Malherbe & S. T. Wu, eds.

doi:10.1017/S1743921313011745

Magnetic reconnection driven by filament eruption in the 7 June 2011 event

L. van Driel-Gesztelyi[1,2,3], D. Baker[1], T. Török[4], E. Pariat[2], L. M. Green[1], D. R. Williams[1], J. Carlyle[1], G. Valori[2], P. Démoulin[2], S. A. Matthews[1], B. Kliem[5] and J.-M. Malherbe[2]

[1]University College London, Mullard Space Science Laboratory, Holmbury St. Mary, Dorking, Surrey RH5 6NT, UK
[2]LESIA, Observatoire de Paris, CNRS, UPMC, Université Paris Diderot, 5 place Jules Janssen, 92190 Meudon, France;email: Lidia.vanDriel@obspm.fr
[3]Konkoly Observatory, Hungarian Academy of Sciences, Budapest, Hungary
[4]Predictive Science Inc., 9990 Mesa Rim Rd., Suite 170, San Diego, CA 92121, USA
[5]Institut für Physik und Astronomie, Universität Potsdam, Karl-Liebknecht-Str. 24-25, 14476 Potsdam, Germany

Abstract. During an unusually massive filament eruption on 7 June 2011, SDO/AIA imaged for the first time significant EUV emission around a magnetic reconnection region in the solar corona. The reconnection occurred between magnetic fields of the laterally expanding CME and a neighbouring active region. A pre-existing quasi-separatrix layer was activated in the process. This scenario is supported by data-constrained numerical simulations of the eruption. Observations show that dense cool filament plasma was re-directed and heated in situ, producing coronal-temperature emission around the reconnection region. These results provide the first direct observational evidence, supported by MHD simulations and magnetic modelling, that a large-scale re-configuration of the coronal magnetic field takes place during solar eruptions via the process of magnetic reconnection.

Keywords. MHD, instabilities, Sun: activity, magnetic fields, coronal mass ejections (CMEs), filaments, methods: numerical, data analysis

---

A spectacular solar eruption occurred on 7 June 2011 observed by the Solar Dynamic Observatory's Atmospheric Imaging Assembly (SDO/AIA: Lemen *et al.* 2012). The CME originated in a complex of three adjacent active regions (ARs, see Figure 1) in the south-western quadrant and carried an unusually massive erupting filament in its core. We carried out a multiwavelength analysis of the event. Using SDO/HMI data we computed the magnetic topology, determining the locations of quasi-separatrix layers in the three-AR complex. We also carried out data-constrained MHD simulations of the eruption.

We found that the strong lateral expansion of the erupting magnetic structure led to flux pile-up, current sheet formation/intensification, and magnetic reconnection along a pre-existing quasi-separatrix layer in the three-AR complex. The onset of reconnection first became apparent in the SDO/AIA images when downward flowing dense, cool filament plasma, originally contained within the erupting flux rope, was re-directed towards a neighbouring active region, tracing the change of large-scale magnetic connectivity. Williams *et al.* (2013) estimated a lower limit of the electron density of the redirected plasma to be 10^{10} cm^{-3}, at least one order of magnitude larger than the typical coronal density. As a result of this unusually high density around the reconnection region, direct plasma heating took place there. The most prominent brightening was seen in the AIA 171 Å waveband (6.3×10^5 K).

These SDO observations provide one of the first direct imaging observations of magnetic reconnection in the solar atmosphere. Furthermore, a combination of observations,

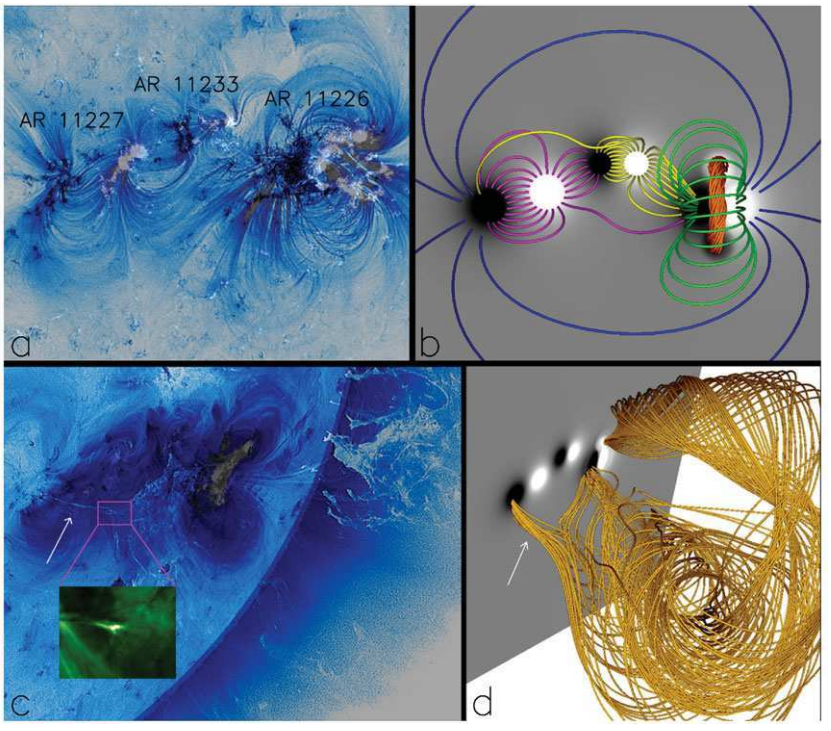

Figure 1. Observations and MHD numerical simulation of the magnetic configuration and the eruption. **(a)** SDO/AIA 171 Å reverse colour scale image over a co-aligned SDO/HMI magnetic field map of the three neighbouring active regions on 3 June 2011 and **(b)** corresponding magnetic configuration in the simulation. Black/white indicate negative/positive magnetic polarity, the pre-eruption magnetic flux rope in the rightmost active region is shown in gold. **(c)** SDO/AIA 171 Å reversed-colour image and **(d)** a simulation snapshot during the CME eruption on 7 June, by when the active regions have rotated close to the solar limb. The new connections, formed by magnetic reconnection between the magnetic flux rope erupting from AR 11226 and magnetic field lines of AR 11227, are indicated by white arrows in **(c)** and **(d)**. The inset in **(c)** is a magnification of the in-situ heated bright reconnection region.

magnetic modelling, and MHD simulations (Figure 1) provides evidence that, during the expansion of a CME's magnetic structure, instantaneous magnetic reconnection can occur with ambient magnetic field leading to large-scale restructuring. For more details see van Driel-Gesztelyi *et al.* (2013).

Acknowledgements

The authors acknowledge funding from the European Commission's Seventh Framework Programme under the grant agreement No. 284461 (eHEROES project) and the Hungarian Research grant OTKA K-081421. TT was supported by NASA's HTP, LWS, SR&T programs and NSF (AGS-1249270). LMG is grateful for a Royal Society Fellowship, and JC for a joint UCL-MPI Impact PhD Studentship. BK acknowledges support by the DFG.

References

Lemen, J. R., Title, A. M., Akin, D. J., *et al.*, 2012, *Solar Phys.* 275, 17

van Driel-Gesztelyi, L., Baker, D., Török, T., Pariat, E., Green, L. M., Williams, D. R., Carlyle, J., Valori, G., Démoulin, P., Matthews, S. A., Kliem, B., & Malherbe, J.-M. 2013, *ApJ*, submitted.

Williams, D. R., Baker, D., & van Driel-Gesztelyi, L. 2013, *ApJ*, 764, 165

Nature of Prominences and their role in Space Weather
Proceedings IAU Symposium No. 300, 2013
B. Schmieder, J.-M. Malherbe & S. T. Wu, eds.

doi:10.1017/S1743921313010971

Initiation of Coronal Mass Ejections by Sunspot Rotation

G. Valori[1], T. Török[2], M. Temmer[3,4], A. M. Veronig[3], L. van Driel-Gesztelyi[1,5,6], and B. Vršnak[7]

[1]LESIA, Observatoire de Paris, CNRS, UPMC, Université Paris Diderot, 5 place Jules Janssen, 92190 Meudon, France; email: gherardo.valori@obspm.fr
[2]Predictive Science Inc., 9990 Mesa Rim Rd., Suite 170, San Diego, CA 92121, USA; email: tibor@predsci.com
[3]IGAM/Kanzelhöhe Observatory, Institute of Physics, Universität Graz, Universitätsplatz 5, A-8010 Graz, Austria
[4]Space Research Institute, Austrian Academy of Sciences, Schmiedlstrasse 6, A-8042 Graz, Austria
[5]University College London, Mullard Space Science Laboratory, Holmbury St. Mary, Dorking, Surrey RH5 6NT, UK
[6]Konkoly Observatory, Hungarian Academy of Sciences, Budapest, Hungary
[7]Hvar Observatory, Faculty of Geodesy, University of Zagreb, Kačićeva 26, HR-10000 Zagreb, Croatia

Abstract. We report observations of a filament eruption, two-ribbon flare, and coronal mass ejection (CME) that occurred in Active Region NOAA 10898 on 6 July 2006. The filament was located South of a strong sunspot that dominated the region. In the evolution leading up to the eruption, and for some time after it, a counter-clockwise rotation of the sunspot of about 30 degrees was observed. We suggest that the rotation triggered the eruption by progressively expanding the magnetic field above the filament. To test this scenario, we study the effect of twisting the initially potential field overlying a pre-existing flux rope, using three-dimensional zero–β MHD simulations. We consider a magnetic configuration whose photospheric flux distribution and coronal structure is guided by the observations and a potential field extrapolation. We find that the twisting leads to the expansion of the overlying field. As a consequence of the progressively reduced magnetic tension, the flux rope quasi-statically adapts to the changed environmental field, rising slowly. Once the tension is sufficiently reduced, a distinct second phase of evolution occurs where the flux rope enters an unstable regime characterized by a strong acceleration. Our simulation thus suggests a new mechanism for the triggering of eruptions in the vicinity of rotating sunspots.

Keywords. MHD, instabilities, Sun: activity, magnetic fields, sunspots, coronal mass ejections (CMEs), filaments, methods: numerical, data analysis

1. Introduction

The eruption on 6 July 2006 in active region NOAA 10898 was a two-ribbon flare accompanied by a filament eruption and a halo CME, the latter being most prominent in the southwest quadrant and reaching a linear plane-of-sky velocity of ≈900 $\mathrm{km\,s^{-1}}$ (Temmer *et al.* 2008). The event was associated with an EIT wave, a type II burst, and very distinct coronal dimming regions. The flare was of class M2.5/2N, located at the heliographic position S9°, W34°. It was observed in soft X-rays (SXR) by GOES (peak time at ≈08:37 UT) as well as in hard-X rays (HXR) with RHESSI, with the two highest peaks of nonthermal HXR emission occurring during 08:20 – 08:24 UT.

The morphology and evolution of the bipolar active region in the days preceding the eruption were studied using photospheric line-of-sight magnetograms obtained by the

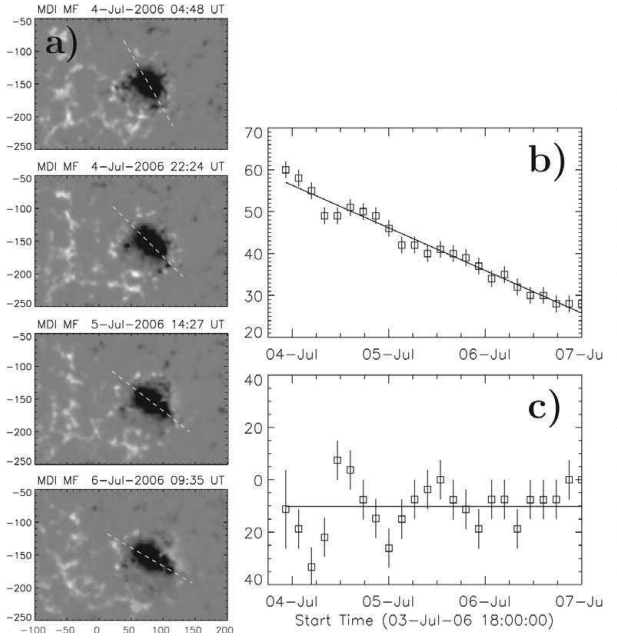

Figure 1. (a) Representative MDI longitudinal magnetic-field maps of the sunspot evolution during 4 – 6 July 2006: The dashed yellow line outlines the major axis of the sunspot that was used to measure the sunspot rotation. The images are all differentially rotated to the first image of the series, when the sunspot was closer to disk centre. **(b)** Sunspot rotation determined from the MDI magnetic-field maps over the period 3 July 2006, 22:00 UT, to 7 July 2006, 8:00 UT, showing the orientation of the sunspot's major axis, measured clockwise from solar East. **(c)** Sunspot rotation rate in degrees per day, determined as the temporal derivative of the rotation measurements.

MDI instrument (Scherrer *et al.* 1995). The region consisted of a compact negative polarity (the sunspot) surrounded by a dispersed positive polarity, most of which was extending eastwards (Fig. 1a). The two polarities were surrounded by a large, "inverse C-shaped" area of dispersed negative flux to the west of the region (Fig. 2a). The magnetic-flux measurements indicate a mere 5% negative surplus flux in this major bipolar active region of 2.1×10^{22} Mx total flux and maximum-field strengths (negative:positive) in a roughly 10:1 ratio. The sequence in Fig. 1a shows that the sunspot is rotating counter-clockwise during the considered period. The total rotation observed over the three days preceding the eruption is about 30°, with sunspot's rotation rate of about 10° day^{-1} (Fig. 1b,c).

The flare and the filament eruption were observed in full-disk Hα filtergrams by the Kanzelhöhe Observatory and, over a smaller field-of-view around the active region, by the Hvar Observatory. These observations reveal that the filament consisted of a double structure before and during the eruption. Significant rising motions of the filament could be seen from about 08:23 UT. The Hα flare started by the appearance of very weak double-footpoint brightening at 08:15 UT. We also estimated the kinematics of the filament and the CME front from a time sequence of running-difference images obtained from TRACE, EIT, and LASCO C2/C3 observations. We obtain that the coronal loops overlying the filament started their slow rising phase at 08:15 UT, i.e., about five – ten minutes before the filament. Similarly, the CME front reached its final, almost constant velocity a few minutes before the filament. More details about the methods employed to obtain the above results can be found in Török *et al.* (2013), hereafter Paper I. We refer to that article and to the references therein for further details on the eruption.

Guo *et al.* (2010) suggested that the eruption was triggered by recurrent chromospheric mass injection in the form of surges or jets into the filament channel. Here we propose a different mechanism: Assuming that the filament was suspended in the corona by a magnetic flux rope, we suggest that the continuous rotation of the sunspot led to a slow expansion of the arcade-like magnetic field overlying the filament, i.e., to a continuous weakening of its stabilizing tension, until a critical point was reached at which equilibrium

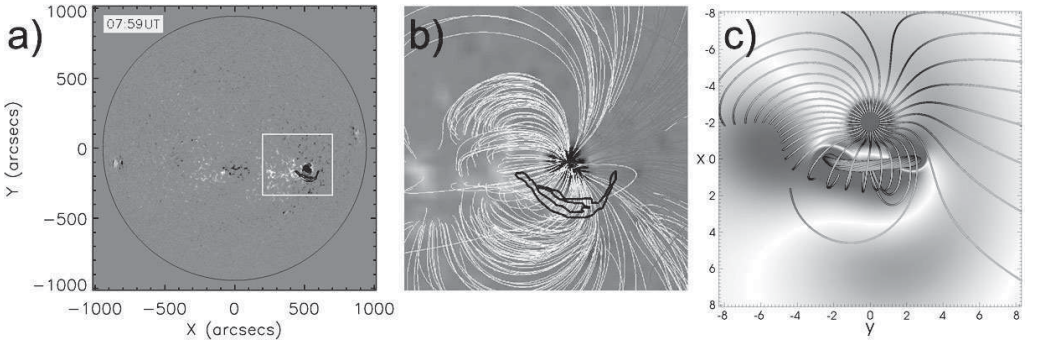

Figure 2. (a) Full-disk MDI magnetogram on 6 July 2006, 07:59 UT. AR10898 is marked by the white box. **(b)** PFSS magnetic field lines in the AR calculated for 6 July 2006, 06:04 UT, overlaid on a synoptic MDI magnetogram. Pink (white) field lines depict open (closed) fields. The outer contours of the filament, based on Hα data taken at 07:59 UT on 6 July 2006, are outlined with black lines. **(c)** Magnetic configuration used in the simulation, after the initial relaxation of the system, showing the core of the TD flux rope (orange field lines) and the ambient potential field (green field lines). $B_z\,(z=0)$ is shown, with red (blue) corresponding to positive (negative) values, and is saturated at 4% $\max(B_z)$ to depict weaker flux distributions.

could not be maintained and the flux rope erupted. We note that we do not claim that the eruption was triggered *exclusively* by this mechanism. Filaments are often observed to spiral into the periphery of sunspots (see,e.g., Green *et al.* 2007), and also in our case an inspection of the TRACE and Hα images during the early phase of the eruption suggests a possible magnetic connection between the western extension of the filament-carrying core field and the sunspot area. Thus, the sunspot rotation may have added stress to this field, thereby possibly contributing to drive it towards eruption. On the other hand, for an injection of twist to occur, the core field must be rooted in the centre of the sunspot, not just in its periphery, which is difficult to establish from observations. It appears reasonable to assume that a clear connection between core field and sunspot centre is not always present, and that the stressing of the overlying ambient field by sunspot rotation may be more relevant for the destabilization of the system in such cases. In order to test this scenario, we perform a three-dimensional (3D) MHD simulation in which we twist the stabilizing potential field overlying a stable coronal flux rope. Differently from previous works (e.g., Amari *et al.* 1996), the photospheric vortex motions we use do not directly affect the flux rope, but solely the field surrounding it.

2. Numerical simulation setup

As in previously published simulations (e.g., Török, Kliem, and Titov 2004; Kliem, Titov, and Török 2004), we integrate the $\beta = 0$ compressible ideal MHD equations, ignoring the effects of thermal pressure and gravity, and we employ the coronal flux rope model of Titov and Démoulin (1999), hereafter TD, to construct the initial magnetic field. The main ingredient of the TD model is a current ring of major radius $[R]$ and minor radius $[a]$ that is placed such that its symmetry axis is located at a depth $[d]$ below a photospheric plane. The outwardly directed Lorentz self-force (or "hoop force") of the ring is balanced by a potential field created by a pair of sub-photospheric point sources $\pm q$ that are placed at the symmetry axis, at distances $\pm L$ from the ring centre. The resulting coronal field consists of an arched and line-tied flux rope embedded in an arcade-like potential field.

We normalize lengths by $l = R - d$ and use a Cartesian grid discretizing the volume $[-40, 40] \times [-30, 30] \times [0, 60]$, resolved by $307 \times 257 \times 156$ points. The grid is nonuniform in all directions, with an almost uniform resolution $\Delta = 0.05$ in the area mimicking the active region. The top and lateral boundaries are closed, which is justified given the large size of the simulation box. Below the photospheric plane, the tangential components of the magnetic field $[B_{x,y}]$ are extrapolated from the integration domain, and the normal component $[B_z]$ is set such that $\nabla \cdot \mathbf{B} = \mathbf{0}$ in $z = 0$ at all times. The vertical velocities are zero there at all times, and the mass density is fixed at its initial values.

Fig. 2b shows a coronal potential-field source-surface model (Schatten, Wilcox, and Ness 1969, PFSS), obtained from a synoptic MDI magnetogram for Carrington Rotation 2045. It can be seen that the field lines rooted in the main polarity (the sunspot) form a fan-like structure, which partly overlies the pre-eruption filament. In order to build an initial magnetic configuration that resembles this coronal field and the underlying highly asymmetric magnetic flux distribution (Sect. 1), we modify the standard TD model by replacing the pair of sub-photospheric point charges by an ensemble of ten sub-photospheric sources. These are adjusted in order to mimic: the approximate flux balance between the concentrated leading negative polarity and the dispersed following positive polarity; the ratio of approximately 10:1 between the peak field strengths in the leading polarity and the following polarity; the size ratio between these polarities; the presence of an "inverse C-shaped" area of dispersed negative flux to the West of the leading polarity; the fan-like shape of the coronal field rooted in the leading polarity. Since the model is still relatively idealized, all these features can be matched only approximately. We then add a TD flux rope, setting $R = 2.75$, $a = 0.8$, and $d = 1.75$. The position of the rope within the ambient field is guided by the observed location of the filament (Fig. 2b), and its magnetic field strength is chosen such that it is in approximate equilibrium with the ambient potential field. We use an initial density distribution $\rho_0(\mathbf{x}) = |\mathbf{B_0}(\mathbf{x})|^2$, corresponding to a uniform initial Alfvén velocity. In order to obtain a numerical equilibrium as a starting point, we first perform a numerical relaxation for $75\,\tau_a$, after which the time is reset to zero.

In order to mimic the observed sunspot rotation, we then twist the main negative flux concentration by imposing tangential velocities at the bottom boundary. They produce a horizontal counterclockwise rotation, chosen such that the velocity vectors always point along the contours of $B_z(x, y, 0, t = 0)$, which assures that the distribution of $B_z(x, y, 0, t)$ is conserved to a very good approximation. The velocities are zero at the polarity centre, located at $(x, y, z) = (-2, 0, 0)$, and decrease towards its edge from their maximum value, equal to 0.005 times the initial Alfvén velocity $[v_{a0}]$. The equations and parameters used to compute the tangential velocities at each time are given in Paper I. The twist injected by such motions is nearly uniform close to the polarity centre and decreases monotonically towards its edge, such that it does not directly affect the flux rope field.

3. Results

The magnetic configuration resulting after the initial numerical relaxation is shown in Fig. 2c and in Fig. 4a. The fan-structure inferred from the PFSS extrapolation is qualitatively well reproduced. The TD flux rope is stabilized by flux rooted towards the southern edge of the main polarity, and the rope is inclined with respect to the vertical, which is due to the asymmetry of the potential field surrounding it.

Figure 4a shows that electric currents are present in the ambient field volume. The strongest current concentrations are located in the front of the flux rope and exhibit an X-shaped pattern in the vertical cut shown. This pattern outlines the locations of quasi-separatrix layers (QSL, see, e.g., Démoulin *et al.* 1996) that separate different connectivity

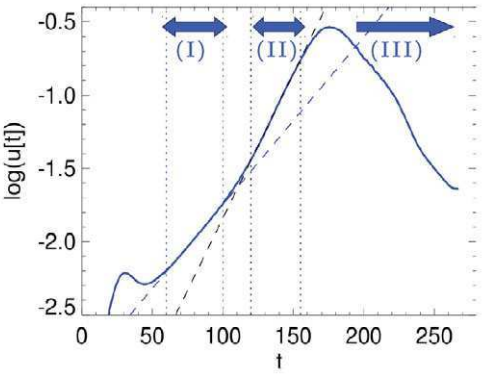

Figure 3. Logarithmic presentation of the velocity of the axis apex of the TD flux rope during the twisting phase, as a function of time. The dashed lines show linear fits, obtained within the time periods marked by the vertical dotted lines of the same color. Thick arrows mark different evolution phases described in the text.

domains. The QSLs are present in the configuration from the very beginning and arise from the complexity of the potential field. Their presence is evident also in the left panel of Fig. 4a: the green field lines show strong connectivity gradients in the northern part of the main polarity and in the vicinity of the western flux rope footpoint. It has been demonstrated that current concentrations form preferably at the locations of QSLs as a system containing such structures is dynamically perturbed (see, e.g., Aulanier, Pariat, and Démoulin 2005). In our case the perturbation results from the – relatively modest – dynamics during the initial relaxation of the system.

After the relaxation, at $t = 0$, we start twisting the main negative polarity, and we quantify the evolution of the TD flux rope by monitoring the velocity at the axis apex of the rope (Fig. 3). Due to the pronounced fan-structure of the field rooted in the main polarity, the photospheric twisting does not lead to the formation of a single twisted flux tube that rises exactly in vertical direction above the TD rope, as it was the case earlier studies (Amari *et al.* 1996; Török and Kliem 2003; Aulanier, Démoulin, and Grappin 2005). Rather, the twisting leads to a slow, global expansion of the fan-shaped field lines, as shown in Fig. 4. Since we are mainly interested in the destabilization of the flux rope, we did not study the detailed evolution of the large-scale field. We expect it to be very similar to the one described in Santos, Büchner, and Otto (2011), since the active region those authors simulated was also dominated by one main polarity, and the field rooted therein had a very similar fan-shaped structure (cf. our Fig. 4 with their Fig.1).

Important for our purpose is the evolution of the arcade-like part of the initial potential field that directly overlies the TD flux rope. Those field lines are directly affected only by a fraction of the boundary flows and therefore get merely sheared (rather than twisted), which still leads to their slow expansion. As a result, the TD rope starts to rise, adapting to the successively decreasing magnetic tension of the overlying field (phase I in Fig. 3). This initial phase of the evolution is depicted in Fig. 4b. Note that some of the flux at the front of the expanding arcade reconnects at the QSL current layer, which can be expected to aid the arcade expansion to some degree. As can be seen in Fig. 3, the TD rope rises, after some initial adjustment, exponentially during this slow initial phase.

As the twisting continues, a transition to a rapid acceleration takes place after $t \approx 100\,\tau_a$, when the rise curve leaves the quasi-static regime. After the transition phase, the TD rope again rises exponentially, but now with a significantly larger growth rate than during the slow rise phase (phase II in Fig. 3). Such a slow (quasi-static) rise phase, followed by a rapid acceleration, is a well-observed property of many filament eruptions in the early evolution of CMEs (see, e.g., Schrijver *et al.* 2008, and references therein), and is also seen for the event studied here (see also Paper I). The evolution of the TD rope after $t \approx 100\,\tau_a$ can be associated with the development of the torus instability

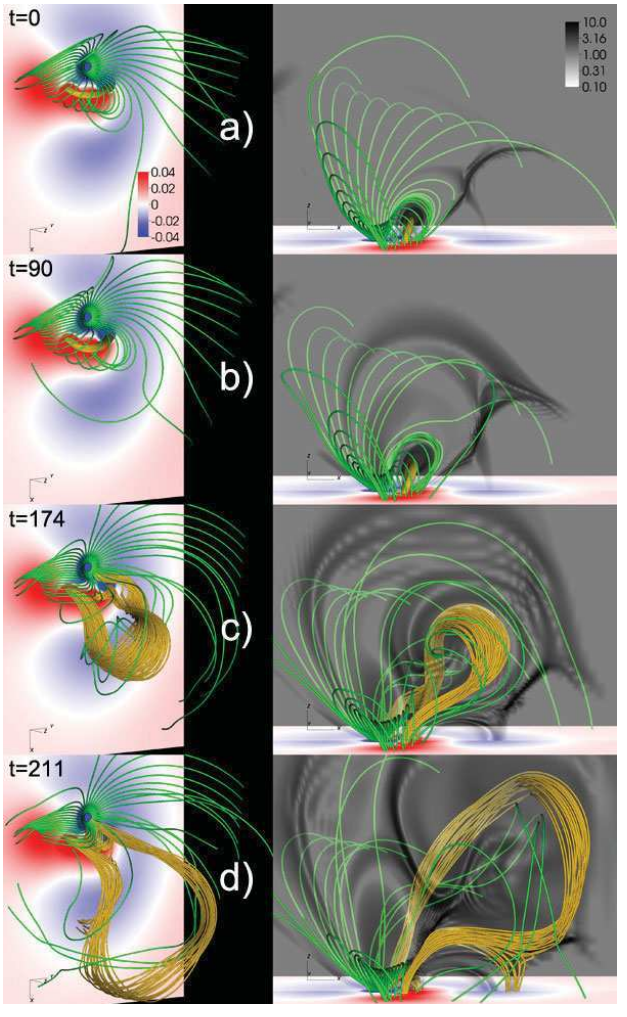

Figure 4. Magnetic configuration after initial relaxation (a), during slow rise phase (b), at time of peak flux rope velocity (c), and during flux rope deceleration (d). The flux rope core is depicted by orange field lines; ambient field lines are green. $B_z\,(z=0)$ is shown, with red (blue) corresponding to positive (negative) values. Left panels use a view similar to the observations (see paper I); right panels show a side view. The transparent grey-scales show a logarithmic distribution of $|\mathbf{j}|/|\mathbf{B}|$ in the plane $x = 0$, outlining the locations of strongest currents. The sub-volume $[-10, 16] \times [-11, 11] \times [0, 18]$ is used for all panels.

(Kliem and Török 2006; Démoulin and Aulanier 2010), as has been shown under similar conditions in various simulations of erupting flux ropes (Török and Kliem 2007; Fan and Gibson 2007; Schrijver *et al.* 2008; Aulanier *et al.* 2010; Török *et al.* 2011). The right panels in Fig. 4 show that the trajectory of the flux rope is far from being vertical. Such lateral eruptions have been reported frequently in both observations and simulations (see, e.g., Williams *et al.* 2005; Panasenco *et al.* 2011; Yang *et al.* 2012), and are usually attributed to an asymmetric structure of the field overlying the erupting core flux. We believe that this causes the lateral rise also in our case.

As the eruption continues, the trajectory of the flux rope becomes increasingly horizontal, resembling the so-called "roll effect" (Panasenco *et al.* 2011) and indicating that the rope cannot overcome the tension of the large-scale overlying field. Moreover, as a

consequence of its increasing expansion, the flux rope strongly pushes against the QSL current layer, which results in reconnection between the front of the rope and the ambient field. Eventually, the rope splits into two parts, similar to what has been found in simulations of confined eruptions (Amari and Luciani 1999; Török and Kliem 2005). These two effects slow down the rise of the rope after $t \approx 175\,\tau_a$ and inhibit its full eruption, i.e., the development of a CME in our simulation (phase III in Fig. 3).

Since QSLs can affect the evolution of an eruption, but are not expected to play a significant role for its initiation, we did not investigate in detail whether or not QSLs were present in the pre-eruption configuration of the 6 July 2006 event. The PFSS extrapolation indicates the presence of a QSL to the North and the West of the main polarity (see the field-line connectivities in Fig. 2b), but less clearly so to its South. Since we merely aim to model the initiation of the eruption rather than its full evolution into a CME, we refrained from further improving our model to obtain a configuration without a strong QSL in front of the flux rope.

4. Summary and Conclusions

We presented a 3D MHD simulation that was designed to test a possible scenario for the initiation and early evolution of the filament eruption and CME that occurred on 6 July 2006 in active region NOAA 10898. Our conjecture was that the slow rotation of the sunspot that dominated the active region progressively reduced the tension of the magnetic field overlying the pre-eruption filament, until the latter could not be stabilized anymore and erupted, resulting in the CME. Using the TD coronal flux rope model as a starting point, we constructed an initial magnetic field that resembles the photospheric flux distribution and coronal magnetic field structure of the active region around the time of the event. In particular, the highly asymmetric flux density and the resulting overall fan-shape of the coronal magnetic field are well captured by the model, while the approximative flux balance of the region is kept. We then mimicked the observed sunspot rotation by imposing photospheric vortex flows localized at the main magnetic polarity of the model. The flows were chosen such that they do not directly affect the flux rope.

As a result of this twisting, the field lines overlying the flux rope start to expand and the rope undergoes a quasi-static adaptation to the changing surrounding field in the simulation, which manifests in a slow rise phase. As the weakening of the overlying field reaches an appropriate level, the torus instability sets in and rapidly accelerates the rope upwards, leading to a second, fast rise phase and eruption. The asymmetry of the ambient field leads to a markedly lateral eruption. This evolution in two phases resembles the often observed slow rise phase and subsequent strong acceleration of filaments in the course of their eruption. However, the presence of a QSL-related current layer in the front of the erupting flux rope in the simulation results in magnetic reconnection which eventually splits the rope before it can evolve into a CME, in contrast to the observations. Although we are not able to follow the expansion of the flux rope beyond this phase, the simulation successfully models the early phases of the eruption (the slow rise and the initial rapid acceleration of the flux rope) in a setting that is qualitatively similar to the observed magnetic configuration around the time of the eruption.

Our simulation thus demonstrates that the continuous expansion due to sunspot rotation of the magnetic field that stabilizes the current-carrying core flux, i.e., the progressive decrease of magnetic tension, can lead to filament eruptions and CMEs.

Acknowledgements

We acknowledge the use of data provided by the SOHO/MDI consortium. SOHO/EIT was funded by CNES, NASA, and the Belgian SPPS. The SOHO/LASCO data used here

are produced by a consortium of the Naval Research Laboratory(USA), Max–Planck–Institut für Aeronomie (Germany), Laboratoire d'Astrophysique de Marseille (France), and the University of Birmingham (UK). SOHO is a mission of international cooperation between ESA and NASA. The *Transition Region and Coronal Explorer* (TRACE) is a mission of the Stanford–Lockheed Institute for Space Research, and part of the NASA Small Explorer program. Hα data were provided by the Kanzelhöhe Observatory, University of Graz, Austria, and by the Hvar Observatory, University of Zagreb, Croatia. The research leading to these results has received funding from the European Commission's Seventh Framework Programme (FP7/2007-2013) under the grant agreements nn° 218816 (SOTERIA project, www.soteria-space.eu) and n° 284461 (eHEROES, http://soteria-space.eu/eheroes/html). TT was partially supported by NASA's HTP, LWS, and SR&T programs. LvDG acknowledges funding through the Hungarian Science Foundation grant OTKA K81421.

References

Amari, T. & Luciani, J. F. 1999, *Astrophys. J. Lett.* 515, L81.

Amari, T., Luciani, J. F., Aly, J. J., & Tagger, M. 1996, *Astrophys. J. Lett.* 466, L39.

Aulanier, G., Démoulin, P., & Grappin, R. 2005, *Astron. Astrophys.* 430, 1067.

Aulanier, G., Pariat, E., & Démoulin, P. 2005, *Astron. Astrophys.* 444, 961.

Aulanier, G., Török, T., Démoulin, P., & DeLuca, E. E. 2010, *Astrophys. J.* 708, 314.

Démoulin, P. & Aulanier, G. 2010, *Astrophys. J.* 718, 1388.

Démoulin, P., Henoux, J. C., Priest, E. R., & Mandrini, C. H. 1996, *Astron. Astrophys.* 308, 643.

Fan, Y. & Gibson, S. E. 2007, *Astrophys. J.* 668, 1232.

Gopalswamy, N., Yashiro, S., Kaiser, M. L., Howard, R. A., & Bougeret, J. L. 2001, *Astrophys. J. Lett.* 548, L91.

Green, L. M., Kliem, B., Török, T., van Driel-Gesztelyi, L., & Attrill, G. D. R. 2007, *Solar Phys.* 246, 365.

Guo, J., Liu, Y., Zhang, H., Deng, Y., Lin, J., & Su, J. 2010, *Astrophys. J.* 711, 1057.

Kliem, B. & Török, T. 2006, *Phys. Rev. Lett.* 96(25), 255002.

Kliem, B., Titov, V. S., & Török, T. 2004, *Astron. Astrophys.* 413, L23.

Panasenco, O., Martin, S., Joshi, A. D., & Srivastava, N. 2011, J. Atmos. Solar-Terr. Phys. 73, 1129.

Santos, J. C., Büchner, J., & Otto, A. 2011, *Astron. Astrophys.* 535, A111.

Schatten, K. H., Wilcox, J. M., & Ness, N. F. 1969, *Solar Phys.* 6, 442.

Scherrer, P. H., Bogart, R. S., Bush, R. I., Hoeksema, J. T., Kosovichev, A. G., Schou, J., Rosenberg, W., Springer, L., Tarbell, T. D., Title, A., Wolfson, C. J., & Zayer, I., MDI Engineering Team 1995, *Solar Phys.* 162, 129.

Schrijver, C. J., Elmore, C., Kliem, B., Török, T., & Title, A. M. 2008, *Astrophys. J.* 674, 586.

Temmer, M., Veronig, A. M., Vršnak, B., Rybák, J., Gömöry, P., Stoiser, S., & Maričić, D. 2008, *Astrophys. J. Lett.* 673, L95.

Titov, V. S. & Démoulin, P. 1999, *Astron. Astrophys.* 351, 707.

Török, T. & Kliem, B. 2003, *Astron. Astrophys.* 406, 1043.

Török, T. & Kliem, B. 2005, *Astrophys. J. Lett.* 630, L97.

Török, T. & Kliem, B. 2007, *Astronom. Nachr.* 328, 743.

Török, T., Kliem, B., & Titov, V. S. 2004, *Astron. Astrophys.* 413, L27.

Török, T., Panasenco, O., Titov, V. S., Mikić, Z., Reeves, K. K., Velli, M., Linker, J. A., & De Toma, G. 2011, *Astrophys. J. Lett.* 739, L63.

Török, T., Temmer, M., Valori, G., Veronig, A. M., van Driel-Gesztelyi, L., & Vršnak, B. 2013, *Solar Phys.* 286, 453. referred to as **Paper I**

Williams, D. R., Török, T., Démoulin, P., van Driel-Gesztelyi, L., & Kliem, B. 2005, *Astrophys. J. Lett.* 628, L163.

Yang, J., Jiang, Y., Yang, B., Zheng, R., Yang, D., Hong, J., Li, H., & Bi, Y. 2012, *Solar Phys.* 279, 115.

Solar Physics
DOI: 10.1007/•••••-•••-•••-••••-•

A Parametric Study of Erupting Flux Rope Rotation

Modeling the "Cartwheel CME" on 9 April 2008

B. Kliem[1,2,3] · **T. Török**[4,5] · **W. T. Thompson**[6]

Abstract The rotation of erupting filaments in the solar corona is addressed through a parametric simulation study of unstable, rotating flux ropes in bipolar force-free initial equilibrium. The Lorentz force due to the external shear field component and the relaxation of tension in the twisted field are the major contributors to the rotation in this model, while reconnection with the ambient field is of minor importance, due to the field's simple structure. In the low-beta corona, the rotation is not guided by the changing orientation of the vertical field component's polarity inversion line with height. The model yields strong initial rotations which saturate in the corona and differ qualitatively from the profile of rotation *vs.* height obtained in a recent simulation of an eruption without preexisting flux rope. Both major mechanisms writhe the flux rope axis, converting part of the initial twist helicity, and produce rotation profiles which, to a large part, are very similar in a range of shear-twist combinations. A difference lies in the tendency of twist-driven rotation to saturate at lower heights than shear-driven rotation. For parameters characteristic of the source regions of erupting filaments and coronal mass ejections, the shear field is found to be the dominant origin of rotations in the corona and to be required if the rotation reaches angles of order 90 degrees and higher; it dominates even if the twist exceeds the threshold of the helical kink instability. The contributions by shear and twist to the total rotation can be disentangled in the analysis of observations if the rotation and rise profiles are simultaneously compared with model calculations. The resulting twist estimate allows one to judge whether the helical kink instability occurred. This is demonstrated for the erupting promi-

[1] Insitut für Physik und Astronomie, Universität Potsdam, Karl-Liebknecht-Str. 24-25, Potsdam 14476, Germany
email: bkliem@uni-potsdam.de
[2] Mullard Space Science Laboratory, University College London, Holmbury St. Mary, Dorking, Surrey RH5 6NT, UK
[3] College of Science, George Mason University, 4400 University Drive, Fairfax, VA 22030, USA
[4] LESIA, Observatoire de Paris, CNRS, UPMC, Université Paris Diderot, 5 place Jules Janssen, 92190 Meudon, France
[5] now at Predictive Science, Inc., 9990 Mesa Rim Road, Ste. 170, San Diego, CA 92121, USA
[6] Adnet Systems Inc., NASA Goddard Space Flight Center, Code 671, Greenbelt, MD 20771, USA

nence in the "Cartwheel CME" on 9 April 2008, which has shown a rotation of $\approx 115^\circ$ up to a height of 1.5 $R_\odot$ above the photosphere. Out of a range of initial equilibria which include strongly kink-unstable (twist $\Phi = 5\pi$), weakly kink-unstable ($\Phi = 3.5\pi$), and kink-stable ($\Phi = 2.5\pi$) configurations, only the evolution of the weakly kink-unstable flux rope matches the observations in their entirety.

Keywords: Corona, Active; Prominences, Dynamics; Coronal Mass Ejections, Initiation and Propagation; Magnetic fields, Corona; Magnetohydrodynamics

1. Introduction

The geoeffectiveness of solar coronal mass ejections (CMEs) depends primarily on two parameters, the velocity and the magnetic orientation of the CME at the impact on the Earth's magnetosphere. The higher the CME velocity and the closer its front side magnetic field to a southward orientation, the more intense the interaction will typically be. Therefore, understanding the physics that determines these CME parameters at 1 AU is one of the key issues in space weather research. This involves the formation and main acceleration of the CME in the solar corona, as well as its propagation through the interplanetary space. The particulars of the trigger process also play a role in some events. It appears that typically the corona is the place where the basic decisions are made: will the CME be fast or slow, and will it keep the orientation given by the source, *i.e.*, will its magnetic axis remain oriented nearly parallel to the photospheric polarity inversion line (PIL), or will it rotate substantially?

In the present paper we employ the technique of MHD simulation to carry out a first systematic, but in view of the problem's complexity necessarily incomplete investigation of a number of processes that cause and influence changes of CME orientation in the corona. Such changes can be described as a rotation of the CME volume, more specifically of the magnetic axis of the flux rope in the CME, about the direction of ascent. This *rotation* should be distinguished from the possible rotation of the flux rope about its own axis, referred to as the *roll effect* (Martin, 2003; Panasenco *et al.*, 2011), which we do not address here.

Understanding the rotation of erupting flux ropes in the corona is also relevant for the question which processes trigger the eruptions, as a substantial rotation may indicate the occurrence of the helical kink instability (KI); see, *e.g.*, Rust and Kumar (1996), Romano, Contarino, and Zuccarello (2003), and Rust and LaBonte (2005). This instability is one of the candidate mechanisms for the initiation of CMEs (Sakurai, 1976; Fan and Gibson, 2003; Kliem, Titov, and Török, 2004). It commences when the twist of the rope exceeds a critical value, $\Phi = 2\pi N > \Phi_{\rm cr}$, where N is the winding number of the field lines about the rope's magnetic axis. The dynamical evolution of the instability has shown very good quantitative agreement with a number of well observed events, which range from confined filament eruptions to the fastest CME on record (Török and Kliem, 2005; Williams *et al.*, 2005). However, Isenberg and Forbes (2007) have pointed out an alternative mechanism for the rotation of line-tied flux ropes, which relies

on the presence of an external toroidal field component, $B_{\rm et}$, due to sources external to the current in the flux rope and pointing along the rope, *i.e.*, an external shear field component. The mechanism can easily be understood in the simplified picture of a current loop in vacuum field. When the loop legs move out of their equilibrium position to a more vertical orientation, the cross product of the loop current with the shear field component yields a sideways Lorentz force on the legs, which is antisymmetric with respect to the vertical line that passes through the apex of the loop. This torque forces the rising top part of the loop to rotate. The effect is also found in a full fluid description (Lynch *et al.*, 2009). For a given chirality of the erupting field, it yields the same direction of rotation as the helical kink. Hence, a comparative study of these two mechanisms is required before firm conclusions about the occurrence of the KI can be drawn from observations of flux rope rotations, which is a further main objective of this paper.

Since the rotations caused by the KI and by the external shear field point in the same direction, they are difficult to disentangle. In fact, from a more general perspective, they are of similar nature. Both cause a writhing of the flux rope which, by conservation of magnetic helicity, reduces the twist of the rope field lines about the writhing axis. Consequently, one can expect that observed flux rope rotations are often consistent with a range of Φ–$B_{\rm et}$ parameter combinations which give the writhing of the flux rope by the helical kink and by the shear field different individual but similar combined strengths.

Other causes of flux rope rotation include magnetic reconnection with the ambient field (Jacobs *et al.*, 2009; Shiota *et al.*, 2010; Cohen *et al.*, 2010; Thompson, 2011; Vourlidas *et al.*, 2011) and the propagation through the overlying field. The latter comprises any asymmetric deflection of the rising flux from radial ascent, *e.g.*, by adjacent coronal holes (see, *e.g.*, Panasenco *et al.*, 2011), and the interaction with the heliospheric current sheet (Yurchyshyn, 2008; Yurchyshyn, Abramenko, and Tripathi, 2009).

One may conjecture that the generally changing orientation of the PIL with height in the corona acts similarly to the heliospheric current sheet at larger heights, *i.e.*, that the upper part of the rising flux continuously adjusts its orientation to align with the PIL. If this were the dominant effect, the rotation of erupting flux could be predicted rather straightforwardly from extrapolation of the photospheric field, since the overlying field is often close to the potential field. However, this conjecture is not valid in the lower corona where $\beta \ll 1$, and where the main part of the total rotation often occurs. We demonstrate this in the Appendix.

The amount of rotation depends on the individual strengths of the four potentially contributing processes. Each of them is controlled by more than a single parameter. This is immediately obvious for the torque by the shear field, which must depend on the height *profile* $B_{\rm et}(z)$, and for the reconnection, which is sensitive to the *structure* of the ambient field, *i.e.*, whether the field is bipolar, quadrupolar, or multipolar and whether the orientation of the line between the resulting new footpoints of the erupting flux differs strongly from the original orientation. The rotation by the KI does not only depend on the initial flux rope twist, $\Phi - \Phi_{\rm cr}$, but also on the strength and height profile of the overlying field (Török, Berger, and Kliem, 2010). If the overlying field decreases only slowly

with height, then the upward expansion develops slowly and, accordingly, its contribution to the relaxation of the field line tension is initially weak. The relaxation is then primarily accomplished by a strong rotation at small heights. In the opposite case of very strong upward expansion, the rotation is distributed across a large height range, which also increases the likelihood of further changes by the onset of reconnection (see Lugaz *et al.*, 2011 for an example). The effect of the heliospheric current sheet can be expected to depend on the angle with the top section of the flux rope's axis, on the horizontal elongation of the CME (whether its horizontal cross section is very elliptical or more nearly circular), and on the magnetic pressure of the CME relative to the pressure of the interplanetary plasma.

Moreover, the total rotation experienced by an erupting flux rope likely depends also on the dynamics of its evolution. For example, a torque strongly localized at low heights, operating on a still small loop, may hurl the flux around more efficiently than a torque which is distributed across a large height range. As another example, in a complex (multipolar) coronal environment the sequence and strength of reconnection with the ambient field may strongly depend upon the height profiles of the rope's angular and rise velocities caused by other processes, *e.g.*, by an ideal MHD instability. The relative velocity between reconnecting flux systems controls how strongly the reconnection with the ambient field is driven. Hence, quantitative studies of flux rope rotation face a very high degree of complexity.

Here we focus on two mechanisms that can cause strong rotations in the corona, the helical kink instability and the torque exerted by an external shear field component. By comparing a parametric study of both mechanisms in a force-free, line-tied flux rope equilibrium with the data of a well observed, strongly rotating erupting prominence, we demonstrate that their contributions can be disentangled to some degree. We also demonstrate the very strong influence of the ambient potential field's height profile on the amount of rotation by the KI, and briefly address the influence of reconnection between the CME flux rope and the ambient field on the rotation.

This investigation was stimulated by the analysis of the strong rotation in a prominence eruption and CME on 9 April 2008, occasionally referred to as the "Cartwheel CME", in Thompson, Kliem, and Török (2011, in the following Paper I). Their stereoscopic reconstruction revealed the height-rotation profile of the erupting filament/prominence in the core of a CME for the first time (Thompson, Kliem, and Toeroek, 2009). This profile provides a strong constraint for the numerical modeling. In combination with the further observations of the event, it allows us to infer the major causes of the rotation and the range of source parameters compatible with the data. The analysis of Paper I has given the following results relevant for the present study. The prominence erupted from the remnants of NOAA active region (AR) 10989 close to the west limb and appeared as a flux rope – a single, weakly to moderately twisted loop – throughout the height range covered by the STEREO EUVI and COR1 telescopes (Howard *et al.*, 2008), *i.e.*, up to 4 $R_\odot$ from Sun center. It rotated counterclockwise by $\approx 115^\circ$ up to a heliocentric height of 2.5 $R_\odot$, where the rotation leveled off. Two thirds of this rotation were acquired within 0.5 $R_\odot$

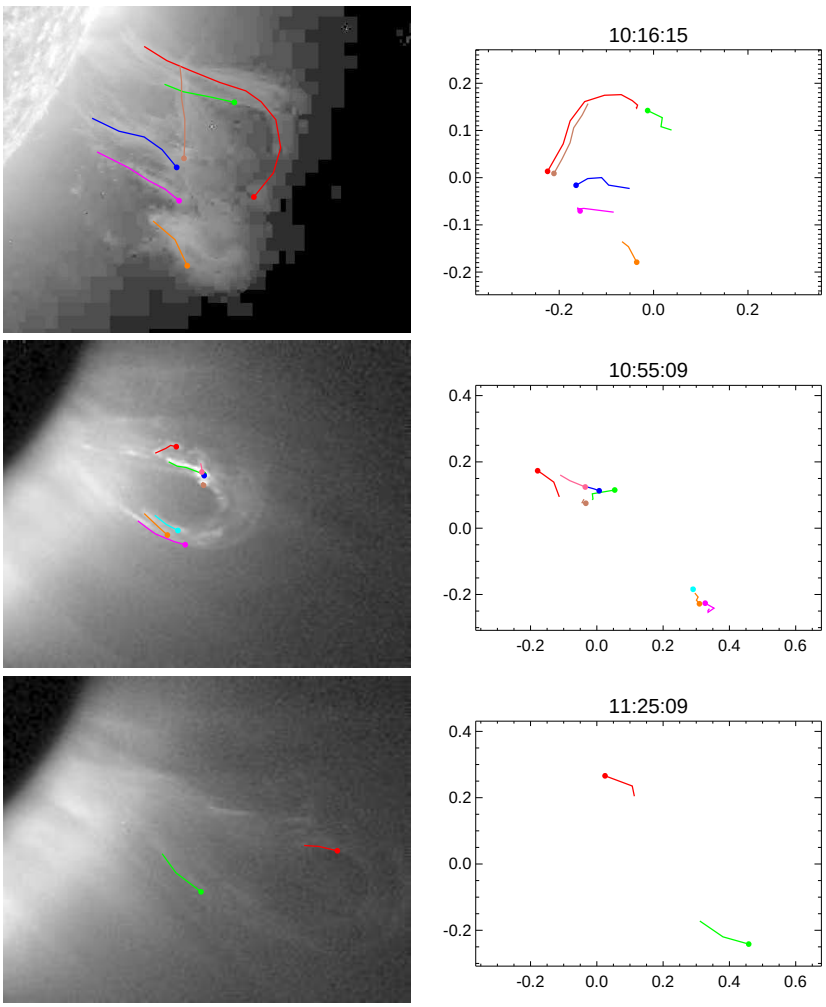

Figure 1. Images and plots of the prominence eruption at 10:16 UT, as seen by the EUVI-Ahead telescope in the 304 Å channel, and at 10:55 and 11:25 UT, as seen in white light by COR1-Ahead. The prominence apex has reached heights of 0.56, 1.6, and 2.3 $R_\odot$ above the photosphere at these times. The right panels display the reconstructed three-dimensional position of the marked prominence threads, using a reprojection to a viewpoint at the position of radial CME propagation, Stonyhurst longitude 98° west (relative to Earth) and latitude 24° south, where the counterclockwise rotation is apparent. The axes are in units of solar radii.

from the photosphere. The data indicate a subsequent gentle backward rotation by $\approx 15°$ in the height range up to 3.3 $R_\odot$. In addition, the analysis of STEREO COR2 data in Patsourakos and Vourlidas (2011) demonstrated that a flux rope structure is consistent also with the three-dimensional shape of the CME at a heliocentric distance of 13 $R_\odot$, where it had changed its orientation by a total of $150° \pm 7°$ from the original one, most likely by further counterclockwise rotation. At this stage the erupting flux was very closely aligned with the heliospheric

current sheet above the active region. The prominence was initially accelerated mainly horizontally along the filament channel. This gradually turned into a radial propagation at a position ≈98W24S as seen from Earth, 15°–20° away from the original location. The prominence experienced most of its upward acceleration in the heliocentric height range up to $\sim 2.5\ R_\odot$ and reached a velocity of $\sim 400\ \mathrm{km\,s^{-1}}$ in the COR2 field of view. At the same time, the leading edge of the CME accelerated to over $700\ \mathrm{km\,s^{-1}}$ (Landi *et al.*, 2010). Representative images of the prominence from STEREO *Ahead*, which had the best perspective at the structure, and the corresponding three-dimensional reconstructions of the location of several prominence threads are compiled in Figure 1 (from Paper I). The rotation (height-rotation) profile and the rise (time-height) profile are included below in the observation-simulation comparisons (Figures 6 and 8, respectively).

As already noted above, we focus our attention here on the coronal evolution of this event, leaving the interaction with the heliospheric current sheet for future investigation. Moreover, we exclude the possible slight backward rotation by $\approx 15°$ in the COR1 height range from our modeling, since we are interested in the generally important effects which cause significant rotations in the corona. This part of the rotation is not fully certain, and, if real, it was likely caused by the particular structure of the large-scale coronal field above the active region, which nearly reversed its horizontal direction at heights $\gtrsim 0.3\ R_\odot$ above the photosphere (Paper I). Thus, we will consider a saturation of the modeled rotation at angles near 115° and heights $h \approx (1.5\text{–}2.3)\ R_\odot$ above the photosphere to be in agreement with the observation data. Furthermore, we will disregard the initial nearly horizontal motion of the prominence along the PIL.

The combined effects of flux dispersal and foreshortening in the course of the source region's rotation to the solar limb made it impossible to obtain a well-defined estimate of the distance between the main flux concentrations in the bipolar region at the time of the eruption, which is a parameter of strong influence on the height profile of the ambient potential field. Only a relatively wide range of $\sim$(40–150) Mm could be estimated by extrapolating the region's evolution in the course of its disk passage through the final three days before the event. It will be seen that this range still sets a useful constraint on the modeling.

In the following we model the radial propagation of the prominence in the Cartwheel CME in the coronal range of heights as the MHD evolution of an unstable force-free and line-tied flux rope (Section 2). A parametric study of the resulting rotation and rise, focusing on the rotation caused by the helical kink instability and by the external shear field, is compared with the observation data, to constrain the parameters in the source of the event and to study whether the relative importance of these mechanisms can be disentangled and individually estimated (Section 3). The discussion in Section 4 addresses the simplifying assumptions made in the modeling and differences to earlier relevant work. Section 5 gives our conclusions. The Appendix relates the rotation of erupting flux ropes in low-beta plasma to the changing orientation of the PIL with height.

2. Numerical Model

We carry out a series of MHD simulations similar to the CME simulation in Török and Kliem (2005). The prominence is modeled as a section of an approximately force-free toroidal current channel embedded in external current-free (potential) field, which represents a modification of the approximate force-free equilibrium by Titov and Démoulin (1999). The current channel creates a flux rope structure of the magnetic field which has a somewhat larger cross section than the channel and is enclosed by a quasi-separatrix layer in the interface to the surrounding field of arcade structure. The chirality of the flux rope is chosen to be left handed, so that the rotation will be counterclockwise (Green *et al.*, 2007). The poloidal component of the external field, $B_{\rm ep}$, is due to a pair of subphotospheric magnetic point sources, which produce a pair of flux concentrations ("sunspots") to the sides of the flux rope (the "prominence") in the magnetogram. This field component holds the current channel in equilibrium; its strength at the position of the rope is exactly proportional to the current in the rope. Consequently, only its spatial profile, determined by the spacing between its sources, can be freely varied. The toroidal component of the external field, $B_{\rm et}$, is due to a pair of subphotospheric dipoles, positioned under the footpoints of the flux rope such that the field lines of $B_{\rm et}$ run parallel to the magnetic axis of the rope to a very good approximation. Therefore, $B_{\rm et}$ introduces only very minor Lorentz forces in the initial configuration, which quickly decrease by numerical relaxation at the beginning of each run, so that the strength of $B_{\rm et}$ can be chosen freely within a wide range. We will refer to the external toroidal field also as the shear field component. Here it decreases faster with height than the external toroidal field in the original Titov-Démoulin equilibrium. A visualization of the configuration is shown in Figure 2.

We integrate the ideal MHD equations but neglect pressure, as appropriate in the active-region corona, and gravity, because the hydrostatic pressure profile along the field is not essential for the flux rope rotation, which is driven by the Lorentz force. These simplifications yield maximum freedom in the scalability of the simulation results to the data. Magnetic reconnection can occur due to the numerical diffusion of the field in regions of strong gradients. The initial density is specified as $\rho_0(\mathbf{x}) = |\mathbf{B}_0(\mathbf{x})|^{3/2}$, where $\mathbf{B}_0(\mathbf{x})$ is the initial magnetic field. This yields a slow decrease of the Alfvén velocity with height, as in the corona. The box is a cube 64 units long on each side, significantly larger than in our previous simulations and in each direction at least twice as large as the biggest size of the structures that will be compared to the data. It is resolved by a nonuniform, fixed Cartesian grid with a resolution of 0.04 units in the central part of the box (a factor of 2 coarser than in Török and Kliem, 2005). Rigid boundary conditions are implemented at the top and side boundaries, while very small velocities are permitted in the bottom boundary. Initially the torus lies in the plane $\{x = 0\}$. The MHD variables are normalized by the initial apex height of the flux rope axis, h_0, by the initial field strength B_0, density ρ_0, and Alfvén velocity $V_{\rm A0}$ at this point, and by the corresponding quantities derived thereof, *e.g.*, the Alfvén time $\tau_A = h_0/V_{\rm A0}$. Thus, the initial apex height of the axis of the current channel and flux rope serves as the length unit.

The parameters of the initial configuration are largely chosen as in Török and Kliem (2005). We fix the major radius of the torus at $R = 1.83$, the depth of the torus center at $d = 0.83$ and the pre-normalization strength of the point sources at $q = 10^{14}$ Tm^2 in all runs. For a base set of the simulation series, discussed below in Figures 3–6 and 8–9, we further fix the distance of the point sources from the z axis at $L = 0.83$ (in units normalized such that h_0 is unity). This value lies in the middle of the estimated range for the corresponding distance of the flux concentrations in AR 10989, given above, when the scaling $h_0 = 0.077\ R_\odot$ adopted in Section 3.1 is applied. It also agrees with the settings in several previous investigations (*e.g.*, Török and Kliem, 2005; Török, Berger, and Kliem, 2010), facilitating comparisons. Variations of this parameter will be considered in the range $L = 0.42$–2.5. We vary the minor radius of the toroidal current channel, $a = 0.32$–0.62, and the strength of the external toroidal field, $B_{\rm et}/B_{\rm ep} = 0$–$1.06$ at the flux rope apex $\mathbf{x} = (0, 0, 1)$, to obtain a range of values for the average twist of the current channel, $\Phi = (2.5\text{–}5.0)\pi$, and for the strength of the shear field component. The twist is influenced by both a and $B_{\rm et}$, with a having the stronger influence within the considered range of parameters. The twist values quoted in this paper represent the initial twist averaged over the cross section of the current channel in the manner described in Török, Kliem, and Titov (2004).

The range of the initial average twist is chosen such that unstable and stable configurations with respect to the helical kink mode are included. The first group is unstable from the beginning of the simulation. Nevertheless, a small upward initial velocity perturbation is applied in the vicinity of the flux rope apex (typically ramped up to 0.05 $V_{\rm A0}$ over 5 τ_A and then switched off), to ensure that the instability displaces the apex upwards, *i.e.*, downward kinking is excluded in these runs which are intended to model CMEs.

For the geometric parameters of the system specified above, the flux rope is initially stable with respect to the torus instability (Kliem and Török, 2006; Török and Kliem, 2007). However, the helical kink instability lifts the rope into the torus-unstable range of heights ($h \gtrsim 2\ h_0$), from where the torus instability accelerates its top part further upwards.[1] The kink-stable cases require that the upward velocity perturbation is applied for a longer time, lifting the apex into the torus-unstable range. This allows us to study the influence of the shear field on the rotation in the absence of the helical kink instability, using uniform geometrical parameters of the initial flux rope (except for the minor flux rope radius a) in all runs. An initial velocity perturbation very close to the required minimum value is applied in each of these cases, to ensure nearly uniform conditions at the onset of the instability throughout the series. The values at the end of the ramp phase stay below 0.12 $V_{\rm A0}$ for all runs. The flux rope velocity falls back to a much smaller value (typically $\approx$0.01 $V_{\rm A0}$) immediately after the perturbation is switched off. The growing instabilities then accelerate the apex to peak upward velocities in the range $\max\{u_{\rm a}\} \approx (0.4\text{–}0.7)\ V_{\rm A0}$, far higher than the initial perturbation.

[1]The torus instability can be considered as a lateral kink of the current channel. However, we choose "kink" and "KI" to refer exclusively to the helical kink mode in this paper.

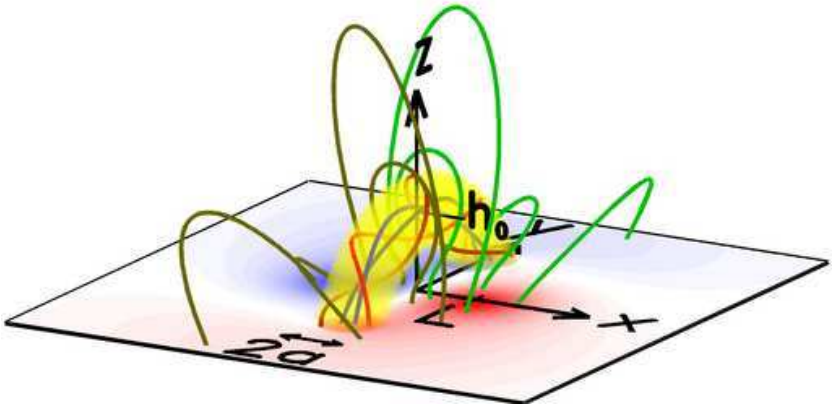

Figure 2. Visualization of the modified Titov-Démoulin flux rope equilibrium used as the initial condition in the simulation runs of this paper; here with an average twist $\Phi = 3.5\pi$ as in Figure 4. The current channel is rendered as a yellow transparent volume. Blue field lines run near the magnetic axis of the flux rope (where the local twist is 2π), red field lines lie in the flux surface at a distance to the axis where the local twist equals the average twist. Green and olive field lines show the ambient potential field. Contours of the magnetogram, $B_z(x, y, 0)$, are shown in the bottom plane. The torus of major radius R and minor radius a is submerged by a distance d, resulting in the apex height $h_0 = R - d$ and the distance of each flux rope footpoint from the origin $D_\mathrm{f} = (R^2 - d^2)^{1/2}$. A bipole, whose components are located at $(\pm L, 0, -d)$, is the source of the external poloidal field component B_ep; see Figure 2 in Titov and Démoulin (1999) for its visualization. A pair of antiparallel, vertically oriented dipoles, placed under the footpoints of the flux rope at $(0, \pm D_\mathrm{f}, -5h_0)$, provides the source of the external toroidal (shear) field component B_et.

On the Sun, the initial lifting of the flux can occur by a variety of effects in addition to the helical kink mode, as has been demonstrated by numerical simulations. These include the shearing and twisting of the coronal field by photospheric flows (*e.g.*, Mikic and Linker, 1994; Török and Kliem, 2003), reconnection associated with flux cancellation in the photosphere (*e.g.*, Aulanier *et al.*, 2010; Amari *et al.*, 2010), and reconnection with newly emerging flux (Chen and Shibata, 2000).

The observations of the Cartwheel event indicate a gradual doubling of the prominence height prior to the eruption (Paper I). The initial lifting of the flux rope apex in the simulations due to the applied perturbation is much smaller for all kink-unstable runs and stays in the range up to this value for the kink-stable cases, except for the run with the highest shear field ($\Phi = 2.5\pi$, $B_\mathrm{et}/B_\mathrm{ep} = 1.06$), which requires a lifting to 2.6 h_0.

3. Comparison Simulations-Observations

3.1. Dependence of Flux Rope Rotation on Twist and Shear

We begin with a case that involves a clear helical kink instability, as one would expect at first sight from the considerable rotation observed in the Cartwheel event.

The initial average twist is chosen to be $\Phi = 5\pi$, a value used previously in the successful modeling of several filament/prominence eruptions (Williams *et al.*, 2005; Török and Kliem, 2005). Even with this considerable amount of twist (and with the sunspot semi-distance $L = 0.83$), we find that a shear field is required to reach the observed rotation. Figure 3 shows the resulting rotation of the flux rope, which reaches the observed value of 115° and is a combined effect of the helical kink instability and the shear field. The field lines visualize a flux bundle in the core of the rope which runs slightly ($\approx$5%) under the rope axis in its top part. This is a likely location for prominence material within a flux rope. Moreover, this is the only selection that allows a favorable comparison with the observed flux rope shape for the weakly twisted case shown below in Figure 5, while the more strongly twisted cases are less sensitive to this vertical offset. Therefore, we adopt this selection as a uniform choice for Figures 3-5 which compare the flux rope rotation for different twist values. The field lines are displayed from perspectives identical to the STEREO images and reconstructions in Figure 1.

Two characteristic morphological features apparent in the COR1 data in Figure 1 are weakly indicated in the simulation: the initial teardrop-like appearance and the elongated shape at large heights (relatively narrow in the horizontal direction). The right panels show that the teardrop shape is a projection effect. The legs of the erupting rope approach each other near the edge of the occulting disk only in projection; they are displaced along the line of sight and actually moving away from each other. The elongated shape is largely also due to the strong rotation.

The legs of the rope appear "wiggly", which results from two effects. First, they reconnect with the ambient field in the vertical current sheet under the flux rope apex in the interval $t \approx$ (32–65) τ_A, which corresponds to apex heights $h \approx$ (5–21) h_0; with the reconnection proceeding at much lower heights inside the edge of the COR1 occulting disk. This leads to a bend in the reconnected flux rope: the field lines have relatively small curvature within the legs of the expanded original rope above the reconnection point but run along a more helical path in the ambient field just outside the original rope below the reconnection point. This bend and the more helical shape of the field lines below it relax upward, along with the overall upward expansion of the reconnected flux rope. Since the flux rope apex has reached a considerable upward velocity, $u_a \lesssim 0.5\, V_A$, the bend needs a large height range for its propagation to the top of the rope. It is located slightly above the dotted line in the third snapshot pair of Figure 3 and at $h \gtrsim 15\ h_0$ in the final snapshot pair. The plots on the right hand side show that the new footpoints of the rope are displaced in counterclockwise direction from the original ones, thus contributing to the overall counterclockwise rotation of the rope. However, this contribution is only a minor one; the major part of the total rotation occurs before the flux rope legs reconnect (which can be seen by comparison with Figure 6 below). This reconnection is similar to the second and third reconnections described in Gibson and Fan (2008, their Section 4.1) and will be addressed in more detail in a future investigation. Second, at the given relatively high value of the twist, the dominant wavelength of the helical kink mode is considerably shorter than the flux rope, so that the characteristic helical shape develops clearly.

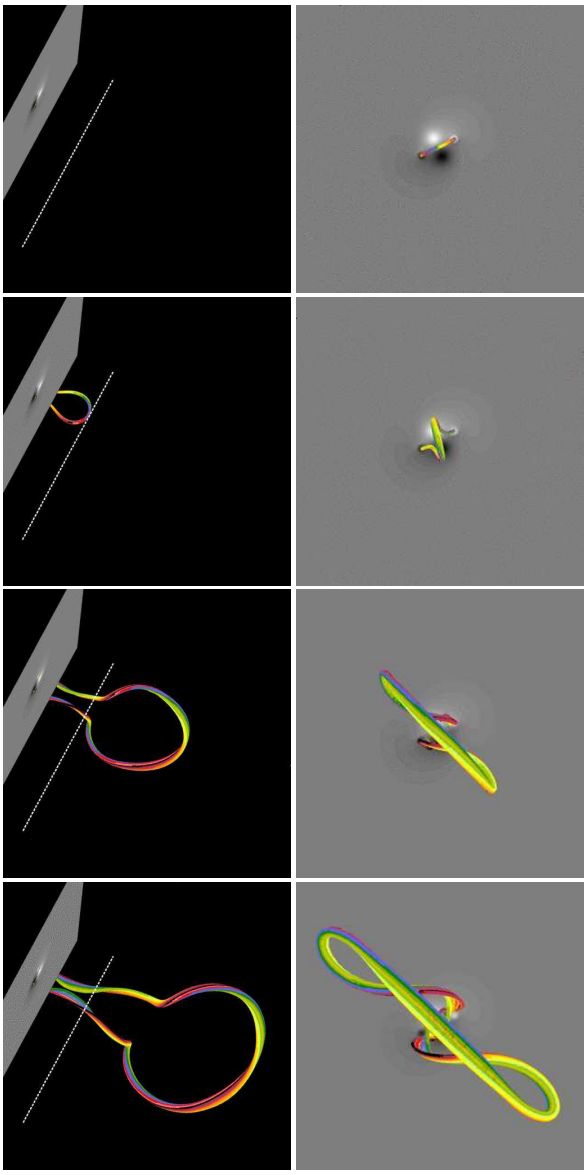

Figure 3. Snapshots of an erupting and rotating, strongly kink-unstable flux rope. The initial average twist is $\Phi = 5\pi$ and the shear field component at the initial flux rope apex position is given by $B_{\rm et}/B_{\rm ep} = 0.42$. Field lines in the core of the rope, traced downward from the apex, are shown in the height range $0 \leq z \lesssim 30$, using the same two perspectives as for the observation data in Figure 1 (in the left panels the line of sight makes an angle of 26° with the y axis, and the z axis is tilted away from the observer by 8°, while the right panels present a vertical view with an initial angle between the flux rope axis and the east-west direction of 26°). The magnetogram, $B_z(x, y, 0, t)$, is displayed in grayscale (seen from below in the left panels). The dotted line indicates where the edge of the COR1 occulting disk is located if the distance between the flux rope footpoints in the simulation, $2D_{\rm f} = 3.3\ h_0$, is scaled to the value of 175 Mm estimated in Paper I. Using this scaling, the simulated heights of $h = 1$, 7.3, 21, and 30 h_0 (at $t = 0$, 36, 64, and 84 τ_A) translate to heights of 0.077, 0.56, 1.6, and 2.3 $R_\odot$ above the photosphere, reached at 10:16, 10:55, and 11:25 UT (for rows 2–4), respectively.

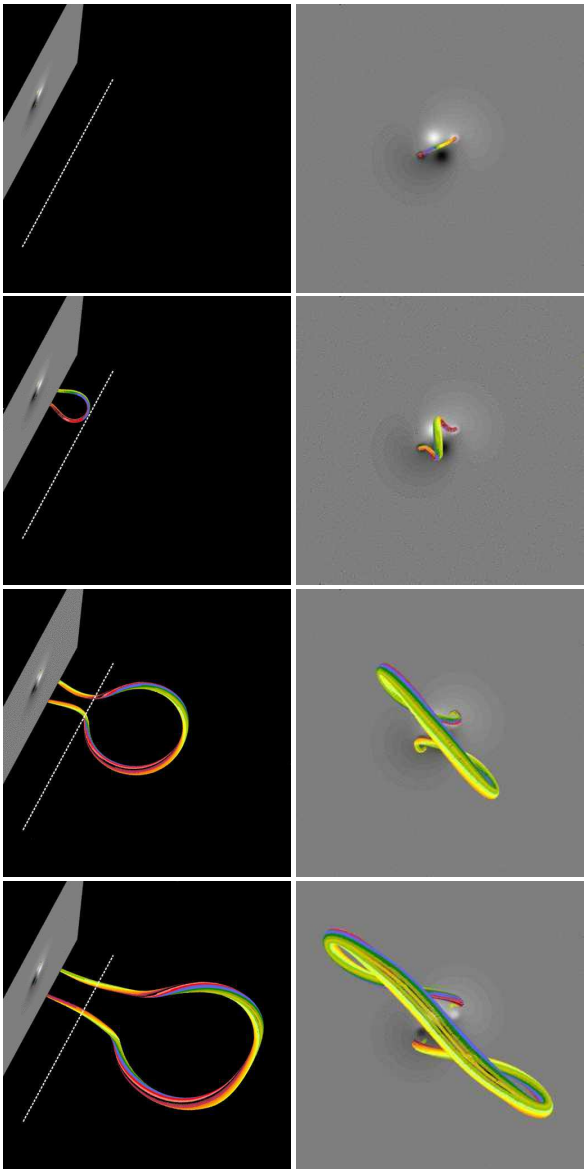

Figure 4. Same as Figure 3 for a weakly kink-unstable case with initial avarage twist $\Phi = 3.5\pi$ and shear field $B_{\rm et}/B_{\rm ep} = 0.67$. The flux rope is shown at the simulation times $t = 0$, 50, 80, and 97 τ_A which yield the same heights as the snapshots in Figure 3, corresponding to the same observation times.

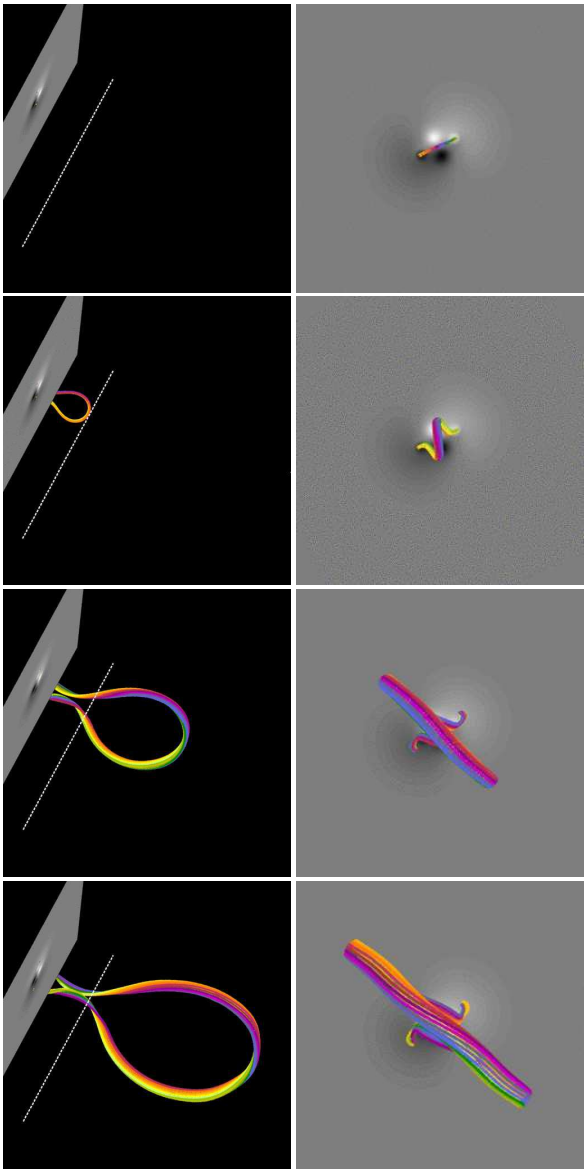

Figure 5. Same as Figure 3 for a kink-stable case with initial avarage twist $\Phi = 2.5\pi$ and shear field $B_{\rm et}/B_{\rm ep} = 1.06$. The flux rope is shown at the simulation times $t = 0$, 77, 109, and 128 τ_A which yield the same heights as the snapshots in Figure 3, corresponding to the same observation times.

Figure 4 shows the evolution in a second run where the KI develops only weakly, using a moderate, only slightly supercritical value of the initial average twist, $\Phi = 3.5\pi$. A stronger shear field is chosen, so that the same total rotation is achieved. The overall properties – accelerated rise into an ejection (CME) and very strong rotation – are identical to the run shown in Figure 3. The morphological details, such as the teardrop shape at small heights and the elongated shape at large heights, match the data slightly better. The indications of wiggly shape at large heights remain weak. Reconnection of the flux rope legs with the ambient field occurs here as well, but the resulting changes in the shape of the flux rope are weaker, since not only the field lines in the rope are less twisted but also the ambient field is less helical, due to the larger $B_{\rm et}$. This morphological difference to the strongly twisted flux rope is one aspect that may allow to distinguish between rotations with strong and weak involvement of the helical kink in observed events. The field line shapes in the present case conform slightly better to the inclination of the prominence threads with respect to the axis of the flux rope in the COR1 data in Figure 1, but this difference is not sufficiently clear to be decisive by itself. Moreover, it depends to a considerable degree upon which part of the erupting flux was outlined by prominence material in the considered event and on the selection of field lines in the plots.

Figure 5 presents a case with subcritical flux rope twist, $\Phi = 2.5\pi$, where the kink instability cannot develop and an even stronger shear field is needed to achieve a similar rotation. Here the parameters were chosen such that the rotation matches the observations as well as the other two runs in the height range $h \lesssim 20\ h_0$, with the total rotation of the rope's magnetic axis at $h = 30\ h_0$ exceeding the rotation in those runs by 20–25 degrees. The elongated teardrop shape at intermediate and large heights yields the best match of the three runs shown in Figures 3–5. However, this is only the case because a flux bundle slightly under the magnetic axis of the flux rope is selected in the visualization. If instead a set of field lines encircling the flux rope axis is chosen, then the high total rotation at the apex height $h = 30\ h_0$ leads to an inverse teardrop shape (narrow at the apex, because at this point the view is nearly along the axis of the rotated flux rope), which is inconsistent with the observations. Again, since it is not known which parts of the erupting flux (rope) were filled with prominence material in the event to be modeled, these morphological comparisons, by themselves, do not allow to rule out the kink-stable run shown in Figure 5.

The similar total rotations in the three simulations confirm that both twist and shear belong to the key parameters which determine the amount of rotation in erupting flux ropes. To analyze this further, we consider a set of characteristic cases from our series of simulation runs with varying strength of the two effects. For each of the twist values $\Phi = 5.0$, 3.5, and 2.5π, we vary the shear field $B_{\rm et}$ from the respective best fitting value used in Figures 3–5. All runs use the same sunspot semi-distance $L = 0.83$ and, hence, the same external poloidal field $B_{\rm ep}$. The variation of L will be considered in Section 3.2.

The rotation of the flux rope in the simulations is measured in two ways. At low heights it is taken from the changing orientation of the magnetic axis at the apex of the flux rope. As the flux rope rises, the apex orientation oscillates increasingly, due to the upward propagation of Alfvénic perturbations which

result from the dynamic onset of reconnection in the vertical current sheet under the rope (the relaxation of the bend in the reconnected field lines mentioned above). The right panels at the two final heights in Figures 4–5 indicate the resulting oscillations of the field orientation at the apex with respect to the bulk orientation of the flux rope's upper part. Therefore, at larger heights we simply use the direction of the horizontal line connecting the flux rope legs at the height where they are most distant from each other. This measurement filters away most of the oscillating variations, which are also not captured by the observed rotation data derived in Paper I and replotted in Figure 6. The difference between the two measurements remains less than 5 percent in a height range $\Delta h \sim$ (3–6) h_0 around $h \sim 10\ h_0$, except for the most strongly rotating and oscillating case in the series ($\Phi = 5\pi$, $B_{\rm et}/B_{\rm ep} = 0.63$) where it reaches ≈ 10 percent. Linear interpolation between the two measurements for each simulation run is applied in the appropriate range of small difference to match them smoothly. (The method to estimate the rotation angle at large heights fails for one of the runs in Figure 6 ($\Phi = 2.5\pi$, $B_{\rm et} = 0$), where reconnection of the flux rope legs with the ambient field leads to jumps that are larger than the oscillations of the magnetic axis at the apex. For this run, whose rotation profile differs strongly from the observed one, we include the rotation angle only at low heights, to show the trend.)

In order to compare the simulated rotation profiles with the observations, a scaling of the length unit in the simulations to distances on the Sun is required. For this purpose, we set the distance between the footpoints of the flux rope in the simulation, $2D_{\rm f} = 3.3\ h_0$, equal to the estimated length of the flux which holds the prominence, 175 Mm (Paper I). This is independent of the actual prominence shape. The apex height of the toroidal Titov-Démoulin flux rope, our length unit, tends to be somewhat high in comparison to solar prominences, which are often quite flat. Here we obtain $h_0 = 0.077\ R_\odot$, relatively close to the estimated initial prominence height of $\approx$ (0.05–0.06) $R_\odot$ (Paper I). If we would instead choose to compare the simulations to the temporal profile of the prominence rotation, then each change of the twist, which implies a change of the KI growth rate, would require a rescaling of the time unit in the simulations, τ_A. The comparison of the simulated rotation profiles with the observed profile is displayed in Figure 6. As discussed in Sections 1 and 4, we disregard the slight backward rotation at $h \gtrsim 1.5\ R_\odot$ above the photosphere in the comparison and assume that the tendency of the rotation to level off at this height would have continued in the absence of the specific complex structure of the large-scale coronal field above AR 10989 and in the absence of the heliospheric current sheet, which are not included in our model. Several conclusions can be drawn from this set of simulations.

(1) Similar height-rotation profiles (not only a similar total rotation) are obtained in a range of Φ-$B_{\rm et}$ combinations. The profiles for $(\Phi, B_{\rm et}/B_{\rm ep}) = (5\pi, 0.42)$, $(3.5\pi, 0.67)$, and $(2.5\pi, 1.06)$ all match the observed profile very well up to a height $h \sim 20\ h_0 \approx 1.5\ R_\odot$ above the photosphere, where a total rotation of $\approx 115°$ is observed. These runs include a strongly and a weakly kink-unstable and a kink-stable case. Hence, even such a strong rotation does not by itself imply the occurrence of the helical kink instability. Further arguments, such as

those given below, are required to draw conclusions about the occurrence of the instability in the modeled event.

(2) To reach the observed total rotation of $\approx 115^\circ$ with the initial configuration and parameter settings chosen in this series, in particular with the chosen value of the sunspot semi-distance L, the shear must contribute. The strongly twisted configuration ($\Phi = 5\pi$) yields only little more than one third of the observed rotation in the absence of shear ($B_{\rm et} = 0$). Therefore, the shear contributes the main part of the total rotation even in this strongly kink-unstable case. Note that this conclusion changes if the sunspot distance is set to larger (however, unrealistic) values, so that the overlying field decreases less steeply with height (see Section 3.2).

(3) The twist also contributes in all runs. The tension of the twisted field relaxes in any case when the flux rope is driven upward out of its initial equilibrium, be it by the helical kink instability, by the torus instability, or by any other process (*e.g.*, by so-called tether-cutting reconnection). This relaxation contributes to the writhing of the flux rope axis regardless of whether or not the helical kink instability is triggered. As a consequence, we do not observe a jump in the achieved rotation as the twist of the initial equilibrium is varied between kink-stable and kink-unstable values. This is most obvious from the runs with $B_{\rm et} = 0$.

(4) The higher the relative contribution of the twist, the lower the height range where most of the rotation is reached. This reflects the fact that the KI tends to reach saturation quickly, often already when the flux rope has risen to a height comparable to the footpoint distance (*e.g.*, Török, Kliem, and Titov, 2004). This property corresponds well to the tendency of the rotation to level off at the relatively low height of $\approx 1.5\ R_\odot$ ($\approx 20\ h_0$) above the photosphere. The rotation by the shear field acts in a larger height range. The different behavior can be made plausible from the fact that the Lorentz force due to the shear field depends on the current through the rope and on the angle between the flux rope legs and the shear field. While the current decreases as the rope ascends (similar to the twist), the angle rises until the legs approach a vertical position, which corresponds to bigger apex heights than the saturation height of the helical kink mode. Hence, the Lorentz force due to the shear field acts strongly in a larger height range than the tension force associated with the twist.

As a consequence, the Titov-Démoulin flux rope with sub-critical twist for KI onset does not allow to match the entire observed rotation profile of the 9 April 2008 event. We have performed considerable numerical experimenting in this range of twists [$\Phi = (2.5\text{–}3)\pi$], including modifications of the height profiles $B_{\rm et}(z)$ and $B_{\rm ep}(z)$ and of the flux rope shape (by varying its major radius R but not the apex height h_0) from the uniform settings for the runs in Figure 6. Either the rotation in the height range $h \lesssim 20\ h_0$ was found to be too small, or the total rotation at $h = 30\ h_0$ was too large. Although the shape of the prominence in the plane of the sky can still be met by the special selection of the field lines in Figure 5, the saturation of the rotation at $h \approx 1.5\ R_\odot$, revealed by the stereoscopic reconstruction, cannot be reproduced. This suggests that at least a weak helical kink instability must have been triggered in this event.

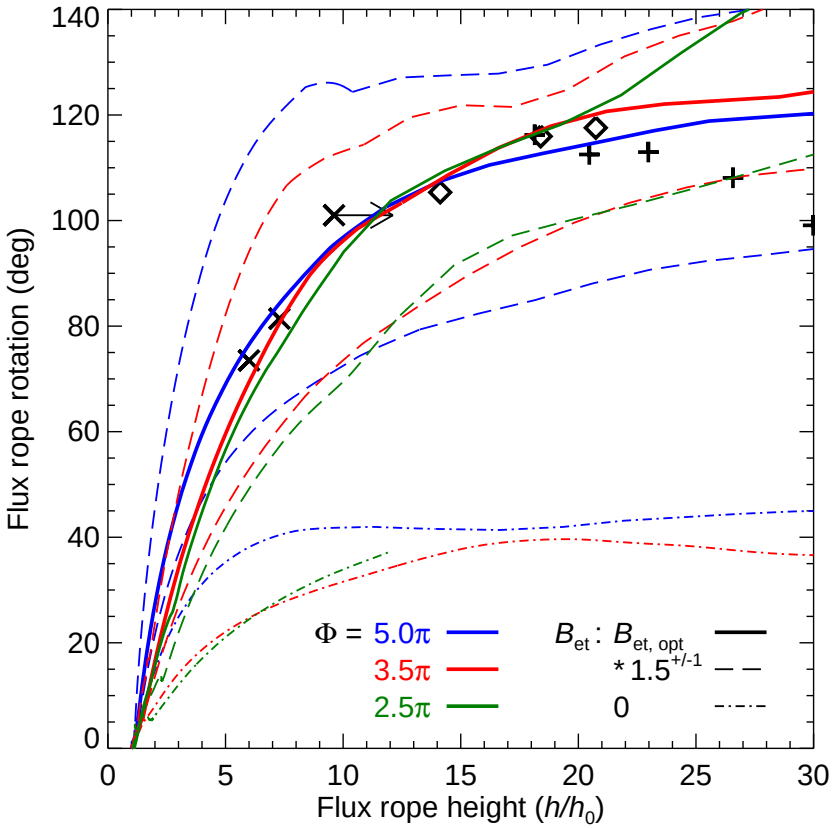

Figure 6. Comparison of flux rope rotation as a function of normalized apex height above the photosphere with the observation data obtained in Paper I. Crosses and diamonds are EUVI data, with the final cross representing a lower limit for the height and the diamonds representing interpolated heights. Plus symbols are COR1 data. The distance between the footpoints of the flux rope in the simulation is scaled to the value of 175 Mm estimated in Paper I, resulting in $h_0 = 0.077\ R_\odot$. The initial average twist, Φ, and the strength of the shear field component (external toroidal field), B_{et}, given by its ratio to the external poloidal field component B_{ep} at the initial flux rope apex, are varied, while the geometrical parameters of the initial flux rope (except the minor radius a) and the spatial structure of the external field components B_{et} and B_{ep} are uniformly chosen throughout the series of runs (see Section 2 for detail). The optimum values for the shear field strength, which yield the best match with the observed rotation profile up to $h \approx 20\ h_0$, found through parametric search, are $B_{et,\,opt}/B_{ep} = 0.42$, 0.67, and 1.06 for $\Phi = 5.0\pi$, 3.5π, and 2.5π, respectively. Changes of B_{et} by a factor 3/2 and the case $B_{et} = 0$ are included.

(5) The range of twist-shear combinations that reproduce the observed rotation profile is bounded not only from below, as outlined in (2) and (4), but also from above. Average twists significantly exceeding 5π are not only unlikely to occur in the corona but also lead to increasingly strong helical deformations of the flux rope, which are favorable for the onset of magnetic reconnection with the overlying field or between the flux rope legs. Such reconnection can strongly distort the rotation profile and can even stop the rise of the flux rope (Török and Kliem, 2005; Shiota *et al.*, 2010). Reconnection with the overlying

field does indeed lead to a confined (failed) eruption in the present simulation series when the initial twist is raised to 6π. Reconnection between the legs of the rope occurs if $\Phi \geq 7\pi$, also leading to confined eruptions. (A detailed description of such reconnection can be found in Kliem *et al.*, 2010.)

Increasing the shear field tends to stabilize the flux rope because any displacement then requires an increasing amount of energy to push the ambient field aside. The low-twist case ($\Phi = 2.5\pi$) with the strongest shear field included in Figure 6 requires a considerable initial perturbation to reach the torus-unstable range of heights ($h > 2.6\ h_0 = 0.2\ R_\odot$ for these parameters); it is completely stable to small perturbations. Similarly, while the 3.5π run with $B_{\rm et} = 0$ is clearly kink-unstable, the corresponding sheared case ($B_{\rm et}/B_{\rm ep} = 0.67$) exceeds the instability threshold only slightly. The initial lifting of the flux rope required in the low-twist case strongly exceeds the observed rise of the prominence to $\approx 0.06\ R_\odot$ prior to the onset of the eruption. This represents a further strong indication against this configuration.

The upper limit for the shear field is not a universal number but depends on other parameters of the system, which include the thickness of the flux rope, the strength of the line tying, and the height profile of the external poloidal field, $B_{\rm ep}(z)$. A systematic study of these dependencies would be beyond the scope of the present investigation. However, we have considered a change of the height profile $B_{\rm ep}(z)$, which is the key parameter for the onset of the torus instability in the absence of shear and significant line tying (Kliem and Török, 2006). In an attempt to ease the occurrence of the instability in the low-twist case ($\Phi = 2.5\pi$, $B_{\rm et}/B_{\rm ep} = 1.06$), the sunspot semi-distance was reduced to the minimum value of the possible range estimated from the observations, $L = 0.4$, leaving the other parameters of the equilibrium unchanged. No reduction of the minimum height for instability was found, which must be due to the strong stabilizing effect by the chosen shear field.

(6) Reconnection of the flux rope legs with the ambient field contributes only a minor part of the total rotation in our simulation series. It appears to remain weaker than the twist-driven rotation, or at most comparable, *i.e.*, considerably weaker than the shear-driven rotation. This can be seen most clearly in the 5π run with $B_{\rm et} = 0$. Here the reconnection of the flux rope legs with the ambient field proceeds while the rope apex rises from $\approx 2\ h_0$ to $\approx 16\ h_0$, with the flux in the core of the rope being involved in the range of apex heights $h \sim$ (4–16) h_0. However, the major part of the total rotation of $\approx 40^\circ$ is already reached at low apex heights, $h \lesssim 5\ h_0$, *i.e.*, due to the helical kink mode. The apex height range during the reconnection of the flux rope legs in the shear-free 3.5π run is similar to the 5π run. The rotation profile of this run in Figure 6 shows about equal amounts of rotation in the height ranges $h \lesssim 5\ h_0$ and $h \sim$ (5–16) h_0, indicating that the reconnection-driven rotation could here be comparable to the twist-driven rotation. Again, both remain considerably smaller than the rotation due to the shear in the 3.5π run that best fits the observation data.

These conclusions are also supported by the fact that the angular distance between the initial and new footpoints of the flux rope's magnetic axis, measured from $\mathbf{x} = 0$, remains far smaller than the total rotation of the rope (see the right panels in Figures 3–5).

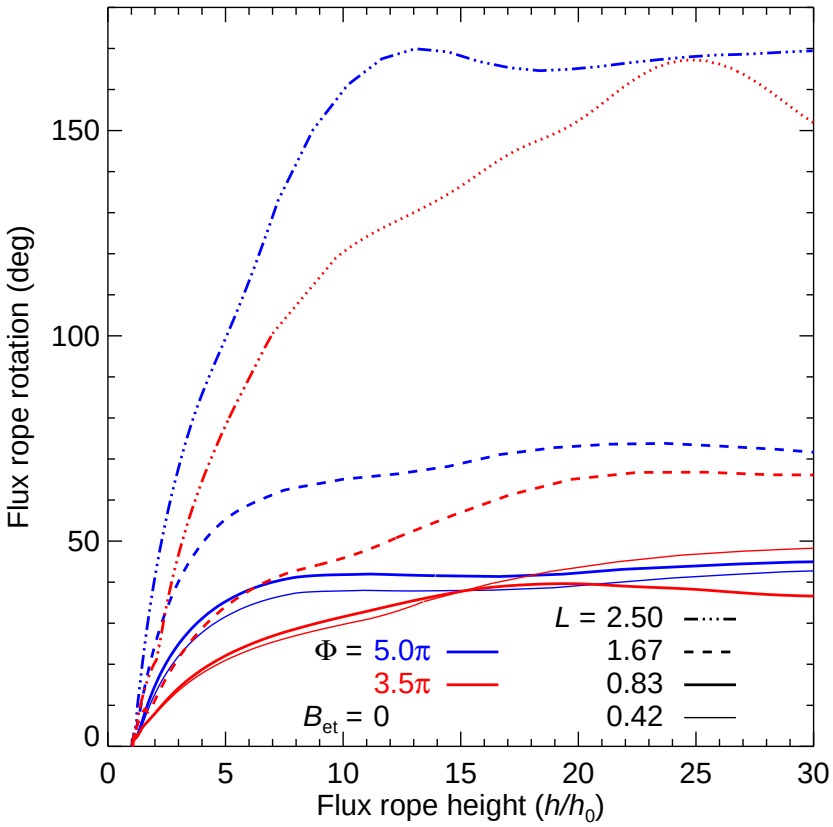

Figure 7. Dependence of flux rope rotation *vs.* height upon the distance L of the main flux concentrations in the source region from the PIL. Kink-unstable flux ropes ($\Phi = 5\pi$ and 3.5π) are considered for vanishing external shear field component, $B_{\rm et} = 0$.

3.2. Influence of the External Poloidal Field

The height profile of the poloidal field which is due to sources external to the flux rope, $B_{\rm ep}$, is a further factor of potentially strong influence on the rotation. Erupting flux ropes rotate more strongly at low heights if the external field initially overlying the flux rope decreases more gradually with increasing height (Török, Berger, and Kliem, 2010). The relaxation of the magnetic tension in the erupting flux rope by rotation is then more pronounced because the relaxation by upward expansion is hindered, at least initially. The relevant length scale, $l_z = -[{\rm d}(\log B_{\rm ep})/{\rm d}z]^{-1}$, increases with increasing distance between the sources of $B_{\rm ep}$, *i.e.*, between the main flux concentrations to the sides of the PIL. This can easily be seen for the Titov-Démoulin equilibrium, where this scale height is $l_z = (z+d)[1+L^2/(z+d)^2]/3$.

Figure 7 shows that this effect remains weak as long as the distance between the sources of $B_{\rm ep}$, $2L$, is smaller than distance between the footpoints of the erupting flux rope, $2D_{\rm f}$, but that it becomes very strong when the reverse relation holds. Here the sunspot semi-distance L is varied for the 5π and 3.5π runs

with no external shear field, $B_{\rm et} = 0$, to be 0.5, 1, 2, and 3 times the value estimated from the observations and used in Section 3.1 (Figures 3–6). The two distances are nearly equal if L is set to twice the estimated value. This is larger than the maximum of the range for L compatible with the observations (see the Introduction). Hence, the conclusions drawn from the series of simulations shown in Figure 6 are not sensitive to the actual value of the parameter L as long as it remains within this range. In particular, an external shear field component of strength close to the optimum values given in this figure is then required to reach the observed rotation.

Rotations even exceeding those produced mainly by the shear field in Figure 6 are achieved in the absence of a shear field for both twists if L exceeds $D_{\rm f}$ by a factor $\gtrsim 1.5$. A similar situation was realized in simulations of erupting flux ropes in Fan and Gibson (2003) and Gibson and Fan (2008), which showed strong rotations of 115–120 degrees with $B_{\rm et} = 0$. However, such large distances of the main polarities, relative to the length of the PIL and a filament channel between them, do not typically occur in fully developed active regions. Hence, the effect of a shear field (Isenberg and Forbes, 2007) will typically be involved if erupting flux rotates by large angles of order 90° and more.

3.3. Rise Profile

The results of Sections 3.1–3.2 lead to the question whether the initial twist and the shear field in the source volume of the eruption can be further constrained individually, although their combined effect on the rotation is similar. The rotation profile obviously is a powerful new diagnostic of the evolution of flux ropes in CMEs, however, for the considered event it does not allow to discriminate between the strongly and weakly kink-unstable cases shown in Figures 3 and 4, respectively. Therefore, we now consider the rise (time-height) profile of the erupting flux. This function reflects the growth rate of the instability driving the eruption. The growth rate varies strongly with the twist if this parameter exceeds the threshold of the helical kink mode (see, *e.g.*, Figure 5 in Török, Kliem, and Titov, 2004). When the variation of the twist is combined with a variation of the shear field strength in the opposite direction (one increasing, the other decreasing), such that the rotation profile stays nearly unchanged, then the rise profile will change even stronger: decreasing (increasing) shear field strength leads to higher (lower) KI growth rate. Thus, the combined comparison can constrain these parameters individually.

In order to compare the simulated rise profiles with the observed one, the time unit in the simulations, τ_A, must also be scaled to a dimensional value. Since $\tau_A = h_0/V_{\rm A0}$ and h_0 is already scaled, this is equivalent to adopting a value for the initial Alfvén velocity $V_{\rm A0}$ in the body of the prominence. So far, this parameter can hardly be derived from observations, since both the field and density structure of prominences are generally only poorly known. Therefore, here we work backwards by first finding the best match between the simulated and observed rise profiles and then checking whether the implied Alfvén velocity falls within an acceptable range. Lower bounds on the Alfvén velocity in filaments have been obtained through the application of seismological techniques to six

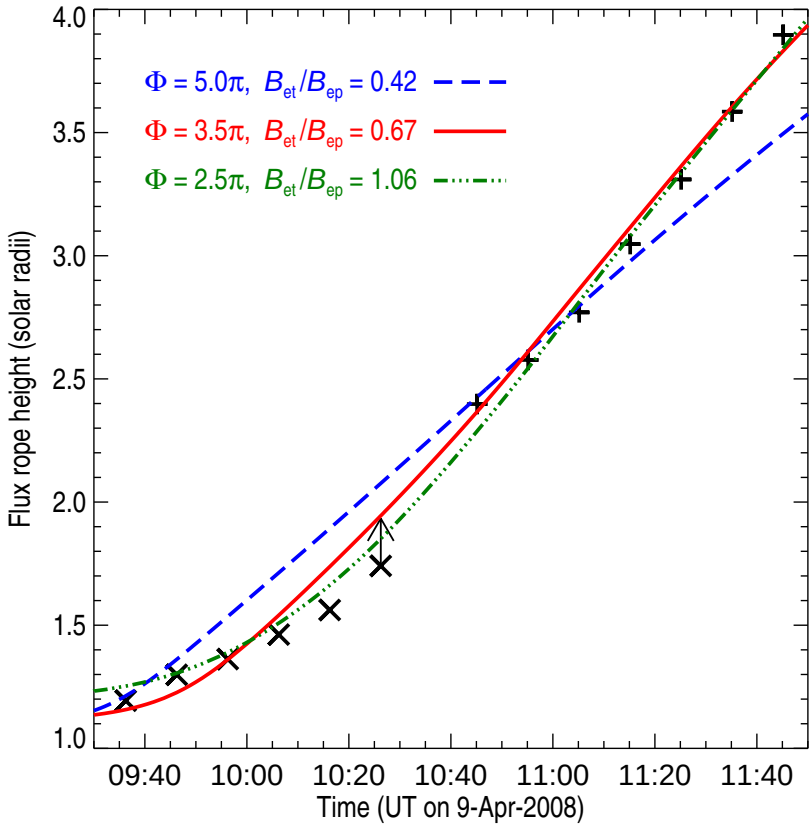

Figure 8. Comparison of the observed and simulated rise profiles of the flux rope apex, using the same scaling of lengths in the simulations as in Figure 6 and a start time of the eruption at 08:48:00 UT. EUVI and COR1 data from Paper I are plotted using the same symbols as in Figure 6. The 5π, 3.5π, and 2.5π runs of Figures 3–5 are scaled to these data assuming Alfvén velocities $V_{A0} = 420$ km s^{-1}, 550 km s^{-1}, and 560 km s^{-1}, respectively.

cases of oscillating filament threads (Terradas *et al.*, 2008). Five of these lie in the range $\sim$(300–600) km s^{-1} if the length of the field lines that pass through the threads is assumed to be $\sim$ 175 Mm, the length of the erupting structure estimated in Paper I. An upper bound of order 1000 km s^{-1} is widely accepted for old, dispersed active regions like the one considered here.

The rise profiles of the simulation runs shown in Figures 3–5 are scaled and matched to the observed profile in Figure 8. In selecting the scaling parameters for the best match, we adopt a start time of the eruption a couple of minutes before 08:51 UT, as estimated in Paper I. The conclusions drawn from the comparison do not depend upon the particular start time if chosen in this range. The value 08:48 UT used in Figure 8 yields the best match of the 3.5π and 2.5π runs with the observations and lies very close to (30 sec before) the last EUVI image prior to the occurrence of motions in the prominence along the path of the CME. Also, we give relatively low priority to the EUVI height data after 10 UT, since these may be smaller than the true heights, as discussed in Paper I.

The scaled rise profile of the simulation with $\Phi = 3.5\pi$ is found to fit the data quite well if the Alfvén velocity is chosen in the range $V_{A0} = (540–560)$ km s^{-1} and the start time of the simulation is placed in the range 08:45–08:50 UT (with the earlier time corresponding to the lower V_{A0}). These values appear very plausible.

We did not succeed to find a satisfactory fit by the higher twisted case. The corresponding curve in Figure 8 demonstrates this, using the same start time as for the 3.5π run and $V_{A0} = 420$ km s^{-1}. Increasing (decreasing) V_{A0} leads to a steeper (flatter) fit curve, *i.e.*, to a better fit at the larger (smaller) heights (if the start time is adjusted simultaneously), but it is obvious that the curve can never fit the combined EUVI and COR1 time-height data. Here the phase of accelerated rise ends too early because the instability grows and saturates too quickly. The rise profile of this simulation can be stretched on the time axis and formally be fit to the data if in addition to an unrealistically low Alfvén velocity of 300 km s^{-1} (lower than the terminal speed of the CME core) an unrealistically large extension of the prominence flux of 360 Mm (twice as large as the estimate in Paper I) are assumed. Both are not acceptable. This comparison with the data thus argues clearly against the occurrence of high twist and a strong helical kink instability in the considered event, in spite of the high total rotation.

Assuming the same start time as for the other two runs, the kink-stable low-twist case ($\Phi = 2.5\pi$) allows an acceptable approximation of the observed rise profile, which yields a plausible value of 560 km s^{-1} for the Alfvén velocity. The match is slightly worse in comparison to the 3.5π run because the curve does not reach the height of the first COR1 data point. Reducing V_{A0}, and adjusting the start time, allows for a nearly perfect match of the COR1 data, similar to the 3.5π run, but this moves the simulation curve, which already runs above all EUVI data points, further away from the measurements in this height range, so that the overall match is degraded.

The origin of the difference lies in the tendency of the torus instability to spread the main upward acceleration of the flux across a larger height range than the helical kink instability, which can be clearly seen in Figure 8. The height range for the torus instability is small only if the field in the source volume of the eruption decreases very rapidly with distance from the flux rope position (see Figure 1 in Kliem and Török, 2006), *i.e.*, in very compact active regions of high field strength, especially in quadrupolar ones. Since AR 10989 was already rather diffuse by the time of the eruption, there is no justification to make the initial configuration in the simulations more compact for a better fit of the rise profile by the kink-stable configuration.

3.4. Implications for the 9 April 2008 Eruption

Based on the good quantitative agreement of the simulated rotation and rise profiles with the observations, Sections 3.1–3.3 yield the following picture. The rotation profile in the height range $h \lesssim 20\ h_0 \approx 1.5\ R_\odot$ above the photosphere is well matched by a strongly kink-unstable case ($\Phi = 5\pi$), a weakly kink-unstable case ($\Phi = 3.5\pi$), and a kink-stable case ($\Phi = 2.5\pi$) if a shear field of appropriate strength is included in each of them. At greater heights, $h \approx$

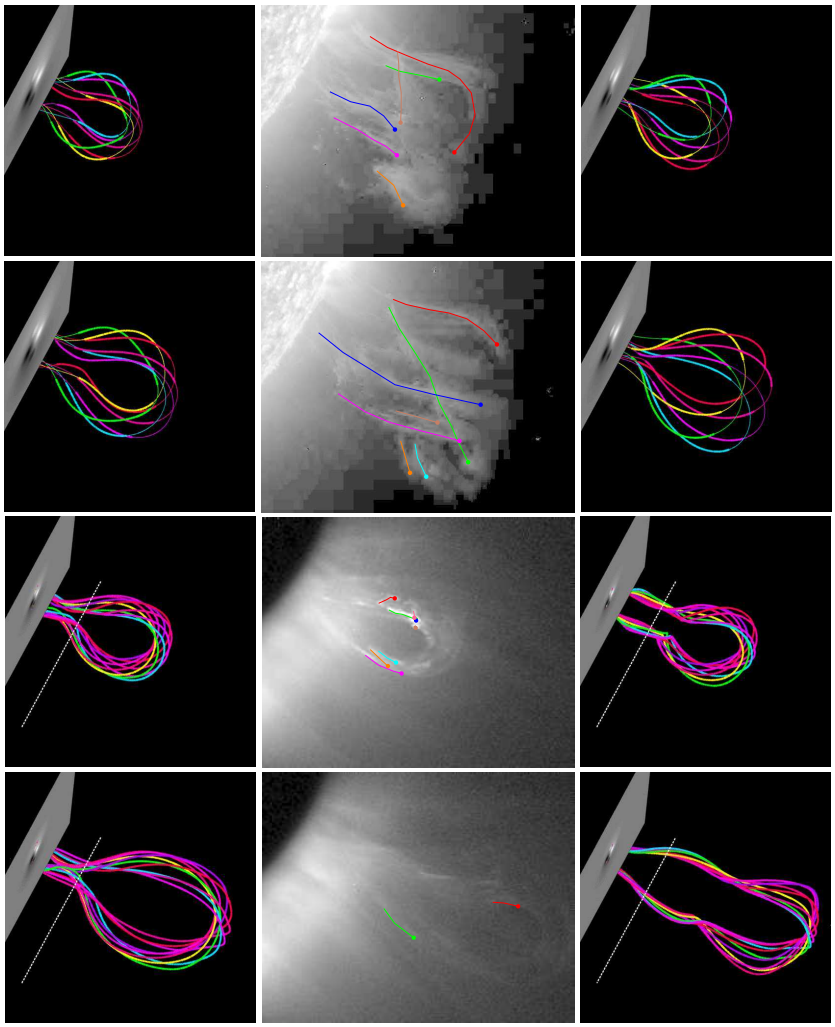

Figure 9. Comparison of simulated and observed flux rope shape for the kink-stable run ($\Phi = 2.5\pi$, $B_{\rm et}/B_{\rm ep} = 1.06$; left panels) and the weakly kink-unstable run ($\Phi = 3.5\pi$, $B_{\rm et}/B_{\rm ep} = 0.67$; right panels) in our parametric search which best match the observed rotation and rise profiles in their entirety. The STEREO images from Figure 1 are supplemented by an additional image at 10:26 UT from Paper I. For both runs, some experimenting with the field line selection was performed until also the observed shape was matched best. This yielded a flux bundle running slightly under the apex point of the rope's magnetic axis for the kink-stable run, as in Figure 5, and a flux bundle enclosing the axis for the kink-unstable run.

(20–30) $h_0 \approx (1.5\text{–}2.3)\ R_\odot$, the comparison yields a clear indication against the kink-stable case, which enters this range with an accelerated rotation, while the observed rotation levels off. The kink-stable case also requires a considerably stronger initial perturbation, lifting the flux rope apex into the torus-unstable range of heights, *i.e.*, to $h \gtrsim 2.6\ h_0 = 0.2\ R_\odot$, a value not supported by the observations. In comparison, the accelerated rise of the kink-unstable cases in

our simulation series starts essentially from $h_0 = 0.077\ R_\odot$, relatively close to the observed onset height of (0.05–0.06) $R_\odot$. The shear field required by the kink-stable case is comparable to the external poloidal field, $B_{\rm et}/B_{\rm ep} = 1.06$. In a bipolar region, this corresponds to a similar distance between the main polarities along and across the PIL, which is not supported by AR 10989 as long as its magnetic structure could be discerned in the approach to the limb (see Figure 4 in Paper I). The rise profile rules out the strongly kink-unstable case and yields a further indication against the kink-stable case, albeit only a weak one. Both the observed shape of the flux rope as a whole and the observed angles between individual threads and the rope axis can be approximately reproduced by all three model systems, but the overall match is best for the weakly kink-unstable case (Figures 3–5). This is substantiated by Figure 9, where we plot the sets of field lines for this and for the kink-stable case which were found to match the observations closest, out of many different sets that were considered.

The shape of the erupting flux rope's magnetic axis in the considered event is not sufficiently well defined by the observations to allow a clear discrimination between the three considered cases based on this property alone. Note that for other events it has proven to be decisive. For example, the shape of the two erupting filaments modeled in Török and Kliem (2005) could be matched only if an initial average twist of 5π was assumed, not with a twist of 4π.

Overall, we conclude that both strongly kink-unstable and kink-stable configurations can be excluded with a high degree of certainty, leaving a weakly kink-unstable initial configuration as the most likely source of the Cartwheel event. This configuration allows to reproduce the event with observationally supported values for several key parameters (flux rope length, distance of the main flux concentrations, initial orientation) and with plausible assumptions for the magnetic structure (flux rope in a simple bipolar active region) and for the remaining free parameters (twist and shear field strength).

Regardless of how definite the rejection of the other two cases is considered to be, the rotation of the erupting flux was primarily caused by a shear field (Isenberg and Forbes, 2007). Weaker contributions came from the relaxation of twist (most likely by a weak helical kink instability) and from reconnection with the ambient field.

4. Discussion

The major simplifying assumptions adopted for the modeling in this paper include (1) the neglect of the initial mainly axial propagation of the prominence, (2) the neglect of any asymmetry and complexity introduced by the large-scale overlying field, and (3) the assumption of a well defined, coherent flux rope (*i.e.*, the Titov-Démoulin model). We discuss these here to assess their potential influence on the results.

While the initial propagation of the prominence introduced an asymmetry and, therefore, definitely had the potential to produce some rotation, we expect that it could not contribute strongly because the propagation was approximately along the flux holding the prominence. This does not principally change the

magnetic configuration and the Lorentz forces which dominate the acceleration of plasma in the low-beta corona.

The effects belonging to category (2) are likely to be relevant primarily at considerable heights. AR 10989 was a relatively isolated region of simple, bipolar structure, and this holds also for its dispersed phase as long as it could be followed in the approach to the limb. The potential-field source-surface extrapolation of the photospheric field in Paper I shows that the large-scale coronal field associated with the polar fields and the heliospheric current sheet began to dominate already at heights $h \gtrsim 0.3\ R_\odot$ above the photosphere, where the horizontal field direction nearly reversed. The force by the field component along the line between the flux rope legs pointed in the direction of a clockwise rotation above this height, opposite to the force low in the corona. However, the shear field above $\sim 0.3\ R_\odot$ was weaker than the shear field in the core of the active region by more than an order of magnitude, so that it could efficiently counteract the continuing, oppositely directed force by the shear field at low heights, and the angular momentum of the already rotating flux rope, only by acting across a considerably larger height range. This is consistent with the fact that the possible weak reverse rotation occurred only at $h > 1.5\ R_\odot$ above the photosphere. Thus, the rotation caused by the shear field and twist inside the bipolar active region (at $h < 0.3\ R_\odot$) must have been dominant factors for the rotation in the height range up to $\sim 1.5\ R_\odot$ modeled here. We cannot exclude that the saturation of the rotation would have occurred at a greater height if the horizontal field had not changed its direction above the active region, however, this weakens only one of the three main arguments against the kink-stable configuration summarized in Section 3.4. The saturation of the rotation profile, at a very similar height, was also seen in another erupting quiescent filament (Bemporad, Mierla, and Tripathi, 2011; see their Figure 5).

The effect of the heliospheric current sheet is expected to become important only at even larger heights. Otherwise, the rotation would not have shown the saturation near $h \sim 1.5\ R_\odot$ and the possible subsequent slight reverse rotation; rather the continuation of the rotation to the value of $\approx 150°$ found at 13 $R_\odot$ would have proceeded already in the COR1 height range.

The assumption that erupting flux in CMEs takes the structure of a flux rope is strongly supported by all available observations. Quantitative differences to our modeling must occur when initial flux ropes of different structure are used. These are not likely to be substantial if only details of the structure differ. The helical kink mode is known to not overly depend on the details of the current channel's radial structure. This can be seen, for example, from the similar instability thresholds found in Mikic, Schnack, and van Hoven (1990), Baty and Heyvaerts (1996), Török, Kliem, and Titov (2004), and Fan and Gibson (2003) although flux ropes with and without a net current and with straight and arched geometries were investigated. Flux ropes with hollow current channels have recently been found to be representative of filament channels which have undergone substantial amounts of flux cancelation (*e.g.*, Su *et al.*, 2011). It is conceivable that their less compact current distribution leads to smaller rotations than the Titov-Démoulin equilibrium with the same twist. This will be a subject of future study. On the other hand, we believe that a strongly kink-unstable configuration of this

type would likely still not match the observed rise profile. The structure and strength of the external poloidal and toroidal field components do not depend upon the details of the flux rope structure, so that two aguments against the kink-stable configuration, which are based on the required initial lifting and on the ratio of $B_{\rm et}$ and $B_{\rm ep}$, would likely still apply.

An overlying current sheet (Birn, Forbes, and Schindler, 2003) may be of stronger influence, but we have argued above that this was not the case for the considered event at the low coronal heights modeled in this paper.

The situation likely changes if the flux rope is far less coherent than the Titov-Démoulin configuration (Green, Kliem, and Wallace, 2011), especially if it is split (Bobra, van Ballegooijen, and DeLuca, 2008). The investigation how such complex cases might change our conclusions must be left for future work.

The comparison of the flux rope rotations found in this paper with the rotation in the simulation of a breakout CME by Lynch *et al.* (2009) suggests a strong dependence upon the existence of a flux rope at the onset of the eruption. In that simulation, the inflating flux of a continuously sheared arcade did not show any significant rotation up to a heliocentric height of $\approx 2\ R_\odot$. Flare reconnection commenced at this point, which progressively transformed the inner part of the arcade into a growing flux rope. The flux rope immediately began to rotate. This process was monitored until the core of the rope reached a heliocentric height of $\approx 3.5\ R_\odot$. Throughout this range, the rope showed a linear increase of its rotation angle with height, and the twist in the rope stayed below the threshold of the helical kink mode. The addition of poloidal flux by flare reconnection was largely complete in the middle of the height interval. The rotation profile in this model differs principally from the data presented here, even if only the height range $> 2\ R_\odot$ is considered, where a flux rope did exist. This suggests that the presence of a flux rope at the onset of the eruption was a key feature of the Cartwheel event.

An interesting result of our parametric study is that the erupting flux rope did always show some amount of rotation, even in the shear-free, kink-stable case included in Figure 6. We expect this to be generally valid if coherent force-free flux ropes are considered as the initial condition, because such ropes always possess twist. An untwisted flux tube, known as a Theta pinch, requires a radial pressure gradient to attain equilibrium. This is not available if the plasma beta is very small, as expected for the lower coronal part of active regions. Whether the observations support the occurrence of rotation in essentially all events does not yet seem to be clear. For example, Muglach, Wang, and Kliem (2009) report that only about 10 cases of unambiguous rotation in erupting filaments not very far from Sun center could be identified in the EUV observations by the EIT instrument (Delaboudinière *et al.*, 1995) for the whole solar cycle 23. However, many cases of only moderate rotation may remain undetected in such data, due to the projection in the plane of the sky. Yurchyshyn, Abramenko, and Tripathi (2009) report 101 partial and full halo CMEs which show a very broad distribution of the difference between the estimated initial and final orientations at distances up to 30 $R_\odot$; these angles do not show a clustering at zero degrees. However, they represent the net effect of rotation in the corona and in the inner solar wind where the heliospheric current sheet likely dominates. If the fraction of

non-rotating events is relatively small, then a plausible explanation is that other processes counteract the rotation by twist relaxation and the shear field in these cases, for example reconnection with the ambient field. If the fraction is large, then such nearly exact cancelation of rotations is unlikely to be the primary explanation. The implication would then be that the current distribution in the erupting field is often less compact or less coherent than in the Titov-Démoulin flux rope, including the possibility that a flux rope does not yet exist at the onset of the eruption.

5. Conclusions

Our parametric study of force-free flux ropes which erupt from simple bipolar source regions with no overlying current sheet and rotate about the direction of ascent yields the following conclusions.

1) Both the force by an external shear field component $B_{\rm et}$ (Isenberg and Forbes, 2007) and the relaxation of twist Φ (*e.g.*, Török, Berger, and Kliem, 2010), are potentially very significant contributors to the rotation.

2) For parameters typical of CME source regions, in particular if the sources of the external stabilizing field (usually the main flux concentrations next to the PIL) have a smaller distance than the footpoints of the erupting flux, the shear field yields the dominant contribution to the rotation for a wide range of shear field strengths. The relaxation of twist remains the weaker contributor under these conditions, even if it is sufficiently high to trigger the helical kink instability. However, since twist always exists in force-free flux ropes, it always causes at least some rotation. Strong rotations ($\gtrsim 90^\circ$) can be produced by the twist alone, but only for considerably larger distances between the sources of the external stabilizing field than typically observed.

3) The rotation in low-beta plasma is not guided by the changing orientation of the PIL with height. For the geometrical conditions typical of CME source regions, it is opposite in direction (see the Appendix).

4) For a given chirality of the configuration, the external shear field and the twist cause flux rope rotation in the same direction, which is clockwise for right-handed field and counterclockwise for left-handed field if seen from above.

5) The two processes are related to each other when considered in terms of magnetic helicity. Both convert initial twist helicity of the flux rope into writhe helicity. The same total rotation, and rotation profiles which are very similar in a substantial part of the total height range of rotation, result in a range of $B_{\rm et}$–Φ combinations.

6) The rotation due to twist relaxation tends to act mainly low in the corona, in a height range up to only a few times the distance between the footpoints of the erupting flux. The rotation by the shear field tends to be distributed across a larger height range.

7) The mere fact that erupting flux rotates does not by itself imply that the helical kink instability occurred.

8) The relative contributions to the total rotation by the shear field and by the twist can be disentangled by comparing both the observed rotation and rise

profiles with the corresponding curves from a model, since these profiles possess a different dependence upon the $B_{\rm et}$–Φ parameter combination. The resulting estimate for the twist allows one to judge the occurrence of the helical kink instability.

9) Magnetic reconnection contributes only weakly (much less than the shear field) to the total rotation in the simple bipolar source regions considered.

From the comparison with the simulation of rotating flux in Lynch *et al.* (2009) we conclude:

10) The rotation profile differs strongly between configurations with and without a flux rope at the onset of the eruption.

The comparison with the stereoscopic observations and three-dimensional reconstruction of the erupting prominence in the 9 April 2008 "Cartwheel CME" additionally shows the following.

11) The rotation profile obtained in Paper I from the stereoscopic reconstruction of STEREO data is equally well reproduced by our model up to heights $\approx 1.5\ R_\odot$ above the photosphere for a range of Φ–$B_{\rm et}$ combinations which include a strongly kink-unstable case ($\Phi = 5\pi$, $B_{\rm et}/B_{\rm ep} = 0.42$), a weakly kink-unstable case ($\Phi = 3.5\pi$, $B_{\rm et}/B_{\rm ep} = 0.67$), and a kink-stable case ($\Phi = 2.5\pi$, $B_{\rm et}/B_{\rm ep} = 1.06$). However, the strongly kink-unstable configuration is ruled out by the simultaneous consideration of the rise profile, and several features of the kink-stable model argue strongly against this configuration. These are the implied high value of the shear field, the rotation profile at greater heights, and the unrealistic start height of the unstable rise of $\approx 0.2\ R_\odot$. Hence, the occurrence of a weak helical kink instability in the Cartwheel event is very likely.

Our results add to the complexity of the phenomenon of flux rope rotation in eruptions which is already known from investigations that focused on the influence of reconnection (*e.g.*, Jacobs *et al.*, 2009; Shiota *et al.*, 2010; Cohen *et al.*, 2010; Thompson, 2011; Lugaz *et al.*, 2011). An overall very complicated dependence on several parameters and on the structure of the ambient field is revealed. Thus, the quantitative prediction of the rotation is a difficult task. The parametric study performed here indicates for simple bipolar source regions that the strength of the external shear field is the primary parameter determining the total rotation. The twist and the height profile of the external poloidal field are of relatively minor importance as long as they stay in the typical ranges indicated by the observations. We did not yet study a possible influence of the height profile of the external shear field. The external shear field of filament channels may be estimated to sufficient precision from a simple linear force-free field extrapolation. It will be worth testing whether numerical modeling starting from such fields, embedded in current-free outer field, yields rotations in agreement with observations of eruptions from bipolar source regions.

Several investigations indicate that erupting flux ropes align with the heliospheric current sheet in the course of their interplanetary propagation (*e.g.*, Bothmer and Schwenn, 1998; Yurchyshyn, 2008; Paper I). This suggests that the coronal rotation merely decides whether a parallel or an antiparallel alignment

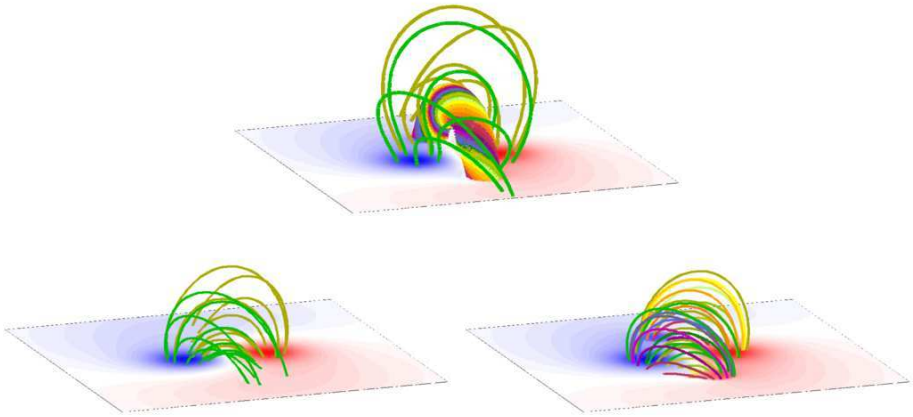

Figure 10. Visualization of the weakly kink-unstable modified Titov-Démoulin equilibrium ($\Phi = 3.5\pi$, $B_{\rm et}/B_{\rm ep} = 0.67$; Figures 2 and 4) whose eruption characteristics match the observations of the Cartwheel CME best (top panel) and of the corresponding external field (bottom left) and potential field (bottom right). The magnetogram and field lines starting in the photospheric flux concentrations are shown.

will result at 1 AU. However, since complex physics is involved and since rotations on the order of 90° may not be rare, the quantitative study of the effects that determine the rotation in the corona remains of high scientific and practical interest.

Appendix

There are quite strong indications that CMEs align with the heliospheric current sheet in the course of their propagation, *i.e.*, with the PIL in the solar wind (see references in Section 5). This leads to the question whether the PIL guides the rotation of erupting flux ropes also in the corona. Here the PIL formed by the external field, due to sources outside the flux rope, must be considered. We use "CPIL" to denote this structure in the corona, where $\beta < 1$. The heliospheric current sheet and the CPIL differ in two properties of relevance here. First, in the solar wind $\beta > 1$, so that the pressure gradient is generally dominant over the Lorentz force, while the opposite is true in the corona. Second, the heliospheric current sheet is the location of pressure gradients and Lorentz forces, while the CPIL generally lacks both. In the low-beta corona, currents are induced at separatrix surfaces, or at quasi separatrix layers, if the equilibrium is perturbed or lost. The CPIL generally does not coincide with these structures. Therefore, the CPIL should not influence the rotation of erupting flux ropes in this height range.

Figure 10 shows the initial equilibrium of the weakly kink-unstable run which matches the Cartwheel event best, the corresponding external field, and the potential field that results when the full magnetogram of the vertical field component of the equilibrium, $B_z(x, y, 0)$, is extrapolated into the volume above. The

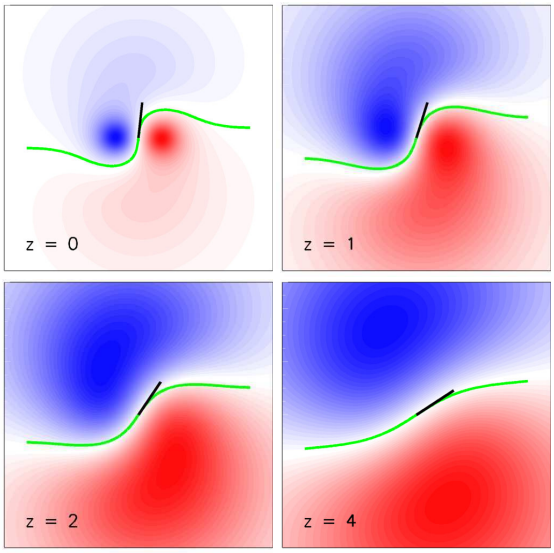

Figure 11. Orientation of the PIL in the external field of the configuration shown in Figure 10 at the position of the flux rope and different heights. The orientation is indicated by a black line.

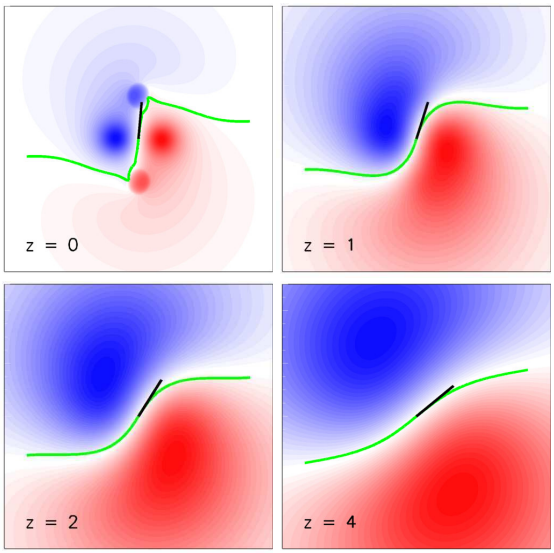

Figure 12. Same as Figure 11 for the potential field of the configuration shown in Figure 10.

full magnetogram includes the contributions from the flux rope, which are excluded from the external field. The CPIL of this configuration at the photospheric and three coronal levels is shown in Figure 11. The CPIL changes its orientation in a clockwise sense if one goes upward, but the unstable flux rope rotates in a counterclockwise direction, since it is left handed. The clockwise changing CPIL orientation results from the dominance of the external toroidal field, $B_{\rm et}$, over

the external poloidal field, $B_{\rm ep}$, at great heights. This situation can typically be expected to occur because $B_{\rm et}$ typically has a larger spatial scale than $B_{\rm ep}$ (set by the distance between the sources in the photosphere). The important fact here is that the CPIL does not appear to have any significant influence on the rotation of the flux rope in the zero-beta simulations performed in this paper. For the reasons given above, this is valid also if other height profiles of $B_{\rm et}$ or $B_{\rm ep}$ lead to a different profile of the CPIL orientation with height.

Finally, we consider the approximation of the true CPIL by the PIL in a potential-field extrapolation of the full photospheric magnetogram, $B_z(x, y, 0)$. In practice, it is difficult or even impossible to determine the external field. This requires the determination of the coronal currents through a nonlinear force-free extrapolation from a vector magnetogram. The former is still difficult to carry out and the latter may not be available. The PIL in the potential field extrapolated from the magnetogram of the weakly kink-unstable configuration in Figure 10 is shown in Figure 12. Its orientation *vs.* height is very similar to the behavior of the true CPIL. This supports the conclusions drawn in Paper I from a potential-field source-surface extrapolation for the source region of the Cartwheel CME.

Acknowledgements We acknowledge the careful reading of the manuscript and the constructive comments by the referee. BK acknowledges support by the DFG, the STFC, and by NASA through Grant NNX08AG44G. TT's work was partially supported by the European Commission through the SOTERIA Network (EU FP7 Space Science Project No. 218816) and by the NASA HTP and LWS programs. WTT's work was supported by by NASA Grant NNG06EB68C.

References

Amari, T., Aly, J., Mikic, Z., Linker, J.: 2010, *Astrophys. J. Lett.* **717**, 26.
Aulanier, G., Török, T., Démoulin, P., DeLuca, E.E.: 2010, *Astrophys. J.* **708**, 314.
Baty, H., Heyvaerts, J.: 1996, *Astron. Astrophys.* **308**, 935.
Bemporad, A., Mierla, M., Tripathi, D.: 2011, *Astron. Astrophys.* **531**, A147.
Birn, J., Forbes, T.G., Schindler, K.: 2003, *Astrophys. J.* **588**, 578.
Bobra, M.G., van Ballegooijen, A.A., DeLuca, E.E.: 2008, *Astrophys. J.* **672**, 1209.
Bothmer, V., Schwenn, R.: 1998, *Annales Geophysicae* **16**, 1.
Chen, P.F., Shibata, K.: 2000, *Astrophys. J.* **545**, 524.
Cohen, O., Attrill, G.D.R., Schwadron, N.A., Crooker, N.U., Owens, M.J., Downs, C., Gombosi, T.I.: 2010, *J. Geophys. Res.* **115**(A14), 10104.
Delaboudinière, J., Artzner, G.E., Brunaud, J., Gabriel, A.H., Hochedez, J.F., Millier, F., Song, X.Y., Au, B., Dere, K.P., Howard, R.A., Kreplin, R., Michels, D.J., Moses, J.D., Defise, J.M., Jamar, C., Rochus, P., Chauvineau, J.P., Marioge, J.P., Catura, R.C., Lemen, J.R., Shing, L., Stern, R.A., Gurman, J.B., Neupert, W.M., Maucherat, A., Clette, F., Cugnon, P., van Dessel, E.L.: 1995, *Solar Phys.* **162**, 291.
Fan, Y., Gibson, S.E.: 2003, *Astrophys. J. Lett.* **589**, 105.
Gibson, S.E., Fan, Y.: 2008, *J. Geophys. Res.* **113**(A12), 9103.
Green, L.M., Kliem, B., Wallace, A.J.: 2011, *Astron. Astrophys.* **526**, A2.
Green, L.M., Kliem, B., Török, T., van Driel-Gesztelyi, L., Attrill, G.D.R.: 2007, *Solar Phys.* **246**, 365.
Howard, R.A., Moses, J.D., Vourlidas, A., Newmark, J.S., Socker, D.G., Plunkett, S.P., Korendyke, C.M., Cook, J.W., Hurley, A., Davila, J.M., Thompson, W.T., Cyr, O.C.S., Mentzell, E., Mehalick, K., Lemen, J.R., Wuelser, J.P., Duncan, D.W., Tarbell, T.D., Wolfson, C.J., Moore, A., Harrison, R.A., Waltham, N.R., Lang, J., Davis, C.J., Eyles,

C.J., Mapson-Menard, H., Simnett, G.M., Halain, J.P., Defise, J.M., Mazy, E., Rochus, P., Mercier, R., Ravet, M.F., Delmotte, F., Auchere, F., Delaboudiniere, J.P., Bothmer, V., Deutsch, W., Wang, D., Rich, N., Cooper, S., Stephens, V., Maahs, G., Baugh, R., Mcmullin, D.: 2008, *Space Sci. Rev.* **136**, 67.
Isenberg, P.A., Forbes, T.G.: 2007, *Astrophys. J.* **670**, 1453.
Jacobs, C., Roussev, I.I., Lugaz, N., Poedts, S.: 2009, *Astrophys. J.* **695**, 171.
Kliem, B., Török, T.: 2006, *Phys. Rev. Lett.* **96**, 255002.
Kliem, B., Titov, V.S., Török, T.: 2004, *Astron. Astrophys.* **413**, 23.
Kliem, B., Linton, M.G., Török, T., Karlický, M.: 2010, *Solar Phys.* **266**, 91.
Landi, E., Raymond, J.C., Miralles, M.P., Hara, H.: 2010, *Astrophys. J.* **711**, 75.
Lugaz, N., Downs, C., Shibata, K., Roussev, I.I., Asai, A., Gombosi, T.I.: 2011, *Astrophys. J.* **738**, 127.
Lynch, B.J., Antiochos, S.K., Li, Y., Luhmann, J.G., DeVore, C.R.: 2009, *Astrophys. J.* **697**, 1918.
Martin, S.F.: 2003, *Advances in Space Research* **32**, 1883.
Mikic, Z., Linker, J.A.: 1994, *Astrophys. J.* **430**, 898.
Mikic, Z., Schnack, D.D., van Hoven, G.: 1990, *Astrophys. J.* **361**, 690.
Muglach, K., Wang, Y., Kliem, B.: 2009, *Astrophys. J.* **703**, 976.
Panasenco, O., Martin, S., Joshi, A.D., Srivastava, N.: 2011, *Journal of Atmospheric and Solar-Terrestrial Physics* **73**, 1129.
Patsourakos, S., Vourlidas, A.: 2011, *Astron. Astrophys.* **525**, A27.
Romano, P., Contarino, L., Zuccarello, F.: 2003, *Solar Phys.* **214**, 313.
Rust, D.M., Kumar, A.: 1996, *Astrophys. J. Lett.* **464**, L199.
Rust, D.M., LaBonte, B.J.: 2005, *Astrophys. J.* **622**, 69.
Sakurai, T.: 1976, *Publ. Astron. Soc. Japan* **28**, 177.
Shiota, D., Kusano, K., Miyoshi, T., Shibata, K.: 2010, *Astrophys. J.* **718**, 1305.
Su, Y., Surges, V., van Ballegooijen, A., DeLuca, E., Golub, L.: 2011, *Astrophys. J.* **734**, 53.
Terradas, J., Arregui, I., Oliver, R., Ballester, J.L.: 2008, *Astrophys. J.* **678**, 153.
Thompson, W.T.: 2011, *Journal of Atmospheric and Solar-Terrestrial Physics* **73**, 1138.
Thompson, W.T., Kliem, B., Toeroek, T.: 2009, In: *AAS/Solar Physics Division Meeting #40*, *AAS/Solar Physics Division Meeting* **40**, 21.11.
Thompson, W.T., Kliem, B., Török, T.: 2011, *Solar Phys.*. doi:10.1007/s11207-011-9868-5.
Titov, V.S., Démoulin, P.: 1999, *Astron. Astrophys.* **351**, 707.
Török, T., Kliem, B.: 2003, *Astron. Astrophys.* **406**, 1043.
Török, T., Kliem, B.: 2005, *Astrophys. J. Lett.* **630**, 97.
Török, T., Kliem, B.: 2007, *Astronomische Nachrichten* **328**, 743.
Török, T., Berger, M.A., Kliem, B.: 2010, *Astron. Astrophys.* **516**, A49.
Török, T., Kliem, B., Titov, V.S.: 2004, *Astron. Astrophys.* **413**, 27.
Vourlidas, A., Colaninno, R., Nieves-Chinchilla, T., Stenborg, G.: 2011, *Astrophys. J. Lett.* **733**, L23.
Williams, D.R., Török, T., Démoulin, P., van Driel-Gesztelyi, L., Kliem, B.: 2005, *Astrophys. J. Lett.* **628**, 163.
Yurchyshyn, V.: 2008, *Astrophys. J.* **675**, 49.
Yurchyshyn, V., Abramenko, V., Tripathi, D.: 2009, *Astrophys. J.* **705**, 426.

Reconciling the electron counterstreaming and dropout occurrence rates with the heliospheric flux budget

M. J. Owens[1] and N. U. Crooker[1]

Received 4 November 2006; revised 29 January 2007; accepted 8 February 2007; published 5 June 2007.

[1] Counterstreaming electrons (CSEs) are treated as signatures of closed magnetic flux, i.e., loops connected to the Sun at both ends. However, CSEs at 1 AU likely fade as the apex of a closed loop passes beyond some distance R, owing to scattering of the sunward beam along its continually increasing path length. The remaining antisunward beam at 1 AU would then give a false signature of open flux. Subsequent opening of a loop at the Sun by interchange reconnection with an open field line would produce an electron dropout (ED) at 1 AU, as if two open field lines were reconnecting to completely disconnect from the Sun. Thus EDs can be signatures of interchange reconnection as well as the commonly attributed disconnection. We incorporate CSE fadeout into a model that matches time-varying closed flux from interplanetary coronal mass ejections (ICMEs) to the solar cycle variation in heliospheric flux. Using the observed occurrence rate of CSEs at solar maximum, the model estimates $R \sim 8-10$ AU. Hence we demonstrate that EDs should be much rarer than CSEs at 1 AU, as EDs can only be detected when the juncture points of reconnected field lines lie sunward of the detector, whereas CSEs continue to be detected in the legs of all loops that have expanded beyond the detector, out to R. We also demonstrate that if closed flux added to the heliosphere by ICMEs is instead balanced by disconnection elsewhere, then ED occurrence at 1 AU would still be rare, contrary to earlier expectations.

Citation: Owens, M. J., and N. U. Crooker (2007), Reconciling the electron counterstreaming and dropout occurrence rates with the heliospheric flux budget, *J. Geophys. Res.*, *112*, A06106, doi:10.1029/2006JA012159.

1. Introduction

[2] Suprathermal electrons have long been used as tracers of the topology of the heliospheric magnetic field (HMF), with a single field-aligned beam (or "strahl") being indicative of open magnetic flux and counterstreaming electron (CSE) beams signifying flux with both foot points rooted at the Sun (the energization of electrons far from the Sun, such as at corotating shocks and planetary sources, is likely to produce a negligible contribution to the total CSE rate observed at 1 AU [e.g., *Wimmer-Schweingruber et al.*, 2006, and references therein]). The closed flux topologies indicated by CSEs are strongly associated with interplanetary coronal mass ejections (ICMEs) [*Gosling et al.*, 1987]. Periods when no field-aligned suprathermal electron beams are observed, termed "heat flux dropouts" (HFDs), were initially thought to be signatures of reconnection between open field lines resulting in flux completely disconnected from the Sun (see also the bottom panels of Figure 1 [*McComas et al.*, 1989]). *McComas et al.* [1989] argued that disconnection must be the means of balancing the closed flux introduced to the heliosphere from CMEs. A balance is required to avoid any buildup over the solar cycle. They also noted, however, that the scarcity of HFDs observed in the solar wind at 1 AU seemed inconsistent with this view. Following *Gosling et al.* [1995], *Crooker et al.* [2002] pointed out that there is no inconsistency if ICME fields open via "interchange reconnection" between the legs of the closed loops and open fields close to the Sun (illustrated in the top panels of Figure 1), in which case no disconnection is required.

[3] *Owens and Crooker* [2006] (hereafter "Paper 1") expanded on the ideas of *Crooker et al.* [2002] to show that if the closed fields in ICMEs open slowly (over many tens of days), their flux contribution is sufficient to explain the solar cycle doubling in HMF intensity observed at 1 AU. They developed a quantitative model of the heliospheric flux consisting of two components: constant open flux from large-scale coronal holes and time-varying closed flux accumulated from CMEs. Here we further develop the model so as to predict suprathermal electron signatures of heliospheric flux buildup from long-lived ICME closed flux. We demonstrate how HFDs can result from interchange reconnection as well as disconnection, and we conclude that the HFD occurrence rate at 1 AU for either process should be much lower than the occurrence rate of CSEs, in agreement with observations.

[1]Center for Space Physics, Boston University, Boston, Massachusetts, USA.

0148-0227/07/2006JA012159

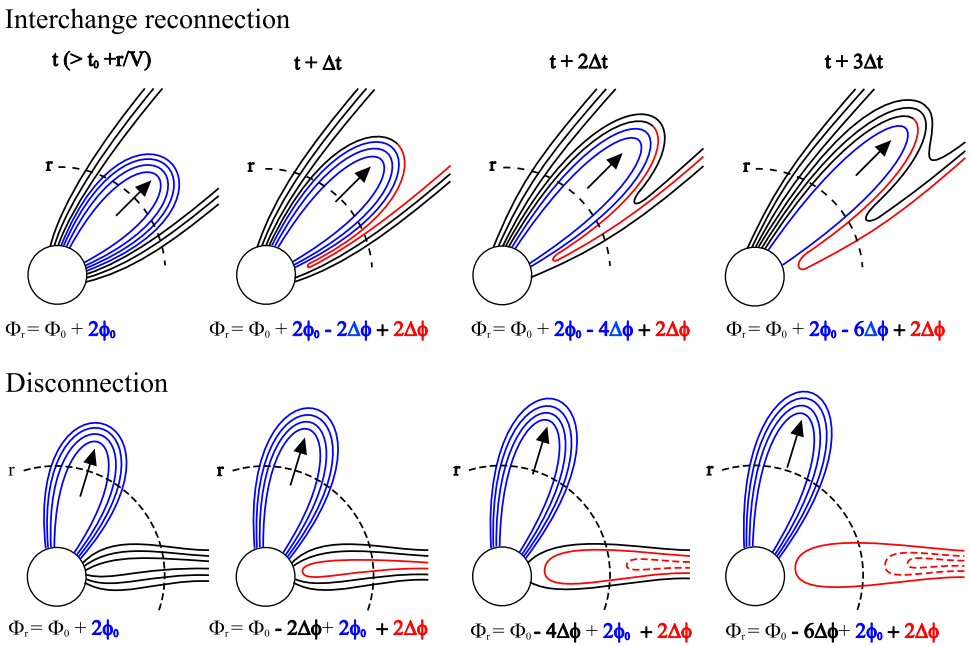

Figure 1. A sketch of the various flux systems that contribute to the total heliospheric flux at a distance r (Φ_r). Each line represents a flux tube containing flux $\Delta\phi$. The top panels show interchange reconnection: The total open flux contribution (Φ_0, shown as black lines) is constant with time. Blue lines indicate closed flux: Initially the CME contributes $2\phi_0$ (where ϕ_0 is the total posteruption axial flux), as each flux tube intersects the sphere of radius r twice. In a time Δt, $\Delta\phi$ of this closed flux will open via interchange reconnection close to the Sun, or $\Delta\phi$ of open flux will disconnect. There is also a contribution to Φ_r from "inverted" flux for interchange reconnection, shown as red lines: This is the result of newly reconnected field lines yet to propagate to r. The bottom panels show disconnection: The injected closed flux is balanced by a reduction in the open flux. Solid red lines show the disconnected flux yet to propagate to r.

[4] Throughout the rest of this paper, we use the more specific "electron dropout" (ED) in place of HFD to designate a drop in total electron number density in the suprathermal energy range, since heat flux can drop through a redistribution in pitch angle as well as through disconnection [e.g., *Pagel et al.*, 2005].

2. Heliospheric Flux From CMEs

[5] To calculate the expected suprathermal electron signatures of long-lived ICME closed flux, we must adapt the model of heliospheric flux outlined in Paper 1 to account for the effects of nonzero propagation time of both the ICME closed loops and newly opened flux. Figure 1 shows an overview of two possible types of heliospheric flux evolution: The top panels show how flux added by ICMEs is removed by opening the ICME flux via interchange reconnection, and the bottom panels show how the ICME-added flux can be balanced by disconnecting the same amount of open flux. Each line represents a flux tube containing flux $\Delta\phi$. We first consider the interchange reconnection scenario. The open flux (black lines) contributes Φ_0 (=$6\Delta\phi$ as shown in the figure) to the total flux threading a sphere at a heliocentric distance r, denoted Φ_r. Although the topology of open flux changes with the evolving ICME flux, Φ_0 remains constant with time.

[6] At time t_0, the CME erupts and carries a posteruption axial flux of ϕ_0 (=$4\Delta\phi$ as shown in the figure), where $\phi_0 = (1 - D)\phi_A$, D being the fraction of flux that opens during CME formation and ϕ_A the total axial flux content of the CME. This new flux system can only contribute to Φ_r once the loops reach r, i.e., when $t \geq t_0 + v/r$, where v is the transit speed of the ICME. (We do not consider the time required for an ICME to move past an observer at r, which depends upon both the ICME radial width and expansion speed.) The closed flux contribution (blue lines) Φ_C at $t \geq t_0 + r/v$ is $2\phi_0$, since each flux tube intersects the sphere of radius r twice, minus any opened flux. Newly opened ICME flux (red lines) takes a time r/v to propagate to r, during which it will continue to contribute to Φ_r as if it were closed. We refer to this flux system as the "inverted flux" Φ_I.

[7] For disconnection, in contrast to interchange reconnection, the closed flux contribution of a CME ϕ is constant. The open flux contribution decays at the exact same rate at which ICME flux opens in the interchange reconnection scenario, since the same amount of flux added to the heliosphere by CMEs must be removed over the solar cycle. Consequently, the instantaneous value of Φ_r is the same for disconnection and interchange reconnection, but the contributing flux systems are different, as shown Figure 1. The disconnected flux contribution (Φ_D, solid red lines) to Φ_r is equal to the inverted flux contribution Φ_I.

[8] Thus Φ_r, the flux threading a heliocentric sphere of radius r, can be considered to consist of three components:

[9] Interchange reconnection:

$$\Phi_r = \Phi_0 + \Phi_C + \Phi_I = \Phi_0 + 2\left(\phi_0 - \int_{t_0}^{t} \frac{\partial \phi_C}{\partial t} dt\right) + 2\left(\int_{t-r/v}^{t} \frac{\partial \phi_C}{\partial t} dt\right)$$

[10] Disconnection:

$$\Phi_r = \Phi_0 + \Phi_C + \Phi_D = \left(\Phi_0 - 2\int_{t_0}^{t} \frac{\partial \Phi_0}{\partial t} dt\right) + 2\phi_0 + 2\left(\int_{t-r/v}^{t} \frac{\partial \Phi_0}{\partial t} dt\right) \quad (1)$$

where ϕ_C is the instantaneous ICME closed flux. The rate of reconnection, involving either open flux disconnection or closed ICME flux opening, is determined by the heliospheric flux budget and must therefore be equal. As in Paper 1, we consider two forms for the reconnection rate: (1) a constant k and (2) proportional to the amount of closed flux. Thus for $t \leq t_0 + \phi/k$:

[11] (1) Constant reconnection rate:

$$\left[\frac{\partial \Phi_0}{\partial t}\right]_{Disc.} = \left[\frac{\partial \phi_C}{\partial t}\right]_{Int.rec.} = -k$$

[12] (2) Reconnection rate proportional to ϕ:

$$\left[\frac{\partial \Phi_0}{\partial t}\right]_{Disc.} = \left[\frac{\partial \phi_C}{\partial t}\right]_{Int.rec.} = -\lambda\phi_C = -\lambda\phi_0 \exp[-\lambda(t - t_0)] \quad (2)$$

For $t > t_0 + \phi/k$, all the closed flux has opened in the constant flux-opening rate model, and thus k becomes zero.

[13] Combining equations (1) and (2) yields the same equations for Φ_r for both disconnection and interchange reconnection:

[14] (1) Constant reconnection rate:

$$\Phi_r = \Phi_0 + 2[\phi_0 - k(t - t_0)] + 2kr/v$$

[15] (2) Reconnection rate proportional to ϕ:

$$\Phi_r = \Phi_0 + 2\phi_0 \exp[-\lambda(t - t_0)] + 2\phi_0 \exp[-\lambda(t - t_0)]\left(\exp\left[\frac{r\lambda}{v}\right] - 1\right) \quad (3)$$

[16] The black lines in Figure 2 show the total flux contribution of a single ICME to a sphere of radius r = 1 AU (i.e., Φ_{1AU}) as a function of time past the CME eruption time. Solid (dashed) lines show the exponential (constant) flux-opening model. The top-left panel gives results for ICME opening via interchange reconnection. There is no contribution to Φ_{1AU} until ~3–4 days, when the leading edge of the ICME reaches 1 AU. (An ICME transit speed of 450 km/s is assumed.) The blue and red lines show the contributions from closed and inverted flux, respectively.

[17] The bottom-left panel of Figure 2 gives results for disconnection. The increase in heliospheric flux at r is shown by the black lines and is identical to that of interchange reconnection. The closed flux contribution (blue lines) is constant, but the overall flux decreases because of a decrease in the open flux (not shown).

[18] To estimate the total ICME contribution to the heliospheric flux, it is necessary to sum over all ICMEs in the heliosphere that have both propagated to r and that still contain some closed flux. Assuming there are N such ejecta at time t, the total flux for both disconnection and interchange reconnection is given by:

[19] (1) Constant reconnection rate:

$$\Phi_r(t) = \Phi_0 + \sum_{n=1}^{N} 2\left[\phi_0^n - k^n\left(t - t_0^n\right)\right] + \sum_{n=1}^{N} 2k^n r/v^n$$

[20] (2) Reconnection rate proportional to ϕ:

$$\Phi_r(t) = \Phi_0 + \sum_{n=1}^{N} 2\phi_0^n \exp\left[-\lambda^n\left(t - t_0^n\right)\right] + \sum_{n=1}^{N} 2\phi_0^n \exp\left[-\lambda^n\left(t - t_0^n\right)\right]\left(\exp\left[\frac{r\lambda^n}{v^n}\right] - 1\right) \quad (4)$$

where the superscript n is used to index the ICMEs (and their properties) in the heliosphere.

3. Implications for Electron Observations

[21] In this section we consider the implications of interchange reconnection and disconnection on observable in situ electron signatures. Figure 3 shows the suprathermal electron strahl direction (red arrows) along magnetic field lines (black lines) for various heliospheric flux systems. The top two sets of panels show ICME flux opening by interchange reconnection. In a "fast" ICME flux-opening scenario (Figure 3a), closed loops always exhibit a CSE signature, whereas open field lines (including the inverted flux) always exhibit a single strahl. For the "slow" ICME flux-opening scenario (Figure 3b), we consider the consequences of suprathermal electron scattering. The blue shaded region shows the heliocentric distance beyond which we assume that sunward electron beams can no longer reach the observing site, having scattered in some unspecified way along the long path from the far foot point. For clarity, the substantial increase in field-line length owing to solar rotation (illustrated in Figure 6) has been ignored here. If ICMEs remain closed for long periods, their CSE signatures will fade when their leading edges reach such distances. When interchange reconnection eventually opens the ICME flux, the remaining antisunward electron beam will be cut off, leaving the inverted flux devoid of suprathermal electrons. This electron dropout was originally thought to signify only flux completely disconnected from the Sun [*McComas et al.* [1989], as discussed below]. In our interpretation, EDs could also be signatures of ICME closed loops opening over very long timescales.

[22] Thus for $t \geq t_0 + R/v$, where R is the distance from the Sun where the field lines are sufficiently long that the sunward electron strahl scatters, the signature of closed flux switches from a CSE signature to a single antisunward strahl (and thus is indistinguishable from open flux), and the signature of inverted flux switches from a sunward single

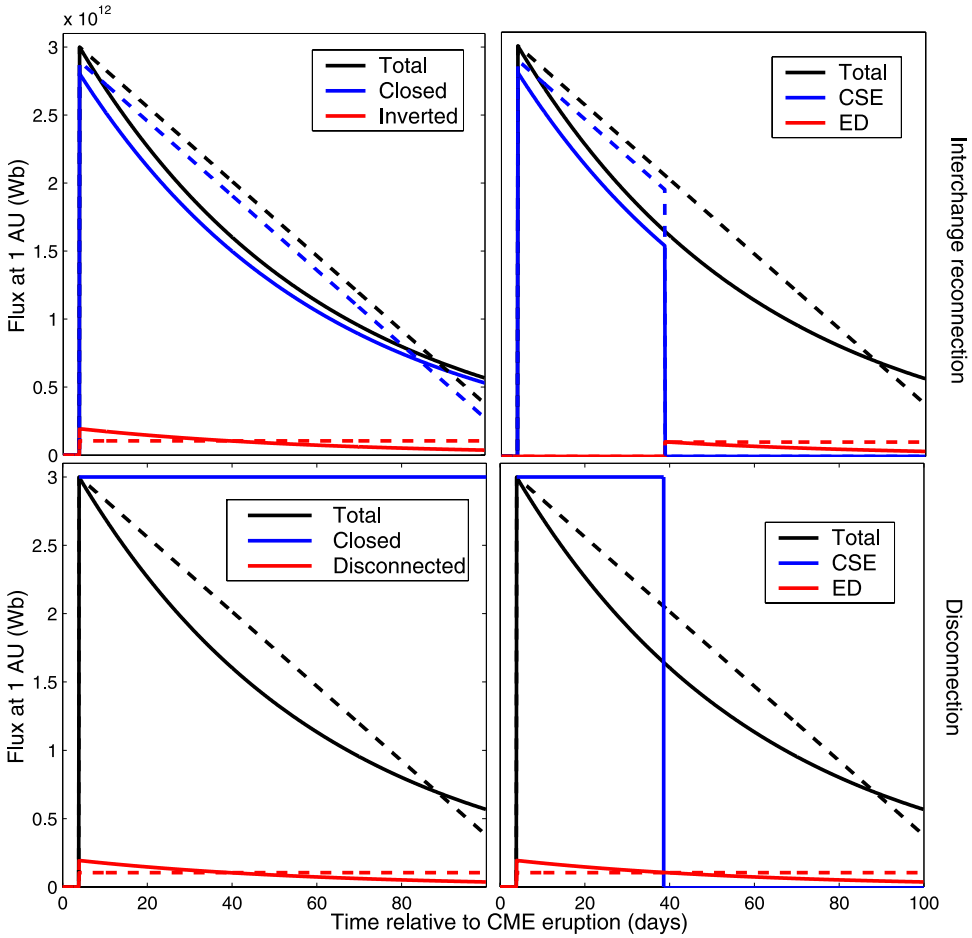

Figure 2. Flux contribution from a single ICME to the total flux threading a heliocentric sphere of radius 1 AU (Φ_{1AU}) as a function of time past CME launch. The top (bottom) two panels show ICME fields opening via interchange reconnection (being balanced by open flux disconnection). Solid (dashed) lines show the exponential (constant) flux-opening model. The left panels show the total contribution of the ICME to Φ_{1AU} (black lines), along with the individual contributions from closed (blue) and inverted/disconnected (red) flux systems. The right panel again shows the total contribution of a single CME to Φ_{1AU} (black lines), but with the fraction of that flux exhibiting counterstreaming electrons (blue) and electron dropouts (red), assuming suprathermal electrons scatter when the leading edge of the CME reaches 10 AU. See also Figure 3.

strahl to an ED. The signature of true open flux remains unchanged as a single strahl throughout this process. The top-right panel of Figure 2 shows the total flux contribution to Φ_r from an ICME as a function of time past CME eruption (black dashed lines), and the fractions of that flux displaying CSEs (red) and EDs (blue), assuming the suprathermal electron strahl scatters at a distance R = 10 AU.

[23] Despite disconnection and interchange reconnection producing the same values for the magnitude of the heliospheric magnetic flux, they may produce different suprathermal electron signatures: Disconnection involves destruction and creation of open flux, which are topologically different from the conservation of open flux that occurs with interchange reconnection. The bottom-right panel of Figure 2 shows the electron signatures for disconnection, with red lines showing EDs resulting from true disconnection. Unlike interchange reconnection, these ED signatures are present both before and after the ICME leading edge reaches the suprathermal electron fadeout distance. The closed field contribution will display CSEs until the ICME leading edge reaches R (blue lines).

[24] In the following sections we use these heliospheric flux models to quantitatively estimate how frequently CSE and ED signatures should be observed at 1 AU.

4. Static Equilibrium

[25] As in Paper 1, it is instructive first to investigate a static equilibrium wherein CMEs are injected into the heliosphere at a constant frequency f. Thus Δt, the time between consecutive CMEs, is simply $1/f$.

[26] At a time t, the last ICME contributing to Φ_r (i.e., the Nth ICME) is the last ejection to reach just to the height of observation (r). Hence $N = 1 + (t - r/v)/\Delta t$. The injection time of the nth CME is then given by:

$$t_0^n = t_0^N - \frac{r}{v} - \Delta t(N - n) = \frac{n-1}{f} \quad (5)$$

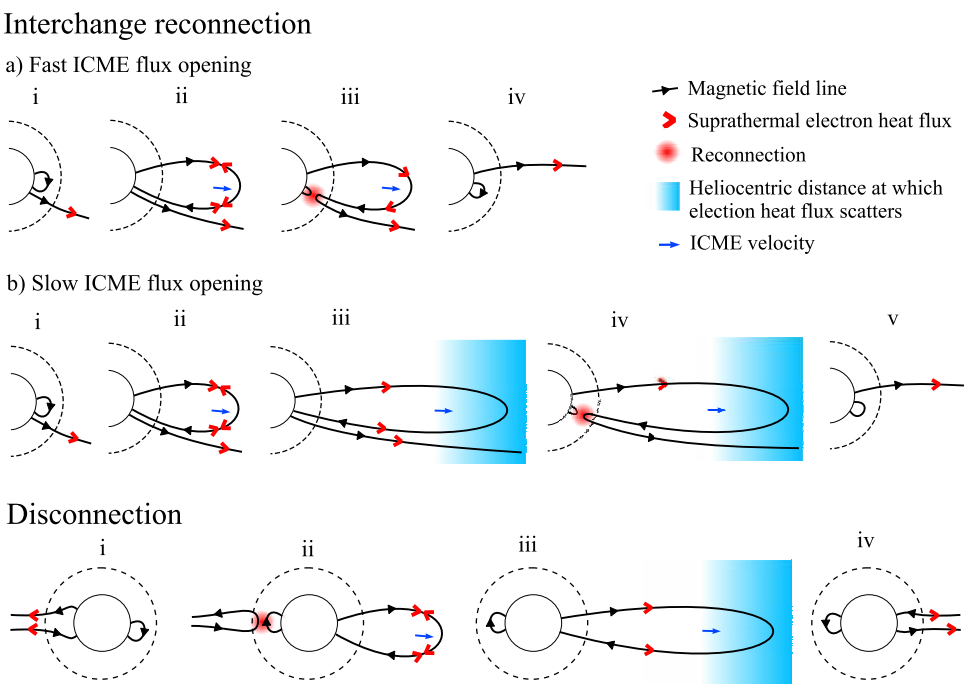

Figure 3. Suprathermal electron signatures of heliospheric flux buildup. Magnetic field lines are shown as solid black lines/arrows and electron beams by red arrows. The dashed line represents a surface at the heliocentric distance at which flux is observed. The top two panels show interchange reconnection: In the case of (a) "fast" ICME flux-opening, closed flux is identifiable by a counterstreaming electron (CSE) signature, which is removed once interchange reconnection opens the loop. However, for (b) "slow" flux-opening, it is necessary to consider the effect of suprathermal electron scattering due to the length of field lines. This can result in no CSE signature on closed loops, and electron dropouts on inverted flux systems. The bottom panel shows ICME flux balanced by disconnection of open flux, which immediately results in ED signatures.

For the constant reconnection rate mode, there is a limit to the number of ICMEs that can contribute to the heliospheric flux: For the interchange reconnection scenario, an ICME has no closed flux after a time $t_C = \phi_0/k$ and will not contribute to the inverted flux after a time $t_F = \phi_0/k + r/v$. Thus the earliest ICME that can still contribute to the closed (inverted) flux system is $n = f[t - t_C]$ ($n = f[t - t_F]$), rounded up to the nearest positive integer.

[27] Assuming all CMEs have the same properties (i.e., ϕ_0^n, λ^n, and v^n can be represented by average values ϕ_0, λ, and v, respectively), we express the flux at r resulting from both disconnection and interchange reconnection as:

[28] (1) Constant reconnection rate:

$$\Phi_r(t) = \Phi_0 + \sum_{n=f(t-t_C)}^{N} 2\left[\Phi_0 - k\left(t - \frac{n-1}{f}\right)\right] + \sum_{n=f(t-t_F)}^{N} 2\frac{kr}{v}$$

$$= \Phi_0 + \sum_{n=1}^{1+f(t_C-r/v)} 2\left[\phi_0 - k\left(t_C - \frac{n-1}{f}\right)\right] + \sum_{n=1}^{1+ft_C} 2\frac{kr}{v}$$

[29] (2) Reconnection rate proportional to ϕ:

$$\Phi_r(t) = \Phi_0 + \sum_{n=1}^{N} 2\phi_0 \exp\left[-\lambda\left(t - \frac{n-1}{f}\right)\right] + \sum_{n=1}^{N} 2\phi_0 \exp\left[-\lambda\left(t - \frac{n-1}{f}\right)\right]\left(\exp\left[\frac{r\lambda}{v}\right] - 1\right) \quad (6)$$

[30] As an equilibrium is attained (i.e., as $t \to \infty$), these expressions simplify to:

[31] (1) Constant reconnection rate:

$$\Phi_r(t) = \Phi_0 + \phi_0\left(1 + \frac{f\phi_0}{k}\right) + \frac{kfr^2 + krv}{v^2}$$

[32] (2) Reconnection rate proportional to ϕ:

$$\Phi_r(t) = \Phi_0 + \frac{2\phi_0}{1 - \exp[\lambda/f]} \quad (7)$$

[33] By considering solar minimum and maximum conditions separately (see Table 1 and Paper 1), and assuming radial flux is constant over the heliocentric sphere (i.e., $\Phi_r = 4\pi r^2|B_{\mathrm{RAD}}|$, where $|B_{\mathrm{RAD}}|$ is the radial magnetic field strength at r), we find the following: (1) k = 1.4 Wb/day, which translates to half the posteruption flux opening (or the equivalent open flux disconnecting) in 55 days, and Φ_0 = 9.3 $\times$ 10^{14} Wb, and (2) λ = 2.1 $\times$ 10^{-7} days, which translates to a closed flux half-life (or timescale for disconnection of open flux) of ~38 days, and Φ_0 = 9.4 $\times$ 10^{14} Wb. These estimates of the reconnection rates are the same as in Paper 1 because the additional inverted/disconnected flux contributions are negligible. This implies that EDs should only comprise a tiny fraction of the total flux, since in the interchange reconnection (disconnection) scenario, EDs can only be produced on this inverted (disconnected) flux system.

Table 1. Observational Estimates for the Parameters of the Heliospheric Flux Budget Calculation

Parameter	Symbol	Value
Average Solar Maximum $\|\mathbf{B}\|$ at 1 AU	$\|\mathbf{B}_{MAX}\|$	8 nT
Average Solar Minimum $\|\mathbf{B}\|$ at 1 AU	$\|\mathbf{B}_{MIN}\|$	5 nT
Average Solar Maximum CME Rate	f_{MAX}	4 day^{-1}
Average Solar Minimum CME Rate	f_{MIN}	1/3 day^{-1}
Typical Axial Flux in an ICME	ϕ_A	3×10^{12} Wb
Typical Fraction of ϕ that Opens at Formation	D	0.5

[34] As in Paper 1, we note that because the axial flux of magnetic clouds is being used as the value for all CMEs, ϕ is probably being overestimated. Hence the derived ICME flux-opening (open flux disconnection) times are best regarded as lower limits. On the other hand, Figure 2 shows that even for a constant (exponential) reconnection half-life as low as 55 (38) days, around a sixth (third) of the CME posteruption flux, which is a 12th (sixth) of the total axial flux, still remains closed after 100 days.

[35] Figure 4 shows the percentage flux at 1 AU expected to exhibit CSE (blue) and ED (red) signatures for CME frequencies at solar minimum (left panel) and solar maximum (right panel) over a range of values for R (the ICME distance beyond which the sunward suprathermal electron strahl at 1 AU fades out). Dashed (solid) lines show constant (exponential) reconnection times with a half-life of (55) 38 days and a background open flux of 9.3×10^{14} (9.4×10^{14}) Wb. The percentage of total flux displaying CSE and ED signatures in Figure 4 directly translates to the percentage of time CSE and ED signatures are expected at 1 AU (i.e., the rate of occurrence). The top panels show the results for interchange reconnection: Our model of heliospheric flux evolution with best observation estimates for the required parameters predicts that ED signatures should be rare (i.e., limited to $\leq$5%), even at solar maximum. CSE signatures are predicted to show a strong solar cycle variation, although the exact numbers depend strongly on the distance at which the strahl scatters.

[36] Ulysses observations have shown that CSEs persist to at least to 5 AU [*Crooker et al.*, 2004; *Riley et al.*, 2004],

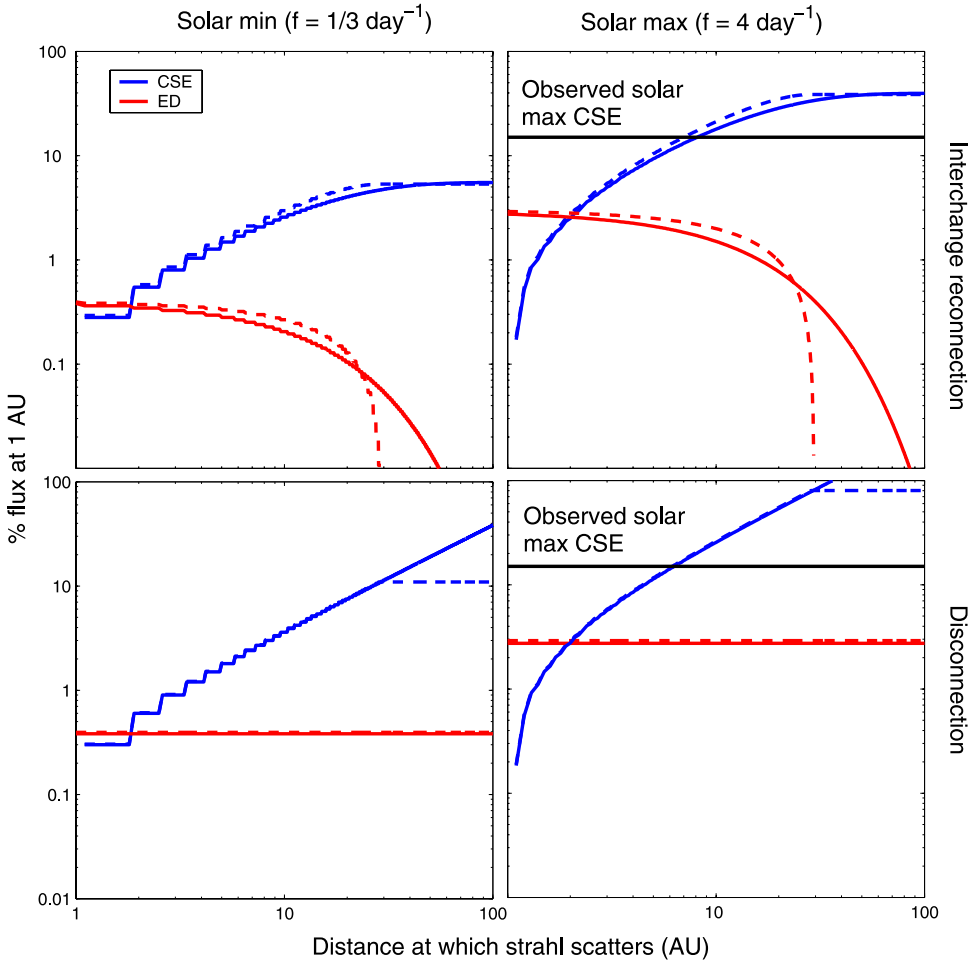

Figure 4. Predicted percentages of CSE (blue) and ED (red) signatures for CME frequencies at solar minimum (left) and maximum (right) at 1 AU, for a range of R, the distance at which the suprathermal electron strahl scatters. Top (bottom) panels show the interchange reconnection (disconnection) methods of reducing heliospheric flux. Dashed (solid) lines show constant (exponential) ICME flux opening with a half-life of (55) 38 days and a background open flux of 9.3×10^{14} (9.4×10^{14}) Wb is used. Note the logarithmic scale on both axes.

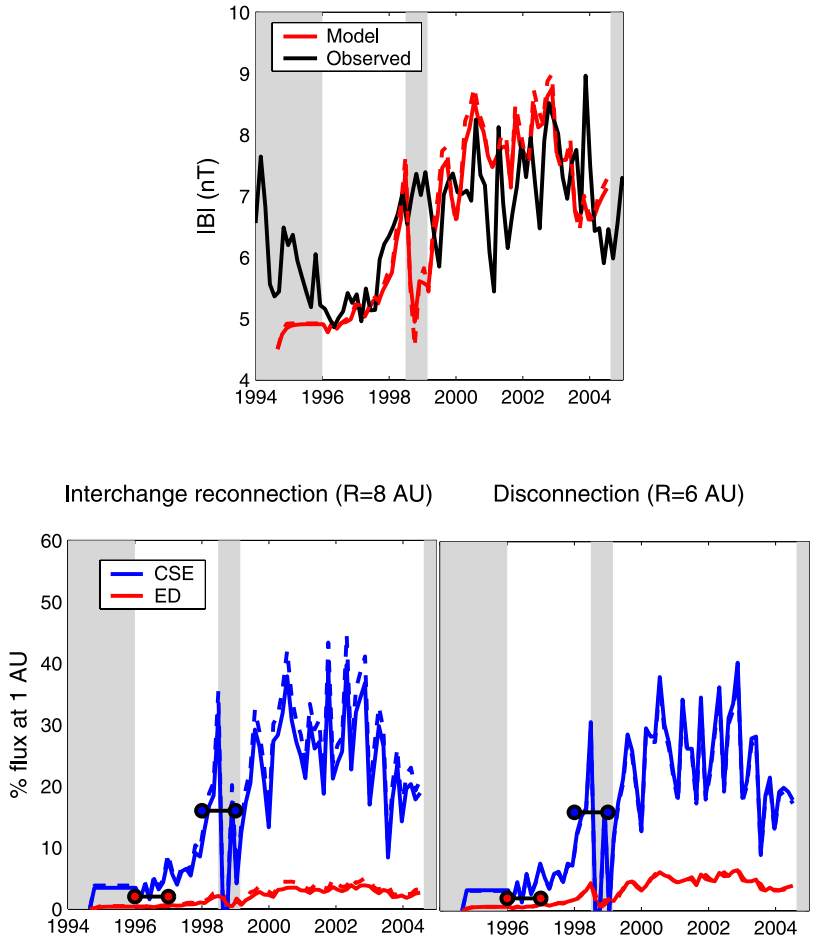

Figure 5. Magnetic flux and suprathermal electron signatures for simulations driven with LASCO-observed CME eruption times. Gray-shaded regions are times when LASCO observations were unavailable. Solid (dashed) lines show the exponential (constant) flux-opening model with a half-life of 38 (55) days. The top panel shows the model-predicted (red) and observed (black) magnetic field intensity at 1 AU: As in Paper 1, a good agreement is found. The bottom-left (bottom-right) panel shows the model-predicted occurrence of CSE and ED signatures at 1 AU for the interchange reconnection (disconnection) process, assuming the strahl scatters at 8 AU (6 AU). Observed occurrence rates of CSEs (EDs) are shown as black lines with blue (red) circles.

which means that a lower bound of 5 AU can be placed on R. This limits the predicted occurrence rate of CSEs to ~1–6% at solar minimum, rising to ~8–40% at solar maximum. *Gosling et al.* [1992] examined the ISEE 3 electron data and observed counterstreaming 15% of the time near maximum of solar cycle 22. From this value we obtain an estimate for R of 8 AU, as indicated by where the black line intersects the blue curves in the top-right panel of Figure 4.

[37] The bottom panels of Figure 4 show the equivalent results for disconnection: Contrary to *McComas et al.* [1992], we find that disconnection should not produce an abundance of ED signatures at 1 AU. However, the disconnection scenario produces more CSE signatures than the interchange reconnection scenario, with the observations of *Gosling et al.* [1992] best matched by R = 6 AU.

5. Dynamic Simulations

[38] In this section, the models are driven using the CME eruption times listed in the LASCO CME catalogue [*Yashiro et al.*, 2004], following an initiation period with a constant rate of 0.5 day^{-1}. At each time step, equation (4) is solved. Figure 5 shows the simulated magnetic flux and suprathermal electron signatures at 1 AU. Gray panels show times when LASCO observations were unavailable. Solid (dashed) lines show the exponential (constant) reconnection model with a half-life of 38 (55) days. The red plots in the top panel show the model-predicted magnetic field intensities at 1 AU, while the black line shows the observed value taken from the National Space Science Center (OMNI) data, averaged over 50 days (this long timescale is required for the observed magnetic field strength to be representative of the heliospheric flux [*Lockwood et al.*, 2004]). As in Paper 1, we find good agreement with the overall solar cycle variation of $|\mathbf{B}|$ at 1 AU.

[39] The bottom-left (bottom-right) panel of Figure 5 shows the model-predicted occurrence of CSE and ED signatures at 1 AU for the interchange reconnection (disconnection) process, assuming the strahl scatters at 8 AU (6 AU). It is immediately obvious that interchange reconnection and

disconnection can produce very similar electron signatures at 1 AU, although different values of R were used. Since here we do not model the latitudinal confinement of CME signatures at solar minimum, the CSE and ED signatures are probably underestimated at this time. At solar maximum, the occurrence of CSEs is highly variable, with a mean value of ~25%, slightly higher than *Gosling et al.*'s [1992] estimate for the previous cycle. At minimum of cycle 22, *Gosling et al.* [1992] found very few periods with CSE signatures (~1%), although the total data coverage at that time was poor (20%). This is also lower than the model prediction for cycle 23. Using data from the ACE spacecraft, *Skoug et al.* [2000] reported a slightly higher occurrence rate for CSEs of ~16% on the rise to the maximum of cycle 23 (shown as black line with blue circles in Figure 5), in close agreement with the model. For both interchange reconnection and disconnection, the occurrence of EDs remains below the 5–7% level throughout the simulation, which is roughly a factor 4–5 lower than the CSE occurrence rate. These low ED percentages suggest consistency with their perceived rarity in the heliosphere [*Pagel et al.*, 2005]. What is new is the model demonstration that this rarity does not imply an imbalance in the heliospheric flux budget. Thus the available suprathermal electron observations for the modeled solar cycle are in general agreement with the model of heliospheric flux evolution via interchange reconnection with $R \sim 8$ AU and via disconnection with $R \sim 6$ AU.

6. Discussion

[40] We have extended the heliospheric flux model of *Owens and Crooker* [2006] to predict the suprathermal electron signatures of heliospheric flux buildup from coronal mass ejections. We assume that either the closed fields of the ejecta open via interchange reconnection or disconnection occurs elsewhere: Both methods produce similar electron signatures at 1 AU. We find that the distance R beyond which suprathermal electrons fail to return to the observing point as sunward counterstreaming beams on closed loops owing to scattering is a critical parameter in determining the predicted occurrence rate of counterstreaming electrons and electron dropouts at 1 AU. Indeed, R may provide a means to differentiate between interchange reconnection and disconnection. CSE observations are best matched when $R \sim 8$ AU for interchange reconnection and when $R \sim 6$ AU for disconnection. The former seems to be the more reasonable value since counterstreaming is commonly observed at 5 AU [e.g., *Crooker et al.*, 2004]. The spiral nature of the field lines means that these R values are equivalent to a scattering distance ~30–40 AU, as illustrated in Figure 6.

[41] Our model assumes only that the sunward suprathermal electron strahl scatters once field lines reach a certain length. Adiabatic effects must also play a role. Figure 6 shows an ICME field line when the leading edge of the ejecta is at 8 AU. Suprathermal electrons must travel ~40 AU to provide the counterstreaming signature at 1 AU. Note that the antisunward (sunward) traveling electrons are moving into weaker (stronger) magnetic fields and therefore will be adiabatically focused (defocused). However, rather than focussing with distance from the Sun, electron beams are observed to broaden owing to scattering [*Hammond et al.*, 1996; *Maksimovic et al.*, 2005]. An adiabatic sunward return of these broadened strahls will then further defocus them. Hence a field line may exhibit CSEs at 8 AU but only a single strahl at 1 AU. This effect implies a slight overprediction of CSE and underprediction of ED occurrence rates over the solar cycle.

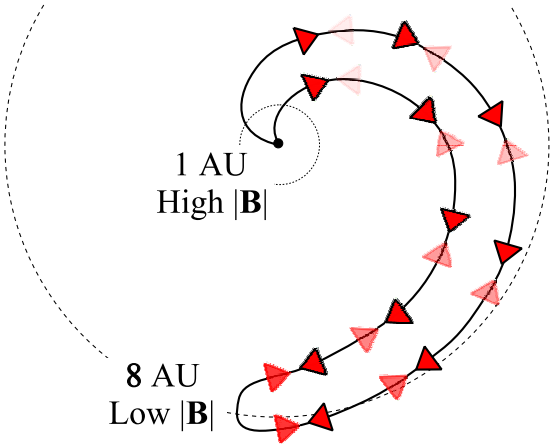

Figure 6. An illustration of the effect of solar rotation on the magnetic field line (black lines) length of ICMEs. When the leading edge of an ICME is at 8 AU, suprathermal electrons (red arrows) must travel ~40 AU to provide the counterstreaming signature at 1 AU. Note also that outward streaming electrons (black outline) are adiabatically focused by moving into weaker magnetic fields, whereas the inward streaming electrons (no outline) are defocused by traveling into stronger fields.

[42] Assuming the counterstreaming electron beam at 1 AU fades when the ICME leading edge is at 6–8 AU, the simulation with LASCO-observed CME times predicts the following 1-AU occurrence rates: CSEs are expected to be observed ~5% of the time at solar minimum, rising to ~25–30% of the time at solar maximum. These numbers are slightly higher than those reported by *Gosling et al.* [1992] for the previous solar cycle but in agreement with those reported by *Skoug et al.* [2000] for the modeled solar cycle. EDs are expected to be rare throughout the solar cycle, varying from $\leq$1% at solar minimum to ~5% at solar maximum. Although ED occurrence rates are difficult to determine, the HFD rate of 6% during the rising phase of solar cycle 23 minus the ~1% rate of those HFDs that are clearly cases of pitch angle scattering gives ~5% as an upper limit [*Pagel et al.*, 2005]. Further analysis is underway to provide a more accurate estimate of the ED occurrence rate.

[43] This prediction of negligible ED occurrence rates compared to CSE rates at 1 AU is one of the most important findings of the model. These contrast with the expectations of *McComas et al.* [1992]. They estimated that during the 18 months leading to the maximum of solar cycle 22, the amount of closed flux introduced by CMEs was four times the amount of disconnected flux created elsewhere, based upon HFD observations, and implied that these should be the same to achieve flux balance. In our models, the amount of closed flux introduced by CMEs is fully balanced by the amount of flux that interchange reconnects or disconnects to produce EDs, as it must be; but the long timescale over which the balancing process occurs compared to the 1-AU

distance of the observing point from the Sun makes a considerable difference in CSE and ED occurrence rates there. EDs can only be observed when the inverted/disconnected fields that carry them lie sunward of 1 AU, whereas CSEs continue to be observed when the leading edges of the loops that carry them lie well beyond 1 AU.

[44] In view of the fact that ultimately all magnetic field lines close somewhere, one might argue that the two scenarios modeled here, one with interchange reconnection opening ICME fields and the other with disconnection elsewhere, could be construed as the same process. An advantage of the former, in addition to providing a possible mechanism for the heliospheric polarity reversal over the solar cycle [*Owens et al.*, 2007] is that open flux is conserved, while the latter requires some unspecified mechanism for balancing the closed flux in ICMEs with the same amount of disconnected flux elsewhere. Once fields have passed far out into the heliosphere, however, keeping track of whether reconnection at the Sun is occurring between the leg of a loop and an open field or between two open fields seems unimportant, since all of the field lines, if followed out far enough, are loops. What is important is that the flux from CMEs does not continue to build, and either interchange reconnection or disconnection can prevent that buildup.

[45] In conclusion, we have proposed that the suprathermal electron signature of the interchange reconnection that opens ICME field-line loops long after their leading edges have passed beyond 1 AU is identical to the signature of disconnection, i.e., a dropout of the electron flux. We have used an analytical model to calculate its occurrence rate at 1 AU, under the assumption that all closed ICME fields eventually open, and find that it should be far less than the occurrence rate of the closed-field signature, in general agreement with observations. The same result holds under the alternative, earlier assumption that closed ICME flux is balanced by true disconnection elsewhere.

[46] **Acknowledgments.** This research was supported by the National Science Foundation Agreement ATM-012950, which funds the CISM project of the STC program, with additional support from NSF grant ATM-0553397.

[47] Amitava Bhattacharjee thanks Adam Rees and Peter Kiraly for their assistance in evaluating this paper.

References

Crooker, N. U., J. Gosling, and T. S. W. Kahler (2002), Reducing heliospheric flux from coronal mass ejections without disconnection, *J. Geophys. Res.*, *107*, (A2), 1028, doi:10.1029/2001JA000236.

Crooker, N. U., R. Forsyth, A. Rees, J. T. Gosling, and S. W. Kahler (2004), Counterstreaming electrons in magnetic clouds near 5 AU, *J. Geophys. Res.*, *109*, A06110, doi:10.1029/2004JA010426.

Gosling, J. T., D. N. Baker, S. J. Bame, W. C. Feldman, and R. D. Zwickl (1987), Bidirectional solar wind electron heat flux events, *J. Geophys. Res.*, *92*, 8519–8535.

Gosling, J. T., D. J. McComas, J. L. Phillips, and S. J. Bame (1992), Counterstreaming solar wind halo electron events—Solar cycle variations, *J. Geophys. Res.*, *97*, 6531–6535.

Gosling, J. T., J. Birn, and M. Hesse (1995), Three-dimensional magnetic reconnection and the magnetic topology of coronal mass ejection events, *Geophys. Res. Lett.*, *103*, 1941–1954.

Hammond, C. M., W. C. Feldman, D. J. McComas, J. L. Phillips, and R. J. Forsyth (1996), Variation of electron-strahl width in the high-speed solar wind: ULYSSES observations, *Astron. Astrophys.*, *316*, 350–354.

Lockwood, M., R. J. Forsyth, A. Balogh, and D. J. McComas (2004), Open solar flux estimates from near-Earth measurements of the interplanetary magnetic field: Comparison of the first two perihelion passes of the Ulysses spacecraft, *Ann. Geophys.*, *22*, 1395–1405Sref-ID:1432-0576/ag/2004-22-1395.

McComas, D. J., J. T. Gosling, J. L. Phillips, S. J. Bame, J. G. Luhmann, and E. J. Smith (1989), Electron heat flux dropouts in the solar wind: Evidence for interplanetary magnetic field reconnection?, *J. Geophys. Res.*, *94*, 6907–6916.

McComas, D. J., J. T. Gosling, and J. L. Phillips (1992), Interplanetary magnetic flux: Measurement and balance, *J. Geophys. Res.*, *97*, 171–177.

Maksimovic, M., et al. (2005), Radial evolution of the electron distribution functions in the fast solar wind between 0.3 and 1.5 AU, *J. Geophys. Res.*, *110*, A09104, doi:10.1029/2005JA011119.

Owens, M. J., and N. U. Crooker (2006), Coronal mass ejections and magnetic flux buildup in the heliosphere, *J. Geophys. Res.*, *111*, A10104, doi:10.1029/2006JA011641.

Owens, M. J., N. A. Schwadron, N. U. Crooker, Spence, W. J. Hughes, and H. E. Spence (2007), Role of coronal mass ejections in the heliospheric Hale cycle, *Geophys. Res. Lett.*, *34*, L06104, doi:10.1029/2006GL028795.

Pagel, C., N. U. Crooker, D. E. Larson, S. W. Kahler, and M. J. Owens (2005), Understanding electron heat flux signatures in the solar wind, *J. Geophys. Res.*, *110*, A01103, doi:10.1029/2004JA010767.

Riley, P., J. T. Gosling, and N. U. Crooker (2004), Ulysses observations of the magnetic connectivity between coronal mass ejections and the Sun, *Astrophys. J.*, *608*, 1100–1105.

Skoug, R. M., W. C. Feldman, J. T. Gosling, D. J. McComas, and C. W. Smith (2000), Solar wind electron characteristics inside and outside coronal mass ejections, *J. Geophys. Res.*, *105*, 23,069–23,084.

Wimmer-Schweingruber, R. F., et al. (2006), Understanding interplanetary coronal mass ejection signatures, *Space Sci. Rev.*, *123*, 177–216, doi:10.1007/s11214-006-9017-x.

Yashiro, S., N. Gopalswamy, G. Michalek, O. C. St. Cyr, S. P. Plunkett, N. B. Rich, and R. A. Howard (2004), A catalog of white light coronal mass ejections observed by the SOHO spacecraft, *J. Geophys. Res.*, *109*, A07105, doi:10.1029/2003JA010282.

N. U. Crooker and M. J. Owens, Center for Space Physics, Boston University, Boston, MA 02215, USA. (mjowens@bu.edu)

Remote sensing of the solar site of interchange reconnection associated with the May 1997 magnetic cloud

N. U. Crooker[1] and D. F. Webb[2]

Received 3 February 2006; revised 19 April 2006; accepted 2 May 2006; published 30 August 2006.

[1] The direction of suprathermal electron flux on open magnetic field lines in the 15 May 1997 magnetic cloud is used to predict the solar location of the interchange reconnection that released one end of what presumably were doubly connected field lines in the coronal mass ejection (CME) of origin on 12 May. A search for an X-ray signature of the interchange reconnection in the predicted location reveals a long-lasting arched structure stretching from high above the CME site to the northern polar coronal hole. At the edge of the coronal hole, coincident with the X-ray feature, are previously reported extreme ultraviolet brightenings (''crinkles''). The observations are consistent with a CME flux rope forming in a near-quadrupolar configuration while overhead open field lines reconnect with the rising, closed, rope fields to open one leg of the rope loop. The pattern is similar to the breakout model except there are no closed overhead field lines through which the rising flux rope must break out. The near-quadrupolar source appears to be responsible for the mismatch between the polarity of the flux rope observed at 1 AU and the sector in which it was embedded. Spacecraft interception of the leg rather than the apex of the flux rope loop may be responsible for the mismatch between the low inclination of the cloud axis and the high inclination predicted from the preexisting filament and magnetic configuration at the source.

Citation: Crooker, N. U., and D. F. Webb (2006), Remote sensing of the solar site of interchange reconnection associated with the May 1997 magnetic cloud, *J. Geophys. Res.*, *111*, A08108, doi:10.1029/2006JA011649.

1. Introduction

[2] Because of its spatial and temporal isolation from similar events, the magnetic cloud that engulfed Earth on 15 May 1997 and its eruption from the Sun in a coronal mass ejection (CME) on 12 May have been the subject of many coordinated studies and publications [e.g., *Plunkett et al.*, 1998; *Thompson et al.*, 1998; *Webb et al.*, 2000; *Arge et al.*, 2004; *Liu*, 2004; *Odstrcil et al.*, 2004, 2005; *Linker et al.*, 2005]. While the event's isolation provided an opportunity to make clear associations between solar and in situ signatures, many aspects of the erupting CME remain poorly understood. Here we add to the body of knowledge about the May 1997 event some new information from in situ suprathermal electron measurements (E > 80 eV) that bear upon models of the configuration of magnetic reconnection back at the Sun.

[3] Since suprathermal electrons continually stream out from the Sun along magnetic field lines, they are commonly used as sensors of whether field lines are connected to the Sun at one or both ends, that is, whether field lines are open or closed. If connected at both ends, the electron distributions are bidirectional, or counterstreaming. While counterstreaming electrons were one of the first signatures used to identify interplanetary coronal mass ejections (ICMEs) on a routine basis [e.g., *Gosling et al.*, 1987, 1990], it was soon recognized that not all fields in ICMEs are connected to the Sun at both ends. In particular, in those ICMEs classified as magnetic clouds [e.g., *Burlaga*, 1991], *Shodhan et al.* [2000] found that fields range from 100% open to 100% closed.

[4] Under the assumption that all field lines in CMEs are originally closed loops, the means by which they open is thought to be interchange reconnection, where an open field line reconnects with one leg of a large CME loop that is expanding into the heliosphere, thereby interchanging it for a small loop at the solar surface [*Gosling et al.*, 1995; *Crooker et al.*, 2002]. Which leg is the site of this interchange reconnection can be determined remotely from the direction of suprathermal electron flow relative to the magnetic field direction on any open field line in an ICME, since the electrons must be flowing from the leg that remains attached to the Sun. We apply this concept for the first time to the 15 May 1997 cloud. We predict where interchange reconnection occurred and find evidence in solar data that both support the prediction and provide information about the large-scale magnetic configuration of the CME site.

2. Analysis

[5] Wind data from the 15 May 1997 cloud were analyzed by *Webb et al.* [2000] and *Arge et al.* [2004]. Of

[1]Center for Space Physics, Boston University, Boston, Massachusetts, USA.
[2]Institute for Scientific Research, Boston College, Chestnut Hill, Massachusetts, USA.

0148-0227/06/2006JA011649

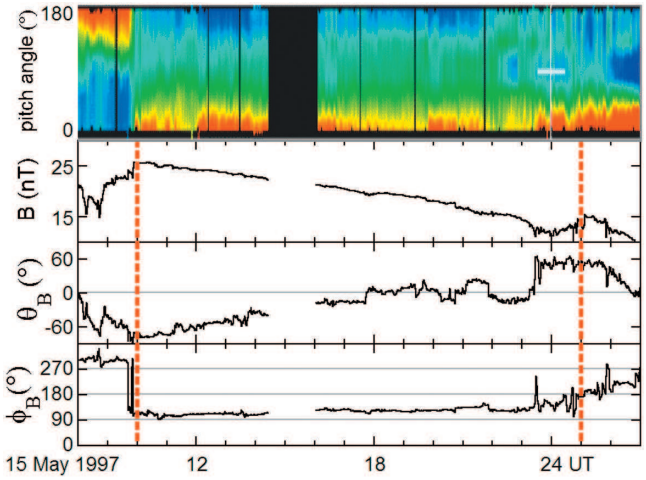

Figure 1. Time variations of color-coded (red is high intensity) electron pitch-angle distributions and magnetic field strength B, latitude angle θ_B, and longitude angle ϕ_B (GSE coordinates) from the Wind spacecraft as it passed through a magnetic cloud bounded by the red dashed vertical lines.

particular relevance here, they showed that the suprathermal electrons were unidirectional and streaming parallel to the magnetic field. Figure 1 illustrates these features in time variations of color-coded 260-eV electron pitch angle distributions from the 3DP instrument [*Lin et al.*, 1995] and of magnetic field parameters from the MFI magnetometer [*Lepping et al.*, 1995]. Between the dashed vertical lines marking the boundaries of the flux rope model fit to the cloud data by *Webb et al.* [2000], there is only a single red-yellow band of streaming electrons at 0° pitch angle, that is, parallel to the magnetic field. The lack of an accompanying band of counterstreaming electrons antiparallel to the field, at 180°, implies that all of the field lines in the cloud were open at 1 AU.

[6] The fact that the suprathermal electrons within the cloud were streaming parallel to the magnetic field means that the field lines on which they resided left the Sun with positive polarity, pointing away from the Sun, independent of any local inversions encountered by the spacecraft. In this case, Figure 1 shows that the magnetic field was not locally inverted, as it might be in some locations within the flux-rope structure of a magnetic cloud [e.g., *Crooker et al.*, 1998]. The magnetic longitude angle within the cloud pointed steadily away from the Sun at ~110°, close to the positive-polarity Parker spiral direction of ~135°, consistent with the positive polarity determined from the electron data.

[7] In the context of the large-scale magnetic sector structure in the heliosphere, the positive polarity of the cloud fields was opposite to the polarity of the sector in which the cloud was immersed, as pointed out by *Arge et al.* [2004]. This is contrary to the pattern in most interplanetary CMEs (ICMEs). Using the direction of the dominant

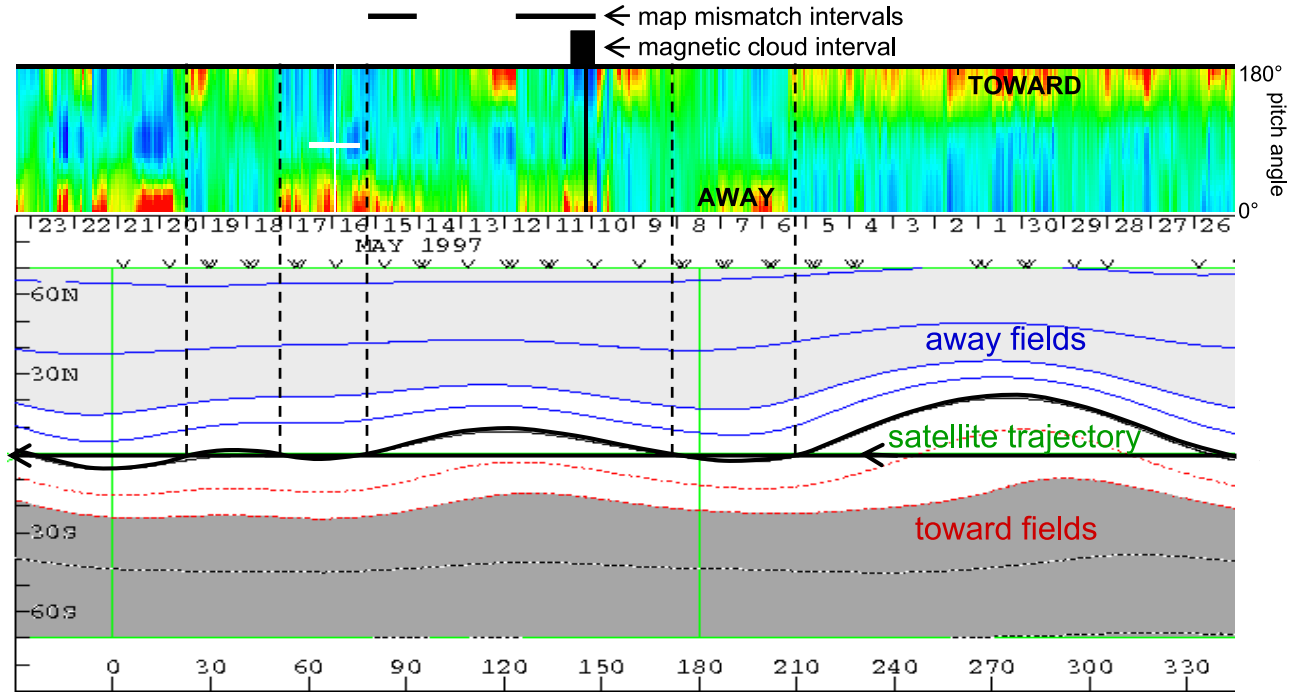

Figure 2. Time variations of color-coded electron pitch-angle distributions plotted from right to left to match the projected spacecraft passage across the potential field source surface map for Carrington Rotation 1922. The map was generated at the Wilcox Solar Observatory using the classic line-of-sight boundary condition and a source surface height of 2.5 solar radii. The contours of magnetic field strength lie at 0 (black curve), ±1, ±2, ±5, and ±10 mT. Dashed vertical lines extending from trajectory intersections with the projected HCS at 0 mT mark predicted polarity changes.

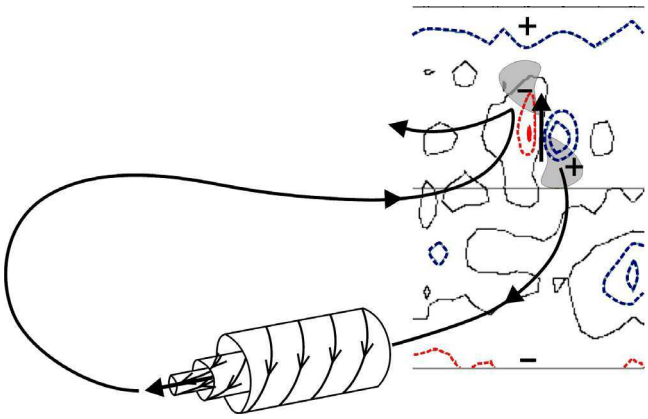

Figure 3. Schematic drawing of a magnetic cloud at 1 AU and its connection back to the solar surface, represented by a section of a photospheric field map from the Wilcox Solar Observatory for Carrington Rotation 1922 covering longitude 90° to 180° and latitude −70° to +70°. The contours of magnetic field strength lie at 0 (black), ±100, and ±200 mT, where the positive contours are blue and the negative red. The gray shapes approximate projected dimmings from EUV observations, and the vertical arrow represents the axis of the associated filament.

electron intensity in a counterstreaming event as an indicator of the polarity of which of the two legs of a closed ICME a spacecraft encounters, *Kahler et al.* [1999] showed that ICME legs are ten times more likely to match the polarity of the sector in which they are encountered than not. Although the study was confined to ICMEs with closed fields, presumably similar statistics apply to open-field ICMEs like the one of concern here. This polarity-matching property reflects the imprint of the dipolar component of the solar magnetic field [*Crooker*, 2000, 2005].

[8] Figure 2 illustrates how this polarity imprint was lacking for the May 1997 cloud. In the top panel, the color-coded electron pitch angle distribution plot for Carrington Rotation 1922 is shown with time running from right to left to match the pattern on the potential field source surface (PFSS) coronal map below it. To help compensate for the variable solar wind transit time from the Sun to the spacecraft in a simple, linear way, the pitch angle plot was displaced and uniformly stretched to maximize the match with polarity change predictions from the coronal map. The pitch angle plot covers ∼26.6 days, beginning midday on 1 May and ending around 0200 UT on 28 May. Compared to the dates on the 28.4-day-long map, beginning on 26 April, the time lag of the pitch angle plot ranges from 5.5 days at the beginning to 3.7 days at the end, corresponding to transit speeds of 314 km/s and 466 km/s, respectively. The average observed speed of 361 km/s during the interval lies within that range, as expected. The predicted polarity changes lie at the vertical dashed lines marking the intersections of the projected trajectory of the Wind spacecraft with the heavy curve outlining the heliomagnetic equator, which traces the predicted projection of the heliospheric current sheet (HCS). These predicted polarity changes match the observed changes in the adjusted pitch angle plot through most of the solar rotation. Where the satellite trajectory runs south of the HCS, starting from the right, the electron beam lies along the top of the plot, at 180° pitch angle, consistent with the predicted immersion in fields with toward polarity. As the trajectory crosses the HCS and passes above it at 210° longitude, the electron beam switches to 0° pitch angle, consistent with the predicted immersion in fields with away polarity. A similar match is present on the left end of the plot, even for the minor excursions above and beneath the predicted HCS. The only exceptions to the pattern lie within the sector containing the magnetic cloud, in the heliographic longitude interval ∼80°–170°. The electrons in two segments of that interval, the first containing the cloud itself, indicate polarity mismatches, as marked. They indicate away polarity in what is clearly predicted to be a toward sector. The mismatch within the cloud provides a clue about the magnetic configuration of the source CME, as discussed in section 3.2.

[9] The primary focus of this paper concerns another clue about the magnetic configuration of the source CME. Suprathermal electrons streaming only parallel and not antiparallel to the magnetic field within the cloud give unequivocal evidence that the positive leg of the structure was connected to the Sun and that the negative leg was not. If the negative leg was originally connected and then lost its connection through interchange reconnection, the data imply that open field lines reconnected with the negative leg back at the Sun. The configuration for this interchange reconnection from the interplanetary point of view is illustrated schematically in Figure 3.

[10] The nested cylindrical coils in Figure 3 represent the flux rope structure of the magnetic cloud. The cylindrical force-free model fit by *Webb et al.* [2000] yields a left-handed twist, a leading magnetic field pointing southward, and an axis that tips below the ecliptic plane at an angle $\theta_c = -11°$ at magnetic longitude $\phi_c = 108°$, where $\phi_c = 0°$ points toward the Sun. Other force-free cylindrical model fits give the same twist and similar angular values of $\theta_c = 0°$, $\phi_c = 108°$ (R. P. Lepping, private communication, 2005) and $\theta_c = -13°$, $\phi_c = 93°$ [*Lynch et al.*, 2005]. A dynamic cylindrical model gives the same twist and a similar axis elevation angle of $\theta_c = -10°$ but a different axis longitude of $\phi_c = 162°$ (K. Marubashi, private communication, 2006), discussed further in section 3.2. Although a cylinder is not a realistic shape for a magnetic cloud [e.g., *Suess*, 1988; *Riley and Crooker*, 2004], most of these cloud properties are probably not highly dependent upon shape and are used here to gain large-scale perspective [cf. *McAllister et al.*, 2001]. The axis tilt comes within at least 23° of matching the ∼10°-upward tilt of the predicted HCS on the coronal map in Figure 2, measured at the heliographic longitude of the cloud (∼145°). This approximate match and the southward leading field appear to reflect the large-scale dipolar properties of the solar field, consistent with earlier studies [*Bothmer and Rust*, 1997; *Mulligan et al.*, 1998; *Crooker*, 2000, and references therein]. This match contrasts with the polarity mismatch described above and is discussed further in section 3.2, along with the differences in model values of ϕ_c.

[11] The solar surface in Figure 3 is represented by a photospheric field map from the Wilcox Solar Observatory. Although this kind of map lacks the more accurate details that can be provided by magnetograms from space-based

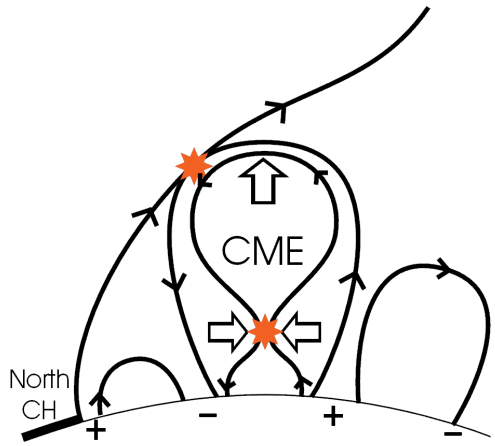

Figure 4. Schematic drawing of the magnetic configuration and reconnection sites (red) of the 12 May 1997 CME. Interchange reconnection high in the corona between open field lines from the northern coronal hole (CH) and closed field lines in the CME acts to open the CME field lines.

measurements, it is suitable for the large-scale analysis discussed here. At this rising phase of solar cycle 23, the northern polar fields were positive (blue contours), and the southern polar fields were negative (red contours). Above the heliographic equator, the map shows the strong bipolar field contours of the active region from which the 12 May CME emerged. The bipolar fields together with the large-scale dipolar fields created a near-quadrupolar structure at the source. The north-pointing arrow between the bipolar contours indicates the preevent orientation of fields in a filament that erupted with the CME. They lay orthogonal to the model cloud axis, in contrast to a statistical tendency toward alignment [e.g., *Zhao and Hoeksema*, 1997], although the left-handed filament chirality matches the cloud twist, as reported by *Webb et al.* [2000]. These parameters are discussed further in section 3.2.

[12] Superposed on the active-region contours in Figure 3 are two shaded areas representing the double-dimming signature seen in images from the Extreme ultraviolet Imaging Telescope (EIT) on the SOHO spacecraft [*Thompson et al.*, 1998]. Following *Webb et al.* [2000], these are treated as the two footpoints of the originally closed flux rope loop comprising the magnetic cloud. *Kahler and Hudson* [2001] raise questions about this kind of association, among them asking why dimmings disappear well before the associated clouds reach 1 AU, where presumably the clouds are still rooted in the Sun. The proposed interchange reconnection, at least in this case, however, may account for the disappearance of the dimming, a possibility foreseen by *Kahler and Hudson* [2001] and discussed further in section 3.1.

[13] The heavy curve in Figure 3 connecting the cylinder to the solar surface represents the core field of the flux rope loop after it lost its connection to the negative footpoint through interchange reconnection with a positive open field line, consistent with the electron data. The field line in what was originally the negative (unsampled) leg of the flux rope acquired positive polarity through the interchange reconnection process, even though it locally points toward the Sun, while the field line in the positive (sampled) leg maintained its original polarity and merely became open.

[14] The configuration in Figure 3 immediately raises the question of the source of open field lines feeding into the interchange reconnection site. Although sometimes PFSS models indicate that open fields stem from active regions [e.g., *Neugebauer et al.*, 2002; *Schrijver and DeRosa*, 2003; *Wang and Sheeley*, 2003a], in this case none was apparent (in three-dimensional (3-D) maps provided by Z. Mikic (private communication, 2004)). The nearest available source of open fields with the required positive polarity was the large reservoir in the northern polar coronal hole, and we assume it was these that fed into the reconnection site.

[15] Figure 4 shows a schematic drawing of the proposed configuration in the corona. Because it is a 2-D rendering of a process with essential 3-D aspects, it fails to show the nonalignment of the active-region bipolar and large-scale dipolar fields, and the implied sequence of reconnection at low and high altitudes should not be treated literally. Nevertheless, the figure captures the essence of the proposed topology. It shows the quadrupolar structure depicted in the well-known breakout model of CME initiation [*Antiochos et al.*, 1999], with a flux rope forming through reconnection under the rising CME [e.g., *Lynch et al.*, 2004]. In 3-D, however, the structure is not the true quadrupole required by the model dynamics because the neutral line on high-resolution magnetograms forms a peninsula rather than an island (J. A. Linker, private communication, 2005). Moreover, nothing breaks out because there is no overlying dipolar field line confining the emerging flux rope. The field line that reconnects at high altitude is open rather than closed, and its reconnection opens the negative leg of the rising CME.

[16] X-ray images from the Yohkoh Soft X-ray telescope (SXT) show a long-lasting feature that may be a signature of the proposed interchange reconnection. To emphasize its longevity, Figure 5 shows three of these images spaced ~3 hours apart. Focused on the upper right-hand (northwestern) quadrant of the Sun, the images prominently display a time sequence of the cusped arcade event associated with the 12 May CME. Cusped arcade events are interpreted as signatures of the reconnection that creates the flux rope, that is, the lower-altitude reconnection illustrated in Figure 4 [e.g., *Shibata et al.*, 1995; *Hundhausen*, 1997]. Fainter but clearly visible in Figure 5 is an arched shape, marked by an arrow in the middle frame, that appears to be at high altitude and extends toward the northern polar region. It is this feature which we interpret as a signature of the higher-altitude interchange reconnection in Figure 4, where the newly closed segment of the originally open field line sunward of the reconnection point represents the illuminated arch. The feature first appeared in an earlier image at 0653 UT and lasted in faint form into the early hours of the next day, consistent with long-lasting interchange reconnection accompanying the flux-rope formation.

[17] We note that the proposed signature of interchange reconnection in Figure 5 is not an uncommon feature. Bright arches that extend from CME sites to coronal hole boundaries have been noted for some time [e.g., *Rust and*

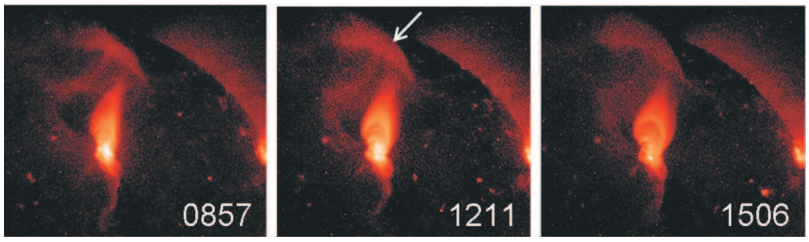

Figure 5. Yohkoh X ray images from three times on 12 May 1997, as marked. The arrow in the middle frame points to the proposed signature of interchange reconnection.

Webb, 1977]. Here we offer a plausible explanation for their occurrence.

3. Discussion

3.1. Interchange Reconnection

[18] The proposed configuration for interchange reconnection in the 12 May event is topologically similar to configurations proposed for two other processes which may be intimately related. The first is interchange reconnection that facilitates the reversal of the solar magnetic field in the course of the solar cycle. *Wang and Sheeley* [2003b] derive nearly the same pattern for the rising phase of the cycle, the same phase in which the May event occurred. The difference between their model and the proposed configuration is that their closed fields are generated by emerging bipoles rather than CMEs, since their model cannot accommodate CME dynamics. Nevertheless, our replication of their topological configuration suggests that their model captures what may be a common reconnection pattern in CMEs.

[19] The second similar configuration is that deduced by *Sterling and Moore* [2001a, 2001b] for what they call "EIT crinkles," bright patterns that intrude into coronal holes in EIT images. *Sterling and Moore* [2001a, 2001b] identified these patterns in a series of CMEs that occurred on 1–2 May 1998. On the basis of an earlier concept called "tether cutting" [*Sturrock*, 1989; *Moore and Roumeliotis*, 1992], they ascribed the crinkles to "external reconnection" between open and closed field lines at the apex of a rising CME, equivalent to the interchange reconnection described here. In their case the open field lines emerged from a low-latitude coronal hole rather than the polar coronal hole. Because the proposed reconnection site was at the outer boundary of the CME, *Sterling and Moore* [2001a, 2001b] cited EIT crinkles as evidence for the breakout model. Here we suggest that EIT crinkles are just evidence of interchange reconnection and not the breakout model, since any overlying fields that are open do not create a barrier from which a CME must break out, as already mentioned in section 2.

[20] *Sterling and Moore* [2001a, 2001b] also analyzed X-ray images of the 1–2 May 1998 events and showed that the EIT crinkles occurred at the extremities of bright X-ray regions that extended back to the active regions from which the CMEs arose. We suggest that these bright regions, aptly named "anemones" by *Shibata et al.* [1994], can thus be treated as the X-ray signature of interchange reconnection. The X-ray signature, reflecting hotter plasma, would appear along the same magnetic field lines at altitudes higher than the EIT signature. For the 12 May 1997 event, the arched X-ray feature in Figure 5 may be a perspective view of an anemone, since it occurred at considerably higher latitudes than the 1–2 May 1998 events. Its lower-altitude EUV counterpart appears to have been already identified by *Thompson et al.* [1998]. They show EIT images with brightening at the edge of the northern coronal hole, presumably the legs of loops rooted in what *Sterling and Moore* [2001a, 2001b] would identify as EIT crinkles. These lasted for more than 7 hours, consistent with our supposition that long-lasting interchange reconnection released the negative leg of the CME. EIT brightenings along coronal hole boundaries, like the X-ray features that extend to the boundaries, are not uncommon accompaniments to CMEs (L. Harra, private communication, 2005) and thus comprise likely signatures of frequently associated interchange reconnection.

[21] Regarding the disappearance of the dimming signatures mentioned in section 2, Figure 3 and Figure 4 illustrate how the proposed interchange reconnection may have eliminated the northern dimming region by filling the footprint of the northern leg of the CME with closed field lines. This process meets the expectations of *Kahler and Hudson* [2001] for reconnection of fields outside the CME and contraction of the outer dimming boundary (in addition to the expected contraction of the inner boundary as the arcade under the CME reformed). Dimming in the presumed footprint of the southern leg may have disappeared owing to interchange reconnection, as well, but in a considerably different way, as proposed by *Attrill et al.* [2006]. These authors recently performed a comprehensive study of the dimming and X-ray signatures of the May 1997 event and independently came to the same conclusions regarding the proposed interchange reconnection configuration in Figure 4. They show that dimming in the two regions disappeared at different rates and suggest that the open field lines rooted in the southern region diffused out of the dimming region through interchange reconnection low in the solar atmosphere with small loops in the magnetic carpet. Thus interchange reconnection may be responsible for the disappearance of dimmings either through a return of closed flux or through a dispersal of open flux. These kinds of interchange reconnection may be part of a larger process of global magnetic footpoint circulation as discussed, for example, by *Fisk and Schwadron* [2001].

3.2. Solar Magnetic Field Imprint and Model Implications

[22] Section 2 notes two ways in which the 15 May 1997 ICME appeared to carry the imprint of the dipolar component of the solar magnetic field (a southward leading field

and cloud axis alignment with the HCS) and one way in which it did not (the mismatch of the polarity of the cloud leg with the sector polarity). Moreover, the cloud did not appear to carry the imprint of the higher-order filament fields, since its axis was orthogonal to the filament axis. These mixed signals may reflect a mix of elements from the breakout model of CMEs, with its focus on quadrupolar structure, as discussed in section 2, and models which focus on the dipolar structure of flux-rope formation through reconnection of helmet streamer field lines [e.g., *Lin and Forbes*, 2000; *Low and Zhang*, 2002; *Linker et al.*, 2003], especially because all of these models, including tether cutting, are closely related [e.g., *Isenberg et al.*, 1993; *Lin et al.*, 2001; *Lynch et al.*, 2004]. On the other hand, Figure 3 suggests a more specific geometrical explanation described below in terms of where the spacecraft intersected the flux rope loop.

[23] The configuration of the magnetic field, of the dimmings, and of the preeruption filament axis at the CME site in Figure 3 and the orientation of the bright arcade in Figure 5 consistently predict the formation of a left-handed flux rope with a north-pointing axis, tilted slightly to the east, and with predominantly eastward leading fields. Studies that use this kind of prediction and assume little change in flux rope orientation as the CME moves out into the heliosphere have been reasonably successful in matching magnetic cloud properties [e.g., *Bothmer and Rust*, 1997; *Zhao and Hoeksema*, 1997; *Crooker et al.*, 1998; *McAllister et al.*, 2001]. In this case, however, the observed cloud, with its southward leading fields and east-pointing axis, lay essentially orthogonal to the predicted one. The only match with a predictive parameter was the near-alignment of the cloud axis with the HCS, and this parameter is an outlier in the sense that it does not agree with those listed above. *Webb et al.* [2000] point out that the flux rope may have rotated counterclockwise as it rose, since the erupting filament, presumably threading the rope [e.g., *Lin and Forbes*, 2000; *Low and Zhang*, 2002], was observed to do so.

[24] An alternative possibility is that the flux rope axis maintained a north-south orientation, reflecting a match with the filament axis rather than the HCS, but that the spacecraft encountered its southern leg rather than the apex of the loop. For flux rope loops that leave the Sun with north-south axes, that orientation can be maintained only at the apex of the loop, while the legs will tend to stretch out along the Parker spiral. Figure 3 attempts to convey this geometry, where the position of the cylindrical form illustrating the flux rope structure, along the southern leg of the loop, sunward of the loop's apex, indicates the proposed site of spacecraft encounter. Consistent with this view, the cloud axis longitude ϕ_c in the leg location agrees better with the more realistic dynamic model fit (162°) compared to the force-free fits (93°, 108°) discussed in section 2, where the latter seem to mistakenly imply encounter with the apex. Even better agreement (ϕ_c = 139° (K. Marubashi, private communication, 2006)), in the sense of being closer to the Parker spiral, is obtained with the dynamic curved cylindrical model of *Marubashi* [1997, 2002], approximated by a torus. Encounter with the southern leg is also consistent with the observed mismatch between the polarity of the cloud leg and the polarity of the sector in which it was imbedded. This mismatch reflects the near-quadrupolar structure at the source, where the footpoint of the southern leg has a polarity opposite that of the southern dipolar field (Figure 3).

4. Conclusions

[25] Using observations of suprathermal electrons in the 15 May 1997 magnetic cloud at 1 AU, we have remotely identified what appear to be signatures of CME-associated interchange reconnection on the Sun in X-ray and EUV observations. These signatures are global in nature, spanning from the active-region source to the polar coronal hole. Since global-scale coronal activity is commonly noted in association with CMEs, it may be that signatures of interchange reconnection are commonly observed but until now have not been recognized as such. Further case studies are needed to test this possibility.

[26] The mixed signatures of the imprint of the solar magnetic field on the 15 May 1997 magnetic cloud were at first surprising in view of the isolation and relative simplicity of the event. Analysis of the cloud parameters in the context of the heliospheric magnetic field and the configuration of the source region, however, suggest that the mixed signatures arose from straightforward geometrical constraints.

[27] **Acknowledgments.** This material is based in part upon work supported by the National Science Foundation under grant ATM-0553397 and under agreement ATM-012950 of the STC program, which funds the Center for Integrated Space Weather Modeling (CISM), and by NASA under grant NNG05GD97G. The authors thank S. W. Kahler and A. C. Sterling for helpful comments.

[28] Zuyin Pu thanks the reviewers for their assistance in evaluating this paper.

References

Antiochos, S. K., C. R. Devore, and J. A. Klimchuk (1999), A model for solar coronal mass ejections, *Astrophys. J.*, *510*, 485–493.

Arge, C. N., J. G. Luhmann, D. Odstrcil, C. J. Schrijver, and Y. Li (2004), Stream structure and coronal sources of the solar wind during the May 12th, 1997 CME, *J. Atmos. Terr. Phys.*, *66*, 1295–1309.

Attrill, G., M. S. Nakwacki, L. K. Harra, L. vanDriel-Gesztelyi, C. H. Mandrini, S. Dasso, and J. Wang (2006), Using the evolution of coronal dimming regions to probe the global magnetic field topology, *Sol. Phys.*, in press.

Bothmer, V., and D. M. Rust (1997), The field configuration of magnetic clouds and the solar cycle, in *Coronal Mass Ejections*, *Geophys. Monogr. Ser.*, vol. 99, edited by N. U. Crooker, J. A. Joselyn, and J. Feynman, pp. 137–146, AGU, Washington, D. C.

Burlaga, L. F. (1991), Magnetic clouds, in *Physics of the Inner Heliosphere II*, edited by R. Schwenn and E. Marsch, pp. 1–22, Springer, New York.

Crooker, N. U. (2000), Solar and heliospheric geoeffective disturbances, *J. Atmos. Sol. Terr. Phys.*, *62*, 1071–1085.

Crooker, N. U. (2005), ICME-CME connections: Outstanding questions, in *Solar Wind Eleven*, edited by B. Fleck and T. H. Zurbuchen, *Eur. Space Agency Spec. Publ.*, *ESA SP 592*, 289–295.

Crooker, N. U., et al. (1998), Sector boundary transformation by an open magnetic cloud, *J. Geophys. Res.*, *103*, 26,859–26,868.

Crooker, N. U., J. T. Gosling, and S. W. Kahler (2002), Reducing heliospheric magnetic flux from coronal mass ejections without disconnection, *J. Geophys. Res.*, *107*(A2), 1028, doi:10.1029/2001JA000236.

Fisk, L. A., and N. A. Schwadron (2001), The behavior of the open magnetic field of the Sun, *Astrophys. J.*, *560*, 425–438.

Gosling, J. T., D. N. Baker, S. J. Bame, W. C. Feldman, and R. D. Zwickl (1987), Bidirectional solar wind electron heat flux events, *J. Geophys. Res.*, *92*, 8519–8535.

Gosling, J. T., S. J. Bame, D. J. McComas, and J. L. Phillips (1990), Coronal mass ejections and large geomagnetic storms, *Geophys. Res. Lett.*, *17*, 901–904.

Gosling, J. T., J. Birn, and M. Hesse (1995), Three-dimensional magnetic reconnection and the magnetic topology of coronal mass ejection events, *Geophys. Res. Lett.*, *22*, 869–872.

Hundhausen, A. J. (1997), Coronal mass ejections, in *Cosmic Winds and the Heliosphere*, edited by J. R. Jokipii, C. P. Sonett, and M. S. Giampapa, pp. 259–296, Univ. of Ariz. Press, Tucson.

Isenberg, P. A., T. G. Forbes, and P. Demoulin (1993), Catastrophic evolution of a force-free flux rope: A model for eruptive flares, *Astrophys. J.*, *417*, 368–386.

Kahler, S. W., and H. S. Hudson (2001), Origin and development of transient coronal holes, *J. Geophys. Res.*, *106*, 29,239–29,248.

Kahler, S. W., N. U. Crooker, and J. T. Gosling (1999), The polarities and locations of interplanetary coronal mass ejections in large interplanetary magnetic sectors, *J. Geophys. Res.*, *104*, 9919–9924.

Lepping, R. L., et al. (1995), The Wind magnetic field investigation, *Space Sci. Rev.*, *71*, 207–229.

Lin, J., and T. G. Forbes (2000), Effects of reconnection on the coronal mass ejection process, *J. Geophys. Res.*, *105*, 2375–2392.

Lin, J., T. G. Forbes, and P. A. Isenberg (2001), Prominence eruptions and coronal mass ejections triggered by newly emerging flux, *J. Geophys. Res.*, *106*, 25,053–25,074.

Lin, R. P., et al. (1995), A three-dimensional plasma and energetic particle investigation for the Wind spacecraft, *Space Sci. Rev.*, *71*, 125–153.

Linker, J. A., Z. Mikic, V. R. Lionello, and P. Riley (2003), Flux cancellation and coronal mass ejections, *Plasma Phys.*, *10*, 1971–1978.

Linker, J. A., Z. Mikic, V. Titov, R. Lionello, and P. Riley (2005), Modeling active region coronal mass ejections, *Eos Trans. AGU*, *86*(18), Jt. Assem. Suppl., Abstract SH54B-05.

Liu, Y. (2004), Photospheric magnetic field observations during the May 12, 1997 CME and their implications for modeling that event, *J. Atmos. Terr. Phys.*, *66*, 1283–1293.

Low, B. C., and M. Zhang (2002), The hydromagnetic origin of the two dynamical types of solar coronal mass ejections, *Astrophys. J.*, *564*, L53–L56.

Lynch, B. J., S. K. Antiochos, P. J. MacNeice, T. H. Zurbuchen, and L. A. Fisk (2004), Observable properties of the breakout model for coronal mass ejections, *Astrophys. J.*, *617*, 589–599.

Lynch, B. J., J. R. Gruesbeck, T. H. Zurbuchen, and S. K. Antiochos (2005), Solar cycle–dependent helicity transport by magnetic clouds, *J. Geophys. Res.*, *110*, A08107, doi:10.1029/2005JA011137.

Marubashi, K. (1997), Interplanetary magnetic flux ropes and solar filaments, in *Coronal Mass Ejections*, *Geophys. Monogr. Ser.*, vol. 99, edited by N. U. Crooker, J. A. Joselyn, and J. Feynman, pp. 147–156, AGU, Washington, D. C.

Marubashi, K. (2002), Interplanetary flux ropes, *J. Commun. Res. Lab.*, *49*, 41–59.

McAllister, A. H., S. F. Martin, N. U. Crooker, R. P. Lepping, and R. J. Fitzenreiter (2001), A test of real-time prediction of magnetic cloud topology from solar signatures, *J. Geophys. Res.*, *106*, 29,185–29,194.

Moore, R. L., and G. Roumeliotis (1992), Triggering of eruptive flares - destabilization of the preflare magnetic field configuration, in *Eruptive Solar Flares*, *Proc. IAU*, vol. 133, edited by Z. Svestka, B. V. Jackson, and M. E. Machado, pp. 69–78, Springer, New York.

Mulligan, T., C. T. Russell, and J. G. Luhmann (1998), Solar cycle evolution of the structure of magnetic clouds in the inner heliosphere, *Geophys. Res. Lett.*, *25*, 2959–2963.

Neugebauer, M., P. C. Liewer, E. J. Smith, R. M. Skoug, and T. H. Zurbuchen (2002), Sources of the solar wind at solar activity maximum, *J. Geophys. Res.*, *107*(A12), 1488, doi:10.1029/2001JA000306.

Odstrcil, D., P. Riley, and X. P. Zhao (2004), Numerical simulation of the 12 May 1997 interplanetary CME event, *J. Geophys. Res.*, *109*, A02116, doi:10.1029/2003JA010135.

Odstrcil, D., V. J. Pizzo, and C. N. Arge (2005), Propagation of the 12 May 1997 interplanetary coronal mass ejection in evolving solar wind structures, *J. Geophys. Res.*, *110*, A02106, doi:10.1029/2004JA010745.

Plunkett, S. P., et al. (1998), LASCO observations of an Earth-directed coronal mass ejection on May 12, 1997, *Geophys. Res. Lett.*, *25*, 2477–2480.

Riley, P., and N. U. Crooker (2004), A kinematic treatment of CME evolution in the solar wind, *Astrophys. J.*, *600*, 1035–1042.

Rust, D. M., and D. F. Webb (1977), Soft X ray observations of large-scale coronal active region brightenings, *Sol. Phys.*, *54*, 403–417.

Schrijver, C. J., and M. L. DeRosa (2003), Photospheric and heliospheric magnetic fields, *Sol. Phys.*, *212*, 165–200.

Suess, S. T. (1988), Magnetic clouds and the pinch effect, *J. Geophys. Res.*, *93*, 5437–5445.

Shibata, K., et al. (1994), A gigantic coronal jet ejected from a compact active region in a coronal hole, *Astrophys J.*, *431*, L51–L53.

Shibata, K., et al. (1995), Hot-plasma ejections associated with compact-loop solar flares, *Astrophys J.*, *451*, L83–L85.

Shodhan, S., et al. (2000), Counterstreaming electrons in magnetic clouds, *J. Geophys. Res.*, *105*, 27,261–27,268.

Sterling, A. C., and R. L. Moore (2001a), Internal and external reconnection in a series of homologous solar flares, *J. Geophys. Res.*, *106*, 25,227–25,238.

Sterling, A. C., and R. L. Moore (2001b), EIT crinkles as evidence for the breakout model of solar eruptions, *Astrophys. J.*, *560*, 1045–1057.

Sturrock, P. A. (1989), The role of eruption in solar flares, *Sol. Phys.*, *121*, 387–397.

Thompson, B. J., S. P. Plunkett, J. B. Gurman, J. S. Newmark, O. C. St. Cyr, and D. J. Michels (1998), SOHO/EIT observations of an Earth-directed coronal mass ejection on May 12, 1997, *Geophys. Res. Lett.*, *25*, 2465–2468.

Wang, Y.-M., and N. R. Sheeley Jr. (2003a), The solar wind and its magnetic sources at sunspot maximum, *Astrophys. J.*, *587*, 818–822.

Wang, Y.-M., and N. R. Sheeley Jr. (2003b), On the topological evolution of the coronal magnetic field during the solar cycle, *Astrophys. J.*, *599*, 1404–1417.

Webb, D. F., et al. (2000), The origin and development of the May 1997 magnetic cloud, *J. Geophys. Res.*, *105*, 27,251–27,259.

Zhao, X.-P., and J. T. Hoeksema (1997), Is the geoeffectiveness of the 6 January 1997 CME predictable from solar observations?, *Geophys. Res. Lett.*, *24*, 2965–2968.

N. U. Crooker, Center for Space Physics, Boston University, 725 Commonwealth Avenue, Boston, MA 02215, USA. (crooker@bu.edu)

D. F. Webb, Air Force Research Laboratory/VSBXS, 27 Randolph Road, Hanscom AFB, MA 01731-3010, USA.

Space Sci Rev (2012) 172:201–208
DOI 10.1007/s11214-011-9748-1

Interchange Reconnection: Remote Sensing of Solar Signature and Role in Heliospheric Magnetic Flux Budget

N.U. Crooker · M.J. Owens

Received: 5 August 2010 / Accepted: 17 January 2011 / Published online: 16 February 2011

Abstract Interchange reconnection at the Sun, that is, reconnection between a doubly-connected field loop and singly-connected or open field line that extends to infinity, has important implications for the heliospheric magnetic flux budget. Recent work on the topic is reviewed, with emphasis on two aspects. The first is a possible heliospheric signature of interchange reconnection at the coronal hole boundary, where open fields meet closed loops. The second aspect concerns the means by which the heliospheric magnetic field strength reached record-lows during the recent solar minimum period. A new implication of this work is that interchange reconnection may be responsible for the puzzling, occasional coincidence of the heliospheric current sheet and the interface between fast and slow flow in the solar wind.

Keywords Coronal hole boundary · Reconnection · Stream interface · Heliospheric magnetic field

1 Introduction

In space physics applications, it is useful to describe magnetic field lines as either open or closed. Open field lines have one end rooted in the magnetized body and the other end extending out to infinity. Closed field lines form loops that have both ends rooted in the magnetized body. Since ultimately all field lines are closed, how infinity is defined for open fields can lead to misconceptions, as will be discussed in the last section. The subject of this paper, interchange reconnection, occurs when an open field line reconnects with a closed field line.

Although the term "interchange reconnection" is relatively new (Crooker et al. 2002), as a concept it has been invoked for some time to account for solar and solar wind

N.U. Crooker (✉)
Center for Space Physics, Boston University, Boston, MA 02215, USA
e-mail: crooker@bu.edu

M.J. Owens
Space Environment Physics Group, Department of Meteorology, University of Reading, Reading, UK

phenomena and, more recently, for magnetospheric phenomena (see review in Merkin and Crooker 2008). Two properties of interchange reconnection are particularly relevant to this paper. First, interchange reconnection transports the foot of the open field line to the far footpoint of the closed loop. This transport has been invoked to explain the rigid rotation of coronal holes, the domain of open field lines on the Sun, in the face of differential rotation (e.g., Nash et al. 1988; Wang and Sheeley 2004). It has also been invoked to effect a global circulation of open flux on the Sun when the Sun's dipole axis is tilted with respect to the pattern of differential rotation (e.g., Fisk 1996; Fisk et al. 1999). The second property involves the exchange of flux between the Sun and the heliosphere. When the apex of the loop that participates in interchange reconnection at the Sun extends out into the heliosphere, the act of reconnection reduces the heliospheric flux from the two legs of the loop to one leg, and a new loop forms on the Sun (e.g., Gosling et al. 1995). The next section addresses the possibility of observing signatures of flux transport across the coronal hole boundary, and the following section addresses whether or not interchange reconnection can account for the dearth of magnetic flux in the heliosphere during the recent solar minimum.

2 Flux Transport at the Coronal Hole Boundary

Crooker et al. (2010) have recently reported on a possible remote signature of interchange reconnection on the Sun at the boundary between open field lines, which are concentrated in coronal holes, and closed field lines comprising the streamer belt that straddles the heliomagnetic equator. Here we review that work and suggest how it may support new ideas about the topology of the boundary as discussed in another paper in this volume.

If interchange reconnection occurs on the Sun across some boundary marked by a change in plasma characteristics, its signature at a spacecraft at 1 AU will be a separation between the plasma and suprathermal electron signatures of that boundary, as noted by Borovsky (2008). The reason for the separation is that suprathermal electrons streaming out from the Sun along magnetic field lines reach 1 AU within a matter of hours compared to days for solar wind plasma convecting radially outward. Crooker et al. (2010) applied that argument to the coronal hole boundary under the assumption (consistent, for example, with Fisk et al. 1999) that its signature in the heliosphere is the stream interface, the boundary between the fast flow emanating from coronal holes and the slow flow emanating from the streamer belt. With superposed epoch analysis they identified a suprathermal electron signature at the interface at 1 AU consisting of a strong peak in 250-eV flux integrated over pitch angle. In individual cases, however, this electron peak was often displaced from the well-known plasma signatures of the interface stemming from the pressure ridge there, where fast flow runs into slow flow. The displacements indicate that the electron flux peaks are not caused by local compression. Whatever the cause of the peaks (see discussion in Crooker et al. 2010 of relevant work by Gosling et al. 1978), the displacements may be signatures of interchange reconnection, as proposed by Borovsky (2008).

Figure 1 illustrates the process of signature displacement at the stream interface before and after interchange reconnection occurs. To understand the diagram, it is best to focus first on the magnetic field lines emanating from the solar surface: They are the same in number and polarity in both views, but their connections change. The field line that has its origin at the coronal hole boundary, that is, the boundary between open field lines in the coronal hole and closed field lines in the streamer belt, is marked with a heavy curve in both views. In Fig. 1a it forms the stream interface between fast flow from the coronal hole, shaded gray,

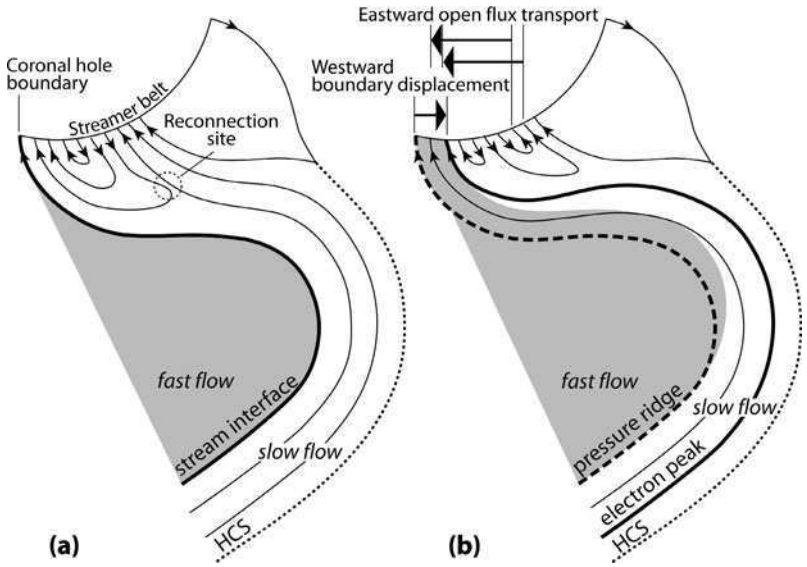

Fig. 1 Schematic illustration of the magnetic configuration (**a**) before and (**b**) after displacement of suprathermal electron and plasma signatures of the stream interface between fast and slow flow resulting from flux transport by interchange reconnection at the coronal hole boundary on the Sun (adapted from Crooker et al. 2010)

and slow flow from the streamer belt surrounding the heliospheric current sheet (HCS). Although with distance from the sun the fast flow slows and the slow flow speeds up near the interface owing to the dynamic interaction, in steady state the interface remains as the boundary between what was originally slow and fast flow.

Figure 1b illustrates a transitional state some time after interchange reconnection acts to displace the coronal hole boundary. In this case the heavy field line marking the coronal hole boundary maps out to the location of the peak suprathermal electron flux, which serves as a nearly instantaneous field-line tracer of the new coronal hole boundary location. The pressure ridge that forms the plasma signature of the stream interface in the heliosphere, however, remains at the original location of the interface, displaced from the electron signature. The field line threading the pressure ridge in the heliosphere is now marked by a heavy dashed curve instead of a solid curve because, closer to the Sun, it diverges from the boundary of the gray area marking the pressure ridge and, thus, no longer connects to the coronal hole boundary. Eventually the plasma at the newly displaced coronal hole boundary convects out into the heliosphere, and a steady state is reached in which a single field line lies along the interface between fast and slow flow, as in Fig. 1a.

The interchange reconnection in Fig. 1 takes place at the encircled reconnection site in Fig. 1a between the outer two of the three nested loops and the two open field lines adjacent to the helmet streamer. (The presence of these open field lines in the purportedly closed-field region of the streamer belt is an approximation that is fully discussed below.) As a result of the reconnection, the footpoints of the two open field lines saltate (leap abruptly) eastward, across the distance originally spanned by the loops, and join the open fields in the coronal hole. To accommodate the transported flux, the coronal hole boundary shifts westward, although by a much smaller distance. The reverse sense of open-field-line transport, from the coronal hole to the streamer belt, is illustrated in Crooker et al. (2010). Their observational

results, which apply only to those sections of the coronal hole boundary where the streamer belt lies west of the coronal hole, as in Fig. 1, suggest that flux transport can be in either direction there.

The lack of evidence for any systematic westward flux transport reported by Crooker et al. (2010) was surprising in view of predictions for the rigid rotation of equatorward extensions of coronal holes, illustrated by Wang and Sheeley (2004), and for the pattern of global footpoint circulation proposed by Fisk et al. (1999). Both of these concepts are specific about the direction of flux transport depending upon whether the coronal hole lies to the east or west of its boundary with the streamer belt. The most intriguing explanation for the lack of systematic transport lies in the recent work by S. Antiochos, J. Linker, and colleagues (e.g., Antiochos et al. 2011; Edmondson et al. 2010), as discussed in another paper in this volume. They propose that the coronal hole boundary can be highly irregular, with deep corrugations. Under these conditions, it seems reasonable to expect that while systematic flux transport may occur on a global scale, its signature may be overcome by the random signature of transport across the locally ragged boundary.

The concept of an irregular coronal hole boundary can be used to explain the presence of open field lines in the streamer belt in Fig. 1a. Strictly speaking, open field lines cannot exist in isolated islands separate from areas of other open field lines of the same polarity (Crooker and Siscoe 1990; Antiochos et al. 2007). If the coronal hole boundary is irregular, however, a cross-section passing from one side to the other may cut through a mix of volumes of open and closed fields, as in Fig. 1a. On the other hand, if we maintain the definition of the coronal hole boundary as the boundary between open and closed fields, then the configuration in Fig. 1 loosens the connection between the coronal hole boundary and the boundary between fast and slow flow. It suggests that the latter lies at the outer envelope of the irregular coronal hole boundary, consistent with the conclusions of the latest version of the Fisk model of global footpoint circulation (Zhao and Fisk 2010).

3 Heliospheric Flux Balance

Interchange reconnection may play a major role in the heliospheric magnetic flux budget. As solar activity increases during the rising phase of the solar cycle, magnetic loops expand into the heliosphere and increase the amount of flux there. Although from the perspective of potential field source surface modeling these loops merely become open flux, from the heliospheric perspective the loops are closed flux that can be detected by the presence of counterstreaming suprathermal electrons emanating from both footpoints on the Sun. Moreover, the loops are nearly always located within interplanetary coronal mass ejections (ICMEs) (e.g., Wimmer-Schweingruber et al. 2006), which implies that coronal mass ejections (CMEs) are nearly the sole source of flux added to the heliosphere. Since flux in the heliosphere does not continue to increase but waxes and wanes with the solar cycle, there must also be some mechanism for losing flux. Two possibilities have been proposed. One is interchange reconnection at the Sun, whereby a loop in an ICME opens through reconnection between one of its legs and an open field line (Gosling et al. 1995; Crooker et al. 2002). The other is disconnection at the Sun, whereby two open field lines reconnect to form a completely disconnected U-shaped field line (e.g., McComas et al. 1989). In both cases flux is returned to the Sun by the formation of a small loop there.

The recent, deep, extended solar minimum has prompted much discussion about whether interchange reconnection or disconnection is responsible for the record-breaking low values of interplanetary field strength (Owens et al. 2008; Connick et al. 2011; Schwadron et al.

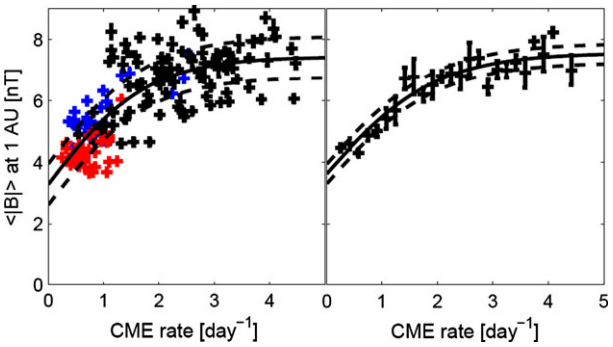

Fig. 2 Scatter plots of Carrington-Rotation averaged CME rate against magnetic field strength in the heliosphere at 1 AU, updated from Crooker and Owens (2010) to include points through the end of 2009. In the *left panel*, points from the recent solar minimum are *red* and points from the previous solar minimum are *blue*. In the *right panel*, points are binned by CME rate. The *solid curves* are tanh fits bracketed by *dashed curves* at the 95% confidence level

2010; Crooker and Owens 2010; Zhao and Fisk 2010). While interchange reconnection has the attractive property of conserving open flux, since reconnection with loops transports but does not destroy the participating open flux, disconnection can proceed ad infinitum, independent of the presence of closed loops. Disconnection is thus capable of reducing the flux to zero, whereas interchange reconnection can proceed only until all of the closed flux opens, leaving the conserved open flux to supply a floor value to heliospheric field strength.

Possible evidence for a floor value to heliospheric field strength has been presented by Svalgaard and Cliver (2007, 2010) using long-term historical records and by Owens et al. (2008) and Crooker and Owens (2010) using measured CME rates over the past solar cycle. An update of the results presented in the latter two papers is shown in Fig. 2. Carrington-Rotation-averages of CME rate and heliospheric field strength are plotted against each other covering the period from the last solar minimum in blue to the recent minimum in red in the left panel. If the loss of flux is accomplished by opening closed loops in ICMEs through interchange reconnection, then the heliospheric field strength should depend upon how many CMEs are fed into the heliosphere. The points in the left panel of Fig. 2 are consistent with this view, although the scatter is broad. When binned by CME rate, in the right panel, a clearer pattern emerges. Evidence for a floor value to the heliospheric field strength is the fact that the hyperbolic tangent curve fit to the points intersects the B axis at a finite value for zero CME rate. That value is ∼3.8 nT, comparable to the lowest averages plotted in the left panel.

The origin has been included in this updated version of the plots in order to obtain a sense of the likelihood that a fitted curve could pass through it, as it would if there were no floor value to the field. While the curve on the right clearly could not pass through the origin, one can imagine a curve with some functional form other than tanh running up from the origin through the unbinned values on the left, owing to the large degree of scatter. Thus at most one can say that the data do not preclude the possibility that interchange reconnection is the primary means of reducing flux in the heliosphere and that open flux is conserved. On the other hand, making this statement may come as a surprise to those who have noted the steady, prolonged decline in heliospheric field strength during the recent minimum.

4 Discussion and Conclusions

Two aspects of interchange reconnection have been addressed primarily from an observational point of view—its possible signature at the coronal hole boundary and its role in the heliospheric flux budget. Here we discuss some relevant points about flux budget models, the expected locations of source and loss processes on the Sun, and how those locations might map to the heliosphere.

Models of the heliospheric flux budget that assume interchange reconnection as the sole means of flux loss (e.g., Owens and Crooker 2006), or, more generally, that flux loss depends upon the amount of closed flux, overestimate the heliospheric field strength during the recent minimum (Owens et al. 2011). The reason may be owing to the simplifying assumption that the rate of interchange reconnection is constant. If it varies, instead, with the degree to which higher order fields dominate the solar configuration, as they did during the recent minimum compared to the previous minimum, then the model can provide a good fit to the observations (Owens et al. 2011). Why the reconnection rate should vary in this way is discussed further below.

Whether it is interchange reconnection or disconnection that reduces flux in the heliosphere once loops have passed beyond about 10 AU is a question that cannot be addressed by suprathermal electron observations (Owens and Crooker 2007; Connick et al. 2011). The counterstreaming signature of a loop is lost at 1 AU once the apex of the loop is so far out that electrons cannot stream out from the Sun and back to the observer along the far leg owing to scattering. All that remains is unidirectional streaming from the Sun along the leg encountered by the observer. Any interchange reconnection between that loop and an open field line will give the signature of disconnection, which is a dropout of electrons, called a "heat flux dropout" (McComas et al. 1989; Crooker and Pagel 2008). These are observed frequently enough that flux budget models can accommodate either interchange reconnection or disconnection as a loss mechanism (Owens and Crooker 2007). Owens et al. (2011) use the term "pinching" for either process at the Sun and generalize the models so that the distinction between the processes is not important, aside from the issue of whether or not open flux is conserved.

Evidence for pinching can be found in white light observations at the Sun and plasma observations in the heliosphere. The location of pinching for disconnection is expected to be at the base of the heliospheric current sheet, where open fields of opposite polarity meet at the tips of helmet streamers, and the location of pinching for interchange reconnection is expected to be at the coronal hole boundary, which can be in the same vicinity. For example, Wang et al. (2000) ascribe the release of blobs from the tips of coronal streamers, as seen in white light images, to either process. Also seen in white light near the current sheet are downflows ascribed to loops returning to the Sun as the result of disconnection (e.g., Sheeley and Wang 2001), although these could as well result from pinching by interchange reconnection. The downflows occur preferentially where the current sheet is highly inclined to the heliographic equator, that is, when the dipole component of the field is strong and tilted or when higher order fields dominate the configuration and produce a highly warped current sheet. Presumably the preferred site for downflows reflects higher rates of reconnection there, driven by differential rotation. It is this property of downflows which motivated Owens et al. (2011) to vary the flux loss rate with the degree of current sheet tilt/warp in the flux budget model. In the heliosphere, the expected site for signatures of interchange reconnection on the Sun is at the stream interface, as illustrated in Fig. 1, and the expected site for signatures of disconnection on the Sun is at the heliospheric current sheet. Heat flux dropouts, which take the form of high-beta plasma sheets, are a likely signature of either, and these occur at and near the heliospheric current sheet, possibly the heliospheric

counterpart of the blobs observed near the Sun (Crooker et al. 2004a). The high degree of variability in measurements of plasma sheets near and at the heliospheric current sheet is consistent with the new concept of a ragged coronal hole boundary that continually changes its configuration through reconnection, as Fig. 1 illustrates.

The Fig. 1 view also offers an explanation for a longstanding question regarding the position of the stream interface relative to the heliospheric current sheet. While at 1 AU it usually takes about 10 hours for a spacecraft to pass from the heliospheric current sheet to the stream interface (Gosling et al. 1978), that distance is highly variable, and sometimes the two features coincide (e.g., Siscoe and Intriligator 1993; Crooker et al. 1999). Antiochos et al. (2011) point out similar variability in related MHD model parameters. Figure 1 shows how the variability could be the result of interchange reconnection, which, at times, might locally remove all open flux between the interface and the current sheet. The view in the right panel shows a reduced space between the features, implying some remaining open flux between them, but the features could as well have been drawn as coincident.

Finally, we consider the question of whether the sources and losses in the flux budget are related, as assumed for the model invoking interchange reconnection to open all of the loops added by CMEs, or not, as assumed for disconnection. Recent findings that bear upon this question concern how CMES, which commonly arise near active regions, can be related to losses at the distant coronal hole boundary. Cohen et al. (2009, 2010) have simulated CME events that are accompanied by coronal waves and confirm the view of Attrill et al. (2007) that the footpoints of these CME loops rapidly saltate laterally through reconnection with other loops until they reach the coronal hole boundary. Thus the loops are rapidly exposed to the site of flux loss by interchange reconnection. Suprathermal electron data suggest that about half of the loops in CMEs open in this manner shortly after ejection (Shodhan et al. 2000; Crooker et al. 2004b). The remaining loops are expected to open over timescales on the order of 40 days (Owens and Crooker 2006). Over these long timescales, however, the observational distinction between interchange reconnection and disconnection becomes moot, as discussed above. Loss by either process might cease when the dominance of higher order fields disappears and the heliospheric current sheet aligns with the heliographic equator, as noted by Owens et al. (2011), in which case it is not clear how the amount of flux lost might match the amount that was added. It is also important to note that interchange reconnection with loops that have not left the solar atmosphere, as pictured in Fig. 1, act only to transport open field lines and does not reduce the flux in the heliosphere.

In conclusion, interchange reconnection may be responsible for a ragged coronal hole boundary, a variable distance between stream interfaces and the heliospheric current sheet, and reducing flux in the heliosphere.

Acknowledgements The authors thank the International Space Science Institute, Bern, for the opportunity to present this research at a workshop in January, 2010. Additionally, N. Crooker thanks the (US) National Science Foundation for support under grant AGS-0962645.

References

S.K. Antiochos, C.R. Devore, J.T. Karpen, Z. Mikić, Astrophys. J. **671**, 936–946 (2007). doi:10.1086/522489

S.K. Antiochos, Z. Mikic, R. Lionello, V. Titov, J. Linker, Astrophys. J. (2011, submitted)

G.D.R. Attrill, L.K. Harra, L. van Driel-Gesztelyi, P. Demoulin, Astrophys. J. **656**, L101–L104 (2007). doi:10.1086/512854

J.E. Borovsky, J. Geophys. Res. **113**, A08110 (2008). doi:10.1029/2007JA012684

O. Cohen, G.D.R. Attrill, W.B. Manchester, M.J. Wills-Davey, Astrophys. J. **705**, 587–602 (2009). doi:10.1088/0004-637X/705/1/587

O. Cohen, G.D.R. Attrill, N.A. Schwadron, N.U. Crooker, M.J. Owens, C. Downs, T.I. Gombosi, J. Geophys. Res. **115**, A10104 (2010). doi:10.1029/2010JA015464
D.E. Connick, C.W. Smith, N.A. Schwadron, Astrophys. J. **727** (2011). doi:10.1088/0004-637X/727/1/8
N.U. Crooker, M.J. Owens, in *SOHO-23: Understanding a Peculiar Solar Minimum*, ed. by S. Cranmer, T. Hoeksema, J. Kohl. ASP Conf. Proc., vol. 428, pp. 279–283 (Astronomical Soc. Pacific, San Francisco, 2010). Also as arXiv:1004.2238v1 [astro-ph.SR]
N.U. Crooker, C. Pagel, J. Geophys. Res. **113**, A02106 (2008). doi:10.1029/2007JA012421
N.U. Crooker, G.L. Siscoe, J. Geophys. Res. **95**, 3795–3799 (1990)
N.U. Crooker, J.T. Gosling et al., in *Corotating Interaction Regions*, ed. by A. Balogh, J.T. Gosling, J.R. Jokipii, R. Kallenbach, H. Kunow. ISSI Space Sci. Ser. (Kluwer Academic, Dordrecht, 1999), pp. 179–220. Also, Space Sci. Rev. **89**, 179–220 (1999)
N.U. Crooker, J.T. Gosling, S.W. Kahler, J. Geophys. Res. **107**(A2), 1028 (2002). doi:10.1029/2001JA000236
N.U. Crooker, C.-L. Huang, S.M. Lamassa, D.E. Larson, S.W. Kahler, H.E. Spence, J. Geophys. Res. **109**, A03107 (2004a). doi:10.1029/2003JA010170
N.U. Crooker, R. Forsyth, A. Rees, J.T. Gosling, S.W. Kahler, J. Geophys. Res. **109**, A06110 (2004b). doi:10.1029/2004JA010426
N.U. Crooker, E.M. Appleton, N.A. Schwadron, M.J. Owens, J. Geophys. Res. **115**, A11101 (2010). doi:10.1029/2010JA015496
J.K. Edmondson, S.K. Antiochos, C.R. DeVore, B.J. Lynch, T.H. Zurbuchen, Astrophys. J. **714**, 517–531 (2010). doi:10.1088/0004-637X/714/1/517
L.A. Fisk, J. Geophys. Res. **101**, 15,547–15,553 (1996)
L.A. Fisk, N.A. Schwadron, T.H. Zurbuchen, J. Geophys. Res. **104**, 19,765–19,772 (1999)
J.T. Gosling, J.R. Asbridge, S.J. Bame, W.C. Feldman, J. Geophys. Res. **83**, 1401–1412 (1978)
J.T. Gosling, J. Birn, M. Hesse, Geophys. Res. Lett. **22**, 869–872 (1995)
D.J. McComas, J.T. Gosling, J.L. Phillips, S.J. Bame, J.G. Luhmann, E.J. Smith, J. Geophys. Res. **94**, 6907–6916 (1989)
V.G. Merkin, N.U. Crooker, J. Geophys. Res. **113**, A00B04 (2008). doi:10.1029/2008JA013140
A.G. Nash, N.R. Sheeley, Jr., Y.-M. Wang, Sol. Phys. **117**, 359–389 (1988)
M.J. Owens, N.U. Crooker, J. Geophys. Res. **111**, A10104 (2006). doi:10.1029/2006JA011641
M.J. Owens, N.U. Crooker, J. Geophys. Res. **112**, A06106 (2007). doi:10.1029/2006JA012159
M.J. Owens, N.U. Crooker, N.A. Schwadron, T.S. Horbury, S. Yashiro, H. Xie, O.C. St. Cyr, N. Gopalswamy, Geophys. Res. Lett. **35**, L20108 (2008). doi:10.1029/2008GL035813
M.J. Owens, N.U. Crooker, M. Lockwood, J. Geophys. Res. (2011, submitted)
N.A. Schwadron, D.E. Connick, C.W. Smith, Astrophys. J. **722**, L132–L136 (2010)
N.R. Sheeley Jr., Y.-M. Wang, Astrophys. J. **562**, L107–L110 (2001)
S. Shodhan, N.U. Crooker, S.W. Kahler, R.J. Fitzenreiter, D.E. Larson, R.P. Lepping, G.L. Siscoe, J.T. Gosling, J. Geophys. Res. **105**, 27,261–27,268 (2000)
G. Siscoe, D. Intriligator, Geophys. Res. Lett. **20**, 2267–2270 (1993)
L. Svalgaard, E.W. Cliver, Astrophys. J. **661**, L203–L206 (2007)
L. Svalgaard, E.W. Cliver, J. Geophys. Res. **115**, A09111 (2010). doi:10.1029/2009JA015069
Y.-M. Wang, N.R. Sheeley Jr., Astrophys. J. **612**, 1196–1205 (2004)
Y.-M. Wang, N.R. Sheeley Jr., D.G. Socker, R.A. Howard, N.B. Rich, J. Geophys. Res. **105**, 25,133–25,142 (2000)
R.F. Wimmer-Schweingruber, N.U. Crooker et al., in *Coronal Mass Ejections*, ed. by H. Kunow et al. ISSI Space Sci. Ser. (Springer, Dordrecht, 2006), pp. 177–216. Also, Space Sci. Rev. **123**, 177–216. doi:10.1007/s11214-006-9017-x
L. Zhao, L. Fisk, in *SOHO-23: Understanding a Peculiar Solar Minimum*, ed. by S. Cranmer, T. Hoeksema, J. Kohl. ASP Conf. Proc., vol. 428 (Astronomical Soc. Pacific, San Francisco, 2010) pp. 229–234. Also as arXiv:1003.4336v1 [astro-ph.SR]

SOLAR IMPRINT ON ICMES, THEIR MAGNETIC CONNECTIVITY, AND HELIOSPHERIC EVOLUTION

N. U. CROOKER[1,*] and T. S. HORBURY[2]
[1]*Center for Space Physics, Boston University, Boston, Massachusetts, USA*
[2]*The Blackett Laboratory, Imperial College, London, UK*
([*]Author for correspondence: E-mail: crooker@bu.edu)

(Received 21 April 2004; Accepted in final form 29 August 2005)

Abstract. Interplanetary outflows from coronal mass ejections (ICMEs) are structures shaped by their magnetic fields. Sometimes these fields are highly ordered and reflect properties of the solar magnetic field. Field lines emerging in CMEs are presumably connected to the Sun at both ends, but about half lose their connection at one end by the time they are observed in ICMEs. All must eventually lose one connection in order to prevent a build-up of flux in the heliosphere; but since little change is observed between 1 AU and 5 AU, this process may take months to years to complete. As ICMEs propagate out into the heliosphere, they kinematically elongate in angular extent, expand from higher pressure within, distort owing to inhomogeneous solar wind structure, and can compress the ambient solar wind, depending upon their relative speed. Their magnetic fields may reconnect with solar wind fields or those of other ICMEs with which they interact, creating complicated signatures in spacecraft data.

1. Introduction

How do the properties of interplanetary coronal mass ejections (ICMEs) relate to their origins on the Sun, and how do the kinematics and dynamics of propagation into the heliosphere affect ICMEs and their environment? These two questions structure the content of this paper. The first concerns internal structure and magnetic connection to the Sun and is addressed in Section 2. The second concerns external processes and is addressed in Section 3.

2. Internal Structure and Connectivity

As reviewed by Zurbuchen and Richardson (2006, this volume), ICMEs range in complexity from fairly simple magnetic clouds characterized by smooth field rotations, high magnetic field strength, and low temperature (e.g., Burlaga, 1988) to complicated, compound structures with signatures that have non-matching boundaries. This section focuses on the simple structures, magnetic clouds, whose magnetic parameters, usually calculated from flux rope model fits, can be classified and related to solar parameters. Sections 2.1, 2.2, and 2.3, respectively, address

Space Science Reviews (2006) 123: 93–109
DOI: 10.1007/s11214-006-9014-0

the imprint of solar magnetic fields on clouds, the remote connections of magnetic field lines in clouds, and the relation between cloud properties and solar features observed in coronagraphs.

2.1. Solar Magnetic Field Imprint

Various aspects of solar magnetic structures are reflected in the structure of magnetic clouds. Section 2.1.1 discusses how CME formation under the helmet streamer belt can create ICMEs that blend into the heliospheric sector structure, and Section 2.1.2 discusses how the chirality, leading magnetic field orientation, and axis orientation of magnetic clouds reflects magnetic properties of filaments and the helmet streamer belt.

2.1.1. *ICMEs and Sector Boundaries*

Coronagraphs have long shown that CMEs arise from the predominantly closed field line regions of the Sun under the umbrella of the helmet streamer belt (e.g., Hundhausen, 1993). The helmet streamer belt, in turn, forms the base from which stems the boundary between sectors of oppositely directed magnetic fields in the heliosphere, or the heliospheric current sheet (HCS) (Figure 1a).If field lines from the arcade of loops comprising the streamer belt rise, shear, and reconnect to form a CME flux rope, as pictured in Figure 1a and commonly modeled (e.g., Mikic

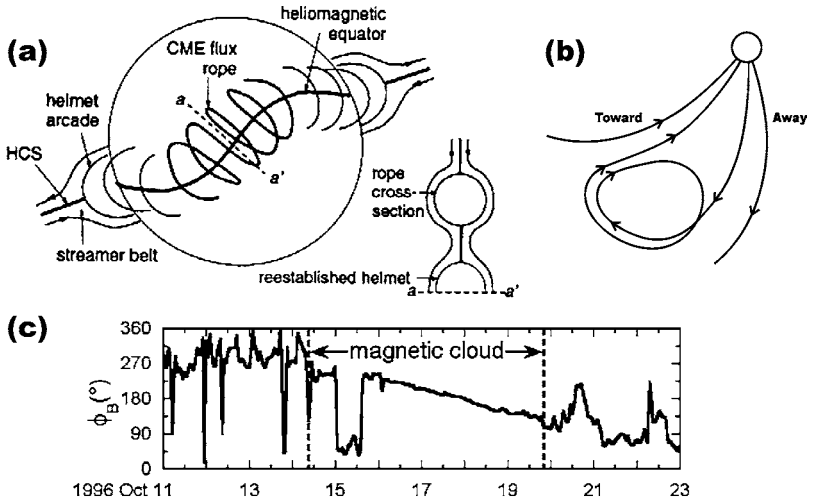

Figure 1. Relationship between magnetic clouds and sector boundaries. (a) A CME flux rope forms from the helmet arcade at the base of the heliospheric current sheet (HCS) separating sectors of opposite magnetic polarity (Crooker *et al*., 1998). (b) Fields in flux rope legs match away and toward polarity of adjacent sectors. (c) Magnetic azimuth angle measured by Ulysses rotates from away to toward polarity across a magnetic cloud (flux rope) at a sector boundary (Forsyth *et al*., 1997).

and Lee, 2006, this volume), it follows that the field lines comprising the flux rope will match the surrounding sector structure. Further into the heliosphere, Figure 1b illustrates how the fields in the legs of the flux rope and the sides of its loops will have the same local polarity as the true polarity of the adjacent open field lines on either side. Moreover, the current that creates the flux rope configuration embeds itself in the HCS so that the CME constitutes a bulge of distributed current in what is otherwise a current sheet.

Some observations clearly support the Figures 1a and 1b views (e.g., Crooker *et al*., 1998). Figure 1c gives an example of the time variation of the magnetic azimuth angle across a magnetic cloud at a sector boundary encountered by Ulysses at 4.4 AU (Forsyth *et al*., 1997). Instead of a sharp change from 270° marking polarity away from the Sun to 90° marking polarity toward the Sun, as expected for an HCS crossing, the polarity change is accomplished through the days-long field rotation intrinsic to the cloud. As noted by Forsyth *et al*. (1997), "The HCS is neither pushed aside nor draped around the CME but is replaced locally by the CME."

Many ICMEs are not encountered at sector boundaries, presumably because ICMEs are large and orbits through them skim the vicinity of the HCS rather than pass through it. Supporting this view, Kahler *et al*. (1999) found that the "polarity" of ICMEs, assuming passage through one leg rather than the apex of an ICME loop (cf. Figure 1b), is 10 times more likely to match than not to match the surrounding sector polarity. In their study, ICME leg "polarity" was determined not from local magnetic fields, which can turn back on themselves, but from the direction of the strongest counterstreaming suprathermal electron beam relative to the magnetic field direction (see Section 2.2). The fact that one beam is usually stronger supports the assumption that passage is through one leg, since the stronger beam presumably comes from the nearest solar connection point (Pilipp *et al*., 1987). The Kahler *et al*. (1999) study is the most thorough confirmation to date that ICMEs blend into the sector structure, consistent with the expected solar imprint.

2.1.2. *Magnetic Cloud Flux Rope Parameters, Filaments, and the Heliomagnetic Equator*

A magnetic flux rope expanding into the heliosphere as a loop of nested coils connected to the Sun at both ends (Figure 2 in Zurbuchen and Richardson, 2006, this volume) can be characterized by the directions of its axial and leading fields at the apex of the loop, which together determine the handedness of the twist (Bothmer and Schwenn, 1998). These parameters carry the imprint of both high- and low-altitude solar features (see review by Crooker (2000) and references therein).

From Figure 1a one might expect the direction of the magnetic field at the leading edge of an ICME flux rope or magnetic cloud to reflect the dipole component of the solar magnetic field inherent in the helmet streamer belt, pointing south (north) from the maximum of an even (odd) cycle to the maximum of an odd (even) cycle. Observations show this to be true for 77% of a total of 79 clouds tested

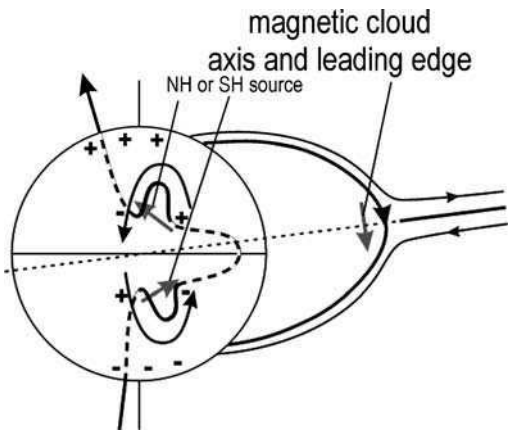

Figure 2. Schematic diagram of solar magnetic features that control magnetic cloud parameters. The direction of the field line distorted by differential rotation gives the direction of the cloud axis, depending upon its hemisphere of origin, and the direction of the dipole component (with a phase lag, see text) gives the direction of the leading field.

in the period spanning 1974 to 1991 (Bothmer and Rust, 1997; Mulligan *et al*., 1998), with the caveat that the sign change expected at solar maximum shifts to the declining phase. This phase shift may reflect higher-order field components lower in the solar atmosphere, where arcades over filaments retain the old cycle polarity until presumably they are shed as CMEs (cf. Gopalswamy *et al*., 2003). Although (Leamon *et al*., 2002) report no correspondence between the solar dipolar component and the leading field direction in magnetic clouds arising from sigmoids in active regions, when the phase shift is taken into account, 65% of their 34 cases fit the pattern.

With the possible exception of the early declining phase, magnetic fields high in the solar atmosphere appear to be systematically related to those in the lower atmosphere (Martin and McAllister, 1997; McAllister *et al*., 2002), with the result that magnetic cloud parameters reflect filament as well as streamer belt characteristics. Filaments align with neutral lines which are convoluted at low altitudes owing to the influence of higher-order fields but map up to the smoother HCS, which serves as the heliomagnetic equator (Figure 1a). Thus there is some correspondence between the tilts of cloud axes and HCS tilt with respect to the ecliptic plane (Mulligan *et al*., 1998) as well as the tilts of filament axes (Marubashi, 1997). Zhao and Hoeksema (1997) have shown that on average cloud axes are less tilted than filament axes by a factor of 0.7, consistent with the influence of higher-order fields on filaments (cf. Section 2 of Forsyth *et al*. (2006, this volume)).

In addition to tilt angle, the handedness of twist determined from filament structure is reflected in magnetic clouds. Although filaments may not be flux ropes themselves (Martin and McAllister, 1997), the pattern of magnetic fields surrounding

filaments, consisting of barbs and fibrils, displays a skew. Martin *et al*. (1994) found the skew to be dextral in the northern hemisphere and sinistral in the southern hemisphere for 89% of 73 quiescent filaments, independent of solar cycle, although no pattern was found for 31 active-region filaments. At higher altitudes, the coronal arcades overlying quiescent filaments have the opposite skew (Martin and McAllister, 1997). When these arcade fields reconnect to form a CME flux rope, the rope will tend to have left-handed twist if it emerges from the northern hemisphere and right-handed twist if it emerges from the southern hemisphere. Rust (1994) found this to be true for 13 out of 16 magnetic clouds. Somewhat surprisingly, for 36 clouds arising from active regions, (Leamon *et al*., 2002) found the same hemispheric pattern for 75% of them.

Figure 2 summarizes the solar magnetic imprint patterns on magnetic clouds. The predicted direction of the axial field of a cloud, marked by a short gray arrow in each hemisphere, is the direction of a field line distorted by differential rotation, as in the Babcock model and in the filament pattern low in the solar atmosphere (cf. Bothmer and Schwenn, 1998). At higher altitudes, one can imagine the tilt of the axis lowering toward the dotted line representing the heliomagnetic equator as the neutral line of the filament channel maps up to the HCS. The bipolar field line arched over each filament axis, as in the Babcock view of sunspot formation, represents a low-level arcade. At higher altitudes, the skew of the arcade fields increases until they point in the direction of the solar dipole component, at least until solar maximum. This is the predicted direction of the leading field of a magnetic cloud, as indicated. For the subsequent cycle, when the dipolar fields have the opposite sign, the directions of both the cloud axes and their leading fields will be reversed, which maintains the observed hemispheric pattern of handedness. While the Figure 2 sketch does not capture the lag between filament and polar fields during the declining phase that can account for the phase shift in the sign change of leading fields, it is physically accurate for the ascending phase and serves as a mnemonic device for most of the solar cycle between maxima.

2.2. Magnetic Connectivity to the Sun

Sketches of ICMEs usually show their magnetic field lines connected to the Sun at both ends, as in Figure 1b. The degree to which this is true, our understanding of how connections change, and implications for the heliospheric magnetic flux budget are the respective topics of Sections 2.2.1, 2.2.2, and 2.2.3.

2.2.1. *Tracing ICME Field Connections*

Particles with energies higher than those that constitute the core of solar wind distributions act as field line tracers. Like core particles, they are confined to gyrating motions about field lines; but their considerably higher velocity components result not only in larger gyroradii but in high field-aligned speeds that create particle beams

that give nearly instant information about solar connections. For example, solar energetic particle (SEP) events observed inside magnetic clouds give incontrovertible evidence of field lines connected to the Sun at least on one end, as opposed to field lines detached at both ends or closing upon themselves in plasmoids (e.g., Richardson, 1997; Malandraki *et al*., 2003; and references therein). Further discussion of ICME tracing with particles in the SEP energy range can be found in Section 4.6 of Wimmer-Schweingruber *et al*. (2006, this volume). This section focuses primarily on the lower-energy suprathermal electrons ($E \gtrsim 80$ eV) as ICME field-line tracers.

Because fluxes are higher at lower energies, suprathermal electrons constitute a continuous source of field-aligned particles from the Sun. They focus into beams as their pitch angles decrease owing to decreasing magnetic field strength with distance from the Sun. While scattering processes, shocks, and other inhomogeneities in the heliospheric magnetic field alter these beams as they propagate outward (Wimmer-Schweingruber *et al*., 2006, this volume), informed use of suprathermal electron data have yielded a large body of information about ICME connections. Counterstreaming beams, used as one of the first widely-accepted signatures of ICMEs (Gosling *et al*., 1987), are interpreted as a signature of closed field lines, connected to the Sun at both ends. Unidirectional beams signal open field lines, connected at only one end. The lack of beams, called a "heat flux dropout" (HFD) because suprathermal electrons carry heat flux away from the Sun, is a necessary but unfortunately not sufficient signature of field lines disconnected from the Sun at both ends (Crooker *et al*., 2002; Crooker *et al*., 2003; Pagel *et al*., 2005; and references therein). Studies of counterstreaming suprathermal electrons as well as higher-energy particles conclude that ICMEs contain a mixture of open, closed, and, on rare occasions, disconnected field lines (Bothmer *et al*., 1996; Larson *et al*., 1997, 2000; Malandraki *et al*., 2003; Crooker *et al*., 2004). For example, in a study of 48 magnetic clouds at 1 AU, Shodhan *et al*. (2000) found counterstreaming only 59% of the time, on average, leaving the clouds 41% open.

2.2.2. *Conceptual Modeling of ICME Connections*

An explanation for how a coherent flux rope in the solar wind can contain a mix of open and closed field lines, as pictured in Figure 3a, has been provided by Gosling *et al*. (1995). The conceptual model is based upon an MHD simulation of flux rope release in Earth's magnetosphere (Hesse and Birn, 1991) in which reconnection between differently-connected field lines occurs seemingly randomly yet progressively disconnects closed field lines. The steps leading to disconnection are illustrated in Figure 3b: (1) closed loops with sheared footpoints reconnect to form a flux rope that is still connected to the Sun at both ends (i.e., closed); (2) an open field line reconnects with a field line in one leg of the flux rope to form an open coil; (3) an open field line reconnects with a field line in the other leg of the flux rope to form a disconnected coil; (4) two open field lines reconnect to form a U-shaped disconnected field line encasing the disconnected coil. Since

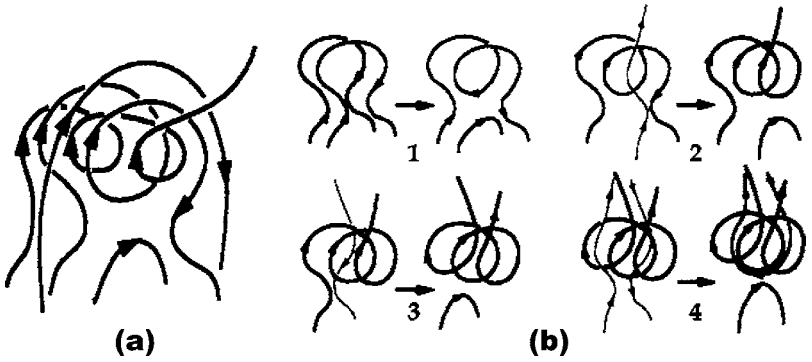

Figure 3. Schematic drawings of magnetic field lines in CME flux rope (Gosling *et al*., 1995). (a) Coherent flux rope with open coil nested in a closed coil. (b) Four steps to disconnection: 1. partial disconnection, two closed loops reconnect to form coil; 2. interchange reconnection, open field line reconnects with closed coil to form open coil; 3. open field line reconnects with open coil to disconnect coil; 4. two open field lines reconnect to form U-shaped disconnected field line.

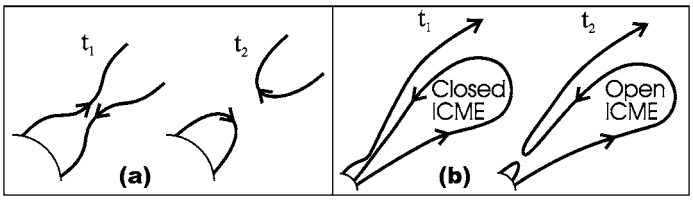

Figure 4. Before (t1) and after (t2) solutions to the problem of magnetic flux build-up from CMEs: (a) disconnection and (b) interchange reconnection (Crooker *et al*., 2002).

observations show that disconnected field lines in ICMEs are rare, steps 3 and 4 are not important for CMEs. Steps 1 and 2, respectively called "partial disconnection" and "interchange reconnection," result in the configuration in Figure 3a and play an important role in the heliospheric magnetic flux budget (Crooker *et al*., 2002), discussed in the following section.

2.2.3. *Heliospheric Magnetic Flux Budget*

Without some mitigating process, the closed flux that CMEs introduce to the heliosphere would result in a continuous build-up of magnetic flux, which is not observed. McComas (1995) argues that the only means of preventing flux build-up from CMEs is to disconnect fields elsewhere through reconnection of open field lines back at the Sun. Figure 4a illustrates the resulting U-shaped field with no connection to the Sun (cf. step 4 in Figure 3b). The problem with this solution is that true signatures of disconnection are rare, as mentioned in Section 2.2.1, not only within ICMEs but throughout the solar wind. About 90% of HFDs at time scales > 1 hr show electrons with reduced intensities and/or at higher energies still

streaming from the Sun along what must be connected field lines (Lin and Kahler, 1992; Pagel *et al*., 2005).

An alternative solution to the problem of magnetic flux build-up is that the closed field lines within ICMEs open through interchange reconnection (Gosling *et al*., 1995; Crooker *et al*., 2002). As illustrated in Figure 4b (cf. step 2 in Figure 3b), an open field line can reconnect with a closed field line in one leg of an ICME back at the Sun with the result that the closed loop in the heliosphere is exchanged for a closed loop in the solar atmosphere. This alternative solution is attractive because interchange reconnection generates no disconnected field lines, in agreement with the observation that they are rare, and it can continue to open CMEs well after they have left the Sun, until they are completely open and add no flux to the heliosphere.

If interchange reconnection is the means by which the flux budget is balanced, one might expect that ICMEs observed by Ulysses beyond 1 AU would be more open than those at 1 AU, but this seems not to be the case. Using counterstreaming electrons as a signature of closed fields, Riley *et al*. (2004) could detect no radial trend in the degree of openness in ICMEs encountered on the way to Jupiter, and (Crooker *et al*., 2004) found that magnetic clouds near 5 AU were not significantly more open on average than those at 1 AU. Both papers conclude that the rate at which a CME opens by interchange reconnection must slow significantly as its leading edge moves out into the heliosphere and that it may take months to years rather than days to open completely, leading to a temporary flux build-up that is consistent with the factor of two solar cycle variation in heliospheric magnetic flux (e.g., Wang *et al*., 2000). On the other hand, as discussed in detail by Crooker (2005), after months to years, closed loops moving out into the heliosphere will likely lose their counterstreaming signature and be indistinguishable from open field lines in spacecraft measurements. The interchange reconnection that eventually opens them will then give the signature of open field lines reconnecting, or disconnection, which reopens the problem of finding sufficient disconnection signatures. A different problem arises if one argues that ICMEs should be completely open by the time they reach 5 AU based upon estimates of the rate of interchange reconnection at the Sun (Reinard and Fisk, 2004). Although this eliminates the need for disconnection signatures, it casts doubt upon the relatively robust and widely-used interpretation of counterstreaming suprathermal electrons as signatures of closed fields. Clearly current understanding of these issues leads to dilemmas that remain to be resolved.

2.3. Imprint of Plasma Origins

Progress in understanding plasma characteristics of ICMEs in terms of what we know about CMEs has been limited owing to a number of constraints on observations. Two topics of interest concern the interpretation of elemental and ionic composition data from ICMEs and ICME manifestations of the three-part structure

of CMEs observed in coronagraphs. The first is treated by Wimmer-Schweingruber *et al*. (2006, this volume), von Steiger and Richardson (2006, this volume), and Gazis *et al*. (2006, this volume). Here, relevant to the discussion in section 2.2.2, we note that the high charge state of heavy ions characteristic of ICMEs and indicative of high-temperature origins may well be a signature of magnetic fields reconnecting during CME liftoff, as argued by Lepri and Zurbuchen (2004).

The second topic, ICME manifestations of CME three-part structure, still raises more questions than it answers. The classic three parts are the bright outer rim, the dark cavity, and the bright core (see, e.g., Schwenn *et al*., 2006, this volume). These have been loosely associated with the pile-up of plasma or streamer material at the leading edge, the flux rope, and the filament, respectively, but these associations raise unsettled issues, particularly about flux rope formation and filament structure. What is assumed to be evidence of cool filament material from low in the solar atmosphere, for example, the presence of He+, is only rarely found in the solar wind (Zurbuchen and Richardson, 2006, this volume; Wimmer-Schweingruber *et al*., 2006, this volume), yet sometimes the bright core is a substantial fraction of the volume of an ICME. Suleiman *et al*. (2005) illustrate such a case and argue that although the bright core may be filament material, it may no longer reside on filament field lines. Through partial disconnection the filament material may gain access to the much larger flux rope formed by that process and thus lose both its magnetic coherence and the imprint of its cold origins (Crooker, 2005).

3. External Forces and Structures

The interaction of ICMEs with the ambient solar wind through which they propagate can significantly alter their properties as well as change the solar wind plasma itself. These interactions need to be understood in order to relate ICME properties to properties at their solar origins and thereby learn about what causes their generation and ejection. These interactions also tend to make ICMEs harder to identify and study. Significant additional effects of solar wind/ICME interactions include the energisation of particles by shocks (e.g., Reames, 1999), increased geoeffectiveness (e.g., Webb *et al*., 2000; Siscoe and Schwenn, 2006, this volume), and the enhanced blocking of energetic particle propagation (e.g., Ifedili, 2004).

The study of ICMEs over the last few decades has led to an increasing appreciation of the complexity that can arise from the dynamics of ICME interactions. These interactions result in extremely structured objects which are highly undersampled with in situ spacecraft data, and it is therefore challenging to deduce their 3D structure. Nevertheless, considerable progress has been made. Increasingly sophisticated simulations of ICME dynamics have shown what behaviours are possible and help interpret in situ data (see Forsyth *et al*., 2006, this volume). Advances have also

been made in analytical models of magnetic flux ropes to take into account the effects of dynamical deformation.

We consider some of the most important consequences of dynamics in this paper. A number of related issues such as ICME deceleration and multi-spacecraft observations are discussed by Forsyth *et al*. (2006, this volume).

3.1. KINEMATIC EVOLUTION

Kinematic aspects of the propagation of an ICME into interplanetary space result in changes to its shape, independent of any interaction with the ambient plasma. ICMEs are typically extended objects and cover a finite solid angle near the Sun. The propagation of the ICME plasma radially away from the Sun results in a preservation of this solid angle and a consequent increase in the extent of the ejecta perpendicular to the radial direction. Therefore, if the ICME retains its radial extent, it will expand into a "pancake" shape far from the Sun. This kinematic effect is shown schematically in Figure 5(a). Riley and Crooker (2004) show that this effect is significant by 1 AU for typical ICMEs. Radial expansion and the interaction with the ambient solar wind will obviously also alter the ICME shape, but this simple

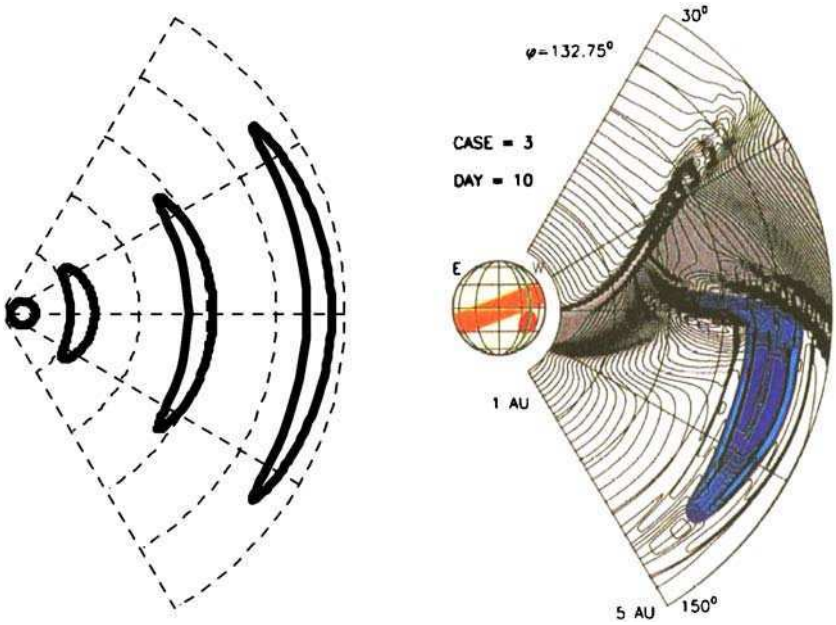

Figure 5. (a) Schematic of the kinematic effects of the radial expansion of ICMEs, leading to a "pancake" shape. (b) Results of a 3D simulation of an ICME propagating through a structured solar wind: the ICME is greatly distorted by its interaction with slow solar wind at low latitudes (after Odstrčil and Pizzo, 1999b).

geometrical effect implies that it is never possible to assume that ICMEs propagate unchanged into interplanetary space.

3.2. Dynamic Evolution

3.2.1. *Overexpanding ICMEs*

The simplest interplanetary signatures of ICMEs were in fact the last to be identified. Ulysses observations within steady, high-speed solar wind at high latitudes at several AU revealed (e.g., Gosling *et al*., 1998) a class of transients lasting a few days, bounded by a forward and reverse shock, the latter being uncommon for low-latitude ICMEs. Their internal structure was remarkably uniform, and all the events were similar in their gross form. As with low-latitude ICMEs, around 1/3 contained magnetic flux ropes. Perhaps most surprisingly, these events tended to have a lower pressure inside than the ambient wind, although they were bounded by compressions and shocks. Gosling *et al*. (1998) showed that these signatures were consistent with ejecta with an initial overpressure relative to the ambient solar wind: this pressure drives the expansion of the ICME, producing a lower density cavity. In addition, simulations (e.g., Schmidt and Cargill, 2001) show that at least parts of ICMEs can propagate in latitude from the streamer belt into polar solar wind (see Section 3.2.3), so the observation of overexpanded ICMEs in high-speed wind does not imply that they originate in coronal holes. The magnetic field of flux rope ICMEs can act to prevent disruption of the large scale ICME structure (Cargill *et al*., 2000).

The remarkable similarity of the observed events implies that, in the presence of uniform solar wind conditions, many or all ICMEs will exhibit this profile. Some events exhibit less symmetric time profiles than others: Gosling *et al*. (1998) showed that this was due to differences in the relative speeds of the solar wind and ejecta.

3.2.2. *Interaction with the Ambient Solar Wind*

While overexpanded ICMEs represent a particularly simple and regular class of ejecta signatures, most observed events are more complex. This is largely due to the complicated interactions between the ejecta and the ambient solar wind plasma. Since many ICMEs do not travel at the same speed as the solar wind in which they are embedded, compressions and rarefactions develop at the edges of the events. Even simple 1D simulations (e.g., Gosling and Riley, 1996) of solar wind dynamics show some of the possible consequences of these interactions, such as shocks and the acceleration or deceleration of ICMEs. The ICME shape can also be greatly distorted. Some of the consequences of these interactions are discussed in the remainder of this paper.

3.2.3. *Low- and High-Latitude Manifestations of the Same ICME*

The observation of relatively simple overexpanded ICMEs in high-latitude fast wind and much more complex structures at low latitudes raises the question as to whether these are two different classes of events or simply different manifestations

of the same phenomenon. Observations of the same ICME at high and low latitudes (Hammond *et al*., 1995) show that these can be the same phenomenon, highlighting the importance of the ambient solar wind in determining the in situ signature of an ICME. As mentioned in Section 3.2.1, simulations (Riley *et al*., 1997; Schmidt and Cargill, 2001) show that ICMEs launched from within the streamer belt can partially penetrate the stream interface and enter high-speed polar wind, resulting in an ICME with different signatures in fast and slow wind, as observed (see Section 4.3 of Forsyth *et al*., 2006, this volume). When an ICME propagates within streams of different speeds, shear of the structure results from the effect of drag to bring speeds closer to that of the ambient solar wind.

The complexity that can arise from ICME-solar wind interactions, and the different character of a single ICME at different locations, is shown in the 3D simulation result in Figure 5(b), taken from Odstrčil and Pizzo (1999b). At high latitudes, the ICME resembles the kinematic ICME in Figure 5(a), although with a larger extent due to expansion caused by internal overpressure. At lower latitudes, the ICME is heavily distorted by solar wind interactions. Such simulations highlight the difficulties in interpreting in situ ICME data.

3.2.4. *Folded Flux Ropes*

If the footpoints of an ICME flux rope are rooted in the Sun, as sketched in Figure 2 of Zurbuchen and Richardson (2006, this volume), then solar rotation would be expected to cause distortion in the structure, just as the large scale magnetic field tends to form Archimedean (Parker) spirals. Such effects are seen in 3D simulations (Vandas *et al*., 2002). Consistent with this view, Owens *et al*. (2004) suggested that west flank passages through ICMEs were around twice as common as east flank. In principle, it could be possible for a single spacecraft to pass through both legs of the same magnetic cloud, as suggested by Crooker *et al*. (1998) on the basis of mirror symmetric patterns in magnetic field elevation angle coincident with counterstreaming electrons trailing magnetic clouds. However, since several ICMEs often exist close to each other, it is difficult unambiguously to distinguish two encounters with one cloud from two separate events. A necessary but not sufficient test is for both events to exhibit the same handedness. Rees and Forsyth (2004) describe two such examples in Ulysses data, while Kahler *et al*. (1999) found only one in 8 possible cases in ISEE 3 data.

3.2.5. *Modelling Dynamic Effects: Non-Circular Flux Rope Models*

Analysis of ICMEs has often concentrated on magnetic flux ropes, despite their occurrence in only around 1/3 to 1/2 of apparent events, for a number of reasons: the relative simplicity of identifying flux ropes; their presumed relation to magnetic structures at the Sun; and because by fitting analytical models to their profiles, it is possible to estimate parameters such as the location and orientation of the rope's axis. The earliest models of flux ropes (e.g., Burlag, 1988) assumed circular cross sections: these often result in good agreement with observations, but deformation

from this shape will occur as a result of both kinematics and dynamics. There is evidence that this deformation can lead to systematic errors in estimates of flux rope parameters derived from circular cross section models. As a result, considerable efforts have been made to extend models to include elliptical cross sections (e.g., Mulligan *et al*., 2001; Hidalgo *et al*., 2002). A more generalised fitting method (Hu and Sonnerup, 2002), assuming $2\frac{1}{2}$D variations, has recently been developed and shows considerable promise. These models are discussed further by Forbes *et al*. (2006, this volume).

3.3. Sheaths and Shocks

Both ICME propagation at a speed different from the ambient solar wind and elevated internal pressure result in compressions and rarefactions. Passage of compressed solar wind plasma and magnetic field in sheath regions upstream of ICMEs at 1 AU can last for many hours. If this compression is strong, the magnetic field can be much larger than typical and, hence, geoeffective (e.g., Tsurutani *et al*., 1999; Siscoe and Schwenn, 2006, this volume). The orientation of the plane of compression in which the magnetic field in the sheath is forced to lie can be determined by minimum variance analysis and used to estimate the local orientation of the leading edge of an ICME (Jones *et al*., 2002; Section 4.3 of Wimmer-Schweingruber *et al*., 2006, this volume).

The shocks driven by speed and pressure differences between the ICME and the surrounding solar wind can propagate significant distances away from the ejecta itself, both radially and perpendicular to the flow. Simulations (e.g., Odstrčil and Pizzo, 1999a) show that the shock and resulting compression can result in profiles in the solar wind which might be mistaken for passage through the ejecta itself. This may explain events such as that reported by Richardson *et al*. (1994) when two spacecraft encountered a shock but only one entered ejecta material. In principle, composition signatures can help to distinguish these cases, since the sheath, being compressed solar wind, should retain solar wind composition. For example, Borrini *et al*. (1982) used enhancements of He/H to identifiy ejecta following shocks and explained the large number of shocks without this marker (48 out of 91) in terms of the much larger extent of shocks compared to ejecta. It is highly likely, however, that some ejecta went undetected owing to the variability of composition patterns in ICMEs (Wimmer-Schweingruber *et al*., 2006, this volume; Crooker, 2005).

3.4. Reconnection

Both simulations and some limited observations suggest that reconnection occurs around and within ICMEs. The large compression ahead of some ICMEs would be expected to trigger reconnection between ICME and sheath magnetic field if their orientations were favourable. McComas *et al*. (1994) presented suprathermal

electron data which could be interpreted as signatures of reconnection ahead of an ICME. Simulations (Cargill and Schmidt, 2002) show that reconnection can occur at the flanks of ICMEs, particularly if they are traveling through the streamer belt. Simulations also imply that reconnection can occur within ICMEs owing to shear by background solar wind inhomogeneity (Schmidt and Cargill, 2001). (See Sections 4.2 and 4.3 of Forsyth *et al*. (2006, this volume) for examples of simulation results.) Farrugia *et al*. (2001) have discussed one possible signature of such an event, and more direct evidence has been reported recently by Gosling *et al*. (2005). Behind ICMEs, simulations by Riley *et al*. (2002) indicate that the in situ signatures of partial reconnection back at the Sun (section 2.2.2) would be a slight velocity and density increase trailing an ICME as a result of an outward reconnection jet. Such signatures have been seen in spacecraft data, but only rarely (Riley *et al*., 2002).

3.5. Interactions of Multiple ICMEs

The ejection of multiple CMEs from the vicinity of individual active regions over several days, combined with their variable velocities and large angular extent, makes it inevitable that ICMEs will sometimes interact. Indeed, as ICMEs propagate into the outer heliosphere, they merge and interact with CIRs and other ICMEs to form global merged interaction regions (GMIRs) – these effects are discussed by Gazis *et al*. (2006, this volume). Like ICME/solar wind interactions, ICME/ICME interactions can also result in complicated structures and spacecraft signatures. For example, Kahler *et al*. (1999) used bidirectional electron fluxes to argue that some magnetic clouds are in fact multiple events. Hu *et al*. (2003) used the reconstruction technique of Hu and Sonnerup (2002) to infer a double rope structure of a magnetic cloud at 1 AU.

Burlaga *et al*. (2002) discussed three sets of multiple halo CMEs and their associated ejecta at 1 AU. They showed that the ejecta were "complex," being fast ($>$ 600 km/s) events that were not magnetic clouds. These events typically showed substructure in parameters such as composition and density, suggesting that they were formed from several structures. They emphasised the challenges in quantitatively describing such events.

Simulations, again, reveal some of the possible consequences of multiple ICME interactions, such as shocks propagating through ejecta (Odstrčil *et al*., 2003) – and, if two flux ropes are of the same chirality and polarity, the merging and reconnection of ICMEs (Schmidt and Cargill, 2004).

3.5.1. *Interacting ICMEs as Particle Accelerators*

Gopalswamy *et al*. (2002a) showed that radio emission occurred at around 10 solar radii when two CMEs came into contact and argued that this was due to either reconnection or the formation of a shock at this location. Gopalswamy *et al*. (2002b) argued that when one CME overtakes a second, slower event, solar energetic particle

acceleration is significantly increased. However, this conclusion was recently disputed by Richardson *et al*. (2003) and remains controversial.

4. Conclusion

There is little question that ICMEs are the interplanetary manifestations of CMEs, but both simulations of their propagation and observations of their complicated signatures indicate that they evolve substantially as they move out into the heliosphere. Magnetic field lines change their connections, the imprint of the magnetic field at their source weakens, shapes and structures distort, and particles accelerate. It appears that many aspects of that evolution can be understood in terms of phenomenological models – a first step toward the long-term goal of understanding in terms of fundamental physical processes – but a number of basic questions remain. Some of the more important of these questions concern how long field lines remain connected to the Sun at both ends, the fate of filament plasma, and the degree to which simulations represent the actual distortion of ICMEs.

Acknowledgements

The authors thank D. Odstrčil for providing Figure 5(b) and the International Space Science Institute, Bern, for their support of this work. T. Horbury is supported by a PPARC (UK) Fellowship and N. Crooker by the (US) National Science Foundation grant ATM-0119700.

References

Borrini, G., Gosling, J. T., Bame, S. J., and Feldman, W. C.: 1982, *J. Geophys. Res.* **87**(16), 4365.

Bothmer, V., Desai, M. I., Marsden, R. G., Sanderson, T. R., Trattner, K. J., Wenzel, K.-P., *et al*.: 1996, *Astron. Astrophys.* **316**, 493.

Bothmer, V. and Rust, D. M.: 1997, In: Crooker, N. U., Joselyn, J. A., and Feynman, J. (eds.): *Coronal Mass Ejections, Geophys. Monogr. Ser.*, Vol. 99. Washington, D. C.: AGU, pp. 137.

Bothmer, V. and Schwenn, R.: 1998, *Ann. Geophys.* **16**, 1.

Burlaga, L. F.: 1988, *J. Geophys. Res.* **93**(12), 7217.

Burlaga, L. F., Plunkett, S. P., and St. Cyr, O. C.: 2002, *J. Geophys. Res.* **107**(A10), 10.1029/2001JA000255.

Cargill, P. J., Schmidt, J., Spicer, D. S., and Zalesak, S. T.: 2000, *J. Geophys. Res.* **105**(A4), 7509.

Cargill, P. J. and Schmidt, J. M.: 2002, *Ann. Geophys.* **20**, 879.

Crooker, N. U.: 2000, *J. Atmos. Sol. Terr. Phys.* **62**, 1071.

Crooker, N. U.: 2005, In: *Solar Wind Eleven*. ESA Spac. Publ. 592, pp 289–295.

Crooker, N. U., Forsyth, R., Rees, A., Gosling, J. T., and Kahler, S. W.: 2004, *J. Geophys. Res.* **109**(A18), 10.1029/2004JA010426.

Crooker, N. U., Gosling, J. T., and Kahler, S. W.: 1998, *J. Geophys. Res.* **103**(12), 301.

Crooker, N. U., Gosling, J. T., and Kahler, S. W.: 2002, *J. Geophys. Res.* **107**(A2), 10.1029/2001JA000236.
Crooker, N. U., Larson, D. E., Kahler, S. W., Lamassa, S. M., and Spence, H. E.: 2003, *Geophys. Res. Lett.* **30**, 10.1029/2003GL017036.
Farrugia, C. J., Vasquez, B., Richardson, I. G., Torbert, R. B., Burlaga, L. F., Biernat, H. K., *et al.*: 2001, *Adv. Space. Res.* **28**, 759.
Forbes, T. G., Linker, J. A., *et al.*: 2006, *Space Sci. Rev.,* this volume, 10.1007/s11214-006-9019-8.
Forsyth, R. J., Balogh, A., Smith, E. J., and Gosling, J. T.: 1997, *Geophys. Res. Lett.* **24**, 3101.
Forsyth, R. J., Bothmer, V., *et al.*: 2006, *Space Sci. Rev.,* this volume, 10.1007/s11214-006-9022-0.
Gazis, P. R., Balogh, A., *et al.*: 2006, *Space Sci. Rev.,* this volume, 10.1007/s11214-006-9023-z.
Gopalswamy, N., Lara, A., Yashiro, S., and Howard, R. A.: 2003, *Astrophys. J.* **598**, L63.
Gopalswamy, N., Yashiro, S., Kaiser, M. L., Howard, R. A., and Bougeret, J.-L.: 2002a, *Geophys. Res. Lett.* **29**, 10.1029/2001GL013606.
Gopalswamy, N., Yashiro, S., Michalek, G., Kaiser, M. L., Howard, R. A., Reames, D. V., *et al.*: 2002b, *Astrophys. J.* **572**, L103.
Gosling, J. T., Baker, D. N., Bame, S. J., Feldman, W. C., Zwickl, R. D., and Smith, E. J.: 1987, *J. Geophys. Res.* **92**(11), 8519.
Gosling, J. T., Birn, J., and Hesse, M.: 1995, *Geophys. Res. Lett.* **22**, 869.
Gosling, J. T. and Riley, P.: 1996, *Geophys. Res. Lett.* **23**, 2867.
Gosling, J. T., Riley, P., McComas, D. J., and Pizzo, V. J.: 1998, *J. Geophys. Res.* **103**(12), 1941
Gosling, J. T., Skoug, R. M., McComas, D. J., and Smith, C. W.: 2005, *J. Geophys. Res.* **110**(A9), 10.1029/2004JA010809.
Hammond, C. M., Crawford, G. K., Gosling, J. T., Kojima, H., Phillips, J. L., Matsumoto, H., *et al.*: 1995, *Geophys. Res. Lett.* **22**, 11690
Hesse, M. and Birn, J.: 1991, *J. Geophys. Res.* **96**(15), 5683.
Hidalgo, M. A., Nieves-Chinchilla, T., and Cid, C.: 2002, *Geophys. Res. Lett.* **29**, 10.1029/2001GL013875.
Hu, Q., Smith, C. W., Ness, N. F., and Skoug, R. M.: 2003, *Geophys. Res. Lett.* **30**, 10.1029/2002GL016653.
Hu, Q. and Sonnerup, B. U. Ö.: 2002, *J. Geophys. Res.* **107**(A7), 10.1029/2001JA000293.
Hundhausen, A. J.: 1993, *J. Geophys. Res.* **98**(17), 113,177–13,200.
Ifedili, S. O.: 2004, *J. Geophys. Res.* **109**(A18), 10.1029/2002JA009814.
Jones, G. H., Rees, A., Balogh, A., and Forsyth, R. J.: 2002, *Geophys. Res. Lett.* **29**, 10.1029/2001GL014110.
Kahler, S. W., Crooker, N. U., and Gosling, J. T.: 1999, *J. Geophys. Res.* **104**(13), 9919–9924.
Larson, D. E., Lin, R. P., McTiernan, J. M., McFadden, J. P., Ergun, R. E., McCarthy, M., *et al.*: 1997, *Geophys. Res. Lett.* **24**, 1911.
Larson, D. E., Lin, R. P., and Steinberg, J.: 2000, *Geophys. Res. Lett.* **27**, 157.
Leamon, R. J., Canfield, R. C., and Pevtsov, A. A.: 2002, *J. Geophys. Res.* **107**(A9), 10.1029/2001JA000313.
Lepri, S. T. and Zurbuchen, T. H.: 2004, *J. Geophys. Res.* **109**(A18), 10.1029/2003JA009954.
Lin, R. P. and Kahler, S. W.: 1992, *J. Geophys. Res.* **97**(16), 8203.
Malandraki, O. E., Sarris, E. T., and Tsiropoula, G.: 2003, *Ann. Geophys.* **21**, 1249.
Martin, S. F., Bilimoria, R., and Tracadas, P. W.: 1994, In: Rutten, R. J. and Schrijver, C. J. (eds.): *Solar Surface Magnetism*, Norwell, Mass.: Kluwer Academic, pp. 303.
Martin, S. F. and McAllister, A. H.: 1997, In: Crooker, N. U., Joselyn, J. A., and Feynman, J. (eds.): *Coronal Mass Ejections, Geophys. Monogr. Ser.*, Vol. 99. Washington, D. C.: AGU, pp. 127.
Marubashi, K.: 1997, In: Crooker, N. U., Joselyn, J. A., and Feynman, J. (eds.): *Coronal Mass Ejections, Geophys. Monogr. Ser.*, Vol. 99. Washington, D. C.: AGU, pp. 147.
McAllister, A. H., Mackay, D. H., and Martin, S. F.: 2002, *Sol. Phys.* **211**, 155.

McComas, D. J.: 1995, *Rev. Geophys. Suppl.* **33**, 603.
McComas, D. J., Gosling, J. T., Hammond, C. M., Moldwin, M. B., Phillips, J. L., and Forsyth, R. J.: 1994, *Geophys. Res. Lett.* **21**, 1751.
Mikic, Z. and Lee, M. A.: 2006, *Space Sci. Rev.,* this volume, 10.1007/s11214-006-9012-2.
Mulligan, T., Russell, C. T., Anderson, B. J., and Acuna, M. H.: 2001, *Geophys. Res. Lett.* **28**, 4417.
Mulligan, T., Russell, C. T., and Luhmann, J. G.: 1998, *Geophys. Res. Lett.* **25**, 2959.
Odstrčil, D. and Pizzo, V. J.: 1999a, *J. Geophys. Res.* **104**(A12), 28225.
Odstrčil, D. and Pizzo, V. J.: 1999b, *J. Geophys. Res.* **104**(A1), 493.
Odstrčil, D., Vandas, M., Pizzo, V. J., and MacNeice, P.: 2003, In: *AIP Conf. Proc. 679: Solar Wind Ten*. pp. 699.
Owens, M. J., Rees, A., and Cargill, P. J.: 2004, submitted to *Ann. Geophys.* unpublished manuscript.
Pagel, C., Crooker, N. U., and Larson, D. E.: 2005, *Geophys. Res. Lett.* **32**, 10.1029/2005GL023043.
Pilipp, W. G., Muehlhaeuser, K.-H., Miggenrieder, H., Rosenbauer, H., and Schwenn, R.: 1987, *J. Geophys. Res.* **92**(11), 1103.
Schwenn, R., Raymond, J. C., *et al.*: 2006, *Space Sci. Rev.,* this volume, 10.1007/s11214-006-9016-y.
Reames, D. V.: 1999, *Space Sci. Rev.* **90**, 413.
Rees, A. and Forsyth, R. J.: 2004, *Geophys. Res. Lett.* **31**, 10.1029/2003GL018330.
Reinard, A. A. and Fisk, L. A.: 2004, *Astrophys. J.* **608**, 533.
Richardson, I. G.: 1997, In: Crooker, N. U., Joselyn, J. A., and Feynman, J. (eds.): *Coronal Mass Ejections, Geophys. Monogr. Ser.*, Vol. 99. Washington, D. C.: AGU, pp. 189.
Richardson, I. G., Farrugia, C. J., and Winterhalter, D.: 1994, *J. Geophys. Res.* **99**(18), 2513.
Richardson, I. G., Lawrence, G. R., Haggerty, D. K., Kucera, T. A., and Szabo, A.: 2003, *Geophys. Res. Lett.* **30**, 10.1029/2002GL016424.
Riley, P. and Crooker, N. U.: 2004, *Astrophys. J.* **600**, 1035.
Riley, P., Gosling, J. T., and Crooker, N. U.: 2004, *Astrophys. J.* **608**, 1100.
Riley, P., Gosling, J. T., and Pizzo, V. J.: 1997, *J. Geophys. Res.* **102**(11), 14677.
Riley, P., Linker, J. A., Mikić, Z., Odstrčil, D., Pizzo, V. J., and Webb, D. F.: 2002, *Astrophys. J.* **578**, 972.
Rust, D. M.: 1994, *Geophys. Res. Lett.* **21**, 241.
Schmidt, J. and Cargill, P. J.: 2004, *Ann. Geophys.* **22**, 2245.
Schmidt, J. M. and Cargill, P. J.: 2001, *J. Geophys. Res.* **106**(15), 8283.
Shodhan, S., Crooker, N. U., Kahler, S. W., Fitzenreiter, R. J., Larson, D. E., Lepping, R. P., *et al.*: 2000, *J. Geophys. Res.* **105**(14), 27261.
Siscoe, G. and Schwenn, R.: 2006, *Space Sci. Rev.,* this volume.
Suleiman, R. M., Crooker, N. U., Raymond, J. C., and Ballegooijen, A. V.: 2005, In: *IAU Symposium*. pp. 71.
Tsurutani, B. T., Kamide, Y., Arballo, J. K., Gonzalez, W. D., and Lepping, R. P.: 1999, *Phys. Chem. Earth (C)* **24**(1–3), 101.
Vandas, M., Odstrčil, D., and Watari, S.: 2002, *J. Geophys. Res.* **107**(A9), 10.1029/2001JA005068.
von Steiger, R. and Richardson, J. D.: 2006, *Space Sci. Rev.,* this volume, 10.1007/s11214-006-9015-z.
Wang, Y.-M., Lean, J., and Sheeley, N. R.: 2000, *Geophys. Res. Lett.* **27**, 505.
Webb, D. F., Cliver, E. W., Crooker, N. U., Cry, O. C. S., and Thompson, B. J.: 2000, *J. Geophys. Res.* **105**(14), 7491.
Wimmer-Schweingruber, R. F., Crookers, N. U., *et al.*: 2006, *Space Sci. Rev.,* this volume, 10.1007/s11214-006-9017-x.
Zhao, X. P. and Hoeksema, J. T.: 1997, *Geophys. Res. Lett.* **24**, 2965.
Zurbuchen, T. H. and Richardson, I. G.: 2006, *Space Sci. Rev.,* this volume, 10.1007/s11214-006-9010-4.

Solar Phys (2013) 284:1–4
DOI 10.1007/s11207-013-0280-1

Preface

N. Gopalswamy · T. Nieves-Chinchilla · M. Hidalgo · J. Zhang · P. Riley · L. van Driel-Gesztelyi · C.H. Mandrini

Published online: 4 April 2013

This Topical Issue (TI) of *Solar Physics*, devoted to the study of flux-rope structure in coronal mass ejections (CMEs), is based on two Coordinated Data Analysis Workshops (CDAWs) held in 2010 (20 – 23 September in Dan Diego, California, USA) and 2011 (5 – 9

Flux-Rope Structure of Coronal Mass Ejections
Guest Editors: N. Gopalswamy, T. Nieves-Chinchilla, M. Hidalgo, J. Zhang, and P. Riley

N. Gopalswamy (✉) · T. Nieves-Chinchilla
Heliophysics Division, NASA Goddard Space Flight Center, Greenbelt, MD, USA
e-mail: nat.gopalswamy@nasa.gov

T. Nieves-Chinchilla
Department of Physics, The Catholic University of America, Washington, DC 20064, USA

M. Hidalgo
SRG-UAH, Alcala de Henares, Madrid, Spain

J. Zhang
School of Physics, Astronomy and Computational Sciences, George Mason University, Fairfax, VA, USA

P. Riley
Predictive Science Inc., San Diego, CA, USA

L. van Driel-Gesztelyi
Observatoire de Paris, LESIA-CNRS UMR 8109, 9295 Meudon Cédex, France

L. van Driel-Gesztelyi
Mullard Space Science Laboratory, University College London, Holmbury St. Mary, UK

L. van Driel-Gesztelyi
Konkoly Observatory of Hungarian Academy of Sciences, Budapest, Hungary

C.H. Mandrini
Instituto de Astronomía y Física del Espacio, CONICET-UBA, CC. 67, Suc. 28, 1428 Buenos Aires, Argentina

September in Alcala, Spain). The primary purpose of the CDAWs was to address the question whether all CMEs have a flux rope structure. Each CDAW was attended by about 50 scientists interested in the origin, propagation, and interplanetary manifestation of CME phenomena.

The backbone of the workshop was a set of 59 interplanetary CMEs (ICMEs) that were driving shocks at Sun–Earth L1 as detected by one or more of the *Solar Heliospheric Observatory* (SOHO), *Wind*, and the *Advanced Composition Explorer* (ACE). The CME-ICME pairs were selected from a set identified by Gopalswamy *et al.* (2010) based on the criterion that the source location should be within $\pm 15^{\circ}$ longitude from the disk center. Many of the papers in this TI used these CME-ICME pairs, referred to as CDAW Events. A revision of the source locations made during the CDAWs reduced the list to 54 events. According to the classical definition of Burlaga *et al.* (1981), 23 ICMEs were classified as magnetic clouds (MCs), the remaining 31 were non-MCs. The reason for limiting the longitude range to $\pm 15^{\circ}$ is that disk-center CMEs are more likely to be identified as MCs according to the geometrical hypothesis that all ICMEs are flux ropes but appear as non-ropes because of observational limitations. The events all occurred during Solar Cycle 23 (bounded by the launch of SOHO to the end of 2005) with exceptional *in-situ* measurements and remote-sensing observations for each. The remote-sensing observations include Hα, EUV, white-light, microwave, and X-ray images from ground- and space-based instruments.

Yashiro *et al.* (2013) focused on the structure of post-eruption arcades (PEAs) associated with MC and non-MC CMEs and found that one cannot distinguish between these two classes of events based on flare data. Gopalswamy *et al.* (2013) compared the Fe and O charge states in MCs and non-MCs and found that an enhanced charge state is a common characteristic of both types of ICMEs. They also concluded that the non-rope models involving magnetic loop expansion are inconsistent with non-MCs because the observed charge state and CME kinematics do not support such a model. Xie, Gopalswamy, and St. Cyr (2013) were able to fit a flux rope to CMEs associated with MCs as well as non-MCs and showed evidence that the propagation effects might turn them into MCs and non-MCs; specifically, that CMEs associated with non-MCs are generally deflected away from the Sun–Earth line, while those associated with MCs were unaffected or were deflected toward the Sun–Earth line (Mäkelä *et al.*, 2013). This result was also supported by the fact that the direction parameter is larger for CMEs associated with MCs than for the non-MC CMEs (Kim *et al.*, 2013). Zhang, Hess, and Poomvises (2013) presented a case study of two ICMEs and also concluded that the difference between the two events observed *in situ* can be explained by the deflection of flux ropes *en route* to Earth. Cho *et al.* (2013) determined the helicity signs in the source active regions of the CDAW events by estimating the cumulative magnetic helicity injected through the photosphere. They found that in 88 % of the cases, the ICME helicity signs are consistent with those of the solar source regions. The authors also suggested that one or more of the following could have caused the deviation in the remaining cases: incorrect identification of the CME source region, a local helicity sign opposite to that of the entire active region, and the helicity sign of the pre-existing coronal magnetic field opposite to the sign of the photospheric helicity injection.

All CDAW events were analyzed using four different magnetic field models and reconstruction techniques: force-free fitting, magnetostatic reconstruction using a numerical solution to the Grad–Shafranov equation, fitting to a self-similarly expanding cylindrical configuration, and elliptical, non-force-free fitting (Al-Haddad *et al.*, 2013). Hidalgo, Nieves-Chinchilla, and Blanco (2013) used an analytical flux rope model to fit the observations and found that the majority of CDAW events contain flux ropes. They also found that the flux-rope noses are generally oriented along the Sun–Earth line. Blanco *et al.* (2013) studied the

Forbush decrease in cosmic rays triggered by the passage of the CDAW events at Earth and found that only 25 % displayed a noticeable decrease. They also found that MCs are more effective in causing Forbush decreases.

The TI also includes papers that expand the context of the CDAW events: Vourlidas *et al.* (2013) presented a statistical analysis of all white-light CMEs observed by SOHO, assisted by 3D MHD simulations. They suggested that a flux rope can be defined as a coherent magnetic twist-carrying coronal structure with angular width of at least 40°, which is able to reach beyond 10 Rs. Isavnin, Vourlidas, and Kilpua (2013) studied 15 ICMEs in Solar Cycle 24, comparing the three-dimensional parameters of CMEs from imaging and *in situ* reconstructions, and focusing on propagation effects. They were able to confirm the flux-rope deflection toward the equator and its rotation. Riley and Richardson (2013) analyzed *Ulysses* spacecraft measurements to assess five possible explanations for why some ICMEs are observed to be MCs and others are not. They concluded that it is difficult to choose between the geometrical hypothesis discussed above and the possibility that there are two distinct initiation mechanisms – one producing MCs, the other non-MCs. Romashets and Vandas (2013) considered a linear force-free configuration consisting of a cylindrical flux rope combined with a compact toroid. This model can be applied for the interpretation of some features observed in solar flux ropes, including prominences. Berdichevsky (2013) studied the isotropic evolution of flux ropes and attempted to estimate the mass of ICMEs. Osherovich, Fainberg, and Webb (2013) provided observational support for a double helix structure within CMEs and MCs. Hu *et al.* (2013) examined the effect of electron pressure on the Grad–Shafranov reconstruction of ICMEs and found that it contributes to a 10 – 20 % discrepancy in the derived physical quantities, such as the magnetic flux content of the ICME flux rope observed at 1 AU.

As in the cases of previous CDAWs, the data collected for the Flux Rope CDAWs are available online: http://cdaw.gsfc.nasa.gov/meetings/2010_fluxrope/LWS_CDAW2010_ICMEtbl.html.

Acknowledgements We would like to express our gratitude to the referees, whose critical assessment of the manuscripts resulted in the high-quality papers in this TI "Flux-rope structure of coronal mass ejections". The CDAW organizers gratefully acknowledge support for the CDAWs from NASA's Living with a Star (LWS) program. We thank Lika Guhathakuta, at NASA Head Quarters, for her assistance. We also thank Predictive Science, Inc. (USA) and the University of Alcala (Spain) for hosting the CDAWs in 2010 and 2011, respectively.

References

Al-Haddad, N., Nieves-Chinchilla, T., Savani, N.P., Möstl, C., Marubashi, K., Hidalgo, M.A., Roussev, I.I., Poedts, S., Farrugia, C.J.: 2013, *Solar Phys.* this issue. doi:10.1007/s11207-013-0244-5.

Berdichevsky, D.: 2013, *Solar Phys.* this issue. doi:10.1007/s11207-012-0176-5

Blanco, J.J., Catalán, E., Hidalgo, M.A., Medina, J., García, O., Rodríguez-Pacheco, J.: 2013, *Solar Phys.* this issue. doi:10.1007/s11207-013-0256-1.

Burlaga, L., Sittler, E., Mariani, F., Schwenn, R.: 1981, *J. Geophys. Res.* **86**, 6673. doi:10.1029/JA086iA08p06673.

Cho, K.-S., Park, S.-H., Marubashi, K., Gopalswamy, N., Akiyama, S., Yashiro, S., Kim, R.-S., Lim, E.-K.: 2013, *Solar Phys.* this issue. doi:10.1007/s11207-013-0224-9.

Gopalswamy, N., Xie, H., Mäkelä, P., Akiyama, S., Yashiro, S., Kaiser, M.L., Howard, R.A., Bougeret, J.-L.: 2010, *Astrophys. J.* **710**, 1111. doi:10.1088/0004-637X/710/2/1111.

Gopalswamy, N., Mäkelä, P., Akiyama, S., Xie, H., Yashiro, S., Reinard, A.A.: 2013, *Solar Phys.* this issue. doi:10.1007/s11207-012-0215-2.

Hidalgo, M.A., Nieves-Chinchilla, T., Blanco, J.J.: 2013, *Solar Phys.* this issue. doi:10.1007/s11207-012-0191-6.

Hu, Q., Farrugia, C.J., Osherovich, V.A., Möstl, C., Szabo, A., Oglivie, K.W., Lepping, R.P.: 2013, *Solar Phys.* this issue. doi:10.1007/s11207-013-0259-y.
Isavnin, A., Vourlidas, A., Kilpua, E.K.J.: 2013, *Solar Phys.* this issue. doi:10.1007/s11207-012-0214-3.
Kim, R.-S., Gopalswamy, N., Cho, K.-S., Moon, Y.-J., Yashiro, S.: 2013, *Solar Phys.* this issue. doi:10.1007/s11207-013-0230-y.
Mäkelä, P., Gopalswamy, N., Xie, H., Mohamed, A.A., Akiyama, S., Yashiro, S.: 2013, *Solar Phys.* this issue. doi:10.1007/s11207-012-0211-6.
Osherovich, V., Fainberg, J., Webb, A.: 2013, *Solar Phys.* this issue. doi:10.1007/s11207-013-0278-8.
Riley, P., Richardson, I.G.: 2013, *Solar Phys.* this issue. doi:10.1007/s11207-012-0006-9.
Romashets, E., Vandas, M.: 2013, *Solar Phys.* this issue. doi:10.1007/s11207-012-0083-9.
Vourlidas, A., Lynch, B.J., Howard, R.A., Li, Y.: 2013, *Solar Phys.* this issue. doi:10.1007/s11207-012-0084-8.
Xie, H., Gopalswamy, N., St. Cyr, O.C.: 2013, *Solar Phys.* this issue. doi:10.1007/s11207-012-0209-0.
Yashiro, S., Gopalswamy, N., Mäkelä, P., Akiyama, S.: 2013, *Solar Phys.* this issue. doi:10.1007/s11207-013-0248-1.
Zhang, J., Hess, P., Poomvises, W.: 2013, *Solar Phys.* this issue. doi:10.1007/s11207-013-0242-7.

Solar Phys (2013) 284:261–274
DOI 10.1007/s11207-013-0278-8

Observational Evidence for a Double-Helix Structure in CMEs and Magnetic Clouds

Vladimir Osherovich · Joseph Fainberg · Alla Webb

Received: 31 March 2012 / Accepted: 12 March 2013 / Published online: 16 April 2013

Abstract We compare recent observations of a solar eruptive prominence as seen in extreme-UV light on 30 March 2010 by the *Solar Dynamics Observatory* (SDO) with the multi-tube model for interplanetary magnetic clouds (Osherovich, Fainberg, Stone, *Geophys. Res. Lett.* **26**, 2597, 1999). Our model is based on an exact analytical solution of the plasma equilibrium with magnetic force balanced by a gradient of scalar gas pressure. Topologically, this solution describes two magnetic helices with opposite magnetic polarity embedded in a cylindrical magnetic flux tube that creates magnetic flux inequality between the two helices by enhancing one helix and suppressing the other. The magnetic field in this model is continuous everywhere and has a finite magnetic energy per unit length of the tube. These configurations have been introduced as MHD bounded states (Osherovich, *Soln. Dannye* **5**, 70, 1975). Apparently, the SDO observations depict two non-equal magnetically interacting helices described by this analytical model. We consider magnetic and thermodynamic signatures of multiple magnetic flux ropes inside the same magnetic cloud, using *in situ* observations. The ratio of magnetic energy density to bulk speed solar wind energy density has been defined as a solar wind quasi-invariant (QI). We analyze the structure of the QI profile to probe the topology of the internal structure of magnetic clouds. From the superposition of 12 magnetically isolated clouds observed by *Ulysses*, we have found that the corresponding QI is consistent with our double helix model.

Joseph Fainberg is Emeritus at NASA Goddard Space Flight Center.

Flux-Rope Structure of Coronal Mass Ejections
Guest Editors: N. Gopalswamy, T. Nieves-Chinchilla, M. Hidalgo, J. Zhang, and P. Riley

V. Osherovich
CUA/NASA Goddard Space Flight Center, Code 673, Greenbelt, MD 20771, USA
e-mail: vladimir.osherovich@gmail.com

J. Fainberg (✉)
NASA Goddard Space Flight Center, Code 673, Greenbelt, MD 20771, USA
e-mail: fainberg@jhu.edu

A. Webb
Montgomery College, 51 Mannakee St., Rockville, MD 20850, USA
e-mail: allawebb@gmail.com

Keywords Quasi-invariant · Solar wind · Magnetic clouds · Coronal mass ejections

1. Introduction

This paper invokes a particular double-helix bounded state solution to an MHD force balance equation (Krat and Osherovich, 1978; Osherovich, Fainberg, and Stone, 1999) and shows that this solution's multi-tube magnetic topology explains a number of plasma, magnetic field, and radio wave signatures observed in some coronal mass ejections (CMEs) and magnetic clouds. After a detailed review of the double helix solution (Section 2), we consider the first observational example: extreme UV observations from SDO on 30 March 2010 of erupting solar prominence material that shows a winding double helix structure (Section 3). As a second example, we consider the 10 – 13 June 1993 magnetic cloud observed by *Ulysses* at 4.6 AU out of the ecliptic plane (Section 4). Fainberg *et al.* (1996) have shown that inside this cloud there are two regions each with a polytropic relation between electron temperature T_e and density N_e. The presence of two polytropes with the first polytrope observations lasting about two days and the second polytrope lasting about one day has been interpreted as a signature of two magnetic flux tubes inside the same cloud with an order-of-magnitude increase of density on the magnetic separatrix situated on the boundary between the tubes (which we call a divider). Magnetic boundaries (defined by the smooth rotation of vector **B**) coincide with the boundaries of the two polytropes. The same boundaries can be seen both in the ratio of electron temperature T_e to proton temperature T_p ($T_e/T_p > 1$ inside the cloud except at the divider) and in the sharp interruption of ion-acoustic waves in the sheath of the magnetic cloud where $T_e/T_p < 1$. Landau damping suppresses ion-acoustic waves inside the sheath on both sides of the cloud (Stone *et al.*, 1995). In addition to considering separately the magnetic field and thermodynamic signatures of the two tubes inside the 10 – 13 June 1993 *Ulysses* magnetic cloud, we also look at the solar wind quasi-invariant (QI) defined as a ratio of the magnetic energy density to the energy density of the bulk flow of the solar wind (Osherovich, Fainberg, and Stone, 1999). The profile of QI for this cloud is consistent with the two-tube interpretation. As a third example of observational evidence of the double-helix topology of some magnetic clouds, we consider the superposition of QI for 12 magnetic clouds observed by *Ulysses*. The double-peak structure of the resulting QI profile we interpret as statistical evidence of the two-magnetic-tube topology with one tube twice as large in diameter as the other. The relation of our double-helix model with other models as well as possible directions for future research are discussed in Section 5.

2. Double-Helix Solution as an MHD Bounded State

Applying MHD equations in solar and heliospheric physics as well as in astrophysics in general does require some discussion. The equilibrium between the magnetic force and gradient of gas pressure P is described by a nonlinear system of partial differential equations for three components of magnetic field **B** (vector) and the scalar pressure function P:

$$\frac{1}{4\pi}(\nabla \times \mathbf{B}) \times \mathbf{B} = \nabla P \text{ (cgs units)}, \tag{1}$$

$$\nabla \cdot \mathbf{B} = 0. \tag{2}$$

This system of four equations for four functions is applied to magnetically confined plasma in laboratory experiments. For axially symmetric configurations, it has been found (Chandrasekhar and Prendergast, 1956) that the system, Equations (1) – (2), has two integrals that must be defined before attempting to solve these equations. After defining these two integrals, we have to define the boundary conditions. In laboratory experiments, metal walls confine the magnetic structure. By truncating the magnetic field on those conducting surfaces, surface currents are introduced. Effectively, this approach guarantees a finite magnetic energy of the whole configuration, but it introduces some elastic forces defined by the shape of the metal container. These forces are difficult to identify in space plasmas. This problem is known from modeling quiescent prominences. Locally, the magnetic force supports the heavy prominence. But one must introduce forces different from gravity, gradient of gas pressure, and magnetic force to support the whole configuration if one chooses to truncate the magnetic field on some surface that surrounds the prominence.

To avoid the truncation of **B**, different boundary conditions have been put forward (Osherovich, 1975). By requiring **B** to be continuous everywhere, but yet having finite magnetic energy, this approach has led to MHD bounded states as a new type of exact MHD solutions. For a cylindrical magnetic flux rope (coordinate z along the axis) the finite energy requirement reduces to the requirement of finite magnetic energy per unit length in the z-direction. The equilibrium system, Equations (1) – (2), with these boundary conditions and the specific choice of two integrals mentioned above has been reduced to a Schrödinger-type equation for an oscillator. The ground-state solution describes a single magnetic toroid; the first excited-state solution describes two interacting toroids with application to sunspot groups (Krat and Osherovich, 1976).

Several models in solar physics and astrophysics have been developed based on MHD bounded state solutions. These are

i) sunspot models, including the return-flux sunspot model (Osherovich, 1975, 1982a; Krat and Osherovich, 1978; Osherovich and Lawrence, 1983);
ii) the solar prominence model based on eigenvalue solutions that describe single and multiple flux ropes in Cartesian coordinates with one ignorable coordinate in constant gravitational field (Osherovich, 1985, 1989);
iii) the multi-toroidal model for coronal loops and transients [coronal mass ejections (CMEs)], which used a similarity assumption for time-dependent solutions (Osherovich, 1982b);
iv) the solar flare model with helicity conservation (Gliner and Osherovich, 1995); and
v) the multi-tube model for interplanetary magnetic clouds (Osherovich, Fainberg, and Stone, 1999).

Gliner (1984) has also used MHD bounded states in a study of the combined effect of potential and non-potential magnetic fields on equilibrium in stellar atmospheres.

We briefly review this multi-tube model based on the MHD ground-state solution with helical symmetry, which we apply below to optical observations of a CME and heliospheric *in situ* observations of magnetic clouds. It is known that not all CMEs become magnetic clouds; however, most of the strong magnetic storms (Dst < -100 nT) are associated with magnetic clouds, which makes them particularly interesting for us.

Introducing a helical variable

$$\xi \equiv \kappa z - m\phi, \tag{3}$$

where κ is constant, m is an integer $= 1, 2, \ldots$ and ϕ is the azimuthal angle in the cylindrical coordinate system, Johnson *et al.* (1958) reduced Equations (1) – (2) to a single partial

differential equation for a magnetic flux function ψ

$$\frac{1}{R}\frac{\partial^2\psi}{\partial\zeta^2}+\frac{1}{R}\frac{\partial}{\partial R}\left[\frac{R}{\kappa^2R^3+m^2}\frac{\partial\psi}{\partial R}\right]+4\pi\frac{\mathrm{d}P}{\mathrm{d}\psi}+\frac{J}{\kappa^2R^2+m^2}\frac{\mathrm{d}J}{\mathrm{d}\psi}+\frac{2\kappa mJ}{(\kappa^2R^2+m^2)^2}=0 \tag{4}$$

where $P(\psi)$ and $J(\psi)$ are the two integrals that must be chosen together with the boundary conditions to search for solutions of the initial system of Equations (1)–(2). The components of **B** can be found from ψ using three equations:

$$B_R=\frac{1}{R}\frac{\partial\psi}{\partial\xi}, \tag{5}$$

$$m\frac{B_\varphi}{R}-\kappa B_z=\frac{1}{R}\frac{\partial\psi}{\partial R}, \tag{6}$$

and

$$mB_z+\kappa RB_\varphi=J. \tag{7}$$

For the choice (Krat and Osherovich, 1978)

$$P=P_0-\frac{\kappa^2}{32\pi}\psi^2, \tag{8}$$

$$J=\frac{3}{2\kappa}\psi, \tag{9}$$

where P_0 is constant, Equation (4) has been reduced to a Schrödinger-type linear partial differential equation and solved analytically. The ground-state solution is

$$\frac{\psi}{\psi_0}=\left[(\kappa R)^2-1+x_0\frac{\kappa R\cos\xi}{\sqrt{2}}\right]\exp\left(\frac{-(\kappa R)^2}{4}\right), \tag{10}$$

where ψ_0 and x_0 are constants. The corresponding magnetic field components are

$$\frac{B_z}{B_0}=\left[-1.5\frac{(\kappa R)^2}{2}+\frac{x_0(\kappa R)\cos\xi}{2\sqrt{2}}\right]\exp\left(\frac{-(\kappa R)^2}{4}\right), \tag{11}$$

$$\frac{B_\varphi}{B_0}=\left[\kappa R+\frac{x_0\cos\xi}{\sqrt{2}}\right]\exp\left(\frac{-(\kappa R)^2}{4}\right), \tag{12}$$

$$\frac{B_R}{B_0}=-x_0\sqrt{2}\sin\xi\exp\left(\frac{-(\kappa R)^2}{4}\right), \tag{13}$$

where B_0 is constant. More general analytical solutions of Equation (4) can be found in Woolley (1975).

With Equations (10)–(13) for the magnetic field and Equation (8) for gas pressure, we can compare our double helix model with observations. In Figures 1 and 2 we show different elements of our double-helix model. In this model, magnetic surfaces can be found when the magnetic flux function ψ is kept constant. For $x_0=0$, ψ depends on R only and the magnetic surfaces are cylindrical. The corresponding non-zero components of magnetic

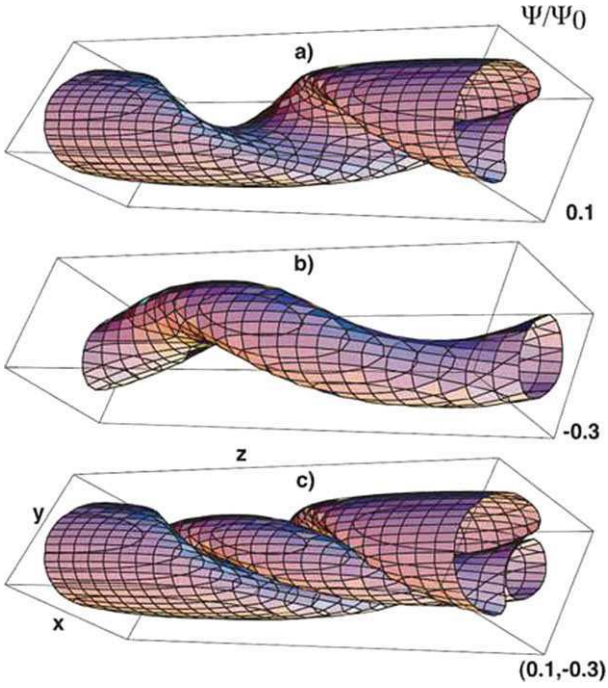

Figure 1 (a, b, c) Two non-equal helical tubes. (a) Large helix represented by the first magnetic surface formed by magnetic lines. (b) Small helix represented by another magnetic surface. (c) Combination of the two helices.

field strength $B_z(R)$ and $B_\varphi(R)$ are given by Equations (11)–(12). Thus, for $x_0 = 0$, we have a cylindrical flux rope with a deficit of gas pressure described by Equation (8). For $x_0 \neq 0$, Equation (10) describes a double-helix magnetic structure embedded in a cylindrical flux rope that enhances one helix and reduces the other. This is how the two non-equal helices shown in Figure 1 are formed. The corresponding cross section (perpendicular to the z-axis) in Figure 2b shows the results for the magnetic field surfaces. The numbers in Figures 1a, b, c and 2b represent values of ψ/ψ_0 of Equation (10). In Figure 1, adapted from Osherovich, Fainberg, and Stone (1999), x_0 is chosen to be five. The magnetic and thermodynamic structures have the same double-helix topology. According to Equation (4), magnetic surfaces coincide with isobaric (constant P) surfaces. The profiles of pressure deficit ΔP (Figure 2a) for our solution with $x_0 = 5$ show two non-equal minima of gas pressure

$$\Delta P \equiv -\frac{\kappa^2}{32\pi}\psi^2 \tag{14}$$

for two helices separated by a gas pressure increase (pressure "pulse").

3. Extreme UV Observations from SDO on 30 March 2010

The *Solar Dynamics Observatory* (SDO: Pesnell, Thompson, and Chamberlin, 2012) has been launched in February 2010. Figure 3 shows an extreme UV picture of an eruptive prominence taken by the SDO *Atmospheric Imaging Assembly* (AIA: Lemen *et al.*, 2012) on 30 March 2010. This image of an eruptive prominence (which we consider to be a CME) does not represent the magnetic measurements of the structure, but rather the thermodynamic consequences of the double-helix magnetic field, *i.e.*, the variations of temperature

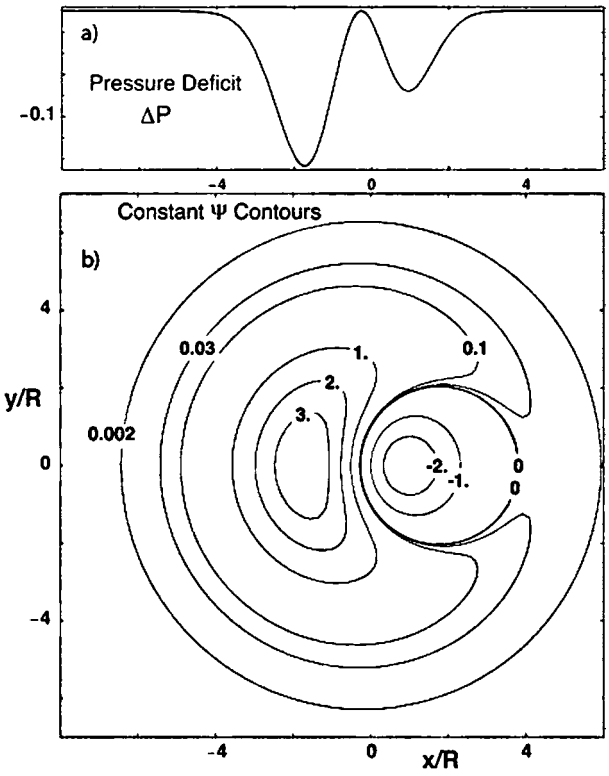

Figure 2 Two-helix magnetostatic solution: (a) Pressure deficit for the solution that describes two non-equal helices of opposite polarity embedded in a cylindrical flux rope. (b) Contours of the magnetic flux function for the cross section in the plane perpendicular to the axis of the cylinder. A cylindrical flux rope wraps around the two helices (adapted from Osherovich, Benson, and Fainberg, 2005).

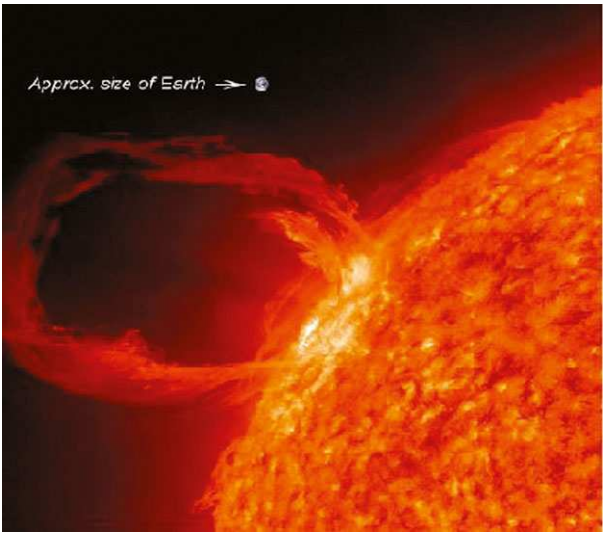

Figure 3 A solar eruptive prominence, with double helix appearance, as seen in extreme UV light (304 Å) on 30 March 2010 by SDO/AIA (with Earth superimposed for a sense of scale; source NASA website, http://sdo.gsfc.nasa.gov/firstlight).

and density in the corona associated with the eruption. It is also true that the filamentary structure and the overall shape and location of the prominence material is related to the magnetic structure in some way. We believe that the double-helix structure of the extreme

UV emission in Figure 3 is consistent with the magnetic field topology of our model for a CME.

4. Possible Double-Helix Topology of Isolated Magnetic Clouds Observed by *Ulysses*

Most of the research for CMEs and ICMEs has been performed for a single magnetic flux rope (Lepping, Jones, and Burlaga, 1990; Marubashi, 1996; Shimazu and Vandas, 2002; Berdichevsky, Lepping, and Farrugia, 2003, and references in a review by Osherovich and Burlaga, 1997). Farrugia, Osherovich, and Burlaga (1995) effectively ended the long competition between the spheromak and magnetic flux tube topology in favor of the latter. Even within the concept of a single flux rope (not necessarily cylindrical and possibly curved as part of a large toroidal structure), determining the tube boundaries from the *in situ* plasma and magnetic field measurements is a difficult task. Our suggestion of a double-helix topology for some magnetic clouds requires that we identify the boundaries for each helix. Sections 4.1 and 4.2 are devoted to this problem.

4.1. Multiple Polytropes and Tubes Within a Magnetic Cloud

The first observational evidence that there are two interacting magnetic tubes within a magnetic cloud (possibly two helices, according to the multi-tube model of Osherovich, Fainberg, and Stone, 1999) came from measurements of the electron temperature T_e and the proton temperature T_p in the 10 – 13 June 1993 cloud observed by *Ulysses* at 4.6 AU. Fainberg *et al.* (1996) have found that the log–log plot of T_e *vs.* N_e for this *Ulysses* magnetic cloud has two straight lines (Figure 4a). Previous observations at 1 AU (Osherovich *et al.*, 1993) had only one straight line, which was interpreted as a consequence of a polytropic relation $P_e \propto N_e^{\gamma_e}$ with the polytropic index $\gamma_e < 1$ where P_e is the total electron pressure and T_e is the total moment electron temperature. The theoretical interpretation with $\gamma_e < 1$ in turn has been drawn from a self-similar model based on an exact MHD solution for magnetic flux ropes (Farrugia, Osherovich, and Burlaga, 1995; Osherovich and Burlaga, 1997 and references therein) Fainberg *et al.* (1996) have found that for the first two days inside the cloud

$$P_{e1} = F_1 N_{e1}^{\gamma_1}, \tag{15}$$

and for the last day

$$P_{e2} = F_2 N_{e2}^{\gamma_2}, \tag{16}$$

where $\gamma_1 = 0.35$ was close to $\gamma_2 = 0.37$. However, the entropy coefficient F_1 was found to be 60 % higher than F_2. This is why the two suggested polytropes in Figure 4a appear as two parallel straight lines. Fainberg *et al.* (1996) pointed out the non-Maxwellian nature of the electron distribution as a possible reason for $\gamma_e < 1$ and the unusual anti-correlation of T_e and N_e. Indeed, the dominant component of pressure is from the electrons where for this cloud $T_e/T_p \sim 20$ (see Figure 5A); also, the electrons gain 50 % of their pressure from the core distribution (Maxwellian portion) and 50 % from the halo distribution (non-Maxwellian portion). Because CMEs and their interplanetary counterparts ICMEs (with magnetic clouds among them) all have a coronal origin, our results are related to the fundamental work of Scudder (1992) concerning non-Maxwellian distributions as an explanation of the inverse temperature density relation in stellar coronas. Further analysis reported by Sittler and Burlaga (1998) for electrons in magnetic clouds observed by

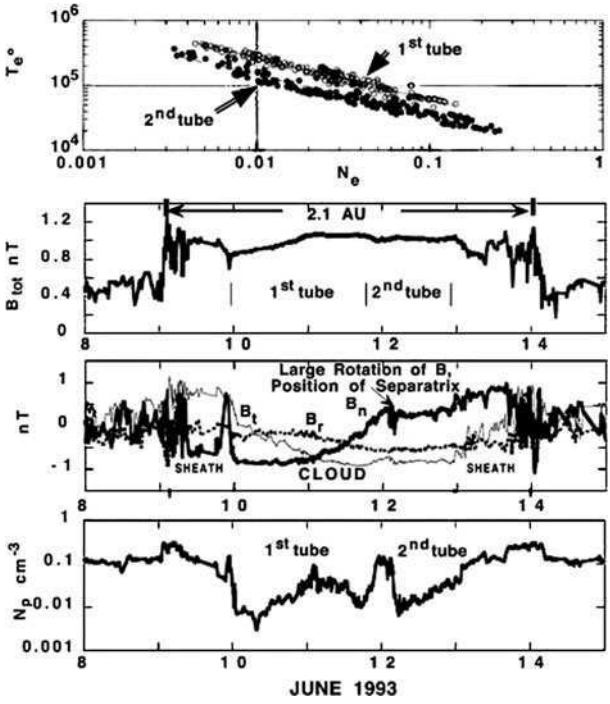

Figure 4 Magnetic cloud observed by *Ulysses* on 10 – 13 June 1993. (a) Log–log plot of T_e *vs.* N_e shows two polytropes: the first for the period 10 – 11 June 1993, the second for 11 – 13 June 1993 (after Fainberg *et al.*, 1996). (b) Total magnetic field of the cloud (after Osherovich, Fainberg, and Stone, 1999). (c) Radial, tangential and normal components of the magnetic field in the heliospheric system of coordinates. The position of the suggested separatrix is marked by fast rotation of **B**. (d) The proton density.

Voyager 2 has confirmed $\gamma_e < 1$ as a consequence of the non-Maxwellian energy distribution. Later, for *Wind* spacecraft observations of magnetic clouds, Nieves-Chinchilla and Viñas (2008) have arrived at the same conclusion, and they refer to attempts to explain the T_e *vs.* N_e anti-correlation without invoking non-Maxwellian distributions. For most of the above research, γ_e was found to be about 0.5. The discovery of two polytropes inside the same magnetic cloud opened up a new opportunity to study the topology of these objects. Not only the existence of multiple magnetic tubes inside the same cloud, but also their boundaries have been determined from the log–log plot of T_e *vs.* N_e. Fainberg *et al.* (1996) have found that the beginning of the first polytrope marks the beginning of the magnetic cloud as determined from the sharp decrease of T_p (usual method of determining magnetic cloud boundaries). Burlaga *et al.* (1981) defined magnetic clouds and included i) a magnetic field enhancement, ii) smooth rotation of **B**, and iii) a low proton temperature T_p. An enhancement of **B** began one day before *Ulysses* entered the magnetic cloud of 10 – 13 June 1993 and this enhancement lasts for five days (Figure 4b). From the beginning of the B enhancement to the T_p drop (one-day interval) there is a sheath that is dominated by protons ($T_e/T_p < 1$), as shown in Figure 5A. A similar one-day sheath follows the back of this cloud. Fainberg *et al.* (1996) showed that from the beginning of the sheath, **B** rotates, but the rotation is not smooth. The beginning of smooth rotation marks the front boundary of the cloud, which coincides with drop of T_p. These two definitions of a magnetic cloud front boundary correspond remarkably well to the beginning of the first tube polytrope in Figure 4a. Effectively, the beginning of the polytrope with $\gamma_e < 1$ presents a third method for determining the front boundary of a magnetic cloud. The end of the first polytrope is marked by the loss of smooth rotation for approximately 40 minutes. This large non-smooth rotation of **B** shown in Figure 4c was interpreted by Fainberg *et al.* (1996) as an indication of a magnetic separatrix that is also marked by an order-of-magnitude increase of N_p

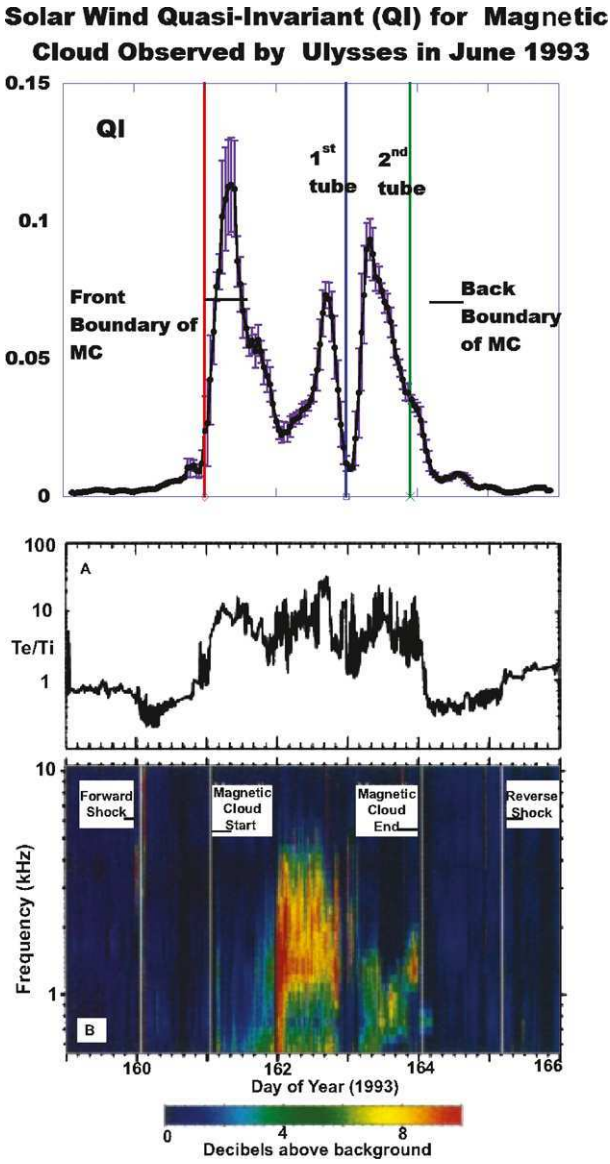

Figure 5 (A) Electron–ion temperature ratio (T_e/T_p) during the interval June 1993 (day 159 to 165), provided by the *Ulysses* solar wind plasma instrument. (B) Dynamic spectrum of electric field data from 0.5 to 10 kHz during the same interval showing intense wave activity occurring throughout the interval that the spacecraft was inside the magnetic cloud. The magnetic boundaries of the cloud and the arrival times of the associated forward and reverse shocks are indicated by vertical bars (adapted from Stone *et al.*, 1995). Top panel shows the QI of this cloud; each point is a five-hour average.

(Figure 4d) and a related increase in proton pressure. This divider, which lasted 40 minutes between the first and second tube, is also shown in our model in Figure 2a as a pressure pulse. Consistent with the two-helix topology in our model, the second polytrope starts after the divider and ends at the back boundary of the magnetic cloud. The back boundary is again marked by an increase in T_p along with the loss of smooth rotation of **B** – all characteristics of the one-day back sheath. In the sheath on both sides of the magnetic cloud, the proton component was found to be close to adiabatic with $\gamma_p \approx 5/3$ (Fainberg *et al.*, 1996; Osherovich and Burlaga, 1997). Inside the cloud the proton component was closer to isothermal with observations of $\gamma_p \approx 1.1 - 1.2$. The expansion of a magnetic cloud with time leads to an increase of T_e/T_p from 6 – 7 at 1 AU to 10 – 20 for the *Ulysses* magnetic cloud of 10 –

13 June 1993 at 4.6 AU. The high T_e/T_p value creates favorable conditions for ion-acoustic waves, which were indeed observed in this cloud (Figure 5B adapted from Stone *et al.*, 1995). In the sheath $T_e/T_p < 1$ (as shown in Figure 5A as T_e/T_i), which satisfies conditions where Landau damping decreases the intensity of ion-acoustic waves. The boundaries of the T_e/T_p increase and the intensity of the ion-acoustic waves are sharp and can be used as a proxy for the magnetic cloud boundary. On the divider, where the first polytrope ends and the second one starts, there is a significant decrease of wave activity because of the low value of T_e/T_p. Thus the ion-acoustic waves also show two parts in this magnetic cloud, consistent with the double-helix model (Figure 5B).

4.2. Probing the Multi-Tube Topology of Magnetic Clouds Using the Solar Wind Quasi-Invariant

Magnetic cloud boundaries and the topology of their internal structure can be determined using a non-dimensional parameter called the solar wind quasi-invariant (QI),

$$\mathrm{QI} \equiv \frac{B^2}{8\pi} \Big/ \frac{\rho v^2}{2} = M_A^{-2}, \tag{17}$$

(cgs system) where M_A is the magnetic Mach number, v is the solar wind speed and ρ is the solar wind density. QI was introduced as a new index of solar wind activity (Osherovich, Fainberg, and Stone, 1999). This ratio of magnetic energy density to the energy density of the solar wind flow on a yearly basis has a high correlation (~ 0.98) for 28 years with sunspot numbers. For short time scales (days, hours, minutes), QI provides a useful measure of the short-term deviation of the solar wind from its normal state caused by interplanetary disturbances. For magnetic clouds, QI is 10 – 100 times higher than QI of the undisturbed solar wind. This QI anomaly was studied for three magnetic clouds associated with three strong magnetic storms (Dst < -100 nT) in Osherovich *et al.* (2007). Recently, Webb, Fainberg, and Osherovich (2012) investigated QI for fast and slow isolated magnetic clouds from the Richardson and Cane (2010) catalog of interplanetary disturbances observed by the *Wind* spacecraft. Webb, Fainberg and Osherovich found that the boundaries of the QI anomaly taken at 20 % of QI maximum in the magnetic cloud are quite close to the traditional magnetic cloud boundaries determined by plasma and magnetic data by Richardson and Cane. The possibility that QI might characterize the internal structure of a magnetic cloud and its boundaries was also examined. For the *Ulysses* 10 – 13 June 1993 magnetic cloud, average (longer than five hours) values of QI are shown in the upper panel of Figure 5, where the error bars result from the averaging of five successive hourly observations. We compared the front and back boundaries of the cloud based on the 20 % of $\mathrm{QI}_{\max}$ with boundaries determined from the T_e/T_p ratio (Figure 5A) as well as from the start and end of the two polytropes in Figure 4a. The above results for the 10 – 13 June 1993 magnetic cloud are consistent with traditionally determined boundaries (Fainberg *et al.*, 1996), and also consistent with results in a recent paper (Webb, Fainberg, and Osherovich, 2012). The profile of QI for this cloud has two main peaks (much larger than the error bars) with a deep minimum at the divider between the two tubes, which we have discussed in Section 4.1 of this paper. The time of the deep narrow QI minimum coincides with the time of the narrow depression in the intensity of ion-acoustic waves in Figure 5B. The agreement of boundaries derived from different instruments reinforces their physical nature. There is also a third somewhat smaller narrow peak with a counterpart in the T_e/T_p profile, which may be suggestive of a

Table 1 List of isolated magnetic clouds observed by *Ulysses* at distances of 3.8 AU to 5.4 AU used in Figure 6.

Cloud No.	Year	Start time (day of the year at QI_{max} 20 %)	QI_{max}	Average distance R (AU)	Mean latitude	Mean v (km s^{-1})
1	1991	213.92	0.44631	3.8	−5.3	412.87
2	1991	239.17	0.2479	4	−5.5	517.21
3	1991	263.75	0.091842	4.2	−5.6	457.35
4	1991	293.17	0.15449	4.5	−5.7	435.3
5	1992	7.4167	0.56615	5.1	−6	526.77
6	1992	307.58	0.1	5.2	−19.4	529.07
7	1992	319.42	0.32718	5.2	−20.1	612.64
8	1992	92.667	0.17718	5.4	−8.6	458.35
9	1992	143.67	0.096644	5.4	−11.1	435.44
10	1993	161	0.18456	4.6	−32.2	736.19
11	1993	202.92	0.095638	4.5	−35.2	608.34
12	1993	72.375	0.1396	4.9	−26.7	536.92

third narrow tube in the *Ulysses* cloud. Our ground-state solution (Equation (10)) describes two non-equal helices embedded in a cylindrical flux rope. Excited states of this model have more than two helices. A cloud observed by *Wind* on 18 October 1995 was found to have eight magnetic tubes based on the analysis of the log–log T_e *vs*. N_e relation (Osherovich *et al.*, 2002). These tubes had polytropic indices below unity except for a few non-coherent structures for which the polytropic relation was not valid.

Table 1 presents a list of the 12 isolated magnetic clouds observed by *Ulysses* at distances between 3.8 and 5.4 AU. For each magnetic cloud in Table 1, the QI profile was calculated (with the density of the proton component only as in Figure 5 for QI of the 10 – 13 June 1993 cloud, which is number 10 in the table). The selection criteria for isolated clouds in Table 1 are the same as in Webb, Fainberg, and Osherovich (2012). At large distances magnetic clouds are very large due to expansion. It took three days for *Ulysses* to cross cloud number 10, whereas a typical cloud at 1 AU is observed within a single day. The sheaths of the clouds in this table are observed typically for one day before and after the cloud. The very large size of these distant clouds helps in studying their internal structure. For the 12 clouds in Table 1, the superposition (average) of QI profiles (where the clouds are lined up at the time of a 20 % of QI maximum) is presented in Figure 6, where the error bars are for the 12 hourly values comprising the average. This combined QI profile is similar to that of cloud number 10 in that there is an order-of-magnitude enhancement (QI anomaly) above the background lasting for about three days. The boundaries shown in Figure 6 correspond to the times when QI is 20 % of maximum. This QI superposition also reveals a two-part structure similar to that of cloud number 10. The first part (first helix in our model) is twice as large (lasting for two days) as the second part (second helix, which in Figure 6 is designated as the second tube), which lasts about one day. A deep minimum of QI separates the two tubes with significance justified by the small error bars. Mostly, the increase in density ρ in the divider is responsible for the minimum in QI in Figure 6, as is the case cloud number 10 alone. The asymmetry by a factor of two in the size of the helices seems to be a characteristic of this group of distant clouds.

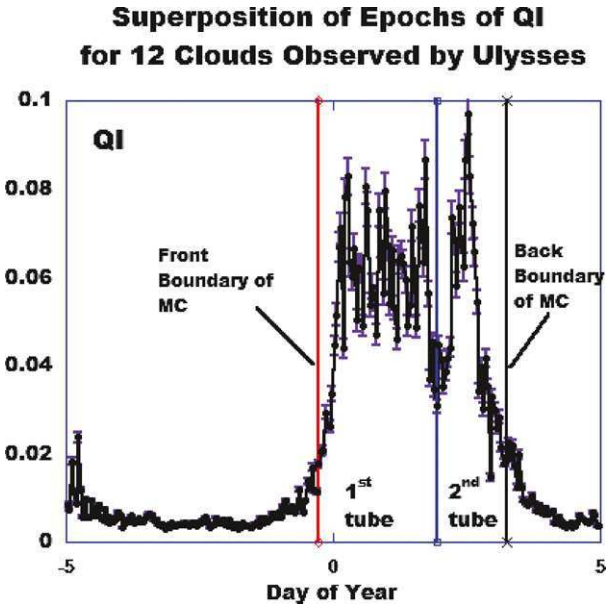

Figure 6 Solar wind quasi-invariant superposition of 12 isolated magnetic clouds (denoted by MC) observed by *Ulysses* between 1991 and 1993, at distances of 3.8 AU to 5.4 AU.

5. Summary and Discussion

The multiple-tube geometry for a magnetic structure can be explained naturally as MHD-excited states in a multi-toroidal axisymmetric model (Osherovich, 1975) of sunspots, in the solar prominence model with one ignorable coordinate (Osherovich, 1985, 1989), and in the time-dependent multi-toroidal self-similar model for CMEs (Osherovich, 1982b). The MHD ground-states in the above models represent a single toroid and single infinite flux rope. For MHD-bounded states with helical symmetry (Equations (10) – (13)), the ground state already has two magnetic tubes – two helices with opposite magnetic polarity. These two helices are not equal since they are embedded in a cylindrical flux rope of one polarity along the z-axis. The transition from a cylindrical rope model to a double helix model with two equal helices is controlled by a non-dimensional parameter x_0. For $x_0 = 0$ there are no helices. For $x_0 = 5$ in Figures 1 and 2 there are two non-equal helices embedded in a cylindrical magnetic container. These two helices magnetically interact with each other and also with the cylindrical magnetic flux rope that surrounds them. Any attempt to describe two magnetic tubes as force-free magnetic flux ropes effectively excludes magnetic interaction. The observed divider between two helices that we identified for the 12 *Ulysses* clouds is evidence of such interaction. Vandas, Fischer, and Geranios (1999) have reported that the double-peak magnetic profile in some magnetic clouds is suggestive of a double flux rope structure of these objects, which would exclude the previous spheromak interpretation. Without a specific MHD solution, it is unclear what prevents the collapse of the two flux ropes. The self-similar evolution of a single cylindrical magnetic flux rope (Osherovich, Farrugia, and Burlaga, 1993) leads to the flattening of the B profile and eventually develops into two humps in the profile for old clouds. This pattern is observed for cases where the same cloud was intercepted by two spacecraft at different heliospheric distances (Osherovich, 1998). For such a single flux rope to expand, the polytropic index γ must be below unity, which we have found to be the case for all clouds studied. Thus, two humps in the B profile do not necessarily mean two flux ropes inside the same cloud. In contrast,

for the self-similar spherical expansion model of a cylindrical tube of Berdichevsky, Lepping, and Farrugia (2003) and Shimazu and Vandas (2002), the B profile does not change in time (no flattening) and $\gamma < 1$ is not required. The two magnetic flux ropes within the same magnetic cloud identified by Hu *et al.* (2003) from the reconstruction procedure based on numerical solutions of the Grad–Shafranov equation provides additional evidence of the multi-tube nature of magnetic clouds. In this model two flux ropes have the same orientation as their magnetic axes. Geometrically, these solutions are similar to the prominence solutions mentioned in Section 2. The difference is twofold: i) the prominence model (Osherovich, 1985, 1989) is based on MHD-bounded state configurations and contains a constant gravitational field, and ii) Hu *et al.* (2003) took only proton pressure as input. All our modeling of magnetic clouds (reviewed in Osherovich and Burlaga, 1997) recognizes that at 1 AU the contribution of the electrons to the total gas pressure is 6 – 7 times higher than the contribution of protons. For distant clouds like cloud no. 10 in Table 1, it is about 20 times higher. Profiles for P_e and P_p are quite different. Thus, solving the Grad–Shafranov equation with proton pressure only does not do justice to the force balance inside the magnetic cloud.

The double-helix model comes from more general symmetry than axial symmetry and therefore is more complex geometrically. But so are the new extreme UV light images provided by the *Solar Dynamics Observatory* like the one shown in Figure 3 for an eruptive prominence. In the view of formulas for magnetic field **B** components for our double-helix model, two spacecraft like STEREO A and STEREO B, when suitably separated, may cross two different helices of the same magnetic cloud. In such a case the orientation of the magnetic axes for the two flux ropes may differ significantly since they belong to two different helices. Even for single-spacecraft observations, different trajectories through the double-helix model suggest the possible existence of a quasi-periodic structure where the periodicity is due to the helical symmetry. The static double helix model should be considered as a starting point for a self-similar time-dependent MHD model with the same magnetic topology. These topics concern the direction of future work and are beyond the scope of this paper.

Acknowledgements The authors appreciate the invitation of Teresa Nieves-Chinchilla to participate in this special issue of *Solar Physics* devoted to magnetic flux rope research. The constructive suggestions of the referee have been incorporated in the paper.

References

Berdichevsky, D., Lepping, R.P., Farrugia, C.J.: 2003, *Phys. Rev. E* **67**, 036405.
Burlaga, L.F., Sittler, E., Mariani, F., Schwenn, R.: 1981, *J. Geophys. Res.* **86**, 6673.
Chandrasekhar, S., Prendergast, K.H.: 1956, *Proc. Natl. Acad. Sci. USA* **42**(1), 5.
Fainberg, J., Osherovich, V.A., Stone, R.G., MacDowall, R.J., Balogh, A.: 1996, In: Winterhalter, D., Gosling, J.T., Habbal, S.R., Kurth, W.S., Neugebauer, M. (eds.) *Proc. Solar Wind Eight Conference* **382**, 554.
Farrugia, C.J., Osherovich, V.A., Burlaga, L.F.: 1995, *J. Geophys. Res.* **100**, 12293.
Gliner, E.B.: 1984, *Astrophys. J.* **283**, 363.
Gliner, E.B., Osherovich, V.A.: 1995, *Solar Phys.* **156**, 95.
Hu, Q., Smith, W., Ness, N.F., Skoug, R.M.: 2003, *Geophys. Res. Lett.* **30**, 1385.
Johnson, J., Oberman, C., Kulsrud, R., Frieman, E.: 1958, In: *Proc. Int. Conf. Peaceful Uses of Atomic Energy*, *Geneva, Switzerland*, 1875.
Krat, K.A., Osherovich, V.A.: 1976, *Solar Phys.* **50**, 65.
Krat, K.A., Osherovich, V.A.: 1978, *Solar Phys.* **59**, 43.
Lemen, J.R., Title, A.M., Akin, D.J., Boerner, P.F., Chou, C., Drake, J.F., *et al.*: 2012, *Solar Phys.* **275**, 17. doi:10.1007/s11207-011-9776-8.
Lepping, R.P., Jones, J.A., Burlaga, L.F.: 1990, *J. Geophys. Res.* **95**, 11957.
Marubashi, K.: 1996, In: *Solar Wind Eight Conf.*, *AIP Conf. Proc.* **382**, 522.

Nieves-Chinchilla, T., Viñas, A.F.: 2008, *J. Geophys. Res.* **113**, A02105.
Osherovich, V.A.: 1975, *Soln. Dannye* **5**, 70.
Osherovich, V.A.: 1982a, *Solar Phys.* **77**, 63.
Osherovich, V.A.: 1982b, *Astrophys. Space Sci.* **86**(2), 453.
Osherovich, V.A.: 1985, *Astrophys. J.* **297**, 314.
Osherovich, V.A.: 1989, *Astrophys. J.* **336**, 1041.
Osherovich, V.A.: 1998, In: Chang, T. (ed.) *Cambridge Symposium on Multiscale Phenomena II in Space Plasmas*, *Cambridge*, 265.
Osherovich, V.A., Benson, R.F., Fainberg, J.: 2005, *IEEE Trans. Plasma Sci.* **33**(2), 599.
Osherovich, V.A., Burlaga, L.F.: 1997, In: Crooker, N., Joselyn, J.A., Feynman, J. (eds.) *Coronal Mass Ejections*, *AGU Geophys. Monogr.* **99**, 157.
Osherovich, V.A., Fainberg, J., Stone, R.G.: 1999, *Geophys. Res. Lett.* **26**, 2597.
Osherovich, V.A., Farrugia, C.J., Burlaga, L.F.: 1993, *Adv. Space Res.* **13**(6), 57.
Osherovich, V.A., Lawrence, J.K.: 1983, *Solar Phys.* **88**, 117.
Osherovich, V.A., Farrugia, C.J., Burlaga, L.F., Lepping, R.P., Fainberg, J., Stone, R.G.: 1993, *J. Geophys. Res.* **98**, 15331.
Osherovich, V.A., Fainberg, J., Viñas, A.F., Fitzenreiter, R.: 2002, In: *Solar Wind Ten Conf*, *AIP Conf. Proc.* **679**, 733.
Osherovich, V.A., Benson, R.F., Fainberg, J., Green, J.L., Garcia, L., Boardsen, S., Tsyganenko, N., Reinisch, B.W.: 2007, *J. Geophys. Res.* **112**, A06247.
Pesnell, W.D., Thompson, B.J., Chamberlin, P.C.: 2012, *Solar Phys.* **275**, 3 – 15. doi:10.1007/s11207-011-9841-3.
Richardson, I.G., Cane, H.V.: 2010, *Solar Phys.* **264**, 189.
Scudder, J.D.: 1992, *Astrophys. J.* **398**, 299.
Shimazu, H., Vandas, M.: 2002, *Earth Planets Space* **54**, 783.
Sittler, E., Burlaga, L.F.: 1998, *J. Geophys. Res.* **103**(A8), 17477.
Stone, R.G., MacDowall, R.J., Fainberg, J., Hoang, S., Kaiser, M.L., Kellogg, P.J., *et al.*: 1995, *Science* **268**(5213), 1026.
Vandas, M., Fischer, S., Geranios, A.: 1999, In: *Solar Wind Nine Conf.*, *AIP Conf. Proc.* **471**, 127.
Webb, A., Fainberg, J., Osherovich, V.: 2012, *Solar Phys.* **277**, 375.
Woolley, M.I.: 1975, *J. Plasma Phys.* **14**, 305.

Solar Phys (2013) 286:453–477
DOI 10.1007/s11207-013-0269-9

Initiation of Coronal Mass Ejections by Sunspot Rotation

T. Török · M. Temmer · G. Valori · A.M. Veronig · L. van Driel-Gesztelyi · B. Vršnak

Received: 28 July 2012 / Accepted: 6 March 2013 / Published online: 4 April 2013

Abstract We study a filament eruption, two-ribbon flare, and coronal mass ejection (CME) that occurred in NOAA Active Region 10898 on 6 July 2006. The filament was located South of a strong sunspot that dominated the region. In the evolution leading up to the eruption, and for some time after it, a counter-clockwise rotation of the sunspot of about 30 degrees was observed. We suggest that the rotation triggered the eruption by progressively expanding the magnetic field above the filament. To test this scenario, we study the effect of twisting the initially potential field overlying a pre-existing flux-rope, using three-dimensional zero-β MHD simulations. We first consider a relatively simple and symmetric system, and

Electronic supplementary material The online version of this article (doi:10.1007/s11207-013-0269-9) contains supplementary material, which is available to authorized users.

T. Török (✉)
Predictive Science, Inc., 9990 Mesa Rim Rd., Suite 170, San Diego, CA 92121, USA
e-mail: tibor@predsci.com

M. Temmer · A.M. Veronig
IGAM/Kanzelhöhe Observatory, Institute of Physics, Universität Graz, Universitätsplatz 5, 8010 Graz, Austria

M. Temmer
Space Research Institute, Austrian Academy of Sciences, Schmiedlstrasse 6, 8042 Graz, Austria

G. Valori · L. van Driel-Gesztelyi
LESIA, Observatoire de Paris, CNRS, UPMC, Université Paris Diderot, 5 place Jules Janssen, 92190 Meudon, France

L. van Driel-Gesztelyi
Mullard Space Science Laboratory, University College London, Holmbury St. Mary, Dorking, Surrey RH5 6NT, UK

L. van Driel-Gesztelyi
Konkoly Observatory, Hungarian Academy of Sciences, Budapest, Hungary

B. Vršnak
Hvar Observatory, Faculty of Geodesy, University of Zagreb, Kačićeva 26, 10000 Zagreb, Croatia

then study a more complex and asymmetric magnetic configuration, whose photospheric-flux distribution and coronal structure are guided by the observations and a potential field extrapolation. In both cases, we find that the twisting leads to the expansion of the overlying field. As a consequence of the progressively reduced magnetic tension, the flux-rope quasi-statically adapts to the changed environmental field, rising slowly. Once the tension is sufficiently reduced, a distinct second phase of evolution occurs where the flux-rope enters an unstable regime characterised by a strong acceleration. Our simulations thus suggest a new mechanism for the triggering of eruptions in the vicinity of rotating sunspots.

Keywords Magnetic fields, corona · Active regions, models · Coronal mass ejections, initiation and propagation · Sunspots, velocity

1. Introduction

Filament (or prominence) eruptions, flares, and coronal mass ejections (CMEs) are the three large-scale eruptive events on the Sun. It has become clear in recent years that they are not independent phenomena, but different observational manifestations of a more general process, namely the sudden and violent disruption and dynamic reconfiguration of a localised volume of the coronal magnetic field (*e.g.* Forbes, 2000). Whether or not all three phenomena occur together appears to depend mainly on the properties of the pre-eruptive configuration. For example, CMEs can occur without a filament eruption (if no filament has formed in the source region of the erupting flux prior to its eruption) and without significant flaring (if the magnetic field in the source region is too weak; *e.g.* Zirin, 1998) or, in extreme cases, even without any low-coronal or chromospheric signature (Robbrecht, Patsourakos, and Vourlidas, 2009). On the other hand, both flares and filament eruptions are not always accompanied by a CME (if, for instance, the magnetic field above the source region is too strong; see, *e.g.*, Moore *et al.*, 2001; Nindos and Andrews, 2004; Török and Kliem, 2005). In large events such as the one studied in this article, however, all three phenomena are observed almost always. Such events typically start with the slow rise of a filament and/or overlying loops (*e.g.* Maričić *et al.*, 2004; Schrijver *et al.*, 2008; Maričić, Vršnak, and Roša, 2009), which is often accompanied by weak pre-flare signatures in EUV or X-rays (*e.g.* Maričić *et al.*, 2004; Chifor *et al.*, 2007). The slow rise is followed by a rapid acceleration and a huge expansion of the eruptive structure, which is then observed as a CME. The rapid acceleration has been found in most cases to be very closely correlated with the flare impulsive phase (*e.g.* Kahler *et al.*, 1988; Zhang *et al.*, 2001; Maričić *et al.*, 2007; Temmer *et al.*, 2008).

Although it is now widely accepted that solar eruptions are magnetically driven, the detailed physical mechanisms that initiate and drive eruptions are still controversial. Accordingly, a large number of theoretical models have been proposed in the past decades (for a recent review see, *e.g.*, Forbes, 2010). Virtually all of these models consider as pre-eruptive configuration a sheared or twisted core field low in the corona, which stores the free magnetic energy required for eruption and is stabilised by the ambient coronal field. The choice of such a configuration is supported by observations of active regions, which often display sheared structures (filaments and soft X-ray sigmoids) surrounded by less sheared, tall loops. An eruption is triggered if the force balance between the core field and the ambient field is destroyed, either by increasing the shear or twist in the core field or by weakening the stabilizing restoring force of the ambient field (see, *e.g.*, Aulanier *et al.*, 2010).

One of the many mechanisms that has been suggested to trigger eruptions is the rotation of sunspots. The idea was put forward by Stenflo (1969), who showed that the order of

magnitude of the energy deposition into coronal structures by sunspot rotations is sufficient to produce flaring activity (see also Kazachenko *et al.*, 2009).

Sunspot rotations have been known for a long time – the first evidence, based on spectral observations, was presented one century ago by Evershed (1910) – and since then they have been the subject of numerous analyses. Still, measurements of sunspot rotation are not straightforward, and, depending on the method employed, can give quite different results (see, *e.g.*, Min and Chae, 2009). Meticulous case studies (*e.g.* Zhang, Li, and Song, 2007; Min and Chae, 2009; Yan *et al.*, 2009), as well as detailed statistical analyses (*e.g.* Brown *et al.*, 2003; Yan and Qu, 2007; Zhang, Liu, and Zhang, 2008; Li and Zhang, 2009; Suryanarayana, 2010) showed that sunspots can rotate significantly, up to several hundreds of degrees over a period of a few days. Interestingly, sunspots do not necessarily rotate as a rigid body: Brown *et al.* (2003) and Yan and Qu (2007) showed that the rotation rate often changes with the distance from the sunspot centre. The rotation of sunspots is commonly interpreted as an observational signature of the emergence of a flux-rope through the photosphere (*e.g.* Gibson *et al.*, 2004) or, more generally, as the transport of helicity from the convection zone into the corona (see, *e.g.*, Longcope and Welsch, 2000; Tian and Alexander, 2006; Tian, Alexander, and Nightingale, 2008; Fan, 2009). On the other hand, observations of strong sunspot rotation without signs of significant flux emergence have been reported (*e.g.* Tian and Alexander, 2006, and references therein), suggesting that intrinsic sunspot rotation of sub-photospheric origin exists. In such cases the rotation rate tends to be smaller than for sunspot rotations associated with flux emergence (*e.g.* Zhu, Alexander, and Tian, 2012).

A number of studies have shown a direct cause–consequence relationship between higher-than-average sunspot rotation and enhanced eruptive activity. For example, Brown *et al.* (2003), Hiremath and Suryanarayana (2003), Hiremath, Lovely, and Kariyappa (2006), Tian and Alexander (2006), Yan and Qu (2007), Zhang, Liu, and Zhang (2008), Li and Zhang (2009), Yan *et al.* (2009, 2012), and Suryanarayana (2010) reported an apparent connection between rotating sunspots (with total rotation angles of up to 200° and more) and eruptive events. In particular, Yan and Qu (2007) attributed eruptive activity in an active region to different rotation speeds in different parts of a sunspot, whereas Yan, Qu, and Kong (2008) found indications that active regions with sunspots rotating opposite to the differential-rotation shear are characterised by high X-class-flare productivity. Romano, Contarino, and Zuccarello (2005) reported a filament eruption that was apparently triggered by photospheric vortex motions at both footpoints of the filament, without any sign of significant flux emergence.

Besides purely observational studies of the relationship between sunspot rotation and eruptive activity, some authors presented a combination of observations and modelling. For example, Régnier and Canfield (2006) utilised multi-wavelength observations and modelling of the coronal magnetic field of the highly flare-productive NOAA Active Region 8210 to show that slow sunspot rotations enabled flaring, whereas fast motions associated with emerging flux did not result in any detectable flaring activity. Moreover, they also showed that the deposition of magnetic energy by photospheric motions is correlated with the energy storage in the corona, which is then released by flaring. Similarly, Kazachenko *et al.* (2009) analysed detailed observations of an M8 flare–CME event and the associated rotating sunspot, and combined them in a minimum-current-corona model. They found that the observed rotation of 34° over 40 hours led to a triplication of the energy content and flux-rope self-helicity, sufficient to power the M8 flare.

Numerical MHD investigations of the relationship between sunspot rotation and eruptive activity started with Barnes and Sturrock (1972), who modelled the coronal magnetic field of

a rotating sunspot surrounded by a region of opposite polarity. They found that the rotation causes an inflation of the magnetic field, and that its energy increases with the rotation angle until, when the rotation angle exceeds $\approx 180°$, it becomes larger than that of the open-field configuration with the same boundary conditions, presumably leading to an eruption.

MHD simulations of the formation and evolution of flux-ropes by twisting line-tied potential fields have been widely performed since then. Calculations were done by either twisting uniform fields in straight, cylindrically symmetric configurations (*e.g.* Mikic, Schnack, and van Hoven, 1990; Galsgaard and Nordlund, 1997; Gerrard, Arber, and Hood, 2002; Gerrard *et al.*, 2003) or by twisting bipolar potential fields; the latter yielding arched flux-ropes anchored at both ends in the same plane (*e.g.* Amari and Luciani, 1999; Gerrard, Hood, and Brown, 2004). Most of these simulations focused on the helical kink instability and its possible role in producing compact flares and confined eruptions. Klimchuk, Antiochos, and Norton (2000) studied the twisting of a bipole with emphasis on the apparently uniform cross-section of coronal loops. Very recently, Santos, Büchner, and Otto (2011) simulated the energy storage for the active region that was studied earlier by Régnier and Canfield (2006). They imposed photospheric flows on an extrapolated potential field and found the formation of pronounced electric currents at the locations of the observed flare sites. The authors concluded that the main flare activity in the active region was caused by the slow rotation of the sunspot that dominated the region.

However, none of the above studies were directly related to CMEs. Amari *et al.* (1996) were the first to show that the formation and continuous twisting of an arched flux-rope in a bipolar potential field can lead to a strong dynamic expansion of the rope, resembling what is observed in CMEs. Later, Török and Kliem (2003) and Aulanier, Démoulin, and Grappin (2005) extended this work by studying in detail the stability properties and dynamic evolution of such a system. The underlying idea of these simulations is that slow photospheric vortex motions can twist the core magnetic field in an active region up to the point where equilibrium cannot be longer maintained, and the twisted core field, *i.e.* a flux-rope, erupts (for the role of increasing twist in triggering a flux-rope eruption see also Chen, 1989; Vršnak, 1990; Fan and Gibson, 2003; Isenberg and Forbes, 2007). What has not been studied yet is whether a twisting of the field *overlying an existing flux-rope* can lead to the eruption of the rope.

In this article, we present observations of a large solar eruption that took place in the vicinity of a rotating sunspot. We suggest that the continuous rotation of the spot triggered the eruption by successively weakening the stabilizing coronal field until the low-lying core field erupted. We support our suggestion by MHD simulations that qualitatively model this scenario.

The remaining part of this article is organised as follows: In Section 2 we describe the observations, focusing on the initial evolution of the eruption and on the rotation of the sunspot. In Section 3 we describe the numerical simulations, the results of which are presented in Section 4. We finally discuss our results in Section 5.

2. Observations

The eruption on 6 July 2006 in NOAA Active Region 10898 was a textbook two-ribbon flare accompanied by a filament eruption and a halo CME, the latter being most prominent in the southwest quadrant and reaching a linear plane-of-sky velocity of ≈ 900 km s^{-1} (Temmer *et al.*, 2008). The event was associated with an EIT wave, a type II burst, and very distinct coronal dimming regions. The flare was of class M2.5/2N, located at the heliographic position S9°, W34°. It was observed in soft X-rays (SXR) by GOES (peak time at $\approx$ 08:37 UT)

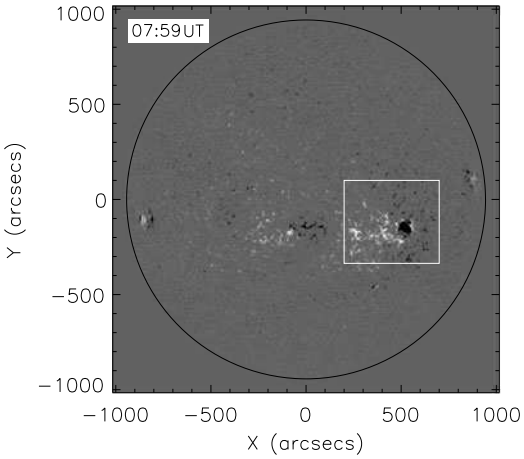

Figure 1 Full-disk line-of-sight SOHO/MDI magnetogram recorded on 6 July 2006, 07:59 UT. The active region under study is marked by the white box.

as well as in hard-X rays (HXR) with RHESSI, with the two highest peaks of nonthermal HXR emission occurring during 08:20 – 08:24 UT.

The evolution of the active region in the days preceding the eruption, and in particular the rotation of the leading sunspot, can be studied using its photospheric signatures. Photospheric line-of-sight magnetograms of the region were obtained by the MDI instrument (Scherrer *et al.*, 1995) onboard the *Solar and Heliospheric Observatory* (SOHO). The active region was a bipolar region of Hale type β, consisting of a compact negative polarity (the sunspot) that was surrounded by a dispersed positive polarity, most of which was extending eastwards (see Figure 1). The maximum of the magnetic-field flux density in the sunspot was about nine times larger than in the dispersed positive polarity. The two polarities were surrounded by a large, "inverse C-shaped" area of dispersed negative flux to the west of the region.

We measured the magnetic flux of the concentrated leading (negative) and dispersed following (positive) polarities using a (re-calibrated) SOHO/MDI synoptic map, which preserves the resolution of the original observation. The map includes magnetic features close to the time of their central meridian passage, when projection effects of the line-of-sight magnetic fields are at minimum. The total magnetic flux (half of the total unsigned flux) was found to be $(2.1 \pm 0.2) \times 10^{22}$ Mx, with the two polarities nearly balanced [$(2.0 \pm 0.2) \times 10^{22}$ and $(-2.2 \pm 0.2) \times 10^{22}$ Mx for the positive and negative flux, respectively]. The error estimates reflect the uncertainty in determining how much of the dispersed positive and negative polarities belonged to the active region. The leading spot, including the penumbral area, had a mean magnetic-field strength (magnetic-flux density over 2340 pixels) of 390 G, reaching 1820 G when a smaller, purely umbral, area was considered (240 pixels). However, since the MDI response becomes non-linear in such a strong, and therefore dark, umbra, the core field strength there was probably higher ($\geq$ 2000 G) (see, *e.g.*, Green *et al.*, 2003). The positive dispersed plage had a much lower mean magnetic-field strength of about 50 ± 10 G, depending on the extent of dispersed positive field measured (magnetic-flux density over 13 060 – 24 600 pixels). Positive flux concentrations (measured over 600 pixels) within the plage had a characteristic field strength of 220 ± 20 G. In summary, magnetic-flux measurements indicate a mere 5 % negative surplus flux in this major bipolar active region of 2.1×10^{22} Mx total flux and maximum-field strengths (negative : positive) in a roughly 10 : 1 ratio.

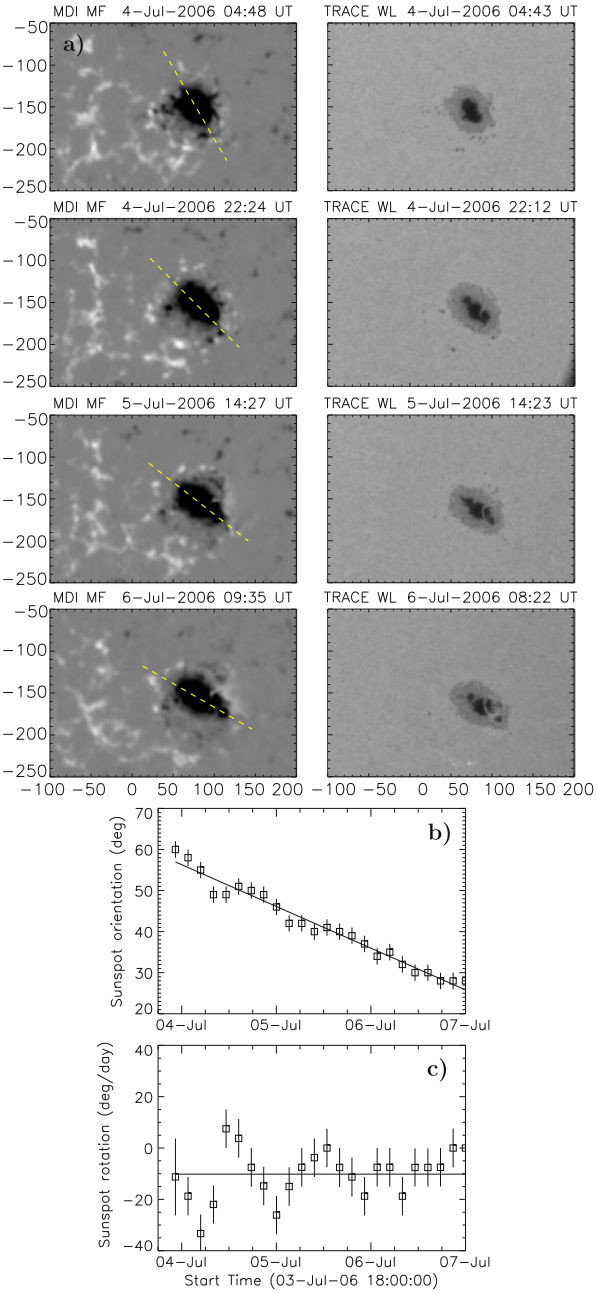

Figure 2 (a) Representative images of the sunspot evolution during 4 – 6 July 2006: MDI longitudinal magnetic-field maps (left column); TRACE white-light images (right column). The TRACE image in the bottom panels corresponds to the time of the M2 flare (starting in soft X-rays at 8:20 UT). The dashed yellow line outlines the major axis of the sunspot that was used to measure the sunspot rotation. The corresponding SOHO/MDI movie is available in the electronic version of the article. (b) Sunspot rotation determined from the MDI magnetic-field maps over the period 3 July 2006, 22:00 UT, to 7 July 2006, 8:00 UT, showing the orientation of the sunspot's major axis, measured clockwise from solar East. (c) Sunspot rotation rate in degrees per day.

In Figure 2(a) we show snapshots of the sunspot evolution as observed by MDI and the *Transition Region and Coronal Explorer* (TRACE: Handy *et al.*, 1999), ranging from two days before the eruption to one day after it. The images are all differentially rotated to the first image of the series, when the sunspot was closer to disk centre. The sequence shows that the sunspot is rotating counter-clockwise during the considered period (see the

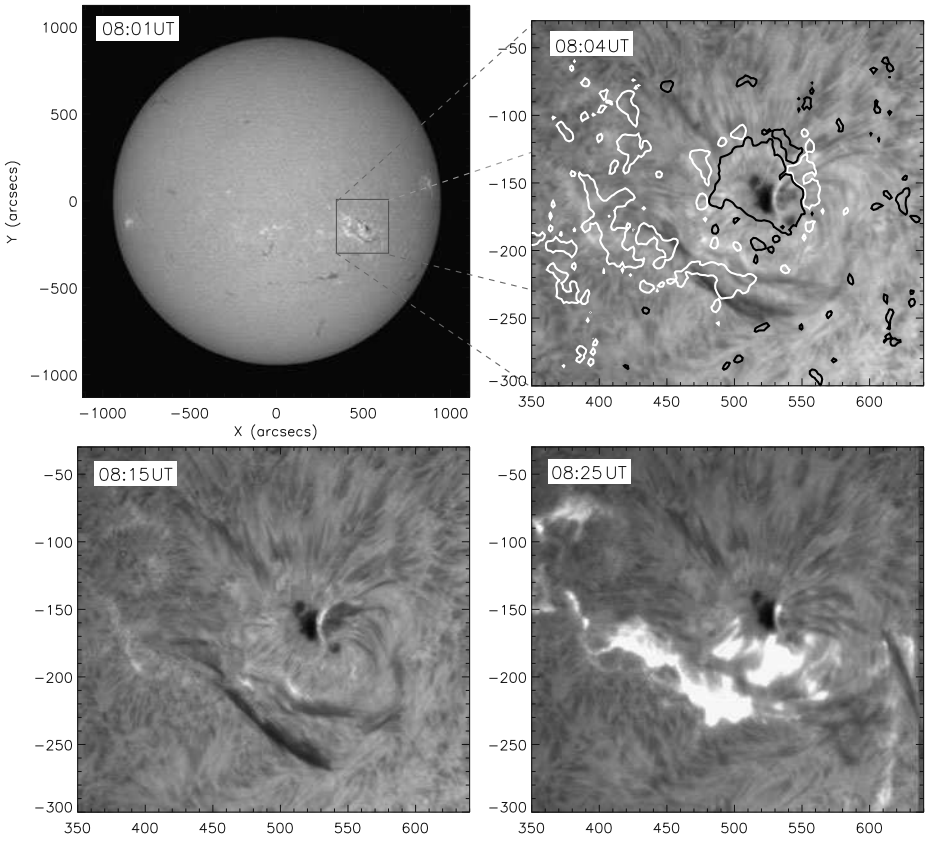

Figure 3 Hα filtergram sequence observed before and during the flare on 6 July 2006 by the Kanzelhöhe (full disk) and Hvar (active region area) Observatories. An apparent double structure of the filament is visible South of the sunspot. Contour levels of 100 G from an MDI magnetogram taken at 07:59 UT are added in the top right panel, with white (black) lines corresponding to positive (negative) values.

Electronic Supplementary Material). From the evolution of the MDI magnetic-field maps, we geometrically determined the major axis of the sunspot and followed its evolution in time. In Figure 2(b) we plot the sunspot's rotation angle over the period 3 July 2006, 22:00 UT, to 7 July 2006, 8:00 UT. The total rotation observed over these three days is about 30°. The sunspot's rotation rate, determined as the temporal derivative of the rotation measurements, yields a mean value of about 10° day^{-1} during the considered time span (Figure 2(c)). For comparison, we determined the rotation also from the TRACE white-light images and found no significant differences.

The flare and the filament eruption were observed in full-disk Hα filtergrams by the Kanzelhöhe Observatory and, over a smaller field-of-view around the active region, by the Hvar Observatory (Figure 3). These observations reveal that the filament consisted of a double structure before and during the eruption (for a similar case of such a double-structured filament, see Liu *et al.*, 2012). Significant rising motions of the filament could be seen from about 08:23 UT on. The Hα flare started by the appearance of very weak double-footpoint brightening at 08:15 UT.

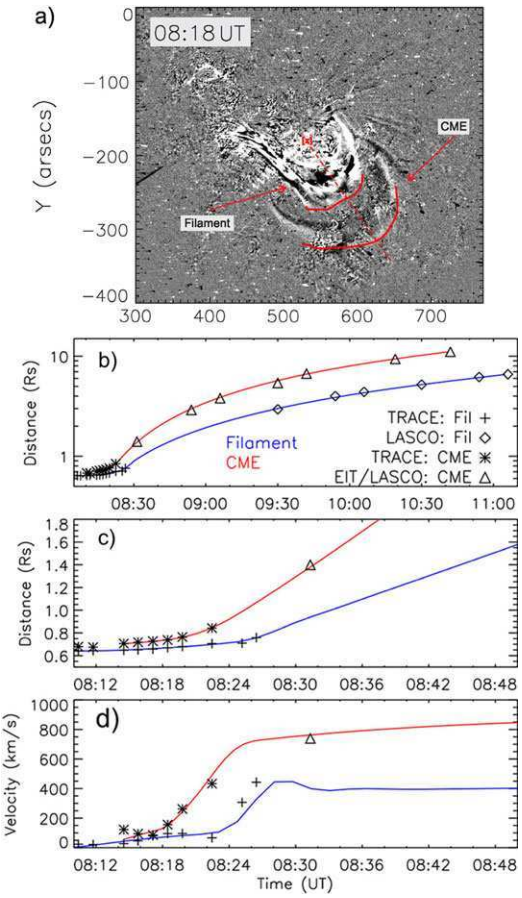

Figure 4 (a) TRACE 171 Å running-difference image showing the erupting filament and the overlying CME front. Distances are measured at crossings of the respective leading edges (red solid lines) with the dashed line, starting from the point marked by [x]. (b) Distance–time plot showing the kinematics of the filament and the CME front for the entire distance range. (c) Distance–time plot for the distance range up to 1.8 $R_{\odot}$. The distance between [x] and the disk centre is added to all TRACE and EIT data points. (d) Velocity–time plot over the distance range up to 1.8 $R_{\odot}$. See text for further details.

Figure 4(a) shows a running-difference image from TRACE 171 Å in which the erupting filament (the CME core) and the preceding CME front can be identified. From a time sequence of similar images by TRACE, EIT, and LASCO C2/C3 we estimated the kinematics of the filament and the CME front, which are shown in Figure 4(b), (c). The distances were measured in the plane of the sky, from disk centre in the LASCO images and from the midpoint of the line connecting the pre-eruption filament footpoints in the TRACE and EIT images. In order to approximately compensate for this discrepancy, we added to the TRACE and EIT measurements the distance between this point and the disk centre, which corresponds to ≈ 400 Mm. The resulting distances are plotted in Figure 4(b), (c), together with spline-smoothed curves. We did not correct for foreshortening effects, as projection effects only result in a multiplication factor and do not alter the profile of the derived kinematical curves (see, *e.g.*, Vršnak *et al.*, 2007). Additionally, Figure 4(d) gives the velocity profiles for the filament and the CME front, as derived from the first derivative of the distance–time measurements and spline-smoothed curves. From these plots we obtain the result that the coronal loops overlying the filament started their slow rising phase at 08:15 UT, *i.e.* about five – ten minutes before the filament. Similarly, the CME front reached its final, almost constant, velocity a few minutes before the filament.

Various other aspects of the event (flare, CME, EIT wave, dimming) were studied by Jiang *et al.* (2007), McIntosh *et al.* (2007), Attrill *et al.* (2008), Temmer *et al.* (2008), Miklenic, Veronig, and Vršnak (2009), Veronig *et al.* (2010), and Guo *et al.* (2010a). We refer to this work for further details as regards the eruption. Guo *et al.* (2010a) suggested that the eruption was triggered by recurrent chromospheric mass injection in the form of surges or jets into the filament channel. Here we propose a different mechanism, assuming that the filament was suspended in the corona by a magnetic flux-rope, a picture that is supported by various magnetic-field models of active regions containing filaments (*e.g.* Lionello *et al.*, 2002; van Ballegooijen, 2004; Guo *et al.*, 2010b; Canou and Amari, 2010). We suggest that the continuous rotation of the sunspot led to a slow expansion of the arcade-like magnetic field overlying the filament (*i.e.* to a continuous weakening of its stabilizing tension), until a critical point was reached at which equilibrium could not be maintained and the flux-rope erupted. We note that we do not claim that the eruption was triggered *exclusively* by this mechanism. Filaments are often observed to spiral into the periphery of sunspots (*e.g.* Green *et al.*, 2007), and also in our case an inspection of the TRACE and Hα images during the early phase of the eruption suggests a possible magnetic connection between the western extension of the filament-carrying core field and the sunspot area. Thus, the sunspot rotation may have added stress to this field, thereby possibly contributing to drive it towards eruption. On the other hand, for an injection of twist as suggested by the simulations mentioned above to occur, the core field must be rooted in the centre of the sunspot, not just in its periphery, which is difficult to establish from observations. It appears reasonable to assume that a clear connection between core field and sunspot centre is not always present, and that the stressing of the overlying ambient field by sunspot rotation may be more relevant for the destabilisation of the system in such cases. In order to test this scenario, we perform a series of three-dimensional (3D) MHD simulations, which are described in the following sections.

3. Numerical Simulations

The purpose of the numerical simulations presented in this article is to show that the rotation of photospheric-flux concentrations can trigger the eruption of an initially stable flux-rope that is embedded in their fields. Differently from previous work (*e.g.* Amari *et al.*, 1996; Török and Kliem, 2003; Aulanier, Démoulin, and Grappin, 2005), the photospheric vortex motions do not directly affect the flux-rope in our simulations, but solely the field surrounding it.

The first simulation (hereafter run 1) involves a relatively simple magnetic configuration, consisting of a flux-rope embedded in a bipolar potential field (see Figure 5(c)). The initially potential field gets twisted at its photospheric-flux concentrations on both sides of the flux-rope in the same manner. This simulation is very idealised with respect to the observations presented in Section 2, in particular because both the initial magnetic configuration and the imposed driving possess a high degree of symmetry.

We then consider a more complex initial magnetic field (hereafter run 2), which is chosen such that it resembles the magnetic-field structure prior to the eruption described in Section 2 (see Figure 5(d)). As in run 1, this configuration contains a flux-rope embedded in a potential field, but the latter is now constructed by a significantly larger number of sub-photospheric sources, in order to mimic the main features of the observed photospheric flux distribution and the extrapolated coronal magnetic field (see Figure 5(c)). Differently from run 1, only one flux concentration is twisted in this case, as suggested by the observations. The purpose of run 2 is to verify that the mechanism studied in run 1 also works in a highly asymmetric

configuration. We do not attempt here to model the full eruption and evolution of the CME, for reasons that are specified below.

To construct our magnetic configurations, we employ the coronal flux-rope model of Titov and Démoulin (1999, hereafter TD). Its main ingredient is a current ring of major radius $[R]$ and minor radius $[a]$ that is placed such that its symmetry axis is located at a depth $[d]$ below a photospheric plane. The outward-directed Lorentz self-force (or "hoop force") of the ring is balanced by a potential field created by a pair of sub-photospheric point sources $[\pm q]$ that are placed at the symmetry axis, at distances $\pm L$ from the ring centre. The resulting coronal field consists of an arched and line-tied flux-rope embedded in an arcade-like potential field. In order to create a shear component of the ambient field, TD added a sub-photospheric line current to the system. Since the latter is not required for equilibrium, we do not use it for our configurations (see also Roussev *et al.*, 2003; Török and Kliem, 2007).

Previous simulations (*e.g.* Török and Kliem, 2005; Schrijver *et al.*, 2008) and analytical calculations (Isenberg and Forbes, 2007) have shown that the TD flux-rope can be subject to the ideal-MHD helical kink and torus instabilities. Therefore, we adjust the model parameters such that the flux-rope twist stays below the typical threshold of the kink instability for the TD flux-rope (see Török, Kliem, and Titov, 2004). To inhibit the occurrence of the torus instability in the initial configurations, we further adjust the locations and magnitude of the potential field sources such that the field drops sufficiently slowly with height above the flux-rope (see Kliem and Török, 2006; Török and Kliem, 2007; Fan and Gibson, 2007; Aulanier *et al.*, 2010). While this is a relatively easy task for the standard TD configuration used in run 1, an extended parameter search was required for the complex configuration used in run 2, until an appropriate numerical equilibrium to start with could be found.

3.1. Numerical Setup

As in our previous simulations of the TD model (*e.g.* Török, Kliem, and Titov, 2004; Kliem, Titov, and Török, 2004), we integrate the $\beta = 0$ compressible ideal-MHD equations:

$$\partial_t \rho = -\nabla \cdot (\rho \mathbf{u}), \tag{1}$$

$$\rho \partial_t \mathbf{u} = -\rho (\mathbf{u} \cdot \nabla)\mathbf{u} + \mathbf{j} \times \mathbf{B} + \nabla \cdot \mathcal{T}, \tag{2}$$

$$\partial_t \mathbf{B} = \nabla \times (\mathbf{u} \times \mathbf{B}), \tag{3}$$

where $\mathbf{B}$, $\mathbf{u}$, and ρ are the magnetic field, velocity, and mass density, respectively. The current density is given by $\mathbf{j} = \mu_0^{-1} \nabla \times \mathbf{B}$. $\mathcal{T}$ denotes the viscous stress tensor, included to improve numerical stability (Török and Kliem, 2003). We neglect thermal pressure and gravity, which is justified for the low corona where the Lorentz force dominates.

The MHD equations are normalised by quantities derived from a characteristic length $[l]$ taken here to be the initial apex height of the axis of the TD current ring above the photospheric plane $[l = R - d]$, the maximum magnetic-field strength in the domain $[B_{0\max}]$, and the Alfvén velocity $[v_{a0}]$. The Alfvén time is given by $[\tau_a = l/v_{a0}]$. We use a Cartesian grid of size $[-40, 40] \times [-40, 40] \times [0, 80]$ for run 1 and $[-40, 40] \times [-30, 30] \times [0, 60]$ for run 2, resolved by $247 \times 247 \times 146$ and $307 \times 257 \times 156$ grid points, respectively. The grids are non-uniform in all directions, with an almost uniform resolution $\Delta = 0.04$ (run 1) and $\Delta = 0.05$ (run 2) in the box centre, where the TD flux-rope and the main polarities are located. The plane $z = 0$ corresponds to the photosphere. The TD flux-rope is oriented along the y-direction in all runs, with its positive-polarity footpoint rooted in the half-plane $y < 0$. We employ a modified two-step Lax–Wendroff method for the integration, and we

additionally stabilise the calculation by artificial smoothing of all integration variables (Sato and Hayashi, 1979; Török and Kliem, 2003).

The boundary conditions are implemented in the ghost layers. The top and lateral boundaries are closed, which is justified given the large size of the simulation box. Below the photospheric plane, the tangential velocities are imposed as described in Section 3.3. The vertical velocities are zero there at all times, and the mass density is fixed at its initial values. The latter condition is not consistent with the imposed vortex flows, but is chosen to ensure numerical stability (see Török and Kliem, 2003). Since we use the $\beta = 0$ approximation, and since the evolution is driven quasi-statically at the bottom plane, fixing the density in $z = -\Delta z$ is tolerable. The tangential components of the magnetic field $[B_{x,y}]$ are extrapolated from the integration domain, and the normal component $[B_z]$ is set such that $\nabla \cdot \mathbf{B} = \mathbf{0}$ in $z = 0$ at all times (see Török and Kliem, 2003). Since our code does not ensure $\nabla \cdot \mathbf{B} = \mathbf{0}$ to rounding error in the rest of the domain, we use a diffusive $\nabla \cdot \mathbf{B}$ cleaner (Keppens *et al.*, 2003), as well as Powell's source-term method (Gombosi, Powell, and de Zeeuw, 1994), to minimise unphysical effects resulting from $\nabla \cdot \mathbf{B}$ errors.

3.2. Initial Conditions

The parameters of the TD equilibrium employed in run 1 are (in normalised units): $R = 2.2$, $a = 0.7$, $d = 1.2$, $L = 1.2$, and $q = 1.27$. The magnetic axis of the TD flux-rope (which is located above the geometrical axis of the current ring, see Valori *et al.*, 2010) has an apex height $z = 1.09$. The potential field connects two fully symmetric flux concentrations and runs essentially perpendicular above the TD flux-rope. The apex of the central field line, *i.e.* the field line connecting the centres of the potential-field polarities, is located at $z = 3.40$. After the initial relaxation of the system (see below), these heights become $z = 1.22$ and $z = 3.62$, respectively. Figures 5(c) and 6(a) show the configuration after the relaxation.

The magnetic configuration used in run 2 is a step towards a more realistic modelling of the coronal field during the 6 July 2006 eruption. Figure 5(b) shows a coronal potential-field source-surface (PFSS) model (Schatten, Wilcox, and Ness, 1969), obtained from a synoptic MDI magnetogram for Carrington Rotation 2045, using the SolarSoft package pfss provided by LMSAL (http://www.lmsal.com/~derosa/pfsspack/). It can be seen that the field lines rooted in the main polarity (the sunspot) form a fan-like structure, which partly overlies the filament. We again consider a standard TD flux-rope, with $R = 2.75$, $a = 0.8$, and $d = 1.75$, but now we use an ensemble of ten sub-photospheric sources (five point sources, and five vertically oriented dipoles like the ones used by Török and Kliem, 2003) for the construction of the ambient field, in order to resemble the main properties of the observed photospheric flux distribution and the corresponding PFSS field. By adjusting the positions and strengths of the sources, we tried to mimic the approximate flux balance between the concentrated leading negative polarity and the dispersed following positive polarity, the ratio of approximately 10:1 between the peak field strengths in the leading polarity and the following polarity, the size ratio between these polarities, the presence of an "inverse C-shaped" area of dispersed negative flux to the West of the leading polarity (see Section 2), as well as the fan-like shape of the coronal field rooted in the leading polarity. The position of the flux-rope within the ambient field is guided by the observed location of the filament (Figure 5(b)). Since the model is still relatively idealised, all of these features can be matched only approximately. The resulting configuration (after initial relaxation) is shown in Figure 5(d) and in Figure 8(a) below. It can be seen that the TD flux-rope is stabilised by flux rooted towards the southern edge of the main polarity. The rope is inclined with respect to the vertical, which is due to the asymmetry of the potential field surrounding it.

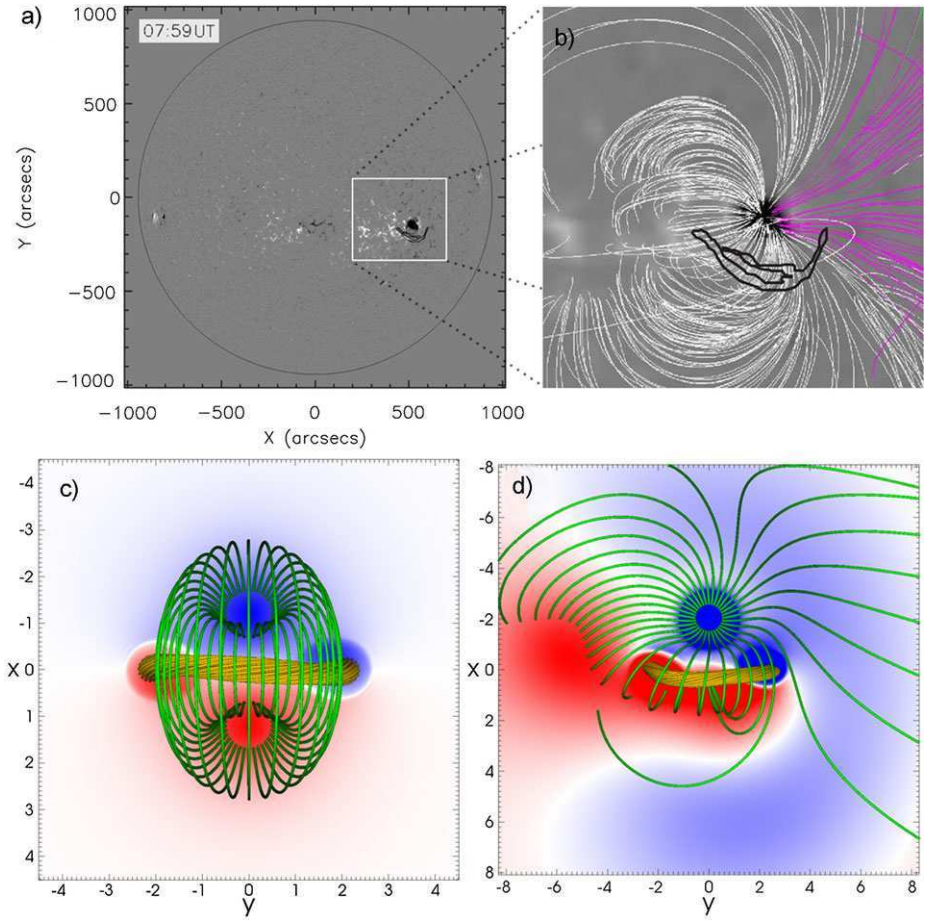

Figure 5 (a) Same as Figure 1. (b) Magnetic-field lines in the active-region area (marked by the white square in panel a) from a potential field source surface (PFSS) model that was calculated for 6 July 2006, 06:04 UT, overlaid on a synoptic MDI magnetogram for the corresponding Carrington Rotation 2045. The model corona is a spherical shell extending from 1.0 to 2.5 $R_\odot$. Pink (white) field lines depict open (closed) fields. The outer contours of the filament, based on Hα data taken at 07:59 UT on 6 July 2006, are outlined with black lines. For better illustration, the area is rotated to disk centre. (c), (d): Top view on the magnetic configurations used in runs 1 and 2, respectively, after the initial relaxation of the system (see Section 3 for details). The core of the TD flux-rope is shown by orange field lines, green field lines depict the ambient potential field. B_z is shown in the bottom plane, where red (blue) colours corresponds to positive (negative) values. The colour scale in panel d) is saturated at about 4 % of the maximum B_z, in order to depict also weaker flux distributions.

In contrast to the configuration used in run 1, the magnetic field in run 2 is dominated by one main polarity. Rather than closing down to an equally strong polarity of opposite sign, the flux emanating from the main polarity now spreads out in all directions, resembling a so-called fan–spine configuration (*e.g.* Pariat, Antiochos, and DeVore, 2009; Masson *et al.*, 2009; Török *et al.*, 2009). Note that this flux does not contain fully open field lines, as was presumably the case during the 6 July 2006 eruption (see Figure 5(b)). This is due to the fact that the flux distribution shown in Figure 5(d) is fully surrounded by weak positive flux in the model (imposed to mimic the isolated "inverse C-shaped" weak negative polarity to the

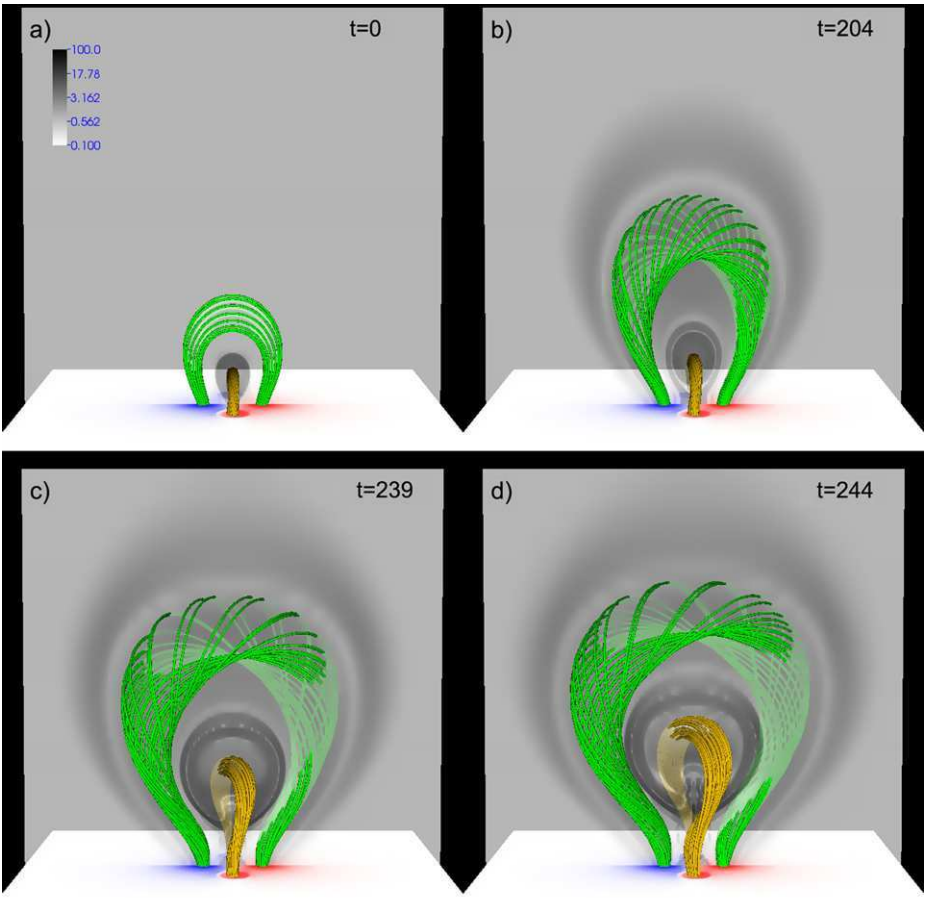

Figure 6 Magnetic-field lines outlining the evolution of the TD flux-rope (orange) and the twisted overlying field (green) for run 1, at $t = 0, 204, 239, 244\tau_A$, respectively; panel (a) shows the system after the initial numerical relaxation. The normal component of the magnetic field $[B_z]$ is shown at the bottom plane $z = 0$, with red (blue) corresponding to positive (negative) values. The transparent grey-scale shows the logarithmic distribution of the current densities divided by the magnetic field strength $[|\mathbf{J}|/|\mathbf{B}|]$ in the plane $x = 0$. The sub-volume $[-8.5, 8.5] \times [-8, 8] \times [0, 16]$ is shown in all panels. An animation of this figure is available in the electronic version of this article.

West of the main polarity), so that the positive flux in the total simulation domain exceeds the negative flux shown in Figure 5(b). Note that this "total" flux ratio shall not be confused with the flux ratio between the main polarity and the dispersed positive polarity to its East, which is approximately balanced in the model, in line with the observations.

As in Amari *et al.* (1996), Török and Kliem (2003) and Aulanier, Démoulin, and Grappin (2005), we use an initial density distribution $\rho_0(\mathbf{x}) = |\mathbf{B}_0(\mathbf{x})|^2$ corresponding to a uniform initial Alfvén velocity. For the configuration used in run 2 we also ran a calculation with $\rho_0(\mathbf{x}) = |\mathbf{B}_0(\mathbf{x})|^{3/2}$, *i.e.* with a more realistic Alfvén velocity that decreases with distance from the flux concentrations. We found that the evolution was qualitatively equivalent, but somewhat less dynamic.

In order to obtain a numerical equilibrium as a starting point of the twisting phase, we first performed a numerical relaxation of the two configurations used. This is done for $54\tau_a$ for the system used in run 1, and for $75\tau_a$ for the system used in run 2, after which the time is reset to zero in both cases.

3.3. Photospheric Driving

The velocity field used to twist the potential fields is prescribed in the plane $z = -\Delta z$ and located at their main flux concentrations. It produces a horizontal counter-clockwise rotation, chosen such that the velocity vectors always point along the contours of $B_z(x, y, 0, t = 0)$, which ensures that the distribution of $B_z(x, y, 0, t)$ is conserved to a very good approximation. The flows are given by

$$u_{x,y}(x, y, -\Delta z, t) = v_0 f(t) \nabla^{\perp} \{ \zeta [B_{0z}(x, y, 0, 0)] \}, \tag{4}$$

$$u_z(x, y, -\Delta z, t) = 0, \tag{5}$$

with $\nabla^{\perp} := (\partial_y, -\partial_x)$. A smooth function

$$\zeta = B_z^2 \exp\left(\left(B_z^2 - B_{z\max}^2 \right) / \delta B^2 \right), \tag{6}$$

chosen as by Amari *et al.* (1996), defines the vortex profile. The parameter δB determines the vortex width (see Figure 3 in Aulanier, Démoulin, and Grappin, 2005). We use $\delta B = 0.7$ for run 1 and $\delta B = 2$ for run 2. The parameter v_0 determines the maximum driving velocity. We choose $v_0 = 0.005 v_{\mathrm{A}}$ for both runs to ensure that the driving is slow compared to the Alfvén velocity. The velocities are zero at the polarity centre and decrease towards its edge from their maximum value to zero (see Figure 2 in Török and Kliem, 2003). The twist injected by such motions is nearly uniform close to the polarity centre and decreases monotonically towards its edge (see Figure 10 below and Figure 9 in Török and Kliem, 2003). The polarity centres are located at $(\pm 1.2, 0, 0)$ for the configuration used in run 1 and the vortex flows are applied at both flux concentrations. In run 2, we twist the potential field only in the main negative polarity, the centre of which is located at $(-2, 0, 0)$. The function $f(t)$ describes the temporal profile of the imposed twisting. The twisting phase starts with a linear ramp $(0 \le t \le t_r)$ from $f(0) = 0$ to $f(t_r) = 1$, which is then held fixed. If a final relaxation phase is added, $f(t)$ is analogously linearly reduced to zero and held fixed. In all simulations in this article $t_r = 10\tau_a$.

In contrast to the symmetric configuration used in run 1, where most of the flux emanating from the main polarities arches over the flux-rope, the flux that initially stabilises the rope in run 2 is concentrated towards the southern edge of the polarity, where the imposed vortex velocities are relatively small. In order to obtain the eruption of the TD rope within a reasonable computational time in run 2, we therefore use a δB that is larger than in run 1.

4. Simulation Results

4.1. Run 1

We first consider the more idealised and symmetric case, in which the vortices are applied at both photospheric polarities of the potential field. As a result of the imposed motions, the field lines rooted in the polarities become increasingly twisted and a relatively wide twisted flux-tube is formed, which expands and rises with increasing velocity (Figure 6).

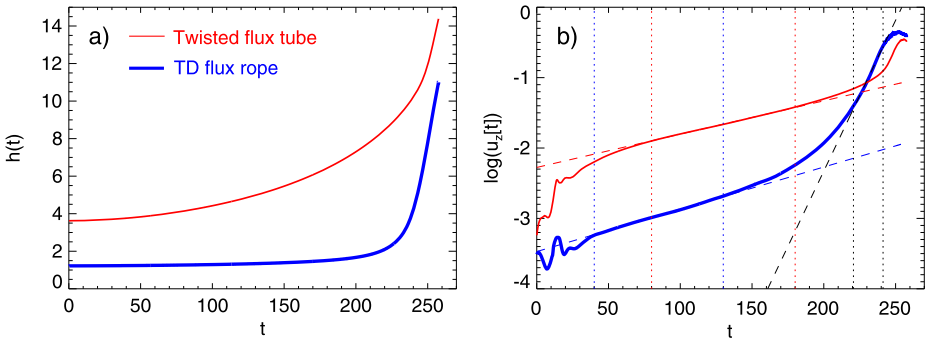

Figure 7 Kinematics of the TD flux-rope (thick blue lines) and of the overlying twisted flux-tube (solid red lines) during the twisting phase in run 1. (a) Height of the axis apex as a function of time. The initial heights are 1.22 for the TD rope and 3.62 for the twisted flux-tube. (b) Logarithmic presentation of the corresponding vertical velocities. The dashed lines show linear fits, obtained within the time periods marked by the vertical dotted lines of the same colour.

Detailed descriptions on the evolution of such twisted fields have been given by Amari *et al.* (1996), Török and Kliem (2003), and Aulanier, Démoulin, and Grappin (2005). Since here we are merely interested in how the rising flux affects the stability of the TD flux-rope, we only note that the rise follows the exponential behaviour found in this earlier work. This is shown in Figure 7, where the kinematics of the two flux systems (the twisted flux-tube and the TD flux-rope) are followed in time by tracking the position of the respective central field-line apex. The exponential rise phase of the twisted flux-tube, preceded by a slower transition, can be clearly seen between $t \approx 80\tau_a$ and $t \approx 180\tau_a$.

The slow rise of the flux-tube successively weakens the stabilizing magnetic tension on the TD rope, so that the latter starts to ascend as well. As can be seen in Figure 7(b), the rise of the TD rope also follows an exponential behaviour up to $t \approx 130\tau_a$. While its growth rate is slightly larger than for the twisted flux-tube, its velocity remains about one order of magnitude smaller. In order to check that this slow exponential rise of the TD rope is indeed an adaptation to the changing ambient field, rather than a slowly growing instability, we performed a relaxation run by ramping down the photospheric driving velocities to zero between $t = 100\tau_a$ and $t = 110\tau_a$ and following the evolution of the system until $t = 181\tau_a$. Both the twisted flux-tube and the TD rope relax towards a numerical equilibrium in this run, without any indication of instability or eruption. Hence, during its slow rise phase until $t \approx 130\tau_a$, the TD rope experiences a quasi-static evolution along a sequence of approximately force-free equilibria, generated by the slowly changing boundary conditions (in particular, the changing tangential components of the magnetic field at the bottom plane).

Starting at $t \approx 130\tau_a$, the TD rope undergoes a successively growing acceleration which ends in a rapid exponential acceleration phase between $t \approx 220\tau_a$ and $t \approx 250\tau_a$ that is characterised by a growth rate significantly larger than during the quasi-static phase (see also the bottom panels of Figure 6). The rope finally reaches a maximum velocity of $0.45v_{a0}$ at $t = 252\tau_a$, after which it starts to decelerate. Such a slow rise phase, followed by a rapid acceleration, is a well-observed property of many filament eruptions in the early evolution of CMEs (see, *e.g.*, Schrijver *et al.*, 2008, and references therein), and is also seen for the event studied in this article (see Figure 4(d)). The evolution of the TD rope after $t \approx 130\tau_a$ can be associated with the development of the torus instability (Bateman, 1978; Kliem and Török, 2006; Démoulin and Aulanier, 2010), as has been shown under similar conditions in

various simulations of erupting flux-ropes (Török and Kliem, 2007; Fan and Gibson, 2007; Schrijver *et al.*, 2008; Aulanier *et al.*, 2010; Török *et al.*, 2011).

During the transition of the TD rope to the torus-unstable regime, the overlying twisted flux-tube continues its slow exponential rise at almost the same growth rate for about 100 Alfvén times, which excludes the possibility that the additional acceleration of the TD rope after $t \approx 130\tau_a$ is due to an adaptation to the evolving environment field. At $t \approx 230\tau_a$, however, the rise speed of the TD rope begins to exceed the rise speed of the flux-tube, and the latter gets significantly accelerated from below by the strongly expanding rope. The overtaking of the twisted flux-tube by the faster TD rope, and the resulting interaction between the two, is reminiscent of the so-called CME cannibalism phenomenon (*e.g.* Gopalswamy *et al.*, 2001; Lugaz, Manchester, and Gombosi, 2005). The investigation of this interaction is, however, beyond the scope of the present article, so that we stopped the simulation at this point.

Run 1 shows that the rotation of the footpoints of a flux system overlying a stable flux-rope can lead to the eruption of the rope, by progressively lowering the threshold for the torus instability. We suggest that this mechanism may have been at the origin of the CME event described in Section 2.

The numerical experiment presented here has a high degree of symmetry, with respect to both the initial magnetic-field configuration and the driving photospheric motions. A practically identical result is obtained if only one of the polarities of the overlying field is twisted, as long as the driving velocity is clearly sub-Alfvénic. In particular, we found that twisting only one flux concentration does not significantly affect the rise direction of the TD rope, indicating that slow asymmetric twisting does not necessarily lead to a non-radial rise of the erupting flux-rope if the overlying field is symmetric. A more general case, which exhibits a strongly non-radial rise, is presented in the following section.

4.2. Run 2

We now consider a much less symmetric initial condition for the magnetic field, together with a driving that is applied to one polarity only. The configuration is still idealised, but closer to the observations (see Sections 2 and 3.2). The purpose of run 2 is to verify that the CME initiation mechanism suggested in Section 4.1 can work also in a more realistic and general setting.

The fan-like structure of the ambient field makes it difficult to follow its evolution during the twisting phase using a single point as a tracer of the whole three-dimensional structure, as was done for run 1. We therefore follow here only the apex of the TD rope axis in time. The inclination of the rope makes it complicated to find the exact position of the axis apex, so we determined it only approximately. Consequently, the trajectories presented in Figure 9 below are somewhat less precise than for run 1.

Figure 8(a) shows that electric currents are formed in the ambient field volume during the initial relaxation of the system. The strongest current concentrations are located in the front of the flux-rope and exhibit an X-shaped pattern in the vertical cut shown. This pattern outlines the locations of quasi-separatrix layers (QSLs: *e.g.* Priest and Forbes, 1992; Démoulin *et al.*, 1996) that separate different flux systems. The QSLs are present in the configuration from the very beginning and arise from the complexity of the potential field (see Section 3.2). Their presence is evident also in the left panel of Figure 8(a): the green field lines show strong connectivity gradients in the northern part of the main polarity and in the vicinity of the western flux-rope footpoint. It has been demonstrated that current concentrations form preferably at the locations of QSLs and other structural

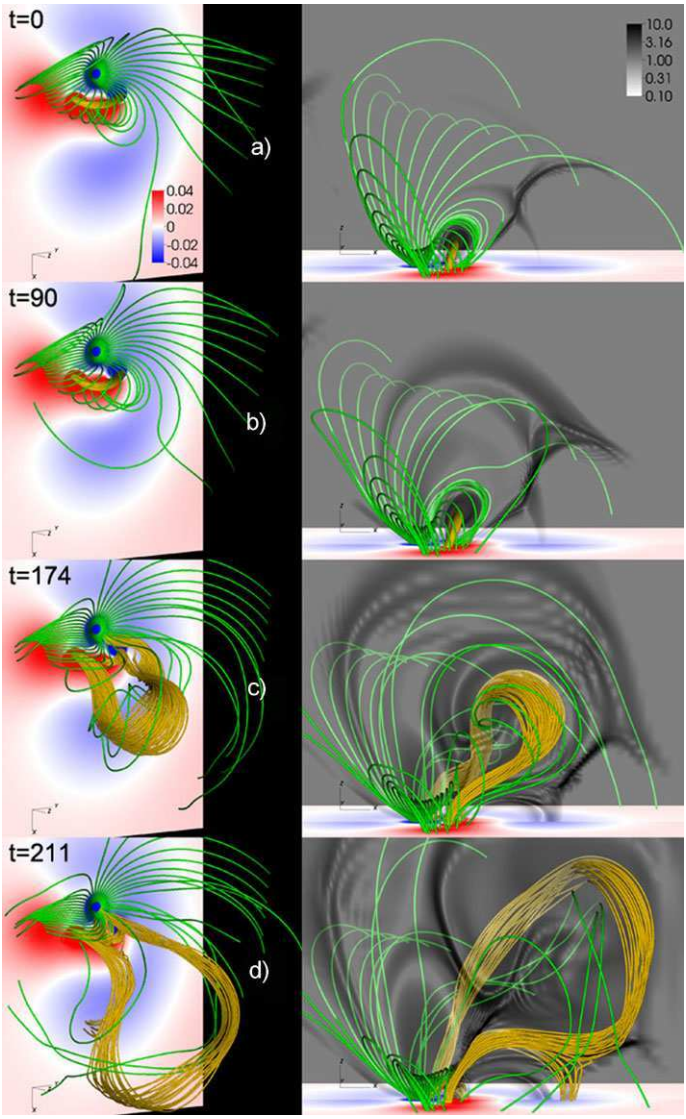

Figure 8 Snapshots of run 2 at times $t = 0$, 90, 174, $211\tau_a$, respectively, showing the same features as in Figure 5(d). The system is shown after the initial relaxation (a), during the slow rise phase (b), at the time of the peak flux-rope velocity (c), and during the deceleration of the flux-rope (d). The left panels use a view similar to the observations presented in Section 2, the right panels show a side view. The transparent grey-scale in the right panels depicts the logarithmic distribution of $|\mathbf{j}|/|\mathbf{B}|$ in the plane $x = 0$, outlining the locations of strong current concentrations. The sub-volume $[-10, 16] \times [-11, 11] \times [0, 18]$ is used for all panels. An animation of this figure is available in the electronic version of this article.

features like null points, separatrix surfaces, and separators, if a system containing such structures is dynamically perturbed (*e.g.* Baum and Bratenahl, 1980; Lau and Finn, 1990; Aulanier, Pariat, and Démoulin, 2005). In our case the perturbation results from the – relatively modest – dynamics during the initial relaxation of the system.

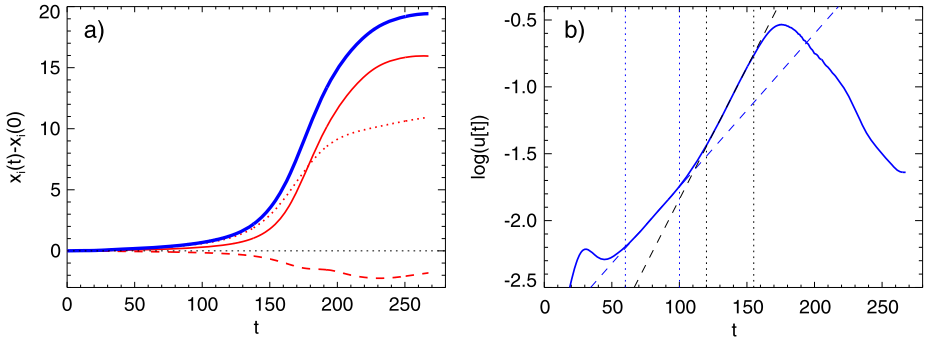

Figure 9 Kinematics of the TD flux-rope in run 2. (a) Red lines show the distances of the axis apex from its initial position, $(x_0, y_0, z_0) = (0.075, 0, 1.076)$, for all three spatial dimensions as a function of time. The solid line shows $x - x_0$, the dashed one $y - y_0$, and the dotted one $z - z_0$. The thick blue line shows the total deviation from the initial position. (b) Logarithmic presentation of the total velocity of the axis apex as a function of time (solid blue line). As in Figure 7, the dashed lines show linear fits obtained for the time periods marked by dotted lines of the same colour.

After the relaxation, at $t = 0$, we start twisting the main negative polarity. Due to the pronounced fan-structure of the field rooted in the main polarity, the photospheric twisting does not lead to the formation of a single twisted flux tube that rises exactly in vertical direction above the TD rope, as was the case in run 1. Rather, the twisting leads to a slow, global expansion of the fan-shaped field lines (see Figure 8 and the corresponding online animations). Since we are mainly interested in the destabilisation of the flux-rope, we did not study the detailed evolution of the large-scale field. We expect it to be very similar to the one described by Santos, Büchner, and Otto (2011), since the active region those authors simulated was also dominated by one main polarity (sunspot), and the field rooted therein had a very similar fan-shaped structure (compare, for example, our Figure 8 with their Figure 1).

Important for our purpose is the evolution of the arcade-like part of the initial potential field that directly overlies the TD flux-rope. Those field lines are directly affected only by a fraction of the boundary flows and therefore get merely sheared (rather than twisted), which still leads to their slow expansion. As was the case for run 1, the TD rope starts to expand as well, adapting to the successively decreasing magnetic tension of the overlying field. This initial phase of the evolution is depicted in Figure 8b. Note that some of the flux at the front of the expanding arcade reconnects at the QSL current layer (see the online animation), which can be expected to aid the arcade expansion to some degree. As in run 1, the TD rope rises, after some initial adjustment, exponentially during this slow initial phase (Figure 9).

As the twisting continues, a transition to a rapid acceleration takes place, which can be seen in Figure 9b after $t \approx 100\tau_a$, when the rise curve leaves the quasi-static regime. After the transition phase, the TD rope again rises exponentially, but now with a significantly larger growth rate than during the slow rise phase. As for run 1, we attribute this transition and rapid acceleration to the occurrence of the torus instability.

The right panels in Figure 8 show that the trajectory of the flux-rope is far from being vertical. As can be seen in Figure 9, the rope axis has reached an inclination of about 45 degrees at the time of its peak rise velocity. Such lateral eruptions have been reported frequently in both observations and simulations (Williams *et al.*, 2005; Aulanier *et al.*, 2010; Bi *et al.*, 2011; Panasenco *et al.*, 2011; Zuccarello *et al.*, 2012; Yang *et al.*, 2012, and references therein), and are usually attributed to an asymmetric

structure of the field overlying the erupting core flux. We believe that this causes the lateral rise also in our case, in particular since we found that asymmetric twisting of a symmetric configuration does not lead to a non-vertical trajectory of the flux-rope (see Section 4.1). We note that such a lateral rise during the very early phase of a CME is different from the often observed deflection of CMEs at coronal holes, where the ejecta is channelled by the structure of the coronal field at larger heights (Kahler, Akiyama, and Gopalswamy, 2012, and references therein). As the eruption continues, the trajectory of the flux-rope becomes increasingly horizontal, resembling the so-called "roll effect" (*e.g.* Panasenco *et al.*, 2011) and indicating that the rope cannot overcome the tension of the large-scale overlying field. Moreover, as a consequence of its increasing expansion, the flux-rope strongly pushes against the QSL current layer, which results in reconnection between the front of the rope and the ambient field. Eventually, the rope splits into two parts, similar to what has been found in simulations of confined eruptions (Amari and Luciani, 1999; Török and Kliem, 2005). These two effects – which both are not present in run 1 – slow down the rise of the rope after $t \approx 175\tau_a$ and inhibit its full eruption (*i.e.* the development of a CME) in our simulation.

Since QSLs can affect the evolution of an eruption, but are not expected to play a significant role for its initiation, we did not investigate in detail whether or not QSLs were present in the pre-eruption configuration of the 6 July 2006 event. The PFSS extrapolation indicates their presence to the North and the West of the main polarity (see the field-line connectivities in Figure 5(b), but less clearly so to its South. The possible absence of a QSL in front of the erupting core field in the real event is in line with the "smooth" evolution of the observed CME, while in our simulation the coherence of the flux-rope is destroyed before it can evolve into a full eruption. Also, the real large-scale field was probably less confining than our model field: the PFSS extrapolation indicates the presence of open field lines, which are fully absent in our simulation. Since, as stated earlier, we merely aim to model the initiation of the eruption rather than its full evolution into a CME, we refrained from further improving our model to obtain a configuration without a strong QSL in front of the flux-rope and with more open flux.

As for run 1, we check how the system evolves when the twisting is stopped before the flux-rope erupts. When the vortex flows are ramped down to zero during $t = (35-45)\tau_a$ – corresponding to an effective twisting time of $35\tau_a$ – no eruptive behaviour is seen in the subsequent evolution for almost $300\tau_a$, after which we stopped the calculation. However, the system does not fully relax to a numerical equilibrium as it was the case for the simpler configuration (see Section 4.1). Rather, the flux-rope continues to rise very slowly, with velocities smaller than $10^{-3}v_{a0}$. This indicates that the system has entered a meta-stable state, which is possibly supported by continuous slow reconnection at the QSL current layer due to numerical diffusion, so that it can be expected that the rope would finally erupt if the integration were continued sufficiently long. When somewhat more twisting is applied, the system behaves as in the continuously driven configuration, *i.e.* a phase of slow rise is followed by a transition to rapid acceleration and the final eruption of the flux-rope, except that the evolution leading up to the eruption takes the longer the less twist is imposed. For example, for an effective twisting period of $45\tau_a$, the rapid acceleration of the rope sets in at $\approx 265\tau_a$, significantly later than in the continuously driven system.

While it is tempting to quantitatively compare the amount of rotation in the simulation with the observed sunspot rotation, we think that such a comparison can be misleading, since the amount of rotation required for eruption will depend on parameters that have not been studied here and are not available from the observations (see Section 5: Summary and Discussion). Moreover, a quantitative comparison is not straightforward, since the model

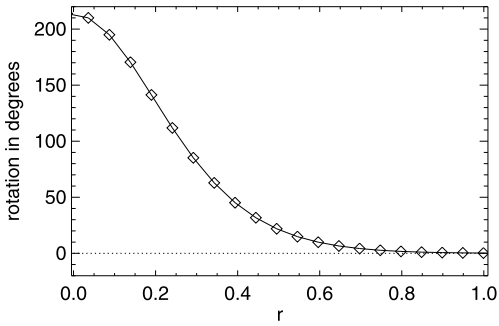

Figure 10 Rotation profile for run 2 as a function of distance from the vortex centre; shown at $t = 100\tau_a$, approximately when the transition from slow to fast rise sets in (see Figure 9(b)).

rotation is highly non-uniform (Figure 10), while in the observed case a rigid rotation of the spot was measured (Figure 2). For example, at $t \approx 100\tau_a$, when the transition from slow to fast rise starts in the continuously driven simulation, the field lines rooted very close to the main polarity centre have rotated by about 200°. However, those field lines do not overlie the TD flux-rope directly, rather they connect to the positive polarity region located to the East of the rope (see Figures 5d and 8) and should therefore not significantly influence the rope's stability. On the other hand, the arcade-like field lines that are located directly above the rope are rooted at a distance of $r \approx 0.4$ from the polarity centre, towards its southern edge. As can be seen in Figure 10, the flux surface containing these field lines is rotated by a much smaller amount, about 40° at $t = 100\tau_a$. For the run with an effective twisting time of $t = 45\tau_a$ mentioned above, the imposed total rotation at this flux surface is even smaller, slightly below 20°. These values are similar to the observed sunspot rotation, but, in addition to the reasons given above, such a comparison should be taken with care. While the expansion of the field lines located directly above the TD flux-rope presumably depends mainly on the driving imposed at their footpoints, it is also influenced to some degree by the expansion of higher-lying fields which, in turn, depends on the (significantly larger) amount of rotation closer to the polarity centre. Moreover, the values obtained from the model refer to an overlying field that is initially potential (except for the QSL-related current layers), while the real overlying field may have already contained some stress at the onset of detectable rotational motions. Finally, as discussed at the end of the Introduction, the sunspot rotation may have injected stress also directly into the filament. In both cases, presumably less rotation as suggested by the model would have been required to trigger the eruption.

In summary, the simulation successfully models the early phases of the eruption (the slow rise and the initial rapid acceleration of the flux-rope) in a setting that is qualitatively similar to the observed configuration of the active region around the time of the CME described in Section 2. Hence, the CME-initiation mechanism described in run 1 can work also in more complex and less symmetric configurations.

5. Summary and Discussion

We analyse a filament eruption, two-ribbon flare, and CME that occurred in NOAA Active Region 10898 on 6 July 2006. The filament was located South of a strong sunspot that dominated the region. In the evolution leading up to the eruption, and for some time after it, a counter-clockwise rotation of the sunspot of about 30° was observed. Similar events, which occurred close to a dominant rotating sunspot, were presented by, *e.g.*, Tian and Alexander (2006) and Régnier and Canfield (2006). The triggering of such eruptions is commonly

attributed to the injection of twist (or helicity) beyond a certain threshold by the sunspot rotation (*e.g.* Török and Kliem, 2003). However, while filaments are frequently observed to spiral into the periphery of main sunspots, the erupting core flux may not always be rooted in the spot itself. Here we suggest that the continuous expansion due to sunspot rotation of the magnetic field that stabilises the current-carrying core flux, *i.e.* the successive decrease of magnetic tension, can also lead to filament eruptions and CMEs in such configurations.

We support this scenario by MHD simulations, in which a potential field overlying and stabilizing a pre-existing flux-rope is slowly twisted at its photospheric-flux concentration(s). The flux-rope is not anchored in these concentrations and is therefore not twisted. In a first configuration, the rope is initially kept in equilibrium by a field rooted in two "sunspots" of opposite polarity that are located at opposite sides of the rope. The twisting of the flux concentrations reproduces the known behaviour of twisted bipolar fields (see, *e.g.*, Amari *et al.*, 1996): a twisted flux tube is generated that expands and rises at an exponentially increasing rate. As a consequence, the magnetic tension of the field above the pre-existing flux-rope is successively weakened. The rope undergoes a quasi-static adaptation to the changing surrounding field, which is manifested in a slow rise phase. As the weakening of the overlying field reaches an appropriate level, the torus instability sets in and rapidly accelerates the rope upwards, leading to a second, fast rise phase and eruption. This evolution in two phases resembles the often-observed slow rise phase and subsequent strong acceleration of filaments in the course of their eruption (see Figure 4, as well as Schrijver *et al.*, 2008, and references therein). Eventually, since the flux-rope erupts faster than the twisted flux-tube rises, the rope catches up and starts to interact with the flux-tube, at which point we stop the simulation.

As a step towards more realistic configurations, we consider a second setup in which the initial ambient field surrounding the flux-rope is created by an ensemble of sub-photospheric sources that qualitatively reproduce the photospheric flux distribution and magnetic-field structure of the active region around the time of the 6 July 2006 event. In particular, the highly asymmetric flux density and the resulting overall fan shape of the active-region field are recovered, while the approximative flux balance of the region is kept. The rotation of the dominant negative polarity (mimicking the observed sunspot rotation) leads to the same qualitative behaviour as in the much more symmetric configuration: after a slow rise phase resembling the quasi-static adaptation of the flux-rope to the expanding ambient field, the rope undergoes a second, strong acceleration phase. In this case, the asymmetry of the ambient field leads to a markedly lateral eruption. However, in contrast to the first configuration, the presence of a QSL-related current layer in the front of the erupting flux-rope leads to reconnection which eventually splits the rope before it can evolve into a CME. Although we are not able to follow the expansion of the flux-rope beyond this phase, we can assert the effectiveness of the proposed mechanism in triggering an eruption also in this more realistic case.

The proposed mechanism requires the presence of a flux-rope in the corona prior to the onset of the twisting motions, which is in line with the relatively small observed rotation of about 30° in our event. Far larger rotations appear to be required to produce a flux-rope that can be driven beyond the threshold of instability by such small additional rotation (*e.g.* Török and Kliem, 2003; Aulanier, Démoulin, and Grappin, 2005; Yan *et al.*, 2012). It can be expected that the amount of rotation required to initiate the eruption of a pre-existing flux-rope by rotating its overlying field depends on two main parameters: i) the "distance" of the flux-rope from an unstable state and ii) the "effectiveness" of the rotation in reducing the stabilisation by the overlying field. For example, it will take a longer time for a low-lying flux-rope to slowly rise to the critical height required for the onset of the torus instability

than it does for a rope that is already close to this height. Also, the required rotation will be larger if mostly high-arching field lines, rather than field lines located directly above the rope, are twisted. Thus, the amount of rotation required for eruption appears to depend strongly on the details of the configuration. A proper assessment of this question demands an extensive parametric study that is beyond the scope of this article. Here we merely aim to provide proof-of-concept simulations that illustrate the physical mechanism.

In summary, the main result of our study is that the rotation of sunspots can substantially weaken the magnetic tension of the field in active regions, in particular in cases where the sunspot dominates the region. This can lead to the triggering of eruptions in the vicinity of the spot, even if the erupting core flux (the filament) is not anchored in it. The mechanism that we suggest provides an alternative to the common scenario in which eruptions in the vicinity of rotating sunspots are triggered by the direct injection of twist into the erupting core flux.

Acknowledgements We thank the anonymous referee for constructive comments that helped to improve the content of the article. We acknowledge the use of data provided by the SOHO/MDI consortium. SOHO/EIT was funded by CNES, NASA, and the Belgian SPPS. The SOHO/LASCO data used here are produced by a consortium of the Naval Research Laboratory(USA), Max–Planck–Institut für Aeronomie (Germany), Laboratoire d'Astrophysique de Marseille (France), and the University of Birmingham (UK). SOHO is a mission of international cooperation between ESA and NASA. The *Transition Region and Coronal Explorer* (TRACE) is a mission of the Stanford–Lockheed Institute for Space Research, and part of the NASA Small Explorer program. Hα data were provided by the Kanzelhöhe Observatory, University of Graz, Austria, and by the Hvar Observatory, University of Zagreb, Croatia. The research leading to these results has received funding from the European Commission's Seventh Framework Programme (FP7/2007 – 2013) under the grant agreements No. 218816 (SOTERIA project, www.soteria-space.eu) and No. 284461 (eHEROES, http://soteria-space.eu/eheroes/html). TT was partially supported by NASA's HTP, LWS, and SR&T programs. LvDG acknowledges funding through the Hungarian Science Foundation grant OTKA K81421.

References

Amari, T., Luciani, J.F.: 1999, *Astrophys. J. Lett.* **515**, L81. doi:10.1086/311971.
Amari, T., Luciani, J.F., Aly, J.J., Tagger, M.: 1996, *Astrophys. J. Lett.* **466**, L39. doi:10.1086/310158.
Attrill, G.D.R., van Driel-Gesztelyi, L., Démoulin, P., Zhukov, A.N., Steed, K., Harra, L.K., Mandrini, C.H., Linker, J.: 2008, *Solar Phys.* **252**, 349. doi:10.1007/s11207-008-9255-z.
Aulanier, G., Démoulin, P., Grappin, R.: 2005, *Astron. Astrophys.* **430**, 1067. doi:10.1051/0004-6361:20041519.
Aulanier, G., Pariat, E., Démoulin, P.: 2005, *Astron. Astrophys.* **444**, 961. doi:10.1051/0004-6361:20053600.
Aulanier, G., Török, T., Démoulin, P., DeLuca, E.E.: 2010, *Astrophys. J.* **708**, 314. doi:10.1088/0004-637X/708/1/314.
Barnes, C.W., Sturrock, P.A.: 1972, *Astrophys. J.* **174**, 659. doi:10.1086/151527.
Bateman, G.: 1978, *MHD Instabilities*, MIT Press, Cambridge.
Baum, P.J., Bratenahl, A.: 1980, *Solar Phys.* **67**, 245. doi:10.1007/BF00149805.
Bi, Y., Jiang, Y.C., Yang, L.H., Zheng, R.S.: 2011, *New Astron.* **16**, 276. doi:10.1016/j.newast.2010.11.009.
Brown, D.S., Nightingale, R.W., Alexander, D., Schrijver, C.J., Metcalf, T.R., Shine, R.A., Title, A.M., Wolfson, C.J.: 2003, *Solar Phys.* **216**, 79. doi:10.1023/A:1026138413791.
Canou, A., Amari, T.: 2010, *Astrophys. J.* **715**, 1566. doi:10.1088/0004-637X/715/2/1566.
Chen, J.: 1989, *Astrophys. J.* **338**, 453. doi:10.1086/167211.
Chifor, C., Tripathi, D., Mason, H.E., Dennis, B.R.: 2007, *Astron. Astrophys.* **472**, 967. doi:10.1051/0004-6361:20077771.
Démoulin, P., Aulanier, G.: 2010, *Astrophys. J.* **718**, 1388. doi:10.1088/0004-637X/718/2/1388.
Démoulin, P., Henoux, J.C., Priest, E.R., Mandrini, C.H.: 1996, *Astron. Astrophys.* **308**, 643.
Evershed, J.: 1910, *Mon. Not. Roy. Astron. Soc.* **70**, 217.
Fan, Y.: 2009, *Astrophys. J.* **697**, 1529. doi:10.1088/0004-637X/697/2/1529.
Fan, Y., Gibson, S.E.: 2003, *Astrophys. J. Lett.* **589**, L105. doi:10.1086/375834.
Fan, Y., Gibson, S.E.: 2007, *Astrophys. J.* **668**, 1232. doi:10.1086/521335.

Forbes, T.: 2010, In: Schrijver, C.J., Siscoe, G.L. (eds.) *Heliophysics: Space Storms and Radiation: Causes and Effects*, Cambridge University Press, Cambridge, 159.
Forbes, T.G.: 2000, *J. Geophys. Res.* **105**, 23153. doi:10.1029/2000JA000005.
Galsgaard, K., Nordlund, Å.: 1997, *J. Geophys. Res.* **102**, 219. doi:10.1029/96JA01462.
Gerrard, C.L., Arber, T.D., Hood, A.W.: 2002, *Astron. Astrophys.* **387**, 687. doi:10.1051/0004-6361:20020491.
Gerrard, C.L., Hood, A.W., Brown, D.S.: 2004, *Solar Phys.* **222**, 79. doi:10.1023/B:SOLA.0000036877.20077.42.
Gerrard, C.L., Brown, D.S., Mellor, C., Arber, T.D., Hood, A.W.: 2003, *Solar Phys.* **213**, 39. doi:10.1023/A:1023281624037.
Gibson, S.E., Fan, Y., Mandrini, C., Fisher, G., Demoulin, P.: 2004, *Astrophys. J.* **617**, 600. doi:10.1086/425294.
Gombosi, T.I., Powell, K.G., de Zeeuw, D.L.: 1994, *J. Geophys. Res.* **99**, 21525.
Gopalswamy, N., Yashiro, S., Kaiser, M.L., Howard, R.A., Bougeret, J.-L.: 2001, *Astrophys. J. Lett.* **548**, L91. doi:10.1086/318939.
Green, L.M., Démoulin, P., Mandrini, C.H., Van Driel-Gesztelyi, L.: 2003, *Solar Phys.* **215**, 307. doi:10.1023/A:1025678917086.
Green, L.M., Kliem, B., Török, T., van Driel-Gesztelyi, L., Attrill, G.D.R.: 2007, *Solar Phys.* **246**, 365. doi:10.1007/s11207-007-9061-z.
Guo, J., Liu, Y., Zhang, H., Deng, Y., Lin, J., Su, J.: 2010a, *Astrophys. J.* **711**, 1057. doi:10.1088/0004-637X/711/2/1057.
Guo, Y., Schmieder, B., Démoulin, P., Wiegelmann, T., Aulanier, G., Török, T., Bommier, V.: 2010b, *Astrophys. J.* **714**, 343. doi:10.1088/0004-637X/714/1/343.
Handy, B.N., Acton, L.W., Kankelborg, C.C., Wolfson, C.J., Akin, D.J., Bruner, M.E., Caravalho, R., Catura, R.C., Chevalier, R., Duncan, D.W., Edwards, C.G., Feinstein, C.N., Freeland, S.L., Friedlaender, F.M., Hoffmann, C.H., Hurlburt, N.E., Jurcevich, B.K., Katz, N.L., Kelly, G.A., Lemen, J.R., Levay, M., Lindgren, R.W., Mathur, D.P., Meyer, S.B., Morrison, S.J., Morrison, M.D., Nightingale, R.W., Pope, T.P., Rehse, R.A., Schrijver, C.J., Shine, R.A., Shing, L., Strong, K.T., Tarbell, T.D., Title, A.M., Torgerson, D.D., Golub, L., Bookbinder, J.A., Caldwell, D., Cheimets, P.N., Davis, W.N., Deluca, E.E., McMullen, R.A., Warren, H.P., Amato, D., Fisher, R., Maldonado, H., Parkinson, C.: 1999, *Solar Phys.* **187**, 229. doi:10.1023/A:1005166902804.
Hiremath, K.M., Suryanarayana, G.S.: 2003, *Astron. Astrophys.* **411**, L497. doi:10.1051/0004-6361:20031618.
Hiremath, K.M., Lovely, M.R., Kariyappa, R.: 2006, *J. Astrophys. Astron.* **27**, 333. doi:10.1007/BF02702538.
Isenberg, P.A., Forbes, T.G.: 2007, *Astrophys. J.* **670**, 1453. doi:10.1086/522025.
Jiang, Y., Yang, L., Li, K., Ren, D.: 2007, *Astrophys. J. Lett.* **662**, L131. doi:10.1086/519490.
Kahler, S.W., Akiyama, S., Gopalswamy, N.: 2012, *Astrophys. J.* **754**, 100. doi:10.1088/0004-637X/754/2/100.
Kahler, S.W., Moore, R.L., Kane, S.R., Zirin, H.: 1988, *Astrophys. J.* **328**, 824. doi:10.1086/166340.
Kazachenko, M.D., Canfield, R.C., Longcope, D.W., Qiu, J., Des Jardins, A., Nightingale, R.W.: 2009, *Astrophys. J.* **704**, 1146. doi:10.1088/0004-637X/704/2/1146.
Keppens, R., Nool, M., Tóth, G., Goedbloed, J.P.: 2003, *Comput. Phys. Commun.* **153**, 317. doi:10.1016/S0010-4655(03)00139-5.
Kliem, B., Török, T.: 2006, *Phys. Rev. Lett.* **96**(25), 255002. doi:10.1103/PhysRevLett.96.255002.
Kliem, B., Titov, V.S., Török, T.: 2004, *Astron. Astrophys.* **413**, L23. doi:10.1051/0004-6361:20031690.
Klimchuk, J.A., Antiochos, S.K., Norton, D.: 2000, *Astrophys. J.* **542**, 504. doi:10.1086/309527.
Lau, Y.-T., Finn, J.M.: 1990, *Astrophys. J.* **350**, 672. doi:10.1086/168419.
Li, L., Zhang, J.: 2009, *Astrophys. J. Lett.* **706**, L17. doi:10.1088/0004-637X/706/1/L17.
Lionello, R., Mikić, Z., Linker, J.A., Amari, T.: 2002, *Astrophys. J.* **581**, 718. doi:10.1086/344222.
Liu, R., Kliem, B., Török, T., Liu, C., Titov, V.S., Lionello, R., Linker, J.A., Wang, H.: 2012, *Astrophys. J.* **756**, 59. doi:10.1088/0004-637X/756/1/59.
Longcope, D.W., Welsch, B.T.: 2000, *Astrophys. J.* **545**, 1089. doi:10.1086/317846.
Lugaz, N., Manchester, W.B. IV, Gombosi, T.I.: 2005, *Astrophys. J.* **634**, 651. doi:10.1086/491782.
Maričić, D., Vršnak, B., Roša, D.: 2009, *Solar Phys.* **260**, 177. doi:10.1007/s11207-009-9421-y.
Maričić, D., Vršnak, B., Stanger, A.L., Veronig, A.: 2004, *Solar Phys.* **225**, 337. doi:10.1007/s11207-004-3748-1.
Maričić, D., Vršnak, B., Stanger, A.L., Veronig, A.M., Temmer, M., Roša, D.: 2007, *Solar Phys.* **241**, 99. doi:10.1007/s11207-007-0291-x.
Masson, S., Pariat, E., Aulanier, G., Schrijver, C.J.: 2009, *Astrophys. J.* **700**, 559. doi:10.1088/0004-637X/700/1/559.

McIntosh, S.W., Leamon, R.J., Davey, A.R., Wills-Davey, M.J.: 2007, *Astrophys. J.* **660**, 1653. doi:10.1086/512665.
Mikic, Z., Schnack, D.D., van Hoven, G.: 1990, *Astrophys. J.* **361**, 690. doi:10.1086/169232.
Miklenic, C.H., Veronig, A.M., Vršnak, B.: 2009, *Astron. Astrophys.* **499**, 893. doi:10.1051/0004-6361/200810947.
Min, S., Chae, J.: 2009, *Solar Phys.* **258**, 203. doi:10.1007/s11207-009-9425-7.
Moore, R.L., Sterling, A.C., Hudson, H.S., Lemen, J.R.: 2001, *Astrophys. J.* **552**, 833. doi:10.1086/320559.
Nindos, A., Andrews, M.D.: 2004, *Astrophys. J. Lett.* **616**, L175. doi:10.1086/426861.
Panasenco, O., Martin, S., Joshi, A.D., Srivastava, N.: 2011, *J. Atmos. Solar-Terr. Phys.* **73**, 1129. doi:10.1016/j.jastp.2010.09.010.
Pariat, E., Antiochos, S.K., DeVore, C.R.: 2009, *Astrophys. J.* **691**, 61. doi:10.1088/0004-637X/691/1/61.
Priest, E.R., Forbes, T.G.: 1992, *J. Geophys. Res.* **97**, 1521. doi:10.1029/91JA02435.
Régnier, S., Canfield, R.C.: 2006, *Astron. Astrophys.* **451**, 319. doi:10.1051/0004-6361:20054171.
Robbrecht, E., Patsourakos, S., Vourlidas, A.: 2009, *Astrophys. J.* **701**, 283. doi:10.1088/0004-637X/701/1/283.
Romano, P., Contarino, L., Zuccarello, F.: 2005, *Astron. Astrophys.* **433**, 683. doi:10.1051/0004-6361:20041807.
Roussev, I.I., Forbes, T.G., Gombosi, T.I., Sokolov, I.V., DeZeeuw, D.L., Birn, J.: 2003, *Astrophys. J. Lett.* **588**, L45. doi:10.1086/375442.
Santos, J.C., Büchner, J., Otto, A.: 2011, *Astron. Astrophys.* **535**, A111. doi:10.1051/0004-6361/201116792.
Sato, T., Hayashi, T.: 1979, *Phys. Fluids* **22**, 1189. doi:10.1063/1.862721.
Schatten, K.H., Wilcox, J.M., Ness, N.F.: 1969, *Solar Phys.* **6**, 442. doi:10.1007/BF00146478.
Scherrer, P.H., Bogart, R.S., Bush, R.I., Hoeksema, J.T., Kosovichev, A.G., Schou, J., Rosenberg, W., Springer, L., Tarbell, T.D., Title, A., Wolfson, C.J., Zayer, I., MDI Engineering Team: 1995, *Solar Phys.* **162**, 129. doi:10.1007/BF00733429.
Schrijver, C.J., Elmore, C., Kliem, B., Török, T., Title, A.M.: 2008, *Astrophys. J.* **674**, 586. doi:10.1086/524294.
Stenflo, J.O.: 1969, *Solar Phys.* **8**, 115. doi:10.1007/BF00150662.
Suryanarayana, G.S.: 2010, *New Astron.* **15**, 313. doi:10.1016/j.newast.2009.09.004.
Temmer, M., Veronig, A.M., Vršnak, B., Rybák, J., Gömöry, P., Stoiser, S., Maričić, D.: 2008, *Astrophys. J. Lett.* **673**, L95. doi:10.1086/527414.
Tian, L., Alexander, D.: 2006, *Solar Phys.* **233**, 29. doi:10.1007/s11207-006-2505-z.
Tian, L., Alexander, D., Nightingale, R.: 2008, *Astrophys. J.* **684**, 747. doi:10.1086/589492.
Titov, V.S., Démoulin, P.: 1999, *Astron. Astrophys.* **351**, 707.
Török, T., Kliem, B.: 2003, *Astron. Astrophys.* **406**, 1043. doi:10.1051/0004-6361:20030692.
Török, T., Kliem, B.: 2005, *Astrophys. J. Lett.* **630**, L97. doi:10.1086/462412.
Török, T., Kliem, B.: 2007, *Astron. Nachr.* **328**, 743. doi:10.1002/asna.200710795.
Török, T., Kliem, B., Titov, V.S.: 2004, *Astron. Astrophys.* **413**, L27. doi:10.1051/0004-6361:20031691.
Török, T., Aulanier, G., Schmieder, B., Reeves, K.K., Golub, L.: 2009, *Astrophys. J.* **704**, 485. doi:10.1088/0004-637X/704/1/485.
Török, T., Panasenco, O., Titov, V.S., Mikić, Z., Reeves, K.K., Velli, M., Linker, J.A., De Toma, G.: 2011, *Astrophys. J. Lett.* **739**, L63. doi:10.1088/2041-8205/739/2/L63.
Valori, G., Kliem, B., Török, T., Titov, V.S.: 2010, *Astron. Astrophys.* **519**, A44. doi:10.1051/0004-6361/201014416.
van Ballegooijen, A.A.: 2004, *Astrophys. J.* **612**, 519. doi:10.1086/422512.
Veronig, A.M., Rybak, J., Gömöry, P., Berkebile-Stoiser, S., Temmer, M., Otruba, W., Vrsnak, B., Pötzi, W., Baumgartner, D.: 2010, *Astrophys. J.* **719**, 655. doi:10.1088/0004-637X/719/1/655.
Vršnak, B.: 1990, *Solar Phys.* **129**, 295. doi:10.1007/BF00159042.
Vršnak, B., Sudar, D., Ruždjak, D., Žic, T.: 2007, *Astron. Astrophys.* **469**, 339. doi:10.1051/0004-6361:20077175.
Williams, D.R., Török, T., Démoulin, P., van Driel-Gesztelyi, L., Kliem, B.: 2005, *Astrophys. J. Lett.* **628**, L163. doi:10.1086/432910.
Yan, X.L., Qu, Z.Q.: 2007, *Astron. Astrophys.* **468**, 1083. doi:10.1051/0004-6361:20077064.
Yan, X.L., Qu, Z.Q., Kong, D.F.: 2008, *Mon. Not. Roy. Astron. Soc.* **391**, 1887. doi:10.1111/j.1365-2966.2008.14002.x.
Yan, X.L., Qu, Z.Q., Xu, C.L., Xue, Z.K., Kong, D.F.: 2009, *Res. Astron. Astrophys.* **9**, 596. doi:10.1088/1674-4527/9/5/010.
Yan, X.L., Qu, Z.Q., Kong, D.-F., Xu, C.L.: 2012, *Astrophys. J.* **754**, 16. doi:10.1088/0004-637X/754/1/16.
Yang, J., Jiang, Y., Yang, B., Zheng, R., Yang, D., Hong, J., Li, H., Bi, Y.: 2012, *Solar Phys.* **279**, 115. doi:10.1007/s11207-012-0002-0.
Zhang, J., Li, L., Song, Q.: 2007, *Astrophys. J. Lett.* **662**, L35. doi:10.1086/519280.

Zhang, J., Dere, K.P., Howard, R.A., Kundu, M.R., White, S.M.: 2001, *Astrophys. J.* **559**, 452. doi:10.1086/322405.
Zhang, Y., Liu, J., Zhang, H.: 2008, *Solar Phys.* **247**, 39. doi:10.1007/s11207-007-9089-0.
Zhu, C., Alexander, D., Tian, L.: 2012, *Solar Phys.* **278**, 121. doi:10.1007/s11207-011-9923-2.
Zirin, H.: 1998, *The Astrophysics of the Sun*, Cambridge University Press, Cambridge.
Zuccarello, F.P., Bemporad, A., Jacobs, C., Mierla, M., Poedts, S., Zuccarello, F.: 2012, *Astrophys. J.* **744**, 66. doi:10.1088/0004-637X/744/1/66.

Solar Phys (2013) 284:275–291
DOI 10.1007/s11207-013-0259-y

Effect of Electron Pressure on the Grad–Shafranov Reconstruction of Interplanetary Coronal Mass Ejections

Qiang Hu · C.J. Farrugia · V.A. Osherovich · C. Möstl · A. Szabo · K.W. Ogilvie · R.P. Lepping

Received: 16 November 2012 / Accepted: 21 February 2013 / Published online: 8 March 2013

Abstract We investigate the effect of electron pressure on the Grad–Shafranov (GS) reconstruction of Interplanetary Coronal Mass Ejection (ICME) structures. The GS method uses *in situ* magnetic field and plasma measurements to solve for a magnetohydrostatic quasi-equilibrium state of space plasmas. For some events, a magnetic flux-rope structure embedded within the ICME can be reconstructed. The electron temperature contributes directly to the calculation of the total plasma pressure, and in ICMEs its contribution often substantially exceeds that of proton temperature. We selected ICME events observed with the *Wind* spacecraft at 1 AU and applied the GS reconstruction method to each event for cases with and without electron temperature measurements. We sorted them according to the proton plasma β (the ratio of proton plasma pressure to magnetic pressure) and the electron-to-proton temperature ratio. We present case studies of three representative events, show the cross sections of GS reconstructed flux-rope structure, and discuss the electron pressure contribution to key quantities in the numerical reconstruction procedure. We summarize and compare the geometrical and physical parameters derived from the GS reconstruction results for cases with and without electron temperature contribution. We conclude that overall the

Flux-Rope Structure of Coronal Mass Ejections
Guest Editors: N. Gopalswamy, T. Nieves-Chinchilla, M. Hidalgo, J. Zhang, and P. Riley

Q. Hu (✉)
Department of Physics/CSPAR, University of Alabama in Huntsville, Huntsville, AL, USA
e-mail: qh0001@uah.edu

C.J. Farrugia
Space Science Center, University of New Hampshire, Durham, NH, USA
e-mail: charlie.farrugia@unh.edu

V.A. Osherovich · A. Szabo · K.W. Ogilvie · R.P. Lepping
NASA Goddard Space Flight Center, Greenbelt, MD, USA

C. Möstl
Space Science Laboratory, University of California, Berkeley, CA, USA

C. Möstl
Kanzelhöhe Observatory-IGAM, Institute of Physics, University of Graz, Graz, Austria

electron pressure effect on the GS reconstruction results contributes to a 10 – 20 % discrepancy in some key physical quantities, such as the magnetic flux content of the ICME flux rope observed at 1 AU.

Keywords ICMEs · Magnetic clouds · Flux rope · Electron temperature · Grad–Shafranov reconstruction

1. Introduction

The Grad–Shafranov (GS) reconstruction technique, based on the so-called Grad–Shafranov equation, was first developed by Sonnerup and Guo (1996) and Hau and Sonnerup (1999). The GS method is capable of deriving a two-and-a-half dimensional (2.5D with a non-vanishing magnetic field component along the invariant/axial direction) cross section of the plasma structure from the single spacecraft measurements along its path across the structure. The GS method was first applied to small-scale interplanetary magnetic flux-rope structures by Hu and Sonnerup (2001) and was subsequently developed and applied to large-scale magnetic cloud (MC) structures in the solar wind (Hu and Sonnerup, 2002). The method uses both *in situ* magnetic field and plasma measurements, including proton density, temperature, and velocity, that characterize a single-fluid magnetohydrostatic equilibrium with a finite plasma pressure gradient.

The plasma pressure, ignoring the alpha-particle contribution, is generated by protons and electrons. Whenever electron temperature measurements were available, they were included for calculating the total plasma pressure, as was done in many previous works that applied the GS reconstruction method to magnetic clouds (*e.g.*, Hu *et al.*, 2003, 2004). Since in general the electron moment data are less readily available than those for protons, especially for *Advanced Composition Explorer* (ACE) spacecraft data and for previous investigations, it is usual to include only the proton plasma pressure. The electron contribution is often not included, which may render the results less reliable when the investigated structure is a magnetic cloud. It has been shown observationally that, while the proton temperature T_p decreases as a consequence of radial expansion – indeed, this is one of the basic properties that characterize magnetic clouds and ICMEs (Richardson and Cane, 2010 and references therein) – the electron temperature T_e, while variable, stays high, with $T_\mathrm{e}/T_\mathrm{p}$ ranging from 2 – 20, as illustrated in the examples below and shown in previous studies (Osherovich *et al.*, 1993; Farrugia *et al.*, 1994; Fainberg *et al.*, 1996; Richardson, Farrugia, and Cane, 1997; Sittler and Burlaga, 1998; Skoug *et al.*, 2000a, 2000b; Nieves-Chinchilla and Viñas, 2008). For example, Sittler and Burlaga (1998) analyzed three magnetic clouds with data from *Voyager* 2 between 2 and 4 AU and obtained average values of $T_\mathrm{e}/T_\mathrm{p} \sim 7.0$. It follows that the dynamics of magnetic clouds are determined mainly by electrons and not by protons. The question is, therefore, if we can trust the results on MC quantities obtained by GS reconstruction if we only take into account the proton contribution to the pressure. We aim here to address this important question, which is particularly relevant in view of the wide use of GS reconstruction in studies of MC *in situ* data. Because the GS method is used for plasmas with a finite pressure gradient, we do not limit our applications to MCs only (*i.e.*, configurations characterized by low proton β values, which represent the ratios between proton plasma pressure and the corresponding magnetic pressure), and we use the terms MC and ICME interchangeably throughout this paper.

Previous studies have revealed and confirmed the flux-rope structure of MCs. Various geometrical and physical properties of ICME flux ropes can be derived. They include the axis

orientation, the approximate transverse size, the closest distance from the flux-rope center to the spacecraft path, the maximum axial magnetic field, the electric current density, the axial and poloidal magnetic flux, the relative magnetic helicity content, *etc*. The validity of the GS reconstruction method and results were well established particularly by a series of works (Sonnerup, Hasegawa, and Paschmann, 2004; Hasegawa *et al.*, 2004, 2005) that used *Cluster* mission data. These authors examined magnetic flux-rope structures embedded within Earth's magnetopause that were often present during flux-transfer events. The separation distances among the four *Cluster* spacecraft were appropriate with respect to the size of the flux rope cross section such that the four spacecraft paths were evenly spread across it. A comparison between the GS reconstruction results and the actual spacecraft measurements showed remarkable agreement.

In recent years, the GS reconstruction method has been used more often, especially in applications to the twin STEREO (*Solar TErrestrial RElations Observatory*) spacecraft data, in addition to traditional ACE and *Wind* spacecraft *in situ* measurements. A number of studies (Liu *et al.*, 2008, 2010; Möstl *et al.*, 2008, 2009a, 2009b, 2009c; Kilpua *et al.*, 2009; Farrugia *et al.*, 2011; Wood *et al.*, 2012) have successfully applied the method to the STEREO data sets, combined with remote-sensing multi-wavelength imaging, which is capable of tracking the propagation of CMEs from their source regions to 1 AU. This combined approach, taking advantage of the STEREO data sets, allows us to compare the GS reconstruction results of ICMEs with their solar sources, following the earlier work of Qiu *et al.* (2007). For instance, Farrugia *et al.* (2011) examined an event in November 2007 that was simultaneously observed by STEREO A and B and the *Wind* spacecraft, at a time when the spacecraft separation between A and B was about 40° on the ecliptic plane. Farrugia and collaborators were able to derive the cross section of the ICME flux rope at each spacecraft location and showed the combined view of the general flux rope shape from all three GS reconstruction results. Their results showed the complexity of the interplanetary transient structures and their interactions by employing multi-point observations.

The original GS reconstruction procedures have been improved recently (Li *et al.*, 2009; Isavnin, Kilpua, and Koskinen, 2011). For example, Li *et al.* (2009) modified the definition of the fitting residue that is used in the GS method for determining the axis orientation of the cylindrical ICME flux rope. Isavnin, Kilpua, and Koskinen (2011) also adjusted the calculation of this residue and adopted a dedicated smooth finite-difference algorithm. Although these authors showed improvements in certain aspects for a few selected events, the significantly enhanced performance resulting from these modifications has yet to be firmly established. For the purpose of this study, we used the original approach as documented in Hu and Sonnerup (2002) and Hu *et al.* (2004). Especially remarkable is an effort by C. Möstl, who developed a software package in Matlab that incorporates the GS reconstruction procedures into a Graphical User Interface (GUI) that enables the users to apply the method with the ease of clicking a mouse button. The results are displayed and visualized through this interactive process. The package has been widely distributed free of charge,[1] and there are more than a dozen research groups using the GS method all over the world. We refer to the original work of Hu and Sonnerup (2002) and the comprehensive review on the GS method by Sonnerup *et al.* (2006) for details. To facilitate the presentation in this paper, a brief description of the GS reconstruction method is given in Section 2. There were other flux-rope modeling efforts and comparisons among different approaches (*e.g.*, Riley *et al.*, 2004; Al-Haddad *et al.*, 2013) as well as an effort to address the limitations that are

[1]Download a copy of the software package and a user manual from ftp://ftp.iwf.oeaw.ac.at/pub/moestl/publicgscode/, or send an email to the author.

intrinsic to all flux-rope models based on a simplified geometry and single-spacecraft data (*e.g.*, Hasegawa *et al.*, 2007; Al-Haddad *et al.*, 2011). We do not intend to address these problems here.

The motivation of the present work is to examine the effects of the electron temperature (pressure), T_e (p_e), on the GS reconstruction results of ICME structures at 1 AU. As we have shown earlier, the GS reconstruction technique has evolved over the years and has been widely used in the study of ICME structures. But a study on the effect of T_e is still lacking. We aim to perform this simple, yet important and much needed study to be able to address the matter in a systematic and definitive manner, especially considering that the T_e measurements are not always available. We stress that the GS method itself does incorporate the finite plasma pressure that includes contributions from both protons and electrons,without a force-free assumption, which enables us to select a wider range of events beyond the traditional classification of magnetic clouds. We selected eight ICME events from *Wind* spacecraft observations. The event selection criteria and specific measurements used are discussed in Section 3. We specifically selected events with a range of proton β values (not limited to low values only) and variable and representative T_e/T_p ratios. The GS reconstructions results of three events of these typical and extreme parameters are presented in Section 4. Each case study is presented both with and without T_e contribution. We summarize and discuss our quantitative results in the last section.

2. A Brief Description of GS Reconstruction Method

The GS reconstruction method for a cylindrical structure is based on the GS equation in a Cartesian coordinate system, (x, y, z), where the invariant axis (flux-rope axis) is along $\hat{\mathbf{z}}$ with $\partial/\partial z \approx 0$, and a definition of a magnetic flux function $A(x, y)$ (or the axial component of the magnetic vector potential)

$$\frac{\partial^2 A}{\partial x^2} + \frac{\partial^2 A}{\partial y^2} = -\mu_0 \frac{\mathrm{d}P_t(A)}{\mathrm{d}A} = -\mu_0 j_z(A). \tag{1}$$

One of the important quantities is the transverse pressure, $P_t(A) = p(A) + B_z^2(A)/2\mu_0$, which is the sum of the total plasma pressure (protons plus electrons) and the axial magnetic pressure, whose derivative yields the axial current density j_z. Once a local reconstruction frame is set up with known (x, y, z) axes, the initial flux function $A(x, 0)$ and transverse pressure $P_t(x, 0)$ are also known from spacecraft *in situ* measurements (with the x axis at $y = 0$ being the projected spacecraft path across the structure). Then, an analytic functional fit $P_t(A)$ is obtained and the right-hand side of the GS equation (1) becomes explicitly known, which facilitates the final solution of A over a cross-sectional domain of the structure. A fitting residue R_f is calculated to assess the goodness-of-fit (Hu *et al.*, 2004). The entire procedure works through a trial-and-error process by optimizing the requirement that P_t is a single-valued function of A by first determining the z axis orientation. Then, a cross-sectional map of $A(x, y)$ is obtained by solving the GS equation (1) with the initial values and the corresponding functional fit $P_t(A)$. A full characterization of all magnetic field components is achieved since the magnetic field vectors are related to A as $\mathbf{B} = (\partial A/\partial y, -\partial A/\partial x, B_z(A))$. For a magnetic flux-rope solution, the magnetic field often exhibits a configuration of spiral field lines lying on nested, cylindrical iso-surfaces of A, winding along the z axis. This characterization also enables the definition of a flux-rope boundary by selecting a specific $A = A_b$ value (Hu *et al.*, 2004; Riley *et al.*, 2004), as we demonstrate below, which is used to calculate the magnetic flux

Table 1 Selected *Wind* spacecraft ICME events.

Event No.	ICME Interval[a]	$\langle T_e/T_p \rangle$	$\langle \beta_p \rangle$	$\langle \beta \rangle$
3	2 June 1998 10:31:30 – 15:49:30	3.4	0.077	0.32
4	6 Nov. 2000 23:8:30 – 7 Nov. 2000 18:46:30	9.8	0.013	0.089
8	20 November 2003 12:11:30 – 21:17:30	0.88	0.15	0.32
9	4 Apr. 2004 3:28:30 – 5 Apr. 2004 14:55:30	9.8	0.017	0.16
10	27 July 2004 1:44:30 – 15:20:30	2.0	0.065	0.14
5	31 October 2005 0:44:30 – 20:59:30	3.9	0.27	0.95
6	20 May 2005 10:19:30 – 21 May 2005 7:1:30	6.4	0.11	0.40
7	14 Jan. 2007 12:1:30 – 15 Jan. 2007 6:53:30	12.5	0.021	0.24

[a]Identified for the GS reconstruction; in UT.

content (Qiu *et al.*, 2007). We here determine A_b by inspecting the single-value behavior of $B_z(A)$ only; A_b is chosen based on the B_z *vs.* A plot (generated with original relatively high-resolution data, typically ~ 1 minute) arbitrarily where the B_z values start to deviate significantly from a single curve beyond certain $A = A_b$ value. Therefore, the electron temperature does not directly contribute to the determination of A_b.

3. Selected *Wind* Spacecraft ICME Events

We selected and compiled a list of ICMEs observed *in situ* at 1 AU from various sources, primarily based on the comprehensive list published by Richardson and Cane (2010). We used *in situ* magnetic field and plasma measurements from the *Wind* spacecraft, because it provides additional electron temperature observations through the publicly accessible NASA Coordinated Data Analysis Web (CDAWeb) interface. The electron temperature T_e measurements were obtained from the *Wind Solar Wind Experiment* (SWE) (Ogilvie *et al.*, 1995) data product of H0 level through the CDAWeb. If the H0 level data were not available, we used the total electron temperature from the SWE H5 data product. The magnetic field and proton measurements, including the magnetic field magnitude B and three components, the proton temperature T_p, number density N_p, and proton velocity, were obtained from the *Wind Magnetic Field Investigation* (MFI) (Lepping *et al.*, 1995) H0 level and SWE K0 level data products, respectively.

In Table 1, we list the ICME events that we were able to successfully apply the GS reconstruction method to. We identify each event by an arbitrarily assigned event number. For each event, we list the data interval selected for the GS reconstruction, the corresponding average T_e/T_p ratio, the average proton β_p ($\equiv N_p k T_p/p_B$, where $p_B = B^2/2\mu_0$, k being the Boltzmann constant and μ_0 the permeability) value, and the average total plasma β ($\equiv N_p k(T_p + T_e)/p_B$) values. These values span a fairly wide range, as shown in Figure 1. The average electron-to-proton temperature ratio has a range from ~ 1 to >10 and the average total plasma β ranges from ~ 0.1 to ~ 1. The average total plasma β value is generally much (from at least one to ten times) higher than the corresponding average proton β_p value, indicating significant contribution from the electrons to the total plasma pressure. The average values of the parameters in Table 1 are 6.1, 0.087, and 0.33, and the corresponding median values are 5.2, 0.071, and 0.28.

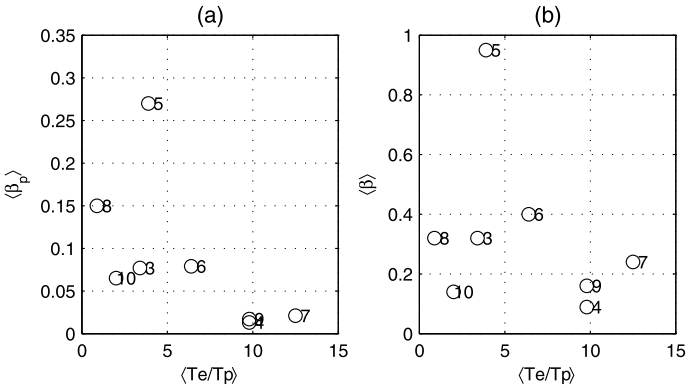

Figure 1 Parameter distribution of (a) $\langle\beta_{\rm p}\rangle$ and (b) $\langle\beta\rangle$ *vs*. the average electron temperature over the proton temperature ratio for each selected *Wind* ICME event. The event number is indicated at the side of each open circle.

4. Case Studies

In this section, we present GS reconstruction results for three events that are representative and extreme in terms of the characteristic plasma parameters from Table 1. As also evident from Figure 1, events No. 5 and 7 have the highest $\langle\beta\rangle$ value and $\langle T_{\rm e}/T_{\rm p}\rangle$ ratio. We present these two events along with event No. 6, which has moderate values of $\langle\beta\rangle$ and the $\langle T_{\rm e}/T_{\rm p}\rangle$ ratio. For each event, we present the results with and without electron temperature contribution to the total plasma pressure. The invariant z axis orientation is determined by the GS reconstruction procedure including the $T_{\rm e}$ contribution and remains unchanged for the case without $T_{\rm e}$ contribution. We discuss the effect of $T_{\rm e}$ on the flux-rope axis determination in the last section.

4.1. Event No. 5: 31 October 2005

Event No. 5 occurred on 31 October 2005 and lasted for nearly one day. Figure 2 shows some *in situ* measurements of the bulk properties of the ICME from the *Wind* spacecraft. The magnetic field magnitude shows a moderate increase to somewhat more than 10 nT, and the magnetic field vector executes a rotation in at least two components for the identified interval. The bulk radial speed is about 400 km s^{-1} and shows little evidence of expansion. The proton temperature $T_{\rm p}$ does become fairly low during the interval, while the electron temperature $T_{\rm e}$ is much higher than $T_{\rm p}$ with an average $T_{\rm e}/T_{\rm p}$ ratio of 3.9. Since the proton $\beta_{\rm p}$ value is fairly moderate for this event, with an average value 0.27, including the electron contribution in the total plasma pressure increases the total plasma β value to ~ 1 on average. Another notable feature, as seen in the last panel of Figure 2, is the apparent variation (gradient) in the axial magnetic pressure p_{Bz} ($\equiv B_z^2/2\mu_0$, red), which seems to exceed that in the corresponding total plasma pressure p (black).

The GS reconstruction was carried out for the time interval between the vertical lines in Figure 2. We note that this interval selection was made for the purpose of GS reconstruction only and does not necessarily coincide with an ICME interval identified based on other criteria (*e.g.*, Richardson and Cane, 2010; Jian *et al.*, 2006). A main criterion for our selection was the decrease in plasma β value (fourth panel of Figure 2) and, as a rule of thumb, we generally selected as long an interval as possible.

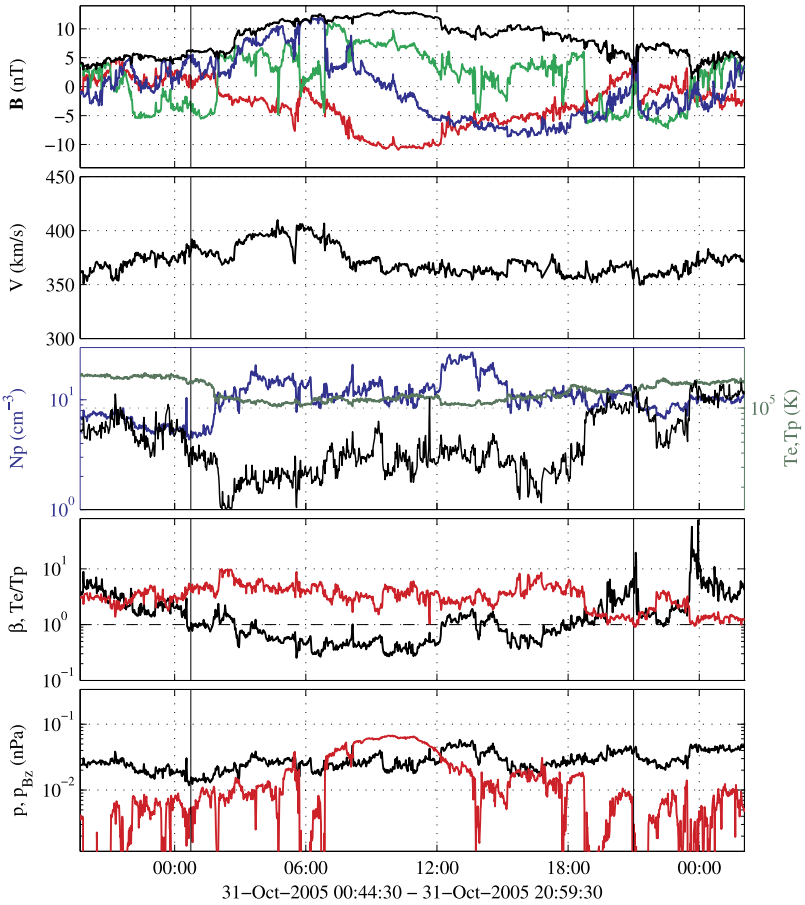

Figure 2 Time series for Event No. 5. The top panel shows the magnetic field GSE-X (red), Y (green), Z (blue) components, and magnitude (black). The second panel shows the bulk solar wind speed. The third panel shows the proton number density $N_{\rm p}$ (blue) in the left vertical axis, and the electron ($T_{\rm e}$, green) and proton ($T_{\rm p}$, black) temperatures in the right vertical axis. The fourth panel shows the plasma β value (black) and the ratio $T_{\rm e}/T_{\rm p}$ (red). A dashed line of value 1.0 is drawn. The bottom panel shows the total plasma pressure p (black) and the axial magnetic field pressure p_{Bz} (red). The vertical lines denote the time interval chosen for the GS reconstruction, as indicated beneath the bottom panel.

The GS reconstruction results, first including $T_{\rm e}$, are given in Tables 2 and 3. These include both geometrical and physical parameters: the axis orientation $\hat{\mathbf{z}}$ of the cylindrical flux rope, the closest approach distance from the spacecraft path to the center of the flux rope Y_0, the highest axial magnetic field component $B_{z\,\max}$, the highest/lowest axial current density j_{z0}, the total axial current I_z, the axial magnetic flux Φ_z, the poloidal magnetic flux $\Phi_{\rm p}$, and the relative magnetic helicity $K_{\rm r}$ (the last two for a cylindrical length of 1 AU; see, *e.g.*, Qiu *et al.*, 2007; Hu and Dasgupta, 2005, and Webb *et al.*, 2010). An additional parameter, $R_{\rm f}$, representing the fitting residue of the transverse pressure $P_{\rm t} \equiv p + p_{Bz}$ *vs.* the flux function A, as defined in Hu *et al.* (2004) and described in Section 2, is also given to evaluate the effect of $T_{\rm e}$ on the fitting of $P_{\rm t}(A)$, a critical step in the GS reconstruction method. The lower the $R_{\rm f}$ value, the more reliable the results. Generally, we expect such a value to be equal to, or lower than, 0.2 for the case to be acceptable. The same set of results

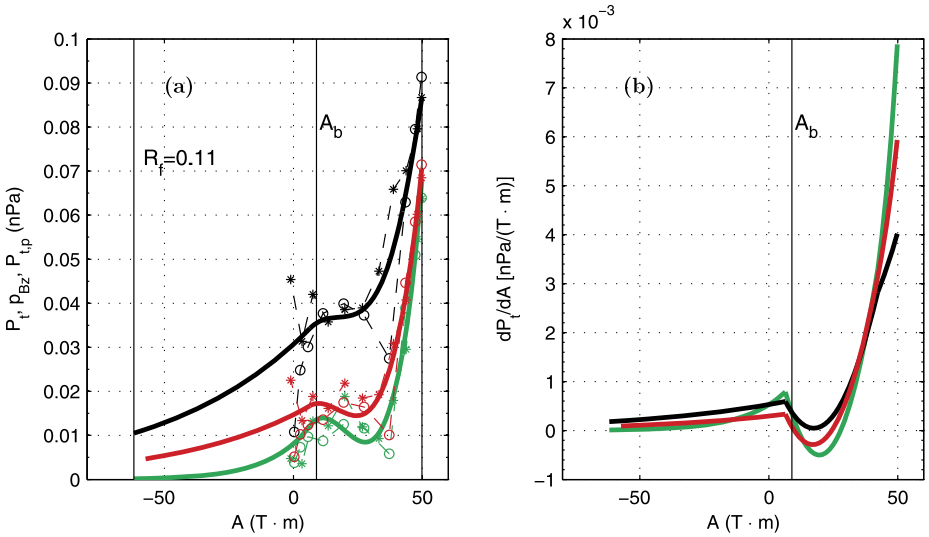

Figure 3 The measured quantities (symbols) and corresponding functional fits (solid curves) of (a) the transverse pressure P_t including T_e (black), $P_{t,p}$ excluding T_e (red), and the axial magnetic pressure p_{Bz} (green) *vs.* the magnetic flux function A and (b) the corresponding gradients of $P_t(A)$ (black), $p_{Bz}(A)$ (green), and $P_{t,p}(A)$ (red) for event No. 5. The circles and stars are the corresponding measurements along the inbound and outbound path of the spacecraft across the flux-rope cross section. The fitting residue R_f for $P_t(A)$ and the boundary value $A = A_b$ are also denoted.

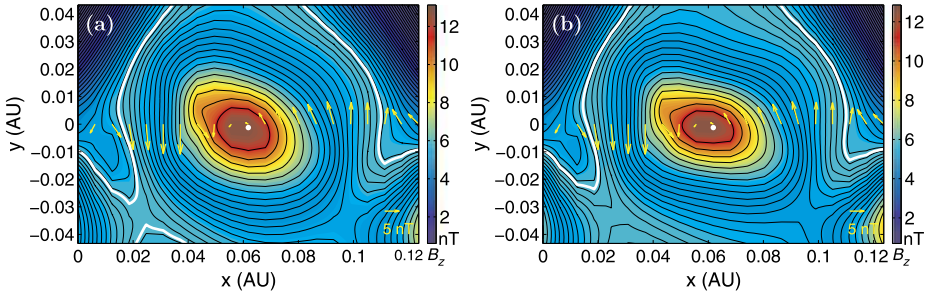

Figure 4 The cross-sectional map of Event No. 5 for (a) the case including T_e, and (b) the case excluding T_e. Each map shows the transverse magnetic field lines (black contour lines of the flux function A) on the plane perpendicular to the flux-rope axis, and the axial magnetic field B_z superposed in color with scales indicated by the color bar. The yellow arrows along $y = 0$ denote measured transverse magnetic field vectors along the projected spacecraft path. The white dot marks the location of the highest B_z. The thick white line indicates the flux-rope boundary of $A = A_b$.

are repeated in Table 3 for the GS reconstruction without T_e ($T_e \equiv 0$) and the same z axis orientation. For this event, the fitting residue R_f slightly decreases for the case without T_e contribution. We compare all derived quantities between the two cases in the last section for all events.

Figure 3a shows the critical measurements of P_t, $P_{t,p}$ ($T_e \equiv 0$), and p_{Bz} *vs.* A (symbols) along the spacecraft path across the ICME flux rope and the corresponding functional fits that were used in the GS reconstruction procedures (specifically, their gradients/derivatives with respect to A, see Equation (1) and Section 2). The flux-rope boundary $A = A_b$ is the

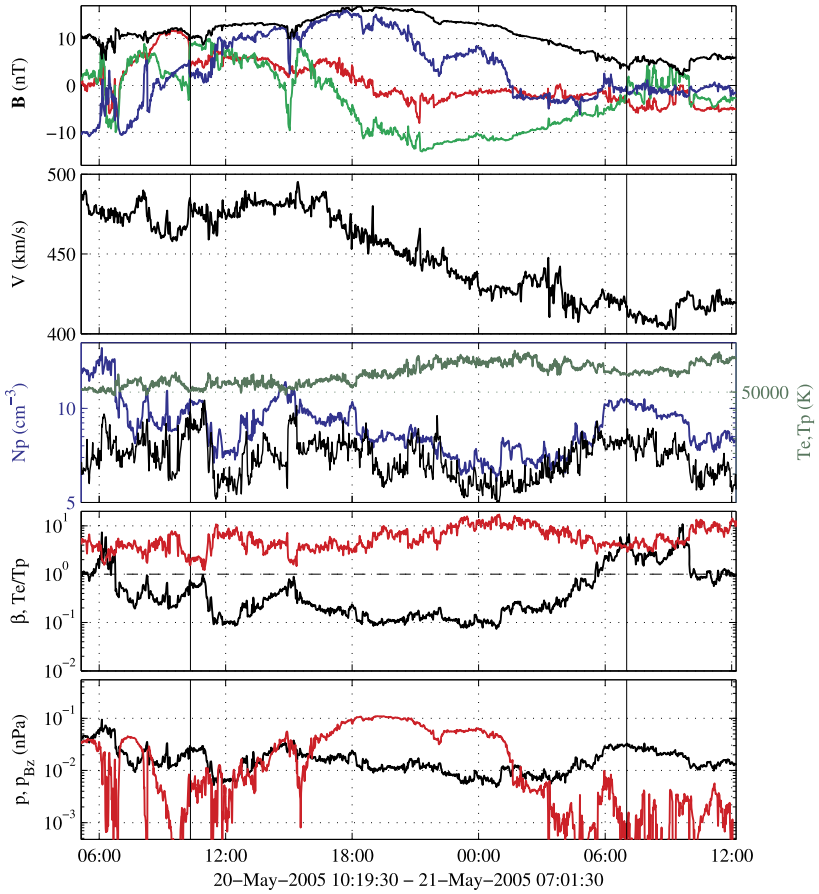

Figure 5 Time series for Event No. 6. The panels show the same parameters as in Figure 2 with the same convention.

same for all three curves because it is determined by the $B_z(A)$ curve, which is the same because the z-axis orientation is the same. The magnitude of P_t (Figure 3a) differs significantly in the cases with and without T_e because the electron pressure is much higher than the proton pressure. However, the gradients of $P_t(A)$ and $P_{t,p}(A)$ differ much less, as shown in Figure 3b, especially for the middle part of $A > A_b$. The most noticeable differences exist near the center the flux rope where the flux function A is highest and near the flux rope boundary $A \sim A_b$. These discrepancies correspond to noticeable deviations in the reconstructed cross sections of the ICME flux rope between the cases with and without T_e contribution, as seen in Figure 4. The major differences between Figure 4a and 4b appear near the center of the flux rope, where the transverse field line changes shape slightly, and near the boundary highlighted by the thick white line at which $A = A_b$. However, the overall magnetic field configuration remains very similar.

4.2. Event No. 6: 20 May 2005

Event No. 6 was observed during 20 – 21 May 2005 and lasted for a little shorter than a day. The temporal profiles of various magnetic field and plasma parameters are plotted in Fig-

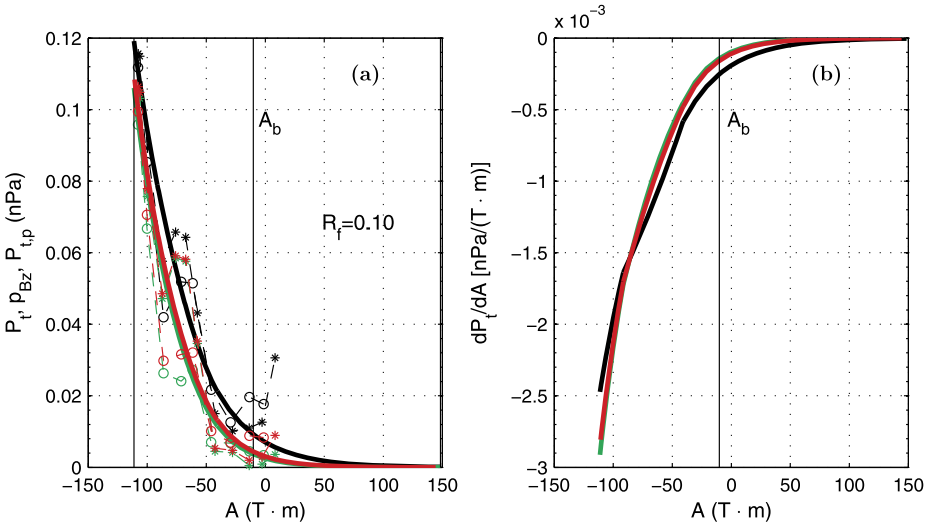

Figure 6 The measured quantities and corresponding functional fits of the transverse pressure, the axial magnetic pressure, and the corresponding gradients for Event No. 6. The panels show the same parameters as in Figure 3 with the same convention.

ure 5, in the same format as in Figure 2. The *in situ* data exhibit typical signatures of an MC event, namely, an enhanced magnetic field magnitude and a smooth rotation of the magnetic field components, and a low proton β value. Throughout most of the MC interval, the β value remains low around 0.1, although the T_e/T_p ratio is rather high, about 6.4 on average, and briefly reaches ~ 10 in the latter half of the interval. The bulk radial velocity decreases gradually from nearly 500 km s^{-1} to about 400 km s^{-1} during the ~ 20 hour interval, which is very modest and would yield a maximum radial expansion speed of ~ 50 km s^{-1} if we attribute the declining radial speed profile solely to kinematic expansion. We estimated the ratio between the dynamic term due to remaining plasma flows in a reference frame that moves with the ICME structure and the Lorentz force of a nominal value 0.19, which effect was omitted from the reconstruction. The axial magnetic pressure again displays more pronounced variations over two orders of magnitude than the total plasma pressure, as indicated in the last panel of Figure 5.

Although the average β value is ~ 0.40 for this event, throughout most of the interval its value is fairly low, ~ 0.1. Therefore, the magnetic pressure dominates most of the time. Since the electron temperature is much higher than the proton temperature, the quantities $P_{t,p}$ and p_{Bz} are nearly identical, but are lower than P_t, as shown in Figure 6a. In Figure 6b, the gradients of $P_t(A)$ and $P_{t,p}(A)$ show very little difference, which leads to very similar cross-section plots in Figure 7. The only noticeable deviation is found at the flux-rope boundary, which was caused by the biggest difference between the two curves near $A = A_b$ in Figure 6b. In Figure 7, the cross-section maps are nearly identical, both showing a large-scale left-handed flux-rope structure with the spacecraft path nearly crossing the center.

4.3. Event No. 7: 14 January 2007

Event No. 7 occurred during an ~ 20-hour interval on 14 – 15 January 2007 and has the highest average T_e/T_p ratio, 12.5, of all events listed in Table 1. This ratio of above 10 persists

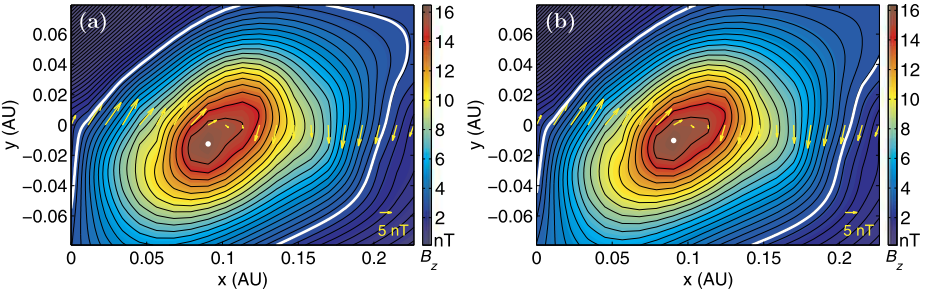

Figure 7 The cross-sectional map of Event No. 6 for (a) the case including T_e, and (b) the case excluding T_e. The convention is the same as in Figure 4.

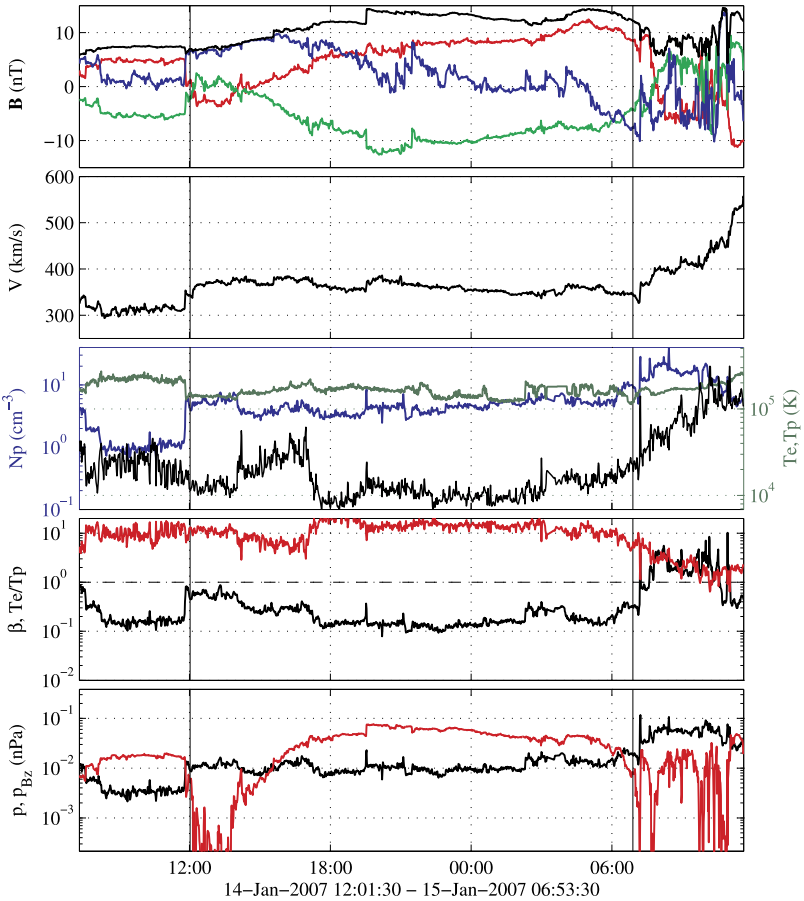

Figure 8 Time series for Event No. 7. The panels show the same parameters as in Figure 2 with the same convention.

throughout the central part of the ICME interval, as shown in Figure 8. In the meantime, the plasma β value remains fairly low near the center of the interval, ~ 0.1. The same is true for

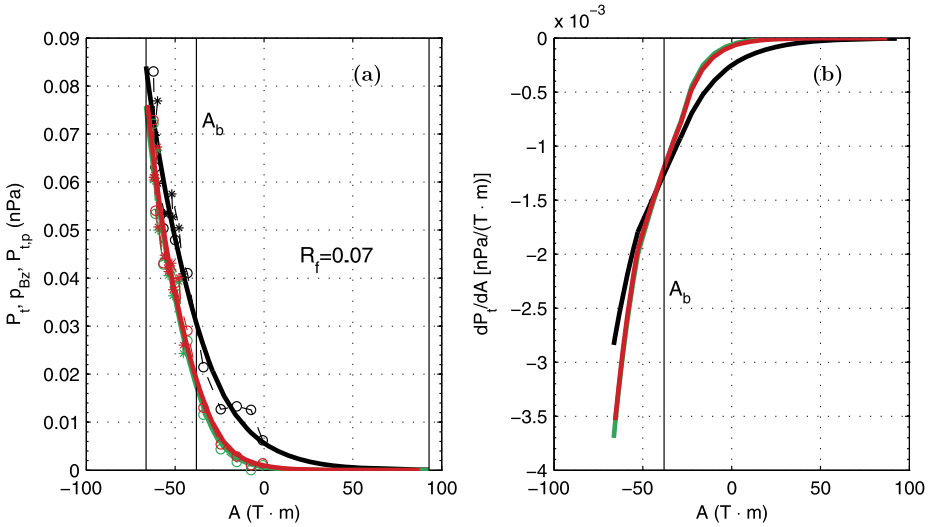

Figure 9 The measured quantities and corresponding functional fits of the transverse pressure, the axial magnetic pressure, and the corresponding gradients for Event No. 7. The convention is the same as in Figure 3.

the proton temperature, which is around 10^4 K. The magnetic field again shows the typical signatures of a flux-rope structure. The radial velocity profile declines moderately, similar to, but less pronounced than, Event No. 6 (the decrease is less than 100 km s^{-1} during the $\sim$ 20-hour interval). The axial magnetic pressure varies by more than one order of magnitude throughout the interval, while the total plasma pressure remains almost constant around 10^{-2} nPa.

The corresponding $P_t(A)$ curves and their gradients are given in Figure 9. They show a behavior similar to those of Event No. 6. The electron temperature is even more dominant over the proton temperature ($T_e/T_p \gtrsim 10$) in this case. Because the proton β_p is rather low, on the order 0.01 on average, the $P_{t,p}(A)$ and $p_{Bz}(A)$ curves lie almost on top of each other. The gradients in the $P_t(A)$ curves shown in Figure 9b are again very similar to each other, especially for $A \lesssim A_b$, which corresponds to the central region of the flux rope within the boundary. As a result, the reconstructed cross sections, given in Figure 10, for the cases with and without T_e contribution, show very little difference. The barely noticeable difference exists mostly beyond the flux-rope boundary, especially near the bottom boundary of the computational domain, which corresponds to the strongest deviation seen in Figure 9b where $A > A_b$. The multiple flux-rope configurations are present for both cases. Therefore, the GS reconstruction without a T_e contribution still preserves the same multiple flux-rope structure in this case. Multiple flux-rope ICME structures like these have been revealed before by Hu *et al.* (2004), where the electron temperature measurements were included.

5. Summary and Conclusion

We have shown the GS reconstruction results in typical graphical representations of cross-section maps on the plane perpendicular to the cylindrical flux-rope axis and the associated behaviors of the $P_t(A)$ functions including and excluding T_e. By visual inspection, we found

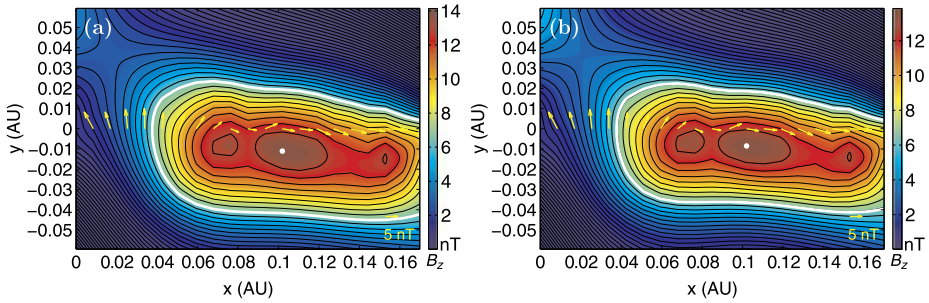

Figure 10 The cross-sectional map of Event No. 7 for (a) the case including T_e and (b) the case excluding T_e. The convention is the same as in Figure 4.

only little qualitative effect of T_e on the GS reconstruction results. This is mainly because overall the gradients of the corresponding $P_t(A)$ functions do not change significantly.

More quantitatively, for the geometrical and physical quantities summarized in Table 3 of all events, this effect is also weak on most, but not all, parameters. The fitting residues are low (all $\lesssim 0.1$) for the cases with and without a T_e contribution, while the invariant z axis remains the same. This indicates that the effect of T_e on the z axis determination is negligible for these events. The closest-approach distances Y_0 are close except for Event No. 10, where they differ by ~ 0.01 AU. The highest axial magnetic field magnitudes $B_{z\,\max}$ are mostly identical. The largest difference was found in the axial current density at the flux-rope center, j_{z0}, which is proportional to the slope of the $P_t(A)$ curve at the location of the extreme A value that represents the center of a flux rope. Therefore, these values of j_{z0} correspond to the extreme values (highest gradients in magnitude) plotted in panel (b) of Figures 3, 6, and 9, where the strongest difference between the two curves (black and red) is observed.

Most importantly, the physical quantities Φ_z, Φ_p, and K_r, concerning the magnetic flux and helicity content, differ by ~ 10 % at most, except for K_r of Events No. 5 and 7. While the first two quantities are area integrals, the last one is volume-integrated, which probably induces a greater error. The change of A_b would modify the values of these quantities. We estimate the change to be very small (< 10 %) for the axial flux since near the boundary the axial field is very small, near zero, and the area change is less than 10 %. The change to the poloidal flux is proportional to the uncertainty in A_b, which is also small (10 % as an upper limit), because the vector potential along $y = 0$ is derived from high-resolution data via numerical integration of $-B_y$ (see Section 2). The relative error is estimated to be $\lesssim 1/12$ based on the composite trapezoidal rule. In addition, the uncertainty in the effective length of a cylindrical flux rope alone would have resulted in an uncertainty of 50 – 100 %, *e.g.*, for an effective length of 1 AU with an uncertainty range 0.5 – 2.0 AU (Qiu *et al.*, 2007), although such an uncertainty can be reduced based on an additional comparison of magnetic helicity (Kazachenko *et al.*, 2012) and actual measurements of field-line lengths (Kahler, Haggerty, and Richardson, 2011). These are important and quantitative outputs from the GS reconstruction that characterizes the flux-rope ICME structures and are useful for studying CME-ICME connections. For instance, in Qiu *et al.* (2007), the magnetic flux contained in ICME flux ropes was compared with the corresponding magnetic flux injected during the magnetic reconnection process in the solar source regions, as manifested by flaring activities accompanied by brightening ribbons in remote-sensing observations of the Sun. That original study provided favorable and quantitative evidence for the important role of magnetic

Table 2 The axial orientations from GS reconstruction (including T_e) for the selected *Wind* spacecraft ICME events.

Event No.	$\hat{\mathbf{z}}$ (GSE)			$\hat{\mathbf{z}}$ (angular GSE)
	(X	Y	Z)	(δ, ϕ)[a]
3	(0.3804	0.8892	0.2541)	(68, 16)
4	(0.2144	0.8901	0.4021)	(78, 24)
8	(–0.1553	0.5504	–0.8204)	(99, 304)
9	(0.4934	–0.2740	0.8255)	(60, 108)
10	(–0.03967	0.9438	–0.3282)	(92, 341)
5	(–0.7696	0.6373	–0.04000)	(140, 356)
6	(–0.1461	–0.5440	0.8263)	(98, 123)
7	(0.2679	–0.9329	0.2405)	(74, 166)

[a]The angle δ ($0-180°$) is the polar angle measured from the positive X direction toward the z axis and the angle ϕ ($0-360°$) is the azimuthal angle measured from the positive Y direction toward the projection of the z axis onto the $Y-Z$ plane.

Table 3 Summary of the GS reconstruction results for the selected *Wind* spacecraft ICME events. For each group of results as identified by the event no. (two rows each), the first (second) row corresponds to the results including (excluding) T_e.

Event No.	R_f	Y_0 (AU)	$B_{z\,max}$ nT	j_{z0} (A/m^2) $\times 10^{-12}$	Φ_z (Wb) $\times 10^{12}$	Φ_p (Wb) $\times 10^{12}$	K_r (Wb^2) $\times 10^{26}$
3	0.062	0.0042	12	−4.08	0.25	2.04	−0.0042
	0.043	0.0039	12	−4.20	0.25	2.04	−0.0041
4	0.040	0.027	25	−3.28	7.67	19.6	−1.29
	0.048	0.027	24	−3.35	7.73	19.8	−1.31
8	0.041	0.0047	53	13.6	6.31	26.8	1.41
	0.042	0.0040	53	15.8	6.21	26.8	1.38
9	0.064	0.028	19	−1.35	13.0	19.1	−2.17
	0.068	0.029	19	−1.27	13.9	19.3	−2.09
10	0.081	−0.034	26	1.92	18.1	30.6	5.43
	0.057	−0.021	26	2.11	17.5	30.3	5.11
5	0.10	−0.0012	13	4.02	1.11	6.10	0.028
	0.078	−0.0012	13	5.94	1.12	6.10	0.023
6	0.098	−0.012	16	−2.49	4.48	15.1	−0.59
	0.10	−0.010	16	−2.83	4.60	15.0	−0.57
7	0.070	−0.011	14	−2.85	1.75	4.22	−0.074
	0.063	−0.0085	14	−3.55	1.59	4.10	−0.064

reconnection in triggering flare-CME activity and the formation of a magnetic flux rope in the low solar corona that was subsequently examined in more detail in several studies (*e.g.*, Möstl *et al.*, 2008, 2009b; Qiu, 2009; Kazachenko *et al.*, 2012).

Overall, we conclude that the effect of the electron temperature T_e (pressure p_e) on the GS reconstruction results of ICME flux ropes at 1 AU contributes to about 10 – 20 % discrepancy in some major physical parameters derived, such as the magnetic flux content. The reason is that the T_e contribution to the total plasma pressure p does not significantly change the gradient of p over a wide range of the interval compared with the gradient of the magnetic pressure, although the magnitude of p is often changed greatly, given $T_e \gg T_p$ in many cases. However, it does affect certain quantities, for instance the current density

near the center of the flux rope (*i.e.*, the maximum axial current density and consequently the total axial current) more significantly. Therefore, the T_e contribution has to be included when these quantities are to be reliably assessed.

We concentrated on a selection of magnetic clouds observed at 1 AU. As these configurations propagate farther outward, their parameters (B_z, B_t, T_e, T_p, and N_p) decrease with heliocentric distance, r_H. But the functional dependence on r_H is not the same (see, *e.g.*, Osherovich, Farrugia, and Burlaga, 1993). Thus, for example, a "flat-topped" B-profile tends to develop. Therefore it is appropriate to extend the current study to a set of events at larger distances, subject to events and data availability. This is the subject of ongoing work.

Acknowledgements HQ and CJF acknowledge NASA grant NNG06GD41G for partial support. Work at UNH was also supported by NASA *Wind* grant NNX10AQ29G and NSF grant AGS-1140211. HQ is also grateful for partial support from NASA grants NNX12AF97G and NNX12AH50G, and NSF SHINE AGS-1062050. CM acknowledges funding from the European Union Seventh Framework Programme (FP7/2007-2013) under grant agreement n°263252 [COMESEP]. This research was supported by a Marie Curie International Outgoing Fellowship within the 7th European Community Framework Programme. We are grateful to NASA CDAWeb for the *Wind* spacecraft data.

References

Al-Haddad, N., Roussev, I.I., Möstl, C., Jacobs, C., Lugaz, N., Poedts, S., Farrugia, C.J.: 2011, On the internal structure of the magnetic field in magnetic clouds and interplanetary coronal mass ejections: writhe *versus* twist. *Astrophys. J. Lett.* **738**, L18. doi:10.1088/2041-8205/738/2/L18.

Al-Haddad, N., Nieves-Chinchilla, T., Savani, N.P., Möstl, C., Marubashi, K., Hidalgo, M.A., Roussev, I.I., Poedts, S., Farrugia, C.J.: 2013, Magnetic field configuration models and reconstruction methods: a comparative study. *Solar Phys.*, in this issue. doi:10.1007/s11207-013-0244-5.

Fainberg, J., Osherovich, V.A., Stone, R.G., MacDowall, R.J., Balogh, A.: 1996, Ulysses observations of electron and proton components in a magnetic cloud and related wave activity. In: Winterhalter, D., Gosling, J.T., Habbal, S.R., Kurth, W.S., Neugebauer, M. (eds.) *American Institute of Physics Conference Series* **382**, 554 – 557. doi:10.1063/1.51513.

Farrugia, C.J., Fitzenreiter, R.J., Burlaga, L.F., Erkaev, N.V., Osherovich, V.A., Biernat, H.K., Fazakerley, A.: 1994, Observations in the sheath region ahead of a magnetic cloud and in the dayside magnetosheath during magnetic cloud passage. *Adv. Space Res.* **14**, 105 – 110. doi:10.1016/0273-1177(94)90055-8.

Farrugia, C.J., Berdichevsky, D.B., Möstl, C., Galvin, A.B., Leitner, M., Popecki, M.A., Simunac, K.D.C., Opitz, A., Lavraud, B., Ogilvie, K.W., Veronig, A.M., Temmer, M., Luhmann, J.G., Sauvaud, J.A.: 2011, Multiple, distant (40°) *in situ* observations of a magnetic cloud and a corotating interaction region complex. *J. Atmos. Solar-Terr. Phys.* **73**, 1254 – 1269. doi:10.1016/j.jastp.2010.09.011.

Hasegawa, H., Sonnerup, B., Dunlop, M., Balogh, A., Haaland, S., Klecker, B., Paschmann, G., Lavraud, B., Dandouras, I., Rème, H.: 2004, Reconstruction of two-dimensional magnetopause structures from Cluster observations: verification of method. *Ann. Geophys.* **22**, 1251 – 1266. doi:10.5194/angeo-22-1251-2004.

Hasegawa, H., Sonnerup, B.U.Ö., Klecker, B., Paschmann, G., Dunlop, M.W., Rème, H.: 2005, Optimal reconstruction of magnetopause structures from Cluster data. *Ann. Geophys.* **23**, 973 – 982. doi:10.5194/angeo-23-973-2005.

Hasegawa, H., Nakamura, R., Fujimoto, M., Sergeev, V.A., Lucek, E.A., Rème, H., Khotyaintsev, Y.: 2007, Reconstruction of a bipolar magnetic signature in an earthward jet in the tail: flux rope or 3D guide-field reconnection? *J. Geophys. Res.* **112**, 11206. doi:10.1029/2007JA012492.

Hau, L.N., Sonnerup, B.U.Ö.: 1999, Two-dimensional coherent structures in the magnetopause: recovery of static equilibria from single-spacecraft data. *J. Geophys. Res.* **104**, 6899 – 6918. doi:10.1029/1999JA900002.

Hu, Q., Dasgupta, B.: 2005, Calculation of magnetic helicity of cylindrical flux rope. *Geophys. Res. Lett.* **32**, 12109. doi:10.1029/2005GL023004.

Hu, Q., Smith, C.W., Ness, N.F., Skoug, R.M.: 2003, Double flux-rope magnetic cloud in the solar wind at 1 AU. *Geophys. Res. Lett.* **30**, 070000. doi:10.1029/2002GL016653.

Hu, Q., Smith, C.W., Ness, N.F., Skoug, R.M.: 2004, Multiple flux rope magnetic ejecta in the solar wind. *J. Geophys. Res.* **109**, 3102. doi:10.1029/2003JA010101.

Hu, Q., Sonnerup, B.U.Ö.: 2001, Reconstruction of magnetic flux ropes in the solar wind. *Geophys. Res. Lett.* **28**, 467 – 470. doi:10.1029/2000GL012232.

Hu, Q., Sonnerup, B.U.Ö.: 2002, Reconstruction of magnetic clouds in the solar wind: orientations and configurations. *J. Geophys. Res.* **107**, 1142. doi:10.1029/2001JA000293.

Isavnin, A., Kilpua, E.K.J., Koskinen, H.E.J.: 2011, Grad–Shafranov reconstruction of magnetic clouds: overview and improvements. *Solar Phys.* **273**, 205 – 219. doi:10.1007/s11207-011-9845-z.

Jian, L., Russell, C.T., Luhmann, J.G., Skoug, R.M.: 2006, Properties of interplanetary coronal mass ejections at one AU during 1995 – 2004. *Solar Phys.* **239**, 393 – 436. doi:10.1007/s11207-006-0133-2.

Kahler, S.W., Haggerty, D.K., Richardson, I.G.: 2011, Magnetic field-line lengths in interplanetary coronal mass ejections inferred from energetic electron events. *Astrophys. J.* **736**, 106. doi:10.1088/0004-637X/736/2/106.

Kazachenko, M.D., Canfield, R.C., Longcope, D.W., Qiu, J.: 2012, Predictions of energy and helicity in four major eruptive solar flares. *Solar Phys.* **277**, 165 – 183. doi:10.1007/s11207-011-9786-6.

Kilpua, E.K.J., Liewer, P.C., Farrugia, C., Luhmann, J.G., Möstl, C., Li, Y., Liu, Y., Lynch, B.J., Russell, C.T., Vourlidas, A., Acuna, M.H., Galvin, A.B., Larson, D., Sauvaud, J.A.: 2009, Multispacecraft observations of magnetic clouds and their solar origins between 19 and 23 May 2007. *Solar Phys.* **254**, 325 – 344. doi:10.1007/s11207-008-9300-y.

Lepping, R.P., Acũna, M.H., Burlaga, L.F., Farrell, W.M., Slavin, J.A., Schatten, K.H., Mariani, F., Ness, N.F., Neubauer, F.M., Whang, Y.C., Byrnes, J.B., Kennon, R.S., Panetta, P.V., Scheifele, J., Worley, E.M.: 1995, The wind magnetic field investigation. *Space Sci. Rev.* **71**, 207 – 229. doi:10.1007/BF00751330.

Li, H.J., Feng, X.S., Zuo, P.B., Xie, Y.Q.: 2009, Inferring interplanetary flux rope orientation with the minimum residue method. *J. Geophys. Res.* **114**, A03102. doi:10.1029/2008JA013331.

Liu, Y., Luhmann, J.G., Huttunen, K.E.J., Lin, R.P., Bale, S.D., Russell, C.T., Galvin, A.B.: 2008, Reconstruction of the 2007 May 22 magnetic cloud: how much can we trust the flux-rope geometry of CMEs? *Astrophys. J. Lett.* **677**, L133 – L136. doi:10.1086/587839.

Liu, Y., Thernisien, A., Luhmann, J.G., Vourlidas, A., Davies, J.A., Lin, R.P., Bale, S.D.: 2010, Reconstructing coronal mass ejections with coordinated imaging and *in situ* observations: global structure, kinematics, and implications for space weather forecasting. *Astrophys. J.* **722**, 1762 – 1777. doi:10.1088/0004-637X/722/2/1762.

Möstl, C., Miklenic, C., Farrugia, C.J., Temmer, M., Veronig, A., Galvin, A.B., Vršnak, B., Biernat, H.K.: 2008, Two-spacecraft reconstruction of a magnetic cloud and comparison to its solar source. *Ann. Geophys.* **26**, 3139 – 3152. doi:10.5194/angeo-26-3139-2008.

Möstl, C., Farrugia, C.J., Biernat, H.K., Leitner, M., Kilpua, E.K.J., Galvin, A.B., Luhmann, J.G.: 2009a, Optimized Grad–Shafranov reconstruction of a magnetic cloud using STEREO-wind observations. *Solar Phys.* **256**, 427 – 441. doi:10.1007/s11207-009-9360-7.

Möstl, C., Farrugia, C.J., Miklenic, C., Temmer, M., Galvin, A.B., Luhmann, J.G., Kilpua, E.K.J., Leitner, M., Nieves-Chinchilla, T., Veronig, A., Biernat, H.K.: 2009b, Multispacecraft recovery of a magnetic cloud and its origin from magnetic reconnection on the Sun. *J. Geophys. Res.* **114**, A04102. doi:10.1029/2008JA013657.

Möstl, C., Farrugia, C.J., Temmer, M., Miklenic, C., Veronig, A.M., Galvin, A.B., Leitner, M., Biernat, H.K.: 2009c, Linking remote imagery of a coronal mass ejection to its *in situ* signatures at 1 AU. *Astrophys. J. Lett.* **705**, L180 – L185. doi:10.1088/0004-637X/705/2/L180.

Nieves-Chinchilla, T., Viñas, A.F.: 2008, Solar wind electron distribution functions inside magnetic clouds. *J. Geophys. Res.* **113**, 2105. doi:10.1029/2007JA012703.

Ogilvie, K.W., Chornay, D.J., Fritzenreiter, R.J., Hunsaker, F., Keller, J., Lobell, J., Miller, G., Scudder, J.D., Sittler, E.C. Jr., Torbert, R.B., Bodet, D., Needell, G., Lazarus, A.J., Steinberg, J.T., Tappan, J.H., Mavretic, A., Gergin, E.: 1995, SWE, a comprehensive plasma instrument for the wind spacecraft. *Space Sci. Rev.* **71**, 55 – 77. doi:10.1007/BF00751326.

Osherovich, V.A., Farrugia, C.J., Burlaga, L.F.: 1993, Dynamics of aging magnetic clouds. *Adv. Space Res.* **13**, 57 – 62. doi:10.1016/0273-1177(93)90391-N.

Osherovich, V.A., Farrugia, C.J., Burlaga, L.F., Lepping, R.P., Fainberg, J., Stone, R.G.: 1993, Polytropic relationship in interplanetary magnetic clouds. *J. Geophys. Res.* **98**, 15331. doi:10.1029/93JA01012.

Qiu, J.: 2009, Observational analysis of magnetic reconnection sequence. *Astrophys. J.* **692**, 1110 – 1124. doi:10.1088/0004-637X/692/2/1110.

Qiu, J., Hu, Q., Howard, T.A., Yurchyshyn, V.B.: 2007, On the magnetic flux budget in low-corona magnetic reconnection and interplanetary coronal mass ejections. *Astrophys. J.* **659**, 758 – 772. doi:10.1086/512060.

Richardson, I.G., Cane, H.V.: 2010, Near-Earth interplanetary coronal mass ejections during solar cycle 23 (1996 – 2009): catalog and summary of properties. *Solar Phys.* **264**, 189 – 237. doi:10.1007/s11207-010-9568-6.

Richardson, I.G., Farrugia, C.J., Cane, H.V.: 1997, A statistical study of the behavior of the electron temperature in ejecta. *J. Geophys. Res.* **102**, 4691 – 4700. doi:10.1029/96JA04001.

Riley, P., Linker, J.A., Lionello, R., Mikić, Z., Odstrcil, D., Hidalgo, M.A., Cid, C., Hu, Q., Lepping, R.P., Lynch, B.J., Rees, A.: 2004, Fitting flux ropes to a global MHD solution: a comparison of techniques. *J. Atmos. Solar-Terr. Phys.* **66**, 1321 – 1331. doi:10.1016/j.jastp.2004.03.019.

Sittler, E.C., Burlaga, L.F.: 1998, Electron temperatures within magnetic clouds between 2 and 4 AU: Voyager 2 observations. *J. Geophys. Res.* **103**, 17447 – 17454. doi:10.1029/98JA01289.

Skoug, R.M., Feldman, W.C., Gosling, J.T., McComas, D.J., Reisenfeld, D.B., Smith, C.W., Lepping, R.P., Balogh, A.: 2000a, Radial variation of solar wind electrons inside a magnetic cloud observed at 1 and 5 AU. *J. Geophys. Res.* **105**, 27269 – 27276. doi:10.1029/2000JA000095.

Skoug, R.M., Feldman, W.C., Gosling, J.T., McComas, D.J., Smith, C.W.: 2000b, Solar wind electron characteristics inside and outside coronal mass ejections. *J. Geophys. Res.* **105**, 23069 – 23084. doi:10.1029/2000JA000017.

Sonnerup, B.U.Ö., Guo, M.: 1996, Magnetopause transects. *Geophys. Res. Lett.* **23**, 3679 – 3682. doi:10.1029/96GL03573.

Sonnerup, B.U.Ö., Hasegawa, H., Paschmann, G.: 2004, Anatomy of a flux transfer event seen by Cluster. *Geophys. Res. Lett.* **31**, L11803. doi:10.1029/2004GL020134.

Sonnerup, B.U.Ö., Hasegawa, H., Teh, W.L., Hau, L.N.: 2006, Grad–Shafranov reconstruction: an overview. *J. Geophys. Res.* **111**, A09204. doi:10.1029/2006JA011717.

Webb, G.M., Hu, Q., Dasgupta, B., Zank, G.P.: 2010, Homotopy formulas for the magnetic vector potential and magnetic helicity: the Parker spiral interplanetary magnetic field and magnetic flux ropes. *J. Geophys. Res.* **115**, 10112. doi:10.1029/2010JA015513.

Wood, B.E., Rouillard, A.P., Möstl, C., Battams, K., Savani, N.P., Marubashi, K., Howard, R.A., Socker, D.G.: 2012, Connecting coronal mass ejections and magnetic clouds: a case study using an event from 22 June 2009. *Solar Phys.* **281**, 369 – 389. doi:10.1007/s11207-012-0036-3.

Solar Phys (2013) 284:167–178
DOI 10.1007/s11207-013-0256-1

Observable Effects of Interplanetary Coronal Mass Ejections on Ground Level Neutron Monitor Count Rates

J.J. Blanco · E. Catalán · M.A. Hidalgo · J. Medina · O. García · J. Rodríguez-Pacheco

Received: 31 March 2012 / Accepted: 11 February 2013 / Published online: 1 March 2013

Abstract In this work, non-recurrent Forbush decreases (FDs) triggered by the passage of shock-driving interplanetary coronal mass ejections (ICMEs) have been analyzed. Fifty-nine ICMEs have been studied, but only 25 % of them were associated to a FD. We find that shock-driving magnetic clouds (MCs) produce deeper FDs than shock-driving ejecta. This fact can be explained regarding the observed growing trends between decreases in neutron monitor (NM) count rate and MC/ejecta speed and its associated rigidity. MCs are faster and have higher associated rigidities than ejecta. Also the deceleration of ICMEs seems to be a cause for producing FDs, as can be inferred from the decreasing trend between NM count rate and deceleration. This probably implies that the interaction between the ICME traveling from the corona to the Earth and the solar wind can play an important role in producing deeper FDs. Finally, we conclude that ejecta without flux rope topology are the ones less effective in unchaining FDs.

Keywords ICME · Magnetic cloud · Ejecta · Forbush decrease

1. Introduction

Ground level neutron monitors (NMs) are able to monitor the galactic cosmic ray (GCR) fluxes arriving to the Earth surface with energies between 0.5 to 20 GeV (Simpson, 2000). The geographical location of a NM determines the minimum energy of GCRs that reach each

Flux-Rope Structure of Coronal Mass Ejections
Guest Editors: N. Gopalswamy, T. Nieves-Chinchilla, M. Hidalgo, J. Zhang, and P. Riley

J.J. Blanco (✉) · E. Catalán · M.A. Hidalgo · J. Medina · J. Rodríguez-Pacheco
Space Research Group, Physics Department, Alcalá University, Ctra. Madrid-Barcelona km 33.600, 28871, Alcalá de Henares (Madrid), Spain
e-mail: juanjo.blanco@uah.es

O. García
Space Research Group, Computing Engineering Department, Alcalá University, Ctra. Madrid-Barcelona km 33.600, 28871, Alcalá de Henares (Madrid), Spain

station. This is traditionally quantified by the geomagnetic cutoff expressed in GV. Particles with less magnetic rigidity than the NM geomagnetic cutoff cannot reach the monitor. The NM count rate can be strongly affected by solar flares (Firoz *et al.*, 2011), coronal mass ejections (CMEs) (Gopalswamy *et al.*, 2012) and solar wind structures such as interplanetary coronal mass ejections (ICMEs) (Jordan *et al.*, 2011), interplanetary shocks (Cane, Richardson, and von Rosenvinge, 1994), and interaction regions (Richardson, Wibberenz, and Cane, 1996). While the first two can produce a significant increase in the NM count rate, known as ground level enhancement (GLE) (Shea and Smart, 2012), the other three may induce decreases in NM count rate called Fosbush decrease (FD). These FDs can be divided into recurrent or non-recurrent, depending on if they are observed along several solar rotations and are associated with corotating stream interaction regions (Richardson, Wibberenz, and Cane, 1996) or if they last for several days and are caused by transient events as interplanetary shocks or ICME passages (Cane, 2000 and Belov, 2008). In this work we focus on non-recurrent decreases and we will refer to them as FDs. A Forbush decrease (FD) is observed as a decrease in the cosmic ray intensity and it was first reported by Forbush (1937). It is characterized by a fast decrease, as much as 20 % in the order of hours, and a slow recovery phase that can last several days. As a first approach, it can be assumed that the decreases in the cosmic ray counts are due to changes in the propagation conditions at the surrounding region where the FD is observed. It can be said that FD is a local phenomenon restricted to a small region when compared with the whole heliosphere. These changes can be related to enhancements in solar wind speed, variation in the magnetic field topology, enhancements in the interplanetary magnetic field magnitude, and the presence of magnetic turbulence. ICMEs are large structures (around 0.1 AU) that propagate at high speeds (up to 2000 km s^{-1}) and produce shocks and magnetic turbulence in the background solar wind. Moreover, about one third of ICMEs show a closed magnetic topology defined by a relatively strong magnetic field and a smooth field rotation which is usually known as magnetic cloud (MC) (Burlaga *et al.*, 1981; Lepping, Jones, and Burlaga, 1990). It is generally accepted that an ICME passage can produce decreases in the count rate of NMs (Cane, 2000; Ifedili, 2004; Papaioannou *et al.*, 2010). These decreases are short-term events with the decreasing phase lasting for about one to two days and the recovery phase over one week of duration.

During a shock-driving ICME passage, the shock may initiate a decrease in NM counts maintained along the sheath region, *i.e.*, the highly turbulent region between the shock and the ICME. This decrement can be steeper at leading edge of the ICME. This scenario is path dependent. This means that depending on the trajectory of the spacecraft or the Earth through the shock/ICME structure one of these two effects might not be observed (Richardson and Cane, 2011).

The FD shape may vary from one event to another, especially if complex structures converge on the observation point. Jordan *et al.* (2011) point out that each FD has to be studied separately and that small-scale structures, between shock and ICME, can greatly affect the FD shape and question the two-step FD picture.

To answer the question "do all the CMEs have a flux rope structure?" we proposed to analyze a list of 59 shock-driving ICMEs extracted from Gopalswamy *et al.* (2010) during Solar Cycle 23 during the Living With a Star Coordinate Data Analysis Workshop hosted in San Diego (2010) and Alcalá (2011). This subset (these 59 events) was selected using a CME source region criterion (E15° $\leq$ source longitude $\leq$ W15°). This roughly implies that only CMEs from the central solar disk region were considered. Although the main goal in this workshop was the study of the magnetic structures observed into ICMEs, we investigated the role of these structures in the propagation of cosmic rays, especially during their arrival at Earth.

In this work we analyze the effect of the ICME passage on Oulu NM station count rates with the goal to study which part of an ICME, *i.e.*, shock, MC or flux rope, magnetic field magnitude and induced turbulence plays the most important role in producing observable FDs.

2. Data Analysis

The 59 shock-driving ICMEs selected from the list in Gopalswamy *et al.* (2010) has been studied from January 1997 to September 2006. In 24 of them, clear signatures of MC were found. We considered that an MC has been detected when the solar wind follows the Burlaga criteria (Burlaga *et al.*, 1981; Lepping, Jones, and Burlaga, 1990), *i.e.* low temperature, smooth magnetic field rotation combined with intense magnetic field, and the magnetic field can be fitted with Hidalgo's model (Hidalgo and Nieves-Chinchilla, 2012). The other 35 events did not show clear evidence of an MC, but a depression in solar wind proton temperature is observed with low plasma beta. Generally speaking, we named them ejecta (Ej). If the magnetic field within the Ej is organized as a flux rope that can be fitted by Hidalgo's model, then this Ej is cataloged as ejecta plus (Ej+), and ejecta minus (Ej−) in the opposite case. The ICME pool was separated into MC (24), Ej+ (23) and Ej− (12). The details of this classification can be found in Hidalgo, Nieves-Chinchilla, and Blanco (2013).

Key parameters with a time resolution of 92 s from the *Solar Wind Experiment* (SWE) (Ogilvie *et al.*, 1995), 1 min time resolution data from the *Magnetic Field Instrument* (FMI) (Lepping *et al.*, 1995) on board the *Wind* spacecraft, 64 s time resolution data from the *Solar Wind Electron, Proton, and Alpha Monitor* (SWEPAM) (McComas *et al.*, 1998), and 4-min resolution data from the magnetic field experiment (MAG) (Smith *et al.*, 1998) on board ACE spacecraft have been used. Data have been retrieved from the CDAWeb web page. In this work, it is assumed that an FD is observed when the NM count rate decreases more than 3 % below the GCR background measured before the shock arrival. Because of its relative low geomagnetic cutoff (0.81 GV), cosmic rays arriving with energies higher than some hundreds of MeV are detected by the Oulu (Finland) NM. Counts of 5 min of time resolution from Oulu have been used (Kananen *et al.*, 1991). This station is located at 65.05°N, 25.47°E and at 15 m above sea level. The monitor is made up by 9 NM-64 tubes. The data from this station have been collected from the Neutron Monitor Database (NMDB) (Mavromichalaki *et al.*, 2011) that integrates the readings of many different NM stations located mainly in Europe and Asia. The high-count cadence lets us perform comparable observations with measurements acquired by space-borne instruments with similar temporal resolution to the one used in our analysis of MC magnetic structure. Although using 5-min NM data is not the standard approach to study FDs, where hourly averaged measurements are commonly used (*e.g.* Cane, 2000; Usoskin *et al.*, 2008; Papaioannou *et al.*, 2010; Richardson and Cane, 2011), this high-count cadence is required to make a direct comparison between the results given by Hidalgo's model, *i.e.* MC and/or Ej+ existence and limits, and the role of MCs, Ej+ and Ej− on the depth of FDs.

Only 15 ICMEs from the selected sample of 59 triggered the detection of an FD in the Oulu NM. Eight of them were MC and other six Ej+. Only one Ej− was able to induce an observable FD at Oulu. The latter Ej was preceded by a strong interplanetary shock. It is clear that flux ropes (MC or Ej+) within ICMEs play a crucial role in producing FD (94 % of FD associated with flux ropes). The decrease percentage of the resulting FD ranged between 5.2 % and 26.1 %, those related to MCs being deeper (Table 1). The transit time, *i.e.* the time that it takes a CME to arrive at Earth, has been calculated using the onset times from the

Table 1 ICME associated with FD. The columns give the year, time interval between the MC nose and its rear as estimated by Hidalgo's model, CME transit time, magnetic rigidity cut off associated with the flux rope, FD percentage, and FD location within the ICME. The asterisk in MC* means a complex event where two consecutive MCs were observed but the FD is not resolved into two separate events.

Year	ICME interval (doy)	Type	Travel time (day)	Rigidity (GV)	FD (%)	FD location
1998	124.442 → 125.234	Ej−	1.95	167	7.5	Ejecta
1999	178.942 → 179.108	Ej+	3.38	27	6.24	Sheath
2000	197.911 → 198.298	MC	1.46	419	16.00	Ejecta
2000	261.221 → 262.599	MC	1.77	283	8.86	Ejecta
2000	311.964 → 312.74	MC	3.2	215	6.96	Ejecta
2000	332.458 → 333.131	Ej+	3.23	80	9.01	behind Ej+
2001	102.367 → 103.279	MC*	2.14	139	12.63	Ejecta
2001	118.892 → 119.662	MC	2.37	106	8.17	Sheath
2001	285.205 → 285.360	Ej+	2.73	24	7.67	Sheath
2003	302.554 → 303.151	MC*	1.07	162	26.13	Ejecta
2004	22.558 → 23.282	Ej+	2.55	142	10.09	Sheath
2004	315.195 → 315.705	MC*	4.11	188	12.42	Sheath
2005	135.464 → 136.004	MC	1.75	354	11.89	Sheath
2005	149.495 → 149.638	Ej+	2.6	27	6.10	Ejecta
2006	232.630 → 233.625	Ej+	3.94	80	5.24	Ejecta

LASCO CME list (http://cdaw.gsfc.nasa.gov/CME_list/) and the ICME *in-situ* times using measurements from instruments on board the *Wind* and ACE spacecraft. From Table 1, it seems that the shorter the travel time, the deeper the FD. This will be discussed in the next section. In our list of 15 ICMEs connected to CMEs from the central region of solar disk, the deepest GCR decrease rate was measured in eight events during the ejecta's passage, in six events during the ICME sheath's and one behind the ejecta's passage. Only in three events, 12 April 2001, 29 October 2003 and 10 November 2004, the FDs could have been affected by other structures. The former two during their recovery phases, because of the presence of a subsequent interaction region and a later ICME, respectively, and the third during its main phase due to a previous ICME which reduced the GCR level before the 10 November MC's arrival. Five events produced decreases higher than 10 %. All of them were ICMEs with MC and in three of them some interaction with previous or subsequent structures might have happened, as has been explained above.

For every event, the shock strength, the Ej size, its mean speed and mean magnetic field have been computed. As an example, the analysis of two events is shown in detail. On 15 May 2005 a shock arrived at *Wind*'s location ($X_{GSE} = 200\ R_E$, near L1) followed by a sheath and three hours later by an ICME with an MC structure. The ICME front is marked by a jump higher than 30 nT and a fast field rotation (less than 4 h) characterized by an elevated thermal speed. This region coincides with the deepest point in the FD measured by the Oulu NM. At the MC nose, *i.e.* when the field begins to rotate due to the MC passage, a magnetic field intensity of 55 nT and a speed of 990 km s^{-1} were observed. Under these conditions, the ICME reached the Earth 23 min later. The arrival of the shock at Earth was observed in coincidence with a steep decrease in the counts measured at Oulu, triggering a clear FD (Figure 1, bottom panel, where 5-min Oulu NM data have been smoothed using a

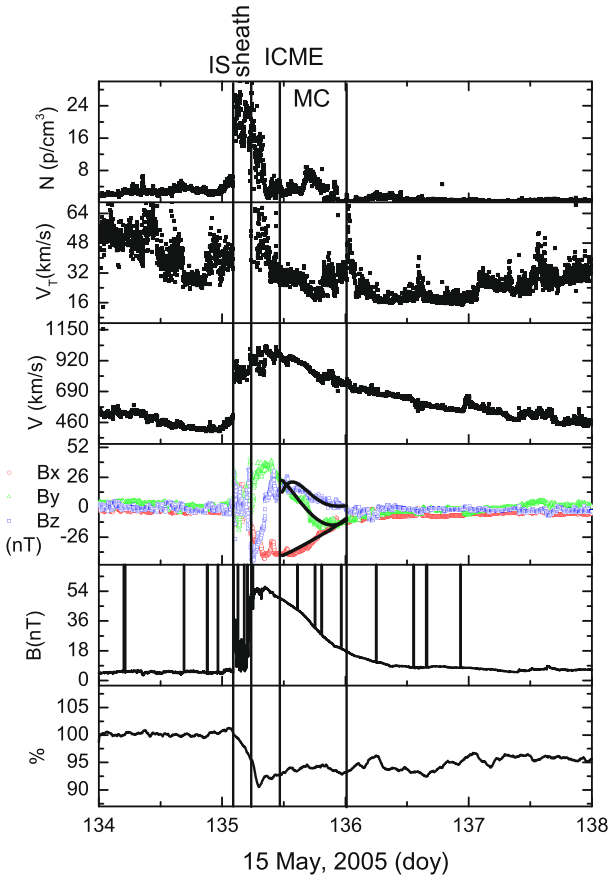

Figure 1 Example of an ICME with an MC. Data from the *Wind* spacecraft and the Oulu neutron monitor have been used.

1-h running average). At ICME front arrival, the FD slope changed, clearly being the second step in this particular FD. In the figure, divided into panels, we show from top to bottom:

i) solar wind density,
ii) thermal velocity,
iii) solar wind speed,
iv) magnetic field components in GSE system (red circles B_x, green triangles B_y and blue squares B_z) over plotted with continuous lines, which are Hidalgo's model results,
v) the magnetic field strength, and
vi) the percentage of the normalized NM count rate.

The decrease was even steeper when the ICME leading edge hit the Earth. The FD's deepest point was measured within the fast rotating region before the MC nose arrival, and a soft recovery phase started during the MC passage (marked with vertical lines in Figure 1). The FD lasted more than five days until the previous neutron monitor count rate was recovered (doy 140, not shown in Figure 1). The MC showed a well-organized magnetic flux rope. This is clear when comparing to the over plotted continuous lines which show Hidalgo's model results. During this FD, the count rate dropped to 12 % with respect to the GCR background before the shock arrival, following, in our opinion, a two-step FD shape. This event has been analyzed by Dasso *et al.* (2009) in terms of the magnetospheric response. They argue for the

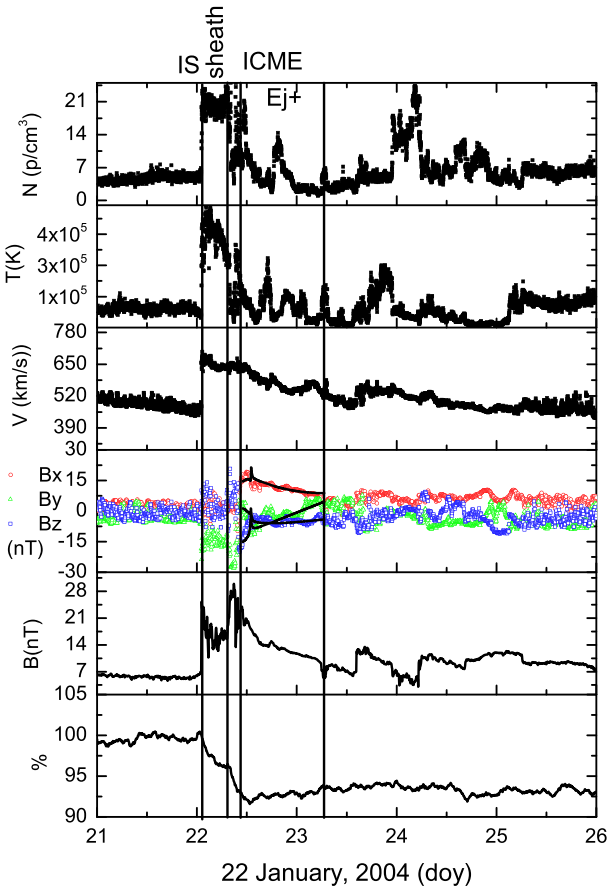

Figure 2 Example of an ICME with Ej+. Data from the ACE spacecraft and the Oulu neutron monitor have been used.

presence of two consecutive MCs. The first one in coincidence with the fast-rotating region mentioned above and the second one with the MC presented in Figure 1. In our opinion, the temperature is too high to be sure that such a rotation may result from a small MC.

On 22 January 2004 a shock arrived at *Wind*'s location in (−210, 42, −2) Earth radii in GSE coordinate system, *i.e.* on the night side of the Earth. To avoid possible interactions with the magnetotail, data from the ACE spacecraft have been used to analyze this event. ACE was located at L1. This event is shown in Figure 2. Plots are organized as in Figure 1. There is one difference though. In the second panel from the top the proton temperature appears instead of the thermal speed. As in Figure 1, the Oulu count rate has been smoothed using a running average of 1 h to get a clearer structure of the FD. The FD started with the interplanetary shock arrival. During the sheath between the shock and the ICME front the NM counts were reduced by 4 %. Six hours later, when the ICME arrived, a change in the FD slope was detected. Two hours later the flux rope nose, confirmed by Hidalgo's model (continuous lines in Figure 2), was observed. The FD minimum and the beginning of the recovery phase occurred within the flux rope. The Ej were characterized by a mean magnetic field of about 10 nT with a smooth field rotation that lasted almost one day and a solar wind speed of 600 km s^{-1} in the low solar wind temperature region. As for the FD shape, it showed a two-step behavior with a harder slope in coincidence with the ICME leading edge passage. The recovery phase was slower than that seen in Figure 1, lasting up

to 10 days. The neutron monitor registered a decrease of 10 % of its counts compared to the GCR background on 21 January.

3. Results

The FD depth can be influenced by various ICME properties. One of the possible causes of an FD can be the size of the magnetic structure and the intensity of its magnetic field. Cane (1993) found a clear correlation between the percentage decrease of GCRs and the magnetic field strength in the ICME. The effect of these two elements can be evaluated by the expression $R = Brc$, which gives the magnetic rigidity in GV, B being the magnetic field intensity, r the particle gyroradii and c the light speed. We assume the value of B to be the mean value inside the ICME and r the size of the ICME section because the particle gyroradius has to be in the order of this size to be affected in its normal movement. In a recent paper, Kubo and Shimazu (2010) analyzed the effect of a finite Larmor radius on GCR penetration into flux ropes, concluding that it can be relevant at 1 AU. The mean B and the structure size have been computed using Hidalgo's model both for MCs and Ej+. As for the only Ej−, its size was assumed to be equal to the size of the ICME. The resulting plot of the FD minimum *versus* the estimated rigidity is presented in Figure 3a. Red circles represent MCs, blue triangles Ej+, and the green square Ej−. The growing trend of GCR count rate percentage with rigidity is clear, ICMEs with MC being more effective than Ej+ and Ej− in producing FDs. This can be understood, as larger MC sizes and more intense magnetic fields imply higher associated rigidity. One of the MCs (the 29 October 2003 event) showed a percentage decrease higher than 25 %. Nevertheless, its rigidity was relatively low. This event had a sheath with a magnetic field as high as 50 nT and an MC mean field of only 12 nT. In this event, the role of the sheath seems to be more important than that of the MC in terms of reducing the Oulu NM count rate.

It can be argued that the shocks observed ahead of some ICMEs play an important role in the FD depth themselves, but what we observed in Figure 3b is that those shocks associated with MCs are related to deeper FD. The shock strength is defined here as the ratio of the difference between the downward and the upward magnetic field at shock passage. It is important to point out that the shock driven by the Ej− (green square) was the third more intense, but it only caused a modest FD of 7 %. The conclusion that can be extracted from Figure 3 is that an MC strengthens the shock effect on the neutron monitor count rate. A red continuous line and a blue dashed line are the linear fits to MCs and Ej+ with slopes of 13.6 and 4.7 and Pearson's coefficients (Pc) of 0.76 and 0.66, respectively. The shock triggers the FD but the MC makes it deeper. This result is in agreement with Richardson and Cane (2011) concerning the role that MCs may play in producing FD. Also the observed relationship between Ej rigidity and FDs could support the argument of MCs being closed magnetic structures.

Another important parameter that deserves to be studied focusing on the causes of FDs is the speed of the ICME. There are three different speeds that can be associated with the ICME propagation. We have the CME emergence speed that is calculated from coronagraph images, the ICME transit speed that can be estimated from the CME onset time and the ICME arrival time at the spacecraft location and the solar wind speed measured within the ICME. A common conclusion inferred from the three speeds is that the faster CME or ICME, the deeper the FD (Figure 4). This result agrees with those by Richardson and Cane (2011) who used a pool of more than 300 ICMEs. As they affirm in their paper, the dependence of the decrease on the CME/ICME/MC speed can be explained arguing that in faster-propagating

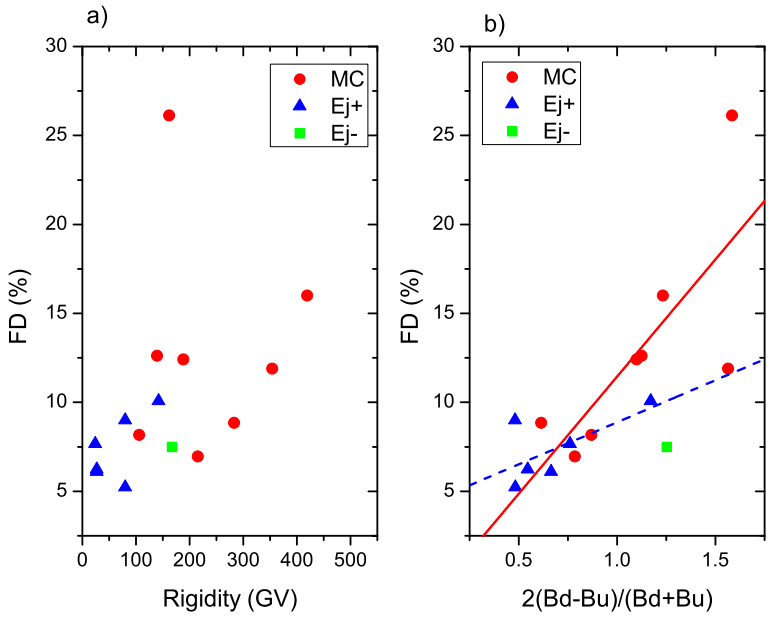

Figure 3 FD dependence on rigidity (a) and shock strength (b).

events GCRs have less time to fill up the closed magnetic structure of an MC. On the other hand, the range of values of the three speeds is different. The CME speed ranges between 300 and 3000 km s^{-1} (Figure 4a), the transit speed between 500 and 2000 km s^{-1} (Figure 4b), and the solar wind speed between 300 and 1300 km s^{-1} (Figure 4c). Again, MCs are, generally speaking, faster than Ej events. On the other hand, taking a closer look at Figure 4c, it is clear that Ej velocities are in a narrow range of 500 km s^{-1} (250 to 750 km s^{-1}) without a clear linear relationship (blue dashed line) with the associated FD ($Pc = 0.33$). Nevertheless, the FDs produced by MCs show a good linear correlation (red continuous line) and a clear growing trend with the MC speed at 1 AU ($Pc = 0.71$).

Non-recurrent FDs are observed by NMs at ground level as local phenomena related to solar wind conditions around Earth, given that most of them can be directly related to the passage of an ICME. No relationship of CME speed, transit speed and FD should be expected other than the dependence between these two velocities on the solar wind speed. Nevertheless, important variations in the speed from the CME onset to the ICME arrival at the Earth are depicted in Figure 4. This can be explained by assuming that an effective interaction between ICMEs and solar wind occurs during the ICME's travel in the interplanetary space (Vršnak, 2001). In almost all the events a deceleration is observed. This deceleration can be due to an effective kinetic energy exchange between the ICME and the solar wind. This exchange can produce intense shock waves and turbulence ahead (sheath) the ICME and therefore make the ICME able to change the propagation conditions of GCRs with energies from hundreds to thousands of MeV. This is expected for propagating diffusive barriers (Wibberenz *et al.*, 1998). The ICME acceleration can be estimated from the difference between the solar wind speed and the CME speed divided by the travel time. In Figure 5, this acceleration is plotted against the percentage decrease of GCRs displaying a clear negative slope. Those ICMEs that are more intensively decelerated produce deeper FDs. Only two of 15 ICMEs show a positive acceleration. Although acceleration could produce an effective

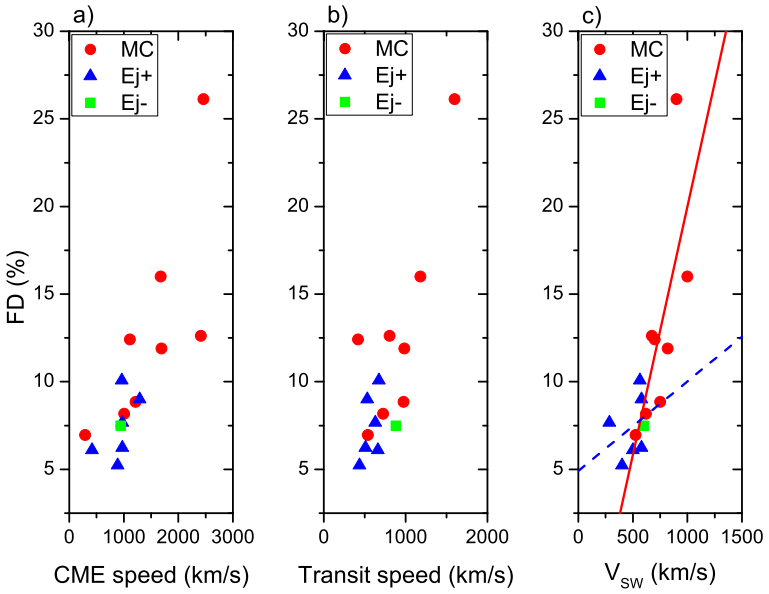

Figure 4 FD dependence on CME speed (a), transit speed (b) and solar wind speed measured during an ICME passage (c).

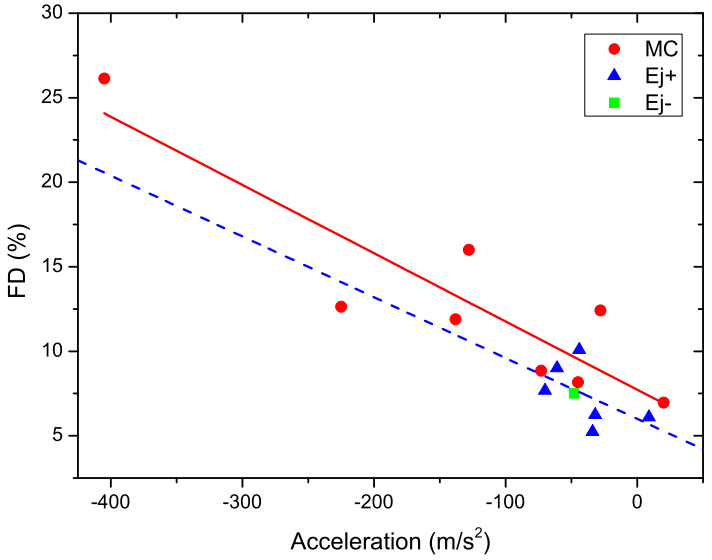

Figure 5 FD dependence on ICME acceleration. This acceleration has been estimated by means of the expression $(V_{SW} - V_{CME}) \times$ ICME travel time.

interaction with the solar wind, two events provide little statistical evidence to affirm that a change in the acceleration slope appears. Moreover, this cannot be considered as a conclusive result because of the uncertainty in CMEs speed estimations. MCs and Ej+ events have

similar slopes (red continuous and blue dashed lines, respectively) of 0.04 and 0.035 but different *Pc*s, −0.89 for MCs and −0.53 for Ej+. MCs are more efficiently decelerated. This may be due to their larger size, more intense magnetic field and higher speed. Moreover, the FD depth is better correlated with MC acceleration than with any other physical quantities considered in this work (rigidity, shock strength, and speed). The deceleration/acceleration of ICMEs plays a very important role in the development of FDs. Intense accelerations imply strong interaction between ICME and solar wind. This interaction drives stronger shocks and makes the solar wind more turbulent. These two features greatly affect the propagation of cosmic rays in the range of the detectable energies by the neutron monitors.

4. Conclusions

The role of CMEs originating from near the center of the solar disk and their associated ICME on FDs detected by the Oulu NM have been analyzed. Cosmic rays with energies higher than a few hundreds of MeV are the main component of the energetic particle population detected by this NM. A pool of 59 shock-driving ICMEs has been classified into three groups, MC (24), ejecta with flux rope (23) and ejecta without apparent flux rope structure (12). Only around 25 % of them were able to produce decreases in the NM count rate higher than 3 %, eight MC, six Ej+ and one Ej−. This result seems to show that an isolated shock is rarely able to produce FD. Moreover, similar shocks may induce stronger FDs if they are driven by an MC or an Ej+. Therefore a closed magnetic structure such as MC or flux rope strengthens the effect of shocks on FDs. Richardson and Cane (2011) reached the same conclusion.

The rigidity associated with MCs and Ej events affects the CGR propagation into ICMEs. This rigidity has been compared with the GCR decreases concluding that higher rigidities are related to deeper FDs. The higher rigidities correspond to MCs because they are larger and their magnetic fields are more intense than those of the Ej events.

The shock strength and its relationship with FD have also been analyzed. Stronger shocks produce higher decreases in the GCR count rate, but when considering similar shocks, those driven by MC are more effective (almost three times more effective) in shielding the Earth from the arriving GCRs. This can be explained assuming that MCs interact more strongly with the underlying solar wind than Ej events driving turbulence into the sheath region and therefore, affecting in a more efficient way the propagation of the GCRs into the ICME.

Another analyzed aspect is the effect of ICME speed on GCR count rates. The observations show that faster structures (MC or Ej) are more efficient to produce FDs, and at least in the sample analyzed, MCs are faster than Ej events. Moreover, FDs associated with ejecta show an increasing trend with CME speed and transit speed but the relation is not so clear with their measured speed at 1 AU ($Pc = 0.33$). As for MCs these three velocities show similar increasing trends with the FD depth and a good correlation between MC speed and FD depth ($Pc = 0.71$). This result is also in agreement with the conclusion by Richardson and Cane (2011).

Finally, we have observed that the deceleration/acceleration of ICME between the Sun and the Earth can play an important role in the development of FDs. Higher decelerations induce deeper FDs. This can be explained in terms of effective energy exchange between the ICME and solar wind. This interaction can lead to the formation of a stronger shock ahead of the ICME. MCs decelerate stronger. Closed magnetic structures as MCs with stronger magnetic field and larger size than those observed in Ej events seem to be more effective in interacting with the solar wind. Moreover, we find the best correlation between deeper

FDs and the MC acceleration. The linear correlation gives a *Pc* equal to −0.89. This value implies that the interaction between MC and solar wind is very important in the shielding effect that an ICME has over GCRs.

Richardson and Cane (2011) propose that MCs are effective in excluding GCRs because they are closed magnetic structures. Our results support this conclusion but also the importance of MC/solar wind interaction on GCR decreases as can be inferred from the clear relationship between MC acceleration and GCR count rates.

Hidalgo, Nieves-Chinchilla, and Blanco (2013) have found that most of the ejecta from the initial list of 59 shock-driving ICMEs showed axes close to the Sun–Earth line. This implies that the passage of the spacecraft through the corresponding ejecta event was probably by its flank and this may be seen as support for the idea of MCs and Ej events being observed at different parts of a flux rope. According to this picture and the results showed in this work we conclude that the effect of shock-driving ICMEs on GCR count rates may also depend on which region of the flux rope hits the Earth.

In conclusion, shock-driving MCs produce deeper FDs than Ej+ and Ej− events, because the MCs have higher rigidity, higher speed, and higher deceleration, and they interact more effectively with the solar wind.

Acknowledgements We acknowledge the NMDB database (www.nmdb.eu), founded under the European Union's FP7 programme (contract no. 213007) for providing data, especially to Oulu neutron monitor station and the Sodankyla Geophysical Observatory of the University of Oulu for the operation of the monitor, also to the MFI and SWE instruments on board Wind and Mag and SWEPAM on board ACE and Coordinated Data Analysis Web (CDAWeb) for the use of data. This work has been supported under the grants: JCCM PPII10-0150-6529 and AYA2011-29727-C02-01. The authors in particular wish to thank the Parque Científico y Tecnológico de Guadalajara (Guadalab) team.

References

Belov, A.V.: 2008, In: Gopalswamy, N., Webb, D. (eds.) *Universal Heliophysical Processes. Proc. IAU Symp.* **257**, Cambridge Univ. Press, Cambridge, 439. doi:10.1017/S1743921309029676

Burlaga, L.F., Sittler, E., Mariani, F., Schwenn, R.: 1981, *J. Geophys. Res.* **86**, 6.

Cane, H.V.: 1993, *J. Geophys. Res.* **98**, 3509.

Cane, H.V.: 2000, *Space Sci. Rev.* **93**, 55.

Cane, H.V., Richardson, I.G., von Rosenvinge, T.T.: 1994, *J. Geophys. Res.* **99**, 21429.

Dasso, S., Mandrini, C.H., Schmieder, B., Cremades, H., Cid, C., Cerrato, Y., Saiz, E., Démoulin, P., Zhukov, A.N., Rodríguez, L., Aran, A., Menvielle, M., Poedts, S.: 2009, *J. Geophys. Res.* **114**, A02109.

Firoz, K.A., Moon, Y.-J., Cho, K.-S., Hwang, J., Park, Y.D., Kudela, K., Dorman, L.I.: 2011, *J. Geophys. Res.* **116**, A04101.

Forbush, S.E.: 1937, *Phys. Rev.* **51**, 1108.

Gopalswamy, N., Xie, H., Makela, P., Akiyama, S., Yashiro, S., Kaiser, M.L., Howard, R.A., Bougeret, J.-L.: 2010, *Astrophys. J.* **710**, 1111.

Gopalswamy, N., Xie, H., Yashiro, S., Akiyama, S., Makela, P., Usoskin, I.G.: 2012, *Space Sci. Rev.* **171**, 23.

Hidalgo, M.A., Nieves-Chinchilla, T.: 2012, *Astrophys. J.* **748**, 109.

Hidalgo, M.A., Nieves-Chinchilla, T., Blanco, J.J.: 2013, *Solar Phys.*, in this issue. doi:10.1007/s11207-012-0191-6.

Ifedili, S.O.: 2004, *J. Geophys. Res.* **109**, A02117.

Jordan, A.P., Spence, H.E., Blake, J.B., Shaul, D.N.A.: 2011, *J. Geophys. Res.* **116**, A11103.

Kananen, H., Tanskanen, P.J., Gentile, L.C., Shea, M.A., Smart, D.F.: 1991, In: *Proc. 22nd ICRC* **3**, 145.

Kubo, Y., Shimazu, H.: 2010, *Astrophys. J.* **720**, 853.

Lepping, R.-P., Jones, J.A., Burlaga, L.F.: 1990, *J. Geophys. Res.* **95**, 11957.

Lepping, R.P., Acuna, M., Burlaga, L., Farrell, W., Slavin, J., Schatten, K., Mariani, F., Ness, N., Neubauer, F., Whang, Y.C., Byrnes, J., Kennon, R., Panetta, P., Scheifele, J., Worley, E.: 1995, *Space Sci. Rev.* **71**, 207.

Mavromichalaki, H., Papaioannou, A., Plainaki, C., Sarlanis, C., Souvatzoglou, G., Gerontidou, M., Papailiou, M., Eroshenko, E., Belov, A.A., Yanke, V., Fluckiger, E.O., Butikofer, R., Parisi, M., Storini, M., Klein, K.-L., Fuller, N., Steigies, C.T., Rother, O.M., Heber, B., Wimmer-Schweingruber, R.F., Kudela, K., Strharsky, I., Langer, R., Usoskin, I., Ibragimov, A., Chilingaryan, A., Hovsepyan, G.A., Reymers, A., Yeghikyan, A., Kryakunova, O., Dryn, E., Nikolayevskiy, M., Dorman, L., Pustilnik, L.: 2011, *Adv. Space Res.* **47**, 2210.

McComas, D.J., Bame, S.J., Barker, P., Feldman, W.C., Phillips, J.L., Riley, P., Griffee, J.W.: 1998, *Space Sci. Rev.* **86**, 563.

Ogilvie, K.W., Chorney, D.J., Fitzenreiter, R.J., Hunsaker, F., Keller, J., Lobell, J., Miller, G., Scudder, J.D., Sittler, E.C. Jr., Torbert, R.B., Bodet, D., Needell, G., Lazarus, A.J., Steinberg, J.T., Tappan, J.H., Mavretic, A., Gergin, E.: 1995, *Space Sci. Rev.* **71**, 55.

Papaioannou, A., Malandraki, O., Belov, A., Skoug, R., Mavromichalaki, H., Eroshenko, E., Abunin, A.S., Lepri, S.: 2010, *Solar Phys.* **266**, 181.

Richardson, I.G., Cane, H.: 2011, *Solar Phys.* **270**, 609.

Richardson, I.G., Wibberenz, G., Cane, H.V.: 1996, *J. Geophys. Res.* **101**, 13483.

Shea, M.A., Smart, D.F.: 2012, *Space Sci. Rev.* **171**, 161.

Simpson, J.A.: 2000, *Space Sci. Rev.* **93**, 11.

Smith, C.W., L'Heureux, J., Ness, N.F., Acuña, M.H., Burlaga, L.F., Scheifele, J.: 1998, *Space Sci. Rev.* **86**, 613.

Usoskin, I.G., Braun, I., Gladysheva, O.G., Horandel, J.R., Jamsen, T., Kovaltsov, G.A., Starodubtsev, S.A.: 2008, *J. Geophys. Res.* **113**, A07102.

Vršnak, B.: 2001, *Solar Phys.* **202**, 173.

Wibberenz, G., Le Roux, J.A., Potgieter, M.S., Bieber, J.W.: 1998, *Space Sci. Rev.* **83**, 309.

Solar Phys (2013) 284:5–15
DOI 10.1007/s11207-013-0248-1

Post-Eruption Arcades and Interplanetary Coronal Mass Ejections

S. Yashiro · N. Gopalswamy · P. Mäkelä · S. Akiyama

Received: 27 July 2012 / Accepted: 28 January 2013 / Published online: 14 February 2013

Abstract We compare the temporal and spatial properties of posteruption arcades (PEAs) associated with coronal mass ejections (CMEs) at the Sun that end up as magnetic cloud (MC) and non-MC events in the solar wind. We investigate the length, width, area, tilt angle, and formation time of the PEAs associated with 22 MC and 29 non-MC events and we find no difference between the two populations. According to current ideas on the relation between flares and CMEs, the PEA is formed together with the CME flux-rope structure by magnetic reconnection. Our results indicate that at the Sun flux ropes form during CMEs in association with both MC and non-MC events; however, for non-MC events the flux-rope structure is not observed in the interplanetary space because of the geometry of the observation, *i.e.* the location of the spacecraft when the structure passes through it.

Keywords Flares · Coronal mass ejections · Posteruption arcades · Flux rope · Magnetic cloud

Flux-Rope Structure of Coronal Mass Ejections
Guest Editors: N. Gopalswamy, T. Nieves-Chinchilla, M. Hidalgo, J. Zhang, and P. Riley

S. Yashiro · P. Mäkelä · S. Akiyama
The Catholic University of America, Washington, DC 20064, USA

S. Yashiro (✉) · N. Gopalswamy · P. Mäkelä · S. Akiyama
NASA Goddard Space Flight Center, Greenbelt, MD 20771, USA
e-mail: seiji.yashiro@nasa.gov

N. Gopalswamy
e-mail: nat.gopalswamy@nasa.gov

P. Mäkelä
e-mail: pertti.makela@nasa.gov

S. Akiyama
e-mail: sachiko.akiyama@nasa.gov

1. Introduction

Two-ribbon flares are characterized by a pair of bright ribbons observed in Hα and ultraviolet (UV) images. The ribbons are located on either side of a magnetic polarity inversion line and they separate from each other as the flare progresses. Two-ribbon flares are often associated with filament eruptions and coronal mass ejections (CMEs). After the launch of the filament, long-lived arcades are formed connecting the two ribbons across the polarity inversion line. The emerged assembly of arches is called a posteruption arcade (PEA). The PEAs are observed at multiple wavelengths and are known also as long-duration (or decay) events (LDEs; Pallavicini, Serio, and Vaiana, 1977) in X-ray observations. The erupting filament becomes the core of the associated CME (Webb and Hundhausen, 1987; Gopalswamy *et al.*, 2003), thus PEAs are considered as surface signatures of CMEs (Tripathi, Bothmer, and Cremades, 2004).

The CSHKP magnetic reconnection model is widely accepted as a model of two-ribbon flares and CME onsets. The acronym "CSHKP" stands for the authors of this model, Carmichael (1964), Sturrock (1966), Hirayama (1974), Kopp and Pneuman (1976). This model suggests that during a filament eruption, a current sheet is formed and magnetic reconnection occurs below the erupting filament. The reconnected field lines arching downward and connected to the solar surface form the PEA, while the upward reconnected field lines envelop the erupting filament and form the flux-rope structure (see *e.g.*, Longcope and Magara, 2004; Longcope and Beveridge, 2007). This model explains well the characteristics of two-ribbon flares: the separation of flare ribbons, the development of the PEAs, and their association with filament eruptions and CMEs (Bruzek, 1964; Sheeley *et al.*, 1975; Kahler, 1977; Munro *et al.*, 1979; Harra-Murnion *et al.*, 1998; Yurchyshyn, 2008). Hα flare ribbons form at the feet of the PEAs at the chromospheric level. At the coronal level, the PEAs are observed as a collection of loops in X-rays, EUV, and even microwaves (*e.g.*, Hanaoka *et al.*, 1994; McAllister *et al.*, 1996; Gopalswamy *et al.*, 1999, 2003; Tripathi, Bothmer, and Cremades, 2004). The model is also supported by a relationship between the reconnected magnetic flux during flares and the magnetic flux of MCs observed near Earth, as reported by Qiu *et al.* (2007).

There is a general consensus that large PEAs appearing near the central meridian of the Sun are good indicators of geoeffective CMEs. The Bastille Day flare on 14 July 2000, with a bright EUV arcade (see Figure 1a, see also Aschwanden and Alexander, 2001), caused an intense geomagnetic storm with a minimum *Dst* of -301 nT. During an earlier event on 14 April 1994, when coronographic observations of CMEs were more limited, the *Soft X-ray Telescope* on the *Yohkoh* satellite observed a giant PEA that extended 150° in longitude. An Earth-directed CME was expected and an alert of a geomagnetic storm was issued (McAllister *et al.*, 1996). Three days after the giant PEA, an intense geomagnetic storm with a minimum *Dst* of -201 nT occurred. We should note that the X-ray intensity of the event was very low; the *X-ray Sensor* on the *Geostationary Operational Environmental Satellites* (GOES) did not detect any significant X-ray enhancement. This case showed that a large-scale PEA is a good indicator of CMEs arriving at Earth and causing geomagnetic storms. The *Extreme-ultraviolet Imaging Telescope* (EIT) on board the *Solar and Heliospheric Observatory* (SOHO) mission started observing PEAs routinely since 1996 and helped to identify the solar sources of CMEs observed by the *Large Angle and Spectrometric Coronagraph* (LASCO; Brueckner *et al.*, 1995).

Two Coordinated Data Analysis workshops (CDAWs) were held in 2010 and 2011 to address the question: Do all CMEs have a flux-rope structure? This question derives from the fact that only a fraction of the interplanetary CMEs (ICMEs; *i.e.* the plasma and magnetic field structure in interplanetary space corresponding to CMEs from the Sun) are observed

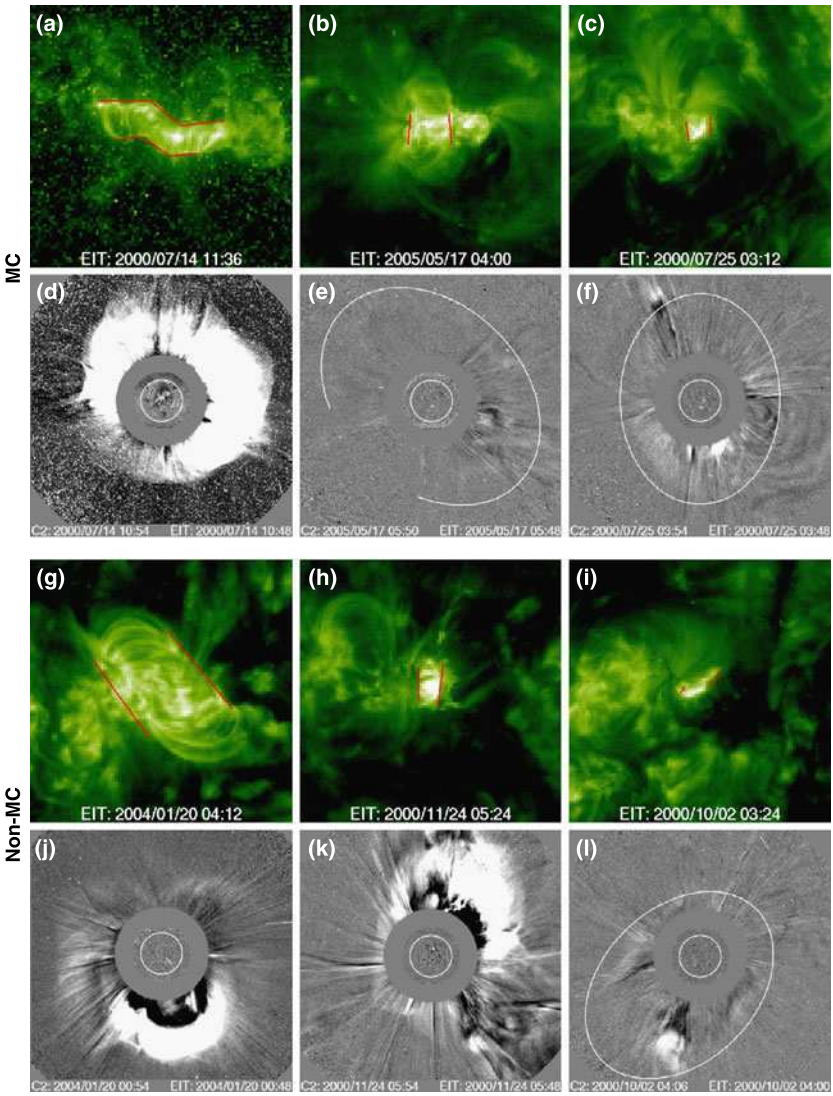

Figure 1 PEAs observed by EIT (first and third rows) and the associated CMEs observed by LASCO (second and fourth rows). The top two rows show the solar sources of MC events, while the bottom two rows are for non-MC events.

as flux ropes or magnetic clouds at 1 AU (MCs; Burlaga *et al.*, 1981). ICMEs without an observable flux-rope structure are called "ejecta" or non-MCs.

It has been suggested that non-MCs may have a flux-rope structure but that it may not be observed in single-point measurements at 1 AU if the observing spacecraft passes through the periphery of the ICME (Gopalswamy, 2006). If this were the case, one does not expect any difference between PEAs associated with MCs and non-MCs at the Sun. Such a view has been supported by the fact that a flux rope can be fit to all white-light in the CDAW list near the Sun, irrespective of their 1-AU manifestation as MCs or non-MCs (Xie, Gopalswamy, and St. Cyr, 2013). As CMEs propagate away from the Sun, the trajectories of those

CMEs associated with non-MCs become non radial (Xie, Gopalswamy, and St. Cyr, 2013; Kim *et al.*, 2013) due to deflection by nearby coronal holes (Mäkelä *et al.*, 2013). Other possibilities are CME-CME interactions leading to complex ejecta (Burlaga, Plunkett, and St. Cyr, 2002) or inherent non flux-rope structure at the Sun (Gosling, 1990). Gopalswamy *et al.* (2013) have shown that both MCs and non-MCs have charge-state enhancements at 1 AU, which is an indication of flare reconnection and flux-rope formation at the Sun, thus ruling out the non flux-rope structure suggested by Gosling (1990).

If CMEs resulting in non-MCs do not have a flux-rope structure and if the flux-rope structure of the MC-associated CMEs is formed by magnetic reconnection, as suggested by the CSHKP model, we should be able to find differences between the MC-associated and the non-MC-associated PEAs. The aim of this paper is to examine this possibility by investigating the differences of the PEAs observed in EUV between the two populations.

2. Data Set and Analysis

The data set used in this study consists of the CDAW events selected from the list of shock-driving ICMEs listed in Gopalswamy *et al.* (2010). From the more than 200 events listed in Gopalswamy *et al.* (2010), 59 events originating from the disk center ($\pm 15^\circ$ from the central meridian) were selected to form the CDAW list. If one assumes that all CMEs have a flux-rope structure then many of the IP drivers at 1 AU should be MCs because solar eruptions launched from disk center are expected to hit Earth head-on. However, only 24 events were MCs and the remaining 35 events were classified as ejecta or non-MCs. Comparisons of these two populations were the suggested agenda of the workshops.

A careful analysis of the selected 59 events was carried out by the meeting participants during and after workshops. It turned out that the revised solar source of five events (No. 6, 11, 12, 22, and 55) did not meet the original location criteria (for details see Gopalswamy *et al.*, 2013). Therefore, the number of events in the CDAW list was reduced to 54. In this study we have excluded two events (No. 1 and 58) because of EIT data gaps. We have also excluded one event (No. 40) because no flare brightening was identified after the filament eruption.

Table 1 summarizes the properties of the 51 PEAs analyzed in our study. Note that the event numbers (column 1) are not sequential because we use the event numbers of the original 59 events. The ICME type is given in the column 2: MC for magnetic clouds and EJ (ejecta) for non-MC. General information on the solar sources are given in columns 3 – 7 (column 3: the flare date in yyyy/mm/dd format; column 4: the flare start time as hh:mm in UT; column 5: the flare location in the heliographic coordinates; column 6: the soft X-ray flare class; column 7: the CME speed in km s^{-1}). Columns 8 – 12 give the PEA information: the length, width, and size in Mm, the tilt angle in degree, and the PEA developing time in hours (see Section 3 for their definitions).

In 31 events, out of the 51 analyzed, we could see well-developed PEAs. Figure 1a shows a PEA observed during the so-called Bastille Day event on 14 July 2000 (No. 19). The X-ray class of the associated flare was X5.7 and the flare duration was 40 minutes. This event was associated with an Earth-directed CME which arrived at Earth 38 hours later as an MC. This event provides a good example of a bright, large PEA associated with an MC. Figure 1g shows another bright PEA but this one was associated with a non-MC (No. 47). The flare was an LDE flare (duration > 4 hours) with peak X-ray class C5.5. The flare occurred at S13W09 and was associated with a halo CME (see Figure 1j). Two days after the corresponding ICME was observed by the *Advanced Composition Explorer* (ACE). The ICME was classified as non-MC since no clear rotation of the magnetic field was observed.

Table 1 List of the CDAW events and the posteruption arcade parameters.

No.	ICME type[a]	Flare				CME speed [km s^{-1}]	Post-eruption arcade				
		Date	Time [UT]	Location	Class[b]		Length [Mm]	Width [Mm]	Size [Mm]	ϕ[c] [deg]	T[d] [hour]
02	MC	1997/05/12	04:42	N21W08	C1.3	464	77	67	65	83	12.1
03	EJ	1997/12/06	10:00	N45W10	EP	397	210	189	169	−45	13.9
04	EJ	1998/05/01	22:36	S18W05	M1.2	585	62	28	40	−68	1.0
05	EJ	1998/05/02	13:31	S15W15	X1.1	938	74	42	56	6	1.4
07	EJ	1998/11/04	07:13	N17W01	C1.6	523	135	159	145	−48	4.4
08	EJ	1998/11/09	17:03	N15W05	C2.5	325	59	103	75	−12	4.2
09	MC	1999/04/13	01:45	N16E00	B4.3	291	188	65	102	−32	2.3
10	EJ	1999/06/24	12:04	N29W13	C4.1	975	169	82	126	−37	3.7
13	EJ	1999/09/20	03:58	S20W05	EP	604	215	90	153	28	3.8
14	EJ	1999/10/17	23:22	S30E15	C1.2	144	50	50	52	89	2.4
15	EJ	2000/01/18	17:07	S19E11	M3.9	739	136	72	90	35	2.1
16	MC	2000/02/17	20:17	S29E07	M1.3	728	100	69	75	−84	1.5
17	EJ	2000/07/07	08:42	N17E10	C5.6	453	90	119	103	89	5.1
18	EJ	2000/07/08	22:58	N18W12	C4.0	483	83	60	65	−34	2.8
19	MC	2000/07/14	10:03	N22W07	X5.7	1674	159	59	87	−9	1.6
20	EJ	2000/07/23	04:11	S13W05	EP	631	118	94	97	38	5.0
21	MC	2000/07/25	02:43	N06W08	M8.0	528	29	45	21	−86	0.5
23	MC	2000/08/09	15:19	N20E12	EP	702	74	97	85	−74	6.3
24	MC	2000/09/16	04:06	N14W07	M5.9	1215	81	59	61	−5	2.5
25	EJ	2000/10/02	02:48	S09E07	C4.1	525	9	70	24	−90	0.6
26	MC	2000/10/09	23:19	N01W14	C6.7	798	165	85	126	27	2.1
27	MC	2000/11/03	18:35	N02W02	C3.2	291	313	106	189	−34	10.6
28	EJ	2000/11/24	04:55	N20W05	X2.0	1289	53	30	41	87	0.5
29	EJ	2001/02/28	13:22	S17W05	B4.2	313	213	122	155	87	3.2
30	EJ	2001/03/19	04:12	S20W00	EP	389	176	72	122	18	2.6
31	EJ	2001/04/09	15:20	S21W04	M7.9	1192	70	57	60	−67	3.1
32	MC	2001/04/10	05:06	S23W09	X2.3	2411	146	65	86	83	2.1
33	MC	2001/04/26	11:26	N20W05	M1.5	1006	167	131	128	−30	4.8
34	EJ	2001/08/09	08:00	N11W14	PEA	479	97	233	140	−80	7.2
35	EJ	2001/10/09	10:46	S28E08	M1.4	973	143	73	98	22	1.6
36	MC	2002/03/15	22:09	S08W03	M2.2	957	169	80	112	48	6.3
37	MC	2002/04/15	03:05	S15W01	M1.2	720	83	64	69	38	3.5
38	EJ	2002/05/08	12:58	S12W07	C4.2	614	34	31	32	−66	1.4
39	MC	2002/05/16	00:11	S23E15	C4.5	600	100	114	91	72	3.2
41	EJ	2002/05/27	12:36	N22E15	C3.7	1106	129	79	97	−62	3.0
42	EJ	2002/07/15	21:03	N19W01	M1.8	1300	93	66	78	58	4.5
43	MC	2002/07/29	10:27	S10W10	M4.7	222	91	29	49	32	0.6
44	MC	2003/08/14	17:12	S10E02	C3.8	378	57	76	64	−87	3.6
45	MC	2003/10/28	11:00	S16E08	X17.2	2459	200	66	109	−37	2.4
46	MC	2003/10/29	20:37	S15W02	X10.0	2029	101	86	93	−77	4.2
47	EJ	2004/01/19	23:46	S13W09	C5.5	965	139	114	124	−52	4.4

Table 1 (*Continued*)

No.	ICME type[a]	Flare				CME speed [km s^{-1}]	Post-eruption arcade				
		Date	Time [UT]	Location	Class[b]		Length [Mm]	Width [Mm]	Size [Mm]	ϕ[c] [deg]	T[d] [hour]
48	MC	2004/07/22	07:41	N04E10	C5.3	899	19	42	27	85	0.7
49	MC	2004/11/06	01:40	N09E05	M3.6	1111	163	52	92	2	1.7
50	EJ	2004/12/08	19:34	N05W03	C2.5	611	75	97	80	−52	2.0
51	EJ	2005/01/15	05:54	N16E04	M8.6	2049	92	73	78	31	5.7
52	EJ	2005/02/13	10:28	S11E09	C2.7	584	30	27	25	−89	0.5
53	MC	2005/05/13	16:13	N12E11	M8.0	1689	86	82	70	−55	12.7
54	MC	2005/05/17	02:31	S15W00	M1.8	449	40	57	49	90	1.5
56	EJ	2005/07/07	16:07	N09E03	M4.9	683	84	36	53	−60	0.9
57	EJ	2005/08/31	10:26	N13W13	C2.0	825	137	80	94	−9	3.4
59	EJ	2006/08/16	14:37	S16W08	C3.6	888	209	155	164	10	7.2

[a]MC = Magnetic cloud; EJ = Ejecta or non-MC.

[b]EP = Eruptive prominence.

[c]ϕ = Tilt angle measured counterclockwise from East–West line in degree.

[d]T = PEA developing time.

In 10 events, we could identify long-lived non-arcade loops (see Figure 1b; No. 54) or short-lived arcades (see Figure 1h; No. 28). These events differ a little bit from the typical appearance of PEAs (long-lived arcades). In the remaining 10 events, we could see short-lived non-arcade flaring loops. Figure 1c shows an example of an M8.0 flare at 02:43 UT on 25 July 2000 (No. 21). The flare was compact (<45 Mm) and impulsive (11 min). Usually, such compact impulsive flares are likely to be confined (Yashiro *et al.*, 2006), but this flare was associated with an EIT dimming and a faint halo CME (Figure 1f). The halo CME appeared in LASCO/C2 at 03:30 UT with an apparent speed of 528 km s^{-1} and, three days later, the associated ICME was observed as an MC. One could not necessarily classify these as PEAs but we have included them in the analysis because, according to the CSHKP flare-CME model, bright flare loops and PEAs are not physically distinct.

The solar source of the non-MC event on 5 October 2000 (No. 25) was a halo CME that appeared in the LASCO/C2 field of view at 03:50 UT on 3 October (Figure 1l). The main body of the CME appeared in the south-east quadrant and the faint envelope surrounding it expanded to cover the occulting disk of the LASCO/C2 coronagraph. The associated flare was the C4.1 flare at S09E07 at 02:48 UT on the same day. The flare was impulsive, so the EIT image observed 27 min after the flare peak (Figure 1i) does not show an arcade. These two examples show that occasionally poor arcade signatures are observed both in MCs and non-MCs.

3. Results

In order to investigate the spatial properties of the PEAs, we measured their lengths, widths, and areas. Since PEAs grow larger in time, we determined their properties when the size reached its maximum. We visually determined the footpoints of the PEAs in EUV images and measured the length, which corresponds to the two flare ribbons in Hα images. The red

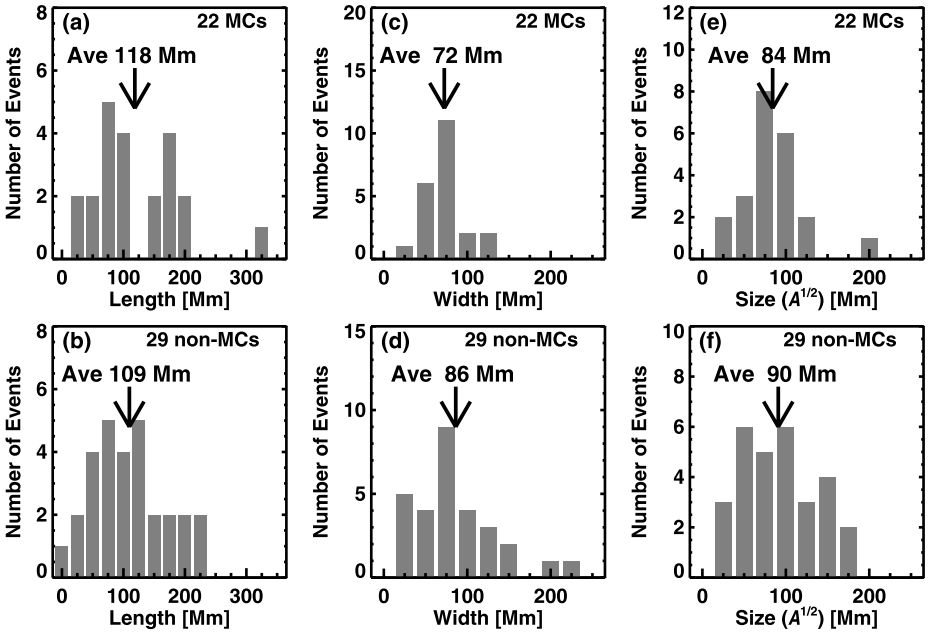

Figure 2 Distributions of lengths (left), widths (center), and sizes ($A^{1/2}$; right) for MC (top) and non-MC (bottom) events. The averages of each distribution are shown in the plot.

lines of Figure 1 show the locations of the footpoints of each PEA. We define the length of the PEAs as the average length of the two ribbons.

Figure 2a shows the distribution of the lengths of PEAs associated with MCs. The lengths are distributed widely from 29 Mm to 313 Mm with an average of 120 Mm. Figure 2b shows the same as 2a but for non-MC events. Similarly, the lengths of non-MC associated PEAs are distributed widely from 9 Mm to 215 Mm. The average length is slightly shorter but the difference in average length between the MC and non-MC events is not significant. Tripathi, Bothmer, and Cremades (2004) examined 236 PEAs using SOHO/EIT and reported that the heliographic length of the PEAs ranged from 2° to 40°, which correspond to 24 Mm to 486 Mm. The lengths of PEAs associated with MCs are distributed within the range of Tripathi *et al.*, but for the non-MCs cases they are not. The minimum length of 9 Mm is out of the range because our data sets include compact flares without the arcade structure (see Figure 1i). We include them because flare loops and PEAs are not physically distinct according to the CSHKP model.

The middle panels compare the width distributions of the PEAs of MC-associated and non-MC-associated events. The width of each PEA is defined as an average distance between footpoints at the two ends. The average widths are similar in both populations. The width distribution of the MC-associated PEAs is narrower than that of the non-MC events.

The right-hand panels of Figure 2 compare the PEA size for the MC-events and non-MC events. We define the PEA size as square root of the area ($A^{1/2}$) between the two ribbons. We found that the PEA size distributions are very similar in both populations. The average PEA size is 85 Mm for the MC events and 90 Mm for the non-MC events.

We define the tilt angle of the PEAs as the angle between the PEA axis and the East–West line, measured counterclockwise in degrees. A horizontal PEA has a tilt angle within $\pm 10°$. For example, the PEA of the Bastille Day event (Figure 1a) has a tilt angle of $-9°$. A

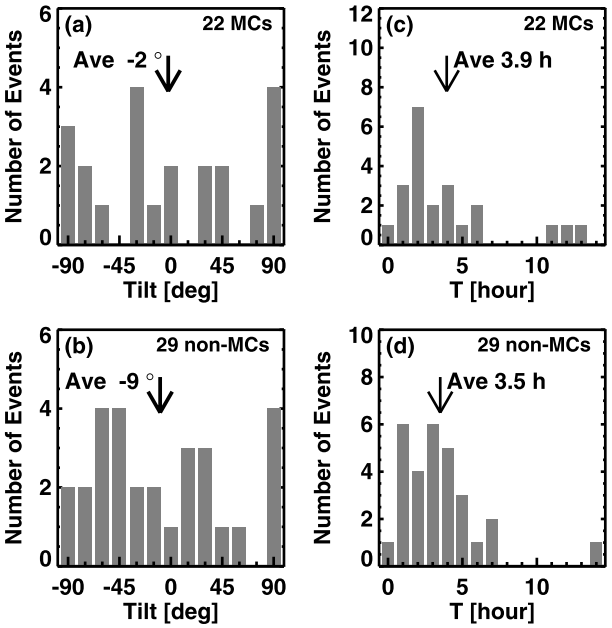

Figure 3 Distributions of PEA tilt angles (left) and PEA developing times (right) for MC (top) and non-MC events (bottom).

vertical PEA (*e.g.* Figures 1b, 1c, and 1h) has a tilt angle larger than 80° or lower than −80°. With this definition, tilt angles +90° and −90° are identical. A PEA axis is determined as the straight line between the two mid points of the ribbons at its ends. We used the same definition even for curved PEAs. The direction of the flux-rope axis is not considered here because it is not a property of the PEA itself.

Figure 3a shows the distribution of the tilt angle of the MC-associated PEAs. The tilt angles are widely distributed from −90° to 90°. No clear trend is found in our sample. Figure 3b is the same as Figure 3a but for non-MC events. We could not find any preferred tilt angle or any difference between the two distributions. One could expect more vertical PEAs than horizontal ones because ordinary sunspots are aligned horizontally; thus, the neutral line between them orients vertically. However, active regions producing many flares and CMEs are highly sheared and complex, thus, such simple consideration could not be valid.

In order to investigate the temporal properties of the PEAs, we use the time between the flare start and the PEA peak, defined as the time when a PEA is fully developed. We refer to this as the PEA developing time. PEA peak times are visually determined, so this is a somewhat subjective parameter. For the same event, different observers would select a different EIT frame as the PEA peak time. Our internal person-to-person check indicated that the errors between different observers are typically within 2 EIT frames or 24 minutes.

The right-hand panels of Figure 3 show the distribution of the PEA developing time for MC-associated (top) and non-MC-associated (bottom) events. As we saw in the other parameters, both distributions are very similar. The PEA developing time ranges from 24 minutes to 15 hours with an average of 3.9 hours for MC-events and 3.5 hours for non-MC-events, respectively. The average developing time is approximately half of the average lifetime (6.8 hours; Tripathi, Bothmer, and Cremades, 2004).

Since PEAs are the essential ingredients of eruptive flares, one might expect a relation between PEA and CME properties: the larger PEAs are more likely to be associated with

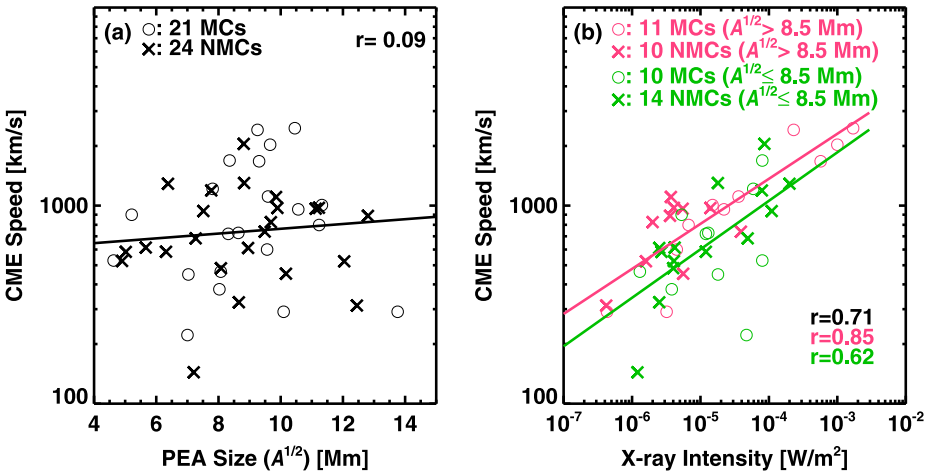

Figure 4 (a) Plot of the PEA sizes ($A^{1/2}$) *versus* CME speeds. Circles and crosses denote the MC-associated and non-MC-associated events, respectively. (b) Plot of the peak X-ray intensity *versus* CME speed. Six events lacking an observed X-ray flare are excluded from the plot. Events with large ($A^{1/2} > 8.5$ Mm) and small sizes ($A^{1/2} \leq 8.5$ Mm) are shown in pink and green, respectively.

faster CMEs. Since all our events originated at the disk center, the observed speed represents the expansion speed which is correlated with the radial speed (Gopalswamy *et al.*, 2009, 2012). Figure 4a plots the PEA size ($A^{1/2}$) against the CME speed, but we cannot see any clear relation between them. The correlation coefficient is 0.08 for both MC and non-MC events and 0.09 for all data points.

It is known that the CME kinetic energy is proportional to the X-ray peak intensity, but the correlation coefficient is only 0.54 (Hundhausen, 1999; Yashiro and Gopalswamy, 2009). Figure 4b shows the correlation between the X-ray peak intensity and the CME speed. The correlation coefficient for all data points increases to 0.71.

We divided our sample into four groups based on the ICME structure, *i.e.* MC (circle) or non-MC (crosses) event, and on the PEA area, *i.e.* large ($A^{1/2} > 8.5$ Mm) or small ($A^{1/2} \leq 8.5$ Mm) PEA. The circles and crosses are highly overlapped so we cannot see any difference between the MC and non-MC events. On the other hand, we can see a difference between the large (pink) and small (green) PEAs. For a given flare intensity, the speeds of CMEs associated with larger PEAs are higher on average. The correlation coefficient is 0.85 for large and 0.62 for small PEA events.

4. Summary and Conclusions

Historic events, *e.g.* the Bastille Day Event on 14 July 2000 and the giant X-ray arcade formation on 14 April 1994, have convinced us that energetic CMEs are likely to be associated with a post-flare arcade formation. This idea is supported by the CSHKP model (*e.g.* Longcope and Magara, 2004; Longcope and Beveridge, 2007), *i.e.* the flux-rope structure of a CME is formed by magnetic reconnection which is also responsible for the formation of the PEA. If the non-MC associated CMEs do not have a flux-rope structure, we expect some difference in the PEA properties between MC and non-MC events. We find no difference in the PEA properties between the MC and non-MC populations.

In Figure 1 we show that the MC-associated CMEs are not necessarily associated with large PEAs. A CME associated with a compact impulsive flare was observed as an MC near Earth. Therefore, the association of a large PEA is not a necessary condition for a CME to have a flux-rope structure. In Figures 2 and 3 we compare the PEA properties between MC and non-MC events and found that there are no significant differences in the PEA properties between the two populations. In Figure 4 we found that the CME speeds weakly depend on the PEA sizes: the CMEs associated with larger PEAs tend to be faster than those associated with smaller ones. These results indicate that there is no difference in the properties of PEAs between the MC and non-MC events during the CME launch.

Xie, Gopalswamy, and St. Cyr (2013) applied a flux-rope model (Krall and St. Cyr, 2006) to the CMEs of the CDAW events and found that on average CMEs associated with MCs (non-MCs) are deflected towards (away from) the disk center. Kim *et al.* (2013) examined the CME direction parameter (Moon *et al.*, 2005) and found that the parameter is smaller for non-MC events indicating that non-MC-associated CMEs are deflected away from the Sun–Earth line. Mäkelä *et al.* (2013) reported that different CME deflections between MC and non-MC events can be explained by the influence of coronal holes. Many studies suggest that there are significant differences in the CME launch direction between MC and non-MC events. Gopalswamy *et al.* (2013) found no clear difference in the flare properties of MC and non-MC events. In addition, we found that there is no significant difference in the properties of post-flare arcades. All these results are consistent with the view that at the Sun a CME flux-rope structure forms both in the MC and non-MC events, but the flux-rope structure is not observed in interplanetary space for non-MC events because of geometrical reasons.

Acknowledgements We would like to thank the local organizers of the LWS CDAW meetings in San Diego, USA, and Alcalá de Henares, Spain. This research was supported by NASA grants NNX10AL50A and NNG11PL10A. SOHO is an international cooperation project between ESA and NASA.

References

Aschwanden, M.J., Alexander, D.: 2001, Flare plasma cooling from 30 MK down to 1 MK modeled from *Yohkoh*, GOES, and TRACE observations during the Bastille Day event (14 July 2000). *Solar Phys.* **204**, 91.

Brueckner, G.E., Howard, R.A., Koomen, M.J., Korendyke, C.M., Michels, D.J., Moses, J.D., Socker, D.G., Dere, K.P., Lamy, P.L., Llebaria, A., Bout, M.V., Schwenn, R., Simnett, G.M., Bedford, D.K., Eyles, C.J.: 1995, The Large Angle Spectroscopic Coronagraph (LASCO). *Solar Phys.* **162**, 357.

Bruzek, A.: 1964, On the association between loop prominences and flares. *Astrophys. J.* **140**, 746.

Burlaga, L.F., Plunkett, S.P., St. Cyr, O.C.: 2002, Successive CMEs and complex ejecta. *J. Geophys. Res.* **107**, 1266.

Burlaga, L., Sittler, E., Mariani, F., Schwenn, R.: 1981, Magnetic loop behind an interplanetary shock – *Voyager*, *Helios*, and IMP 8 observations. *J. Geophys. Res.* **86**, 6673.

Carmichael, H.: 1964, In: Hess, W.N. (ed.) *Physics of Solar Flares*, *NASA* **SP-50**, 451.

Gopalswamy, N.: 2006, Properties of interplanetary coronal mass ejections. *Space Sci. Rev.* **124**, 145.

Gopalswamy, N., Nitta, N., Manoharan, P.K., Raoult, A., Pick, M.: 1999, X-ray and radio manifestations of a solar eruptive event. *Astron. Astrophys.* **347**, 684.

Gopalswamy, N., Shimojo, M., Lu, W., Yashiro, S., Shibasaki, K., Howard, R.A.: 2003, Prominence eruptions and coronal mass ejection: a statistical study using microwave observations. *Astrophys. J.* **586**, 562.

Gopalswamy, N., Dal Lago, A., Yashiro, S., Akiyama, S.: 2009, The expansion and radial speeds of coronal mass ejections. *Cent. Eur. Astrophys. Bull.* **33**, 115.

Gopalswamy, N., Xie, H., Mäkelä, P., Akiyama, S., Yashiro, S., Kaiser, M.L., Howard, R.A., Bougeret, J.-L.: 2010, Interplanetary shocks lacking type II radio bursts. *Astrophys. J.* **710**, 1111.

Gopalswamy, N., Mäkelä, P., Yashiro, S., Davila, J.M.: 2012, The relationship between the expansion speed and radial speed of CMEs confirmed using quadrature observations of the 2011 February 15 CME. *Sun Geosph.* **7**, 7.

Gopalswamy, N., Mäkelä, P., Akiyama, S., Xie, H., Yashiro, S., Reinard, A.A.: 2013, The solar connection of enhanced heavy ion charge states in the interplanetary medium: implications for the flux-rope structure of CMEs, *Solar Phys.*, in this issue. doi:10.1007/s11207-012-0215-2.

Gosling, J.T.: 1990, *Coronal Mass Ejections and Magnetic Flux Ropes in Interplanetary Space*, *Geophys. Monogr. Ser.* **58**, AGU, Washington, 343.

Hanaoka, Y., Kurokawa, H., Enome, S., Nakajima, H., Shibasaki, K., Nishio, M., *et al.*: 1994, Simultaneous observations of a prominence eruption followed by a coronal arcade formation in radio, soft X-rays, and H. *Publ. Astron. Soc. Japan* **46**, 205.

Harra-Murnion, L.K., Schmieder, B., van Driel-Gesztelyi, L., Sato, J., Plunkett, S.P., Rudawy, P., Rompolt, B., Akioka, M., Sakao, T., Ichimoto, K.: 1998, Multi-wavelength observations of POST flare loops in two long duration solar flares. *Astron. Astrophys.* **337**, 911.

Hirayama, T.: 1974, Theoretical model of flares and prominences. I: evaporating flare model. *Solar Phys.* **34**, 323.

Hundhausen, A.: 1999, Coronal mass ejections. In: Strong, K.T., Saba, J.L.R., Haisch, B.M., Schmelz, J.T. (eds.) *The Many Faces of the Sun: A Summary of the Results from NASA's Solar Maximum Mission*, 143.

Kahler, S.: 1977, The morphological and statistical properties of solar X-ray events with long decay times. *Astrophys. J.* **214**, 891.

Kim, R.-S., Gopalswamy, N., Cho, K.-S., Moon, Y.-J., Yashiro, S.: 2013, Propagation characteristics of CMEs associated magnetic clouds and ejecta. *Solar Phys.*, in this issue. doi:10.1007/s11207-013-0230-y.

Kopp, R.A., Pneuman, G.W.: 1976, Magnetic reconnection in the corona and the loop prominence phenomenon. *Solar Phys.* **50**, 85.

Krall, J., St. Cyr, O.C.: 2006, Flux-rope coronal mass ejection geometry and its relation to observed morphology. *Astrophys. J.* **652**, 1740.

Longcope, D.W., Beveridge, C.: 2007, A quantitative, topological model of reconnection and flux rope formation in a two-ribbon flare. *Astrophys. J.* **669**, 621.

Longcope, D.W., Magara, T.: 2004, A comparison of the minimum current corona to a magnetohydrodynamic simulation of quasi-static coronal evolution. *Astrophys. J.* **608**, 1106.

Mäkelä, P., Gopalswamy, N., Xie, H., Mohamed, A., Akiyama, S., Yashiro, S.: 2013, Coronal hole influence on the observed structure of interplanetary CMEs. *Solar Phys.*, in this issue. doi:10.1007/s11207-012-0211-6.

McAllister, A.H., Dryer, M., McIntosh, P., Singer, H., Weiss, L.: 1996, A large polar crown coronal mass ejection and a "problem" goemagnetic storm: April 14 – 23, 1994. *J. Geophys. Res.* **101**, 13497.

Moon, Y.J., Cho, K.S., Dryer, M., Kim, Y.H., Bong, S.C., Chae, J., Park, Y.D.: 2005, New geoeffective parameters of very fast halo coronal mass ejection. *Astrophys. J.* **624**, 414.

Munro, R.H., Gosling, J.T., Hildner, E., MacQueen, R.M., Poland, A.I., Ross, C.L.: 1979, The association of coronal mass ejection transients with other forms of solar activity. *Solar Phys.* **61**, 201.

Pallavicini, R., Serio, S., Vaiana, G.S.: 1977, A survey of soft X-ray limb flare images – the relation between their structure in the corona and other physical parameters. *Astrophys. J.* **216**, 108.

Qiu, J., Hu, Q., Howard, T.A., Yurchyshyn, V.B.: 2007, On the magnetic flux budget in low-corona magnetic reconnection and interplanetary coronal mass ejections. *Astrophys. J.* **659**, 758.

Sheeley, N.R., Bohlin, J.D. Jr., Brueckner, G.E., Purcell, J.D., Scherrer, V.E., Tousey, R., Smith, J.B., Speich, D.M. Jr., Tandberg-Hanssen, E., Wilson, R.M.: 1975, Coronal changes associated with a disappearing filament. *Solar Phys.* **45**, 377.

Sturrock, P.A.: 1966, Model of the high-energy phase of solar flares. *Nature* **211**, 695.

Tripathi, D., Bothmer, V., Cremades, H.: 2004, The basic characteristics of EUV post-eruptive arcades and their role as tracers of coronal mass ejection source regions. *Astron. Astrophys.* **422**, 337.

Webb, D.F., Hundhausen, A.J.: 1987, Activity associated with the solar origin of coronal mass ejections. *Solar Phys.* **108**, 383.

Xie, H., Gopalswamy, N., St. Cyr, O.C.: 2013, Near-Sun flux rope structure of CMEs. *Solar Phys.*, in this issue. doi:10.1007/s11207-012-0209-0.

Yashiro, S., Gopalswamy, N.: 2009, Statistical relationship between solar flares and coronal mass ejections. In: Gopalswamy, N., Webb, D.F. (eds.) *Universal Heliophysical Processes*, *IAU Symp.* **257**, Cambridge Univ. Press, London, 233.

Yashiro, S., Akiyama, S., Gopalswamy, N., Howard, R.A.: 2006, Different power-law indices in the frequency distributions of flares with and without coronal mass ejections. *Astrophys. J. Lett.* **650**, L143.

Yurchyshyn, V.: 2008, Relationship between EIT posteruption arcades, coronal mass ejections, the coronal neutral line, and magnetic clouds. *Astrophys. J. Lett.* **675**, L49.

Solar Phys (2013) 284:129–149
DOI 10.1007/s11207-013-0244-5

Magnetic Field Configuration Models and Reconstruction Methods for Interplanetary Coronal Mass Ejections

N. Al-Haddad · T. Nieves-Chinchilla · N.P. Savani · C. Möstl · K. Marubashi · M.A. Hidalgo · I.I. Roussev · S. Poedts · C.J. Farrugia

Received: 8 April 2012 / Accepted: 23 January 2013 / Published online: 20 February 2013

Abstract This study aims to provide a reference for different magnetic field models and reconstruction methods for interplanetary coronal mass ejections (ICMEs). To understand the differences in the outputs of these models and codes, we analyzed 59 events from the Coordinated Data Analysis Workshop (CDAW) list, using four different magnetic field models

Flux-Rope Structure of Coronal Mass Ejections
Guest Editors: N. Gopalswamy, T. Nieves-Chinchilla, M. Hidalgo, J. Zhang and P. Riley

N. Al-Haddad (✉) · S. Poedts
Centrum voor Plasma-Astrofysica, Katholieke Universiteit Leuven, Celestijnenlaan 200B, 3001 Leuven, Belgium
e-mail: nada.alhaddad@student.kuleuven.be

T. Nieves-Chinchilla
Heliospheric Physics Lab., GSFC-NASA, Greenbelt, MD, USA

T. Nieves-Chinchilla
IACS-CUA, Washington, DC, USA

N.P. Savani
UCAR, Boulder, CO, USA

N.P. Savani
NASA Goddard Space Flight Center, Greenbelt, MD, USA

C. Möstl
Space Science Laboratory, University of California, Berkeley, CA, USA

C. Möstl
Space Research Institute, Austrian Academy of Sciences, Graz 8042, Austria

C. Möstl
Kanzelhöhe Observatory-IGAM, Institute of Physics, University of Graz, Universitätsplatz 5, 8010 Graz, Austria

K. Marubashi
Korea Astronomy and Space Science Institute, Daejeon 305-348, Republic of Korea

and reconstruction techniques; force-free fitting, magnetostatic reconstruction using a numerical solution to the Grad–Shafranov equation, fitting to a self-similarly expanding cylindrical configuration and elliptical, non-force-free fitting. The resulting parameters of the reconstructions for the 59 events are compared statistically and in selected case studies. The ability of a method to fit or reconstruct an event is found to vary greatly; this depends on whether the event is a magnetic cloud or not. We find that the magnitude of the axial field is relatively consistent across models, but that the axis orientation of the ejecta is not. We also find that there are a few cases with different signs of the magnetic helicity for the same event when we leave the boundaries free to vary, which illustrates that this simplest of parameters is not necessarily always clearly constrained by fitting and reconstruction models. Finally, we examine three unique cases in depth to provide a comprehensive idea of the different aspects of how the fitting and reconstruction codes work.

Keywords Sun: corona · Sun: coronal mass ejections (CMEs)

1. Introduction

Coronal mass ejections (CMEs) are large-scale eruptions of plasma and magnetic flux with a typical size of 0.25 AU at 1 AU (*e.g.*, see Bothmer and Schwenn, 1998; Savani *et al.*, 2009; or Nieves-Chinchilla *et al.*, 2012). In the interplanetary space, they typically move at supersonic speeds between 200 and 2000 km s^{-1}, propagating from the solar corona to 1 AU in a few days. They can interact with the Earth's magnetosphere, resulting in geomagnetic storms (Gold, 1959). Once CMEs drive through and interact with the interplanetary medium, they are often referred to as interplanetary CMEs (ICMEs). These ICMEs, measured *in situ*, for example at L1, may be composed of a fast forward shock, a dense sheath and ejecta material. Slow CMEs typically do not drive a shock. Hereafter, we use the term ICME once it is propagating in the interplanetary medium after leaving the corona (more or less after $10-20\ R_{\odot}$).

Interplanetary CMEs, measured *in situ*, are typically characterized by a low proton temperature, the presence of bi-directionally streaming electrons, unusual charge states of oxygen and iron, and various magnetic signatures (*e.g.* Lynch *et al.*, 2003; Zurbuchen and Richardson, 2006; Richardson and Cane, 2010). However, there is no single characteristic that is consistently observed. Lists of ICMEs measured by ACE and STEREO are maintained by Jian *et al.* (2006), Lepping *et al.* (2006), Richardson and Cane (2010), and Gopalswamy *et al.* (2008), among others. ICMEs have been classified into three different classes based on their magnetic field and plasma properties (Zurbuchen and Richardson, 2006):

K. Marubashi
660-73 Mizuno, Sayama, Saitama 3350-1317, Japan

M.A. Hidalgo
SRG-UAH, Alcala de Henares, Madrid, Spain

I.I. Roussev
Institute for Astronomy, University of Hawaii, 2680 Woodlawn Dr., Honolulu, HI 96822, USA

C.J. Farrugia
Space Science Center and Department of Physics, University of New Hampshire, Durham, NH, USA

i) Magnetic clouds (MCs): characterized by low plasma beta, low proton temperature and featuring a strong magnetic field with a smooth rotation (Burlaga *et al.*, 1981). To explain this last characteristic, Goldstein (1983) suggested that the magnetic field in an MC can be described by a force-free flux rope structure, where $\nabla \times \mathbf{B} = \alpha \mathbf{B}$. Burlaga (1988) assumed a constant α, in which case the flux rope satisfies the Lundquist solution (Lundquist, 1950) and can be expressed in terms of Bessel functions. This became the most widely used model to describe the magnetic field structure of MCs. MCs are believed to represent about one third of the total number of ICMEs (Gosling, 1990; Richardson and Cane, 2010). However, a number of other studies proposed that an even higher percentage of ICMEs are MCs; for example, the study by Li *et al.* (2011) and Marubashi (2000) estimated the proportion of MCs to be 50 % and 80 %, respectively. Other authors have studied the variation of the proportion of MCs among ICMEs during the solar cycle (Kilpua *et al.*, 2011; Richardson and Cane, 2010) and found that it varies from close to 100 % near solar minimum to about 20 – 25 % near solar maximum.

ii) Ejecta or irregular and weak magnetic field ICMEs: These configurations have some but not all the properties of MCs. Typically, their magnetic field is too weak and/or irregular or has little rotation. Some of these ejecta can be additionally classified into subcategories, for example, "magnetic-cloud-like" (Zhang *et al.*, 2007) or magnetic flux rope (Rouillard, 2011). It has been proposed recently that some of these events are actually MCs whose legs passed through the observing spacecraft (Marubashi and Lepping, 2007), which has been confirmed with STEREO observations (Möstl *et al.*, 2010). According to these studies, ejecta are MCs but are not observed as such due to an observational bias.

iii) Complex ICMEs (complex ejecta), which may result from the interaction of successive CMEs or from the interaction of CMEs with complex solar wind structures and streams (Burlaga, Plunkett, and St. Cyr, 2002; Wang, Ye, and Wang, 2003; Lugaz, Manchester, and Gombosi, 2005b). Double rotation within one MC has also been reported from *Ulysses* (Rees and Forsyth, 2004) and ACE observations (Steed *et al.*, 2011), showing that even isolated ICMEs may produce complex ejecta.

Understanding the nature of the magnetic field in ICMEs (magnetic clouds and ejecta) is a crucial part of comprehending their behavior and the way they affect the interplanetary medium and Earth's magnetosphere throughout their propagation. Thus there have been several attempts to describe the structure of the magnetic field in ICMEs using models and magnetic field reconstruction codes. Figures 1 and 2 give some examples of proposed models.

To explain the behavior of the magnetic field in MCs, early models were developed to accommodate the definition of Burlaga *et al.* (1981) of an MC. Most of these models restrict the internal structure of the magnetic field to the force-free configuration where the magnetic field, $\mathbf{B}$, is described as $\nabla \times \mathbf{B} = \alpha \mathbf{B}$. Several magnetic field reconstructions and fitting models have been built upon this definition; among the most often used is the model by Burlaga (1988) and Lepping, Burlaga, and Jones (1990), which assumes a cylindrically symmetric solution and a constant α across the cloud.

Marubashi (1986) also adopted a force-free model, but without assuming a constant α. Farrugia *et al.* (1993) and Farrugia, Osherovich, and Burlaga (1995) introduced a cylindrical model that incorporated self-similar expansion in two initially force-free constant-α codes, a cylindrical and a spherical model, and noted that the cylindrical configuration did not maintain the force-free state after it starts to expand. Thereafter, Shimazu and Vandas (2002) provided a modification of the mathematical formalism to keep the self-similarly expanding cylindrical model force-free.

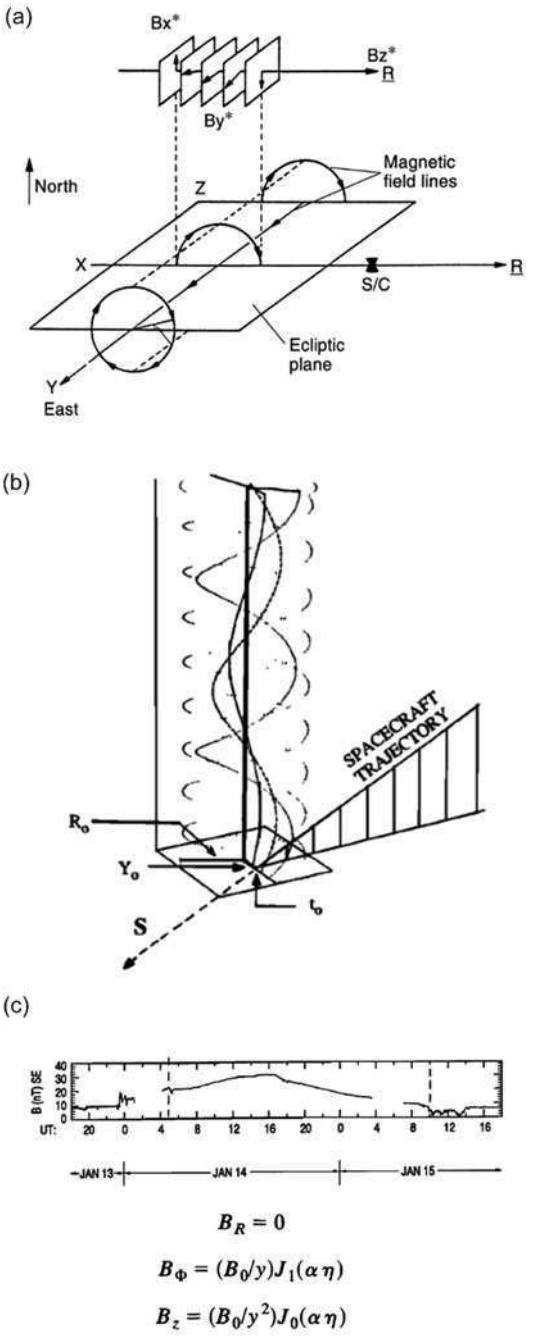

Figure 1 Overview of different MC models. (a) Goldstein (1983) proposed that MCs are force-free structures, which was confirmed by Marubashi (1986) (figure adapted from Bothmer and Schwenn, 1998). (b) Lepping, Burlaga, and Jones (1990) succeeded in fitting the Lundquist model to *in situ* magnetic field observations after an idea by Burlaga (1988). (c) Farrugia *et al.* (1993) included expansion in the model.

Several other models have emerged thereafter that made different assumptions: fitting to a cylinder of elliptical cross-section by Hidalgo, Nieves-Chinchilla, and Cid (2002) and Hidalgo (2003); fitting to a kinematically distorted flux rope (Owens, Merkin, and Riley, 2006;

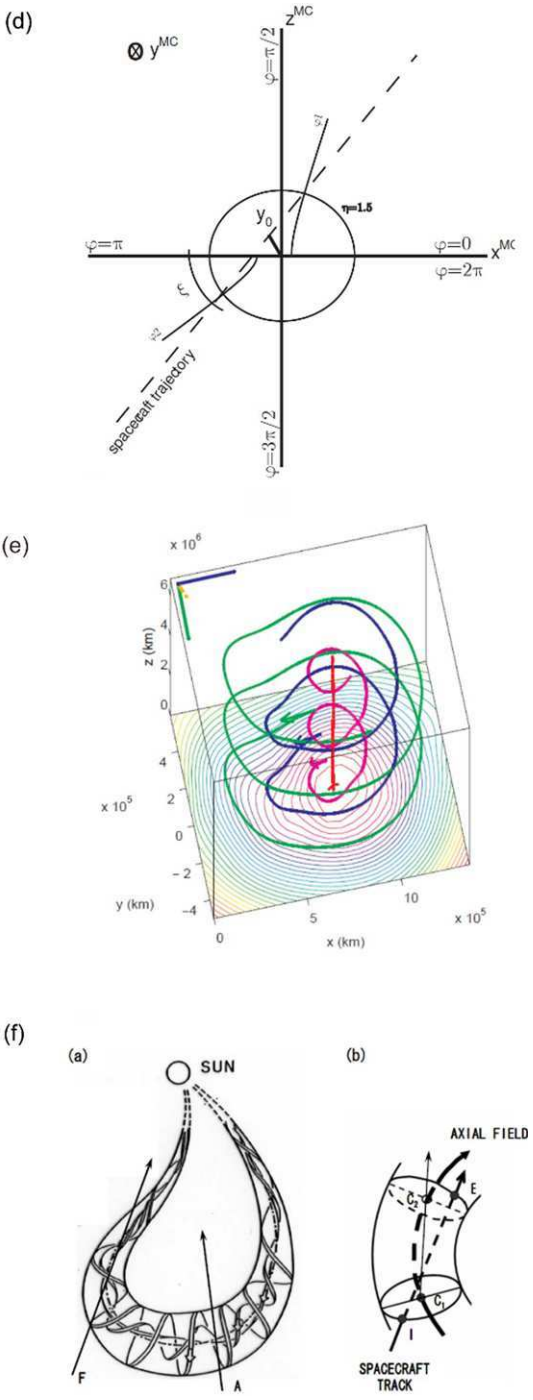

Figure 2 Overview of different MC models (*continued*). (d) Schematic representation of the spacecraft trajectory inside an MC of elliptical cross-section following the model of Hidalgo, Nieves-Chinchilla, and Cid (2002). (e) Hu and Sonnerup (2001) modeled magnetic flux ropes using a magneto-hydrostatic reconstruction technique without a predefined geometry. (f) Marubashi and Lepping (2007) included curvature in the classical model.

Vandas and Romashets, 2003; Vandas *et al.*, 2006; Démoulin and Dasso, 2009); non-cylindrical flux rope fitting (Mulligan and Russell, 2001; Owens *et al.*, 2012); torus fitting (Romashets and Vandas, 2003; Marubashi and Lepping, 2007). The Grad–Shafranov reconstruction technique (Hu and Sonnerup, 2002; Möstl *et al.*, 2009b) assumes a structure in magneto-hydrostatic (MHS) equilibrium with an invariant direction, and uses the Grad–Shafranov equation to describe the magnetic field in the structure. Therefore, this model does not only use the magnetic field measurements but also measurements of the plasma pressure, and it is only applicable to a structure possessing axial symmetry. The Grad–Shafranov technique has been tested using multi-spacecraft measurements (Liu *et al.*, 2008; Kilpua *et al.*, 2009; Möstl *et al.*, 2009a) and, recently, improvements to the algorithm have been presented by Isavnin, Kilpua, and Koskinen (2011).

While most techniques reconstruct or fit ICMEs as some type of twisted flux ropes, this result is not necessarily well tested. It has recently been shown by Al-Haddad *et al.* (2011) that the Grad–Shafranov technique is designed in a way that it will always reconstruct a helical flux rope from a rotating magnetic field observed by a single spacecraft, even if the magnetic field is not a helical flux rope in 3D. This is precisely the reason why the Grad–Shafranov reconstruction assumes an invariance along the cloud axis (so-called 2.5D method). As was shown in Al-Haddad *et al.* (2011), this is equivalent to assuming a helical solution from the beginning. The assumption of invariance along the cloud axis is also made in all the other fitting techniques used in this article. Other recent observations pointing toward a more complicated geometry of ICMEs at 1 AU have been made by Kahler, Krucker, and Szabo (2011), Farrugia *et al.* (2011) and Nieves-Chinchilla *et al.* (2012).

Using 2D and 3D numerical simulations, it is possible to show that a CME initiated at the solar surface (for example using a twisted flux rope) evolves through its interaction with the solar wind into a typical ICME (Riley, Gosling, and Pizzo, 1997; Riley *et al.*, 2003; Odstrčil and Pizzo, 1999; Manchester *et al.*, 2004; Chané *et al.*, 2006; Shen *et al.*, 2007). This idea has now been confirmed by STEREO observations (see, for example, Savani *et al.*, 2010). In these simulations, synthetic satellite measurements made at 1 AU show a typical ICME structure with a fast shock, preceding a dense sheath and an ejecta. Synthetic coronagraphic and heliospheric images are also able to reproduce typical views of CMEs (Lugaz, Manchester, and Gombosi, 2005a; Manchester *et al.*, 2008; Riley *et al.*, 2008; Lugaz *et al.*, 2009; Odstrčil and Pizzo, 2009).

Riley *et al.* (2004) compared magnetic field reconstructions and fitting models for ICMEs by fitting two different time series of a simulated ICME with five different techniques: three force-free models, the elliptical model by Hidalgo, Nieves-Chinchilla, and Cid (2002), and the Grad–Shafranov reconstruction code. The results of the reconstructions were then compared again to the 2.5D MHD simulation. One of the difficulties that the authors encountered was choosing the boundaries. Another difficulty was recognizing an MC within the provided time series. It is particularly hard to observe the properties characterizing an MC when the minimum variance technique is used and the impact parameter is large.

Three of the models used in the study by Riley *et al.* (2004) were also used in the present study. We also added the self-similarly expanding cylindrical fitting of Marubashi and Lepping (2007) and only kept one classical – no expansion – force-free model. However, it is important to stress that in this project we applied the comparison to a list of observed events. Here, the authors address some of the problems discussed in Riley *et al.* (2004) by performing more detailed analyses and proposing fixed boundaries.

In this study, we compare the reconstruction of four different magnetic field fitting techniques for most of the fast ICMEs and MCs observed during Solar Cycle 23, for which a source region can be identified (see details in Section 2). Our goals are to acquire a broader

understanding of the magnetic field structure in MCs and to investigate if there are statistical differences between the codes for MCs and non-MC ejecta, and take steps toward deciphering if all ICMEs can be expressed as flux ropes if a sufficiently sophisticated model is used. We do this by comparing the results of the different fitting techniques. In Section 2, we describe the data used in this study followed by a succinct description of the different codes. In Section 3, we discuss the full results for the 59 selected events and in Section 4, we present two events for which we used the same boundaries for all codes. We conclude and discuss our results for the nature of magnetic fields in ICMEs in Section 5.

2. Data and Model Overview

2.1. CDAW Data

The data are taken from the list of the Coordinated Data-analysis Workshop (CDAW) of MCs and ejecta during Solar Cycle 23. The list can be found at http://cdaw.gsfc.nasa.gov/meetings/2010_fluxrope/LWS_CDAW2010_ICMEtbl.html.

This list contains all shock-driving ICMEs from Solar Cycle 23 for which it was possible to determine the source region, and for which the source region was within $\pm 15^\circ$ of the disk center. This list is a subset of the list of all interplanetary shocks observed during Solar Cycle 23 from Gopalswamy *et al.* (2010). The list contains 59 ICMEs classified as follows: 24 events classified as magnetic clouds (MCs) and 35 events classified as ejecta (EJ).

2.2. Grad–Shafranov Reconstruction Technique

For the Grad–Shafranov (GS) reconstruction, we used the code by Hu and Sonnerup (2002) and followed the guidelines for using it discussed by Möstl *et al.* (2009b). This is based on magneto-hydrostatic equilibrium of a system with an invariant direction and is a solution for what is basically a numerical boundary problem. The GS equation is

$$\frac{\partial^2 A}{\partial x^2} + \frac{\partial^2 A}{\partial y^2} = -\mu_0 \frac{\mathrm{d}P_\mathrm{t}(A)}{\mathrm{d}A}, \tag{1}$$

where $A(x, y)$ is the magnetic vector potential and P_t is the transverse pressure defined as $P_\mathrm{t} = p + B_z^2/(2\mu_0)$, with p being the thermal pressure. The total magnetic field is given by $\mathbf{B} = \nabla A \times \mathbf{e}_z + B_z \mathbf{e}_z$. The first step to solving this equation is to determine the invariant axis, z. This is done first using a minimum variance analysis on the magnetic field components and by finding a frame in which the transverse pressure is a single-value function of the magnetic vector potential, A. After this, the GS equation can be solved numerically.

The main assumptions of the technique are that the structure is assumed to be invariant along the ICME axis (so-called 2.5D), and that it is assumed to be time-independent during the whole measurement by the spacecraft. Compared to other techniques, it does not include expansion or a toroidal geometry. One of the potential problems with the Grad–Shafranov technique is the stability of the integration and the influence of the solver and stabilization procedure on the results. However, the Grad–Shafranov reconstruction has been tested by using observations of ICMEs by two spacecraft at a significant separation with respect to the ICME size (Liu *et al.*, 2008; Möstl *et al.*, 2009a, 2009b). Some of the stability problems have also recently been addressed in Isavnin, Kilpua, and Koskinen (2011).

One of the main advantages of the GS method is that the shape of the flux rope's cross-section and the number of flux ropes inside the reconstructed interval are both not pre-defined, but are an output of the technique. Another advantage is that the boundaries of the ICMEs are chosen through an optimization procedure to render the $P_t(A)$ function as close to single-valued as possible. The $P_t(A)$ function is fitted with a polynomial function with exponential tail(s), and only the events for which the fitting residue is low (typically less than 0.1) and for which the fitting appears to be visually correct are deemed successfully reconstructed. More details can be found in Hu *et al.* (2004).

The GS reconstruction gives the following results: flux rope orientation (longitude and latitude), impact parameter (closest approach of the spacecraft to the MC axis), magnetic flux (axial and poloidal), axial current, the cross–section shape and the central field strength. The GS reconstruction feasibility was checked for every event in the CDAW list. We primarily used data from the *Wind* spacecraft (MFI (Lepping *et al.*, 1995) and SWE (Ogilvie *et al.*, 1995) instruments), and switched to ACE (MAG (Smith *et al.*, 1998) and SWEPAM (McComas *et al.*, 1998) instruments if there was a data gap at *Wind*. The GS reconstruction method was successful for

- full list: 20 events out of 59 (34 %),
- 17 MC events out of 24 (71 %),
- 3 EJ events out of 35 (8 %).

This means that the applicability of using GS reconstruction is closely tied to the definition of a magnetic cloud (higher-than-average field strength, smoothly rotating magnetic field vector, low β, low T_p). Typically, this means that for these cases, one magnetic field component (B_y or B_z) needs to be bipolar and the other unipolar, depending on the orientation of the flux rope (see discussion in Bothmer and Schwenn, 1998). Moreover, we were able to reconstruct about 1/3 of the events in the complete list, which is similar to the often-quoted ratio between all ICMEs and those that contain parts that satisfy the MC definition.

2.3. Self-similarly Expanding Cylinder Fitting Technique

This model is a force-free model that assumes a spatially constant α and performs the fitting in cylindrical coordinates. Here, α is chosen fixed for every event and equal to 2.4. The model takes into account self-similar expansion, as was initially suggested by Farrugia *et al.* (1992, 1993). The original inclusion of the self-similar expansion has been found to cause a deviation from the force-free state during expansion. Some refinements proposed by Shimazu and Vandas (2002) have been incorporated into the model to preserve the force-free state for the duration of the MC travel. As a result, the magnetic field intensity B and the radius r of the fitted MC at a given time as produced by the model are defined as follows:

$$\mathbf{B} = \frac{B_0}{(1 + \frac{t}{t_{\rm exp}})^2}, \tag{2}$$

$$\mathbf{r} = r_0\left(1 + \frac{t}{t_{\rm exp}}\right), \tag{3}$$

where B_0 is the magnetic field intensity on the axis of the CME cylinder, $t_{\rm exp}$ is the expansion time, t is the time since the first encounter of the spacecraft with the CME, and r_0 is the distance between the cylinder axis and the spacecraft at the time of the first encounter.

The model also provides values for the longitude and latitude of the axis, as well as the impact parameter, which is defined as the distance between the closest axis of the cylinder and the path of the spacecraft. The model simultaneously fits the following quantities for both chiralities (positive and negative): B_0, r_0, $t_{\exp}$, the longitude, latitude, and impact parameter. The final selection was made by choosing the sign of the chirality that gives the best fit. The details of the model can be found in Appendix A of Marubashi and Lepping (2007). The self-similarly expanding cylinder fitting method was successful for

- full list: 50 events out of 59 (85 %),
- 22 MC events out of 24 (91.5 %),
- 28 EJ events out of 35 (80 %).

There were seven events that were found to be contracting (negative $t_{\exp}$) and three events whose expansion time was longer than 500 hours, which corresponds to less than 10 % change in the axial magnetic field strength over the crossing of a typical magnetic cloud ($\sim$ 1 day).

2.4. Force-Free Constant-α Reconstruction

This force-free fitting model is based on the force-free flux constant-α (FFCA) rope developed by Burlaga (1988) and subsequently optimized by Lepping, Burlaga, and Jones (1990). In our model, α is fixed to equal 2.4. This implies that the flux rope's magnetic field on the outer shell is almost completely poloidal. The value of 2.4 is not optimized and could be changed (*i.e.*, reduced in value) if it was believed that on the outer shell of the flux rope the field lines were still helical. This might be the case if the rear or front edge of the flux has been "eroded" away from its ideal case (perhaps by reconnection), as proposed by Dasso *et al.* (2006) and recently confirmed by Ruffenach *et al.* (2012). The α parameter has also been used as a free variable in some models (*e.g.* Lepping, Burlaga, and Jones, 1990). Since α is constant and fixed to equal 2.4 for the FFCA and for the self-similarly expanding cylinder models, it is clear that these two models are identical when the expansion is equal to 0.

The flux rope axis was calculated by a minimum variance analysis (MVA). This is a technique originally developed for solving the normals to a tangential discontinuity (TD) (Sonnerup and Scheible, 1998). To obtain the orientation of an ICME, the axis is determined by the intermediate eigenvector, as pointed out by Goldstein (1983).

The chirality of the flux rope is determined by the sense of direction in which the magnetic field rotates in the MVA reference frame. The impact parameter and magnetic field magnitude are the only two free variables. They are optimized using a nonlinear optimization routine (Nelder and Mead, 1965). For each event, the fitting was attempted with two different boundaries: those from Lepping *et al.* (2006) and those selected by K. Marubashi. In addition, for eight events, a different set of boundaries was chosen directly by N.P. Savani because the other two sets of boundaries were judged to be unsatisfactory for these events. Overall, the method was successful for

- full list: 55 events out of 59 (93 %),
- 24 MC events out of 24 (100 %),
- 31 EJ events out of 35 (88.5 %).

2.5. Elliptical Cross-Section Fitting Model

The elliptical, non-force-free model (Hidalgo, Nieves-Chinchilla, and Cid, 2002; Hidalgo, 2003) considers that ICMEs have elliptical cross-section due to their interaction with the

solar wind. In this model, the expansion of the local cross-section is taken into account. Two characteristics distinguish this model from the others used in this paper: i) non-force-free condition is assumed, and, ii) an elliptical cylindrical coordinate system is chosen to solve the Maxwell equations. The model assumes a flux rope magnetic field geometry and treats the radial and axial electric currents separately. The local solutions of the Maxwell equations provide the three magnetic field components that are to be transformed into spacecraft coordinates. The only assumptions are that the radial and axial components of the current density are constant. The cross-section of the flux ropes is not required to be circular. This model was compared with the circular cross-section model of Lepping, Burlaga, and Jones (1990) in Nieves-Chinchilla, Hidalgo and Sequeiros (2005) and compared with information from remote-sensing measurements in Nieves-Chinchilla *et al.* (2012).

The ellipticity, the current density components, the expansion time of the cloud, and the axial magnetic field are determined by fitting the magnetic field data as explained in Section 2 of Hidalgo (2003). Multiple regression analysis is used to infer the spacecraft trajectory through the flux rope. The method converged for all events. However, the fit goodness was reported with a flag: 0 = poor; 1 = good; and, 2 = very good. This "goodness" is based on the correlation coefficient, fitting residue, and visual goodness. In the rest of the analysis, we take into account only fitting results with quality 1 or 2 (*i.e.*, removing poor fits). In that case, the elliptical cross-section fitting method was successful for

- full list: 39 events out of 59 (66 %),
- 24 MC events out of 24 (100 %),
- 15 EJ+ events out of 35 (43 %).

2.6. Selection of the ICME Boundaries

Selecting the boundaries of an ICME is still a challenging problem. This is because there is no single definitive characteristic of ICMEs. Some authors based the ICME boundaries purely on magnetic properties; others used a low proton temperature as one of the criteria; while others used charge state information. Many of the *in situ* signatures have been taken into account to determine the boundaries of ICMEs. However, each of these indicators provided different boundaries, which leaves the problem still unsolved. In this study, we let each group determine the boundaries for the ICMEs. For three events, we re-ran the analysis using pre-set boundaries as given by the self-similarly expanding cylinder fitting technique.

3. Comparative Analysis of the Fitting Parameters – Results

Out of 59 events on the CDAW list, the magnetic field was successfully reconstructed for 20 events by the GS technique, mostly for MCs. By comparison, the FFCA fitting and the self-similarly expanding cylinder methods were able to fit more than 85 % of the list, and the elliptical cylinder fitting method 66 %. In the following sections, we compare the fitted parameters from different codes with those from the FFCA code because i) it is the simplest code in our study, and ii) it succeeded in fitting most of the cases with the least deviation from the results of the other models. The number of cases that were analyzed in common by the FFCA code and the other codes is as follows: 20 with the GS reconstruction technique, 45 with the self-similarly expanding cylinder fitting method, and 37 with the elliptical cylinder fitting method.

3.1. Chirality

For all the 20 events reconstructed by the GS code, the chirality (sign of the magnetic helicity) is the same as for the self-similarly expanding cylinder and the FFCA model. There are three events for which the FFCA and self-similarly expanding cylinder found opposite signs for the helicity (events 13, 15, and 52 in the CDAW online list). This shows that even the simplest result of fitting and reconstruction methods is not necessarily well constrained. The difference is primarily due to the choice of boundaries. In two of these three cases (13 and 15), when the FFCA fit was performed again with a different choice for the boundaries, it returned the same sign of helicity as that found by the self-similarly expanding cylinder. In fact, it is worth noting that the chirality found with the FFCA differs for seven events depending on whether the boundaries are chosen following Lepping *et al.* (2006) or chosen specifically for this study by K. Marubashi.

One event is more ambiguous. For event 52, the FFCA fit is relatively poor and gives left-handed ejecta for the boundaries selected by K. Marubashi as well as for those from Lepping *et al.* (2006), whereas the self-similarly expanding cylinder fit gives right-handed ejecta. We note that the best-fit axial magnetic field by FFCA for this event is less than 6 nT for the two sets of boundaries, reflecting very weak ejecta.

This overall result about the chirality may appear inconsistent with what was found in previous studies by Dasso *et al*. (2003, 2006), who found the magnetic flux and helicity to be nearly independent of the fitting and reconstruction model for two well-observed MCs. Here, we find that this is generally true and consistent with our results. However, we also show that for ejecta whose boundaries are not clearly defined because of incomplete rotation, fittings with different boundaries can yield opposite chirality for the same event.

3.2. Maximum Magnetic Field Strength

For all cases in common between the FFCA code and one of the other codes in this study, we calculated the correlation of the fitted axial magnetic fields. For the self-similarly expanding cylinder fitting method, we used the axial magnetic field halfway through the cloud, corresponding approximately to the magnetic field at the closest approach to the cylinder axis, as calculated from Equation (2). We did not compare the value of the axial magnetic field for the elliptical cross-section fitting model with that of the other models. This is because the axial magnetic field in this model is the sum of two fields: the magnetic field created by the currents and the axial field that is a parameter of the model. Figure 3 summarizes the magnetic field results.

Overall, the correlation between the FFCA, GS, and self-similarly expanding cylinder code is quite good (~ 0.84). The axial magnetic field value from the GS code tends to be slightly higher than that from the FFCA especially for stronger magnetic fields, whereas the self-similarly expanding cylinder code tends to return higher values for the magnetic field for weak magnetic fields.

3.3. Orientation of the ICME Axis: Longitude and Latitude

The orientation of the ICME as it arrives at Earth is an essential parameter because it is often used to determine rotation of the CME as it propagates in the heliosphere (Yurchyshyn *et al.*, 2001). In addition, precisely knowing the orientation of an ICME is particularly important because the orientation of an ICME is known to be related to its geo-effectiveness (see, for example Zhao and Hoeksema, 1998). As can be seen in Figure 4, the orientation of some

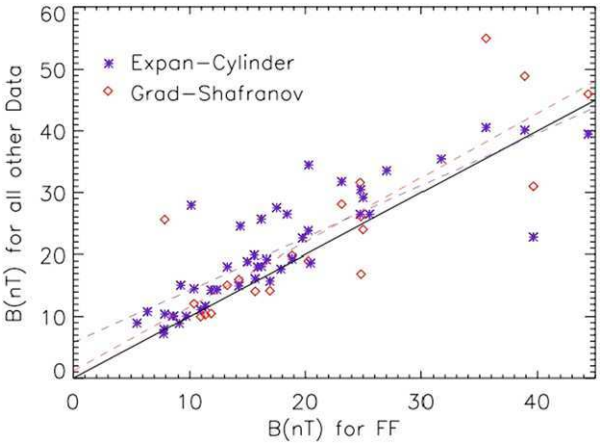

Figure 3 Axial magnetic field for the Grad–Shafranov (red diamonds) and self-similarly expanding cylinder (purple stars) models compared with the axial magnetic field for the FFCA model. The red and purple dashed lines show the best linear fits to the Grad–Shafranov and self-similarly expanding cylinder models.

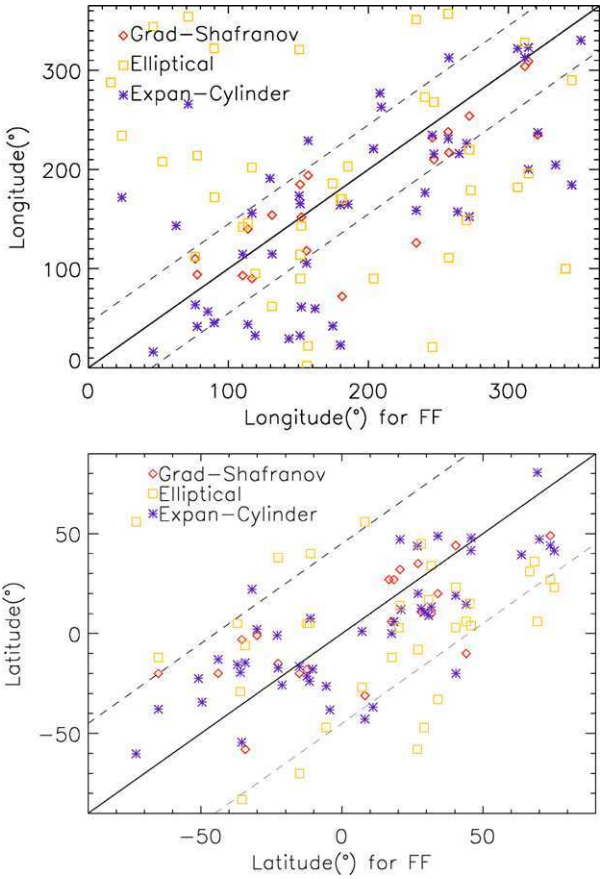

Figure 4 Same as Figure 3 but for the longitude and latitude of the reconstructed ICME axis. The yellow squares are for the elliptical cross-section fitting model. The dashed lines highlight the angles $\pm 45°$ from the FFCA angle.

ICME events differs greatly depending on which model is used. Indeed, only for one CME (event 44) did all events give an orientation of the axis within $\pm 45°$ of each other.

First, we focus on a comparison of the orientation between the Grad–Shafranov, self-similarly expanding cylinder and FFCA models for the 20 events successfully reproduced by all three methods. For seven events, the three methods give an orientation within $\pm 45°$ of each other. For eleven other events, the Grad–Shafranov reconstruction technique gives an orientation of the axis within $\pm 45°$ of one of the other two methods (but not the other). In fact, although the FFCA and self-similarly expanding cylinder fitting methods are closely related, the axis of the fitted cylinder is found to agree for only about 45 % of the events (21 out of the 45 common cases; for 14 of these, the orientation is within $\pm 30°$). While this may appear surprising considering the similarities between the two methods, it should be noted that the force-free method without expansion relies on the minimum-variance analysis to obtain the orientation of the flux rope, whereas the expanding cylinder method relies on a multi-parameter fitting procedure to minimize the deviation between the model and the measurements. In addition, for many events, the two methods used different boundaries.

Comparing the direction obtained from the elliptical cross-section model with that from the force-free cylindrical models (with and without expansion), we find that the direction from all three models only agree for one event. For seven additional events, the direction from the elliptical cross-section model is within $\pm 45°$ of the direction from the FFCA fitting model; for three additional cases, the same is true as compared to the direction from the self-similarly expanding cylinder model, and for one event it is true as compared with the direction for the Grad–Shafranov reconstruction technique.

Overall, there are only 34 events reconstructed by three or more methods. For 30 of these events, the orientation of the axis of the reconstructed ICME is consistent between at least two methods. The same is only true for three out of the 18 events reconstructed by two methods only. Finally, seven events were reconstructed by one method only.

3.4. Difference Between MCs and Non-MC Ejecta

Here, we briefly compare the average values of some parameters for the MCs with those for the non-MC ejecta. We only focus on the FFCA and self-similarly expanding cylinder, because the Grad–Shafranov reconstruction method is only able to reconstruct three non-MC ejecta (out of 35) and the elliptical cross-section fitting has a different set of parameters than these two models. Consistent with their definitions, non-MC ejecta are found to have, on average, a weaker magnetic field than MCs: 13.75 nT *vs*. 22.1 nT (FFCA) and 17.7 nT *vs*. 34.4 nT (expanding cylinder). We also find that the average impact parameter is larger for non-MC ejecta than for MCs: 0.73 *vs*. 0.54 (expanding cylinder) and 0.32 *vs*. 0.29 (FFCA). This may indicate that ejecta are indeed flux-rope-like magnetic clouds but are measured at a large impact parameter, resulting in a weaker magnetic field and less clearly defined properties. The average impact parameter for the events reconstructed by the GS method is 0.29 (FFCA) and 0.47 (expanding cylinder), once again showing that the GS method was only successful for MCs or MC-like ejecta.

4. Detailed Analyses of Three Events

We focus on events 10, 20, and 27, which we fitted using the same boundaries. These were the events chosen for the self-similarly expanding cylinder fitting method.

4.1. Event 10

This event is a left-handed non-MC ejectum observed in 26 – 28 June 1999. This was one of the events resulting in a poor fit for the elliptical cross-section model and was not initially

Table 1 Intervals used by different researchers for the events 10, 20, and 27. In bold are given the intervals chosen for events compared with the same boundaries. In parentheses are given the day of the month corresponding to the interval boundary. Events 10, 20, and 27 took place in June 1999, July 2000, and November 2000, respectively.

Event	10 (June)	20 (July)	27 (Nov.)
GS	N/A	08:36(27) – 19:24(27)	23:56(06) – 17:20(07)
FFCA	06:00(26) – 22:00(26)	07:30 – 19:30	22:10(06) – 17:10(07)
Exp. Cylind.	**06:00(26) – 19:00(26)**	**07:30 – 19:30**	**22:10 – 17:10**
Ellip	22:36(26) – 02:36(27)	10:10 – 20:40	23:08 – 17:45

successfully reconstructed by the Grad–Shafranov method. For this method, one problem was the presence of a shock propagating inside the ICME at 19:16 UT on 26 June. Because the GS reconstruction method attempts to find the best orientation of the ICME by requiring the function $P_t(A)$ to be single-valued, the presence of a shock in the magnetic and plasma pressure in one side of the cloud makes this an impossible task. This has been previously noted in Kilpua *et al.* (2009) and Möstl *et al.* (2009a). It is not a problem encountered by the other fitting methods.

Initially, some researchers found two possible flux rope intervals: one shortly after the shock wave on 26 June lasting about 16 hours (referred to hereafter as 10a) and one corresponding to the initial interval fitted with the self-similarly expanding cylindrical code of 6.5 hours at the end of 27 June and the beginning of 28 June (referred to hereafter as 10b from 20:30 UT on 27 June to 03:00 UT on 28 June). We discuss here the results from the longer, first interval. The intervals found by different researchers are shown in Table 1.

The analysis was performed again for interval 10a using the interval of 26 June from 06:00 to 19:00. In Figure 5, we show the fitting results for the different methods corresponding to this interval. Using the same interval for all the methods, the magnitude of the magnetic field in the ICME is found to agree relatively well between the two force-free and the Grad–Shafranov methods; it corresponds to a value $\sim 15-20$ nT. The orientation of the cloud is found to be consistent with a latitude of $0^\circ \pm 12^\circ$ and a longitude of $65^\circ \pm 25^\circ$ between these three methods, whereas the elliptical cross-section model finds a value about 90° away. This example illustrates the importance of the choice of boundaries for the study of magnetic clouds and ICMEs, because three of the four codes find very similar parameters for same boundaries.

4.2. Event 20

This event is a left-handed non-cloud ejectum observed on 27 July 2000. It is one of the three nonmagnetic cloud ejecta successfully reconstructed with the Grad–Shafranov reconstruction method. Initially, as we let each researcher select the ejectum boundaries, the direction of the cloud axis agreed well between the four methods: a longitude of $212^\circ \pm 32^\circ$ and a latitude of $22^\circ \pm 12^\circ$. All methods were within 45° of each other, except for the self-similarly expanding cylinder and the elliptical cross-section cylinder, which were about 55° apart.

The impact parameter was found to be close to 0 for the Grad–Shafranov method, but larger than 0.5 for the other three methods. The magnitude of the axial magnetic field was about 20 nT for the Grad–Shafranov method and about 8 nT for the two force-free constant-alpha models.

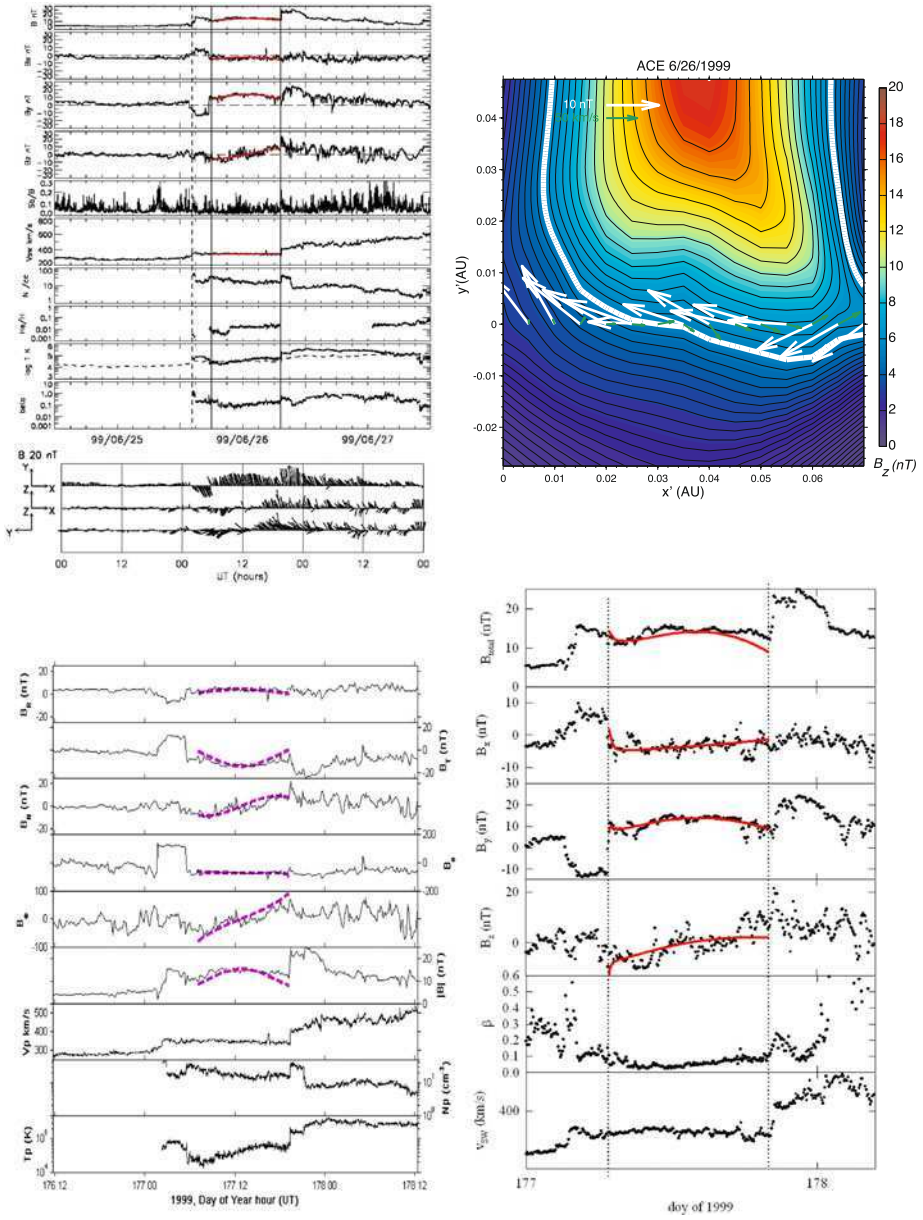

Figure 5 Fitting for event 10a by the different codes. Top left: Self-similarly expanding cylinder code fit shown in red. The different panels are the total magnetic field, B_x, B_y, B_z, the magnetic field fluctuation, the solar wind speed, proton density, alpha-to-proton ratio, temperature, and plasma β from top to bottom. Bottom left: FFCA code fit shown in purple. The panels show from top to bottom the radial, tangential, normal (R, T and N) components, the longitude and latitude angles (in RTN) and the magnitude of the magnetic field, the proton velocity, density, and temperature. Top right: GS reconstruction map, the axial magnetic field is color-coded and the black contours are magnetic field lines in the plane of the cross-section of the ICME. Observed magnetic field components in this plane are shown with white vectors and velocity is depicted in green. Bottom right: Elliptical cross-section fit in red. The different panels show the magnetic field, its three components, the plasma β, and the solar wind speed from top to bottom.

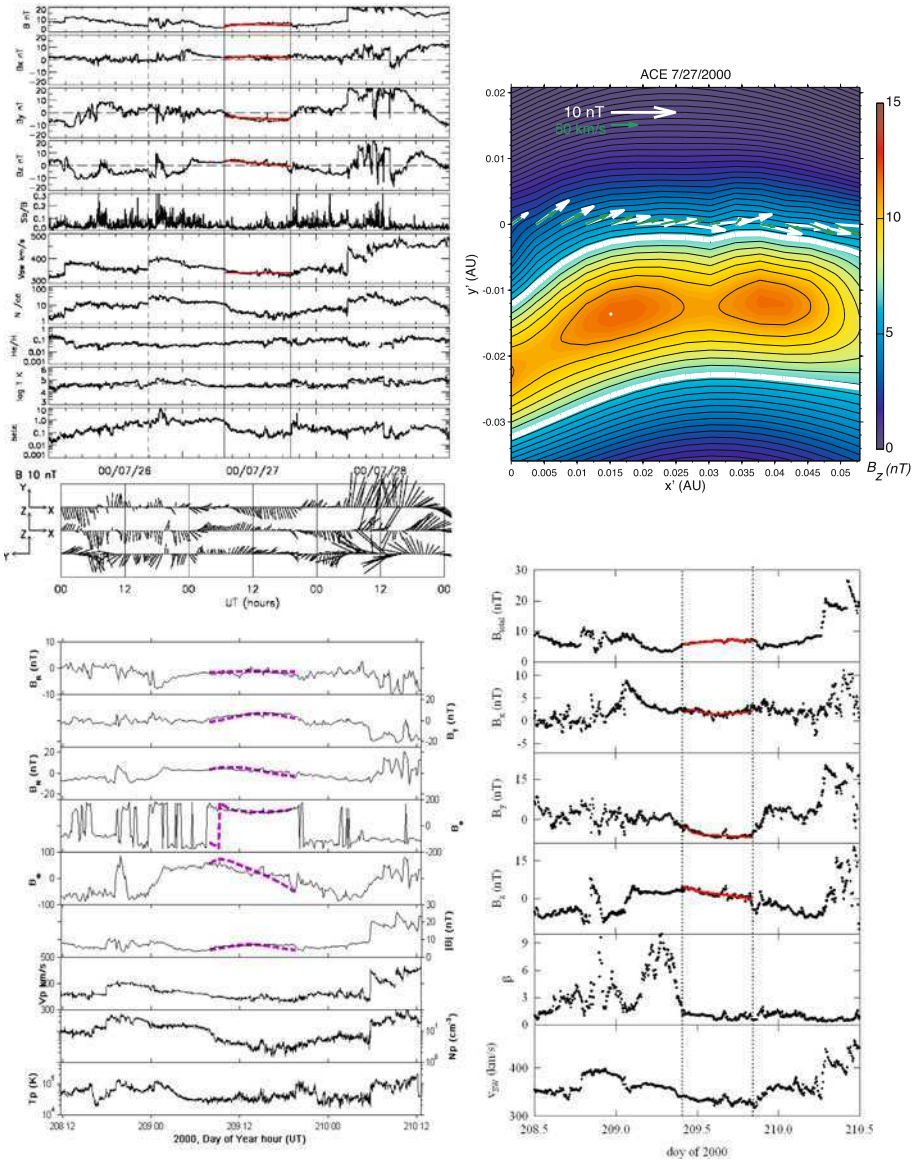

Figure 6 Same as Figure 5 but for event 20.

As can be seen from Table 1, the different researchers chose boundaries very close to each other, and choosing exactly the same boundaries does not drastically change the results, except that the maximum axial magnetic field for the Grad–Shafranov model was 12 nT with an impact parameter of about 0.25, more consistent with the values found by the other models. In Figure 6, we show the results of the fit using the boundaries chosen for the self-similarly expanding cylinder fit.

4.3. Event 27

This event is a left-handed magnetic cloud observed on 6 – 7 November 2000. All methods agree on the maximum magnetic field strength (~ 25 nT for Grad–Shafranov and the FFCA model and ~ 31.5 nT for the self-similarly expanding cylinder). However, there is initially little agreement regarding the orientation of the magnetic cloud with a latitude of $14^\circ \pm 14^\circ$ and a longitude of $145^\circ \pm 55^\circ$ for the four methods. As for the previous event, the boundaries chosen independently by different researchers were relatively consistent. One significant difference is the inclusion or exclusion of a region of strong magnetic field without much rotation at the "back" of the MC (until 02:40 on 8 November). Previous studies (Dasso *et al.*, 2006, 2007; Möstl *et al.*, 2008) have discussed how reconnection between an MC and the ambient solar wind during the ICME propagation may result in this type of region which strictly speaking belongs to the MC. Each researcher decided exactly where to end the MC. Since there is no counterpart flux on the MC front to the flux on the back of the MC, it is probably better not to take this region into account.

Using the same boundaries, there is a better agreement that the magnetic cloud has a low inclination (latitude $\sim 5^\circ$) but an only slightly better agreement about the precise orientation or the value of the impact parameter. The fits and reconstructions are shown in Figure 7.

5. Summary and Conclusions

In this article, we have presented a comparison of the reconstruction results of 59 ICMEs measured *in situ* during Solar Cycle 23 using four different reconstruction or fitting methods. The events our study focused on were chosen because their source region was known and was within $\pm 15^\circ$ of the central meridian. Our data included 24 events identified as magnetic clouds (MCs) following the definition of Burlaga *et al.* (1981) and 35 non-MC ejecta. We find that the two force-free techniques (with or without expansion) are able to fit the vast majority of the events (≥ 85 %) including more than 75 % of the ejecta. The Grad–Shafranov reconstruction method, which assumes magneto-hydrostatic equilibrium and uses the plasma pressure is found to only work for clear magnetic clouds, because it was only successful in reconstructing 8 % of the non-cloud ejecta (3/35). In addition, the Grad–Shafranov reconstruction is not able to reconstruct ICMEs into which a shock is propagating because it violates its initial assumption. However, one of the advantages of this method is the fact that the boundaries of the ICME are a result of the reconstruction, and they do not need to be chosen before performing the fits, as for the other methods. The expanding elliptical cross-section was able to fit about two-thirds of the events with a reasonably good result (all magnetic clouds and about 40 % of the ejecta).

We have found that even the ICME chirality (sign of the magnetic helicity), one of the simplest possible reconstruction parameters, is not necessarily clearly constrained, and opposite chirality can be found for the same event because of differences in the choice of the boundaries. In most cases, the choice of boundaries alone explains the difference between different methods.

Regarding the maximum magnetic field strength, we have found that, typically, the results of the Grad–Shafranov method, the FFCA, and self-similarly expanding fittings are well correlated and agree to within about 25 %. The Grad–Shafranov method returns higher values than the FFCA fitting method for strong magnetic fields, whereas the force-free model, which includes self-similar expansion, returns higher values than the FFCA fitting method for weak magnetic fields. Gulisano *et al.* (2005) previously compared the maximum magnetic field at the cloud axis for 20 magnetic clouds using four fitting methods and found

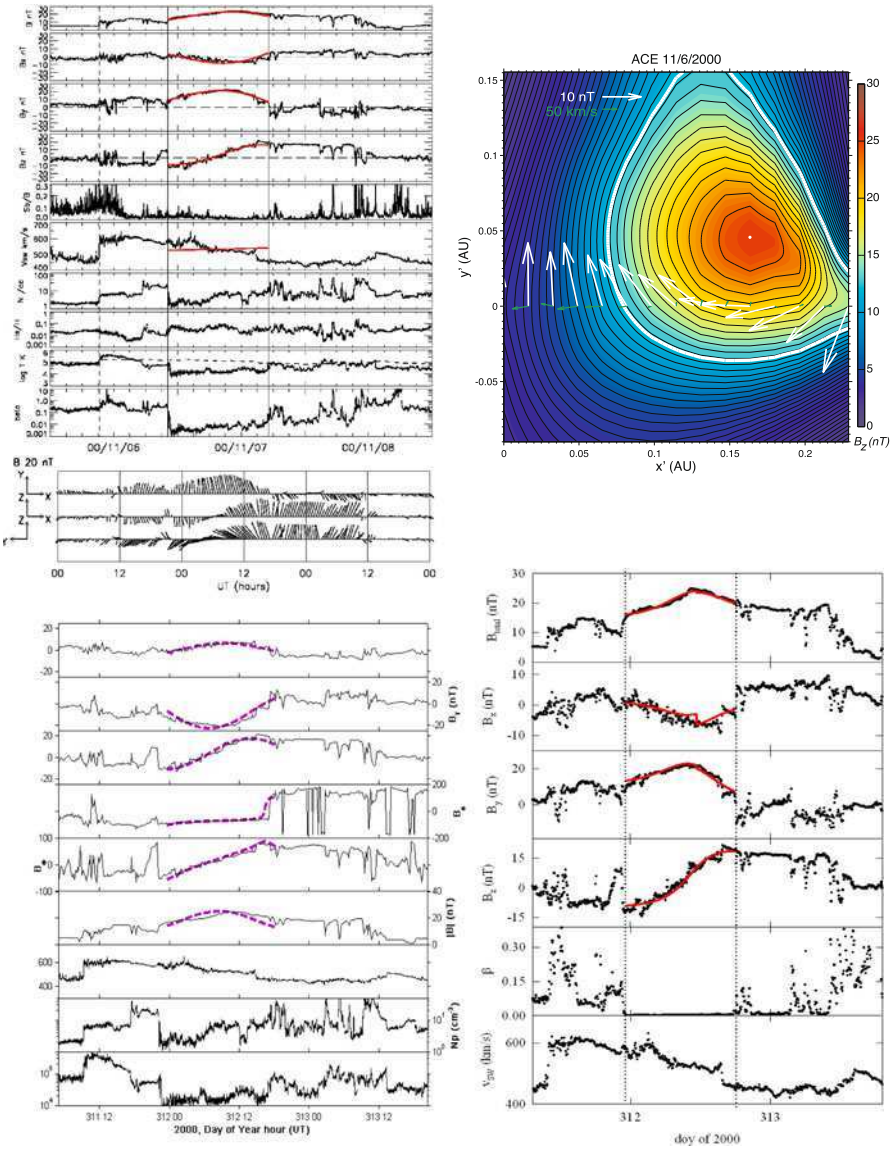

Figure 7 Same as Figure 5 but for event 27.

that the variability between methods for the same event was significantly lower than the variability between events for the same method (see their Figure 4).

For only one event, all four methods found an orientation of the ICME axis within $\pm 45°$. Considering only the two force-free fitting methods (with and without expansion) and the Grad–Shafranov reconstruction method, this is the case for about 30 % of the ICMEs (seven out the 20 common cases). Directly comparing the two force-free constant-α codes (with and without expansion), they return ICME axis within $\pm 30°$ in only ~ 30 % of the cases and within $\pm 45°$ in only ~ 45 % of the cases. While these two methods assumed very sim-

ilar geometries for the ICME, the fitting procedures are very different: a minimum-variance analysis was used to determine the axis' direction for the FFCA code, whereas a fitting procedure was used for the expanding cylinder method. This is likely to account for the difference in the direction of the ICME axis. Finally, the elliptical cross-section model typically gives different orientation as compared to the other methods, which agrees with at least one other method for only about 30 % of the events. These results were found by letting researchers select their own boundaries.

When only two methods successfully reconstructed an event, the orientation found by these two methods usually disagreed (by more than $\pm 45°$ in 15 out the 18 cases). When the two force-free constant-α fitting methods and the Grad–Shafranov reconstruction method successfully reconstructed an event, the orientation from the Grad–Shafranov method was within $\pm 30°$ of that from one of the force-free constant-α methods in 70 % of the cases (14 out of 20 events). Combining all four methods, more than 65 % (23/34) of the events reconstructed by three or more methods had at least two methods that yielded an orientation within $\pm 30°$. It is therefore clear that having multiple methods able to successfully fit or reconstruct the same event gives more reliable results regarding the orientation of the ICME axis.

We furthermore quantified the importance of the boundary selection by performing the analyses again for three events using the same boundaries for all methods. This way we found a better agreement between the different codes regarding the ICME magnetic field strength, and, for one event, a better agreement for the ICME orientation.

Finally, for two methods we compared the impact parameter and magnetic field strength of MCs and non-MC ejecta. We found that the non-MC ejecta have, as expected, a weaker magnetic field but we also found some evidence that the impact parameter is, on average, larger for non-MC ejecta than for MCs. This is a first statistical hint that most (or all) ICMEs observed at 1 AU may in fact be magnetic flux ropes, but depending on how they impact the observing spacecraft, they may be recognized as magnetic clouds or not. After performing fitting and reconstructions for 59 ICMEs with four different codes, we will investigate the nature of the magnetic fields in ICMEs in more detail and also aim improve the reconstruction methods in the future.

Acknowledgements We would like to thank the referee for his/her very useful comments, which helped improve and clarify our study and manuscript.

N. A. and I. R. were supported by a NSF grant AGS-0639335 (CAREER). This work was initiated at two Coordinated Data Analysis Workshops (CDAWs) held at Predictive Science Inc. in San Diego, CA and at the University of Alcala in Alcala de Henares, Spain with support from NASA and from Spain. N. P. S. was supported by the NASA LWS Jack Eddy Postdoctoral Fellowship Program, administrated by the UCAR Visiting Scientist Program and hosted by the Naval Research Laboratory. C. M. was supported by a Marie Curie International Outgoing Fellowship within the 7th European Community Framework Programme. The presented work has received funding from the European Union Seventh Framework Programme (FP7/2007-2013) under grant agreement n°263252 [COMESEP]. C. J. F. acknowledges support from NASA grant NNX10AQ29G and NAS5-0313. N. A. would like to thank the Space Science Center at the University of New Hampshire for providing a nice work environment during the final revisions of this manuscript.

References

Al-Haddad, N., Roussev, I.I., Möstl, C., Jacobs, C., Lugaz, N., Poedts, S., Farrugia, C.J.: 2011, *Astrophys. J. Lett.* **738**, L18. doi:10.1088/2041-8205/738/2/L18.

Bothmer, V., Schwenn, R.: 1998, *Ann. Geophys.* **16**, 1. doi:10.1007/s00585-997-0001-x.

Burlaga, L.F.: 1988, *J. Geophys. Res.* **93**, 7217. doi:10.1029/JA093iA07p07217.

Burlaga, L.F., Plunkett, S.P., St. Cyr, O.C.: 2002, *J. Geophys. Res.* **107**, 1266.

Burlaga, L., Sittler, E., Mariani, F., Schwenn, R.: 1981, *J. Geophys. Res.* **86**, 6673.

Chané, E., van der Holst, B., Jacobs, C., Poedts, S., Kimpe, D.: 2006, *Astron. Astrophys.* **447**, 727. doi:10.1051/0004-6361:20053802.
Dasso, S., Mandrini, C.H., Démoulin, P., Farrugia, C.J.: 2003, *J. Geophys. Res.* **108**, 1362. doi:10.1029/2003JA009942.
Dasso, S., Mandrini, C.H., Démoulin, P., Luoni, M.L.: 2006, *Astron. Astrophys.* **455**, 349. doi:10.1051/0004-6361:20064806.
Dasso, S., Nakwacki, M.S., Démoulin, P., Mandrini, C.H.: 2007, *Solar Phys.* **244**, 115.
Démoulin, P., Dasso, S.: 2009, *Astron. Astrophys.* **507**, 969. doi:10.1051/0004-6361/200912645.
Farrugia, C.J., Osherovich, V.A., Burlaga, L.F.: 1995, *J. Geophys. Res.* **100**, 12293. doi:10.1029/95JA00272.
Farrugia, C.J., Burlaga, L.F., Osherovich, V.A., Lepping, R.P.: 1992, In: Marsch, E., Schwenn, R. (eds.) *Solar Wind Seven Colloquium*, 611.
Farrugia, C.J., Burlaga, L.F., Osherovich, V.A., Richardson, I.G., Freeman, M.P., Lepping, R.P., Lazarus, A.J.: 1993, *J. Geophys. Res.* **98**, 7621. doi:10.1029/92JA02349.
Farrugia, C.J., Berdichevsky, D.B., Möstl, C., Galvin, A.B., Leitner, M., Popecki, M.A., Simunac, K.D.C., Opitz, A., Lavraud, B., Ogilvie, K.W., Veronig, A.M., Temmer, M., Luhmann, J.G., Sauvaud, J.A.: 2011, *J. Atmos. Solar-Terr. Phys.* **73**, 1254. doi:10.1016/j.jastp.2010.09.011.
Gold, T.: 1959, *J. Geophys. Res.* **64**, 1219. doi:10.1029/JZ064i009p01219.
Goldstein, H.: 1983, In: *NASA Conference Publication* **228**, 731.
Gopalswamy, N., Akiyama, S., Yashiro, S., Michalek, G., Lepping, R.P.: 2008, *J. Atmos. Solar-Terr. Phys.* **70**, 245. doi:10.1016/j.jastp.2007.08.070.
Gopalswamy, N., Xie, H., Mäkelä, P., Akiyama, S., Yashiro, S., Kaiser, M.L., Howard, R.A., Bougeret, J.L.: 2010, *Astrophys. J.* **710**, 1111. doi:10.1088/0004-637X/710/2/1111.
Gosling, J.T.: 1990, In: *AGU Geophys. Monogr. Ser.* **58**, 343.
Gulisano, A.M., Dasso, S., Mandrini, C.H., Démoulin, P.: 2005, *J. Atmos. Solar-Terr. Phys.* **67**, 1761. doi:10.1016/j.jastp.2005.02.026.
Hidalgo, M.A.: 2003, *J. Geophys. Res.* **108**, 1320. doi:10.1029/2002JA009818.
Hidalgo, M.A., Nieves-Chinchilla, T., Cid, C.: 2002, *Geophys. Res. Lett.* **29**(13), 1637. doi:10.1029/2001GL013875.
Hu, Q., Sonnerup, B.U.Ö.: 2001, *Geophys. Res. Lett.* **28**, 467. doi:10.1029/2000GL012232.
Hu, Q., Sonnerup, B.U.Ö.: 2002, *J. Geophys. Res.* **107**, 1142. doi:10.1029/2001JA000293.
Hu, Q., Smith, C.W., Ness, N.F., Skoug, R.M.: 2004, *J. Geophys. Res.* **109**, A03102. doi:10.1029/2003JA010101.
Isavnin, A., Kilpua, E.K.J., Koskinen, H.E.J.: 2011, *Solar Phys.* **273**, 205. doi:10.1007/s11207-011-9845-z.
Jian, L., Russell, C.T., Luhmann, J.G., Skoug, R.M.: 2006, *Solar Phys.* **239**, 393. doi:10.1007/s11207-006-0133-2.
Kahler, S.W., Krucker, S., Szabo, A.: 2011, *J. Geophys. Res.* **116**, A01104. doi:10.1029/2010JA015328.
Kilpua, E.K.J., Liewer, P.C., Farrugia, C., Luhmann, J.G., Möstl, C., Li, Y., Liu, Y., Lynch, B.J., Russell, C.T., Vourlidas, A., Acuna, M.H., Galvin, A.B., Larson, D., Sauvaud, J.A.: 2009, *Solar Phys.* **254**, 325. doi:10.1007/s11207-008-9300-y.
Kilpua, E.K.J., Lee, C.O., Luhmann, J.G., Li, Y.: 2011, *Ann. Geophys.* **29**, 1455. doi:10.5194/angeo-29-1455-2011.
Lepping, R.P., Burlaga, L.F., Jones, J.A.: 1990, *J. Geophys. Res.* **95**, 11957.
Lepping, R.P., Acuna, M.H., Burlaga, L.F., Farrell, W.M.: 1995, *Space Sci. Rev.* **71**, 207.
Lepping, R.P., Berdichevsky, D.B., Wu, C.C., Szabo, A., Narock, T., Mariani, F., Lazarus, A.J., Quivers, A.J.: 2006, *Ann. Geophys.* **24**, 215. doi:10.5194/angeo-24-215-2006.
Li, Y., Luhmann, J.G., Lynch, B.J., Kilpua, E.K.J.: 2011, *Solar Phys.* **270**, 331. doi:10.1007/s11207-011-9722-9.
Liu, Y., Luhmann, J.G., Huttunen, K.E.J., Lin, R.P., Bale, S.D., Russell, C.T., Galvin, A.B.: 2008, *Astrophys. J. Lett.* **677**, 133. doi:10.1086/587839.
Lugaz, N., Manchester, W.B., Gombosi, T.I.: 2005a, *Astrophys. J.* **627**, 1019.
Lugaz, N., Manchester, W.B., Gombosi, T.I.: 2005b, *Astrophys. J.* **634**, 651.
Lugaz, N., Vourlidas, A., Roussev, I.I., Morgan, H.: 2009, *Solar Phys.* **256**, 269. doi:10.1007/s11207-009-9339-4.
Lundquist, S.: 1950, *Ark. Fys.* **2**, 361.
Lynch, B.J., Zurbuchen, T.H., Fisk, L.A., Antiochos, S.K.: 2003, *J. Geophys. Res.* **108**, 1239. doi:10.1029/2002JA009591.
Manchester, W.B., Gombosi, T.I., Roussev, I., Ridley, A., De Zeeuw, D.L., Sokolov, I.V., Powell, K.G., Tóth, G.: 2004, *J. Geophys. Res.* **109**, A02107.
Manchester, W.B., Vourlidas, A., Tóth, G., Lugaz, N., Roussev, I.I., Sokolov, I.V., Gombosi, T.I., De Zeeuw, D.L., Opher, M.: 2008, *Astrophys. J.* **684**, 1448. doi:10.1086/590231.
Marubashi, K.: 1986, *Adv. Space Res.* **6**, 335. doi:10.1016/0273-1177(86)90172-9.

Marubashi, K.: 2000, *Adv. Space Res.* **26**, 55. doi:10.1016/S0273-1177(99)01026-1.
Marubashi, K., Lepping, R.P.: 2007, *Ann. Geophys.* **25**, 2453. doi:10.5194/angeo-25-2453-2007.
McComas, D.J., Bame, S.J., Barker, P., Feldman, W.C.: 1998, *Space Sci. Rev.* **86**, 563.
Möstl, C., Miklenic, C., Farrugia, C.J., Temmer, M., Veronig, A., Galvin, A.B., Vršnak, B., Biernat, H.K.: 2008, *Ann. Geophys.* **26**, 3139. doi:10.5194/angeo-26-3139-2008.
Möstl, C., Farrugia, C.J., Miklenic, C., Temmer, M., Galvin, A.B., Luhmann, J.G., Kilpua, E.K.J., Leitner, M., Nieves-Chinchilla, T., Veronig, A., Biernat, H.K.: 2009a, *J. Geophys. Res.* **114**, A04102. doi:10.1029/2008JA013657.
Möstl, C., Farrugia, C.J., Biernat, H.K., Leitner, M., Kilpua, E.K.J., Galvin, A.B., Luhmann, J.G.: 2009b, *Solar Phys.* **256**, 427. doi:10.1007/s11207-009-9360-7.
Möstl, C., Temmer, M., Rollett, T., Farrugia, C.J., Liu, Y., Veronig, A.M., Leitner, M., Galvin, A.B., Biernat, H.K.: 2010, *Geophys. Res. Lett.* **37**, L24103. doi:10.1029/2010GL045175.
Mulligan, T., Russell, C.T.: 2001, *J. Geophys. Res.* **106**, 10581. doi:10.1029/2000JA900170.
Nelder, J.A., Mead, R.: 1965, *Comput. J.* **7**, 308.
Nieves-Chinchilla, T., Hidalgo, M.A., Sequeiros, J.: 2005, *Solar Phys.* **232**, 105.
Nieves-Chinchilla, T., Colaninno, R., Vourlidas, A., Szabo, A., Lepping, R.P., Boardsen, S.A., Anderson, B.J., Korth, H.: 2012, *J. Geophys. Res.* **117**, A06106.
Odstrčil, D., Pizzo, V.J.: 1999, *J. Geophys. Res.* **104**(13), 483.
Odstrčil, D., Pizzo, V.J.: 2009, *Solar Phys.* **259**, 297. doi:10.1007/s11207-009-9449-z.
Ogilvie, K.W., Chornay, D.J., Fritzenreiter, R.J., Hunsaker, F.: 1995, *Space Sci. Rev.* **71**, 55.
Owens, M.J., Merkin, V.G., Riley, P.: 2006, *J. Geophys. Res.* **111**, A03104. doi:10.1029/2005JA011460.
Owens, M.J., Démoulin, P., Savani, N.P., Lavraud, B., Ruffenach, A.: 2012, *Solar Phys.*, **278**, 435. doi:10.1007/s11207-012-9939-2.
Rees, A., Forsyth, R.J.: 2004, *Geophys. Res. Lett.* **31**, L06804. doi:10.1029/2003GL018330.
Richardson, I.G., Cane, H.V.: 2010, *Solar Phys.* **264**, 189. doi:10.1007/s11207-010-9568-6.
Riley, P., Gosling, J.T., Pizzo, V.J.: 1997, *J. Geophys. Res.* **102**, 14677. doi:10.1029/97JA01131.
Riley, P., Linker, J.A., Mikić, Z., Odstrcil, D., Zurbuchen, T.H., Lario, D., Lepping, R.P.: 2003, *J. Geophys. Res.* **108**, 1272. doi:10.1029/2002JA009760.
Riley, P., Linker, J.A., Lionello, R., Mikić, Z., Odstrcil, D., Hidalgo, M.A., Cid, C., Hu, Q., Lepping, R.P., Lynch, B.J., Rees, A.: 2004, *J. Atmos. Solar-Terr. Phys.* **66**, 1321. doi:10.1016/j.jastp.2004.03.019.
Riley, P., Lionello, R., Mikić, Z., Linker, J.: 2008, *Astrophys. J.* **672**, 1221. doi:10.1086/523893.
Romashets, E.P., Vandas, M.: 2003, *Geophys. Res. Lett.* **30**(20), 2065. doi:10.1029/2003GL017692.
Rouillard, A.P.: 2011, *J. Atmos. Solar-Terr. Phys.* **73**, 1201.
Ruffenach, A.B., Lavraud, B., Owens, M.J., *et al.*: 2012, *J. Geophys. Res.* doi:10.1029/2012JA017624
Savani, N.P., Rouillard, A.P., Davies, J.A., Owens, M.J., Forsyth, R.J., Davis, C.J., Harrison, R.A.: 2009, *Ann. Geophys.* **27**, 4349 – 4358. doi:10.5194/angeo-27-4349-2009.
Savani, N.P., Owens, M.J., Rouillard, A.P., Forsyth, R.J., Davies, J.A.: 2010, *Astrophys. J. Lett.* **714**, 128. doi:10.1088/2041-8205/714/1/L128.
Shen, F., Feng, X., Wu, S.T., Xiang, C.: 2007, *J. Geophys. Res.* **112**, A06109. doi:10.1029/2006JA012164.
Shimazu, H., Vandas, M.: 2002, *Earth Planets Space* **54**, 783.
Smith, C.W., L'Heureux, J., Ness, N.F., Acuna, M.H.: 1998, *Space Sci. Rev.* **86**, 613.
Sonnerup, B.U.Ö., Scheible, M.: 1998, *ISSI Sci. Rep. Ser.* **1**, 185.
Steed, K., Owen, C.J., Démoulin, P., Dasso, S.: 2011, *J. Geophys. Res.* **116**, A01106. doi:10.1029/2010JA015940.
Vandas, M., Romashets, E.P.: 2003, *Astron. Astrophys.* **398**, 801. doi:10.1051/0004-6361:20021691.
Vandas, M., Romashets, E.P., Watari, S., Geranios, A., Antoniadou, E., Zacharopoulou, O.: 2006, *Adv. Space Res.* **38**, 441. doi:10.1016/j.asr.2004.11.026.
Wang, Y.M., Ye, P.Z., Wang, S.: 2003, *J. Geophys. Res.* **108**, 1370.
Yurchyshyn, V.B., Wang, H., Goode, P.R., Deng, Y.: 2001, *Astrophys. J.* **563**, 381. doi:10.1086/323778.
Zhang, J., Richardson, I.G., Webb, D.F., Gopalswamy, N., Huttunen, E., Kasper, J.C., Nitta, N.V., Poomvises, W., Thompson, B.J., Wu, C.C., Yashiro, S., Zhukov, A.N.: 2007, *J. Geophys. Res.* **112**. A10102. doi:10.1029/2007JA012321.
Zhao, X.P., Hoeksema, J.T.: 1998, *J. Geophys. Res.* **103**, 2077. doi:10.1029/97JA03234.
Zurbuchen, T.H., Richardson, I.G.: 2006, *Space Sci. Rev.* **123**, 31. doi:10.1007/s11214-006-9010-4.

Solar Phys (2013) 284:89–104
DOI 10.1007/s11207-013-0242-7

A Comparative Study of Coronal Mass Ejections with and Without Magnetic Cloud Structure near the Earth: Are All Interplanetary CMEs Flux Ropes?

J. Zhang · P. Hess · W. Poomvises

Received: 13 July 2012 / Accepted: 21 January 2013 / Published online: 8 February 2013

Abstract An outstanding question concerning interplanetary coronal mass ejections (ICMEs) is whether all ICMEs have a magnetic flux rope structure. We test this question by studying two different ICMEs, one having a magnetic cloud (MC) showing smooth rotation of magnetic field lines and the other not. The two ICMEs are chosen in such a way that their progenitor CMEs are very similar in remote sensing observations. Both CMEs originated from close to the central meridian directly facing the Earth. Both CMEs were associated with a long-lasting post-eruption loop arcade and appeared as an elliptical halo in coronagraph images, indicating a flux rope origin. We conclude that the difference in the *in-situ* observation is caused by the geometric selection effect, contributed by the deflection of flux ropes in the inner corona and interplanetary space. The first event had its nose pass through the observing spacecraft; thus, the intrinsic flux rope structure of the CME appeared as a magnetic cloud. On the other hand, the second event had the flank of the flux rope intercept the spacecraft, and it thus did not appear as a magnetic cloud. We further argue that a conspicuous long period of weak magnetic field, low plasma temperature, and density in the second event should correspond to the extended leg portion of the embedded magnetic flux rope, thus validating the scenario of the flank-passing. These observations support the idea that all CMEs arriving at the Earth include flux rope drivers.

Flux-Rope Structure of Coronal Mass Ejections
Guest Editors: N. Gopalswamy, T. Nieves-Chinchilla, M. Hidalgo, J. Zhang, and P. Riley

J. Zhang (✉) · P. Hess
School of Physics, Astronomy and Computational Sciences, George Mason University,
4400 University Dr., MSN 6A2, Fairfax, VA 22030, USA
e-mail: jzhang7@gmu.edu

W. Poomvises
Catholic University of America, Washington, DC 20064, USA

W. Poomvises
NASA Goddard Space Flight Center, Greenbelt, MD 20771, USA

1. Introduction

Coronal mass ejections (CMEs) are an energetic phenomenon originated in the Sun's corona, but subsequently propagating into the interplanetary space. CMEs are now well known to be the cause of intense geomagnetic storms (Gosling *et al.*, 1991; Zhang *et al.*, 2007) and to be a direct driver of severe space weather that may have disruptive effects on advanced human technological systems in space and on the ground. The underlying physical structure of a CME is believed to be a magnetic flux rope, a self-contained magnetic system with helical magnetic field lines wrapping around its center axis (Chen, 1996). The first direct observational evidence of the presence of magnetic flux ropes was from near-Earth *in-situ* solar wind observations of the so-called magnetic clouds, seen as a large rotation in the field's direction, enhanced field strength and a low plasma β (Burlaga *et al.*, 1981; Lepping, Jones, and Burlaga, 1990). Improved coronagraphic observations of CMEs from the *Solar and Heliospheric Observatory* (SOHO) showed that CMEs in the outer corona often contain a circular intensity pattern when CMEs are observed from the side, thus suggesting the presence of flux ropes (Dere *et al.*, 1999).

Recent observations from the *Advanced Imaging Assembly* (AIA) on-board *Solar Dynamic Observatory* (SDO) showed that a magnetic flux rope exists prior to the eruption and continuously transforms from a sigmoidal structure to a semi-circular shape (Zhang, Cheng, and Ding, 2012). In SDO observations, magnetic flux ropes are best seen in hot temperature passbands ($> \sim 6$ MK), but are completely absent in cool temperatures ($< \sim 3$ MK) (Liu *et al.*, 2010; Cheng *et al.*, 2011; Zhang, Cheng, and Ding, 2012). Earlier observations of sigmoidal structures in soft X-ray images prior to eruptions (Sterling and Hudson, 1997; Canfield, Hudson, and McKenzie, 1999), are often interpreted as a magnetic flux rope (Rust, 1994; Titov and Démoulin, 1999; McKenzie and Canfield, 2008). The physical origin of flux ropes has been suggested either to be sub-photospheric emergence into the corona (Gibson *et al.*, 2002; Schrijver, 2009), or the transformation of a sheared arcade through photospheric flux cancellation (Green and Kliem, 2009; Tripathi *et al.*, 2009).

Magnetic flux ropes probably play an essential role in CME initiation and acceleration, *i.e.*, the CME initiation is triggered by the structural instability of the flux rope. One such mechanism is so-called the Torus Instability (TI) (Kliem and Török, 2006; Olmedo and Zhang, 2010), an ideal magneto-hydrodynamic (MHD) process responsible for the loss of equilibrium of a toroidal current ring. In this model, a critical gradient of the external magnetic field determines the onset of the instability. Three-dimensional MHD simulations further demonstrate that the transition of a flux rope from equilibrium to eruption follows the TI onset criterion (Fan and Gibson, 2007; Aulanier *et al.*, 2010). However, there also exist opposing models that assume no flux rope prior to the eruption, and assume a sheared arcade instead (Antiochos, DeVore, and Klimchuk, 1999; Moore *et al.*, 2001; Amari *et al.*, 2003). Nevertheless, these models allow magnetic reconnection to transfer the sheared arcade into a fully developed magnetic flux rope. Therefore, on both observational and theoretical grounds, all sizable CMEs following the eruption (*e.g.*, tens of minutes) are likely to contain a magnetic flux rope in the structure.

An interesting and important question is then about the CME structure near the Earth after the tens-of-hour-long journey through the interplanetary space. *In-situ* observations of solar wind magnetic field and plasma properties have clearly revealed the existence of interplanetary CMEs (ICMEs), the counterpart phenomena of CMEs from the Sun. The *in-situ* signatures of ICMEs are many, including enhanced magnetic field, reduced magnetic field variance, abnormally low proton temperature, upstream forward shock, elevated

oxygen charge state, enhancement of Fe/O ratio, and bidirectional strahl electrons *etc.* (Zurbuchen and Richardson, 2006). Not all signatures exist at the same time, but the presence of several signatures set ICMEs apart from the ambient solar wind. One can also set ICMEs apart from other transient features, such as CME-driven sheath regions and corotating interaction regions (CIRs).

It has been found that only a subset of ICMEs show the presence of a magnetic cloud structure or flux rope. These magnetic-cloud ICMEs are abbreviated as MC-ICME hereafter. The complementary set of ICMEs, which do not show a systematic rotation of magnetic field lines, are abbreviated NMC-ICMEs (non-magnetic-cloud ICME). MC-ICMEs only constitute a fraction of all ICMEs detected in solar wind, The estimated fraction ranges from ~ 30 % to ~ 50 % (Gosling, 1990; Bothmer and Schwenn, 1996; Henke *et al.*, 2001). Richardson and Cane (2004) found a solar cycle variation of the fraction of MC-ICMEs, *i.e.*, ~ 15 % at solar maximum but as high as almost 100 % at solar minimum. MC-ICMEs are usually more geoeffective than other transient events. Zhang *et al.* (2007) found that for those ICME-driven intensive geomagnetic storms, 43 % of the storms are caused by MCs, and only 18 % of them are produced by NMC-ICMEs; the others are related to ICME-driven shock sheaths (27 %) and shocks propagating into preceding ICMEs (12 %). Gopalswamy *et al.* (2007) also found that MC-associated CMEs are faster and wider on the average and originate within ± 30 degree from the solar disk center.

The challenging question is whether or not a NMC-ICME is a flux rope, given that there is a large fraction of NMC-ICMEs at 1 AU. We intend to address this issue through a careful comparative study of MC-ICME and NMC-ICME events. If one assumes that all CMEs borne on the Sun are a flux rope, there are several known factors that might cause the flux rope to appear as a non-magnetic-cloud:

i) Geometric selection effect. This effect is caused by the one-point sampling of *in-situ* observations, *i.e.*, the appearance of an ICME is highly dependent on the sampling path of the spacecraft through the ICME structure. This selection effect, as well as the contributing deflection effect of flux ropes, will be addressed in detail in this paper (see the Discussion section).
ii) Multiple CME-interaction effect (Gopalswamy *et al.*, 2001; Wang *et al.*, 2003), in which the interaction possibly destroys the coherence of a flux rope.

We can safely exclude the self-evolution effect of a single flux rope, since it is unlikely that a flux rope topology, while expanding in the interplanetary space, will alter and change itself into some structures different from a flux rope. The interaction between flux rope and the ambient solar wind will possibly compress the flux rope, the so-called pancake effect (Riley and Crooker, 2004), but will not change the overall topology of helical field lines. In this paper, we make a comparative study of two ICMEs, one MC and one NMC. The ICMEs are such chosen so that we remove or limit all the known effects affecting the evolution of flux ropes. Both events are isolated single CMEs, thus eliminating the effect of CME interaction. Both progenitor CMEs originated close to the central meridian of the Sun, thus limiting the difference of initial launching angles. Further, both CMEs were associated with long-lasting post-eruption arcades and elliptic-shaped halo CMEs, suggesting a flux rope origin.

The organization of the paper is as follows. Observations and event selection are given in Section 2, the results of comparative analysis are presented in Section 3, and Section 4 provides discussion and conclusions.

2. Observations and Event Selection

The two events studied in this paper are carefully chosen from a large set of 59 ICME events from 1997 to 2006 whose solar progenitor CMEs and source regions are well defined. These events are the database of two Coordinated Data Analysis Workshops (CDAW), one took place in 2010 and the other in 2011, for the purpose of addressing the question discussed in Section 1. The database of 59 events is available on-line at http://cdaw.gsfc.nasa.gov/meetings/2010_fluxrope/. For each event, the database provides

i) the ICME information, including the arrival time of the shock, the start time and end time of the ICME,
ii) the progenitor CME information near the Sun, including the CME onset time, the width, average velocity and average acceleration, and
iii) CME source region information, including the heliographic coordinates of the source surface region, the associated GOES soft X-ray flare onset time and magnitude.

Among the 59 events, only 25 events can be classified as MC CMEs.

One approach to address the all-flux-rope hypothesis is to make a comparative study of two types of ICME event. A task group in the 2010 workshop was established to select the two types of "well behaved" ICME. The criteria of "well behaved" ICMEs are many, including having low proton temperature, low plasma density, high charge state, expansion velocity profile, enhanced magnetic field, and large scale in duration and size. The only difference between the two types is whether or not the magnetic field shows rotation. Further, the two types are comparable in the properties of progenitor CMEs, *i.e.*, they are all full halo CMEs and comparable in velocities. The properties of their source surface regions are also comparable, in particular, they all originated within 15° of central meridian. After working through the database, the task group down selected the following four events as "well behaved" NMC-ICMEs: 22 September 1999, 22 January 2004, 17 February 2005, and 19 August 2006, which are events numbered as 13, 47, 52, and 59, respectively, in the database. For comparison, the following four events were selected as "well behaved" MC-ICMEs: 11 August 2000, 12 October 2000, 18 May 2002 and 24 July 2004, which are numbered as 23, 26, 39, and 48, respectively, in the database.

In this paper, we choose one event from each type and carry out a detailed analysis on all relevant properties of the events from the Sun to the Earth. The representative MC-ICME occurred on 12 October 2000, while the representative NMC-ICME arrived at the Earth on 22 September 1999.

3. Comparative Analysis and Results

3.1. Properties of the MC Event

The event on 12 October 2000 is a typical MC-ICME. Figure 1 shows the *in-situ* solar wind data obtained from the ACE spacecraft. The time-series data show two distinct periods, one corresponding to the magnetic cloud (the period between two vertical blue lines), and the other corresponding to the shock sheath region (the period between the vertical red line and the vertical solid blue line). The arrival of the event at 1 AU was first signaled by the conspicuous shock at 21:42 UT on 12 October 2000, at which the solar wind velocity, density and temperature as well as the magnetic field showed an abrupt jump in strength. These elevated solar wind parameters continued for about 19 hours, forming the so-called shock

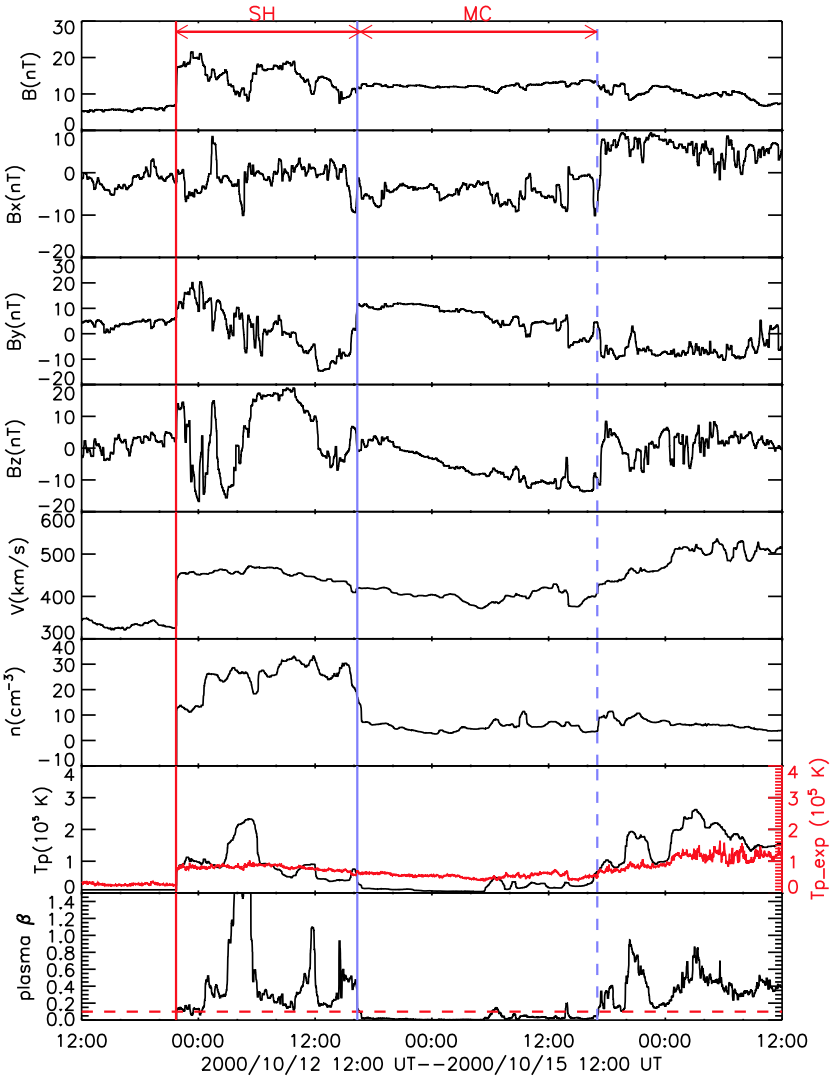

Figure 1 *In-situ* solar wind observations of the ICME event on 12 October 2000. The panels from top to bottom show, respectively, (1) solar wind magnetic field total intensity, (2) magnetic field B_x component, (3) magnetic field B_y component, (4) magnetic field B_z component, (5) solar wind plasma velocity, (6) plasma density, (6) proton temperature (black) overlaid with the expected temperature (red), and (7) the derived plasma β. The solar wind data are from the ACE spacecraft in GSE coordinates. The solid and dashed blue vertical lines indicate the starting and ending times of the ICME, which in this case is a magnetic cloud. The vertical red line indicates the arrival time of the ICME-driven shock.

sheath region. The sheath region ended at 16:20 UT on 13 October 2002, at which time the magnetic cloud, or the CME ejecta started to appear. The onset of the MC was characterized by an abrupt reduction of plasma temperature and density, thus the plasma β, likely caused by the quasi-adiabatic expansion of the magnetic cloud. The magnetic cloud lasted for about 25 hours, ending at about 17:00 UT on 14 October 2000. During the whole period of the magnetic cloud, the magnetic field clearly showed a smooth profile, in contrast to the fluc-

tuating profile in the sheath region. In particular, the magnetic field showed a clear rotation of its vector direction, as evident in the monotonic continuous change of its Z component from the northward maximum to southward maximum. The duration of the magnetic cloud is also well demarcated by the abnormal low temperature, relative to the expected temperature which is empirically determined from the observed solar wind velocity but assuming a normal solar wind condition (as shown in the red line profile in the temperature panel of Figure 1) (Richardson and Cane, 1995).

The solar wind data within the period of the magnetic cloud can be well fitted by the cylinder-shaped force-free flux rope model (Lepping, Jones, and Burlaga, 1990). One can find a catalog of magnetic clouds and their fitting parameters on-line at http://wind.nasa.gov/mfi/clouds/mag_cloud.html. The axis of the fitting flux rope has a direction of latitude $-24°$ (pointing toward the South or negative Z along the Z direction; also called the inclination angle) and longitude 140° (pointing toward the Earth or negative X along the X direction, and toward the East or positive Y along the Y direction; also called the azimuthal angle) in the GSE coordinates. This axial direction will be compared later with the orientations available from various solar observations. The diameter of the flux rope is 0.21 AU, the size of a typical magnetic cloud. The closest approach, defined as the ratio between the spacecraft-axis distance and the radius of the flux rope, is about 17 %.

The orientation of the flux rope determined at 1 AU is largely consistent with the inferred orientations from various remote-sensing observations (Figures 2 and 3). The four panels in Figure 2 shows the progenitor CME (panel d) observed by the LASCO C2 coronagraph, the surface source active region (panel c) observed by the SOHO MDI instrument and the coronal source region by SOHO EIT (panel a and b). The white line in panel b shows the axial orientation of the post-eruption loop arcade associated with the progenitor CME. The accompanying C6.7 GOES X-ray flare located at the heliographic location of N01°W14° is indicated by the plus symbol. This accompanying flare had an onset time at 23:19 UT on 09 October 2000, which should be also the onset time of the CME (Zhang *et al.*, 2001). Thus, it took about 70 hours for the CME-driven shock to reach the Earth, and about 88 hours for the CME ejecta itself to arrive. The latitudinal orientation of the post-eruption loop arcade is found to be 32°, which is about 8° different from the value of 24° of the axial orientation of the magnetic cloud. The difference is rather small, given the uncertainty of the fitting of the magnetic cloud. The orientation of the post-eruption loop arcade aligns well with the polarity inversion line of the magnetic field in the source active region as seen in Figure 2(b). Thus, the orientation of the magnetic cloud is consistent with the orientation of the erupted flux rope inferred from the post-eruption loop arcade and the source region magnetic field.

We can also infer the orientation of the flux rope in the outer corona from coronagraph observations. A halo CME usually has its leading front in all position angles forming an oval shape, as shown by the plus symbols and the fitted elliptical shape in Figure 3. The orientation of the major axis of the fitted ellipse likely indicates the axial orientation of the underlying flux rope. We illustrate this point using the so-called cone model fitting and the difference between the cone-projected ellipse and the observed ellipse. The geometric cone model of CMEs assumes that a CME has an intrinsic cone shape, uniquely determined by the following four parameters: longitude and latitude of the cone axis, angular width, and the height of the cone (Zhao, Plunkett, and Liu, 2002; Xie, Ofman, and Lawrence, 2004). While the cross section of the cone has a perfect circular shape, its projection onto the plane of the sky has usually an elliptic shape when the axis of the cone is not oriented perfectly along the line of sight. We fitted the observed ellipse (the black oval) with the four-parameter cone

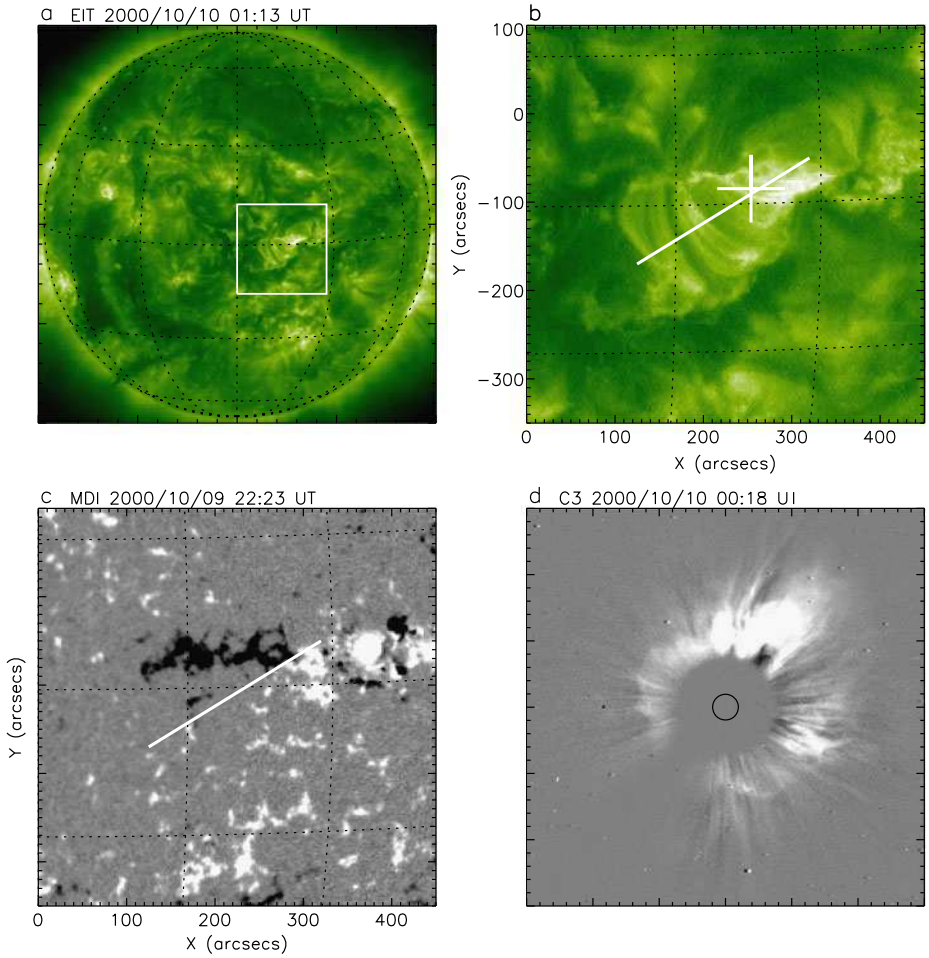

Figure 2 Solar remote-sensing observations of the source region and progenitor CME of the ICME event on 12 October 2000. (a) A full disk SOHO EIT image showing the location of the source region (inside the white square), (b) A zoom-in image of the white square area in panel (a), showing the post-eruption arcade associated with the CME. The white line indicates the orientation of the arcade, while the cross symbol indicates the location of the accompanying flare. (c) A SOHO MDI line-of-sight magnetogram image showing the photospheric magnetic field structure of the CME source region. The white line is the same as in panel (b), indicating that the orientation of the post-eruption arcade follows the polarity inversion line of the magnetic field on the surface. (d) The progenitor halo CME observed by the SOHO LASCO C2 coronagraph.

model, and then projected the cone onto the plane of the sky using the fitting parameters. The result of the cone projection is the ellipse shown in red color in Figure 3. Apparently, the orientation of the major axis of the cone-projected ellipse is much different from that of the observed ellipse; the two major axes are almost orthogonal to each other. We believe that the difference is caused by the shape of the CME, which should be intrinsically an elongated flux rope, instead of a circular cone. The axial orientation of the flux rope gives rise to the major axis of the observed ellipse. It is found that the major axis of the ellipse has a tilt angle of 34°, which is very close to the inferred flux rope orientation based on the post-eruption loop arcade (32°).

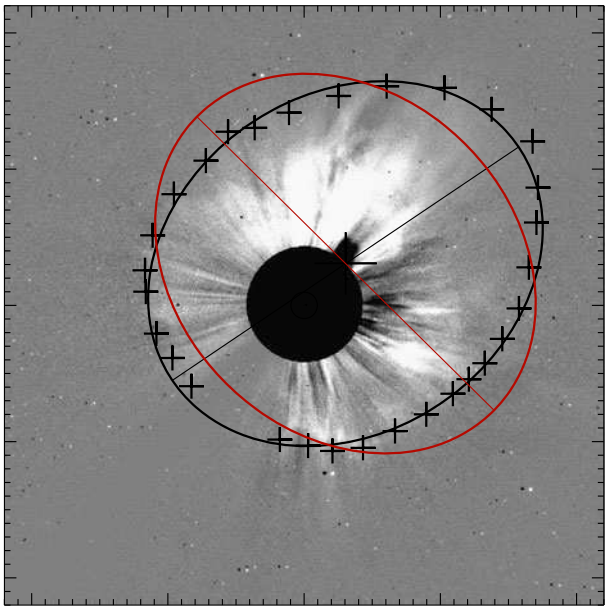

Figure 3 The geometric fitting to the observed progenitor halo CME of the ICME event on 12 October 2000. The black plus symbols are visually selected to outline the edge of the halo CME, which is fitted into an elliptic shape as indicated by the black curve; the straight black line indicates the major axis of the fitted ellipse. The ellipse shape in red line is the expected CME shape assuming a circular cone geometry of the CME, with the red straight line indicating the major axis of the ellipse. Apparently, the observed shape deviates from the circular cone model, indicating a possible flux rope structure of the CME.

We note that it is likely that the elliptical fitting is made on the shock front instead of the CME flux rope itself. In white light coronagraph images, CME-driven shocks usually appear as a diffuse front running ahead of the ejecta, which usually has a sharper contrast in brightness (Vourlidas *et al.*, 2003; Wood and Howard, 2009). Nevertheless, we believe that the elongated shape of the shock front should be similar to that of the flux rope. The flux rope is the underlying driver of the shock, thus any asymmetry in the geometry of the driver will likely to show up in the appearance of the driven front. The shape of the shock may be further deformed if there exists a nearby coronal hole, which allows the shock to propagate faster inside the hole than in surrounding regions (Wood *et al.*, 2012). For the event studied here, the coronal hole effect does not seem to be important; the overall shape outlined is fitted well with a smooth elliptical shape.

3.2. Properties of the NMC Event

While the event discussed above is a classical flux rope event that contains a magnetic cloud, the event on 22 September 1999 is an interesting non-magnetic-cloud one. The latter event shows very similar properties as for the earlier event in solar remote-sensing observations, *e.g.*, originating from close to the central meridian, post-eruption loop arcade and an elongated halo CME, thus one can expect a magnetic cloud structure. However, the magnetic cloud is not observed in the *in-situ* observations, leading to the question whether a flux rope is present in this CME or not.

Figure 4 shows the *in-situ* solar wind data of the event. The *in-situ* signal of the event started at 11:45 UT on 22 September 1999, at which a shock front (indicated by the vertical red line) appeared with apparent jump in plasma temperature, density and velocity and magnetic field intensity. The shock sheath lasted for about eight hours with elevated temperature and magnetic field until 20:00 UT (indicated by the vertical solid blue line). After 20:00 UT, the solar wind plasma temperature became abnormally low, while the magnetic

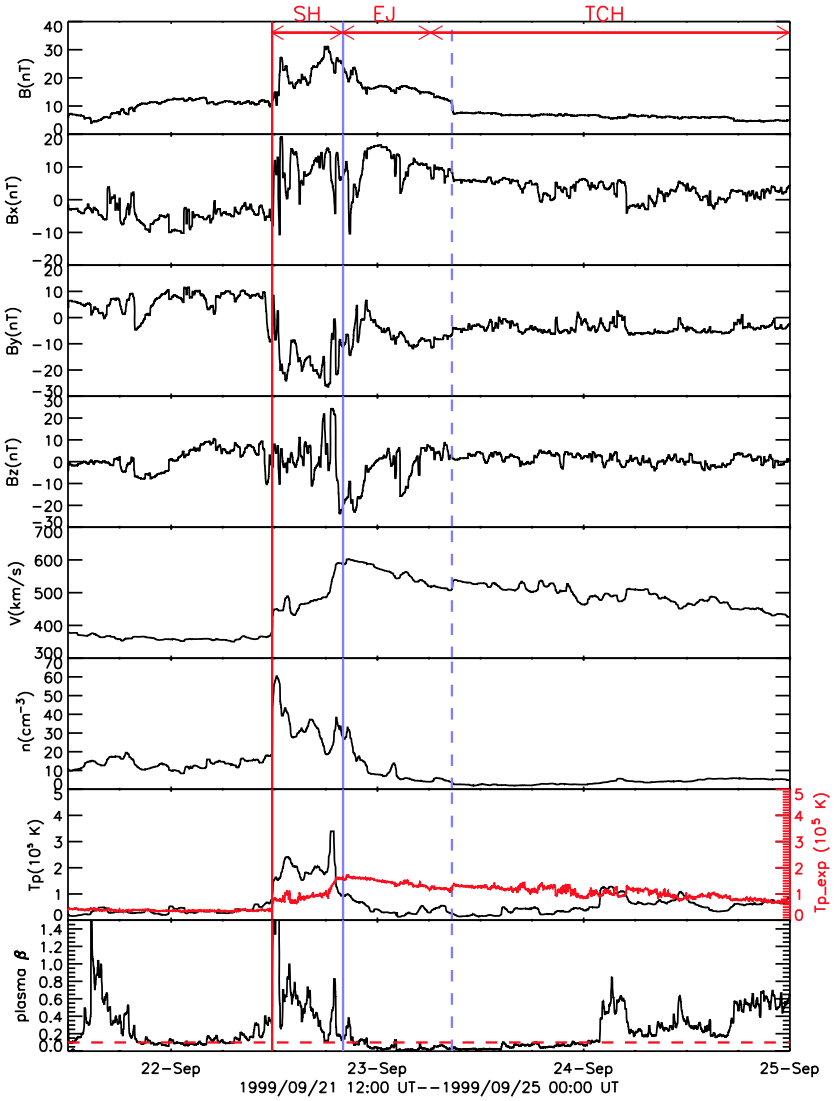

Figure 4 *In-situ* solar wind observations of the ICME event on 22 September 1999. The panels from top to bottom show, respectively, (1) solar wind magnetic field total intensity, (2) magnetic field B_x component, (3) magnetic field B_y component, (4) magnetic field B_z component, (5) solar wind plasma velocity, (6) plasma density, (6) proton temperature (black) overlaid with the expected temperature (red), and (7) the derived plasma β. The solar wind data are from the ACE spacecraft in GSE coordinates. The solid and dashed blue vertical lines indicate the starting and ending times of the ICME, which in this case is not a magnetic cloud. The vertical red line indicates the arrival time of the ICME-driven shock. The identified transient coronal hole (TCH) following the ICME or ejecta (EJ) is characterized by a long period of weak magnetic field and low plasma temperature and density.

field remained to be high until 08:40 UT on 23 September. This high-magnetic-field–low-plasma-temperature period lasted for about 13 hours, apparently corresponding to an ICME ejecta. However, this ICME ejecta did not appear as a magnetic cloud: there was no systematic rotation of the magnetic field direction. Further, the temporal profiles of the magnetic

field are rather bumpy, not as smooth as that expected from a magnetic cloud. The relatively short duration of the ejecta is also smaller than the typical size of a magnetic cloud.

Immediately following the period of the ejecta of strong magnetic field, there is a conspicuous long period of weak magnetic field, low temperature and low density that lasts for at least 39 hours, until the ending time of the display at 00:00 UT on 25 September 1999. The property of the solar wind during this period is much different from any usual transients. Neither does it correspond to a shock sheath nor ICME ejecta, since these structures usually contain a strong magnetic field. It cannot be the rear part of a corotating interaction region (CIR), albeit of weak magnetic field and low density; a typical CIR, which is believed to originate from a long-lasting low-latitude coronal hole, usually has a high plasma temperature.

What could be the solar origin of this unusual solar wind structure? We argue that it originates from a transient coronal hole (TCH) that has been forming at the footpoints of the magnetic flux rope contained in the progenitor CME. The coronal hole origin naturally explains the observed property of low plasma density and relatively weak magnetic field due to strong over-expansion of magnetic field lines, as in a usual long-lasting coronal hole. On the other hand, the low plasma temperature might be a hallmark property of a transient coronal hole, in which the ongoing cooling effect caused by the flux rope expansion still dominates the usual heating mechanism occurring in a coronal hole. Nevertheless, this argument is highly speculative, and further theoretical consideration is needed.

The existence of TCH explains why this particular ICME lacks a magnetic cloud: the *in-situ* spacecraft intercepted the leg of the flux rope instead of the nose. It is highly possible that one of the flux rope legs aligned well along the Sun–Earth line, giving rise to the long-lasting structure of weak magnetic field and low plasma temperature and density.

Since the ejecta and the TCH structures aforementioned do not appear as a magnetic cloud, we cannot fit these structures using the usual force-free flux rope model. Instead, we assume that, as a first order approximation, the structure is a simple untwisted flux tube, *i.e.*, all magnetic field lines have the same direction in the 3D space. This approximation is still valid even though the flux tube is weakly twisted. With this assumption, we can find that the overall direction of the ejecta has an inclination angle of -14° and azimuthal angle of 326° in the GSE coordinates. On the other hand, the TCH has an inclination angle of 13° and azimuthal angle of 306°. Therefore, the two structures have a very similar azimuthal angle on the equatorial plane. The inclination angles differ by about 27°, which is not surprising considering the uncertainty introduced by the averaging method.

The solar remote-sensing observations of this event support its flux rope origin (Figure 5). The progenitor CME originated from a decayed active region (panel c) located near the central meridian at W00°S23°. There appeared a large post-eruption arcade in EIT images (panels a and b). The CME was also associated with a filament eruption and a long-duration C2.8 GOES X-ray flare. The eruption produced a halo CME as seen in LASCO images (panel d). The axial orientation of the post-eruption arcade has a tilt angle with respect to the East–West direction of 31° as shown in panel b. This tilt angle is consistent with the polarity inversion line of the magnetic source region on the photospheric surface (panel c). The existence of an apparent post-eruption arcade indicates that this is an eruptive event, and the resulting CME might contain a magnetic flux rope. The axial orientation of the resulting flux rope shall follow the axis of the arcade, if the flux rope axis has not rotated during the eruption. By fitting the CME with an ellipse and further with the cone model (Figure 6), it is shown that the flux rope has a tilt angle of 10°. The difference indicates that the CME flux rope has probably rotated to have its axis more aligned with the equator than the original tilt angle at the source region. The tilt angle of the CME is highly consistent with the inclination angle of the corresponding ICME ejecta derived from *in-situ* observations.

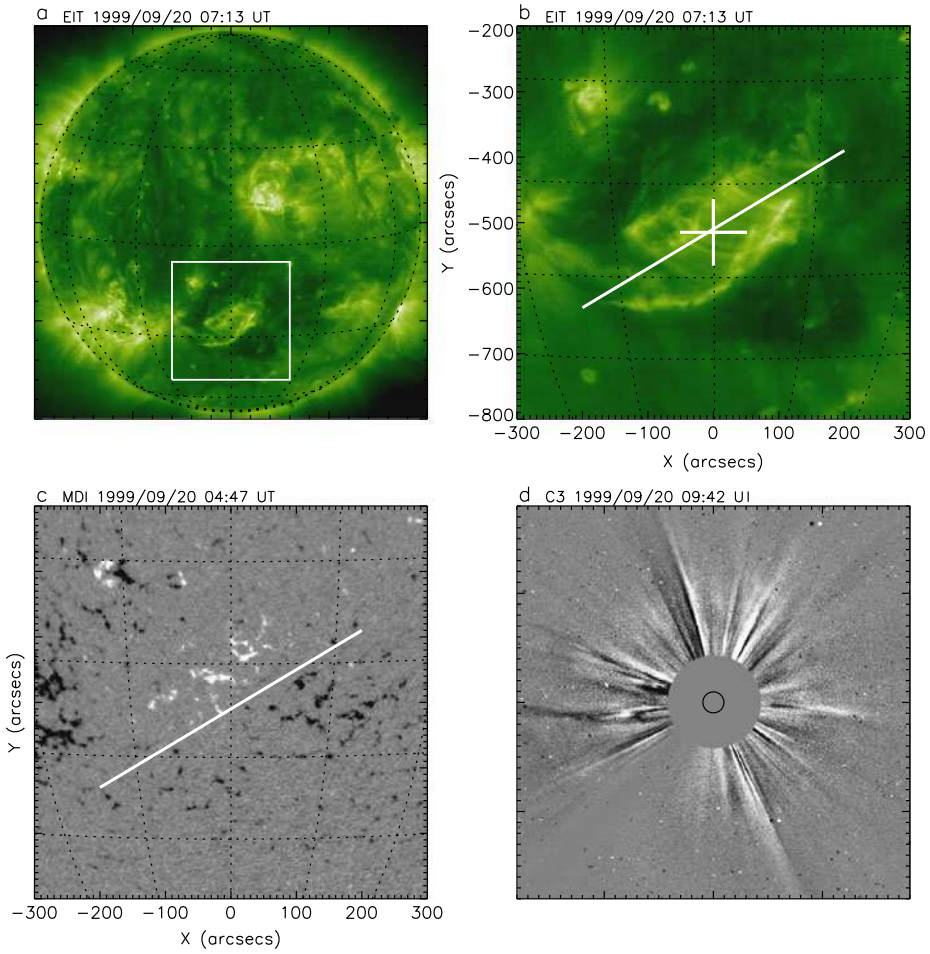

Figure 5 Solar remote-sensing observations of the source region and progenitor CME of the ICME event on 22 September 1999. (a) A full disk SOHO EIT image showing the location of the source region (inside the white square), (b) A zoom-in image of the white square area in panel (a), showing the post-eruption arcade associated with the CME. The white line indicates the orientation of the arcade, while the cross symbol indicates the location of the accompanying flare. (c) A SOHO MDI line-of-sight magnetogram image showing the photospheric magnetic field structure of the CME source region. The white line is the same as in panel (b), indicating that the orientation of the post-eruption arcade follows the polarity inversion line of the magnetic field on the surface. (d) The progenitor halo CME observed by the SOHO LASCO C2 coronagraph.

4. Discussions and Conclusion

To facilitate the discussion of the results presented above, we put together all relevant parameters of the two CME-ICME events in Table 1. The first six rows outline the timings of the Sun–Earth event chain: flare onset time, CME first-appearance time in LASCO/C2 coronagraphs, ICME-driven shock arrival time, ICME arrival time, ICME ending time, and the transient coronal hole ending time (only for the second event). The next two rows indicate the strength of the CMEs and flares, respectively. The next five rows show the geometric

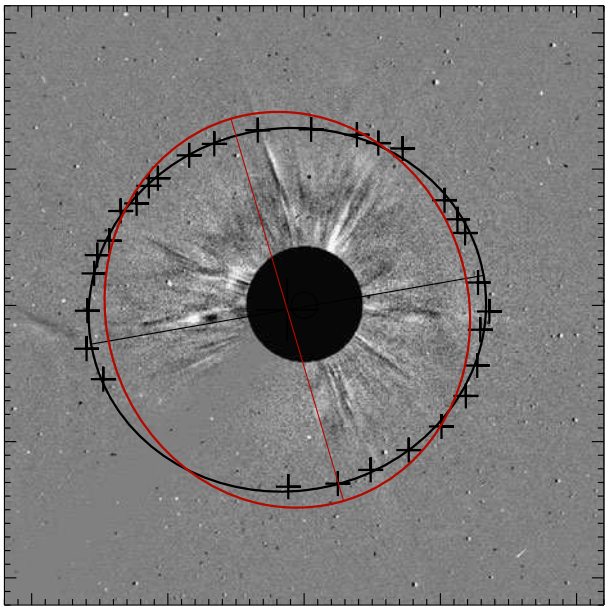

Figure 6 The geometric fitting to the observed progenitor halo CME of the ICME event on 22 September 1999. The black plus symbols are visually selected to outline the edge of the halo CME, which is fitted into an elliptic shape as indicated by the black curve; the straight black line indicates the major axis of the fitted ellipse. The ellipse shape in red line is the expected CME shape assuming a circular cone geometry of the CME, with the red straight line indicating the major axis of the ellipse. Apparently, the observed shape deviates from the circular cone model, indicating a possible flux rope structure of the CME.

parameters of the CMEs close to the Sun from remote-sensing observations, while the remaining four rows indicate the geometric parameters at 1 AU from *in-situ* observations.

Apparently, both CMEs originated from a region close to the central meridian. They also had similar appearance in coronal images with a straight post-eruption arcade and in coronagraph images with an elongated full halo shape. These similar features strongly indicate that both CMEs shall have the same magnetic structure as in their origin, very likely a magnetic flux rope. However, they differed strongly in their appearance in the near-Earth space: the first CME is a magnetic cloud, while the second is apparently not.

The question that arises from these comparative observations is why the second CME does not contain a magnetic cloud structure at 1 AU. Our answer to this question is because of the geometric selection effect at 1 AU, *i.e.*, the *in-situ* spacecraft intercepted the flank of the flux rope instead of near the nose for the second event. The conclusion of a flank interception is supported by the observation that the extended leg of the flux rope passed the near-Earth space, appearing as a TCH characterized by a long-period of weak magnetic field and low plasma temperature and density.

The cause of such a geometric effect for the central meridian CME is a non-radial propagation of the flux rope near the Sun and in the interplanetary space. One would expect that the central-meridian-originated CME should have the bulk of the flux rope or the nose pass the Earth, assuming a simple radial propagation. However, a non-radial propagation of CME is possible, depending on the magnetic field configuration in the low plasma β regime near the Sun and the relative CME-solar-wind velocity in the high plasma β regime in the interplanetary space. In the regions near the Sun, coronagraph observations have shown well that CMEs usually experience a latitudinal deflection, *e.g.*, deflected mostly from high latitude sources toward the low latitudes or equators, especially during the solar minimum (Schwenn, 2000; Gopalswamy *et al.*, 2003; Cremades, Bothmer, and Tripathi, 2006; Wang *et al.*, 2011). The non-radial longitudinal deflection, while being difficult to be directly observed in coronagraph images due to the plane-of-sky projection effect, has been inferred from comparing remote-sensing and *in-situ* observations. Such observa-

Table 1 Properties of the CME events with and without magnetic cloud.

Event	MC	NMC
Time Flare Onset (UT)	2000/10/09 23:19	1999/09/20 05:46
Time CME (UT)[a]	2000/10/09 23:50	1999/09/20 06:06
Time Shock Arrival (UT)	2000/10/12 12:42	1999/09/22 11:45
Time ICME Arrival (UT)	2000/10/13 16:20	1999/09/22 20:00
Time ICME Ending (UT)	2000/10/14 17:00	1999/09/23 08:40
Time TCH Ending (UT)[b]	NA	1999/09/25 00:00
Speed of CME (km s^{-1})	798	604
Magnitude of Flare	C6.7	C2.8
Surface Location of Flare	W14°N01°	E00°S23°
Direction of CME	W27°N27°	E24°S07°
Half Cone Angle of CME	65°	77°
INC of Eruption Arcade[c]	32°	31°
INC of CME Major Axis[c]	34°	10°
INC of ICME Axis[d]	−24°	−14°
INC of TCH Axis[d]	NA	13 °
AZI of ICME Axis[e]	140°	326°
AZI of TCH Axis[e]	NA	306°

[a]The time of the CME first appearance in LASCO C2 FOV.

[b]Approximate ending time of transient coronal hole, only for the NMC event.

[c]Inclination angle with respect to the heliospheric equator.

[d]Inclination angle with respect to the ecliptic plane as in the GSE coordinates. The angular difference between the heliospheric equator and the ecliptic plane is ignored in this study.

[e]Azimuthal angle in the GSE coordinates. Zero degree is toward the Sun, 90 degree is to the East.

tions include the apparent East–West asymmetry of solar sources of intense geomagnetic storms with more events originated in the western hemisphere (Wang *et al.*, 2002; Zhang *et al.*, 2003) and a similar asymmetry of the sources of magnetic clouds (Gopalswamy *et al.*, 2007). The longitudinal deflection can also be inferred from how individual CMEs with different source longitudes either encounter or miss the Earth (Wang *et al.*, 2006), and in particular, the identification of the unexpected "driverless" shocks at 1 AU with their solar sources close to the central meridian (Gopalswamy *et al.*, 2009). Direct evidence of longitudinal deflection was recently made possible from the measurement of the 3D trajectory of CMEs based on the twin STEREO spacecraft observations (Gui *et al.*, 2011). The research work discussed above indicates that a CME could be deflected either along the latitudinal direction or longitudinal direction.

Theoretically, a CME's trajectory can be influenced by the ambient magnetic field in the corona where a CME has to push through. It is well known that the inner corona, *e.g.*, $< \sim 3$ solar radii, is in the regime of low plasma β, *i.e.*, the magnetic force dominates plasma pressure force and other forces, and as a result, the magnetic field lines rooted in the photosphere are highly non-radial in the inner corona until they reach the heights where the momentum of solar wind flow starts to dominate the magnetic force. Thus, it is expected that in the inner corona the trajectory of the rising motion of the flux rope should be at least partially guided by the non-radial orientation of the ambient

magnetic field. It has been recognized that such magnetic deflection effect is mainly attributed to coronal holes (Cremades, Bothmer, and Tripathi, 2006; Gopalswamy *et al.*, 2009; Mohamed *et al.*, 2012), whose magnetic field is highly non-radial and also comparable in size to that of flux ropes. This kind of deflection has been empirically quantified by the so-called coronal hole influence parameter (CHIP), whose magnitude for each coronal hole depends on the distance between the coronal hole centroid and the eruption area, the coronal hole area and the average magnetic field at the photospheric level (Gopalswamy *et al.*, 2009; Mohamed *et al.*, 2012). Recently, Shen *et al.* (2011) proposed a more general parameter, the magnetic energy density parameter that includes the contributions from all fields instead of only that from coronal holes; in this model, the flux rope is deflected toward the region of minimum coronal magnetic energy density.

Far from the inner corona, STEREO observations have also provided evidence that a CME may deflect or deviate from the radial direction in the interplanetary space (Lugaz *et al.*, 2010). The deflection is probably caused by the Parker spiral magnetic field embedded in the radially flowing solar wind (Wang *et al.*, 2004). A CME traveling faster than the ambient solar wind is expected to deflect toward the East, due to the piling-up of the interplanetary magnetic field in front of the CME; Such enhanced magnetic field has a force component pointing toward the East along the transverse direction. On the other hand, a slow CME is expected to be deflected toward the West. Nevertheless, since the magnetic field in the interplanetary space is weak and the plasma is in the regime of high β, the rate of deflection in the interplanetary space should be smaller than that in the inner corona.

In summary, we have studied two carefully chosen CME events, both of which originated close to the central meridian and showed similar properties near the Sun in remote-sensing observations. We argue that the difference in the *in-situ* observations, *i.e.*, a magnetic cloud appearing in the first event but not in the second event, is caused by the geometric selection effect. The first event had its nose pass through the observing spacecraft, thus the intrinsic flux rope structure of the CME appeared as a magnetic cloud. On the other hand, the second event had the flank of the flux rope intercept the spacecraft, thus did not appear as a magnetic cloud. We further argue that a conspicuous long period of weak magnetic field, low plasma temperature and density in the second event should correspond to the extended leg portion of the embedded magnetic flux rope in the interplanetary space, thus validating the scenario of flank-passing. These observations support the idea that all CMEs arriving at the Earth include flux ropes.

Acknowledgements We acknowledge the support from NSF ATM-0748003 and NSF AGS-1156120. The ACE plasma, magnetic field, and composition/charge state data were provided by the ACE Science Center. SOHO is a project of international cooperation between ESA and NASA. The LASCO instrument was constructed by a consortium of the Naval Research Laboratory, University of Birmingham (England), the Max-Planck-Institute für Aeronomie (Germany) and the Laboratoire d'Astronomie Spatiale (France).

References

Amari, T., Luciani, J.F., Aly, J.J., Mikic, Z., Linker, J.: 2003, Coronal mass ejection: initiation, magnetic helicity, and flux ropes. I. Boundary motion-driven evolution. *Astrophys. J.* **585**, 1073. doi:10.1086/345501.

Antiochos, S.K., DeVore, C.R., Klimchuk, J.A.: 1999, A model for solar coronal mass ejections. *Astrophys. J.* **510**, 485. doi:10.1086/306563.

Aulanier, G., Török, T., Démoulin, P., DeLuca, E.E.: 2010, Formation of torus-unstable flux ropes and electric currents in erupting sigmoids. *Astrophys. J.* **708**, 314. doi:10.1088/0004-637X/708/1/314.

Bothmer, V., Schwenn, R.: 1996, Signatures of fast CMEs in interplanetary space. *Adv. Space Res.* **17**, 319.

Burlaga, L., Sittler, E., Mariani, F., Schwenn, R.: 1981, Magnetic loop behind an interplanetary shock: Voyager, Helios, and IMP 8 observations. *J. Geophys. Res.* **86(A8)**, 6673.

Canfield, R.C., Hudson, H.S., McKenzie, D.E.: 1999, Sigmoidal morphology and eruptive solar activity. *Geophys. Res. Lett.* **26**, 627. doi:10.1029/1999GL900105.

Chen, J.: 1996, Theory of prominence eruption and propagation: interplanetary consequences. *J. Geophys. Res.* **101**, 27499. doi:10.1029/96JA02644.

Cheng, X., Zhang, J., Liu, Y., Ding, M.D.: 2011, Observing flux rope formation during the impulsive phase of a solar eruption. *Astrophys. J. Lett.* **732**, L25. doi:10.1088/2041-8205/732/2/L25.

Cremades, H., Bothmer, V., Tripathi, D.: 2006, Properties of structured coronal mass ejections in solar cycle 23. *Adv. Space Res.* **38**, 461. doi:10.1016/j.asr.2005.01.095.

Dere, K.P., Brueckner, G.E., Howard, R.A., Michels, D.J., Delaboudinière, J.P.: 1999, LASCO and EIT observations of helical structure in coronal mass ejections. *Astrophys. J.* **516**, 465. doi:10.1086/307101.

Fan, Y., Gibson, S.E.: 2007, Onset of coronal mass ejections due to loss of confinement of coronal flux ropes. *Astrophys. J.* **668**, 1232. doi:10.1086/521335.

Gibson, S.E., Fletcher, L., Del Zanna, G., Pike, C.D., Mason, H.E., Mandrini, C.H., Démoulin, P., Gilbert, H., Burkepile, J., Holzer, T., Alexander, D., Liu, Y., Nitta, N., Qiu, J., Schmieder, B., Thompson, B.J.: 2002, The structure and evolution of a sigmoidal active region. *Astrophys. J.* **574**, 1021. doi:10.1086/341090.

Gopalswamy, N., Yashiro, S., Kaiser, M.L., Howard, R.A., Bougeret, J.L.: 2001, Radio signatures of coronal mass ejection interaction: coronal mass ejection cannibalism? *Astrophys. J. Lett.* **548**, L91.

Gopalswamy, N., Shimojo, M., Lu, W., Yashiro, S., Shibasaki, K., Howard, R.A.: 2003, Prominence eruptions and coronal mass ejection: a statistical study using microwave observations. *Astrophys. J.* **586**, 562. doi:10.1086/367614.

Gopalswamy, N., Akiyama, S., Yashiro, S., Michalek, G., Lepping, R.P.: 2007, Solar sources and geospace consequences of interplanetary magnetic clouds observed during solar cycle 23. *J. Atmos. Solar-Terr. Phys.* doi:10.1016/j.jastp.2007.08.070.

Gopalswamy, N., Mäkelä, P., Xie, H., Akiyama, S., Yashiro, S.: 2009, CME interactions with coronal holes and their interplanetary consequences. *J. Geophys. Res.* **114**. doi:10.1029/2008JA013686.

Gosling, J.T.: 1990, Coronal mass ejections and magnetic flux ropes in interplanetary space. In: Russell, C.T., Priest, E.R., Lee, L.C. (eds.) *Physics of Magnetic Flux Ropes*, *Geophys. Monogr. Ser.* **58**, AGU, Washington, 343.

Gosling, J.T., McComas, D.J., Phillips, J.L., Bame, S.J.: 1991, Geomagnetic activity associated with Earth passage of interplanetary shock disturbances and coronal mass ejections. *J. Geophys. Res.* **96**, 7831.

Green, L.M., Kliem, B.: 2009, Flux rope formation preceding coronal mass ejection onset. *Astrophys. J. Lett.* **700**, L83. doi:10.1088/0004-637X/700/2/L83.

Gui, B., Shen, C., Wang, Y., Ye, P., Liu, J., Wang, S., Zhao, X.: 2011, Quantitative analysis of CME deflections in the corona. *Solar Phys.* **271**, 111. doi:10.1007/s11207-011-9791-9.

Henke, T., Woch, J., Schwenn, R., Mall, U., Gloeckler, G., von Steiger, R., Forsyth, R.J., Balogh, A.: 2001, Ionization state and magnetic topology of coronal mass ejections. *J. Geophys. Res.* **106**, 10597. doi:10.1029/2000JA900176.

Kliem, B., Török, T.: 2006, Torus instability. *Phys. Rev. Lett.* **96**, 255002. doi:10.1103/PhysRevLett.96.255002.

Lepping, R.P., Jones, J.A., Burlaga, L.F.: 1990, Magnetic field structure of interplanetary magnetic clouds at 1 AU. *J. Geophys. Res.* **95**, 11957.

Liu, R., Liu, C., Wang, S., Deng, N., Wang, H.: 2010, Sigmoid-to-flux-rope transition leading to a loop-like coronal mass ejection. *Astrophys. J. Lett.* **725**, L84. doi:10.1088/2041-8205/725/1/L84.

Lugaz, N., Hernandez-Charpak, J.N., Roussev, I.I., Davis, C.J., Vourlidas, A., Davies, J.A.: 2010, Determining the azimuthal properties of coronal mass ejections from multi-spacecraft remote-sensing observations with STEREO SECCHI. *Astrophys. J.* **715**, 493. doi:10.1088/0004-637X/715/1/493.

McKenzie, D.E., Canfield, R.C.: 2008, Hinode XRT observations of a long-lasting coronal sigmoid. *Astron. Astrophys.* **481**, L65. doi:10.1051/0004-6361:20079035.

Mohamed, A.A., Gopalswamy, N., Yashiro, S., Akiyama, S., Mäkelä, P., Xie, H., Jung, H.: 2012, The relation between coronal holes and coronal mass ejections during the rise, maximum, and declining phases of solar cycle 23. *J. Geophys. Res.* **117**(A16), 1103. doi:10.1029/2011JA016589.

Moore, R.L., Sterling, A.C., Hudson, H.S., Lemen, J.R.: 2001, Onset of the magnetic explosion in solar flares and coronal mass ejections. *Astrophys. J.* **552**, 833. doi:10.1086/320559.

Olmedo, O., Zhang, J.: 2010, Partial torus instability. *Astrophys. J.* **718**, 433. doi:10.1088/0004-637X/718/1/433.

Richardson, I.G., Cane, H.V.: 1995, Regions of abnormally low proton temperature in the solar wind (1965 – 1991) and their association with ejecta. *J. Geophys. Res.* **100**, 23397. doi:10.1029/95JA02684.

Richardson, I.G., Cane, H.V.: 2004, The fraction of interplanetary coronal mass ejections that are magnetic clouds: evidence for a solar cycle variation. *Geophys. Res. Lett.* **31**, L18804.
Riley, P., Crooker, N.U.: 2004, Kinematic treatment of coronal mass ejection evolution in the solar wind. *Astrophys. J.* **600**, 1035. doi:10.1086/379974.
Rust, D.M.: 1994, Spawning and shedding helical magnetic fields in the solar atmosphere. *Geophys. Res. Lett.* **21**, 241.
Schrijver, C.J.: 2009, Driving major solar flares and eruptions: a review. *Adv. Space Res.* **43**, 739. doi:10.1016/j.asr.2008.11.004.
Schwenn, R.: 2000, Heliospheric 3d structure and CME propagation as seen from SOHO: recent lessons for space weather predictions. *Adv. Space Res.* **26**, 43. doi:10.1016/S0273-1177(99)01025-X.
Shen, C., Wang, Y., Gui, B., Ye, P., Wang, S.: 2011, Kinematic evolution of a slow CME in corona viewed by STEREO-B on 8 October 2007. *Solar Phys.* **269**, 389. doi:10.1007/s11207-011-9715-8.
Sterling, A.C., Hudson, H.S.: 1997, YOHKOH SXT observations of X-ray "dimming" associated with a halo coronal mass ejection. *Astrophys. J. Lett.* **491**, L55.
Titov, V.S., Démoulin, P.: 1999, Basic topology of twisted magnetic configurations in solar flares. *Astron. Astrophys.* **351**, 707.
Tripathi, D., Kliem, B., Mason, H.E., Young, P.R., Green, L.M.: 2009, Temperature tomography of a coronal sigmoid supporting the gradual formation of a flux rope. *Astrophys. J. Lett.* **698**, L27. doi:10.1088/0004-637X/698/1/L27.
Vourlidas, A., Wu, S.T., Wang, A.H., Subramanian, P., Howard, R.A.: 2003, Direct detection of a coronal mass ejection-associated shock in large angle and spectrometric coronagraph experiment white-light images. *Astrophys. J.* **598**, 1392. doi:10.1086/379098.
Wang, Y.M., Ye, P.Z., Wang, S., Zhou, G.P., Wang, J.X.: 2002, A statistical study on the geoeffectiveness of Earth-directed coronal mass ejections from March 1997 to December 2000. *J. Geophys. Res.* **107**, 1340. doi:10.1029/2002JA009244.
Wang, Y.M., Ye, P.Z., Wang, S., Xue, X.H.: 2003, An interplanetary cause of large geomagnetic storms: fast forward shock overtaking preceding magnetic cloud. *Geophys. Res. Lett.* **30**, 1700. doi:10.1029/2002GL016861.
Wang, Y., Shen, C., Ye, P., Wang, S.: 2004, Deflection of coronal mass ejection in the interplanetary medium. *Solar Phys.* **222**, 329.
Wang, Y., Xue, X., Shen, C., Ye, P., Wang, S., Zhang, J.: 2006, Impact of major coronal mass ejections on geospace during 2005 September 7 – 13. *Astrophys. J.* **646**, 625. doi:10.1086/504676.
Wang, Y., Chen, C., Gui, B., Shen, C., Ye, P., Wang, S.: 2011, Statistical study of coronal mass ejection source locations: understanding CMEs viewed in coronagraphs. *J. Geophys. Res.* **116**, 4104. doi:10.1029/2010JA016101.
Wood, B.E., Howard, R.A.: 2009, An empirical reconstruction of the 2008 April 26 coronal mass ejection. *Astrophys. J.* **702**, 901. doi:10.1088/0004-637X/702/2/901.
Wood, B.E., Wu, C.-C., Rouillard, A.P., Howard, R.A., Socker, D.G.: 2012, A coronal hole's effects on coronal mass ejection shock morphology in the inner heliosphere. *Astrophys. J.* **755**, 43. doi:10.1088/0004-637X/755/1/43.
Xie, H., Ofman, L., Lawrence, G.: 2004, Cone model for halo CMEs: application to space weather forecasting. *J. Geophys. Res.* **109**, A03109.
Zhang, J., Cheng, X., Ding, M.-D.: 2012, Observation of an evolving magnetic flux rope before and during a solar eruption. *Nat. Commun.* **3**, 747. doi:10.1038/ncomms1753.
Zhang, J., Dere, K.P., Howard, R.A., Kundu, M.R., White, S.M.: 2001, On the temporal relationship between coronal mass ejections and flares. *Astrophys. J.* **559**, 452. doi:10.1086/322405.
Zhang, J., Dere, K.P., Howard, R.A., Bothmer, V.: 2003, Identification of solar sources of major geomagnetic storms between 1996 and 2000. *Astrophys. J.* **582**, 520.
Zhang, J., Richardson, I.G., Webb, D.F., Gopalswamy, N., Huttunen, E., Kasper, J.C., Nitta, N.V., Poomvises, W., Thompson, B.J., Wu, C.-C., Yashiro, S., Zhukov, A.N.: 2007, Solar and interplanetary sources of major geomagnetic storms (Dst ≤ -100 nT) during 1996 – 2005. *J. Geophys. Res.* **112**, 10102. doi:10.1029/2007JA012321.
Zhao, X.P., Plunkett, S.P., Liu, W.: 2002, Determination of geometrical and kinematical properties of halo coronal mass ejections using the cone model. *J. Geophys. Res.* **107**, 1223. doi:10.1029/2001JA009143.
Zurbuchen, T.H., Richardson, I.G.: 2006, *In-situ* solar wind and magnetic field signatures of interplanetary coronal mass ejections. *Space Sci. Rev.* **123**, 31. doi:10.1007/s11214-006-9010-4.

Solar Phys (2013) 284:77–88
DOI 10.1007/s11207-013-0230-y

Propagation Characteristics of CMEs Associated with Magnetic Clouds and Ejecta

R.-S. Kim · N. Gopalswamy · K.-S. Cho · Y.-J. Moon · S. Yashiro

Received: 6 April 2012 / Accepted: 15 January 2013 / Published online: 5 February 2013

Abstract We have investigated the characteristics of magnetic cloud (MC) and ejecta (EJ) associated coronal mass ejections (CMEs) based on the assumption that all CMEs have a flux rope structure. For this, we used 54 CMEs and their interplanetary counterparts (interplanetary CMEs: ICMEs) that constitute the list of events used by the NASA/LWS Coordinated Data Analysis Workshop (CDAW) on CME flux ropes. We considered the location, angular width, and speed as well as the direction parameter, D. The direction parameter quantifies the degree of asymmetry of the CME shape in coronagraph images, and shows how closely the CME propagation is directed to Earth. For the 54 CDAW events, we found the following properties of the CMEs: i) the average value of D for the 23 MCs (0.62) is larger than that for the 31 EJs (0.49), which indicates that the MC-associated CMEs propagate more directly toward the Earth than the EJ-associated CMEs; ii) comparison between the direction parameter and the source location shows that the majority of the MC-associated CMEs are ejected along the radial direction, while many of the EJ-associated CMEs are ejected non-radially; iii) the mean speed of MC-associated CMEs (946 km s^{-1}) is faster than that of EJ-associated CMEs (771 km s^{-1}). For seven very fast CMEs ($\geq$ 1500 km s^{-1}), all CMEs with large D ($\geq$ 0.4) are associated with MCs and the CMEs with small D are associated with EJs. From the statistical analysis of CME parameters, we found the superiority of the

Flux-Rope Structure of Coronal Mass Ejections
Guest Editors: N. Gopalswamy, T. Nieves-Chinchilla, M. Hidalgo, J. Zhang, and P. Riley

R.-S. Kim (✉) · K.-S. Cho
Korea Astronomy and Space Science Institute, Daejeon, 305-348, Korea
e-mail: rskim@kasi.re.kr

N. Gopalswamy · S. Yashiro
NASA Goddard Space Flight Center, Greenbelt, MD, USA

Y.-J. Moon
School of Space Research, Kyunghee University, Yongin-shi, 446-701, Korea

S. Yashiro
Department of Physics, The Catholic University of America, Washington, DC, USA

direction parameter. Based on these results, we suggest that the CME trajectory essentially determines the observed ICME structure.

Keywords Coronal mass ejections, ejecta · Interplanetary coronal mass ejections, magnetic clouds

1. Introduction

Coronal mass ejections (CMEs) are extremely dynamical events in which closed coronal magnetic field lines are ejected into the interplanetary (IP) space from the Sun (Hundhausen, 1993). When they arrive at the Earth, they are detected as interplanetary CMEs (ICMEs). According to Burlaga *et al.* (1981), ICMEs are classified into two types: magnetic cloud (MC) and ejecta (EJ). An MC is an extension of magnetic flux rope into IP space and defined by above-average magnetic field magnitude, low variance with smooth rotating magnetic field, low plasma beta (ratio of thermal to magnetic pressure), unusual alpha/proton density ratio, and low ion temperature. An MC is a well-structured ICME and about 30 % of ICMEs are MCs (Gosling, 1990). Often, however, identification of an MC can be ambiguous because these characteristics are presented in the literature in various combinations. When the smoothly rotating magnetic field signature is not observed, we refer to the ICME as an EJ (Burlaga *et al.*, 2001).

To understand the ICME structures, several authors have examined the evolution of CME's flux rope structures (Nakwacki *et al.*, 2011; Howard and DeForest, 2012). Numerical simulations show that a flux rope expanding from the solar surface will evolve into an MC with all required plasma characteristics (Roussev *et al.*, 2003; Manchester *et al.*, 2004; Thompson, Kliem, and Török, 2012). According to Gosling (1990), some ICMEs consist of untwisted loops and hence do not show any MC structures. Jacobs *et al.* (2009) successfully simulated a CME with typical characteristics of an MC, but without an underlying helical flux rope structure. On the other hand, Gopalswamy (2006) suggested that all ICMEs have a magnetic flux rope structure, but the passing direction of the spacecraft decides the appearance of ICME as shown in Figure 1. He explained that we can observe an MC only when the observer's trajectory goes through the nose of the magnetic cloud (tracks 3 and 6). In this case, the azimuthal field changes sign at the axis and the magnitude of the azimuthal component also changes, peaking at the axis and falling off on either side. If the spacecraft passes along tracks 4 or 5, the magnetic field will not change and the ICME will be observed as an EJ. It is not clear whether MCs and EJs have intrinsically different structures (flux rope, non-flux rope) or the observed structure is due to different propagation directions. We cannot exclude the possibility of ejected flux ropes being distorted or shredded on their journey from the Sun to the Earth.

Regarding this issue, we are motivated by the proposal of Gopalswamy (2006) that the propagation direction of the CME could be the key to understanding the difference between the two types of ICME. The propagation of CMEs toward the Earth can be investigated using the solar source location and the direction parameter (D) of CMEs. The direction parameter quantifies the degree of asymmetry of the CME shape and shows how closely the CME propagation is directed toward Earth (Moon *et al.*, 2005; Kim *et al.*, 2008). This parameter can be determined directly from coronagraph observations and is applicable to most of the halo CMEs. Note that D is very useful to determine the propagation direction especially for CMEs that are not ejected radially from the source region. In addition, CMEs might experience a distortion of their flux rope structure due to interaction with the background solar wind (Odstrcil and Pizzo, 1999). We expect that the speed of CME could be another important parameter to classify the structure of ICME.

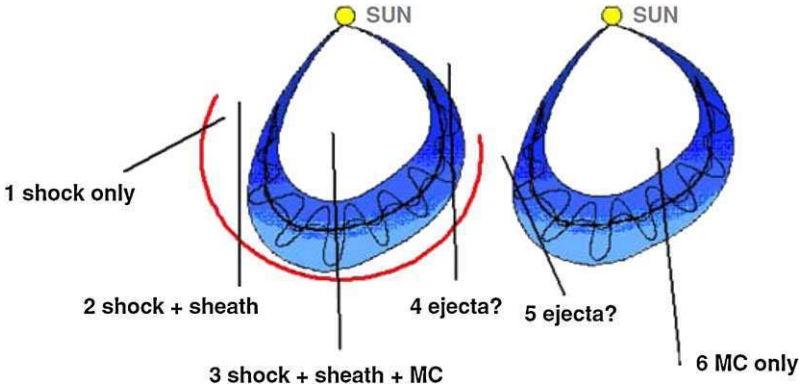

Figure 1 Six possible tracks of an observing spacecraft through an MC with a leading shock (left) and another without (right). Tracks 1 and 2 never encounter the MC proper. Track 3 passes through the nose of the MC. Trajectory 4 passes through the shock, sheath, and through the edge of the MC. Tracks 5 and 6 are similar to 4 and 3, respectively, except that the MC is slow and hence it does not drive a shock. Only trajectories 3 and 6 are expected to observe an MC structure (Gopalswamy, 2006).

In this study, we examined the location, angular width, speed, and the direction parameter of the 54 CDAW events to inspect the different characteristics of MC- and EJ-associated CMEs. We explain our data in Section 2 and present the results in Section 3. Our summary and discussion are given in Section 4.

2. Data

To examine the different characteristics of the CMEs, we used the CDAW list developed for the NASA/LWS Coordinated Data Analysis Workshop (CDAW) on CME flux ropes.[1] The CDAW list contains shock-driving ICMEs during Solar Cycle 23 whose source longitude (l) are located in between E15° and W15°. The list gives us detailed information of the CMEs, which are considered as the sources of ICMEs, and the associated flares. Among the 54 ICMEs, 23 events are classified as MCs (43 %) and 31 events are EJs (57 %). Details of their classification can be found in Gopalswamy *et al.* (2010). From the CDAW list, we used the properties of CMEs, such as the onset date and time, angular width, linear speed, and the location of flare or eruptive prominence for each ICME event.

Adopting the method from Kim *et al.* (2008), we measured the direction parameters, D, for 54 CMEs using the running difference images of the LASCO. For this, we first plotted an ellipse to follow the CME front (see Figure 1 in Kim *et al.*, 2008), and then we drew a line that passes through the centers of both the Sun and the ellipse. The ratio of the shorter to longer distance of the CME front from the solar center along this line is the direction parameter. D is always between 0 and 1, and a larger D indicates a closer orientation toward the Earth. In Table 1, the first three columns are ICME data and the next four columns are related CME data including the direction parameter. The last column is the location of flare or eruptive prominence associated with the ICMEs on the solar surface.

The *Large Angle and Spectrometric Coronagraph* (LASCO: Brueckner *et al.*, 1995) on board the *Solar and Heliospheric Observatory* (SOHO) mission has revealed the various

[1] http://cdaw.gsfc.nasa.gov/meetings/2010_fluxrope/LWS_CDAW2010_ICMEtbl.html.

Table 1 List of shock-driving ICMEs during Solar Cycle 23 (E15° ≤ l ≤ W15°).

CDAW #	ICME		CME				Solar source location
	Type	Start date/time	Onset date/time	Angular width (°)	Speed (km s^{-1})	D	
1	MC	1997/01/10 05:18	01/06 15:10	360	136	0.78	S18E06
2	MC	1997/05/15 09:06	05/12 05:30	360	464	0.78	N21W08
3	EJ	1997/12/11 03:45	12/06 10:27	223	397	0.14	N45W10
4	EJ	1998/05/03 19:00	05/01 23:40	360	585	0.77	S18W05
5	EJ	1998/05/04 10:00	05/02 14:06	360	938	0.58	S15W15
7	EJ	1998/11/07 22:00	11/04 07:54	360	523	0.25	N17W01
8	EJ	1998/11/13 04:30	11/09 18:18	190	325	0.38	N15W05
9	MC	1999/04/16 20:18	04/13 03:30	261	291	0.79	N16E00
10	EJ	1999/06/27 21:30	06/24 13:31	360	975	0.48	N29W13
13	EJ	1999/09/22 21:00	09/20 06:06	360	604	0.95	S20W05
14	EJ	1999/10/21 18:30	10/18 00:06	240	144	0.41	S30E15
15	EJ	2000/01/22 18:00	01/18 17:54	360	739	0.58	S19E11
16	MC	2000/02/21 09:48	02/17 21:30	360	728	0.74	S29E07
17	EJ	2000/07/11 01:30	07/07 10:26	360	453	0.80	N04E00
18	EJ	2000/07/11 22:48	07/08 23:50	161	483	0.13	N18W12
19	MC	2000/07/15 21:06	07/14 10:54	360	1674	0.71	N22W07
20	EJ	2000/07/27 08:28	07/23 05:30	181	631	0.83	S13W05
21	MC	2000/07/28 21:06	07/25 03:30	360	528	0.69	N06W08
23	MC	2000/08/12 06:06	08/09 16:30	360	702	0.73	N20E12
24	MC	2000/09/18 01:54	09/16 05:18	360	1215	0.46	N14W07
25	EJ	2000/10/05 13:13	10/02 03:50	360	525	0.74	S09E07
26	MC	2000/10/13 18:24	10/09 23:50	360	798	0.49	N01W14
27	MC	2000/11/06 23:06	11/03 18:26	360	291	0.79	N02W02
28	EJ	2000/11/27 05:00	11/24 05:30	360	1289	0.57	N20W05
29	EJ	2001/03/04 04:00	02/28 14:50	232	313	0.43	S17W05
30	EJ	2001/03/22 22:30	03/19 05:26	360	389	0.79	S20W00
31	EJ	2001/04/11 22:30	04/09 15:54	360	1192	0.69	S21W04
32	MC	2001/04/12 07:54	04/10 05:30	360	2411	0.49	S23W09
33	MC	2001/04/29 01:54	04/26 12:30	360	1006	0.30	N20W05
34	EJ	2001/08/13 07:00	08/09 10:30	175	479	0.33	N11W14
35	EJ	2001/10/12 03:30	10/09 11:30	360	973	0.53	S28E08
36	MC	2002/03/19 22:54	03/15 23:06	360	957	0.61	S08W03
37	MC	2002/04/18 04:18	04/15 03:50	360	720	0.86	S15W01
38	EJ	2002/05/11 13:00	05/08 13:50	360	614	0.67	S12W07
39	MC	2002/05/19 03:54	05/16 00:50	360	600	0.41	S23E15
40	EJ	2002/05/20 11:00	05/17 01:27	45	461	0.19	S20E14
41	EJ	2002/05/30 07:09	05/27 13:27	161	1106	0.12	N22E15
42	EJ	2002/07/18 12:00	07/15 21:30	188	1300	0.39	N19W01
43	MC	2002/08/01 11:54	07/29 12:07	161	222	0.75	S10W10
44	MC	2003/08/18 11:36	08/14 20:06	360	378	0.44	S10E02
45	MC	2003/10/29 08:00	10/28 11:30	360	2459	0.94	S16E08

Table 1 (*Continued*)

CDAW #	ICME		CME				Solar source location
	Type	Start date/time	Onset date/time	Angular width (°)	Speed (km s^{-1})	D	
46	MC	2003/10/31 02:00	10/29 20:54	360	2029	0.83	S15W02
47	EJ	2004/01/22 08:00	01/20 00:06	360	965	0.76	S13W09
48	MC	2004/07/24 12:48	07/22 08:30	132	899	0.01	N04E10
49	MC	2004/11/09 20:54	11/06 02:06	214	1111	0.72	N09E05
50	EJ	2004/12/12 12:00	12/08 20:26	360	611	0.73	N05W03
51	EJ	2005/01/16 14:00	01/15 06:30	360	2049	0.07	N16E04
52	EJ	2005/02/18 15:00	02/13 11:06	151	584	0.13	S11E09
53	MC	2005/05/15 05:42	05/13 17:12	360	1689	0.79	N12E11
54	MC	2005/05/20 07:18	05/17 03:26	273	449	0.21	S15W00
56	EJ	2005/07/10 10:30	07/07 17:06	360	683	0.16	N09E03
57	EJ	2005/09/02 19:03	08/31 11:30	360	825	0.69	N13W13
58	EJ	2005/09/15 14:24	09/13 20:00	360	1866	0.31	S09E10
59	EJ	2006/08/20 00:00	08/16 16:30	360	888	0.44	S16W08

shapes of CMEs as shown in Figure 2(a) and (c). The CME observed on 28 October 2003 (CDAW #45) was associated with a strong X-ray flare (X17.2) at S16E08, and observed as a symmetric halo with a speed of 2456 km s^{-1} (Gopalswamy *et al.*, 2005; see Figure 2(a)). This CME was detected as an MC when it arrived at the Earth on 29 October 2003 as shown in Figure 2(b). The figure shows a smoothly rotating and increasing magnetic field, which is an indicator of MC. Another CME observed on 15 January 2005 (CDAW #51) was associated with an M8.6 class flare from N16E04 as shown in Figure 2(c). It was also a halo event with high speed (2049 km s^{-1}) from the solar center. In this case, the CME turned into an EJ when observed by *in-situ* spacecraft on 16 January 2005 (Figure 2(d)). As shown in the figure, there was no distinct rotation of magnetic field and the strength remained less than 10 nT during the passage of the EJ. The direction parameters for these two events were compiled as 0.94 (28 October 2003) and 0.07 (15 January 2005). The northward bias of the latter event resulted in a smaller D.

3. Results

3.1. Source Location and Angular Width

Since we have already selected only the CMEs with source regions close to the solar center, it is clear that both MCs and EJs originate near the central meridian as listed in Table 1. The distribution of source locations for the 54 CMEs in Figure 3(a) shows that the mean longitude ($|l|$) for the 23 MCs is 6.6°, which is similar to that for 31 EJs (7.6°). As shown in the figure, there is no significant difference between the source locations for MCs and EJs. The p value of the T test for two groups of MC and EJ is 0.199, which is much higher than the significance level (0.05).

The distribution of angular widths of the CMEs in Figure 3(b) shows that a large portion (38/54, 70 %) of the 54 CMEs are full halos (AW = 360°) with the mean angular width

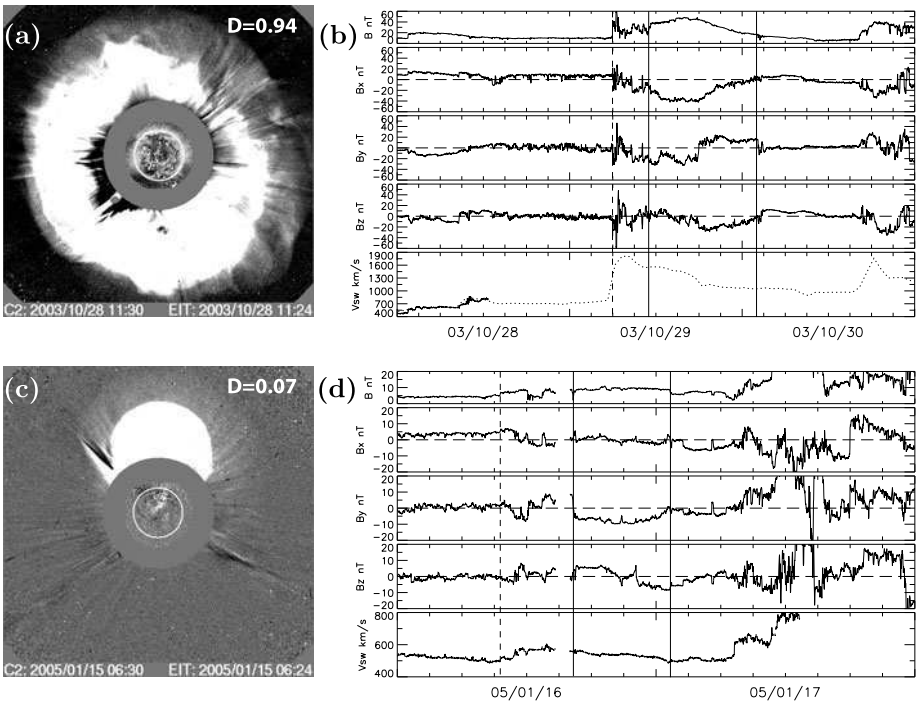

Figure 2 LASCO C2 running difference images for the CMEs on 28 October 2003 (a) and on 15 January 2005 (c). (b) and (d) show the time profiles of magnetic field intensity, B_X, B_y, B_z components in geocentric solar ecliptic (GSE) coordinates, and the solar wind bulk velocity observed by the *Solar Wind Electron, Proton, and Alpha Monitor* (SWEPAM) on board the *Advanced Composition Explorer* (ACE; Gloeckler *et al.*, 1998). We also use the data from the *Solar Wind Ion Composition Spectrometer* (SWICS) on board the ACE when the SWEPAM does not give solar wind parameters because the speed is too high, as represented by dotted line (b). The start time of IP shock and the boundaries of ICME are denoted by vertical dashed (shock) and solid lines (ICME).

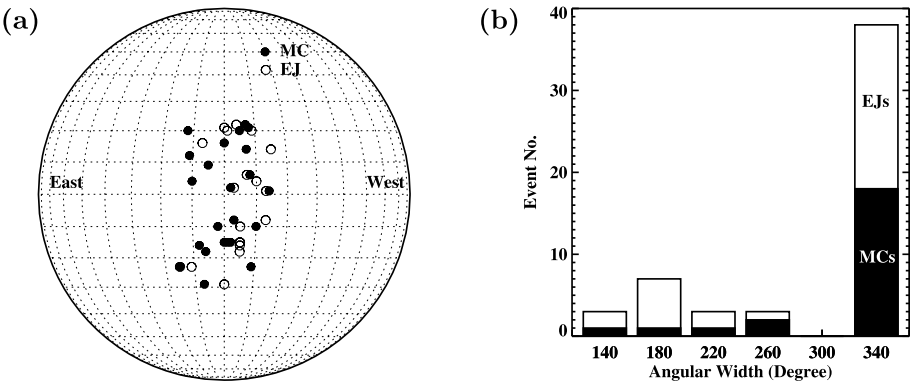

Figure 3 Distribution of the source region locations (a) and the angular width (b) of MC and EJ events.

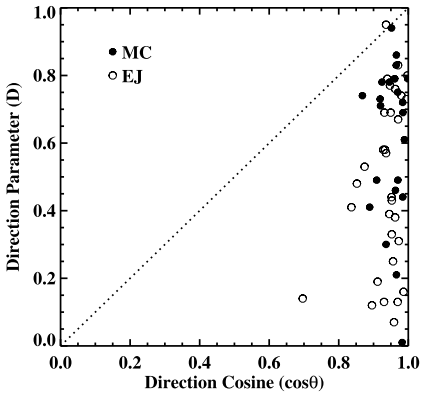

Figure 4 The relationship between the direction cosine of the CME source location and the direction parameter. The filled and empty circles represent MCs and EJs, respectively.

of 309°. Among the halos, there are 18 MC-associated CMEs and 20 EJ-associated CMEs. Among the 16 non-halo CMEs, five events are MC-associated CMEs and 11 events are EJ-associated CMEs. The mean angular widths for MC and EJ are 327° and 295°, respectively. We found that there is no big difference between them in the angular width distribution because the majority of CMEs in the two groups are full halo events.

3.2. Direction Parameter

The source locations of the two events in Figure 2 have similar distances from the solar center (S16E08 and N16E04), but they show different ICME structures; one is detected as an MC and the other an EJ. This is a typical example showing a possibility that even though all events occurred near the solar center, their propagation directions might be different, leading to different ICME structures at 1 AU. Thus, we inspected the propagation direction using D for all the events in the CDAW list. Recall that the 28 October 2003 CME has a large D (0.94), but the one on 15 January 2005 has a small D (0.07).

To verify the hypothesis that the propagation directions of CMEs might be different even though they originate from the vicinity of the central median on the Sun, we examined the relation between the source locations and the propagation directions for 54 CDAW events, supposing that CMEs propagate radially. In Figure 4, we compare D with the direction cosine, $\cos\theta$, where θ is the angular distance of the source region from the solar center. The direction cosine is between 0 to 1 and it should be 1 when the source location is exactly at the solar center. For the 54 CDAW events, we found that $\cos\theta$ occupies a narrow range $(0.8-1)$ except for one event as shown in the figure (mean $= 0.94$), while D is randomly scattered over the entire range (mean $= 0.54$). If all CMEs are ejected radially, these two values should be similar for each event. In this case, the events should fall near the dotted line in the figure, but the distribution in the figure deviates significantly from the dotted line. This result shows that many of the CMEs are not ejected along the radial direction and their noses may not reach the Earth even though they are ejected from the vicinity of the center of the solar disk.

We also examined the dependence of D on the ICME type: MC and EJ. The average D values for 23 MCs and 31 EJs are 0.62 and 0.49, respectively. These values are relatively high, since the CDAW events are from the disk center. However, EJ's D value is only slightly higher ($+0.06$) than the average D for the 486 halo CMEs ($D = 0.43$; Kim *et al.*, 2008), in spite of the data set from the disk center. Please note that MC's D value is almost 1.5 times of that for entire sample of halo CMEs. Figure 5(a) and (b) show that Ds for MC-associated

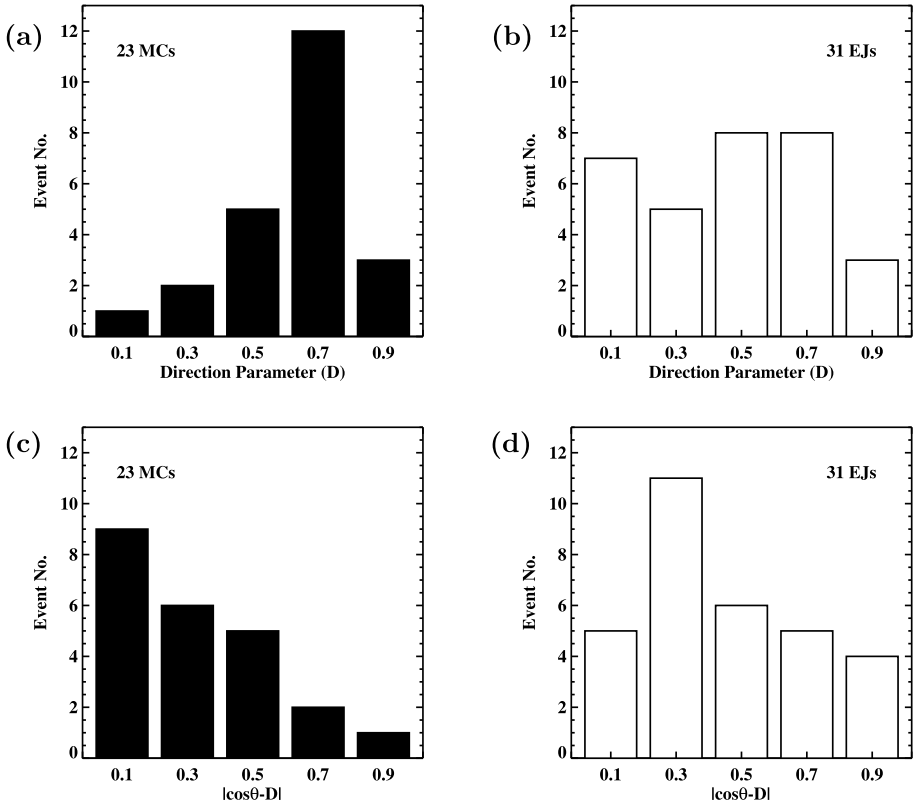

Figure 5 The distributions of the direction parameter for MC and EJ events (a and b) and the amount of deflection of MC and EJ events (c and d).

CMEs follow a Gaussian distribution with the median value of 0.72, while those of EJ-associated CMEs are evenly spread (median = 0.48). The p value of the T test between the two groups is 0.048 (< 0.05), which means that the difference is statistically significant.

We also examined the difference between $\cos\theta$ and D ($|\cos\theta - D|$) for each event as shown in Figure 5(c) and (d). This value can be regarded as a proxy of the CME deflection from the radial direction. We found that the majority of MC-associated CMEs are not deflected much with peak difference between 0 and 0.2 as shown in Figure 5(c). On the other hand, many of EJs show some deflection with peak value between 0.2 and 0.4 in Figure 5(d). This result suggests a tendency in our dataset that EJs either erupt non-radially or experience more deflection than MCs.

3.3. CME Speed

The association between the CMEs and MCs can be explained by the direction parameter, but the association between the CMEs and EJs is difficult to explain with the direction parameter as shown in Figure 5(a) and (b). To inspect other effects on the EJ-associated CMEs, we considered the linear speed of CMEs and examined the combined effect of the speed and direction parameter. In Figure 6(a) and (b), we can see a tendency that slow CMEs are more likely to be associated with EJs. Of the 31 EJ-associated CMEs, 25 have

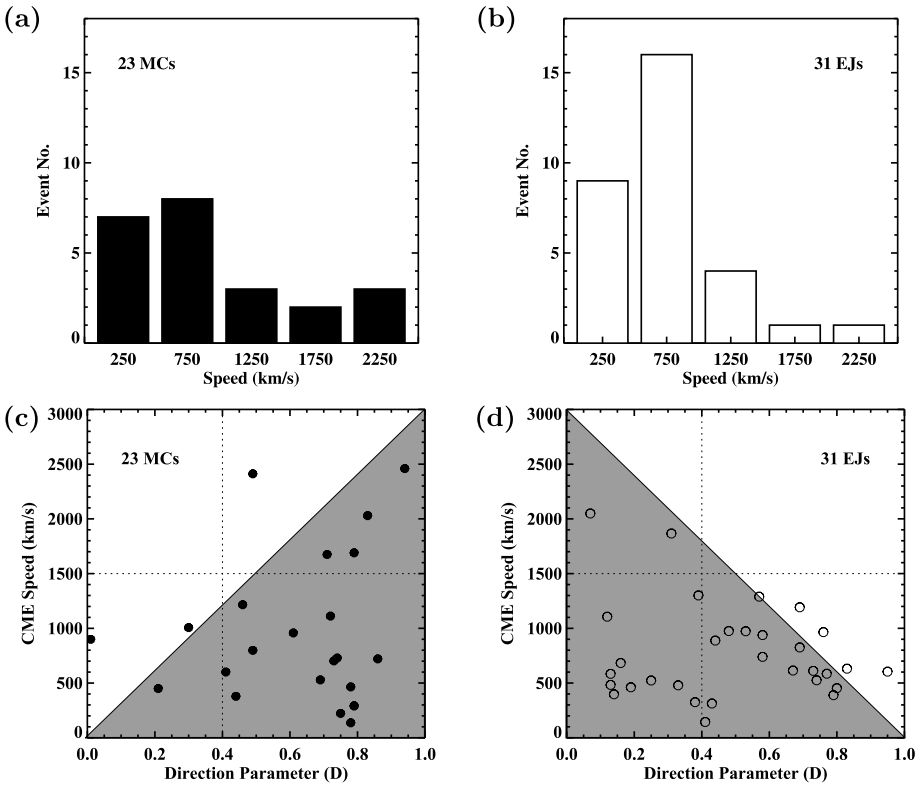

Figure 6 Associated CME speed for MCs (a) and EJs (b), and the distribution of MCs (c) and EJs (d) as a function of the speed and the direction parameter. The horizontal dotted lines indicate $V = 1500$ km s^{-1} and the vertical dotted lines indicate $D = 0.4$.

lower speeds than 1000 km s^{-1} (81 %), while the 23 MC-associated CMEs do not show any strong dependences as the EJs-associated CMEs do. The mean speed for the CDAW events is 846 km s^{-1} and those for MC- and EJ-associated CMEs are 946 km s^{-1} and 771 km s^{-1}, respectively.

Although the difference in mean speed is not statistically significant (p value $= 0.253$), we can find a combined effect of speed and direction parameter as shown in Figure 6(c) and (d). The majority of the MCs are located beneath the increasing diagonal line (increasing speed with D) and a large portion of the EJs are located beneath the decreasing diagonal line (decreasing speed with D) as shown in the gray portions of Figure 6(c) and (d), respectively. This result implies that, for the faster CME, D is more important to classify the ICME. This becomes clearer in the case of seven very fast CMEs (≥ 1500 km s^{-1}), since all large-D events (≥ 0.4) are MCs, and all small-D events are EJs.

Contrary to our result, Gopalswamy *et al.* (2010) reported that the MC-associated CMEs have lower speeds than EJ-associated CMEs using 222 IP shock–CME pairs. They explained that the difference in CME speeds stem from the fact that the MC-associated CMEs mostly originate close to the disk center, and the EJ-associated CMEs originate at intermediate central meridian distances. Then MC-associated CMEs are more subject to projection effects than EJ-associated CMEs. However, since our data set is selected from the central events,

Table 2 Definition of verification statistics.

	Observed MC	Observed EJ	Total
Predicted MC	hit (a)	false (b)	a + b
Predicted EJ	miss (c)	null (d)	c + d
Total	a + c	b + d	a + b + c + d
Probability of detection, yes (PODy)			a/(a + c)
Probability of detection, no (PODn)			d/(b + d)
Critical success index (CSI)			a/(a + b + c)

Table 3 Three contingency tables with criteria of the average values of 486 halo CMEs (Kim *et al.*, 2008).

CME parameters				PODy	PODn	CSI	χ^2 (p value)
$\cos\theta = 0.7$	MC	EJ	Total				
Inner	23	30	53	1.00	0.03	0.43	0.76 (0.385)
Outer	0	1	1				
Total	23	31	54				
$D = 0.4$	MC	EJ	Total				
Large D	20	19	39	0.87	0.39	0.48	4.34 (0.037)
Small D	3	12	15				
Total	23	31	54				
$V = 800$ km s^{-1}	MC	EJ	Total				
Fast	10	12	22	0.43	0.61	0.29	0.12 (0.724)
Slow	13	19	32				
Total	23	31	54				

even the EJ-associated CMEs cannot avoid the projection effects. Therefore, our result is in line with the result of Gopalswamy *et al.* (2010).

3.4. Statistical Significance

To evaluate the capability of ICME classification using the CME parameters, we adopted a contingency table that has been widely used in the meteorological forecasting literature. Table 2 is a general form of the contingency table, which provides us with the information of the success or failure (or degree thereof) of the forecasting experience in real time (Smith *et al.*, 2000). In this table, the 'hit' means correctly predicted for an MC. The 'false' means predicted for an MC, but observed as an EJ. Similarly, the 'miss' is predicted for an EJ, but observed as an MC, and the 'null' is correctly predicted for an EJ. The statistics, such as the probability of detection 'yes' (PODy) and the critical success index (CSI), may then be computed as shown in the table. CSI ranges from 0 to 1, with a value of 1 indicating a perfect forecast.

Table 3 shows three 2 × 2 contingency tables based on the CME location, direction parameter, and speed. As the criteria for parameters, we applied 0.7 for $\cos\theta$, 0.4 for D, and 800 km s^{-1} for speed based on the average values of the 486 general halo CMEs (Kim *et al.*,

2008). If an event has larger value than each criterion, we expect the ICME as an MC, otherwise as an EJ. Since the data set already selected the events from the central meridian, almost all CMEs are so biased inner events that we cannot discern MC or EJ using their location as shown in the first contingency table. In this case, PODy, PODn, and CSI are estimated to be 1.00, 0.03, and 0.43, respectively. Similarly, it also seems hard to classify CME into MC or EJ using only the speed of CME. The events are evenly distributed in each cell as shown in the third contingency table. PODy, PODn, and CSI are estimated to be 0.43, 0.61, and 0.29, respectively. The p values from χ^2 test of the directional cosine and the speed are 0.385 and 0.724, respectively. These values are too high to have any significance on the classification of the ICME. In contrast, the direction parameter can provide reliable classification with sufficient statistical significance (p value $= 0.037$). As shown in the second contingency table, its PODy, PODn, and CSI are estimated to be 0.87, 0.39, and 0.48, respectively.

4. Summary and Discussion

We examined the CME parameters to check whether all the CMEs have flux rope structure using the 54 CME–ICME pairs compiled for the NASA/LWS Coordinated Data Analysis Workshop. We did not find any significant difference between 23 MCs and 31 EJs from the comparison of their source locations and angular widths. The average value of D for MC events (0.62) is larger than that for EJ events (0.49). We found a tendency that the EJ-associated CMEs are ejected non-radially or experience deflections more than the MC-associated CMEs. Regarding the CME speed, the mean value for MCs is 946 km s^{-1} and that for EJs is 771 km s^{-1}. Among the 31 EJs, 25 events have low CME speeds (< 1000 km s^{-1}, 81 %), while the MCs have less slow CMEs (15/23, 65 %, *cf.* the fraction of slow CME from Kim *et al.* (2008) is 72 %). We also examined the combined effect of the direction parameter and speed. It is found that the majority of the MCs have large D (≥ 0.4) and the majority of the EJs have slow speed (< 1500 km s^{-1}). This result can be summarized that EJ-associated CMEs have slow speeds, and MC-associated CMEs have large D. We also found a clear tendency in the case of seven very fast CMEs (≥ 1500 km s^{-1}) that all large-D events (≥ 0.4) are MCs, and all small-D events are EJs.

Our study is a simple analysis, but it provides a clue to answer the question whether all CME have flux rope structure. If we use only the CME source information to classify ICMEs, it seems hard to find any differences between MCs and EJs. However, if we use the CME propagation direction and speed, we can find a hint for the answer. Based on our results, we suggest that some of the CMEs are not ejected along the radial direction and they may not reach the Earth by their noses. In this case, we may not detect the flux rope structure even if they have one. Our result is consistent with those by Xie, Gopalswamy, and Cyr (2013), who reported that the EJ-associated CMEs were deflected more away from the disk center, while the MC-associated CMEs were deflected more towards the disk center using the Krall flux rope model. Our result is also consistent with those by Mäkelä *et al.* (2013) who found that the EJ-associated CMEs are prone to deflection by nearby coronal holes.

If the CMEs associated with MCs and EJs have originally different flux rope structures, they should be observed differently without no dependence on the CME speed. However, our observation shows that slow CMEs are more likely to be EJs than fast CMEs, and fast CMEs are to be EJs, only when they have small Ds. Based on the above results, we suggest that all CMEs have a flux rope structure and the trajectory of the CMEs essentially decides the observed ICME structure.

Acknowledgements This work benefited from the NASA/LWS Coordinated Data Analysis Workshops on CME flux ropes in 2010 and 2011. We acknowledge the workshop support provided by NASA/LWS, Predictive Sciences, Inc. (San Diego, CA), University of Alcala (Alcala de Henares, Spain), and Ministerio de Ciencia e Innovacion (Reference number AYA2010-12439-E), Spain. This work was partially supported by the Construction of Korean Space Weather Center as the project of KASI, the KASI Basic Research Fund, and Research Fellowship for Young Scientists of KRCF. Y.-J.M. has been supported by the WCU program (No. R31-10016) and Basic Research Promotion Fund (20090071744 and 20100014501) through the National Research Foundation of Korea funded by the Ministry of Education, Science and Technology.

References

Brueckner, G.E., Howard, R.A., Koomen, M.J., Korendyke, C.M., Michels, D.J., Moses, J.D., *et al.*: 1995, The Large Angle Spectroscopic Coronagraph (LASCO). *Solar Phys.* **162**, 357.

Burlaga, L.F., Sittler, E., Mariani, F., Schwenn, R.: 1981, Magnetic loop behind an interplanetary shock: *Voyager*, *Helios*, and IMP 8 observations. *J. Geophys. Res.* **86**, 6673.

Burlaga, L.F., Skoug, R.M., Smith, C.W., Webb, D.F., Zurbuchen, T.H., Reinard, R.: 2001, Fast ejecta during the ascending phase of solar cycle 23: ACE observations, 1998 – 1999. *J. Geophys. Res.* **106**(A10), 20957.

Gloeckler, G., Cain, J., Ipavich, F.M., Tums, E.O., Bedini, P., Fisk, L.A., *et al.*: 1998, Investigation of the composition of solar and interstellar matter using solar wind and pickup ion measurements with SWICS and SWIMS on the ACE spacecraft. *Space Sci. Rev.* **86**, 497.

Gopalswamy, N.: 2006, Properties of interplanetary coronal mass ejections. *Space Sci. Rev.* **124**, 145.

Gopalswamy, N., Yashiro, S., Liu, Y., Michalek, G., Vourlidas, A., Kaiser, M.L., Howard, R.A.: 2005, Coronal mass ejections and other extreme characteristics of the 2003 October – November solar eruptions. *J. Geophys. Res.* **110**, A09S15. doi:10.1029/2004JA010958.

Gopalswamy, N., Xie, H., Mäkelä, P., Akiyama, S., Yashiro, S., Kaiser, M.K., Howard, R.A., Bougeret, J.-L.: 2010, Interplanetary shocks lacking type II radio burst. *Astrophys. J.* **710**, 1111.

Gosling, J.T.: 1990, In: *Physics of Magnetic Flux Ropes*, *Geophys. Monogr. Ser.* **58**, AGU, Washington, 343.

Howard, T.A., DeForest, C.E.: 2012, Inner heliospheric flux rope evolution via imaging of coronal mass ejection. *Astrophys. J.* **746**, 64.

Hundhausen, A.J.: 1993, Size and locations of coronal mass ejections – SMM observations from 1980 and 1984 – 1989. *J. Geophys. Res.* **98**(A8), 13177.

Jacobs, C., Roussev, I.I., Lugaz, N., Poedts, S.: 2009, The internal structure of coronal mass ejections: are all regular magnetic clouds flux ropes? *Astrophys. J. Lett.* **695**, L171.

Kim, R.-S., Cho, K.-S., Moon, Y.-J., Dryer, M., Yi, Y., Lee, J., Kim, K.-H., Wang, H., Song, H., Park, Y.-D.: 2008, CME earthward direction as an important geoeffectiveness indicator. *Astrophys. J.* **677**, 1378.

Mäkelä, P., Gopalswamy, N., Xie, H., Mohamed, A.A., Akiyama, S., Yashiro, S.: 2013, Coronal hole influence on the observed structure of interplanetary CMEs. *Solar Phys.*, in this issue. doi:10.1007/s11207-012-0211-6.

Manchester, W.B., Gombosi, T.I., Roussev, I., DeZeeuw, D.L., Sokolov, I.V., Powell, K.G., Tóth, G., Opher, M.: 2004, Three-dimensional MHD simulation of a flux rope driven CME. *J. Geophys. Res.* **109**(A1), A01102.

Moon, Y.-J., Cho, K.-S., Dryer, M., Kim, Y.-H., Bong, S.-C., Chae, J., Park, Y.D.: 2005, New geoeffective parameters of very fast halo coronal mass ejections. *Astrophys. J.* **624**, 414.

Nakwacki, M.S., Dasso, S., Démoulin, P., Mandrini, C.H., Gulisano, A.M.: 2011, Dynamical evolution of a magnetic cloud from the Sun to 5.4 AU. *Astron. Astrophys.* **535**, 52.

Odstrcil, D., Pizzo, V.J.: 1999, Distortion of the interplanetary magnetic field by three-dimensional propagation of coronal mass ejections in a structured solar wind. *J. Geophys. Res.* **104**(A12), 28225.

Roussev, I.I., Gombosi, T.I., Sokolov, I.V., Velli, M., Manchester, W., DeZeeuw, D.L. IV, *et al.*: 2003, A three-dimensional model of the solar wind incorporating solar magnetogram observations. *Astrophys. J. Lett.* **595**, L57.

Smith, Z., Dryer, M., Ort, E., Murtagh, W.: 2000, Performance of interplanetary shock prediction model: STOA and ISPM. *J. Atmos. Solar-Terr. Phys.* **62**, 1265.

Thompson, W.T., Kliem, B., Török, T.: 2012, 3D reconstruction of a rotating erupting prominence. *Solar Phys.* **276**, 241.

Xie, H., Gopalswamy, N., St. Cyr, O.C.: 2013, Near-Sun flux rope structure of CMEs. *Solar Phys.*, in this issue. doi:10.1007/s11207-012-0209-0.

Solar Phys (2013) 284:105–127
DOI 10.1007/s11207-013-0224-9

Comparison of Helicity Signs in Interplanetary CMEs and Their Solar Source Regions

K.-S. Cho · S.-H. Park · K. Marubashi · N. Gopalswamy · S. Akiyama · S. Yashiro · R.-S. Kim · E.-K. Lim

Received: 6 April 2012 / Accepted: 5 January 2013 / Published online: 7 February 2013

Abstract If all coronal mass ejections (CMEs) have flux ropes, then the CMEs should keep their helicity signs from the Sun to the Earth according to the helicity conservation principle. This study presents an attempt to answer the question from the Coordinated Data Analysis Workshop (CDAW), "Do all CMEs have flux ropes?", by using a qualitative helicity sign comparison between interplanetary CMEs (ICMEs) and their CME source regions. For this, we select 34 CME–ICME pairs whose source active regions (ARs) have continuous SOHO/MDI magnetogram data covering more than 24 hr without data gap during the passage of the ARs near the solar disk center. The helicity signs in the ARs are determined by estimation of cumulative magnetic helicity injected through the photosphere in the entire source ARs. The helicity signs in the ICMEs are estimated by applying the cylinder model developed by Marubashi (*Adv. Space. Res.*, **26**, 55, 2000) to 16 second resolution magnetic field data from the MAG instrument onboard the ACE spacecraft. It is found that 30 out of 34 events (88 %) are helicity sign-consistent events, while four events (12 %) are sign-inconsistent. Through a detailed investigation of the source ARs of the four sign-inconsistent events, we find that those events can be explained by the local helicity sign opposite to that of the entire AR helicity (28 July 2000 ICME), incorrectly reported solar source region in the CDAW list (20 May 2005 ICME), or the helicity sign of the pre-existing coronal magnetic field (13 October 2000 and 20 November 2003 ICMEs). We conclude that the helicity

Flux-Rope Structure of Coronal Mass Ejections
Guest Editors: N. Gopalswamy, T. Nieves-Chinchilla, M. Hidalgo, J. Zhang, and P. Riley

K.-S. Cho (✉) · S.-H. Park · K. Marubashi
Korea Astronomy and Space Science Institute, Daejeon 305-348, Republic of Korea
e-mail: kscho@kasi.re.kr

K.-S. Cho · N. Gopalswamy · S. Akiyama · S. Yashiro · R.-S. Kim
NASA Goddard Space Flight Center, Greenbelt, MD 20771, USA

K.-S. Cho · S. Akiyama · S. Yashiro · R.-S. Kim
Department of Physics, The Catholic University of America, Washington, DC 20064, USA

E.-K. Lim
Big Bear Solar Observatory, New Jersey Institute of Technology, Newark, CA, USA

signs of the ICMEs are quite consistent with those of the injected helicities in the AR regions from where the CMEs erupted.

Keywords Coronal mass ejections · Magnetic cloud · Photospheric helicity · Solar surface magnetic field · Interplanetary magnetic field

1. Introduction

Coronal mass ejections (CMEs) are one of the means by which the Sun ejects plasma and magnetic field into interplanetary space. When CMEs are detected near the Earth, they are known as interplanetary CMEs (ICMEs). ICMEs are further classified into magnetic clouds (MC) and complex ejecta (EJ) depending on the observed magnetic structure. MCs exhibit a smooth rotation of magnetic field vector, while EJs do not show a significant rotation signature (*e.g.* Burlaga *et al.*, 1981). It is still not clear whether MC and EJ have intrinsically different structure or the observed structure is due to different propagation of the ejecta relative to the observing spacecraft. The main purpose of the Coordinated Data Analysis Workshop (CDAW) this article results from is to answer the question: "Do all CMEs have flux ropes?" There are two different views. One view is that some CMEs have inherently non-flux rope structure (Gosling *et al.*, 1990; Jacobs *et al.*, 2009), and the other view is that all the CMEs have flux ropes but sometimes they are not detected as flux ropes since a magnetic cloud observed far from its apex (nose) may not exhibit a clear flux rope structure (Gopalswamy, 2006; Kim *et al.*, 2013). For example, Chen *et al.* (1997) compared LASCO C2 and C3 CME images with a magnetic flux rope model, and concluded that the dynamics and morphology of the observed CME on 13 April 1997 were consistent with those of the three-dimensional (3D) MHD flux rope model developed by Chen (1996).

Magnetic helicity quantifies the signed amount of twists, kinks, and inter-linkages of the magnetic field lines in a given magnetic field system (Berger and Field, 1984). Magnetic helicity is an approximately conserved quantity in resistive MHD with low resistivity (Berger, 1984) – this is the 'helicity conservation principle'. Therefore, an ICME is expected to carry the same amount of helicity as its corresponding CME from the solar source region, and the helicity sign of the ICME should be consistent with that of the solar source region. Several attempts have been made to match the helicity sign of ICMEs with that inferred from the morphological features of their source active region such as sunspot whorls, filament barbs, sigmoids, and flare ribbons (*e.g.* Ali *et al.*, 2007; Démoulin, 2008). However, the helicity sign of the solar source region was not always found to agree with that of the ICME (Leamon *et al.*, 2004). These observational features have been commonly used for qualitative comparison of helicity signs of CMEs and ICMEs. In this study, we use the helicity signs of solar source regions and ICMEs that are determined in the following ways:

i) measurement of the rate of the helicity transfer into the corona across the photosphere by inferring the motion of the surface field lines from photospheric magnetogram data, and
ii) inferring the rotation of the magnetic field vector from *in situ* data obtained by spacecraft located near the Earth.

If we find complete agreement of the helicity signs between CMEs and ICMEs, this result would support the hypothesis that all ICMEs are flux ropes. We investigate 34 CME–ICME events. To obtain the helicity sign of the ICMEs, we employ the fitting technique developed by Marubashi (2000) using the constant-α force-free field solution, assuming the

flux rope to be a cylinder with self-similar expansion. We do not consider the amount of helicity in this study since it could be different depending on the fitting model employed (Hu and Dasgupta, 2005; Marubashi and Lepping, 2007). On the contrary, we note that the sign of helicity determined by different fitting models is consistent between models. For this reason, we compare the helicity sign in ICMEs and to that in their source regions.

The rest of the paper is organized as follows. In Section 2, we describe briefly the methods used to determine the helicity injection rate. The helicity sign comparison between photospheric injection and ICME is given in Section 3, with detailed inspection of the four sign-inconsistent events. Section 4 summarizes the findings of this study.

2. Data and Analysis

The CDAW events (http://cdaw.gsfc.nasa.gov/meetings/2010_fluxrope/) have been selected from the list of shock-driving ICMEs in Gopalswamy *et al.* (2010), which originate from the vicinity of central meridian of the Sun (E15° $\leq$ source longitude $\leq$ W15°). To get a reliable helicity injection avoiding the projection effect on the line-of-sight magnetic field, we need continuous SOHO/MDI magnetogram (Scherrer *et al.*, 1995) data of the solar source region covering more than 24 hr without data gaps during the transit of the source region across the solar disk center. With this criterion, we select 28 events from the 54 CDAW events and also select six events from the list in Sung *et al.* (2009). Details of the identification of solar source regions associated with the 28 ICMEs are described in Gopalswamy *et al.* (2010), and those of the additional six CME–MC pairs can be found in Manoharan *et al.* (2004) and Qiu *et al.* (2007).

Detailed information on the 34 CME–ICME pairs are given in Table 1. The first column of Table 1 denotes the event number. Year, appearance time, speed, and angular width of the CMEs determined from SOHO/LASCO observations are listed from the second to fifth columns. The sixth to ninth columns contain information on the associated flare onset time and class, active region number, and solar source location, respectively. The last three columns give the start and end times of ICMEs, and their classification as listed in the CDAW ICME data table. Note that there are 24 MCs and 10 EJs in the dataset. We determined the geometry of the ICMEs and derived the helicity sign by assuming that the ICMEs have flux rope structure.

2.1. Photospheric Helicity Injection

The helicity sign in the solar source ARs of the selected events is obtained from the helicity flux density (*i.e.*, helicity injection per unit area per unit time) at the photospheric level of the ARs. To calculate the helicity flux density, we use the formula proposed by Pariat, Démoulin, and Berger (2005) and the numerical calculation method developed by Chae (2007).

Following the method of Chae (2007), we estimate the normal component of magnetic field (B_n) from the line-of-sight component of magnetic field (B_l), assuming that the magnetic field at the photosphere is normal to the solar surface and the transverse component of the magnetic field is negligible compared to B_l. This assumption is valid only in the case of active regions located near the solar disk center.

The time-dependent measurement of B_l is obtained from a set of the full-disk 96 minutes SOHO/MDI (Scherrer *et al.*, 1995) magnetogram data. To reduce the geometrical projection effects in the calculation of B_n, we restrict to solar source regions located within 60 % of

Table 1 Characteristics of flare, CME, and ICME.

No[a]	Year	CME appearance Time	CME speed (km s^{-1})	CME AW (deg)	Flare onset (UT)	Flare class	AR	Solar source Loc	ICME start[c] (UT)	ICME end (UT)	MC/EJ
C2	1997	05/12 05:30	464	360	04:42	C1.3	8038	N21W08	05/15 09:06	05/16 01:06	MC
S11	1998	02/28 12:48	176	169	–	–	8171	S24W01[b]	03/04 19:00	03/06 05:00	MC
C5	1998	05/02 14:06	938	360	13:31	X1.1	8210	S15W15	05/04 10:00	05/05 01:15	EJ
S13	1998	06/21 05:35	192	163	–	–	8243	N17W25[b]	06/24 13:00	06/25 22:00	MC
C16	2000	02/17 21:30	728	360	20:17	M1.3	8872	S29E07	02/21 09:48	02/22 13:18	MC
C17	2000	07/07 10:26	453	360	08:42	C5.6	9070	N17E10	07/11 01:30	07/11 11:22	EJ
C18	2000	07/08 23:50	483	161	22:58	C4.0	9070	N18W12	07/11 22:48	07/13 02:25	EJ
C19	2000	07/14 10:54	1674	360	10:03	X5.7	9077	N22W07	07/15 21:06	07/16 09:54	MC
C21	2000	07/25 03:30	528	360	02:43	M8.0	9097	N06W08	07/28 21:06	07/29 10:06	MC
C23	2000	08/09 16:30	702	360	15:19	–	9114	N20E12	08/12 06:06	08/13 05:06	MC
C24	2000	09/16 05:18	1215	360	04:06	M5.9	9165	N14W07	09/18 01:54	09/18 15:06	MC
C26	2000	10/09 23:50	789	360	23:19	C6.7	9182	N01W14	10/13 18:24	10/14 16:54	MC
S26	2001	03/16 03:50	271	281	–	–	9384	N11W09[b]	03/19 19:00	03/22 06:00	MC
C32	2001	04/10 05:30	2411	360	05:06	X2.3	9415	S23W09	04/12 07:54	04/12 17:54	MC
C27	2001	04/19 12:30	392	129	–	–	9434	N20W20[b]	04/22 00:00	04/23 00:00	MC
C33	2001	04/26 12:30	1006	360	11:26	M1.5	9433	N20W05	04/29 01:54	04/29 12:54	MC
S30	2002	03/20 17:54	603	360	–	–	9871	S17W20[b]	03/24 03:00	03/25 22:00	MC
C37	2002	04/15 03:50	720	360	03:05	M1.2	9906	S15W01	04/18 04:18	04/19 02:18	MC
C39	2002	05/16 00:50	600	360	00:11	C4.5	9948	S23E15	05/19 03:54	05/19 23:24	MC
C42	2002	07/15 21:30	1300	180	21:03	M1.8	10030	N19W01	07/18 12:00	07/19 08:10	EJ

Table 1 (*Continued*)

No[a]	Year	CME appearance Time	CME speed ($km\,s^{-1}$)	CME AW (deg)	Flare onset (UT)	Flare class	AR	Solar source Loc	ICME start[c] (UT)	ICME end (UT)	MC/EJ
C44	2003	08/14 20:06	378	360	17:12	–	10431	S10E02	08/18 11:36	08/19 04:24	MC
C45	2003	10/28 11:30	2459	360	11:00	X17.2	10486	S10E08	10/29 08:00	10/30 04:00	MC
C46	2003	10/29 20:54	2029	360	20:37	X10.0	10486	S15W02	10/31 02:00	10/31 13:00	MC
S32	2003	11/18 08:50	1660	360	08:30	M3.9	10501	N03E08[b]	11/20 11:00	11/21 01:00	MC
C48	2004	07/22 08:30	899	132	07:41	C5.3	10652	N04E10	07/24 12:48	07/25 13:18	MC
C49	2004	11/06 02:06	1111	214	01:40	M3.6	10696	N09E05	11/09 20:54	11/10 03:24	MC
C50	2004	12/08 20:26	611	360	19:34	C2.5	10709	N05W03	12/12 12:00	12/13 06:00	EJ
C51	2005	01/15 06:30	2049	360	05:54	M8.6	10720	N16E04	01/16 14:00	01/17 06:30	EJ
C52	2005	02/13 11:06	584	151	10:28	C2.7	10733	S11E09	02/18 15:00	02/19 08:15	EJ
C53	2005	05/13 17:12	1689	360	16:13	M8.0	10759	N12E11	05/15 05:42	05/15 22:12	MC
C54	2005	05/17 03:26	449	273	02:31	M1.8	10763	S15W00	05/20 07:18	05/21 05:18	MC
C55	2005	05/26 21:26	420	199	20:57	C8.6	10767	S08E11	05/29 10:15	05/29 14:45	EJ
C56	2005	07/07 17:06	683	360	16:07	M4.9	10786	N09E03	07/10 10:30	07/12 04:00	EJ
C57	2005	08/31 11:30	825	360	10:26	C2.0	10803	N13W13	09/02 19:03	09/03 06:00	EJ

[a] 'C' denotes that the CME–ICME pair is selected from the CDAW ICME list. 'S' denotes that CME–ICME pair is selected from Sung *et al.* (2009).

[b] Source ARs given by Manoharan *et al.* (2004) and Qiu *et al.* (2007) are used.

[c] ICME start time is the time when the leading boundary of the ICME is observed *in situ*, determined from fitting of the cylinder model.

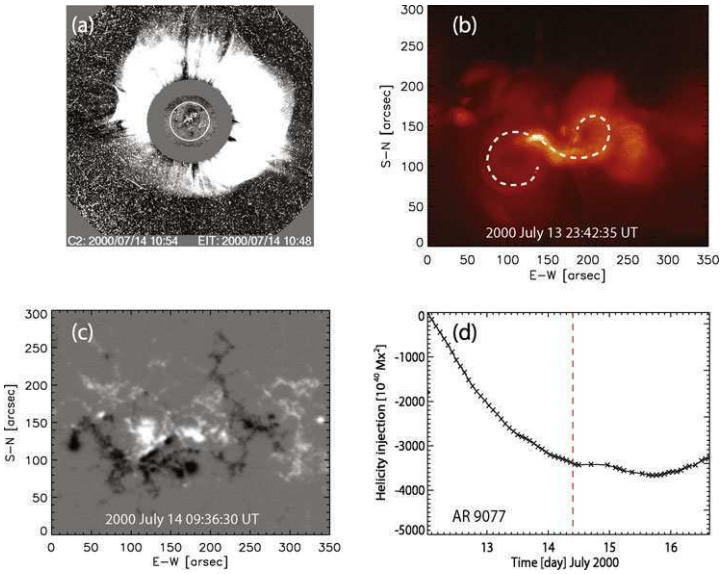

Figure 1 (a) A SOHO/LASCO running difference image of the 14 July 2000 CME, (b) inverse-S shape sigmoid in a *Yohkoh* soft X-ray image of AR 9077, (c) MDI magnetogram of the AR, (d) estimated helicity injection in the AR from 12 to 16 July in 2000. The dashed vertical line in panel (d) denotes the start time of the flare associated with the CME.

the solar radius ($R_\odot$) from the apparent disk center. The velocity of the apparent horizontal motion of field line footpoints is determined by applying the differential affine velocity estimator (DAVE) method (Schuck, 2006). It is noted by Chae and Sakurai (2008) that the performance of DAVE is degraded in the presence of superpixel motions, even though DAVE outperforms the local correlation tracking (LCT) method. This comes from the linear assumption in DAVE that the speed of the motion is low enough.

We integrate the helicity flux density over the area of the region of interest (ROI) and also with respect to time to obtain the helicity injection (ΔH) in the ROI. Finally, the sign of helicity in the ROI of the ARs is determined by the sign of ΔH at the occurrence time of the CMEs. Note that the start time of the helicity measurements is determined as soon as the ROI appears or rotates to a position within 0.6 $R_\odot$ from the disk center. Details of the procedure for the calculation of the photospheric helicity injection can be found in Chae (2007).

Figure 1 shows (a) the 14 July 2000 CME observed by SOHO/LASCO (Brueckner *et al.*, 1995) C2, (b) a *Yohkoh*/SXT (Tsuneta *et al.*, 1991) soft X-ray image of the source AR of the CME, NOAA 9077, (c) a SOHO/MDI magnetogram of the AR, and (d) helicity injection (ΔH) in the entire AR. The vertical dashed line in Figure 1(d) indicates the start time of the flare associated with the CME. As shown in Figure 1(d), helicity with a negative (left-handed) sign was continuously injected through the entire photospheric surface of the AR from 12 July up to the onset of the flare. We therefore conjecture that the CME produced in the AR has helicity with a negative sign.

In fact, the CME was observed as an ICME near the Earth on 15 July 2000, and the cylinder fitting models of the ICME indicate that it had a flux rope structure and its helicity sign was negative. In Section 2.2, we describe in detail the ICME fitting model that was used in this study.

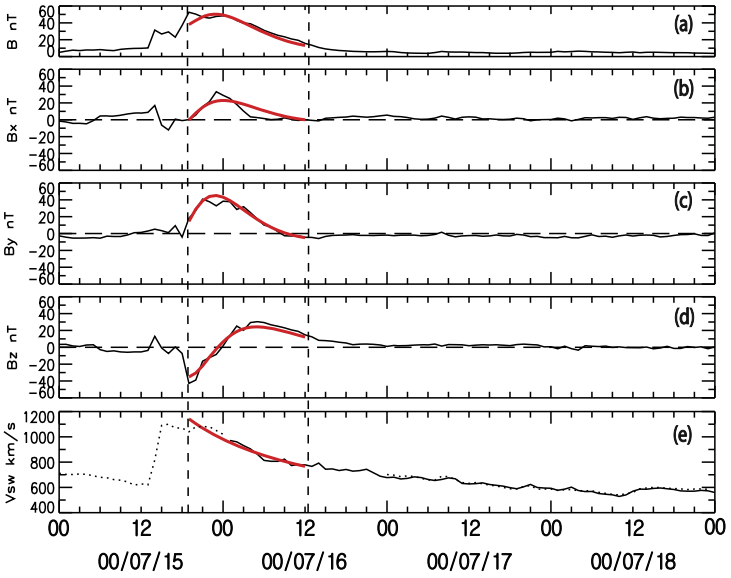

Figure 2 *In situ* interplanetary space data from the ACE spacecraft showing (a) total magnetic field strength, (b) to (d) magnetic field vector in GSE coordinates and (e) solar wind speed. The result of the fitting of the cylinder model is shown by the thick, solid, red lines. The ICME boundaries are located at 19:00 UT on 15 July and 12:00 UT on 16 July 2000, indicated by the two vertical dashed lines.

2.2. Magnetic Cloud Helicity Sign

We perform the cylinder model fitting for 34 ICMEs with either the 15, 20, 30, or 60 mins averaged magnetic field data from the *Magnetic Field Experiment* (MAG: Smith *et al.*, 1998) on the *Advanced Composition Explorer* (ACE) spacecraft, depending on the duration of the ICME. We select the ICME time interval in which the magnetic field vectors change direction smoothly in the $Y - Z$ GSE plane. We then adjust the time span of the ICMEs and the optimum fitting parameters, such as the bulk velocity, intensity of the magnetic field at the cylinder axis, radius of the cylinder, geometry and expansion rate of the cylinder, and the helicity sign of the ICME, which are selected when the least-squares fitting procedure returns a result that is most consistent with the magnetic field observations. In general the helicity sign of an ICME can be judged from the direction of magnetic field rotation with respect to the Earth–Sun line: the helicity is positive (negative) when the rotation has right-handed chirality (left-handed chirality). However, there are some cases where the magnetic field rotation is not very clear. Therefore, we tried the fitting for positive and negative helicity sign when necessary, and selected the helicity sign which yielded a better fit. It is noted that adjustment of the start and end times of the fitting is sometimes necessary for the best fit. We have found that the adjustment is usually less than a few hours and only a little different from Lepping's fit, which can be found in the CDAW list. The difference does not give significantly different results. A detailed description of the cylinder model, the parameters, and fitting procedure are explained by Marubashi and Lepping (2007), and references therein. The start and end times of ICMEs for the best fit using the cylinder model are listed in Table 2.

Figure 2 presents the results of the cylinder fitting for the ICME detected on 15 July 2000 at 21:06 UT associated with the 14 July 2000 CME (Figure 1(a)). From top to bottom, the

Table 2 Estimated helicity injections in the active region and inferred quantities of the magnetic flux in the ICMEs.

No[a]	Active region					ICME				
	Start date[c]	Start time[c]	H_{acc} (10^{40} Mx^2)	AR sig.	Arcade clear?	Start time	End time	Cylinder θ[d]	Cylinder ϕ[e]	Helicity sign
C2	970509	14:28	−100	IS	Yes	05/15 09:50	05/16 02:20	−5	95	LH
S11	980226	11:12	−15	IS(?)	No	03/04 19:00	03/06 5:00	28	77	LH
C5	980428	19:10	2300	S	Yes	05/05 13:00	05/06 02:00	7	309	RH
S13	980616	17:36	−450	IS	No	06/24 13:00	06/25 22:00	34	131	LH
C16	000216	06:23	600	S	Yes	02/21 13:00	02/22 12:00	80	322	RH
C17	000706	00:00	−2700	IS	Yes	07/11 03:30	07/11 13:30	−7	343	LH
C18	000706	00:00	−4800	IS	Yes	07/11 22:30	07/13 04:30	47	61	LH
C19	000712	00:00	−4500	IS	Yes	07/15 19:30	07/16 12:30	19	63	LH
C21[b]	000722	07:59	950	IS(?)	No	07/28 14:00	07/29 00:30	58	376	LH
C23	000806	11:15	−3100	IS	Yes	08/12 05:00	08/13 06:00	15	115	LH
C24	000913	09:33	−2300	IS	Yes	09/17 23:20	09/18 14:20	41	226	LH
C26[b]	001006	12:47	−200	S(?)	Yes	10/13 16:30	10/14 14:00	−24	42	RH
S26	010313	08:00	−50	?	No	03/19 20:00	03/22 6:00	−65	128	LH
C32	010407	04:48	210	S(?)	Yes	04/12 06:00	04/13 03:00	1	353	RH
S27	010418	08:00	−6	S	Yes	04/22 00:00	04/23 03:00	−50	308	LH
C33	010423	11:12	−6200	IS	Yes	04/29 00:30	04/29 14:00	0	115	LH
S30	020317	03:15	700	IS	Yes	03/24 20:30	03/25 20:30	23	203	RH
C37	020412	09:36	6500	S	Yes	04/18 01:00	04/19 10:00	−17	323	RH
C39	020514	19:15	400	IS(?)	Yes	05/19 02:45	05/19 22:45	9	234	RH
C42	020713	12:51	−1100	?	No	07/18 12:00	07/18 21:40	39	29	LH

Table 2 (*Continued*)

No[a]	Active region					ICME				
	Start date[c]	Start time[c]	H_{acc} (10^{40} Mx^2)	AR sig.	Arcade clear?	Start time	End time	Cylinder θ[d]	Cylinder ϕ[e]	Helicity sign
C44	030812	22:23	2400	S	Yes	08/18 10:30	08/19 15:30	−15	312	RH
C45	031027	07:59	−6700	IS	Yes	10/29 11:00	10/30 02:00	−54	229	LH
C46	031027	07:59	−10600	IS(?)	Yes	10/31 02:30	11/01 00:30	49	235	LH
S32[b]	031117	04:51	−450	IS	Yes	11/20 11:00	11/21 00:30	−66	137	RH
C48	040720	23:59	4000	S	No	07/24 17:30	07/25 06:30	−13	41	RH
C49	041103	23:59	−4500	S	Yes	11/10 03:00	11/11 01:00	−33	160	LH
C50	041206	08:00	−290	IS	Yes	12/13 07:00	12/13 21:00	−25	162	LH
C51	050113	12:47	−2100	IS	No	01/16 16:20	01/17 01:20	−2	237	LH
C52	050211	09:39	610	S	No	02/18 17:30	02/19 04:00	22	277	RH
C53	050512	01:35	−240	IS	Yes	05/15 06:00	05/16 04:00	49	159	LH
C54[b]	050514	11:15	10	S(?)	No	05/20 15:10	05/21 06:10	20	231	LH
C55	050525	14:23	−400	S(?)	No	05/29 10:30	05/29 14:45	11	184	LH
C56	050705	01:35	−700	IS	No	07/10 17:00	07/11 00:30	−36	23	LH
C57	050828	06:23	210	S	Yes	09/02 19:20	09/03 04:00	1	173	RH

[a] 'C' denotes that the CME–ICME pair is selected from the CDAW ICME list. 'S' denotes that CME–ICME pair is selected from Sung *et al.* (2009).

[b] Exceptional events whose helicity signs of MC and AR are not consistent.

[c] Start date and time of helicity measurement of the source region.

[d] θ is the latitude angle of the cylinder axis magnetic field.

[e] ϕ is the longitude angle of the cylinder axis magnetic field.

panels show the total magnetic field intensity, X-, Y-, and Z-components of the magnetic field in the GSE coordinates, and solar wind speed, respectively. The vertical dashed lines denote the start and end times of the ICME that give the best fit to the observations. The thick red solid lines are the results of the fitting with the cylinder model, which show excellent agreement with the observations. The determined helicity sign of the ICME is negative, and the latitude (θ) and longitude (ϕ) of the axis of the ICME are 19° and 63°, respectively. The fitting results for the rest of the events are shown in Table 2.

3. Results

3.1. Helicity Sign Comparison

Table 2 summarizes the results on helicity accumulation in the source ARs and the fitting results for the 34 ICMEs. The first four columns give the event number, the start date and time of helicity accumulation measurements, and the accumulated helicity within the AR between the start time of the accumulation and the onset time of the flare. The fifth and sixth columns present the deduced sigmoid shape of the AR using *Yohkoh*/SXT images and the clearness of the post-eruption arcade (PEA) structure after the eruption to identify whether it has S- or Inverse S-shape. Those with a shape and a question mark *e.g.* 'IS(?)' events are where we think the sigmoid shape is an inverse S, but there is some uncertainty, while those with just a question mark do not show any evidence of the presence of a sigmoid.

According to the coronal flux rope (CFR) model (Titov and Démoulin, 1999), a toroidal flux rope is embedded in an active region with a dipolar flux system. The projected magnetic separatrix surface has an S-shape when the flux rope is right-handed (positive helicity), while it has an inverse S-shape when it is left-handed (negative helicity). Employing the CFR model, we find that about 61 % (21/34) of the ICMEs have the same helicity sign as that deduced from the X-ray sigmoid shape, while for 11 % (4/34) of the ICMEs the deduced signs disagree. However, we find that there are many ambiguities (9/34, 26 %) in the determination of the sigmoid shape through inspection directly from soft X-ray images. We thus conclude that the sigmoid analysis needs careful treatment and high resolution loop observations.

The next five columns present the start and end times of ICMEs for the fitting, the θ and ϕ of the cylinder axis in GSE coordinates, and the helicity sign of ICME determined from the cylinder model. The orientation of magnetic cloud axes is described in terms of θ and ϕ, where θ is the angle between the magnetic cloud axis and the ecliptic plane and ϕ is the angle between Xgse and the projection of the magnetic cloud axis on the ecliptic plane, measured positive when anti-clockwise (right-handed chirality). The direction of the ICME axis projected onto the Y–Z plane can be estimated using the equation given by Marubashi *et al.* (2012).

For statistical evaluation of the sign consistency, we have compared the accumulated helicity sign of the solar source region with the relative helicity sign inferred from the structure of the ensuing ICME as shown in Table 3. We find that 30 events (88 %) have the same helicity sign while four events (C21, C26, S32, and C54 in Table 2) have different signs.

3.2. Sign-Inconsistent Events

Based on the helicity conservation principle, we have investigated the four exceptional events in detail with the speculation that their signs may be inconsistent for one of the following reasons:

Table 3 Helicity sign comparison between ICME and solar source active region.

ICME	Solar source AR		Total
	Positive	Negative	
Positive	10	3	13
Negative	1	20	21
Total	11	23	34

i) wrong identification of the solar source region,
ii) the wrong selection of CME–ICME pair, or
iii) localized helicity injection with different helicity sign than the sign of helicity in the entire source active region.

3.2.1. 28 July 2000 ICME (Event C21 in Table 2)

According to the *Solar Geophysical Data* (SGD; ftp://ftp.ngdc.noaa.gov/STP/space-weather/solar-data/solar-features/solar-flares/x-rays/goes/), an M8.0 flare occurred at 02:43 UT on 25 July 2000 in AR9097 near the disk center (N06W08). After the flare, a halo CME appeared in the LASCO C2 field of view at 03:30 UT as seen in Figure 3(b). The CME arrived at the Earth with an IP shock on July 28. The IP shock was detected by the ACE satellite at 05:43 UT on the same day, as denoted by a vertical dashed line in Figure 3(c). We set the start and end times of the ICME to July 28 14:00 UT and July 29 00:30 UT for the boundaries of the flux rope structure, respectively, and determine its helicity sign by using the cylinder model. The deduced helicity sign of the ICME is negative. The estimated axis direction of the ICME projected on the $Y - Z$ GSE plane using the cylinder model for the above boundaries of the ICME is about 80°.

We examine AR9097, which is reported in the CDAW ICME list as the solar source region of the CME. The helicity injections through the entire active region and the polarity inversion line (PIL) region, marked with a white box in Figure 3(a), have positive signs which are not the same as that of the ICME. It is noted that there are several filaments which might be related to the CME as shown in BBSO Hα image (Figure 3(d)). We have considered the filaments as possible candidates for the CME, and we have investigated the Hα images taken before and after the flare. In the case of the filament North of the AR, it disappeared at 01:44 UT, before the flare. There were two filaments in regions F1 and F2 which disappeared after the flare. Due to a data gap in the Hα observations, the exact times of these filament eruptions cannot be identified. We inspect the helicity injection in these regions. As shown in Figure 3(i), the accumulated helicity in the F1 region has a negative sign but there is no significant helicity injection in the region F2, so the filament from the region F1 seems to be the most likely candidate for the source region of the CME.

During the flare time, there was another eruption from AR 9096 located to the South of AR 9097 as marked by the yellow box in Figure 3(a). The filament eruption can be clearly seen in Hα data from Yunnan observatory and in the movie from the SOHO/LASCO CME catalog (http://cdaw.gsfc.nasa.gov/CME_list; Yashiro *et al.*, 2004; Gopalswamy *et al.*, 2009). The eruption started at about 02:46 UT and we can see a clear Post-Eruption Arcade (PEA) structure in the *Yohkoh* SXT image shown in Figure 4(c). For the filament region, R3, we estimate the helicity injection and find a negative helicity sign, the same as that of the ICME.

We find two candidate solar source regions (F1 and F3) for the CME, which have negative helicity accumulation. If we assume that the flux rope of a CME that erupts from an AR

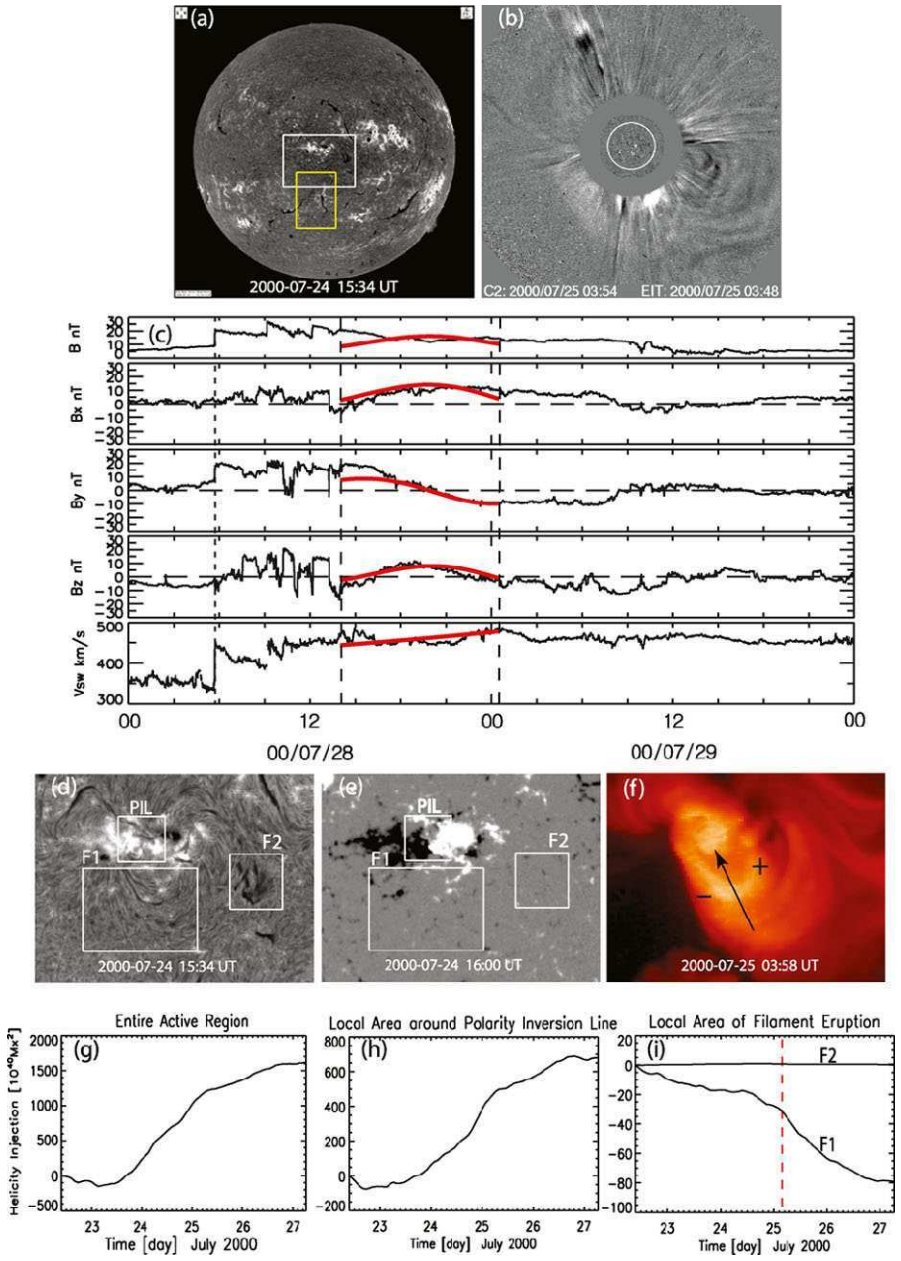

Figure 3 The 25 July 2000 CME, the associated 28 July 2000 ICME and the candidate solar source regions. (a) Full disk BBSO Hα image. The white and yellow boxes denote the locations of AR 9097 and AR 9096, respectively. (b) Shows LASCO C2 observations of the CME that produced the ICME observed *in situ* near Earth, shown in (c). Solid, red lines denote a fitting result of the cylinder model. The vertical dotted and dashed lines represent the time of arrival of the interplanetary shock and the boundaries of the ICMEs, respectively. Submaps focusing on AR 9097 prior to the CME eruption are shown in (d) Hα and (e) a magnetogram from SOHO/MDI. (f) Shows *Yohkoh*/SXT observations of the same region post-eruption. Estimates of helicity injection in the regions of interest are shown for (g) the entire active region, (h) the polarity inversion line (PIL) and (i) the regions labeled 'F1' and 'F2'. The red, vertical line indicates when the flare occurred.

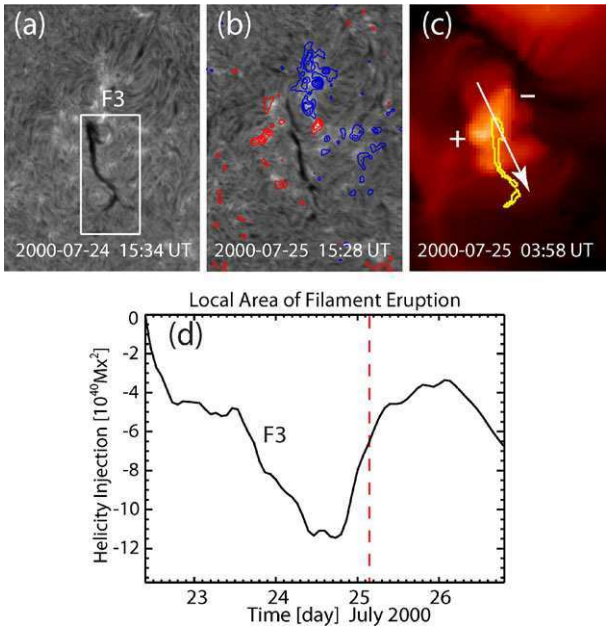

Figure 4 BBSO Hα submap images of AR 9096 (a) before and (b) after the CME. (c) Shows a *Yohkoh* SXT submap image after the CME and (d) shows the helicity injection in the filament region of AR 9096. The filament region (F3) is denoted by a white box in the local Hα image. The red and blue contours on the BBSO Hα image after the CME denote positive and negative magnetic fields observed by SOHO/MDI, respectively. The red vertical line indicates when the flare occurred.

maintains its axis orientation (Yurchyshyn *et al.*, 2001) as it propagates from the Sun to the Earth and the flux rope is assumed to be observed at (or near) the apex of the ICME loop, the orientation of the ICME axis projected onto the $Y-Z$ plane may be aligned with the direction of the flux rope structure near the Sun, which can be estimated from the orientation of the PEA associated with the eruption. Based on this assumption, we adopt the alignment of the flux rope axes as a second constraint to select the solar source region of ICME, and measure the orientation angles of the axes of PEAs. Figure 3(f) and Figure 4(c) show the PEAs in the regions F1 and F3. By considering the helicity sign and magnetic polarities from MDI data, we can determine the axial direction of each of the PEAs by measuring the angle from the East on the Sun in a clockwise (left-handed chirality) direction. For the F1 region in AR 9097, the estimated PEA axis angle is about 65° as marked by an arrow in Figure 3(f) and that of the PEA in AR 9096 is about 270°. Since the axis angle of the PEA in AR 9097 is roughly similar to that (80°) of the ICME estimated using the cylinder model and their helicity signs are same, we conclude that the region F1 in AR9097 is the most probable source region of the 28 July 2000 ICME. Prior to this study, an incorrect association had been made between the ICME and its source region, which originally led to the incorrect conclusion that the helicity sign was not conserved between the solar source region of the CME and the associated ICME.

3.2.2. 13 October 2000 ICME (Event C26 in Table 2)

According to the CDAW ICME list, the ICME of 13 October 18:24 UT to 14 October 16:54 UT was associated with the halo CME that appeared at 00:26 UT on 10 October 2000 in the LASCO C2 FOV as shown in Figure 5(b). The linear speed of the CME in the plane of sky from SOHO/LASCO observations is 527 km s^{-1}. This CME is related to the C6.7 flare from AR 9182 (the box in Figure 5(a)) at 23:19 UT located near the disk center (N01W41). The cylinder fitting result for the ICME during the period between 13 October 16:30 UT

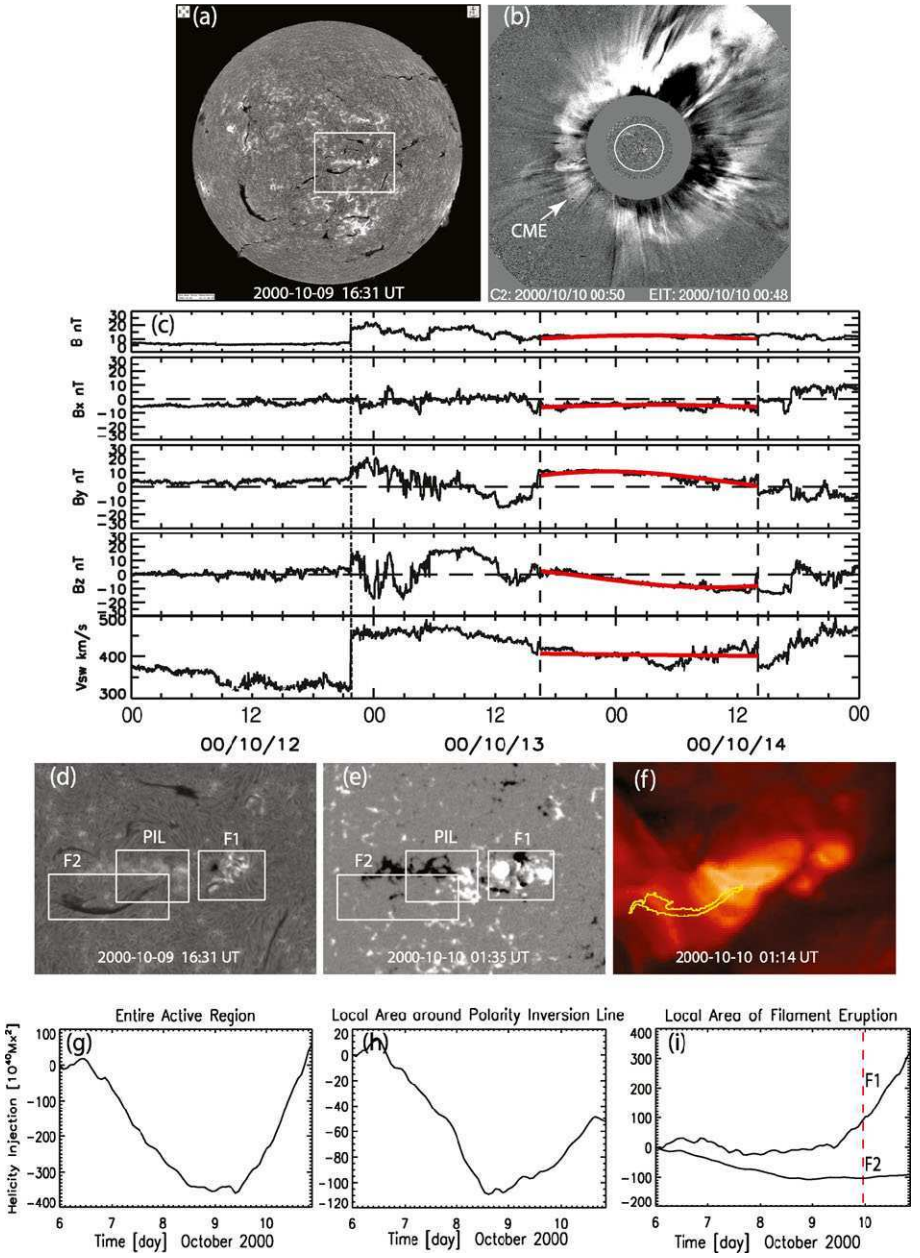

Figure 5 The 9 October 2000 CME, the associated 13 – 14 October 2000 ICME and the candidate solar source regions. (a) Full disk BBSO Hα image. The white box denotes the location of AR 9182. (b) Shows LASCO C2 observations of the halo CME that produced the ICME observed *in situ* near Earth, shown in (c). Solid red lines denote a fitting result of the cylinder model. The vertical dotted and dashed lines represent the arrival time of the interplanetary shock and the boundaries of the ICME. Submaps focusing on AR 9182 prior to the CME eruption are shown in (d) Hα and (e) a magnetogram from SOHO/MDI. (f) Shows *Yohkoh*/SXT observations of the same region post-eruption. Estimates of helicity injection in the regions of interest are shown for (g) the entire active region, (h) the polarity inversion line (PIL), and (i) the regions labeled 'F1', and 'F2'. The red vertical line indicates when the flare occurred.

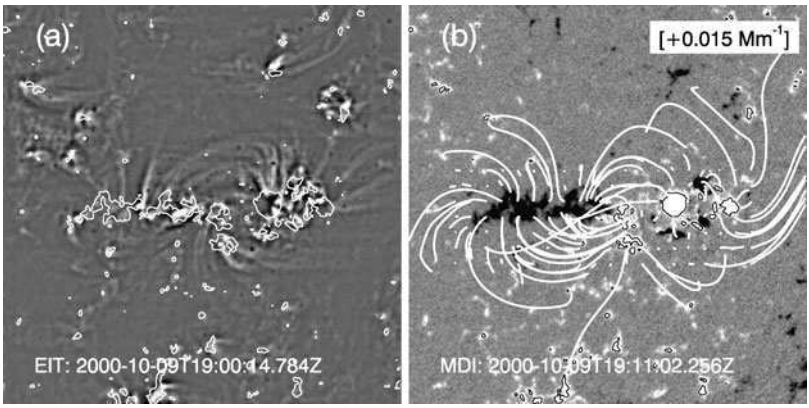

Figure 6 Determination of the coronal magnetic helicity sign of AR9182, and its comparison with observed coronal loops. (a) SOHO/EIT image in gray scale with the magnetic field strength contours at ± 200 G overlaid. (b) SOHO/MDI magnetogram in gray scale and the computed magnetic field lines projected onto the surface. The obtained best-fit α is $+0.015$ Mm^{-1}.

and 14 October 14:00 UT reveals that the ICME has a positive helicity sign, but the signs of injected helicity through the entire active region (AR 9182) and PIL are both negative (Figure 5(g) and (h)).

To identify the solar source region of the ICME, we have determined helicity signs for the local regions F1 and F2. As shown in Figure 5(i), it is found that the region F1 has positive, while the region F2 has negative injected helicity. There was a previous CME that was associated with the region F1. The CME appeared at 23:50 UT on 9 October in the LASCO C2 FOV with narrow angular width ($\sim 40°$). The linear speed of the CME was about 800 km s^{-1}. The CME from F1 could be a possible candidate for being the source region of the ICME. However, this does not look plausible, since it is difficult to explain how a narrow limb CME with small direction parameter can be detected near Earth as an ICME.

In addition to the helicity injection through the photosphere, we also have measured the sign of the helicity content in the corona using the linear force-free field (LFFF) model. The reliability of the LFFF model to measure the coronal magnetic helicity was demonstrated by previous studies (Démoulin *et al.*, 2002; Lim, Jeong, and Chae, 2007). The coronal magnetic field is extrapolated from the SOHO/MDI line-of-sight magnetogram using the Fourier transform method suggested by Alissandrakis (1981) by changing the value of the force-free α. Then the computed coronal model is compared with the observed coronal loops to determine the best-fit α. The best-fit α has the same sign as that of the coronal magnetic helicity.

Figure 6 shows the LFFF model with the obtained best-fit α (Figure 6(b)) compared with the observed coronal loops in the SOHO/EIT 171 Å image (Figure 6(a)). Since our concern is the sign of the coronal magnetic helicity, we have compared the overall topology of the coronal loops and the LFFF model. As a result, we obtain a positive value for the force-free α indicating that the AR9181 has positive magnetic helicity in the corona. The sign of the coronal magnetic helicity is the same as that of the helicity of the ICME. Projection effects have not been considered since the active region was near the disk center. Moreover, the barb structures of the filament shown in the Hα image (F2 in Fig. 5(d)) indicate that the chirality of the filament is sinistral, in other words, it has positive helicity. Therefore, the sign of the computed coronal helicity is also consistent with that of the filament chirality

(Lim and Chae, 2009). The same filament was also visible on 5 October, and showed a sinistral structure. Therefore, it is likely that the sign of the coronal magnetic helicity was already positive at least from 5 October.

It has been reported that the local helicity sign can be opposite to that of the whole active region helicity (Hao and Zhang, 2011), and the injection of helicity with the opposite sign to that of the pre-existing helicity plays an important role in eruptive events such as flares and CMEs (Park *et al.*, 2012; Jing *et al.*, 2012). We speculate that overall the coronal field in AR9181 had pre-existing positive helicity and the local injection of negative helicity in the F1 region played a role through magnetic reconnection in the ejection of the pre-existing positive coronal helicity via the CME and ensuing ICME. We conclude that the helicity sign of the ICME is not consistent with the sign of injected helicity during the analyzed period, but it is consistent with that of the coronal helicity in the whole active region (AR9182).

3.2.3. 20 November 2003 ICME (Event S32 in Table 2)

The ICME of 20 November 11:00 UT to 21 November 01:00 UT was caused by a halo CME (1660 $\mathrm{km\,s^{-1}}$) that appeared at 08:50 UT on 18 November 2003 in the LASCO C2 FOV as seen in Figure 7(b). This CME is related to an M3.9 flare in AR 10501 (the box in Figure 7(a)) at 08:30 UT near the disk center (N03E08) and is known to be the most probable solar source of the ICME (Gopalswamy *et al.*, 2005). The cylinder fitting result for the ICME reveals that the ICME has a positive helicity sign, but the signs of injected helicity in the entire active region and along the PIL are negative as shown in Figure 7(g) and (h). The projected axis orientation angles of the ICMEs using the cylinder model is about 290°.

There was an erupting filament with a curved shape in region F1 as marked in Figure 7(d). The SOHO/EIT image after the eruption shows a PEA structure in the region as seen in Figure 7(f). The yellow contour in Figure 7(f) depicts the filament just before the flare. The EIT movie in the CDAW CME catalog also shows that the filament was gradually rising from 18 November 04:36 UT to 08:00 UT, and finally it erupted before 09:20 UT on 18 November. We speculate that this filament is the source of the CME because there is no other filament present at 09:20 UT in the Catania Hα image. We estimate the injected helicity signs in the entire AR region and each local region such as the PIL region and the region F1 where the filament was located as shown in Figure 7(d). As a result, we find that the sign of injected helicity in the region F1 is positive, as shown in Figure 7(i), which is the same sign as that of the MC.

In fact, this event was reported by Chandra *et al.* (2010), who studied the solar source of the ICME, and by Gopalswamy *et al.* (2005), who studied the relationship between the CME and ICME. Chandra *et al.* (2010) examined the spatial distribution of magnetic helicity injection, and concluded that the positive helicity in the eastern part (F1a in Figure 8) of the filament was consistent with the ICME. However, Gopalswamy *et al.* (2005) reported that the eastern leg had erupted before the halo CME. They proposed that the entire filament erupted during the halo CME and the North-South segment (F1b in Figure 8) was the largest and may be responsible for the halo CME. In addition, they pointed out that the axis angle of the segment is consistent with the ICME axis orientation from the cylinder model.

Since the helicity sign in the corona where the helicity of both the filament and the CME originated from has not been fully explained in the work of Chandra *et al.* (2010), we have investigated this active region in detail. Similar to Section 3.2.2, we also apply the LFFF model to check the sign of the coronal helicity before the halo CME occurred. The overall coronal loops in the TRACE image agree with either the negative or near zero force-free α, as in Chandra *et al.* (2010), except for the local dark loops indicated by an arrow in

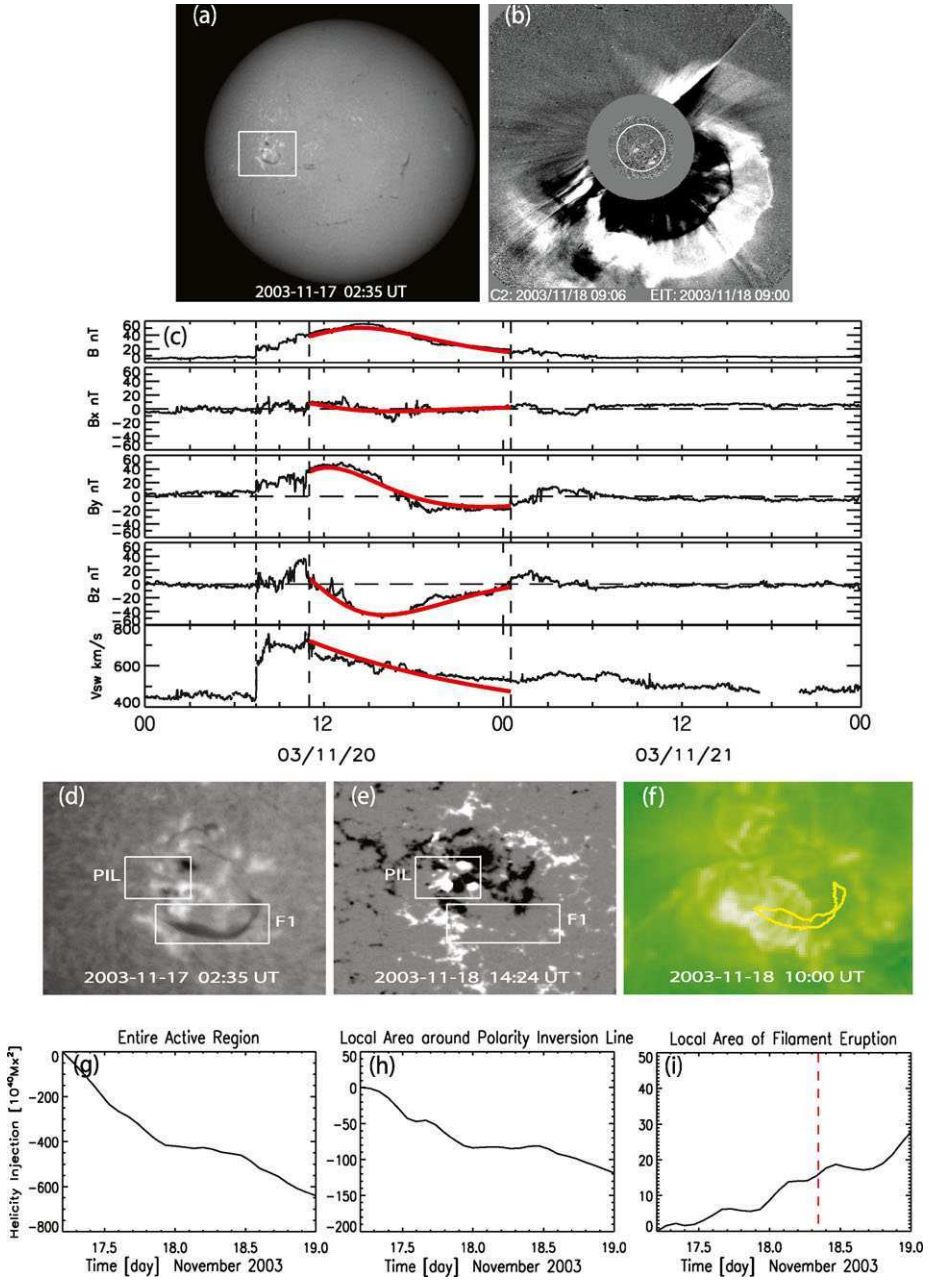

Figure 7 The 18 November 2003 CMEs, the associated 20 November 2003 ICME, and the candidate solar source regions. The white box in the full disk Hα image (a) of Yunnan observatory denotes AR 10501. The CME in a LASCO C2 image (b) produced the ICME (c). Red thick lines in the panel (c) denote fitting results of the cylinder model and the vertical dotted and dashed lines represent the IP shock arrival time and the boundary of the ICME. Submap Hα images before (d) the CME are presented with a magnetic map of the same region from SOHO/MDI (e) and a SOHO/EIT image (f). Helicity injections are estimated for the entire AR 10501 (g), 'PIL' (h), and 'F1' regions (i), respectively. The red dashed vertical line indicates when the flare occurred.

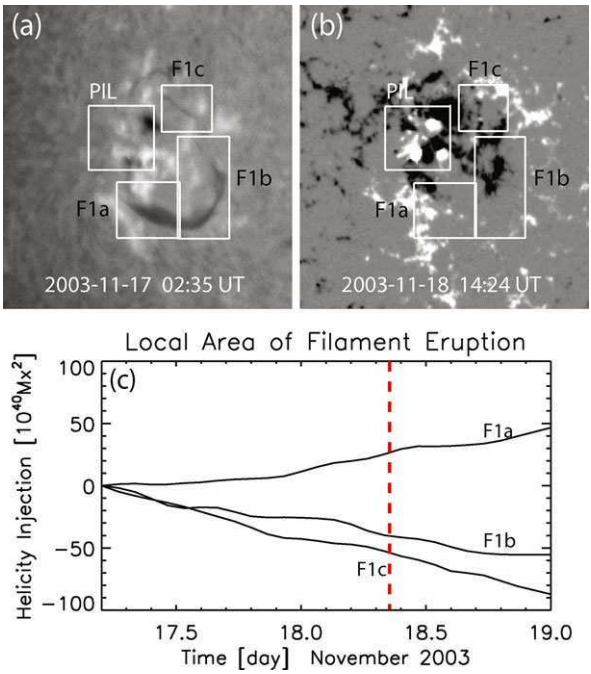

Figure 8 Yunnan Hα submap image (a) and SOHO/MDI magnetogram (b) of AR 10501 before the CME. The helicity injections (c) are estimated for each segment of the filament. The red dashed vertical line indicates when the flare occurred.

Figure 9(a). Those dark loops seen in the TRACE image are the same filament shown in Figure 7(d) and Figure 8(a). We can reconstruct those dark loops in the lower region with positive force-free α (red field lines in Figure 9(b)), and the loops in the upper region with negative α (blue field lines on the right-hand side of the red lines). We have also overlaid the contour of the filament segment that erupted during the halo CME (black contour in Figure 9(b)). We find that the erupted filament has positive helicity in the corona. Our result supports the idea that the positive helicity sign of the ICME of interest originates from the locally positive coronal helicity, and this region becomes unstable and erupts facilitated by the opposite sign of helicity in this region to that of the surroundings (Park *et al.*, 2012; Jing *et al.*, 2012).

3.2.4. 20 May 2005 ICME (Event C54 in Table 2)

The 20 May 2005 ICME had been reported by the CDAW to be caused by the 17 May 2005 CME that appeared at 03:26 UT in the LASCO C2 FOV. The CME is a partial halo CME and has a slow speed of 450 km s^{-1}. The deduced helicity sign of the ICME using the cylinder model is negative, and the fitting result shows good agreement with the observations, as shown in Figure 10(c).

In the solar source region of the CME (AR 10763), three flares occurred on 17 May. The first, second, and third flares started at 02:31 UT, 03:58 UT, and 05:47 UT in the western, middle, and eastern parts of the AR, respectively. There were two small filaments in the active region marked as F1 and F2 in Figure 10(d). The signs of injected helicity over the entire active region and the region of PIL are both positive as shown in Figure 10(g) and (h). The filament in the region F1 has negative helicity sign while the filament in the region F2 has positive sign (Figure 10(i)). Considering its time of appearance (03:26 UT), the CME is probably related to the first flare that occurred in the West of the AR at 02:31 UT on 17 May

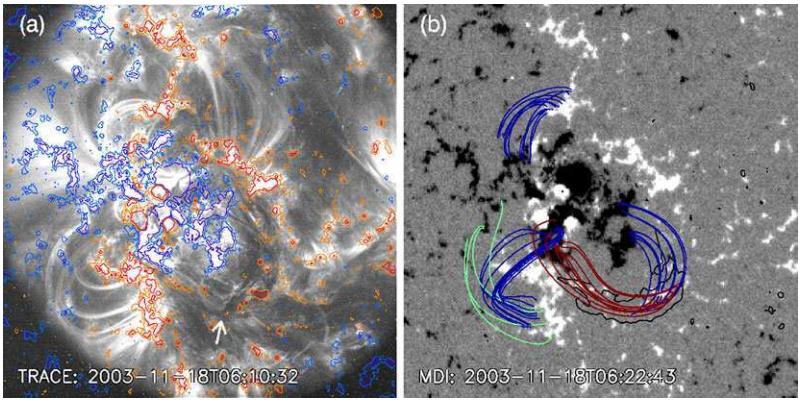

Figure 9 Determination of the coronal magnetic helicity sign in AR10501, through magnetic extrapolation and its comparison with observed coronal loops. (a) TRACE 171 Å image and line-of-sight magnetic field contours from SOHO/MDI overlaid corresponding to (−200, −50, 50, 200 G) levels. (b) SOHO/MDI magnetogram and selected magnetic field lines computed from the linear force-free field extrapolation with different α values (green: 0, blue: negative, red: positive). Black contour represents the filament that disappeared after the CME (flare) obtained from Hα images taken by Kanzelhöhe Solar Observatory at 07:39:51 and 12:16:08 UT on 18 November 2003.

2005. The filament F1 seems to be a possible source of the ICME since it has the same helicity sign as that of the ICME, if the CME–ICME pair is correctly selected. However, we note that the filament in the F1 region can still be seen at 07:07 UT on 17 May in the Hα movies from the *Hida Domeless Solar Telescope* (http://fw.hida.kyoto-u.ac.jp), and no clear PEA structure can be seen in the EIT image, as shown in Figure 10(f). It is also noted that no PEA signature is found in SXI images. For these reasons, we conclude that the region F1 is not the source region of the ICME.

Meanwhile, another candidate solar source of the ICME was proposed by Zhang *et al.* (2007), who suggested that the 20 May 2005 MC may be due to a partial halo CME that appeared at 13:50 UT on 16 May 2005 in the LASCO C2 FOV as seen in Figure 11(b). The solar source region of the CME, AR 10759, located at N13W29 is denoted by a white box in Figure 11(a). We note that the CME was related to the eruptive filament located in region F1 of Figure 11(c). The eruption of the filament occurred at 12:12 UT on 16 May, and the eruption can be clearly seen in the Hα movie by the *Solar Telescope of Argentina* (HASTA, http://www.oafa.fcefn.unsj-cuim.edu.ar). We inspect helicity injections over the entire region, PIL region, and F1 filament region of AR 10759, and find that they all have negative signs (Figure 11(f) – (h)), which is the same as the sign of the ICME.

It is noted that deduced axis direction ($\sim 155°$) of the ICME by applying the cylinder fitting model is not consistent with the orientation angle (60°) of the PEA axis, as shown in Figure 11(e). One possible explanation for this disagreement is that the axis of the PEA rotates during propagation from the Sun to the Earth as reported by Cohen *et al.* (2010) and Vourlidas *et al.* (2011).

It is noteworthy that the researchers who participated in CDAW had selected the 17 May CME, not strong but faintly erupted, as the likely candidate of the ICME, because its source region was located close to disk center, while the source location of 16 May CME was far from the disk center. Recently, the 16 May CME was accepted as an alternative candidate for the ICME by CDAW, after the discovery that the eruptive filament near the disk center is related to the arcade formation in AR 10759. Based on our study, we conclude that the solar

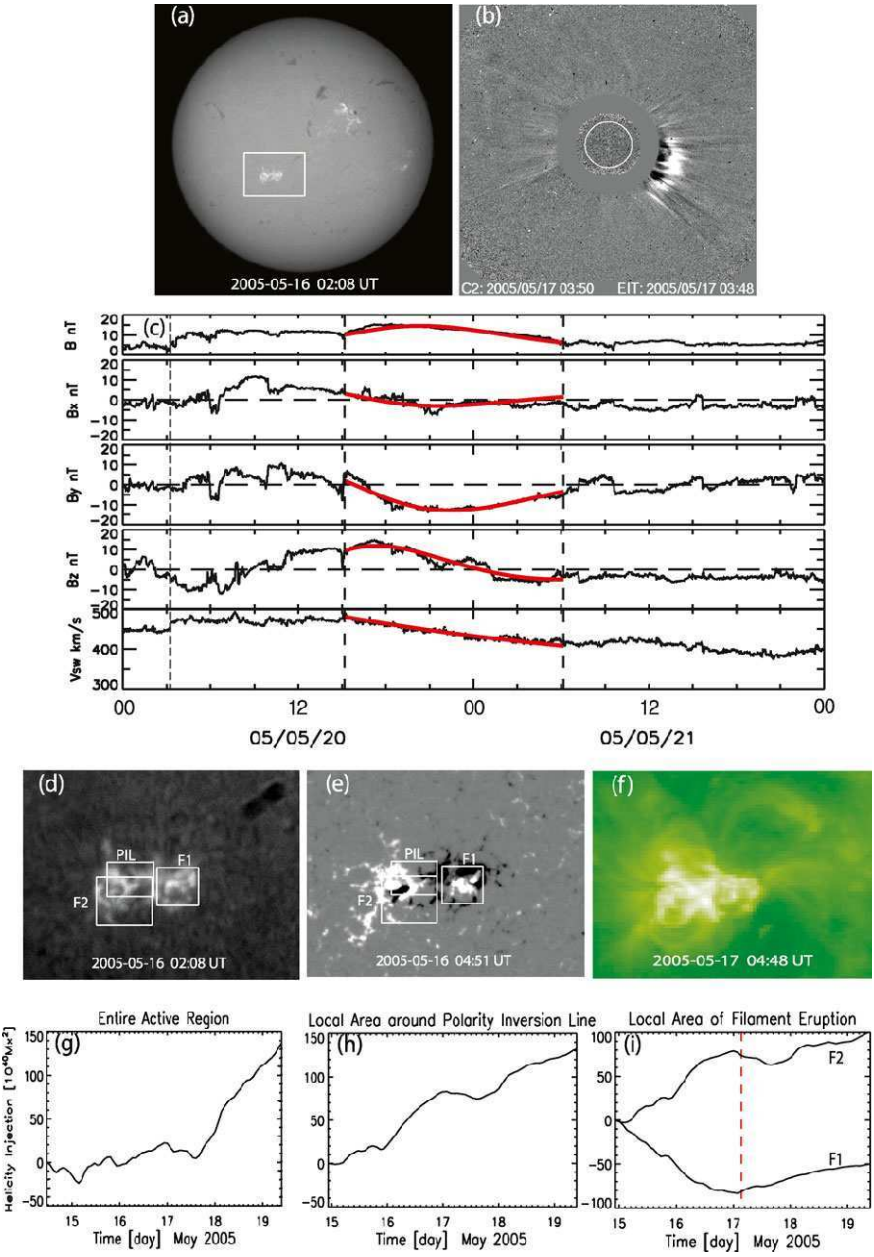

Figure 10 The 17 May 2005 CME, the possibly associated 20 May 2005 ICME, and their candidate solar source regions. (a) Full disk Yunnan Hα image. The white box denotes the location of AR 10763. (b) LASCO C2 observations of the CME that could produce the ICME observed *in situ* near Earth, shown in (c). Solid red lines denote a fitting result by the cylinder model. The vertical dotted and dashed lines represent the interplanetary shock arrival time and the boundaries of the ICME, respectively. Submaps focusing on AR 9097 prior to the CME eruption are shown in (d) Hα and (e) a magnetogram from SOHO/MDI. (f) Shows SOHO/EIT observations of the same region post-eruption. Estimates of helicity injection in the regions of interest are shown for (g) the entire active region, (h) the polarity inversion line (PIL) and (i) the regions labeled 'F1' and 'F2'. The red dashed vertical line indicates when the flare occurred.

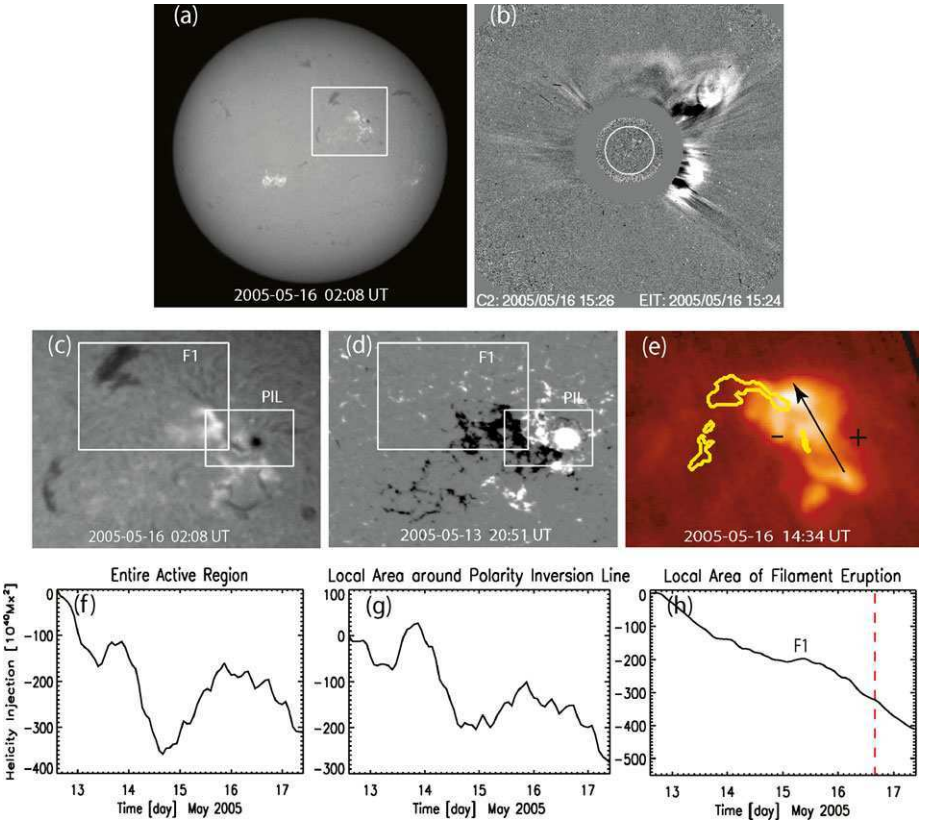

Figure 11 The 16 May 2005 CME and its potential solar source regions. (a) Full disk Yunnan Hα image. The white box denote the location of AR 10759. (b) LASCO C2 observations of the CME that produced the 20 May 2005 ICME. Submaps focusing on AR 10759 prior to the CME eruption are shown in (c) Hα and (d) a magnetogram from SOHO/MDI. (e) Shows GOES/SXI observations of the same region post-eruption. Estimates of helicity injection in the regions of interest are shown for (f) the entire active region, (g) the polarity inversion line (PIL) and (i) the region labeled 'F1'. The red dashed vertical line indicates when the flare occurred.

source of the 20 May 2005 ICME is more likely to be 16 May 2005 CME, rather than the 17 May 2005 CME.

4. Summary and Conclusions

We determined the accumulated amount of helicity injection in the source active regions of CMEs using SOHO/MDI magnetograms, and the helicity sign of the associated ICMEs by fitting the cylinder model developed by Marubashi (2000), assuming a self-similar expansion of the flux rope, to the solar wind data. We confirmed that the helicity signs of ICMEs are generally consistent with that of their solar source regions, in 88 % of the cases. We also compared helicity signs deduced from the X-ray sigmoid shapes with the helicity signs of the ICMEs, and found that about 61 % of the ICMEs have the same helicity signs, while 12 % of the ICMEs have helicity signs that are not in agreement with that of the sigmoid.

However, it was noted that there are many cases (26 %) when the sigmoid's shape is ambiguous in the soft X-ray images. These results indicate that most CMEs contain flux ropes which maintain their helicity signs in the interplanetary space.

By studying four events where the helicity signs differ between the active regions and the ICMEs, we found that the sign inconsistency in two events may be due to one of the following reasons: either incorrect identification of the CME source region (20 May 2005 ICME), or a localised region having a different helicity sign than that of the entire source active region (28 July 2000). The other two events (the 13 – 14 October 2000 ICME and the 20 November 2003 ICME) do not show clear consistency of the sign between the helicity injection through the photosphere and the helicity of the ICMEs. However, we found in both cases that the ICMEs have the same helicity signs as that of the pre-existing coronal magnetic fields in their solar source regions, which were determined by using the LFFF model. These results suggest that the origin of the ICME helicity can be found from the pre-existing magnetic helicity already accumulated in the corona, and the injection of helicity of the opposite sign through the photosphere may result in magnetic reconnection and lead to filament eruptions.

We note that the sigmoid shapes of the source regions of 28 July 2000 and 13 – 14 October 2000 events do indicate a sign of helicity in agreement with the ICME. The sigmoid shape can represent the coronal helicity, opposite to the sign of the photospheric helicity injection. This might illustrate the importance of not relying on a single signature of source region helicity sign when comparing the signs of helicity of CMEs and their associated ICMEs.

In summary, we have found that all ICMEs in this study have the same helicity signs as their solar source regions. Our result reveals that all the CMEs studied in this article have flux rope structure and their helicity signs are conserved while the CMEs propagate from the Sun to the Earth.

Acknowledgements We are grateful to the referee for helpful and constructive comments. SOHO is a project of international cooperation between ESA and NASA. We thank the ACE Science center for the ACE data and to the *Yohkoh* SXT team and GOES SXI team for the solar X-ray images. This work benefited from the NASA/LWS Coordinated Data Analysis Workshops on CME flux ropes in 2010 and 2011. We acknowledge the workshop support provided by NASA/LWS, Predictive Science, Inc. (San Diego, CA), University of Alcala (Alcala de Henares, Spain), and Ministerio de Ciencia e Innovacion (Reference number AYA2010-1239-E), Spain. E.-K.L. is supported by AFOSR (FA 9550-12-1-0066). K.-S.C. was supported by the "Development of Korean Space Weather Center" of KASI and the KASI basic research funds.

References

Alissandrakis, C.E.: 1981, *Astron. Astrophys.* **100**, 197.
Ali, S.S., Uddin, W., Chandra, R., Mary, D.L., Vršnak, B.: 2007, *Solar Phys.* **240**, 89.
Berger, M.A.: 1984, *J. Geophys. Res.* **240**, 89.
Berger, M.A., Field, G.B.: 1984, *J. Fluid Mech.* **147**, 133.
Brueckner, G.E., Howard, R.A., Koomen, M.J., Korendyke, C.M., Michels, D.J., Moses, J.D., Socker, D.G., *et al.*: 1995, *Solar Phys.* **162**, 357.
Burlaga, L., Sittler, E., Mariani, F., Schwenn, R.: 1981, *J. Geophys. Res.* **86**, 6673.
Chae, J.: 2007, *Adv. Space Res.* **39**, 1700.
Chae, J., Sakurai, T.: 2008, *Astrophys. J.* **689**, 593.
Chandra, R., Pariat, E., Schmieder, B., Mandrini, C.J., Uddine, W.: 2010, *Solar Phys.* **261**, 127.
Chen, J.: 1996, *J. Geophys. Res.* **101**, 27499.
Chen, J., Howard, R.A., Brueckner, G.E., Santoro, R., Krall, J., Paswaters, S.E., *et al.*: 1997, *Astrophys. J.* **490**, L191.
Cohen, O., Attrill, G.D.R., Schwadron, N.A., Crooker, N.U., Owens, M.J., Downs, C., Gombosi, T.I.: 2010, *J. Geophys. Res.* **115**, A10104.

Démoulin, P.: 2008, *Ann. Geophys.* **26**, 3113.
Démoulin, P., Mandrini, C.H., van Driel-Gesztelyi, L., Thompson, B.J., Plunkett, S., Kovári, Zs., Aulanier, G., Young, A.: 2002, *Astron. Astrophys.* **382**, 650.
Gosling, J.T., Bame, S.J., McComas, D.J., Phillips, J.L.: 1990, *Geophys. Res. Lett.* **17**, 901.
Gopalswamy, N., Yashiro, S., Michalek, G., Xie, H., Lepping, R.P., Howard, R.A.: 2005, *Geophys. Res. Lett.* **32**, 12.
Gopalswamy, N.: 2006, *Space Sci. Rev.* **124**, 145.
Gopalswamy, N., Yashiro, S., Michalek, G., Stenborg, G., Vourlidas, A., Freeland, S., Howard, R.: 2009, *Earth Moon Planets* **104**, 295.
Gopalswamy, N., Xie, H., Mäkelä, P., Akiyama, S., Yashiro, S., Kaiser, M.K., Howard, R.A., Bougeret, J.-L.: 2010, *Astrophys. J.* **710**, 1111.
Hao, J., Zhang, M.: 2011, *Astrophys. J. Lett.* **733**, L27.
Hu, Q., Dasgupta, B.: 2005, *Geophys. Res. Lett.* **32**, L12109.
Jacobs, C., Roussev, I.I., Lugaz, N., Poedts, S.: 2009, *Astrophys. J. Lett.* **695**, L171.
Jing, J., Park, S.-H., Liu, C., Lee, J., Wiegelmann, T., Xu, Y., Deng, N., Wang, H.: 2012, *Astrophys. J. Lett.* **752**, L9.
Kim, R.-S., Gopalswamy, N., Cho, K.-S., Moon, Y.-J., Yashiro, S.: 2013, *Solar Phys.* doi:10.1007/s11207-013-0230-y
Leamon, R.J., Canfield, R.C., Jones, S.L., Lamdberg, B.J., Pevtsov, A.A.: 2004, *J. Geophys. Res.* **109**, 5106.
Lim, E.-K., Chae, J.: 2009, *Astrophys. J.* **692**, 104.
Lim, E.-K., Jeong, K., Chae, J.: 2007, *Astrophys. J.* **656**, 1167.
Manoharan, P.K., Gopalswamy, N., Yashiro, S., Lara, A., Michalek, G., Howard, R.A.: 2004, *J. Geophys. Res.* **109**, A06109.
Marubashi, K.: 2000, *Adv. Space Res.* **26**, 55.
Marubashi, K., Lepping, R.P.: 2007, *Ann. Geophys.* **25**, 2453.
Marubashi, K., Cho, K.-S., Kim, Y.-H., Park, Y.-D., Park, S.-H.: 2012, *J. Geophys. Res.* **117**, A01101.
Pariat, E., Démoulin, P., Berger, M.A.: 2005, *Astron. Astrophys.* **439**, 1191.
Park, S.-H., Cho, K.-S., Bong, S.-C., Kumar, P., Chae, J., Liu, R., Wang, H.: 2012, *Astrophys. J.* **750**, 48.
Qiu, J., Hu, Q., Howard, T.A., Yurchyshyn, V.B.: 2007, *Astrophys. J.* **659**, 758.
Scherrer, P.H., Bogart, R.S., Bush, R.I., Hoeksema, J.T., Kosovichev, A.G., Schou, J., Rosenberg, W., *et al.*: 1995, *Solar Phys.* **162**, 129.
Schuck, P.W.: 2006, *Astrophys. J.* **646**, 1358.
Smith, C.W., L'Heureux, J., Ness, N.F., Acuña, M.H., Burlaga, L.F., Scheifele, J.: 1998, *Space Sci. Rev.* **86**, 613.
Sung, S.-K., Marubashi, K., Cho, K.-S., Kim, Y.-H., Kim, K.-H., Chae, J., Moon, Y.-J., Kim, I.-H.: 2009, *Astrophys. J.* **699**, 298.
Titov, V.S., Démoulin, P.: 1999, *Astron. Astrophys.* **351**, 707.
Tsuneta, S., Acton, L., Bruner, M., Lemen, J., Brown, W., Caravalho, R., Catura, R.: 1991, *Solar Phys.* **136**, 37.
Vourlidas, A., Colaninno, R., Nieves-Chinchilla, T., Stenborg, G.: 2011, *Astrophys. J. Lett.* **733**, L23.
Yashiro, S., Gopalswamy, N., Michalek, G., St. Cyr, O.C., Plunkett, S.P., Rich, N.B., Howard, R.A.: 2004, *J. Geophys. Res.* **109**, A07105.
Yurchyshyn, V.B., Wang, H., Goode, P.R., Deng, Y.: 2001, *Astrophys. J.* **563**, 381.
Zhang, J., Richardson, I.G., Webb, D.F., Gopalswamy, N., Huttunen, E., Kasper, J., Nitta, N.V.: 2007, *J. Geophys. Res.* **112**, A12103.

Solar Phys (2012) 281:137–166
DOI 10.1007/s11207-012-9990-z

A Parametric Study of Erupting Flux Rope Rotation

Modeling the "Cartwheel CME" on 9 April 2008

B. Kliem · T. Török · W.T. Thompson

Received: 10 November 2011 / Accepted: 27 March 2012 / Published online: 24 April 2012

Abstract The rotation of erupting filaments in the solar corona is addressed through a parametric simulation study of unstable, rotating flux ropes in bipolar force-free initial equilibrium. The Lorentz force due to the external shear-field component and the relaxation of tension in the twisted field are the major contributors to the rotation in this model, while reconnection with the ambient field is of minor importance, due to the field's simple structure. In the low-beta corona, the rotation is not guided by the changing orientation of the vertical field component's polarity inversion line with height. The model yields strong initial rotations which saturate in the corona and differ qualitatively from the profile of rotation *vs.* height obtained in a recent simulation of an eruption without preexisting flux rope. Both major mechanisms writhe the flux rope axis, converting part of the initial twist helicity, and

The Sun 360
Guest Editors: Bernhard Fleck, Bernd Heber, Angelos Vourlidas

B. Kliem (✉)
Insitut für Physik und Astronomie, Universität Potsdam, Karl-Liebknecht-Str. 24-25, Potsdam 14476, Germany
e-mail: bkliem@uni-potsdam.de

B. Kliem
Mullard Space Science Laboratory, University College London, Holmbury St. Mary, Dorking, Surrey RH5 6NT, UK

B. Kliem
College of Science, George Mason University, 4400 University Drive, Fairfax, VA 22030, USA

T. Török
LESIA, Observatoire de Paris, CNRS, UPMC, Université Paris Diderot, 5 place Jules Janssen, 92195 Meudon, France

Present address:
T. Török
Predictive Science, Inc., 9990 Mesa Rim Road, Ste. 170, San Diego, CA 92121, USA

W.T. Thompson
Adnet Systems Inc., NASA Goddard Space Flight Center, Code 671, Greenbelt, MD 20771, USA

produce rotation profiles which, to a large part, are very similar within a range of shear-twist combinations. A difference lies in the tendency of twist-driven rotation to saturate at lower heights than shear-driven rotation. For parameters characteristic of the source regions of erupting filaments and coronal mass ejections, the shear field is found to be the dominant origin of rotations in the corona and to be required if the rotation reaches angles of order 90 degrees and higher; it dominates even if the twist exceeds the threshold of the helical kink instability. The contributions by shear and twist to the total rotation can be disentangled in the analysis of observations if the rotation and rise profiles are simultaneously compared with model calculations. The resulting twist estimate allows one to judge whether the helical kink instability occurred. This is demonstrated for the erupting prominence in the "Cartwheel CME" on 9 April 2008, which has shown a rotation of $\approx 115^\circ$ up to a height of 1.5 $R_\odot$ above the photosphere. Out of a range of initial equilibria which include strongly kink-unstable (twist $\Phi = 5\pi$), weakly kink-unstable ($\Phi = 3.5\pi$), and kink-stable ($\Phi = 2.5\pi$) configurations, only the evolution of the weakly kink-unstable flux rope matches the observations in their entirety.

Keywords Corona, active · Prominences, dynamics · Coronal mass ejections, initiation and propagation · Magnetic fields, corona · Magnetohydrodynamics

1. Introduction

The geoeffectiveness of solar coronal mass ejections (CMEs) depends primarily on two parameters, the velocity and the magnetic orientation of the CME at the impact on the Earth's magnetosphere. The higher the CME velocity and the closer its front side magnetic field to a southward orientation, the more intense the interaction will typically be. Therefore, understanding the physics that determines these CME parameters at 1 AU is one of the key issues in space weather research. This involves the formation and main acceleration of the CME in the solar corona, as well as its propagation through the interplanetary space. The particulars of the trigger process also play a role in some events. It appears that typically the corona is the place where the basic decisions are made: will the CME be fast or slow, and will it keep the orientation given by the source, *i.e.*, will its magnetic axis remain oriented nearly parallel to the photospheric polarity inversion line (PIL), or will it rotate substantially?

In the present paper we employ the technique of MHD simulation to carry out a first systematic, but in view of the problem's complexity necessarily incomplete investigation of a number of processes that cause and influence changes of CME orientation in the corona. Such changes can be described as a rotation of the CME volume, more specifically of the magnetic axis of the flux rope in the CME, about the direction of ascent. This *rotation* should be distinguished from the possible rotation of the flux rope about its own axis, referred to as the *roll effect* (Martin, 2003; Panasenco *et al.*, 2011), which we do not address here.

Understanding the rotation of erupting flux ropes in the corona is also relevant for the question which processes trigger the eruptions, as a substantial rotation may indicate the occurrence of the helical kink instability (KI); see, *e.g.*, Rust and Kumar (1996), Romano, Contarino, and Zuccarello (2003), and Rust and LaBonte (2005). This instability is one of the candidate mechanisms for the initiation of CMEs (Sakurai, 1976; Fan and Gibson, 2003; Kliem, Titov, and Török, 2004). It commences when the twist of the rope exceeds a critical value, $\Phi = 2\pi N > \Phi_{\rm cr}$, where N is the winding number of the field lines about the rope's magnetic axis. The dynamical evolution of the instability has shown very good quantitative agreement with a number of well observed events, which range from confined

filament eruptions to the fastest CME on record (Török and Kliem, 2005; Williams *et al.*, 2005). However, Isenberg and Forbes (2007) have pointed out an alternative mechanism for the rotation of line-tied flux ropes, which relies on the presence of an external toroidal field component, $B_{\rm et}$, due to sources external to the current in the flux rope and pointing along the rope, *i.e.*, an external shear-field component. The mechanism can easily be understood in the simplified picture of a current loop in vacuum field. When the loop legs move out of their equilibrium position to a more vertical orientation, the cross product of the loop current with the shear-field component yields a sideways Lorentz force on the legs, which is antisymmetric with respect to the vertical line that passes through the apex of the loop. This torque forces the rising top part of the loop to rotate. The effect is also found in a full fluid description (Lynch *et al.*, 2009). For a given chirality of the erupting field, it yields the same direction of rotation as the helical kink. Hence, a comparative study of these two mechanisms is required before firm conclusions about the occurrence of the KI can be drawn from observations of flux rope rotations, which is a further main objective of this paper.

Since the rotations caused by the KI and by the external shear field point in the same direction, they are difficult to disentangle. In fact, from a more general perspective, they are of similar nature. Both cause a writhing of the flux rope which, by conservation of magnetic helicity, reduces the twist of the rope field lines about the writhing axis. Consequently, one can expect that observed flux rope rotations are often consistent with a range of Φ–$B_{\rm et}$ parameter combinations which give the writhing of the flux rope by the helical kink and by the shear field different individual but similar combined strengths.

Other causes of flux rope rotation include magnetic reconnection with the ambient field (Jacobs *et al.*, 2009; Shiota *et al.*, 2010; Cohen *et al.*, 2010; Thompson, 2011; Vourlidas *et al.*, 2011), the straightening from an initial S shape (*e.g.*, Török, Berger, and Kliem, 2010), and the propagation through the overlying field. The latter comprises any asymmetric deflection of the rising flux from radial ascent, *e.g.*, by adjacent coronal holes (see, *e.g.*, Panasenco *et al.*, 2011), and the interaction with the heliospheric current sheet (Yurchyshyn, 2008; Yurchyshyn, Abramenko, and Tripathi, 2009).

One may conjecture that the generally changing orientation of the PIL with height in the corona acts similarly to the heliospheric current sheet at larger heights, *i.e.*, that the upper part of the rising flux continuously adjusts its orientation to align with the PIL. If this were the dominant effect, the rotation of erupting flux could be predicted rather straightforwardly from extrapolation of the photospheric field, since the overlying field is often close to the potential field. However, this conjecture is not valid in the lower corona where $\beta \ll 1$, and where the main part of the total rotation often occurs. We demonstrate this in Appendix A.

The amount of rotation depends on the individual strengths of the five potentially contributing processes. Four of them are controlled by more than a single parameter. This is immediately obvious for the torque by the shear field, which must depend on the height *profile* $B_{\rm et}(z)$, and for the reconnection, which is sensitive to the *structure* of the ambient field, *i.e.*, whether the field is bipolar, quadrupolar, or multipolar and whether the orientation of the line between the resulting new footpoints of the erupting flux differs strongly from the original orientation. The rotation by the KI does not only depend on the initial flux rope twist, $\Phi - \Phi_{\rm cr}$, but also on the strength and height profile of the overlying field (Török, Berger, and Kliem, 2010). If the overlying field decreases only slowly with height, then the upward expansion develops slowly and, accordingly, its contribution to the relaxation of the field line tension is initially weak. The relaxation is then primarily accomplished by a strong rotation at small heights. In the opposite case of very strong upward expansion, the rotation is distributed across a large height range, which also increases the likelihood of further changes by the onset of reconnection (see Lugaz *et al.*, 2011 for an example). The effect of

the heliospheric current sheet can be expected to depend on the angle with the top section of the flux rope's axis, on the horizontal elongation of the CME (whether its horizontal cross section is very elliptical or more nearly circular), and on the magnetic pressure of the CME relative to the pressure of the interplanetary plasma.

Moreover, the total rotation experienced by an erupting flux rope likely depends also on the dynamics of its evolution. For example, a torque strongly localized at low heights, operating on a still small loop, may hurl the flux around more efficiently than a torque which is distributed across a large height range. As another example, in a complex (multipolar) coronal environment the sequence and strength of reconnection with the ambient field may strongly depend upon the height profiles of the rope's angular and rise velocities caused by other processes, *e.g.*, by an ideal MHD instability. The relative velocity between reconnecting flux systems controls how strongly the reconnection with the ambient field is driven. Hence, quantitative studies of flux rope rotation face a very high degree of complexity.

Here we focus on two mechanisms that can cause strong rotations in the corona, the helical kink instability and the torque exerted by an external shear-field component. By comparing a parametric study of both mechanisms in a force-free, line-tied flux rope equilibrium with the data of a well observed, strongly rotating erupting prominence, we demonstrate that their contributions can be disentangled to some degree. We also demonstrate the very strong influence of the ambient potential field's height profile on the amount of rotation by the KI, and briefly address the influence of reconnection between the CME flux rope and the ambient field on the rotation.

This investigation was stimulated by the analysis of the strong rotation in a prominence eruption and CME on 9 April 2008, occasionally referred to as the "Cartwheel CME", in Thompson, Kliem, and Török (2012, in the following: Paper I). Their stereoscopic reconstruction revealed the height–rotation profile of the erupting filament/prominence in the core of a CME for the first time (Thompson, Kliem, and Toeroek, 2009). This profile provides a strong constraint for the numerical modeling. In combination with the further observations of the event, it allows us to infer the major causes of the rotation and the range of source parameters compatible with the data. The analysis of Paper I has given the following results relevant for the present study. The prominence erupted from the remnants of NOAA active region (AR) 10989 close to the west limb and appeared as a flux rope – a single, weakly to moderately twisted loop – throughout the height range covered by the STEREO EUVI and COR1 telescopes (Howard *et al.*, 2008), *i.e.*, up to 4 $R_\odot$ from Sun center. It rotated counterclockwise by $\approx 115^\circ$ up to a heliocentric height of 2.5 $R_\odot$, where the rotation leveled off. Two thirds of this rotation were acquired within 0.5 $R_\odot$ from the photosphere. The data indicate a subsequent gentle backward rotation by $\approx 15^\circ$ in the height range up to 3.3 $R_\odot$. In addition, the analysis of STEREO COR2 data in Patsourakos and Vourlidas (2011) demonstrated that a flux rope structure is consistent also with the three-dimensional shape of the CME at a heliocentric distance of 13 $R_\odot$, where it had changed its orientation by a total of $150^\circ \pm 7^\circ$ from the original one, most likely by further counterclockwise rotation. At this stage the erupting flux was very closely aligned with the heliospheric current sheet above the active region. The prominence was initially accelerated mainly horizontally along the filament channel. This gradually turned into a radial propagation at a position $\approx$98W24S as seen from Earth, $15^\circ - 20^\circ$ away from the original location. The prominence experienced most of its upward acceleration in the heliocentric height range up to ~ 2.5 $R_\odot$ and reached a velocity of ~ 400 km s^{-1} in the COR2 field of view. At the same time, the leading edge of the CME accelerated to over 700 km s^{-1} (Landi *et al.*, 2010). Representative images of the prominence from STEREO *Ahead*, which had the best perspective at the structure, and the corresponding three-dimensional reconstructions of the location of several prominence

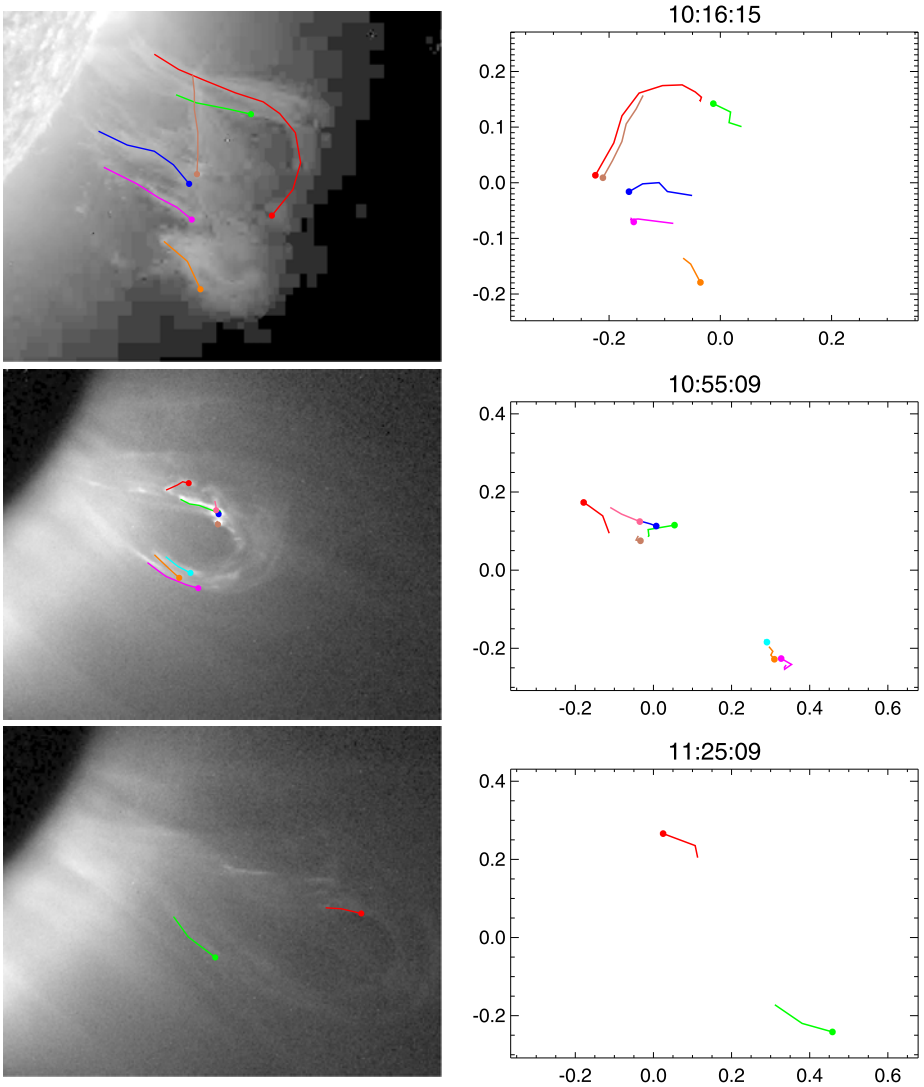

Figure 1 Images and plots of the prominence eruption at 10:16 UT, as seen by the EUVI-*Ahead* telescope in the 304 Å channel, and at 10:55 and 11:25 UT, as seen in white light by COR1-*Ahead*. The prominence apex has reached heights of 0.56, 1.6, and 2.3 $R_{\odot}$ above the photosphere at these times. The right panels display the reconstructed three-dimensional position of the marked prominence threads, using a reprojection to a viewpoint at the position of radial CME propagation, Stonyhurst longitude 98° west (relative to Earth) and latitude 24° south, where the counterclockwise rotation is apparent. The axes are in units of solar radii.

threads are compiled in Figure 1 (from Paper I). The rotation (height–rotation) profile and the rise (time–height) profile are included below in the observation-simulation comparisons (Figures 6 and 8, respectively).

As already noted above, we focus our attention here on the coronal evolution of this event, leaving the interaction with the heliospheric current sheet for future investigation. Moreover, we exclude the possible slight backward rotation by $\approx 15°$ in the COR1 height

range from our modeling, since we are interested in the generally important effects which cause significant rotations in the corona. This part of the rotation is not fully certain, and, if real, it was likely caused by the particular structure of the large-scale coronal field above the active region, which nearly reversed its horizontal direction at heights $\gtrsim 0.3\ R_\odot$ above the photosphere (Paper I). Thus, we will consider a saturation of the modeled rotation at angles near 115° and heights $h \approx (1.5-2.3)\ R_\odot$ above the photosphere to be in agreement with the observations. Furthermore, we will disregard the initial nearly horizontal motion of the prominence along the PIL.

The combined effects of flux dispersal and foreshortening in the course of the source region's rotation to the solar limb made it impossible to obtain a well-defined estimate of the distance between the main flux concentrations in the bipolar region at the time of the eruption, which is a parameter of strong influence on the height profile of the ambient potential field. Only a relatively wide range of $\sim(40-150)$ Mm could be estimated by extrapolating the region's evolution in the course of its disk passage through the final three days before the event. It will be seen that this range still sets a useful constraint on the modeling.

In the following we model the radial propagation of the prominence in the Cartwheel CME in the coronal range of heights as the MHD evolution of an unstable force-free and line-tied flux rope (Section 2). A parametric study of the resulting rotation and rise, focusing on the rotation caused by the helical kink instability and by the external shear field, is compared with the observations, to constrain the parameters in the source of the event and to study whether the relative importance of these mechanisms can be disentangled and individually estimated (Section 3). The discussion in Section 4 addresses the simplifying assumptions made in the modeling and differences to earlier relevant work. Section 5 gives our conclusions. Appendix A relates the rotation of erupting flux ropes in low-beta plasma to the changing orientation of the PIL with height, and Appendix B considers options for inferring the occurrence of the helical kink in the presence of shear-field-driven rotation.

2. Numerical Model

We carry out a series of MHD simulations similar to the CME simulation in Török and Kliem (2005). The prominence is modeled as a section of an approximately force-free toroidal current channel embedded in external current-free (potential) field, which represents a modification of the approximate force-free equilibrium by Titov and Démoulin (1999). The current channel creates a flux rope structure of the magnetic field which has a somewhat larger cross section than the channel and is enclosed by a quasi-separatrix layer in the interface to the surrounding field of arcade structure. The chirality of the flux rope is chosen to be left handed, so that the rotation will be counterclockwise (Green *et al.*, 2007). The poloidal component of the external field, $B_{\rm ep}$, is due to a pair of subphotospheric magnetic point sources, which produce a pair of flux concentrations ("sunspots") on the sides of the flux rope (the "prominence") in the magnetogram. This field component holds the current channel in equilibrium; its strength at the position of the rope is exactly proportional to the current in the rope. Consequently, only its spatial profile, determined by the spacing between its sources, can be freely varied. The toroidal component of the external field, $B_{\rm et}$, is due to a pair of subphotospheric dipoles, positioned under the footpoints of the flux rope such that the field lines of $B_{\rm et}$ run parallel to the magnetic axis of the rope to a very good approximation. Therefore, $B_{\rm et}$ introduces only very minor Lorentz forces in the initial configuration, which quickly decrease by numerical relaxation at the beginning of each run, so that the strength of $B_{\rm et}$ can be chosen freely within a wide range. We will also refer to the external toroidal field as the

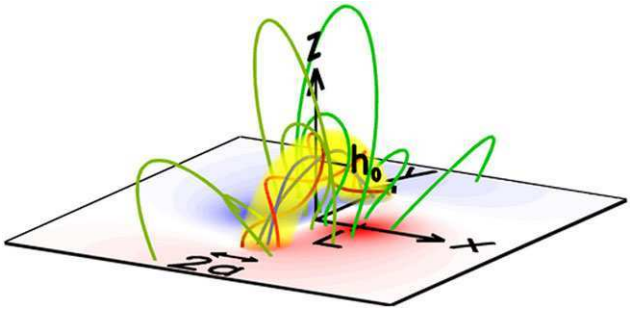

Figure 2 Visualization of the modified Titov–Démoulin flux rope equilibrium used as the initial condition in the simulation runs of this paper; here with an average twist $\Phi = 3.5\pi$ as in Figure 4. The current channel is rendered as a yellow transparent volume. Blue field lines run near the magnetic axis of the flux rope (where the local twist is 2π; note that their color is modified by the yellow transparent volume around them), red field lines are embedded in the flux surface at a distance to the axis where the local twist equals the average twist. Two symmetric sets of green and olive field lines show the ambient potential field. Contours of the magnetogram, $B_z(x, y, 0)$, are shown in the bottom plane. The torus of major radius R and minor radius a is submerged by a distance d, resulting in the apex height $h_0 = R - d$ and the distance of each flux rope footpoint from the origin $D_f = (R^2 - d^2)^{1/2}$. A bipole, whose components are located at $(\pm L, 0, -d)$, is the source of the external poloidal field component B_{ep}; see Figure 2 in Titov and Démoulin (1999) for its visualization. A pair of antiparallel, vertically oriented dipoles, placed under the footpoints of the flux rope at $(0, \pm D_f, -5h_0)$, provides the source of the external toroidal (shear) field component B_{et}.

shear-field component. Here it decreases faster with height than the external toroidal field in the original Titov–Démoulin equilibrium. A visualization of the configuration is shown in Figure 2.

We integrate the ideal MHD equations but neglect pressure, as appropriate in the active-region corona, and gravity, because the hydrostatic pressure profile along the field is not essential for the flux rope rotation, which is driven by the Lorentz force. These simplifications yield maximum freedom in the scalability of the simulation results to the data. Magnetic reconnection can occur due to the numerical diffusion of the field in regions of strong gradients. The initial density is specified as $\rho_0(\mathbf{x}) = |\mathbf{B}_0(\mathbf{x})|^{3/2}$, where $\mathbf{B}_0(\mathbf{x})$ is the initial magnetic field. This yields a slow decrease of the Alfvén velocity with height, as in the corona. The box is a cube 64 units long on each side, significantly larger than in our previous simulations and in each direction at least twice as large as the biggest size of the structures that will be compared to the data. It is resolved by a nonuniform, fixed Cartesian grid with a resolution of 0.04 units in the central part of the box (a factor of two coarser than in Török and Kliem, 2005). Rigid boundary conditions are implemented at the top and side boundaries, while very small velocities are permitted in the bottom boundary. Initially the torus lies in the plane $\{x = 0\}$. The MHD variables are normalized by the initial apex height of the flux rope axis, h_0, by the initial field strength B_0, density ρ_0, and Alfvén velocity V_{A0} at this point, and by the corresponding quantities derived thereof, *e.g.*, the Alfvén time $\tau_A = h_0/V_{A0}$. Thus, the initial apex height of the axis of the current channel and flux rope serves as the length unit.

The parameters of the initial configuration are largely chosen as in Török and Kliem (2005). We fix the major radius of the torus at $R = 1.83$, the depth of the torus center at $d = 0.83$ and the pre-normalization strength of the point sources at $q = 10^{14}$ Tm^2 in all runs. For a base set of the simulation series, discussed below in Figures 3 – 6, 8, and 9, we further fix the distance of the point sources from the z axis at $L = 0.83$ (in units normalized such that h_0 is unity). This value lies in the middle of the estimated range for the corresponding dis-

tance of the flux concentrations in AR 10989, given above, when the scaling $h_0 = 0.077\ R_\odot$ adopted in Section 3.1 is applied. It also agrees with the settings in several previous investigations (*e.g.*, Török and Kliem, 2005; Török, Berger, and Kliem, 2010), facilitating comparisons. Variations of this parameter will be considered in the range $L = 0.42 - 2.5$. We vary the minor radius of the toroidal current channel, $a = 0.32 - 0.62$, and the strength of the external toroidal field, $B_{\rm et}/B_{\rm ep} = 0 - 1.06$ at the flux rope apex $\mathbf{x} = (0, 0, 1)$, to obtain a range of values for the average twist of the current channel, $\Phi = (2.5 - 5.0)\pi$, and for the strength of the shear-field component. The twist is influenced by both a and $B_{\rm et}$, with a having the stronger influence within the considered range of parameters. The twist values quoted in this paper represent the initial twist averaged over the cross section of the current channel in the manner described in Török, Kliem, and Titov (2004).

The range of the initial average twist is chosen such that unstable and stable configurations with respect to the helical kink mode are included. The first group is unstable from the beginning of the simulation. Nevertheless, a small upward initial velocity perturbation is applied in the vicinity of the flux rope apex (typically ramped up to 0.05 $V_{\rm A0}$ over 5 $\tau_{\rm A}$ and then switched off), to ensure that the instability displaces the apex upwards, *i.e.*, downward kinking is excluded in these runs which are intended to model CMEs.

For the geometric parameters of the system specified above, the flux rope is initially stable with respect to the torus instability (Kliem and Török, 2006; Török and Kliem, 2007). However, the helical kink instability lifts the rope into the torus-unstable range of heights ($h \gtrsim 2\ h_0$), from where the torus instability accelerates its top part further upwards.[1] The kink-stable cases require that the upward velocity perturbation is applied for a longer time, lifting the apex into the torus-unstable range. This allows us to study the influence of the shear field on the rotation in the absence of the helical kink instability, using uniform geometrical parameters of the initial flux rope (except for the minor flux rope radius a) in all runs. An initial velocity perturbation very close to the required minimum value is applied in each of these cases, to ensure nearly uniform conditions at the onset of the instability throughout the series. The values at the end of the ramp phase stay below 0.12 $V_{\rm A0}$ for all runs. The flux rope velocity falls back to a much smaller value (typically $\approx 0.01\ V_{\rm A0}$) immediately after the perturbation is switched off. The growing instabilities then accelerate the apex to peak upward velocities in the range $\max\{u_{\rm a}\} \approx (0.4 - 0.7)\ V_{\rm A0}$, far higher than the initial perturbation.

On the Sun, the initial lifting of the flux can occur by a variety of effects in addition to the helical kink mode, as has been demonstrated by numerical simulations. These include the shearing and twisting of the coronal field by photospheric flows (*e.g.*, Mikic and Linker, 1994; Török and Kliem, 2003), reconnection associated with flux cancellation in the photosphere (*e.g.*, Aulanier *et al.*, 2010; Amari *et al.*, 2010), and reconnection with newly emerging flux (Chen and Shibata, 2000).

The observations of the Cartwheel event indicate a gradual doubling of the prominence height prior to the eruption (Paper I). The initial lifting of the flux rope apex in the simulations due to the applied perturbation is much smaller for all kink-unstable runs and stays in the range up to this value for the kink-stable cases, except for the run with the highest shear field ($\Phi = 2.5\pi$, $B_{\rm et}/B_{\rm ep} = 1.06$), which requires a lifting to 2.6 h_0.

[1] The torus instability can be considered as a lateral kink of the current channel. However, we choose "kink" and "KI" to refer exclusively to the helical kink mode in this paper.

3. Comparison of Simulations and Observations

3.1. Dependence of Flux Rope Rotation on Twist and Shear

We begin with a case that involves a clear helical kink instability, as one would expect at first sight from the considerable rotation observed in the Cartwheel event. The initial average twist is chosen to be $\Phi = 5\pi$, a value used previously in the successful modeling of several filament/prominence eruptions (Williams *et al.*, 2005; Török and Kliem, 2005). Even with this considerable amount of twist (and with the sunspot semi-distance $L = 0.83$), we find that a shear field is required to reach the observed rotation. Figure 3 shows the resulting rotation of the flux rope, which reaches the observed value of 115° and is a combined effect of the helical kink instability and the shear field. The field lines visualize a flux bundle in the core of the rope which runs slightly (≈ 5 %) under the rope axis in its top part. This is a likely location for prominence material within a flux rope. Moreover, this is the only selection that allows a favorable comparison with the observed flux rope shape for the weakly twisted case shown below in Figure 5, while the more strongly twisted cases are less sensitive to this vertical offset. Therefore, we adopt this selection as a uniform choice for Figures 3, 4 and 5 which compare the flux rope rotation for different twist values. The field lines are displayed from perspectives identical to the STEREO images and reconstructions in Figure 1.

Two characteristic morphological features apparent in the COR1 data in Figure 1 are weakly indicated in the simulation: the initial teardrop-like appearance and the elongated shape at large heights (relatively narrow in the horizontal direction). The right panels show that the teardrop shape is a projection effect. The legs of the erupting rope approach each other near the edge of the occulting disk only in projection; they are displaced along the line of sight and actually moving away from each other. The elongated shape is largely also due to the strong rotation.

The legs of the rope appear "wiggly", which results from two effects. First, they reconnect with the ambient field in the vertical current sheet under the flux rope apex in the interval $t \approx (32-65)\ \tau_A$, which corresponds to apex heights $h \approx (5-21)\ h_0$; with the reconnection proceeding at much lower heights inside the edge of the COR1 occulting disk. This leads to a bend in the reconnected flux rope: the field lines have relatively small curvature within the legs of the expanded original rope above the reconnection point but run along a more helical path in the ambient field just outside the original rope below the reconnection point. This bend and the more helical shape of the field lines below it relax upward, along with the overall upward expansion of the reconnected flux rope. Since the flux rope apex has reached a considerable upward velocity, $u_a \lesssim 0.5\ V_A$, the bend needs a large height range for its propagation to the top of the rope. It is located slightly above the dotted line in the third snapshot pair of Figure 3 and at $h \gtrsim 15\ h_0$ in the final snapshot pair. The plots on the right hand side show that the new footpoints of the rope are displaced in counterclockwise direction from the original ones, thus contributing to the overall counterclockwise rotation of the rope. However, this contribution is only a minor one; the major part of the total rotation occurs before the flux rope legs reconnect (which can be seen by comparison with Figure 6 below). This reconnection is similar to the second and third reconnections described in Gibson and Fan (2008, their Section 4.1) and will be addressed in more detail in a future investigation. Second, at the given relatively high value of the twist, the dominant wavelength of the helical kink mode is considerably shorter than the flux rope, so that the characteristic helical shape develops clearly.

Figure 4 shows the evolution in a second run where the KI develops only weakly, using a moderate, only slightly supercritical value of the initial average twist, $\Phi = 3.5\pi$. A stronger

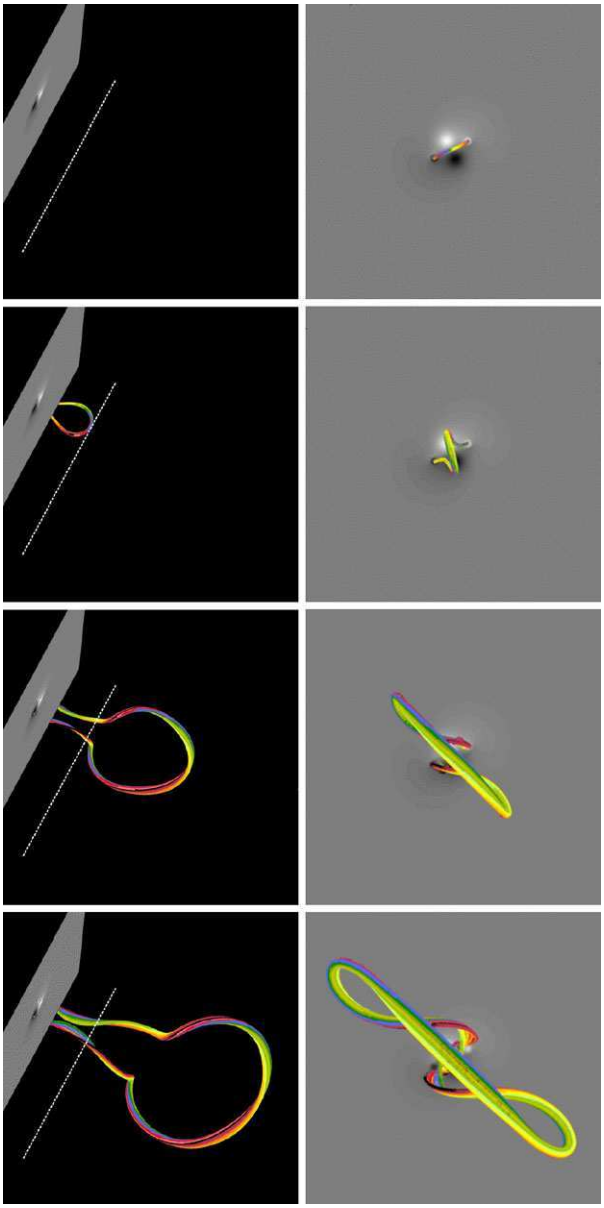

Figure 3 Snapshots of an erupting and rotating, strongly kink-unstable flux rope. The initial average twist is $\Phi = 5\pi$ and the shear-field component at the initial flux rope apex position is given by $B_{\rm et}/B_{\rm ep} = 0.42$. Field lines in the core of the rope, traced downward from the apex, are shown in the height range $0 \le z \lesssim 30$, using the same two perspectives as for the observations in Figure 1 (in the left panels the line of sight makes an angle of 26° with the y axis, and the z axis is tilted away from the observer by 8°, while the right panels present a vertical view with an initial angle between the flux rope axis and the east–west direction of 26°). The magnetogram, $B_z(x, y, 0, t)$, is displayed in grayscale (seen from below in the left panels). The dotted line indicates where the edge of the COR1 occulting disk is located if the distance between the flux rope footpoints in the simulation, $2D_{\rm f} = 3.3\ h_0$, is scaled to the value of 175 Mm estimated in Paper I. Using this scaling, the simulated heights of $h = 1$, 7.3, 21, and 30 h_0 (at $t = 0$, 36, 64, and 84 $\tau_{\rm A}$) translate to heights of 0.077, 0.56, 1.6, and 2.3 $R_\odot$ above the photosphere, reached at 10:16, 10:55, and 11:25 UT (for rows 2 – 4), respectively.

shear field is chosen, so that the same total rotation is achieved. The overall properties – accelerated rise into an ejection (CME) and very strong rotation – are identical to the run shown in Figure 3. The morphological details, such as the teardrop shape at small heights and the elongated shape at large heights, match the data slightly better. The indications of wiggly shape at large heights remain weak. Reconnection of the flux rope legs with the ambient field occurs here as well, but the resulting changes in the shape of the flux rope are weaker, since not only the field lines in the rope are less twisted but also the ambient field is less helical, due to the larger $B_{\rm et}$. This morphological difference to the strongly twisted

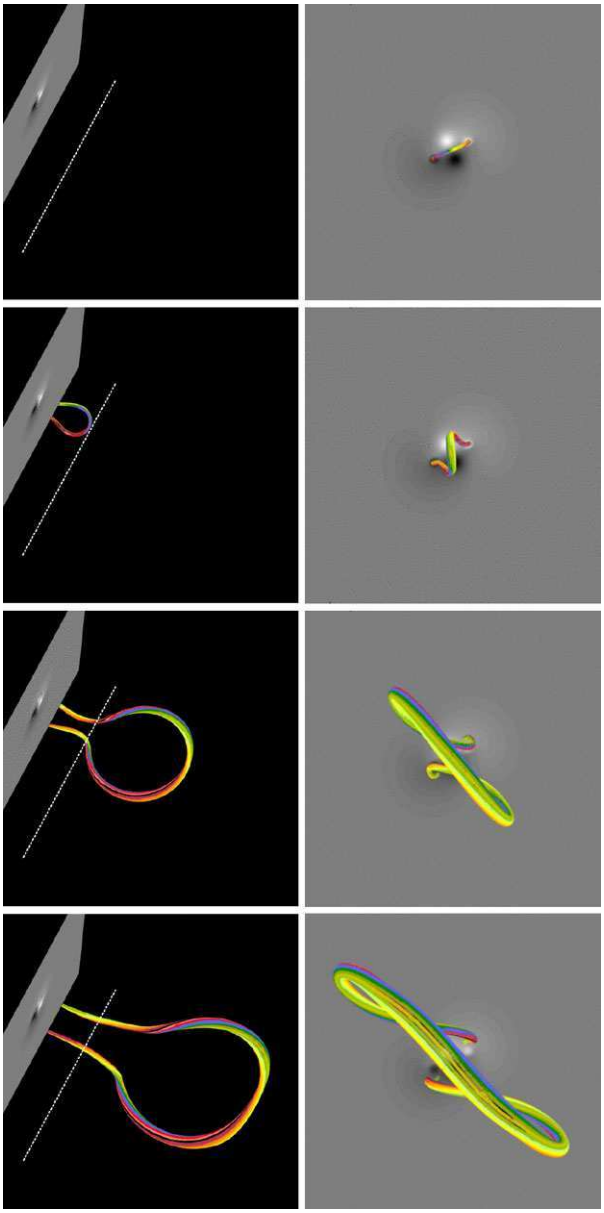

Figure 4 Same as Figure 3 for a weakly kink-unstable case with initial average twist $\Phi = 3.5\pi$ and shear field $B_{et}/B_{ep} = 0.67$. The flux rope is shown at the simulation times $t = 0$, 50, 80, and 97 τ_A which yield the same heights as the snapshots in Figure 3, corresponding to the same observation times.

flux rope is one aspect that may allow to distinguish between rotations with strong and weak involvement of the helical kink in observed events. The field line shapes in the present case conform slightly better to the inclination of the prominence threads with respect to the axis of the flux rope in the COR1 data in Figure 1, but this difference is not sufficiently clear to be decisive by itself. Moreover, it depends to a considerable degree upon which part of the erupting flux was outlined by prominence material in the considered event and on the selection of field lines in the plots.

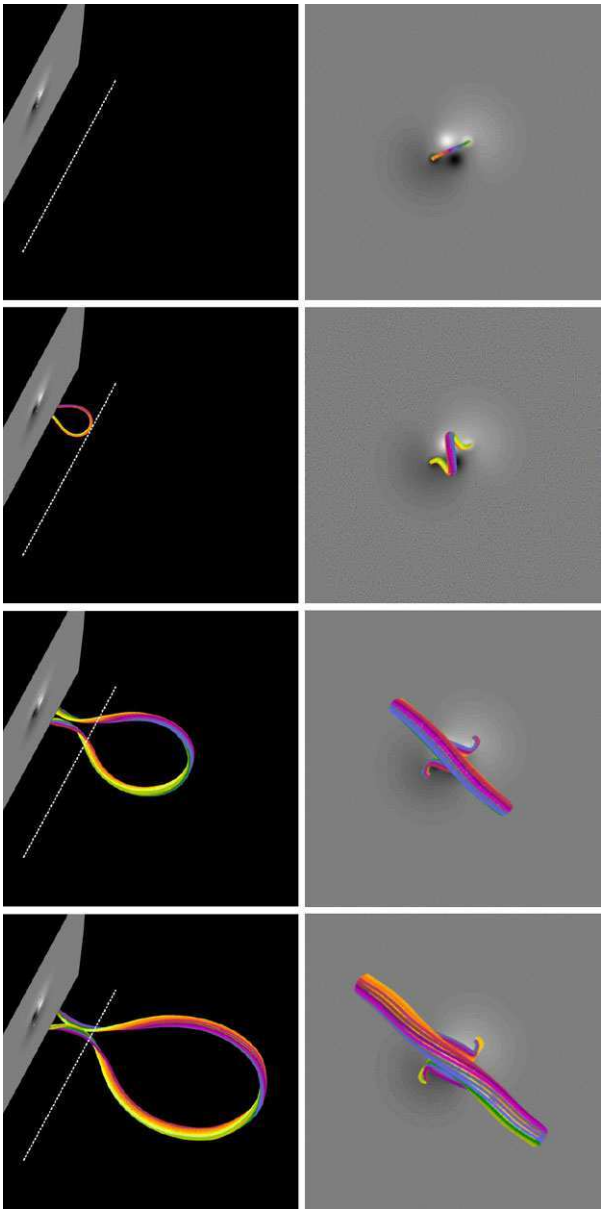

Figure 5 Same as Figure 3 for a kink-stable case with initial average twist $\Phi = 2.5\pi$ and shear field $B_{\rm et}/B_{\rm ep} = 1.06$. The flux rope is shown at the simulation times $t = 0$, 77, 109, and 128 $\tau_{\rm A}$ which yield the same heights as the snapshots in Figure 3, corresponding to the same observation times.

Figure 5 presents a case with subcritical flux rope twist, $\Phi = 2.5\pi$, where the kink instability cannot develop and an even stronger shear field is needed to achieve a similar rotation. Here the parameters were chosen such that the rotation matches the observations as well as the other two runs in the height range $h \lesssim 20\ h_0$, with the total rotation of the rope's magnetic axis at $h = 30\ h_0$ exceeding the rotation in those runs by 20 – 25 degrees. The elongated teardrop shape at intermediate and large heights yields the best match of the three runs shown in Figures 3, 4 and 5. However, this is only the case because a flux bundle slightly under the magnetic axis of the flux rope is selected in the visualization. If instead

a set of field lines encircling the flux rope axis is chosen, then the high total rotation at the apex height $h = 30\ h_0$ leads to an inverse teardrop shape (narrow at the apex, because at this point the view is nearly along the axis of the rotated flux rope), which is inconsistent with the observations. Again, since it is not known which parts of the erupting flux (rope) were filled with prominence material in the event to be modeled, these morphological comparisons, by themselves, do not allow to rule out the kink-stable run shown in Figure 5.

The similar total rotations in the three simulations confirm that both twist and shear belong to the key parameters which determine the amount of rotation in erupting flux ropes. To analyze this further, we consider a set of characteristic cases from our series of simulation runs with varying strength of the two effects. For each of the twist values $\Phi = 5.0$, 3.5, and 2.5π, we vary the shear field $B_{\rm et}$ from the respective best fitting value used in Figures 3–5. All runs use the same sunspot semi-distance $L = 0.83$ and, hence, the same external poloidal field $B_{\rm ep}$. The variation of L will be considered in Section 3.2.

The rotation of the flux rope in the simulations is measured in two ways. At low heights it is taken from the changing orientation of the magnetic axis at the apex of the flux rope. As the flux rope rises, the apex orientation oscillates increasingly, due to the upward propagation of Alfvénic perturbations which result from the dynamic onset of reconnection in the vertical current sheet under the rope (the relaxation of the bend in the reconnected field lines mentioned above). The right panels at the two final heights in Figures 4 and 5 indicate the resulting oscillations of the field orientation at the apex with respect to the bulk orientation of the flux rope's upper part. Therefore, at larger heights we simply use the direction of the horizontal line connecting the flux rope legs at the height where they are most distant from each other. This measurement filters away most of the oscillating variations, which are also not captured by the observed rotation data derived in Paper I and replotted in Figure 6. The difference between the two measurements remains less than five percent in a height range $\Delta h \sim (3-6)\ h_0$ around $h \sim 10\ h_0$, except for the most strongly rotating and oscillating case in the series ($\Phi = 5\pi$, $B_{\rm et}/B_{\rm ep} = 0.63$) where it reaches ≈ 10 percent. Linear interpolation between the two measurements for each simulation run is applied in the appropriate range of small differences to match them smoothly.

(The method to estimate the rotation angle at large heights fails for one of the runs in Figure 6 ($\Phi = 2.5\pi$, $B_{\rm et} = 0$), where reconnection of the flux rope legs with the ambient field leads to jumps that are larger than the oscillations of the magnetic axis at the apex. For this run, whose rotation profile differs strongly from the observed one, we include the rotation angle only at low heights, to show the trend.)

In order to compare the simulated rotation profiles with the observations, a scaling of the length unit in the simulations to distances on the Sun is required. For this purpose, we set the distance between the footpoints of the flux rope in the simulation, $2D_{\rm f} = 3.3\ h_0$, equal to the estimated length of the flux which holds the prominence, 175 Mm (Paper I). This is independent of the actual prominence shape. The apex height of the toroidal Titov–Démoulin flux rope, our length unit, tends to be somewhat high in comparison to solar prominences, which are often quite flat. Here we obtain $h_0 = 0.077\ R_\odot$, relatively close to the estimated initial prominence height of $\approx (0.05-0.06)\ R_\odot$ (Paper I). If we would instead choose to compare the simulations to the temporal profile of the prominence rotation, then each change of the twist, which implies a change of the KI growth rate, would require a rescaling of the time unit in the simulations, $\tau_{\rm A}$. The comparison of the simulated rotation profiles with the observed profile is displayed in Figure 6. As discussed in Sections 1 and 4, we disregard the slight backward rotation at $h \gtrsim 1.5\ R_\odot$ above the photosphere in the comparison and assume that the tendency of the rotation to level off at this height would have continued in the absence of the specific complex structure of the large-scale coronal field above AR 10989

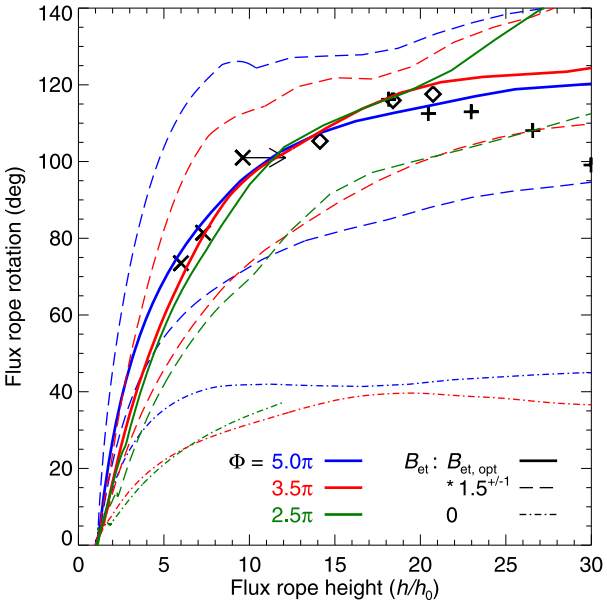

Figure 6 Comparison of flux rope rotation as a function of normalized apex height above the photosphere with the observations obtained in Paper I. Crosses and diamonds are EUVI data, with the final cross representing a lower limit for the height and the diamonds representing interpolated heights. Plus symbols are COR1 data. The distance between the footpoints of the flux rope in the simulation is scaled to the value of 175 Mm estimated in Paper I, resulting in $h_0 = 0.077\ R_\odot$. The initial average twist, Φ, and the strength of the shear-field component (external toroidal field), B_{et}, given by its ratio to the external poloidal field component B_{ep} at the initial flux rope apex, are varied, while the geometrical parameters of the initial flux rope (except the minor radius a) and the spatial structure of the external field components B_{et} and B_{ep} are uniformly chosen throughout the series of runs (see Section 2 for details). The optimum values for the shear-field strength, which yield the best match with the observed rotation profile up to $h \approx 20\ h_0$, found through parametric search, are $B_{et,\,opt}/B_{ep} = 0.42$, 0.67, and 1.06 for $\Phi = 5.0\pi$, 3.5π, and 2.5π, respectively. Changes of B_{et} by a factor 3/2 and the case $B_{et} = 0$ are included.

and in the absence of the heliospheric current sheet, which are not included in our model. Several conclusions can be drawn from this set of simulations.

i) Similar height–rotation profiles (not only a similar total rotation) are obtained in a range of Φ–B_{et} combinations. The profiles for $(\Phi, B_{et}/B_{ep}) = (5\pi, 0.42)$, $(3.5\pi, 0.67)$, and $(2.5\pi, 1.06)$ all match the observed profile very well up to a height $h \sim 20\ h_0 \approx 1.5\ R_\odot$ above the photosphere, where a total rotation of $\approx 115°$ is observed. These runs include a strongly and a weakly kink-unstable and a kink-stable case. Hence, even such a strong rotation does not by itself imply the occurrence of the helical kink instability. Further arguments, such as those given below, are required to draw conclusions about the occurrence of the instability in the modeled event.

ii) To reach the observed total rotation of $\approx 115°$ with the initial configuration and parameter settings chosen in this series, in particular with the chosen value of the sunspot semi-distance L, the shear must contribute. The strongly twisted configuration ($\Phi = 5\pi$) yields only little more than one third of the observed rotation in the absence of shear ($B_{et} = 0$). Therefore, the shear contributes the main part of the total rotation even in this strongly kink-unstable case. Note that this conclusion changes if the sunspot distance

is set to larger (however, unrealistic) values, so that the overlying field decreases less steeply with height (see Section 3.2).

iii) The twist also contributes in all runs. The tension of the twisted field relaxes in any case when the flux rope is driven upward out of its initial equilibrium, be it by the helical kink instability, by the torus instability, or by any other process (*e.g.*, by so-called tether-cutting reconnection). This relaxation contributes to the writhing of the flux rope axis regardless of whether or not the helical kink instability is triggered. As a consequence, we do not observe a jump in the achieved rotation as the twist of the initial equilibrium is varied between kink-stable and kink-unstable values. This is most obvious from the runs with $B_{\rm et} = 0$.

iv) The higher the relative contribution of the twist, the lower the height range where most of the rotation is reached. This reflects the fact that the KI tends to reach saturation quickly, often already when the flux rope has risen to a height comparable to the foot-point distance (*e.g.*, Török, Kliem, and Titov, 2004). This property corresponds well to the tendency of the rotation to level off at the relatively low height of $\approx 1.5\ R_\odot$ ($\approx 20\ h_0$) above the photosphere. The rotation by the shear field acts in a larger height range. The different behavior can be made plausible from the fact that the Lorentz force due to the shear field depends on the current through the rope and on the angle between the flux rope legs and the shear field. While the current decreases as the rope ascends (similar to the twist), the angle rises until the legs approach a vertical position, which corresponds to bigger apex heights than the saturation height of the helical kink mode. Hence, the Lorentz force due to the shear field acts strongly in a larger height range than the tension force associated with the twist.

As a consequence, the Titov–Démoulin flux rope with subcritical twist for KI onset does not allow to match the entire observed rotation profile of the 9 April 2008 event. We have performed considerable numerical experimenting in this range of twists [$\Phi = (2.5-3)\pi$], including modifications of the height profiles $B_{\rm et}(z)$ and $B_{\rm ep}(z)$ and of the flux rope shape (by varying its major radius R but not the apex height h_0) from the uniform settings for the runs in Figure 6. Either the rotation in the height range $h \lesssim 20\ h_0$ was found to be too small, or the total rotation at $h = 30\ h_0$ was too large. Although the shape of the prominence in the plane of the sky can still be met by the special selection of the field lines in Figure 5, the saturation of the rotation at $h \approx 1.5\ R_\odot$, revealed by the stereoscopic reconstruction, cannot be reproduced. This suggests that at least a weak helical kink instability must have been triggered in this event.

v) The range of twist-shear combinations that reproduce the observed rotation profile is bounded not only from below, as outlined in ii) and iv), but also from above. Average twists significantly exceeding 5π are not only unlikely to occur in the corona but also lead to increasingly strong helical deformations of the flux rope, which are favorable for the onset of magnetic reconnection with the overlying field or between the flux rope legs. Such reconnection can strongly distort the rotation profile and can even stop the rise of the flux rope (Török and Kliem, 2005; Shiota *et al.*, 2010). Reconnection with the overlying field does indeed lead to a confined (failed) eruption in the present simulation series when the initial twist is raised to 6π. Reconnection between the legs of the rope occurs if $\Phi \geq 7\pi$, also leading to confined eruptions. (A detailed description of such reconnection can be found in Kliem *et al.*, 2010.)

Increasing the shear field tends to stabilize the flux rope because any displacement then requires an increasing amount of energy to push the ambient field aside. The low-twist case ($\Phi = 2.5\pi$) with the strongest shear field included in Figure 6 requires a considerable initial perturbation to reach the torus-unstable range of heights

($h > 2.6\ h_0 = 0.2\ R_\odot$ for these parameters); it is completely stable to small perturbations. Similarly, while the 3.5π run with $B_{et} = 0$ is clearly kink-unstable, the corresponding sheared case ($B_{et}/B_{ep} = 0.67$) exceeds the instability threshold only slightly. The initial lifting of the flux rope required in the low-twist case strongly exceeds the observed rise of the prominence to $\approx 0.06\ R_\odot$ prior to the onset of the eruption. This represents a further strong indication against this configuration.

The upper limit for the shear field is not a universal number but depends on other parameters of the system, which include the thickness of the flux rope, the strength of the line tying, and the height profile of the external poloidal field, $B_{ep}(z)$. A systematic study of these dependencies would be beyond the scope of the present investigation. However, we have considered a modification of the height profile $B_{ep}(z)$, which is the key parameter for the onset of the torus instability in the absence of shear and significant line tying (Kliem and Török, 2006). In an attempt to ease the occurrence of the instability in the low-twist case ($\Phi = 2.5\pi$, $B_{et}/B_{ep} = 1.06$), the sunspot semi-distance was reduced to the minimum value of the possible range estimated from the observations, $L = 0.4$, leaving the other parameters of the equilibrium unchanged. No reduction of the minimum height for instability was found, which must be due to the strong stabilizing effect by the chosen shear field.

vi) Reconnection of the flux rope legs with the ambient field contributes only a minor part of the total rotation in our simulation series. It appears to remain weaker than the twist-driven rotation, or at most comparable, *i.e.*, considerably weaker than the shear-driven rotation. This can be seen most clearly in the 5π run with $B_{et} = 0$. Here the reconnection of the flux rope legs with the ambient field proceeds while the rope apex rises from $\approx 2\ h_0$ to $\approx 16\ h_0$, with the flux in the core of the rope being involved in the range of apex heights $h \sim (4-16)\ h_0$. However, the major part of the total rotation of $\approx 40°$ is already reached at low apex heights, $h \lesssim 5\ h_0$, *i.e.*, due to the helical kink mode. The apex height range during the reconnection of the flux rope legs in the shear-free 3.5π run is similar to the 5π run. The rotation profile of this run in Figure 6 shows about equal amounts of rotation in the height ranges $h \lesssim 5\ h_0$ and $h \sim (5-16)\ h_0$, indicating that the reconnection-driven rotation could here be comparable to the twist-driven rotation. Again, both remain considerably smaller than the rotation due to the shear in the 3.5π run that best fits the observations.

These conclusions are also supported by the fact that the angular distance between the initial and new footpoints of the flux rope's magnetic axis, measured from $\mathbf{x} = 0$, remains far smaller than the total rotation of the rope (see the right panels in Figures 3–5).

3.2. Influence of the External Poloidal Field

The height profile of the poloidal field which is due to sources external to the flux rope, B_{ep}, is a further factor of potentially strong influence on the rotation. Erupting flux ropes rotate more strongly at low heights if the external field initially overlying the flux rope decreases more gradually with increasing height (Török, Berger, and Kliem, 2010). The relaxation of the magnetic tension in the erupting flux rope by rotation is then more pronounced because the relaxation by upward expansion is hindered, at least initially. The relevant length scale, $l_z = -[\mathrm{d}(\log B_{ep})/\mathrm{d}z]^{-1}$, increases with increasing distance between the sources of B_{ep}, *i.e.*, between the main flux concentrations to the sides of the PIL. This can easily be seen for the Titov–Démoulin equilibrium, where this scale height is $l_z = (z+d)[1 + L^2/(z+d)^2]/3$.

Figure 7 shows that this effect remains weak as long as the distance between the sources of B_{ep}, $2L$, is smaller than the distance between the footpoints of the erupting flux rope,

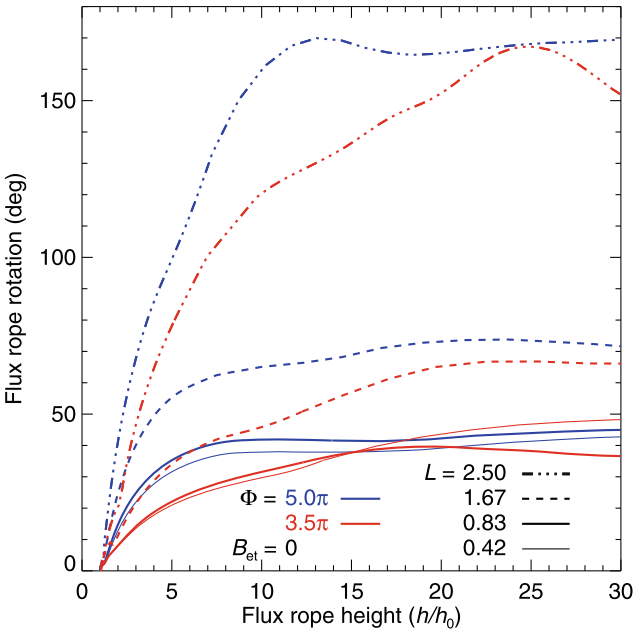

Figure 7 Dependence of flux rope rotation *vs.* height upon the distance L of the main flux concentrations in the source region from the PIL. Kink-unstable flux ropes ($\Phi = 5\pi$ and 3.5π) are considered for vanishing external shear-field component, $B_{et} = 0$.

$2D_f$, but that it becomes very strong when the reverse relation holds. Here the sunspot semi-distance L is varied for the 5π and 3.5π runs with no external shear field, $B_{et} = 0$, to be 0.5, 1, 2, and 3 times the value estimated from the observations and used in Section 3.1 (Figures 3 – 6). The two distances are nearly equal if L is set to twice the estimated value. This is larger than the maximum of the range for L compatible with the observations (see the Introduction). Hence, the conclusions drawn from the series of simulations shown in Figure 6 are not sensitive to the actual value of the parameter L as long as it remains within this range. In particular, an external shear-field component of strength close to the optimum values given in this figure is then required to reach the observed rotation.

Rotations even exceeding those produced mainly by the shear field in Figure 6 are achieved in the absence of a shear field for both twists if L exceeds D_f by a factor $\gtrsim 1.5$. A similar situation was realized in simulations of erupting flux ropes in Fan and Gibson (2003) and Gibson and Fan (2008), which showed strong rotations of 115 – 120 degrees with $B_{et} = 0$. However, such large distances of the main polarities, relative to the length of the PIL and a filament channel between them, do not typically occur in fully developed active regions. Hence, the effect of a shear field (Isenberg and Forbes, 2007) will typically be involved (and significant) if erupting flux rotates by large angles of order 90° and more.

3.3. Rise Profile

The results of Sections 3.1 and 3.2 lead to the question whether the initial twist and the shear field in the source volume of the eruption can be further constrained individually, although their combined effect on the rotation is similar. The rotation profile obviously is a powerful new diagnostic of the evolution of flux ropes in CMEs, however, for the considered event it

does not allow to discriminate between the strongly and weakly kink-unstable cases shown in Figures 3 and 4, respectively. Therefore, we now consider the rise (time–height) profile of the erupting flux. This function reflects the growth rate of the instability driving the eruption. The growth rate varies strongly with the twist if this parameter exceeds the threshold of the helical kink mode (see, *e.g.*, Figure 5 in Török, Kliem, and Titov, 2004). When the variation of the twist is combined with a variation of the shear-field strength in the opposite direction (one increasing, the other decreasing), such that the rotation profile stays nearly unchanged, then the rise profile will change even stronger: decreasing (increasing) shear-field strength leads to higher (lower) KI growth rate. Thus, the combined comparison can constrain these parameters individually.

In order to compare the simulated rise profiles with the observed one, the time unit in the simulations, τ_A, must also be scaled to a dimensional value. Since $\tau_A = h_0/V_{A0}$ and h_0 is already scaled, this is equivalent to adopting a value for the initial Alfvén velocity V_{A0} in the body of the prominence. So far, this parameter can hardly be derived from observations, since both the field and density structure of prominences are generally only poorly known. Therefore, here we work backwards by first finding the best match between the simulated and observed rise profiles and then checking whether the implied Alfvén velocity falls within an acceptable range. Lower bounds on the Alfvén velocity in filaments have been obtained through the application of seismological techniques to six cases of oscillating filament threads (Terradas *et al.*, 2008). Five of these lie in the range $\sim(300-600)$ km s^{-1} if the length of the field lines that pass through the threads is assumed to be ~ 175 Mm, the length of the erupting structure estimated in Paper I. An upper bound of order 1000 km s^{-1} is widely accepted for old, dispersed active regions like the one considered here.

The rise profiles of the simulation runs shown in Figures 3, 4 and 5 are scaled and matched to the observed profile in Figure 8. In selecting the scaling parameters for the best match, we adopt a start time of the eruption a couple of minutes before 08:51 UT, as estimated in Paper I. The conclusions drawn from the comparison do not depend upon the particular start time if chosen in this range. The value 08:48 UT used in Figure 8 yields the best match of the 3.5π and 2.5π runs with the observations and lies very close to (30 sec before) the last EUVI image prior to the occurrence of motions in the prominence along the path of the CME. Also, we give relatively low priority to the EUVI height data after 10 UT, since these may be smaller than the true heights, as discussed in Paper I.

The scaled rise profile of the simulation with $\Phi = 3.5\pi$ is found to fit the data quite well if the Alfvén velocity is chosen in the range $V_{A0} = (540-560)$ km s^{-1} and the start time of the simulation is placed in the range 08:45 – 08:50 UT (with the earlier time corresponding to the lower V_{A0}). These values appear very plausible.

We did not succeed to find a satisfactory fit by the higher twisted case. The corresponding curve in Figure 8 demonstrates this, using the same start time as for the 3.5π run and $V_{A0} = 420$ km s^{-1}. Increasing (decreasing) V_{A0} leads to a steeper (flatter) fit curve, *i.e.*, to a better fit at the larger (smaller) heights (if the start time is adjusted simultaneously), but it is obvious that the curve can never fit the combined EUVI and COR1 time–height data. Here the phase of accelerated rise ends too early because the instability grows and saturates too quickly. The rise profile of this simulation can be stretched on the time axis and formally be fit to the data if in addition to an unrealistically low Alfvén velocity of 300 km s^{-1} (lower than the terminal speed of the CME core) an unrealistically large extension of the prominence flux of 360 Mm (twice as large as the estimate in Paper I) are assumed. Both are unacceptable. This comparison with the data thus argues clearly against the occurrence of high twist and a strong helical kink instability in the considered event, in spite of the high total rotation.

Assuming the same start time as for the other two runs, the kink-stable low-twist case ($\Phi = 2.5\pi$) allows an acceptable approximation of the observed rise profile, which yields

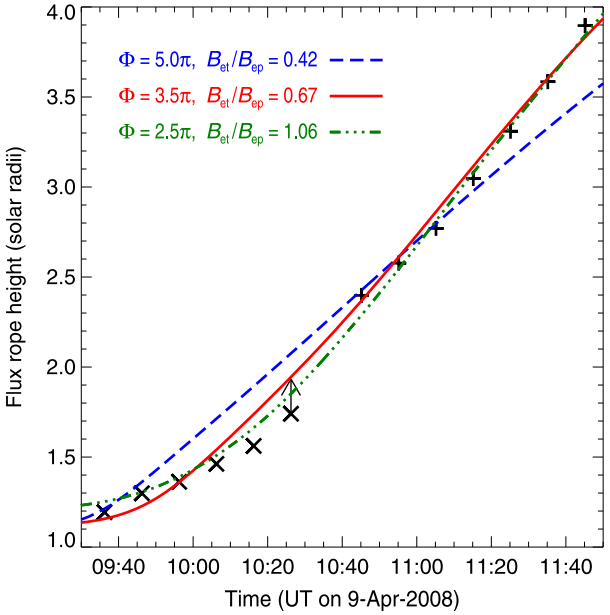

Figure 8 Comparison of the observed and simulated rise profiles of the flux rope apex, using the same scaling of lengths in the simulations as in Figure 6 and a start time of the eruption at 08:48:00 UT. EUVI and COR1 data from Paper I are plotted using the same symbols as in Figure 6. The 5π, 3.5π, and 2.5π runs of Figures 3 – 5 are scaled to these data assuming Alfvén velocities $V_{A0} = 420$ km s^{-1}, 550 km s^{-1}, and 560 km s^{-1}, respectively.

a plausible value of 560 km s^{-1} for the Alfvén velocity. The match is slightly worse in comparison to the 3.5π run because the curve does not reach the height of the first COR1 data point. Reducing V_{A0}, and adjusting the start time, allows for a nearly perfect match of the COR1 data, similar to the 3.5π run, but this moves the simulation curve, which already runs above all EUVI data points, further away from the measurements in this height range, so that the overall match is degraded.

The origin of the difference lies in the tendency of the torus instability to spread the main upward acceleration of the flux across a larger height range than the helical kink instability, which can be clearly seen in Figure 8. The height range for the torus instability is small only if the field in the source volume of the eruption decreases very rapidly with distance from the flux rope position (see Figure 1 in Kliem and Török, 2006), *i.e.*, in very compact active regions of high field strength, especially in quadrupolar ones. Since AR 10989 was already rather diffuse by the time of the eruption, there is no justification to make the initial configuration in the simulations more compact for a better fit of the rise profile by the kink-stable configuration.

3.4. Implications for the 9 April 2008 Eruption

Based on the good quantitative agreement of the simulated rotation and rise profiles with the observations, Sections 3.1, 3.2 and 3.3 yield the following picture. The rotation profile in the height range $h \lesssim 20\, h_0 \approx 1.5\, R_\odot$ above the photosphere is well matched by a strongly kink-unstable case ($\Phi = 5\pi$), a weakly kink-unstable case ($\Phi = 3.5\pi$), and a kink-stable case ($\Phi = 2.5\pi$) if a shear field of appropriate strength is included in each of them. At greater heights, $h \approx (20-30)\, h_0 \approx (1.5-2.3)\, R_\odot$, the comparison yields a clear indication against the kink-stable case, which enters this range with an accelerated rotation, while the observed rotation levels off. The kink-stable case also requires a considerably stronger initial perturbation, lifting the flux rope apex into the torus-unstable range of heights, *i.e.*, to $h \gtrsim 2.6\, h_0 = 0.2\, R_\odot$, a value not supported by the observations. In comparison, the accelerated

rise of the kink-unstable cases in our simulation series starts essentially from $h_0 = 0.077\ R_\odot$, relatively close to the observed onset height of $(0.05 - 0.06)\ R_\odot$. The shear field required by the kink-stable case is comparable to the external poloidal field, $B_{\rm et}/B_{\rm ep} = 1.06$. In a bipolar region, this corresponds to a similar distance between the main polarities along and across the PIL, which is not supported by AR 10989 as long as its magnetic structure could be discerned in the approach to the limb (see Figure 4 in Paper I). The rise profile rules out the strongly kink-unstable case and yields a further indication against the kink-stable case, albeit only a weak one. Both the observed shape of the flux rope as a whole and the observed angles between individual threads and the rope axis can be approximately reproduced by all three model systems, but the overall match is best for the weakly kink-unstable case (Figures 3, 4 and 5). This is substantiated by Figure 9, where we plot the sets of field lines for this and for the kink-stable case which were found to match the observations closest, out of many different sets that were considered.

The shape of the erupting flux rope's magnetic axis in the considered event is not sufficiently well defined by the observations to allow a clear discrimination between the three considered cases based on this property alone. Note that for other events it has proven to be decisive. For example, the shape of the two erupting filaments modeled in Török and Kliem (2005) could be matched only if an initial average twist of 5π was assumed, not with a twist of 4π.

Overall, we conclude that both strongly kink-unstable and kink-stable configurations can be excluded with a high degree of certainty, leaving a weakly kink-unstable initial configuration as the most likely source of the Cartwheel event. This configuration allows to reproduce the event with observationally supported values for several key parameters (flux rope length, distance of the main flux concentrations, initial orientation) and with plausible assumptions for the magnetic structure (flux rope in a simple bipolar active region) and for the remaining free parameters (twist and shear-field strength).

Regardless of how definite the rejection of the other two cases is considered to be, the rotation of the erupting flux was primarily caused by a shear field (Isenberg and Forbes, 2007). Weaker contributions came from the relaxation of twist (most likely by a weak helical kink instability) and from reconnection with the ambient field.

4. Discussion

The major simplifying assumptions adopted for the modeling in this paper include

i) the neglect of the initial mainly axial propagation of the prominence,
ii) the neglect of any asymmetry and complexity introduced by the large-scale overlying field, and
iii) the assumption of a well-defined, coherent flux rope (*i.e.*, the Titov–Démoulin model).

We discuss these here to assess their potential influence on the results. We also compare our results with other recent relevant work.

While the initial propagation of the prominence introduced an asymmetry and, therefore, definitely had the potential to produce some rotation, we expect that it could not contribute strongly because the propagation was approximately along the flux holding the prominence. This does not principally change the magnetic configuration and the Lorentz forces which dominate the acceleration of plasma in the low-beta corona.

The effects belonging to category ii) are likely to be relevant primarily at considerable heights. AR 10989 was a relatively isolated region of simple, bipolar structure, and this

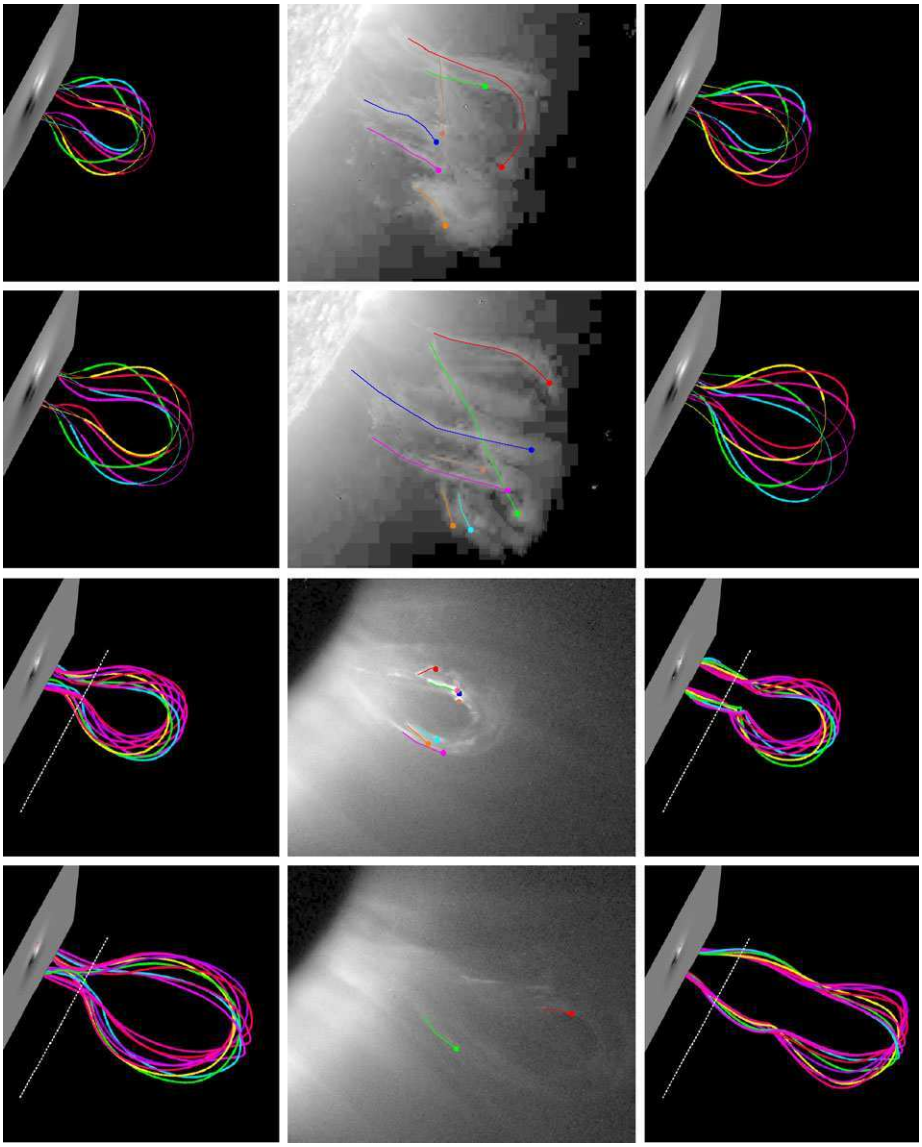

Figure 9 Comparison of simulated and observed flux rope shapes for the kink-stable run ($\Phi = 2.5\pi$, $B_{et}/B_{ep} = 1.06$; left panels) and the weakly kink-unstable run ($\Phi = 3.5\pi$, $B_{et}/B_{ep} = 0.67$; right panels) in our parametric search which best match the observed rotation and rise profiles in their entirety. The STEREO images from Figure 1 are supplemented by an additional image at 10:26 UT from Paper I. For both runs, some experimenting with the field line selection was performed until also the observed shape was matched best. This yielded a flux bundle running slightly under the apex point of the rope's magnetic axis for the kink-stable run, as in Figure 5, and a flux bundle enclosing the axis for the kink-unstable run.

holds also for its dispersed phase as long as it could be followed in the approach to the limb. The potential-field source-surface extrapolation of the photospheric field in Paper I shows that the large-scale coronal field associated with the polar fields and the heliospheric current

sheet began to dominate already at heights $h \gtrsim 0.3\ R_\odot$ above the photosphere, where the horizontal field direction nearly reversed. The force by the field component along the line between the flux rope legs pointed in the direction of a clockwise rotation above this height, opposite to the force low in the corona. However, the shear field above $\sim 0.3\ R_\odot$ was weaker than the shear field in the core of the active region by more than an order of magnitude, so that it could efficiently counteract the continuing, oppositely directed force by the shear field at low heights, and the angular momentum of the already rotating flux rope, only by acting across a considerably larger height range. This is consistent with the fact that the possible weak reverse rotation occurred only at $h > 1.5\ R_\odot$ above the photosphere. Thus, the rotation caused by the shear field and twist inside the bipolar active region (at $h < 0.3\ R_\odot$) must have been dominant factors for the rotation in the height range up to $\sim 1.5\ R_\odot$ modeled here. We cannot exclude that the saturation of the rotation would have occurred at a greater height if the horizontal field had not changed its direction above the active region, however, this weakens only one of the three main arguments against the kink-stable configuration summarized in Section 3.4. The saturation of the rotation profile, at a very similar height, was also seen in another erupting quiescent filament (Bemporad, Mierla, and Tripathi, 2011; see their Figure 5).

The effect of the heliospheric current sheet is expected to become important only at even larger heights. Otherwise, the rotation would not have shown the saturation near $h \sim 1.5\ R_\odot$ and the possible subsequent slight reverse rotation; rather the continuation of the rotation to the value of $\approx 150°$ found at 13 $R_\odot$ would have proceeded already in the COR1 height range.

The assumption that erupting flux in CMEs takes the structure of a flux rope is strongly supported by all available observations. Quantitative differences to our modeling must occur when initial flux ropes of different structure are used. These are not likely to be substantial if only details of the structure differ. The helical kink mode is known to not overly depend on the details of the current channel's radial structure. This can be seen, for example, from the similar instability thresholds found in Mikic, Schnack, and van Hoven (1990), Baty and Heyvaerts (1996), Török, Kliem, and Titov (2004), and Fan and Gibson (2003) although flux ropes with and without a net current and with straight and arched geometries were investigated. Flux ropes with hollow current channels have recently been found to be representative of filament channels which have undergone substantial amounts of flux cancellation (*e.g.*, Su *et al.*, 2011). It is conceivable that their less compact current distribution leads to smaller rotations than the Titov–Démoulin equilibrium with the same twist. This will be a subject of future study. On the other hand, we believe that a strongly kink-unstable configuration of this type would likely still not match the observed rise profile. The structure and strength of the external poloidal and toroidal field components do not depend upon the details of the flux rope structure, so that two arguments against the kink-stable configuration, which are based on the required initial lifting and on the ratio of $B_{\rm et}$ and $B_{\rm ep}$, would likely still apply.

An overlying current sheet (Birn, Forbes, and Schindler, 2003) may be of stronger influence, but we have argued above that this was not the case for the considered event at the low coronal heights modeled in this paper.

The situation likely changes if the flux rope is far less coherent than the Titov–Démoulin configuration (Green, Kliem, and Wallace, 2011), especially if it is split (Bobra, van Ballegooijen, and DeLuca, 2008). The investigation how such complex cases might change our conclusions must be left for future work.

The comparison of the flux rope rotations found in this paper with the rotation in the simulation of a breakout CME by Lynch *et al.* (2009) suggests a strong dependence upon the existence of a flux rope at the onset of the eruption. In that simulation, the inflating flux of a

continuously sheared arcade did not show any significant rotation up to a heliocentric height of $\approx 2\ R_\odot$. Flare reconnection commenced at this point, which progressively transformed the inner part of the arcade into a growing flux rope. The flux rope immediately began to rotate. This process was monitored until the core of the rope reached a heliocentric height of $\approx 3.5\ R_\odot$. Throughout this range, the rope showed a linear increase of its rotation angle with height, and the twist in the rope stayed below the threshold of the helical kink mode. The addition of poloidal flux by flare reconnection was largely complete in the middle of the height interval. The rotation profile in this model differs principally from the data presented here, even if only the height range $> 2\ R_\odot$ is considered, where a flux rope did exist. This suggests that the presence of a flux rope at the onset of the eruption was a key feature of the Cartwheel event.

An interesting result of our parametric study is that the erupting flux rope did always show some amount of rotation, even in the shear-free, kink-stable case included in Figure 6. We expect this to be generally valid if coherent force-free flux ropes are considered as the initial condition, because such ropes always possess twist. An untwisted flux tube, known as a Theta pinch, requires a radial pressure gradient to attain equilibrium. This is not available if the plasma beta is very small, as expected for the lower coronal part of active regions. Whether the observations support the occurrence of rotation in essentially all events does not yet seem to be clear. For example, Muglach, Wang, and Kliem (2009) report that only about 10 cases of unambiguous rotation in erupting filaments not very far from Sun center could be identified in the EUV observations by the EIT instrument (Delaboudinière *et al.*, 1995) for the whole Solar Cycle 23. However, many cases of only moderate rotation may remain undetected in such data, due to the projection on the plane of the sky. Thernisien, Howard, and Vourlidas (2006) find that only 13 out of 34 events fitted by a geometric flux rope model showed rotations (between 5° and 90°) at distances up to 30 $R_\odot$, but the rotation angles obtained through this method appear to possess a considerable uncertainty (Thernisien, Vourlidas, and Howard, 2009). Yurchyshyn, Abramenko, and Tripathi (2009) report 101 partial and full halo CMEs which show a very broad distribution of the difference between the estimated initial and final orientations in the same distance range; these angles do not show a clustering at zero degrees. However, the latter two investigations yield the net effect of rotation in the corona and in the inner solar wind where the heliospheric current sheet likely dominates. If the fraction of non-rotating events is relatively small, then a plausible explanation is that other processes counteract the rotation by twist relaxation and the shear field in these cases, for example reconnection with the ambient field. If the fraction is large, then such nearly exact cancellation of rotations is unlikely to be the primary explanation. The implication would then be that the current distribution in the erupting field is often less compact or less coherent than in the Titov–Démoulin flux rope, including the possibility that a flux rope does not yet exist at the onset of the eruption.

5. Conclusions

Our parametric study of force-free flux ropes which erupt from simple bipolar source regions with no overlying current sheet and rotate about the direction of ascent yields the following conclusions.

i) Both the force by an external shear-field component $B_{\rm et}$ (Isenberg and Forbes, 2007) and the relaxation of twist Φ (*e.g.*, Török, Berger, and Kliem, 2010), are potentially very significant contributors to the rotation.

ii) For parameters typical of CME source regions, in particular if the sources of the external stabilizing field (usually the main flux concentrations next to the PIL) have a smaller distance than the footpoints of the erupting flux, the shear field yields the dominant contribution to the rotation for a wide range of shear-field strengths. The relaxation of twist remains the weaker contributor under these conditions, even if the twist is sufficiently high to trigger the helical kink instability. However, since twist always exists in force-free flux ropes, it always causes at least some rotation. Strong rotations ($\gtrsim 90°$) can be produced by the twist alone, but only for considerably larger distances between the sources of the external stabilizing field than typically observed.

iii) The rotation in low-beta plasma is not guided by the changing orientation of the PIL with height. For the geometrical conditions typical of CME source regions, it is opposite in direction (see Appendix A).

iv) For a given chirality of the configuration, the external shear field and the twist cause flux rope rotation in the same direction, which is clockwise for right-handed field and counterclockwise for left-handed field if seen from above.

v) The two processes are related to each other when considered in terms of magnetic helicity. Both convert initial twist helicity of the flux rope into writhe helicity. The same total rotation, and rotation profiles which are very similar in a substantial part of the total height range of rotation, result in a range of $B_{\rm et}$–Φ combinations.

vi) The rotation due to twist relaxation tends to act mainly low in the corona, in a height range up to only a few times the distance between the footpoints of the erupting flux. The rotation by the shear field tends to be distributed across a larger height range.

vii) The mere fact that erupting flux rotates does not by itself imply that the helical kink instability occurred. Inferring this instability requires deriving a supercritical twist or finding features incompatible with rotation driven (nearly) exclusively by the shear field, like more than one helical turn of the erupting structure, approaching legs, or a rotation exceeding $\approx 130°$ at coronal heights (in the absence of other contributions). A somewhat smaller rotation angle may be sufficient if the rotation profile and the shear-field strength in the source region can be estimated (see Appendix B).

viii) The relative contributions to the total rotation by the shear field and by the twist can be disentangled by comparing both the observed rotation and rise profiles with the corresponding curves from a model, since these profiles possess a different dependence upon the $B_{\rm et}$–Φ parameter combination. The resulting estimate for the twist allows one to judge the occurrence of the helical kink instability.

ix) Magnetic reconnection contributes only weakly (much less than the shear field) to the total rotation in the simple bipolar source regions considered.

From the comparison with the simulation of rotating flux in Lynch *et al.* (2009) we conclude:

x) The rotation profile differs strongly between configurations with and without a flux rope at the onset of the eruption.

The comparison with the stereoscopic observations and three-dimensional reconstruction of the erupting prominence in the 9 April 2008 "Cartwheel CME" additionally shows the following.

xi) The rotation profile obtained in Paper I from the stereoscopic reconstruction of STEREO data is equally well reproduced by our model up to heights $\approx 1.5\ R_\odot$ above the photosphere for a range of Φ–$B_{\rm et}$ combinations which include a strongly kink-unstable case ($\Phi = 5\pi$, $B_{\rm et}/B_{\rm ep} = 0.42$), a weakly kink-unstable case ($\Phi = 3.5\pi$, $B_{\rm et}/B_{\rm ep} = 0.67$),

and a kink-stable case ($\Phi = 2.5\pi$, $B_{et}/B_{ep} = 1.06$). However, the strongly kink-unstable configuration is ruled out by the simultaneous consideration of the rise profile, and several features of the kink-stable model argue strongly against this configuration. These are the implied high value of the shear field, the rotation profile at greater heights, and the unrealistic start height of the unstable rise of $\approx 0.2\ R_\odot$. Hence, the occurrence of a weak helical kink instability in the Cartwheel event is very likely.

Our results add to the complexity of the phenomenon of flux rope rotation in eruptions which is already known from investigations that focused on the influence of reconnection (*e.g.*, Jacobs *et al.*, 2009; Shiota *et al.*, 2010; Cohen *et al.*, 2010; Thompson, 2011; Lugaz *et al.*, 2011). An overall very complicated dependence on several parameters and on the structure of the ambient field is revealed. Thus, the quantitative prediction of the rotation is a difficult task. The parametric study performed here indicates for simple bipolar source regions that the strength of the external shear field is the primary parameter determining the total rotation. The flux rope twist and the height profile of the external poloidal field are of relatively minor importance as long as they stay in the typical ranges indicated by the observations. We did not yet study a possible influence of the height profile of the external shear field. The external shear field of filament channels may be estimated to sufficient precision from a simple linear force-free field extrapolation. It will be worth testing whether numerical modeling starting from such fields, embedded in current-free outer field, yields rotations in agreement with observations of eruptions from bipolar source regions.

Several investigations indicate that erupting flux ropes align with the heliospheric current sheet in the course of their interplanetary propagation (*e.g.*, Bothmer and Schwenn, 1998; Yurchyshyn, 2008; Paper I). This suggests that the coronal rotation merely decides whether a parallel or an antiparallel alignment will result at 1 AU. However, since complex physics is involved and since rotations on the order of 90° may not be rare, the quantitative study of the effects that determine the rotation in the corona remains of high scientific and practical interest.

Acknowledgements We acknowledge the careful reading of the manuscript and the constructive comments by the referee. BK acknowledges support by the DFG, the STFC, and by NASA through Grant NNX08AG44G. TT's work was partially supported by the European Commission through the SOTERIA Network (EU FP7 Space Science Project No. 218816) and by the NASA HTP and LWS programs. WTT's work was supported by NASA Grant NNG06EB68C.

Appendix A: Influence of the Coronal Polarity Inversion Line

There are quite strong indications that CMEs align with the heliospheric current sheet in the course of their propagation, *i.e.*, with the PIL in the solar wind (see references in Section 5). This leads to the question whether the PIL guides the rotation of erupting flux ropes also in the corona. Here the PIL formed by the external field, due to sources outside the flux rope, must be considered. We use "CPIL" to denote this structure in the corona, where $\beta < 1$. The heliospheric current sheet and the CPIL differ in two properties of relevance here. First, in the solar wind $\beta > 1$, so that the pressure gradient is generally dominant over the Lorentz force, while the opposite is true in the corona. Second, the heliospheric current sheet is the location of pressure gradients and Lorentz forces, while the CPIL generally lacks both. In the low-beta corona, currents are induced at separatrix surfaces, or at quasi-separatrix layers, if the equilibrium is perturbed or lost. The CPIL generally does not coincide with these structures. Therefore, the CPIL should not influence the rotation of erupting flux ropes in this height range.

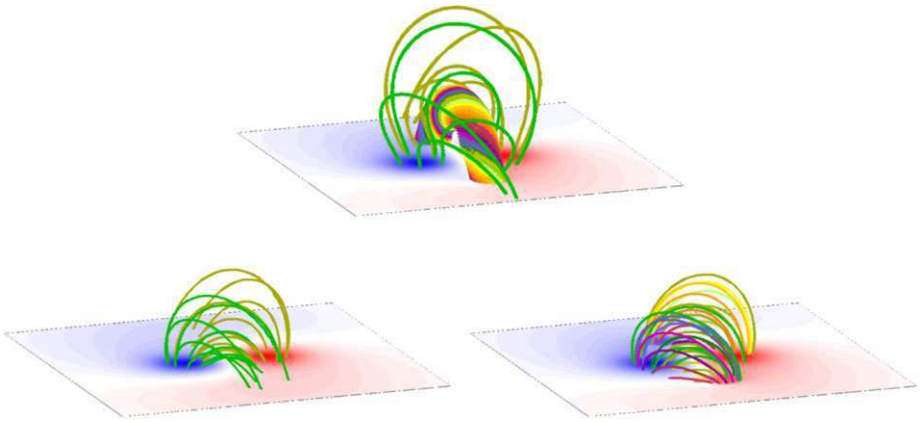

Figure 10 Visualization of the weakly kink-unstable modified Titov–Démoulin equilibrium ($\Phi = 3.5\pi$, $B_{et}/B_{ep} = 0.67$; Figures 2 and 4) whose eruption characteristics match the observations of the Cartwheel CME best (top panel) and of the corresponding external field (bottom left) and potential field (bottom right). The magnetogram and field lines starting in the photospheric flux concentrations are shown.

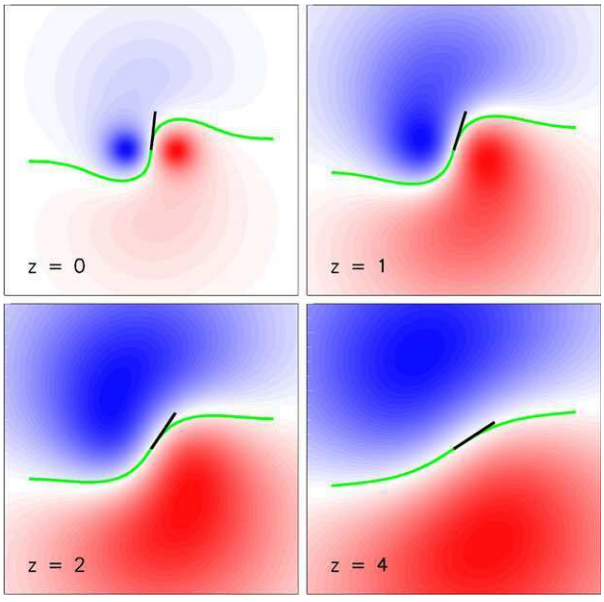

Figure 11 Orientation of the PIL in the external field of the configuration shown in Figure 10 at the position of the flux rope and different heights. The orientation is indicated by a black line.

Figure 10 shows the initial equilibrium of the weakly kink-unstable run which matches the Cartwheel event best, the corresponding external field, and the potential field that results when the full magnetogram of the vertical field component of the equilibrium, $B_z(x, y, 0)$, is extrapolated into the volume above. The full magnetogram includes the contributions from the flux rope, which are excluded from the external field. The CPIL of this configuration at the photospheric and three coronal levels is shown in Figure 11. The CPIL changes its orientation in a clockwise sense if one goes upward, but the unstable flux rope rotates in a counterclockwise direction, since it is left handed. The clockwise changing CPIL orientation results from the dominance of the external toroidal field, B_{et}, over the external poloidal

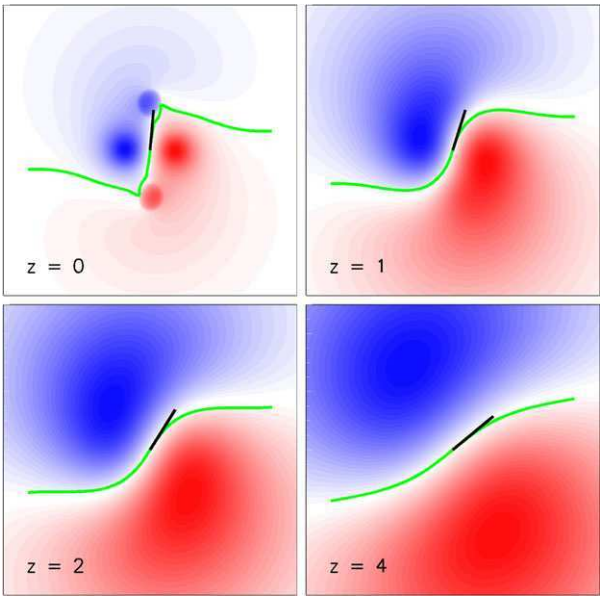

Figure 12 Same as Figure 11 for the potential field of the configuration shown in Figure 10.

field, $B_{\rm ep}$, at great heights. This situation can typically be expected to occur because $B_{\rm et}$ typically has a larger spatial scale than $B_{\rm ep}$ (set by the distance between the sources in the photosphere). The important fact here is that the CPIL does not appear to have any significant influence on the rotation of the flux rope in the zero-beta simulations performed in this paper. For the reasons given above, this is valid also if other height profiles of $B_{\rm et}$ or $B_{\rm ep}$ lead to a different profile of the CPIL orientation with height.

We also consider the approximation of the true CPIL by the PIL in a potential-field extrapolation of the full photospheric magnetogram, $B_z(x, y, 0)$. In practice, it is difficult or even impossible to determine the external field. This requires the determination of the coronal currents through a nonlinear force-free extrapolation from a vector magnetogram. The former is still difficult to carry out and the latter may not be available. The PIL in the potential field extrapolated from the magnetogram of the weakly kink-unstable configuration in Figure 10 is shown in Figure 12. Its orientation *vs.* height is very similar to the behavior of the true CPIL. This supports the conclusions drawn in Paper I from a potential-field source-surface extrapolation for the source region of the Cartwheel CME.

Appendix B: Inferring the Helical Kink Instability

Finally, we consider the question how the occurrence of the helical kink instability can be inferred in spite of the typical dominance of shear-field-driven rotation above KI-driven rotation in CMEs, which is suggested by the present study. The writhing of erupting flux loops into a helical shape, *i.e.*, the apex rotation, has often been regarded to be a clear indication if not a proof of the occurrence, but from Isenberg and Forbes (2007), Lynch *et al.* (2009), and the present investigation it is obvious that the apex rotation, by itself, is not conclusive in general. To infer the occurrence unambiguously, one needs to find a supercritical amount of twist or features incompatible with the shear-field-driven writhing (if other rotation processes can be excluded, such as reconnection with the ambient field and the straightening from a strong initial S shape).

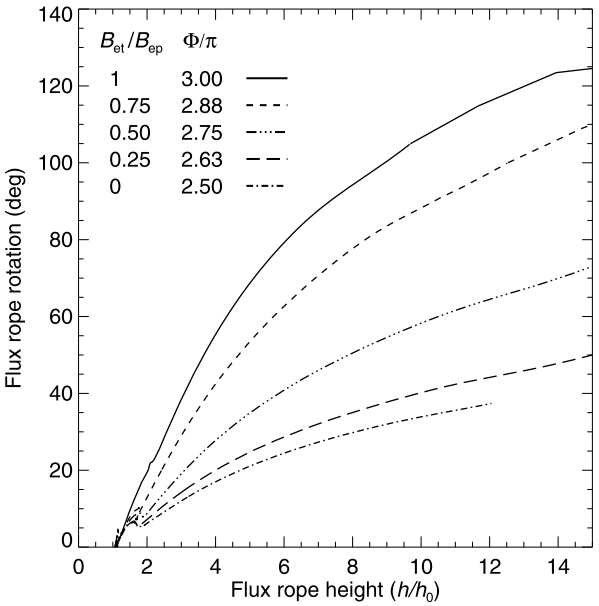

Figure 13 Flux rope rotation *vs.* normalized apex height for a range of B_{et}–Φ combinations that yield stable flux rope equilibria near the threshold of the helical kink mode. The normalized sunspot semi-distance is $L = 0.83$ as in Figure 6. Observed rotation profiles which exceed the rotations plotted here for the same ratio B_{et}/B_{ep} indicate the occurrence of the helical kink.

The twist can be calculated from extrapolated magnetic fields, or be estimated from the observation of twisted substructures or from parametric studies like the one performed here. The second option yields indications for supercritical values only rarely (*e.g.*, Vrsnak, Ruzdjak, and Rompolt, 1991; Romano, Contarino, and Zuccarello, 2003), and the other options are computationally demanding. In particular, the extrapolation must at least be based on the nonlinear force-free field assumption (Leka, Fan, and Barnes, 2005; Valori *et al.*, 2010), which additionally requires a vector magnetogram.

Features incompatible with purely shear-field-driven rotation are approaching flux rope legs, an apex rotation considerably exceeding 90°, and the development of more than one helical turn in the shape of the erupting structure as a whole (*i.e.*, in its axis). The shear field causes the flux rope legs to lean aside in opposite direction perpendicular to its own direction, *i.e.*, to move away from each other. The legs of a kinking flux rope approach each other if the initial twist exceeds $\approx 6\pi$ (Kliem *et al.*, 2010). However, this will occur only rarely, due to the high twist required.

The rotation resulting from the opposite bending of the flux rope legs by the shear field would always stay below 90° if there were no further contributing effect. As discussed in Section 3.1, an additional contribution from the relaxation of the twist in a force-free flux rope does, in fact, always exist, even if the twist is insufficient to trigger the helical kink. This contribution reaches $\sim 40°$ if the shear field is very small (Figure 6) (and the sunspot distance stays within the typical range observed; see Section 3.2 and Figure 7). It is expected to remain smaller when a larger shear field reduces the twist through its own enforced rotation. Consequently, a rotation exceeding 130° (in the absence of other contributions) is a strong indication that the helical kink instability occurred.

Figure 6 also shows that the instability is indicated already by somewhat smaller values of the rotation if the angle rises quickly at low heights. To quantify this, we have computed the family of rotation curves shown in Figure 13, which all represent initial conditions stable against the helical kink mode but close to its marginal stability boundary in the B_{et}–Φ plane. Any rotation profile lying clearly above the corresponding curve in this figure, with the shear

field set to the value in the eruption's source region, indicates a contribution by the helical kink. This requires estimating the shear field $B_{\rm et}$ and the footpoint distance, $2D_{\rm f}$, of the erupting flux. A linear force-free field extrapolation yields a reliable estimate of the shear field, and the consideration of the distances of the main polarities along and across the PIL may yield a rough estimate in source regions of relatively simple structure.

These considerations are valid only as long as no other processes contribute to the rotation, which could be reconnection, the straightening from a strong initial S shape, and, at heights above the corona, the alignment with the heliospheric current sheet. The straightening from an initial S shape can simply be subtracted from the total rotation angle before the comparison with the plots in Figure 13 is made.

Since the shear-field-driven writhing is caused by antiparallel forces on the legs, the erupting flux rope's axis will never develop more than one helical turn. Some eruptions indicate more than one turn, from an S shape of one or both legs (*e.g.*, Ji *et al.*, 2003; Maričić *et al.*, 2004) or from a very writhed shape as a whole (*e.g.*, Romano, Contarino, and Zuccarello, 2003). The helical kink instability can be inferred in such cases from the shape of the structure (Török and Kliem, 2005; Kumar *et al.*, 2012).

References

Amari, T., Aly, J., Mikic, Z., Linker, J.: 2010, *Astrophys. J. Lett.* **717**, L26.
Aulanier, G., Török, T., Démoulin, P., DeLuca, E.E.: 2010, *Astrophys. J.* **708**, 314.
Baty, H., Heyvaerts, J.: 1996, *Astron. Astrophys.* **308**, 935.
Bemporad, A., Mierla, M., Tripathi, D.: 2011, *Astron. Astrophys.* **531**, A147.
Birn, J., Forbes, T.G., Schindler, K.: 2003, *Astrophys. J.* **588**, 578.
Bobra, M.G., van Ballegooijen, A.A., DeLuca, E.E.: 2008, *Astrophys. J.* **672**, 1209.
Bothmer, V., Schwenn, R.: 1998, *Ann. Geophys.* **16**, 1.
Chen, P.F., Shibata, K.: 2000, *Astrophys. J.* **545**, 524.
Cohen, O., Attrill, G.D.R., Schwadron, N.A., Crooker, N.U., Owens, M.J., Downs, C., Gombosi, T.I.: 2010, *J. Geophys. Res.* **115**(A14), 10104.
Delaboudinière, J., Artzner, G.E., Brunaud, J., Gabriel, A.H., Hochedez, J.F., Millier, F., Song, X.Y., Au, B., Dere, K.P., Howard, R.A., Kreplin, R., Michels, D.J., Moses, J.D., Defise, J.M., Jamar, C., Rochus, P., Chauvineau, J.P., Marioge, J.P., Catura, R.C., Lemen, J.R., Shing, L., Stern, R.A., Gurman, J.B., Neupert, W.M., Maucherat, A., Clette, F., Cugnon, P., van Dessel, E.L.: 1995, *Solar Phys.* **162**, 291.
Fan, Y., Gibson, S.E.: 2003, *Astrophys. J. Lett.* **589**, L105.
Gibson, S.E., Fan, Y.: 2008, *J. Geophys. Res.* **113**(A12), 9103.
Green, L.M., Kliem, B., Wallace, A.J.: 2011, *Astron. Astrophys.* **526**, A2.
Green, L.M., Kliem, B., Török, T., van Driel-Gesztelyi, L., Attrill, G.D.R.: 2007, *Solar Phys.* **246**, 365.
Howard, R.A., Moses, J.D., Vourlidas, A., Newmark, J.S., Socker, D.G., Plunkett, S.P., Korendyke, C.M., Cook, J.W., Hurley, A., Davila, J.M., Thompson, W.T., Cyr, O.C.S., Mentzell, E., Mehalick, K., Lemen, J.R., Wuelser, J.P., Duncan, D.W., Tarbell, T.D., Wolfson, C.J., Moore, A., Harrison, R.A., Waltham, N.R., Lang, J., Davis, C.J., Eyles, C.J., Mapson-Menard, H., Simnett, G.M., Halain, J.P., Defise, J.M., Mazy, E., Rochus, P., Mercier, R., Ravet, M.F., Delmotte, F., Auchere, F., Delaboudiniere, J.P., Bothmer, V., Deutsch, W., Wang, D., Rich, N., Cooper, S., Stephens, V., Maahs, G., Baugh, R., Mcmullin, D.: 2008, *Space Sci. Rev.* **136**, 67.
Isenberg, P.A., Forbes, T.G.: 2007, *Astrophys. J.* **670**, 1453.
Jacobs, C., Roussev, I.I., Lugaz, N., Poedts, S.: 2009, *Astrophys. J. Lett.* **695**, 171.
Ji, H., Wang, H., Schmahl, E.J., Moon, Y.-J., Jiang, Y.: 2003, *Astrophys. J. Lett.* **595**, 135.
Kliem, B., Török, T.: 2006, *Phys. Rev. Lett.* **96**, 255002.
Kliem, B., Titov, V.S., Török, T.: 2004, *Astron. Astrophys. Lett.* **413**, L23.
Kliem, B., Linton, M.G., Török, T., Karlický, M.: 2010, *Solar Phys.* **266**, 91.
Kumar, P., Cho, K.-S., Bong, S.-C., Park, S.-H., Kim, Y.H.: 2012, *Astrophys. J.* **746**, 67.
Landi, E., Raymond, J.C., Miralles, M.P., Hara, H.: 2010, *Astrophys. J.* **711**, 75.
Leka, K.D., Fan, Y., Barnes, G.: 2005, *Astrophys. J.* **626**, 1091.
Lugaz, N., Downs, C., Shibata, K., Roussev, I.I., Asai, A., Gombosi, T.I.: 2011, *Astrophys. J.* **738**, 127.
Lynch, B.J., Antiochos, S.K., Li, Y., Luhmann, J.G., DeVore, C.R.: 2009, *Astrophys. J.* **697**, 1918.

Maričić, D., Vršnak, B., Stanger, A.L., Veronig, A.: 2004, *Solar Phys.* **225**, 337.
Martin, S.F.: 2003, *Adv. Space Res.* **32**, 1883.
Mikic, Z., Linker, J.A.: 1994, *Astrophys. J.* **430**, 898.
Mikic, Z., Schnack, D.D., van Hoven, G.: 1990, *Astrophys. J.* **361**, 690.
Muglach, K., Wang, Y., Kliem, B.: 2009, *Astrophys. J.* **703**, 976.
Panasenco, O., Martin, S., Joshi, A.D., Srivastava, N.: 2011, *J. Atmos. Solar-Terr. Phys.* **73**, 1129.
Patsourakos, S., Vourlidas, A.: 2011, *Astron. Astrophys.* **525**, A27.
Romano, P., Contarino, L., Zuccarello, F.: 2003, *Solar Phys.* **214**, 313.
Rust, D.M., Kumar, A.: 1996, *Astrophys. J. Lett.* **464**, L199.
Rust, D.M., LaBonte, B.J.: 2005, *Astrophys. J. Lett.* **622**, L69.
Sakurai, T.: 1976, *Publ. Astron. Soc. Japan* **28**, 177.
Shiota, D., Kusano, K., Miyoshi, T., Shibata, K.: 2010, *Astrophys. J.* **718**, 1305.
Su, Y., Surges, V., van Ballegooijen, A., DeLuca, E., Golub, L.: 2011, *Astrophys. J.* **734**, 53.
Terradas, J., Arregui, I., Oliver, R., Ballester, J.L.: 2008, *Astrophys. J. Lett.* **678**, L153.
Thernisien, A., Vourlidas, A., Howard, R.A.: 2009, *Solar Phys.* **256**, 111.
Thernisien, A.F.R., Howard, R.A., Vourlidas, A.: 2006, *Astrophys. J.* **652**, 763.
Thompson, W.T.: 2011, *J. Atmos. Solar-Terr. Phys.* **73**, 1138.
Thompson, W.T., Kliem, B., Toeroek, T.: 2009, In: *AAS/Solar Physics Division Meeting* **40**, 21.11.
Thompson, W.T., Kliem, B., Török, T.: 2012, *Solar Phys.* **276**, 241.
Titov, V.S., Démoulin, P.: 1999, *Astron. Astrophys.* **351**, 707.
Török, T., Kliem, B.: 2003, *Astron. Astrophys.* **406**, 1043.
Török, T., Kliem, B.: 2005, *Astrophys. J. Lett.* **630**, L97.
Török, T., Kliem, B.: 2007, *Astron. Nachr.* **328**, 743.
Török, T., Kliem, B., Titov, V.S.: 2004, *Astron. Astrophys. Lett.* **413**, L27.
Török, T., Berger, M.A., Kliem, B.: 2010, *Astron. Astrophys.* **516**, A49.
Valori, G., Kliem, B., Török, T., Titov, V.S.: 2010, *Astron. Astrophys.* **519**, A44.
Vourlidas, A., Colaninno, R., Nieves-Chinchilla, T., Stenborg, G.: 2011, *Astrophys. J. Lett.* **733**, L23.
Vrsnak, B., Ruzdjak, V., Rompolt, B.: 1991, *Solar Phys.* **136**, 151.
Williams, D.R., Török, T., Démoulin, P., van Driel-Gesztelyi, L., Kliem, B.: 2005, *Astrophys. J. Lett.* **628**, L163.
Yurchyshyn, V.: 2008, *Astrophys. J. Lett.* **675**, L49.
Yurchyshyn, V., Abramenko, V., Tripathi, D.: 2009, *Astrophys. J.* **705**, 426.

Solar Phys (2013) 284:17–46
DOI 10.1007/s11207-012-0215-2

The Solar Connection of Enhanced Heavy Ion Charge States in the Interplanetary Medium: Implications for the Flux-Rope Structure of CMEs

N. Gopalswamy · P. Mäkelä · S. Akiyama · H. Xie · S. Yashiro · A.A. Reinard

Received: 21 April 2012 / Accepted: 10 December 2012 / Published online: 9 January 2013

Abstract We investigated a set of 54 interplanetary coronal mass ejection (ICME) events whose solar sources are very close to the disk center (within $\pm 15^\circ$ from the central meridian). The ICMEs consisted of 23 magnetic-cloud (MC) events and 31 non-MC events. Our analyses suggest that the MC and non-MC ICMEs have more or less the same eruption characteristics at the Sun in terms of soft X-ray flares and CMEs. Both types have significant enhancements in ion charge states, although the non-MC structures have slightly lower levels of enhancement. The overall duration of charge-state enhancement is also considerably smaller than that in MCs as derived from solar wind plasma and magnetic signatures. We find very good correlation between the Fe and O charge-state measurements and the flare properties such as soft X-ray flare intensity and flare temperature for both MCs and non-MCs. These observations suggest that both MC and non-MC ICMEs are likely to have a flux-rope structure and the unfavorable observational geometry may be responsible for the appearance of non-MC structures at 1 AU. We do not find any evidence for an active region expansion resulting in ICMEs lacking a flux-rope structure because the mechanism of producing high charge states and the flux-rope structure at the Sun is the same for MC and non-MC events.

Keywords Coronal mass ejections · Flares · Flux rope · Magnetic cloud, charge state

Flux-Rope Structure of Coronal Mass Ejections
Guest Editors: N. Gopalswamy, T. Nieves-Chinchilla, M. Hidalgo, J. Zhang, and P. Riley

N. Gopalswamy (✉)
NASA Goddard Space Flight Center, Greenbelt, MD, USA
e-mail: nat.gopalswamy@nasa.gov

P. Mäkelä · S. Akiyama · H. Xie · S. Yashiro
The Catholic University of America, Washington, DC, USA

A.A. Reinard
NOAA Space Weather Prediction Center, Boulder, CO, USA

1. Introduction

The occurrence of high charge states of elements such as oxygen, silicon, and iron at times of low solar wind kinetic temperature was attributed to heated flare plasma long ago (Bame *et al.*, 1979). The low solar wind kinetic temperature is one of the indicators of coronal mass ejections (CMEs) in the interplanetary space (*i.e.*, ICMEs). Bame *et al.* (1979) also suggested that "magnetic bottles" might carry the flare-heated plasma with the higher charge-state ions created due to the higher temperature of the flare plasma low in the corona. Furthermore, they compared synthetic ion spectra with observations and estimated a source temperature of 3.4 MK for O ions and 2.9 MK for Fe ions. The charge states are unchanged when the plasma, containing heavy elements (solar wind or CME), leaves the corona because the recombination time scale far exceeds the expansion time scale of the plasma. This is known as the freezing-in concept (Hundhausen, Gilbert, and Bame, 1968). Thus the charge states of heavy elements observed in the interplanetary medium preserve the coronal conditions at which they originated. Henke *et al.* (1998, 2001) suggested that the ICMEs with enhanced charge state have the magnetic-cloud (MC) structure, which is the same as the flux rope. In this paper we use MC and flux rope interchangeably, but observationally, MCs are characterized by enhanced magnetic field with a smooth rotation of one of the components transverse to the Sun–Earth direction, and low values of proton temperature or plasma beta (Burlaga *et al.*, 1981). Henke *et al.* (1998) analyzed 56 ICMEs observed by the *Ulysses* spacecraft and found that those with MC structure have an increased O^{7+}/O^{6+} ratio (herein after referred to as O^7O^6) with respect to the ambient solar wind whereas non-MC ICMEs seldom show such enhancement. Furthermore, the events with enhanced O^7O^6 also showed an enhancement in the Fe^{12+}/Fe^{11+} charge-state ratio. Aguilar-Rodriguez, Blanco-Cano, and Gopalswamy (2006) considered a much larger sample of ICMEs (28 MCs and 117 non-MCs) observed at Sun–Earth L1 by the ACE spacecraft and confirmed the result of Henke *et al.* (1998, 2001). Reinard (2008) examined the source location and flare size at the Sun and the *in-situ* density and temperature for a large numbers of ICMEs and found that ICMEs may have a basic structure consisting of a core (or cores) of magnetic-cloud plasma surrounded by an envelope with weaker charge-state signatures. These studies indicate that the presence of enhanced charge states observed in interplanetary space is likely due to a CME at the Sun that is magnetically connected to a flare. In light of these findings, we are left to question why some ICMEs exhibit a flux-rope structure, while others do not.

How do we distinguish between MC and non-MC ICMEs? The simplest classification is to lump all the ICMEs that do not have flux-rope structure as non-MC ICMEs. These are also referred to as non-cloud ICMEs or ejecta. The flux rope is thought to be formed out of a sheared arcade via reconnection during the eruption process and is observed as an MC in the interplanetary medium (see *e.g.*, Qiu *et al.*, 2007). On the other hand, it is possible that a set of loops from an active region on the Sun can simply expand into the IP medium and can be detected as an enhancement in the magnetic field with respect to the ambient medium (Gosling, 1990) without any flux-rope structure. Clearly, the magnetic signatures will be different in the two cases. A spacecraft passing through the flux rope will see a smooth rotation of the magnetic field throughout the body of the ICME, while the expanded loop system will show no rotation. If we take just the IP observations, we may be able to explain MCs as flux ropes and non-MCs as expanding loops. However, they should show different charge-state characteristics because of the different solar origins. The flux-rope forms during the flare process and hence is accessed by the hot plasma resulting in high charge states inside MCs when observed at 1 AU. Expanding loops on the other hand should not have high charge states because there may not be any reconnection involved (Uchida

et al., 1992). Under such a scheme, the non-MC events should not have a flare association and the associated CME, if any, is expected to be generally slow. However, all the non-MC ICMEs are also associated with flares and the corresponding white-light CMEs are fast and wide (Gopalswamy *et al.*, 2010a, 2010b).

An alternative approach is to understand the difference between MCs and non-MCs as a direct consequence of the observing geometry. According to this view, all ICMEs are flux ropes, but they do not appear so if they are not heading towards the observer (Marubashi, 1997; Owens *et al.*, 2005; Gopalswamy, 2006a; Riley *et al.*, 2006). Gopalswamy (2006a) and Gopalswamy *et al.* (2009a) compared the solar source locations of MCs, non-MCs, and shocks not followed by discernible ejecta ("driverless" shocks) and found a distinct pattern. As one moves from the disk center to the limb, one first encounters mostly MCs, then mostly non-MC ICMEs, and finally the driverless shocks. MCs are associated with CMEs heading directly towards Earth. The shocks without discernible ejecta are due to CMEs ejected almost orthogonal to the Sun–Earth line. This gives a clue that the CMEs ejected at intermediate angles may turn up as non-MCs for an observer along the Sun–Earth line. So, the viewing angle may be the reason that certain ICMEs do not have a flux-rope structure. Gopalswamy *et al.* (2009a) noted two major exceptions to this pattern.

i) There are some driverless shocks from the disk center. This was shown to be due to the deflection of CMEs by nearby coronal holes.
ii) There are too many non-MC ICMEs that have their solar sources close to the disk center, contradicting the geometrical approach.

In this paper, we examine these disk-center events in more detail to see if the geometrical approach still holds and why they deviate from the geometrical hypothesis.

Two Coordinated Data Analysis Workshops (CDAWs) addressed this central question: Do all ICMEs contain a flux-rope structure? Solar and interplanetary data from space- and ground-based instruments were assembled and analyzed during the CDAWs to answer this question. Data analyses were combined with modeling near the Sun as well as in the interplanetary medium to check if observing geometry is responsible for not observing the flux-rope structure. In this paper, we make use of the charge-state information of ICMEs to address the question of flux-rope structure of CMEs.

2. Data Description

The CDAW events were extracted from the list of shock-driving ICMEs published in Gopalswamy *et al.* (2010a) in the electronic supplement (http://iopscience.iop.org/0004-637X/710/2/1111/fulltext/apj_710_2_1111.tables.html) with the criterion that the solar sources of the ICMEs should be within the longitude range $\pm 15°$. There are 59 events meeting this criterion, but further examination revealed that the solar sources had to be revised in five cases reducing the number of events to 54, of which 23 are MCs and the remaining 31 are non-MC ICMEs. According to the geometrical hypothesis, all the CMEs originating from close to the disk center should be observed as a flux rope by an Earth observer. Obviously this is not the case. We attempt to find out why using flare and CME observations near the Sun and charge-state observations of ICMEs near Earth.

This paper uses two measures of charge states in analyzing MC and non-MC structures. The first one is the average Fe charge state denoted by Q_{Fe} (see Lepri *et al.*, 2001) and is given by $\sum n_i Q_i$, where n_i is the density of the Fe ions with charge state Q_i (the subscript i numbers the Fe charge states present in the plasma). The density is normalized such that $\sum n_i = 1$. As Lepri *et al.* (2001) showed, $Q_{\mathrm{Fe}} \sim 11$ corresponds to the

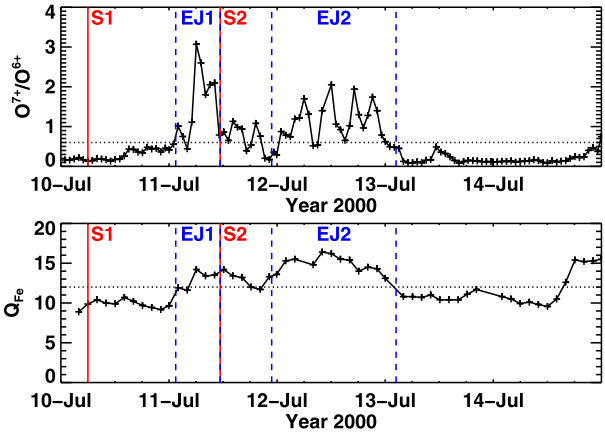

Figure 1 Charge-state time profile of the 10 and 11 July 2000 ICME events with O^7O^6 ratio (top) and Q_{Fe} (bottom) plotted with a 1-h and 2-h time resolution, respectively. The boundaries derived from plasma and magnetic signatures of the ICMEs (EJ1, EJ2) are denoted by the vertical dashed lines. EJ1 happens to be second largest O^7O^6 event among the non-MC events. The leading shocks (S1, S2) of the ICMEs are denoted by the vertical solid lines. Clearly the two ICMEs are very close to each other, with the second shock already inside the first ICME. In fact, the sheath of the second shock consists mostly of the first CME.

slow solar wind. $Q_{Fe} > 11$ indicates hotter plasma typically found inside ICMEs (see also Lepri and Zurbuchen, 2004). The second measure of charge states is the ratio of densities of O ions ionized seven and six times (O^{7+} and O^{6+}), denoted by O^{7+}/O^{6+} or simply O^7O^6 (Henke *et al.*, 1998, 2001; Aguilar-Rodriguez, Blanco-Cano, and Gopalswamy, 2006; Reinard, 2005, 2008). The average value of O^7O^6 is ~ 0.3 in the slow solar wind (see Zhao, Zurbuchen, and Fisk, 2009 for the range of O^7O^6 values in different types of solar wind). We take twice this value (0.6) as the threshold to indicate ICME plasma. In previous papers, slightly larger values (0.7, 0.8 or 1) have been used to minimize the number of false identifications (see *e.g.*, Reinard, 2008). Here we are concerned with maximizing the number of enhancements in identified ICMEs, so 0.6 is justified.

A typical ICME event analyzed in this paper has a leading shock followed by an interval of ICME identified from plasma and magnetic (plasmag) signatures. For identifying an ICME, the primary characteristic used is the depressed solar wind proton temperature (a plasma signature). In addition, magnetic signatures such as enhanced field strength and smooth rotation of the vertical or azimuthal component are used to identify a MC event. We also refer to MC events as flux-rope events. Figure 1 shows the O^7O^6 and Q_{Fe} values for two events that occurred in quick succession, taken from the CDAW list. The sheath following the shock S1 has low charge-state values, similar to the upstream plasma. At the first ICME (EJ1) boundary, the charge states climb to large values. The peak value of O^7O^6 in the EJ1 interval is 3.1 and the average value is 1.6. Similarly, the peak and average values of Q_{Fe} are 14.2 and 12.9, respectively. All these numbers are above the threshold values set above and hence represent the hot plasma from the flare site that entered into the ICME when it formed near the Sun. The rear boundary of EJ1 is not clear, because it coincides with the second shock S2 driven by the second ICME (EJ2). Both O^7O^6 and Q_{Fe} show enhancements in the downstream of S2. According to the charge-state signature, the rear boundary of EJ1 should be around 18 UT on 11 July 2000, which is only a few hours ahead of EJ2. Clearly, S2 has penetrated into EJ1 and the sheath of S2 is mostly EJ1. In this case, the sheath of S2 will have enhanced charge state, but it is not the property of the sheath; the origin is the

preceding ICME. The Q_{Fe} is enhanced and relatively smooth within EJ2 with peak and average values of 16.4 and 14.9, respectively. On the other hand, the O^7O^6 is fluctuating with at least five peaks, which seems to be a characteristic of many O^7O^6 events. The duration of O^7O^6 is also slightly lower than that of Q_{Fe}. The actual duration of O^7O^6 is even smaller if we exclude intervals when O^7O^6 drops below 0.6. The peak and average O^7O^6 are 2.0 and 1.0, respectively. Following this procedure, we compute the following quantities for each of the CDAW events: i) the peak and average Q_{Fe} within the ICME interval identified by plasmag signatures, ii) the peak and average O^7O^6 within the ICME interval, iii) the charge-state duration ignoring the rear boundary of ICME (similar to EJ1 in Figure 1, where the charge-state signatures extend beyond the EJ1 boundary obtained from plasmag signatures), and iv) the duration within the ICME boundary when the charge state remains above the threshold. We analyze these six parameters for MC and non-MC events taken separately and as a combined set.

We also compile the properties of CMEs associated with the ICMEs as observed by the *Large Angle and Spectrometric Coronagraph* (LASCO) on board the *Solar and Heliospheric Observatory* (SOHO) and listed in the on line CME catalog (http://cdaw.gsfc.nasa.gov/CME_list, see Yashiro *et al.*, 2004; Gopalswamy *et al.*, 2009b). We specifically use CME speed, apparent angular width, and acceleration without correcting for projection effects.

Finally, we compile the flare properties of the CMEs such as the flare size given by the peak soft X-ray flux ($W\,m^{-2}$) in the 1 – 8 Å GOES channel (used to classify the flare importance). Since the flare temperature is an important quantity that decides the heavy-ion charge state in the flare plasma that enters into the CMEs, we compute it using the method outlined by Garcia (1994). The method involves obtaining the ratios of soft X-ray flux in the 1 – 8 Å and 0.5 – 4 Å GOES channels to get the temperature. A software routine is available in SolarSoft, which we make use of in obtaining the flare temperature.

Table 1 shows the list 59 events selected for the two CDAW sessions. Column 1 gives the original serial number of the events used in the CDAW sessions. The date and time of the interplanetary shocks are given in columns 2 and 3. Information on the shock-driving ICMEs is given in columns 4 – 8 with the ICME type (MC for magnetic clouds and EJ (ejecta) for non-MC ICMEs in column 4) followed by the start and end times. Information on the white-light CMEs identified in the field of view of the SOHO/LASCO telescopes is given in columns 9 – 13 with date and time followed by CME properties (width, speed, and acceleration). Columns 14 – 16 give the solar source information of the CMEs: flare onset, flare location (heliographic coordinates), and the soft X-ray flare importance. If the associated flare is not seen above the background, the onset time of the associated eruptive prominence (EP) or post-eruption arcade (PEA) is listed with EP or PEA entered in the flare importance column. Column 17 indicates whether the event is associated with type II bursts in the metric and/or longer wavelength domains. Columns 18 – 23 give the Fe charge-state information: Q_{Fe} peak, Q_{Fe} averaged over the event duration, duration of Q_{Fe} enhancement from the first plasmag boundary until the charge state drops to the background level (dur1), cumulative duration of Q_{Fe} enhancement above the threshold value of 12 (dur2), ratio of dur1 to the plasmag duration of the ICME, and the ratio of dur2 to the plasmag duration. Columns 24 – 29 give the same information as in columns 18 – 23, but for O^7O^6. We analyze these data to understand the difference between MC and EJ-associated CMEs and how the results can be used to find out if all CMEs have a flux-rope structure.

3. Analysis and Results

Several results can be directly extracted from Table 1.

Table 1 List of ICMEs originating from the disk center with the solar source and 1 AU charge-state information.

Event #	Shock		ICME					CME					Solar source			Type II?	Charge states											
	Date	Time [UT]	Type	Start		End		Onset		Width [deg]	Speed [km s^{-1}]	Acc. [m s^{-2}]	Onset [UT]	Loc	Flare Imp.		Q_{Fe}						O^{+7}/O^{+6}					
				Date [mm/dd]	Time [UT]	Date [mm/dd]	Time [UT]	Date	Time [UT]								Peak	Ave	Dur1	Dur2	Fr1	Fr2	Peak	Ave	Dur1	Dur2	Fr1	Fr2
1	1997/01/10	00:52	MC	01/10	05:18	01/11	02:18	01/06	15:10	360	136	4.1	14:54	S18E06	A1.1	Yes	–	–	–	–	–	–	–	–	–	–	–	–
2	1997/05/15	01:15	MC	05/15	09:06	05/16	01:06	05/12	05:30	360	464	− 15.0	04:42	N21W08	C1.3	Yes	–	–	–	–	–	–	–	–	–	–	–	–
3	1997/12/10	04:30	EJ+	12/11	03:45	12/11	09:00	12/06	10:27	223	397	9.0	10:00	N45W10	EP	Yes	–	–	–	–	–	–	–	–	–	–	–	–
4	1998/05/03	17:00	EJ?	05/03	19:00	05/04	00:00	05/01	23:40	360	585	8.0	22:36	S18W05	M1.2	No	10.6	9.2	14.0	–	2.80	–	0.6	0.4	–	–	–	–
5	1998/05/04	02:00	EJ+	05/04	10:00	05/05	01:15	05/02	14:06	360	938	− 28.8	13:31	S15W15	X1.1	Yes	15.6	15.5	4.0	4.0	0.26	0.26	0.7	0.6	15.0	9.0	0.98	0.59
6	1998/06/25	16:10	EJ+	06/26	02:00	06/26	19:00	06/22	07:34	119	278	6.7	05:56	S28W35	EP	No	12.3	11.6	–	–	–	–	0.6	0.4	–	–	–	–
7	1998/11/07	08:00	EJ+	11/07	22:00	11/08	02:00	11/04	07:54	360	523	19.6	07:13	N17W01	C1.6	No	11.8	11.0	37.5	–	9.37	–	0.7	0.5	1.0	1.0	0.25	0.25
8	1998/11/13	01:40	EJ+	11/13	04:30	11/14	10:15	11/09	18:18	190	325	2.6	17:03	N15W05	C2.5	Yes	13.4	10.9	2.0	2.0	0.07	0.07	0.5	0.3	–	–	–	–
9	1999/04/16	11:10	MC	04/16	20:18	04/17	21:18	04/13	03:30	261	291	0.2	01:45	N16E00	B4.3	No	14.9	13.3	27.9	22.0	1.12	0.88	1.0	0.6	16.0	11.0	0.64	0.44
10	1999/06/26	19:25	EJ+	06/27	21:30	06/28	01:00	06/24	13:31	360	975	32.4	12:04	N29W13	C4.1	Yes	12.2	11.9	8.0	2.0	2.29	0.57	0.4	0.3	–	–	–	–
11	1999/07/02	00:23	EJ+	07/02	06:00	07/02	07:30	06/29	19:54	360	560	− 8.9	19:07	S14E01	M1.6	Yes	–	–	–	–	–	–	0.3	0.3	–	–	–	–
12	1999/08/08	17:44	MC	08/09	10:48	08/10	15:48	08/02	07:26	189	286	− 0.5	06:12	N13E24	EP	?	11.1	10.3	–	–	–	–	0.9	0.6	–	–	–	–
13	1999/09/22	12:00	EJ+	09/22	21:00	09/24	02:00	09/20	06:06	360	604	− 14.5	03:58	S20W05	EP	No	15.6	14.5	44.0	30.0	1.52	1.03	1.3	0.8	28.0	21.0	0.97	0.72
14	1999/10/21	02:13	EJ+	10/21	18:30	10/22	05:50	10/18	00:06	240	144	3.5	23:22	S30E15	C1.2	No	14.4	13.0	14.0	8.0	1.24	0.71	0.8	0.5	1.0	3.0	0.09	0.26
15	2000/01/22	00:23	EJ+	01/22	18:00	01/23	02:00	01/18	17:54	360	739	− 7.1	17:07	S19E11	M3.9	Yes	10.8	10.5	4.0	–	0.50	0.00	0.6	0.3	7.0	–	0.88	–
16	2000/02/20	21:00	MC	02/21	09:48	02/22	13:18	02/17	21:30	360	728	− 22.9	20:17	S29E07	M1.3	Yes	16.8	14.6	41.9	22.0	1.52	0.80	1.3	0.6	17.0	13.0	0.62	0.47
17	2000/07/10	06:00	EJ+	07/11	01:30	07/11	11:22	07/07	10:26	360	453	10.8	06:24	N04E00	EP	No	14.2	12.9	14.1	6.0	1.43	0.61	3.1	1.6	18.0	9.0	1.82	0.91
18	2000/07/11	11:22	EJ+	07/11	22:48	07/13	02:25	07/08	23:50	161	483	− 7.2	22:58	N18W12	C4.0	Yes	16.4	14.9	26.1	24.0	0.94	0.87	2.0	1.0	22.0	21.0	0.80	0.76
19	2000/07/15	14:18	MC	07/15	21:06	07/16	09:54	07/14	10:54	360	1674	− 96.1	10:03	N22W07	X5.7	Yes	17.7	16.9	15.8	12.0	1.23	0.94	2.0	1.2	17.0	10.0	1.33	0.78
20	2000/07/26	18:58	EJ+	07/27	08:28	07/27	19:35	07/23	05:30	181	631	− 20.4	04:11	S13W05	EP	No	–	–	–	–	–	–	1.1	0.8	9.0	10.0	0.81	0.90
21	2000/07/28	06:39	MC	07/28	21:06	07/29	10:06	07/25	03:30	360	528	− 5.8	02:43	N06W08	M8.0	Yes	15.8	12.8	11.9	8.0	0.92	0.62	4.1	1.0	10.0	6.0	0.77	0.46
22	2000/08/10	05:10	EJ+	08/10	19:00	08/11	12:00	08/06	23:06	40	597	− 7.0	22:36	S24W15	?	No	11.1	10.7	–	–	–	–	0.9	0.8	–	–	–	–
23	2000/08/11	18:51	MC	08/12	06:06	08/13	05:06	08/09	16:30	360	702	2.8	15:19	N20E12	EP	No	15.4	13.6	38.2	20.0	1.66	0.87	2.5	0.9	37.0	13.0	1.61	0.57
24	2000/09/17	17:00	MC	09/18	01:54	09/18	15:06	09/16	05:18	360	1215	− 12.3	04:06	N14W07	M5.9	Yes	17.3	15.9	47.9	14.0	3.63	1.06	5.3	2.0	22.0	12.0	1.67	0.91
25	2000/10/05	03:23	EJ+	10/05	13:13	10/07	13:00	10/02	03:50	360	525	− 4.9	02:48	S09E07	C4.1	No	12.7	11.7	37.1	12.0	0.78	0.25	0.6	0.4	–	2.0	–	0.04
26	2000/10/12	22:36	MC	10/13	18:24	10/14	16:54	10/09	23:50	360	527	− 24.2	23:19	N01W14	C6.7	Yes	16.1	14.4	19.8	20.0	0.88	0.89	1.3	0.8	15.0	18.0	0.67	0.80
27	2000/11/06	09:20	MC	11/06	23:06	11/07	18:06	11/03	18:26	360	291	16.4	18:35	N02W02	C3.2	Yes	14.8	12.5	44.0	12.0	2.32	0.63	2.1	0.9	10.0	13.0	0.53	0.68
28	2000/11/26	05:30	EJ+	11/27	05:00	11/28	04:00	11/24	05:30	360	1289	2.1	04:55	N20W05	X2.0	Yes	15.6	13.7	60.0	24.0	2.61	1.04	1.4	0.8	17.0	18.0	0.74	0.78
29	2001/03/03	11:30	EJ+	03/04	04:00	03/05	01:30	02/28	14:50	232	313	1.9	13:22	S17W05	B4.2	No	14.5	12.1	8.0	8.0	0.37	0.37	1.2	0.8	6.0	17.0	0.28	0.79
30	2001/03/22	14:00	EJ+	03/22	22:30	03/23	04:00	03/19	05:26	360	389	− 2.4	04:12	S20W00	PEA	No	9.8	9.7	–	–	–	–	0.4	0.3	–	–	–	–
31	2001/04/11	14:12	EJ+	04/11	22:30	04/12	03:00	04/09	15:54	360	1192	1.3	15:20	S21W04	M7.9	Yes	15.3	15.1	10.0	4.0	2.23	0.89	4.8	1.9	7.0	5.0	1.56	1.11
32	2001/04/11	16:19	MC	04/12	07:54	04/12	17:54	04/10	05:30	360	2411	211.6	05:06	S23W09	X2.3	Yes	16.2	14.6	22.0	8.0	2.20	0.80	1.3	1.0	24.0	9.0	2.40	0.90
33	2001/04/28	05:02	MC	04/29	01:54	04/29	12:54	04/26	12:30	360	1006	21.1	11:26	N20W05	M1.5	Yes	16.7	15.9	48.0	12.0	4.36	1.09	2.0	1.5	47.0	9.0	4.27	0.82
34	2001/08/12	11:10	EJ-	08/13	07:00	08/13	10:00	08/09	10:30	175	479	4.4	08:00	N11W14	PEA	Yes	12.6	11.6	2.0	2.0	0.67	0.67	0.3	0.2	–	–	–	–
35	2001/10/11	16:50	EJ+	10/12	03:30	10/12	08:30	10/09	11:30	360	973	− 41.5	10:46	S28E08	M1.4	Yes	15.1	14.0	6.0	6.0	1.20	1.20	1.7	1.0	2.0	5.0	0.40	1.00
36	2002/03/18	13:13	MC	03/19	22:54	03/20	15:24	03/15	23:06	360	957	− 17.4	22:09	S08W03	M2.2	Yes	13.7	13.7	–	2.0	–	0.12	1.5	1.0	18.0	12.0	1.09	0.73

Table 1 (*Continued*)

Event #[a]	Shock		ICME					CME					Solar source			Type II?	Charge states											
	Date	Time [UT]	Type[b]	Start		End		Onset		Width [deg]	Speed [km s^{-1}]	Acc. [m s^{-2}]	Onset [UT]	Loc	Flare Imp.[c]		Q_{Fe}						O^{+7}/O^{+6}					
				Date [mm/dd]	Time [UT]	Date [mm/dd]	Time [UT]	Date	Time [UT]								Peak	Ave	Dur1[d]	Dur2[e]	Fr1[f]	Fr2[g]	Peak	Ave	Dur1[d]	Dur2[e]	Fr1[f]	Fr2[g]
37	2002/04/17	11:01	MC	04/18	04:18	04/19	02:18	04/15	03:50	360	720	2.1	03:05	S15W01	M1.2	Yes	14.9	14.6	22.0	4.0	1.00	0.18	4.1	2.2	16.0	11.0	0.73	0.50
38	2002/05/11	10:30	EJ+	05/11	13:00	05/11	14:00	05/08	13:50	360	614	78.9	12:58	S12W07	C4.2	No	11.4	11.4	6.0	–	6.01	–	0.3	0.3	4.0	–	4.00	–
39	2002/05/18	19:51	MC	05/19	03:54	05/19	23:24	05/16	00:50	360	600	− 6.6	00:11	S23E15	C4.5	Yes	10.7	10.1	–	–	–	–	0.2	0.1	–	–	–	–
40	2002/05/20	03:40	EJ−	05/20	11:00	05/20	22:00	05/17	01:27	45	461	5.5	00:23	S20E14	EP	No	11.6	11.1	–	–	–	–	0.4	0.2	–	–	–	–
41	2002/05/30	02:15	EJ−	05/30	07:09	05/31	11:20	05/27	13:27	161	1106	3.8	12:36	N22E15	C3.7	No	12.1	11.0	2.0	2.0	0.07	0.07	0.7	0.5	–	3.0	–	0.11
42	2002/07/17	15:50	EJ+	07/18	12:00	07/19	08:10	07/15	21:30	188	1300	− 7.3	21:03	N19W01	M1.8	Yes	–	–	–	–	–	–	1.1	0.6	15.0	9.0	0.74	0.45
43	2002/08/01	05:10	MC	08/01	11:54	08/01	22:36	07/29	12:07	161	222	3.3	10:27	S10W10	M4.7	Yes	15.2	13.5	17.9	12.0	1.67	1.12	2.6	1.3	17.0	10.0	1.59	0.93
44	2003/08/17	13:40	MC	08/18	11:36	08/19	04:24	08/14	20:06	360	378	4.4	17:12	S10E02	C3.8	No	14.3	12.9	37.7	14.0	2.24	0.83	2.1	1.4	37.0	17.0	2.20	1.01
45	2003/10/29	06:00	MC	10/29	08:00	10/30	04:00	10/28	11:30	360	2459	− 105.2	11:00	S16E08	X17.2	Yes	17.0	15.3	60.1	18.0	3.01	0.90	1.2	0.6	34.0	12.0	1.70	0.60
46	2003/10/30	16:20	MC	10/31	02:00	10/31	13:00	10/29	20:54	360	2029	− 146.5	20:37	S15W02	X10.0	Yes	17.3	16.7	48.0	10.0	4.36	0.91	8.5	3.0	45.0	8.0	4.09	0.73
47	2004/01/22	01:10	EJ+	01/22	08:00	01/23	17:00	01/20	00:06	360	965	17.2	23:46	S13W09	C5.5	No	14.2	11.6	13.8	12.0	0.42	0.36	3.1	0.8	21.0	16.0	0.64	0.48
48	2004/07/24	05:32	MC	07/24	12:48	07/25	13:18	07/22	08:30	132	899	− 12.6	07:41	N04E10	C5.3	No	14.5	13.5	52.0	6.0	2.12	0.24	3.2	1.5	50.0	19.0	2.04	0.78
49	2004/11/09	09:05	MC	11/09	20:54	11/10	03:24	11/06	02:06	214	1111	18.8	01:40	N09E05	M3.6	Yes	13.7	13.1	48.0	6.0	7.39	0.92	1.3	0.8	48.0	4.0	7.38	0.62
50	2004/12/11	13:03	EJ+	12/12	12:00	12/13	06:00	12/08	20:26	360	611	− 87.2	19:34	N05W03	C2.5	Yes	13.9	11.4	21.6	6.0	1.20	0.33	0.6	0.4	5.0	–	0.28	–
51	2005/01/16	09:27	EJ+	01/16	14:00	01/17	06:30	01/15	06:30	360	2049	− 30.7	05:54	N16E04	M8.6	Yes	15.1	13.2	34.8	16.0	2.11	0.97	0.8	0.3	–	1.0	–	0.06
52	2005/02/17	21:59	EJ+	02/18	15:00	02/19	08:15	02/13	11:06	151	584	− 13.0	10:28	S11E09	C2.7	Yes	14.6	13.5	14.0	12.0	0.81	0.70	1.2	0.6	5.0	8.0	0.29	0.46
53	2005/05/15	02:19	MC	05/15	05:42	05/15	22:12	05/13	17:12	360	1689	–	16:13	N12E11	M8.0	Yes	16.2	14.7	30.0	18.0	1.82	1.70	3.7	1.6	28.0	17.0	1.70	1.03
54	2005/05/20	03:34	MC	05/20	07:18	05/21	05:18	05/17	03:26	273	449	18.1	02:31	S15W00	M1.8	Yes	16.8	14.7	21.8	18.0	0.99	0.82	2.1	1.0	37.0	18.0	1.68	0.82
55	2005/05/29	09:15	EJ+	05/29	10:15	05/29	14:45	05/26	15:06	360	586	− 1.6	13:10	S11E19	B7.5	?	11.2	11.0	–	–	–	–	0.7	0.4	–	–	–	–
56	2005/07/10	02:56	EJ+	07/10	10:30	07/12	04:00	07/07	17:06	360	683	− 8.7	16:07	N09E03	M4.9	Yes	16.8	13.5	50.0	24.0	1.21	0.58	1.6	0.7	43.0	17.0	1.04	0.41
57	2005/09/02	13:32	EJ+	09/02	19:03	09/03	06:00	08/31	11:30	360	825	42.9	10:26	N13W13	C2.0	Yes	12.6	10.9	2.0	2.0	0.18	0.18	0.5	0.2	–	–	–	–
58	2005/09/15	08:25	EJ+	09/15	14:24	09/15	18:00	09/13	20:00	360	1866	11.5	19:42	S09E10	X1.5	Yes	14.1	14.1	6.0	2.0	1.67	0.56	0.5	0.4	–	–	–	–
59	2006/08/19	10:51	EJ+	08/20	00:00	08/21	15:30	08/16	16:30	360	888	1.9	14:37	S16W08	C3.6	Yes	15.1	14.0	8.0	8.0	0.20	0.20	0.6	0.3	1.0	1.0	0.03	0.03

[a] List of shock-driving ICMEs during the solar cycle 23 (E 15° ≤ source longitude ≤ W15°) (Gopalswamy *et al.*, 2010a).

[b] MC = Magnetic cloud; EJ = Ejecta; the suffix + indicates that it was possible fit a flux rope to the ejecta by adjusting the plasmag boundaries; − indicates it was not possible to fit a flux rope.

[c] EP = Eruptive prominence; PEA = post-eruption arcade.

[d] dur1 = duration of charge-state enhancements, without considering the second plasmag boundary.

[e] dur2 = duration of charge-state enhancements, within the plasmag boundaries.

[f] Fr1 = Fractional duration of charge-state enhancements with respect to the plasmag ICME duration.

[g] Fr2 = Fractional duration of charge-state enhancements within the plasmag boundaries, considering only intervals during which the charge states are above the thresholds.

#6, #12, #55 Dropped from the analysis because the revised solar source location fell outside the longitude criterion.
#11 Dropped from the analysis because this is a known "driverless" event.
#22 Dropped from the analysis because of the uncertainty in identifying the solar source; multiple candidates exist.

i) Out of the 23 MC events, two had Q_{Fe} data gaps. Of the remaining 21 events, 20 had peak $Q_{Fe} \geq 12.0$. In all these cases, there was a definite increase in Q_{Fe} sometime during the MC interval obtained from plasma signatures. Only one event did not have any Q_{Fe} signature (the Q_{Fe} value remained the same before the shock, in the sheath, and in the MC interval). This means, 95 % of the MC events had Q_{Fe} enhancement. Three of the 31 non-MC events had Q_{Fe} data gap. Out of the remaining 28, only six events had $Q_{Fe} < 12.0$, which means 79 % of the non-MC events had Q_{Fe} enhancement. If we use the nominal solar wind value of $Q_{Fe} = 11$, then only three non-MC events had $Q_{Fe} < 11$, indicating ~ 89 % of non-MC events having high charge state. This is only slightly smaller than what was found in the MC events.

ii) The O^7O^6 within the ICME interval exceeded 0.6 in all but one of the MC events, which means 95 % of the MC events had enhanced O charge-state ratio. On the other hand, eight of the non-MC events had O^7O^6 ratio < 0.6, which means about 73 % of the EJ events had enhanced O^7O^6 during the ICME interval. These two results suggest that most of the non-MC events behave similar to the MC events in terms of the enhanced Q_{Fe} and O^7O^6 during the ICME interval.

iii) All but three of the non-MC events have a '+' sign following the 'EJ' symbols in column 3 of Table 1. EJ+ means it was possible to fit a flux rope to the solar wind data of these ICMEs by adjusting the boundary of the ICMEs and using either a cylindrical or toroidal geometry for the flux rope (see Marubashi *et al.*, under preparation, for more details regarding the flux-rope fitting). This result is consistent with the fact that most of the ICMEs have Q_{Fe} and O^7O^6 ratio increases within the ICME interval. Of the three "EJ−" events, two were associated with weak flare signatures and no charge-state enhancement, and the third had marginal charge-state enhancement.

These three events are discussed in more detail in Section 3.5.

3.1. Charge-State Distributions

Figure 2 shows the Q_{Fe} distributions inside all ICMEs in the CDAW list in comparison with MC and non-MC events. The mean (13.2) and median (13.5) Q_{Fe} values of the combined set clearly exceed the nominal slow solar wind value (11). The corresponding values for MC and non-MC events lie above and below those of the combined set. Note also that all the mean and median values are at or above the nominal solar wind values. In the distribution of average Q_{Fe}, the lower mean value results because there are intervals of low charge state during the ICME interval, when Q_{Fe} dropped below the threshold value. In addition, we see that highest Q_{Fe} was attained in MCs, but only in the next bin (17.5 *vs*. 16.5 for peak Q_{Fe} and 16.5 *vs*. 15.5 for average Q_{Fe}).

The distributions of O^7O^6 values follow a pattern similar to the Q_{Fe} values (see Fig. 3). MCs clearly have the highest O^7O^6. When peak O^7O^6 inside the ICME intervals are considered, MC intervals have a mean and median values of 2.54 and 2.1, respectively. The corresponding values for non-MC intervals are 1.12 and 0.7, respectively. Clearly, there is enhancement in both MCs and non-MC events, but higher O^7O^6 ratios are found for MCs. When we consider event-averaged O^7O^6 values, we see that the mean and median values are still above the threshold for MCs, but slightly below for non-MC events. This may be due to the fact that the O^7O^6 values have time structure within the ICME interval (see Figure 1), which might have caused smaller O^7O^6 when averaged over the event. Comparing the Q_{Fe} and O^7O^6 values, we see that Q_{Fe} is a better indicator of ICMEs than O^7O^6.

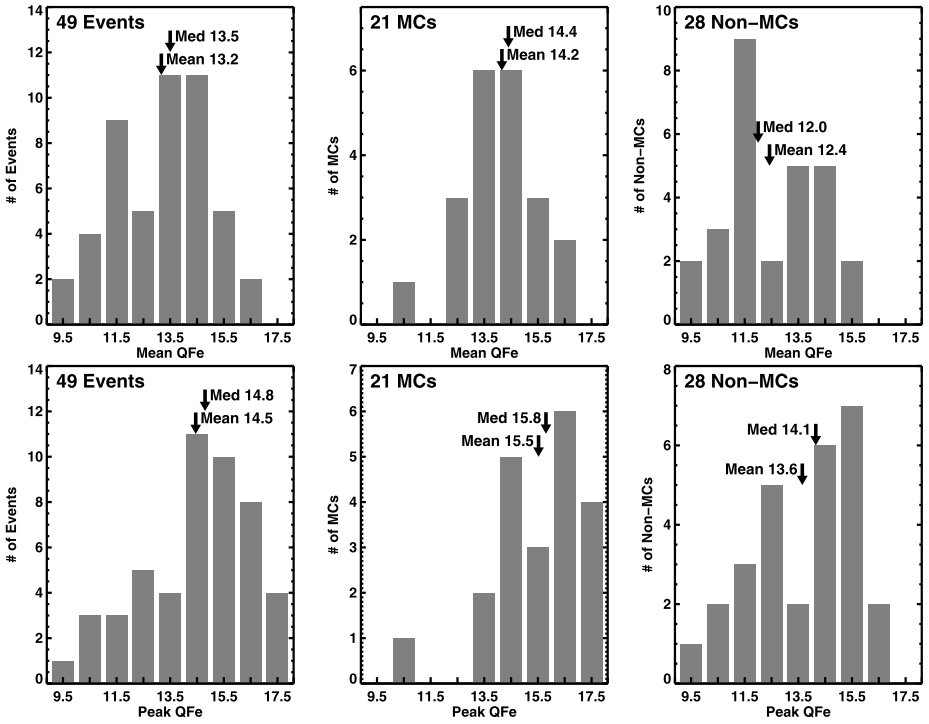

Figure 2 Distribution of Q_{Fe} inside ICMEs using average (top) and peak (bottom) values within the ICME intervals with MCs and non-MC ICMEs distinguished. The mean and median values are shown on the plots.

3.2. Charge State and ICME Durations

The ICME boundaries given in Table 1 were obtained from plasma and magnetic (plasmag) signatures. In order to check the durations of ICME events from the charge states alone, we measured the duration when Q_{Fe} and O^7O^6 remained above the threshold values ignoring the ICME ending time. In other words, if the charge state remained above the threshold, we counted the duration until the values dropped to the threshold values. In some cases the value never came down, so the end time is the end time of the data set. The distributions in Figure 4 show that the mean and median plasmag durations are 16.5 and 16.9 h, respectively for all the ICMEs. The MC and non-MC durations taken separately are not substantially different from these values. However, when Q_{Fe} is used (middle panel of Figure 4), the MC distribution gets much wider and the mean and median values are substantially higher (34.5 and 37.7 h, respectively). The O^7O^6 values also had a wider distribution (bottom panels of Figure 4), but to a less extent (mean and median O^7O^6 values: 23 and 27.7 h, respectively). In non-MC events, the plasmag and Q_{Fe} durations were similar, whereas the O^7O^6 durations were slightly smaller. One problem with these durations is that we have not paid attention to the solar wind structure beyond the rear boundary of the ICMEs. The charge-state enhancement may be due to poor definition of the boundaries from plasmag signatures or due to weaker ICMEs that follow the ICME in question.

We have also not considered the fact that the ICME interval may contain subintervals of low charge states from prominence material (Burlaga *et al.*, 1998; Gopalswamy *et al.*, 1998;

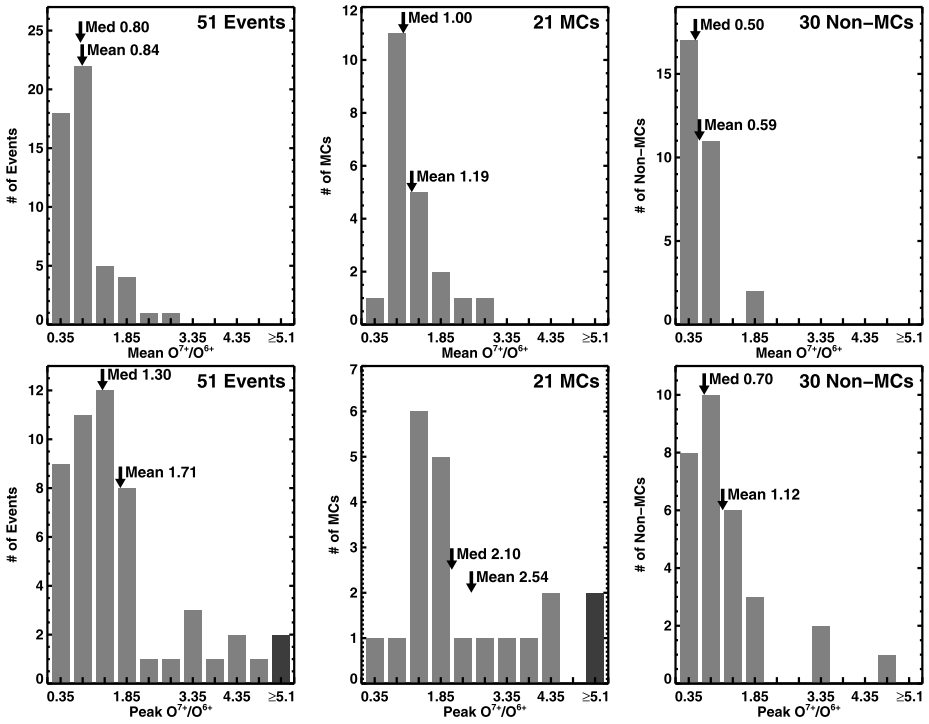

Figure 3 Distribution of O^7O^6 inside ICMEs using average (top) and peak (bottom) values within the ICME intervals with MCs and non-MC ICMEs distinguished. The mean and median values shown on the plots.

Lepri and Zurbuchen, 2010; Gilbert *et al.*, 2012). In order to avoid the uncertainty on the ICME signatures outside of the plasmag boundaries, we computed the duration within the plasma ICME boundaries, by summing up only those subintervals when the charge states remained above the threshold values. As Figure 1 shows, in the 11 July 2000 event, the plasmag duration of EJ2 is ∼ 27.6 h, whereas the Q_{Fe} and O^7O^6 values remain above the threshold only for 24 and 21 h, respectively. The reduction is essentially due to time structure in the charge-state profiles (especially for O^7O^6). This suggests that the ICME may not be uniformly filled with hot plasma, but in patches as in Figure 1 (EJ2). Numerical simulations also suggest such spatial inhomogeneity within the CME flux rope (see, *e.g.*, Lynch *et al.*, 2011). Figure 5 shows the distributions of these reduced durations. Now, the Q_{Fe} and O^7O^6 enhancements have similar durations that are substantially below the plasmag durations given in Figure 4. Just by comparing the mean values, we see that the charge-state durations constitute a fraction of the plasmag duration in the range 0.56 to 0.74. Taking the average durations in columns 23 and 28 in Table 1, we see that the ICMEs are filled with 67 % enhanced Q_{Fe} and 63 % enhanced O^7O^6. This suggests that the hot plasma is filling only part of the CMEs when they are released near the Sun. Furthermore, both the Q_{Fe} and O^7O^6 durations in MCs are generally longer than those in non-MC events. This is significant because this may be related to the fact that the observing spacecraft may not be passing through the nose of the ICME in the case of non-MC events thereby intercepting less number of patches of high charge state. Such an interpretation would be consistent with the non-radial motion of the CMEs that result in non-MC ICMEs.

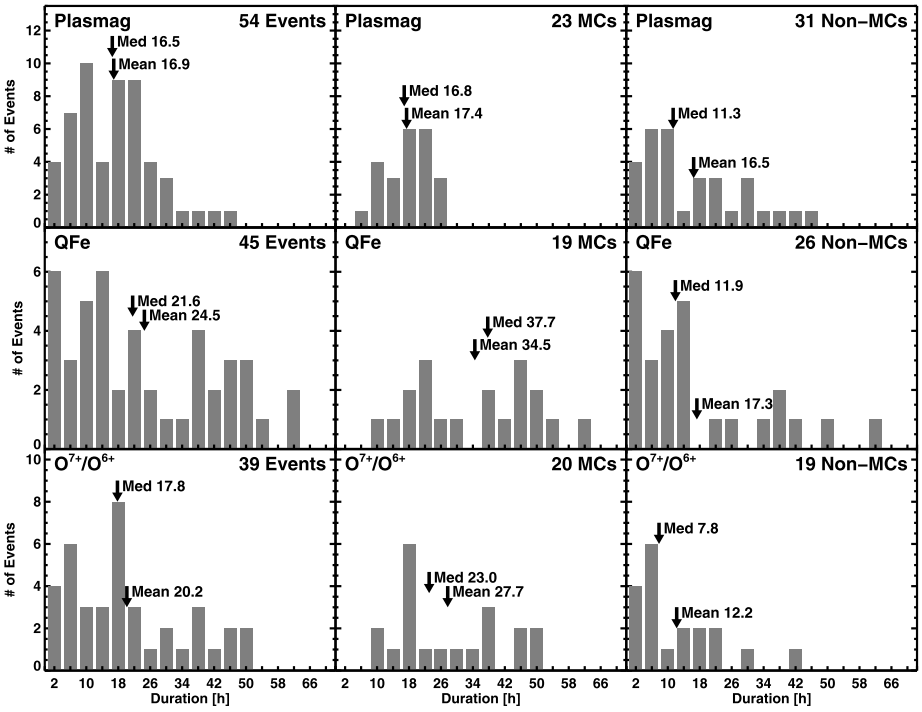

Figure 4 ICME durations based on plasma signatures (top – plasmag), Q_{Fe} (middle), and O^7O^6 (bottom). The mean and median durations (in hours) are noted on the plots.

3.3. Flare Comparisons

Since flare heating is ultimately responsible for the injection of hot plasma into the CMEs, it is imperative that we compare the flare properties of the MC and non-MC events. Figure 6 shows the flare size distributions for MC, non-MC, and the combined set. The mean and median flare size of flares associated with the ICMEs in general fall in the M class suggesting that most of the flares are major ones. When MC and non-MC events are considered separately, we see that the flares of the non-MC events are slightly smaller in size. For MCs, the median size remains in M class whereas it is in C class for the non-MC events. The mean sizes are higher than the median sizes because of the asymmetry, but even there the MC-associated flares are one class higher. Thus there is some indication that we are dealing with slightly weaker flares in the case of non-MC events, although there is a heavy overlap in flare sizes between the two populations. What is really needed in the flare is that the plasma temperature should reach sufficient level to ionize a high enough number of ions to be detected as a charge-state enhancement at 1 AU. To see this, we used the soft X-ray intensities in the two GOES energy channels to obtain the flare temperature. We were able to determine the flare temperature for 22 MC events. There were several weak events identified as eruptive prominence (EP) event or an event with weak post-eruption arcade (PEA). The solar source of one of the CMEs is an eruptive prominence (EP) event (11 August 2000). The others were non-MC events with low soft X-ray flux that we were not able to determine the flare temperature. We discuss these weak events separately in a later subsection.

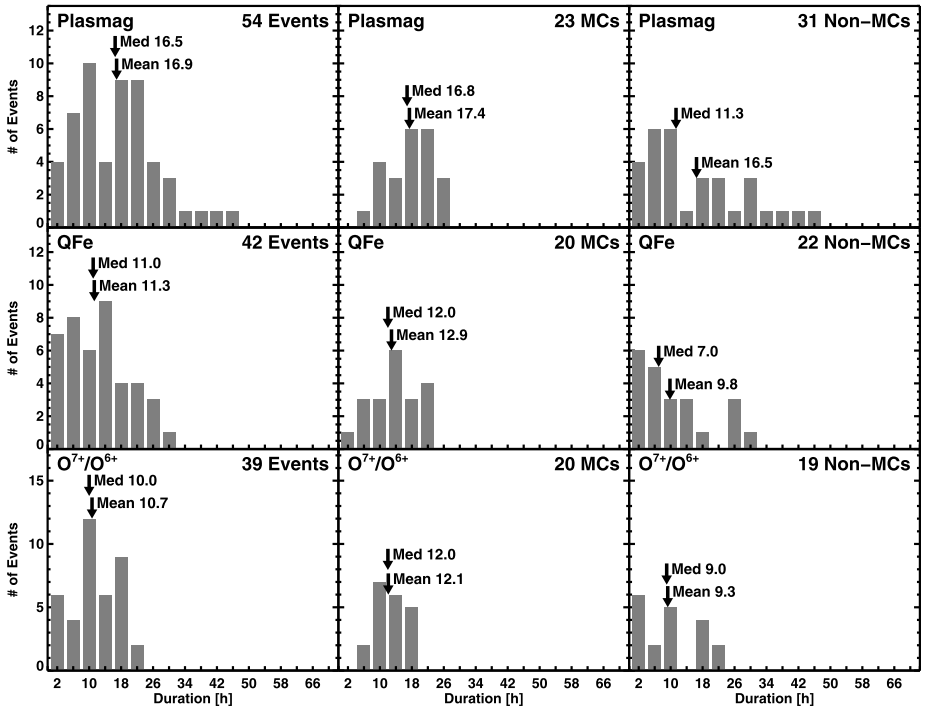

Figure 5 ICME durations based on plasmag signatures (top) compared with reduced durations obtained from Q_{Fe} (middle), and O^7O^6 (bottom) signatures. The mean and median durations (in hours) are noted on the plots.

Figure 6 also shows the flare temperature distributions for 22 MCs and 23 non-MC events. The flare temperatures range from 5 MK to 25 MK. The mean and median flare temperatures are nearly the same for both MC and EJ events. The range of temperatures is more than adequate in producing the observed Q_{Fe} and O^7O^6 enhancements (Bame *et al.*, 1979; Lepri *et al.*, 2001). Thus we conclude that the flares involved in both MC and non-MC events have similar flare sizes and temperatures, suggesting that the availability of hot plasmas is about the same for the two populations.

3.3.1. Correlation Between Flare Size, Flare Temperature and Charge States

Reinard (2005, 2008) reported a general increase in charge-state ratios as a function of the flare size. She grouped the flares into C, M, and X classes and found that both O^7O^6 and Q_{Fe} values were enhanced the greatest in the case of X flares and the least in the case of C-class flares. In our sample, we have even X-class flares, so we use scatter plots between the flare size and temperature on the one hand and the charge states on the other. For the eight EP events, there is no flare information available, so we have not used them. Excluding events with data gaps, we have 20 MC and 23 non-MC events for which we show the scatter plots in Figure 7 between the flare intensity and the peak and event-averaged Q_{Fe} values. The high degree of overlap between the MC and non-MC data points is quite obvious. There is definitely a positive correlation between Q_{Fe} and flare size for all the three cases shown: MC events, non-MC events and for the combined set. The correlation coefficient

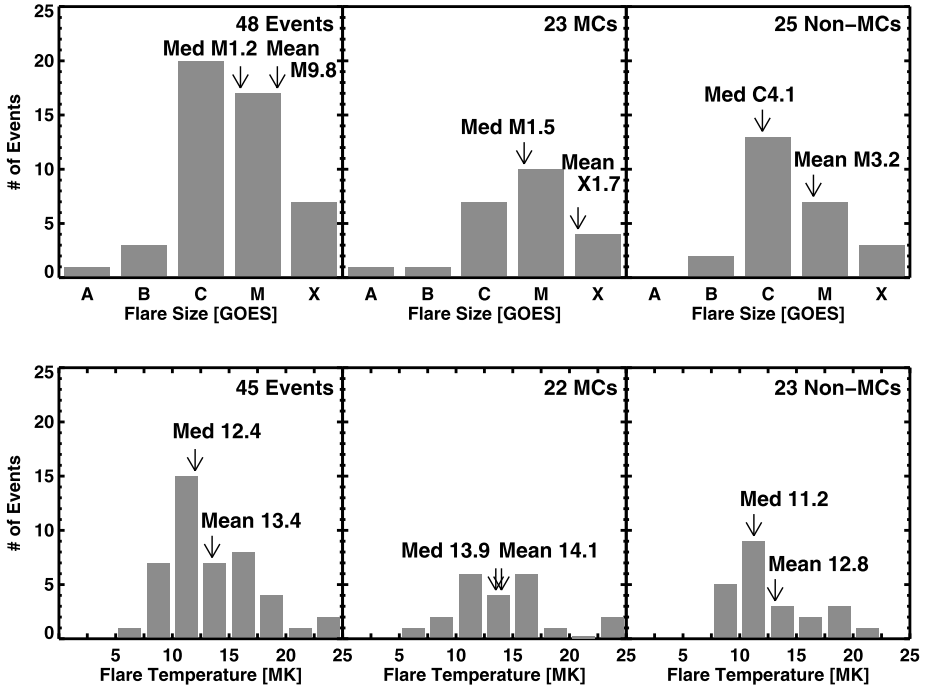

Figure 6 Size and temperature distributions of GOES soft X-ray flares for the selected ICME events with the flares associated with MCs and non-MC ICMEs distinguished. The mean and medium values of the distributions are marked on the plots. For nine events, the soft X-ray intensity was too low to calculate the temperature.

(r) is 0.5 for the peak Q_{Fe} within the ICME interval. The probability (p) that the observed correlation is by chance is very low: 4.9×10^{-4}. When the event-averaged Q_{Fe} is used, the correlation is even better ($r = 0.59$) with $p = 1.9 \times 10^{-5}$. The correlation coefficient is reasonably high for MC events ($r = 0.56$ for peak Q_{Fe} and 0.61 for the averaged Q_{Fe} with p values of 9.0×10^{-3} and 3.2×10^{-3}, respectively). For the non-MC events, the correlation is somewhat weaker ($r = 0.31$ with $p = 0.16$ for peak Q_{Fe} and $r = 0.46$ with $p = 0.027$ for event-averaged Q_{Fe}). In Figure 7 we see some outliers at low values of Q_{Fe}. These outliers could be due to incomplete heating of prominence material or merely because the spacecraft observations did not sample the portion of the ICME that contained enhancements (due to geometrical constraints, *in-situ* observations of charge-state enhancements provide only a lower limit on the initial heating). When the outliers at the bottom of the plot are excluded, the correlation improves significantly: For peak Q_{Fe}, the correlation coefficients are 0.60 ($p = 2.6 \times 10^{-5}$, combined set), 0.58 (7.4×10^{-3}, MC events), and 0.49 ($p = 0.023$, non-MC events). For event-averaged Q_{Fe}, the correlation is even better: 0.68 ($p = 6.8 \times 10^{-7}$, combined set), 0.63 (3.2×10^{-3}, MC events), and 0.63 ($p = 1.7 \times 10^{-3}$, non-MC events). The correlation analysis confirms the flare-size dependence of Q_{Fe}. Furthermore, the high overlap between the data points from MC and non-MC events suggests that they should be similar objects.

The correlation analysis done for O^7O^6 values against flare size are shown in Figure 8. One can see significant overlap between MC and non-MC events, but the non-MC events

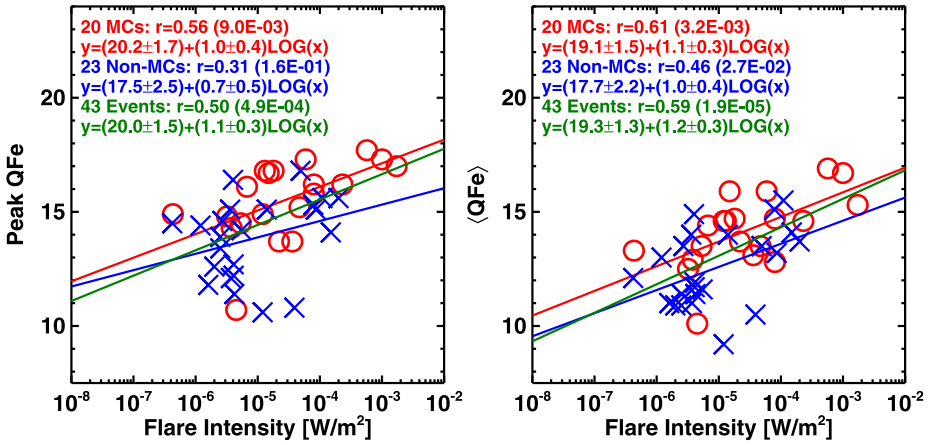

Figure 7 Scatter plots between the soft X-ray flare size and the peak (left) and average (right) Q_{Fe} in ICMEs. MCs and non-MCs are denoted by circles and crosses, respectively. The correlation coefficients (r) and the regression lines for the MC and non-MC events as well as the combined set (43 events) are shown on the plots. The probability of obtaining the correlation by chance is indicated in parentheses.

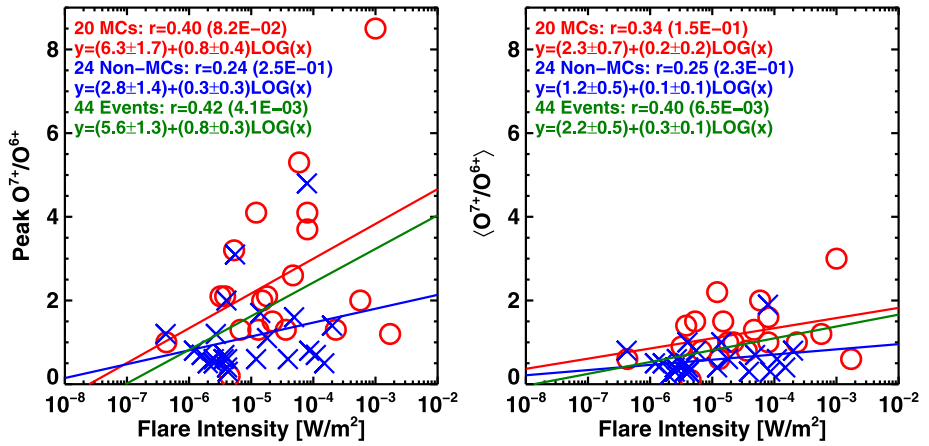

Figure 8 Scatter plots between the soft X-ray flare size and the peak (left) and average (right) O^7/O^6 ratios in ICMEs. MCs and non-MC are denoted by circles and crosses, respectively. The correlation coefficients (r) and the regression lines for the MC and non-MC events as well as the combined set (44 events) are shown on the plots. The probability of obtaining the correlation by chance is indicated in parentheses.

are generally concentrated toward the lower charge-state values as we also showed using the distributions in Figure 3. This is particularly clear in the event-averaged O^7O^6 values shown in the right-side panel of Figure 3. Even though the correlation is positive, it is much weaker compared to the Q_{Fe} – flare size correlation. For the combined set, the correlation coefficients are similar for peak ($r = 0.42$ with $p = 7.0 \times 10^{-3}$) and event-averaged (0.4 with $p = 6.5 \times 10^{-3}$) O^7O^6. The correlation is still reasonable for MC events: $r = 0.4$ ($p = 0.08$) and 0.32 ($p = 0.15$) for peak and event-averaged O^7O^6, respectively. The lowest correlation is for the non-MC events: 0.24 ($p = 0.25$, peak O^7O^6), 0.25 ($p = 0.23$, event-averaged

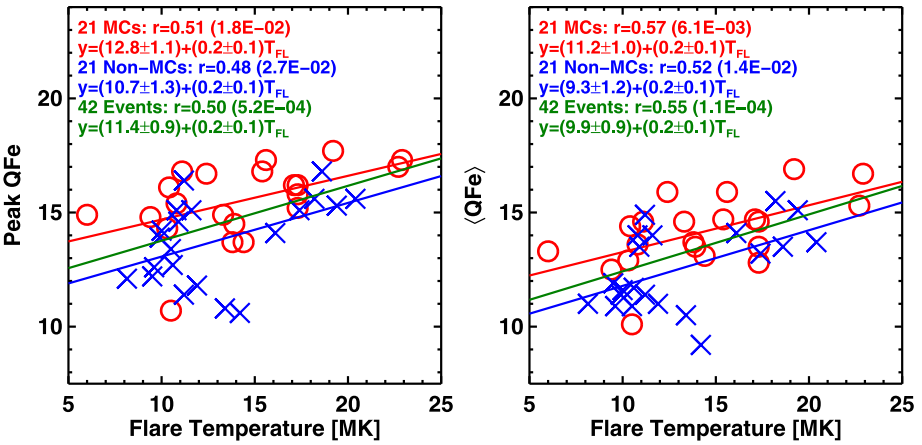

Figure 9 Scatter plots between flare temperature and the peak (left) and average (right) Q_{Fe} in ICMEs. MCs and non-MCs are denoted by circles and crosses, respectively. The correlation coefficients (r) and the regression lines for the MC and non-MC events as well as the combined set (42 events) are shown on the plots. The probability of obtaining the correlation by chance is indicated in parentheses.

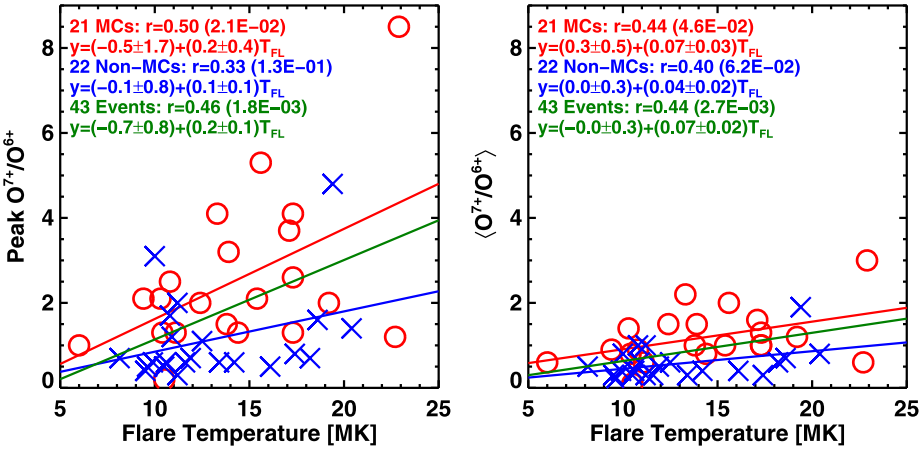

Figure 10 Scatter plots between flare temperature and the peak (left) and average (right) O^7/O^6 ratio in ICMEs. MCs and non-MCs are denoted by circles and crosses, respectively. The correlation coefficients (r) and the regression lines for the MC and non-MC events as well as the combined set (43 events) are shown on the plots. The probability of obtaining the correlation by chance is indicated in parentheses.

O^7O^6). Note that the p values are high indicating low confidence levels (75 % and 77 %) for the peak and event-averaged O^7O^6 vales.

The correlations of charge states measures with flare temperature are similar to those with the peak soft X-ray flux. The correlation coefficients and the p-values shown in Figures 9 and 10 indicate that all the correlations are highly significant, confirming the importance of flares in creating the high charge states observed inside ICMEs of both types. The lowest correlation obtained is for peak O^7O^6 in non-MC events: $r = 0.33$ with $p = 0.13$. The confidence level of this correlation is only 87 %.

3.4. CME Comparisons

We have seen in the previous sections that there is no significant difference between flares associated with the MC and non-MC events. The flare signatures are contained within the CME as the charge-state enhancements. Is there any characteristic difference between the CMEs associated with the two types of ICME? In order to check this we have plotted the speed, width, and acceleration distributions of the MC and non-MC events in Figure 11. The speeds of white-light CMEs near the Sun are about two times larger than the average speed of the general population of CMEs. The speeds of MC-associated CMEs (mean 934 km s^{-1}) are similar to speeds (mean 782 km s^{-1}) reported before without the longitude restriction (Gopalswamy, Yashiro, and Akiyama, 2007; Gopalswamy *et al.*, 2010b). This is because the solar sources of MC-associated CMEs tend to be closer to the disk center. On the other hand, the solar sources of non-MC ICMEs are generally at larger distances from the central meridian, so their speed measurement is subject to less projection effects. Accordingly, the average speed of CMEs associated with non-MC events is somewhat higher (955 km s^{-1} *vs.* 772 km s^{-1}). The events in Figure 11 are both from disk center, and hence subject to similar projection effects resulting in similar speeds.

Such high speed CMEs from the disk center are expected to appear as halo CMEs in the coronagraphic field of view. The width of the halo CMEs is not known, but measurements of limb CMEs reveal that faster CMEs are generally wider (Gopalswamy *et al.*, 2009c). Again wider CMEs are more massive (Gopalswamy *et al.*, 2005), indicating that faster CMEs are generally more energetic. In other words, halo CMEs are expected to be generally more energetic. In fact, the fraction of halo CMEs in a population is an indicator of the average energy of the population: higher the halo fraction, larger is the kinetic energy. Gopalswamy *et al.* (2010b) found that the majority of CMEs arriving at Earth are halos: 59 % of CMEs associated with MCs and 60 % associated with non-MCs. Figure 11 shows even a larger fraction of halo CMEs (70 % for MC+non-MC events) in the present study because they originate closer to the disk center compared to all halos. The halo fraction is the highest with 76 % for MC-associated CMEs, while somewhat smaller (65 %) for the non-MC CMEs. A CME needs to be relatively fast to become a halo CME when it originates farther from the disk center (Gopalswamy *et al.*, 2010c).

The acceleration measurement is generally difficult and is accurate only for slow CMEs from the limb: because there are no projection effects for limb CMEs and many data points can be obtained for slow CMEs. The CMEs in question are subject to projection effects, because they all come from close to the disk center. Fortunately, comparing the acceleration of MC and non-MC CMEs is possible because both sets are subject to similar projection effects. We see from Figure 11 that the accelerations are similar for MC, non-MC, and the combined set. Gopalswamy (2010) showed that for a large number of limb CMEs, the mean acceleration was -3.1 m s^{-2}, which is only slightly larger than the mean values in Figure 11. One small difference is that the distribution peaks in the $0-10$ m s^{-2} bin. A closer examination of these events in this bin reveals that most of these CMEs are radio quiet, *i.e.*, they did not produce a type II radio burst anywhere between the Sun and Earth, even though they were associated with IP shocks at 1 AU. Accelerating CMEs become fast enough to drive shocks generally far away from the Sun (beyond 10 R_s), so they either produce type II bursts at kilometric wavelengths (Gopalswamy, 2006b) or none at all (Gopalswamy *et al.*, 2010a). When we examined the type II burst association of the 54 events, we found that 17 were radio quiet (no type II burst association). The vast majority of the radio-quiet CMEs were non-MC events (14 *vs.* 3 MCs), consistent with the positive acceleration bias seen in Figure 11. Only four of the 14 radio-quiet CMEs associated with non-MC events were decelerating.

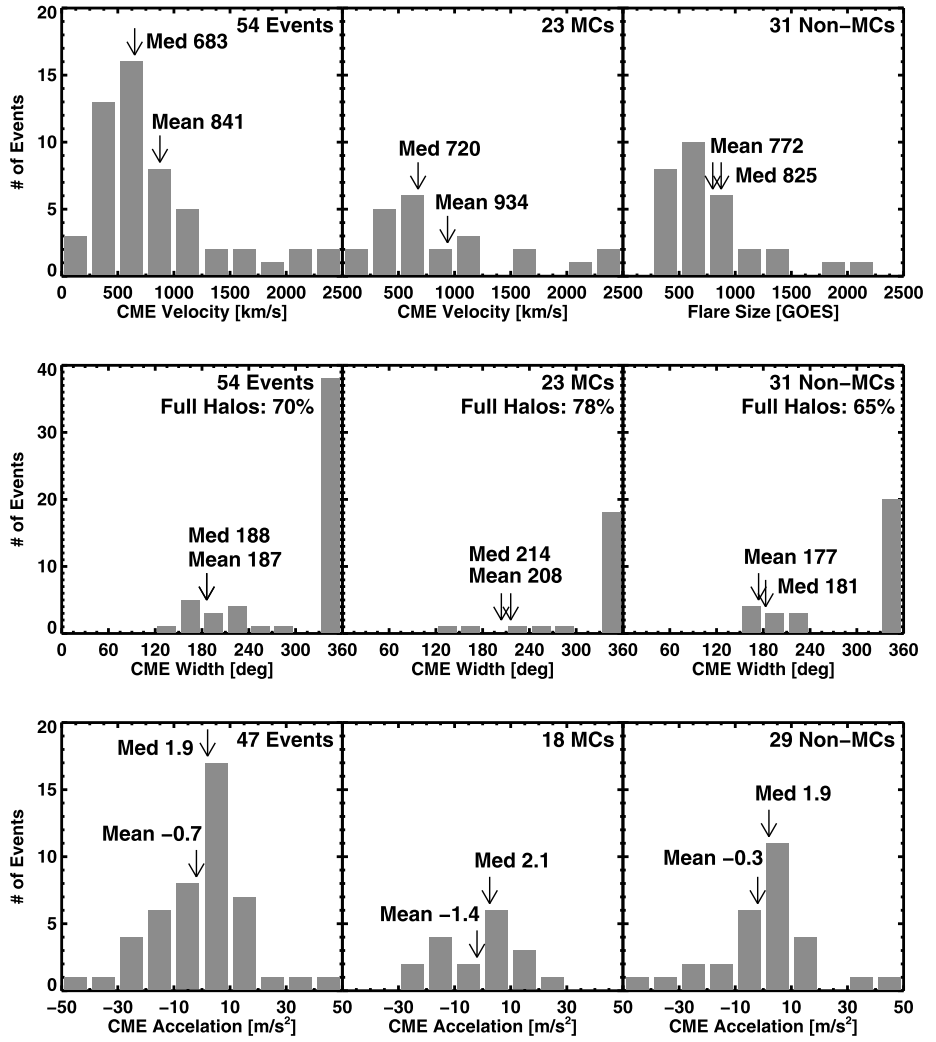

Figure 11 Speed, width and acceleration of CMEs associated with the ICMEs in question. MC and non-MC values are compared with each other and with the combined set. In the width distributions, the fraction of halo CMEs is indicated.

In summary, we see that the basic properties of CMEs (speed, width, and acceleration) in the MC and non-MC events are very similar. The only exception we find is a slightly larger number of radio-quiet CMEs among the non-MC events (14 out of 31 non-MC events or 45 % are radio quiet, while three out of 23 MC events or 13 % are radio quiet). Now let us look at the correlation between CME speed and charge-state measures.

There is generally a positive correlation between the CME speed and Q_{Fe}. Figure 12 shows that the correlation coefficients range from 0.26 to 0.58. The weakest correlation ($r = 0.26$) is for peak Q_{Fe} with $p = 0.19$ indication that the confidence level is only 81 %. On the other hand the CME speed is poorly correlated with O^7O^6 values as can be seen in Figure 13. We think the CME speed – charge-state correlation essentially reflects the

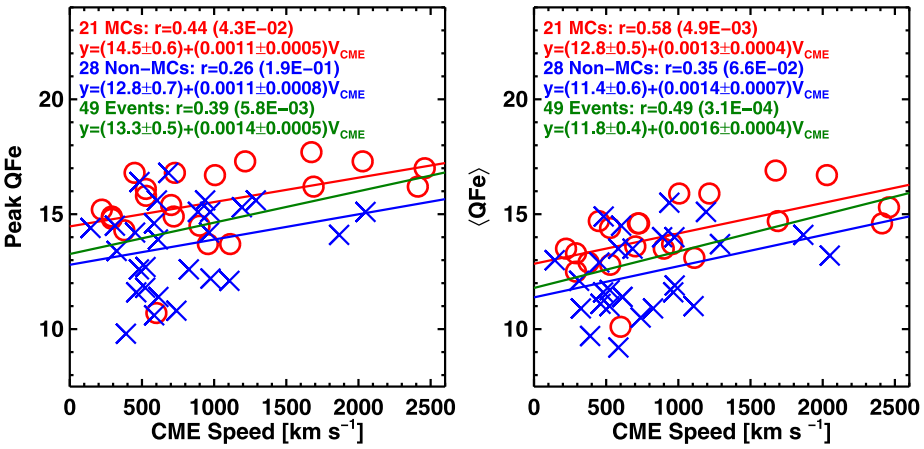

Figure 12 Scatter plots between CME speed and the peak (left) and average (right) Q_{Fe} in ICMEs. MCs and non-MCs are denoted by circles and crosses, respectively. The correlation coefficients (r) and the regression lines for the MC and non-MC events as well as the combined set (51 events) are shown on the plots. The probability of obtaining the correlation by chance is indicated in parentheses.

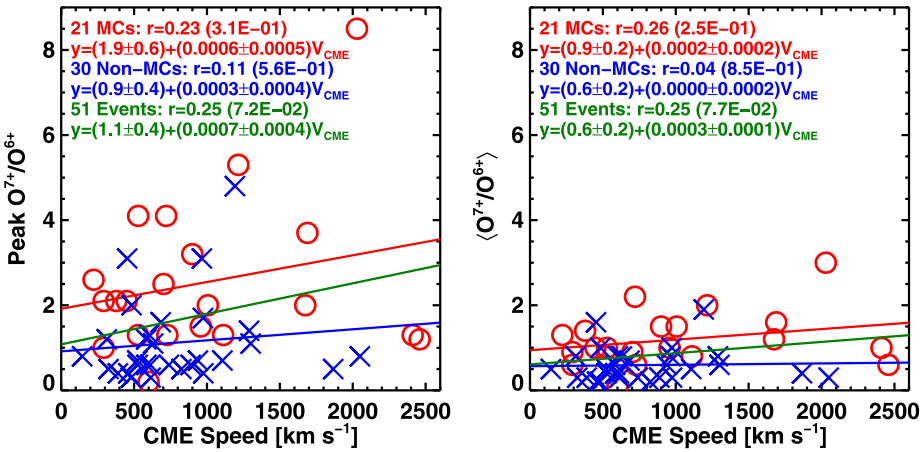

Figure 13 Scatter plots between CME speed and the peak (left) and average (right) Q_{Fe} in ICMEs. MCs and non-MC are denoted by circles and crosses, respectively. The correlation coefficients (r) and the regression lines for the MC and non-MC events as well as the combined set (49 events) are shown on the plots. The probability of obtaining the correlation by chance is indicated in parentheses.

correlation between CME speed and flare size (see, *e.g.*, Gopalswamy, 2010) because CMEs do not play any role in the creation of high charge states.

Table 2 summarizes various correlation coefficients discussed above for Q_{Fe} and O^7O^6. The probability that a correlation is by chance is given by the number in parentheses. Any p value more a few percent is an indication that we have low confidence in the correlation. The confidence level is roughly $1 - p$. We have listed the correlation of Q_{Fe} and O^7O^6 with flare intensity, flare temperature, and CME speed. We have also listed the correlation coefficients obtained by eliminating a few outliers. These cases are denoted by the "XO" (for excluding outliers). Barring one or two cases, the charge states have generally a high correlation for

Table 2 Correlation coefficients for flare/CME properties and Q_{Fe} and O^7O^6.

	Correlation coefficient for Q_{Fe}[d]			Correlation coefficient for O^7/O^6[d]		
	MC	Non-MC	MC+non-MC	MC	Non-MC	MC+non-MC
Flare Size	0.56 (0.9 %)	0.31 (16 %)	0.50 (0.05 %)	0.40 (8.2 %)	0.24 (25 %)	0.42 (0.4 %)
	0.61 (0.3 %)	0.46 (2.7 %)	0.59 (0.002 %)	0.34 (15 %)	0.25 (23 %)	0.40 (0.7 %)
Flare Size XO[a]	0.58 (0.7 %)	0.49 (2.3 %)	0.60 (0.003 %)	0.16 (51 %)	0.24 (25 %)	0.29 (6.1 %)
	0.63 (0.3 %)	0.63 (0.2 %)	0.68 (0.00006 %)	0.11 (66 %)	0.07 (75 %)	0.25 (12 %)
Flare T[b]	0.51 (1.8 %)	0.48 (2.7 %)	0.50 (0.05 %)	0.50 (2.1 %)	0.33 (13 %)	0.46 (0.2 %)
	0.57 (0.6 %)	0.52 (1.4 %)	0.55 (0.01 %)	0.44 (4.6 %)	0.40 (6.2 %)	0.44 (0.4 %)
Flare T XO[a]	0.51 (1.9 %)	0.67 (0.2 %)	0.59 (0.008 %)	0.27 (26 %)	0.26 (27 %)	0.28 (7.5 %)
	0.57 (0.8 %)	0.66 (0.2 %)	0.62 (0.002 %)	0.44 (4.6 %)	0.17 (47 %)	0.41 (0.7 %)
CME V[c]	0.44 (4.3 %)	0.26 (19 %)	0.39 (0.6 %)	0.23 (31 %)	0.11 (56 %)	0.25 (7.2 %)
	0.58 (0.5 %)	0.35 (6.6 %)	0.49 (0.03 %)	0.26 (25 %)	0.04 (84 %)	0.25 (7.7 %)
CME V XO[a]	0.49 (2.8 %)	0.26 (19 %)	0.38 (0.7 %)	−0.04 (87 %)	0.03 (90 %)	0.08 (60 %)
	0.63 (0.2 %)	0.35 (6.6 %)	0.49 (0.04 %)	0.26 (25 %)	−0.01 (96 %)	0.27 (6.7 %)

[a]XO indicates that a few outliers were excluded.

[b]Flare temperature derived from GOES soft X-ray intensities.

[c]Speed of white-light CMEs from LASCO; the upper (lower) entries are peak (average) charge-state values within the ICME interval.

[d]The percentage values in parentheses denote the probability that the observed correlation is due to chance. The smaller is this probability, the higher is the confidence level in reality of the correlation.

Q_{Fe}. On the other hand, O^7O^6 correlations are generally weaker, especially with CME speed. The poorest correlations are between O^7O^6 and CME speed for non-MC events. The lower correlations with CME properties are understandable because CME properties do not decide the creation of charge states.

3.5. Weak Events

We saw that there were eight weak events in terms of flare size. These were eruptive prominence events with clear post-eruption arcades. Even though the flare signature in these events was extremely weak, the post-eruption arcades (in soft X-rays, EUV, or microwaves) were very prominent. The soft X-ray flux derived from imaging observations (*Yohkoh*/SXT) is well below the GOES soft X-ray background level, so these events do not have flares listed in the SGD. All but three of these EP events had a charge-state enhancement. The exceptions are the 22 March 2001, 12 August 2001, and 20 May 2002 events. Figure 14 shows the solar source of the 22 March 2001 non-MC event as an SXR arcade on 19 March 2001 from *Yohkoh*/SXT. The weak east–west arcade overlying the neutral line (see Figure 14a, b). The EIT images had a clear filament channel with only a tiny filament visible in Hα (not shown). Figure 14c shows that the duration of the ejecta was very small suggesting the possibility that the spacecraft passed through only the northern flank of the ICME. The presence of a coronal hole to the northeast of the eruption region (see Figure 14a) might have also deflected the CME to the south. Note that our selection criterion restricts source longitudes to $\pm 15°$, but not in latitudes. Therefore, CMEs could still go north or south of Earth (especially when deflected by coronal holes) and that might be why we do not always see flux ropes. The lack of charge-state enhancement in this event (see Figure 14c) is likely due to the fact that the observing spacecraft is passing through the edge of the ICME and hence might have missed the charge-state enhancement. The 12 August 2001 event also did not

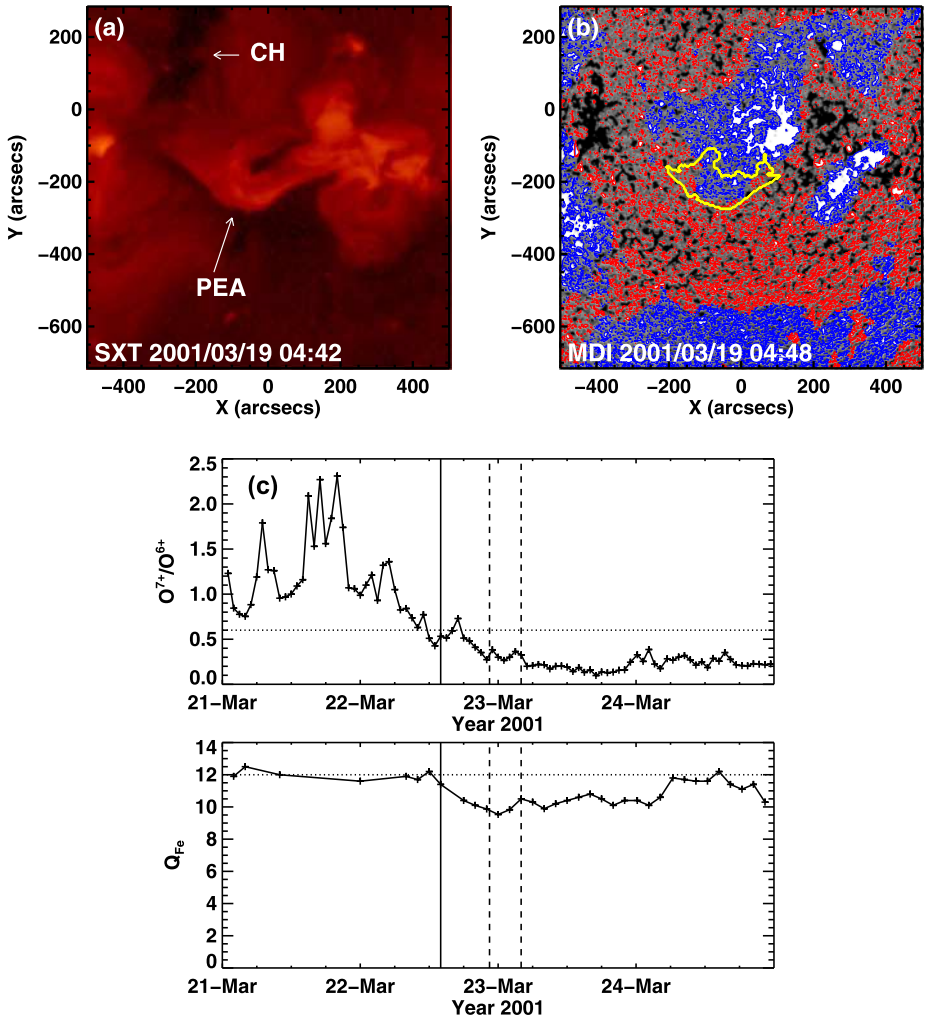

Figure 14 (a) The post-eruption arcade (PEA) as observed by *Yohkoh*/SXT. (b) The PEA superposed on SOHO/MDI magnetogram showing that the arcade straddles the polarity inversion line like in any eruptive event. (c) The Q_{Fe} and O^7O^6 plots showing no charge-state enhancement after the shock (vertical solid line) or during the ICME interval (marked by the vertical dashed lines). The only EP event among the MCs is the 10 August 2000 event associated with a complex filament eruption on 9 August 2000 accompanied by a halo CME at 16:30 UT. The O^7O^6 ratio was ~ 2.5 and $Q_{Fe} \sim 15$. The arcade was observed in *Yohkoh*/SXT and SOHO/EIT images, but was very weak, so the event was not seen in the GOES light curve.

have charge-state enhancement and has a similar solar source environment. The event had a clear north–south arcade in *Yohkoh*/SXT and SOHO/EIT images at the western edge of a north–south coronal hole. Clearly the CME was deflected to the west, away from the Sun–Earth line, consistent with a very short duration ejecta (~ 3 h). Therefore, it is not surprising that we do not see charge-state enhancement in this event. This event was already reported as a coronal-hole deflection event (Gopalswamy *et al.*, 2004, their Figure 3). Finally, the 20 May 2002 event is also associated with the eruption of a long north–south filament. The

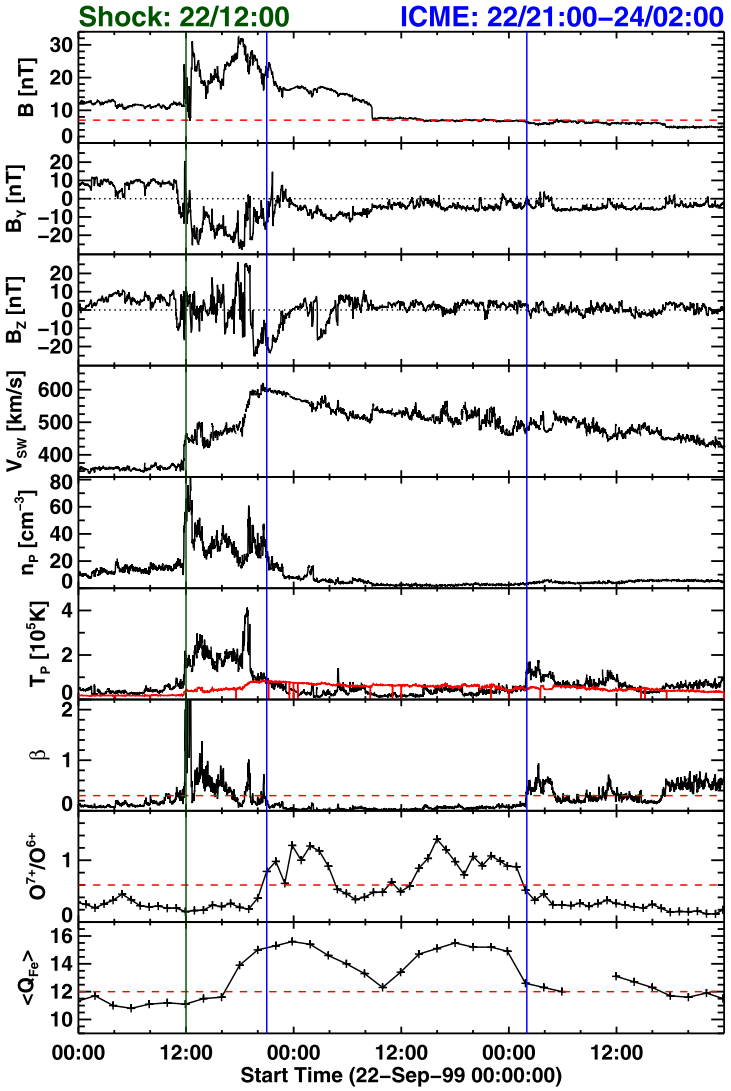

Figure 15 The non-MC ICME of 22 September 1999 showing total magnetic field strength (B), B_y component, B_z component, solar wind speed (V_{SW}), proton density (n_p), proton temperature (T_p), plasma betta, O^7O^6 and Q_{Fe}. This is a non-MC because the neither the B_z nor the B_y component shows a smooth rotation. The ICME boundaries from the plasmag signatures are shown by the vertical blue lines. The shock is denoted by the vertical black line.

associated CME was relatively narrow (45°) in the plane of the sky. The solar source of this event has some ambiguity because there are other CME candidates (see Cho *et al.*, 2013).

One of the characteristics of the EP events is that the flare structure is extremely weak, so the question arises whether high charge states can be produced in such weak flares. We already saw that four of the seven events did have enhanced charge states, and in two other events, the spacecraft might have missed the flux rope. How do we reconcile these observations? In order to do this we perform a case study of the 22 September 1999 non-MC event (see Figure 15). Both Q_{Fe} and O^7O^6 plots show a double structure, similar to many of the

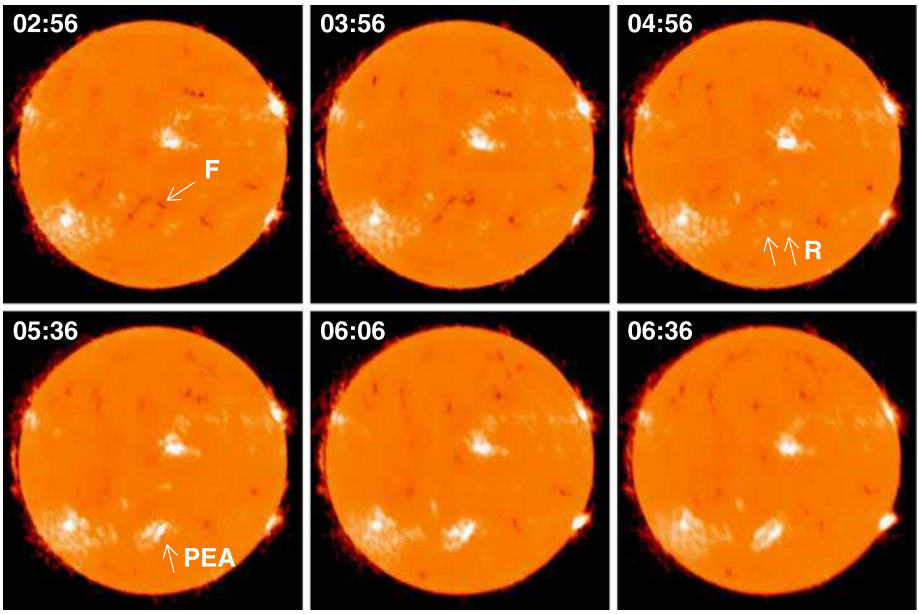

Figure 16 A series of 17 GHz microwave images obtained by the *Nobeyama radioheliograph* on 19 September 1999 showing the filament (F), its disappearance resulting in a two-ribbon flare (R), and the formation of the post-eruption arcade (PEA). The PEA was also observed by *Yohkoh*/SXT and SOHO/EIT beyond the 06:36 UT (not shown).

EP events. The O^7O^6 boundaries above the threshold value of 0.6 coincide well with the boundaries derived from plasmag signatures. However, the Q_{Fe} signature starts 2 – 3 hours earlier. The peak (event-averaged) Q_{Fe} and O^7O^6 values are 15.6 (14.5) and 1.3 (0.8), respectively. The Q_{Fe} values are typical (see the distribution in Figure 2), while the O^7O^6 value is somewhat smaller (Figure 3).

The solar source of the CME associated with the 22 September 1999 non-MC event is identified by an eruptive filament followed by a post-eruption arcade observed in microwave, soft X-rays and EUV. Figure 16 shows the U-shaped filament at 02:36 UT, which erupts resulting in a two-ribbon flare and post-eruption arcade (PEA) all imaged by the *Nobeyama radioheliograph* at 17 GHz. The peak brightness temperature (T_b) of the PEA in microwaves (17 GHz) is 3.87×10^4 K. The average brightness temperature of the arcade is 1.53×10^4 K. The radio emission from the arcade is optically thin, so the kinetic temperature (T) of the arcade plasma is given by $T = T_b/\tau$, where τ is the free-free optical depth of the arcade given by $\tau = 0.2n^2L/f^2T^{3/2}$, where f is the observing frequency (17 GHz), n is the electron density of the arcade plasma, and L is the line-of-sight thickness of the arcade. We need $\tau \leq 0.004$ so that the observed average T_b translates into an average kinetic temperature $T \geq 3.5$ MK needed to produce the observed charge states (Bame *et al.*, 1979). Taking the arcade height as its observed width ($L = 9.8 \times 10^9$ cm), one can readily get the required optical depth for an electron density of $(2-2.2) \times 10^9$ cm^{-3}. Such densities have been derived from simultaneous soft X-ray imaging observations in other post-eruption arcades (Hanaoka *et al.*, 1994). Thus, the temperature in the PEA is adequate to produce the observed charge-state enhancements in the EP event. We expect a similar situation for most of the EP events and hence conclude that even in such events with poor flare signatures, high charge states can be produced.

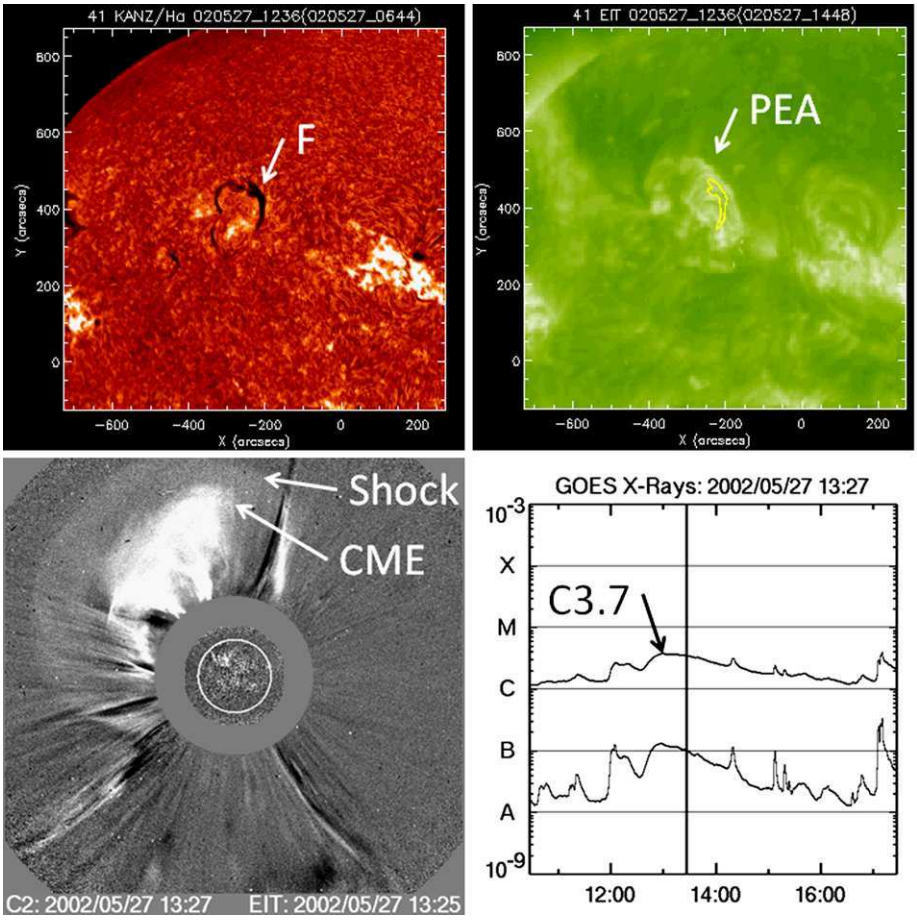

Figure 17 The solar source of the 30 May 2002 non-MC event (one of the three events for which flux-rope fitting did not succeed) as a filament (F) eruption event accompanied by a wide shock-driving CME and a weak post-eruption arcade (PEA) responsible for the weak (C3.7) GOES soft X-ray flare on 27 May 2002.

We also note that two of the EP events without charge-state enhancement are also EJ-events, *i.e.*, we were not able to fit a flux-rope event with boundary adjustments. The third EJ-event is the one on 30 May 2002 associated with a C3.7 flare and a filament eruption in the NE quadrant. The filament in the pre-eruption stage (F), the post-eruption arcade (PEA) overlying the filament location, the associated white-light CME, and the GOES soft X-ray light curve are all shown in Figure 17. Note that the white-light CME was clearly surrounded by a shock, but the whole structure is mostly heading to the northwest. In particular, there is only a small section of the CME that crosses the ecliptic, suggesting that the ACE spacecraft measuring the charge states might have passed through only the edge of the ICME. This might be the reason that the observed ICME could not be fit with a flux rope.

3.6. Is There Charge-State Enhancement in the Shock Sheath?

In a preliminary study, Gopalswamy (2006c) did not find any Q_{Fe} enhancement in MC sheaths. They found the average Q_{Fe} in sheaths is ~ 11.3, which is same as the value in

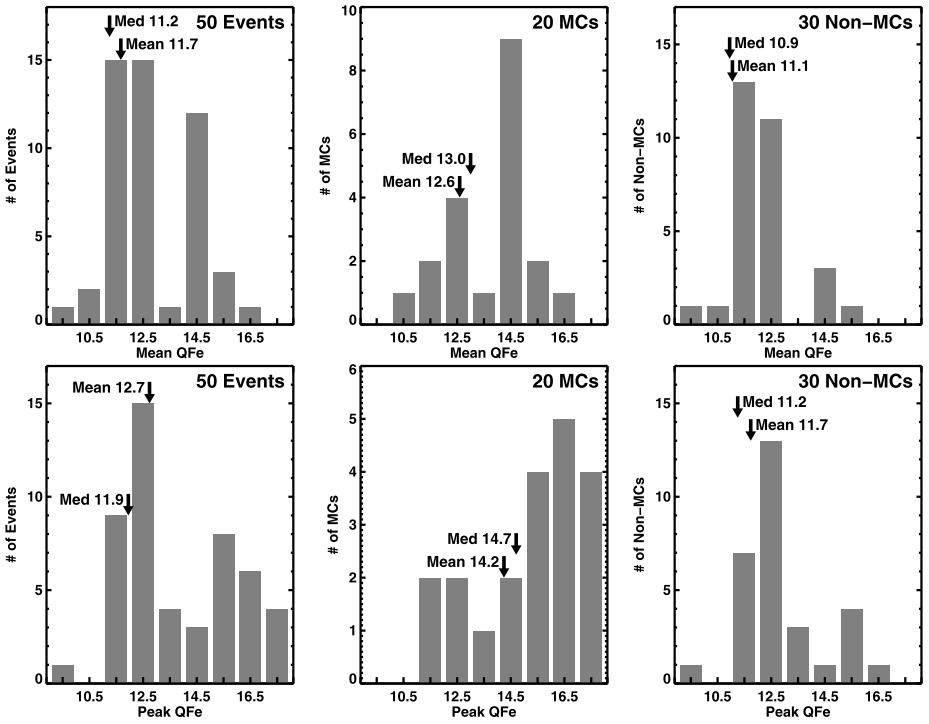

Figure 18 Distribution of average (top) and peak (bottom) Q_{Fe} values in the sheaths of MC and non-MC ICMEs.

slow solar wind reported by Lepri *et al.* (2001). Figure 18 shows the distribution of Q_{Fe} in the sheath regions for MC and non-MC events and for the combined set. It is clear that the peak and average Q_{Fe} in the sheath are enhanced with respect to the threshold values. The enhancement is more prominent in sheaths of MCs than in non-MC sheaths.

In order to examine the charge-state enhancements in sheaths, we have listed the events numbers that do and do not show charge-state enhancement in sheaths in Table 3. The first three events in Table 1 do not have charge-state data, so the remaining 51 are used. First of all we note that more than half of the events (27 out of 51 or 53 %) do not have any charge-state enhancement in the sheaths. These events are noted as category i) events in Table 3. Among the remaining 24 events, four (or 8 %) were marginal in that only one of Q_{Fe} and O^7O^6 showed enhancement in the sheath, also with just one or two data points above the threshold values (categories ii) and iii)). Twelve events had charge-state enhancements in the tail end of the sheaths. Comparison of the plasmag and charge-state signatures revealed that these enhancements can be attributed to the ambiguity in identifying the starting boundary of the ICME based on plasmag signatures. In fact, all these cases, the plasma beta coincided with the onset of charge-state enhancement, although there are some short-term fluctuations in the beta value. These events are noted as category iv) events in Table 3 and add up to 23 % of the 51 events. The event shown in Figure 15 is a good example of this type of event. In another six events (marked as category v) in Table 3), there was definitely preceding ICME material into which the shock was propagating and hence the charge-state enhancement can be attributed to the preceding ICME as in Figure 1. Only for two events, marked as

Table 3 Charge-state enhancement in sheaths.

Charge State in Sheath	Event Numbers (Table 1)	Fraction	Remark
i) No enhancement	4, 7, 8, 9, 10, 14, 15, 16, 17, 20, 25, 27, 29, 31, 38, 39, 40, 41, 42, 45, 47, 50, 51, 53, 56, 57, 59	27/51 or 53 %	
ii) Marginal cases: O^7O^6 – No, $\langle Q_{Fe} \rangle$ – Yes	5, 54	2/51 or 4 %	Only Q_{Fe} enhancement
iii) Marginal cases: O^7O^6 – Yes, $\langle Q_{Fe} \rangle$ – No	30, 34	2/51 or 4 %	Only O^7O^6 enhancement
iv) Enhancement before plasmag starting boundary	13, 19, 21, 23, 24, 26, 28, 32, 33, 35, 36, 44	12/51 or 23 %	Charge-state signatures precedes plasmag signature in all cases
v) Enhancement due to preceding ICME	18, 43, 46, 48, 49, 58	6/51 or 12 %	Plasmag signatures indicate preceding ICME
vi) Other enhancements	37, 52	2/51 or 4 %	#52 – marginal enhancement

category vi) events in Table 3, one can say there is charge-state enhancement in the sheath. In the case of event #52 (15 February 2005), there were only two consecutive O^7O^6 data points and a single Q_{Fe} data point above the respective thresholds. Thus the enhancement is marginal and could be due to fluctuation. In the case of event #37 (17 April 2002), there were two intervals of charge-state enhancements, one close to the plasmag starting boundary and the other in the middle of the sheath. The enhancement near the plasmag boundary is similar to that in category iv) events. However, the enhancement in the middle is during the interval of high beta. Thus, there is only one event among the 51 that can be said to have a charge-state enhancement in the sheath. This event needs to be further investigated.

Since the sheath is not connected to the flare site, it is unlikely that the flare plasma enters into the sheath region. Is it possible that the temperature jump across the shock is high enough to enhance the charge state when the shock is very close to the Sun? Comparing the events with no charge-state enhancement in Table 3 with their association with type II bursts, we find that more than half of them (15 out of 27) have type II burst association. This means the CMEs were driving strong shocks near the Sun, but there was no charge-state enhancement in the sheath. Similarly, there are other events (#23, 44, and 48) that have no type II burst near the Sun (weak shocks) yet they had charge-state enhancement. These observations support our conclusion that the temperature jump at the shock may not be related to charge-state enhancements observed in the interplanetary medium.

Direct comparison between shock formation observed in EUV images (Gopalswamy *et al.*, 2012) and the frequency of the associated metric type II burst suggests that the shock formation can occur at a heliocentric distance as short as 1.2 R_s. The density jump across the shock has been estimated to be only by a factor of ~ 1.5. If the temperature of the upstream quiet corona is ~ 1.5 MK, the downstream temperature due to shock heating is expected to be too low to cause the charge-state enhancement. Besides, the density in the shock downstream is also expected to be much smaller than in the flare site, which also works against this possibility. However, it must be pointed out that numerical simulation results are not conclusive and give conflicting charge-state charge state enhancements in sheaths with respect to the driving CME and the core (see Lynch *et al.*, 2011).

4. Discussion

The primary finding of this paper is that the Fe and O charge-state measures found inside ICMEs are closely related to the flares that accompany the CMEs. The high temperature resulting from flare heating is responsible for the production of high charge states in the flare plasma, which is injected into the CME flux rope and carried into the IP medium. Charge-state enhancement events are excellent examples in which flares and CMEs act in tandem to produce the observed charge state at 1 AU. Without CMEs, the ions cannot get into the IP medium as the charge state data presented here and elsewhere and indicated by models (see *e.g.*, Rakowski, Laming, and Lepri, 2007). Two types of magnetic structure are created during an eruptive process: an arcade anchored to the Sun and a flux rope ejected into the heliosphere. This standard model of an eruption elucidated by many authors requires the formation of the two structures, except in confined flares in which all the energy goes into plasma heating and none goes into mass motion (Gopalswamy, Akiyama, and Yashiro, 2009). For example, temperatures exceeding 30 MK may be produced in confined flares, but these flares are not accompanied by CMEs (Schmahl *et al.*, 1990; Gopalswamy *et al.*, 1995; Gopalswamy, Akiyama, and Yashiro, 2009). We did not find any significant difference in the flare and CME properties of eruptions associated with MC and non-MC ICMEs. Therefore, there is no obvious reason to expect a difference in the topology of the CME structure in the IP medium. The charge-state distributions indicate that the charge-state signatures are more prominent in MCs than in non-MC ICMEs. The lower charge-state ratio observed in non-MC CMEs can be attributed to the non-radial propagation of the associated CMEs near the Sun, resulting in a less favorable observing geometry. The observing spacecraft does not pass through the axis of the flux rope and thus encounters less of the flare plasma that entered into the flux rope. Such a suggestion was made in Gopalswamy (2006a), which is supported by the charge-state analysis presented in this paper.

Many studies have revealed that the high ionization states observed in the IP medium are indicative of a hot source region at the Sun (Bame *et al.*, 1979; Henke *et al.*, 2001; Lepri *et al.*, 2001; Reinard *et al.*, 2001; Reinard, 2005, 2008). Apart from the interior of the Sun where thermonuclear reactions occur, one can find temperatures of several to tens of MK only in solar flares. Our analysis finds that the temperature attained in the flaring region ranges from a few MK to 25 MK for both MC and non-MC cases, thus identifying the hot source region on the Sun. The connection between flares and CMEs is that the reconnection produces a flux-rope structure (see *e.g.*, Qiu *et al.*, 2007) and the process also injects hot plasma into the flux rope (Lin, Raymond, and van Ballegooijen, 2004). The propagation characteristics of the flux rope into the IP medium and how the observing spacecraft passes through the flux rope seem to decide the appearance of the flux rope as an MC or non-MC.

There is considerable observational support that both MCs and non-MCs have a flux-rope structure and that the flux ropes associated with non-MCs propagate non-radially. The observational support can be found in the accompanying papers that show that i) white-light CMEs associated with both MCs and non-MC ICMEs can be fit to flux ropes near the Sun (Xie *et al.*, 2013), ii) propagation direction obtained from the flux-rope fit and the CME direction parameter suggest that the CMEs associated with non-MC ICMEs seem to propagate non-radially (Xie *et al.*, 2013; Kim *et al.*, 2013), iii) coronal-hole deflection of CMEs is one of the major causes for the non-radial motion of CMEs, and iv) a flux rope can be fit to even non-MC ICMEs either by slightly modifying the ICME boundaries derived from plasmag signatures or using a torus-type flux rope instead of the conventional cylindrical flux ropes (Marubashi *et al.*, 2012). Thus, all evidence points to the conclusion that almost all of the ICMEs reaching far into the IP medium seem to contain a flux-rope structure.

The results of this study do not support the idea that some ICMEs may be inherently non-flux ropes, as suggested by Gosling (1990). When active regions slowly expand into the IP medium, one does not expect flares or mass motions faster than the slow solar wind. In fact, Uchida *et al.* (1992) ruled out that the active region loop expansion involves reconnection. These authors also found that the speed of the expanding loops near the Sun is typically tens of km s^{-1}. We saw that almost all the ICME events (MC or non-MC) have charge-state enhancements and are associated with flares and fast CMEs. Thus we can rule out active region expansion as a mechanism for non-MC ICMEs (Gosling, 1990). Whether active region expansion leads to any ICMEs is an open question. Antiochos, DeVore, and Klimchuk (1999) speculated that CMEs associated with polar crown filaments may not be CMEs, but loop expansions. However, even CMEs associated with polar crown filaments have post-eruption arcades, similar to the EP events discussed in this paper. Thus we confirm that none of the solar sources of the non-MC ICMEs are active region expansions.

Our study confirms the earlier suggestion by Reinard (2008) that the peripheries of ICMEs may contain weaker charge-state signatures. In addition, we think the patchiness of the charge-state enhancement within the ICME might contribute to the weaker charge-state signals observed in non-MC ICMEs. The patchy reconnection at the flare site might have contributed to such a situation inside ICMEs. When combined with the fact that the observing spacecraft does not pass through the central axes in the case of non-MC ICMEs, one might expect lower charge-state enhancement. The Q_{Fe} enhancement seems to be more robust that the O^7O^6 enhancement, probably due to the higher ionization potential of O^{6+} ions (see also Henke *et al.*, 2001). We find much larger fraction of events with enhanced charge states than in earlier works (Henke *et al.*, 2001; Aguilar-Rodriguez, Blanco-Cano, and Gopalswamy, 2006) because we have selected events originating from the solar disk center, which seems to be the preferred location for high charge-state events (Reinard, 2008). We also find significant overlap between MC and non-MC events in the charge-state *vs*. flare properties scatter plots.

In terms of the solar sources, there is one clear difference between the MC and non-MC events: there are far more eruptive prominence and dimming events in the non-MC population (7 *vs*. 1). It is not clear if this is significant because even in these EP events, there are clear flare structures in the form of post-eruption arcades. The temperature attained in these events are also high enough to produce the observed charge states, as illustrated using a case study of the 22 September 1999 non-MC ICME and its solar source.

5. Summary and Conclusions

We investigated a set of 54 ICMEs whose solar sources were very close to the disk center (within $\pm 15^\circ$ from the central meridian). The motivation behind this longitude criterion is that CMEs originating from such locations are expected to reach Earth directly and produce MC signatures. More than half of these ICMEs were non-MC events, thus questioning the geometrical hypothesis. We compared the charge-state properties at 1 AU between the MC and non-MC events and the corresponding flare and CME properties at the Sun. Our analyses suggest that the MC and non-MC ICMEs had more or less the same eruption characteristics at the Sun. Both types had significant enhancement in charge states. These observations suggest that both MC and non-MC ICMEs are likely to have a flux-rope structure and the observational geometry may be responsible for the appearance of non-MC structures at 1 AU. Specific conclusions of the paper are listed below.

i) Both MC and non-MC ICMEs are associated with major solar flares, although there are even A- and B-class flares involved in some cases. The median flare class for non-MC events is slightly smaller than that of the MC events.
ii) The flare temperatures derived from GOES soft X-ray data are in the range 5 – 25 MK for both MC and non-MC events. Even in the case of eruptive prominence events in which the flare temperature could not be derived from GOES data, there is radio evidence of flare temperature high enough to produce the observed charge states.
iii) The CME properties are similar between MC and non-MC events in terms of their sky-plane speed, width, and acceleration. The CMEs are more energetic than ordinary CMEs. The fraction of halo CMEs in the two populations is very high, exceeding 70 %.
iv) There is good correlation between Fe and O charge-state enhancements in ICMEs and the flare properties such as soft X-ray peak flux and flare temperature. The correlation with CME speed is moderate for Fe charge states, but poor for O charge states. CMEs are not directly involved in the production of high charge states, so the observed correlation simply reflects the correlation between CME kinetic energy and soft X-ray peak flux known before (see, *e.g.*, Yashiro and Gopalswamy, 2009).
v) There is significant difference in the boundaries derived from the solar wind plasma and magnetic signatures and from the charge signatures: the charge-state signatures systematically start before the starting ICME boundary. This may be responsible for the enhanced charge states observed in many ICME sheaths. Charge-state enhancements in shock sheaths are also found when the shock moves through a preceding ICME. There is only one clear case in our sample in which true charge-state enhancement was found in the sheath and needs further investigation.
vi) The durations of charge-state enhancement above the Fe and O thresholds is considerably smaller than the ICME duration derived from the solar wind plasma and magnetic signatures. This suggests that the charge-state enhancement within the ICMEs is patchy.
vii) Combined with the results of the accompanying papers, we find that CMEs associated with non-MC ICMEs are prone to deflection by coronal holes resulting in non-radial propagation, which might have contributed to the observation of non-MCs at 1 AU. The patchiness of enhanced charge state in CMEs also lowers the probability of observing the flux-rope structure at 1 AU.
viii) We conclude that the production mechanism for high charge states and the flux-rope structure are the same for MC and non-MC ICMEs. However, the observing geometry is different, resulting from propagation differences.
ix) We do not find any evidence for active region expansion resulting in ICMEs lacking a flux-rope structure.

Acknowledgements We thank the ACE, *Wind*, and SOHO teams for providing the data on line. SOHO is a project of international collaboration between ESA and NASA.

References

Aguilar-Rodriguez, E., Blanco-Cano, X., Gopalswamy, N.: 2006, Composition and magnetic structure of interplanetary coronal mass ejections at 1 AU. *Adv. Space Res.* **38**, 522.

Antiochos, S.K., DeVore, C.R., Klimchuk, J.A.: 1999, A model for solar coronal mass ejections. *Astrophys. J.* **510**, 485.

Bame, S.J., Asbridge, J.R., Feldman, W.C., Fenimore, E.E., Gosling, J.T.: 1979, Solar wind heavy ions from flare-heated coronal plasma. *Solar Phys.* **62**, 179.

Burlaga, L., Sittler, E., Mariani, F., Schwenn, R.: 1981, Magnetic loop behind an interplanetary shock – Voyager, Helios, and IMP 8 observations. *J. Geophys. Res.* **86**, 6673.
Burlaga, L., Fitzenreiter, R., Lepping, R., Ogilvie, K., Szabo, A., Lazarus, A., *et al.*: 1998, A magnetic cloud containing prominence material – January 1997. *J. Geophys. Res.* **10**, 277.
Cho, K.-S., Park, S.-H., Marubashi, K., Gopalswamy, N., Akiyama, S., Yashiro, S., Kim, R.-S.: 2013, Comparison of helicity signs in interplanetary CMEs and their solar source regions. *Solar Phys.*, in this issue.
Garcia, H.: 1994, Temperature and emission measure from GOES soft X-ray measurements. *Solar Phys.* **154**, 275.
Gilbert, J.A., Lepri, S.T., Landi, E., Zurbuchen, T.H.: 2012, First measurements of the complete heavy-ion charge state distributions of C, O, and Fe associated with interplanetary coronal mass ejections. *Astrophys. J.* **751**, 20.
Gopalswamy, N.: 2006a, Properties of interplanetary coronal mass ejections. *Space Sci. Rev.* **124**, 145.
Gopalswamy, N.: 2006b, Coronal mass ejections and type II radio bursts. In: Gopalswamy, N., Mewaldt, R., Torsti, J. (eds.) *Solar Eruptions and Energetic Particles*, *Geophys. Monogr. Ser.* **165**, AGU, Washington, 207.
Gopalswamy, N.: 2006c, Consequences of coronal mass ejections in the heliosphere. *Sun Geosph.* **1**, 5.
Gopalswamy, N.: 2010, Coronal mass ejections: a summary of recent results. In: *Proceedings of the 20th National Solar Physics Meeting*, *held 31 May – 4 June, 2010*, *Papradno, Slovakia*, 108 – 130.
Gopalswamy, N., Akiyama, S., Yashiro, S.: 2009, Major solar flares without coronal mass ejections. In: Gopalswamy, N., Webb, D.F. (eds.) *Proceedings of IAU Symposium* **257**, *Universal Heliophysical Processes*, 283.
Gopalswamy, N., Yashiro, S., Akiyama, S.: 2007, Geoeffectiveness of halo coronal mass ejections. *J. Geophys. Res.* **112**, A06112. doi:10.1029/2006JA012149.
Gopalswamy, N., Raulin, J.-P., Kundu, M.R., Nitta, N., Lemen, J.R., Herrmann, R., Zarro, D., Kosugi, T.: 1995, VLA and YOHKOH observations of an M1.5 flare. *Astrophys. J.* **455**, 715.
Gopalswamy, N., Hanaoka, Y., Kosugi, T., Lepping, R.P., Steinberg, J.T., Plunkett, S., *et al.*: 1998, On the relationship between coronal mass ejections and magnetic clouds. *Geophys. Res. Lett.* **25**, 2485.
Gopalswamy, N., Yashiro, S., Krucker, S., Stenborg, G., Howard, R.A.: 2004, Intensity variation of large solar energetic particle events associated with coronal mass ejections. *J. Geophys. Res.* **109**, A12105. doi:10.1029/2004JA010602.
Gopalswamy, N., Aguilar-Rodriguez, E., Yashiro, S., Nunes, S., Kaiser, M.L., Howard, R.A.: 2005, Type II radio bursts and energetic solar eruptions. *J. Geophys. Res.* **110**, A12S07. doi:10.1029/2005JA011158.
Gopalswamy, N., Mäkelä, P., Xie, H., Akiyama, S., Yashiro, S.: 2009a, CME interactions with coronal holes and their interplanetary consequences. *J. Geophys. Res.* **114**, A00A22. doi:10.1029/2008JA013686.
Gopalswamy, N., Yashiro, S., Michalek, G., Stenborg, G., Vourlidas, A., Freeland, S., Howard, R.: 2009b, The SOHO/LASCO CME catalog. *Earth Moon Planets* **104**, 295.
Gopalswamy, N., Dal Lago, A., Yashiro, S., Akiyama, S.: 2009c, The expansion and radial speeds of coronal mass ejections. *Cent. Eur. Astrophys. Bull.* **33**, 115.
Gopalswamy, N., Xie, H., Mäkelä, P., Akiyama, S., Yashiro, S., Kaiser, M.L., Howard, R.A., Bougeret, J.-L.: 2010a, Interplanetary shocks lacking type II radio bursts. *Astrophys. J.* **710**, 1111.
Gopalswamy, N., Akiyama, S., Yashiro, S., Mäkelä, P.: 2010b, Coronal mass ejections from sunspot and non-sunspot regions. In: Hasan, S.S., Rutten, R.J. (eds.) *Magnetic Coupling Between the Interior and Atmosphere of the Sun*, *Astrophysics and Space Science Proceedings*, Springer, Berlin, 289.
Gopalswamy, N., Yashiro, S., Michalek, G., Xie, H., Mäkelä, P., Vourlidas, A., Howard, R.A.: 2010c, A catalog of halo coronal mass ejections from SOHO. *Sun Geosph.* **5**, 7.
Gopalswamy, N., Nitta, N., Akiyama, S., Mäkelä, P., Yashiro, S.: 2012, Coronal magnetic field measurement from EUV images made by the solar dynamics observatory. *Astrophys. J.* **744**, 72.
Gosling, J.T.: 1990, *Coronal Mass Ejections and Magnetic Flux Ropes in Interplanetary Space in Physics of Magnetic Flux Ropes*, *Geophys. Monogr. Ser.* **58**, 343.
Hanaoka, Y., Kurokawa, H., Enome, S., Nakajima, H., Shibasaki, K., Nishio, M., *et al.*: 1994, Simultaneous observations of a prominence eruption followed by a coronal arcade formation in radio, soft X-rays, and H(alpha). *Publ. Astron. Soc. Japan* **46**, 205.
Henke, T., Woch, J., Mall, U., Livi, S., Wilken, B., Schwenn, R., *et al.*: 1998, Differences in the O^{7+}/O^{6+} ratio of magnetic cloud and non-cloud coronal mass ejections. *Geophys. Res. Lett.* **25**, 3465.
Henke, T., Woch, J., Schwenn, R., Mall, U., Gloeckler, G., von Steiger, R., *et al.*: 2001, Ionization state and magnetic topology of coronal mass ejections. *J. Geophys. Res.* **106**, 10613.
Hundhausen, A.J., Gilbert, H.E., Bame, S.J.: 1968, Ionization state of the interplanetary plasma. *J. Geophys. Res.* **73**, 5485.
Kim, R.-S., Gopalswamy, N., Cho, K.-S., Moon, Y.-J., Yashiro, S.: 2013, Propagation characteristics of CMEs associated magnetic clouds and ejecta. *Solar Phys.*, in this issue.

Lepri, S.T., Zurbuchen, T.H.: 2004, Iron charge state distributions as an indicator of hot ICMEs: possible sources and temporal and spatial variations during solar maximum. *J. Geophys. Res.* **109**, A01112. doi:10.1029/2003JA009954.

Lepri, S.T., Zurbuchen, T.H.: 2010, Direct observational evidence of filament material within interplanetary coronal mass ejections. *Astrophys. J. Lett.* **723**, L22.

Lepri, S.T., Zurbuchen, T.H., Fisk, L.A., Richardson, I.G., Cane, H.V., Gloeckler, G.: 2001, Iron charge state distributions as an identifier of interplanetary coronal mass ejections. *J. Geophys. Res.* **106**, 29231.

Lin, J., Raymond, J.C., van Ballegooijen, A.A.: 2004, The role of magnetic reconnection in the observable features of solar eruptions. *Astrophys. J.* **602**, 422.

Lynch, B.J., Reinard, A.A., Mulligan, T., Reeves, K.K., Rakowski, C.E., Allred, J.C., *et al.*: 2011, Ionic composition structure of coronal mass ejections in axisymmetric magnetohydrodynamic models. *Astrophys. J.* **740**, 112.

Marubashi, K.: 1997, Interplanetary magnetic flux ropes and solar filaments. In: Crooker, N., Joselyn, J.A., Feynman, J. (eds.) *Coronal Mass Ejections*, *Geophys. Monogr. Ser.* **99**, AGU, Washington, 147.

Owens, M.J., Cargill, P.J., Pagel, C., Siscoe, G.L., Crooker, N.U.: 2005, Characteristic magnetic field and speed properties of interplanetary coronal mass ejections and their sheath regions. *J. Geophys. Res.* **110**, A01105. doi:10.1029/2004JA010814.

Qiu, J., Hu, Q., Howard, T.A., Yurchyshyn, V.B.: 2007, On the magnetic flux budget in low-corona magnetic reconnection and interplanetary coronal mass ejections. *Astrophys. J.* **659**, 758.

Rakowski, C.E., Laming, M.J., Lepri, S.T.: 2007, Ion charge states in halo coronal mass ejections: what can we learn about the explosion? *Astrophys. J.* **667**, 602.

Reinard, A.: 2005, Comparison of interplanetary CME charge state composition with CME-associated flare magnitude. *Astrophys. J.* **620**, 501.

Reinard, A.A.: 2008, Analysis of interplanetary coronal mass ejection parameters as a function of energetics, source location, and magnetic structure. *Astrophys. J.* **682**, 1289.

Reinard, A.A., Zurbuchen, T.H., Fisk, L.A., Lepri, S.T., Skoug, R.M., Gloeckler, G.: 2001, Comparison between average charge states and abundances of ions in CMEs and the slow solar wind. *AIP Conf. Proc.* **598**(1), 139.

Riley, P., Schatzman, C., Cane, H.V., Richardson, I.G., Gopalswamy, N.: 2006, On the rates of coronal mass ejections: remote solar and *in situ* observations. *Astrophys. J.* **647**, 648.

Schmahl, E.J., Schmelz, J.T., Saba, J.L.R., Strong, K.T., Kundu, M.R.: 1990, Microwave and X-ray observations of a major confined solar flare. *Astrophys. J.* **358**, 654.

Uchida, Y., McAllister, A., Strong, K.T., Ogawara, Y., Shimizu, T., Matsumoto, R., Hudson, H.S.: 1992, Continual expansion of the active region corona observed by the Yohkoh soft X-ray telescope. *Publ. Astron. Soc. Japan* **44**, L155.

Xie, H., Gopalswamy, N., St. Cyr, O.C.: 2013, Near-Sun flux rope structure of CMEs. *Solar Phys.* in this issue. doi:10.1007/s11207-012-0209-0.

Yashiro, S., Gopalswamy, N.: 2009, Statistical relationship between solar flares and coronal mass ejections. In: Gopalswamy, N., Webb, D.F. (eds.) *IAU Symposium 257, Universal Heliophysical Processes*, Cambridge Univ. Press, London, 233.

Yashiro, S., Gopalswamy, N., Michalek, G., St. Cyr, O.C., Plunkett, S.P., Rich, N.B., Howard, R.A.: 2004, A catalog of white light coronal mass ejections observed by the SOHO spacecraft. *J. Geophys. Res.* **109**, A07105. doi:10.1029/2003JA010282.

Zhao, L., Zurbuchen, T.H., Fisk, L.A.: 2009, Global distribution of the solar wind during solar cycle 23: ACE observations. *Geophys. Res. Lett.* **36**, L14104. doi:10.1029/2009GL039181.

Solar Phys (2013) 284:203–215
DOI 10.1007/s11207-012-0214-3

Three-Dimensional Evolution of Erupted Flux Ropes from the Sun ($2-20\ R_{\odot}$) to 1 AU

A. Isavnin · A. Vourlidas · E.K.J. Kilpua

Received: 29 March 2012 / Accepted: 10 December 2012 / Published online: 4 January 2013

Abstract Studying the evolution of magnetic clouds entrained in coronal mass ejections using *in-situ* data is a difficult task, since only a limited number of observational points is available at large heliocentric distances. Remote sensing observations can, however, provide important information for events close to the Sun. In this work we estimate the flux rope orientation first in the close vicinity of the Sun ($2-20\ R_{\odot}$) using forward modeling of STEREO/SECCHI and SOHO/LASCO coronagraph images of coronal mass ejections and then *in situ* using Grad–Shafranov reconstruction of the magnetic cloud. Thus, we are able to measure changes in the orientation of the erupted flux ropes as they propagate from the Sun to 1 AU. We present both techniques and use them to study 15 magnetic clouds observed during the minimum following Solar Cycle 23 and the rise of Solar Cycle 24. This is the first multievent study to compare the three-dimensional parameters of CMEs from imaging and *in-situ* reconstructions. The results of our analysis confirm earlier studies showing that the flux ropes tend to deflect towards the solar equatorial plane. We also find evidence of rotation on their travel from the Sun to 1 AU. In contrast to past studies, our method allows one to deduce the evolution of the three-dimensional orientation of individual flux ropes rather than on a statistical basis.

Keywords Coronal mass ejections, interplanetary · Magnetic fields, interplanetary · Magnetic fields, models

Flux-Rope Structure of Coronal Mass Ejections
Guest Editors: N. Gopalswamy, T. Nieves-Chinchilla, M. Hidalgo, J. Zhang, and P. Riley

A. Isavnin (✉) · E.K.J. Kilpua
Department of Physics, University of Helsinki, P.O. Box 64, 00014, Helsinki, Finland
e-mail: Alexey.Isavnin@helsinki.fi

A. Vourlidas
Space Science Division, Naval Research Laboratory, Washington, DC, USA

1. Introduction

Coronal mass ejections (CMEs) are massive bursts of plasma and magnetic field from the Sun into the interplanetary space. Interplanetary coronal mass ejections (ICMEs) are the heliospheric counterparts of the CMEs. ICMEs are one the main drivers of space weather (Tsurutani *et al.*, 1988; Huttunen, Koskinen, and Schwenn, 2002; Zhang *et al.*, 2007). ICMEs show a variety of signatures in *in-situ* observations at 1 AU. Some of them such as the enhancement of the magnetic field, smooth monotonic rotation of the magnetic field through a large angle, low proton temperature and low plasma β indicate the existence of a flux rope structure within the body of the ICME. ICMEs with embedded magnetic flux ropes are called magnetic clouds (MCs). The list of signatures found in *in-situ* measurements of MCs can be found in the paper of Zurbuchen and Richardson (2006). Approximately one-third of all ICMEs observed at 1 AU show magnetic cloud signatures (Gosling, 1990), but there is indirect evidence that all ICMEs might have central flux ropes. Krall (2007) concluded after analyzing *Solar Maximum Mission* (SMM) coronagraph data that all CMEs in his sample may share a similar hollow-flux-rope structure (see also Vourlidas *et al.*, 2013, this volume). As suggested by Jian *et al.* (2006), the absence of MC signatures in many ICMEs may be a positional effect: their analysis showed that in about two-thirds of the cases the spacecraft encounters the ICME so far from the center that the central flux rope is not identifiable. Since the southward magnetic field has the strongest influence on the Earth's magnetosphere, the geoeffectivity of MCs depends on their orientation. The orientation of the MC in the low solar corona and at 1 AU can differ greatly, so it is crucial to understand how the orientation of MCs changes on their journey from the Sun to 1 AU. This knowledge will help us to better understand the processes affecting CME propagation in the heliosphere, improve the solar and heliosphere magnetohydrodynamics simulation techniques and hence improve space weather forecasting.

The orientation of MCs during their journey from the Sun to 1 AU can change significantly. The change of the orientation can be decomposed into latitudinal deflection, longitudinal deflection and rotation. The latitudinal deflection of CMEs in the low corona was reported already by MacQueen, Hundhausen, and Conover (1986). According to their work, CMEs tend to deflect towards the solar equatorial plane by about two degrees on average while traveling from $2R_{\odot}$ to $4R_{\odot}$ during solar minimum. Plunkett *et al.* (2001) found that the latitude distribution of CMEs in the outer corona near solar minimum is very different from the distribution in the inner corona, suggesting that the propagation of CMEs in the inner corona is controlled by the large-scale solar magnetic field which tends to push the CME towards the equatorial streamer belt as it propagates outward. On the other hand, CMEs show no average latitudinal deflection during solar maximum. Cremades, Bothmer, and Tripathi (2006) has shown that the deviation of CMEs with respect to their source regions is always equatorward near solar minimum, while deviations to higher latitudes are also frequent during solar maximum. They also found a significant correlation of the deviation with the number of coronal holes, their area and their distance to the CME source regions. Kilpua *et al.* (2009) pointed that the spatial dimensions of the erupting CME might play a role in determining whether a CME will be deflected towards the equator, *i.e.* slower CMEs with wide longitudinal extent could not penetrate through the background coronal fields.

The evidence for longitudinal deflection is based on the statistics of the solar source regions of geoeffective halo CMEs (*i.e.* CMEs that arrived at the Earth and produced geomagnetic storms). It was found by Wang *et al.* (2002) that the East–West distribution of the CME sources is asymmetrical – the number of geoeffective halo CMEs originating from

the western hemisphere is larger by 57 % compared to the ones originating from the eastern hemisphere. In the paper by Wang *et al.* (2011) the CME deflections were classified into three types:

i) asymmetrical expansion of the CME,
ii) nonradial ejection and
iii) deflected propagation. Deflected propagation in the lower corona can be caused by the interaction of the CME with other neighboring large-scale magnetic field structures such as coronal holes.

MCs can also experience rotation on their journey to 1 AU. The possible reason for MC rotation can be the interaction with neighboring magnetic field structures and the kink instability (Török and Kliem, 2003). But CME rotation is not expected at large distances when the ambient magnetic field is weak (Lynch *et al.*, 2009). Sometimes MCs can suffer rather rapid rotation, however. Vourlidas *et al.* (2011) reported an MC rotating at a rate of 60° per day in the low corona. Based on statistical evidence MCs seem to rotate towards the heliospheric current sheet (HCS) so that the MC stays aligned with the local HCS as shown by Yurchyshyn (2008) and Yurchyshyn, Abramenko, and Tripathi (2009).

It is difficult to study the evolution of MCs from the Sun to 1 AU, since there is only a limited number of observing points for analysis of such a complicated and large structure. The launch of the STEREO mission (Kaiser *et al.*, 2008) made it possible to obtain stereoscopic coronagraph images of the Sun which gave rise to forward modeling (Thernisien, Vourlidas, and Howard, 2009; Thernisien, 2011). Paired with *in-situ* measurements it allows to obtain the geometrical parameters of MCs in different temporal and spatial stages of their evolution. In this work we study the evolution of MCs registered during the minimum following Solar Cycle 23 and the rise of Solar Cycle 24. We use forward modeling technique to study the properties of MCs close to the Sun ($5-20\ R_{\odot}$) and Grad–Shafranov reconstruction at 1 AU.

Our paper is organized as follows: in Section 2 we will describe our method of estimating the orientation of MCs using one example from our list of 15 events, in Section 3 we present the results of our analysis and discuss them in Section 4.

2. Methodology Using an Example Event

A coronagraph is a telescope pointed at the Sun with an occulter blocking the solar disk light. The solar disk is about $10^6 - 10^9$ times brighter than the inner corona, thus the occulter is necessary to observe the solar corona with sufficient contrast to reveal faint structures. There are three coronagraphs on board the SOHO spacecraft with fields of view of $1.1-3\ R_{\odot}$ (C1), $2.2-6\ R_{\odot}$ (C2) and $3.5-30\ R_{\odot}$ (C3), part of the LASCO (*Large Angle and Spectrometric Coronagraph*) experiment (Brueckner *et al.*, 1995). The STEREO spacecraft are supplied with two coronagraphs each with fields of view of $1.5-4\ R_{\odot}$ (COR1) and $2.5-15\ R_{\odot}$ (COR2) and a heliospheric imager (HI) pointed towards the Sun–Earth line, part of the SECCHI (*Sun Earth Connection Coronal and Heliospheric Investigation*: Howard *et al.*, 2008) package. In our study we tracked each CME from 2 to $20-40\ R_{\odot}$ using LASCO C2 and C3 and SECCHI COR2 and HI telescopes. We required that each CME was captured *in-situ* by at least one spacecraft (STEREO and/or *Wind*).

The method we developed in this paper to study the evolution of an MC is based on the forward modeling of coronagraph data (Thernisien, Vourlidas, and Howard, 2009) and Grad–Shafranov reconstruction of *in-situ* MCs (Hu and Sonnerup, 2002). We present this

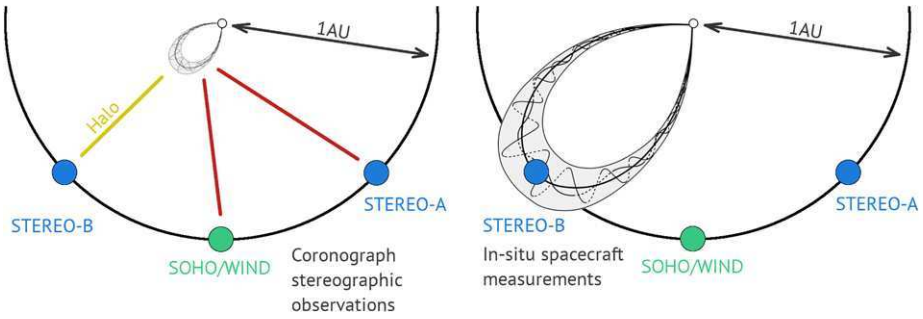

Figure 1 Scheme of an event suitable for our analysis.

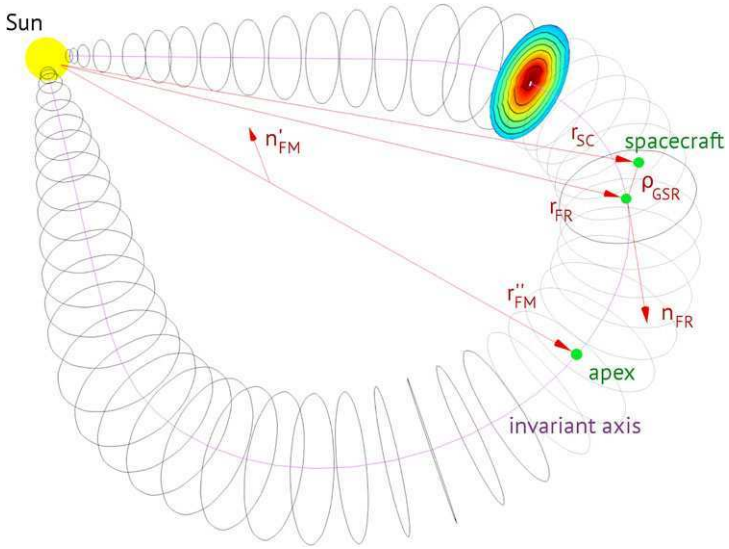

Figure 2 Three-dimensional scheme of a magnetic cloud. $\hat{\mathbf{r}}''_{\mathrm{FM}}$ is the global axis of the flux rope, $\hat{\mathbf{n}}_{\mathrm{FR}}$ is the local invariant axis of the flux rope at the point of intersection with the spacecraft, ρ_{GSR} is the impact parameter.

method alongside an example event of the CME on 4 November 2010 and the associated *in-situ* MC measured on 8 November 2010 by the STEREO-B spacecraft. The schematic representation of this event is depicted on Figure 1.

We assume that the invariant axis of a MC lies in a single plane (Figure 2), so that when the MC changes its orientation, the plane containing the invariant axis changes its orientation accordingly. We will refer to it as the MC plane from now on. The orientation of the MC can be characterised by the normal to the MC plane and the direction from the Sun to the apex of the MC (Figure 2).

The multi-spacecraft forward modeling (FM) was introduced by Thernisien, Vourlidas, and Howard (2009) and is implemented in the SolarSoft package. The technique is based on the fitting of a three-dimensional hollow-croissant-shaped structure to stereoscopic coronagraph images of a CME. It is preferable to use all three spacecraft observations for a fitting procedure since at least one of them will observe the CME as halo or partial halo resulting in

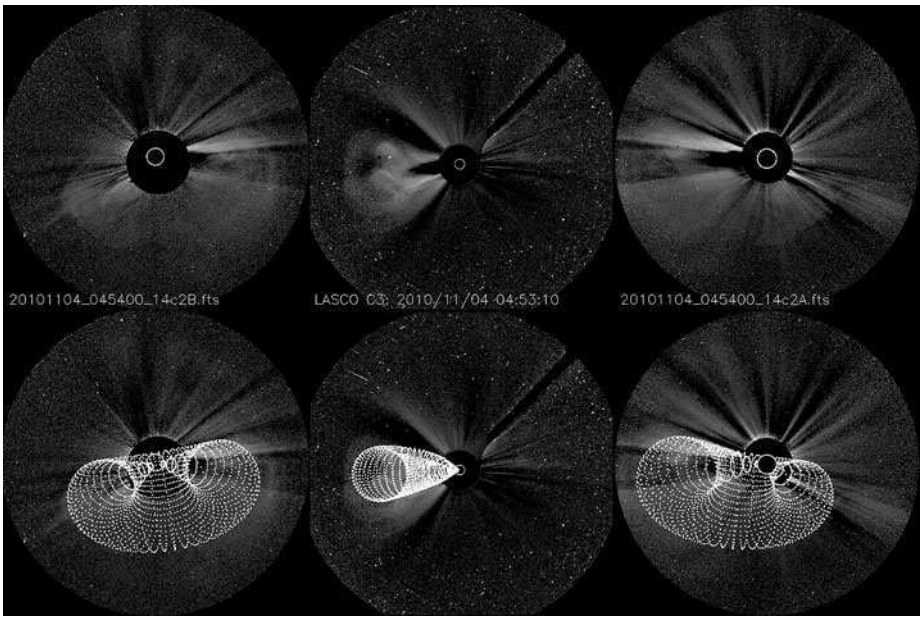

Figure 3 Example of forward modeling (lower panels) of the CME of 4 November 2010 (upper panels). The gray-scale images from left to right are the coronagraph images obtained by STEREO-B/SECCHI COR2, SOHO/LASCO C3 and STEREO-A/SECCHI COR2 telescopes.

faint coronagraph images. Figure 3 shows the FM fitting for the CME on 4 November 2010. The separation between the STEREO spacecraft was about 166°, so both STEREO spacecraft observed partial halo CME (backside partial halo CME for STEREO-A). LASCO, at the same time, observed the CME on the Eastern part of the limb. The output of FM that we are interested in are the direction of radial CME propagation ($\theta_{\rm FM}, \phi_{\rm FM}$) and its rotation angle $\gamma_{\rm FM}$. These outputs are given in the Stonyhurst coordinate system (Thompson, 2006). The direction of CME propagation $\hat{\mathbf{r}}_{\rm FM}$ and the normal to the MC plane $\hat{\mathbf{n}}_{\rm FM}$ in the lower corona are determined then as

$$\hat{\mathbf{r}}_{\rm FM} = \cos\theta_{\rm FM}\cos\phi_{\rm FM}\hat{\mathbf{e}}_x + \cos\theta_{\rm FM}\sin\phi_{\rm FM}\hat{\mathbf{e}}_y + \sin\theta_{\rm FM}\hat{\mathbf{e}}_z, \tag{1}$$

$$\hat{\mathbf{n}}_{\rm FM} = \text{rotate}\big([\hat{\mathbf{r}}_{\rm FM} \times \hat{\mathbf{e}}_y] \times \hat{\mathbf{r}}_{\rm FM}, \hat{\mathbf{r}}_{\rm FM}, \gamma_{\rm FM}\big), \tag{2}$$

where we defined vector rotation operator "rotate" as

$$\text{rotate}(\hat{\mathbf{v}}, \hat{\mathbf{a}}, \gamma) = \hat{\mathbf{v}}\cos\gamma + (\hat{\mathbf{v}}\cdot\hat{\mathbf{a}})(1-\cos\gamma)\hat{\mathbf{a}} + [\hat{\mathbf{a}}\times\hat{\mathbf{v}}]\sin\gamma, \tag{3}$$

which rotates $\hat{\mathbf{v}}$ around $\hat{\mathbf{a}}$ by angle γ counterclockwise.

After having determined the orientation of the CME close to the Sun we turn our attention to *in-situ* observations near 1 AU. The Grad–Shafranov reconstruction (GSR) (Hu and Sonnerup, 2002) is used for the estimation of the local direction of the invariant axis of MC and reconstruction of a slice of the MC. We use the modified version of GSR described in Isavnin, Kilpua, and Koskinen (2011). The output we are interested in is the local direction of the invariant axis of the flux rope ($\theta_{\rm GSR}, \phi_{\rm GSR}$)

$$\hat{\mathbf{n}}_{\rm FR} = \cos\theta_{\rm GSR}\cos\phi_{\rm GSR}\hat{\mathbf{e}}_x + \cos\theta_{\rm GSR}\sin\phi_{\rm GSR}\hat{\mathbf{e}}_y + \sin\theta_{\rm GSR}\hat{\mathbf{e}}_z, \tag{4}$$

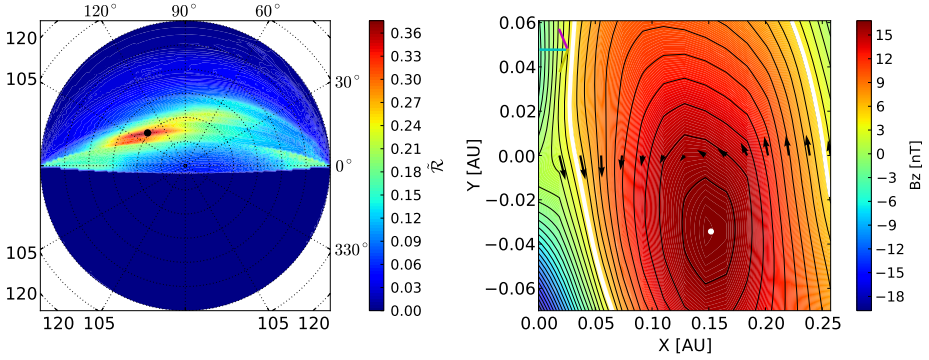

Figure 4 Residual map (left) and magnetic field map (right) for the MC registered on 8 November 2010 by STEREO-B spacecraft. The projected RTN coordinate axes are R_{RTN} (cyan), T_{RTN} (magenta) and N_{RTN} (yellow).

and the impact parameter ρ_{GSR}. The impact parameter is the measure of the closest approach of the spacecraft to the invariant axis of the flux rope, calculated either as the distance of the closest approach (in astronomical units) or the distance of the closest approach divided by the radius of the flux rope cross-section. Knowing the position of the spacecraft which crossed the MC $(\theta_{\mathrm{SC}}, \phi_{\mathrm{SC}})$

$$\hat{\mathbf{r}}_{\mathrm{SC}} = \cos\theta_{\mathrm{SC}} \cos\phi_{\mathrm{SC}} \hat{\mathbf{e}}_x + \cos\theta_{\mathrm{SC}} \sin\phi_{\mathrm{SC}} \hat{\mathbf{e}}_y + \sin\theta_{\mathrm{SC}} \hat{\mathbf{e}}_z \tag{5}$$

and the impact parameter ρ_{GSR} we can estimate the vector pointing to the part of the of flux rope closest to the spacecraft trajectory using the following equation:

$$\hat{\mathbf{r}}_{\mathrm{FR}} = \mathrm{rotate}\left(\hat{\mathbf{r}}_{\mathrm{SC}}, \hat{\mathbf{n}}_{\mathrm{FR}}, 2\arcsin\frac{\mathrm{sign}(\hat{\mathbf{n}}_{\mathrm{FR}} \cdot \hat{\mathbf{e}}_y)\rho_{\mathrm{GSR}}}{2}\right). \tag{6}$$

The vector defined by Equation (6) lies in the MC plane. We can estimate the normal to the MC plane at 1 AU as

$$\hat{\mathbf{n}}_{\mathrm{GSR}} = \hat{\mathbf{n}}_{\mathrm{FR}} \times \hat{\mathbf{r}}_{\mathrm{FR}}. \tag{7}$$

The MC associated with the CME in the example event was registered *in situ* by the STEREO-B spacecraft on 8 November 2010. Figure 4 shows the residual map and the reconstructed magnetic field map for this event. The residual map shows the process of the search for the local direction of the invariant axis of the flux rope. It represents the hemisphere of all possible orientations of the axis and the direction with the minimal residue is the estimated invariant axis of the flux rope. The reconstructed magnetic field map is essentially the cross-section of the flux rope in the vicinity of the spacecraft trajectory. Black arrows show the magnetic field measured *in situ* and projected onto the plane perpendicular to the invariant axis of the flux rope. Black contour lines denote the equipotential levels, where the absolute values of the vector potential are considered. The white dot represents the invariant axis of the flux rope. The thick white contour line shows the boundary of the unperturbed part of the flux rope.

Wang *et al.* (2004) introduced the kinetic interpretation of the longitudinal deflection of MCs which conforms with the statistics of observations of geoeffective MCs and their sources (Wang *et al.*, 2002). According to these authors the longitudinal deflection of MCs

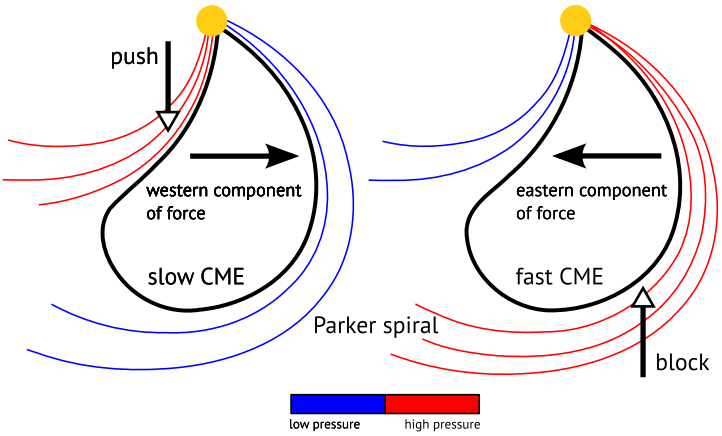

Figure 5 Interaction of a slow (left) and fast (right) CME with Parker-spiral-structured solar wind (adapted from Wang *et al.*, 2004).

is caused by the interaction of the MC with the Parker-spiral-structured solar wind (see Figure 5). If an MC propagates slower than the background solar wind it is pushed by the faster solar wind thus getting the westward component of the force. On the other hand, a fast MC is blocked by the slower background solar wind thus getting the eastward component of the force. Longitudinal deflection can be estimated using the following equation:

$$\Delta\phi = \Omega\left(\frac{1}{V_{\mathrm{MC}}} - \frac{1}{V_{\mathrm{SW}}}\right) \cdot 1\ \mathrm{AU}, \tag{8}$$

where V_{MC} is the average speed of the MC propagation, V_{SW} is the average velocity of the background solar wind and $\Omega \approx 2.7 \times 10^{-6}\ \mathrm{rad\,s^{-1}}$ is the angular velocity of the Sun's rotation. The positive value of $\Delta\phi$ represents westward deflection, while the negative value of $\Delta\phi$ shows eastward deflection of the MC. MCs which propagate with the velocity close to the background solar wind velocity do not experience longitudinal deflection on average. It should be noted that this is a rough estimate since the speed of the MC can change on its journey from the Sun to 1 AU. Since we are studying only events registered near the solar minimum, most of which are slow CMEs, the simplicity of Equation (8) should not affect the results of the analysis significantly. For our example event the MC propagation velocity at 1 AU is slightly lower than the background solar wind. So we estimate the westward deflection using Equation (8) to be $\Delta\phi = 1°$.

Longitudinal deflection is taken into account by rotating the initial MC direction $\hat{\mathbf{r}}_{\mathrm{FM}}$ by $\Delta\phi$ around $\hat{\mathbf{e}}_z$:

$$\hat{\mathbf{r}}'_{\mathrm{FM}} = \mathrm{rotate}(\hat{\mathbf{r}}_{\mathrm{FR}}, \hat{\mathbf{e}}_z, \Delta\phi). \tag{9}$$

Since $\hat{\mathbf{r}}'_{\mathrm{FM}}$ is directed along the global axis of the MC through its apex, the possible rotation of the MC around its axis will not affect $\hat{\mathbf{r}}'_{\mathrm{FM}}$. Then only latitudinal deflection can change $\hat{\mathbf{r}}'_{\mathrm{FM}}$:

$$\hat{\mathbf{r}}''_{\mathrm{FM}} = \mathrm{rotate}\left(\hat{\mathbf{r}}'_{\mathrm{FM}}, \hat{\mathbf{e}}'_y, \Delta\theta\right), \tag{10}$$

where $\hat{\mathbf{e}}'_y = \hat{\mathbf{e}}_z \times \hat{\mathbf{r}}'_{\rm FM}$ and $\Delta\theta$ is latitudinal deflection angle. The vectors $\hat{\mathbf{r}}''_{\rm FM}$ and $\hat{\mathbf{r}}_{\rm FR}$ both lie in the MC plane (see Figure 2) and its normal at 1 AU can be estimated as

$$\hat{\mathbf{n}}'_{\rm FM} = \hat{\mathbf{r}}_{\rm FR} \times \hat{\mathbf{r}}''_{\rm FM}. \tag{11}$$

Latitudinal deflection is determined as such an angle $\Delta\theta$ for which $\hat{\mathbf{n}}_{\rm GSR} \cdot \hat{\mathbf{n}}'_{\rm FM} = 1$. The positive value of $\Delta\theta$ represents North-to-South deflection and negative value shows South-to-North rotation. For our example event we found the latitudinal deflection to be $\Delta\theta = -17°$. The MC deflected from the Southern to the Northern hemisphere, crossing the helioequatorial plane.

After estimating the $\Delta\phi$ and $\Delta\theta$ deflections, the rotation can be calculated using the following equation:

$$\Delta\gamma = \arctan\left(\frac{\hat{\mathbf{r}}_{\rm FR} \cdot \hat{\mathbf{e}}'_z}{\hat{\mathbf{r}}_{\rm FR} \cdot \hat{\mathbf{e}}'_y}\right) - \gamma_{\rm FM}, \tag{12}$$

where $\hat{\mathbf{e}}'_z = \hat{\mathbf{r}}''_{\rm FM} \times \hat{\mathbf{e}}'_y$. The positive value of $\Delta\gamma$ represents counterclockwise rotation, while the negative value of $\Delta\gamma$ shows clockwise rotation of the MC around its global axis. Using Equation (12) we estimate a rotation by $\Delta\gamma = 30°$ for our example event. It should be noted that the FM fit contains no information about polarity or chirality of the flux rope. Thus, the estimated initial rotation angle of the flux rope has an ambiguity of 180 degrees. This implies that Equation (12) shows the change of the tilt angle of the MC plane, but not the real direction or full amount of rotation.

3. Results

For the analysis we selected the MCs which were observed during the minimum following the Solar Cycle 23 and the rise of the Solar Cycle 24, *i.e.* years 2008 – 2010. Such a choice is based on several considerations, *i.e.* sufficiently large angular distance (at least 30 – 40 degrees) between the STEREO spacecraft which was launched in 2006 is required for the FM technique results to be reliable (Thernisien, Vourlidas, and Howard, 2009). The separation between the STEREO and SOHO spacecraft grew from 26° to 87° during that period. The minimum of solar activity is also characterised by a less dynamic structure of the heliospheric current sheet (HCS) and coronal holes which facilitate studies of interaction of an MC with these structures.

Similar to other flux rope fitting techniques, GSR works best for small impact parameter events (Isavnin, Kilpua, and Koskinen, 2011), so we conducted analysis only for MCs which were crossed close to their invariant axis by the spacecraft at 1 AU. We have selected 15 events for our analysis, the results of analysis are summarized in Table 1.

The diagrams in Figure 6 visualize the estimated deflection and rotation experienced by the analyzed MCs when they propagated from the Sun to 1 AU. Also, the last three columns of Table 1 give the longitudinal and latitudinal deflection angles (calculated from Equations (8) – (11)) and the rotation angle estimated from Equation (12) for each event. In the left diagram of Figure 6 the x-components of the lines connecting the red squares and green diamonds show the amount of longitudinal deflection, while the y-components of the lines represent the amount of latitudinal deflection. In the right panel, the longer the angular distance covered by a curve between the red squares and green diamonds the more the MC has rotated during its interplanetary propagation.

As shown by Figure 6 and Table 1 for all studied events the longitudinal deflection was small, less than 6 degrees. The latitudinal deflection was clearly larger than the longitudinal,

Table 1 The results of the analysis of MC deflection for 15 events. The CME part of the table represents the results of FM analysis at 5 – 20 $R_{\odot}$, the MC part of the table represents the results of GSR analysis at 1 AU, the Δ orientation represents the estimated deflection angles. The columns from left to right are as follows: # – event number, date – date of the CME event start, ϕ_{FM}, θ_{FM} – direction of the CME propagation, γ_{FM} – initial rotation angle of the CME, date – date of MC registration at 1 AU, SC – spacecraft which observed the MC at 1 AU, ϕ_{SC}, θ_{SC} – coordinates of the spacecraft, ϕ_{GSR}, θ_{GSR} – direction of the invariant axis of the MC, ρ_{GSR} – impact parameter, $\Delta\phi$ – longitudinal deflection (positive for East-to-West), $\Delta\theta$ – latitudinal deflection (positive for North-to-South), $\Delta\gamma$ – change of the rotation angle (positive for counterclockwise).

#	CME				MC							Δ orientation		
	Date	ϕ_{FM}	θ_{FM}	γ_{FM}	Date	SC	ϕ_{SC}	θ_{SC}	ϕ_{GSR}	θ_{GSR}	ρ_{GSR} [AU]	$\Delta\phi$	$\Delta\theta$	$\Delta\gamma$
1	2008-06-02	−31.85	−2.23	−48.49	2008-06-06	STB	−24.97	−3.77	−152.9	58.0	−0.0045	−0.58	−13.62	−14.20
2	2008-07-07	−22.39	−18.88	−2.20	2008-07-10	STB	−27.20	0.10	88.3	−28.6	0.0195	−0.05	−14.65	−29.16
3	2008-08-31	3.10	−9.85	−1.64	2008-09-03	*Wind*	0.08	7.18	−107.4	12.9	0.0085	−0.77	−15.92	−14.00
4	2008-12-12	8.19	7.20	63.11	2008-12-17	*Wind*	0.08	−1.17	115.7	−15.8	−0.0279	−0.31	9.26	−80.26
5	2008-12-27	−38.37	16.37	13.74	2008-12-31	STB	−45.20	3.40	24.5	−12.7	0.0264	1.66	16.62	−28.03
6	2009-09-27	−52.16	4.82	15.49	2009-10-02	STB	−56.73	5.60	75.1	−42.7	−0.0031	−5.38	−1.92	−64.17
7	2010-01-15	−72.40	6.00	15.69	2010-01-20	STB	−69.07	3.90	−180.0	−25.8	−0.0045	−0.15	3.54	10.54
8	2010-02-01	64.54	−17.59	24.64	2010-02-05	STA	64.10	−6.20	−51.9	−31.2	−0.0163	−0.16	−14.76	10.31
9	2010-04-03	4.60	−23.66	7.93	2010-04-05	*Wind*	−0.24	−6.30	140.6	−3.4	0.0144	−3.93	−16.59	−21.31
10	2010-05-23	12.25	6.23	54.98	2010-05-28	*Wind*	0.03	−1.02	67.6	−60.1	0.0007	4.05	34.75	67.43
11	2010-05-27	72.92	−11.73	62.35	2010-05-31	STA	71.70	6.50	132.7	0.1	0.0165	−2.28	−17.46	−65.27
12	2010-06-13	97.22	20.04	−17.36	2010-06-16	STA	73.68	7.30	−3.4	15.2	−0.0078	−0.25	18.85	1.66
13	2010-11-04	−76.07	−6.56	11.06	2010-11-08	STB	−82.20	6.40	−139.0	−35.3	0.0341	1.11	−16.84	29.69
14	2010-12-12	48.40	−16.87	6.02	2010-12-15	STA	85.20	−7.30	10.1	10.9	−0.0158	2.00	−17.86	−21.52
15	2010-12-12	−87.88	−10.46	−11.40	2010-12-17	STB	−87.30	7.30	−166.0	0.2	0.0158	2.78	−2.02	−9.85

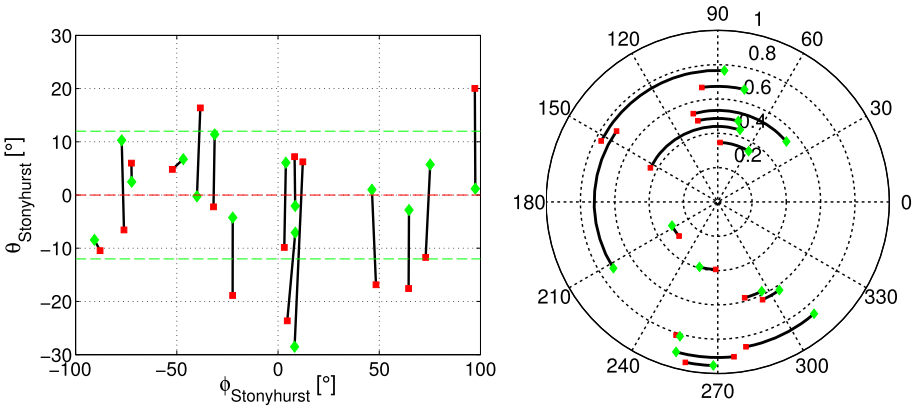

Figure 6 Diagrams of deflection (left) and rotation (right) of the studied MCs. Red squares denote the direction of MC propagation (left) and the direction of the normal to the MC plane (right) close to the Sun, *i.e.* in the initial position. Green diamonds denote the direction of MC propagation (left) and the direction of the normal to the MC plane (right) at 1 AU, *i.e.* in the final position.

exceeding 10° for the majority of events with the largest deflection of 35° (event #10). According to our study 14 out of 15 analyzed MCs deflected towards the helioequatorial plane, often crossing it. The only exception is event #6 for which the deflection by 2° away from helioequatorial plane was found. This event is also the one with the smallest amount of latitudinal deflection among the 15 events we studied.

The amount of rotation of the studied MCs ranged from events that experienced practically no rotation (event #12) to events that rotated as much as 80 degrees (event #4). The average absolute value of rotation angle for our data set was 31 degrees.

From Figure 6 (left) it can be seen that the directions of propagation of 14 out of 15 MCs deflected to or stayed in the latitude range of $\theta_{\text{Stonyhurst}} = [-12°, 12°]$ after their travel from the Sun to 1 AU. Thus, MCs seem to align the direction of their expansion with the solar equatorial plane.

4. Discussion

We have presented the first detailed study of the three-dimensional evolution of the orientation of MCs from the Sun to 1 AU. The analysis makes use of coronagraph images of CMEs and *in-situ* observations of erupted flux ropes and is capable of more precise identification of the three-dimensional orientation of individual flux ropes and their evolution than was possible in the past. This method utilizes the FM and GSR techniques for estimation of the flux rope orientation close to the Sun and at 1 AU, respectively. The approach is constrained by certain limitations on the quality of the studied events. The flux rope structure within the CME associated with the analyzed MC has to be clear enough to be easily distinguishable in the coronagraph images. The separation between the STEREO spacecraft has to be large enough (at least 30 – 40 degrees) to get three-dimensional representation of the CME and hence a better FM fit. The impact parameter of the MC observed at 1 AU has to be small to estimate the orientation of MC at 1 AU more precisely using GSR technique, which works better for small impact parameters.

Based on these considerations we have selected 15 clear events during the years 2008–2010 and used our method to study their three-dimensional evolution from the Sun to 1 AU. The events were observed during the minimum following Solar Cycle 23 and the rise of Solar Cycle 24. Our analysis shows that MCs tend to deflect towards the solar equatorial plane on their journey from the Sun to 1 AU. This result is in agreement with previous statistical studies by MacQueen, Hundhausen, and Conover (1986), Plunkett *et al.* (2001) and Cremades, Bothmer, and Tripathi (2006), though in our work we were able to calculate the evolution of MCs' orientation directly from the multi-spacecraft observations. In this study we have not considered the source regions of CMEs but we started tracking MCs from 2 $R_{\odot}$, hence we showed that the latitudinal deflection of MC can happen not only in the lower corona, but the orientation of MC continues to evolve all the way to 1 AU. A possible reason for the latitudinal deflection may be the kinematic interaction between CMEs and fast solar wind.

The studied events showed very little longitudinal deflection. As discussed in the Introduction, Wang *et al.* (2002) observed an obvious East–West asymmetry in the source region distribution of geoeffective halo CMEs. While the sample of Wang *et al.* (2002) covers the rising phase of solar activity and solar maximum, our study period coincides with relatively low solar activity conditions, and thus most of our CMEs were slow and embedded into solar wind of the speed close to the CME speed, *i.e.* were not pushed by fast solar wind or blocked by slow solar wind. Thus, it is possible that our data set represents events that were not much influenced by the ambient solar wind flow. We also expect that forward modeling based on the coronagraph data gives a more reliable estimate of the CME propagation direction than the analysis of their source regions based on the solar disk observation. Our results are also consistent with the analysis by Rodriguez *et al.* (2011) who found that the predictions of ICME detections based on the forward modeling of STEREO/COR2 data matched well with the actual *in-situ* observations. Our results thus imply that at least near solar minimum the CME propagation direction in longitude can be predicted accurately based on the coronagraph data and this direction does not change significantly from a few tens of solar radii from the Sun to 1 AU. It should be noted that although Equation (8) is a rough estimate of the longitudinal deflection, it does not affect the accuracy of the presented technique dramatically. For instance, introducing an error $\delta\Delta\phi = 10^{\circ}$ to the longitudinal deflection estimate leads to the average error $\delta\Delta\theta = 3^{\circ}$ of latitudinal deflection estimate and $\delta\Delta\gamma = 0.1^{\circ}$ of rotation angle estimate for the studied MCs.

The rotation of the studied MCs could be caused by the disconnection of one of the flux rope footpoints early in the eruption (Vourlidas *et al.*, 2011; Nieves-Chinchilla *et al.*, 2012), interaction with large-scale magnetic structures in the solar wind and HCS (Yurchyshyn, 2008). Analysis of these possibilities in relation to each event will be the subject of our upcoming research.

Acknowledgements The work of A. Isavnin and E. Kilpua was supported by the Academy of Finland. The work of A. Vourlidas is supported by NASA contract S-136361-Y to the Naval Research Laboratory. LASCO was constructed by a consortium of institutions: NRL (USA), MPI fur Aeronomie (Germany), LAS (France) and University of Birmingham (UK). The SECCHI data are produced by an international consortium of the NRL, LMSAL and NASA GSFC (USA), RAL and University of Birmingham (UK), MPS (Germany), CSL (Belgium), IOTA and IAS (France).

References

Brueckner, G.E., Howard, R.A., Koomen, M.J., Korendyke, C.M., Michels, D.J., Moses, J.D., Socker, D.G., Dere, K.P., Lamy, P.L., Llebaria, A., Bout, M.V., Schwenn, R., Simnett, G.M., Bedford, D.K.,

Eyles, C.J.: 1995, The large angle spectroscopic coronagraph (LASCO). *Solar Phys.* **162**, 357 – 402. doi:10.1007/BF00733434.
Cremades, H., Bothmer, V., Tripathi, D.: 2006, Properties of structured coronal mass ejections in solar cycle 23. *Adv. Space Res.* **38**, 461 – 465. doi:10.1016/j.asr.2005.01.095.
Gosling, J.T.: 1990, Coronal mass ejections and magnetic flux ropes in interplanetary space. In: Priest, E.R., Lee, L.C., Russel, C.T. (eds.) *Geophys. Monogr. Ser.* **58**, 343 – 364.
Howard, R.A., Moses, J.D., Vourlidas, A., Newmark, J.S., Socker, D.G., Plunkett, S.P., Korendyke, C.M., Cook, J.W., Hurley, A., Davila, J.M., Thompson, W.T., St. Cyr, O.C., Mentzell, E., Mehalick, K., Lemen, J.R., Wuelser, J.P., Duncan, D.W., Tarbell, T.D., Wolfson, C.J., Moore, A., Harrison, R.A., Waltham, N.R., Lang, J., Davis, C.J., Eyles, C.J., Mapson-Menard, H., Simnett, G.M., Halain, J.P., Defise, J.M., Mazy, E., Rochus, P., Mercier, R., Ravet, M.F., Delmotte, F., Auchere, F., Delaboudiniere, J.P., Bothmer, V., Deutsch, W., Wang, D., Rich, N., Cooper, S., Stephens, V., Maahs, G., Baugh, R., McMullin, D., Carter, T.: 2008, Sun Earth connection coronal and heliospheric investigation (SECCHI). *Space Sci. Rev.* **136**, 67 – 115. doi:10.1007/s11214-008-9341-4.
Hu, Q., Sonnerup, B.U.Ö.: 2002, Reconstruction of magnetic clouds in the solar wind: orientations and configurations. *J. Geophys. Res.* **107**, 1142. doi:10.1029/2001JA000293.
Huttunen, K.E.J., Koskinen, H.E.J., Schwenn, R.: 2002, Variability of magnetospheric storms driven by different solar wind perturbations. *J. Geophys. Res.* **107**, 1121 – 1128. doi:10.1029/2001JA900171.
Isavnin, A., Kilpua, E.K.J., Koskinen, H.E.J.: 2011, Grad–Shafranov reconstruction of magnetic clouds: overview and improvements. *Solar Phys.* **273**, 205 – 219. doi:10.1007/s11207-011-9845-z.
Jian, L., Russel, C.T., Luhmann, J.G., Skoug, R.M.: 2006, Properties of interplanetary coronal mass ejections at one AU during 1995 – 2004. *Solar Phys.* **239**, 393 – 436. doi:10.1007/s11207-006-0133-2.
Kaiser, M.L., Kucera, T.A., Davila, J.M., Cyr, O.C.S., Guhathakurta, M., Crhistian, E.: 2008, The STEREO mission: an introduction. *Space Sci. Rev.* **136**, 5 – 16. doi:10.1007/s11214-007-9277-0.
Kilpua, E.K.J., Pomoell, J., Vourlidas, A., Vainio, R., Luhmann, J., Li, Y., Schroeder, P., Galvin, A.B., Simunac, K.: 2009, STEREO observations of interplanetary coronal mass ejections and prominence deflection during solar minimum period. *Ann. Geophys.* **27**, 4491 – 4503. doi:10.5194/angeo-27-4491-2009.
Krall, J.: 2007, Are all coronal mass ejections hollow flux ropes? *Astrophys. J.* **657**, 559 – 566. doi:10.1086/510191.
Lynch, B.J., Antiochos, S.K., Li, Y., Luhmann, J.G., DeVore, C.R.: 2009, Rotation of coronal mass ejections during eruption. *Astrophys. J.* **697**, 1918 – 1927. doi:10.1088/0004-637X/697/2/1918.
MacQueen, R.M., Hundhausen, A.J., Conover, C.W.: 1986, The propagation of coronal mass ejection transients. *J. Geophys. Res.* **91**, 31 – 38. doi:10.1029/JA091iA01p00031.
Nieves-Chinchilla, T., Colaninno, R., Vourlidas, A., Szabo, A., Lepping, R.P., Boardsen, S.A., Anderson, B.J., Korth, H.: 2012, Remote and *in situ* observations of an unusual Earth-directed coronal mass ejection from multiple viewpoints. *J. Geoph. Res.* **117**, A017243. doi:10.1029/2011JA017243.
Plunkett, S.P., Thompson, B.J., Cyr, O.C.S., Howard, R.A.: 2001, Solar source regions of coronal mass ejections and their geomagnetic effects. *J. Atmos. Solar-Terr. Phys.* **63**, 389 – 402. doi:10.1016/S1364-6826(00)00166-8.
Rodriguez, L., Mierla, M., Zhukov, A.N., West, M., Kilpua, E.: 2011, Linking of remote-sensing and *in situ* observations of CMEs using STEREO. *Solar Phys.* **270**, 561 – 573. doi:10.1007/s11207-011-9784-8.
Thernisien, A.: 2011, Implementation of the graduated cylindrical shell model for the three-dimensional reconstruction of coronal mass ejections. *Astrophys. J. Suppl.* **194**, 33. doi:10.1088/0067-0049/194/2/33.
Thernisien, A., Vourlidas, A., Howard, R.A.: 2009, Forward modeling of coronal mass ejections using STEREO/SECCHI data. *Solar Phys.* **256**, 111 – 130. doi:10.1007/s11207-009-9346-5.
Thompson, W.T.: 2006, Coordinate systems for solar image data. *Astron. Astrophys.* **449**, 791 – 803. doi:10.1051/0004-6361:20054262.
Török, T., Kliem, B.: 2003, The evolution of twisting coronal magnetic flux tubes. *Astron. Astrophys.* **406**, 1043 – 1059. doi:10.1051/0004-6361:20030692.
Tsurutani, B.T., Gonzalez, W.D., Tang, F., Akasofu, S.I., Smith, E.J.: 1988, Origin of interplanetary southward magnetic fields responsible for major magnetic storms near solar maximum (1978 – 1979). *J. Geophys. Res.* **93**, 8519 – 8531. doi:10.1029/JA093iA08p08519.
Vourlidas, A., Colaninno, R., Noeves-Chinchilla, T., Stenborg, G.: 2011, The first observation of a rapidly rotating coronal mass ejection in the middle corona. *Astrophys. J. Lett.* **733**, L23. doi:10.1088/2041-8205/733/2/L23.
Vourlidas, A., Lynch, B.J., Howard, R.A., Li, Y.: 2013, How many CMEs have flux ropes? Deciphering the signatures of shocks, flux ropes, and prominences in coronagraph observations of CMEs. *Solar Phys.* in this issue. doi:10.1007/s11207-012-0084-8.
Wang, Y.M., Ye, P.Z., Wang, S., Zhou, G.P., Wang, J.X.: 2002, A statistical study on the geoeffectiveness of Earth-directed coronal mass ejections from March 1997 to December 2000. *J. Geophys. Res.* **107**, 1340. doi:10.1029/2002JA009244.

Wang, Y., Chen, C., Gui, B., Shen, C., Ye, P., Wang, S.: 2011, Statistical study of coronal mass ejection source locations: understanding CMEs viewed in coronagraphs. *J. Geophys. Res.* **116**, A04104. doi:10.1029/2010JA016101.

Wang, Y., Shen, C., Wang, S., Ye, P.: 2004, Deflection of coronal mass ejection in the interplanetary medium. *Solar Phys.* **222**, 329 – 343. doi:10.1023/B:SOLA.0000043576.21942.aa.

Yurchyshyn, V.: 2008, Relationship between EIT post eruption arcades, coronal mass ejections, coronal neutral line and magnetic clouds. *Astrophys. J. Lett.* **675**, L49 – L52. doi:10.1086/533413.

Yurchyshyn, V., Abramenko, V., Tripathi, D.: 2009, Rotation of white-light coronal mass ejection structures as inferred from LASCO coronagraph. *Astrophys. J.* **705**, 426 – 435. doi:10.1088/0004-637X/705/1/426.

Zhang, J., Richardson, I.G., Webb, D.F., Gopalswamy, N., Huttunen, E., Kasper, J.C., Nitta, N.V., Poomvises, W., Thompson, B.J., Wu, C.C., Yashiro, S., Zhukov, A.N.: 2007, Solar and interplanetary sources of major geomagnetic storms (Dst ≤ -100 nT) during 1996 – 2005. *J. Geophys. Res.* **112**, A10102. doi:10.1029/2007JA012321.

Zurbuchen, T.H., Richardson, I.G.: 2006, *In-situ* solar wind and magnetic field signatures of interplanetary coronal mass ejections. *Space Sci. Rev.* **123**, 31 – 43. doi:10.1007/s11214-006-9010-4.

Solar Phys (2013) 284:59–75
DOI 10.1007/s11207-012-0211-6

Coronal Hole Influence on the Observed Structure of Interplanetary CMEs

P. Mäkelä · N. Gopalswamy · H. Xie · A.A. Mohamed · S. Akiyama · S. Yashiro

Received: 31 March 2012 / Accepted: 3 December 2012 / Published online: 4 January 2013

Abstract We report on the coronal hole (CH) influence on the 54 magnetic cloud (MC) and non-MC associated coronal mass ejections (CMEs) selected for studies during the Coordinated Data Analysis Workshops (CDAWs) focusing on the question if all CMEs are flux ropes. All selected CMEs originated from source regions located between longitudes 15E–15W. Xie, Gopalswamy, and St. Cyr (2013, *Solar Phys.*, doi:10.1007/s11207-012-0209-0) found that these MC and non-MC associated CMEs are on average deflected towards and away from the Sun–Earth line, respectively. We used a CH influence parameter (CHIP) that depends on the CH area, average magnetic field strength, and distance from the CME source region to describe the influence of all on-disk CHs on the erupting CME. We found that for CHIP values larger than 2.6 G the MC and non-MC events separate into two distinct groups where MCs (non-MCs) are deflected towards (away) from the disk center. Division into two groups was also observed when the distance to the nearest CH was less than 3.2×10^5 km. At CHIP values less than 2.6 G or at distances of the nearest CH larger than 3.2×10^5 km

Flux-Rope Structure of Coronal Mass Ejections
Guest Editors: N. Gopalswamy, T. Nieves-Chinchilla, M. Hidalgo, J. Zhang, and P. Riley

P. Mäkelä (✉) · H. Xie · A.A. Mohamed · S. Akiyama · S. Yashiro
The Catholic University of America, Washington, DC, USA
e-mail: pertti.makela@nasa.gov

H. Xie
e-mail: hong.xie@nasa.gov

A.A. Mohamed
e-mail: amaal.shahin@nasa.gov

S. Akiyama
e-mail: sachiko.akiyama@nasa.gov

S. Yashiro
e-mail: seiji.yashiro@nasa.gov

P. Mäkelä · N. Gopalswamy · H. Xie · A.A. Mohamed · S. Akiyama · S. Yashiro
NASA Goddard Space Flight Center, Greenbelt, USA

N. Gopalswamy
e-mail: nat.gopalswamy@nasa.gov

the deflection distributions of the MC and non-MCs started to overlap, indicating diminishing CH influence. These results give support to the idea that all CMEs are flux ropes, but those observed to be non-MCs at 1 AU could be deflected away from the Sun–Earth line by nearby CHs, making their flux rope structure unobservable at 1 AU.

Keywords Sun · Coronal holes · Coronal mass ejections · Magnetic clouds · Ejecta

1. Introduction

Coronal mass ejections (CMEs) are magnetized plasma structures that are expelled from the solar corona into interplanetary space. If the CME is launched near the center of the visible solar disk, the CME will hit Earth within few days, possibly causing a severe geomagnetic storm. When the interplanetary counterpart of the CME near the Sun, known as interplanetary CME (ICME), arrives at Earth, an observer near Earth can measure the plasma and magnetic field properties of the passing ICME (see *e.g.*, Burlaga *et al.*, 1981; Gopalswamy, 2006; Zurbuchen and Richardson, 2006; Richardson and Cane, 2010). Therefore if we assume that all CMEs are flux ropes, ICMEs associated with near-disk-center CMEs should show at 1 AU magnetic signatures of flux rope structure, *i.e.* smooth rotation of magnetic field. These structures with smoothly rotating magnetic fields are known as magnetic clouds (MCs) (see *e.g.*, Burlaga *et al.*, 1981; Klein and Burlaga, 1982). However, observations show that some ICMEs originating from the disk-center sources do not have a flux rope structure (see *e.g.*, Gopalswamy, 2006) and a few even appear to have no ejecta at all (Gopalswamy *et al.*, 2009). A possible solution for this is that the flux rope structure of the ICME exists but cannot be identified from the *in situ* measurements, because the identification of the flux rope signatures becomes more difficult as the spacecraft distance from the flux rope center axis increases (see *e.g.*, Gopalswamy, 2006; Jian *et al.*, 2006; Kilpua *et al.*, 2011). It is known that the propagation of CMEs is not always radial, indicating that the CME propagation direction must be affected by surrounding coronal structures. The assumption here is that the dominant CME deflection occurs near the Sun, and not later during the ICME propagation in interplanetary space. Wang *et al.* (2004) have suggested that ICMEs traveling faster than the solar wind speed are deflected to the west and those traveling slower to the east. We do not consider this possible ICME deflection because the solar wind is not fully formed in the height range we are interested in. Already the early white-light observations during the *Skylab* and *Solar Maximum Mission* (SMM) missions revealed that CMEs are deflected towards lower latitudes (Hildner, 1977; MacQueen, Hundhausen, and Conover, 1986). More recently it has been shown that CME–CME collision (Gopalswamy *et al.*, 2001) and CME interaction with coronal holes (CHs) (Gopalswamy *et al.*, 2004, 2005) can significantly change the trajectory of the CME. Furthermore, Gopalswamy *et al.* (2009) suggested that CME–CH interaction could explain why no ejecta is observed at 1 AU behind traveling interplanetary shocks that were associated with CMEs launched near the solar disk center, and hence expected to hit Earth. They proposed that combined effects of nearby coronal holes deflect the CME away from the Sun–Earth line, causing the driver behind the shock to miss Earth and the observing spacecraft, resulting in apparently driverless shocks at 1 AU (see also *e.g.*, Gopalswamy, 2006; Jian *et al.*, 2006; Riley *et al.*, 2006). The CH influence on CMEs was modeled using an *ad hoc* force depending on the area, average magnetic field strength, and distance of CHs (Cremades, Bothmer, and Tripathi, 2006). Mohamed *et al.* (2012) performed a statistical study that included all disk-center CMEs observed by the *Large Angle and Spectrometric*

Coronagraph (LASCO) (Brueckner *et al.*, 1995) on the *Solar and Heliospheric Observatory* (SOHO) during Solar Cycle 23. They found some evidence supporting the CH influence on the CME propagation. In both studies the measurement position angle (MPA), *i.e.* the direction of fastest CME propagation in the sky plane, was used as a proxy of the propagation direction of the CMEs and compared with the position angle (FPA) of the calculated direction of the total CH influence F (see Equation (1) in Section 2.2).

It this report we study a set of CME–ICME pairs that were especially selected for the two Living With the Star (LWS) Coordinated Data Analysis Workshops (CDAWs) addressing the question if all CMEs are flux ropes or not. The workshops were held in San Diego, USA, in 2010 and in Alcalá de Henares, Spain, in 2011. We investigate in detail if the geometrical explanation for driverless shocks by Gopalswamy *et al.* (2009) could also explain why all the selected CDAW ICMEs do not have a flux rope structure at 1 AU even though they originate near the disk center. The idea is that the flux rope structure is not observed because the CME is deflected away from the Sun–Earth line so that the spacecraft at 1 AU crosses the flank of the corresponding ICME (see Gopalswamy, 2006). We compare the CH influence parameter obtained by Gopalswamy *et al.* (2009) and Mohamed *et al.* (2012) with the flux rope fitting results by Xie, Gopalswamy, and St. Cyr (2013). Xie, Gopalswamy, and St. Cyr (2013) found that on average the MC associated CMEs are deflected towards and the non-MC associated CMEs away from the Sun–Earth line.

We expect that the CME direction obtained from the flux rope fitting to give a better understanding of the CME propagation direction than the MPA used in the previous studies. The flux rope fitting uses a three-dimensional model for CMEs and, therefore, results should provide a more realistic estimate of the CME trajectory. Because the MPA is the sky-plane direction of the CME, it cannot describe the three-dimensional deflection of CMEs accurately, and that can in some cases create problems when the MPA values are compared with the predictions of the CH influence model. For example if a southern polar CH pushes the CME from the southern hemisphere source towards north, but the CME propagation direction still remains in southern hemisphere, the observed MPA value of the CME will be close to 180°, erroneously indicating a southward deflection of the CME.

2. Data Analysis

2.1. Coronal Mass Ejections

The final data set used in this study consists of 54 CME–ICME pairs of which 23 were labeled as MCs based on the list by R. Lepping (http://wind.gsfc.nasa.gov/mfi/mag_cloud_pub1.html). The rest of the events were identified as non-MC events (ejecta). The events were originally selected from a list of CME-driven shocks by Gopalswamy *et al.* (2010b). Selected events were limited to the CMEs that had their solar source location in the longitude range 15E – 15W without any limits in the source latitude. The estimated deflection of the CME is based on the analysis by Xie, Gopalswamy, and St. Cyr (2013). They obtained the CME propagation directions by fitting a flux rope model (Krall and St. Cyr, 2006) to the white-light images taken by the LASCO experiment on the SOHO.

2.2. Coronal Holes

Coronal holes obtained their name because in the EUV and X-ray images of the solar corona they appear as areas darker than the surrounding corona. However, in images taken at other

wavelengths, *e.g.* in images taken using the He I 10830 Å line or microwaves (Zirker, 1977; Gopalswamy *et al.*, 1999), CHs are brighter than the surrounding solar disk. In the photospheric magnetograms these dark CHs are observed to correspond regions of unipolar magnetic field. It is believed that CHs are filled with open magnetic field lines that extend out into interplanetary space.

In the identification of CH regions and their boundaries we used both EUV images by the *Extreme Ultraviolet Imaging Telescope* (EIT) (Delaboudinière *et al.*, 1995) and photospheric magnetograms by the *Michelson Doppler Imager* (MDI) (Scherrer *et al.*, 1995), both instruments on the SOHO spacecraft. First we searched for dark regions in the full-disk EUV 284 Å images and selected for further analysis areas where the EUV intensity was below half of the median EUV intensity of the full solar disk. Filament channels and other interfering dark areas were excluded. Then we looked at the corresponding region in the photospheric magnetogram and defined the CH boundaries to be the boundaries of the major polarity region within the selected region. Further details of the CH identification can be found in Gopalswamy *et al.* (2009) and Mohamed *et al.* (2012).

In the analysis the influence of the CH is described as a force ($\boldsymbol{f}$) deflecting the CME away from the CH (see Equation (1)). The direction of this force is assumed to be from the centroid of the CH towards the source region of the CME. The magnitude of the force equals the average magnetic field strength ($\langle B \rangle$) within the CH multiplied by the area (A) of the CH and divided by the square of the distance (d) between the CH centroid and the CME source region. Both the average magnetic field $\langle B \rangle$ and area A of the CH are the line-of-sight corrected values (see Gopalswamy *et al.*, 2009; Mohamed *et al.*, 2012). The total force ($\boldsymbol{F}$) of all CHs on the visible disk is calculated as a vector sum of all CH forces and the magnitude of $\boldsymbol{F}$ is called coronal hole influence parameter (CHIP).

$$\boldsymbol{F} = \sum_{\mathrm{CHs}} \boldsymbol{f} = \frac{\langle B \rangle A}{d^2} \hat{\boldsymbol{e}}, \tag{1}$$

where $\hat{\boldsymbol{e}}$ is a unit vector pointing from the CH centroid to the CME source region. The corresponding position angle of the F direction is called FPA. The unit of the force is Gauss. One should note that this model includes only the possible CH influence. If there are any other mechanisms that deflect CMEs, the model cannot describe their effects or separate the possible CH contribution to the total CME deflection.

2.3. Data Table

We have collected all data used in our analysis into Table 1. The first column of Table 1 lists the CDAW event number, the seven next columns give the information regarding the CME (column 2: date in yyyy/mm/dd format; column 3: time as hh:mm in UT; column 4: source location in heliographic coordinates; column 5: angular distance of the source from the disk center in degrees; column 6: type of the associated ICME; column 7: sky-plane speed in km s^{-1}; column 8: MPA in degrees). Next two columns list the FPA (column 9) and CHIP (column 10) calculated using our CH influence model. Last two columns are results from the flux rope fitting to the LASCO white-light images of the CME (column 11: propagation direction in heliographic coordinates; column 12: angular distance of the propagation direction from the disk center in degrees). We recalculated the CHIP for the 7 July 2000 (N17) CME because we changed the location of the source region to N04E00. The new CHIP value is 0.3 G. We corrected the errors in the calculation of the CHIP values given in Mohamed *et al.* (2012) for four events: N08 (CHIP = 1.1 G), N24 (CHIP = 6.0 G), N28 (CHIP = 12.0 G), and N32 (CHIP = 5.7 G).

Table 1 List of the CDAW events and their CH influence and best-fit flux rope parameters.

N	CME							CHIP[a]		Flux Rope Fitting[b]	
	Date	Time [UT]	Source	θ_{Source} [deg]	Type	Speed km s^{-1}	MPA [deg]	FPA [deg]	F [G]	Direction	θ_{Fit} [deg]
01	1997/01/06	15:10	S18E06	15.5	MC	136	180	25	0.8	S18W01	14.3
02	1997/05/12	05:30	N21W08	25.2	MC	464	264	352	0.2	N01W02	4.4
03	1997/12/06	10:27	N45W10[c]	46.0	EJ	397	296	315	0.5	N15W30	33.2
04	1998/05/01	23:40	S18W05	14.8	EJ	585	126	189	0.2	S16E14	18.3
05	1998/05/02	14:06	S15W15	18.5	EJ	938	331	298	0.2	N08W05	13.0
07	1998/11/04	07:54	N17W01	13.0	EJ	523	349	324	0.1	N25W01	21.0
08	1998/11/09	18:18	N15W05	12.6	EJ	325	338	320[d]	1.1[d]	N15W05	12.6
09	1999/04/13	03:30	N16E00	21.8	MC	291	194	301	1.9	S02W06	7.1
10	1999/06/24	13:31	N29W13	29.7	EJ	975	335	332	0.8	N25W15	27.2
13	1999/09/20	06:06	S20W05	27.5	EJ	604	14	48	37.0	S20W05	27.5
14	1999/10/18	00:06	S30E15	38.3	EJ	144	184	58	9.8	S30E15	38.3
15	2000/01/18	17:54	S19E11	17.8	EJ	739	45	29	2.5	S10E29	29.4
16	2000/02/17	21:30	S29E07	23.1	MC	728	184	336	0.3	S12W02	5.5
17	2000/07/07	10:26	N04E00	0.4	EJ	453	193	19[d]	0.3[d]	S17W05	21.2
18	2000/07/08	23:50	N18W12	18.5	EJ	483	339	279	1.7	N18W06	15.4
19	2000/07/14	10:54	N22W07	19.0	MC	1674	273	201	5.4	N18W14	19.5
20	2000/07/23	05:30	S13W05	18.8	EJ	631	166	268	1.4	S13E04	18.5
21	2000/07/25	03:30	N06W08	8.0	MC	528	168	291	8.2	S15E04	20.6
23	2000/08/09	16:30	N20E12	18.1	MC	702	12	159	1.0	N17E05	11.7
24	2000/09/16	05:18	N14W07	9.8	MC	1215	3	323[d]	6.0[d]	N08W07	7.0

Table 1 (*Continued.*)

N	CME							CHIP[a]		Flux Rope Fitting[b]	
	Date	Time [UT]	Source	θ_{Source} [deg]	Type	Speed km s^{-1}	MPA [deg]	FPA [deg]	F [G]	Direction	θ_{Fit} [deg]
25	2000/10/02	03:50	S09E07	17.1	EJ	525	107	61	10.0	S19E08	26.8
26	2000/10/09	23:50	N01W14	14.9	MC	798	318	195	1.1	N20W14	19.6
27	2000/11/03	18:26	N02W02	2.9	MC	291	57	178	0.8	N02E05	5.4
28	2000/11/24	05:30	N20W05	19.0	EJ	1289	313	110[d]	12.0[d]	N30W18	33.1
29	2001/02/28	14:50	S17W05	11.0	EJ	313	263	342	1.9	S05W15	15.2
30	2001/03/19	05:26	S20W00	12.9	EJ	389	184	300	0.7	N05W10	15.6
31	2001/04/09	15:54	S21W04	15.5	EJ	1192	211	336	2.6	S12E01	6.1
32	2001/04/10	05:30	S23W09	19.2	MC	2411	166	336[d]	5.7[d]	S23W05	17.7
33	2001/04/26	12:30	N20W05	25.1	MC	1006	37	62	0.5	N20W03	24.8
34	2001/08/09	10:30	N11W14	14.7	EJ	479	255	270	1.2	N02W18	18.5
35	2001/10/09	11:30	S28E08	35.1	EJ	973	184	316	1.5	S28E01	34.3
36	2002/03/15	23:06	S08W03	3.1	MC	957	309	240	0.9	N15W01	22.2
37	2002/04/15	03:50	S15W01	9.5	MC	720	198	335	1.1	S01W05	6.8
38	2002/05/08	13:50	S12W07	11.1	EJ	614	229	323	2.3	S09W09	10.6
39	2002/05/16	00:50	S23E15	25.2	MC	600	158	360	1.3	S23E05	21.0
40	2002/05/17	01:27	S20E14	22.3	EJ	461	145	50	0.6[e]	S28E20	32.0
41	2002/05/27	13:27	N22E15	27.4	EJ	1106	35	165	4.6	N32E20	38.2
42	2002/07/15	21:30	N19W01	14.6	EJ	1300	45	355	4.4	N29E15	28.6
43	2002/07/29	12:07	S10W10	18.4	MC	222	161	203	4.4	S02W10	12.5
44	2003/08/14	20:06	S10E02	16.7	MC	378	25	93	1.3	N12E10	11.3
45	2003/10/28	11:30	S16E08	22.2	MC	2495	15	160	1.1	S16E20	28.5

Table 1 (*Continued.*)

N	CME							CHIP[a]		Flux Rope Fitting[b]	
	Date	Time [UT]	Source	θ_{Source} [deg]	Type	Speed km s^{-1}	MPA [deg]	FPA [deg]	F [G]	Direction	θ_{Fit} [deg]
46	2003/10/29	20:54	S15W02	19.7	MC	2029	190	255	4.6	S15E05	20.2
47	2004/01/20	00:06	S13W09	12.0	EJ	965	224	87	1.8	S25W10	22.3
48	2004/07/22	08:30	N04E10	10.1	MC	899	210	193	1.6	N06E05	5.1
49	2004/11/06	02:06	N09E05	7.2	MC	1111	21	94	2.5	N07W00	3.2
50	2004/12/08	20:26	N05W03	6.0	EJ	611	301	233	1.2	S05W06	7.7
51	2005/01/15	06:30	N16E04	21.0	EJ	2049	359	113	0.6	N25W01	29.6
52	2005/02/13	11:06	S11E09	9.9	EJ	584	129	218	5.8	S21E19	23.6
53	2005/05/13	17:12	N12E11	18.4	MC	1689	2	42	0.7	N05E11	13.5
54	2005/05/17	03:26	S15W00	12.6	MC	449	54	334	2.0	N08E05	11.5
56	2005/07/07	17:06	N09E03	6.2	EJ	683	39	154	1.7	N12E26	27.2
57	2005/08/31	11:30	N13W13	14.2	EJ	825	287	191	3.4	N08W25	25.0
58	2005/09/13	20:00	S09E10	19.0	EJ	1866	149	100	1.3	S29E21	41.1
59	2006/08/16	16:30	S16W08	24.0	EJ	888	161	182	0.4	S28W01	34.7

[a]Data from Gopalswamy *et al.* (2009) and Mohamed *et al.* (2012).

[b]Data from Xie, Gopalswamy, and St. Cyr (2013).

[c]Xie, Gopalswamy, and St. Cyr (2013) assumed the source location to be N25W40.

[d]Data value recalculated.

[e]Typo in Mohamed *et al.* (2012) corrected.

3. Results

3.1. CME Deflection by Coronal Holes

In order to characterize the CME deflection from the radial propagation we calculated the angular distances from the Sun–Earth line, *i.e.* from the disk center, for the CME source region (θ_{Source}) and the flux rope propagation direction (θ_{Fit}). The CME source regions and flux rope propagation directions were taken from Table 1 by Xie, Gopalswamy, and St. Cyr (2013). Xie, Gopalswamy, and St. Cyr (2013) used white-light images by the SOHO/LASCO coronagraph to forward model the flux rope orientation and propagation near the Sun. In Figure 1 we have plotted the estimated CME deflection $\theta_{\mathrm{Fit}} - \theta_{\mathrm{Source}}$ *vs.* the CHIP (Figure 1a) and the nearest CH distance (Figure 1b). The negative values of $\theta_{\mathrm{Fit}} - \theta_{\mathrm{Source}}$ indicate deflection towards the Sun–Earth line, *i.e.* it is more likely that an observer at 1 AU should detect an MC structure, assuming that all CMEs are flux ropes. The red circles (blues crosses) mark MC (non-MC) events, respectively.

The CHIP values plotted in Figure 1 are from Tables 2 and 3 in the paper by Mohamed *et al.* (2012) that includes data from Gopalswamy *et al.* (2009). Some data values were recalculated as mentioned in Section 2.3. The nearest CH distances are extracted from the data used in the calculations of CHIP values. In the plots and our discussions we have excluded the event N13 on 20 September 1999 because it is a very faint halo CME with an exceptionally large CHIP value due to a large CH at SW from the source region at S20W05. As discussed by Mohamed *et al.* (2012) this large CH should push the CME towards the NE direction. The measurement position angle (MPA) for this event is 14°, indicating that the fastest part of the CME travels approximately to the NE direction as expected. However, the result from the flux rope fitting for this event shows no deflection at all, *i.e.* the CME should appear to propagate radially towards south. We think that the faintness of the CME makes this event very difficult to accurately fit with a flux rope model, therefore we have excluded it from our analysis.

The general conclusion from Figure 1 is that the majority of MCs (red circles) lie below the dotted horizontal line marking the zero deflection. This indicates that MCs are favorably deflected towards the Sun–Earth line as discussed in the paper by Xie, Gopalswamy, and St. Cyr (2013). Only seven out of 23 (30 %) MC events appear to have been deflected further away from the Sun–Earth line, and only two out of the seven events (events N21 and N36) are deflected more than 10° away from the Sun–Earth direction. Similarly most of the non-MC events (blue crosses) lie above the zero level, *i.e.* they are deflected away from the disk center. Only eight non-MC events out of 30 (27 %) are deflected towards the disk center. The non-MC events N03 and N31 are the two extreme events out of the eight events with a towards-disk-center deflection. There are two non-MC events with no deflection.

When considering the CH influence and how well our model of that can explain the estimated CME deflection we notice in Figure 1a that the range of CHIP values can be divided roughly into two regions. Events with CHIP larger than 2.6 G show clear separation of MC and non-MC deflection. The MC events are deflected towards the Sun–Earth line and non-MC event away, with two exceptions: the non-MC event N14 with CHIP = 9.8 G and no observed CME deflection and the MC event N21 with CHIP = 8.2 and deflection away from the Sun–Earth line. We will discuss these two events below in detail. In the CHIP value region less than 2.6 G the deflection distributions of the MC and non-MC events are overlapping. Most of the events are concentrated between $-10° < \theta_{\mathrm{Fit}} - \theta_{\mathrm{Source}} < 10°$. But still in the region of lower CHIP values the majority of MC events (13 out of 17 or 76 %) are

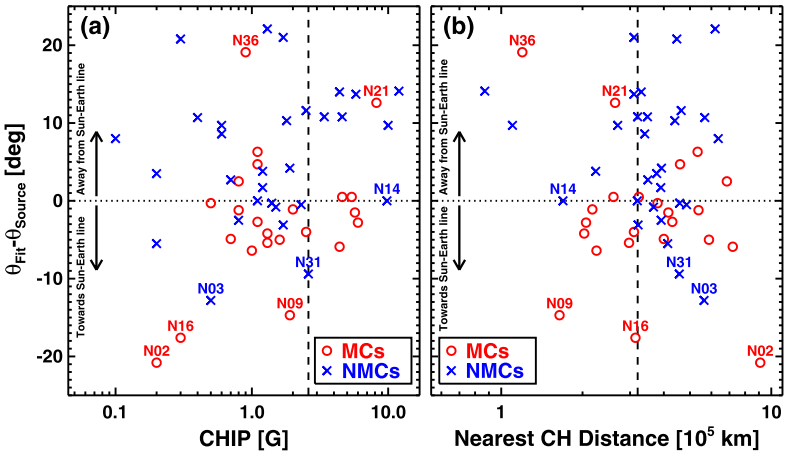

Figure 1 Deflection of the CME direction relative to the Sun–Earth line based on the flux rope fitting by Xie, Gopalswamy, and St. Cyr (2013) as a function of (a) the CHIP (b) the distance of the nearest CH. θ_{Source} and θ_{Fit} are angular distance of the source location and the CME propagation direction from flux rope fitting relative to the disk center, respectively. Blue crosses (red circles) mark MC (non-MC) events. Dashed lines in Figures (a) and (b) mark the CHIP value of 2.6 G and the distance of 3.2×10^5 km, respectively. The event number is plotted next to few selected data points. These events are discussed in more detail in the text.

deflected towards disk center and that of non-MC events (14 out of 23 or 61 %) are deflected away from the disk center. The three more extreme cases are MC events N02 and N16 that show larger deflection even though both events have the low CHIP value, and the event N09 with a moderate CHIP value of 1.9 G. We discuss also these events later in this section.

In Figure 1b we have plotted the nearest CH distance *vs*. the CME deflection. Also the range of the nearest CH distances can be divided into two regions with differing CME deflection distributions. Again the events N21 and N36 form an exception discussed later. If the distance to the nearest CH is less than 3.2×10^5 km the groups of the MC and non-MC events are clearly separated. This distance corresponds to approximately a quarter of the solar radius. When the CH distance increases the deflection distributions start to overlap. We did not find a similar clear division for the area times the average magnetic field strength of CHs. Clearly the distance of the nearest CH is a significant factor for the CH influence.

Figure 1 also shows that the magnitude of CME deflection for MC events is confined between $-7^\circ \leq \theta \leq 7^\circ$, only five MC events (event number plotted next to the data point in Figure 1) show larger values of CME deflection. On the other hand, non-MC events have CME deflection values that are scattered into a wider range between $-6^\circ \leq \theta \leq 23^\circ$. In the region where CHIP value are larger than 2.6 G the non-MC events have CME deflection values near and above 10°, which supports the idea that CHs influence the CME propagation. The CME deflection values for the MC events do not show similar shift at large CHIP values. On the other hand the number of MC events in this region is low, so this could be by chance. It is also possible that it is an intrinsic characteristic of the CME population associated with MCs to be less deflected than those associated with the non-MCs.

3.2. 18 October 1999 Non-MC Event

The CME (N14) in question is a faint and slow partial halo on 18 October 1999 at 00:06 UT with MPA = 184° at S30E15. Another narrow and slow CME with MPA = 40° occurs

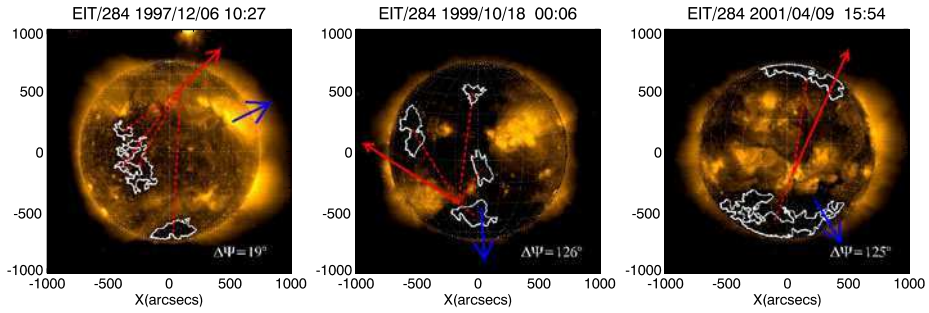

Figure 2 EUV images showing the coronal holes for the 6 December 1997 (left), 18 October 1999 (middle), and 9 April 2001 (right) non-MC events discussed in the text. Blue arrow marks the MPA of the CME, red arrow the direction of the CH influence and $\Delta\Psi$ is the angle between them. Figures from Mohamed (2011).

at the same time as the partial-halo CME. The conclusion that these events are two separate CMEs is based on a slight difference in speeds of the emerging loop structures towards the NE and S directions, but the sequence of events is complex and open to interpretations. This event is difficult to fit with a flux rope model accurately. The locations of the selected CHs are shown in Figure 2, middle. Therefore we consider the CME deflection in this event to be uncertain.

3.3. 6 December 1997 Non-MC Event

The CME (N03) on 6 December 1997 at 10:27 UT has the largest deflection towards the disk center of all non-MC events, but the estimated CHIP value is only 0.5 G. On the other hand the CME source region is farthest away from the Sun–Earth line of all events. The estimation of the source location for this event is somewhat complicated. The first indication of the possible CME eruption was an eruptive prominence at high northern latitude (N45W10), followed by a formation of large arcades about four hours later near active regions 8115 and 8113. We selected the source to be at N45W10, but Xie, Gopalswamy, and St. Cyr (2013) used in their calculations the later source location at N25W40. In either case the angular distance of the source for this event is over 40° from the disk center, making it the most distant event of all the CDAW events. The fitted propagation direction of the CME is N15W30, which is still about 33° from the disk center. Therefore, even though the CME was deflected towards the Sun–Earth line, the distance from the Sun–Earth line remained large. The MPA of the CME is 315°, indicating propagation in the NW quadrant. If the location used in flux rope fitting is accurate then the event is beyond the longitudinal range of our study. Because this latter location is so close to the western limb the calculations are unreliable because they do not include the influence from the possible CHs near the western limb (see Figure 2, left). The Kitt Peak CH map shows near the west limb a long, narrow elongation of the northern polar CH reaching almost to the N20 latitude. In the EUV images this CH appears to be masked by the bright loops in the forefront. Because of these ambiguities in the location of the source region and CHs we must consider this event uncertain.

3.4. 9 April 2001 Non-MC Event

The halo CME (N31) on 9 April 2001 at 15:54 UT is another non-MC event with $\sim 10°$ deflection towards the Sun–Earth line. This event is the one which we used as a limit between

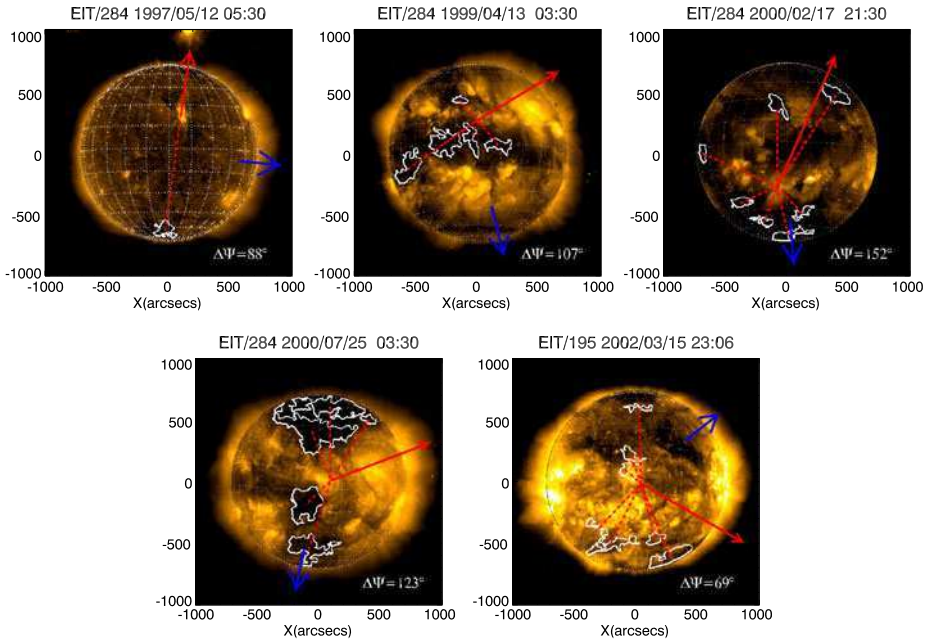

Figure 3 EUV images showing the coronal holes for the 12 May 1997 (top left), 13 April 1999 (top middle), 17 February 2000 (top right), 25 July 2000 (bottom left), and 15 March 2002 (bottom left) MC events discussed in the text. Blue arrow marks the MPA of the CME, red arrow the direction of the CH influence and $\Delta\Psi$ is the angle between them. Figures from Mohamed (2011).

the two CHIP ranges, so the corresponding CHIP value is 2.6 G. The CME occurred at S21W04 and the fitted propagation direction is S12E01. The MPA angle of the CME is 221°, again indicating that the CME propagated towards south. The nearest CH was the southern polar CH, which should push the CME towards north exactly as the flux rope fitting indicated (Figure 2, right). The question then is why this event was classified as a non-MC event even though its propagation direction was less than 10° from the Sun–Earth line? It is quite possible that the associated ICME was misidentified because the CME was followed by another faster halo CME (N32) from the same region on 10 April 2001 at 05:30 UT. The speed of the 9 April CME was 1192 km s^{-1} and the 10 April CME had a speed twice of that of the preceding CME, 2411 km s^{-1}. The corresponding shocks were detected only two hours apart at 14:12 UT and 16:19 UT, respectively. Therefore, we think that the corresponding ICMEs were merging and the flux rope structure of the 9 April CME was destroyed in the process. This means also that our CHIP limit could be lowered to $\sim$2 G.

3.5. 12 May 1997 MC Event

The slow halo CME (N02) on 12 May 1997 at 05:30 UT occurred at N21W08 during the period of minimum solar activity. We identified only one polar CH far away in the southern pole as is typical during a solar minimum (Figure 3, top left). Therefore the CHIP value we obtained is only 0.2 G. We do not expect the southern polar CH have any significant influence on the CME propagation. The CME propagation direction was N01W02, only 4°

from the disk center. So what explains the relatively large deflection of the CME towards the disk center? The possible cause is the global solar magnetic field, which during the solar minimum is a well-organized dipole field associated with strong magnetic fields in the polar CHs that are known to exist in the polar regions during solar minimum. CME deflection towards lower latitudes during solar minima was first observed by Hildner (1977) and MacQueen, Hundhausen, and Conover (1986). Probably our CH selection method cannot identify the near-limb northern polar CH if it has only a small area on the visible side of the Sun. Therefore the large CME deflection in this case can be attributed to the effects of the large-scale solar magnetic field configuration due to polar CHs (see also *e.g.*, Gopalswamy and Thompson, 2000; Filippov, Gopalswamy, and Lozhechkin, 2001; Plunkett *et al.*, 2001; Cremades, Bothmer, and Tripathi, 2006; Kilpua *et al.*, 2009).

3.6. 13 April 1999 MC Event

The partial-halo CME (N09) on 13 April 1999 occurred at 03:30 UT when the solar X-ray emission was low. The CME was relatively faint with an uncertain width ($> 261°$), and it was expanding fastest towards south (MPA $= 194°$). The selected source for this event is a disappearing filament at N16E00 with the post-flare arcade loops reaching a B3.4 class in the X-ray intensity. However, another possible source candidate for this event is an EUV dimming at S13E21. The fitted flux rope direction was S02W06 matching with the observed MPA towards south. The three nearest CHs were located in the SE, S, and SW direction from the selected source (see Figure 3, top middle), and they were of average size. The calculated CHIP value for this event is 1.9 G with the direction towards NW. The large deflection obtained by the flux rope fitting suggests that there was a CH near the source as observed, but the calculated direction of the CHIP deviates significantly from the expected deflection towards south. A better agreement with observations would be achieved if the source was located south of the CHs as suggested by the EUV dimming. But if the source was located at S13E12 then the CME propagation direction from the flux rope fitting (S02W06) would indicate deflection towards north. Because we identified a total of four low-latitude CHs, which is an unusually large number, it is possible that our CH selections in this case are not correct. The inspection of the EUV image shows bands of bright regions at mid-latitudes in the southern and northern hemisphere and a dark equatorial region in between. A few long and faint transequatorial loops appear to connect these bright regions in south and north, so it could be that the magnetic field lines are closed in the equatorial region. Otherwise unless we have misidentified the associated CME, which seems unlikely, this event is difficult to explain based on the CH influence model.

3.7. 17 February 2000 MC Event

The halo CME (N16) on 17 February 2000 at 21:30 UT was launched from a location at S29E07. The fitted propagation direction was S12W02 and the MPA was 184°. The estimated CHIP values was 0.3 G. We identified three relatively small CHs at almost equal distance ($3.1 - 3.8 \times 10^5$ km) at SE, S, and SW directions from the source (Figure 3, top right). In addition there was a southern polar CH (5.5×10^5 km) and another three CHs were in NE, N, and NW directions but at large distances ($6.3 - 8.8 \times 10^5$ km). The calculated force $\boldsymbol{F}$ was towards N–NE direction, which coincides well with the result from flux rope fitting. Why then our CHIP value is so low if the CME was deflected by the nearby CHs? Because CHs are surrounding the CME source region in all directions, the low CHIP value might be an indication that our simple model overestimates the influence of CHs far

away from the source region. Considering that the Sun is a sphere it is possible that the influence of CHs more than a solar radius away is less than predicted by our model.

3.8. 25 July 2000 MC Event

The 25 July 2000 CME (N21) at 03:30 UT occurred at N06W08, but the flux rope was observed first above the southern solar limb (MPA = 168°). Also the flux rope fitting shows deflection towards the S–SE direction, as the fitted propagation direction was S15E04. However, from Figure 3 (bottom left) we see that the nearest CH on disk was in the SE direction from the source region. This CH had also a strong average magnetic field ($\langle B \rangle = 11.9$ G). Our calculations show that this CH dominates the total influence of all the on-disk CHs and therefore the CME should be pushed towards the NW direction. There were large northern polar CHs relatively nearby ($\langle B \rangle = 2.6 - 4.8$ G) but according to our estimation their effect did suffice only to turn the total CH influence direction slightly towards west. However, this CME has an uncertain source region. There was a M8.0 flare eruption at 02:43 UT in the active region 9097 at N06W08 and approximately at the same time an eruptive prominence occurred further south at S14W04. Interestingly the flux rope fitted propagation direction of the CME is close to this eruptive prominence location. Therefore, we conclude that the complex events at the Sun make the identification of the CME source location uncertain, and according to our CH influence model the eruptive prominence would be a more favored source of the CME.

3.9. 15 March 2002 MC Event

The 15 March 2002 event (N36) was a halo CME first observed at 23:06 UT expanding towards the NW direction (MPA = 309°). Its solar source was the M2.2 flare at S08W03 at 22:09 UT. Our CH identification found multiple small CHs scattered around the solar disk (see Figure 3, bottom right). The influence of each CH was calculated to be relatively weak ranging from 0.2 G to 1.6 G, resulting in a weak total influence (CHIP = 0.9 G) pushing the CME towards the SW direction. The fitted propagation direction was N15W01, so the CME appears to be deflected towards north. In this case there is no ambiguity in the source location. In addition, the solar south pole is inclined towards Earth in mid March, so the CME source is very close to the disk center. Therefore, we cannot expect the deflection away from the Sun–Earth line will necessarily mean that an observer at 1 AU cannot detect the flux rope structure of the CME. The question remains what caused this deflection. There could be some uncertainty in the identification of the CHs, because there is a nearby filament channel north of the source region extending from the central meridian towards the E-NE direction. This filament channel might interfere with the identification of the two CHs near the CME source region. In any case, it appears that there is no clear CH close enough in the S–SE direction from the source region, which could push the CME towards the N–NW direction. However, this event occurred during the solar maximum, when the solar magnetic field is very complex, so distorted local magnetic structures could result in the CME deflection.

3.10. FPA *versus* the CME Propagation Direction

In Figure 4 we have plotted the FPA angles together with arrows that start from the source region and end at the estimated CME propagation direction from the flux rope fitting by Xie, Gopalswamy, and St. Cyr (2013). As can be seen the alignment of the green arrows (FPA) with the red (MCs) and blue (non-MCs) is not particularly good. The CH influence model

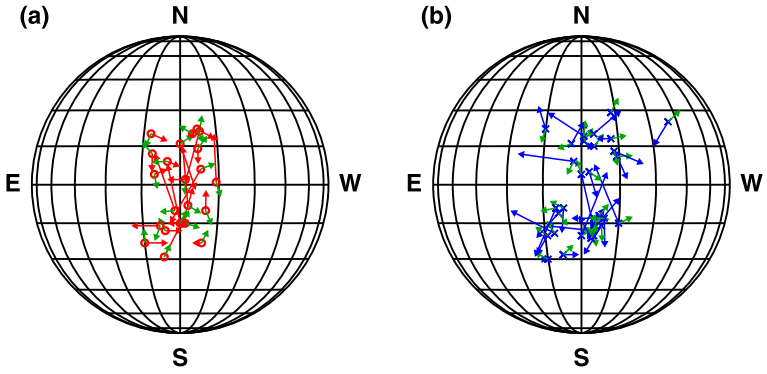

Figure 4 FPA from the CH deflection model (Table 1, column 9) compared with the shift of the CME propagation direction by Xie, Gopalswamy, and St. Cyr (2013) relative to the source location. The red (a) and blue (b) arrows correspond to MC and non-MC events. The red and blue arrows start at the CME source location (Table 1, column 4) and end at the CME propagation direction (Table 1, column 11). The green arrows show the direction of the CHIP.

clearly provides less accurate estimates for the FPA than for the CHIP. We believe that the moderate correspondence of the FPA with the shift of the CME propagation direction relative to the source location is partly due to simplified description of the CH as a single point (the centroid of the CH area) in the model. Especially when the CH has very elongated shape, the CH section nearest to the source most likely contributes more in the CME deflection than the rest of the CHs. Figure 1b showed that the distance of the CH is significant parameter for the CME deflection. In addition the identification of CH areas has uncertainties. As discussed by Gopalswamy *et al.* (2009) the selection method of the CH area may not fully select open field regions due to the foreground coronal emission. Other features on the Sun can interfere with the CH identification as might be the case in the 13 April 1999 event we discussed in Section 3.6, where long faint transequatorial loops possibly interfered with the CH identification resulting in unusually large number of CHs.

In our study we have not considered the possible uncertainties in the fitting of the flux rope model. When the CME appears very faint in the coronagraphic images or when parts of the successively launched CMEs overlap each other, the identification of features of the CME becomes difficult. This results in not easily quantifiable uncertainties in the fitting of the flux rope model and in the estimation of the CME propagation direction.

4. Summary and Conclusions

Our report is one of the contributions originating from collaborations during the LWS CDAW meetings focusing on the question if all CMEs are flux ropes. In a recent study Gopalswamy *et al.* (2009) analyzed ICMEs that originated from disk-center sources and therefore were expected to be directed towards Earth, but which did not have an observed ejecta at 1 AU. As an explanation they suggested that nearby CHs pushed the CMEs near the Sun away from the Sun–Earth line far enough that the driving ejecta of the corresponding ICME became unobservable at 1 AU. Gopalswamy *et al.* (2009) described the CH influence on CMEs by using a simple parameter called CHIP (see Equation (1)) depending on the area, average magnetic field and distance from the source of the CH (see also Cremades, Bothmer, and Tripathi, 2006). Mohamed *et al.* (2012) performed an expanded statistical study of the

CH influence on CMEs during the whole Cycle 23. They found some evidence supporting the CH influence. In our study we have utilized results from the flux rope fitting reported by Xie, Gopalswamy, and St. Cyr (2013), who found that on average CMEs associated with MCs are deflected closer to the disk center and those associated with non-MCs away from the disk center.

When we compared the CME deflection (Xie, Gopalswamy, and St. Cyr, 2013) to the CH influence parameter CHIP (Gopalswamy *et al.*, 2009; Mohamed *et al.*, 2012) we found support to the CH influence as described by CHIP on the CME propagation. We found that for the CHIP values larger than 2.6 G the CME deflection distributions are divided into two separate groups where the MCs are deflected towards and non-MCs away from the Sun–Earth line. At CHIP values lower than 2.6 G the deflection distributions of MC and non-MC events overlap but still the average deflection direction for MC is towards and non-MCs away from the Sun–Earth line. We also found that the deflection as a function of the distance of the nearest CH is divided into two distance regions. If the nearest CH is closer than 3.2×10^5 km from the CME source region, the deflection distributions of the MCs and non-MCs again are separated into two groups: MCs are deflected towards the Sun–Earth line and non-MCs correspondingly away. When the distance to the nearest CHs increases the CH influence on CMEs decreases and the deflection distributions start to overlap. This indicates that the distance to the nearest CH is an important parameter for the CME deflection. We also found the scatter of the CME deflection values to be larger for a non-MC event than for the MC events.

There were few events that had exceptionally large values of the CME deflection, which we discussed in more detail. Most of the events revealed unavoidable uncertainties in identifying CME solar sources and CHs using the methods applied here, and which resulted in uncertain predictions of the CH influence. In addition to the problems in the identification of the features on the Sun, the model used to calculate the CHIP reduces the CH to a single point (the centroid of the CH). This assumption is incorrect especially if the CH has a very elongated shape, because then the nearest section of the CH to the CME source is the most likely area pushing the CME. During the solar minimum the global dipole magnetic field due to strong magnetic fields in the polar CHs deflects CMEs towards the lower latitudes (see *e.g.*, Hildner, 1977; MacQueen, Hundhausen, and Conover, 1986; Gopalswamy and Thompson, 2000; Filippov, Gopalswamy, and Lozhechkin, 2001; Plunkett *et al.*, 2001; Cremades, Bothmer, and Tripathi, 2006; Kilpua *et al.*, 2009). During solar maximum the solar magnetic field configuration can be very complex, so that local magnetic structures near the CME source may direct the CME to propagate non-radially. We cannot separate or exclude these other effects in our calculations.

As a final point we like to mention that the CHIP estimates might improve if one modifies Equation (1) so that the CH force is proportional to the square of the average magnetic field strength of the CH as suggested by Gopalswamy *et al.* (2010a). They proposed this modification because B^2 represents magnetic pressure and therefore could be a better CH parameter in the calculations of the CH influence.

In summary, we found evidence by using a simple CH influence model that CHs probably deflect CMEs and that the deflection pattern of the MC and non-MC associated CMEs near the Sun as reported by Xie, Gopalswamy, and St. Cyr (2013) is at least partly explained by the CH influence.

Acknowledgements We would like to thank the local organizers of the LWS CDAW meetings in San Diego, USA, and Alcalá de Henares, Spain. This research was supported by NASA grants NNX10AL50A and NNG11PL10A. SOHO is an international cooperation project between ESA and NASA.

References

Brueckner, G.E., Howard, R.A., Koomen, M.J., Korendyke, C.M., Michels, D.J., Moses, J.D., Socker, D.G., Dere, K.P., Lamy, P.L., Llebaria, A., Bout, M.V., Schwenn, R., Simnett, G.M., Bedford, D.K., Eyles, C.J.: 1995, The Large Angle Spectroscopic Coronagraph (LASCO). *Solar Phys.* **162**, 357 – 402. doi:10.1007/BF00733434.

Burlaga, L., Sittler, E., Mariani, F., Schwenn, R.: 1981, Magnetic loop behind an interplanetary shock – Voyager, Helios, and IMP 8 observations. *J. Geophys. Res.* **86**, 6673 – 6684. doi:10.1029/JA086iA08p06673.

Cremades, H., Bothmer, V., Tripathi, D.: 2006, Properties of structured coronal mass ejections in solar cycle 23. *Adv. Space Res.* **38**, 461 – 465. doi:10.1016/j.asr.2005.01.095.

Delaboudinière, J.P., Artzner, G.E., Brunaud, J., Gabriel, A.H., Hochedez, J.F., Millier, F., Song, X.Y., Au, B., Dere, K.P., Howard, R.A., Kreplin, R., Michels, D.J., Moses, J.D., Defise, J.M., Jamar, C., Rochus, P., Chauvineau, J.P., Marioge, J.P., Catura, R.C., Lemen, J.R., Shing, L., Stern, R.A., Gurman, J.B., Neupert, W.M., Maucherat, A., Clette, F., Cugnon, P., van Dessel, E.L.: 1995, EIT: Extreme-Ultraviolet Imaging Telescope for the SOHO mission. *Solar Phys.* **162**, 291 – 312. doi:10.1007/BF00733432.

Filippov, B.P., Gopalswamy, N., Lozhechkin, A.V.: 2001, Non-radial motion of eruptive filaments. *Solar Phys.* **203**, 119 – 130.

Gopalswamy, N.: 2006, Properties of interplanetary coronal mass ejections. *Space Sci. Rev.* **124**, 145 – 168. doi:10.1007/s11214-006-9102-1.

Gopalswamy, N., Thompson, B.J.: 2000, Early life of coronal mass ejections. *J. Atmos. Solar-Terr. Phys.* **62**, 1457 – 1469. doi:10.1016/S1364-6826(00)00079-1.

Gopalswamy, N., Shibasaki, K., Thompson, B.J., Gurman, J., DeForest, C.: 1999, Microwave enhancement and variability in the elephant's trunk coronal hole: comparison with SOHO observations. *J. Geophys. Res.* **104**, 9767 – 9780. doi:10.1029/1998JA900168.

Gopalswamy, N., Yashiro, S., Kaiser, M.L., Howard, R.A., Bougeret, J.L.: 2001, Radio signatures of coronal mass ejection interaction: coronal mass ejection cannibalism? *Astrophys. J. Lett.* **548**, L91 – L94. doi:10.1086/318939.

Gopalswamy, N., Yashiro, S., Krucker, S., Stenborg, G., Howard, R.A.: 2004, Intensity variation of large solar energetic particle events associated with coronal mass ejections. *J. Geophys. Res.* **109**, A12105. doi:10.1029/2004JA010602.

Gopalswamy, N., Yashiro, S., Michalek, G., Xie, H., Lepping, R.P., Howard, R.A.: 2005, Solar source of the largest geomagnetic storm of cycle 23. *Geophys. Res. Lett.* **32**, 12. doi:10.1029/2004GL021639.

Gopalswamy, N., Mäkelä, P., Xie, H., Akiyama, S., Yashiro, S.: 2009, CME interactions with coronal holes and their interplanetary consequences. *J. Geophys. Res.* **114**, A00A22. doi:10.1029/2008JA013686.

Gopalswamy, N., Mäkelä, P., Xie, H., Akiyama, S., Yashiro, S.: 2010a, Solar sources of "Driverless" interplanetary shocks. In: *Twelfth International Solar Wind Conference* **1216**, 452 – 458. doi:10.1063/1.3395902.

Gopalswamy, N., Xie, H., Mäkelä, P., Akiyama, S., Yashiro, S., Kaiser, M.L., Howard, R.A., Bougeret, J.L.: 2010b, Interplanetary shocks lacking type II radio bursts. *Astrophys. J.* **710**, 1111 – 1126. doi:10.1088/0004-637X/710/2/1111.

Hildner, E.: 1977, Mass ejections from the solar corona into interplanetary space. In: Shea, M., Smart, D., Wu, S. (eds.) *Study of Travelling Interplanetary Phenomena*, *Astrophys. Space Sci. Libr.* **71**, D. Reidel Publ. Co., Dordrecht, 3 – 20.

Jian, L., Russell, C.T., Luhmann, J.G., Skoug, R.M.: 2006, Properties of interplanetary coronal mass ejections at one AU during 1995 – 2004. *Solar Phys.* **239**, 393 – 436. doi:10.1007/s11207-006-0133-2.

Kilpua, E.K.J., Pomoell, J., Vourlidas, A., Vainio, R., Luhmann, J., Li, Y., Schroeder, P., Galvin, A.B., Simunac, K.: 2009, STEREO observations of interplanetary coronal mass ejections and prominence deflection during solar minimum period. *Ann. Geophys.* **27**, 4491 – 4503. doi:10.5194/angeo-27-4491-2009.

Kilpua, E.K.J., Jian, L.K., Li, Y., Luhmann, J.G., Russell, C.T.: 2011, Multipoint ICME encounters: pre-STEREO and STEREO observations. *J. Atmos. Solar-Terr. Phys.* **73**, 1228 – 1241. doi:10.1016/j.jastp.2010.10.012.

Klein, L.W., Burlaga, L.F.: 1982, Interplanetary magnetic clouds at 1 AU. *J. Geophys. Res.* **87**, 613 – 624. doi:10.1029/JA087iA02p00613.

Krall, J., St. Cyr, O.C.: 2006, Flux-rope coronal mass ejection geometry and its relation to observed morphology. *Astrophys. J.* **652**, 1740 – 1746. doi:10.1086/508337.

MacQueen, R.M., Hundhausen, A.J., Conover, C.W.: 1986, The propagation of coronal mass ejection transients. *J. Geophys. Res.* **91**, 31 – 38. doi:10.1029/JA091iA01p00031.

Mohamed, A.A.: 2011, Some aspects of solar activity and their impact on space environment near Earth. Ph.D. thesis, School of Physics, University of Sydney, Australia.

Mohamed, A.A., Gopalswamy, N., Yashiro, S., Akiyama, S., Mäkelä, P., Xie, H., Jung, H.: 2012, The relation between coronal holes and coronal mass ejections during the rise, maximum, and declining phases of solar cycle 23. *J. Geophys. Res.* **117**, A1103. doi:10.1029/2011JA016589.

Plunkett, S.P., Thompson, B.J., St. Cyr, O.C., Howard, R.A.: 2001, Solar source regions of coronal mass ejections and their geomagnetic effects. *J. Atmos. Solar-Terr. Phys.* **63**, 389 – 402. doi:10.1016/S1364-6826(00)00166-8.

Richardson, I.G., Cane, H.V.: 2010, Near-Earth interplanetary coronal mass ejections during solar cycle 23 (1996 – 2009): catalog and summary of properties. *Solar Phys.* **264**, 189 – 237. doi:10.1007/s11207-010-9568-6.

Riley, P., Schatzman, C., Cane, H.V., Richardson, I.G., Gopalswamy, N.: 2006, On the rates of coronal mass ejections: remote solar and *in situ* observations. *Astrophys. J.* **647**, 648 – 653. doi:10.1086/505383.

Scherrer, P.H., Bogart, R.S., Bush, R.I., Hoeksema, J.T., Kosovichev, A.G., Schou, J., Rosenberg, W., Springer, L., Tarbell, T.D., Title, A., Wolfson, C.J., Zayer, I., MDI Engineering Team: 1995, The solar oscillations investigation – Michelson Doppler Imager. *Solar Phys.* **162**, 129 – 188. doi:10.1007/BF00733429.

Wang, Y., Shen, C., Wang, S., Ye, P.: 2004, Deflection of coronal mass ejection in the interplanetary medium. *Solar Phys.* **222**, 329 – 343. doi:10.1023/B:SOLA.0000043576.21942.aa.

Xie, H., Gopalswamy, N., St. Cyr, O.C.: 2013, Near-Sun flux rope structure of CMEs. *Solar Phys.*, this issue. doi:10.1007/s11207-012-0209-0.

Zirker, J.B. (ed.): 1977, *Coronal Holes and High-Speed Wind Streams*, Colorado Assoc. Univ. Press, Boulder.

Zurbuchen, T.H., Richardson, I.G.: 2006, In-situ solar wind and magnetic field signatures of interplanetary coronal mass ejections. *Space Sci. Rev.* **123**, 31 – 43. doi:10.1007/s11214-006-9010-4.

Solar Phys (2013) 284:47–58
DOI 10.1007/s11207-012-0209-0

Near-Sun Flux-Rope Structure of CMEs

H. Xie · N. Gopalswamy · O.C. St. Cyr

Received: 27 March 2012 / Accepted: 3 December 2012 / Published online: 4 January 2013

Abstract We have used the Krall flux-rope model (Krall and St. Cyr, *Astrophys. J.* 2006, **657**, 1740) (KFR) to fit 23 magnetic cloud (MC)-CMEs and 30 non-cloud ejecta (EJ)-CMEs in the Living With a Star (LWS) Coordinated Data Analysis Workshop (CDAW) 2011 list. The KFR-fit results shows that the CMEs associated with MCs (EJs) have been deflected closer to (away from) the solar disk center (DC), likely by both the intrinsic magnetic structures inside an active region (AR) and ambient magnetic structures (*e.g.* nearby ARs, coronal holes, and streamers, *etc.*). The mean absolute propagation latitudes and longitudes of the EJ-CMEs (18°, 11°) were larger than those of the MC-CMEs (11°, 6°) by 7° and 5°, respectively. Furthermore, the KFR-fit widths showed that the MC-CMEs are wider than the EJ-CMEs. The mean fitting face-on width and edge-on width of the MC-CMEs (EJ-CMEs) were 87 (85)° and 70 (63)°, respectively. The deflection away from DC and narrower angular widths of the EJ-CMEs have caused the observing spacecraft to pass over only their flanks and miss the central flux-rope structures. The results of this work support the idea that all CMEs have a flux-rope structure.

Keywords Coronal mass ejections · Initiation and propagation

Flux-Rope Structure of Coronal Mass Ejections
Guest Editors: N. Gopalswamy, T. Nieves-Chinchilla, M. Hidalgo, J. Zhang, and P. Riley

H. Xie (✉)
Solar Physics Lab, IACS/CUA – NASA Goddard Flight Center, Greenbelt, MD 20771, USA
e-mail: hong.xie@nasa.gov

N. Gopalswamy · O.C. St. Cyr
NASA Goddard Space Flight Center, Code 671, Greenbelt, MD 20771, USA

N. Gopalswamy
e-mail: nat.gopalswamy@nasa.gov

O.C. St. Cyr
e-mail: chris.stcyr@nasa.gov

1. Introduction

In recent years, a great deal of research in both modeling and observations (see, *e.g.*, Chen *et al.*, 1997; Dere *et al.*, 1999; Gibson and Low, 2000; Krall *et al.*, 2001; Cremades and Bothmer, 2004; Krall and St. Cyr, 2006; Thernisien, Howard, and Vourlidas, 2006; Krall, 2007) has been focused on coronal mass ejections (CMEs) having the "three-part" morphology, namely, a bright front, a dark void and a bright core of prominence material (Illing and Hundhausen, 1985). Concave-outward trailing features were noted in the *Solar Maximum Mission* (SMM) coronagraph images (Illing and Hundhausen, 1985; Burkepile and St. Cyr, 1993), but the high-resolution *Large Angle and Spectrometric COronagraph* (LASCO) observations revealed that these three-part CMEs often create the appearance of a helical or flux-rope (FR) structure.

The interplanetary (IP) counterpart of CMEs are called ICMEs. They are featured with high magnetic fields, low ion temperatures, high alpha/proton density ratios and occasionally bidirectional streaming of electrons and ions (*e.g.*, Gosling, 1990). Depending on whether they have a smooth rotating magnetic field, *i.e.*, a signature of flux rope, and fulfill other conditions, ICMEs are further classified into i) magnetic clouds (MCs), and ii) non-cloud ejecta (or simply ejecta) (EJs) (see, *e.g.*, Burlaga *et al.*, 1981; Gosling, 1990). Gopalswamy (2006) suggested that all CMEs have magnetic FR structures, but their propagation directions determine whether they can be seen *in-situ*.

Based on the coronagraphic observations, simple FR models of CMEs using a torus geometry have been developed by various authors. Krall and St. Cyr (2006) (hereafter KS06) described a FR model as having an elliptical curved axis with a circular cross-section of varying radius along the axis and the width (minor diameter) being narrowest at the footpoints on the solar surface. It was shown that the KS06 FR model (KFR) geometry reproduced the statistical measures (average angular widths) of a subset of FR-like CMEs observed by LASCO (St. Cyr *et al.*, 2004). Thernisien, Howard, and Vourlidas (2006) used the graduated cylindrical shell (GCS) model, a FR model with a conical curved axis, and demonstrated that the GCS model fits the CME morphologies for 34 FR-like CMEs selected from Cremades and Bothmer (2004). A more recent study (Krall, 2007) extended the work of KS06 by comparing the FR model synthetic images to 111 limb CMEs observed by SMM (Burkepile *et al.*, 2004). Their results suggested that the FR morphology can be applied not only to FR-like CMEs but also to the general population of CMEs.

In this work, we apply the KFR to the 2011 Living With a Star (LWS) Coordinated Data Analysis Workshop (CDAW) CME list to determine the radial speeds, angular widths, and the propagation directions of the CMEs. We studied 53 shock-driving CMEs during Solar Cycle 23 whose source regions are located within E15° and W15°. We have excluded complex event number 3 with multiple solar sources: an eruptive prominence (EP) (N45W10), active region (AR) 8115 (N32W32), and AR 8113 (N25W40). To zeroth order, it is supposed that MCs associated CMEs (MC-CMEs) come from the disk center, ejecta-CMEs come from intermediate longitudes, and driverless shocks come from near the limb (*e.g.*, Gopalswamy, 2006). Since all the CDAW CMEs originate nearly from the disk center, it is expected that they are observed as MCs at Earth, assuming that all CMEs have FR structures and erupt radially. However, for the 53 CDAW events, 23 events are associated with MCs and 30 events are EJs. One likely reason is the non-radial eruption of CMEs (see, *e.g.*, St. Cyr *et al.*, 2000; Gopalswamy *et al.*, 2009; Xie *et al.*, 2009). In this paper, we are looking into the characteristics that distinguish two CME populations: MC-CMEs and EJ-CMEs. By performing a detailed investigation of CME origins and propagations, we hope to answer the CDAW's focusing question: Do all CMEs have flux-rope structure, but sometimes they are not observed

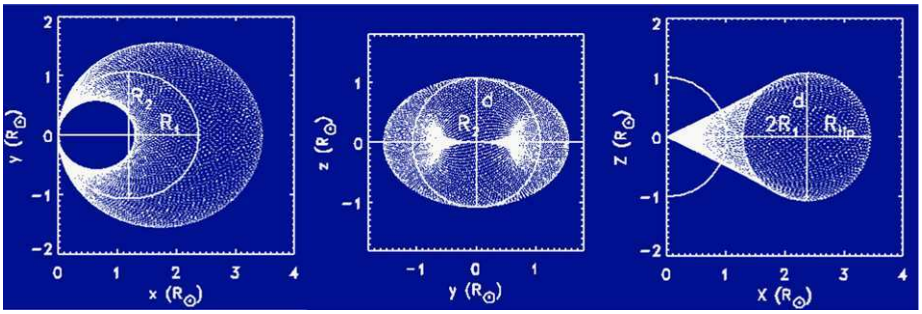

Figure 1 Illustrative plot of the flux-rope model morphology. From left to right: broadside (face-on), top, and edge-on views of a flux rope.

so because of geometry (the observing spacecraft does not pass through the flux rope) or do some CMEs have inherently non-flux-rope structure?

The rest of the paper is organized as follows. Section 2 describes data selection and detailed FR model fitting procedures. Section 3 presents the fitting results and statistical analysis. Finally, the summary and conclusions are presented in Section 4.

2. Data and Model

The CDAW 2011 list is a subset of the list in Gopalswamy *et al.* (2010). This subset was selected based on two criteria: i) the CMEs originate from close to the central meridian (E15° ≤ source longitude ≤ W15°), ii) the CMEs are associated with shock-driving interplanetary CMEs (ICMEs). The CDAW 2011 list consists of 23 MC-CMEs and 30 EJ-CMEs.

To determine the radial speeds, angular widths, and propagation directions of the CMEs, we applied the KS06 FR model fit (KFR-fit) to LASCO C2 and C3 images. The KS06 model is also called the elliptical FR model, which assumes that the FR has an elliptical axis with varying radial circular cross-sections. Figure 1 gives the broadside (face-on), top, and edge-on views of the FR model, with apex pointing to the west limb.

The geometry of the flux rope can be described by two parameters: the ratio of the semi-minor to semi-major axes of the ellipse, $\lambda_\epsilon = R_2/R_1$ and the axial aspect ratio, $\Lambda_\alpha = 2R_1/d$, where R_1, R_2, and d are semi-major axis, semi-minor axis and width of the flux rope at its apex, as shown in Figure 1. The orientation of the flux rope is defined by three angles: latitude λ, longitude ϕ, and tilt angle α, where the tilt angle is the rotation angle clockwise with respect to the East direction.

We used an iterative method to parameterize the flux-rope model. First, we chose initial test parameters of the model based on the coronagraphic observations; we then iteratively adjusted the test parameters until the best fit of the FR model to LASCO images was obtained. The fitted CME radial speed is given by $V_{\rm CME} = \Delta(R_{\rm tip})/{\rm d}t$, where $R_{\rm tip}$ is the radial distance from the origin to the apex of the FR. The widths of the CME are given by $\omega_{\rm edge} = 2 \times {\rm tg}^{-1}(0.5/\Lambda_\alpha)$, $\omega_{\rm broad} = 2 \times {\rm tg}^{-1}(\lambda_\epsilon)$, where $\omega_{\rm edge}$ and $\omega_{\rm broad}$ are the widths of the CME from edge-on and face-on views, respectively.

Figure 2 shows an example of the model fit for the 20 January 2004 CME. The CME was a halo CME associated with a C5.5 soft X-ray flare recorded by GOES in AR 10540 (S13W09), with a peak at 00:45 UT. The left panel of Figure 2 is an *Extreme Ultraviolet Imaging Telescope* (EIT) 195 Å image, which shows the post-eruption arcade titled ∼52°

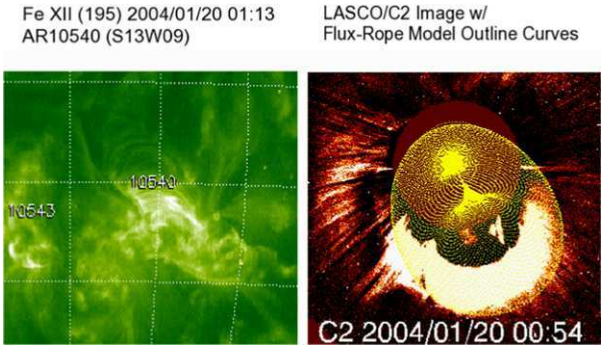

Figure 2 An example of the flux-rope model fit for the 20 January 2004 CME. (Left) EIT 195 Å image showing the flare post-eruption arcade at 01:13 UT. (Right) LASCO/C2 image at 00:54 UT superimposed with the flux-rope model outline curves (yellow curves).

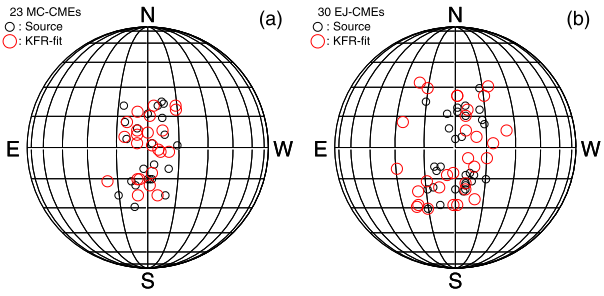

Figure 3 Comparison between the source locations (black circles) and the KFR-fit propagation directions (red circles) for (a) 23 MC-CMEs and (b) 30 EJ-CMEs.

relative to the E–W direction at 01:13 UT. The right panel shows the model outline curves (yellow curves) superimposed on a LASCO/C2 image at 00:54 UT. The fitting gave a CME radial speed $V_{\rm CME} = 1441$ km s^{-1}, $\omega_{\rm broad} = 90°$, and $\omega_{\rm edge} = 71°$; the best fit for the propagation direction was $(\lambda, \phi, \alpha) = (-25°, 10°, 60°)$. The fitting results showed that the CME erupted non-radially and was deflected from S13 to S25; the longitude and tilt angle of the KFR-fit direction were relatively consistent with the CME source location.

3. Statistical Analysis and Results

Table 1 summarizes the flux-rope fitting results for the 53 CMEs. Columns 1 – 8 are the event number, shock date, time, ICME type, CME date, first appearance time at LASCO C2, sky-plane speed, and source location identified based on solar surface activities: flare, EIT wave and dimming, eruptive prominence or disappearing filament. Columns 9 – 13 are outputs of the KFR-fit edge-on width and face-on (broadside) width, radial speed, propagation direction and tilt angle.

3.1. Spatial Relationship Between CME Source Locations and Propagation Directions

Previous studies have shown that CMEs may erupt non-radially and be deflected by the ambient magnetic environment such as coronal holes (*e.g.* Gopalswamy *et al.*, 2009; Mohamed *et al.*, 2012), streamers, and nearby ARs or complex intrinsic structures of associated ARs (*e.g.*, Xie *et al.*, 2009). Figure 3 shows the CME source locations (black circles) and the KFR-fit propagation directions (red circles) for (a) 23 MC-CMEs and (b) 30 EJ-CMEs. From Figure 3a we can see that both the CME source locations and the KFR-fit propagation directions for the MC-CMEs are relatively clustered close to disk center (DC).

Table 1 List of the CDAW 2011 CMEs and the best-fit flux-rope model parameters.

No.	ICME		Type[a]	CME				Flux-rope model fit output				
	Date	Time [UT]		Date	Time [UT]	V_{sky} [km s^{-1}]	Source	ω_e [◦]	ω_b [◦]	V_{cme} [km s^{-1}]	Direction	Tilt[b] [◦]
01	1997/01/10	00:52	MC	1997/01/06	15:10	136	S18E06	55	70	258	S18W01	−60.00
02	1997/05/15	01:15	MC	1997/05/12	05:30	464	N21W08	53	70	670	N01W02	−80.00
04	1998/05/03	17:00	EJ	1998/05/02	23:40	585	S18W05	79	90	826	S16E14	42.00
05	1998/05/04	02:00	EJ	1998/05/02	14:06	938	S15W15	79	90	2097	N08W05	22.00
07	1998/11/07	08:00	EJ	1998/11/04	07:54	523	N17W01	71	95	706	N25W01	92.00
08	1998/11/13	01:40	EJ	1998/11/09	18:18	325	N15W05	53	70	712	N15W05	16.00
09	1999/04/16	11:10	MC	1999/04/13	03:30	291	N16E00	79	90	560	S02W06	−10.00
10	1999/06/26	19:25	EJ	1999/06/24	13:31	975	N29W13	71	90	1531	N25W15	45.00
13	1999/09/22	12:00	EJ	1999/09/20	06:06	604	S20W05	31	70	868	S20W05	−35.00
14	1999/10/21	02:13	EJ	1999/10/18	00:06	144	S30E15	48	90	217	S30E15	60.00
15	2000/01/22	00:23	EJ	2000/01/18	17:54	739	S19E11	71	90	1179	S10E29	−25.00
16	2000/02/20	21:00	MC	2000/02/17	21:30	728	S29E07	71	84	994	S12W02	70.00
17	2000/07/10	06:00	EJ	2000/07/07	10:26	453	N04E00	48	90	739	S17W05	70.00
18	2000/07/11	11:22	EJ	2000/07/09	23:50	483	N18W12	58	77	1152	N18W06	15.00
19	2000/07/15	14:18	MC	2000/07/14	10:54	1674	N22W07	90	16	2281	N18W14	30.00
20	2000/07/26	18:58	EJ	2000/07/23	05:30	631	S13W05	71	84	1119	S13E04	−15.00
21	2000/07/28	06:39	MC	2000/07/25	03:30	528	N06W08	64	84	960	S15E04	−95.00
23	2000/08/11	18:51	MC	2000/08/09	16:30	702	N20E12	53	77	1024	N17E05	−85.00
24	2000/09/17	17:00	MC	2000/09/16	05:18	1215	N14W07	64	90	1574	N08W07	45.00
25	2000/10/05	03:23	EJ	2000/10/02	03:50	525	S09E07	53	90	1104	S19E08	−65.00
26	2000/10/12	22:36	MC	2000/10/10	23:50	798	N01W14	58	95	1287	N20W14	−55.00
27	2000/11/06	09:20	MC	2000/11/03	18:26	291	N02W02	64	87	542	N02E05	25.00

Table 1 (*Continued.*)

No.	ICME		Type[a]	CME				Flux-rope model fit output				
	Date	Time [UT]		Date	Time [UT]	V_{sky} [km s^{-1}]	Source	ω_e [◦]	ω_b [◦]	V_{cme} [km s^{-1}]	Direction	Tilt[b] [◦]
28	2000/11/26	05:30	EJ	2000/11/24	05:30	1289	N20W05	79	95	1745	N30W18	−55.00
29	2001/03/03	11:30	EJ	2001/02/28	14:50	313	S17W05	71	90	522	S05W15	−65.00
30	2001/03/22	14:00	EJ	2001/03/19	05:26	389	S20W00	71	90	691	N05W10	85.00
31	2001/04/11	14:12	EJ	2001/04/09	15:54	1192	S21W04	79	84	1813	S12E01	75.00
32	2001/04/11	16:19	MC	2001/04/10	05:30	2411	S23W09	71	95	3735	S23W05	−85.00
33	2001/04/28	05:02	MC	2001/04/26	12:30	1006	N20W05	79	77	1093	N20W03	30.00
34	2001/08/12	11:10	EJ	2001/08/09	10:30	479	N11W14	45	90	842	N02W18	80.00
35	2001/10/11	16:50	EJ	2001/10/09	11:30	973	S28E08	58	84	1449	S28E01	−20.00
36	2002/03/18	13:13	MC	2002/03/16	23:06	957	S08W03	79	00	1151	N15W01	−50.00
37	2002/04/17	11:01	MC	2002/04/15	03:50	720	S15W01	79	84	1302	S01W05	−10.00
38	2002/05/11	10:30	EJ	2002/05/08	13:50	614	S12W07	48	90	1231	S09W09	55.00
39	2002/05/18	19:51	MC	2002/05/16	00:50	600	S23E15	48	84	900	S23E05	−70.00
40	2002/05/20	03:40	EJ	2002/05/17	01:27	461	S20E14	31	66	743	S28E20	−60.00
41	2002/05/30	02:15	EJ	2002/05/27	13:27	1106	N22E15	58	84	1362	N32E20	80.00
42	2002/07/17	15:50	EJ	2002/07/15	21:30	1300	N19W01	90	95	2046	N29E15	−40.00
43	2002/08/01	05:10	MC	2002/07/29	12:07	222	S10W10	64	84	448	S02W10	−70.00
44	2003/08/17	13:40	MC	2003/08/14	20:06	378	S10E02	48	84	662	N12E10	−65.00
45	2003/10/29	06:00	MC	2003/10/28	11:30	2459	S16E08	90	90	2916	S16E20	75.00
46	2003/10/30	16:20	MC	2003/10/29	20:54	2029	S15W02	90	95	3474	S15E05	80.00
47	2004/01/22	01:10	EJ	2004/01/20	00:06	965	S13W09	90	71	1441	S25W10	60.00
48	2004/07/24	05:32	MC	2004/07/22	08:30	700	N04E10	71	84	1359	N06E05	−10.00
49	2004/11/09	09:05	MC	2004/11/06	02:06	1111	N09E05	90	95	1319	N07W00	12.00

Table 1 (*Continued.*)

No.	ICME		Type[a]	CME				Flux-rope model fit output				
	Date	Time [UT]		Date	Time [UT]	V_{sky} [km s^{-1}]	Source	ω_e [◦]	ω_b [◦]	V_{cme} [km s^{-1}]	Direction	Tilt[b] [◦]
50	2004/12/11	13:03	EJ	2004/12/08	20:26	611	N05W03	79	77	754	S05W06	45.00
51	2005/01/16	09:27	EJ	2005/01/15	06:30	2049	N16E04	58	84	2503	N25W01	−80.00
52	2005/02/17	21:59	EJ	2005/02/13	11:06	584	S11E09	60	84	587	S21E19	75.00
53	2005/05/15	02:19	MC	2005/05/13	17:12	1689	N12E11	90	90	2384	N05E11	45.00
54	2005/05/20	03:34	MC	2005/05/17	03:26	449	S15W00	64	84	596	N08E05	85.00
56	2005/07/10	02:56	EJ	2005/07/07	17:06	683	N09E03	48	87	1040	N12E26	91.00
57	2005/09/02	13:32	EJ	2005/08/31	11:30	825	N13W13	58	90	1161	N08W25	−5.00
58	2005/09/15	08:25	EJ	2005/09/13	20:00	1866	S09E10	79	95	2171	S29E21	−52.00
59	2006/08/19	10:51	EJ	2006/08/16	16:30	888	S16W08	71	90	1351	S28W01	−15.00

Notes:
Columns 1 – 4: the event number, shock date, time and ICME type. Columns 5 – 8: CME date, first appearance time at LASCO C2, sky-plane speed and source location. Columns 9 – 13: flux-rope model fit edge-on width, broadside width, radial speed, propagation direction and tilt angle.
[a]MC = Magnetic cloud; EJ = Ejecta.
[b]With respect to East clockwise.

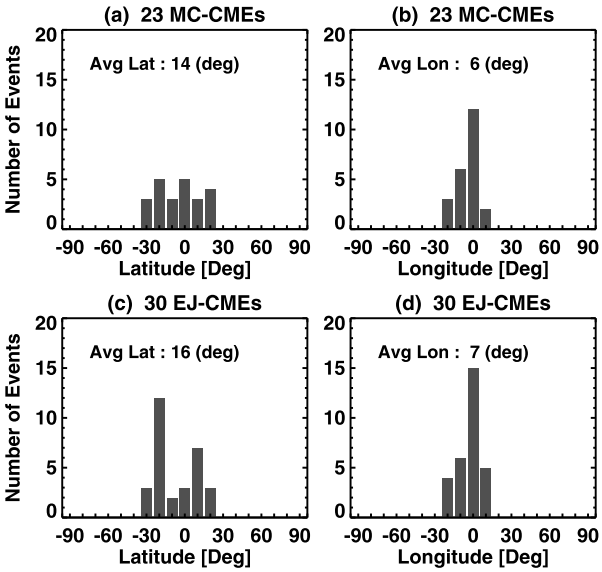

Figure 4 Histograms of the source locations: (a) latitude and (b) longitude for 23 MC-CMEs, (c) latitude and (d) longitude for 30 EJ-CMEs. The average absolute values are indicated in each plot.

Histograms of the source locations (Figures 4a and b) show that the mean absolute latitude and longitude of the source locations for the MC-CMEs are (14°, 6°); and the mean latitude and longitude of the KFR-fit propagation directions are (11°, 6°) (Figure 5a and b). While from Figure 3b, we see that the KFR-fit propagation directions of the EJ-CMEs are relatively scattered away from DC, compared to their source locations, indicating some degree of CME deflection. These deflections of the EJ-CMEs are also shown in Figure 5. In Figure 4 the mean latitude and longitude of the source locations for the EJ-CMEs are (16°, 7°), but the mean latitude and longitude of the KFR-fit propagation directions for the EJ-CMEs are (18°, 11°) (Figure 5c and d).

Figure 6 plots histograms of: (a) $\Delta_{\rm lat}$ and (b) $\Delta_{\rm lon}$ for 23 MC-CMEs, and (c) $\Delta_{\rm lat}$ and (d) $\Delta_{\rm lon}$ for 30 EJ-CMEs, where $\Delta_{\rm lat} = |Lat_{\rm fr}| - |Lat_{\rm sc}|$ and $\Delta_{\rm lon} = |Lon_{\rm fr}| - |Lon_{\rm sc}|$ are the latitudinal and longitudinal differences between CME source locations ($Lat_{\rm sc}$, $Lon_{\rm sc}$) and KFR-fit propagation directions ($Lat_{\rm fr}$, $Lon_{\rm fr}$). The mean $\Delta_{\rm lat}$ and $\Delta_{\rm lon}$ for the MC-CMEs are $-2.7°$ and $-0.3°$, and the mean $\Delta_{\rm lat}$ and $\Delta_{\rm lon}$ for the EJ-CMEs are 2.0° and 4.1°. Since positive (negative) values of $\Delta_{\rm lat}$ and $\Delta_{\rm lon}$ indicate that the CMEs were deflected away from (towards) DC, both Figure 5 and Figure 6 suggest that the EJ-CMEs were deflected farther from DC while the MC-CMEs were deflected closer to DC during their eruption and propagation near the Sun.

3.2. Comparison of Angular Widths Between MC-CMEs and EJ-CMEs

Figure 7 presents histograms of (a) $\omega_{\rm edge}$ and (b) $\omega_{\rm broad}$ for 23 MC-CMEs, and histograms of (c) $\omega_{\rm edge}$ and (d) $\omega_{\rm broad}$ for 30 EJ-CMEs, where $\omega_{\rm edge}$ and $\omega_{\rm broad}$ are the KFR-fit widths of the CMEs from edge-on and face-on views, respectively. The mean broadside (face-on) widths are 87° and 85° for the MC-CMEs and EJ-CMEs, and the mean edge-on widths are 70° and 63° for the MC-CMEs and EJ-CMEs, respectively. The MC-CMEs are wider than the EJ-CMEs by 2° in the mean broadside width and 7° in the mean edge-on width. This indicates that the MC-CMEs are not only deflected toward DC, but also are slightly larger in widths, thus their central FR structures are more likely observed *in-situ*.

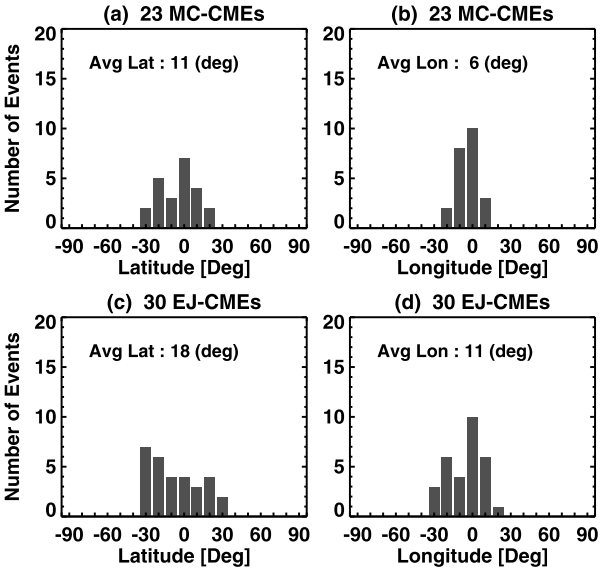

Figure 5 Histograms of the KFR-fit propagation directions: (a) latitude and (b) longitude for 23 MC-CMEs, (c) latitude and (d) longitude for 30 EJ-CMEs. The average absolute values are indicated in each plot.

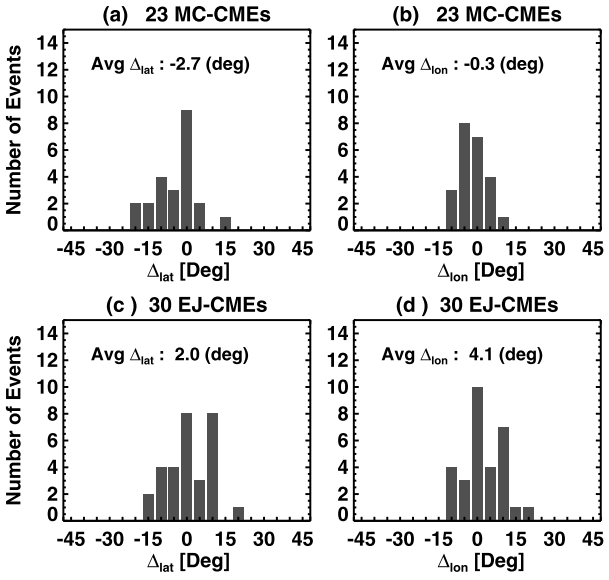

Figure 6 Histograms of latitudinal difference between the CME source locations and propagation directions Δ_{lat} for (a) 23 MC-CMEs and (c) 30 EJ-CMEs, and histograms of longitudinal difference Δ_{lon} for (b) 23 MC-CMEs and (d) 30 EJ-CMEs. The average values are indicated in each plot.

3.3. Comparison of Radial Speeds Between MC-CMEs and EJ-CMEs

Figure 8 shows histograms of radial speeds for: (a) 23 MC-CMEs and (b) 30 EJ-CMEs. The mean radial speeds are 1369 km s^{-1} and 1190 km s^{-1} for the MC-CMEs and EJ-CMEs, respectively. The MC-CMEs are faster than EJ-CMEs by 121 km s^{-1} concerning their mean radial speeds. This might be one of other factors affecting the observed ICME properties. It is expected that the FR structures in the slow CMEs become more distorted by their interactions with the background solar wind and/or with other CMEs (*cf.*, Kim *et al.*, 2012) during their propagation.

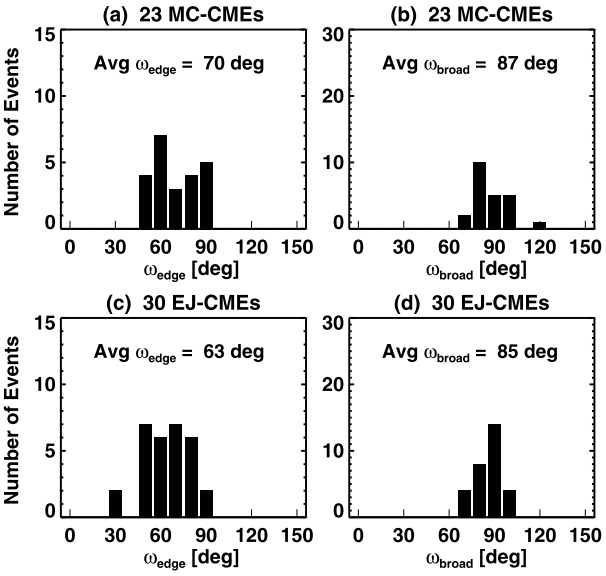

Figure 7 Histograms of KFR-fit widths: (a) edge-on width ω_{edge} and (b) broadside width ω_{broad} for 23 MC-CMEs, (c) ω_{edge} and (d) ω_{broad} for 30 EJ-CMEs. The average values are indicated in each plot.

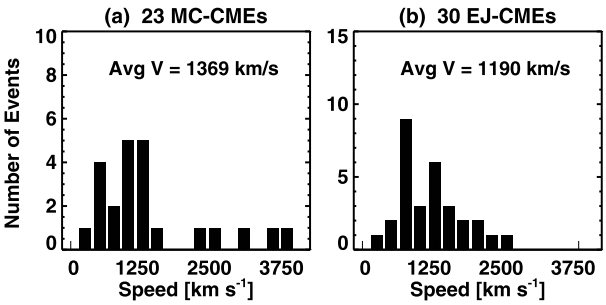

Figure 8 Histograms of KFR-fit radial speed V_{cme} for (a) 23 MC-CMEs and (b) 30 EJ-CMEs. The average values are indicated in each plot.

4. Summary and Conclusion

We studied a set of the CDAW 2011 CMEs which consisted of 23 MC-CMEs and 30 EJ-CMEs. These two groups of CMEs originated from similar source locations, with mean latitude and longitude of the MC-CMEs (EJ-CMEs) of 14 (16)° and 6 (7)°, respectively. We applied the KFR-fit to determine the CME radial speeds, angular widths, and propagation directions. The KFR-fit results have revealed that the properties of these two groups of CMEs showed no characteristic differences.

However, there exist distinguishing features between the two groups in terms of their propagation directions and angular widths. It is found that the EJ-CMEs tend to propagate in higher latitudinal and longitudinal directions. The mean propagation latitude and longitude of the EJ-CMEs were larger than those of the MC-CMEs by 7° and 5° (Figure 5), respectively. The likely reasons of the CME non-radial eruption are the complex intrinsic structures of the associated ARs, deflections from the ambient magnetic structures such as coronal holes, streamers, and nearby ARs. It is shown in Figure 6 that the EJ-CMEs were deflected away from DC, while the MC-CMEs were deflected towards DC. Similar results are also found in Gopalswamy *et al.* (2009) and Mohamed *et al.* (2012), where they studied the interaction of CMEs with coronal holes. Gopalswamy *et al.* (2009) showed that some fast

and wide CMEs from DC were deflected away from the Sun–Earth line and the spacecraft at L1 only observed driveless-like shocks. Mohamed *et al.* (2012) calculated the coronal hole deflection parameters, which are smaller for MCs. The non-radial eruption and deflection of the CMEs has caused the FR eruptions originating from near DC to propagate away from DC and the observing spacecraft passed only by their flank and missed the central FR structures. In addition, the MC-CMEs were also found to be wider than the EJ-CMEs. The mean broadside and edge-on widths of the MC-CMEs were larger than those of the EJ-CMEs by 2° and 7°, respectively. The obtained results suggest that the FR structures in the MC-CMEs are caught *in-situ* not only because they were deflected toward DC, but also because they were larger in size.

In conclusion, both the MC-CMEs and EJ-CMEs had similar solar sources and possible flux-rope structures; their different propagation directions and angular widths determine whether they are viewed as clouds or non-clouds by the observing spacecraft. The results of this work support the conjecture that "all CMEs have flux-rope structure".

Acknowledgements This work uses data from the NASA/LWS Coordinated Data Analysis Workshops on CME/flux-ropes in 2010 and 2011. We acknowledge the workshop support provided by NASA/LWS, Predictive Sciences, Inc. (San Diego, CA), University of Alcala (Alcala de Henares, Spain), and Ministerio de Ciencia e Innovacion (Reference number AYA2010-12439-E), Spain. The authors acknowledge support of NASA grant LWSTRT08-0029.

References

Burkepile, J.T., Hundhausen, A.J., Stanger, A.L., St. Cyr, O.C., Seiden, J.A.: 2004, Role of projection effects on solar coronal mass ejection properties: 1. A study of CMEs associated with limb activity. *J. Geophys. Res.* **109**, 3103. doi:10.1029/2003JA010149.

Burkepile, J.T., St. Cyr, O.C.: 1993, A revised and expanded catalogue of mass ejections observed by the Solar Maximum Mission coronagraph. NASA STI/Recon Technical Report N 93, 26556.

Burlaga, L., Sittler, E., Mariani, F., Schwenn, R.: 1981, Magnetic loop behind an interplanetary shock – Voyager, Helios, and IMP 8 observations. *J. Geophys. Res.* **86**, 6673 – 6684. doi:10.1029/JA086iA08p06673.

Chen, J., Howard, R.A., Brueckner, G.E., Santoro, R., Krall, J., Paswaters, S.E., St. Cyr, O.C., Schwenn, R., Lamy, P., Simnett, G.M.: 1997, Evidence of an erupting magnetic flux rope: LASCO coronal mass ejection of 1997 April 13. *Astrophys. J. Lett.* **490**, L191. doi:10.1086/311029.

Cremades, H., Bothmer, V.: 2004, On the three-dimensional configuration of coronal mass ejections. *Astron. Astrophys.* **422**, 307 – 322. doi:10.1051/0004-6361:20035776.

Dere, K.P., Brueckner, G.E., Howard, R.A., Michels, D.J., Delaboudiniere, J.P.: 1999, LASCO and EIT observations of helical structure in coronal mass ejections. *Astrophys. J.* **516**, 465 – 474. doi:10.1086/307101.

Gibson, S.E., Low, B.C.: 2000, Three-dimensional and twisted: an MHD interpretation of on-disk observational characteristics of coronal mass ejections. *J. Geophys. Res.* **105**, 18187 – 18202. doi:10.1029/1999JA000317.

Gopalswamy, N.: 2006, Properties of interplanetary coronal mass ejections. *Space Sci. Rev.* **124**, 145 – 168. doi:10.1007/s11214-006-9102-1.

Gopalswamy, N., Mäkelä, P., Xie, H., Akiyama, S., Yashiro, S.: 2009, CME interactions with coronal holes and their interplanetary consequences. *J. Geophys. Res.* **114**, A00A22. doi:10.1029/2008JA013686.

Gopalswamy, N., Xie, H., Mäkelä, P., Akiyama, S., Yashiro, S., Kaiser, M.L., Howard, R.A., Bougeret, J.-L.: 2010, Interplanetary shocks lacking type II radio bursts. *Astrophys. J.* **710**, 1111 – 1126. doi:10.1088/0004-637X/710/2/1111.

Gosling, J.T.: 1990, *Coronal Mass Ejections and Magnetic Flux Ropes in Interplanetary Space*. *Geophys. Monogr. Ser.* **58**, AGU, Washington, 343 – 364.

Illing, R.M.E., Hundhausen, A.J.: 1985, Observation of a coronal transient from 1.2 to 6 solar radii. *J. Geophys. Res.* **90**, 275 – 282. doi:10.1029/JA090iA01p00275.

Kim, R.-S., Gopalswamy, N., Cho, K.-S., Moon, Y.-J., Yashiro, S.: 2012, Different characteristics of MC associated CME and EJ associated CME. *Solar Phys.*, submitted (this issue).

Krall, J.: 2007, Are all coronal mass ejections hollow flux ropes? *Astrophys. J.* **657**, 559 – 566. doi:10.1086/510191.

Krall, J., St. Cyr, O.C.: 2006, Flux-rope coronal mass ejection geometry and its relation to observed morphology. *Astrophys. J.* **652**, 1740 – 1746. doi:10.1086/508337.

Krall, J., Chen, J., Duffin, R.T., Howard, R.A., Thompson, B.J.: 2001, Erupting solar magnetic flux ropes: theory and observation. *Astrophys. J.* **562**, 1045 – 1057. doi:10.1086/323844.

Mohamed, A.A., Gopalswamy, N., Yashiro, S., Akiyama, S., Mäkelä, P., Xie, H., Jung, H.: 2012, The relation between coronal holes and coronal mass ejections during the rise, maximum, and declining phases of Solar Cycle 23. *J. Geophys. Res.* **117**, 1103. doi:10.1029/2011JA016589.

St. Cyr, O.C., Plunkett, S.P., Michels, D.J., Paswaters, S.E., Koomen, M.J., Simnett, G.M., Thompson, B.J., Gurman, J.B., Schwenn, R., Webb, D.F., Hildner, E., Lamy, P.L.: 2000, Properties of coronal mass ejections: SOHO LASCO observations from January 1996 to June 1998. *J. Geophys. Res.* **105**, 18169 – 18186. doi:10.1029/1999JA000381.

St. Cyr, O.C., Cremades, H., Bothmer, V., Krall, J., Burkepile, J.T.: 2004, Morphology Indicators of the three-dimensional size of flux rope CMEs: a prediction for STEREO. AGU Fall Meeting Abstracts, SH22A-04.

Thernisien, A.F.R., Howard, R.A., Vourlidas, A.: 2006, Modeling of flux rope coronal mass ejections. *Astrophys. J.* **652**, 763 – 773. doi:10.1086/508254.

Xie, H., St. Cyr, O.C., Gopalswamy, N., Yashiro, S., Krall, J., Kramar, M., Davila, J.: 2009, On the origin, 3D structure and dynamic evolution of CMEs near solar minimum. *Solar Phys.* **259**, 143 – 161. doi:10.1007/s11207-009-9422-x.

Solar Phys (2013) 284:151–166
DOI 10.1007/s11207-012-0191-6

On the Flux-Rope Topology of Ejecta Observed in the Period 1997 – 2006

M.A. Hidalgo · T. Nieves-Chinchilla · J.J. Blanco

Received: 7 April 2012 / Accepted: 5 November 2012 / Published online: 27 November 2012

Abstract In the following study our aim is to analyse the magnetic flux-rope topology of some events observed in the interplanetary medium related to ejecta. The magnetic field structures associated with interplanetary coronal mass ejections are globally classified in magnetic clouds and ejecta. One of the main questions regarding these phenomena concerns their flux-rope or non-flux-rope magnetic field line configuration. From the experimental measurements the only way to elucidate such a question is analysing the corresponding data by means of a flux-rope physical model. After selecting the ejecta events observed during the period 1997 – 2006, we have analysed them in light of an analytical model with that topology for the magnetic field components, initially developed for magnetic clouds, and with a non-force-free character; then, incorporating the expansion of the magnetic structure during their evolution in the interplanetary medium. Different parameters obtained from the fitting of the model are related to the orientation of the axis of the magnetic flux-rope structure and, additionally, the closest distance approach of the spacecraft to its axis. One of the main conclusions achieved concerns the fact that the axes of most of those structures are close to the Sun–Earth line, which implies that the passage of the spacecraft through the corresponding ejecta event is by its flank. In general, we show a rough procedure for the analysis and classification of ejecta in terms of their magnetic field topology.

Flux-Rope Structure of Coronal Mass Ejections
Guest Editors: N. Gopalswamy, T. Nieves-Chinchilla, M. Hidalgo, J. Zhang, and P. Riley

M.A. Hidalgo (✉) · J.J. Blanco
Departamento de Física, Universidad de Alcalá, Alcalá de Henares, Madrid, Spain
e-mail: miguel.hidalgo@uah.es

J.J. Blanco
e-mail: juanjo.blanco@uah.es

T. Nieves-Chinchilla
Catholic University of America, Washington, DC, USA

T. Nieves-Chinchilla
Heliosphysics Science Division, GSFC/NASA, Greenbelt, MD, USA
e-mail: teresa.nieves-chinchil-1@nasa.gov

1. Introduction

Looking at the *in situ* measurements, the coronal mass ejections (CMEs) originating in the Sun's lower atmosphere and propagating in the interplanetary medium appear to be more complex than thought at the beginning; they present magnetic and plasma profiles, some of them without showing any well-defined topology. Once CMEs drive through and interact with the interplanetary medium they are often referred to as interplanetary CMEs (ICMEs). These are globally classified in magnetic clouds (MCs) and ejecta (EJ), nowadays being an active subject of interest in solar physics, above all because they have been revealed to be one of the most determinant phenomena in the relationship between Sun and Earth, mainly for the implication they have in the generation of many geomagnetic storms (Wu and Lepping, 2002; Jian *et al.*, 2006).

Observations of ICMEs show that some of them are associated with structured and ordered magnetic field topologies, in particular, the phenomena of MCs have been well established after Burlaga *et al.* (1981) fixed the criteria on the signatures appearing in *in situ* measurements in the behaviour of the magnetic field and plasma. An MC is a structure in the solar wind that, in most cases, follows an interplanetary shock, shows a smooth rotation of the magnetic field, presents a low proton temperature (or pressure) and has a relatively high magnetic field strength, over the usual values of the solar wind. Even more, recently they have added the presence of bi-directional electrons and unusual charge states of oxygen and iron.

However, there are many ICMEs that correspond to magnetic structures coming from the Sun that do not follow all these requirements. Then, an important global question has arisen about the topology of all these phenomena: do they have a flux-rope magnetic field configuration? Thus, although the phenomenon of MC is considered a well-defined magnetic field configuration, the nature and structure of the EJ are still an open question. In fact, this was the origin of the "Living with a Star Coordinated Data Analysis Workshop: Do all CMEs have flux rope structure?", one held in San Diego, in September 2010, and the second one in Alcalá de Henares (Spain), in September 2011. The approach was twofold: on one hand, from the remote sensing point of view looking at the surface of the Sun, and, on the other hand, analysing *in situ* measurements at 1 AU in light of analytical models and numerical simulations. The latter option was ours.

From the beginning various models and techniques have appeared in the literature to analyse the physics of MCs, with the goal to understand the global structure, the initiation and connection with the Sun, as well as the interactions with the ambient solar wind along the MCs' trajectory in the interplanetary medium and the Earth's magnetosphere. Local models deal with circular cross section (Marubashi, 1986; Burlaga, 1988; Lepping, Jones, and Burlaga, 1990; Hidalgo *et al.*, 2002), including distortion (Mulligan and Russell, 2001; Hidalgo, Nieves-Chinchilla, and Cid, 2002) or local expansion (Farrugia *et al.* 1992, 1993, 1995; Osherovich, Farrugia, and Burlaga, 1993, 1995; Marubashi, 1997; Hidalgo 2003, 2005). Concerning this aspect recent work has shown that the main reason for the expansion of the magnetic structures in the interplanetary medium is the decrease of the external solar wind pressure (Démoulin and Dasso, 2009); this has been confirmed in the inner (Gulisano *et al.*, 2010) and in the 'near' outer heliosphere (up to 5 AUs) (Gulisano *et al.*, 2012). However, the relaxation of force-free and cylindrical approximation conditions is necessary in order to connect the local to the global structure in a more realistic scene. Then, models relaxing the force-free condition (Hidalgo 2003, 2005, and references therein) have been proposed; and these models, therefore, include the

plasma pressure to incorporate the expansion of the MC, or relax the cylindrical approximation (Marubashi, 1997). They are key to deal with the global topology of the magnetic structure. Concerning the latter aspect several topologies have been proposed: plasmoid, toroidal (assuming a uniform cross section along the torus) (Farrugia *et al.*, 1995; Romashets and Vandas, 2001; Romashets, Vandas, and Poedts, 2010), or, more recently, a torus geometry with non-uniform (variable maximum radius) cross section (Hidalgo and Nieves-Chinchilla, 2012).

A research line parallel to analytical models is a numerical approach. At present the number of publications related to phenomena in the interplanetary medium using this approach is increasing (*e.g.*, Riley *et al.*, 2003; Riley and Crooker, 2004), many times confirming the physics deduced from analytical models (distortion of the cross sections (Hu and Sonnerup, 2002), elliptic shape for some orientations respecting the equatorial plane (Taubenschuss *et al.*, 2010)).

However, in many respects analytical models are more useful, easier to apply and more practical than numerical models, above all because they extract information directly from experimental data and investigate the physics involved in a phenomenon like the ICME (Linton and Moldwin, 2009).

The main feature of all analytical models is their assumed flux-rope topology. In particular, this fact allows us to use them for elucidating the presence of this magnetic field configuration in EJ.

More precisely, we will classify ICMEs as follows:

i) MCs, structures with a clear flux-rope topology, clearly seen most of the time in the behaviour of the magnetic field components and proton temperature or pressure.
ii) EJ; in spite of lacking well-defined signatures in the magnetic field, these may have a flux-rope topology.
iii) Complex ejecta (CE), resulting from the interaction of successive CMEs or from the interaction of CMEs with complex solar wind structures and streams. They are apparent in the complex behaviour of the magnetic field components and plasma.

The second class is evident when the plasma presents clear signatures of some well-defined structure, for example Figures 3 or 4, which are associated with the events on November 1998 and March 2001, respectively. They show a low pressure at the time interval of the ejecta. The third class can be seen in Figure 1, which is associated with the event on May 2002; a detailed study of this last kind of structures can be found in Burlaga *et al.* (2001).

Hence, in the present work we plan to analyse the magnetic flux-rope character of some EJ observed in the interplanetary medium during the period 1997 – 2006. The outline of the paper is as follows. In the next section we briefly describe the data used for the present study. In the third one we summarise the flux-rope magnetic field model taking into account a fit to the data. Section 4 corresponds to the body of the present work, being devoted to the analysis of the set of EJ observed in the period of time of interest; we have previously put aside the examples clearly associated with complex ejecta. In light of the results of our analysis, we have been capable to make a first classification between non-flux-rope ejecta (N-FRE) and flux-rope ejecta (FRE). Section 5 is devoted to a discussion of the results.

2. Data

As we have already mentioned, during the two workshops "Living with a Star Coordinated Data Analysis Workshop: Do all CMEs have flux rope structure?", the first in San Diego

(US, 2010) and the second in Alcalá de Henares (Spain, 2011), a strategy was designed to study and analyse with different models and techniques 59 ICMEs observed in the time period 1997 – 2006.

To start with, from the selected 59 events, 24 were unambiguously associated with MCs, *i.e.*, the times series of the magnetic field components and the plasma measurements follow the criteria and signatures established more than 30 years ago by Burlaga *et al.* (1981). (A detailed description and study of these MCs has been reported by Ron Lepping at http://wind.nasa.gov/mfi/mag_cloud_S1.html.) The remaining events, around two thirds and all EJ, do not present so clear simultaneous signatures in the data. Even more, in this set there are EJs that show complex behaviour in most of the main physical magnitudes measured, which will lead us to include them in the subgroup named complex ejecta (CE); we will show below that in our dataset they are represented by four events.

Therefore, the challenge of the workshop has been to make some contributions to the knowledge of the flux or non-flux-rope character of these EJs. For that task we have used data and information coming from the ISTP (International Solar-Terrestrial Physics) program and OMNIWeb.

3. Theoretical Model

We now summarise the analytical magnetic field model used in the present study, which is explained in more detail in Hidalgo and Nieves-Chinchilla (2012); this model was initially developed for MCs. Its starting point is to assume a torus geometry, relaxing the cylindrical approximation, as a key to deal with the global topology of the magnetic structure; a similar focus had previously been presented by Marubashi (1997), but in our case it comes with non-uniform (variable maximum radius) cross section, and with flux-rope topology. Thus, we solve the corresponding Maxwell equations for the magnetic field, together with the plasma continuity equation, and we obtain $\mathbf{B} = B_\varphi \mathbf{e}_\varphi + B_\psi \mathbf{e}_\psi + B_\eta \mathbf{e}_\eta$ and $\mathbf{j} = j_\varphi \mathbf{e}_\varphi + j_\psi \mathbf{e}_\psi + j_\eta \mathbf{e}_\eta$; the latter is the plasma current density, where $\mathbf{j} = \mathbf{j}^e + \mathbf{j}^p$; $\mathbf{j}^e$ and $\mathbf{j}^p$ are the electron and proton current densities, respectively.

Because we are interested in the analysis of ICMEs at 1 AU, we will assume for the torus a large mean radius, much larger than the minor one, and a circular cross section along it. Then, the analytical solution for the poloidal component of the magnetic field is given by the equation

$$B_\varphi = B_\varphi^0(\psi)\cos(\varphi) - \mu_0 j_\psi r \cosh\bigl(-\rho_0\eta + f(\psi)\bigr), \tag{1}$$

where $B_\varphi^0(\psi)$ is the integration constant and $f = f(\psi)$ is an auxiliary function (see below). On the other hand, for the axial component of the magnetic field we obtain

$$B_\psi = B_\psi^0(\psi) + \mu_0 j_\varphi r \cosh\bigl(-\rho_0\eta + f(\psi)\bigr), \tag{2}$$

$B_\psi^0(\psi)$ is the axial magnetic field at the axis of the torus. In order to introduce the expansion of the cross section of the MC, we assume a linear dependence with time in the components of the plasma current density and the integration constants of both components of the magnetic field. Concerning the time dependence of the plasma current density (and, therefore, of the magnetic field), this must be linear to have a physically consistent model (Hidalgo, 2011).

To be able to use the analytical expressions of the components of the magnetic field, we have to make some hypothesis about the behaviour of the auxiliary function $f(\psi)$: in a first

approach we assume it to be $f(\psi) = C\sin(\psi/2)$, C being an adjustable constant (making it zero the torus would have a uniform cross section). Moreover, on the one hand, considering magnetic flux conservation along the torus, we write the poloidal magnetic field integration constant as $B^0_\varphi(\psi) = B^0_{0\varphi}\sin(\psi/2)$, where $B^0_{0\varphi}$ depends on r. For the axial magnetic field at the axis of the torus we write $B^0_\psi(\psi) = B^0_{0\psi}|\cos(\psi/2)|$, imposing $B^0_{0\psi}$ to be constant. On the other hand, for the poloidal component of the current density we take $j_\varphi = \alpha(t_0 - t)r|\cos(\psi/2)|$, whereas for the axial component $j_\psi = \lambda(t_0 - t)\sin(\psi/2)$, where λ and α are parameters of the model.

Finally, the expression for the solution for the third component of the magnetic field is given by

$$B_\eta = -2\cos(\varphi)S\left\{B^0_{0\psi}\sin\left(\frac{\psi}{2}\right) + \frac{1}{C}\mu_0\alpha(t_0 - t)r^2\cosh\big(-\rho_0\eta + f(\psi)\big)\right\}, \tag{3}$$

where the term $S = \sqrt{\sin^2(\psi)}/\sin(\psi)$ corresponds to the Heaviside function. Thus, we now have analytical expressions for the three components of the magnetic field (Equations (1) – (3) (Hidalgo and Nieves-Chinchilla, 2012).

Then, taking into account the parameters related to the orientation of the magnetic flux-rope structure (the attitude of the axis of the flux rope, both the latitude, θ, and the longitude, ϕ, and the minimum distance between the spacecraft path and its axis, y_0), not only the theoretical local magnetic field components in the GSE system can be determined, but also the coordinates of the spacecraft at any time t inside the magnetic field structure.

Therefore, fitting the model we not only can establish if the event has, or does not have, a flux-rope character, but it allows us to determine the orientation of its axis, which in turn allows us to know the relative trajectory of the spacecraft through the EJ (see below).

4. Ejecta

From the potential 59 events initially considered in the time period 1997 – 2006, our purpose in the present work is to focus on the 35 events related to EJ, trying to elucidate their flux-rope topologies. For such an analysis we will take into account the flux-rope model presented in the previous section.

In general, EJ correspond to magnetic structures with a low magnetic field – lower than that observed in MCs. To establish the boundaries of every EJ we have taken into account the behaviour of the plasma pressure (although the same signatures appear in proton temperature or plasma beta), and the magnetic field profile, in particular, searching for an increase in the magnetic field magnitude with respect to the mean values in the calm solar wind.

Moreover, by only having a quick look at the corresponding graphs, we have found that among all these EJs there are four events without any kind of well-defined topology (no clear signatures: neither in the magnetic field components, which present a complex profile, nor in the plasma behaviour). An obvious example is shown in Figure 1, which corresponds to the event of May 2002. We have eventually grouped these events with complex magnetic field profiles in the set of non-flux-rope ejecta (N-FREJ), appearing in Table 1 with CE label (see below). Additionally, in Figure 2 we present a typical fit obtained with our model to such kind of structures, in particular for the event on August 2001. In view of the results obtained from the fits of flux-rope models to these EJ cases, we can conclude that these magnetic structures have more complex topologies.

The next step will be to study the remaining 31 EJs, fitting the flux-rope model to them. After analysing those events we will be able to group this set of events in two main groups:

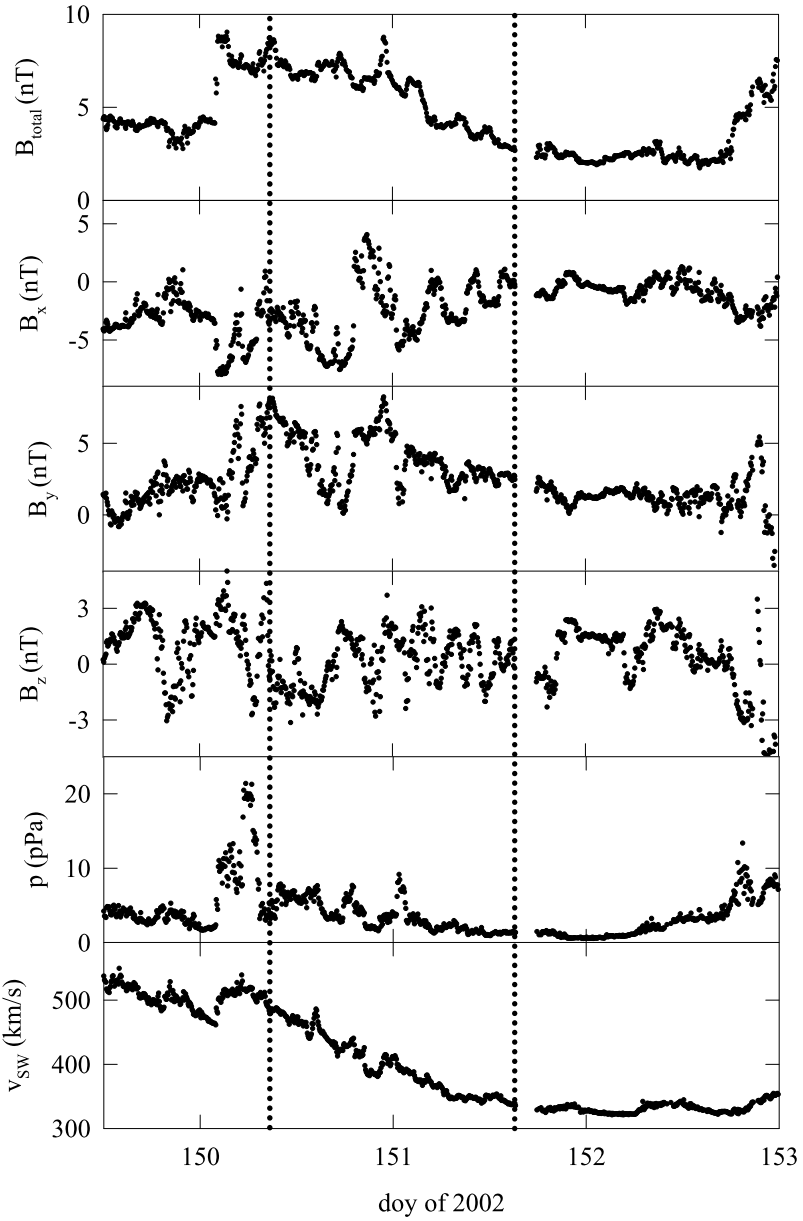

Figure 1 Complex ejecta (CE) corresponding to the event 20020530. From the top down we show the magnetic field strength, **B**, the Cartesian GSE-components (B_x, B_y, B_z), the proton pressure and the bulk solar wind velocity. The vertical dotted lines represent the start and end times of the CE (see text for details).

EJ without flux-rope structure (N-FREJ, see Table 1), and EJ with flux-rope topology (FREJ, see Table 2).

In Table 3 we summarise the results of our analyses over the whole family of events considered.

Table 1 Non-flux-rope ejecta found in the period analysed, 1997 – 2006. In the second column the corresponding time interval is specified. In the third column we show the mean velocity and in the fourth the type of non-flux-rope ejecta: CE (complex ejecta), N-FREJ (ejecta without flux-rope topology). See text for details.

Ejecta (yyyymmdd)	Time interval (doy)	Mean velocity ($km\,s^{-1}$)	Type
19980504	123.851 → 124.065	460	N-FREJ
19980505	124.442 → 125.234	600	N-FREJ
19981113	317.235 → 317.873	385	N-FREJ
19990702	183.223 → 183.560	600	CE
19991022	294.656 → 295.256	470	N-FREJ
20000710	193.155 → 193.511	450	N-FREJ
20010305	63.721 → 64.098	430	N-FREJ
20010323	81.985 → 82.552	400	N-FREJ
20010813	225.332 → 225.886	400	CE
20020511	131.591 → 131.811	420	CE
20020520	140.564 → 140.954	450	N-FREJ
20020530	150.353 → 151.636	410	CE

4.1. Ejecta Without Flux-Rope Topology

Among the 31 EJs we find events which present a proton pressure (or temperature or plasma beta) much lower than the corresponding ambient solar wind, implying that the EJ could be a stable magnetic structure propagating in the interplanetary medium. However, the magnetic field component profiles do not present the smooth and regular behaviour expected for a flux-rope topology, but large fluctuating profiles during the time interval.

There are eight of such events, all detailed in Table 1, where they have been labelled as N-FREJ). Choosing the boundaries of these EJ mainly through the well-defined signatures in the proton pressure, we have tried to fit the model to all cases. The results obtained for such events are illustrated in Figures 3 and 4, corresponding to the events 19981113 and 20010305, respectively.

In Table 1 we give the whole list of the EJ without flux-rope topology found during the interval of interest (1997 – 2006) and studied with our model. The columns detail the identification for each event, the corresponding time interval, the mean velocity and, finally, the type of event: CE (complex ejecta) or N-FREJ (non-flux-rope ejecta).

For all the N-FREJ events the fits obtained are similar to the ones presented in Figures 3 and 4. The model cannot reproduce large fluctuations due to the irregular behaviour of some magnetic field components; we can only fit smoothly the components for some of them. Another main consequence of those fluctuations in comparison with the theoretical model appears in the magnitude of the magnetic field, where it is clearly seen that any flux-rope model has to fail for this kind of magnetic field structure.

4.2. Ejecta with Flux-Rope Topology

We study now the remaining 23 events. All of them present very regular magnetic field component profiles (with no large fluctuations in the corresponding time interval) during their durations. Moreover, the proton pressure and temperature are well defined (see for example the graph of the pressure in Figure 5, corresponding to the event 20000712).

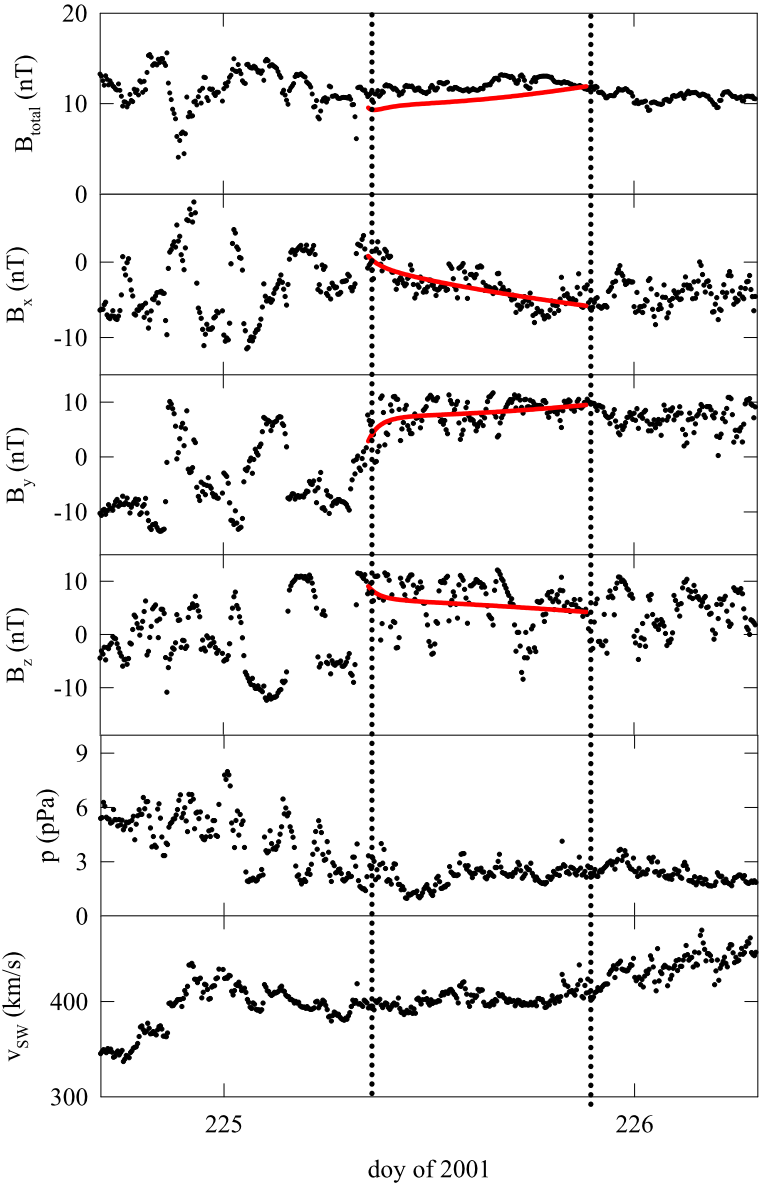

Figure 2 Complex ejecta (CE) corresponding to the event 20010813 and the fitting obtained with the model. From the top down we show the magnetic field strength, **B**, the Cartesian GSE-components (B_x, B_y, B_z), the proton pressure and the bulk solar wind velocity. The vertical dotted lines represent the start and end times of the CE. Superimposed to the experimental data the predictions of the model for the three magnetic field components and its magnitude are shown with solid red lines (see text for details).

Fitting the flux-rope model to every EJ of these 23 we can appreciate the quality of the fits, which leads us to assume unambiguously that they have flux-rope topologies. We have selected, as examples, the results of the analysis for the events 20000712, 20010412, and 20050529, shown in Figures 5, 6 and 7, respectively.

Table 2 Flux-rope ejecta (FREJ) events found in the period analysed, 1997 – 2006. In the second column the corresponding time interval is specified, and the mean velocity at the time interval of the EJ in the third one. The last three columns of the table correspond to the latitude, longitude and the closet approach of the spacecraft to the axis of the flux-rope structure, y_0, expressed in AU, all of them as obtained from the fitting of the model to the experimental data. See text for details.

Ejecta (yyyymmdd)	Time interval (doy)	Mean velocity ($km\,s^{-1}$)	Latitude (°)	Longitude (°)	y_0 (AU)
19971211	344.822 → 345.458	360	91	179	0.0002
19980626	177.526 → 177.812	460	37	92	0.02
19981108	311.957 → 312.191	470	60	177	0.001
19990628	178.942 → 179.108	580	23	188	0.09
19990923	266.415 → 267.047	520	106	154	0.01
20000123	22.785 → 23.099	370	31	180	0.0002
20000712	194.153 → 195.116	500	51	181	0.013
20000727	209.424 → 209.863	330	65	173	0.00003
20000811	223.886 → 224.756	420	77	191	0.002
20001005	279.967 → 280.678	450	0	128	0.03
20001127	332.458 → 333.131	580	26	270	0.14
20010412	102.367 → 103.279	675	52	160	0.23
20011012	285.205 → 285.360	285	33	179	0.003
20020717	199.546 → 200.342	450	36	182	0.02
20040122	22.558 → 23.282	565	37	180	0
20041211	347.984 → 348.316	400	47	161	0.03
20050116	16.718 → 17.300	540	58	161	0.02
20050217	49.349 → 49.873	525	83	191	0.003
20050529	149.495 → 149.638	500	75	173	0.0005
20050710	192.113 → 192.298	420	0	180	0.05
20050902	245.944 → 246.209	650	58	103	0.012
20050915	258.685 → 258.715	850	59	146	0.02
20060820	232.630 → 233.625	400	7	109	0.05

Table 3 Classification of all the events considered in the present work. MC-ICME: Interplanetary coronal mass ejections corresponding to magnetic clouds. Non MC-ICME: Interplanetary coronal mass ejection corresponding to ejecta. CE: Complex ejecta. EJ: Ejecta with simple structure. FREJ: Ejecta with flux-rope structure. N-FREJ: Ejecta without flux-rope structure.

59 events					
MC-ICME	24 events				
Non MC-ICME	35 events	CE	4 events		
		EJ	31 events	FREJ	23 events
				N-FREJ	8 events

In Table 2 we give the list of events with flux-rope ejecta (FREJ) found in the period studied, after analysing the data with the model. In the second column the corresponding time interval is specified, and in the third one the mean velocity, used in the fitting procedure

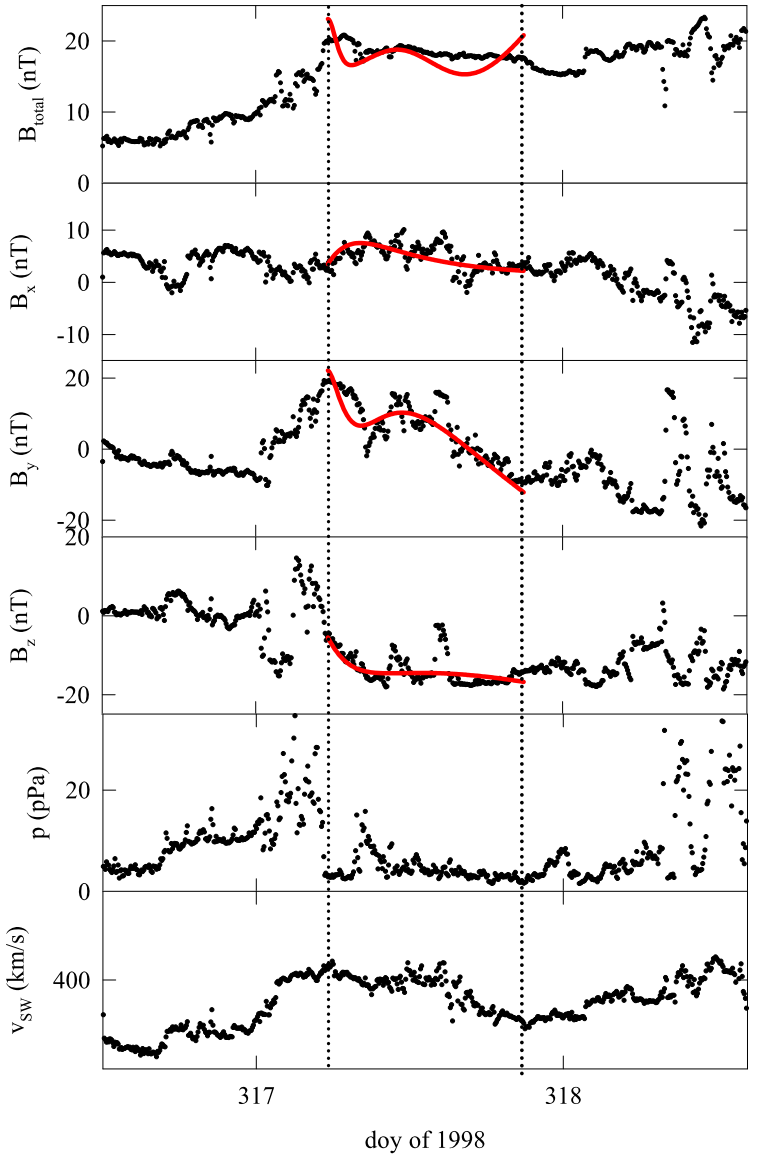

Figure 3 Non-flux-rope ejecta (N-FREJ) corresponding to the event 19981113. From the top down, we show the magnetic field strength, **B**, the Cartesian GSE-components (B_x, B_y, B_z), the proton pressure and the bulk solar wind velocity. The vertical dotted lines represent the start and end times of the EJ. Superimposed to the experimental data the predictions of the model for the three magnetic field components are shown with solid red lines.

for each EJ at the corresponding interval. In the last three columns of the table we give three of the parameters obtained from the fitting: the latitude, longitude and the closet approach of the spacecraft to the axis of the flux-rope structure, y_0, expressed in AU (Astronomical Units).

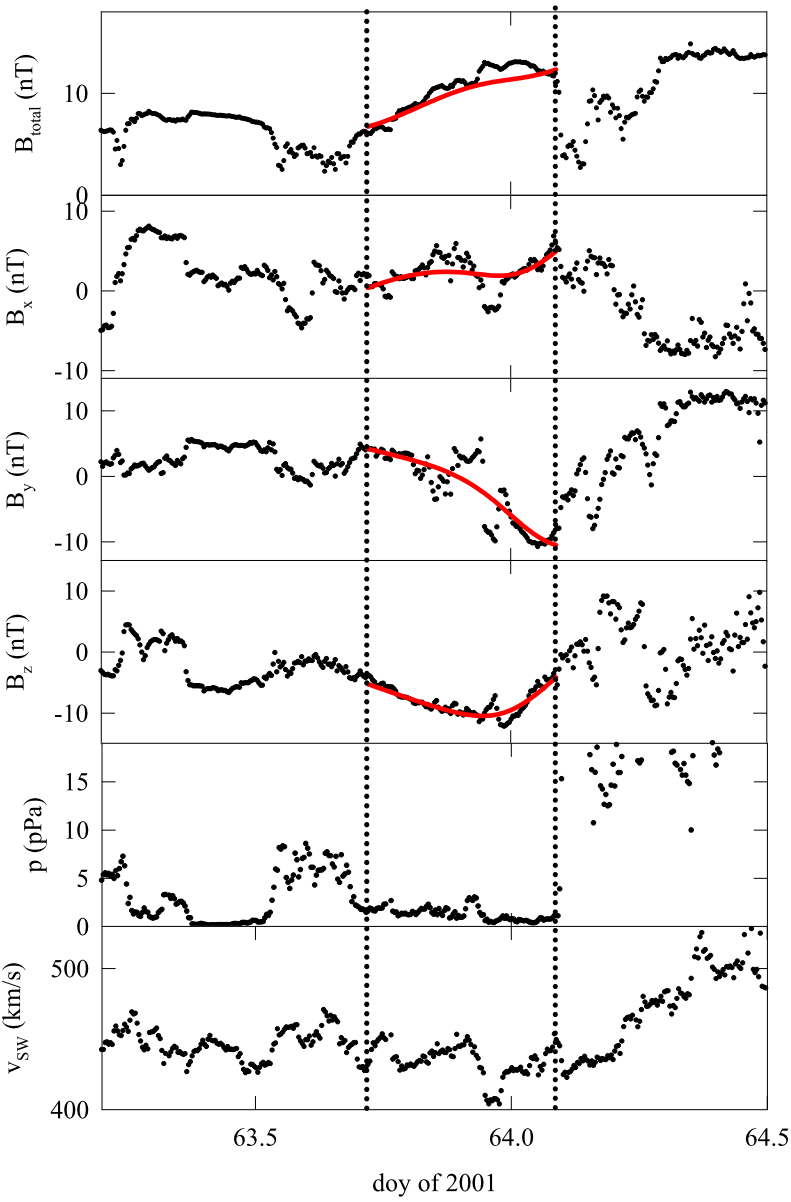

Figure 4 The same as in Figure 3; in this case for the non-flux-rope ejecta (N-FREJ) corresponding to event 20010305.

5. Comments and Discussion

Statistically, based on the 35 events analysed, we conclude that 65 % are FREJ, *i.e.*, it can be assumed that they have flux-rope topology without ambiguity. The remaining events are N-FREJ and do not have this magnetic field configuration. In fact, there are four events showing

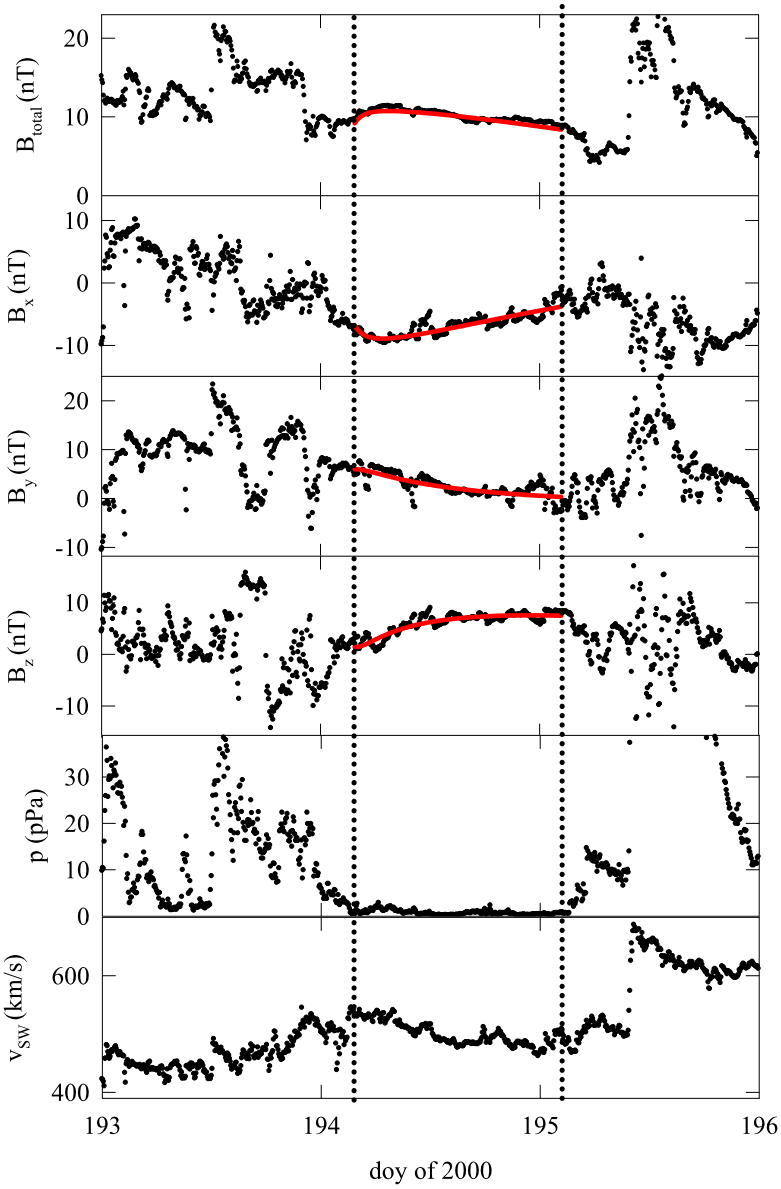

Figure 5 Flux-rope ejecta (FREJ) corresponding to the event 20000712. The graphs are the magnetic field strength, **B**, the Cartesian GSE-components (B_x, B_y, B_z), the proton pressure and the bulk solar wind velocity. The vertical dotted lines represent the start and end times of the EJ. Superimposed to the experimental data the predictions of the model for the three magnetic field components are shown with solid red lines.

complex behaviour in their corresponding physical magnitudes (Table 1) and presenting important fluctuations along their durations (Figure 1).

Then, from the fitting of the flux-rope model, described in Section 3, to the data we can ensure the presence of such a topology in a particular event and, additionally, find phys-

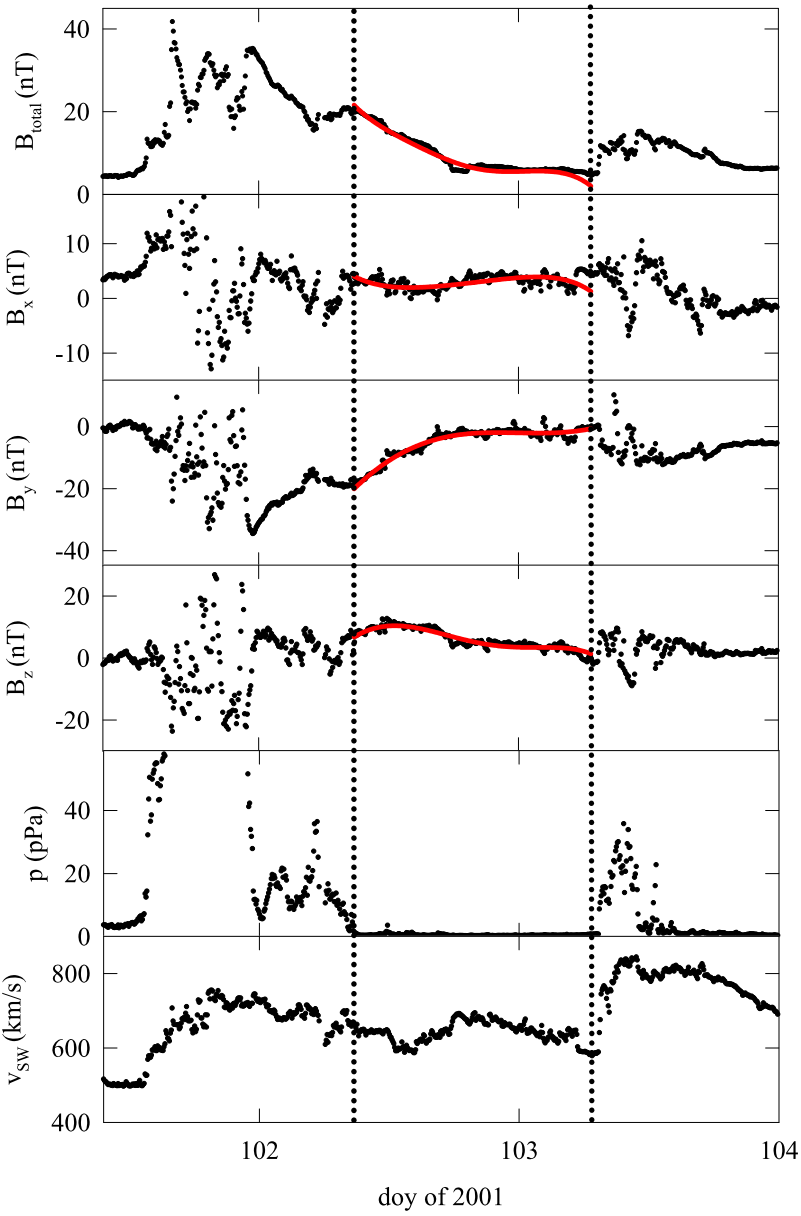

Figure 6 Flux-rope ejecta (FREJ) corresponding to the event 20010412. The graphs are the same as in Figure 5.

ical information on the phenomenon itself; specifically, the attitude of the corresponding flux-rope structure (the latitude with respect to the ecliptic plane, θ, and the longitude in the ecliptic plane with respect to the Sun–Earth line, ϕ) (Table 2). In Figure 8 we represent in polar plots the results obtained for both magnitudes for all the FREJ in the period 1997 – 2006. Whereas the latitude obtained for this set of events meets a wide range

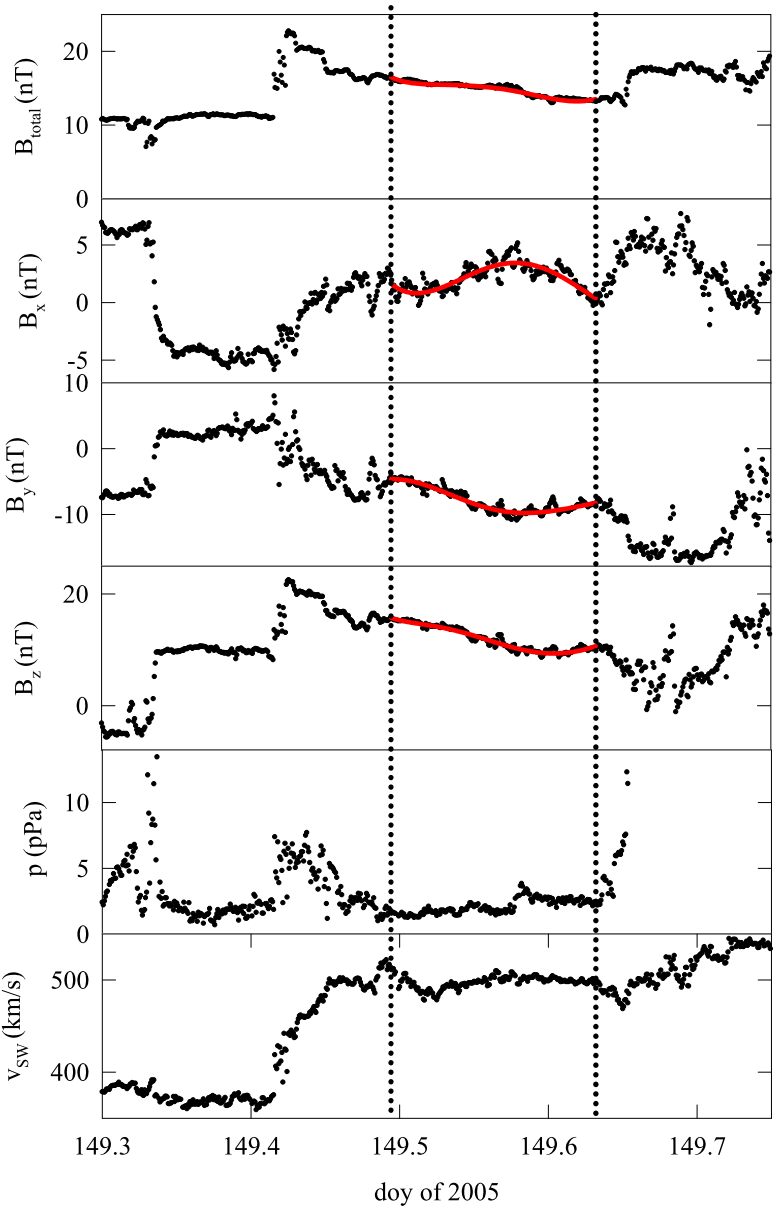

Figure 7 Flux-rope ejecta (FREJ) corresponding to the event 20050529. The graphs shown are the same as in Figure 5. The vertical dotted lines represent the start and end times of the EJ. Superimposed to the experimental data the predictions of the model for the three magnetic field components are shown with solid red lines.

of values, the longitudes obtained for most of the events have values close to 180°, *i.e.*, they are oriented in a direction loosely around the Sun–Earth line. This means that the satellite passage through these EJ has to be close to the flank of their flux-rope structure.

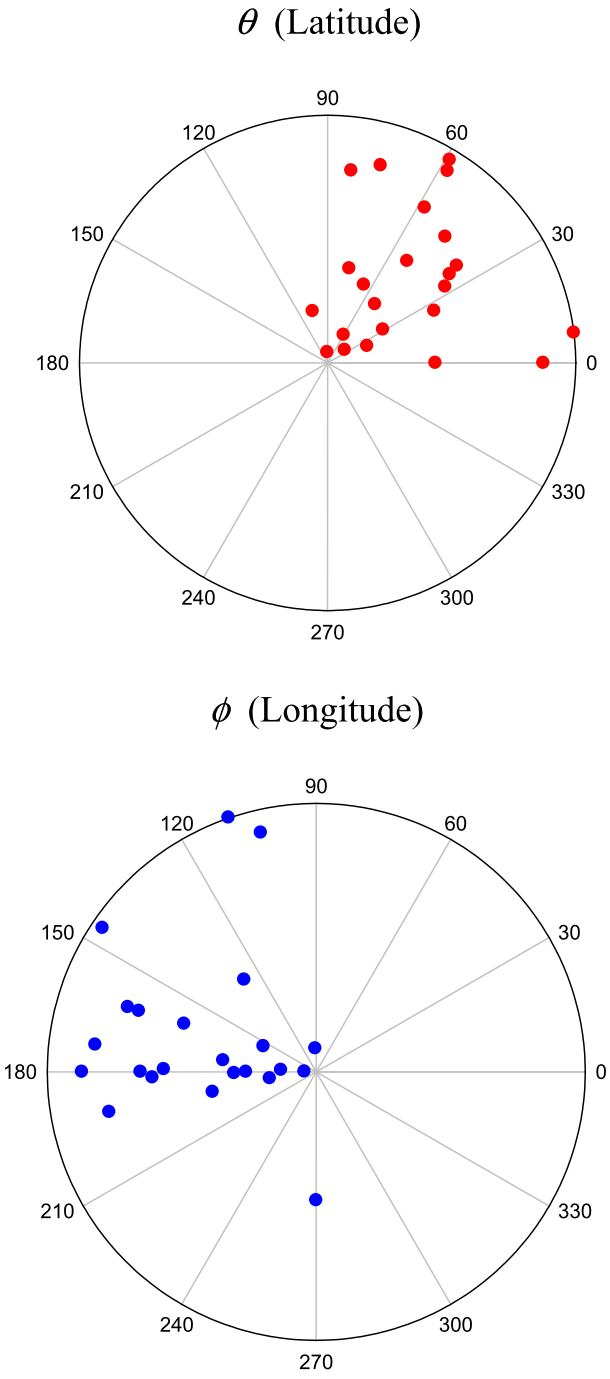

Figure 8 Results obtained for the attitude of all the flux-rope ejecta (FREJ) seen during the time period 1997 – 2006. The values for the latitude (θ) and longitude (ϕ) obtained from the fitting of the model have been represented in polar plots. The possible angle intervals for the axes of the FREJ are $(0, 180)$ for latitude and $(0, 360)$ for longitude.

Eventually, for the sake of completeness of the present study on EJ, after classifying them as above, a question remains open: what is the real nature and structure of the complex ejecta?

Acknowledgements The authors wish to acknowledge data and information obtained from the ISTP program, OMNIWeb. This work has been supported by the Comisión Interministerial de Ciencia y Tecnología (CICYT) of Spain. Project Reference: AYA2011-29727-C02-01.

References

Burlaga, L.F., Sittler, E., Mariani, F., Schwenn, R.: 1981, *J. Geophys. Res.* **86**, 6673.
Burlaga, L.F.: 1988, *J. Geophys. Res.* **93**, 7217.
Burlaga, L.F., Skoug, R.M., Smith, C.W., Webb, D.F., Zurbuchen, T.H., Reinard, A.: 2001, *J. Geophys. Res.* **106**, 20957.
Démoulin, P., Dasso, S.: 2009, *Astron. Astrophys.* **498**, 551.
Farrugia, C.J., Burlaga, L.F., Osherovich, V.A., Lepping, R.P.: 1992, In: Marsch, E., Schwenn, R. (eds.) *Solar Wind Seven*, Pergamon Press, Elmsford, 611.
Farrugia, C.J., Burlaga, L.F., Osherovich, V.A., Richardson, I.G., Freeman, M.P., Lepping, R.P., Lazarus, A.: 1993, *J. Geophys. Res.* **98**, 7621.
Farrugia, C.J., Burlaga, L.F., Osherovich, V.A., Lepping, R.P.: 1995, *J. Geophys. Res.* **100**, 12293.
Gulisano, A.M., Démoulin, P.M., Dasso, S., Ruiz, M.E., Marsch, E.: 2010, *Astron. Astrophys.* **509**, A39.
Gulisano, A.M., Démoulin, P.M., Dasso, S., Rodriguez, L.: 2012, *Astron. Astrophys.* **543**, A107.
Hidalgo, M.A.: 2003, *J. Geophys. Res.* **108**, 1320. doi:10.1029/2002JA009818.
Hidalgo, M.A.: 2005, *J. Geophys. Res.* **110**, 3207.
Hidalgo, M.A.: 2011, *J. Geophys. Res.* **116**, A02101.
Hidalgo, M.A., Nieves-Chinchilla, T.: 2012, *Astrophys. J.* **748**, 109.
Hidalgo, M.A., Nieves-Chinchilla, T., Cid, C.: 2002, *Geophys. Res. Lett.* **29**, 1637. doi:10.1029/2001GL013875.
Hidalgo, M.A., Cid, C., Viñas, A.-F., Sequeiros, J.: 2002, *J. Geophys. Res.* **107**, 1002. doi:10.1029/2001JA900100.
Hu, Q., Sonnerup, U.Ö.: 2002, *J. Geophys. Res.* **107**, 1142. doi:10.1029/2001JA000293.
Jian, L., Russell, C.T., Luhmann, J.G., Skoug, R.M.: 2006, *Solar Phys.* **239**, 393.
Lepping, R.P., Jones, J.A., Burlaga, L.F.: 1990, *J. Geophys. Res.* **95**, 11957.
Linton, M.G., Moldwin, M.B.: 2009, *J. Geophys. Res.* **114**, A00B09.
Marubashi, K.: 1986, *Adv. Space Res.* **6**, 335.
Marubashi, K.: 1997, In: *AGU Geophys. Monogr.* **99**, AGU, Washington, 147.
Mulligan, T., Russell, C.T.: 2001, *J. Geophys. Res.* **106**, 10581.
Osherovich, V.A., Farrugia, C.J., Burlaga, L.F.: 1993, *Adv. Space Res.* **13**, 57.
Osherovich, V.A., Farrugia, C.J., Burlaga, L.F.: 1995, *J. Geophys. Res.* **100**, 12,307.
Riley, P., Crooker, N.U.: 2004, *Astrophys. J.* **600**, 1035.
Riley, P., Linker, J.A., Mikic, Z., Odstrcil, D., Zurbuchen, T.H., Lario, D., Lepping, R.P.: 2003, *J. Geophys. Res.* **108**, 1272.
Romashets, E.P., Vandas, M.: 2001, *J. Geophys. Res.* **106**, 10615.
Romashets, E.M., Vandas, M., Poedts, S.: 2010, *Solar Phys.* **261**, 271.
Taubenschuss, U., Erkaev, N.V., Biernat, H.K., Farrugia, C.J., Mostl, C., Amerstorfer, U.V.: 2010, *Ann. Geophys.* **28**, 1075.
Wu, C.-C., Lepping, R.P.: 2002, *J. Geophys. Res.* **107**, 1314. doi:10.1029/2001JA000161.

Solar Phys (2013) 284:245–259
DOI 10.1007/s11207-012-0176-5

On Fields and Mass Constraints for the Uniform Propagation of Magnetic-Flux Ropes Undergoing Isotropic Expansion

Daniel Benjamín Berdichevsky

Received: 31 March 2012 / Accepted: 14 October 2012 / Published online: 21 November 2012

Abstract An analytical 3-D magnetohydrodynamic (MHD) solution of a magnetic-flux rope (FR) is presented. This FR solution may explain the uniform propagation, beyond ~ 0.05 AU, of coronal mass ejections (CMEs) commonly observed by today's missions like *The Solar Mass Ejection Imager* (SMEI), *Solar and Heliospheric Observatory* (SOHO) and *Solar Terrestrial Relations Observatory* (STEREO), tracked to tens of times the radius of the Sun, and in some cases up to 1 AU, and/or beyond. Once a CME occurs, we present arguments regarding its evolution based on its mass and linear momentum conservation. Here, we require that the gravitational and magnetic forces balance each other in the framework of the MHD theory for a simple model of the evolution of a CME, assuming it interacts weakly with the steady solar wind. When satisfying these ansätze we identify a relation between the transported mechanical mass of the interplanetary CME with its geometrical parameters and the intensity of the magnetic field carried by the structure. In this way we are able to estimate the mass of the interplanetary CME (ICME) for a list of cases, from the *Wind* mission records of ICME encountered near Earth, at 1 AU. We obtain a range for masses of $\sim 10^9$ to 10^{13} kg, or assuming a uniform distribution, of ~ 0.5 to 500 cm^{-3} for the hadron density of these structures, a result that appears to be consistent with observations.

Keywords CME/ICME mass · Time dependent MHD flux-rope model · Magnetohydrodynamics · Transient flows in inner heliosphere

1. Introduction

The displacement of the magnetic field and plasma suddenly ejected from the Sun, *i.e.*, solar ejecta, also known as interplanetary coronal mass ejection (ICME), is of high interest, not only scientifically but also socio-economically, because when directed toward Earth, they

Flux-Rope Structure of Coronal Mass Ejections
Guest Editors: N. Gopalswamy, T. Nieves-Chinchilla, M. Hidalgo, J. Zhang, and P. Riley

D.B. Berdichevsky (✉)
College Park, MD 20740-4111, USA
e-mail: dbberdi@gmail.com

may effect a large range of human resources that among others include communications, pipe-lines, and power grids (*e.g.*, Garrett, 1981; Lanzerotti *et al.*, 1998; Pirjola and Lehtinen, 1985; Czech *et al.*, 1992; Albertson *et al.*, 1973).

The interest on the subject of ICME/CME started well before the advent of the space era. As reviews of the literature on the subject of the solar wind (SW) show, matter escaping the Sun and making an impact on Earth's magnetic field has been the subject of conjecture and study because of the influence on its secular changes. One may find these perturbations to the Earth's magnetic field reported since the 19th century (at http://www.ngdc.noaa.gov/stp/geomag/aastar.html), and the continuous changes in geomagnetic indices (at http://www.wdc.bgs.ac.uk/catalog/master.html); see also Bartels (1962). As such it was possible to identify particular occasions when a temporal relationship was apparent between the Earth's magnetic storm and the earlier observation, within a day or a few days, of a bright, at times optically visible, flare on the surface of the Sun, see, *e.g.*, Carrington (1859).

Today we know that these flows result from the sudden expulsion from a region, often low in the corona, *i.e.*, ~ 1.03 to 1.3 times the solar radius ($R_{\rm Sun}$), of matter and magnetic field that has cumulated there over a period of time of days or even months. From the observations of the solar corona during total eclipses of the Sun such findings became an accepted possibility, which was later confirmed in continuous observations with mainly Hα solar telescopes; see *e.g.* Zirin (1966).

The presence of a permanent fine plasma gas emerging from the Sun was another subject of great interest in the astrophysical community before the advent of the space era. Among the models advanced in the middle of the 20th century were those by Chapman (1957), Parker (1958), Chamberlain (1960, 1961), with the observations giving *overall validity* to the prediction of the SW by Parker.

The focus of this work is to address the conjecture that ICME(s) frequently *neither* slow down *nor* speed up within 1 AU from the Sun as we illustrate in Figure 1 for several Sun-Earth connections during the rising phase of the solar cycle 23. This happens despite the expected presence of other interactions, such as (a) the gravitational pull of the Sun, or (b) the drag caused by the presence of *other* SW streams. Regarding the data in Figure 1, this plot uses *ejecta* mid-point: i) travel-times, and ii) velocities, for a subset of the cases listed in Table 4 in Berdichevsky *et al.* (2002).

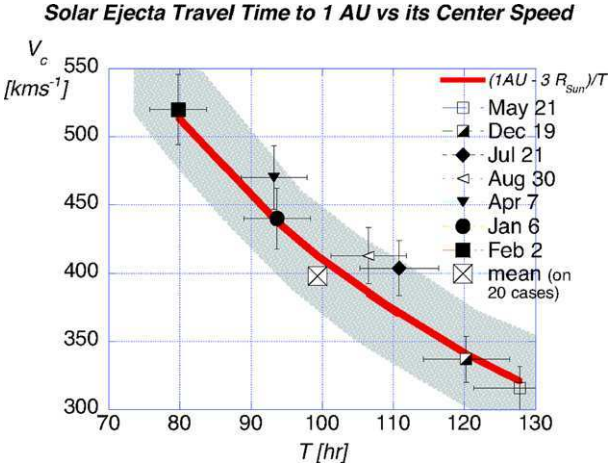

Figure 1 Red: curve with shading shows *in-situ* central speed $V_c \pm \sqrt{2}\sigma$ (standard deviation) as a function of time for a constant uniform displacement of the center of a solar eject, from three solar radii to Earth. Symbols identify the corresponding *in situ* values for a selected set of Sun-Earth connections, identified by date of launch (all in year 1997, but December event in 1996). Plotted data are from the list of cases in Table 4, in Berdichevsky *et al.* (2002).

In addition we ask ourselves if we can address the above conjecture while ignoring for a few hundreds of solar radii (up to ~ 1 AU) the drag caused by the presence of the aforementioned steady flow of plasma and magnetic field, *i.e.*, the SW. SW has been seen by the *Voyager* mission to be flowing away from the Sun at locations beyond the Sun's furthest planet (see *e.g.*, Richardson *et al.*, 2008).

Here we limit our scope to *addressing the conjecture(s)* within the frame of the ideal magneto-hydrodynamics (MHD) theory for a magnetic-flux rope (FR) with a uniform translation – and isotropic expansion of such a mass-carrying transient – in the presence of a central gravitational field.

Section 2 presents the derivation of the model, which extends the solution of a propagating, free expanding magnetic structure of a FR kind in a force-free environment, developed from first principles in Berdichevsky, Lepping, and Farrugia (2003). This we will refer to next as BLF (see also Shimazu and Vandas, 2002). Section 3 discusses the implications of *this* extended model on the carried mass by the FR structure, including a discussion of the mass ranges carried by a CME moving at constant speed. Conclusions are drawn in Section 4.

2. The Propulsion of a Transient of the Flux Rope Type

For the propulsion of the ICME we start with Newton's well known *second law of mechanics*,

$$\mathrm{d}/\mathrm{d}t\mathbf{P} = \mathbf{F}, \tag{1}$$

relating the linear momentum of a point-like mass with the resultant of the forces applied to it, see *e.g.*, Equation (1) in Chapter 1 of the fourth edition of the treaty on *Classical Mechanics*, by Goldstein (1956), where we assume that for a flux rope the momentum $\mathbf{P}$ has a mechanical and an electromagnetic part. Here, the mechanical part

$$\mathbf{P}_{\mathrm{mec}} = M_{\mathrm{mec}}\mathbf{V}_{\mathrm{CM}} \tag{2a}$$

contains essentially the particles momentum of a dilute ionized gas of mass M_{mec}. For the electromagnetic part, see, *e.g.*, Jackson (1966), and in the case that the expansion speed is much less than the translational speed $|\mathbf{V}_{\mathrm{CM}}|$

$$\mathbf{P}_{\mathrm{EM}} = \mathbf{V}_{\mathrm{CM}}/\big(c^2\mu_0\big)\int_{Vol}\mathbf{B}^2\,\mathrm{d}Vol, \tag{2b}$$

from Berdichevsky, Stenborg, and Vourlidas (2011), with

$$\mathbf{B} = B_0(t_0/t)^2\big[\mathscr{J}_0\big(a(t,\rho)\big)\mathbf{e}_x + H\,\mathscr{J}_1\big(a(t,\rho)\big)\mathbf{e}_\varphi\big], \tag{3a}$$

where $a(t,\rho) = A(t)\rho$ and $A(t) = j_0/R_{\mathrm{FRcore}}$. $\mathscr{J}_{0,1}$ are the well known orthogonal, grade 0 and 1, cylindrical Bessel functions of the first kind, see *e.g.*, Abramowitz and Stegun (1972). The value of $\rho = R_{\mathrm{FRcore}}$ defines the radius of *'the circular cross section'* of a cylinder, at the location where the axial magnetic field is identically zero, *i.e.*, $\mathscr{J}_0(j_0) = 0$. In this evolution the volume (*Vol*) of the FR changes with time as

$$Vol(t) = (t/t_0)^3 Vol(t_0) \tag{3b}$$

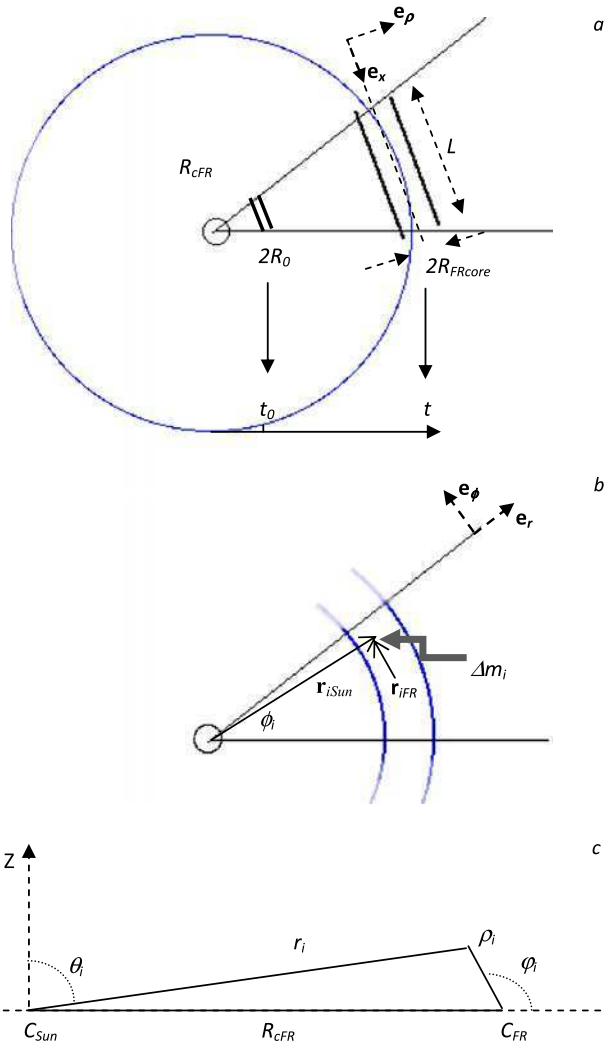

Figure 2 (a) Top. Evolution of a circular cross-section cylinder-shaped FR, derived in BLF, projected in the plane defined by the spherical coordinate $\theta = \pi/2$, illustrated at time t_0 and t ($t_0 < t$), where radius and length are R_0, L_0 and R_{FRcore}, L at times t_0 and t respectively. Dashed line in cylinder drawn for time t indicates its axis at a distance R_{cFR} from center of the Sun. On top of the larger cylinder are also indicated the unit vectors $\mathbf{e}_\rho$ and $\mathbf{e}_x$ in FR coordinates. (b) Middle. The same as on top, but shown only at time t, for this model of a curved FR that has its magnetic stresses in equilibrium with a central gravitational force. The figure further illustrates the coordinates of the fraction of mass Δm_i of the FR when observed from the center of curvature ($\mathbf{r}_{i\mathrm{Sun}}$), and from the center of the FR ($\mathbf{r}_{i\mathrm{FR}}$). (c) Bottom. A view of the relationship between the spherical coordinates centered at the Sun and the cross section of the FR coordinates (polar) centered at the FR axis, as seen in a plane defined by the spherical coordinate $\phi_i =$ constant.

(see BLF). It corresponds to the analytical MHD evolution in time and space of any piece of plasma 'Δm_i' relative to the center of mass (CM), given by

$$\mathbf{r}_i(t) = t/t_0 \mathbf{r}_i(t_0), \tag{3c}$$

for $t > t_0$, within a tube of a magnetic-field flux and plasma, when the displacement of its CM describes a rectilinear uniform motion, in this case away from the Sun, given by

$$\mathbf{R}_{\mathrm{CM}}(t) = \mathbf{V}_{\mathrm{CM}}(t - t_0) + \mathbf{R}_{\mathrm{CM}}(t_0). \tag{3d}$$

This evolution is sketched in Figure 2a with a truncated cylinder at times t_0 and $t > t_0$ expanding while moving away from the center (Sun). This assumption appears justified by observation, as illustrated in Figure 1, and for single study cases, as in the weak event recently observed *in situ* by MESSENGER, and *Venus-Express*, from May 24 to 26, 2007, and

remotely with STEREO from May 20 to 22 (Rouillard *et al.*, 2009; Berdichevsky, Stenborg, and Vourlidas, 2011). Another supporting example is the well documented (Special Issue '*Bastille Day, Year 2000*,' in Solar Phys. **204**, 2001) *in situ* observed passage of the magnetic cloud (MC) corresponding to the large and fast moving CME released on Bastille's day, of the year 2000, which we can check from the discussion by Lepping *et al.* (2001a).

However, a closer look at the problem reveals that in the presence of an approximately spherical gravitational field like the one of the Sun,

$$\mathbf{F}_{\mathrm{G}} = -GM_{\mathrm{Sun}}M_{\mathrm{FR}}/|\mathbf{R}_{\mathrm{CM}}|^2\left[\mathbf{R}_{\mathrm{CM}}/|\mathbf{R}_{\mathrm{CM}}|\right] \tag{4}$$

the required condition

$$\sum_i \mathbf{F}_i = 0, \tag{5}$$

is not satisfied without the presence of another force. Here, we consider for the purpose of satisfying Equation (5)

$$\mathbf{F}_{\mathrm{EM}} = \int_{\mathrm{Vol}} \mathbf{J}_{\mathrm{c}} \times \mathbf{B}/\mu_0 \, \mathrm{d}Vol, \tag{6}$$

the force acting on the FR, resulting from the magnetic field of the FR, where the integration is over the FR volume, and $\mathbf{J}_{\mathrm{c}}$ is the convection current; see *e.g.*, Jackson (1966). In the case of an evolving FR with a cylinder with circular cross-section geometry, Equation (3a) gives the solution for $\mathbf{B}$. This is a solution describing a self-similar evolution of the magnetic field which possesses the property of being free of magnetic stresses on its plasma, *i.e.* it satisfies $\mathbf{J}_{\mathrm{c}} \times \mathbf{B} \equiv \mathbf{0}$.

Hence, the uniform, isotropic motion of any plasma element 'Δm_i' in the FR becomes inconsistent with the presence of the gravitational pull of the Sun. This due to Equations (3c) and (3d), for the topology of the magnetic fields in Equation (3a), valid for a cylinder, with circular cross-section geometry. This would cause a deceleration and an observable time delay in going from ~ 0.05 to near 1 AU for any ICME moving with a radial speed of less than $\sim 800\ \mathrm{km\,s^{-1}}$, as is shown in Figure 3. The solid line in the figure illustrates the error in the identification of the launching time if the passing speed of the center point of the ejecta (FR) were to be used. The dashed line gives the error in identifying the start time of the event at the Sun, when fully considering the pull of the Sun on the FR from the energy relationship for the gravitational central force of the Sun when using

$$t(1\ \mathrm{AU}) - t_0 = \int_{r_0}^{1\ \mathrm{AU}} \mathrm{d}r/\sqrt{\left[V_{\mathrm{c}}^2 - 2GM_{\mathrm{Sun}}/r_0 + 2GM_{\mathrm{Sun}}/r\right]}$$

– see, *e.g.*, Landau and Lifchitz (1966) – with $r_0 = 10R_{\mathrm{Sun}}$, and comparing it to the correct observational identification of the evolution while traveling at a constant velocity. Figure 3 shows that the mismatch when considering exactly the pull of the Sun would still be large for the range enclosed by the dashed rectangle on its upper left corner, which corresponds to the events in Figure 1. These are the events that served as the basis for the conjecture that the displacement of the FR is at constant speed between approximately ten solar radii and 1 AU. Detailed tracking (*e.g.*, Rouillard *et al.*, 2009; Wood and Howard, 2009; Wood *et al.*, 2011) confirms that frequently the conjecture of a constant speed for the propagation of elements of ICMEs appears to be quite good.

Here we address this problem of uniform propagation of the center of the structure by incorporating magnetic stresses to equilibrate the pull of the gravitational field, assuming

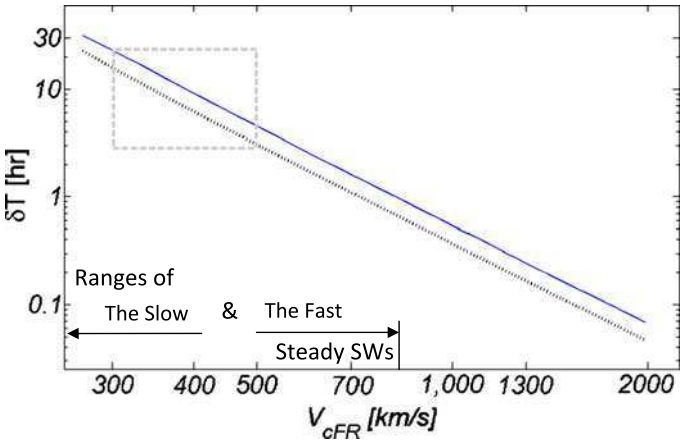

Figure 3 The top curve shows the delay δT in reaching 1 AU when covering a distance from $10R_S$ to 1 AU as a function of the measured speed of the FR at 1 AU ($215R_{\rm Sun}$) from the center of the Sun when the pull of gravitation is considered approximately, *i.e.*, the motion is assumed to be rounded to the observed speed of the FR at 1 AU. The dotted line is the delay when integrating the time exactly. The rectangular dashed gray box shows the range of speeds observed for the CMEs in Figure 1. On the bottom left side of the figure are further shown the slow and fast SW speed ranges commonly observed.

that the ejected FR possesses the curvature in the sketch of Figure 2b. As will be shown later, we need to consider only the mechanical linear momentum, $\mathbf{P}_{\rm mec}$ (Equation (2a)), when considering equilibrium in Equation (1). Other authors, *e.g.*, Holzer (1979), have considered the possibility (or the need) of the existence of such force(s) counteracting the pull of the Sun, enabling plasma and field to be displaced upward.

Figure 2b shows the axial symmetric FR magnetic field curved along a circular arc, with its *major* radius of curvature $R_{\rm cFR}$ with origin at the CM of the Sun. Further, Figure 2b shows the radius vector, $\mathbf{r}_{i\rm Sun} = r_i\mathbf{e}_r$, connecting the element of mass 'Δm_i' of FR-plasma to the center of the Sun ($C_{\rm Sun}$), in the (horizontal) plane defined by the spherical coordinate $\theta_0 = \pi/2$. Also in Figure 2b it is shown how the same element of mass is connected to the center of the FR, $C_{\rm FR}$, with

$$\mathbf{r}_{i\rm FR} = \rho_i\mathbf{e}_\rho + x_i\mathbf{e}_x,$$

where ρ_i is defined with respect to the axis of symmetry of the FR, and x_i to $C_{\rm FR}$ along its axis.

With the help of the relationship illustrated in Figure 2c between the spherical coordinates r_i, and θ_i, centered at the Sun, and the cylindrical-FR coordinates ρ_i, and φ_i, under the constraint $\nabla\cdot\mathbf{B} = 0$, it is determined that a torus shape, *i.e.*, the curvature of the FR geometry *imposes* a distortion to the geometry of its cross section that can be expressed through a modified magnetic field argument,

$$A(t,\rho,\varphi) = a(t,\rho)\big[1 + \rho/R_{\rm cFR}\big(\cos(\varphi) - \big|\sin(\varphi)\big|\big)\big], \tag{7}$$

instead of the argument '$a(t,\rho)$' of the cylindrical Bessel functions of the first kind in the magnetic field expression of the model, as shown in Equation (3a). The sketch of Figure 4 illustrates with the thick dotted line the deviation of the contour from the unperturbed case, the circular solid line (*i.e.*, deviation from the case when $R_{\rm cFR}\to\infty$). These are the loci of the points where the axial component of the field is identically zero, *i.e.*, when $A(t,\rho,\varphi) =$

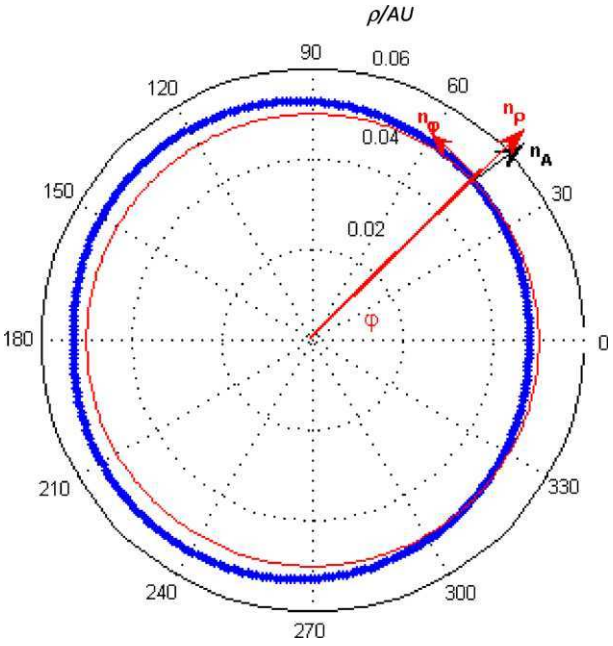

Figure 4 The thin, red, circular curve represents the location where the magnetic field is fully poloidal for the circular cross-section cylinder-shaped FR, when we have evolution in the absence of external forces, see, *e.g.*, BLF. The thick, blue, curve with its broken circular symmetry in a mirror symmetric cross section represents the new model shape for the region where the magnetic field is fully poloidal for the bended, truncated-torus FR shape with major axis of curvature $R_{\rm cFR}$. It corresponds to the case in which there is a gravitational field centered at distance $R_{\rm cFR}$ from the FR-axis in equilibrium with the magnetic stresses of the structure modeled in this work. $\mathbf{n}_A$ is the normal unit vector to the thick curve, and $\mathbf{n}_\rho$ and $\mathbf{n}_\varphi$ are polar unit vectors for the coordinate system corresponding to the center of the circular curve. The scale corresponds to *in-situ* FR observations for the event discussed in Berdichevsky, Stenborg, and Vourlidas (2011).

j_0, for $R_{\rm FRcore}/R_{\rm cFR} = 0.1$. This is exact to order $n = 1$ on a $(R_{\rm FRcore}/R_{\rm cFR})^n$ perturbation expansion, derived for this model *with* curvature by modifying perturbatively the force-free evolution of the magnetic field of BLF.

The argument $A(t, \rho, \varphi)$ modifies the convection current '$\mathbf{J}_{\rm c} = \nabla \times \mathbf{B}/\mu_0$' into

$$
\begin{aligned}
J_{{\rm c}\rho} &= -A(t)/\mu_0 B_\varphi \rho / R_{\rm cFR}\big(\sin(\varphi) + \partial_\varphi \big|\sin(\varphi)\big|\big),\\
J_{{\rm c}\varphi} &= A(t)/\mu_0 B_\varphi \big[1 - 2\rho/R_{\rm cFR}\big(\cos(\varphi) - \big|\sin(\varphi)\big|\big)\big],\\
J_{{\rm c}x} &= A(t)/\mu_0 B_x \big[1 - 2\rho/R_{\rm cFR}\big(\cos(\varphi) - \big|\sin(\varphi)\big|\big)\big]
\end{aligned}
$$

along the $\mathbf{e}_\rho$, $\mathbf{e}_\varphi$, and $\mathbf{e}_x$ directions, respectively, in the FR-intrinsic system of '*cylindrical*' coordinates. Without loss of generality, we can consider the truncated-torus structure composed as a succession of n contiguous, narrow cylinder rings for each of which there is defined the set of ρ_n, φ_n, x_n, FR coordinates introduced earlier; see the sketch in Figure 2b. In this approximation the explicit expressions for the current $\mathbf{J}_{\rm c}$ and magnetic field $\mathbf{B}$ allow a straightforward evaluation to be made of the force $\mathbf{F}_{\rm EM}$; see Equation (6).

The result gives the component of $\mathbf{F}_{\rm EM}$ along the radial direction from the center of the Sun, equal to

$$
(\mathbf{F}_{\rm EM})_r = \pi/(4\mu_0)(0.5201/0.4158)^2\big[\Phi_\varphi^2 (R_{\rm FRcore}/L_{1/2})(V_{\rm cFR}/v_{\rm Rcore})\big]/|\mathbf{R}_{\rm cFR}|^2. \qquad (8)
$$

This is a force of the magnetic field pointing outward from the Sun, where: i) Φ_φ is the poloidal flux of the magnetic FR, in the case that the main axis of the truncated-torus structure is orthogonal to $\mathbf{e}_r$ ($= \mathbf{R}_{\rm cFR}/|\mathbf{R}_{\rm cFR}|$; see Figure 2b), the radial direction from the Sun; ii) $V_{\rm cFR}$ is the speed away from the Sun at the center of the FR; with iii) $\mathbf{v}_{\rm Rcore}$ the velocity expansions of the FR surfaces at its minor radius of curvature, the surface-boundaries are at $R_{\rm FRcore}$, and $L_{1/2}$ (half the arc-length extension of the FR along its major radius of curvature $R_{\rm cFR}$). Notice that we neglected terms order c^{-2}, and $(R_{\rm FRcore}/R_{\rm cFR})^2$.

Then, if other forces are not included (*e.g.*, drag caused by a solar wind stream in which the FR evolves) the uniform evolution of each mass element in the FR, given by the ansatz in Equations (3c) and (3d), is *on average* enabled, without perturbations, in the radial direction away from the Sun when

$$\text{(a)} \qquad \mathbf{R}_{\rm cFR} = \mathbf{R}_{\rm CM}$$

i.e., the centers of the electromagnetic fields and masses of the structure coincide, and on average Equation (5) is satisfied when the FR physical mechanical and electromagnetic properties satisfy

$$\text{(b)} \qquad -GM_{\rm Sun}M_{\rm mec} + \pi/(4\mu_0)(0.5201/0.4158)^2\big[\Phi_\varphi^2(R_{\rm FRcore}/L_{1/2})(V_{\rm cFR}/v_{\rm FRcore})\big] = 0.$$

Then, without loss of generality, it is possible to state that the value of

$$M_{\rm mec} = (0.5201/0.4158)^2\pi/(4\mu_0)/[GM_{\rm Sun}]\big[\Phi_\varphi^2(R_{\rm FRcore}/L_{1/2})(V_{\rm cFR}/v_{\rm FRcore})\big] \qquad (9)$$

is required for the above described simple evolution of the FR, which is propagating as a whole at constant speed $V_{\rm cFR}$ away from the Sun.

When interpreting in our ideal MHD model the above developed connection between $M_{\rm mec}$ and the structure's poloidal magnetic flux Φ_φ, it is necessary to check the intrinsic consistency of the above derived relationship, given that, as we know, the electromagnetic field of the expelled magnetic structure has a weight, which due to the explicit dependence of the fields on the inverse square power of the time, changes with time as t^{-1} (see Section 4.4 in Berdichevsky, Stenborg, and Vourlidas, 2011). There,

$$\mathbf{P}_{\rm EM} = \mathbf{V}_{\rm CM}5.547\pi\, B_0^2/\mu_0\big[\big(R_{\rm FRcore}^2 L_0\big)/c^2\big]t_0/t \qquad (10)$$

is the electromagnetic lineal momentum. It presents this t^{-1} dependence, in its simplified case, corresponding to the cylindrical symmetry of the FR electrodynamics.

In this case, for $t > t_0$ and the $R_{\rm CM}(t) > 10R_{\rm Sun}$, *i.e.*, already in a collision-less region, and for constant $V_{\rm CM}$, we can write

$$\mathbf{P}_{\rm EM} = \mathbf{V}_{\rm CM}5.547\pi\, B_0^2/\mu_0\big[\big(R_{\rm FRcore}^2 L_0\big)/c^2\big]\big[R_{\rm CM}(t_0)/R_{\rm CM}\big].$$

In this way we identify the electromagnetic mass

$$m_{\rm EM}(R_{\rm CM}) = 5.547\pi\, B_0^2/\mu_0\big[\big(R_{\rm FRcore}^2 L_0\big)/c^2\big]\big[R_{\rm CM}(t_0)/R_{\rm CM}\big]$$

contributing to the mass of the FR ($M_{\rm FR}$), which we then rearrange in terms of the poloidal magnetic flux Φ_φ, thereby obtaining

$$m_{\rm EM}(R_{\rm CM}) = 32.08\pi/\big(\mu_0 c^2\big)\big[\Phi_\varphi^2/R_{\rm CM}\big]$$

Table 1 Top: *quantities used to calculate* $M_{\rm FR}$, bottom: *approximations made deriving the FR model*.

Quantity	Mean	Sigma	Units[a]
$B_0(1\ \text{AU})$ – magnetic field strength	18.8	9.1	nT (10^{-9} Tesla)
$R_{\rm FRcore}(1\ \text{AU})$ – FR minor radius	0.123	0.6	AU (150×10^9 m)
$\phi_{\rm FR}$ – CME/FR angular extent	57.30°	30°	
$V_{\rm FR}$ – average FR velocity	500	130	$\text{km}\,\text{s}^{-1}$
μ_0 – vacuum magnetic permeability	$4\pi \times 10^{-7}$		$\text{kg}\,\text{m}\,\text{C}^{-2}$ (Coulomb^2)
$M_{\rm Sun}$ – mass of the Sun	2×10^{30}		kg (Kilogram)
G – gravitation constant	6.7×10^{-11}		m^3 ($\text{s}^{-2}\,\text{kg}^{-1}$)
$(R_{\rm FRcore}/R_{\rm cFR})^2$, $V_{\rm cFR}/c$ – neglected terms	$O \times 10^{-2}$, 10^{-3}		

The ratios in the table show the ranges in the derivation of the relations used. The approximations considered are appropriate when $V_{\rm cFR}/c$ and $(R_{\rm FRcore}/R_{\rm cFR})^2 \ll 1$.

[a]Values are listed in the rationalized MKS system of units.

by assuming the same angular extension as before: $\alpha = 57.30°$. In this way we readily find that the ratio is

$$M_{\rm mec}/m_{\rm EM}(\mathbf{R}_{\rm CM}) \propto (c/v_{\rm FRcore})^2.$$

A closer evaluation of this ratio (for $v_{\rm FRcore} \leq 10^2\ \text{km}\,\text{s}^{-1}$) gives $m_{\rm EM}(10R_{\rm Sun})/M_{\rm mec} \sim \text{O} \times 10^{-6}$ (here 'O' stands for 'order'). Therefore, in our velocity range it is possible to consider the FR mass $M_{\rm FR}$ as constant, and to consider as valid its interpretation as the mechanical mass, $M_{\rm mec}$, of the FR at distances $R_{\rm cFR} \geq 10R_{\rm Sun}$ from the Sun, as was evaluated in Equation (9). This allows us to proceed to the evaluation of the mass transported (or propelled) by this MHD FR model with the help of limited information on the structure, as listed in Table 1.

3. Model Prediction on FR-Masses (-Particle Densities)

Compilations on CME extensions and speeds suggest that the length ratio and velocity ratio in Equation (9) is likely confined to a narrow range, while to some extent they are independent between themselves. *In-situ* observations also suggest ejecta amenable to the Lundquist magnetostatic model fitted to the data assumed to be associated with a FR (commonly named magnetic cloud, *i.e.*, MC). Here, we emphasize once more that the plasma structure with a magnetic field of the FR type that concerns us in this work is extensively discussed empirically in the literature under the common name of a MC; see, *e.g.*, Burlaga (1988). There, a rich number of plasma properties have been identified with the help of the magnetostatic model (Lundquist (1951); see also, *e.g.*, Lepping, Jones, and Burlaga, 1990). These MCs are interpreted to be our FRs frozen in time. This allows us to use the average MC magnetic field, dimension, and mean propagation velocity parameters, in Table 1, from a set of more than 100 cases listed on the extension and magnetic characteristics, in Lepping *et al.* (2006).

Hence, we assume in Equation (9) that

$$x = L_{1/2}/R_{\rm FRcore}, \quad \text{and} \tag{11a}$$

$$y = V_{\rm cFR}/v_{\rm FRcore} \tag{11b}$$

constitute independent parameters. They are both dimensionless ratios, while the third independent parameter,

$$z = \Phi_{\varphi}^2, \tag{11c}$$

is the magnetic poloidal flux square, Φ_{φ}^2, of the structure in units of zetta-Wb^2 ($\equiv 10^{21}$ Wb^2).

Armed with the center FR speed, $V_{\rm cFR} \sim \langle |V_{\rm MC}| \rangle$, the FR (or MC) mean velocity, its orientation, magnetic field strength, B_0, and time duration T of its passage at 1 AU, the variable 'y' is determined, and we are left with two undetermined ranges in two variables 'x, and z, when lacking information on $L_{1/2}$.' However, solar observations can be used to constrain the indetermination of the value of this MHD evolution model to a much narrower range for the mass. In the particular case of the tracked May 20, 2007, CME directed toward Venus, we observationally identify $x \cong 6$, to less than 1 % of uncertainty, assuming isotropic propagation, further validated by observations of the time passage and remote monitoring of the evolution of the structure. In this case the model mass formula results in $M_{\rm mec}({\rm FR}) = 4.4 \times 10^{11}$ kg, *which is within less than two standard deviations of the estimate of* $2.0 \pm 1.2 \times 10^{11}$ kg, *reached*, *through extrapolation, for the FR-part of the identified ICME tracked from May 20 to 26*, in Berdichevsky, Stenborg, and Vourlidas (2011).

Next we consider the evaluation of a 'generic' mass transported (or propelled) by this MHD FR model with the help of a few constants, and assumptions made, listed in Table 1. Henceforth, we extract from Equation (9), with the help of relations in Equations (11a)–(11c), a $M_{\rm mec}$ for *a generic* CME whose parameters are obtained from the mean values over several years of observations (see, *e.g.*, Bothmer and Schwenn, 1998; Huttunen *et al.*, 2005; Lepping *et al.*, 2006).

From Table 1 we define the generic FR as having the average properties observed near Earth listed in Lepping *et al.* (2006): i) a magnetic field strength, $\langle B_0 \rangle = 18$ nT, ii) $R_{\rm cFR} = 1$ AU (*i.e.*, Earth-Sun distance), iii) a cross section with a radius value $\langle R_{\rm coreFR} \rangle = 0.123$ AU; and iv) a mean velocity $\langle V_{\rm MC} \rangle$ of approximately 500 km s^{-1}. To that we add the assumption that it has an angular extension of 1 radian, *i.e.*, $L = 1$ AU; then $L_{1/2} = 0.5$ AU, with

$$\left\langle |\Phi_{\varphi}| \right\rangle = 0.4158 \left(\langle B_0 \rangle \langle R_{\rm FRcore} \rangle L \right) \tag{12a}$$

having a value 2.15×10^{13} Wb. Then, with the uniform propagation and expansion from 0.05 AU to Earth's location, the ratio

$$V_{\rm cFR}/1 \text{ AU} = v_{\rm FRcore}/\langle R_{\rm FRcore} \rangle \tag{12b}$$

holds approximately, implying $v_{\rm FRcore} \cong 40$ km s^{-1}, when we incorporate width, and extension of the FR at its launch in the low corona near $R_{\rm Sun}$. This gives at 1 AU a FR with mean dimensions that will support the uniform rectilinear propagation away from the Sun with a mass $M_{\rm FR} \cong 1.0 \times 10^{13}$ kg.

At Earth's distance, a mean density $N(1 \text{ AU}) = 38$ hadrons cm^{-3} for the generic FR is obtained by dividing $M_{\rm FR}$ by the volume ($\cong \pi \langle R_{\rm FRcore} \rangle^2 L$) of the truncated-torus shaped magnetic structure. Here we consider a mass of hadron of 1.67×10^{-27} kg ($= m_p$). When comparing with the density of the protons observed we take into consideration the empirically determined composition of an eject, where fully ionized He^{++} (αs) are about 10 % of the density and also there is often enhancement of heavy ions (see *e.g.*, Hirshberg, Bame, and Robbins, 1972; Richardson and Cane, 2004) reducing the number of protons in the FR to about 2/5 to 1/2 of the total hadrons carried by the FR. This means we have a proton-density estimate of $\langle N_p \rangle \sim 17$ p cm^{-3} for the generic FR.

When we restrict ourselves to the rising phase of Solar Cycle 23, analyzed in detail in Lepping *et al.* (2003), $\langle B_0 \rangle$ becomes 72 % of the value listed in Table 1, and consequently the predicted model poloidal flux Φ_φ is reduced by a factor of 0.75^2, considering that the mean radius is $\langle R_{\rm FRcore} \rangle = 0.14$ AU, and assuming the same $L_{1/2}$. For this set the mean MC speed is $\langle V \rangle = 400\ {\rm km\,s^{-1}}$, interpreted as before to be $V_{\rm cFR}$. The measured mean expansion speed of the core boundary for the set is $\langle v_{\rm FRcore} \rangle = 27\ {\rm km\,s^{-1}}$. Then, assuming the same hadronic partition of the plasma as in the case of the '*generic*' FR gives a model with $N_p = 13\ {\rm p\,cm^{-3}}$. For this particular set a mean value of $\langle N_p \rangle = 11.5 \pm 3.0\ {\rm p\,cm^{-3}}$ is the result of observations carried out with the SWE instrument in the *Wind* mission, which is in excellent agreement with the model.

The relatively large standard deviation in any compilation of MCs, *e.g.* for the standard deviations presented in Table 1, suggest the exploration here of their ranges in mass given by the relationship

$$M_{\rm mec} = 7.3 \times 10^{-15} x y z\ {\rm kg\,Wb^{-2}} \tag{13}$$

with $x = R_{\rm FRcore}/L_{1/2}$, $y = V_{\rm CM}/v_{\rm FRcore}$, $z = \Phi_\varphi^2$, with the mass $M_{\rm mec}$ of the FR in kg (rationalized MKS system of physical units). Hence, in the corona of the environment of the Sun and its ensuing 'steady' SW presence there is a set of possible CME/ICMEs with the FR properties empirically described above, where Table 1 shows us a set of ranges for our parameters.

However, we choose to select a range for the FR parameters directly from the observational record of MCs, *i.e.*, FR-like structures tabulated by different authors on the field (*e.g.*, Huttunen *et al.*, 2005; Lepping *et al.*, 2006). Here again we use Lepping *et al.* (2006), to choose the ranges of properties of the MC: i) $\langle |V_{\rm MC}| \rangle$, the FR (or MC) mean velocity; ii) magnetic field strength, B_0; and iii) minor radius of the truncated torus $R_{\rm MC}$. All estimated quantities of their MCs are kept by the magnetic field experiment in the table-page of the WIND MFI Science Team (1995), running until present. Therein is a list of over 130 events compiled so far, starting with observations after its launch in November 1994, and still being compiled. Table 2 presents the range we extract for them. To these parameters we add the needed arc-length extension of the CME, $L_{\rm CME}$, from Yashiro *et al.* (2004) (see also Thernisien, Vourlidas, and Howard, 2009), and which we assume to be the same for the ICME. In this analysis of mass ranges for the FR structure possibly to be observed we use the simple evolution described above. The range then obtained for the ejected mass, carried in the isotropic evolution of the FR, is

$$1.0 \times 10^9 < M_{\rm mec}/{\rm kg} < 1.6 \times 10^{13}. \tag{14a}$$

We see that it covers a range of four orders of magnitude, and while obviously the FRs with the strongest magnetic field strength will have no problem plowing their way through any steady SW condition ahead of them, such a propagation will become problematic for a MC with the weakest magnetic field strength even in the presence of average SW conditions. In such a case, dragging effects on the evolution of the structure with respect to time would likely be substantial.

The ranges of masses and volumes estimated for the FR correspond to a density range per hadron of

$$\sim 0.40\ {\rm cm^{-3}}\ \text{to} \sim 400\ {\rm cm^{-3}} \tag{14b}$$

when considering the second and third column values from Table 2.

Interestingly, during the time interval extending from the beginning of 1995 to the present, the MCs with the weakest observed strength have occurred recently, beginning

Table 2 Relevant parameters for finding the $M_{\rm mec}$ carried by this FR model of an ICME.

Input	Low value	High value	Units
$B_{0\rm MC}$	6	70	nT
$\langle \lvert V_{\rm MC} \rvert \rangle$	300	1000	km s^{-1}
$R_{\rm MC}$	0.03	0.21	AU
$\phi_{\rm CME}$	10°	120°	
Mass dependence			
$x\ (= L_{1/2}/R_{\rm FRcore})$	5.8	10	
$y\ (= [V_{\rm cFR}/v_{\rm FRcore}]^2)$	10	30	
$z\ (= \Phi_\varphi^2)$	8.0×10^{22}	1.0×10^{28}	Wb^2

around the year 2008, when several cases with a strength $B_0 < 10$ nT were observed. It is during this time interval that the interplanetary magnetic field was extremely weak, with an average value well below 5 nT (see, *e.g.*, Lepping *et al.*, 2011).

4. Discussion, and Concluding Remarks

Starting perturbatively from a force-free MHD evolution of a flux rope, and introducing a curvature to the geometry of the structure such that the minor-to-major axes ratio satisfies $(R_{\rm coreFR}/R_{\rm cFR})^2 \ll 1$, we find:

i) Magnetic stresses in the FR can be accommodated to compensate for the pull of the gravitational force allowing the structure to evolve undergoing isotropic expansion, while moving as a whole at constant speed away from the Sun.
ii) This modified, non-'magnetic force-free' MHD solution of the FR has a non-circular cross section, as illustrated in Figure 4.
iii) The condition of a constant speed evolution relates the mass of the structure to its geometry and magnetic poloidal flux in the manner shown in Equation (9).

Further expanding on finding (i), this truncated-torus MHD solution extends the ideal MHD solution for a cylindrical geometry, with a circular *cross section*, of an evolving FR found in BLF to the case in which the structure is curved. The electromagnetic fields are distorted such that a magnetic force $\mathbf{J}_{\rm c} \times \mathbf{B} \neq \mathbf{0}$ appears to equilibrate the pull of a gravitational force possessing spherical symmetry. This is shown to be a consequence of the ansatz of Equation (5), Section 2.

In this case each of its elements would appear to move on average '*freely*', while as a whole the FR-structure undergoes a self-similar expansion. This mass ($M_{\rm mec}$), then, depends on the extension and width, translational and expansion velocity, and the square of the poloidal magnetic flux carried by the magnetized plasma structure.

The ubiquitous encounter with MCs that appear to have Lundquist's magnetic solution at each instant in time – by unmanned, interplanetary plasma laboratories (scientific spacecraft devoted to the study of the solar wind) – suggests that the right conditions for such a 'simple' evolution are frequently met in nature.

In the case of the Sun, Equation (9) gives the relationship between the mass carried and the magnetic flux, as well as its size and velocity parameters. Then we find that this model, predicting a mass for the magnetic FR-structure escaping the Sun, appears in reasonable agreement with observations as shown for: i) a generic magnetic cloud, ii) *Wind* MCs observed from the rising phase of Solar Cycle 23, and iii) a case study.

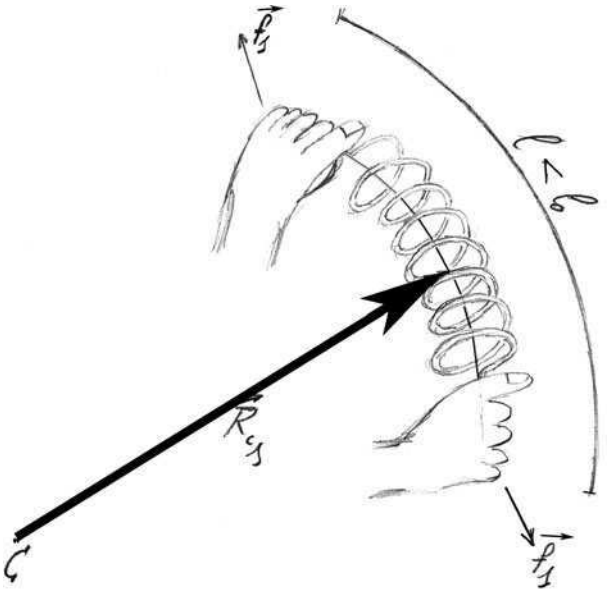

Figure 5 Hand-made sketch showing a spring compressed and bent into acquiring a major 'spring-radius' of curvature, R_{cs}, from a center C to the axis of the spring (dashed line). In this way we show its stresses represented by the forces $\mathbf{f}_s$, ready to propel the spring outward from its center of curvature while expanding toward achieving its proper length l_0 (indicated with the curve on top of the spring). This is illustrative of the manner in which the model of the FR presented possesses magnetic stresses with the right conditions given; it results in its outward direction from the Sun enabling it to equilibrate the gravitational pull of the Sun on the structure's mass.

When considering the parameter 'y,' Equation (11b), to be constant while $V_{cFR} \to 0$ for the particular case that the FR neither undergoes motion relative to the Sun, nor expansion, the solution would be valid. Also the FR, if unperturbed, would under such circumstances be in equilibrium, *i.e.*, levitated magnetically with respect to the Sun surface. However, it should be subject of further study to find if additional stability conditions are met for such a quiescent state of the FR to exist in nature over time intervals that would allow their observation.

When considering this kind of evolution we expect it to be possible in other environments; for example, as the evolution of a flux transfer structure after detaching itself from Earth's magnetosphere like those observed at Earth's magnetopause (see *e.g.*, Le *et al.*, 1999, 2008), or the Earth's magnetosphere tail (see *e.g.*, Slavin *et al.*, 2002), as well as from more exotic structures, or possibly present too as transients in stellar structures with much stronger electromagnetic winds than the Sun. They could also be related to processes connecting to nebulas, and/or be generated in the neighborhood of (active) galactic nuclei.

In the cases referred to in our work through Figure 1, the effects of the drag force are observed to affect mainly volumes of plasma neighboring the contact regions between the ICME and the plasma stream in which the ejected structure is immersed. These effects have been observed under a diverse set of conditions (see *e.g.*, Lepping *et al.*, 2001b). This may not always be true and their influence on the FR when drag dominates (*e.g.*, Farrugia and Berdichevsky, 2004; Berdichevsky *et al.*, 2005) is beyond the scope of the present work. For the possible presence of a combination of SW streams responsible for *global* deformation of the FR cross section into elliptical or more general shapes, see *e.g.*, Hu and Sonnerup (2001), Hidalgo, Nieves-Chinchilla, and Cid (2002). Also beyond this study are considerations regarding the thermal evolution of the structure, which observations appear to indicate the polytropic index γ of the FR to be smaller than one due to the electrons (*e.g.*, Osherovich *et al.*, 1997; Sittler and Burlaga, 1998).

The propulsion mechanism here presented can be understood as the result of the difference in the tightening of the poloidal magnetic field (B_φ) in the rear (closer to Sun) relative

to the front (further away from the Sun) of the FR. The consequence is that while the FR propagates away from the Sun, it produces a force on its mechanical mass, M_{mec}, pushing it *in the opposite direction to the pull of the Sun's gravitational force*. This is similar to what happens to a straight spring when we compress the spring and bend its axis of symmetry as in the form illustrated in Figure 5.

One of the predictions raised in this work which it would be possible to investigate is if the model here discussed is capable of giving quantitative agreement of observation for the mass of specific ICMEs.

Acknowledgements I acknowledge my father Carlos David, for his unconditional support of a whole life. Also I acknowledge the professional support of Santiago Berdichevsky, who helped to put this text in better English, making it more understandable.

References

Abramowitz, M., Stegun, I.A.: 1972, *Handbook of Mathematical Functions*, 9th edn. Dover, New York.
Albertson, V.D., Thorson, J.M., Clayton, R.E., Tripathy, R.E.: 1973, Solar induced currents in power systems: cause and effects. *IEEE Trans. Power Appar. Syst.* **PAS-92**, 471.
Bartels, J.: 1962, *Collection of Geomagnetic Planetary Indices KP and Derived Daily Indices, AP and CP for the Years 1932 to 1961*, AGU, Washington. QC811.B28.
Berdichevsky, D.B., Lepping, R.P., Farrugia, C.J.: 2003, Geometric considerations of the evolution of magnetic flux ropes. *Phys. Rev. E* **67**, 036405. doi:10.1103/PhysRevE.036405.
Berdichevsky, D.B., Stenborg, G., Vourlidas, A.: 2011, Deriving the physical parameters of a solar ejection with an isotropic magnetohydrodynamic evolutionary model. *Astrophys. J.* **741**, 47. doi:10.1088/0004-637X/741/1/47.
Berdichevsky, D.B., Farrugia, C.J., Thompson, B.J., Lepping, R.P., Reames, V.V., Kaiser, M.L., Steinberg, J.T., Plunkett, S.P., Michels, D.J.: 2002, Halo-coronal mass ejections near the 23rd solar minimum: lift-off, inner heliosphere, and in situ (1 AU) signatures. *Ann. Geophys.* **20**, 891.
Berdichevsky, D.B., Richardson, I., Lepping, R.P., Martin, S., 2005, On the origin and configuration of the 20 March 2003 interplanetary shock and magnetic cloud at 1 AU. *J. Geophys. Res.* **110**, A09105. doi:10.1029/2004JA010662.
Bothmer,V., Schwenn, R.: 1998, The structure of magnetic clouds in the solar wind. *Ann. Geophys.* **16**, 1.
Burlaga, L.F.: 1988, Magnetic clouds and force-free fields with constant alpha. *J. Geophys. Res.* **93**, 7217.
Carrington, R.C.: 1859, Description of a singular appearance seen in the Sun on September 1, 1859. *Mon. Not. Roy. Astron. Soc.* **20**, 13.
Chamberlain, J.W.: 1960, Interplanetary gas II. Expansion of a model solar corona. *Astrophys. J.* **131**, 47.
Chamberlain, J.W.: 1961, Interplanetary gas III. A hydrodynamical model of the corona. *Astrophys. J.* **133**, 675.
Chapman, S.: 1957, Notes on the solar corona and the terrestrial ionosphere. *Smithson. Contrib. Astrophys.* **2**, 1.
Czech, P., Chano, S., Huynh, H., Dutil, A.: 1992, The hydro-Quebec system blackout of 13 March 1989: system response to geomagnetic disturbance. In: *Proc. EPRI Conf. Geomagnetically Induced Currents EPRI TR-100450, Burlingame, CA*. 19-1.
Farrugia, C.J., Berdichevsky, D.B.: 2004, Evolutionary signatures in complex ejecta and their driven shocks. *Ann. Geophys.* **22**, 3679.
Goldstein, H.: 1956, *Classical Mechanics*, 4th edn. Addison Wesley, Cambridge.
Garrett, H.B.: 1981, The charging of spacecraft surfaces. *Rev. Geophys.* **19**, 577.
Hidalgo, M.A., Nieves-Chinchilla, T., Cid, C.: 2002, Elliptical cross-section model for the magnetic topology of magnetic clouds. *Geophys. Res. Lett.* **29**, 1637. doi:10.1029/2001GL013875.
Hirshberg, J., Bame, S.J., Robbins, D.E.: 1972, Solar flares and solar wind helium enrichments: July 1965. *Solar Phys.* **23**, 467.
Holzer, T.E.: 1979. In: Parker, E.N., Kennel, C.F., Lanzerotti, L.J. (eds.): *Solar and Solar Wind Plasma Physics*. **1**, North-Holland, Amsterdam, 101.
Hu, Q., Sonnerup, U.O.: 2001, Reconstruction of magnetic flux-ropes in the solar wind. *Geophys. Res. Lett.* **28**, 467.
Huttunen, K.E.J., Schwenn, R., Bothmer, V., Koskinen, H.E.J.: 2005, Properties and geoffectiveness of magnetic clouds in the rising, maximum and early declining phases of solar cycle 23. *Ann. Geophys.* **23**, 625.

Jackson, J.D.: 1966, *Electrodinámica Clásica*, 1st Spanish edn. Alhambra, Madrid.
Landau, L., Lifchitz, E.: 1966, *Physique Théorique, Tome i, Mécanique*, 2me edn. MIR, Moscow.
Lanzerotti, L.J., Breglia, C., Maurer, D.W., Maclennan, C.G.: 1998, Studies of spacecraft charging on a geosynchronous telecommunications satellite. *Adv. Space Res.* **22**, 79.
Le, G., Gosling, J.T., Russell, C.T., Elphic, R.C., Thomsen, M.F., Newbury, J.A.: 1999, The magnetic and plasma of flux transfer events. *J. Geophys. Res.* **104**, 233.
Le, G., Zheng, Y., Russell, C.T., Pfaff, R.F., Slavin, J.A., Lin, N., Mozer, F., Parks, G., Wilber, M., Petrinec, S.M., Lucek, E.A., Réme, H.: 2008, Flux transfer events simultaneously observed by Polar and Cluster: flux rope in the subsolar region and flux tube addition to the polar cusp. *J. Geophys. Res.* **113**, A01205.
Lepping, R.P., Jones, J.E., Burlaga, L.F.: 1990, Magnetic field structure of interplanetary magnetic clouds at 1 AU. *J. Geophys. Res.* **108**, 11957.
Lepping, R.P., Berdichevsky, D.B., Burlaga, L.F., Lazarus, A.J., Kasper, J., Desch, M.D., Wu, C.C., Reames, D.-V., Singer, H.J., Smith, C.W., Ackerson, K.L.: 2001a, The Bastille day magnetic clouds and upstream shocks: near earth interplanetary observations. *Solar Phys.* **204**, 287.
Lepping, R.P., Berdichevsky, D.B., Szabo, A., Lazarus, A.J., Thompson, B.J.: 2001b, Upstream shocks and interplanetary magnetic cloud speed and expansion: Sun, Wind, and Earth observations. In: Chao, K. (ed.) *COSPAR 2000*. *Adv. Space Res.*, **26**, 87.
Lepping, R.P, Berdichevsky, D.B., Szabo, A., Arqueros, C., Lazarus, A.J.: 2003, Profile of an average magnetic cloud at 1 AU for the quiet solar phase: Wind observations. *Solar Phys.* **212**, 425.
Lepping, R.P., Berdichevsky, D.B., Wu, C.-C., Szabo, A., Narock, T., Mariani, F., Lazarus, A.J., Quivers, A.J.: 2006, A summary of Wind magnetic clouds for years 1995 – 2003: model-fitted parameters, associated errors and classifications. *Ann. Geophys.* **24**, 215.
Lepping, R.P., Wu, C.-C., Berdichevsky, D.B., Szabo, A: 2011, Magnetic clouds at/near the 2007 – 2009 solar minimum: frequency of occurrence and some unusual properties. *Solar Phys.* **274**, 345.
Lundquist, S.: 1951, Magnetohydrostatic fields. *Ark. Fys.* **2**, 61.
Osherovich, V.A., Fainberg, J., Stone, R.G., MacDowall, R.J., Berdichevsky, D.B.: 1997 In: *Proc. 31st. ESLAB Symp., Correlated Phenomena at the Sun, in the Heliosphere and in Geospace, SA* **SP-415**, ESA, Noordwijk, 771.
Parker, E.N.: 1958, Dynamics of the interplanetary gas and magnetic fields. *Astrophys. J.* **124**, 664.
Pirjola, R., Lehtinen, M.: 1985, Currents produced in the Finnish natural gas pipeline by geomagnetically induced electric fields. *Ann. Geophys.* **3**, 485.
Richardson, I.J., Cane, H.V.: 2004, Identification of interplanetary coronal mass ejections at 1 AU using multiple solar wind plasma composition anomalies. *J. Geophys. Res.* **109**, A09104.
Richardson, D.J., Kasper, C., Wang, C., Belcher, J.W., Lazarus, A.J.: 2008, Cool heliosheath plasma and deceleration of the upstream solar wind at the termination shock. *Nature* **454**(3), 63.
Rouillard, A.P., Davies, J.A., Forsyth, R.J., Savani, N., Sheeley, R., Thernisien, A., Burlaga, L.F., Zhang, T.-L., Vourlidas, A., Howard, R.A., Wang, Y.-M., Rees, A., Anderson, B., Krimiges, T., Slavin, J., Carr, C.M., Tsang, S., Lockwood, M., Davis, C.J., Harrison, R.A., Bewsher, D., Crothers, S.R, Eyles, C.J., Brown, D.S., Habgood, M., Perry, C.H., Whittaker, I., Jones, G.H., Coates, A.J., Reande, M., Frahm, R.A., Winningan, J.D.: 2009, A solar storm observed from the Sun to Venus using the STEREO Venus-Express, and MESSENGER spacecraft. *J. Geophys. Res.* **114**, 07106. doi:10.1029/2008JA014034.
Sittler, E.C. Jr., Burlaga, L.F.: 1998, Electron temperatures within magnetic clouds between 2 and 4 AU: Voyager 2 observations. *J. Geophys. Res.* **103**, 17447.
Shimazu, H., Vandas, M.: 2002, A self-similar solution of expanding cylindrical flux ropes for any polytropic index value. *Earth Planet Sci. J.* **54**, 783.
Slavin, J.A., Fairfield, D.H., Lepping, R.P., Hesse, M., Ieda, A., Tanskanen, E., Østgaard, N., Mukai, T., Nagai, T., Singer, H.J., Sutcliffe, P.R.: 2002, Simultaneous observations of earthward flow bursts and plasmoid ejection during magnetospheric substorms. *J. Geophys. Res.* **107**, A7. doi:10.1029/2000JA003501.
Thernisien, A., Vourlidas, A., Howard, R.A.: 2009, A catalog of white light coronal mass ejections observed by the STEREO/SECCHI data. *Solar Phys.* **256**, 111.
WIND MFI Science Team: 1995, (– start date), Page (–Table 2, 'a living document') at http://wind.gsfc.nasa.gov/mfi/mag_cloud_S1.html.
Wood, B.E., Howard, R.A.: 2009, An empirical reconstruction of the 2008 april 26 coronal mass ejection. *Astrophys. J.* **702**, 901. doi:10.1088/0004-637X/702/2/901.
Wood, B.E., Wu, C.-C., Howard, R.A., Socker, D.G., Rouillard, A.P.: 2011, Empirical reconstruction and numerical modeling of the first geoeffective coronal mass ejection of solar cycle 24. *Astrophys. J.* **729**, 70. doi:10.1088/0004-637X/729/1/70.
Yashiro, S., Gopalswamy, N., Michalek, G., St. Cyr, O.-C., Plunkett, S.P., Rich, N.B., Howard, R.A.: 2004, A catalog of white light coronal mass ejections observed by the SOHO spacecraft. *J. Geophys. Res.* **109**, A07105. doi:101029/2003JA010282.
Zirin, H.: 1966, *The Solar Atmosphere*, Blaisdell, Waltham.

Solar Phys (2013) 284:179–201
DOI 10.1007/s11207-012-0084-8

How Many CMEs Have Flux Ropes? Deciphering the Signatures of Shocks, Flux Ropes, and Prominences in Coronagraph Observations of CMEs

A. Vourlidas · B.J. Lynch · R.A. Howard · Y. Li

Received: 31 March 2012 / Accepted: 17 July 2012 / Published online: 21 August 2012

Abstract We intend to provide a comprehensive answer to the question on whether all Coronal Mass Ejections (CMEs) have flux rope structure. To achieve this, we present a synthesis of the LASCO CME observations over the last 16 years, assisted by 3D MHD simulations of the breakout model, EUV and coronagraphic observations from STEREO and SDO, and statistics from a revised LASCO CME database. We argue that the bright loop often seen as the CME leading edge is the result of pileup at the boundary of the erupting flux rope irrespective of whether a cavity or, more generally, a three-part CME can be identified. Based on our previous work on white light shock detection and supported by the MHD simulations, we identify a new type of morphology, the 'two-front' morphology. It consists of a faint front followed by diffuse emission and the bright loop-like CME leading edge. We show that the faint front is caused by density compression at a wave (or possibly shock) front driven by the CME. We also present highly detailed multi-wavelength EUV observations that clarify the relative positioning of the prominence at the bottom of a coronal cavity with a clear flux rope structure. Finally, we visually check the full LASCO CME database for flux rope structures. In the process, we classify the events into two clear flux rope classes ('three-part', and 'Loop'), jets and outflows (no clear structure). We find that at least 40 % of the observed CMEs have clear flux rope structures and that ∼29 % of the database entries are either misidentifications or inadequately measured and should be discarded from statistical analyses. We propose a new definition for flux rope CMEs (FR-CMEs) as a coherent magnetic, twist-carrying coronal structure with angular width of at

Flux-Rope Structure of Coronal Mass Ejections
Guest Editors: N. Gopalswamy, T. Nieves-Chinchilla, M. Hidalgo, J. Zhang, and P. Riley

Electronic supplementary material The online version of this article (doi:10.1007/s11207-012-0084-8) contains supplementary material, which is available to authorized users.

A. Vourlidas (✉) · R.A. Howard
Space Sciences Division, Naval Research Laboratory, Washington, DC, USA
e-mail: vourlidas@nrl.navy.mil

B.J. Lynch · Y. Li
Space Sciences Laboratory, University of California, Berkeley, CA, USA

least 40° and able to reach beyond 10 $R_{\odot}$ which erupts on a time scale of a few minutes to several hours. We conclude that flux ropes are a common occurrence in CMEs and pose a challenge for future studies to identify CMEs that are clearly *not* FR-CMEs.

Keywords Coronal mass ejections, low coronal signatures · Coronal mass ejections, initiation and propagation

1. Introduction

Since their detection in the early 1970s, Coronal Mass Ejections (CMEs) have been the subject of intense investigation with regard to their initiation mechanisms, their effects on the corona and their association with other coronal phenomena (*e.g.*, flares and prominences). The *Topical Issue* this article is published in presents results from a Coordinated Data Analysis Workshop (CDAW) devoted to the question: "Do All Coronal Mass Ejections (CMEs) Have Flux Rope Structures?". Such a specific physics-based question shows that we have come a long way towards understanding the nature of these explosive events especially when we consider the original definition of a CME: "a relatively short scale white light feature propagating in a coronagraph's field of view" (paraphrasing Hundhausen *et al.*, 1984).

Traditionally, CMEs were observed with visible-light coronagraphs and clues on their origin and nature were based on their morphology in those images (Munro *et al.*, 1979; Howard *et al.*, 1985; Burkepile and St. Cyr, 1993). Despite the apparently large variation in the appearance of CMEs, two particular morphologies stand out: the 'loop'-CME where a bright narrow loop-like structure comprises the CME front, and the 'three-part'-CME (Illing and Hundhausen, 1985) where the bright front is followed by a darker cavity, which frequently contains a bright core. It has become the archetypical morphology of a CME even though the 'three-part' morphology could be identified in only about a third of the events (Munro *et al.*, 1979). It is still unclear whether the remaining variation is the result of projection effects due to the optically thin nature of the emission or not.

It was recognized early that the cavity rather than the prominence in the core drove the CME (Hundhausen, 1987). An initial controversy on whether CMEs were planar (*i.e.*, ejected loops) or three-dimensional (*i.e.*, bubbles) structures was largely resolved by the end of the 1980s. Crifo, Picat, and Cailloux (1983) demonstrated, using polarization analysis, that the loop front was indeed a bubble. The identification of halo CMEs by Howard *et al.* (1982) with their quasi-circular appearance established their three-dimensional (3D) nature and led to the adoption of the 'ice-cream' model to describe and fit the kinematics of these events (Howard *et al.*, 1982; Zhao, Plunkett, and Liu, 2002; Xie, Ofman, and Lawrence, 2004; Xue, Wang, and Dou, 2005). A bubble or spherical structure is the intrinsic assumption behind this model which is not a proper description as we will discuss later.

As theories progressed towards a more physical basis for the CME initiation, they focused on 3D magnetic topologies that could account for the 'three-part' morphology and the frequent association with prominences. This quickly led to scenarios of rising loop arcades, overlying a prominence, which underwent reconnection to form magnetic flux ropes (FR, hereafter; Anzer and Pneuman, 1982; Forbes, 1990). Alternatively, the FR could pre-exist and rise under the driving of Lorenz forces (Kuperus and Raadu, 1974; Chen and Garren, 1993). While the question of whether the FR is formed before or during the eruption remains open, the overwhelming majority of magnetohydrodynamic (MHD) models and simulations agree on one thing. Namely, the erupting structure is always a FR

(Chen, 2011). There is no physical mechanism that can produce a large-scale fast eruption from the corona without ejecting a flux rope, to the best of our knowledge.

At the same time, *in-situ* measurements of interplanetary CMEs (ICMEs) often encounter structures with smooth rotation in one, or more, components of the magnetic field which can be fitted with FR models (Klein and Burlaga, 1982; Lepping, Burlaga, and Jones, 1990; Isavnin, Kilpua, and Koskinen, 2011, to name a few). These so-called Magnetic Clouds (MCs) can be considered then as the interplanetary manifestations of the ejected FR predicted by theory and possibly detected as the cavity in the 'three-part'-CMEs (Burlaga *et al.*, 1982). Cane and Richardson (2003) found that 100 % of ICMEs detected during solar minimum were MCs reducing to < 20 % during solar maximum.

So the CDAW question regarding the nature of CMEs, at least in the case of 'three-part'-CMEs, seems to have been answered. A CME is simply the ejection of a magnetic FR structure from the lower corona which takes the form of a 'three-part'-CME or a MC depending on the instrumentation used (images or *in-situ*, respectively) to detect it.

But if a FR is a necessary ingredient for an ejection, why do not all CMEs show evidence for such a structure? In other words, why are all CMEs not 'three-part'-CMEs? Some have just a loop front while others appear as jets or structureless clouds or blobs. For example, Howard *et al.* (1985) categorized CMEs, between $6-10$ $R_{\odot}$, into ten morphological classes based on their appearance in *Solwind* observations. Why is there such a large variety of shapes? Could there be other types of magnetic structure, besides FRs, ejected from the Sun? If they do exist, they would suggest a major gap in our understanding of eruptive processes, given the prevalence of FR in our theories.

Second, not all ICMEs exhibit MC signatures. Is this simply a result of 'glancing' cuts between *in-situ* instruments and the ICME? Or do CME FRs lose their coherence as they travel in the interplanetary space, through reconnection with the ambient solar wind for example (Dasso *et al.*, 2007)?

Third, many fast ICMEs are driving a shock followed by a sheath of post-shocked plasma. The resulting five-part ICME (shock, sheath, dense front, cavity, and dense plug) does not have a coronal counterpart. Where are the five-part CMEs or more precisely, where are the shock and sheath signatures in the coronagraph images? Shocks could deflect streamers and generally affect the ambient corona, ahead and at the flanks of a CME, thus creating complex brightness distributions in the images. Could such effects be responsible for misidentifications, and hence misinterpretations, of CME morphologies, kinematic profiles, and associations with structures in the low corona or the inner heliosphere?

Fourth, and related point: the emission processes in both low (EUV) and middle (white light) corona are optically thin resulting in images that are projections on the plane of sky (POS). Do these projections affect our ability to properly interpret observations and how can we account for them? We will address this problem throughout this paper.

The *Large Angle and Spectrometric Coronagraph* (LASCO; Brueckner *et al.*, 1995) project has accumulated the largest and longest database of coronagraphic observations of CMEs since 1996. Spanning more than a complete solar cycle, it is reasonable to expect that events of every possible orientation, size, speed, mass, and morphologies have been captured. We should be in a position to understand the role of projection effects on the images, identify the origin of the various features (CME or not) in a given LASCO image, and hence answer the question posed in this *Topical Issue*.

To accomplish this task comprehensively we have given this paper a relatively large scope. It represents a synthesis of the observational knowledge gained over the 16 years of LASCO observations. In the following sections, we will provide: evidence for the FR structure within CME cavities (Section 2), evidence for the existence of white-light shock and

tips on distinguishing the shock front from the CME front (Section 3), theoretical support for these interpretations using synthetic images from 3D MHD simulations (Section 4), observations that clarify the connection between prominence and erupting cavity (Section 5), and finally statistics on the occurrence of 'three-part' or more precisely FR-CMEs, along with a discussion on the constraints of event lists (Section 6). We discuss and conclude in Section 7.

We will support several of our predictions and conclusions by using two-viewpoint imaging afforded by the *Sun-Earth Connection Coronal and Heliospheric Investigation* (SECCHI; Howard *et al.*, 2008) on-board the *Solar TErrestial RElations Observatory (STEREO)* (Kaiser *et al.*, 2008). We will use the SECCHI observations as necessary but we want to focus on the single viewpoint from LASCO for two reasons. First, this article is part of a workshop devoted to the analysis of events observed with LASCO. Second, and more important, the *STEREO* mission has a finite lifetime. Budgetary and other concerns suggest that future observations (whether research or operationally oriented) will be obtained from a single vantage point. It is therefore crucial that future observers can interpret such single viewpoint observations accurately.

2. Where is the Flux Rope? The Three-Part CME

As we noted, the three-part morphology has been identified since the early coronagraph observations. The prototypical event is an event similar to the CME in Figure 1. All three components can be readily identified in this snapshot (the movie is available as an electronic supplement to this article) which was constructed by dividing the original image with a long-term background to remove the effects of the F-corona but to avoid removal of the ambient electron corona. An inspection of the accompanying movie reveals that the brightness of the front originates from the pile-up of the overlying streamer material. The core has sufficient structure to identify it unambiguously with the pre-eruption prominence (we will not discriminate between the terms 'filament' and 'prominence' here since they both refer to the same structure). Note that the cavity, while not completely devoid of plasma, does contain less electrons (it is less bright) than its surroundings. These aspects have been noted before. The question here: Where is the evidence that the cavity is (or contains) a 'flux rope'-like structure?

Let us focus on the concave upward features labeled as 'horns'. They seem to originate within the core and to outline the extent of the cavity. Such a configuration is consistent with models of prominence suspension at the bottom of a coronal flux rope cavity (Low and Hundhausen, 1995). Plunkett *et al.* (2000) commented on the appearance of these 'horns' in EIT images before the eruption as an indication of the formation of the flux rope which subsequently erupted and they also noted that the prominence lay at the trailing edge of the CME. Similar structures were observed by Wood *et al.* (1999) and Dere *et al.* (1999) and interpreted in a similar way as direct evidence of the FR nature of the CME cavity.

Although these features have been observed in many events since, their FR association does not seem to be widely recognized. This may be because the low densities within the cavity do not permit an easy visualization of the FR structure when only the lower part (the 'horns') are illuminated. The missing 'link' would be a three-part CME, where the cavity would be filled with a sufficient amount of plasma to illuminate the full volume and structure of the FR. Figure 2 shows such an example. The event is associated with a slow eruption of a quiet Sun prominence from the northern hemisphere. The last traces of 304 Å disappear from the *Extreme Ultraviolet Imager* (EUVI)-A field of view at 1:56 UT on 4 November

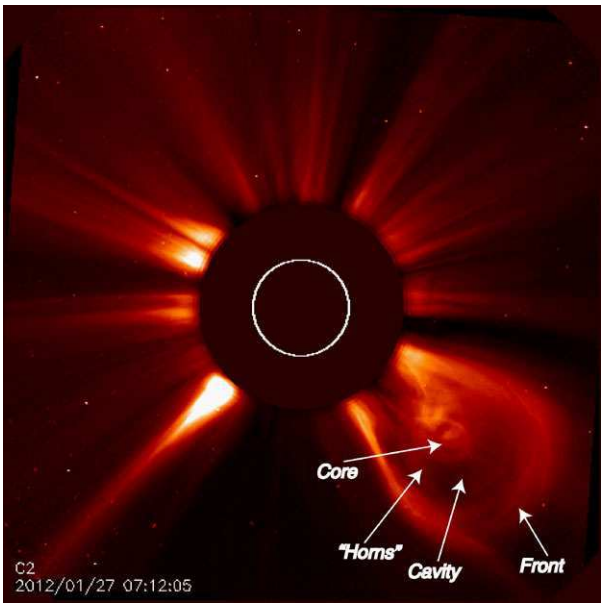

Figure 1 A typical three-part CME as it appeared in LASCO/C2 on 27 January 2012. The three components are identified on this snapshot image. The full movie is available online.

2007. This is by far the clearest detection of an FR within a CME despite observations of thousands of events with LASCO. We believe that the rarity of such detections is due to four reasons:

i) The clearest signatures will appear at middle corona heights (say, > 7 $R_{\odot}$) where the background streamer emission is weaker and the CME has finished evolving (Vourlidas *et al.*, 2010).
ii) The lower spatial resolution of the LASCO/C3 coronagraph (it is about $4\times$ coarser than the LASCO/C2) washes out some of the fine-scale detail.
iii) The FR must have a large size along the line of sight (LOS).
iv) The FR must be oriented almost exactly perpendicular to the POS to produce bright emission throughout the cavity.

The highly structured core of the CME in the COR2-A image has an almost identical appearance in the EUVI-A 195 Å images (not shown here), which suggests that most of the core material was at coronal temperatures (~ 1.4 MK), thus erasing any obvious connections to the prominence (see Robbrecht, Patsourakos, and Vourlidas (2009) for a very similar example). We will return to this point in Section 5.

Even such clear observations would not probably convince the skeptics that the cavity and FR are the same structure. The images are 2D projections on the POS leaving some room for misinterpretation. A comparison to theoretical predictions is therefore required. The high sensitivity of the LASCO images enabled the first opportunity for a detailed comparison between observations and theoretically derived 2D FR structures (Chen *et al.*, 1997, 2000). Krall and St. Cyr (2006) extended these comparisons to a larger sample of LASCO 'three-part'-CMEs in an effort to extract some 3D information (aspect ratio, eccentricity) of the FR. Krall (2007) attempted to answer the same question as us by comparing statistical distributions of the width and the rate of occurrence of concave-upward structures (essentially 'horns' seen in visible light) from observations to synthetic FR images with satisfactory agreement. Extensive measurements of the geometric proper-

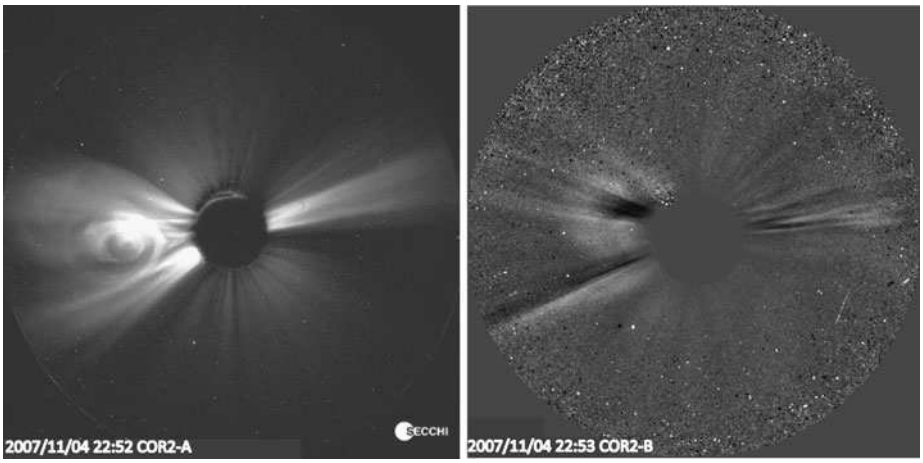

Figure 2 Left: An exceptionally clear example of flux rope structure entrained within a CME observed by SECCHI/COR2-A on 11 November 2007. There is no 'cavity' in this case, since emission from the dense flux rope fills that region. Multiple striations including a tip at the back end of the structure can be discerned. The lack of a bright front is likely due to the low speed and high starting height for this event. Right: Simultaneous image of the same event from COR2-B. The CME appears as a partial halo and a base difference image is used to enhance the faint emission. There is no evidence of FR structure from this viewpoint.

ties of many three-part CMEs led Cremades and Bothmer (2004) to conclude that three-part CMEs were not simply spherical bubbles, but structures elongated along the axis parallel to photospheric neutral line in their source regions. These results were subsequently confirmed by forward modeling methods which demonstrated that a 3D geometric representation of a FR-like shape could account for the observed CME density envelopes and shapes (Thernisien, Howard, and Vourlidas, 2006). This issue has now been consolidated with the successful application of FR-like geometric structures on stereoscopic observations from STEREO (Thernisien, Vourlidas, and Howard, 2009, 2011; Rouillard, 2011; Wood *et al.*, 2011). There should be little doubt, therefore, that 'three-part'-CMEs are indeed systems of ejected FRs, where the cavity is the actual FR.

Our examples, and the events exhibiting clear three-part structures in general, must lie close to the POS to provide an edge-on view of the FR. But CMEs occur in all longitudes. Occasionally, a 'three-part'-CME will be observed along the Sun-Earth line. How can we then tell whether a halo CME has a three-part structure and how can we identify the erupted FR against the backdrop of deflected streamers and material outflows? For this, we first need to identify the signatures of the other erupting structures starting with the shock.

3. Where is the Shock? The Five-Part CME

It is common knowledge that sudden changes in plasma motion will launch compressive waves through the medium. If the motion occurs faster than the characteristic speed of the medium (*i.e.*, sound speed for an unmagnetized plasma or fast-mode speed for a magnetized plasma), the waves will then steepen into shock waves. In either case, the propagating wave will manifest itself as a propagating compression of density (and magnetic field where applicable). In our case, the propagating FR will generate a plasma wave, which

may look as another propagating front in a coronagraph (or EUV) image sequence. Depending on various factors, such as the impulsiveness and starting height of the event, and the magnetic and plasma configuration in the ambient corona, the density compression of the wave front could become strong enough to be detected (Vourlidas *et al.*, 2003). Because waves (and shocks) are an intrinsic component of any eruption, their coronagraphic signatures have been the subject of debate since the first CME observations (see Vourlidas and Ontiveros (2009) for a historical discussion). It was generally accepted that distant streamer deflections were a reliable, but indirect, proxy for these waves (Gosling *et al.*, 1974; Sheeley, Hakala, and Wang, 2000).

The first identification of the density enhancement from a CME-driven shock was reported by Vourlidas *et al.* (2003) thanks to the high sensitivity of the LASCO observations. Such signatures are now commonly reported in the literature (Yan *et al.*, 2006; Ontiveros and Vourlidas, 2009; Vourlidas and Ontiveros, 2009; Gopalswamy *et al.*, 2009; Bemporad and Mancuso, 2010; Vourlidas and Bemporad, 2012; Kim *et al.*, 2012). We now know that the CME-induced waves can be detected in coronagraph images, that they are faint, and that they are located ahead of the FR front. So it should be straightforward to identify them in any image (assuming there is a reasonable expectation of a wave occurrence due to the speed of the CME, for example). Because these wave signatures are faint, the best approach is to use calibrated, excess-mass images (to remove effects such as vignetting, background streamers, etc.) and display them with high contrast.

An illustrative example is shown in the upper panels of Figure 3, where the same frame from a fast CME is shown with two different contrast ratios. On the left, the CME has the classical three-part appearance with a very clear loop front. On the right, the higher contrast ratio allows to see a fainter front ahead which extends around the bright loop front and connects to the deflected streamer on the eastern flank. A series of other deflected streamers (or more likely intrastreamer structures) can be seen as radial striations occupying position angles from the deflected streamer, around the CME to the western equator. The faint front appears to be the outer envelope of these deflected streamers consistent with being a wave driven by the CME and propagating within a large-scale streamer. Two more examples of such fronts are shown in the bottom panels of Figure 3. On the left, a C2 image from a CME on 11 June 2000 shows a bright filamentary front (a 'Loop'-CME) preceded by an extensive faint front connecting to a deflected streamer in the north. On the right, a C3 image shows again a faint front terminating at a deflected streamer but this time the front extends only to one side of the CME. No fronts, and tellingly no loop front either, are seen along the northern CME flank.

These images serve to illustrate our earlier point that the detectability of these shock fronts is highly dependent on the sensitivity of the observations. It is thus unsurprising (in retrospective) that such features have eluded detection in the pre-LASCO coronagraph experiments which lacked CCD detectors, large fields of view, and long-term uninterrupted observations. For many events, only the bright loop would be detected (Figure 3, top left) thus only allowing rather indirect and ambiguous arguments on the existence of a shock (Sime and Hundhausen, 1987).

A plausible criticism that may arise from our interpretation of these images is how can one be sure that the faint front is indeed related to density pile-up at a wave front and is not simply ejected material, *i.e.*, coronal loops moving ahead of the CME in direct analogy to the bright front ahead of the cavity. This can be best answered by careful inspection of excess-mass movies of these events. If the front in question is due to ejected material, then a density depletion should form behind it as it does behind the CME proper. If the front is caused by a wave, then the enhancement is due to density compression and not

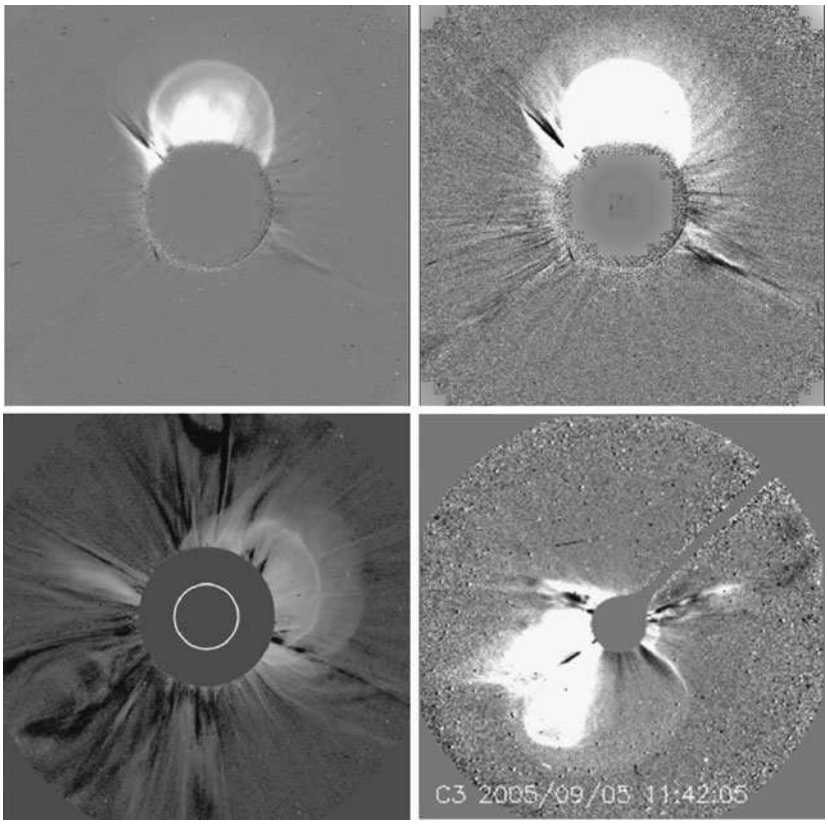

Figure 3 Upper left: An excess-mass image of a CME in the LASCO/C2 field of view on 15 January 2005 at 6:30 UT. The event can be easily classified as a three-part CME. A deflected streamer is located to the east without an apparent connection to the CME. Upper right: The same image displayed with a higher contrast ratio. A faint arch front terminating at the eastern deflected streamer is now visible. Indications of several other deflected streamers (or sub-streamer structures) can be seen. Bottom panels: Other examples of shock fronts ahead of CMEs in C2 on 11 June 2000 (left) and C3 on 5 September 2005 (right).

material transport; therefore, no density depletion should occur. The latter is the observed behavior for the events in Figure 3. MHD simulations have provided further support for this interpretation by matching the location and density compression ratio between observations and model (Vourlidas *et al.*, 2003; Manchester *et al.*, 2008). Recently, similar fronts have been detected in high-cadence EUV images (Ma *et al.*, 2011; Cheng *et al.*, 2012).

Returning to the white-light morphology, the identification of the faint front ahead of the bright loop-like CME front simplifies greatly the interpretation of CME images. The bright loop is the pile-up of material at the outer boundary of the erupted FR (the cavity) and hence it is bright while the outer front originates from a temporary compression of the ambient plasma as the wave (or shock) propagates through and hence is much fainter (see Ontiveros and Vourlidas (2009) for density profiles of these structures). Our examination of thousands of CME images (Section 6) reveals that the "faint front followed by a bright loop" is a common occurrence and can constitute a reliable signature for the identification of *both the shock and FR fronts* in the images. An important benefit from this identification is a better interpretation of the structures in images of halo CMEs.

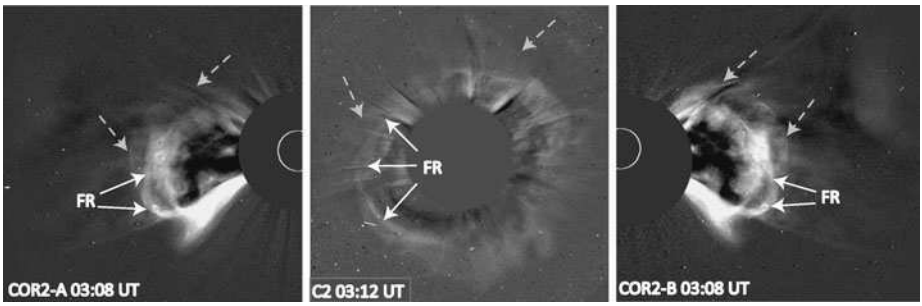

Figure 4 A demonstration of the appearance of 'two-front' morphology in a weak halo CME as viewed from LASCO/C2 (center). The CME appears as a 'loop'-CME in the SECCHI/COR2-A (left) and -B (right) coronagraphs. All three images are taken nearly simultaneously. The pile-up at the FR edge is marked by solid white arrows. The edge of the much fainter wave is marked by the dashed gray arrows. The existence of a shock is likely since the CME is propagating at $\sim 750\ \mathrm{km\,s^{-1}}$ in the LASCO field. The event occurred on 15 February 2011 in association with an X-class flare. For similar examples see Vourlidas and Ontiveros (2009), Vourlidas and Bemporad (2012).

3.1. Halo CMEs

There is no physical reason to expect that halo CMEs are a different class of CMEs. 'Loop' and 'three-part'-CMEs should occur as halos and their FR should appear on the images … sometimes. The common approach has been to identify the outer envelope of the halo with the FR and proceed to fit it with a circular or elliptical cone models to extract kinematic parameters (Howard *et al.*, 1982; Zhao, Plunkett, and Liu, 2002; Xie, Ofman, and Lawrence, 2004; Xue, Wang, and Dou, 2005). However, this approach is inconsistent with our theoretical understanding of FRs as more or less cylindrical structures, elongated along their axis. It is also inconsistent with the analyses of the CME projection effects (Cremades and Bothmer, 2004; Thernisien, Vourlidas, and Howard, 2009). Our discussion above solves this problem. To identify the FR in a halo CME image, we have to look for evidence of the 'two-front' morphology or of the bright loop structure alone when the CME is not fast enough to expect significant pileup at its wave front. Indeed, these structures are visible in the majority (if not all) of halo CMEs.

We picked a recent halo CME as an example (Figure 4). The event, which occurred on 15 February 2011, was the most symmetrical halo of the current solar cycle. It was associated with a large X-class solar flare, metric and decimetric Type-II emissions, and an EUV wave. We chose an event with relatively weak halo emission to demonstrate the robustness of the feature detection. Much clearer examples are presented in Vourlidas and Bemporad (2012). See also Vourlidas and Ontiveros (2009) and Figure 7 (bottom left) for a single LASCO view. Returning to Figure 4, we see that the halo CME appears as a regular 'loop', or even 'three-part'-CME in the COR2-A and -B fields of view. Note that all three images were taken nearly simultaneously and are differenced from a pre-event image. The FR boundary is readily identified in the COR2 images as a bright loop structure (marked by the white arrows and the label 'FR'). The same structure appears as a (fainter) loop in the C2 image. A still fainter front can be seen ahead of the loop. A wave compression, and possibly a shock, is expected in this event given its LASCO speed of $\sim 750\ \mathrm{km\,s^{-1}}$ and the Type-II radio emission. The wave is more difficult to discern in the side views from COR2 (dashed gray arrows) because the CME is projected against, and propagating through, a background corona disturbed by an earlier event. Even the streamer deflection and the wave associated

with it can be detected, albeit barely, in the north (topmost gray arrow). The rugged set of features along the southern-southeastern part of the halo originate in the bright southern streamer, seen in the COR2 images.

This exercise shows that, with a little effort, we can identify the origins of the various features in a halo CME image and delineate the boundaries of the ejected FR with some precision. The important point here is that we do not have to rely on simplistic, rough approximations for the envelop of the CME. These would lead to imprecise measurements of the CME speed, size, and orientation with corresponding implications for Space Weather predictions.

4. Theoretical Support: Synthetic Images from MHD Simulations

Thus far, we have only used coronagraph images to support our interpretation of CMEs as three-part (five-part when a wave front appears) structures resulting from the expulsion of a magnetic FR from the Sun. We now turn to a numerical MHD simulation to determine which aspects of the coronal signatures identified in the LASCO images can be produced by an erupting three-dimensional FR. We analyze results obtained with an Adaptively Refined MHD Solver (ARMS; DeVore and Antiochos, 2008) simulation of the 'magnetic breakout' CME initiation mechanism (Antiochos, DeVore, and Klimchuk, 1999; Lynch *et al.*, 2004, 2008) and the subsequent FR-CME propagation in the low corona to construct synthetic coronagraph images we can directly compare to observations.

4.1. Description of the MHD Simulations and Eruption Overview

The ARMS simulation data analyzed herein come from the 'Left-Handed' CME eruption described by Lynch *et al.* (2009) in a fully three-dimensional, globally multipolar magnetic field configuration. The solar atmosphere is initially in gravitationally stratified equilibrium with spherically symmetric density, pressure, and temperature profiles given in Lynch *et al.* (2008). The maximum field strengths in the AR are ± 40 G which, while lower than observed values in the range 10 – 100, yield a low-β plasma in the CME source region ($\beta \sim 10^{-3}$) and throughout the computational domain. Thus, the ARMS simulation data provide a physically valid, albeit idealized, representation of the magnetically driven eruption process. Here, we briefly review the phases of the moderate speed Lynch *et al.* (2009) breakout CME eruption:

i) *Energization* ($0 \leq t \leq 10000$ s): Surface shearing flows are applied adjacent to the polarity inversion line (PIL) of the active region (AR) resulting in the gradual accumulation of magnetic energy ($E_{\rm M} \sim 10^{31}$ ergs) as the low-lying, strong AR fields are stressed. This sheared field component parallel to the AR PIL will become the FR-CME axial field.

ii) *Breakout Reconnection* ($t \gtrsim 5000$ s): As the sheared portion of the AR flux expands, the overlying coronal null point becomes distorted and flattened, forming a current sheet at the separatrix between the AR and background flux system. Continued expansion compresses the current sheet and drives magnetic reconnection which transfers overlying restraining background flux out of the way of the expanding stressed field which, in turn, increases expansion, and drives more reconnection in a runaway positive feedback scenario. The breakout reconnection facilitated expansion shows up as a smooth increase in kinetic energy to $E_{\rm K} \sim 3 \times 10^{29}$ ergs.

iii) *Eruptive Flare Reconnection* ($t \gtrsim 10000$ s): The runaway sheared arcade expansion drive the formation and elongation of a radial current sheet above the PIL leading to the start of flare reconnection in the shear channel. The eruptive flare reconnection rapidly releases stored magnetic energy ($\Delta E_M \sim 7 \times 10^{30}$ ergs) through the magnetic reconfiguration and formation of flare loop arcades, supplies material and momentum to the ejecta via strong reconnection jet outflow (E_K increases to 1.05×10^{30} ergs), and, in the breakout model, *creates* the magnetic flux rope during the eruption process by generating highly twisted flux surrounding the erupting sheared field core.

The top row of Figure 5 plots representative magnetic field lines for $t = \{11\,000, 12\,000, 13\,000\}$ seconds during the CME eruption. Field lines representing the FR sheared field core are plotted in green, the reconnection-created FR-CME twist component in magenta, and the background field in dark blue.

There are two primary challenges associated with MHD modeling of very fast CMEs and their subsequent shock generation in the low corona. The first is a correct description of the thermodynamics, field and plasma structures of the steady-state background solar wind. The lack of a single, widely accepted theory for coronal heating means, in practice, every simulation relies on idealized, parametrized heating terms and calculates the resulting solar wind and open field structure from the balance of forces. The second major modeling challenge is overcoming the computational limitations associated with the magnetic field strength in CME source regions. The MHD numerical time step is limited by the Alfvén speed which makes the temporal evolution of kilogauss fields that are routinely observed in large active regions prohibitively expensive. Despite these model limitations, numerical MHD simulations are becoming increasingly sophisticated and capable. For example, the

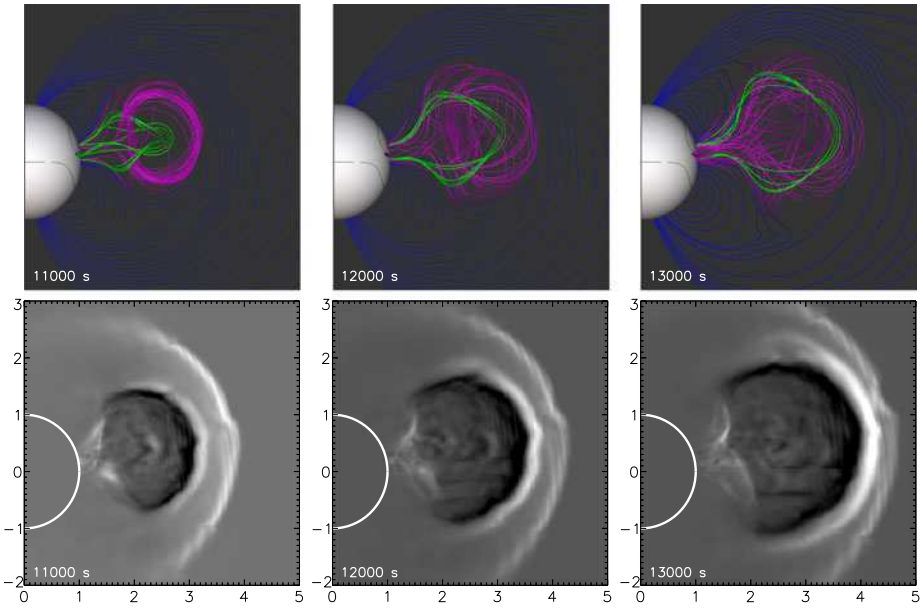

Figure 5 Top row: MHD simulation results of a breakout CME eruption in the coronagraph field of view for a limb event. The FR ejecta field lines are green, magenta for the sheared field core and reconnection generated twisted flux. Bottom row: Synthetic running-difference (RD) coronagraph images constructed from the simulation's density evolution.

field strengths and self-consistent pre-eruption energization used by Lynch *et al.* (2008) and Roussev, Lugaz, and Sokolov (2008) were sufficient to initiate CMEs with eruption speeds on the order of 1200 – 1400 $\mathrm{km\,s^{-1}}$. In simulations that bypass the difficulty of the pre-eruption evolution, fast eruptions can be generated with CME speeds $> 2000\ \mathrm{km\,s^{-1}}$, drive shock formation as low as $\sim 1.6\ \mathrm{R_\odot}$, and can produce complex white-light structures in synthetic coronagraph and HI images (Roussev, Lugaz, and Sokolov, 2008; Manchester *et al.*, 2008; Lugaz *et al.*, 2011).

4.2. Comparison Between Synthetic and LASCO CME Images

To construct synthetic coronagraph images, we use a version of the SolarSoft routine `eltheory.pro` to calculate the total brightness in a regular 2D Cartesian array of lines of sight that sample the spherical 3D MHD density data at every simulation output time. From these synthetic total brightness images we then construct base-difference (BD) images as $B(t) - B(0)$ and running-difference (RD) images as $B(t) - B(t - \Delta t)$. The temporal cadence, Δt, of our simulated data is 250 s. The bottom row of Figure 5 plots the synthetic RD images such that the radial propagation of the center of the FR-CME lies exactly in the RD image plane of the sky (POS) corresponding to the viewpoint of the 3D field line visualization.

In Figure 6 we have constructed a series of viewpoint orientations to examine morphological features of the synthetic coronagraph images. The top row indicates schematically the CME orientation with respect to the image POS and the middle, bottom rows plot the corresponding BD, RD images respectively. From left to right, the angles between the radial propagation of the center of the FR-CME and the image POS are {0, 45, 90, 0} degrees, with

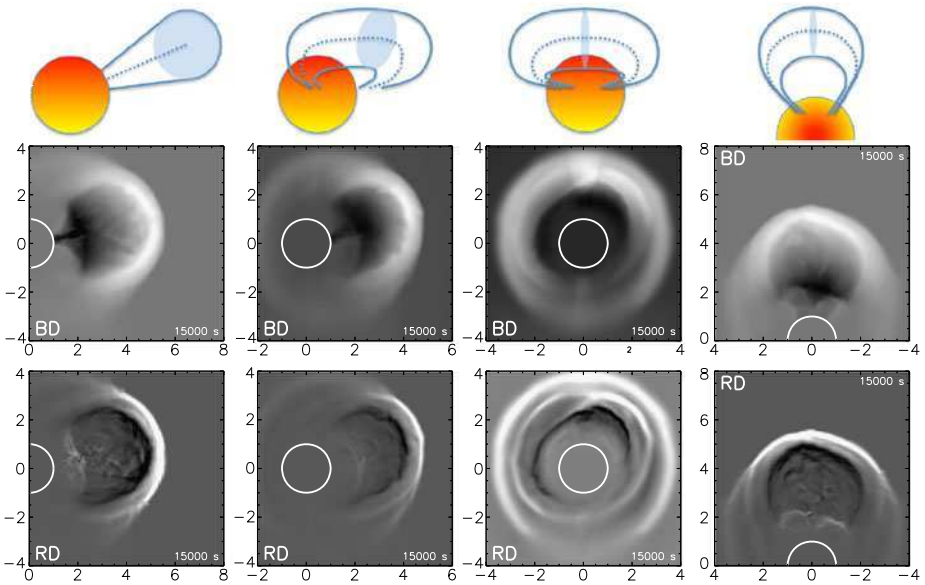

Figure 6 Top row: Schematic images depicting the 3D FR orientation with respect to the synthetic image POS. The middle, bottom rows plot the synthetic base-difference (BD), running-difference (RD) images, respectively. Both the bright CME front and the CME-driven shock/expansion wave can be seen in these images.

the fourth column representing a vantage point from the North solar pole looking down on the eruption.

The shock front, the bright CME front, and the FR cavity are each clearly seen in either the RD or BD images. The CME front morphology varies between a loop-like CME (within 45° from the limb) to a halo CME (at 90° from the limb) similarly to the actual observations.

While the idealized MHD simulation produces both the shock front/expansion wave and the bright leading edge of the ejecta ahead of the FR-CME driver, there is no corresponding high density plug of material associated with the FR core. This limitation was also present in the axisymmetric models (*e.g.*, Lynch *et al.*, 2004) and is due largely to our simplified pre-eruption coronal density distribution which does not include prominence material along the low-lying sheared field or the enhanced densities associated with either ARs or that would arise in a closed-field streamer belt geometry. Our simplified model background results in two main consequences. First, without dense material tracing the topology of the FR-CME core, it is difficult to distinguish between the edge-on view (Figure 6 first column, looking at the FR cross-section; compare to Figure 1) and the top-down view (Figure 6 fourth column, FR axis lies in the image POS; compare to Figure 3, bottom left) in the synthetic images. Second, the relative brightness of the CME leading edge and the shock/expansion wave do not have the same ratio as commonly observed in the coronagraph images (which, as discussed earlier, require significant contrast enhancement). Furthermore, the lack of a background with coronal streamer structures in various locations does not allow us to compare streamer deflections or the effects of coronal hole locations in this particular simulation, although these issues are an area of active research (see, *e.g.*, Lugaz *et al.*, 2011; Zuccarello *et al.*, 2012).

We also note that the synthetic shock appears very close to the CME leading edge (the driver) which is not the case for the LASCO images we have presented so far. This is an evolutionary effect, however, as Figure 5 has already shown. In our simulations, the shock is initially clearly ahead of the CME which catches up to it within $\sim$2000 sec. Of course, different speed profiles and ambient coronal configurations will result in different standoff distances. Again, our comparison here is not an attempt to model a specific CME event with a realistic background density distribution, but rather to present an idealized general case of the appearance of a generic shock-driving FR-CME in a coronagraph field of view.

It is precisely the generality of our simulation that makes the comparison to two LASCO events especially striking, as illustrated in Figure 7. The simulated synthetic BD images (right column) show the diffuse intensity region leading the bright CME front which is associated with the boundary of the magnetic FR structure, exactly as we proposed in Sections 2 and 3. Yellow arrows denote the shock front, green arrows denote the CME leading edge. Despite not capturing the observed sharpness or intensity of the CME front, the simulations do show that the faint halo outline in the LASCO images corresponds to the shock envelope. Therefore, our five-part CME structure is a completely straight-forward interpretation and a natural consequence of the eruption of a 3D FR-CME.

5. The Relationship between Ejected Prominence and CME Flux Rope

Having discussed the nature of the front and the cavity, we turn our attention to the core, the last component of 'three-part'-CMEs. The core has been associated with the erupting prominence ever since combined Hα and coronagraphic observations demonstrated the co-location of the two structures (*e.g.*, Hildner *et al.*, 1975; Illing and Hundhausen, 1985). The fuzziness of the core compared to the filamentary structure of prominences in Hα and He I

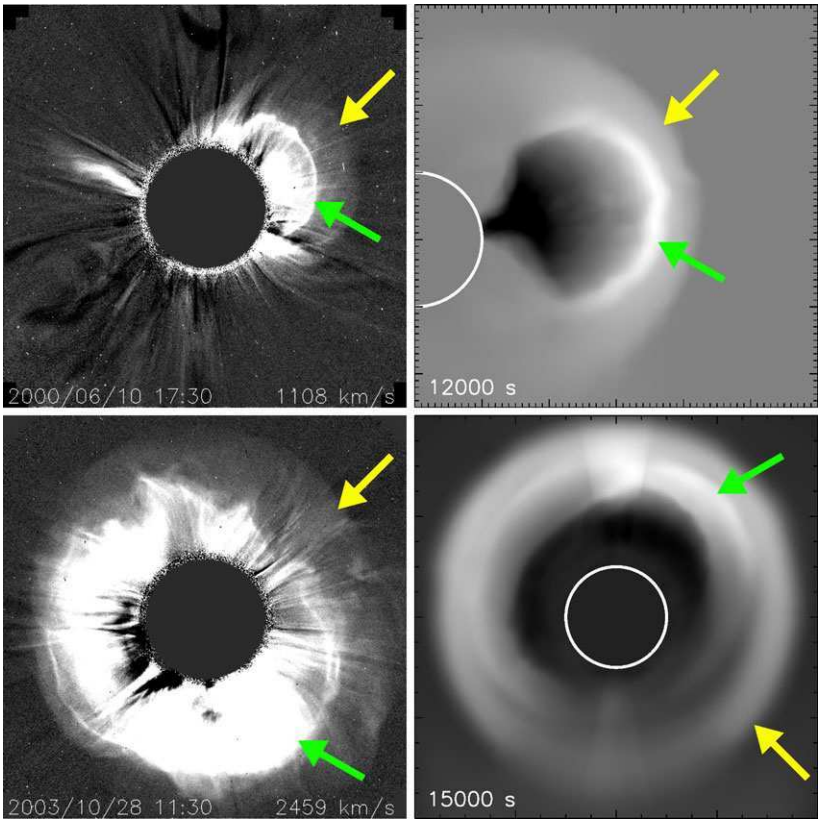

Figure 7 Comparison between LASCO excess mass images (left column) and synthetic base-difference images from our MHD simulations (right column). There is a very good correspondence between observed and simulated structures, despite the idealized nature of the simulation. The yellow arrows denote the shock/expansion wave front and the green arrows denote the CME leading edge density enhancement. The projected speeds for the LASCO CMEs are also shown.

observations is attributed to the progressive ionization and heating of the chromospheric plasma within the prominence as the structure is erupting outwards.

Of the many unclear aspects on the role and evolution of prominence in eruptive events, there are two that pertain to our discussion here. Namely, what the spatial relationship is between the core (and prominence) to the cavity and, why *in-situ* detections of chromospheric material within CMEs are so rare.

The first question stems from the early interpretations of the prominence as a flux rope and its identification with the CME cavity (Low and Hundhausen, 1995). Although prominences exhibit helical structures when they erupt, the large number of combined observations with LASCO (in white light) and EIT (in He I 304 Å) have shown that the cavity is not the prominence itself. They have also shown that the core does not lie in the center of the cavity as was thought in the past (see Figure 10 in Cliver *et al.*, 1986). Rather the prominence lies at the bottom of the cavity, the cool plasma suspended in the dips of the FR field lines by the balance between gravity and magnetic tension forces.

While these concepts are widely accepted thanks to the extensive observations of quiescent cavities and prominences (Gibson *et al.*, 2006), there seems to be a lingering confusion

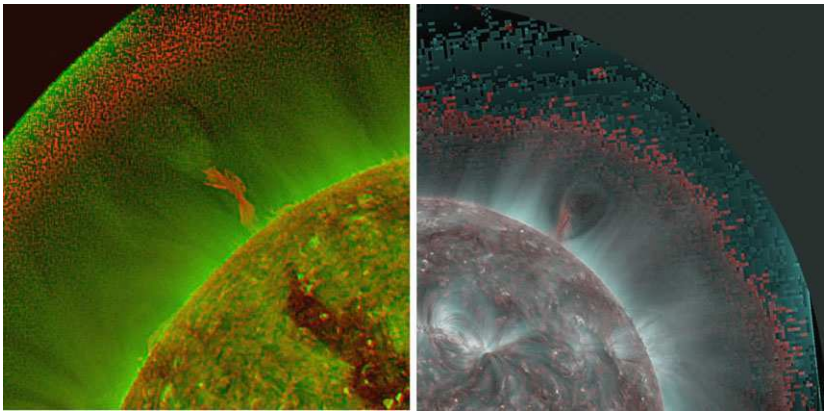

Figure 8 Left: Image of a prominence eruption at the northeast limb on 12 June 2010 using a composite of AIA 193 Å (green) and 304 Å (red) channels. Right: Snapshot of a prominence eruption at the northwest limb on 28 February 2010 using a composite of EUVI-A 195 Å (silver) and 304 Å (red) channels. Both images are snapshots from the online movies.

on the location and importance of the prominence relative to the erupting FR or cavity. The high-resolution observations from SECCHI and the *Atmospheric Imaging Assembly* (AIA; Lemen *et al.*, 2012) can now put this issue to rest. For example, Régnier, Walsh, and Alexander (2011) have presented multi-wavelength AIA observations of a polar crown filament during its early eruption stages where they image both the cool prominence and the hotter FR. The high spatial resolution of AIA reveals cool prominence plasma in 304 Å embedded in field lines at the bottom of the FR visible in 193 Å ($\sim$1.4 MK). The 193 Å emission has the typical 'horn' morphology we discussed in Section 2 and frequently seen in the EIT images during Cycle 23. To demonstrate how common these structures are, we present two more examples in Figure 8.

On the left, we show a snapshot from a prominence eruption at the northeast limb on 12 June 2010 captured by the AIA instrument. To demonstrate the relative locations of the FR and prominence we combined the 193 Å (green) and 304 Å (red) AIA channels after enhancing the individual images through our wavelet processing algorithm (Stenborg, Vourlidas, and Howard, 2008). The accompanying movie demonstrates two important aspects of the eruption:

i) the pre-existing cavity is not actually empty but it is filled with plasma at coronal temperatures, and
ii) most of the cool prominence material returns to the surface and is not ejected with the rest of the CME.

On the right, we show a similar observation from SECCHI/EUVI-A taken on 28 February 2010. Here the 195 Å images are shown in silver color. We observe strong circular motions in the center of the cavity during the early part of the event previously noted by Wang and Stenborg (2010) who did not comment on the temperature characteristics on these motions. Here, we see that the motions are associated with extensions of 304 Å emission into the center of the cavity which exhibits a very clear FR morphology. The cool plasma seems to disappear after its injection until a new extension brings in another quantity of cool material into the cavity. Hence, the rotations within the cavity seem to be driven by the episodes of heating of chromospheric plasma. In contrast to the 12 June 2010 event, the prominence

erupts carrying a significant amount of cool plasma outwards. No return flows are evident in this event.

These EUV observations are quite clear. The prominence is not the cavity. It is the core. The core is not located at the center of the cavity. It is located at the trailing edge. It may, however, appear to be at the center or at other locations due to projection effects. Much of the chromospheric material either drains back to the surface or heats to coronal temperatures or both during the early stages of the eruption. This is likely the reason for the scarcity of *in-situ* detections of such cool material in the inner heliosphere.

Finally, one may question the generality of our conclusions since we have used as examples prominence eruptions from polar crown and generally quiescent areas of the corona. This was done mainly for convenience. Polar crown filament eruptions are both spectacular and slow thus providing a large sample of clear highly detailed structures at various stages of activity. It is much harder to find fast, explosive events with clear structures due to their fast evolution and the large disturbances they create in the surrounding corona. However, detailed analyses of impulsive events do reach the same conclusions. For example, Patsourakos, Vourlidas, and Stenborg (2010) were able to detect the expanding cavity and follow the formation of the three-part structure within the center of an active region during a very impulsive event (peak acceleration $\sim 1.5\ \mathrm{km\,s^{-2}}$). Similarly, Cheng *et al.* (2012) obtained clear distance–time plots for an expanding cavity followed by a spectacular filament for an event reaching (short-lived) accelerations close to $3\ \mathrm{km\,s^{-2}}$.

6. Revisiting the LASCO Statistics: How Many FR-CMEs Are There?

Having addressed the origins of the various sub-structures of a CME in the coronagraph and EUV images, we are now in position to answer one of the most common questions on CME studies: How many FR-CMEs are there? As noted in the introduction, the last studies to undertake that question used *Solar Maximum Mission* (SMM) data (Burkepile and St. Cyr, 1993; Krall, 2007). The answer (~ 30 %) has been quoted ever since. But does it still hold after the observations of thousands of CMEs? Besides, we want to make sure that our examples of FR-indicative CME morphologies are indeed representative of the CME phenomenon as a whole.

6.1. Morphological Classification of the CDAW Database

We have undertaken the task to go over the full CDAW database and visually classify the events according to their morphology. Based on our discussion so far, and on our personal experience with the LASCO images, we decided to classify the events into five categories (to be compared to the ten categories in Howard *et al.*, 1985) as follows.

Flux Rope: CMEs that exhibit a clear three-part morphology (Figure 1).

Loop: CMEs with a bright, filamentary loop but otherwise lacking a cavity and/or a core. Good indicators for the existence of shock ('two-front' morphology, Section 3).

Jet: Narrow CMEs ($\lesssim 40°$) lacking a sharp front, detailed sub-structure, or circular morphology.

Failed: Events that disappear in the C3 field of view despite being bright enough in the C2 field to be labeled as 'CMEs'. Their disappearance cannot be explained by lack of observations, overlapping CMEs, or other instrumental reasons. These events were discussed in Vourlidas *et al.* (2010).

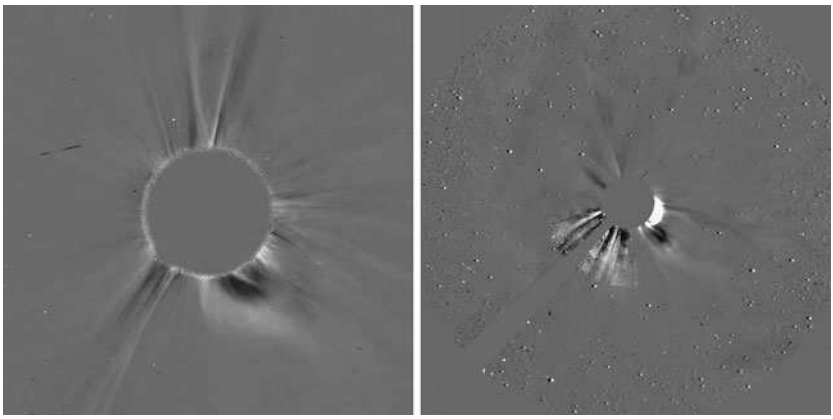

Figure 9 Left: Example of an 'Outflow' event. The CME lacks a three-part morphology, it is too wide to be a 'Jet' event, and the front is not sharp enough to be classified as a 'Loop'-CME. Right: Example of an 'Unknown' category event. The event propagating along the C3 occulter does not show any of the characteristics of a CME and it is too faint to provide accurate measurements for any parameter. Such events should not be included in CME lists. Both images are snapshots from the online movies.

Outflow: Events wider that jets, without clear loop front or cavity. They may be as large as regular CMEs and may contain filamentary material (Figure 9, left).

Unknown: This 'catch-all' category contains mostly wrongly identified events, events with too few observations (<4), and events that cannot be classified in any of the other categories due to poor observations, such as presence of cosmic rays or data dropouts (Figure 9, right).

First, we excluded events with width less than 20° and with less than four observations. For the classification, we used only mass images (Vourlidas *et al.*, 2010). We displayed all available mass images (LASCO C2 and C3) for each event with the same contrast ($\pm 5 \times 10^{10}$ gr pix^{-1}). When the morphology was not apparent, we used a movie of the mass images to get a better sense for the development of the event as a function of time and distance. We excluded the events in the 'Unknown' category from the statistics since we consider them as erroneous and/or unreliable detections. Our results are shown in Table 1.

Table 1 Sampling the distribution of CME types and the ratio of flux-rope CMEs through the solar cycle.

Type	1997	1998	2000	2002	2004	2008	2010
Flux Rope	29	42	86	54	53	35	154
Loop	31	43	191	100	79	9	56
Outflow	48	96	282	145	126	56	209
Jet	5	16	85	17	32	5	32
Failed	10	33	54	10	67	14	30
Unknown	74	98	276	161	220	42	113
Total	224	357	984	597	587	162	476
FR-CMEs	40 %	33 %	39 %	35 %	36 %	37 %	43 %

6.2. Statistical Results

For the purposes of this work, we analyzed seven out of the 16 years of available CDAW mass measurements spread over Cycle 23. This is a sufficiently large sample to extract robust estimates for the rates of occurrence of the various morphologies. We plan to report on the statistics of the full CDAW catalog in a forthcoming publication.

One of the first interesting results from this exercise is the rather large percentage of 'Unknown' events. They comprise 984 out of 3387 events or 29 % of the sample. Recall that the 'Unknown' category includes events that are not CMEs or even outflows, events that are part of a larger CME and should not count as separate entries, and events with measurements ending prematurely. In other words, these events should not be counted in the statistics or other analyses of the CDAW catalog.

Excluding the 'Unknown' events, we find that the class of unambiguous FR-CMEs, *which consists of the sum of 'Flux Rope' plus 'Loop' classes*, comprises 40 % of the total number of CMEs (962/2403 events). There is no obvious correlation with solar cycle but there is a slight hint. The highest percentages of FR-CMEs occur in 1997 and 2010. It remains to be seen whether this result is statistically significant. We emphasize that the 40 % of FR-CMEs is a *lower* limit for the existence of FRs. Some of the 'Outflow' events could be FRs. Indeed many contain hints of 'three-part' structures or cavities, but they are either too faint or the background corona is too disturbed by previous events, to make a conclusive classification. So we choose to err on the side of caution and not include them in the FR-related classes, at this point.

7. Discussion and Conclusions

Our aim is to provide convincing evidence of the CME as an erupting FR. To that end, we have used a variety of EUV and white light observations, MHD simulations, statistics, and have considered projection effects and theoretical predictions. Leaving the question of CME initiation aside, we found that the following picture can lead to a self-consistent interpretation of the observations across many wavelength ranges and is in agreement with the majority (if not all) of our current theoretical understanding of explosive energy release from the Sun.

Basically, a CME is the eruption of a magnetic flux rope with its emission measure dominated by coronal-temperature plasma, carrying a prominence along its bottom dips, piling up the overlying streamer plasma, and driving a wave ahead (if the acceleration is sufficiently high). This interpretation has long been adopted for the 'three-part'-CMEs, as we discussed earlier.

The novelty in this work is the interpretation of the bright loop front as the pileup of material *at the boundary of the flux rope* irrespective of the 'three-part' appearance. The interpretation is strongly supported by the MHD simulations and straightforward physical reasoning (Section 4). A FR structure propagating through plasma presents an extended obstacle against which the material is piled up and transported outwards. The narrow width and brightness of that front further suggests that the pileup occurs over a sharp boundary. Such a boundary is expected between the closed FR fields and the ambient magnetic field. The sharpness of the boundary may depend on the rate of magnetic field influx in the FR during its formation or the initial acceleration and starting height. Such effects have important connections to theories of CME initiation and can be investigated now.

The other novelty is the introduction of the *'two-front'* morphology by pointing out the existence of faint, relatively sharp, fronts ahead of the bright loop front. The interpretation

of the faint front as density compression by a wave (or shock, depending on speed) is again supported by MHD simulations, observations and physical expectations. The stark observational differences between the bright loop front and diffuse outer front clearly point to a different origin. The diffuse fronts are well-defined, faint, followed by diffuse emission, and they can be very extended, and envelope the loop fronts. The loop fronts, in turn, are sharp, bright, followed by emission depletions; they have well-defined extents and are behind the diffuse fronts. The faint diffuse fronts appear only during fast eruptions, and their characteristics, especially the weakness of their emission and lack of post-front depletion, are strong indications that these fronts are results of local density compression and not of transported piled-up plasma. The, albeit few, 3D reconstructions of the density profile across the front (Ontiveros and Vourlidas, 2009) can readily explain the profile as a result of LOS integration and recover compression ratios in agreement with theoretical expectations (less than four). Besides its importance for understanding coronal shocks, the identification of the 'two-front' morphology allows an understanding of the geometry of halo CMEs, as it can help us distinguish among shock, streamer deflections and FR signatures in the coronagraph images. In that way, we can now obtain accurate outlines of the FR (or the shock, depending on the problem at hand) which should lead to better input to CME propagation models.

The identification of these two features leads to a much simpler classification of CME white light morphologies. We used four categories (ignoring the 'Unknown' category) compared to nine in Howard *et al.* (1985). Two of them ('FR' and 'Loop') refer to the same FR intrinsic structure as we have argued. Jet-CMEs also contain helical structures as recent research has shown (Patsourakos *et al.*, 2008; Pariat, Antiochos, and DeVore, 2009; Nisticò *et al.*, 2010). Thus, our classification is essentially reduced to events with and events without *apparent* helical topologies. The helical topology may not be visible in the latter for several reasons. They may propagate at large angles from the POS (Sheeley and Wang, 2007) or through areas disturbed by previous events. They may be too compact to discern their cavity morphology without favorable projections (Wang and Sheeley, 2006). Finally some of these events do not appear to be CMEs in the first place, failing to reach large distances in the corona (called 'failed' CMEs by Vourlidas *et al.*, 2010). A certain number of the remaining events appear to be related to Hα and/or 304 Å surges similar to the event studied by Vourlidas *et al.* (2003). The low coronal signatures of these events do not exhibit any particular morphology or geometry, and hence they tend to appear as semi-amorphous clouds, with the occasional traces of cool material.

Our final estimate of 41 % for the rate of occurrence of FR-CMEs in the LASCO data may not look very different from the widely quoted number of 30 %. However, one must first consider the size of the event samples in past morphological works. Munro *et al.* (1979) reported a 26 % occurrence of 'Loop'-CMEs in a sample of 77 SMM CMEs, while Wagner (1984) found loop and bubble CMEs in 80 % of 65 SMM CMEs. Obviously, selection bias is important with such small event samples. The largest morphological study to date categorized 998 *Solwind* CMEs, of which 31.3 % belonged to an FR-CME class (we summed the statistics for the following structural classes: curved front, loop, streamer blowout, fan) (Howard *et al.*, 1985). We base our statistics here on a sample of 2970 events, 3× larger than the *Solwind* sample, and it is still expanding. We will classify the full LASCO database in the near future. Therefore, we feel that our numbers in Table 1 are quite robust and a large improvement over past work.

The central question of this *Topical Issue* is whether all CMEs are flux ropes. To provide a conclusive answer (to the extent possible in science), we attacked the problem in several ways: multiple viewpoint coronagraphic observations of CMEs, multi-thermal EUV observations of the pre-erupting structures, 3D MHD simulations, and large sample statistics. We summarize our findings as follows:

- The detection of a bright filamentary front in CMEs is a clear indication of the existence of an FR even if the event does not exhibit the classical three-part morphology.
- At least 41 % of CMEs exhibit clear FR signatures ('three-part' or 'loop') in the coronagraph images.
- The 'two-front' morphology (faint front followed by a bright loop) is a reliable indicator of a CME-driven wave (or shock, depending on speed).
- The FR can be separated from the shock signatures in images of halo CMEs, at least in locations where the bright loop appears.
- MHD simulations are able to capture the main structural properties of white light CMEs.
- The prominence is not the cavity and is not the FR, but it is the core. The cool prominence material rests on the dips of the field lines comprising the FR (in the case of pre-existing FR, at least).
- The majority of the prominence material either drains to the surface or is heated to coronal temperatures during the early phases of the eruption. This may be the reason for the scarcity of *in-situ* detections of cool material.
- A typical fast CME comprises five parts: shock front, diffuse sheath, bright front, cavity, and core.

Our discussion suggests that it is time to rethink the original definition for a CME (Hundhausen *et al.*, 1984), as expressed in Schwenn (2006): "*We define a CME to be an observable change in coronal structure that* 1) *occurs on a time scale of a few minutes and several hours and* 2) *involves the appearance* (*and outward motion*) *of a new, discrete, bright, white light feature in the coronagraph field of view*." This definition manages to be broad (no mention of the physical origin or nature of the 'structure') and narrow (CME is defined as a white light feature observed by a coronagraph) at the same time. It may have been an appropriate definition during the times of exploratory CME research, sparse wavelength coverage, and simplified physical models. But times have changed. We are regularly studying CMEs with multiple instruments and wavelengths, have accumulated CME observations spanning a full solar cycle, and are asking highly detailed questions with their modeling. Thus, it may be useful to derive a more precise CME definition, using physically based terms, at least for the events exhibiting clear FR structures (FR-CMEs). Based on the work presented here and in Vourlidas *et al.* (2010), we propose the following definition:

We define an FR-CME to be the eruption of a coherent magnetic, twist-carrying coronal structure with angular width of at least 40° *and able to reach beyond* 10 $R_\odot$ *which occurs on a time scale of a few minutes to several hours*.

The next challenge now is whether we can apply this definition to all CMEs (hence replace 'FR-CME' with 'CME' above). In other words, we propose that the proper questions we should be asking is not *'are all CMEs flux ropes?'* but rather '*Are there any CMEs that are not FR-CMEs?*'

Acknowledgements The work of AV and RAH is supported by NASA contract S-136361-Y to the Naval Research Laboratory. BJL and YL acknowledge support from AFOSR YIP FA9550-11-1-0048, NASA NNX11AJ65G, and NNX08AJ04G. We thank G. Stenborg for his continuing efforts to provide better quality solar images. SOHO is an international collaboration between NASA and ESA. LASCO was constructed by a consortium of institutions: the Naval Research Laboratory (Washington, DC, USA), the Max-Planck-Institut fur Aeronomie (Katlenburg-Lindau, Germany), the Laboratoire d'Astronomie Spatiale (Marseille, France) and the University of Birmingham (Birmingham, UK). The LASCO CME catalog is generated and maintained at the CDAW Data Center by NASA and The Catholic University of America in cooperation with the Naval Research Laboratory. The SECCHI data are produced by an international consortium of the NRL, LMSAL and NASA GSFC (USA), RAL and Univ. Bham (UK), MPS (Germany), CSL (Belgium), IOTA and IAS (France).

References

Antiochos, S.K., DeVore, C.R., Klimchuk, J.A.: 1999, *Astrophys. J.* **510**, 485. doi:10.1086/306563.

Anzer, U., Pneuman, G.W.: 1982, *Solar Phys.* **79**, 129. doi:10.1007/BF00146978.

Bemporad, A., Mancuso, S.: 2010, *Astrophys. J.* **720**, 130. doi:10.1088/0004-637X/720/1/130.

Brueckner, G.E., Howard, R.A., Koomen, M.J., Korendyke, C.M., Michels, D.J., Moses, J.D., Socker, D.G., Dere, K.P., Lamy, P.L., Llebaria, A., Bout, M.V., Schwenn, R., Simnett, G.M., Bedford, D.K., Eyles, C.J.: 1995, *Solar Phys.* **162**, 357. doi:10.1007/BF00733434.

Burkepile, J.T., St. Cyr, O.C.: 1993, *Tech. Note TN-369+STR* **93**, 26556.

Burlaga, L.F., Klein, L., Sheeley, N.R. Jr., Michels, D.J., Howard, R.A., Koomen, M.J., Schwenn, R., Rosenbauer, H.: 1982, *Geophys. Res. Lett.* **9**, 1317. doi:10.1029/GL009i012p01317.

Cane, H.V., Richardson, I.G.: 2003, *J. Geophys. Res.* **108**, 1156. doi:10.1029/2002JA009817.

Chen, J., Garren, D.A.: 1993, *Geophys. Res. Lett.* **20**, 2319. doi:10.1029/93GL02426.

Chen, J., Howard, R.A., Brueckner, G.E., Santoro, R., Krall, J., Paswaters, S.E., St. Cyr, O.C., Schwenn, R., Lamy, P., Simnett, G.M.: 1997, *Astrophys. J. Lett.* **490**, L191. doi:10.1086/311029.

Chen, J., Santoro, R.A., Krall, J., Howard, R.A., Duffin, R., Moses, J.D., Brueckner, G.E., Darnell, J.A., Burkepile, J.T.: 2000, *Astrophys. J.* **533**, 481. doi:10.1086/308646.

Chen, P.F.: 2011, *Living Rev. Solar Phys.* **8**, 1.

Cheng, X., Zhang, J., Olmedo, O., Vourlidas, A., Ding, M.D., Liu, Y.: 2012, *Astrophys. J. Lett.* **745**, L5. doi:10.1088/2041-8205/745/1/L5.

Cliver, E.W., Dennis, B.R., Kiplinger, A.L., Kane, S.R., Neidig, D.F., Sheeley, N.R. Jr., Koomen, M.J.: 1986, *Astrophys. J.* **305**, 920. doi:10.1086/164306.

Cremades, H., Bothmer, V.: 2004, *Astron. Astrophys.* **422**, 307.

Crifo, F., Picat, J.P., Cailloux, M.: 1983, *Solar Phys.* **83**, 143. doi:10.1007/BF00148249.

Dasso, S., Nakwacki, M.S., Démoulin, P., Mandrini, C.H.: 2007, *Solar Phys.* **244**, 115. doi:10.1007/s11207-007-9034-2.

Dere, K.P., Brueckner, G.E., Howard, R.A., Michels, D.J., Delaboudiniere, J.P.: 1999, *Astrophys. J.* **516**, 465. doi:10.1086/307101.

DeVore, C.R., Antiochos, S.K.: 2008, *Astrophys. J.* **680**, 740. doi:10.1086/588011.

Forbes, T.G.: 1990, *J. Geophys. Res.* **95**, 11919. doi:10.1029/JA095iA08p11919.

Gibson, S.E., Foster, D., Burkepile, J., de Toma, G., Stanger, A.: 2006, *Astrophys. J.* **641**, 590. doi:10.1086/500446.

Gopalswamy, N., Thompson, W.T., Davila, J.M., Kaiser, M.L., Yashiro, S., Mäkelä, P., Michalek, G., Bougeret, J.-L., Howard, R.A.: 2009, *Solar Phys.* **259**, 227. doi:10.1007/s11207-009-9382-1.

Gosling, J.T., Hildner, E., MacQueen, R.M., Munro, R.H., Poland, A.I., Ross, C.L.: 1974, *J. Geophys. Res.* **79**, 4581. doi:10.1029/JA079i031p04581.

Hildner, E., Gosling, J.T., Hansen, R.T., Bohlin, J.D.: 1975, *Solar Phys.* **45**, 363. doi:10.1007/BF00158456.

Howard, R.A., Michels, D.J., Sheeley, N.R. Jr., Koomen, M.J.: 1982, *Astrophys. J. Lett.* **263**, L101. doi:10.1086/183932.

Howard, R.A., Sheeley, N.R. Jr., Michels, D.J., Koomen, M.J.: 1985, *J. Geophys. Res.* **90**, 8173.

Howard, R.A., Moses, J.D., Vourlidas, A., Newmark, J.S., Socker, D.G., Plunkett, S.P., Korendyke, C.M., Cook, J.W., Hurley, A., Davila, J.M., Thompson, W.T., St Cyr, O.C., Mentzell, E., Mehalick, K., Lemen, J.R., Wuelser, J.P., Duncan, D.W., Tarbell, T.D., Wolfson, C.J., Moore, A., Harrison, R.A., Waltham, N.R., Lang, J., Davis, C.J., Eyles, C.J., Mapson-Menard, H., Simnett, G.M., Halain, J.P., Defise, J.M., Mazy, E., Rochus, P., Mercier, R., Ravet, M.F., Delmotte, F., Auchere, F., Delaboudiniere, J.P., Bothmer, V., Deutsch, W., Wang, D., Rich, N., Cooper, S., Stephens, V., Maahs, G., Baugh, R., McMullin, D., Carter, T.: 2008, *Space Sci. Rev.* **136**, 67. doi:10.1007/s11214-008-9341-4.

Hundhausen, A.J.: 1987, In: Pizzo, V.J., Holzer, T., Sime, D.G. (eds.) *Sixth International Solar Wind Conference*, 181.

Hundhausen, A.J., Sawyer, C.B., House, L., Illing, R.M.E., Wagner, W.J.: 1984, *J. Geophys. Res.* **89**, 2639. doi:10.1029/JA089iA05p02639.

Illing, R.M.E., Hundhausen, A.J.: 1985, *J. Geophys. Res.* **90**, 275. doi:10.1029/JA090iA01p00275.

Isavnin, A., Kilpua, E.K.J., Koskinen, H.E.J.: 2011, *Solar Phys.* **273**, 205. doi:10.1007/s11207-011-9845-z.

Kaiser, M.L., Kucera, T.A., Davila, J.M., St. Cyr, O.C., Guhathakurta, M., Christian, E.: 2008, *Space Sci. Rev.* **136**, 5. doi:10.1007/s11214-007-9277-0.

Kim, R.-S., Gopalswamy, N., Moon, Y.-J., Cho, K.-S., Yashiro, S.: 2012, *Astrophys. J.* **746**, 118. doi:10.1088/0004-637X/746/2/118.

Klein, L.W., Burlaga, L.F.: 1982, *J. Geophys. Res.* **87**, 613. doi:10.1029/JA087iA02p00613.

Krall, J.: 2007, *Astrophys. J.* **657**, 559. doi:10.1086/510191.

Krall, J., St. Cyr, O.C.: 2006, *Astrophys. J.* **652**, 1740. doi:10.1086/508337.

Kuperus, M., Raadu, M.A.: 1974, *Astron. Astrophys.* **31**, 189.

Lemen, J.R., Title, A.M., Akin, D.J., Boerner, P.F., Chou, C., Drake, J.F., Duncan, D.W., Edwards, C.G., Friedlaender, F.M., Heyman, G.F., Hurlburt, N.E., Katz, N.L., Kushner, G.D., Levay, M., Lindgren, R.W., Mathur, D.P., McFeaters, E.L., Mitchell, S., Rehse, R.A., Schrijver, C.J., Springer, L.A., Stern, R.A., Tarbell, T.D., Wuelser, J.-P., Wolfson, C.J., Yanari, C., Bookbinder, J.A., Cheimets, P.N., Caldwell, D., Deluca, E.E., Gates, R., Golub, L., Park, S., Podgorski, W.A., Bush, R.I., Scherrer, P.H., Gummin, M.A., Smith, P., Auker, G., Jerram, P., Pool, P., Soufli, R., Windt, D.L., Beardsley, S., Clapp, M., Lang, J., Waltham, N.: 2012, *Solar Phys.* **275**, 17. doi:10.1007/s11207-011-9776-8.

Lepping, R.P., Burlaga, L.F., Jones, J.A.: 1990, *J. Geophys. Res.* **95**, 11957. doi:10.1029/JA095iA08p11957.

Low, B.C., Hundhausen, J.R.: 1995, *Astrophys. J.* **443**, 818. doi:10.1086/175572.

Lugaz, N., Downs, C., Shibata, K., Roussev, I.I., Asai, A., Gombosi, T.I.: 2011, *Astrophys. J.* **738**, 127. doi:10.1088/0004-637X/738/2/127.

Lynch, B.J., Antiochos, S.K., MacNeice, P.J., Zurbuchen, T.H., Fisk, L.A.: 2004, *Astrophys. J.* **617**, 589. doi:10.1086/424564.

Lynch, B.J., Antiochos, S.K., DeVore, C.R., Luhmann, J.G., Zurbuchen, T.H.: 2008, *Astrophys. J.* **683**, 1192. doi:10.1086/589738.

Lynch, B.J., Antiochos, S.K., Li, Y., Luhmann, J.G., DeVore, C.R.: 2009, *Astrophys. J.* **697**, 1918. doi:10.1088/0004-637X/697/2/1918.

Ma, S., Raymond, J.C., Golub, L., Lin, J., Chen, H., Grigis, P., Testa, P., Long, D.: 2011, *Astrophys. J.* **738**, 160. doi:10.1088/0004-637X/738/2/160.

Manchester, W.B. IV, Vourlidas, A., Tóth, G., Lugaz, N., Roussev, I.I., Sokolov, I.V., Gombosi, T.I., De Zeeuw, D.L., Opher, M.: 2008, *Astrophys. J.* **684**, 1448. doi:10.1086/590231.

Munro, R.H., Gosling, J.T., Hildner, E., MacQueen, R.M., Poland, A.I., Ross, C.L.: 1979, *Solar Phys.* **61**, 201. doi:10.1007/BF00155456.

Nisticò, G., Bothmer, V., Patsourakos, S., Zimbardo, G.: 2010, *Ann. Geophys.* **28**, 687. doi:10.5194/angeo-28-687-2010.

Ontiveros, V., Vourlidas, A.: 2009, *Astrophys. J.* **693**, 267. doi:10.1088/0004-637X/693/1/267.

Pariat, E., Antiochos, S.K., DeVore, C.R.: 2009, *Astrophys. J.* **691**, 61. doi:10.1088/0004-637X/691/1/61.

Patsourakos, S., Vourlidas, A., Stenborg, G.: 2010, *Astrophys. J. Lett.* **724**, L188. doi:10.1088/2041-8205/724/2/L188.

Patsourakos, S., Pariat, E., Vourlidas, A., Antiochos, S.K., Wuelser, J.P.: 2008, *Astrophys. J. Lett.* **680**, L73. doi:10.1086/589769.

Plunkett, S.P., Vourlidas, A., Šimberová, S., Karlický, M., Kotrč, P., Heinzel, P., Kupryakov, Y.A., Guo, W.P., Wu, S.T.: 2000, *Solar Phys.* **194**, 371.

Régnier, S., Walsh, R.W., Alexander, C.E.: 2011, *Annu. Rev. Astron. Astrophys.* **533**, L1. doi:10.1051/0004-6361/201117381.

Robbrecht, E., Patsourakos, S., Vourlidas, A.: 2009, *Astrophys. J.* **701**, 283. doi:10.1088/0004-637X/701/1/283.

Rouillard, A.P.: 2011, *J. Atmos. Solar-Terr. Phys.* **73**, 1201. doi:10.1016/j.jastp.2010.08.015.

Roussev, I.I., Lugaz, N., Sokolov, I.V.: 2008, In: Li, G., Hu, Q., Verkhoglyadova, O., Zank, G.P., Lin, R.P., Luhmann, J.G. (eds.) *American Institute of Physics Conference Series*, *American Institute of Physics Conference Series* **1039**, 286. doi:10.1063/1.2982460.

Schwenn, R.: 2006, *Living Rev. Solar Phys.* **3**, 2.

Sheeley, N.R., Hakala, W.N., Wang, Y.-M.: 2000, *J. Geophys. Res.* **105**, 5081. doi:10.1029/1999JA000338.

Sheeley, N.R. Jr., Wang, Y.-M.: 2007, *Astrophys. J.* **655**, 1142. doi:10.1086/510323.

Sime, D.G., Hundhausen, A.J.: 1987, *J. Geophys. Res.* **92**, 1049. doi:10.1029/JA092iA02p01049.

Stenborg, G., Vourlidas, A., Howard, R.A.: 2008, *Astrophys. J.* **674**, 1201. doi:10.1086/525556.

Thernisien, A., Vourlidas, A., Howard, R.A.: 2009, *Solar Phys.* **256**, 111. doi:10.1007/s11207-009-9346-5.

Thernisien, A., Vourlidas, A., Howard, R.A.: 2011, *J. Atmos. Solar-Terr. Phys.* **73**, 1156. doi:10.1016/j.jastp.2010.10.019.

Thernisien, A.F.R., Howard, R.A., Vourlidas, A.: 2006, *Astrophys. J.* **652**, 763. doi:10.1086/508254.

Vourlidas, A., Bemporad, A.: 2012, A Decade of Coronagraphic and Spectroscopic Studies of CME-Driven Shocks, American Institute of Physics Conference Series, in print.

Vourlidas, A., Ontiveros, V.: 2009, In: Ao, X., Burrows, G.Z.R. (eds.) *American Institute of Physics Conference Series*, **1183**, 139. doi:10.1063/1.3266770.

Vourlidas, A., Wu, S.T., Wang, A.H., Subramanian, P., Howard, R.A.: 2003, *Astrophys. J.* **598**, 1392. doi:10.1086/379098.

Vourlidas, A., Howard, R.A., Esfandiari, E., Patsourakos, S., Yashiro, S., Michalek, G.: 2010, *Astrophys. J.* **722**, 1522. doi:10.1088/0004-637X/722/2/1522.

Wagner, W.J.: 1984, *Annu. Rev. Astron. Astrophys.* **22**, 267. doi:10.1146/annurev.aa.22.090184.001411.

Wang, Y.-M., Sheeley, N.R. Jr.: 2006, *Astrophys. J.* **650**, 1172. doi:10.1086/506611.

Wang, Y.-M., Stenborg, G.: 2010, *Astrophys. J. Lett.* **719**, L181. doi:10.1088/2041-8205/719/2/L181.

Wood, B.E., Karovska, M., Chen, J., Brueckner, G.E., Cook, J.W., Howard, R.A.: 1999, *Astrophys. J.* **512**, 484. doi:10.1086/306758.
Wood, B.E., Wu, C.-C., Howard, R.A., Socker, D.G., Rouillard, A.P.: 2011, *Astrophys. J.* **729**, 70. doi:10.1088/0004-637X/729/1/70.
Xie, H., Ofman, L., Lawrence, G.: 2004, *J. Geophys. Res.* **109**, 3109. doi:10.1029/2003JA010226.
Xue, X.H., Wang, C.B., Dou, X.K.: 2005, *J. Geophys. Res.* **110**, 8103. doi:10.1029/2004JA010698.
Yan, Y., Pick, M., Wang, M., Krucker, S., Vourlidas, A.: 2006, *Solar Phys.* **239**, 277. doi:10.1007/s11207-006-0202-6.
Zhao, X.P., Plunkett, S.P., Liu, W.: 2002, *J. Geophys. Res.* **107**, 1223. doi:10.1029/2001JA009143.
Zuccarello, F.P., Bemporad, A., Jacobs, C., Mierla, M., Poedts, S., Zuccarello, F.: 2012, *Astrophys. J.* **744**, 66. doi:10.1088/0004-637X/744/1/66.

Solar Phys (2013) 284:235–243
DOI 10.1007/s11207-012-0083-9

Modeling Irregularities in Solar Flux Ropes

E. Romashets · M. Vandas

Received: 15 March 2012 / Accepted: 17 July 2012 / Published online: 14 August 2012

Abstract To model irregularities in the magnetic structure of solar flux ropes or in interplanetary magnetic clouds, we propose the following approach. A local irregularity in the form of a compact toroid is added into a cylindrical linear force-free magnetic structure. The radius of the cylinder and the small radius of the toroid are the same, since the force-free parameter α is constant, that is, we have in total a linear force-free configuration, too. Meanwhile, the large radius of the toroid can be smaller. The effect of such modeling depends on the aspect ratio of the compact toroid, its location and orientation, and on its magnetic field magnitude in comparison with that of the cylinder.

Keywords Sun: magnetic field · Sun: flares · Sun: coronal mass ejections

1. Introduction

Recent analysis of solar observations reveals that magnetic flux ropes in the corona are common. High resolution observations of S-shaped loops, sigmoids, from space-based solar telescopes like SDO/AIA (*Solar Dynamic Observatory/Atmospheric Imaging Assembly*) and *Hinode*/XRT (*X-Ray Telescope*) demonstrate that these objects have flux rope structures (Behm, DeLuca, and Savcheva, 2012; Savcheva, van Ballegooijen, and DeLuca, 2012). The interpretation of new high quality data on the detailed magnetic structure inside active region filaments, provided by vector magnetograms from THEMIS/MTR (*Heliographic Telescope for the Study of the Magnetism and Instabilities on the Sun/multi-lines operating mode*) (Guo

Flux-Rope Structure of Coronal Mass Ejections
Guest Editors: N. Gopalswamy, T. Nieves-Chinchilla, M. Hidalgo, J. Zhang, and P. Riley

E. Romashets (✉)
Prairie View A&M University, Prairie View, TX 77446, USA
e-mail: romashets@yahoo.com

M. Vandas
Astronomical Institute, Academy of Sciences, Prague, Czech Republic
e-mail: vandas@asu.cas.cz

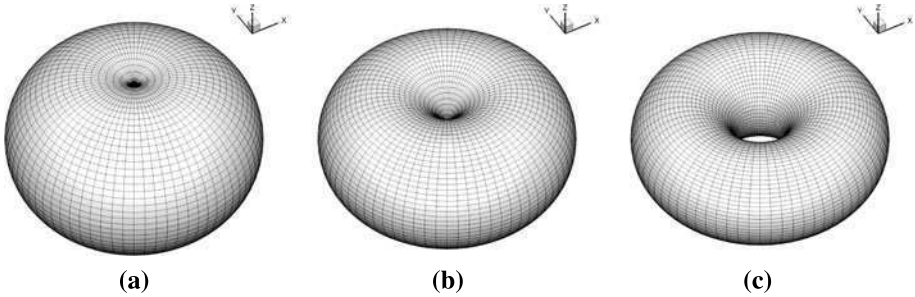

Figure 1 Three-dimensional view of toroids with various aspect ratios R_0/r_0: (a) smaller than unity (0.5), (b) equal to unity, and greater than unity (1.5). In the first case the toroid's surface intersects itself.

et al., 2010, 2011) and VTT/TIP (*Vacuum Tower Telescope/Tenerife Infrared Polarimeter*) (Yelles Chaouche *et al.*, 2012) and other ground based instruments, also suggests that flux ropes are involved in these structures. Theoretical studies demonstrate that linear force-free flux rope models are applicable for filaments and prominences (Démoulin, Priest, and Anzer, 1989; Litvinenko and Wheatland, 2005).

It has been shown by numerical magnetohydrodynamic (MHD) simulations (Detman *et al.*, 1991; Vandas *et al.* 1997, 1998) that spheromacs (spherical magnetic configurations) could evolve into toroidal flux ropes. In terms of the toroid's aspect ratio (ratio of the major R_0 to the minor r_0 radii) the phenomenon is a transformation from the state with its value much less than unity to one comparable to unity or larger. Until recently there was a difficulty to consider and model theoretically such processes because there were no analytical solutions for compact toroidal magnetic fields. The solution has been derived by Romashets and Vandas (2009) and it was utilized to describe local magnetic field enhancements in solar flux ropes by Romashets, Vandas, and Poedts (2010). Their model assumed that the radius of a cylindrical flux rope was equal to both the small and large radii of the toroid ($R_0 = r_0$, *i.e.*, aspect ratio 1). We realized in a subsequent analysis that this solution can describe even cases with aspect ratios lower than one and we use them in the current paper. Figure 1 demonstrates how the topology of a toroid changes with aspect ratio. In the next section the detailed description of the method is given. Section 3 presents the results of the modeling, followed by possible applications discussed in Section 4.

2. Method

Romashets and Vandas (2009) derived a toroidal linear force-free magnetic field. It was constructed as a sum of linear force-free cylindrical magnetic fields. Their generating cylinders with radii r_0 were tangent to a generating toroid with the minor radius r_0 and major radius R_0. Cross sections of a cylinder and the toroid coincided at their tangent place and the magnetic field of each cylinder was given by the Lundquist (1950) solution (see Equations (4)–(6) below). In the limiting case of an infinite number of uniformly distributed cylinders, a toroidal field was obtained:

$$B_r = B_0 \frac{\pi\alpha r z}{2R_0} \sum_{k=1}^{\infty} \frac{(-1)^{k+1}}{(k+1)!} \left(\frac{\alpha R_0}{2}\right)^{2k} \sum_{j=1}^{k} \frac{(2j)!}{j!(k-j)!} \left(\frac{z}{R_0}\right)^{2k-2j} \times \sum_{i=0}^{j-1} \frac{1}{i!(i+1)!(2j-2i-1)!} \left(\frac{r}{2R_0}\right)^{2i}, \quad (1)$$

$$B_\varphi = B_0 \frac{\pi r}{R_0} \sum_{k=1}^{\infty} \frac{(-1)^{k+1}}{k!} \left(\frac{\alpha R_0}{2}\right)^{2k} \sum_{j=1}^{k} \frac{(2j)!}{j!(k-j)!} \left(\frac{z}{R_0}\right)^{2k-2j} \times \sum_{i=0}^{j-1} \frac{1}{i!(i+1)!(2j-2i-1)!} \left(\frac{r}{2R_0}\right)^{2i}, \tag{2}$$

$$B_z = -\frac{r}{z} B_r + B_0 \pi \alpha R_0 \left\langle 1 + \sum_{k=1}^{\infty} \frac{(-1)^k}{(k+1)!} \left(\frac{\alpha R_0}{2}\right)^{2k} \left\{ \frac{1}{k!} \left(\frac{z}{R_0}\right)^{2k} + \sum_{j=1}^{k} \frac{1}{j!(k-j)!} \left(\frac{z}{R_0}\right)^{2k-2j} \left[1 + \sum_{i=1}^{j} \frac{(2j)!}{(i!)^2 (2j-2i)!} \left(\frac{r}{2R_0}\right)^{2i} \right] \right\} \right\rangle. \tag{3}$$

Here r, φ, and z constitute a cylindrical coordinate system, the axis z of which is a rotational axis of the generating toroid. B_0 scales the magnetic field magnitude and the constant α is from the definition of a linear force-free field, $\mathrm{rot}\,\mathbf{B} = \alpha \mathbf{B}$; as usual, it is related to the radius via $r_0 = 2.41/\alpha$, where 2.41 stands for the first root of the Bessel function J_0. Romashets and Vandas (2009) discussed toroidal flux ropes with $R_0 > r_0$, but later they realized that the solution is also applicable under $R_0 \le r_0$. Figure 2 shows toroidal flux ropes for various aspect ratios of generating toroids, including one case with $R_0 < r_0$. We see that the flux ropes have a rotational symmetry around the z axis, but their cross sections are not circular.

Romashets, Vandas, and Poedts (2010) considered the magnetic field (1) – (3) (with $R_0 = r_0$) as a local irregularity of a regular flux rope field determined by the Lundquist (1950) formulas,

$$B'_{r'} = 0, \tag{4}$$

$$B'_{\varphi'} = B_1 \mathrm{J}_1(\alpha r'), \tag{5}$$

$$B'_Z = B_1 \mathrm{J}_0(\alpha r'), \tag{6}$$

where r', φ', and Z are from another cylindrical coordinate system. J_0 and J_1 are the Bessel functions and B_1 scales the magnetic field. Both the regular field and the additional field are linear force-free systems with the same α, so their superposition is also a linear force-free field (with α).

In the present paper, we assume more general cases: the additional magnetic field (1) – (3) may have $R_0 < r_0$ and its generating toroid can be placed arbitrarily in position and orientation with respect to the regular cylindrical flux rope. The superposition is schematically shown in Figure 3. The regular cylindrical flux rope is described in the coordinate system X, Y, and Z (or r', φ', and Z) where the axis of the cylinder with the radius r_0 coincides with the Z axis. The additional toroidal field, determined by the generating toroid with R_0 and r_0, is described in the coordinate system x, y, and z (or r, φ, and z) which can be shifted and inclined with respect to the system X, Y, and Z (as shown in Figure 3).

The total magnetic field configuration, as well as each part of it separately, Equations (4) – (6) and Equations (1) – (3), are in stable minimum energy states, and therefore they preserve their shapes.

3. Results

A series of calculations were made for all possible combinations of parameters involved, namely B_0/B_1, R_0/r_0, inclination angle δ, and shift d of the toroid. The relationship between the systems was

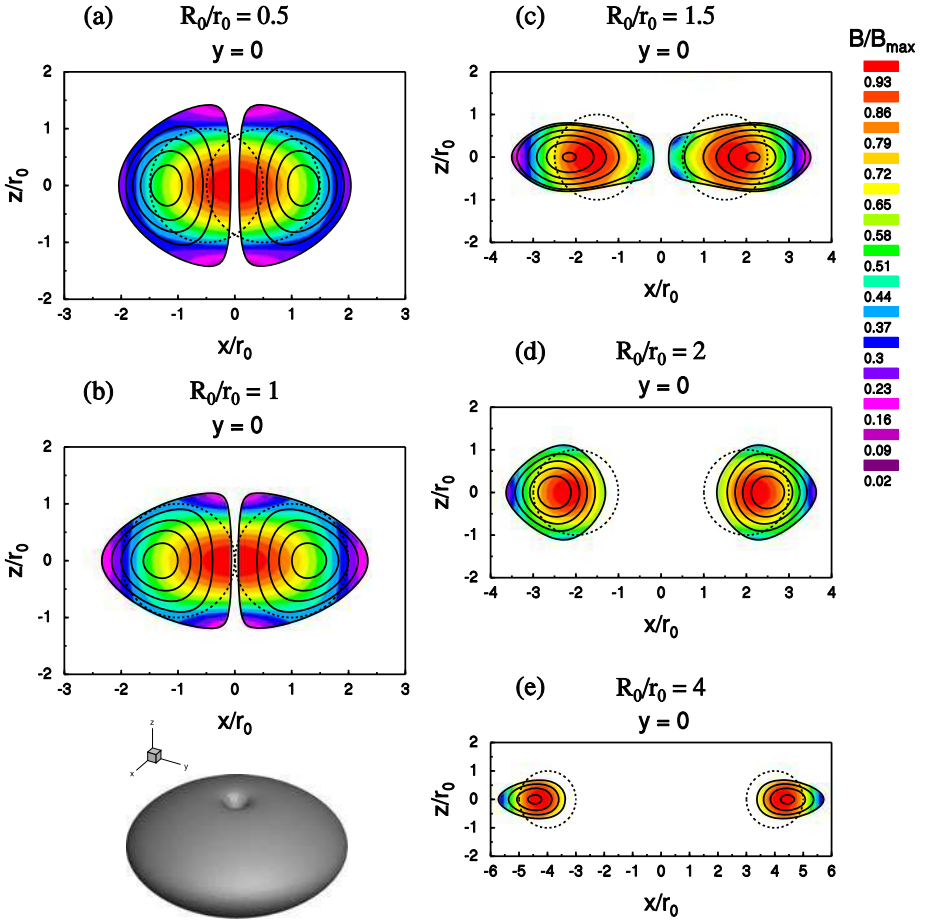

Figure 2 Toroidal flux ropes for various aspect ratios. Magnetic field magnitude distribution is shown by color contours and scaled by the respective field maxima in each plot. Solid lines are cross sections of magnetic surfaces on which helical magnetic field lines lie. Dashed circles are cross sections of a generating toroid. Case (b) is supplemented by a three-dimensional view of the flux rope. Three-dimensional views of the generating toroids from cases (a), (b), and (c) are displayed in Figures 1a, 1b, and 1c, respectively.

$$X = d + x\cos\delta + z\sin\delta, \tag{7}$$

$$Y = y, \tag{8}$$

$$Z = -x\sin\delta + z\cos\delta. \tag{9}$$

The total magnetic field was a vector sum of an unperturbed cylindrical flux rope (Equations (4)–(6) expressed in the XYZ system) and the toroidal field (Equations (1)–(3) related to the xyz system). The toroidal field was not numerically computed from Equations (1)–(3), because the sums converge slowly, but using alternative formulas given by Romashets and Vandas (2009):

$$B_r = B_0 \int_0^{2\pi} \mathrm{J}_1(\alpha\rho)\frac{z\cos\tilde{\varphi}}{\rho}\,\mathrm{d}\tilde{\varphi}, \tag{10}$$

$$B_\varphi = B_0 \int_0^{2\pi} \mathrm{J}_0(\alpha\rho)\cos\tilde{\varphi}\,\mathrm{d}\tilde{\varphi}, \tag{11}$$

$$B_z = -\frac{r}{z}B_r + B_0 \int_0^{2\pi} \mathrm{J}_1(\alpha\rho)\frac{R_0}{\rho}\,\mathrm{d}\tilde{\varphi}, \tag{12}$$

where $\rho = \sqrt{(r\cos\tilde{\varphi} - R_0)^2 + z^2}$ (note that there is a misprint in Equation (12) of Romashets and Vandas (2009) for B_z; it should read J_1 instead of J_0).

A characteristic change of magnetic structure due to insertion of the toroidal field was found for $R_0/r_0 = 0.75$ and $B_1/B_0 \approx 15$ (more specifically, B_0 has such a value that the maximum of the toroidal field is $0.25B_1$; the maximum magnetic field magnitude of the toroidal field for the above given aspect ratio approximately is $3.65B_0$ and is located at the origin; the condition $0.25B_1 \doteq 3.65B_0$ yields $B_1/B_0 \approx 15$). With these values, the following situations were considered in detail: i) parallel case ($\delta = 0°$, $d = 0$), that is, the rotational toroid's axis is aligned with the cylindrical flux rope axis, the magnetic field vectors of the two fields at the origin are parallel, and there is no shift; ii) antiparallel case ($\delta = 180°$, $d = 0$), that is, the axes are aligned, the magnetic field vectors at the origin are antiparallel, and there is no shift; iii) perpendicular case ($\delta = 90°$, $d = 0$), that is, the axes are perpendicular and there is no shift; iv) antiparallel case with a shift ($\delta = 180°$, $d = 0.3r_0$). These configurations are presented in Figures 4–7.

Figure 4a shows a cross section (in the XZ plane) of the flux rope for the parallel case. The boundary of the flux rope is determined by the magnetic surface which has the largest convex cross section perpendicular to Z (all flux rope boundaries in the paper were identified in such a way). Magnetic field magnitude distribution is shown by color contours. Solid lines are cross sections of magnetic surfaces on which helical magnetic field lines lie. Distribution of these surfaces does not represent density of magnetic field lines, because the surfaces are given by the quantity $rB_{\varphi'} = \text{const}$. (it is due to axial symmetry, see Romashets and Vandas, 2009). The fields are parallel near the origin, therefore the resulting field is intensified and the flux rope is thinner here. But there are two widenings away from the origin. Figure 7a is a three-dimensional view of this flux rope. Figure 4b displays the same quantities for the

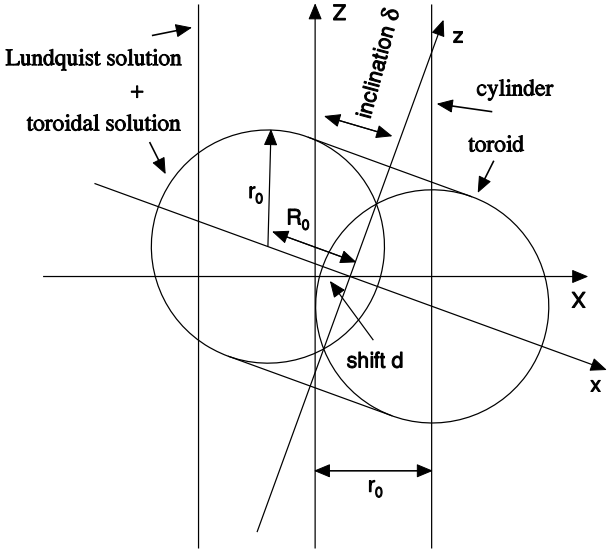

Figure 3 Illustration of how a disturbed magnetic field is constructed in a general case. The field consists of a regular cylindrical field (described in the system X, Y, and Z) and an additional toroidal field (determined in the system x, y, and z).

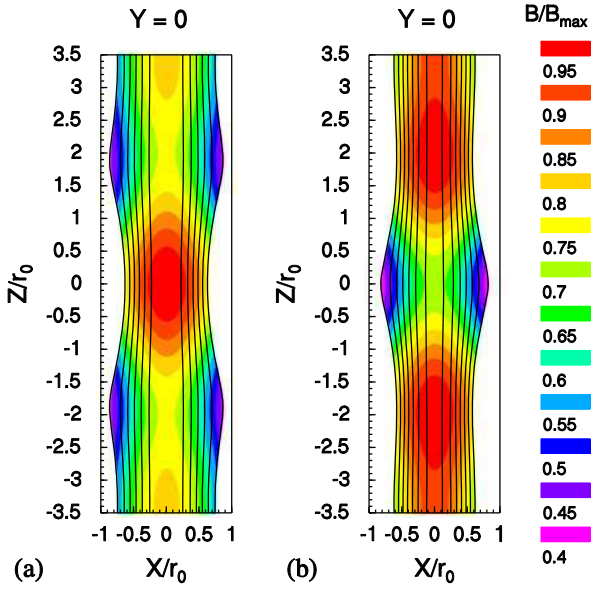

Figure 4 Magnetic field magnitude distribution in flux ropes for (a) parallel and (b) antiparallel cases. A cylindrical flux rope is modified by insertion of the toroidal field. The rotational toroid's axis coincides with the Z axis and the cylinder's and toroid's origins coincide, too. The field magnitudes are scaled by corresponding field maxima. The solid lines show cross sections of magnetic surfaces. The magnetic field configuration is axially symmetric in both cases.

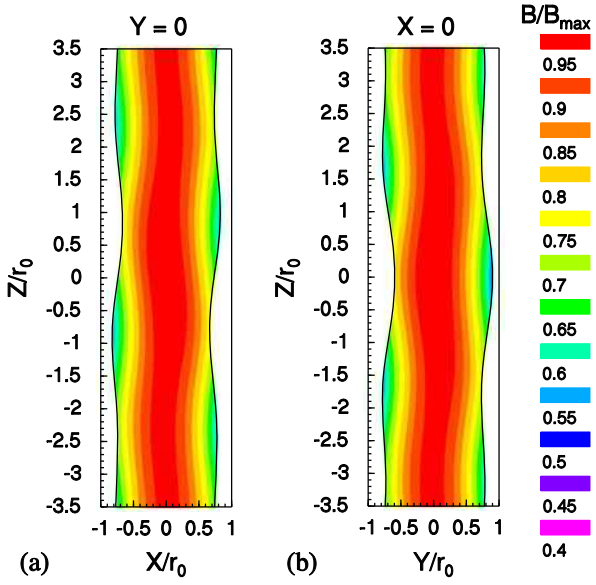

Figure 5 Magnetic field magnitude distribution in the flux rope for the perpendicular case is shown in two planes, (a) $Y = 0$, and (b) $X = 0$. A cylindrical flux rope is modified by insertion of the toroidal field, where the rotational axis coincides with the X axis and the cylinder's and toroid's origins are the same. The field magnitude is scaled by its maximum value in the flux rope. Magnetic surfaces (except of the boundary) are not shown because the case is not axisymmetric and it is not possible to apply a simple mapping as could be done for the symmetric cases.

antiparallel case. The field is weaker around the origin and the flux rope is thicker here. The three-dimensional view is shown in Figure 7b.

Figure 5 displays the perpendicular case. The flux rope is plotted in two cross sections, in the XZ and YZ planes. Mutual comparison reveals asymmetry and warping of the flux rope which is also seen in Figure 7c.

When the toroid's origin is shifted away from the cylinder's axis, the resulting flux rope becomes much thinner, it is also asymmetric and warped. Figures 6 and 7d depict the situation.

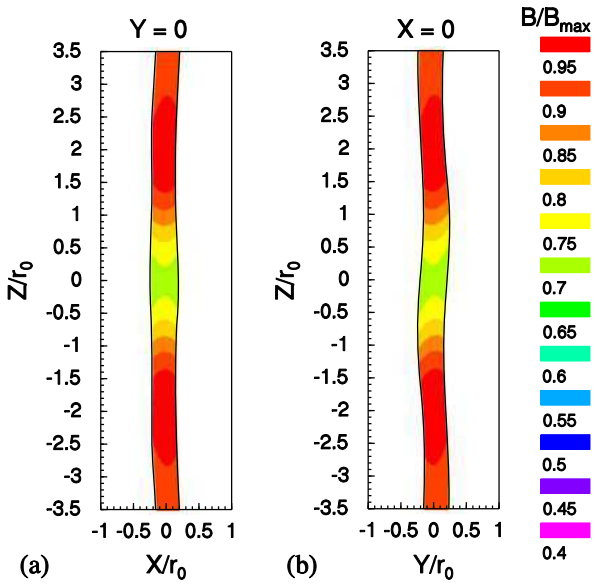

Figure 6 Antiparallel case with a shift; it is similar to Figure 4b but the toroid is shifted by $0.3r_0$ along the X axis to the right. Similar to Figure 5, magnetic field magnitude distribution is shown in two planes, (a) $Y = 0$ and (b) $X = 0$.

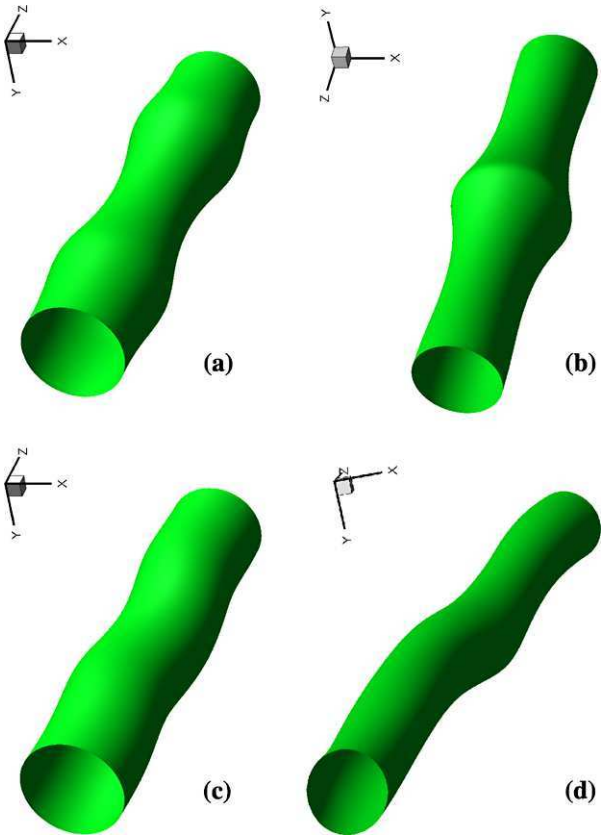

Figure 7 Magnetic surfaces representing boundaries of irregular flux ropes from Figures 4 – 6: (a) parallel case, (b) antiparallel case, (c) perpendicular case, and (d) antiparallel case with a shift.

We selected specific values of the parameters of the model where changes of the cylindrical flux rope were most pronounced: varying thickness and warping. Changing these parameters, the qualitative picture will be the same, but mostly less pronounced, or the flux rope becomes too thin (mainly when the shift is included).

4. Discussion and Conclusions

New mathematical formulas describing a force-free magnetic field with a constant α inside a compact toroid have been developed for modeling local irregularities inside solar magnetic flux ropes. The new compact-toroid solution has been superposed onto the well-known force-free cylindrical solution. In principle, the model can be applied for interpretation of some features observed in solar flux ropes. Within the proposed approach such local irregularities are considered as a superposition of a compact toroid with the cylindrical tube. Figure 8 shows a prominence with irregularities similar to those on Figure 7a (source http://stereo-ssc.nascom.nasa.gov/browse/2010/10/24/index.shtml). It was observed with the STEREO A (*Solar Terrestrial Relations Observatory/Ahead*) satellite SECCHI/EUVI (*Sun Earth Connection Coronal and Heliospheric Investigation/Extreme Ultraviolet Imager*) (304 Å) on November 22, 2011. On the other hand, the image does not show field lines, but plasma. And, because of this, the shape could be attributed to other effects, such as part of the flux rope not being lit up. There is an ongoing discussion whether flux ropes are involved in the formation of filaments (*e.g.* Guo *et al.*, 2010) or not. The former point of view may be supported by presence of helical magnetic field lines visible in the snapshot. The method can also be applied in the future to interpret observations of irregularities inside interplanetary magnetic clouds.

The model presented in this paper yields a static description of the magnetic field. The structure is in equilibrium and can keep its shape for a long time, since force-free structures are minimum energy states. The prominence in Figure 8 was seen for more than 20 hours without significant changes in its shape. Romashets and Poedts (2007) and Dalakashvili *et al.* (2009) developed a procedure to show how plasma parameters (pressure

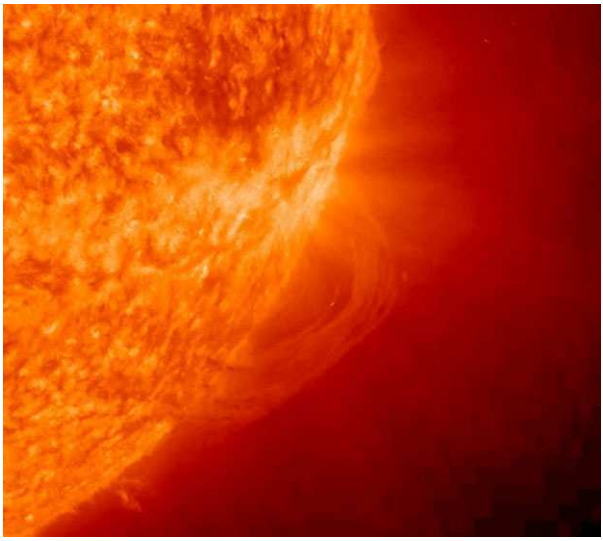

Figure 8 STEREO A SECCHI/EUVI view of a coronal prominence with changes in thickness (similar to Figure 7a). Image courtesy of the STEREO (SECCHI/EUVI) team.

and temperature) can be constructed for such a magnetic-field configuration. If the system is non-stable and time-dependent, the MHD equations need to be solved numerically.

Acknowledgements This work was supported by the program of the Czech–US collaboration in science and technology (ME09032). MV acknowledges support from the AV ČR grant RVO:67985815 and by the GA ČR grant 205/09/0170.

References

Behm, T., DeLuca, E., Savcheva, A.: 2012, Nonlinear force-free modeling of Aug 4 & 10, 2010 sigmoids via flux rope insertion method. *Astron. Astrophys. Suppl.* **219**, 144.04.

Dalakashvili, G., Poedts, S., Fichtner, H., Romashets, E.: 2009, Characteristics of magnetized plasma flow around stationary and expanding magnetic clouds. *Astron. Astrophys.* **507**, 611 – 616.

Démoulin, P., Priest, E.R., Anzer, U.: 1989, A three-dimensional model for solar prominences. *Astron. Astrophys.* **221**, 326 – 337.

Detman, T.R., Dryer, M., Yeh, T., Han, S.M., Wu, S.T.: 1991, A time-dependent, three-dimensional MHD numerical study of interplanetary magnetic draping around plasmoids in the solar wind. *J. Geophys. Res.* **96**, 9531 – 9540.

Guo, Y., Schmieder, B., Démoulin, P., Wiegelmann, T., Aulanier, G., Török, T., Bommier, V.: 2010, Coexisting flux rope and dipped arcade sections along one solar filament. *Astrophys. J.* **714**, 343 – 354.

Guo, Y., Schmieder, B., Démoulin, P., Wiegelmann, T., Aulanier, G., Török, T., Bommier, V.: 2011, A filament supported by different magnetic field configurations. In: *The Physics of Sun and Star Spots*, *IAU Symp.* **273**, 328 – 332.

Litvinenko, Y.E., Wheatland, M.S.: 2005, A simple dynamical model for filament formation in the solar corona. *Astrophys. J.* **630**, 587 – 595.

Lundquist, S.: 1950, Magnetohydrostatic fields. *Ark. Phys.* **2**, 361 – 365.

Romashets, E., Poedts, S.: 2007, Plasma flows around magnetic obstacles in the solar wind. *Astron. Astrophys.* **475**, 1093 – 1100.

Romashets, E.P., Vandas, M.: 2009, Linear force-free field of a toroidal symmetry. *Astron. Astrophys.* **499**, 17 – 20.

Romashets, E., Vandas, M., Poedts, S.: 2010, Modeling of local magnetic field enhancements within solar flux ropes. *Solar Phys.* **261**, 271 – 280.

Savcheva, A.S., van Ballegooijen, A.A., DeLuca, E.E.: 2012, Field topology analysis of a long-lasting coronal sigmoid. *Astrophys. J.* **744**, 78.

Vandas, M., Fischer, S., Pelant, P., Dryer, M., Smith, Z., Detman, T.: 1997, Propagation of a spheromak 1. Some comparisons of cylindrical and spherical magnetic clouds. *J. Geophys. Res.* **102**, 24183 – 24194.

Vandas, M., Fischer, S., Dryer, M., Smith, Z., Detman, T.: 1998, Propagation of a spheromak 2. Three-dimensional structure of a spheromak. *J. Geophys. Res.* **103**, 23717 – 23726.

Yelles Chaouche, L., Kuckein, C., Martínez, P.V., Moreno-Insertis, F.: 2012, The three-dimensional structure of an active region filament as extrapolated from photospheric and chromospheric observations. *Astrophys. J.* **748**, 23.

Solar Phys (2013) 284:217–233
DOI 10.1007/s11207-012-0006-9

Using Statistical Multivariable Models to Understand the Relationship Between Interplanetary Coronal Mass Ejecta and Magnetic Flux Ropes

P. Riley · I.G. Richardson

Received: 30 January 2012 / Accepted: 18 April 2012 / Published online: 17 May 2012

Abstract *In-situ* measurements of interplanetary coronal mass ejections (ICMEs) display a wide range of properties. A distinct subset, "magnetic clouds" (MCs), are readily identifiable by a smooth rotation in an enhanced magnetic field, together with an unusually low solar wind proton temperature. In this study, we analyze *Ulysses* spacecraft measurements to systematically investigate five possible explanations for why some ICMEs are observed to be MCs and others are not: i) An observational selection effect; that is, all ICMEs do in fact contain MCs, but the trajectory of the spacecraft through the ICME determines whether the MC is actually encountered; ii) interactions of an erupting flux rope (FR) with itself or between neighboring FRs, which produce complex structures in which the coherent magnetic structure has been destroyed; iii) an evolutionary process, such as relaxation to a low plasma-β state that leads to the formation of an MC; iv) the existence of two (or more) intrinsic initiation mechanisms, some of which produce MCs and some that do not; or v) MCs are just an easily identifiable limit in an otherwise continuous spectrum of structures. We apply quantitative statistical models to assess these ideas. In particular, we use the Akaike information criterion (AIC) to rank the candidate models and a Gaussian mixture model (GMM) to uncover any intrinsic clustering of the data. Using a logistic regression, we find that plasma-β, CME width, and the ratio O^7/O^6 are the most significant predictor variables for the presence of an MC. Moreover, the propensity for an event to be identified as an MC decreases with heliocentric distance. These results tend to refute ideas ii) and iii). GMM clustering analysis further identifies three distinct groups of ICMEs; two of which match (at

Flux-Rope Structure of Coronal Mass Ejections
Guest Editors: N. Gopalswamy, T. Nieves-Chinchilla, M. Hidalgo, J. Zhang, and P. Riley

P. Riley (✉)
Predictive Science, Inc., 9990 Mesa Rim Road, Suite 170, San Diego, CA, USA
e-mail: pete@predsci.com

I.G. Richardson
Astroparticle Physics Laboratory, Code 661, NASA Goddard Space Flight Center, Greenbelt, MD, USA
e-mail: ian.g.richardson@nasa.gov

I.G. Richardson
CRESST and Department of Astronomy, University of Maryland, College Park, MD, USA

the 86 % level) with events independently identified as MCs, and a third that matches with non-MCs (68 % overlap). Thus, idea v) is not supported. Choosing between ideas i) and iv) is more challenging, since they may effectively be indistinguishable from one another by a single *in-situ* spacecraft. We offer some suggestions on how future studies may address this.

Keywords Coronal mass ejections · Magnetic flux ropes · Magnetic clouds

1. Introduction

Coronal mass ejections (CMEs) produce spectacular visual displays involving the sometimes-explosive release of plasma and magnetic field from the solar corona into interplanetary space. Although they have been studied for many years since their discovery in the early 1970s by *Skylab* (Tousey, 1973) and they have the potential to wreak substantial damage to our technologically reliant society (Schieb, 2011), many of their basic properties are not well understood.

A CME can be defined as a large-scale, bright (and dark) transient feature observed in white-light (coronagraph) images of the Sun (see, *e.g.*, Hundhausen, 1993). The limitations of this definition are important. It relies only on white-light observations, which trace electron density. Moreover, these observations are integrated along the line of sight, weighted by the ray path's closest distance to the solar surface. CMEs are, of course, known to be violent eruptions of coronal magnetic fields, which, when viewed in the plane of the sky give rise to "bulb-like" structures or, on the disk, to "halo" structures. The classic three-part structure of a CME consists of a bright front, cavity, and core (see, *e.g.*, Riley *et al.*, 2008). However, we do not observe the magnetic field; we must infer its properties from a combination of numerical models driven by observations of the photospheric field. Clearly, though, the magnetic field must play a central role in the origin and dynamics of the CME, since there are no other sufficient sources of energy to power the eruption. Based on this, we infer that the white-light features we see are the manifestation of a flux rope (FR) structure propagating through the corona.

In the solar wind, interplanetary CMEs (ICMEs) are observed to display a wide range of features in *in-situ* measurements (Zurbuchen and Richardson, 2006). These include: counterstreaming suprathermal electrons, low proton temperature, declining speed profile, enhanced solar wind ion charge states and/or variable composition, and helium abundance enhancements. ICMEs are often (but not always) preceded by interplanetary shock waves (Marubashi, 1997; Bothmer and Schwenn, 1998). We can further distinguish a subset of ICMEs, termed "magnetic clouds" (MCs), that include a coherent structure with a large, smooth rotation of the magnetic field through the event, in concert with an enhanced magnetic field strength and relatively low proton temperature and plasma-β (Burlaga *et al.*, 1981; Klein and Burlaga, 1982). The terms "magnetic cloud" and "flux rope" are often used interchangeably. However, the latter is less rigorously defined, typically requiring only a coherent rotation in the magnetic field. Here, we will reserve FR to describe the magnetic structure near the Sun and MC to describe the relevant *in-situ* measurements.

Few ICMEs display all of these signatures. To compound this, *in-situ* measurements (with the notable exceptions of composition and charge states) are a convolution of intrinsic and evolutionary effects, and disentangling them can be difficult, if not impossible. Clearly, ICMEs are related to CMEs, yet the connection is not always obvious (Riley *et al.*, 2006; Möstl *et al.*, 2009).

ICMEs that are not MCs, or do not obviously contain an MC, need their own moniker. Burlaga *et al.* (2001) suggested the term "complex ejecta" (CE), while others have used the

phrase "non-MC ICME" (*e.g.*, Richardson and Cane, 2004a; Zurbuchen and Richardson, 2006; Gopalswamy, 2010). Since ejecta are observed that could be classified as "simple" but do not contain a clear rotation in the magnetic field, for our purposes the former definition could be misleading (although it could be used for a specific set of events that are complex but do not contain FRs). For clarity, we will refer to the ICMEs with no obvious MC association as non-magnetic clouds, or non-MCs. Thus, $N_{\rm ICME} = N_{\rm MC} + N_{\rm non\text{-}MC}$.

A number of studies have investigated the statistical properties of ICMEs and/or MCs. Burlaga *et al.* (2001) studied the properties of fast solar wind ejecta observed by the *Advanced Composition Explorer* (ACE) during 1998 – 1999 identifying two distinct classes. Although limited to only nine events, they found that, compared to MCs, the CEs had: i) weaker magnetic fields, ii) higher proton temperatures, iii) higher plasma-β, and iv) comparable speeds. Of more significance, the CEs were twice as wide (in the radial direction) as the MCs. Since CMEs near the Sun are inferred to occasionally interact with one another (*e.g.*, Gopalswamy *et al.*, 2001), this led Burlaga *et al.* (2001) to suggest that CEs were the result of the interaction of two or more MCs nearer to the Sun than the point of observation.

The importance of the spacecraft's trajectory through an event in determining the observed properties has been suspected for a long time. For example, Cane (1988) showed that He abundance enhancements, indicating the presence of ejecta, tended to disappear with increasing angular (longitudinal) distance from the source, suggesting that the flank of the shock, but not the ejecta itself, was being intercepted. Cane, Richardson, and Wibberenz (1997) also concluded that MCs originated, on average, closer to central meridian than non-cloud ICMEs based on *Helios* observations. More recently, Gopalswamy (2006), distinguishing between MCs, non-MCs, and driverless shocks, found that MCs originated close to central meridian longitude ($< 30°$), whereas non-MCs were distributed more broadly across the disk. Most of the driverless shocks originated near the solar limbs (both east and west). These results are consistent with the idea that the observer's position governs whether one sees an MC. However, some exceptions had to be accounted for; in particular, several driverless shocks, as well as numerous non-MCs that originated from disk center.

Richardson and Cane (2010) updated and expanded their earlier studies (Cane and Richardson, 2003; Richardson and Cane, 2004a) of ICMEs observed near Earth to encompass all events from 1996 through 2009. Of relevance to the present study, they found that solar sources (halo, partial halo, Hα, or flare reports) could not be found for 46 % of the ICMEs observed at Earth. For the events for which a source could be found, 95 % lay within 50° of central meridian and 57/43 % of the events lay to the west/east, although the mean location was W3.2°. They also extended an earlier analysis of the relative fraction of ICMEs that were magnetic clouds as a function of solar cycle (Cane and Richardson, 2003; Richardson and Cane, 2004b; Riley *et al.*, 2006). Previously, they had shown a tentative result that the MC fraction was larger at solar minimum than at maximum. While the more recent period (2004 – 2009) was not inconsistent with this, the results (albeit based on a small number of events) did not increase support. They also found a modest correlation (0.6) between the speed and maximum magnetic field strength for those events that were MCs; in contrast, the correlation was weak (0.28) for events that were not MCs. Finally, they noted that, frequently, MC structures were observed to be substructures of larger, more complex ICME regions.

Du, Zuo, and Zhang (2010) developed a comprehensive list of 181 ICMEs observed by the *Ulysses* spacecraft, of which 43 % were identified as MCs. Again, limiting our discussion to relevant points, they found no clear change in the MC fraction with heliolatitude: While there were more MCs than non-MCs in the northern hemisphere (above 50°), the reverse was true in the southern hemisphere.

Most recently, Richardson and Cane (2011) applied the same types of analyses previously performed on near-Earth events to 270 ICMEs they identified in the *Ulysses* measurements. Of these, 125 events overlapped with the events identified by Du, Zuo, and Zhang (2010). Once again, they found a trend for the MC fraction to increase at solar minimum. However, unlike their near-Earth study, the increase was clearer during the most recent minimum (2008). They also concluded that there was a tendency for the MC fraction to increase away from the solar equator, which they argued was consistent with the idea of preferentially intercepting the axis of a flux rope embedded within an ICME when at the latitude of the solar active regions. Additionally, they identified 11 ICMEs that were observed both at *Ulysses* and near Earth when the two spacecraft were separated by less than 30° longitude. Of these, four contained flux rope structure at both locations; five contained flux rope structure at *Ulysses* but not at Earth; one contained flux rope structure at Earth but not at *Ulysses*; and one was devoid of flux rope structure at both locations.

In an attempt to better understand the relationship between MCs and ICMEs, we have identified five possible ideas that might explain why either MCs or non-MCs might appear in *in-situ* measurements. These are described next.

1.1. Is the Presence or Absence of an MC an Observational Selection Effect?

One possible explanation for the relationship between MCs and ICMEs, as discussed above, is that of an "observational selection" effect (*e.g.*, Riley *et al.*, 2003, 2006): Whether one observes an MC depends on the spacecraft's trajectory through the ejecta (Figure 1). In this scenario, all ICMEs have an MC embedded within a larger ejecta. If MCs are observed only when the spacecraft is fortuitously positioned so that it passes sufficiently close to the flux rope's axis, then geometrical considerations can be used to assess this hypothesis. For example, consider a flux rope launched with its axis parallel to, and in the heliographic equator. The cross section is shown in Figure 1. We might anticipate intercepting an MC over a broad range of longitudes, but confined to near-equatorial latitudes. At higher latitudes, the spacecraft would likely intercept a shock and sheath region, and then enter an ejecta-like structure, for example, with depressed temperature and compositional anomalies, but without a rotation of the magnetic field. In practice, CMEs are launched from a range of latitudes, which tend to cluster at mid-latitudes where active regions form, and this pattern changes during the course of the solar cycle. Nevertheless, if this picture holds, we might expect the MC fraction to decrease at sufficiently high latitudes.

1.2. Do MC–MC Interactions Destroy Flux Rope Structure?

A second possibility is that two or more MCs interact with one another to produce a CE (or non-MC), destroying the coherent MC structure in the process (Burlaga *et al.*, 2001). Thus, near the Sun the CME contained a FR that was subsequently destroyed prior to being observed at 1 AU or beyond. In this case, we make the explicit association of non-MCs with the "complex ejecta" structures described by Burlaga *et al.* (2001). In their study, they found that the average radial width of such an event was more than twice that for an MC. Thus, hypothesizing that CEs are created by CME-CME interactions suggests that, on average, they should be two or, for three-body interactions, even three times as wide as MCs. Note that the events in the Burlaga *et al.* (2001) study were carefully chosen. The interval was limited to a 1.8-year period in 1998/1999, which coincided with the ascending phase of Solar Cycle 23. Only fast ejecta ($v > 600$ km s^{-1}) were considered, which resulted in a total of nine events: four MCs and five CEs, or an MC fraction of ≈ 44 %.

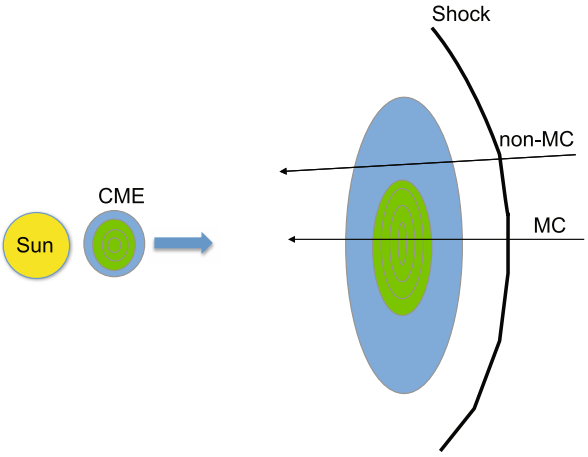

Figure 1 Schematic illustrating how the spacecraft's trajectory through an ICME might lead to either the identification of a magnetic cloud or a non-MC (or CE).

Although Burlaga *et al.* (2001) analyzed the duration of the structure as it passed the spacecraft, in view of the hypothesis that aggregations of MCs produce CEs (or non-MCs), the width of the event would appear to be a more appropriate parameter. This is given by: $d \approx \langle v_{\mathrm{CME}} \rangle \times \tau_{\mathrm{CME}}$, where $\langle v_{\mathrm{CME}} \rangle$ is the average speed of the CME and τ_{CME} is the duration of the CME as it passes over the spacecraft. In summary, if MC–MC interactions are a major effect in producing non-MCs, we would expect, on average, that the latter are larger than the former.

1.3. Do Evolutionary Processes in the Solar Wind Produce Flux Ropes?

A third and related possibility is that evolutionary processes within the CME produce a flux rope. In a sense, this reflects the opposite outcome to idea ii). Observations and modeling suggest that CMEs are born as high-pressure structures close to the Sun, due to the large fields and/or densities. As they move farther away and expand, they relax to a more force-free configuration, potentially allowing a complex magnetic field structure to evolve into a more coherent structure (see Figure 2). In this scenario, ICMEs would evolve into MCs with increasing distance from the Sun (J.T. Gosling, personal communication, 1996). In a similar vein, Bellan (2000) argued that a Taylor-like relaxation, whereby the plasma inside a fusion device is driven toward a force-free helical state (Taylor, 1974), might apply to prominences in the corona, in part based on laboratory experiments. If such a scenario holds, we might expect to observe a greater proportion of MCs to ICMEs at larger heliocentric distances; that is, the MC fraction should increase with increasing distance from the Sun. However, Richardson and Cane (2004b), analyzing *Helios* data, did not find a systematic trend in MC fraction and heliocentric distance.

1.4. Are There Two (or More) Intrinsic Mechanisms that Produce Flux-Rope and Non-flux-Rope CMEs?

A superficially obvious explanation for the apparent bimodal presence of MCs and non-MCs is that there are two (or more) distinct mechanisms producing them. A range of self-consistent models of CME initiation and eruption have already been developed, all of which naturally produce FRs in the corona, and, by inference, MCs in the solar wind (see, *e.g.*, Riley *et al.*, 2004). On the other hand, only *ad hoc* schemes, such as pressure pulses, or

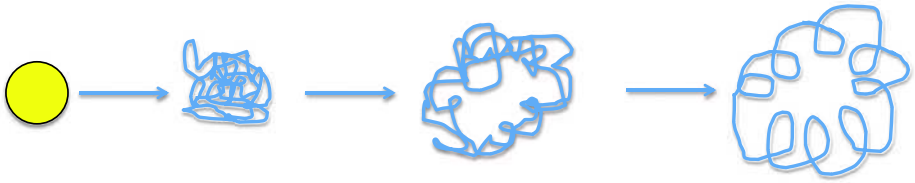

Figure 2 Schematic illustrating how a Taylor relaxation process might produce magnetic clouds from initial non-MCs. For simplicity, the magnetic field is shown as detached from the Sun, but in reality, field lines threading the ejecta would connect back to the Sun. Adapted for ICMEs from a drawing by Bellan (2000).

blast waves (see, *e.g.*, Odstrcil, 2009), can even claim to produce interplanetary transient structures that have no FR component. Thus, as yet there is no self-consistent mechanism starting at or below the photosphere capable of producing a large-scale eruption that does not contain helical fields within it. Therefore, we must appeal to either a new, as yet undiscovered process, or the modification of an existing one that is capable of producing something sufficiently complex. Given the intrinsically more complicated geometry of the "break out" configuration (see, *e.g.*, Lynch *et al.*, 2008), one could posit that it might naturally produce a non-MC, whereas eruption from within a dipolar configuration would be more likely to produce an MC. Of course one could assemble other combinations of "simple" *versus* "complex" scenarios, such as eruptions within active regions *versus* polar crown filaments. However, without a clear set of predictions that can be differentially tested in the data, it would be impossible to confirm or refute a specific pairing.

1.5. Are MCs Merely a Limiting, Easily Identifiable Subset of a Continuum Range of Magnetic Fluctuations Within Ejecta?

As scientists (or humans), we are driven by a desire to classify objects. MCs represent an obvious coherent structure that can be easily identified in multi-day time series of the interplanetary magnetic field, which makes them an obvious candidate for receiving a name and definition. Since non-MC ICMEs share similar plasma attributes, differing primarily in their magnetic properties, it is natural for us to create two classifications into which all cases neatly fit. But what if the classification is merely threshold based? That is, what if a broad and relatively flat spectrum of event types is produced, but only those that are sufficiently "clear" are identified as MCs? To assess this, we must use a technique that is not "biased" with our tendency to subjectively find patterns in the objects we see.

Thus, in this study we will analyze *Ulysses in-situ* measurements from launch through 2008 to uncover evidence that either supports or refutes one or more of these ideas concerning the relationship between MCs and ICMEs. In particular, we will use a logistic regression analysis to develop a statistical model relating CME properties to the likelihood that an MC is present within the ejecta, using the Akaike information criterion (AIC) to assess which predictor variables best define the model. We will then apply a clustering analysis using a Gaussian mixture model (GMM) to determine whether the data support grouping ICMEs into two or more specific groups, and if so, whether these clusters match the subjective delineation of events into MCs and non-MC ICMEs.

2. Statistical Analysis of *Ulysses* ICMEs

To investigate the relationship between MCs and ICMEs, we use *Ulysses* one-hour averaged data from launch through 2008, obtained from COHOweb at the Space Physics Data Fa-

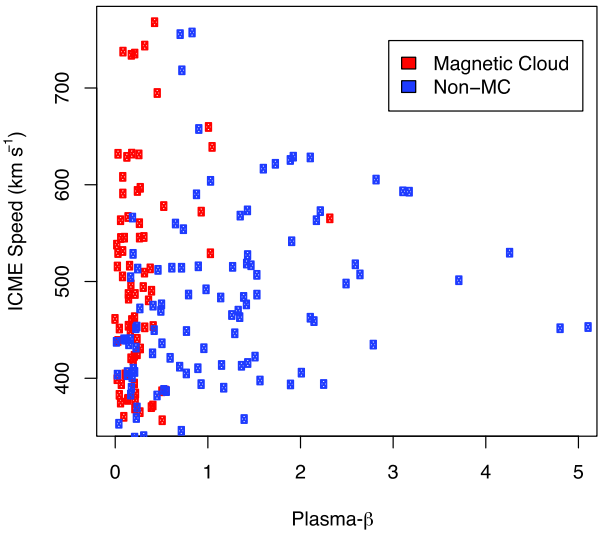

Figure 3 ICME speed *versus* plasma-β for 181 ICMEs identified by Du, Zuo, and Zhang (2010), color-coded according to whether they were (red) or were not (blue) magnetic clouds.

cility (SPDF) at NASA/GSFC (http://cohoweb.gsfc.nasa.gov/). Several comprehensive lists of ICMEs observed by *Ulysses* have been developed in recent years (Ebert *et al.*, 2009; Du, Zuo, and Zhang, 2010; Richardson and Cane, 2011). While there is a significant overlap between these lists (Richardson and Cane, 2011), there are a notable number of differences. Du, Zuo, and Zhang (2010)'s list is the most sparse, containing a total of 181 ICMEs, while Richardson and Cane (2011)'s list is the most extensive, with 270 events. When conducting a statistical analysis, it makes sense to err on the conservative side, provided a sufficiently large number of events are present. Thus, here we restrict our analysis to those events identified by Du, Zuo, and Zhang (2010). Of their identified 181 ICMEs, 77 (or 43 %) were MCs.

In Figure 3 we present all 181 events separated into MCs and non-MCs as a function of solar wind speed and plasma-β, where the plasma-β is defined as $\frac{2n_{\rm p}k_{\rm B}T_{\rm p}}{B^2/\mu_0}$, where $k_{\rm B}$ is the Boltzmann constant, and $n_{\rm p}$ and $T_{\rm p}$ are the proton density and temperature, respectively. This clearly demonstrates the strong dependence on low values of plasma-β for MCs. This is not surprising, given that MCs are defined by their high magnetic field strength, and, because they are often observed to be expanding, their low density. The figure also hints at a possible dependence on speed, with a tendency for MCs to display a broader range in speed. However, this plot does not separate the two classifications fully: a significant number of the non-MCs are also low-β ($\ll 1$) objects (although there are no low-β, high-speed non-MCs).

In the following sections we apply two statistical analysis techniques to these events: logistic regression and Gaussian mixture models.

2.1. Logistic Regression of the *Ulysses* ICMEs

Logistic regression is a useful technique for predicting a binary outcome from a set of continuous predictor variables (Hosmer and Lemeshow, 2000); that is, it can be used for classification purposes. In our case, the outcome variable is whether the ICME is an MC or not, and the predictor variables are a set of continuous (but averaged for each event) parameters, including plasma-β, speed, width, magnetic field strength, plasma density, α/P ratio, temperature, average charge state of iron (QFe), the ratio of O^7 to O^6 (O^7/O^6), heliocentric

distance, latitude, and sunspot number (SSN). This is not an exhaustive list, but it does include the primary variables used to describe the properties of ICMEs. We note that the last three parameters – distance, latitude, and SSN – are not intrinsic parameters of the event; in fact, distance and latitude are sensitive to the position of the spacecraft. However, they can still be useful for assessing whether the likelihood of identifying an MC, rather than a non-MC, is dependent on the spacecraft's position in the heliosphere. Similarly, the presence or absence of MCs can be related to the phase of the solar cycle by including SSN as a predictor variable.

We define our binary outcome variable (y) to be 0 or 1, where the latter is the identification of an MC, and write the probability, p, that $y = 1$:

$$\text{logit}(p) = \ln\big(p/(1-p)\big) = \beta_0 + \beta_1 \times x_1 + \cdots + \beta_k \times x_k. \tag{1}$$

This represents the logistic regression of y on the predictor variables $x_1, \ldots, x_k$ through the estimation of the parameters β_0 through β_k, and, practically speaking, gives the probability that an event described by the observed quantities $x_1, \ldots, x_k$ will be an MC. The *logit* function, $\text{logit}(p) = \ln(p/(1-p))$, is the logarithm of the odds $(p/(1-p))$, *i.e.*, the chance of a given probability of an outcome occurring. Thus, the logistic regression coefficients give the change in the log odds of the outcome for a unit change in the predictor variable.

In practice, the best estimates of the parameters β_0 through β_k are obtained using the method of maximum likelihood via an interactively reweighed least squares method (Hosmer and Lemeshow, 2000). In contrast to the more familiar least-squares approach, which minimizes variation from the model, maximum likelihood finds the model equation with the highest probability (*i.e.*, likelihood) of explaining the outcome variable, given the predictor variables. In the following analysis, we use the generalized linear model (GLM) implemented in the statistical package R, which includes the logistic regression method described above (Faraway, 2006).

To assess the quality of a particular statistical model, we apply the Akaike Information criterion (AIC), which measures the relative goodness-of-fit (Akaike, 1974). It is based on the idea of minimizing the amount of information lost when a particular model is used to approximate reality. In general, the AIC can be defined as:

$$\text{AIC} = 2K - 2\ln(L), \tag{2}$$

where K is the number of parameters in the statistical model and L is the maximized likelihood function for the model. The likelihood function expresses the probability of the observed data as a function of the unknown parameters. Thus, the maximized likelihood function involves the selection of those parameters that give the observed data the greatest probability. Practically speaking, the "best" model for a set of predictor variables is the one that minimizes the AIC value. Since AIC includes the number of parameters (*i.e.*, predictor variables), K, the AIC value is penalized for each parameter added; thus, parsimonious models are encouraged. It is important to note that the AIC does not tell us which is the correct model from a physical point of view, only the one that best matches the data. From a different perspective, the AIC score allows us to discount models that perform poorly.

For our purposes, we will treat the AIC score as a defensible method for assessing whether the presence or absence of MCs is dependent on a particular predictor variable, which, in turn, allows us to argue in favor of or against one or more of the ideas that we introduced earlier to explain the MC/ICME relationship.

One final potentially useful statistical tool to apply in our analysis is the variation inflation factor (VIF). It is well known that some solar wind parameters display strong collinearity

with one another, which, if both were included in the statistical model, would be misleading. Plasma-β and magnetic field strength are obvious examples. While we could perform correlation tests for pairs of predictor variables, looking for large positive or negative correlations, this approach has drawbacks. For example, it is possible that a strong linear dependence exists between three or more variables, yet pairwise correlations between them are small. Computing the VIF circumvents this problem by estimating the factor by which the variance increases for each estimated coefficient β_k. We define the VIF for the kth variable to be:

$$\mathrm{VIF}_k = \frac{1}{1 - R_k^2}, \tag{3}$$

where R_k^2 is the multiple correlation between the kth variable and all other variables (Afifi, Clark, and May, 2011). Thus, as R_k approaches 1, signaling the presence of collinearity, the VIF becomes large. Typically, multicollinearity is considered high when VIF > 5.

Table 1 summarizes an initial logistic regression analysis of the *Ulysses* CMEs. The first column lists the 13 predictor variables that were included. We note that two temperatures are computed from the *Ulysses* ion instrument measurements, ($T_{\min}$ and $T_{\max}$) which are both reported to the SPDF. With no compelling reason to choose one over the other, at least initially, we retain both. The last column ($\Pr(>|z|)$), known as the "p-value," gives a measure of the significance of a particular predictor variable. Typically values < 0.01 provide convincing evidence of the significance of a variable. However, we emphasize that this is only statistical evidence and not proof of a causal relationship. Thus, employing a 5 % threshold, we infer that plasma-β, width, O^7/O^6, and heliocentric distance are "parameters of interest," worthy of further scrutiny. Also note that high p-values do not prove the null hypothesis, *i.e.*, that the variable is not significant, they only tell us that our dataset coupled with the analysis technique was not able to identify such a relationship. Of these, plasma-β, width, and O^7/O^6 are most significant. The second column gives the best-fit coefficient for each predictor variable, $\hat{\beta}_k$ (where the $\hat{}$ denotes the maximum likelihood estimate of the kth variable). Thus, the likelihood of identifying an ICME as an MC depends strongly on it having: i) a low plasma-β, ii) a large width, and iii) high O^7/O^6. Note that, at least during this initial analysis, speed, density, α/P ratio, QFe, and latitude do not appear to be significant. Although not as important for our study, we note that column three gives the standard error of the estimated coefficients, and column four displays the ratios of the estimated coefficients to their estimated standard error.

Next, we assess the effects on the AIC score of dropping any one predictor variable for the model. Table 2 summarizes this. Again, column one lists each of the predictor variables. The initial AIC score is given in the first cell of column four, with the remaining cells giving the revised AIC score if that variable is dropped. Columns two, three, and five give the degrees of freedom, deviance, and likelihood ratio test (LRT). The deviance is a "quality of fit" statistic and essentially measures the deviation of the reduced model to the full model, while the LRT gives a measure as to the statistical significance of the variable in the multivariate model. For example, we conclude that dropping SSN, that is, the phase of the solar cycle, reduces the AIC score modestly, while dropping the plasma-β raises it dramatically. Since our objective is to lower the AIC score, this suggests that SSN is not a significant variable but that plasma-β and width are.

Before culling parameters from our list of predictor variables based on AIC rankings, as a check for collinearity, we estimated the VIFs for each variable. Not surprisingly, we found $\mathrm{VIF}_{T_{\min}} = 10.3$, since $T_{\min}$ and $T_{\max}$ are highly correlated. However, since neither $T_{\min}$ nor $T_{\max}$ was found to be sufficiently significant, both were removed from the analysis.

Table 1 Results of logistic regression analysis. Column one lists the predictor variables used in the statistical model, column two (Estimate) gives the estimated value of the regression coefficient for each variable, column three (Std. error) gives the standard error for these estimates, column four (z value) gives the results of the z test, and column five (Pr($>|z|$)) provides the p-values.

Predictor variable	Estimate	Std. error	z value	Pr($>|z|$)
(Intercept)	0.6030	3.3528	0.180	0.8573
SSN	−0.0046	0.0086	−0.537	0.5910
Plasma-β	−2.9918	0.8938	−3.347	0.0008
Speed	0.0027	0.0043	0.622	0.5337
Width	1.5982	0.4878	3.276	0.0011
Field strength	0.1269	0.0740	1.715	0.0863
Proton density	0.0781	0.0778	1.004	0.3155
α/P ratio	−15.0391	16.9151	−0.889	0.3740
$T_{\min}$	0.0000	0.0000	1.278	0.2013
$T_{\max}$	−0.0000	0.0000	−1.694	0.0903
QFe	0.0290	0.1899	0.153	0.8786
O^7/O^6	2.3950	0.8686	2.757	0.0058
Heliocentric distance	−0.8605	0.3765	−2.285	0.0223
Latitude	−0.0173	0.0185	−0.932	0.3512

Table 2 Variation in AIC score when each predictor variable is dropped from the analysis. Column one lists each predictor variable, column two (Df) gives the number of degrees of freedom, column three gives the deviance, column four gives the AIC score, column five gives the results of the likelihood ratio test (*i.e.*, the deviance change), and column six gives the p-value.

Predictor variable	Df	Deviance	AIC	LRT	Pr(Chi)
⟨none⟩		117.2	145.2		
SSN	1	117.5	143.5	0.289	0.59059
Plasma-β	1	137.4	163.4	20.182	0.00001
Speed	1	117.6	143.6	0.391	0.53200
Width	1	128.9	154.9	11.642	0.00064
Field strength	1	120.4	146.4	3.138	0.07647
Proton density	1	118.2	144.2	0.987	0.32057
α/P ratio	1	118.1	144.1	0.826	0.36355
$T_{\min}$	1	118.8	144.8	1.572	0.20992
$T_{\max}$	1	120.0	146.0	2.716	0.09933
QFe	1	117.3	143.3	0.024	0.87615
O^7/O^6	1	125.8	151.8	8.576	0.00341
Heliocentric distance	1	123.2	149.2	5.971	0.01454
Latitude	1	118.2	144.2	0.911	0.33979

Rerunning the logistic regression with the new subset of predictor variables yielded the results in Table 3: plasma-β, CME width, and O^7/O^6 remain the strongest variables, with heliocentric distance the weakest. Importantly, these results strongly imply that the likeli-

Table 3 Logistic regression analysis for subset of most significant predictor variables. See Table 1 for a description of the column headings.

Predictor variable	Estimate	Std. error	z value	Pr($>\|z\|$)
(Intercept)	0.4651	0.7744	0.601	0.5481
Plasma-β	−2.9253	0.7473	−3.915	0.0001
Width	1.5000	0.4470	3.356	0.0008
O^7/O^6	2.4366	0.7385	3.299	0.0010
Heliocentric distance	−0.3542	0.1799	−1.969	0.0490

Table 4 Variation in AIC score when each of the most significant predictor variables is dropped from the analysis. See Table 2 for a description of the column headings.

Predictor variable	Df	Deviance	AIC	LRT	Pr(Chi)
⟨none⟩		134.8	144.8		
Plasma-β	1	166.4	174.4	31.536	0.00000
Width	1	147.3	155.3	12.505	0.00041
O^7/O^6	1	153.5	161.5	18.678	0.00002
Heliocentric distance	1	138.9	146.9	4.059	0.04395

hood of observing an MC increases with CME width and higher O^7/O^6, but decreases with heliocentric distance and plasma-β.

For completeness, and as a complementary check, we repeated the exercise of dropping each predictor variable from the statistical model and recomputed the AIC score. This is shown in Table 4. Focusing on column four, this reinforces the result that, in decreasing order of significance, plasma-β, O^7/O^6, width, and then heliocentric distance best predict the presence of an MC.

2.2. Gaussian Mixture Model Analysis of *Ulysses* ICMEs

In the previous section we used logistic regression analysis to build a statistical model that related continuous predictor variables to a known (at least subjectively) binary outcome variable (MC or non-MC). However, a complementary question is whether the ICME parameters (*i.e.*, the predictor variables) are clustered into subpopulations. Thus, whereas the logistic regression analysis relied on our identification of the ICME as being either an MC or a non-MC, clustering analysis attempts to find natural groups based only on the predictor variables; *i.e.*, it uses statistical inference derived from the entire population of events without any prior knowledge of the sub-populations. Therefore, to address the question of whether MCs are really a distinct class, we can attempt to identify distinct clusters and see if they match with the events that were identified as either MCs or non-MCs in the *Ulysses* ICME list by Du, Zuo, and Zhang (2010).

The approach we use here is known as the Gaussian mixture model (GMM) (Everitt and Hand, 1981; McLachlan and Peel, 2000). We assume that N observed variables are distributed according to a mixture of K components, where each component belongs to some parametric family, each of which has a different set of parameters. Here, we further assume that the families are Gaussian, being defined by their own mean and variance. That is, each cluster is defined by a Gaussian distribution in the predictor variable parameter space

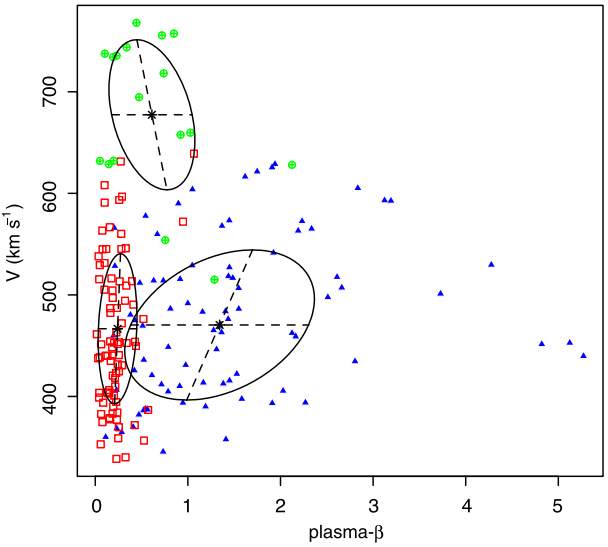

Figure 4 ICME speed *versus* plasma-β for *Ulysses*-observed ICMEs. The CMEs are color-coded according to the three components identified by the GMM analysis.

with a unique mean and variance. Computationally, we use the MCLUST routine developed for the statistical package *R*, which relies on a Bayesian information criterion (BIC) score to estimate the best clusters. (See also Press *et al.*, 2007 for a discussion on implementing this technique numerically.) BIC and AIC are similar but distinct criteria for model selection, with BIC penalizing free parameters more strongly than AIC. While the number of clusters in GMMs can be specified *a priori*, here, we allow the algorithm to minimize the BIC score by varying the number of components from 1 through 9. For this analysis, we used a subset of parameters listed in Table 1 (plasma-β, speed, width, and O^7/O^6). The results are shown in Figures 4 and 5.

The GMM analysis found that the data were best fit by three components, as identified in Figure 4. Two of the clusters (red and green) tend to have low plasma-β but are separated by speed, whereas the third cluster (blue) has a larger plasma-β and more moderate speed. Comparing these clusters with the events identified subjectively by Du, Zuo, and Zhang (2010) to be either MCs or non-MCs (Figure 3) shows that the red/green clusters overlap well with the MCs, while the blue cluster overlaps with the non-MCs. In fact, the fraction of red/green events that were also MCs was 86 %, while the fraction of the blue events that were also non-MCs was 68 %; both significantly larger than would be expected by chance.

In Figure 5, a scatter-plot matrix is shown, summarizing the relationship between these three clusters and the parameters of the ICMEs. In addition to the relatively obvious clustering in plasma-β – speed space (column 1, row 2) already discussed in relation to Figure 4, the ICMEs are also well separated in width – O^7/O^6 space (column 3, row 4). Specifically, what distinguishes the fast MCs (green) is that they are also wider and have a lower O^7/O^6 ratio than the red component. Finally, we note that the dependence on CME width in the likelihood of an event being an MC rather than a non-MC ICME cannot be discerned in Figure 5. While this relationship is statistically significant, the difference between the mean width of MCs (0.77 AU) and non-MC ICMEs (0.73 AU) is only 0.04 AU, and is clearly not visible between these distributions.

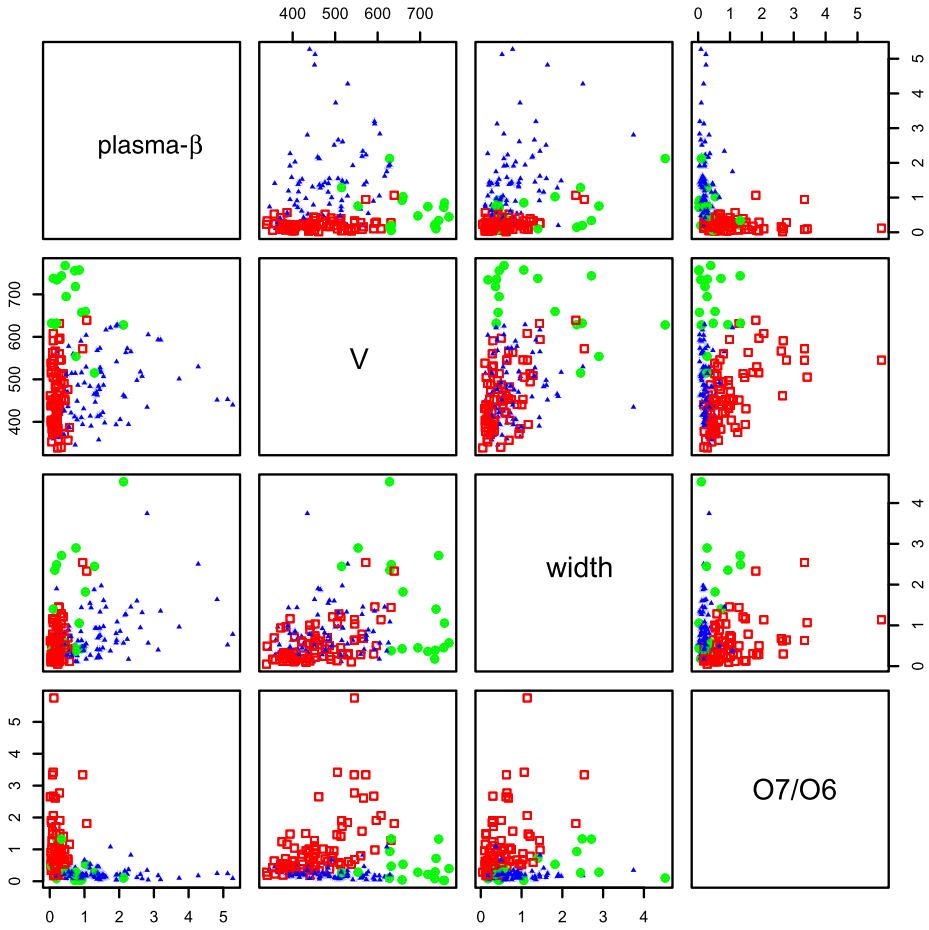

Figure 5 Scatter-plot matrix of plasma-β, speed (V), width, and O^7/O^6 of the ICMEs observed by *Ulysses*. Each panel is color-coded according to the three components identified by the GMM analysis.

3. Summary and Discussion

In this study, we have analyzed the properties of 181 ICMEs observed by the *Ulysses* spacecraft, in an attempt to understand the basic relationship between MCs and non-MCs. We applied two statistical techniques, logistic regression and Gaussian mixture models, to provide a more rigorous assessment of five ideas proposed to resolve the relationship between these two types of ejecta. Our results lead us to the conclusion that only ideas i) and iv) are consistent with the observations. That is, that either (a) an observational selection effect, or (b) the presence of two or more mechanisms is responsible for the MC/ICME relationship.

CME-CME interactions (idea ii)) cannot account for the presence of MCs and non-MCs. Logistic regression analysis strongly suggests that the propensity for an event to be identified as an MC is coupled to the width of the ejecta. Although we found only a modest difference in the size of MCs and non-MCs (0.77 AU *versus* 0.73 AU, respectively), the result was both statistically significant and in the wrong sense for CME-CME interactions to account for the creation of non-MCs: MCs are likely to be broader than non-MCs. However, a basic

prediction from the Burlaga *et al.* (2001) study was that MCs should be at least half the size of non-MCs, since MC-MC interactions would be unlikely to produce narrower structures. Of course, it is possible that such interactions may account for a small number of cases. In fact, this may explain why our results apparently contradict those of Burlaga *et al.* (2001): In their study, a small number of events (nine) were carefully chosen based on specific criteria.

Evolutionary processes (idea iii)), at least those envisaged through a Taylor-like relaxation process (Bellan, 2000), also cannot explain the relationship between MCs and non-MCs. If it were true, we would expect a trend for more MCs to be identified with increasing distance from the Sun. However, our analysis shows that exactly the opposite effect holds: MCs are less likely to be identified with increasing distance from the Sun.

Finally, we cannot relegate the MC/non-MC relationship to a figment of our imagination (idea v)). Clustering analysis suggests the existence of three distinct classes of ejecta, two of which overlap strongly with the MCs identified by Du, Zuo, and Zhang (2010), and a third which overlaps significantly with non-MCs.

Distinguishing between the remaining two ideas is challenging. First-principle models, which inevitably produce a well-formed flux rope, tend to support the idea that a flux rope is always present, and suggest that an ICME's identification as MC or non-MC in the solar wind must be related to where the observing spacecraft is located and its trajectory with respect to the ICME. However, this can be easily countered by the fact that current global CME models are highly idealized, and, by definition, must produce the simplest of structures. It is conceivable that as the realism of the models improves, they will be able to generate more and more complex structures – to the point that some events may be "complex" while others are "simple." It is also possible that the degree of complexity might vary spatially within a single event.

An argument for or against a selection effect explanation could be resolved by geometrical arguments. As we have noted, other studies (*e.g.*, Cane, Richardson, and Wibberenz, 1997; Gopalswamy, 2006) suggest that MCs tend to be launched in longitude closer to central meridian (as viewed by the observing spacecraft) than non-MCs. On the other hand, Richardson and Cane (2011) found a weak tendency for the *Ulysses*-observed MC fraction to increase away from the equator, at least up to mid-latitudes. However, the logistic regression analysis described here finds no statistical support for the MC fraction to depend on latitude.

Ultimately, there is little to separate ideas i) and iv) at the location of Earth or *Ulysses*. Like the proverbial blind men feeling different parts of an elephant, relying only on *in-situ* measurements does not afford us the global view that we need to connect everything. Large-scale MHD models should eventually be able to assist us, but, as we have lamented, they are currently too idealized.

An intriguing result from the cluster analysis concerns the presence of three, not two (MC, non-MC) populations of *Ulysses* ICMEs, with MCs being divided into slower events with higher oxygen charge states, and faster, wider events with lower charge states. In particular, the inverse dependence of O^7/O^6 on MC speed appears to be contrary to previous studies based on near-Earth observations (*e.g.*, Richardson and Cane, 2004a) that indicate at least a modest increase in O^7/O^6 with MC speed. We suggest that the two populations of MCs arise principally from i) the *Ulysses* orbit, which extends to high latitudes; ii) the tendency for faster ICMEs to be found at higher latitudes because of the latitude dependence of the solar wind speed, especially around solar minimum when several of the MCs are observed; and iii) the fact that higher charge states in ICMEs are confined to latitudes below $\approx 30-40^\circ$. For example, Figure 6(a) shows average O^7/O^6 against ICME speed for the Du *et al.* ICMEs with the symbol type indicating the three groups identified in our study. The

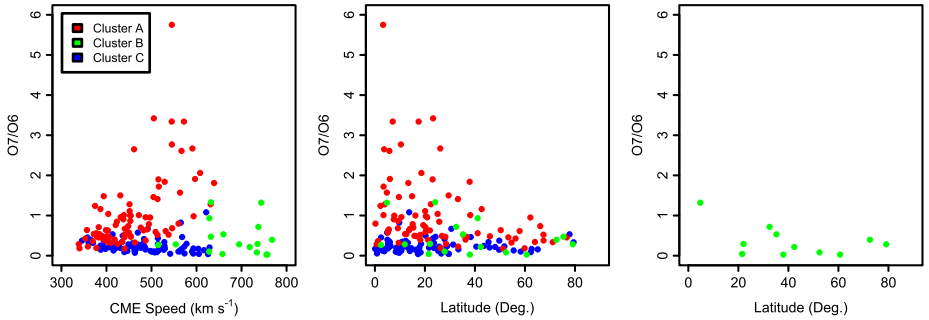

Figure 6 O^7/O^6 *versus* (a) ICME speed, (b) latitude, and (c) latitude of those "green" ICMEs traveling faster than 650 km s^{-1}.

tendency for the fast (green) MCs to have lower O^7/O^6 than slower MCs is clearly evident. However, the slower, red events do show evidence of an increase in O^7/O^6 with speed to values that exceed those in the green events. Figure 6(b) shows O^7/O^6 *versus* ICME heliolatitude, indicating that higher values (say > 1) are observed at low latitudes, below $\approx 40°$. A possible interpretation is that the high charge states arising from plasma heating during CME formation and ejection are preferentially observed close to the location of the related solar event and hence are not detected at higher latitudes (see, *e.g.*, Lepri and Zurbuchen, 2004). Figure 6(c) shows only those "green" events with speeds > 650 km s^{-1}, illustrating that they were predominantly observed at higher latitudes, where higher charge states are more rarely observed. Thus, we suggest that the two populations of MCs indicated by the cluster analysis correspond to lower latitude MCs that typically do not reach high speeds but may have high ion charge states (red events), and a second population of faster ICMEs observed at higher latitudes but which have lower charge states (green events).

This work naturally suggests several possible avenues for future studies. First, it would be interesting to study the properties of the source locations for the "red" (slow and cool) and "green" (fast and hot) types of MCs hinted at by the clustering analysis (Figure 4). Does anything about their origin point to unique properties or processes? Second, how do the *in-situ* composition/charge state properties of the two types of MCs differ? Richardson and Cane (2004a), for example, noted that iron charge states tend to increase with magnetic cloud speed near the Earth, and a similar dependence was found for *Ulysses* events (Richardson and Cane, 2011). This, too, might hint at different origins. Third, do these results hold for ICMEs observed by near-Earth spacecraft? We focused here on ICMEs observed by *Ulysses* so that we could fold both latitude and heliocentric distance into our analysis; however, the database of near-Earth events is considerably larger (Richardson and Cane, 2010). Fourth, can ideas i) and iv) be distinguished from a larger and more systematic study of multi-spacecraft ICMEs? In addition to events observed simultaneously by near-Earth spacecraft (*Geotail*, *Wind*, and ACE) and *Ulysses* (see, *e.g.*, Hammond *et al.*, 1995; Riley *et al.*, 2003; Du, Wang, and Hu, 2007; Rodriguez *et al.*, 2008; Richardson and Cane, 2011), events have been measured by *Helios* 1 and 2 (see, *e.g.*, Kallenrode *et al.*, 1993; Cane, Richardson, and Wibberenz, 1997; Burlaga, Behannon, and Klein, 1987) and STEREO A and B (see, *e.g.*, Liu *et al.*, 2008). If combined, these may result in a sufficiently large and statistically significant database from which the final two ideas can be distinguished.

Acknowledgements P.R. gratefully acknowledges the support of NSF's FESD program as well as NASA SR&T and GI programs, the latter through a subcontract with NRL. We also acknowledge the use of *Ulysses*

observations from NASA/GSFC's Space Physics Data Facility's COHOWeb service, and thank the *Ulysses* PIs who have made their observations available via this source.

References

Afifi, A., Clark, V., May, S.: 2011, *Practical Multivariate Analysis*, 5th edn. *Texts in Statistical Science*, Taylor & Francis, London. ISBN9781439816806.

Akaike, H.: 1974, A new look at the statistical model identification. *IEEE Trans. Autom. Control* **19**(6), 716 – 723.

Bellan, P.M.: 2000, Simulating solar prominences in the laboratory. *Am. Sci.* **88**, 136. doi:10.1511/2000.2.136.

Bothmer, V., Schwenn, R.: 1998, The structure and origin of magnetic clouds in the solar wind. *Ann. Geophys.* **16**, 1 – 24.

Burlaga, L.F., Behannon, K.W., Klein, L.W.: 1987, Compound streams, magnetic clouds, and major geomagnetic storms. *J. Geophys. Res.* **92**, 5725 – 5734. doi:10.1029/JA092iA06p05725.

Burlaga, L.F., Sittler, E.C.J., Mariani, F., Schwenn, R.: 1981, Magnetic loop behind an interplanetary shock – *Voyager*, *Helios*, and IMP-8 observations. *J. Geophys. Res.* **86**, 6673 – 6684.

Burlaga, L.F., Skoug, R.M., Smith, C.W., Webb, D.F., Zurbuchen, T.H., Reinard, A.: 2001, Fast ejecta during the ascending phase of solar cycle 23: ACE observations, 1998–1999. *J. Geophys. Res.* **106**(A10), 20957 – 20978.

Cane, H.V.: 1988, The large-scale structure of flare-associated interplanetary shocks. *J. Geophys. Res.* **93**, 1 – 6. doi:10.1029/JA093iA01p00001.

Cane, H.V., Richardson, I.G.: 2003, Interplanetary coronal mass ejections in the near-Earth solar wind during 1996–2002. *J. Geophys. Res.* **108**, 1156. doi:10.1029/2002JA009817.

Cane, H.V., Richardson, I.G., Wibberenz, G.: 1997, Helios 1 and 2 observations of particle decreases, ejecta, and magnetic clouds. *J. Geophys. Res.* **102**, 7075 – 7086. doi:10.1029/97JA00149.

Du, D., Wang, C., Hu, Q.: 2007, Propagation and evolution of a magnetic cloud from ACE to *Ulysses*. *J. Geophys. Res.* **112**, 9101. doi:10.1029/2007JA012482.

Du, D., Zuo, P.B., Zhang, X.X.: 2010, Interplanetary coronal mass ejections observed by *Ulysses* through its three solar orbits. *Solar Phys.* **262**, 171 – 190. doi:10.1007/s11207-009-9505-8.

Ebert, R.W., McComas, D.J., Elliott, H.A., Forsyth, R.J., Gosling, J.T.: 2009, Bulk properties of the slow and fast solar wind and interplanetary coronal mass ejections measured by *Ulysses*: Three polar orbits of observations. *J. Geophys. Res.* **114**, 1109. doi:10.1029/2008JA013631.

Everitt, B.S., Hand, D.J.: 1981, *Finite Mixture Distributions* **2**, Chapman & Hall, London, 652 – 658.

Faraway, J.J.: 2006, *Extending Linear Models with r: Generalized Linear, Mixed Effects and Nonparametric Regression Models*, Chapman & Hall/CRC, London. ISBN1-584-88424-X. http://www.maths.bath.ac.uk/~jjf23/ELM/.

Gopalswamy, N.: 2006, Properties of interplanetary coronal mass ejections. *Space Sci. Rev.* **124**, 145 – 168. doi:10.1007/s11214-006-9102-1.

Gopalswamy, N.: 2010, Corona mass ejections: A summary of recent results. In: Dorotovic, I. (ed.) *20th National Solar Physics Meeting*, 108 – 130.

Gopalswamy, N., Yashiro, S., Kaiser, M.L., Howard, R.A., Boueret, J.L.: 2001, Radio signatures of coronal mass ejection interaction: Coronal mass ejection cannibalism? *Astrophys. J. Lett.* **548**(1), L91 – L94.

Hammond, C.M., Crawford, G.K., Gosling, J.T., Kojima, H., Phillips, J.L., Matsumoto, H., Balogh, A., Frank, L.A., Kokubun, S., Yamamoto, T.: 1995, Latitudinal structure of a coronal mass ejection inferred from *Ulysses* and Geotail observations. *Geophys. Res. Lett.* **22**(10), 1169 – 1172.

Hosmer, D., Lemeshow, S.: 2000, *Applied Logistic Regression*, *Wiley Series in Probability and Statistics: Texts and References Section*, Wiley, New York. ISBN9780471356325.

Hundhausen, A.J.: 1993, Sizes and locations of coronal mass ejections – SMM observations from 1980 and 1984 – 1989. *J. Geophys. Res.* **98**, 13177 – 13200.

Kallenrode, M.B., Wibberenz, G., Kunow, H., Müller-Mellin, R., Stolpovskii, V., Kontor, N.: 1993, Multispacecraft observations of particle events and interplanetary shocks during November/December 1982. *Solar Phys.* **147**, 377 – 410. doi:10.1007/BF00690726.

Klein, L.W., Burlaga, L.F.: 1982, Interplanetary magnetic clouds at 1 AU. *J. Geophys. Res.* **87**, 613 – 624.

Lepri, S.T., Zurbuchen, T.H.: 2004, Iron charge state distributions as an indicator of hot ICMEs: Possible sources and temporal and spatial variations during solar maximum. *J. Geophys. Res.* **109**, 6101. doi:10.1029/2003JA009954.

Liu, Y., Luhmann, J.G., Huttunen, K.E.J., Lin, R.P., Bale, S.D., Russell, C.T., Galvin, A.B.: 2008, Reconstruction of the 2007 May 22 magnetic cloud: How much can we trust the flux-rope geometry of CMEs? *Astrophys. J. Lett.* **677**, L133 – L136. doi:10.1086/587839.

Lynch, B.J., Antiochos, S.K., DeVore, C.R., Luhmann, J.G., Zurbuchen, T.H.: 2008, Topological evolution of a fast magnetic breakout CME in three dimensions. *Astrophys. J.* **683**, 1192 – 1206. doi:10.1086/589738.

Marubashi, K.: 1997, Interplanetary magnetic flux ropes and solar filaments, in coronal mass ejections. In: Crooker, N.U., Joselyn, J.A., Feynman, J. (eds.) *Coronal Mass Ejections*, *Geophys. Monogr. Ser.* **99**, AGU, Washington, 147.

McLachlan, G., Peel, D.: 2000, *Finite Mixture Models* **44**, Wiley-Interscience, New York, 82. http://pubs.amstat.org/doi/abs/10.1198/tech.2002.s651.

Möstl, C., Farrugia, C.J., Temmer, M., Miklenic, C., Veronig, A.M., Galvin, A.B., Leitner, M., Biernat, H.K.: 2009, Linking remote imagery of a coronal mass ejection to its *in situ* signatures at 1 AU. *Astrophys. J. Lett.* **705**, L180 – L185. doi:10.1088/0004-637X/705/2/L180.

Odstrcil, D.: 2009, Numerical simulation of interplanetary disturbances. In: Pogorelov, N.V., Audit, E., Colella, P., Zank, G.P. (eds.) *Numerical Modeling of Space Plasma Flows* **CS-406**, Astron. Soc. Pac., San Francisco, 141 – 148.

Press, W.H., Teukolsky, S.A., Vetterling, W.T., Flannery, B.P.: 2007, *Numerical Recipes: The Art of Scientific Computing* **29**, Cambridge University Press, Cambridge 501. http://www.jstor.org/stable/1269484?origin=crossref.

Richardson, I.G., Cane, H.V.: 2004a, Identification of interplanetary coronal mass ejections at 1 AU using multiple solar wind plasma composition anomalies. *J. Geophys. Res.* **109**, 9104. doi:10.1029/2004JA010598.

Richardson, I.G., Cane, H.V.: 2004b, The fraction of interplanetary coronal mass ejections that are magnetic clouds: Evidence for a solar cycle variation. *Geophys. Res. Lett.* **31**, 18804. doi:10.1029/2004GL020958.

Richardson, I.G., Cane, H.V.: 2010, Near-Earth interplanetary coronal mass ejections during Solar Cycle 23 (1996 – 2009): Catalog and summary of properties. *Solar Phys.*, 189 – 237. doi:10.1007/s11207-010-9568-6.

Richardson, I.G., Cane, H.V.: 2011, Identification of interplanetary coronal mass ejections at *Ulysses* using multiple solar wind signatures, and comparison with ICMEs observed at the Earth and in the inner heliosphere. AGU Fall Meeting Abstracts, SH31B – 1979.

Riley, P., Linker, J.A., Mikić, Z., Odstrcil, D., Zurbuchen, T.H., Lario, D., Lepping, R.P.: 2003, Using an MHD simulation to interpret the global context of a coronal mass ejection observed by two spacecraft. *J. Geophys. Res.* **108**, 1272.

Riley, P., Linker, J.A., Lionello, R., Mikić, Z., Odstrcil, D., Hidalgo, M.A., Cid, C., Hu, Q., Lepping, R.P., Lynch, B.J., Rees, A.: 2004, Fitting flux ropes to a global MHD solution: A comparison of techniques. *J. Atmos. Solar-Terr. Phys.* **66**, 1321 – 1331.

Riley, P., Schatzman, C., Cane, H.V., Richardson, I.G., Gopalswamy, N.: 2006, On the rates of coronal mass ejections: Remote solar and *in situ* observations. *Astrophys. J.* **647**, 648 – 653. doi:10.1086/505383.

Riley, P., Lionello, R., Mikić, Z., Linker, J.: 2008, Using global simulations to relate the three-part structure of coronal mass ejections to *in situ* signatures. *Astrophys. J.* **672**, 1221 – 1227. doi:10.1086/523893.

Rodriguez, L., Zhukov, A.N., Dasso, S., Mandrini, C.H., Cremades, H., Cid, C., Cerrato, Y., Saiz, E., Aran, A., Menvielle, M., Poedts, S., Schmieder, B.: 2008, Magnetic clouds seen at different locations in the heliosphere. *Ann. Geophys.* **26**, 213 – 229. doi:10.5194/angeo-26-213-2008.

Schieb, P.A.: 2011, Geomagnetic storms. Technical report. http://www.oecd.org/dataoecd/57/25/46891645.pdf.

Taylor, J.B.: 1974, Relaxation of toroidal plasma and generation of reverse magnetic fields. *Phys. Rev. Lett.* **33**, 1139 – 1141. doi:10.1103/PhysRevLett.33.1139.

Tousey, R.: 1973, First results from Skylab. *Bull. Am. Astron. Soc.* **5**, 419.

Zurbuchen, T.H., Richardson, I.G.: 2006, *In-situ* solar wind and magnetic field signatures of interplanetary coronal mass ejections. *Space Sci. Rev.* **123**, 31 – 43. doi:10.1007/s11214-006-9010-4.

Ann. Geophys., 27, 4057–4067, 2009
www.ann-geophys.net/27/4057/2009/

Annales Geophysicae

The expected imprint of flux rope geometry on suprathermal electrons in magnetic clouds

M. J. Owens[1], **N. U. Crooker**[2], **and T. S. Horbury**[1]

[1]Space and Atmospheric Physics, The Blackett Laboratory, Imperial College London, Prince Consort Road, London SW7 2BW, UK
[2]Center for Space Physics, Boston University, Boston MA 02215, USA

Received: 1 June 2009 – Revised: 20 August 2009 – Accepted: 14 October 2009 – Published: 26 October 2009

Abstract. Magnetic clouds are a subset of interplanetary coronal mass ejections characterized by a smooth rotation in the magnetic field direction, which is interpreted as a signature of a magnetic flux rope. Suprathermal electron observations indicate that one or both ends of a magnetic cloud typically remain connected to the Sun as it moves out through the heliosphere. With distance from the axis of the flux rope, out toward its edge, the magnetic field winds more tightly about the axis and electrons must traverse longer magnetic field lines to reach the same heliocentric distance. This increased time of flight allows greater pitch-angle scattering to occur, meaning suprathermal electron pitch-angle distributions should be systematically broader at the edges of the flux rope than at the axis. We model this effect with an analytical magnetic flux rope model and a numerical scheme for suprathermal electron pitch-angle scattering and find that the signature of a magnetic flux rope should be observable with the typical pitch-angle resolution of suprathermal electron data provided ACE's SWEPAM instrument. Evidence of this signature in the observations, however, is weak, possibly because reconnection of magnetic fields within the flux rope acts to intermix flux tubes.

Keywords. Interplanetary physics (Interplanetary magnetic fields; Energetic particles) – Solar physics, astrophysics, and astronomy (Flares and mass ejections)

1 Introduction

Coronal mass ejections (CMEs) are huge expulsions of solar plasma and magnetic field through the corona and out into the heliosphere, known to be the major cause of severe geomagnetic disturbances (e.g., Cane and Richardson, 2003). The interplanetary manifestations of CMEs (ICMEs) provide critical information about their magnetic configuration and orientation, which may prove key in constraining theories of CME initiation as well as aiding our understanding of the evolution of ejecta during their transit from the Sun to 1 AU. A variety of signatures are used to identify ICMEs from in situ data, including, but not limited to, low proton temperatures, counterstreaming suprathermal electrons, reduced magnetic field variance and enhanced ion charge states. See Wimmer-Schweingruber et al. (2006) for a more complete review. Magnetic clouds (MCs), a subset of ICMEs comprising somewhere between a quarter to a third of all ejecta (e.g., Cane and Richardson, 2003), are further characterized by a smooth rotation in the magnetic field direction and an enhanced magnetic field magnitude (Burlaga et al., 1981). The field rotation has been attributed to a magnetic flux-rope (MFR, Lundquist, 1950) and commonly modeled as a constant-α force-free MFR (Burlaga, 1988; Lepping et al., 1990), where currents are assumed to be field aligned and α is the constant relating the current density $\boldsymbol{J}$ to the magnetic field vector $\boldsymbol{B}$. This enables single-point, in situ, time series to be interpreted in terms of the large-scale structure of the ejection.

The present study addresses the behavior of suprathermal electrons in magnetic clouds. In general, suprathermal electrons (i.e., >70 eV) are of key interest to studies of the solar wind because the field-aligned "strahl" acts as an effective tracer of heliospheric magnetic field topology. A single strahl indicates open magnetic flux (Feldman et al., 1975; Rosenbauer et al., 1977), while counterstreaming electrons (CSEs) often signal the presence of closed magnetic loops with both foot points rooted at the Sun (Gosling et al., 1987). A strong field-aligned strahl is expected and observed in the ambient solar wind near 1 AU, as even an initially isotropic distribution near the Sun will undergo pitch-angle focusing due to conservation of magnetic moment in a decreasing magnetic field intensity. Strahl widths at 1 AU, however, are much

Correspondence to: M. J. Owens
(m.owens@imperial.ac.uk)

broader than would be expected from focusing alone, suggesting significant pitch-angle scattering must occur (e.g., Pilipp et al., 1987). Indeed, with increasing distance from the Sun, pitch-angle scattering becomes increasingly important because the rate of focusing decreases owing to the increasing angle between the spiraling magnetic field direction and intensity gradient (Owens et al., 2008). This results in the strahl width increasing with heliocentric distances (Hammond et al., 1996). For closed magnetic loops in an ICME, the antisunward motion of the loop apex will mean that in-transit scattering on the increasingly longer field-line will result in eventual loss of the sunward beam and, hence, loss of the CSE signature, which has important implications for the interpretation of the solar cycle evolution of the heliospheric magnetic field (Owens and Crooker, 2006, 2007).

The flux rope structure of magnetic clouds means the field-line length is shortest at the axis of the MFR, increasing toward the edge as the field winds about the axis. Indirect evidence for the varying length of field lines in magnetic clouds was found in the arrival-time dispersion of solar flare electrons intermittently injected into the October 1995 magnetic cloud (Larson et al., 1997). (Chollet et al., 2007) recently used bursts within energetic particle dispersions within an ICME to infer a jumbled mix of field-line lengths from $\sim$1 to 3.5 AU. While energetic particle events can only be used to calculate field-line length in a very limited number of ICMEs, field-line length should also have an effect on suprathermal electrons, which continually stream away from the Sun along field lines. Since the suprathermal electron time of flight and, hence, pitch-angle scattering time, increases with field-line length, the strahl width should exhibit a characteristic signature as a flux rope convects past an observer at 1 AU.

To characterize the expected imprint of flux rope geometry on suprathermal electron observations, we combine two forms of modeling. In Sect. 2, an analytical MFR model is used to calculate the length of magnetic field lines which connect an observer inside an MC to the Sun. In Sect. 3 a numerical model of suprathermal electron evolution is used to estimate the suprathermal electron strahl widths corresponding to the MFR magnetic field line lengths. Finally, in Sect. 5 we look for the predicted variation in strahl width in ACE observations of magnetic clouds.

2 Magnetic flux rope model

The classic model for a magnetic cloud-associated flux rope, the constant-α force-free flux rope (Burlaga, 1988; Lepping et al., 1990), assumes the magnetic cloud can locally be approximated as a 2-dimensional cylindrical structure with a circular cross-section. The field is entirely axial at the center of the rope, becoming increasingly poloidal toward the outer edge. It is useful to define a parameter Y, the ratio of the distance from the flux rope axis, r, to radius of the flux rope, r_0. The magnetic field of a force-free flux rope is then given by:

$$\begin{aligned} B_{\mathrm{AX}}(Y) &= B_0 J_0(\alpha Y) \\ B_{\mathrm{POL}}(Y) &= \pm B_0 J_1(\alpha Y) \end{aligned} \quad (1)$$

where B_{AX} and B_{POL} are the magnetic field strengths along the axial and poloidal directions, respectively. The poloidal component takes positive or negative values depending on the sense of rotation of the magnetic field about the axis (i.e., the chirality of the flux rope). J_0 and J_1 are zero and first order Bessel functions of the first kind, respectively. α is a constant which determines the outer edge of the flux rope. It is normally assumed to be 2.408, which effectively sets the outer edge of the flux rope at the point where the field first becomes entirely poloidal (Burlaga, 1988; Lepping et al., 1990).

The angle of the magnetic field to the axial direction, θ, is a function of Y:

$$\tan\theta = \frac{B_{\mathrm{AX}}}{B_{\mathrm{POL}}} = \frac{J_0(\alpha Y)}{J_1(\alpha Y)} \quad (2)$$

We initially adopt this simple force-free geometry, later modifying the model to incorporate effects which will substantially alter the estimate of field-line length L connecting a 1-AU observer to the Sun. The left-hand panel of Fig. 1 defines the basic parameters: The rope is of radius r_0. At a distance r from the axis, the field takes the form of a helix about the axis, shown as the solid/dashed blue line, and makes an angle θ to the axis. The field makes one complete revolution about the axis in a height, H, along the axis. For an axis of length L_{AX}, the field makes N revolutions (in the example shown, $N\sim$1.8). The right-hand panel shows the curved face of the cylinder unrolled to form a flat plane. The relations between θ, H, L_{AX}, N, r, r_0 and the length of the field line, L, are easier to visualize in this way. It can immediately be seen that the length of the field line is:

$$L = \sqrt{L_{\mathrm{AX}}^2 + (2N\pi r)^2} \quad (3)$$

and substituting $NH{=}L_{\mathrm{AX}}$ and $H{=}2\pi r/\tan\theta$ gives:

$$L = \frac{L_{\mathrm{AX}}}{\cos\theta} \quad (4)$$

Thus for a force-free flux rope, the length of the magnetic field line depends only on θ (which, in turn, is solely a function of Y) and the length of the axial field line. L is independent of the radius of the flux rope, as the number of revolutions per unit axial length is linearly related to r, the distance from the axis.

To estimate L_{AX}, it is necessary to extend the 2-dimensional force-free model to a more global configuration. Assuming the flux rope plasma moves radially but the foot points of the flux rope remain connected to the Sun, as suggested by observations (Gosling et al., 1987), the axial field

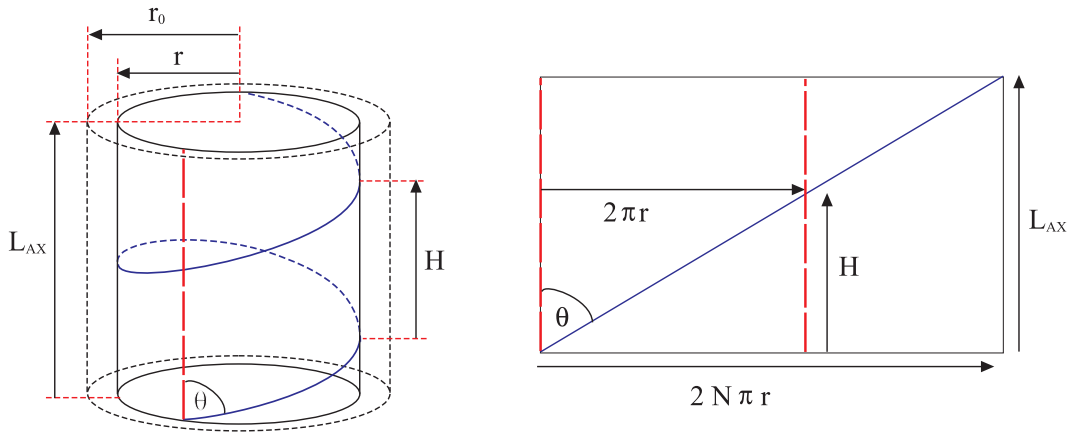

Fig. 1. The left-hand panel shows the cylindrical geometry implied by a force-free flux rope. The rope is of radius r_0. At a distance r from the axis, the field takes the form of a helix about the axis, shown as the solid/dashed blue line, and makes an angle θ to the axis. The field makes one complete revolution about the axis in a height, H, along the axis. For an axis of length L_{AX}, the field makes N revolutions (in the case shown $N\sim1.8$). The right-hand panel shows the curved face of the cylinder unrolled to form a flat plane. The relations between θ, H, L_{AX}, N, r, r_0 and the length of the field line, L are easier to visualize in this way.

will lie predominantly along the Parker Spiral. Thus at a heliocentric distance R, the axis makes an angle γ to the radial:

$$\gamma = \arctan\left(\frac{\Omega R}{V_{CR}}\right)\cos\lambda \tag{5}$$

where λ is the heliographic latitude, $\Omega{=}2\pi/T_{SID}$, and T_{SID} is the sidereal rotation period of the Sun. L_{AX} is therefore given by:

$$L_{AX} = \int_0^{1\,AU} \frac{dR}{\cos\gamma} \tag{6}$$

We now include the effect of expansion to allow for axial curvature effects, and later in this section, we incorporate a more realistic cross-sectional topology. Expansion is assumed to be self-similar about the axis, consistent with the linearly declining speed profiles observed within magnetic clouds (Owens et al., 2005). Thus while the axis of the flux rope moves antisunward at a cruise speed V_{CR}, the edges of the flux rope move away from the axis at a speed V_{EX}. The radius of the flux rope therefore varies with heliocentric distance as:

$$r_0 = \frac{V_{EX}R}{V_{CR}} \tag{7}$$

The left panel of Fig. 2 shows a snapshot of the model flux rope using paramters $V_{CR}{=}400$ km/s and $V_{EX}{=}100$ km/s, typical magnetic cloud values (Owens et al., 2005). A heliocentric distance of 1 AU is shown as the black dotted curve, while the Sun is represented by a solid black circle. Only the half of the flux rope which provides the shortest magnetic connection between the Sun and 1 AU is shown. Field lines at $Y{=}0$, 0.3, 0.6 and 0.9 are shown by black, blue, green and red lines, respectively. Numerically integrating the distance along each helical path gives field-line lengths of 1.17, 1.23, 1.68 and 5.19 AU, respectively.

The open circles in the right panel of Fig. 2 show the field-line length between 1 AU and the Sun as a function of distance from the MFR axis. We find the following functional form, shown as the solid black line, adequately describes the model points:

$$L[AU] = 0.631 - 0.1176\tan(-0.288Y - 1.285) \tag{8}$$

Finally, we include the effect of MFR cross-sectional elongation in the non-radial direction. Magnetic clouds at 1 AU are known to be highly distorted from the circular cross-section assumed by the force-free approximation. Even if a flux rope has a circular cross-section near the Sun, it will become elongated in the non-radial direction by maintaining a constant angular width as it travels to 1 AU (e.g., Newkirk et al., 1981; McComas et al., 1988; Riley and Crooker, 2004; Owens, 2006). While it is difficult to analytically incorporate this effect into the flux rope model presented here, the increase in field-line length can be approximated by considering the increase in path length around the flux rope cross section. The solid lines in the middle panel of Fig. 2 represent model field non-elongated field lines for $Y{=}0.3$, 0.6 and 0.9 for a force-free flux rope with its axis at 1 AU, which has traveled from the Sun at $V_{CR}{=}400$ km/s and undergone expansion at $V_{EX}{=}100$ km/s. Thus at 1 AU, the flux rope has a radial width of $2V_{EX}AU/V_{CR}$. The dashed lines represent the equivalent cross-section for a flux rope with the same characteristic speeds and, hence, radial width at 1 AU as the force-free example but for a MFR which has undergone the kinematic distortion expected from radial propagation (Owens et al., 2006). The increase in field-line length per turn of the magnetic field about the axis is found to be

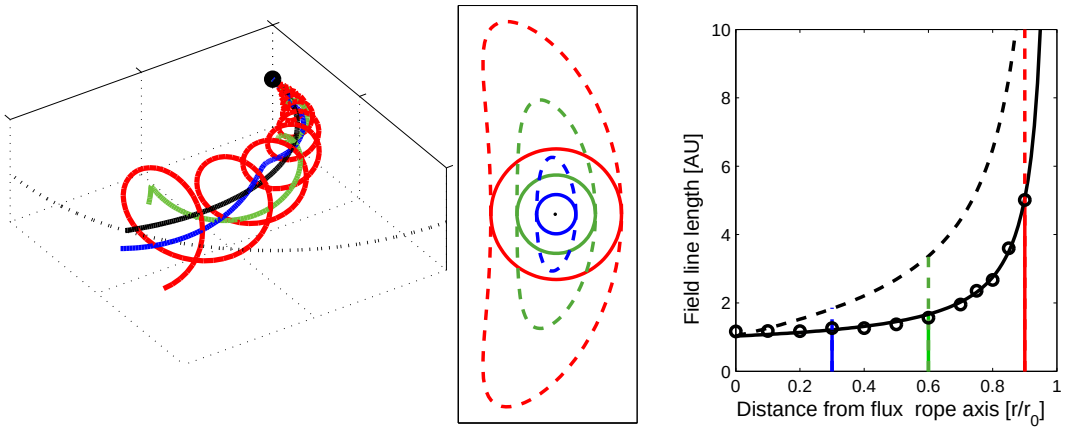

Fig. 2. The left panel shows a snapshot of the model magnetic flux rope. A heliocentric distance of 1 AU is shown as the black dotted curve, while the Sun is represented by a solid black circle. Only the half of the flux rope which provides the shortest magnetic connection between the Sun and 1 AU is shown. Field lines at Y=0, 0.3, 0.6 and 0.9 are shown by black, blue, green and red lines, respectively. Solid lines in the center panel show a cross-section of the flux rope at 1 AU, while the dashed lines show how the cross-section is modified by kinematic distortion. The right panel shows the length of the field lines connecting 1-AU to the Sun as a function of distance from the flux rope axis, with solid (dashed) lines indicating a flux rope with a circular (kinematically-distorted) cross section.

$\sim 1.7Y$. This correction is applied to circular cross section estimates of field line length to approximate the effect of cross-sectional elongation, shown as the dashed line in the right-hand panel of Fig. 2. The best fit is given by:

$$L[AU] = 1.07 - 0.20\tan(-0.288Y - 1.285) \quad (9)$$

3 Suprathermal electron evolution

The model of Owens et al. (2008) is used to determine the expected strahl width for a given pitch-angle scattering rate and field-line length. This numerical scheme iteratively solves electron heliocentric distance and pitch-angle, allowing for movement along the magnetic field direction and convection with the bulk solar wind motion. Electrons undergo the competing effects of adiabatic focusing from conservation of magnetic moment and pitch-angle scattering toward an isotropic distribution. The radial evolution of the suprathermal electron strahl width in the fast solar wind can be well matched by this scheme (Owens et al., 2008).

In this study we use a grid of 500 cells in electron pitch-angle (PA) space, equally spaced in cos PA. Grid cells are spaced by 0.01 AU in heliocentric distance. Although we are interested in strahl widths at 1 AU, the simulation domain extends out to 2 AU to capture the contribution of electrons which are scattered to pitch angles greater than 90° and thus propagate sunward. A time step of 100 s and a solar wind speed (V_{SW}) of 400 km/s are used. Electron energy is set at 272 eV, as this is the center value of the most commonly-used suprathermal electron energy band for characterizing the strahl (e.g., Anderson et al., 2008).

The model field-line length is adjusted by over- or under-winding a Parker Spiral magnetic field (though the bulk solar wind speed experienced by electrons is held constant at 400 km/s). We choose not to use the exact MFR field geometry outlined in the previous section, as it would require extremely high spatial and temporal resolution due to the large gradients in the magnetic field direction, making it computationally prohibitive. Note that the electron model used in this study only accounts for the two major effects: Changing magnetic field strength, which adiabatically focuses electrons, and time of flight, which allows greater pitch-angle scattering to occur. The orientation of the field does not have a direct effect, other than directing electrons into regions of different field strength. Thus while the over/under-wound Parker spiral field will not capture the repeated adiabatic focusing and defocusing of electrons traversing the helical magnetic field of a flux rope, it will capture the net pitch-angle focusing and the net amount of scattering experienced by the electrons.

Pitch-angle scattering is performed in an ad-hoc manner, by Gaussian broadening the PA distribution at each time step, pushing the distribution toward isotropy. A broadening factor of σ=0.0014 applied each second was found to best match the observed strahl width in the fast solar wind (Hammond et al., 1996; Owens et al., 2008). In this study, three levels of scattering are used: The fast solar wind level, taken as "medium" scattering, and "low" and "high" levels of scattering at half and double this value, respectively. The model width at 1 AU is then computed from the model PA distribution using the same fitting procedure as Hammond et al. (1996) and Owens et al. (2008). Suprathermal electron pitch-angle distributions are fit with the following functional form:

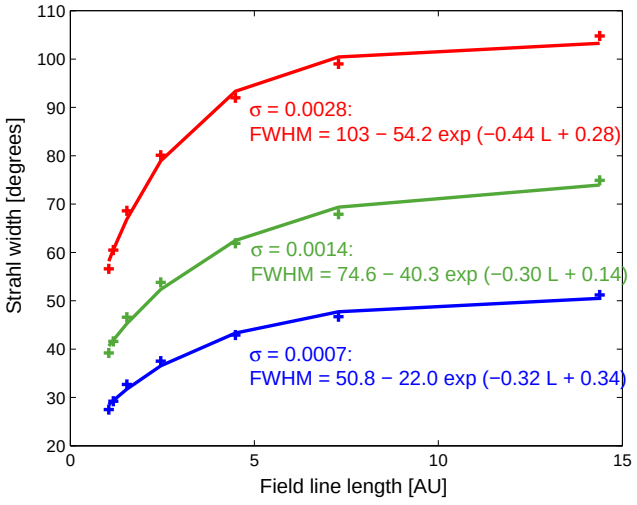

Fig. 3. The effect of varying scattering rate and field-line length on the strahl FWHM at 1 AU. As expected, the increased time of flight along longer field lines results in a broader strahl. As $L \rightarrow \infty$, however, the strahl width asymptotes well before isotropy is achieved. This is because the time of flight of the electrons, from the Sun to the observer, has a maximum value of $1\,\mathrm{AU}/V_{SW}$ due to the convection of the magnetic field line with the bulk solar wind.

$$j(PA) = K_0 + K_1 \exp\left[\frac{-PA^2}{K_3}\right] \tag{10}$$

where $j(PA)$ is the differential electron flux at pitch angle PA, K_0 describes the electron density of the halo and K_3 determines the width of the strahl (the full width at half maximum is given by FWHM$=2\sqrt{(\ln 2)K_3}$). K_1 is the maximum electron density of the strahl above K_0.

Figure 3 shows the effect of varying scattering rate and field-line length on the strahl width at 1 AU. As expected, the increased time of flight along longer field lines results in a broader strahl. The three levels of scattering are fit with an exponential function, to give the following relations:

$$\begin{aligned}
&\sigma = 0.0007[s^{-1}]: \\
&\qquad \mathrm{FWHM}(^\circ) = 51 - 22\exp\left[0.34 - 0.32 L_{AU}\right] \\
&\sigma = 0.0014[s^{-1}]: \\
&\qquad \mathrm{FWHM}(^\circ) = 75 - 40\exp\left[0.14 - 0.30 L_{AU}\right] \\
&\sigma = 0.0028[s^{-1}]: \\
&\qquad \mathrm{FWHM}(^\circ) = 103 - 54\exp\left[0.28 - 0.44 L_{AU}\right]
\end{aligned} \tag{11}$$

where L_{AU} is the field-line length in AU. As $L \rightarrow \infty$, however, the strahl width asymptotes well before isotropy is achieved. This is because the total radial velocity of an electron is given by $V_{SW} + V_{\parallel}\cos\gamma$, where $V_{\parallel}$ is the electron speed along the magnetic field direction and γ is the angle of the field to the radial direction. The first term represents the propagation of magnetic field lines out from the Sun at the bulk solar wind speed. Thus regardless of the field-line length, the maximum time of flight of an anti-sunward propagating electron to a $1-AU$ observer will be $1\,\mathrm{AU}/V_{SW}$.

4 Model time series

We now combine the MFR and electron scattering models to produce the expected suprathermal electron time series at 1 AU. The first step is to generate field-line lengths connecting an observer at 1 AU to the Sun as a magnetic cloud propagates out through the heliosphere. As the expansion speed of magnetic clouds is often a significant fraction of the cruise speed (Owens et al., 2005), we build up a true time series of the model parameters by time evolving past a fixed point at 1 AU rather than take a radial slice through a snapshot of the MFR model.

For this initial time series, the observer is assumed to pass directly through the axis of the flux rope (i.e., through $Y=0$), but this is later relaxed when comparing to observations. A cruise (expansion) speed of 400 (100) km/s is used. The top panel of Fig. 4 shows the resulting time series of the magnetic field line length in the flux rope connecting the 1-AU observer to the Sun, with solid (dashed) lines representing a circular cross-section (kinematically distorted) flux rope. Note the logarithmic scale on the y-axis. The second panel shows the result of combining the field-line length with the scattering code to produce a time series of 272 eV electron pitch-angle density at 1 AU. This type of plot is commonly used to display suprathermal electron observations. It shows the electron flux at a given energy level, normalized to the maximum and minimum densities at each time step, as a function of pitch angle and time. The strahl width exhibits a clear broad-narrow-broad trend. The third panel shows the computed strahl widths for high (red), medium (green) and low (blue) levels of pitch-angle scattering, for circular cross-section (solid) and kinematically-distorted (dashed) flux rope models. The bottom panel shows the strahl width normalized to the mean strahl width in the event. This normalized width is independent of the scattering rate and only a function of field-line length.

The maximum change in strahl width expected through a MFR, ΔFWHM, is a useful parameter for assessing whether or not the flux rope signature should be observable with a given instrument: If ΔFWHM is below the pitch-angle resolution, the effect cannot be measured. Figure 5 shows ΔFWHM as a function of the closest approach of the observer to the axis of a MFR (i.e., the minimum value of Y, often referred to as the "impact parameter"). The color code is the same as in Fig. 4. Very few magnetic clouds are actually encountered "on axis", and thus the minimum value of Y sampled by the observer is normally >0. Although ΔFWHM drops with impact parameter, there is still significant variation in the strahl width even when the observer passes far (e.g., $Y \sim 0.5$) from the axis of the flux rope, particularly for higher scattering rates. For extreme glancing encounters of

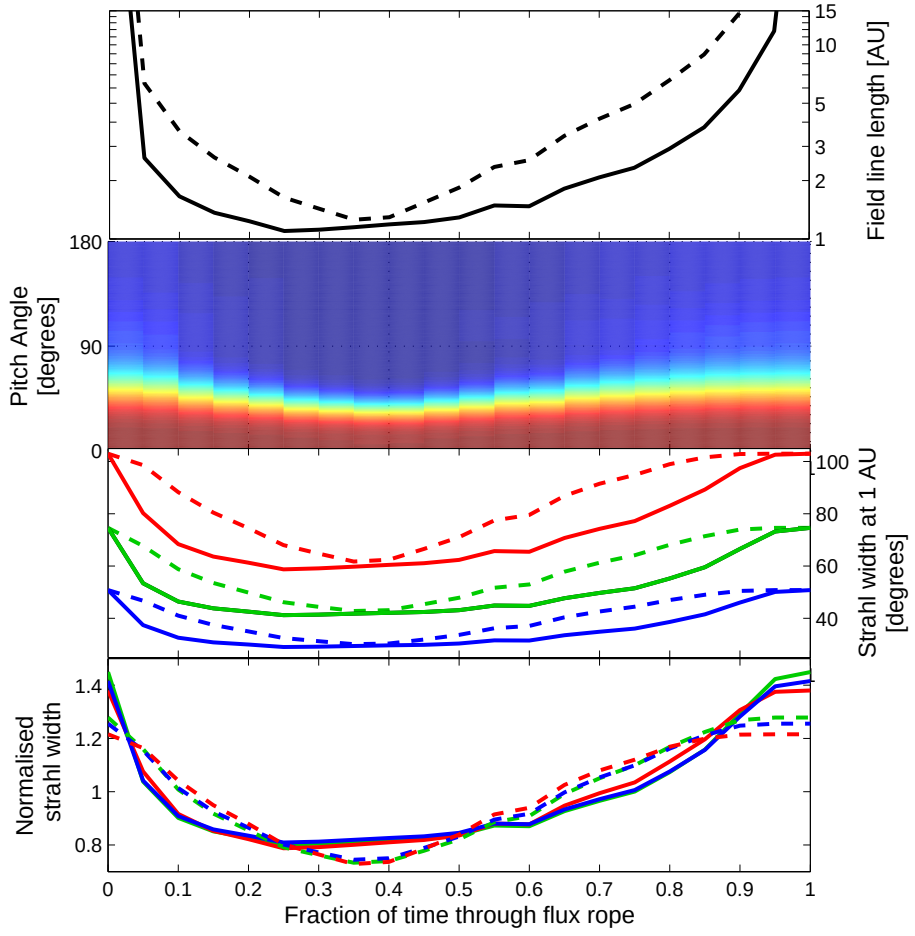

Fig. 4. The model flux rope field-line lengths and expected suprathermal electron signatures. Solid (dashed) lines represent a circular cross-section (kinematically-distorted) flux rope. The top panel shows a time series of field line length connecting an observer to the Sun. Note the logarithmic scale on the y-axis. The second panel shows the normalized 272eV electron pitch-angle density, which exhibits a clear broad-narrow-broad trend through the flux rope. The third panel shows strahl FWHM for high (red), medium (green) and low (blue) levels of pitch-angle scattering. The bottom panel shows the strahl width normalized to the mean width, in the same format.

flux ropes, where the minimum Y intersected by an observing spacecraft is >0.5, the field rotation signature will be significantly weaker, and the event is unlikely to be classified as a magnetic cloud.

The SWEPAM instrument (McComas et al., 1998) on the ACE spacecraft collects electron data in approximately $6^\circ \times 20^\circ$ angular bins. For the standard SWEPAM suprathermal electron data set, the data is then binned into 9° resolution in pitch-angle space. Figure 5 shows that under most circumstances the difference in strahl width across a flux rope should be more than twice this SWEPAM resolution angle and thus clearly observable.

5 Observations

5.1 Case studies

In this section we look for the expected suprathermal electron signature of a magnetic flux rope in the ACE SWEPAM (McComas et al., 1998) data. Three magnetic clouds, listed as A, B, and C in Table 1, have been selected from the Cane and Richardson (2003) ICME list (available at http://www.ssg.sr.unh.edu/mag/ace/ACElists/ICMEtable.html) for their classic form and range of strahl widths.

Figure 6 shows data from Event A. There is a clear rotation in the magnetic field direction, indicative of a magnetic flux rope. This is reflected in the ratios of the eigenvectors in the magnetic field variance directions listed in Table 1 (High ratios, typically >4, indicate strong flux rope signatures (e.g., Bothmer and Schwenn, 1998)). Fitting the Owens et al.

Table 1. Start and end times of three examples of classic magnetic clouds selected from the Cane and Richardson (2003) ICME list. $\lambda_{INT}/\lambda_{MIN}$ and $\lambda_{MAX}/\lambda_{INT}$ are the ratios of magnetic field variances in the variance directions. Y is the closest approach of the observing spacecraft to the flux rope axis inferred from a flux rope model fit.

Event	Start	End	$\lambda_{INT}/\lambda_{MIN}$	$\lambda_{MAX}/\lambda_{INT}$	Y
A	20 Aug 1998 06:00 UT	21 Aug 1998 20:00 UT	23.4	3.75	0.12
B	4 Mar 1998 13:00 UT	6 Mar 1998 09:00 UT	15.5	4.13	0.10
C	28 Oct 2000 21:00 UT	29 Oct 2000 22:00 UT	3.15	7.03	0.27

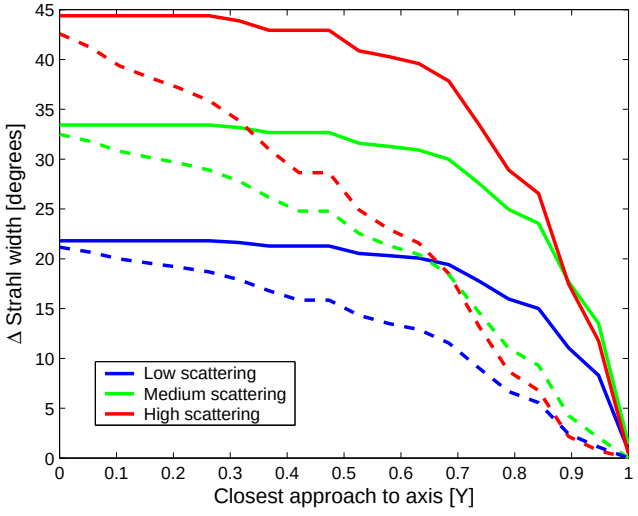

Fig. 5. The maximum expected change in strahl width, a measure of how readily the flux rope signature should be observable, as a function of the closest approach of the observer to the axis of the event (i.e., the minimum value of Y, often referred to as the "impact parameter"). The color code is the same as Fig. 4. Although ΔFWHM drops off with impact parameter, there is significant variation in the strahl width even when the observer passes far (e.g., $Y \sim 0.5$) from the axis of the flux rope.

(2006) magnetic cloud model to the observed time series suggests the spacecraft passed close to the axis (Y=0.12). Despite the apparently near-perfect conditions, the expected signature of a dip in suprathermal electron strahl width is not present. This conclusion would not change if alternative cloud boundaries were chosen as the strahl observed immediately before and after the period of magnetic field rotation is narrower, not wider, than inside the event. Note, however, that in the ambient solar wind, the strahl width is generally broader than in the magnetic cloud. As the field-line length is expected to be shorter in the ambient solar wind than in the cloud, pitch-angle scattering must be greatly suppressed in this magnetic cloud compared to ambient conditions. See, however, Event B.

The magnetic field data for Events B and C are not shown, but Table 1 lists the ratios of the eigenvalues in the variance directions to quantify the quality of the flux rope signature. Also listed are model values of Y, the closest approach of the spacecraft to the axis, which are both small.

The top panels of Fig. 7 show the 272 eV suprathermal electron pitch-angle distributions, normalized at each time step, for the three magnetic cloud intervals. For each event, we compute the flux in the 0° and 180° strahls (i.e., K_1 in Eq. 10) throughout the magnetic cloud interval, and define the dominant strahl as that with the highest flux. For Event A the dominant strahl is at 180° pitch angle, with an order of magnitude higher electron flux than any 0° strahl. We note, however, that the dominant strahl is not always as easy to define, particularly in events with a strong counterstreaming signature. For Event A, there is a clear broadening of the strahl near the center of the cloud and evidence of counterstreaming near the rear of the cloud. This intermingling of apparently open and closed fields is not uncommon within magnetic clouds (e.g., Crooker et al., 2008). The dominant strahl for Event B is at 0° pitch angle. It is much broader than the strahl in Event A. Finally, Event C has a very narrow strahl at 180°, close to, but above the pitch-angle resolution of the standard SWEPAM suprathermal electron data, with intermittent counterstreaming throughout the cloud. These three events highlight the large event-to-event variability in the suprathermal electron properties of magnetic clouds (see also Anderson et al., 2008).

The black lines in the middle panels of Fig. 7 show the strahl width, computed from the observed pitch-angle distributions using Eq. (10). Solid (dashed) colored lines show the model strahl widths for circular (kinematically-distorted) cross-section flux ropes using the inferred values of Y listed in Table 1. Low, medium and high levels of pitch-angle scattering are shown by the blue, green and red lines, respectively. The bottom panels show the normalized strahl widths in the same format. In all three magnetic clouds, the expected imprint of flux rope geometry on the suprathermal electrons is absent.

5.2 Statistical survey

In this section we statistically survey magnetic cloud suprathermal electron profiles. All the events classified as magnetic clouds in the Cane and Richardson (2003) ICME list observed between 1998 and 2007 (74 events) are considered. For each event, the dominant strahl is determined

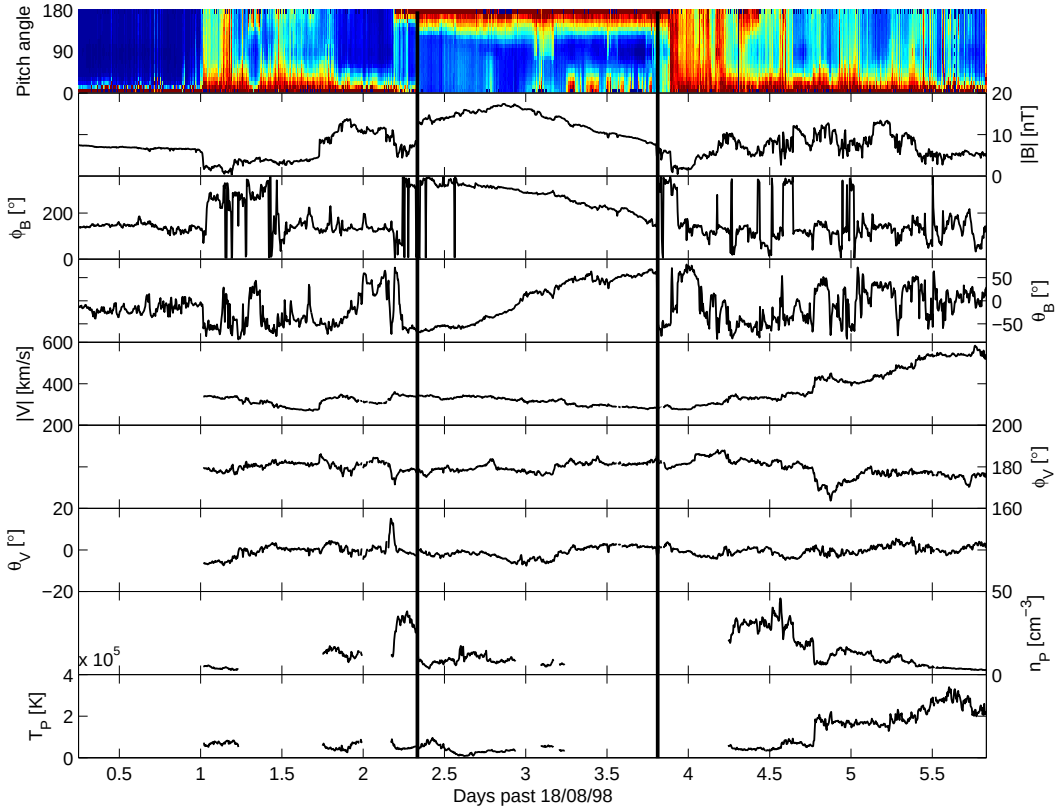

Fig. 6. Event A: A magnetic cloud observed in August 1998. The panels, from top to bottom are: The 272 eV electron pitch-angle distribution, the magnetic field magnitude, the in- and out-of-ecliptic magnetic field angles, the solar wind flow speed, the in- and out-of-ecliptic solar wind flow angles, the proton density and proton temperature. The boundaries of the magnetic cloud are shown by the solid vertical lines. A kinematically-distorted flux rope model fit to the observed magnetic field time series (not shown), suggests the axis of the flux rope passed within r/r_0=0.12 of ACE at the point of closest approach. The dominant strahl, at 180° pitch angle, remains ∼75° width throughout the magnetic cloud. Thus the expected suprathermal electron signature of a magnetic flux rope is not present.

within the given magnetic cloud boundaries, and the strahl width is fit using Eq. (10). The left-hand panel of Fig. 8 shows a superposed epoch plot of the strahl width as a function of time, expressed as a fraction of the event's duration. The colored lines show the model predictions in the same format as Fig. 4, assuming on-axis encounters of magnetic clouds. In this view, which covers a wide range of strahl widths to accommodate the full range of scattering constants, the superposed epoch plot shows little variation, and the predicted flux rope signature does not appear to be present. In contrast, the right-hand panel shows the same strahl width data normalized to the mean strahl width within an event. In this format, there is some evidence of the predicted trend in the observations, with an asymmetric dip in strahl width toward the center of magnetic clouds. The trend, however, is much weaker than predicted by the models.

6 Conclusions

Inside a magnetic flux rope, the varying pitch of the helical field lines means that their lengths vary substantially between the Sun and an observer. This, in turn, affects the suprathermal electron time of flight and, hence, the pitch-angle scattering time. The strahl width observed as a flux rope convects past a 1-AU observer is therefore expected to exhibit a characteristic variation from a broad strahl at the outer edge that narrows toward the axis and then broadens again toward the opposite edge.

We have combined an analytical magnetic flux rope model with a numerical suprathermal electron scattering code to estimate this expected imprint of flux rope geometry on suprathermal electrons in magnetic clouds. The field-line length is found to increase by more than an order of magnitude from the axis to the edge of the flux rope. The associated variation in strahl width at 1 AU, however, is not as extreme because convection of magnetic field lines with

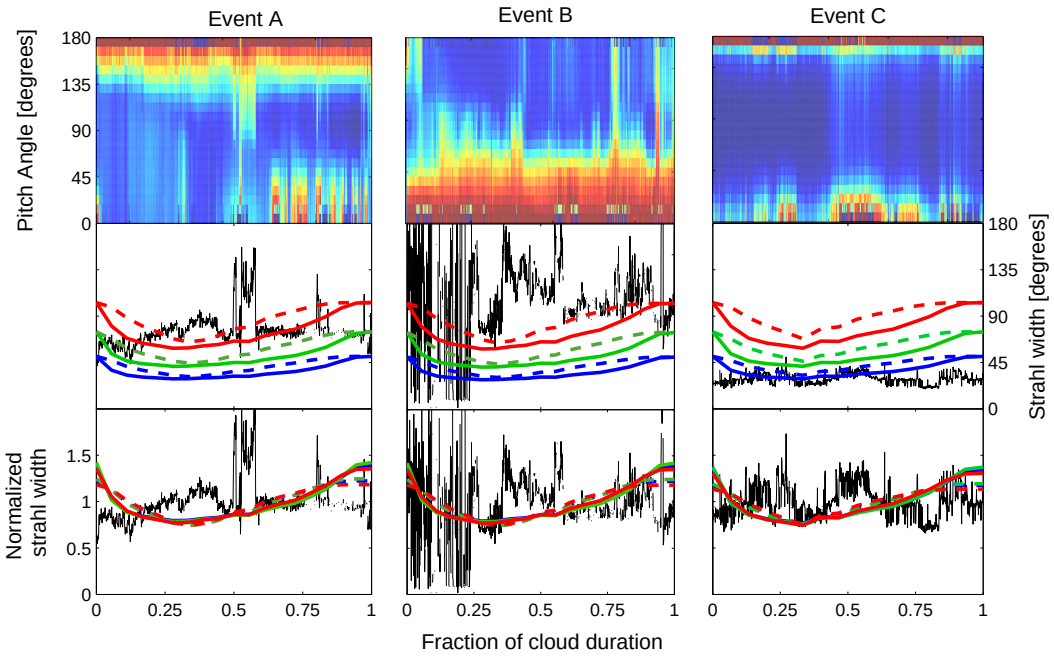

Fig. 7. The suprathermal electron properties inside the three magnetic cloud case studies. The top panels show the normalized pitch-angle distribution within the clouds. The black lines in the middle panels show the widths of the dominant strahls, computed from a Gaussian fit in pitch-angle space, with the colored lines showing the expected strahl width variations for different flux rope encounters (in the same format as Fig. 4). The bottom panels show the normalized strahl widths in the same format.

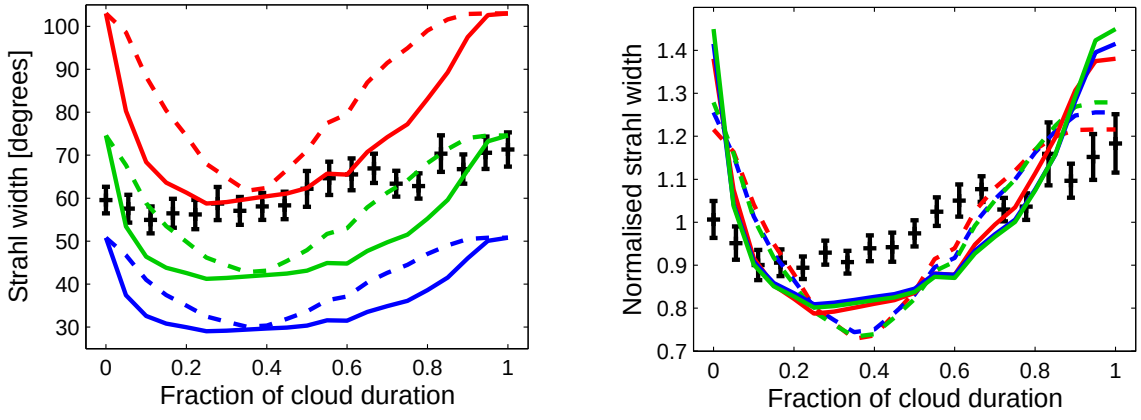

Fig. 8. A superposed epoch plot of the strahl widths in all 74 magnetic clouds catalogued by Cane and Richardson (2003) between 1998 and 2007. Coloured lines show the model predictions in the same format as Fig. 4. In the right panel there is some evidence of the predicted trend in the normalized strahl width observations.

the ambient solar wind imposes a maximum electron time of flight of 1 AU/V_{SW}, independent of field-line length.

The expected variation in strahl width is found to be dependent on the level of scattering in the sense that magnetic clouds with broader strahls throughout should exhibit a more pronounced flux rope imprint. If, however, the strahl width is normalised to the average strahl width observed in the event, the flux rope signature is independent of the scattering rate. For the flux rope signature to be observable, the maximum change in strahl width through a flux rope, ΔFWHM, must be above the pitch-angle resolution of the instrument used to measure the suprathermal electron distribution. For the standard ACE SWEPAM data set (McComas et al., 1998), this cut-off point is 9°. Even for magnetic cloud encounters far from the axis of the flux rope, this signature should, in principle, be observable for a range of scattering rates.

Suprathermal electron observations for three classic examples of magnetic clouds were examined. There was large event-to-event variation in strahl widths, but none of the events exhibited the expected flux rope signature. We also performed an statistical survey of 74 magnetic clouds. Although the superposed epoch analysis performed here removes much of the information about event-to-event variability, there is nevertheless some evidence of the expected strahl width variation, though it is a much weaker signature than the models predict. This aspect of the study clearly merits further, more detailed, investigation.

Possible reasons why the observed strahl width variation is weaker than predicted can be broadly categorized into unmet assumptions about the magnetic field structure of magnetic clouds and the suprathermal electron scattering.

Assuming first that the field-line length has been accurately determined, it is necessary to consider the assumptions made in determining the associated strahl width at 1 AU. The model of Owens et al. (2008) assumes that all scattering undergone by suprathermal electrons occurs in pitch-angle space, and electrons do not lose or gain energy. There is support for this assumption in the observed conservation of electrons scattered from the strahl to the halo at a given energy (Maksimovic et al., 2005), but the postulated energy loss by cross-field drift in the motional electric field has yet to be evaluated (J. R. Jokipii and N. A. Schwadron, personal communication, 2008, 2009). We are also assuming that there is no systematic variation in the scattering properties within a MFR by applying the same scattering rate throughout the structure. If scattering is enhanced at the axis of a flux rope and reduces toward the outer edge, it will act against the field-line length variation and reduce the flux rope signature on suprathermal electrons. There is no reason to expect this behavior, but we cannot discount the possibility.

The most fundamental assumption we have made about the structure of a magnetic cloud is that, locally at least, it forms a flux rope with helical fields that increase in pitch from the straight central axis to the tightly wound edge. This is the widely accepted explanation for the observed magnetic field rotation and is thus unlikely to be an unmet assumption responsible for the weak flux rope imprint, however, there has been recent speculation that a field rotation may not always indicate a flux rope structure (Jacobs et al., 2009).

Setting α equal to 2.408, which implicitly assumes the flux rope edge to be occur where the field becomes entirely poloidal, also has implications for the findings in this study. If the flux rope field is not so tightly wound, or the outer, tightest-wound fields are removed by magnetic reconnection with the ambient solar wind (Schmidt and Cargill, 2003), then the expected variation in field-line length, and hence strahl width, will be reduced. The fact that the field in the maximum variance direction is often seen to rotate through a full 180°, however, as in Event A, argues in favor of our assumption about α.

Magnetic reconnection may be at least a partial explanation for the weak flux rope signature in suprathermal electrons. Near the Sun reconnection is known to open up the closed loops within magnetic clouds (Crooker and Webb, 2006). This process will move the flux rope foot points about at the photosphere but is unlikely to significantly affect the field-line length. Magnetic reconnection between different flux tubes within the magnetic cloud (Gosling et al., 2007), however, would serve to mix field lines of different length and possibly reduce the suprathermal electron signature.

A second possibility is a systematic increase in adiabatic focusing with distance from the magnetic cloud axis, counteracting the extra scattering time from increased field line length. The peak magnetic field intensity is often located close to the centre of a magnetic cloud, so if the foot point field strength back at the Sun is uniform, this suggests that there is a greater variation in field strength between the Sun and 1 AU close to the edges of the flux rope, and hence a stronger focusing effect. Further observational analysis and modelling efforts are required to establish the significance of this effect.

Acknowledgements. Research at Imperial College London is funded by STFC (UK), NC is funded by NSF grant ATM-0553397. We have benefited from the availability of ACE magnetic field (PI: C. Smith) and SWEPAM (PI: D. McComas) data. MO thanks Benoit Lavraud of CESR (Toulouse), for useful discussions.

Editor in Chief W. Kofman thanks S. Kahler and another anonymous referee for their help in evaluating this paper.

References

Anderson, B. R., Skoug, R. M., Steinberg, J. T., and McComas, D. J.: Comparison of the Width and Intensity of the Suprathermal Electron Strahl in General Solar Wind and ICME Solar Wind., AGU Fall Meeting Abstracts, pp. A1580+, 2008.

Bothmer, V. and Schwenn, R.: The structure and origin of magnetic clouds in the solar wind, Ann. Geophys., 16, 1–24, 1998, http://www.ann-geophys.net/16/1/1998/.

Burlaga, L. F.: Magnetic clouds: Constant alpha force-free configurations, J. Geophys. Res., 93, 7217–7224, 1988.

Burlaga, L. F., Sittler, E., Mariani, F., and Schwenn, R.: Magnetic loop behind and interplanetary shock: Voyager, Helios, and IMP 8 observations, J. Geophys. Res., 86, 6673–6684, 1981.

Cane, H. V. and Richardson, I. G.: Interplanetary coronal mass ejections in the near-Earth solar wind during 1996–2002, J. Geophys. Res., 108, A41156, doi:10.1029/2002JA009817, 2003.

Chollet, E. E., Giacalone, J., Mazur, J. E., and Al Dayeh, M.: A New Phenomenon in Impulsive-Flare-Associated Energetic Particles, Astrophys. J., 669, 615–620, doi:10.1086/521670, 2007.

Crooker, N. U. and Webb, D. F.: Remote sensing of the solar site of interchange reconnection associated with the May 1997 magnetic cloud, J. Geophys. Res., 111, A08108, doi:10.1029/2006JA011649, 2006.

Crooker, N. U., Kahler, S. W., Gosling, J. T., and Lepping, R. P.: Evidence in magnetic clouds for systematic open flux trans-

port on the Sun, J. Geophys. Res., 113, 12107, doi:10.1029/2008JA013628, 2008.

Feldman, W. C., Asbridge, J. R., Bame, S. J., Montgomery, M. D., and Gary, S. P.: Solar wind electrons, J. Geophys. Res., 80, 4181–4196, 1975.

Gosling, J. T., Baker, D. N., Bame, S. J., Feldman, W. C., and Zwickl, R. D.: Bidirectional solar wind electron heat flux events, J. Geophys. Res., 92, 8519–8535, 1987.

Gosling, J. T., Eriksson, S., McComas, D. J., Phan, T. D., and Skoug, R. M.: Multiple magnetic reconnection sites associated with a coronal mass ejection in the solar wind, J. Geophys. Res., 112, 8106, doi:10.1029/2007JA012418, 2007.

Hammond, C. M., Feldman, W. C., McComas, D. J., Phillips, J. L., and Forsyth, R. J.: Variation of electron-strahl width in the high-speed solar wind: ULYSSES observations, Astron. Astrophys., 316, 350–354, 1996.

Jacobs, C., Roussev, I. I., Lugaz, N., and Poedts, S.: The Internal Structure of Coronal Mass Ejections: Are all Regular Magnetic Clouds Flux Ropes?, Astrophys. J. Lett., 695, L171–L175, doi:10.1088/0004-637X/695/2/L171, 2009.

Larson, D. E., Lin, R. P., McTiernan, J. M., McFadden, J. P., Ergun, R. E., McCarthy, M., Rème, H., Sanderson, T. R., Kaiser, M., Lepping, R. P., and Mazur, J.: Tracing the topology of the October 18-20, 1995, magnetic cloud with $\sim 0.1-10^2$ keV electrons, Geophys. Res. Lett., 24, 1911–1914, doi:10.1029/97GL01878, 1997.

Lepping, R. P., Jones, J. A., and Burlaga, L. F.: Magnetic field structure of interplanetary clouds at 1 AU, J. Geophys. Res., 95, 11957–11965, 1990.

Lundquist, S.: Magnetostatic fields, Arkiv foer Fysik, 2, 361–365, 1950.

Maksimovic, M., Zouganelis, I., Chaufray, J.-Y., Issautier, K., Scime, E. E., Littleton, J. E., Marsch, E., McComas, D. J., Salem, C., Lin, R. P., and Elliott, H.: Radial evolution of the electron distribution functions in the fast solar wind between 0.3 and 1.5 AU, J. Geophys. Res., 110, A09104, doi:10.1029/2005JA011119, 2005.

McComas, D. J., Gosling, J. T., Winterhalter, D., and Smith, E. J.: Interplanetary magnetic field draping about fast coronal mass ejecta in the outer heliosphere, J. Geophys. Res., 93, 2519–2526, doi:10.1029/JA093iA04p02519, 1988.

McComas, D. J., Bame, S. J., J., B. S., Feldman, W. C., Phillips, J. L., Riley, P., and Griffee, J. W.: Solar wind electron proton alpha monitor (SWEPAM) for the Advanced Composition Explorer, Space Sci. Rev., 86, 563, 1998.

Newkirk, Jr., G., Hundhausen, A. J., and Pizzo, V.: Solar cycle modulation of galactic cosmic rays - Speculation on the role of coronal transients, J. Geophys. Res., 86, 5387–5396, 1981.

Owens, M. J.: Magnetic cloud distortion resulting from propagation through a structured solar wind: Models and observations, J. Geophys. Res., 111, A12109, doi:10.1029/2006JA011903, 2006.

Owens, M. J. and Crooker, N. U.: Coronal mass ejections and magnetic flux buildup in the heliosphere, J. Geophys. Res., 111, A10104, doi:10.1029/2006JA011641, 2006.

Owens, M. J. and Crooker, N. U.: Reconciling the electron counterstreaming and dropout occurrence rates with the heliospheric flux budget, J. Geophys. Res., 112, A06106, doi:10.1029/2006JA012159, 2007.

Owens, M. J., Cargill, P. J., Pagel, C., Siscoe, G. L., and Crooker, N. U.: Characteristic magnetic field and speed properties of interplanetary coronal mass ejections and their sheath regions, J. Geophys. Res., 110, A01105, doi:10.1029/2004JA010814, 2005.

Owens, M. J., Merkin, V. G., and Riley, P.: A kinematically distorted flux rope model for magnetic clouds, J. Geophys. Res., 111, A03104, doi:10.1029/2005JA011460, 2006.

Owens, M. J., Crooker, N. U., and Schwadron, N. A.: Suprathermal electron evolution in a Parker spiral magnetic field, J. Geophys. Res., 113, A11104, doi:10.1029/2008JA013294, 2008.

Pilipp, W. G., Muehlhaeuser, K.-H., Miggenrieder, H., Rosenbauer, H., and Schwenn, R.: Variations of electron distribution functions in the solar wind, J. Geophys. Res., 92, 1103–1118, 1987.

Riley, P. and Crooker, N. U.: Kinematic treatment of CME evolution in the solar wind, Astrophys. J., 600, 1035–1042, 2004.

Rosenbauer, H., Schwenn, R., Marsch, E., Meyer, B., Miggenrieder, H., Montgomery, M. D., Muehlhaeuser, K. H., Pilipp, W., Voges, W., and Zink, S. M.: A survey on initial results of the HELIOS plasma experiment, Journal of Geophysics Zeitschrift Geophysik, 42, 561–580, 1977.

Schmidt, J. M. and Cargill, P. J.: Magnetic reconnection between a magnetic cloud and the solar wind magnetic field, J. Geophys. Res., 108, 1023, doi:10.1029/2002JA009325, 2003.

Wimmer-Schweingruber, R. F., Crooker, N. U., Balogh, A., Bothmer, V., Forsyth, R. J., Gazis, P., Gosling, J. T., Horbury, T., Kilchmann, A., Richardson, I. G., Riley, P., Rodriguez, L., von Steiger, R., Wurz, P., and Zurbuchen, T. H.: Understanding interplanetary coronal mass ejection signatures, Space Sci. Rev., 123, 177–216, doi:10.1007/s11214-006-9017-x, 2006.

The Astrophysical Journal Letters, 782:L10 (6pp), 2014 February 10 doi:10.1088/2041-8205/782/1/L10

DISTRIBUTION OF ELECTRIC CURRENTS IN SOLAR ACTIVE REGIONS

T. Török[1], J. E. Leake[2], V. S. Titov[1], V. Archontis[3], Z. Mikić[1], M. G. Linton[4], K. Dalmasse[5], G. Aulanier[5], and B. Kliem[6]

[1] Predictive Science, Inc., 9990 Mesa Rim Road, Suite 170, San Diego, CA 92121, USA
[2] College of Science, George Mason University, 4400 University Drive, Fairfax, VA 22030, USA
[3] School of Mathematics and Statistics, University of St. Andrews, North Haugh, St. Andrews, Fife KY16 9SS, UK
[4] U.S. Naval Research Lab, 4555 Overlook Avenue, SW Washington, DC 20375, USA
[5] LESIA, Observatoire de Paris, CNRS, UPMC, Univ. Paris Diderot, 5 place Jules Janssen, F-92190 Meudon, France
[6] Institut für Physik und Astronomie, Universität Potsdam, Karl-Liebknecht-Str. 24-25, D-14476 Potsdam, Germany
Received 2013 September 26; accepted 2014 January 14; published 2014 January 27

ABSTRACT

There has been a long-standing debate on the question of whether or not electric currents in solar active regions are neutralized. That is, whether or not the main (or direct) coronal currents connecting the active region polarities are surrounded by shielding (or return) currents of equal total value and opposite direction. Both theory and observations are not yet fully conclusive regarding this question, and numerical simulations have, surprisingly, barely been used to address it. Here we quantify the evolution of electric currents during the formation of a bipolar active region by considering a three-dimensional magnetohydrodynamic simulation of the emergence of a sub-photospheric, current-neutralized magnetic flux rope into the solar atmosphere. We find that a strong deviation from current neutralization develops simultaneously with the onset of significant flux emergence into the corona, accompanied by the development of substantial magnetic shear along the active region's polarity inversion line. After the region has formed and flux emergence has ceased, the strong magnetic fields in the region's center are connected solely by direct currents, and the total direct current is several times larger than the total return current. These results suggest that active regions, the main sources of coronal mass ejections and flares, are born with substantial net currents, in agreement with recent observations. Furthermore, they support eruption models that employ pre-eruption magnetic fields containing such currents.

Key words: magnetohydrodynamics (MHD) – Sun: corona – Sun: coronal mass ejections (CMEs)

Online-only material: color figures

1. INTRODUCTION

The energy required to power solar flares and coronal mass ejections (CMEs) is stored in current-carrying magnetic fields in the corona. Active regions (ARs), the main source regions of eruptions, carry a total electric current of ∼1 TA (e.g., Wilkinson et al. 1992), which is commonly inferred from applying Ampère's law, $\mathbf{j} = (\nabla \times \mathbf{B})/\mu_0$, to photospheric vector magnetograms. Since such data are hampered by limited resolution and various uncertainties (e.g., Wiegelmann et al. 2006), it is not yet well understood how AR currents are distributed.

The observations indicate that the currents in magnetically well-isolated ARs are *balanced* to a very good approximation, i.e., the total current, I, calculated by integrating the vertical current density, j_z, over the *whole* photospheric AR extension vanishes, as expected from $\nabla \cdot \mathbf{j} = 0$ (e.g., Georgoulis et al. 2012). What remains controversial is to what extent the currents are *neutralized*, meaning that I calculated over a *single* AR polarity vanishes as well. Full neutralization requires the main (or direct) currents, which connect the AR polarities, to be surrounded by shielding (or return) currents of equal total strength and opposite direction (see, e.g., Figure 1 in Melrose 1995). Both observations and theoretical considerations are not yet fully conclusive regarding the existence or amount of return currents in ARs, which has led to an ongoing debate (e.g., Parker 1996; Melrose 1996; Georgoulis et al. 2012).

AR currents are believed to be formed by two main mechanisms: (1) the stressing of the coronal magnetic field by photospheric and sub-surface flows (e.g., Klimchuk & Sturrock 1992) and (2) the emergence of current-carrying flux from the solar interior into the corona (e.g., Leka et al. 1996). At first glance, mechanism (1) is expected to produce neutralized currents. To illustrate this, we show in Figures 1(a) and (b) a simple AR model created from a bipolar potential field by photospheric vortex flows (Amari et al. 1996; Török & Kliem 2003; Aulanier et al. 2005; Török et al. 2013). Such an isolated, symmetric system must be current-balanced. To see if it is also neutralized, we calculate $I = \oint_C \mathbf{B} \cdot d\mathbf{l}$ in *one* AR polarity along a photospheric path C that runs fully outside and sufficiently far from the vortex flows. Since the horizontal field components along C do not change much during the twisting (Figure 1(b)) and the initial field is current-free, I remains close to zero at all times, i.e., the generated currents remain nearly neutralized. However, as shown by Török & Kliem (2003), net currents develop in the system if the vortices are close enough to each other to also shear the magnetic field at the polarity inversion line (PIL). The resulting handedness is the same as in the core of the flux rope, i.e., the sheared flux carries direct current. Some recent observations, based on high-resolution vector magnetograms, indeed suggest the presence of substantial net currents in ARs with strong shear along their main PIL (Ravindra et al. 2011; Georgoulis et al. 2012).

As for mechanism (2), it is believed that flux ropes rising through the convection zone are magnetically well-isolated (Fan 2009a), which implies that the currents they carry are well-neutralized (Figure 1(c)). Whether or not the neutralization breaks down when such flux ropes emerge into the corona has not yet been investigated systematically. Ravindra et al. (2011) analyzed a case of strong flux emergence and found it to

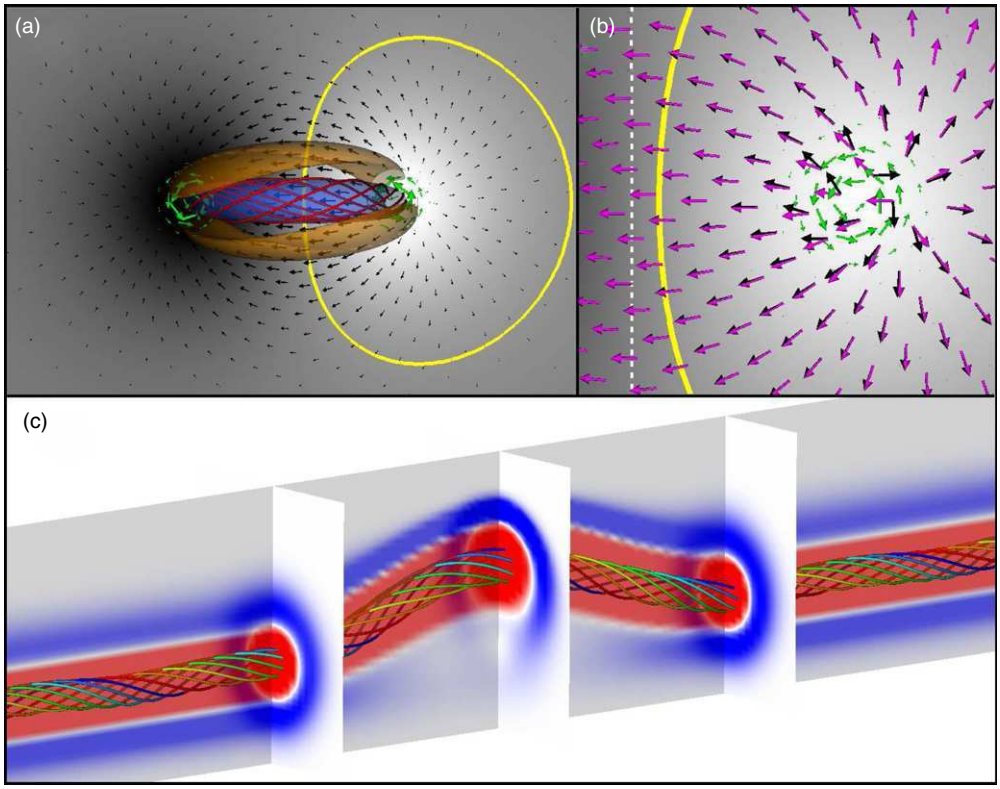

Figure 1. Electric currents in two numerical models of AR formation. (a) Bipolar AR containing a flux rope (red field lines) created by photospheric vortex flows (green arrows). Black (white) colors outline negative (positive) vertical magnetic fields. Currents are visualized by transparent iso-surfaces of $\alpha = (\mathbf{j} \cdot \mathbf{B})/B^2$, with $\alpha = -2$ (blue; direct current) and 0.65 (orange; return current). Black arrows show horizontal field components. The yellow line is an example path for calculating the total current in one polarity (see text). (b) Zoom into AR center, showing additionally the initial horizontal potential field (magenta arrows) and the polarity inversion line (white dotted line). (c) Buoyant flux rope from the simulation investigated in this Letter, before it emerges through the photosphere. Red (blue) colors outline direct (return) currents; field lines show the flux rope core.

(A color version of this figure is available in the online journal.)

be associated with the development of strong net currents and strong shear at the PIL. Longcope & Welsch (2000) suggested, based on a simplified analytical model, that return currents may even completely remain below the corona during the emergence of magnetically isolated flux tubes.

Improving our understanding of the current distribution in ARs is particularly important for theoretical and numerical models of solar eruptions. Many CME simulations (e.g., Roussev et al. 2003; Török & Kliem 2005; Manchester et al. 2008; Lugaz et al. 2011; Török et al. 2011) employed the analytical coronal flux rope configuration developed by Titov & Démoulin (1999), which does not contain return currents. Other investigations used coronal field models constructed through flux rope insertion and numerical relaxation (van Ballegooijen 2004), which are similarly dominated by direct currents, to represent the source-region field prior to an eruption (e.g., Bobra et al. 2008; Savcheva et al. 2012). Based on the assumption that AR currents are neutralized, it has been argued, however, that such configurations are not suitable for CME modeling, as the inclusion of return currents may inhibit their eruption (see a summary in Forbes 2010).

Since theory and observations are not yet conclusive, MHD simulations can be used as a viable tool to address the question of current neutralization in ARs. Surprisingly, while the development of return currents has been reported in simulations where ARs were produced by photospheric flows (e.g., Aulanier et al. 2005; Delannée et al. 2008), the *amount* of current neutralization was quantified in such simulations only by Török & Kliem (2003). To the best of our knowledge, this has not yet been done for ARs produced in flux emergence simulations, which is the purpose of this Letter.

2. NUMERICAL SETUP

The simulation analyzed here is identical to the run "SD" in Leake et al. (2013; hereafter L13), except for a shift in the z coordinate and slightly different boundary and wave damping conditions, which do not affect the system evolution noticeably. It uses the standard, Cartesian setup for the emergence of a buoyant magnetic flux rope into a stratified, plane-parallel atmosphere in hydrostatic equilibrium (Fan 2001). In contrast to previous simulations, where often a field-free corona was considered, the flux rope here emerges into a pre-existing magnetic arcade (Figure 2). We refer the reader to L13 for details, here we only note that (1) the dimensionless lengths, times, magnetic field strengths, current densities, and total currents shown below are normalized by 170 km, 25 s, 1200 G, 0.56 Am^{-2}, and 0.016 TA, respectively; (2) the height range $20 < z < 30$ ($0 < z < 10$ in L13) corresponds to the photosphere/chromosphere layer (PCL); and (3) the initial magnetic field consists of a horizontal sub-photospheric flux rope that runs along the y direction and a background dipole field that is translationally invariant along the rope axis. The axis is placed at $z = 8$ and the field strength at it is set to 6000 G. The dipole field is much weaker, so initially the flux rope currents are almost perfectly neutralized. The rope is made buoyant by a localized, internal density perturbation applied around $y = 0$.

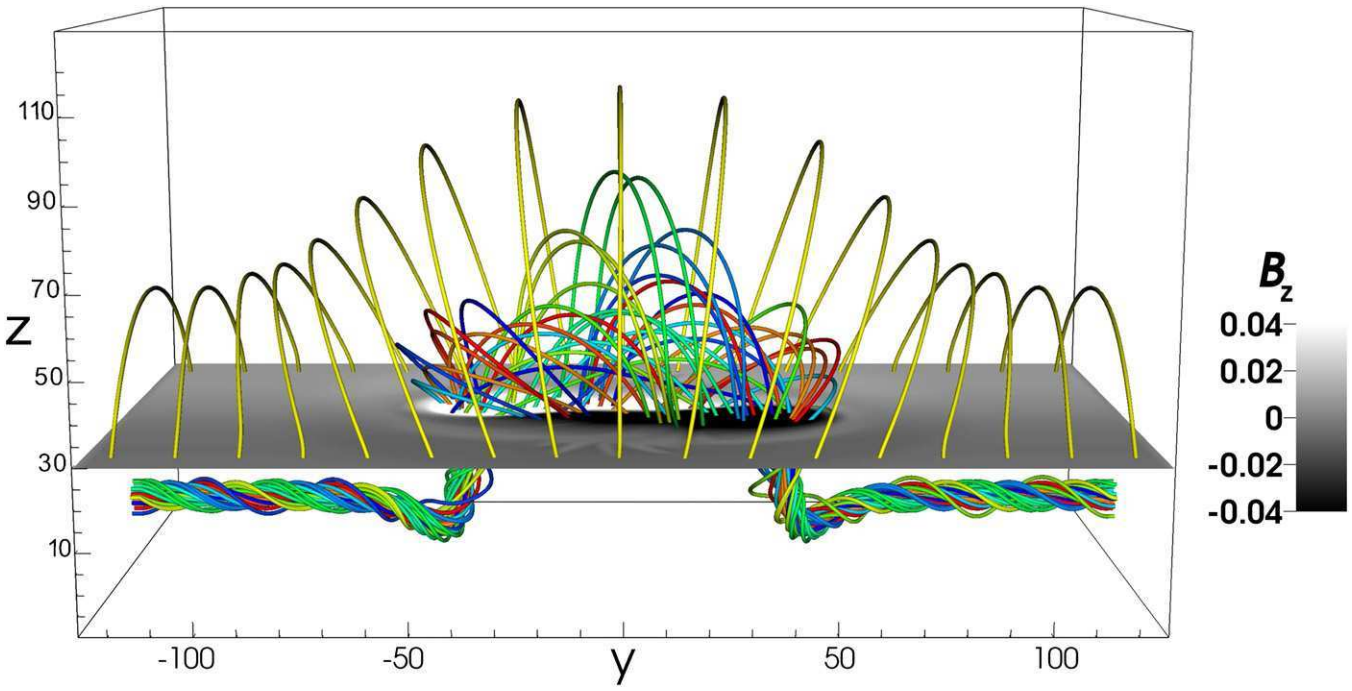

Figure 2. Perspective view on magnetic field lines of the emerging flux rope (random colors) and the ambient coronal dipole field (yellow; drawn for $z > 30$) at $t = 170$. The "magnetogram" $B_z(x, y, z = 30)$ is shown in grayscale.

(A color version of this figure is available in the online journal.)

3. RESULTS

The subsequent evolution is very similar to previous flux emergence simulations (see L13). Here we only show the magnetic configuration at the time when there is no longer significant flux emergence into the atmosphere and a bipolar AR containing a stable flux rope has formed in the corona (Figure 2). The eruption of the rope, observed in previous simulations (Manchester et al. 2004; Archontis & Török 2008), is inhibited here by the stabilizing dipole field, the orientation of which was chosen to minimize magnetic reconnection with the emerging flux. Figure 3 shows that the strongest AR currents are located above the PIL and exhibit a sigmoidal shape when viewed from above. Return currents are present but are rather narrow and located at the AR edges, while the AR center and the flux rope contain only direct currents. Note that the quantity α represents the direct and return currents reasonably well, since the coronal configuration evolves toward a force-free state as the emergence of flux into the atmosphere slows down (see Figure 13 in L13).

In order to quantify the AR currents, we calculate $I = \int j_z\, dx\, dy$ at the top of the PCL ($z = 30$). Integration over the whole AR shows that the total current is balanced at all times, as expected. To check the amount of current neutralization, we restrict the integration to the positive AR polarity, $B_z(z = 30) > 0$. The emerging flux rope has a right-handed twist, so the total direct (return) current, I_d (I_r), is obtained by integrating $j_z(z = 30) > 0\,(< 0)$ over this polarity.

Figure 4(a) shows the evolution of I_d, I_r, $I = I_d + I_r$ (blue symbols), and the total positive magnetic flux (black curve). The initial flux is non-zero due to the presence of the background dipole field. Early in the evolution ($t \lesssim 50$) there is very little flux emergence and the currents remain small and almost perfectly neutralized. No significant shear develops along the PIL during this phase. Strong emergence starts at $t \approx 50$, accompanied by a rapid increase of the currents, and ceases at $t \approx 160$. I_r saturates at $t \approx 100$, while I_d increases until $t \approx 130$ and slowly decreases afterward.

Figure 4(b) shows the ratio $|I_d/I_r|$ (red diamonds). The total direct current starts to exceed the total return current from the onset of strong emergence and remains several times larger during the whole evolution. The same pattern can be found if I_d and I_r are computed deeper in the PCL (at $z = 22$ and 26), with somewhat smaller values of $|I_d/I_r|$.

The red symbols in Figure 4(a) show I_d, I_r, and I in the center of the positive polarity, where the strongest magnetic fields are located. The integration area was defined by the ad-hoc condition $B_z(z = 30, t) > B_{z_{max}}(z = 30, t)/3$ (see the black contour lines in Figures 5(a) and (c)). It can be seen that I_r in the AR center drops to zero shortly after the onset of strong emergence, i.e., the strongest AR fields become connected solely by direct currents as the emergence proceeds. This is visualized in Figures 5(a)–(d). At $t = 55$, right after the onset of strong emergence, the direct and return currents are still quite compact and more or less equally distributed within each polarity of the forming AR. No significant shear along the PIL has yet developed. The PILs of B_z and j_z are very different, indicating that the system is far from a force-free state at this height and time. As the emergence proceeds the picture changes considerably. At $t = 170$, when flux emergence has ceased and strong shear along the PIL has developed, two J-shaped regions of strong direct current occupy the AR center, while the much weaker and narrower return currents are located solely in the AR's periphery. The PILs of B_z and j_z in the AR center now coincide, indicating that the coronal configuration has evolved to an approximately force-free state. This pattern persists during the remaining evolution of the system, except that as the AR polarity centers separate, the current concentrations between them progressively narrow, plausibly causing the decrease of I_d after $t \approx 130$.

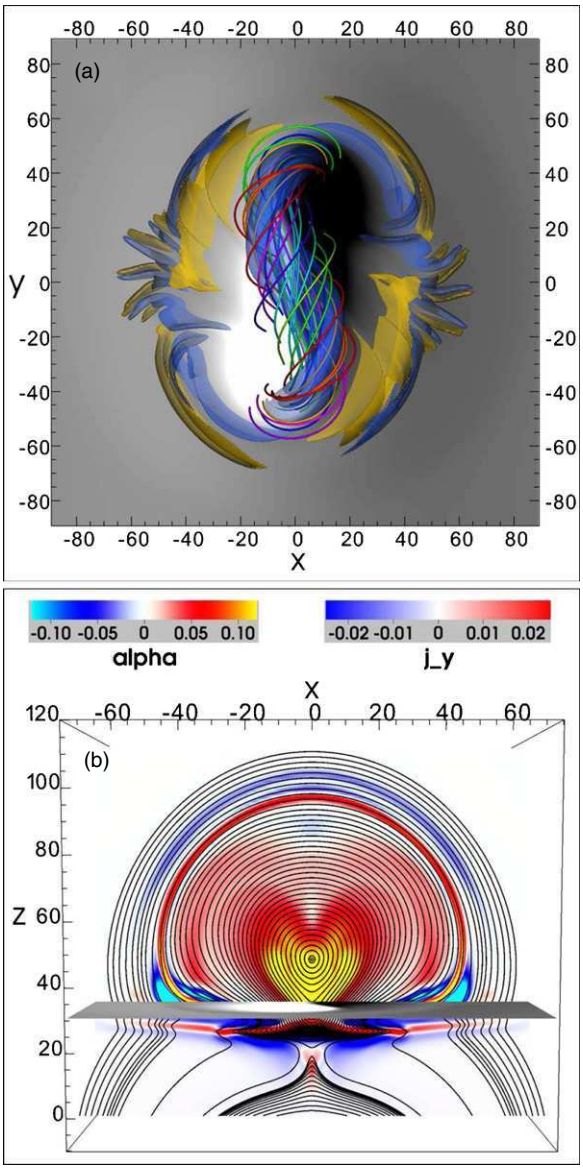

Figure 3. (a) Top view of the system shown in Figure 2 (without arcade field lines). Direct (return) currents are visualized by a blue (orange) transparent iso-surface of $\alpha = 0.12$ (-0.08). Note that the flux rope is right-handed ($\alpha > 0$), while the flux rope in Figure 1(a) is left-handed ($\alpha < 0$). (b) Perspective view along the rope axis, showing field lines of $(B_x, 0, B_z)$ and color-scales of α (for $z > 30$) and j_y (for $z < 30$) in the plane $\{y = 0\}$ (j_y is used to visualize the current direction for $z < 30$ since the field is far from a force-free state there).

(A color version of this figure is available in the online journal.)

4. DISCUSSION

We quantified the amount of electric current neutralization in bipolar solar ARs by considering an MHD simulation of the emergence of a current-neutralized magnetic flux rope from the solar interior into the corona. We find that a rapid and strong deviation from current-neutralization occurs simultaneously with the onset of significant flux emergence. The emergence process is accompanied by the development of strong magnetic shear along the AR's PIL. By the end of the emergence phase $|I_d|$ is several times larger than $|I_r|$ for the model parameters considered here, in reasonable agreement with the ratios obtained from observed data by Ravindra et al. (2011) and Georgoulis et al. (2012). The strong magnetic fields in the AR center are connected solely by direct currents, while the weaker and narrower return currents reside in the AR's periphery. In order to assess the role of shielding on the strength of the return currents, we repeated the simulation using a three times stronger dipole field, and also compared it with emergence into a field-free corona (run "ND" in L13). The deviation from current neutralization is strong in all cases and increases with the ambient field strength, opposite to expectation if shielding were dominant. These results suggests that:

1. ARs are born with substantial net currents, in agreement with recent observations (Ravindra et al. 2011; Georgoulis et al. 2012).
2. Coronal flux rope models that neglect return currents (e.g., Titov & Démoulin 1999; Su et al. 2011) are a valid representation of pre-eruption configurations on the Sun. Indeed, simulations that use such models reproduce important eruption characteristics (e.g., rise profiles and morphological evolution) in very good quantitative agreement with the observations (e.g., Török & Kliem 2005; Williams et al. 2005; Schrijver et al. 2008; Kliem et al. 2010, 2012, 2013).

The question arises of how fully neutralized sub-photospheric currents transform into strongly non-neutralized coronal currents during flux emergence. This transformation is not trivial, since (1) the current paths become highly complex during the rise and emergence of the flux rope, (2) only a fraction of the sub-photospheric currents enter the corona, and (3) new currents may develop as a result of the shearing and converging flows associated with emerging flux ropes (Manchester et al. 2004; Archontis 2008) or of the transport of twist from below the surface via torsional Alfvén waves (Longcope & Welsch 2000; Fan 2009b; L13).

The complexity of the problem calls for a detailed investigation beyond the scope of this Letter. A preliminary analysis indicates that during the flux pile-up that occurs when the rising flux rope approaches the photosphere, return currents located at the top of the rope are pushed aside by subjacent direct currents. Moreover, some of them short-circuit with adjacent direct currents (Figure 5(e)), which supports this process. It appears that most of the return currents thus relocated to the periphery of the emergence area never enter the corona (otherwise the flux emergence would start with an increase of the return current). Figure 5(f) shows that the direct currents that occupy the AR center after emergence are rooted in the center of the sub-photospheric flux rope. This suggests that they emerge bodily, rather than being produced by shearing flows.

It also needs to be studied how parameters such as the initial flux rope twist and diameter (relative to the PCL width), and the structure and strength of the pre-existing coronal field affect the final current distribution.

The results presented here refer to newly emerging flux, in particular to emerging ARs. While the most powerful eruptions tend to arise from relatively young and compact ARs, many filament eruptions and CMEs originate within or between decaying ARs characterized by dispersed photospheric flux distributions (Martin 1973; Tang 1987). The corresponding pre-eruption configurations (typically filament channels) are believed to be formed and energized primarily by persistent shear flows and flux cancellation at PILs (e.g., van Ballegooijen & Martens 1989; Martens & Zwaan 2001; Green & Kliem 2009; Green et al. 2011), rather than by newly emerging flux. Their magnetic structure has been modeled using two complementary approaches.

The flux rope insertion method (van Ballegooijen 2004) yields static models by inserting a flux rope into the potential-field

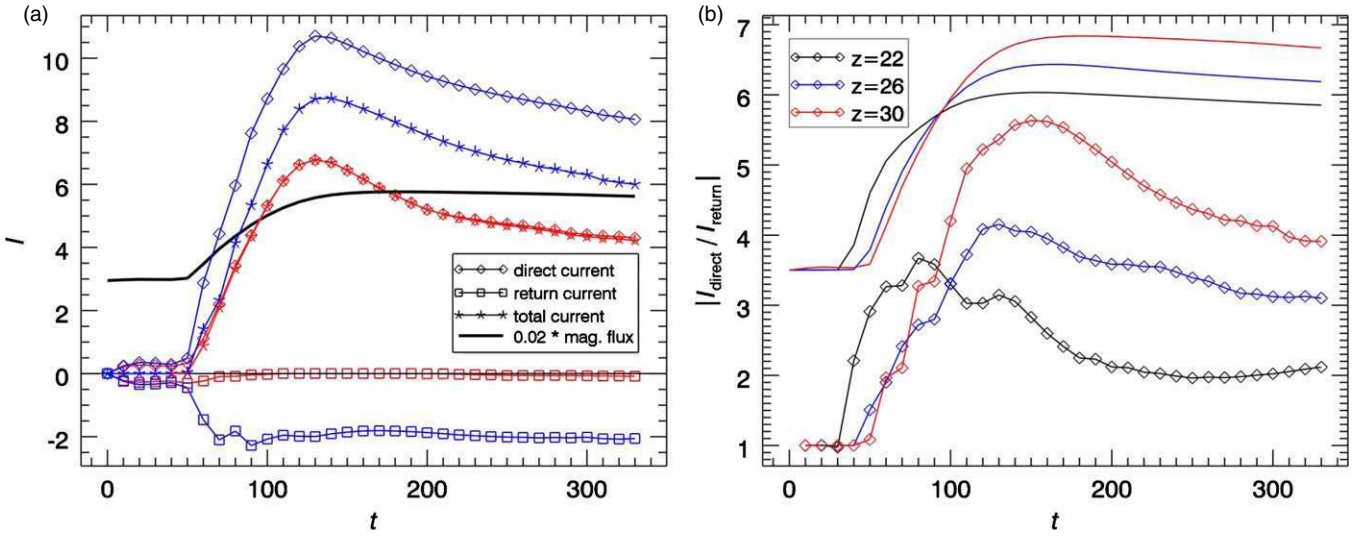

Figure 4. Electric currents integrated over the positive polarity region, $B_z(z) > 0$. (a) Integration at $z = 30$ over the whole polarity (blue symbols) and over the polarity center ($B_z > B_{z_{max}}/3$; red symbols). The total positive magnetic flux is shown by a black line (scaled to fit into the plot). (b) Ratio of total direct and total return current integrated over the whole positive polarity at heights $z = 22$, 26, and 30 (black, blue, and red diamonds, respectively). The total positive magnetic flux at these heights is shown by solid lines of the same color, scaled to the same initial value.

(A color version of this figure is available in the online journal.)

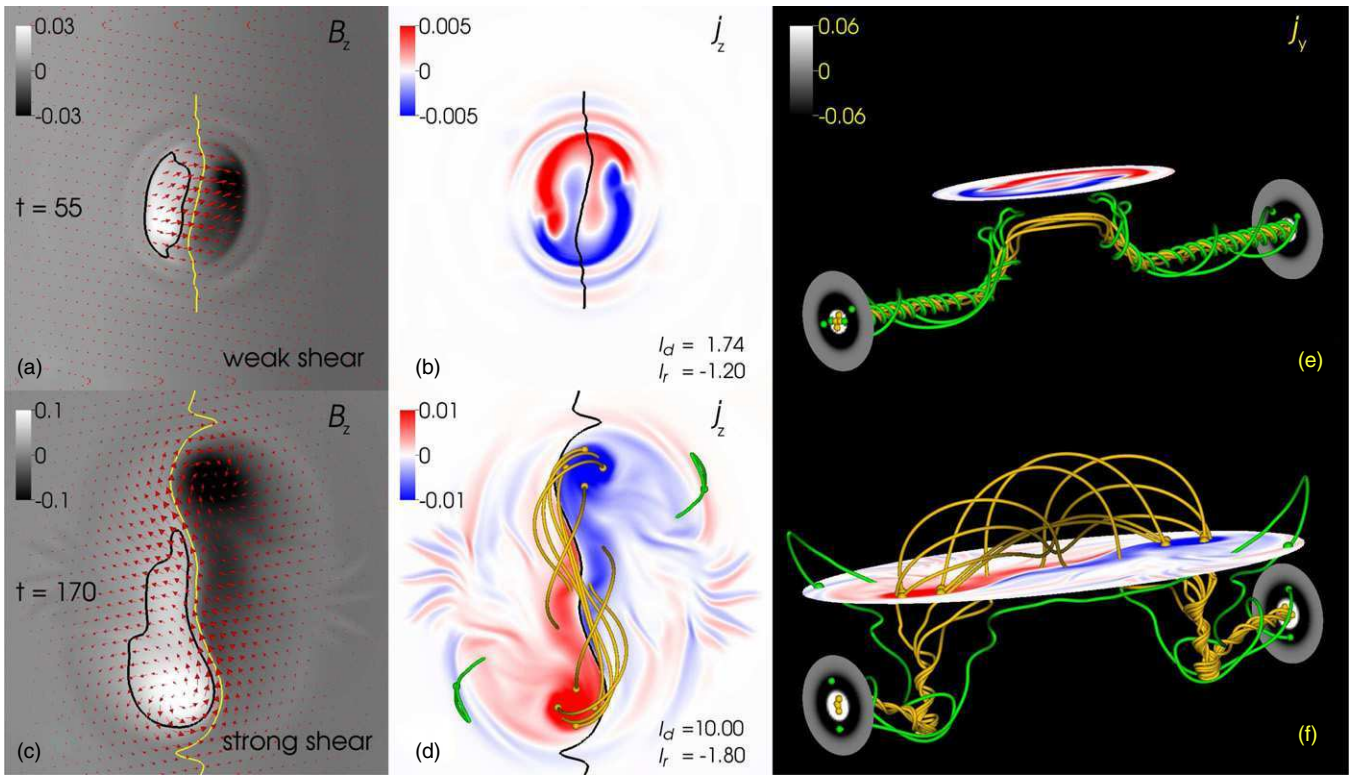

Figure 5. Development of net currents in the corona. The top shows an early state of emergence, when little shear has developed and the currents are relatively well neutralized. The bottom shows a mature state of emergence, after strong shear has developed and the currents are strongly non-neutralized. (a–d) B_z and j_z at $z = 30$. On the left, red arrows, yellow and black lines outline $(B_x, B_y, 0)$, $B_z = 0$, and contours of $B_{z_{max}}/3$, respectively. On the right, $B_z = 0$ is drawn in black. The current field lines in (d) are the same as in (f). (e–f) Oblique view showing $j_z(z = 30)$, field lines of **j**, and vertical slices of j_y at $y = \pm 75$, with white (black) regions outlining the locations of sub-photospheric direct (return) currents. Current field lines start at $y = \pm 75$ in (e) and at $z = 30$ in (f), and are terminated at $y = \pm 75$ in both panels. Orange (green) lines start in regions of direct (return) current. Green current field lines in (e) have short-circuited, i.e., they connect to the direct current region in the same flux rope leg.

(A color version of this figure is available in the online journal.)

extrapolation of an observed magnetogram and subsequently relaxing the coronal field numerically (e.g., Bobra et al. 2008; Savcheva & van Ballegooijen 2009; Su et al. 2011). After relaxation, the currents in these models tend to be strongly non-neutralized (see Figure 3 in Kliem et al. 2013). In particular, the use of a potential ambient field neglects the possible introduction of return currents by localized shearing flows. Nevertheless, the models have been very successful in representing stable as well as unstable fields of dispersed and decaying ARs.

MHD simulations involving flux cancellation have produced fully dynamic models of such ARs (e.g., Linker et al. 2003; Amari et al. 2003; Titov et al. 2008; Aulanier et al. 2010). These simulations impose various combinations of photospheric shearing, converging flows, and field diffusion on an initial potential field; thus, possible return currents resulting from the shearing are kept. Figure 12 in Titov et al. (2008) and Figure 7 in Aulanier et al. (2010) show that return currents are produced in these models, but they appear to be too weak to neutralize the strong direct currents that form above the PIL. For example, the simulation in Titov et al. (2008) yields $|I_d/I_r| \approx 3$, rather similar to the values shown in Figure 4.

All three models (flux emergence, flux rope insertion, and flux cancellation) appear to produce strongly non-neutralized current configurations, though their quantitative differences have yet to be investigated systematically. The same is true for configurations produced by localized vortex flows (Figure 1(a)) if these flows extend close to the PIL. Moreover, these configurations are morphologically similar, typically consisting of a low-lying, sigmoidal layer of strong and concentrated currents and a flux rope with weaker and more diffuse current above it (Török & Kliem 2003; Archontis & Hood 2009; Aulanier et al. 2010; Savcheva et al. 2012). This suggests that young eruptive ARs and mature CME source regions have analogous current distributions, dominated by net currents located close to the PIL, though this conjecture needs to be substantiated by further analysis of numerical models and observations.

Finally, all models show an association between the presence of net currents and magnetic shear along the PIL, regardless of whether the currents are produced by horizontal photospheric flows or emerge bodily into the corona. While the shear at the PIL is causal for the current to be non-neutralized in the vortex-driven case, it may not be causal in the emergence process. The exact nature and validity range of the relationship requires further study as well.

We thank the referee for helpful comments and Brian Welsch for stimulating discussions. The contributions of T.T., V.S.T., and Z.M. were supported by NASA's HTP, LWS, and SR&T programs. J.E.L and M.G.L. were supported by NASA/LWS. M.G.L. received support also from the ONR 6.1 program. The simulation was performed under grant of computer time from the D.o.D. HPC Program. B.K. was supported by the DFG. V.A. acknowledges support through the IEF-272549 grant.

REFERENCES

Amari, T., Luciani, J. F., Aly, J. J., Mikic, Z., & Linker, J. 2003, ApJ, 595, 1231
Amari, T., Luciani, J. F., Aly, J. J., & Tagger, M. 1996, ApJL, 466, L39
Archontis, V. 2008, JGRA, 113, 3
Archontis, V., & Hood, A. W. 2009, A&A, 508, 1469
Archontis, V., & Török, T. 2008, A&A, 492, L35
Aulanier, G., Démoulin, P., & Grappin, R. 2005, A&A, 430, 1067
Aulanier, G., Török, T., Démoulin, P., & DeLuca, E. E. 2010, ApJ, 708, 314
Bobra, M. G., van Ballegooijen, A. A., & DeLuca, E. E. 2008, ApJ, 672, 1209
Delannée, C., Török, T., Aulanier, G., & Hochedez, J.-F. 2008, SoPh, 247, 123
Fan, Y. 2001, ApJL, 554, L111
Fan, Y. 2009a, LRSP, 6, 4
Fan, Y. 2009b, ApJ, 697, 1529
Forbes, T. 2010, in Heliophysics: Space Storms and Radiation: Causes and Effects, ed. C. J. Schrijver & G. L. Siscoe (Cambridge: Cambridge Univ. Press), 159
Georgoulis, M. K., Titov, V. S., & Mikić, Z. 2012, ApJ, 761, 61
Green, L. M., & Kliem, B. 2009, ApJL, 700, L83
Green, L. M., Kliem, B., & Wallace, A. J. 2011, A&A, 526, A2
Kliem, B., Linton, M. G., Török, T., & Karlický, M. 2010, SoPh, 266, 91
Kliem, B., Su, Y., van Ballegooijen, A., & DeLuca, E. 2013, ApJ, 779, 129
Kliem, B., Török, T., & Thompson, W. T. 2012, SoPh, 281, 137
Klimchuk, J. A., & Sturrock, P. A. 1992, ApJ, 385, 344
Leake, J. E., Linton, M. G., & Török, T. 2013, ApJ, 788, 99
Leka, K. D., Canfield, R. C., McClymont, A. N., & van Driel-Gesztelyi, L. 1996, ApJ, 462, 547
Linker, J. A., Mikić, Z., Lionello, R., et al. 2003, PhPl, 10, 1971
Longcope, D. W., & Welsch, B. T. 2000, ApJ, 545, 1089
Lugaz, N., Downs, C., Shibata, K., et al. 2011, ApJ, 738, 127
Manchester, W., IV, Gombosi, T., DeZeeuw, D., & Fan, Y. 2004, ApJ, 610, 588
Manchester, W. B., IV, Vourlidas, A., Tóth, G., et al. 2008, ApJ, 684, 1448
Martens, P. C., & Zwaan, C. 2001, ApJ, 558, 872
Martin, S. F. 1973, SoPh, 31, 3
Melrose, D. B. 1995, ApJ, 451, 391
Melrose, D. B. 1996, ApJ, 471, 497
Parker, E. N. 1996, ApJ, 471, 489
Ravindra, B., Venkatakrishnan, P., Tiwari, S. K., & Bhattacharyya, R. 2011, ApJ, 740, 19
Roussev, I. I., Forbes, T. G., Gombosi, T. I., et al. 2003, ApJL, 588, L45
Savcheva, A., & van Ballegooijen, A. 2009, ApJ, 703, 1766
Savcheva, A. S., van Ballegooijen, A. A., & DeLuca, E. E. 2012, ApJ, 744, 78
Schrijver, C. J., Elmore, C., Kliem, B., Török, T., & Title, A. M. 2008, ApJ, 674, 586
Su, Y., Surges, V., van Ballegooijen, A., DeLuca, E., & Golub, L. 2011, ApJ, 734, 53
Tang, F. 1987, SoPh, 107, 233
Titov, V. S., & Démoulin, P. 1999, A&A, 351, 707
Titov, V. S., Mikic, Z., Linker, J. A., & Lionello, R. 2008, ApJ, 675, 1614
Török, T., & Kliem, B. 2003, A&A, 406, 1043
Török, T., & Kliem, B. 2005, ApJL, 630, L97
Török, T., Panasenco, O., Titov, V. S., et al. 2011, ApJL, 739, L63
Török, T., Temmer, M., Valori, G., et al. 2013, SoPh, 286, 453
van Ballegooijen, A. A. 2004, ApJ, 612, 519
van Ballegooijen, A. A., & Martens, P. C. H. 1989, ApJ, 343, 971
Wiegelmann, T., Inhester, B., & Sakurai, T. 2006, SoPh, 233, 215
Wilkinson, L. K., Emslie, A. G., & Gary, G. A. 1992, ApJL, 392, L39
Williams, D. R., Török, T., Démoulin, P., van Driel-Gesztelyi, L., & Kliem, B. 2005, ApJL, 628, L163

The Astrophysical Journal Letters, 739:L63 (5pp), 2011 October 1 doi:10.1088/2041-8205/739/2/L63

A MODEL FOR MAGNETICALLY COUPLED SYMPATHETIC ERUPTIONS

T. Török[1], O. Panasenco[2], V. S. Titov[1], Z. Mikić[1], K. K. Reeves[3], M. Velli[4], J. A. Linker[1], and G. De Toma[5]
[1] Predictive Science, Inc., 9990 Mesa Rim Road, Suite 170, San Diego, CA 92121, USA
[2] Helio Research, La Crescenta, CA 91214, USA
[3] Harvard-Smithsonian Center for Astrophysics, 60 Garden Street, Cambridge, MA 02138, USA
[4] Jet Propulsion Laboratory, California Institute of Technology, Pasadena, CA 91109, USA
[5] HAO/NCAR, P.O. Box 3000, Boulder, CO 80307-3000, USA
Received 2011 July 20; accepted 2011 August 9; published 2011 September 14

ABSTRACT

Sympathetic eruptions on the Sun have been observed for several decades, but the mechanisms by which one eruption can trigger another remain poorly understood. We present a three-dimensional MHD simulation that suggests two possible magnetic trigger mechanisms for sympathetic eruptions. We consider a configuration that contains two coronal flux ropes located within a pseudo-streamer and one rope located next to it. A sequence of eruptions is initiated by triggering the eruption of the flux rope next to the streamer. The expansion of the rope leads to two consecutive reconnection events, each of which triggers the eruption of a flux rope by removing a sufficient amount of overlying flux. The simulation qualitatively reproduces important aspects of the global sympathetic event on 2010 August 1 and provides a scenario for the so-called twin filament eruptions. The suggested mechanisms are also applicable for sympathetic eruptions occurring in other magnetic configurations.

Key words: methods: numerical – Sun: corona – Sun: coronal mass ejections (CMEs) – Sun: filaments, prominences – Sun: flares – Sun: magnetic topology

Online-only material: animations, color figures

1. INTRODUCTION

Solar eruptions are observed as filament (or prominence) eruptions, flares, and coronal mass ejections (CMEs). It is now well established that these three phenomena are different observational manifestations of a *single eruption*, which is caused by the destabilization of a localized volume of the coronal magnetic field. The detailed mechanisms that trigger and drive eruptions are still under debate, and a large number of theoretical models have been developed (e.g., Forbes 2010).

Virtually all existing models consider single eruptions. The Sun, however, also produces *sympathetic eruptions*, which occur within a relatively short period of time—either in one, typically complex, active region (e.g., Liu et al. 2009) or in different source regions, which occasionally cover a full hemisphere (the so-called global eruptions; Zhukov & Veselovsky 2007). It has been debated whether the close temporal correlation between sympathetic eruptions is purely coincidental, or whether they are causally linked (e.g., Biesecker & Thompson 2000). Both statistical investigations (e.g., Moon et al. 2002; Wheatland & Craig 2006) and detailed case studies (e.g., Wang et al. 2001) indicate that physical connections between them exist.[6]

The exact nature of these connections has yet to be established. They have been attributed, for instance, to convective motions or destabilization by large-scale waves (e.g., Ramsey & Smith 1966; Bumba & Klvana 1993). At present, it seems most likely that the mechanisms by which one eruption can trigger another act in the corona and are of a magnetic nature. Perturbations traveling along field lines that connect source regions of eruptions (e.g., Jiang et al. 2008) and changes in the background field due to reconnection (e.g., Ding et al. 2006; Zuccarello et al. 2009) have been considered. In an analysis of a global sympathetic event (see Section 2), Schrijver & Title (2011) found evidence for connections between all involved source regions via structural features like separators and quasi-separatrix layers (QSLs; Priest & Forbes 1992; Démoulin et al. 1996), suggesting the importance of the structural properties of the large-scale coronal field in the genesis of sympathetic eruptions.

A magnetic configuration that appears to be prone to producing sympathetic eruptions is a unipolar streamer or pseudo-streamer (PS; e.g., Hundhausen 1972; Wang et al. 2007). A PS is morphologically similar to a helmet streamer, but divides open fields of like polarity and contains an even number (typically two) of closed flux lobes below its cusp. PSs are quite common in the corona (e.g., Eselevich et al. 1999; Riley & Luhmann 2011) and occasionally harbor two filaments. It seems that if one of these erupts, the other one follows shortly thereafter (the so-called twin filament eruptions; Panasenco & Velli 2010).

Here, we present a numerical simulation that suggests two possible magnetic trigger mechanisms for sympathetic eruptions. It was inspired by the global sympathetic event on 2010 August 1, which involved a twin filament eruption in a PS.

2. THE SYMPATHETIC ERUPTIONS ON 2010 AUGUST 1

A detailed account of the individual eruptions that occurred in this global event can be found in Schrijver & Title (2011). Here we focus on a subset of three consecutive filament eruptions, all of which evolved into a separate CME. Figures 1(a), (b), and (c) show, respectively, the eruptions as seen by *STEREO*/EUVI (Howard et al. 2008), the pre-eruptive filaments, and a synoptic magnetogram obtained from the *Solar and Heliospheric Observatory*/Michelson Doppler Imager (*SOHO*/MDI; Scherrer et al. 1995) data. The large filaments 2 and 3 were located along the inversion lines dividing an elongated positive polarity and two bracketing negative polarities; the small filament 1 was located at the edge of the southern negative polarity. A potential field source surface extrapolation

[6] We do not distinguish here between sympathetic flares and sympathetic CMEs, since both are part of the same eruption process.

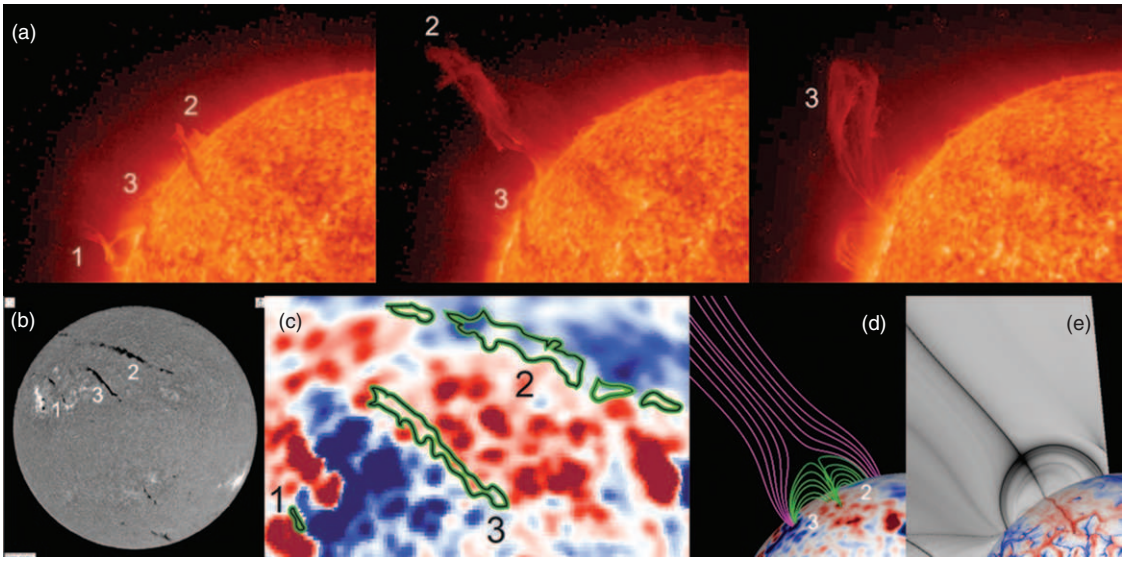

Figure 1. (a) *STEREO-Ahead*/EUVI 304 Å observations of three subsequent prominence eruptions (marked by their order of eruption) on 2010 August 1, shown at 02:56, 09:16, and 22:06 UT (from left to right). (b) Big Bear Observatory Hα observation on 2010 July 30, showing the corresponding pre-eruptive filaments. (c) Filament contours (drawn by eye) overlaid on a synoptic magnetogram for Carrington rotation 2099, with red (blue) showing positive (negative) radial fields. (d) Magnetic field lines from a corresponding PFSS extrapolation, revealing a pseudo-streamer. Green lines outline the lobes in which filaments 2 and 3 were located, pink lines show adjacent coronal holes. (e) Coronal distribution of Q (gray scale) and photospheric distribution of slog Q, where red (blue) outlines positive (negative) magnetic fluxes.

(A color version of this figure is available in the online journal.)

(PFSS; e.g., Schatten et al. 1969) for Carrington rotation 2099 reveals that filaments 2 and 3 were located in the lobes of a PS (Figure 1(d); see also Panasenco & Velli 2010).

Figure 1(e) shows a cut through the coronal distribution of the squashing factor Q (Titov et al. 2002) above filaments 2 and 3. The dark lines of high Q outline structural features and exhibit here a shape characteristic for a PS (compare with Figure 3(b) below). The photospheric distribution shows slog Q (Titov et al. 2011), depicting the footprints of (quasi-) separatrix surfaces. The structural skeleton of a PS consists of two separatrix surfaces, one vertical and one dome-like, which are both surrounded by a thin QSL (Masson et al. 2009) and intersect at a separator (Titov et al. 2011). It has been demonstrated that current sheet formation and reconnection occur preferably at such separators (e.g., Baum & Bratenahl 1980; Lau & Finn 1990).

The presence of the PS above filaments 2 and 3 suggests that the CME associated with filament eruption 1 may have triggered the subsequent eruptions by destabilizing the PS, presumably by inducing reconnection at its separator. We now describe an MHD simulation that enabled us to test this scenario using an idealized model.

3. NUMERICAL SIMULATION

The basic simulation setup is as in Török et al. (2011), where two instances of the coronal flux rope model by Titov & Démoulin (1999, hereafter TD) were used to simulate the interaction of two flux ropes in a PS. Here we add a TD configuration on each side of the PS (Figure 2(a)). The new configuration on the left is used to model the CME associated with filament eruption 1, while the new one on the right is merely used to obtain a (line-)symmetric initial configuration, which facilitates the construction of a numerical equilibrium. It does not significantly participate in the dynamic evolution described below. The flux ropes FR1-3 are intended to model filaments 1–3.

We integrate the zero β compressible ideal MHD equations, neglecting thermal pressure and gravity. The equations are normalized by the initial TD torus axis apex height, $R-d$ (see TD), the maximum initial magnetic field strength and Alfvén velocity, $\boldsymbol{B}_{0\max}$ and $v_{a0\max}$, and derived quantities. The Alfvén time is $\tau_a = (R-d)/v_{a0\max}$. We use a nonuniform Cartesian grid of size $[-25, 25] \times [-25, 25] \times [0, 50]$ with resolution $\simeq 0.04$ in the flux rope area. The initial density distribution is $\rho_0(\boldsymbol{x}) = |\boldsymbol{B}_0(\boldsymbol{x})|^{3/2}$, such that $v_a(\boldsymbol{x})$ decreases slowly with distance from the flux concentrations. For further numerical details we refer to Török & Kliem (2003).

The model parameters are chosen such that all flux ropes are initially stable with respect to the helical kink (Török et al. 2004) and torus instabilities (TI; Kliem & Török 2006). The ropes are placed along the y-direction, at $x = \pm 1.5$ and ± 5.5, and have identical parameters ($R = 2.75$, $a = 0.8$, $d = 1.75$, $L = 0.5$, $q = 4.64$; see TD). The signs of the sub-photospheric point charges, $\pm q$, are set according to the signs of the polarities surrounding filaments 1–3 (Figure 1(c)). The half-distance between the charges, L, is such that the TI can be triggered by a relatively weak perturbation (Schrijver et al. 2008). To obtain a numerically stable initial configuration that contains (semi-)open field above the PS lobes, the two charges associated with each flux rope are adjusted to $-0.55\,q/0.65\,q$ (for FR1 and FR4) and to $-0.34\,q/0.24\,q$ (for FR2 and FR3). The twist is chosen to be left-handed for all ropes to account for the observed dextral chirality of filaments 2 and 3 (Panasenco & Velli 2010).

We first relax the system for 85 τ_a and reset the time to zero. Then we trigger the eruption of FR1 by imposing localized converging flows at the bottom plane (as in Török et al. 2011), which slowly drive the polarities surrounding FR1 toward the local inversion line, yielding a quasi-static expansion of the rope's ambient field. The flows are imposed for 25 τ_a (including phases of linear increase (decrease) to a maximum velocity of $0.02\,v_{a0\max}$ (to zero), each lasting 5 τ_a).

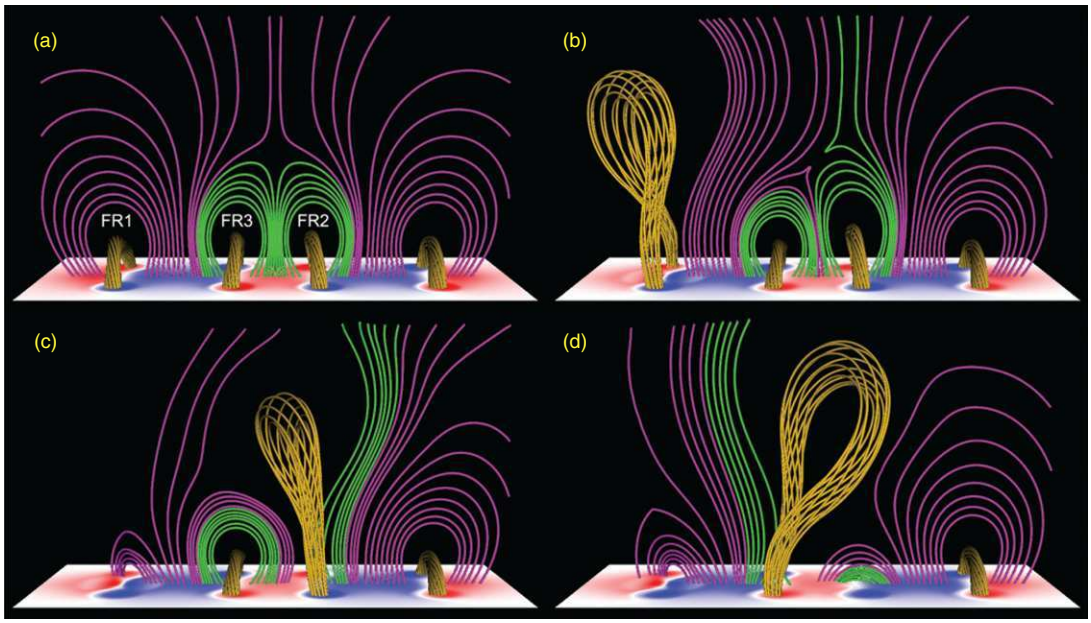

Figure 2. Snapshots from the simulation, showing magnetic field lines with fixed footpoints and the normal component of the magnetic field at the bottom plane, where red (blue) depicts positive (negative) fields. Orange lines belong to the flux ropes, green ones to the initial pseudo-streamer lobes, and pink ones to initially closed or (semi-)open overlying flux. Panel (a) shows the configuration after initial relaxation and panels (b)–(d) show the successive flux rope eruptions and ambient field evolution at $t = 85$, 126, and 181 τ_a, respectively. "Already erupted" flux ropes are omitted for clarity.

(An animation and a color version of this figure are available in the online journal.)

Though we solve the ideal MHD equations, extra diffusion is introduced by numerical differencing (as in every MHD code that models solar magnetic fields). This numerical diffusion is localized in regions where the current density is largest and leads to reconnection of magnetic field lines. Although it is much larger than the diffusion expected on the Sun, experience has shown that simulations produce solutions with physically expected behavior, as long as the numerical diffusion is sufficiently small. We therefore expect that our simulation indicates the true evolution of the system, but that the reconnection rates might differ from those present on the Sun.

4. RESULTS

Figures 2 and 3 summarize the main dynamics and reconnection occurring in the simulation. Figure 3(a) shows the initial configuration and Figures 2(a) and 3(b) show the system after relaxation, during which weak current layers form at the PS separatrix surfaces, but no noticeable reconnection occurs. Note the correspondence between the current layer pattern and the Q-distribution shown in Figure 1(e).

As the converging flows are applied, FR1 starts to rise slowly, in response to the quasi-static expansion of its ambient field. In contrast to other simulations, where such flows have been used to create a flux rope from a sheared arcade (e.g., Amari et al. 2000), here they do not lead to noticeable reconnection. The slow rise lasts until the rope reaches the critical height for TI onset at $t \approx 40\,\tau_a$, after which it rapidly accelerates upward driven by the instability (Török & Kliem 2007; Fan & Gibson 2007; Schrijver et al. 2008; Aulanier et al. 2010). FR1 attains a maximum velocity of $\approx 0.45\,v_{a0\max}$ at $t \approx 90\,\tau_a$ before it slowly decelerates. Figure 2(b) shows the system in the course of this eruption. The rise of the rope is slightly inclined, due to the asymmetry of its ambient field (e.g., Filippov et al. 2001). The rope rotates counterclockwise about its rise direction (as seen from above), due to the conversion of its twist into a writhe (e.g., Green et al. 2007).

The expansion of FR1's ambient field compresses the field between FR1 and the PS, particularly at larger heights where it is weak (see online animations). As a result, a tilted arc-shaped current layer forms around the PS separator (Figures 3(c) and 4). Further compression by the eruption steepens the current densities until reconnection (R1) between the open flux to the left of the PS and the closed flux in the right PS lobe sets in. The lobe flux then starts to open up, while the open flux starts to close down above the left PS lobe (Figures 2(b) and 3(c)). This successively decreases (increases) the magnetic tension above FR2 (FR3), so that FR2 rises slowly, while FR3 is slowly pushed downward. At $t \approx 95\,\tau_a$ FR2 reaches the critical height for TI onset and erupts, attaining a maximum velocity of $\approx 0.60\,v_{a0\max}$ at $t \approx 120\,\tau_a$. Figure 2(c) shows that FR2 also rises non-radially, but rotates less than FR1. The apparently smaller rotation of FR2 is due to the faster decay of its overlying field with height, which leads to a distribution of the total rotation over a larger height range than for FR1 (Török et al. 2010). By the time shown, FR1 has fully erupted, an elongated vertical current layer has formed in its wake (Figure 3(d)), and reconnection therein has produced cusp-shaped field lines below it. As FR2 erupts, it rapidly pushes the arc-shaped current layer to large heights (Figure 3(d)). While R1 still commences for some time, it does not anymore play a significant role in the following evolution.

A vertical current layer also forms below FR2. The subsequent reconnection (R2) initially involves the very same flux systems that took part in R1. The flux previously closed down by R1 opens up again, and the flux previously opened up by R1—and by the expansion of FR2—closes down to form cusp-shaped field lines below the current layer (Figure 3(e)). After these fluxes are exhausted, R2 continues, now involving the left PS lobe and the open flux to the right of the PS. While the former opens up, the latter closes down as part of the growing cusp (Figure 3(f)). Thus, R2 continuously removes closed flux above FR3. As before, this progressive weakening of magnetic tension leads to a slow rise of the rope, followed by its erup-

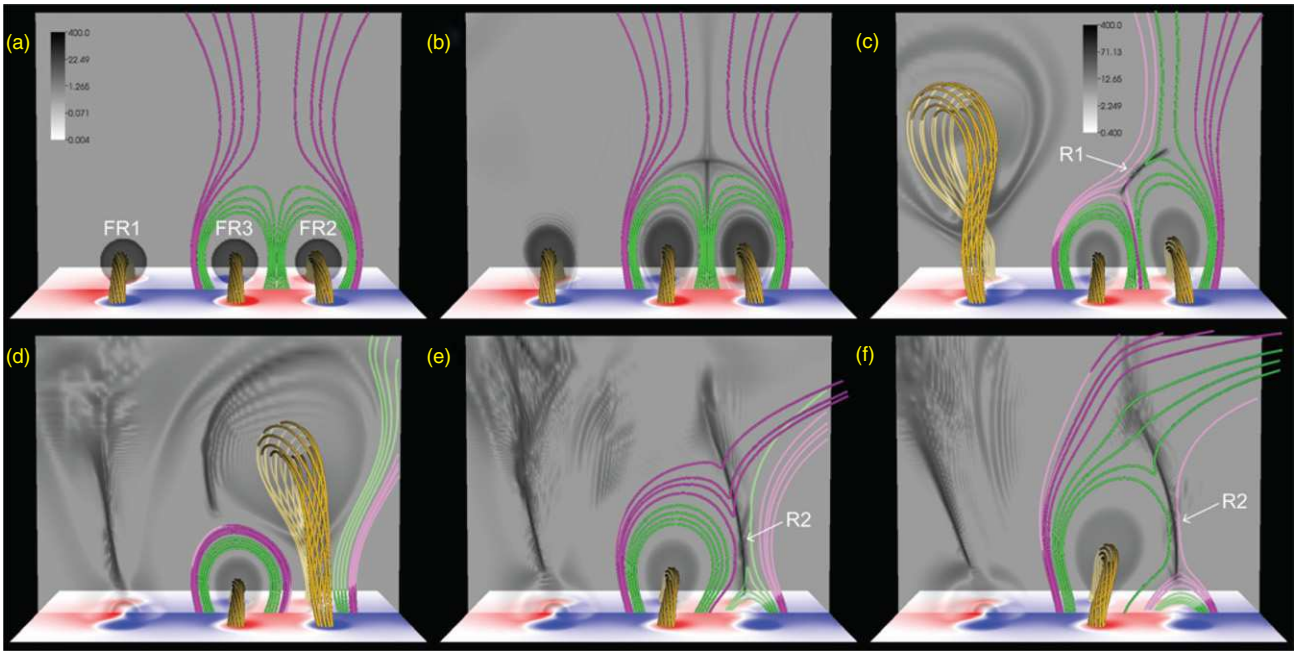

Figure 3. Illustration of the two reconnection phases that trigger the successive flux rope eruptions in the pseudo-streamer. Field lines are colored the same as in Figure 2. The transparent inverted gray scale in the central plane, $\{y = 0\}$, shows the logarithmic distribution of $|\mathbf{j}|/|\mathbf{B}|$, where $\mathbf{j}$ is the electric current density, outlining flux rope currents and thin current layers. Fainter field line segments are located behind the transparent layer. Panel (a) shows the initial configuration, panel (b) the system after relaxation, and panels (c)–(f) show the dynamic evolution, at $t = 85, 126, 142$, and $158\,\tau_a$, respectively. Panels (a) and (b) and (c)–(f) use a different scaling of $|\mathbf{j}|/|\mathbf{B}|$, respectively. Panel (c) shows reconnection R1, which triggers the eruption of FR2, and panels (e) and (f) show reconnection R2, which triggers the eruption of FR3. Panel (d) shows a state between the two reconnection phases.

(An animation and a color version of this figure are available in the online journal.)

tion (Figures 3(f) and 2(d)). The rapid acceleration of FR3 by the TI starts at $t \approx 138\,\tau_a$, yielding a maximum velocity of $\approx 0.35\,v_{a0\max}$ at $t \approx 175\,\tau_a$. The rope shows a significant rotation and an inclined rise which is now mainly directed toward the positive x-direction.

5. DISCUSSION

The eruptions of FR2 and FR3 are initiated by the removal of a sufficient amount of stabilizing flux above the flux ropes via reconnection. R1 is similar to quadrupolar "breakthrough" or "breakout" reconnection (Syrovatskii 1982; Antiochos et al. 1999). Here it is driven by a nearby CME rather than by an expanding arcade and, in contrast to the breakout model, a flux rope is present prior to eruption. R2, on the other hand, corresponds to standard flare reconnection in the wake of a CME. Here it removes flux from the adjacent PS lobe, thereby triggering the eruption of FR3. A similar mechanism for the initiation of a second eruption in a PS was suggested by Cheng et al. (2005), who, however, attributed it to reconnection inflows rather than to flux removal. We emphasize that R1 and R2 merely *trigger* the eruptions, which are *driven* by the TI and supported by the associated flare reconnection (e.g., Vršnak 2008). Thus, in the system studied here, both PS eruptions require the presence of a pre-eruptive flux rope. We further note that the reconnections do not have to commence for the whole time period until the TI sets in. It is sufficient if they remove enough flux for the subsequently slowly rising flux ropes to reach the critical height for TI onset.

R1 is driven by a perturbation of limited duration—the lateral expansion of a nearby CME—and is slow since it involves only weak fields, around a separator at a significant height in the corona. Therefore, its success in triggering an eruption depends on parameters like the distance of the CME from the PS and the amount of pre-eruptive flux within the PS lobes. Indeed, if we sufficiently increase these parameters in the simulation we find that R1 still commences, but does not last long enough to trigger an eruption. In contrast, R2 is driven by the rise of FR2 and involves strong fields. It is therefore faster and more efficient, which supports the finding by Panasenco & Velli (2010) that an eruption in one lobe of a PS is often followed by an eruption in the neighboring lobe.

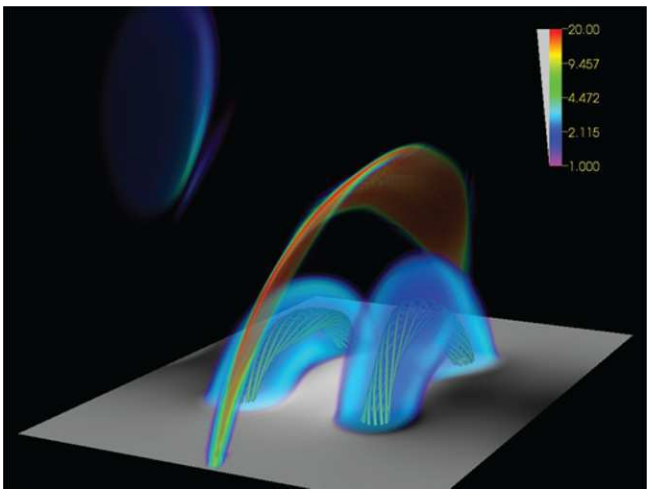

Figure 4. Volume rendering of $|\mathbf{j}|/|\mathbf{B}|$ in the pseudo-streamer area at the same time as in Figures 2(b) and 3(c), outlining the tilted arc-shaped current layer that forms around the separator.

(A color version of this figure is available in the online journal.)

Figure 2 shows that the simulation correctly reproduces the order of the eruptions shown in Figure 1(a) and yields a good match of their inclinations and rotations. Assuming that the first eruption indeed triggered the subsequent ones, it is surprising

that the filament located further away from it went off first. While filament 2 may simply have been closer to its stability limit than filament 3 (as indicated by its larger height; see Figure 1(a)), the simulation provides an alternative explanation: the perturbation of the separator yields an orientation of the current layer that leads to a removal of closed flux only in the right PS lobe (Figure 3(c)), thus enforcing the eruption of FR2. Hence, although we could not find observational signatures of R1 (presumably because the involved fields were too weak), the observed eruption sequence supports its occurrence. The time intervals between the simulated eruptions exhibit a ratio different to the observed ones. Matching the observed ratio requires a search for the appropriate model parameters and a more realistic modeling of reconnection, which are beyond the scope of this work.

FR2 reaches a velocity about 35% larger than that of FR1, which is in line with Liu (2007) and Fainshtein & Ivanov (2010), who found that CMEs associated with PSs are, on average, faster than those associated with helmet streamers. Liu (2007) suggested that this difference is due to the typically smaller amount of closed flux the former have to overcome. Indeed, FR1 has to pass through flux that is closed at all heights above it, while FR2 faces much less closed flux, a significant fraction of which is, moreover, removed by R1. FR3 remains significantly slower than FR2, most likely because it encounters more closed flux at eruption onset, and only partially opened flux later on (Figures 3(e) and (f)).

6. CONCLUSIONS

We present an MHD simulation of two successive flux rope eruptions in a PS, and we demonstrate how they can be triggered by a preceding nearby eruption. The simulation suggests a mechanism for twin filament eruptions and provides a scenario for a subset of the sympathetic eruptions on 2010 August 1. More realistic initial configurations and a more sophisticated treatment of reconnection are needed for a quantitative comparison with observations.

Our results support the conjecture that the trigger mechanisms of sympathetic eruptions can be related to the structural properties of the large-scale coronal field. However, while structural features are present in our model configuration, they do not connect the source region of the first eruption with the source regions of the subsequent ones. Moreover, the mere presence of such features in a source region is not a sufficient criterion for the occurrence of a sympathetic event, even if reconnection at structural features is triggered by a distant eruption. The conditions in the source region must be such that the resulting perturbation forces the region to cross the stability boundary.

The two trigger mechanisms presented here are independent and applicable also to other magnetic configurations. Triggering a sympathetic eruption by R1 requires the presence of a separator (or null point) above closed flux that stabilizes a pre-eruptive flux rope, which can be realized, in the simplest case, in a so-called fan-spine configuration (e.g., Antiochos 1998; Pariat et al. 2009; Török et al. 2009). Triggering a sympathetic eruption by R2 requires the presence of an adjacent closed flux system overlying a flux rope, which can exist, for example, in quadrupolar configurations.

We thank P. Démoulin, B. Kliem, and K. Schrijver for stimulating discussions. The contribution of T.T, V.S.T., Z.M., and J.A.L. was supported by NASA's HTP, LWS, and SR&T programs, CISM (an NSF Science and Technology Center), and a contract from Lockheed-Martin to Predictive Science, Inc. O.P. was supported by NASA grant NNX09AG27G, G.D.T. by NASA/SHP grant NNH09AK02I, and K.K.R. by contract SP02H1701R from Lockheed-Martin to SAO. M.V's. contribution was carried out at JPL (Caltech) under a contract with NASA. Computational resources were provided by NSF TACC in Austin and by NASA NAS at the Ames Research Center. This work was partially supported by the International Space Science Institute via International Team 174 on Solar Prominence Formation and Equilibrium.

REFERENCES

Amari, T., Luciani, J. F., Mikic, Z., & Linker, J. 2000, ApJ, 529, L49
Antiochos, S. K. 1998, ApJ, 502, L181
Antiochos, S. K., DeVore, C. R., & Klimchuk, J. A. 1999, ApJ, 510, 485
Aulanier, G., Török, T., Démoulin, P., & DeLuca, E. E. 2010, ApJ, 708, 314
Baum, P. J., & Bratenahl, A. 1980, Sol. Phys., 67, 245
Biesecker, D. A., & Thompson, B. J. 2000, J. Atmos. Sol.Terr. Phys., 62, 1449
Bumba, V., & Klvana, M. 1993, Ap&SS, 199, 45
Cheng, J., Fang, C., Chen, P., & Ding, M. 2005, Chin. J. Astron. Astrophys., 5, 265
Démoulin, P., Henoux, J. C., Priest, E. R., & Mandrini, C. H. 1996, A&A, 308, 643
Ding, J. Y., Hu, Y. Q., & Wang, J. X. 2006, Sol. Phys., 235, 223
Eselevich, V. G., Fainshtein, V. G., & Rudenko, G. V. 1999, Sol. Phys., 188, 277
Fainshtein, V. G., & Ivanov, E. V. 2010, Sun Geosphere, 5, 28
Fan, Y., & Gibson, S. E. 2007, ApJ, 668, 1232
Filippov, B. P., Gopalswamy, N., & Lozhechkin, A. V. 2001, Sol. Phys., 203, 119
Forbes, T. 2010, in Models of Coronal Mass Ejections and Flares, ed. C. J. Schrijver & G. L. Siscoe (Cambridge: Cambridge Univ. Press), 159
Green, L. M., Kliem, B., Török, T., van Driel-Gesztelyi, L., & Attrill, G. D. R. 2007, Sol. Phys., 246, 365
Howard, R. A., Moses, J. D., Vourlidas, A., et al. 2008, Space Sci. Rev., 136, 67
Hundhausen, A. J. 1972, Coronal Expansion and Solar Wind (Berlin: Springer)
Jiang, Y., Shen, Y., Yi, B., Yang, J., & Wang, J. 2008, ApJ, 677, 699
Kliem, B., & Török, T. 2006, Phys. Rev. Lett., 96, 255002
Lau, Y.-T., & Finn, J. M. 1990, ApJ, 350, 672
Liu, C., Lee, J., Karlický, M., et al. 2009, ApJ, 703, 757
Liu, Y. 2007, ApJ, 654, L171
Masson, S., Pariat, E., Aulanier, G., & Schrijver, C. J. 2009, ApJ, 700, 559
Moon, Y., Choe, G. S., Park, Y. D., et al. 2002, ApJ, 574, 434
Panasenco, O., & Velli, M. M. 2010, AGU Fall Meeting Abstracts, A1663
Pariat, E., Antiochos, S. K., & DeVore, C. R. 2009, ApJ, 691, 61
Priest, E. R., & Forbes, T. G. 1992, J. Geophys. Res., 97, 1521
Ramsey, H. E., & Smith, S. F. 1966, AJ, 71, 197
Riley, P., & Luhmann, J. G. 2011, Sol. Phys., submitted
Schatten, K. H., Wilcox, J. M., & Ness, N. F. 1969, Sol. Phys., 6, 442
Scherrer, P. H., Bogart, R. S., Bush, R. I., et al. 1995, Sol. Phys., 162, 129
Schrijver, C. J., Elmore, C., Kliem, B., Török, T., & Title, A. M. 2008, ApJ, 674, 586
Schrijver, C. J., & Title, A. M. 2011, J. Geophys. Res. (Space Phys.), 116, A04108
Syrovatskii, S. I. 1982, Sol. Phys., 76, 3
Titov, V. S., & Démoulin, P. 1999, A&A, 351, 707
Titov, V. S., Hornig, G., & Démoulin, P. 2002, J. Geophys. Res. (Space Phys.), 107, 1164
Titov, V. S., Mikić, Z., Linker, J. A., Lionello, R., & Antiochos, S. K. 2011, ApJ, 731, 111
Török, T., Aulanier, G., Schmieder, B., Reeves, K. K., & Golub, L. 2009, ApJ, 704, 485
Török, T., Berger, M. A., & Kliem, B. 2010, A&A, 516, A49
Török, T., Chandra, R., Pariat, E., et al. 2011, ApJ, 728, 65
Török, T., & Kliem, B. 2003, A&A, 406, 1043
Török, T., & Kliem, B. 2007, Astron. Nachr., 328, 743
Török, T., Kliem, B., & Titov, V. S. 2004, A&A, 413, L27
Vršnak, B. 2008, Ann. Geophys., 26, 3089
Wang, H., Chae, J., Yurchyshyn, V., et al. 2001, ApJ, 559, 1171
Wang, Y., Sheeley, N. R., Jr., & Rich, N. B. 2007, ApJ, 658, 1340
Wheatland, M. S., & Craig, I. J. D. 2006, Sol. Phys., 238, 73
Zhukov, A. N., & Veselovsky, I. S. 2007, ApJ, 664, L131
Zuccarello, F., Romano, P., Farnik, F., et al. 2009, A&A, 493, 629

The Evolution of Writhe in Kink-Unstable Flux Ropes and Erupting Filaments

T. Török [1], B. Kliem [2], M. A. Berger [3], M. G. Linton [4], P. Démoulin [5], L. van Driel-Gesztelyi [6,5,7]

ABSTRACT

The helical kink instability of a twisted magnetic flux tube has been suggested as a trigger mechanism for solar filament eruptions and coronal mass ejections (CMEs). In order to investigate if estimations of the pre-eruptive twist can be obtained from observations of writhe in such events, we quantitatively analyze the conversion of twist into writhe in the course of the instability, using numerical simulations. We consider the line tied, cylindrically symmetric Gold–Hoyle flux rope model and measure the writhe using the formulae by Berger and Prior which express the quantity as a single integral in space. We find that the amount of twist converted into writhe does not simply scale with the initial flux rope twist, but depends mainly on the growth rates of the instability eigenmodes of higher longitudinal order than the basic mode. The saturation levels of the writhe, as well as the shapes of the kinked flux ropes, are very similar for considerable ranges of initial flux rope twists, which essentially precludes estimations of pre-eruptive twist from measurements of writhe. However, our simulations suggest an upper twist limit of $\sim 6\pi$ for the majority of filaments prior to their eruption.

Subject headings: Magnetohydrodynamics (MHD); Sun: corona; Sun: filaments

1. Introduction

The $m = 1$ kink mode or helical kink instability (hereafter KI) is a current-driven, ideal magnetohydrodynamic (MHD) instability. It occurs in a magnetic flux rope if the winding of the

[1]Predictive Science Inc., 9990 Mesa Rim Rd., Ste 170, San Diego, CA 92121, USA

[2]Institut für Physik und Astronomie, Universität Potsdam, Karl-Liebknecht-Str. 24-25, 14476 Potsdam, Germany

[3]University of Exeter, SECAM, Exeter, EX4 4QE, UK

[4]U.S. Naval Research Lab, 4555 Overlook Ave., SW Washington, DC 20375, USA

[5]LESIA, Observatoire de Paris, CNRS, UPMC, Univ. Paris Diderot, 5 place Jules Janssen, 92190 Meudon, France

[6]University College London, Mullard Space Science Laboratory, Holmbury St Mary, Dorking, Surrey, RH5 6NT, UK

[7]Konkoly Observatory of the Hungarian Academy of Sciences, Budapest, Hungary

field lines about the rope axis (the twist) exceeds a critical value (e.g., Shafranov 1957; Kruskal & Tuck 1958; Freidberg 1982; Priest 1982). The instability lowers the magnetic energy of the flux rope by reducing the bending of field lines, which leads to a characteristic helical deformation (writhe) of the rope axis. Such writhing is often observed in erupting filaments or prominences in the solar corona (Figure 1), which has led to the suggestion that the KI can trigger filament eruptions and CMEs (e.g., Sakurai 1976; Sturrock et al. 2001; Török & Kliem 2005; Fan 2005).

The KI has been studied extensively for laboratory plasmas (see, e.g., Bateman 1978; Goedbloed et al. 2010, and references therein). In applications relevant to the low-β solar corona, typically force-free, cylindrically symmetric flux rope configurations of finite length are considered. The anchoring of coronal loops and prominences in the solar surface is modeled by imposing line tied boundary conditions at the flux rope ends. Properties of the KI such as the instability threshold and growth rate, as well as the formation of current sheets, have been investigated for various radial twist profiles in both straight and arched flux rope geometries (e.g., Hood & Priest 1981; Mikić et al. 1990; Baty & Heyvaerts 1996; Gerrard et al. 2001; Török et al. 2004). MHD simulations of kink-unstable flux ropes have been employed to model coronal loop heating and bright-point emission (Galsgaard & Nordlund 1997; Haynes & Arber 2007), soft X-ray sigmoids (Kliem et al. 2004), energy release in compact flares (Gerrard & Hood 2003), microwave sources in eruptive flares (Kliem et al. 2010), and rise profiles, rotation, and writhing of erupting filaments and CMEs (Török & Kliem 2005; Williams et al. 2005; Fan 2005; Kliem et al. 2012). In spite of this large body of work, the amount and evolution of the writhing in kink-unstable flux ropes was quantified only very rarely (Linton et al. 1998; Török et al. 2010). Systematic investigations of the dependence of the writhe on parameters such as the initial flux rope twist or geometry have not yet been undertaken.

The quantity *writhe* measures the net self-coiling of a space curve. It is related to the total torsion along the curve: the sum of writhe and total torsion remains constant under deformations, unless the curve develops an inflexion point, where curvature vanishes (Moffatt & Ricca 1992). Twist and writhe of a thin flux rope are related to its magnetic helicity via $H = F^2(T+W)$, where F is the axial magnetic flux, T is the number of field line turns, and W is the writhe of the rope axis (Călugăreanu 1959; Berger & Prior 2006). The writhe for flux ropes with footpoints on a boundary (such as the photosphere) can be defined by the same formula, using relative helicity for H (Berger & Field 1984). W depends only on the shape of the axis of the rope; while T measures the net twist of the field lines in the rope about the axis. Since magnetic helicity is conserved in ideal MHD, the KI converts twist into an equal amount of writhe. Here we quantify this process for the first time systematically for a range of initial flux rope twists, using MHD simulations.

For our study we consider the straight, uniformly twisted, force-free flux rope equilibrium by Gold & Hoyle (1960, hereafter GH), line tied at both ends. In the absence of knowledge about

typical twist profiles in coronal flux ropes and due to its force freeness, the equilibrium serves as a convenient reference model. Mechanisms other than the KI that may cause writhing (see Kliem et al. 2012 for a detailed discussion) are excluded. Furthermore, the KI of the GH model does not lead to the formation of a helical current sheet, which triggers reconnection in the nonlinear development of other flux rope equilibria (e.g., Baty & Heyvaerts 1996; Gerrard & Hood 2003). Therefore, the evolution of the axis deformation can be followed well into the saturation phase of the writhe, which makes this equilibrium particularly suited for our purpose. We measure the axis writhe using the formulae by Berger & Prior (2006), which express the quantity as a single integral in space, facilitating its calculation.

Our motivation for this study is derived from the interest in obtaining estimates of the twist in pre-eruptive solar configurations from the amount of writhing observed during an eruption. At present, the twist cannot be obtained directly, since the magnetic field cannot be measured in the coronal volume and since extrapolations from photospheric vector magnetograms are not yet sufficiently reliable in practice, especially for volumes containing a filament (McClymont et al. 1997; Schrijver et al. 2008). Twist estimations based on the observations of pre-eruptive coronal configurations are hampered with substantial uncertainties (see Section 4). The writhe of erupting filaments, on the other hand, can be obtained with a reasonable accuracy if the filament displays a coherent shape (Figure 1) and if observations from more than one viewing angle are available (for example from the *STEREO* mission; Kaiser et al. 2008) or if the eruption is directed toward the observer (Török et al. 2010). Although twist estimates from the writhe can only be obtained in retrospect, they may facilitate systematic studies of this possibly critical parameter for CME initiation and may be useful for comparison with other means of estimation.

2. Flux Rope Model and Numerical Setup

The GH model used in this study is given by

$$B_\theta = \frac{B_0 b r}{1 + b^2 r^2}, \quad B_z = \frac{B_0}{1 + b^2 r^2} \tag{1}$$

and represents a uniformly twisted, force-free flux rope of infinite radial extent. The constant b is related to the axial length of one field line turn, Λ, often referred to as the pitch, by $b = 2\pi/\Lambda$ and, at the same time, represents the inverse scale length of the radial field profile. Using the customary form of the expression for the twist angle,

$$\Phi(r) = \frac{L\, B_\theta(r)}{r\, B_z(r)}, \tag{2}$$

a GH rope of length L has a twist of $\Phi = bL$. This is related to the number of field line turns $T = L/\Lambda$ by $\Phi = 2\pi T$. In our calculations we fix the scale $b = \pi$, so that the radial field profiles

are identical in all simulations, and we vary the initial twist by varying the flux rope length.

The numerical set–up for the simulations is the same as in our previous studies of the kink and torus instabilities (e.g., Török & Kliem 2005, 2007); for a detailed description see Török & Kliem (2003). The compressible ideal MHD equations are integrated using the simplifying assumptions of vanishing pressure and gravity on a discretized Cartesian box $[-L_x, L_x] \times [-L_y, L_y] \times [0, L_z]$ with uniform spacing $\Delta = 0.04$ and $L_x = 8$, $L_z = 16$. In order to take advantage of the z-axis line symmetry inherent in the configurations considered, we orient the flux rope parallel to the y axis, so that the integration need be carried out only in the "half box" $\{y > 0\}$. The flux rope length equals the full box length $2L_y$. Except for $\{y = 0\}$, where mirroring according to the z-axis line symmetry is applied, the MHD variables are held fixed at their initial values at all boundaries (and for consistency the velocity is kept at zero also one grid layer inside the boundaries). This models line-tying at the ends of the rope, $|y| = L_y$.

We vary the initial twist, $\Phi_0 = 2\pi L_y$, in the range (3–10.6)π by varying L_y in our series of runs. Since the rope expands strongly and in different ways in the different runs (Figure 2), we minimize the influence of the top and bottom boundaries by positioning the rope axis at appropriate initial heights $z = h_0$. See Table 1 for the values of L_y, Φ_0, and h_0 used in this investigation.

The initial density distribution is specified to be $\rho_0 = B_0^{3/2}$, such that the Alfvén velocity decreases slowly with distance from the flux rope axis (which corresponds to the conditions in the solar corona). The MHD variables are normalized by quantities derived from a characteristic length of the initial equilibria, chosen to be $\Lambda/2$, and the initial magnetic field strength and Alfvén velocity at the flux rope axis. All runs start with the fluid at rest. A small initial velocity perturbation localized at the flux rope center is imposed in all runs (analogous to Török et al. 2004).

L_y	Φ_0	h_0	W
1.48	$3.0\,\pi$	4	0.96
2.24	$4.5\,\pi$	4	0.97
3.00	$6.0\,\pi$	4	1.01
3.76	$7.5\,\pi$	6	1.04
4.48	$9.0\,\pi$	8	1.79
5.28	$10.6\,\pi$	10	1.76

Table 1: Parameters of the simulations. $2L_y$–length of the flux rope; $\Phi_0 = 2\pi L_y$–initial twist; h_0–initial z position of the rope axis; W–writhe (peak writhe for $\Phi_0 \geq 9\pi$ and final writhe for $\Phi_0 \leq 7.5\pi$).

3. Results

Since the chosen initial twists in the series all exceed the KI threshold for the line tied GH equilibrium of $\Phi_{\rm cr} \approx 2.5\pi$ (Hood & Priest 1981), all configurations are unstable. The helical nature of the growing perturbation is clearly visible in the linear phase (the early phase of the instability during which the exponentially growing amplitude of the axis displacement remains small; top two rows in Figure 2). In the nonlinear phase (when the amplitude of the axis displacement becomes large) the flux rope starts to expand strongly by the action of the hoop force, which comes into play as soon as the flux rope develops some overall curvature between its line tied ends (bottom two rows in Figure 2 and Section 4).

3.1. Flux rope axis evolution

We measure the growth of writhe at the axis of the flux rope using Equations (4)–(6) in Török et al. (2010); see also Berger & Prior (2006). Note that flux surfaces away from the axis undergo a smaller deformation, with less twist converted into writhe, but Figure 2 indicates that a substantial cross section of the GH rope attains similar writhe. For our strongly twisted cases, the measurements are reliable only until the perturbed flux surfaces start to approach the boundaries of the box.

Figure 3(a) shows the development of writhe by the KI. The writhe grows exponentially in the linear phase and then reaches saturation in the nonlinear phase of the instability. It can be seen that the saturation level of the writhe does not scale linearly with the initial twist, which is different from what one might intuitively expect.

The flux ropes with the smallest twist, $\Phi_0 = 3\pi$ and 4.5π, exhibit a very similar behavior, except for a significantly faster initial evolution of the run with $\Phi_0 = 4.5\pi$. The writhe saturates at $W \approx 0.95$ in both runs, corresponding to a converted twist of $\Phi \approx 1.9\pi$ in the vicinity of the flux rope axis. The morphological evolution and the resulting axis shapes are very similar too (Figure 2). In both cases, the axis deforms into a one-turn helix. Figure 3(b) shows that the evolution of writhe coincides well with the release of magnetic energy by the KI and the displacement of the flux rope axis.

A somewhat different evolution takes place for $\Phi_0 = 7.5\pi$: the writhe first reaches a maximum after the initial exponential growth phase, then decreases by ≈ 20 percent, but subsequently starts to increase again slowly, reaching $W \approx 1.05$ at the end of the simulation. Figure 3(b) shows that the flux rope continues to rise (at a slower rate) after the writhe has reached its first maximum, accompanied by ongoing magnetic energy release. The energy saturates when the writhe reaches its temporary minimum. Some further release occurs later on in the evolution; this appears to be

related to reconnection that occurs at outer flux surfaces when those approach the boundary of the simulation box. The morphological evolution is somewhat different from the smaller-twist cases: the axis shape obtained in the nonlinear phase of the instability is still dominated by a one-turn helix, but it becomes internally helically deformed (see Figure 2). The decrease of the writhe appears to be related to the reversal of the orientation of the flux rope legs in the vicinity of the $\pm L_y$ boundaries (see the second and fourth panel for $\Phi_0 = 7.5\,\pi$ in Figure 2), which occurs at the same time as the writhe decrease. This is a consequence of the line-tying that would be absent in infinitely extended flux ropes, and it implies a temporary increase of twist in the vicinity of the flux rope axis. The subsequent increase of the writhe is most likely associated with the development of the internal axis deformation, but may be related to some degree also to the reconnection mentioned above.

The run with $\Phi_0 = 6.0\,\pi$ is an intermediate case: both the temporary decrease of the writhe and the internal helical axis deformation are present but rather weak, and the writhe at the end of the simulation ($W \approx 1.0$) lies in between the corresponding values for the smaller-twist runs and the run with $\Phi_0 = 7.5\pi$.

The cases with the largest twists ($\Phi_0 = 9\pi$ and 10.6π) show a very different behavior. After the fast initial rise, the writhe continues to grow at a much smaller rate until it reaches a maximum of $W \approx 1.75 - 1.8$, after which it slowly decreases (the decrease is not visible for $\Phi_0 = 9\pi$ in the figure, since the evolution during the nonlinear phase is significantly slower than for $\Phi_0 = 10.6\pi$). The flux rope axis now develops a helix with about two turns (see Figure 2 for $\Phi_0 = 9\,\pi$). We attribute the slow increase and decrease of the writhe to the complex morphological evolution of the flux rope for large twists: the development of two expanding helices within the finite domain forces approaching flux rope sections to give way to one another – an effect that is much less pronounced in cases where only one helix develops. The decrease may be also a consequence of the strongly expanding helices approaching the boundaries of the simulation box.

3.2. What determines the amount of twist converted into writhe?

From Figure 3(a) it is obvious that the conversion of twist into writhe depends on the initial twist in a non-trivial manner. Figures 2 and 3 indicate that it is related to the number of helical turns the rope axis develops in the course of the instability. This number depends on the wavelength of the most unstable mode and on the range of unstable modes permitted by the finite length of the rope. In the linear phase of the instability, the helical eigenmode with the highest growth rate dominates the way the rope starts to deform. The finite length of the line tied rope modifies this picture in the nonlinear phase.

The growth rate as a function of axial wavelength for the GH equilibrium is shown in Figure 4 (from Linton et al. 1998). This plot is for the case of infinite axial but finite radial extent of the rope, $R = 3\pi/2b$. Linton et al. (1998) find the peak growth rate and its location to be unchanged for larger R (our x-z box sizes correspond to $R \sim 8\pi/b$). The growth of the helical kink mode peaks at the wavelength $\lambda = 1.85\Lambda$, meaning that the KI grows fastest at a writhe wavelength of about twice the twist pitch. For our choice $b = \pi$ we have $2\Lambda = 4$. Therefore, for a double helix to dominate in the linear phase, the required box length is $2L_y > 8$, equivalent to a required twist $\Phi = 2\pi L_y > 8\pi$.

Although this corresponds nicely to the jump of the final writhe in Figure 2 between twists $\Phi_0 = 7.5\pi$ and 9π, it does not actually explain the occurrence of a jump. From the stability analysis we know that the most rapidly growing mode at $\lambda \approx 2\Lambda$ is permitted to occur as soon as the box length satisfies $2L_y > 2\Lambda = 4$. Therefore, for $2L_y > 2\Lambda = 4$ non-integer values for the number of turns of $\approx L_y/\Lambda$ can occur at the peak growth rate in the linear phase. This agrees with the simulation results shown in the two upper rows of Figure 2. The dominant mode in this phase exhibits a little more than one turn for $\Phi_0 = 4.5\pi$, nearly two turns for $\Phi_0 = 7.5\pi$ and a little more than two turns for $\Phi_0 = 9\pi$.

The jump in the writhe can only be understood from the nonlinear evolution of the instability. This shows a clear tendency to develop an integer number of turns. As long as two axial wavelengths don't fit into the box, the mode with a single turn dominates in this phase. Contributions of the linearly most strongly growing mode, which then has a shorter wavelength, are clearly present (most obviously for $\Phi_0 = 7.5\pi$), but no longer dominate. We attribute this result to the action of the hoop force for kinking flux ropes of finite length. The line-tying leads to an axial dependence of the displacement which is absent for infinitely extended ropes. For $\Phi_0 \leq 7.5\pi$ the displacement is largest in the mid-plane $\{y = 0\}$ of our symmetric simulations and tapers off toward the line tied ends at $y = \pm L_y$ (see the two upper rows in Figure 2). An overall net bending of the rope in the direction of the displacement in the mid-plane (which points along the z axis in all our simulations) results. This introduces a Lorentz self-force in the rope, known as hoop force, pointing in the direction of the bending (Bateman 1978). The hoop force amplifies the perturbation of the rope axis in the mid-plane above its purely KI-driven displacement, thus creating a one-turn helix for $\Phi_0 \leq 7.5\pi$. Such amplification occurs at a pair of symmetrically located displacements for $\Phi_0 \geq 9\pi$, creating a helix with two turns. We discuss the implications of this result for filament eruptions in the following section.

4. Discussion

We studied the conversion of twist into writhe in a simulation series of the KI in the GH model, considering initial flux rope twists in the range $3.0\,\pi \leq \Phi_0 \leq 10.6\,\pi$. We found in all cases a saturation of writhe in the nonlinear phase of the instability, after an initial exponential increase during the linear phase. However, the final writhe does not scale simply with the initial flux rope twist. Rather, the amount of twist converted into writhe seems to be determined predominantly by the number of helical turns the flux rope axis develops in the nonlinear phase.

For $3.0\,\pi \lesssim \Phi_0 \lesssim 7.5\,\pi$, the rope axis develops a one-turn helix. For twists close to the upper end of this range, internal helical deformations of the one-turn helix develop, due to helical eigenmodes with wavelengths $\lambda < 2L_y$. However, the axis shape remains to be dominated by one turn in the nonlinear phase of the instability. The resulting writhe is close to unity for all cases, corresponding to a converted twist of $\sim 2\,\pi$ in the vicinity of the flux rope axis. If the twist is increased beyond this range, the rope axis develops more than one helical turn, and considerably more twist is converted into writhe ($\sim 3.5\,\pi$ in our simulations with $\Phi_0 = 9.0\,\pi$ and $\Phi_0 = 10.6\,\pi$). We attributed the relatively similar writhe values obtained in each respective range, as well as the pronounced increase of the writhe between them, to the action of the hoop force on line-tied, kink-unstable flux ropes of finite length.

The basically discontinuous dependence of the final writhe upon the initial twist displayed in Figure 3 essentially precludes a reasonable estimation of the initial twist from observations of the writhe in solar filament eruptions and CMEs. The saturation levels of the writhe are very similar for initial twists up to $\Phi_0 \approx 8\pi$, requiring an accuracy of writhe determination for such an estimate that cannot be reached in solar observations. Moreover, the final writhe, as any other property of the KI, depends on the radial twist profile of the initial equilibrium. Therefore, a precise knowledge of this profile, combined with a parametric simulation study like the one in Figures 2 and 3 for a range of different profiles, would be required to permit a reliable estimate of twist. Further effects of importance for the final writhe enter when arched flux rope equilibria are considered (see Török et al. 2010), rendering a twist estimation from writhe observations even more difficult.

In order to compare our results with the KI in force-free equilibria with non-uniform radial twist profile, we performed simulation series similar to the one presented here for the straight flux rope model termed "Equilibrium 2" in Gerrard et al. (2001) and the arched flux rope model by Titov & Démoulin (1999). Unfortunately, in all runs the flux rope axis was destroyed by reconnection at current sheets before the writhe would clearly saturate (see Amari & Luciani 1999, Haynes et al. 2008, and Valori et al. 2010 for examples of such reconnection), so that these simulations cannot be used for the purpose of this study.

However, our writhe measurements for the KI in the GH equilibrium provide at least a rough

upper limit for the initial twist of erupting filaments. It is observed that kinking filaments typically do not display more than one helical turn and hardly any significant internal helical deformation of their axis. Combined with our simulations, this suggests that the initial twist typically does not exceed values $\Phi_0 \sim 6\pi$. This is supported by simulations of the KI in the Titov-Démoulin model, which show strong internal helical deformations for twists above this value (see, e.g., Figure 1 in Kliem et al. 2010 and Figure 12 in Török et al. 2010).

Occasionally, however, the Sun seems to succeed in building up higher twists. Several examples can be found in Vršnak et al. (1991), whose estimates of the end-to-end twist fall in the range $(3\text{–}15)\,\pi$ for a sample of prominences close to the time of eruption. A particularly clear indication of very high twist (of $\sim 10\pi$) was obtained by Romano et al. (2003) for a filament eruption on 19 July 2000 (Figure 1c). These estimations are based on measurements of the pitch angle of selected helical prominence threads, which are then converted into twist assuming a uniform radial twist profile both along and across the axis of the underlying flux rope. The latter assumption may be a severe oversimplification, since force-free flux ropes embedded in potential field must generally have a nonuniform radial twist profile in order to match the field at the surface of the rope (see, e.g., Figure 2 in Török et al. 2004). Still, the simulations presented here support the existence of such a high twist at least for the case shown in Figure 1c, based on the strong bending in the lower part of the filament legs (see also Figure 12b in Török et al. 2010, where a strongly nonuniform radial twist profile was used). A further observed case of very high twist may have been an apparently three-fold helix described in Gary & Moore (2004).

While these estimations remain uncertain to a considerable degree, we can ask how such large twists, if present, may be produced in the solar corona. It is widely believed that twist is accumulated prior to an eruption by flux emergence (e.g., Leka et al. 1996), photospheric vortex flows (e.g., Romano et al. 2005), or the slow transformation of a sheared magnetic arcade into a flux rope (e.g., Moore et al. 2001; Aulanier et al. 2010). It has been argued that flux ropes that form by one or more of these mechanisms will become kink-unstable long before the large twists mentioned above can be reached. While this is likely true for the majority of cases, several scenarios for the build-up of large twists appear to plausible. First, the KI threshold can vary in a wide range as a function of the thickness of the rope (e.g., Hood & Priest 1979; Baty 2001; Török et al. 2004), so sufficiently thin flux ropes may be able to harbor large twist in a stable state. Second, sufficiently flat highly twisted flux ropes may be stabilized by strong ambient shear fields (Török et al. 2010), or by gravity if they contain sufficient filament material. Third, significant twist may be added by reconnection to the rising flux in the course of an eruption (e.g., Qiu et al. 2007). Finally, flux ropes may reconnect and merge prior to an eruption, thereby adding up their respective twists (e.g., Pevtsov et al. 1996; Canfield & Reardon 1998; Schmieder et al. 2004; van Ballegooijen 2004).

We thank the anonymous referees for very helpful suggestions and Z. Mikić for providing a routine that was helpful for the writhe calculations. The contribution of T.T. was supported by NASA's HTP, LWS, and SR&T programs and by the NSF. M.G.L. received support from NASA/LWS and the ONR 6.1 programs. B.K. was supported by the DFG. The research leading to these results has received funding from the European Commission's Seventh Framework Programme under the grant agreement No. 284461 (eHEROES project). L.vDG.'s work work was supported by the STFC Consolidated Grant ST/H00260X/1 and the Hungarian Research grant OTKA K-081421.

REFERENCES

Amari, T., & Luciani, J. F. 1999, ApJ, 515, L81

Aulanier, G., Török, T., Démoulin, P., & DeLuca, E. E. 2010, ApJ, 708, 314

Bateman, G. 1978, MHD instabilities (Cambridge, Mass., MIT Press)

Baty, H. 2001, A&A, 367, 321

Baty, H., & Heyvaerts, J. 1996, A&A, 308, 935

Berger, M. A., & Field, G. B. 1984, Journal of Fluid Mechanics, 147, 133

Berger, M. A., & Prior, C. 2006, Journal of Physics A Mathematical General, 39, 8321

Canfield, R. C., & Reardon, K. P. 1998, Sol. Phys., 182, 145

Călugăreanu. 1959, Czechoslovak Math. J., 11, 588ñ625

Fan, Y. 2005, ApJ, 630, 543

Freidberg, J. P. 1982, Reviews of Modern Physics, 54, 801

Galsgaard, K., & Nordlund, Å. 1997, J. Geophys. Res., 102, 219

Gary, G. A., & Moore, R. L. 2004, ApJ, 611, 545

Gerrard, C. L., Arber, T. D., Hood, A. W., & Van der Linden, R. A. M. 2001, A&A, 373, 1089

Gerrard, C. L., & Hood, A. W. 2003, Sol. Phys., 214, 151

Goedbloed, J. P., Keppens, R., & Poedts, S. 2010, Advanced Magnetohydrodynamics (Cambridge University Press)

Gold, T., & Hoyle, F. 1960, MNRAS, 120, 89

Haynes, M., & Arber, T. D. 2007, A&A, 467, 327

Haynes, M., Arber, T. D., & Verwichte, E. 2008, A&A, 479, 235

Hood, A. W., & Priest, E. R. 1979, Sol. Phys., 64, 303

—. 1981, Geophysical and Astrophysical Fluid Dynamics, 17, 297

Kaiser, M. L., Kucera, T. A., Davila, J. M., St. Cyr, O. C., Guhathakurta, M., & Christian, E. 2008, Space Sci. Rev., 136, 5

Kliem, B., Linton, M. G., Török, T., & Karlický, M. 2010, Sol. Phys., 266, 91

Kliem, B., Titov, V. S., & Török, T. 2004, A&A, 413, L23

Kliem, B., Török, T., & Thompson, W. T. 2012, Sol. Phys., 281, 137

Kruskal, M., & Tuck, J. L. 1958, Royal Society of London Proceedings Series A, 245, 222

Leka, K. D., Canfield, R. C., McClymont, A. N., & van Driel-Gesztelyi, L. 1996, ApJ, 462, 547

Linton, M. G., Dahlburg, R. B., Fisher, G. H., & Longcope, D. W. 1998, ApJ, 507, 404

McClymont, A. N., Jiao, L., & Mikić, Z. 1997, Sol. Phys., 174, 191

Mikić, Z., Schnack, D. D., & van Hoven, G. 1990, ApJ, 361, 690

Moffatt, H. K., & Ricca, R. L. 1992, Proc. Roy. Soc. A, 439, 411

Moore, R. L., Sterling, A. C., Hudson, H. S., & Lemen, J. R. 2001, ApJ, 552, 833

Pevtsov, A. A., Canfield, R. C., & Zirin, H. 1996, ApJ, 473, 533

Priest, E. R. 1982, Solar magneto-hydrodynamics (Dordrecht, Holland; Boston: D. Reidel Pub. Co.; Hingham)

Qiu, J., Hu, Q., Howard, T. A., & Yurchyshyn, V. B. 2007, ApJ, 659, 758

Romano, P., Contarino, L., & Zuccarello, F. 2003, Sol. Phys., 214, 313

—. 2005, A&A, 433, 683

Sakurai, T. 1976, PASJ, 28, 177

Schmieder, B., Mein, N., Deng, Y., Dumitrache, C., Malherbe, J., Staiger, J., & Deluca, E. E. 2004, Sol. Phys., 223, 119

Schrijver, C. J., Elmore, C., Kliem, B., Török, T., & Title, A. M. 2008, ApJ, 674, 586

Shafranov, V. D. 1957, Journal of Nuclear Energy II, 5, 86

Sturrock, P. A., Weber, M., Wheatland, M. S., & Wolfson, R. 2001, ApJ, 548, 492

Titov, V. S., & Démoulin, P. 1999, A&A, 351, 707

Török, T., Berger, M. A., & Kliem, B. 2010, A&A, 516, A49

Török, T., & Kliem, B. 2003, A&A, 406, 1043

—. 2005, ApJ, 630, L97

—. 2007, Astron. Nachr., 328, 743

Török, T., Kliem, B., & Titov, V. S. 2004, A&A, 413, L27

Valori, G., Kliem, B., Török, T., & Titov, V. S. 2010, A&A, 519, A44+

van Ballegooijen, A. A. 2004, ApJ, 612, 519

Vršnak, B., Ruždjak, V., & Rompolt, B. 1991, Sol. Phys., 136, 151

Williams, D. R., Török, T., Démoulin, P., van Driel-Gesztelyi, L., & Kliem, B. 2005, ApJ, 628, L163

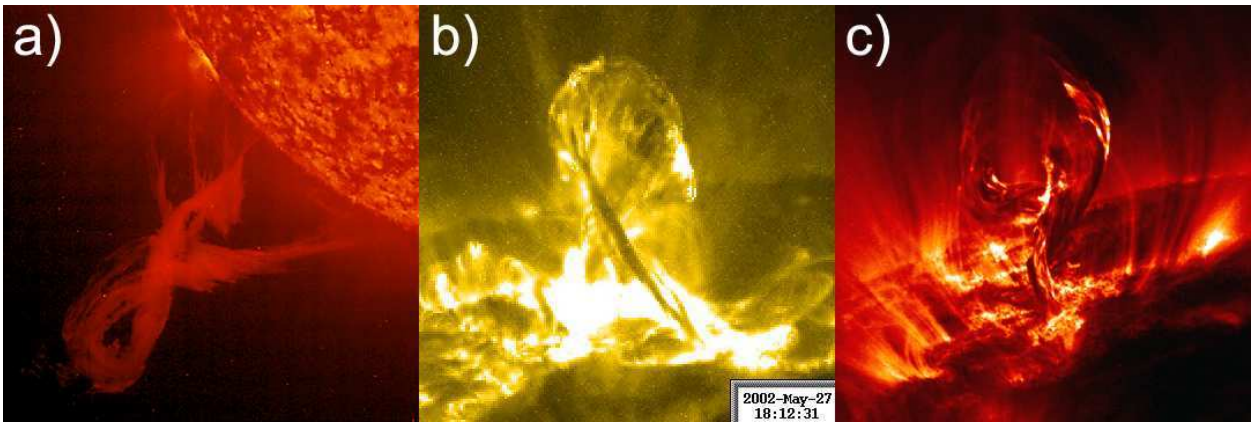

Fig. 1.— Erupting and writhing solar filaments observed in extreme ultraviolet (EUV) wavelengths. **a):** A full eruption (evolving into a CME) on 18 January 2000, observed in 304 Å by the EIT telescope onboard the SOHO spacecraft. **b):** A confined eruption (trapped in the low corona) on 27 May 2002, observed in 195 Å by the TRACE satellite. **c):** An eruption, which most likely remained confined, on 19 July 2000, observed in 171 Å by TRACE.

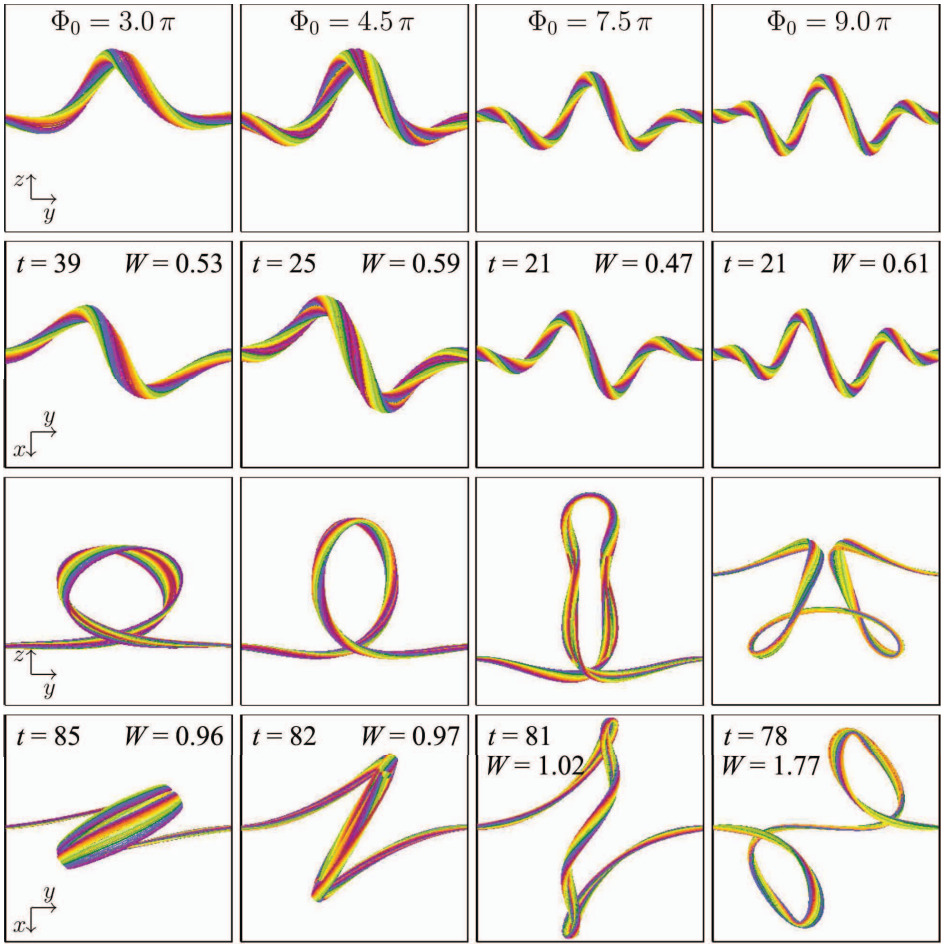

Fig. 2.— Helical deformation of the kink-unstable Gold-Hoyle flux rope. Magnetic field lines start at circles of radius R centered at the axis endpoints, $(0, \pm L_y, h_0)$. The full box range in y direction, $-L_y \le y \le L_y$, is shown in all panels. Endpoint locations are the same for each column, while the x and z ranges are changed to account for the expansion of the flux rope. The two upper rows show flux surfaces with $R = 0.1$ during or shortly after the linear phase of the instability in a side view and a top view, respectively. The range $h_0 - 2 \le z \le h_0 + 2$ is displayed in the side views and $-L_y \le x \le L_y$ in the top views. The two lower rows show flux surfaces with $R = 0.05$ at the end, or toward the end, of the simulations in the same views, using the vertical ranges $[2, 10]$, $[2, 10]$, $[4, 14]$, and $[0, 14]$ (from left to right) in the side views and $-L_y \le x \le L_y$ in the top views. Simulation times and the value of writhe are shown in the top view panels for all cases.

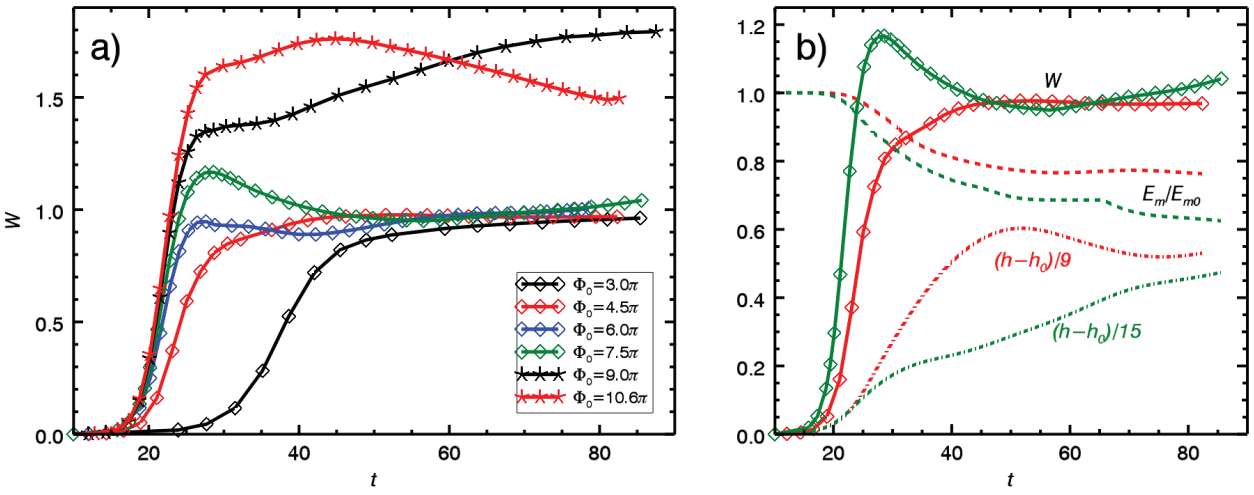

Fig. 3.— **(a):** Development of writhe by the KI of the GH flux rope for different values of the initial twist. **(b):** Writhe (diamonds), vertical displacement of the flux rope axis from its initial position on the z axis (dash-dotted lines; scaled to fit into the plot), and total magnetic energy (dashed lines; normalized to initial value) for $\Phi_0 = 4.5\,\pi$ (red) and $\Phi_0 = 7.5\,\pi$ (green).

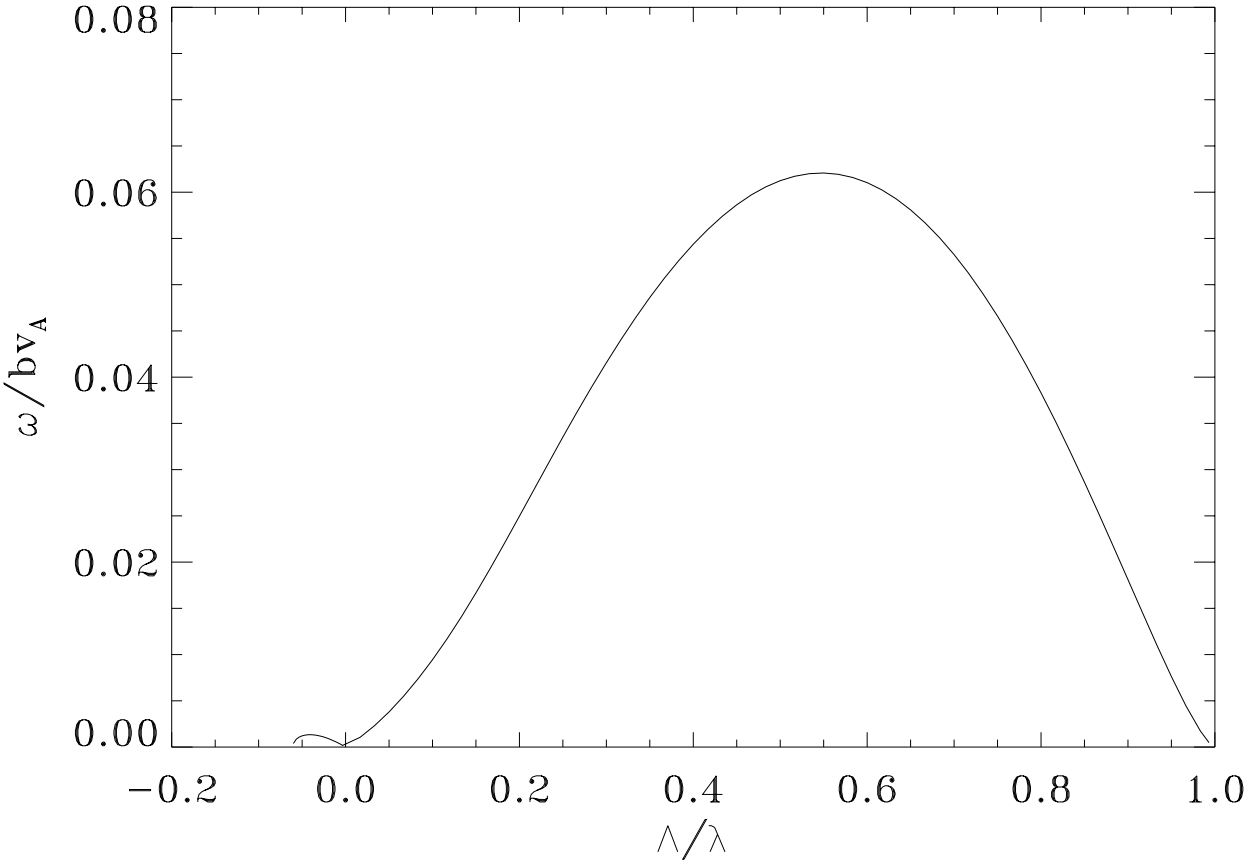

Fig. 4.— Helical kink instability growth rates ω vs. axial wavelength Λ/λ for the Gold-Hoyle equilibrium of infinite axial but finite radial extent of $R = 3\pi/2b$ (from Linton *et al.*, 1998; © AAS. Reproduced with permission). $b = B_\theta/(rB_z)$ is the twist per unit length and v_A is the initial Alfvén velocity at the flux rope axis.

The Astrophysical Journal, 778:99 (12pp), 2013 December 1 doi:10.1088/0004-637X/778/2/99

SIMULATIONS OF EMERGING MAGNETIC FLUX. I. THE FORMATION OF STABLE CORONAL FLUX ROPES

James E. Leake[1], Mark G. Linton[2], and Tibor Török[3]
[1] College of Science, George Mason University, 4400 University Drive, Fairfax, VA 22030, USA; jleake@gmu.edu
[2] US Naval Research Laboratory 4555 Overlook Ave., SW Washington, DC 20375, USA
[3] Predictive Science Inc., 9990 Mesa Rim Rd., Ste. 170, San Diego, CA 92121, USA
Received 2013 July 18; accepted 2013 September 17; published 2013 November 8

ABSTRACT

We present results from three-dimensional visco-resistive magnetohydrodynamic simulations of the emergence of a convection zone magnetic flux tube into a solar atmosphere containing a pre-existing dipole coronal field, which is orientated to minimize reconnection with the emerging field. We observe that the emergence process is capable of producing a coronal flux rope by the transfer of twist from the convection zone, as found in previous simulations. We find that this flux rope is stable, with no evidence of a fast rise, and that its ultimate height in the corona is determined by the strength of the pre-existing dipole field. We also find that although the electric currents in the initial convection zone flux tube are almost perfectly neutralized, the resultant coronal flux rope carries a significant net current. These results suggest that flux tube emergence is capable of creating non-current-neutralized stable flux ropes in the corona, tethered by overlying potential fields, a magnetic configuration that is believed to be the source of coronal mass ejections.

Key words: magnetohydrodynamics (MHD) – Sun: coronal mass ejections (CMEs) – Sun: magnetic fields

Online-only material: color figures

1. INTRODUCTION

Coronal mass ejections (CMEs) are a primary source of space weather and almost all theoretical models of CMEs require the presence or formation of a coronal magnetic flux rope (e.g., Forbes 2000). There exists observational evidence that many CMEs, particularly those originating from quiet Sun regions, are composed of a bright core associated with an erupting prominence and a relatively dark cavity that is associated with a magnetic flux rope (e.g., Gibson & Fan 2006). Moreover, a magnetic flux rope geometry has been fit to coronagraphic observations of propagating CMEs (e.g., Vourlidas et al. 2013). In addition, there is also growing evidence that these flux ropes are formed *before* the eruption. This evidence exists for both quiet Sun regions (Robbrecht et al. 2009; Vourlidas et al. 2013) and active regions (e.g., Green & Kliem 2009; Green et al. 2011; Patsourakos et al. 2013). Although identification of flux rope magnetic geometry is more difficult for active regions than for the quiet Sun due to differences in size and complexity, the existence of active region flux ropes has been supported by recent non-linear force free extrapolations (e.g., Canou & Amari 2010; Guo et al. 2010; Yelles Chaouche et al. 2012).

It has long been postulated that the source of the magnetic field in the corona is a magnetic field in the deep convection zone, created by dynamo action (Parker 1979), and that the process by which this field arrives in the corona is the buoyant rise of twisted flux tubes to the surface and their subsequent emergence. The partial emergence of twisted flux tubes into the solar atmosphere has been extensively studied and a review by Archontis (2008) summarizes the various types of theoretical investigations. Early three-dimensional (3D) simulations found that an emerging sub-surface flux tube does not rise bodily into the corona, but that only the upper portion of the tube emerges, while the tube axis remains near the solar surface (Fan 2001; Magara 2001; Archontis et al. 2004; Murray et al. 2006). More recent simulations found that a new flux rope structure forms in the corona within the partially emerged flux tube and that this flux rope rises slowly in the corona (Manchester et al. 2004; Fan 2009). Archontis & Török (2008) and Archontis & Hood (2012) demonstrated that the rise of the flux rope came to a halt, due to the stabilizing magnetic tension of the surrounding (envelope) flux tube field. Fan (2009) associated the coronal flux rope formation mechanism with the transfer of twist from the convection zone, while Manchester et al. (2004) suggested that the mechanism is due to the reconnection of sheared magnetic fields. By imposing a pre-existing strong horizontal field in the corona, Archontis et al. (2006) found that reconnection between the emerging flux tube and the coronal field can create horizontal jets and plasmoids at relatively low heights in the corona. Later simulations also found that favorably orientated and sufficiently weak horizontal fields can remove part of the envelope field constraining the newly formed flux rope, allowing a strong upward acceleration of the rope resembling eruptive behavior (Archontis & Török 2008; Archontis & Hood 2012).

In this paper, we focus on the formation of stable coronal flux ropes as a result of flux emergence. Creating such configurations is an important step in improving initial equilibrium magnetic field configurations for models of CMEs. A primary example of a pre-eruption configuration is the flux rope model of Titov & Démoulin (1999, hereafter the TD model), in which a coronal flux rope is confined by an overlying potential field. This model has been successfully applied as the initial condition of a number of CME simulations (Roussev et al. 2003; Török & Kliem 2005; Manchester et al. 2008). A specific property of the TD model is that the coronal flux rope carries a net current, since there is no return current in the configuration (see Török et al. 2013 for a detailed discussion of return currents in active regions).

Our aim in this paper is to use numerical magnetohydrodynamic (MHD) simulations to investigate how flux emergence from the convection zone into the solar atmosphere can create a stable coronal flux rope with a net current that is confined by an overlying magnetic field. To do this, we model the partial emergence of a buoyant convection zone twisted flux tube into a pre-existing dipole coronal magnetic field, the strength of which

we vary. The coronal dipole field is intended to represent the remnant field of an old, dispersed active region, into which a new magnetic field emerges. This simulation of flux emergence into a pre-existing dipole follows a paradigm similar to that of the simulation presented in MacTaggart (2011). That study focused on reconnection between the emerging field and the pre-existing field in the corona, whereas in this study we focus on the formation and stability of a coronal flux rope formed within the emerging field. In addition, for reference, we also model flux emergence into a field-free corona, to compare with the simulations of Archontis & Hood (2012) and Manchester et al. (2004).

In Section 2, the model is described. The results are presented in Section 3 and the consequences of these simulations for the theory of coronal flux rope formation and CME initiation are discussed in Section 4.

2. NUMERICAL METHOD

2.1. Equations

The evolution of a magnetic field in a plasma domain that includes the upper layers of the solar convection zone plus a photosphere/chromosphere, transition region, and corona is modeled using the visco-resistive MHD Lagrangian-remap code Lare3D (Arber et al. 2001). The equations solved by Lare3D are presented here in Lagrangian form:

$$\frac{D\rho}{Dt} = -\rho\nabla\cdot\mathbf{v}, \tag{1}$$

$$\frac{D\mathbf{v}}{Dt} = -\frac{1}{\rho}\left[\nabla P + \mathbf{j}\times\mathbf{B} + \rho\mathbf{g} + \nabla\cdot\mathcal{S}\right], \tag{2}$$

$$\frac{D\mathbf{B}}{Dt} = (\mathbf{B}\cdot\nabla)\mathbf{v} - \mathbf{B}(\nabla\cdot\mathbf{v}) - \nabla\wedge(\eta\mathbf{j}), \tag{3}$$

$$\frac{D\epsilon}{Dt} = \frac{1}{\rho}\Big[-P\nabla\cdot\mathbf{v} + \varsigma_{ij}\mathcal{S}_{ij} + \eta j^2\Big]. \tag{4}$$

Here, ρ is the mass density, $\mathbf{v}$ is the velocity, $\mathbf{B}$ is the magnetic field, and ϵ is the specific energy density. The current density is given by $\mathbf{j} = \nabla\times\mathbf{B}/\mu_0$, where μ_0 is the permeability of free space and the resistivity $\eta = 14.6\,\Omega$m. The gravitational acceleration is denoted by $\mathbf{g}$ and is set to the gravity at the mean solar surface ($\mathbf{g}_{\rm sun} = -274\,{\rm m\,s^{-2}}\hat{\mathbf{z}}$). $\mathcal{S}$ is the stress tensor that has components $\mathcal{S}_{ij} = \nu(\varsigma_{ij} - (1/3)\delta_{ij}\nabla\cdot\mathbf{v})$, with $\varsigma_{ij} = (1/2)((\partial v_i/\partial x_j) + (\partial v_j/\partial x_i))$. The viscosity ν is set to $3.35\times10^3\,{\rm kg\,m^{-1}\,s^{-1}}$ and δ_{ij} is the Kronecker delta function. Assuming an ideal gas law, the gas pressure, P, and the specific internal energy density, ϵ, are

$$P = \rho k_B T/\mu_m, \tag{5}$$

$$\epsilon = \frac{k_B T}{\mu_m(\gamma-1)}, \tag{6}$$

respectively, where k_B is Boltzmann's constant and γ is 5/3. The reduced mass, μ_m, is given by $\mu_m = m_f m_p$, where m_p is the mass of a proton and $m_f = 1.25$ is a pre-factor designed to include the effect of elements heavier than hydrogen. In this study, as in many previous simulations of flux emergence, we assume that the plasma is fully ionized and so the reduced mass is spatially independent. In the partially ionized plasma of the Sun, the reduced mass changes as the ionization changes, as discussed in Leake & Linton (2013). In this study, however, we use the average value of $\mu_m = m_f m_p$, which was shown in Leake & Linton (2013) to give the best constant-μ_m match to one-dimensional (1D) models of the solar atmosphere that include partial ionization effects (e.g., Vernazza et al. 1981; Fontenla et al. 2006). The plasma variables ϵ and ρ are defined at cell centers. The magnetic field is defined at cell faces and the velocity is defined at cell vertices. The staggered grid preserves $\nabla\cdot\mathbf{B}$ during the simulation.

2.2. Normalization

The equations are non-dimensionalized by dividing each variable (C) by its normalizing value (C_0). The set of equations requires a choice of three normalizing values. We choose normalizing values for the length ($L_0 = 1.7\times10^5$ m), magnetic field ($B_0 = 0.12$ T), and gravitational acceleration ($g_0 = g_{\rm sun} = 274\,{\rm m\,s^{-2}}$). From these values, the normalizing values for the gas pressure ($P_0 = B_0^2/\mu_0 = 1.14\times10^4$ Pa), density ($\rho_0 = B_0^2/(\mu_0 L_0 g_0) = 2.46\times10^{-4}\,{\rm kg\,m^{-3}}$), velocity ($v_0 = \sqrt{L_0 g_0} = 6.82\times10^3\,{\rm m\,s^{-1}}$), time ($t_0 = \sqrt{L_0/g_0}$ =24.9 s), temperature ($T_0 = m_p L_0 g_0/k_B = 5.64\times10^3$ K), current density ($j_0 = B_0/(\mu_0 L_0) = 0.56\,{\rm Am^2}$), viscosity ($\nu_0 = B_0^2\sqrt{L_0/g_0}/\mu_0 = 2.85\times10^5\,{\rm kg\,m^{-2}\,s^{-1}}$), and resistivity ($\eta_0 = \mu_0 L_0^{3/2} g_0^{1/2} = 1.46\times10^3\,\Omega$m) can be derived. With these values of normalization and the values of ν and η given above, the Reynolds number $R_e = (\rho_0 L_0 v_0)/\nu$ and magnetic Reynolds number $R_m = (\mu_0 L_0 v_0)/\eta$ in this simulation are both 100. The value of resistivity used in this simulation ($0.01\eta_0 = 14.6\,\Omega$m), although comparable to upper estimates of the resistivity in the lower chromosphere, is much larger than typical values in the corona. We use this large value to ensure that the explicit resistivity is larger than the numerical value for the scheme used in regions where electric current densities build up. The normalized numerical resistivity is $\hat{v}_A\hat{\Delta}_x^2/\hat{L}$, where $\hat{\Delta}_x$ is the normalized grid size, $\hat{v}_A$ is the normalized local Alfvén speed, and $\hat{L}$ is a typical normalized length scale over which the magnetic field varies (Arber et al. 2007). In regions of increased current density, we find $\hat{\Delta}_x = 0.66$, $\hat{v}_A = 0.05$, and $\hat{L} = 5$, which give a value for the normalized numerical resistivity of $\eta/\eta_0 = 0.0044$.

2.3. Numerical Domain

The simulations use an irregular Cartesian grid with 304 cells in each direction. In the vertical direction, z, the grid extends from $-30\,L_0$ to $210.45\,L_0$ with a resolution of $0.428\,L_0$ at the bottom boundary and $1.99\,L_0$ at the top boundary. In the horizontal directions, x and y, the grid is centered on 0 and has side boundaries at $\pm126.85\,L_0$. The resolution at $x = y = 0$ is $0.658\,L_0$ and the resolution at the side boundaries is $2.61\,L_0$. This irregular grid has the following form:

$$x, y = \pm\left[(1+f_h)\chi_h + f_h w\ln\left(\frac{\cosh(\frac{\chi_h - L_h}{w})}{\cosh(\frac{-L_h}{w})}\right)\right] \tag{7}$$

$$z = -30\,L_0 + \left[(1+f_v)\chi_v + f_v w\ln\left(\frac{\cosh(\frac{\chi_v - L_v}{w})}{\cosh(\frac{-L_v}{w})}\right)\right], \tag{8}$$

where $\chi_h = [0, 1, 2..., 152]100\,L_0/152$, $\chi_v = [0, 1, 2, ..., 304]$ $130\,L_0/304$, $f_h = 2.1$, $f_v = 1.83$, $L_h = 95\,L_0$, $L_v = 100\,L_0$,

and $w = 10\,L_0$. We also perform one additional simulation (called ND1), which has a higher top boundary at $270\,L_0$, with $f_v = 2.83$.

At the boundaries, all components of the velocity and the gradients of magnetic field, gas density, and specific energy density are set to zero. The resistivity is smoothly decreased to zero close to the side boundary to reduce the diffusion of the magnetic field at the boundary to its numerical value and ensure line-tied boundary conditions as much as possible:

$$\eta = 0.01\left[\tanh(-\frac{(r_\eta - L_\eta)}{w_\eta}) + 1\right]\frac{\eta_0}{2}, \quad (9)$$

where $r_\eta = \sqrt{x^2 + y^2}$, $L_\eta = 100\,L_0$, and $w_\eta = 5\,L_0$. In addition, a damping region is applied to the velocity at all four side boundaries and the top boundary. For a given coordinate ($\kappa = x, y, z$), the velocity Equation (2) has an additional term when $|\kappa| > \kappa_d$:

$$\frac{D\mathbf{v}}{Dt} = -\frac{1}{\rho}\left[\nabla P + \mathbf{j}\wedge\mathbf{B} + \rho\mathbf{g} + \nabla\cdot\mathcal{S}\right] - N\mathbf{v}, \quad (10)$$

with $x_d = y_d = 96\,L_0$ and $z_d = 170\,L_0$ (simulation ND1 has $z_{d1} = 254\,L_0$). The parameter N is designed to increase linearly from 0 at κ_d to 1 at the boundary: $N = (|\kappa| - \kappa_d)/(\max|\kappa| - \kappa_d)$. This approach is used to prevent any reflected waves from interfering with the solution in the interior.

2.4. Initial Conditions

The initial conditions consist of a hydrostatic background atmosphere that represents the upper solar convection zone ($-30\,L_0 \leqslant z < 0$), the photosphere/chromosphere ($0 \leqslant z < 10\,L_0$), the transition region ($10\,L_0 \leqslant z < 20\,L_0$), and the corona ($20\,L_0 \leqslant z$). The transition region in this model is thicker than a typical width derived from semi-implicit models of the Sun, which compare the observed spectrum of the Sun with radiative transfer calculations (e.g., Fontenla et al. 2006). In those studies, the typical width is about 0.1 Mm ($\approx L_0$). As in previous simulations of flux emergence (see the review by Archontis 2008), we use a thicker transition region of 1.7 Mm. This artificial increase of the transition region is required to resolve the large changes in density and temperature that occur across this region for the given spatial resolution that is limited by the large total simulation domain and computational costs. A magnetic field is imposed on this background atmosphere. This field consists of a background dipole field that permeates the entire domain and a localized twisted flux tube in the model convection zone. The flux tube's pressure and density are perturbed to initiate its buoyant rise into the model solar atmosphere. The initial conditions are shown in Figures 1 and 2.

The initial hydrostatic atmosphere is created by first defining the temperature:

$$\frac{dT}{dz} = a\left(\frac{dT}{dz}\right)_{\rm ad} = -\frac{\gamma - 1}{\gamma}\frac{T_0}{L_0}, \quad z \leqslant 0, \quad (11)$$

$$T(z) = T_{\rm ph}, \quad 0 < z < 10\,L_0, \quad (12)$$

$$T(z) = T_{\rm cor}^{(z-10\,L_0)/10\,L_0}, \quad 10\,L_0 \leqslant z < 20\,L_0, \quad (13)$$

$$T(z) = T_{\rm cor}, \quad z \geqslant 20\,L_0, \quad (14)$$

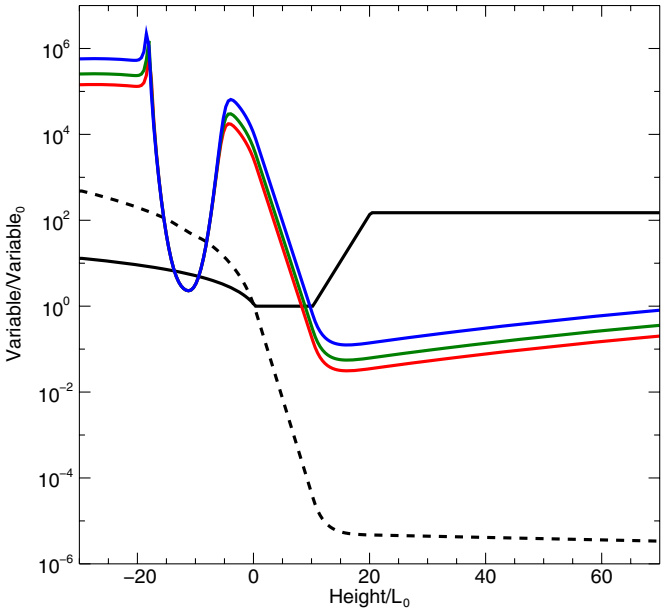

Figure 1. Initial 1D configuration (along $x = y = 0$) for part of the vertical domain. The ordinate represents normalized plasma variables (C/C_0 for a given variable C) and the abscissa represents height. The black solid line shows the temperature. The black dashed line shows gas pressure P. The red, green, and blue lines show the plasma β for the three simulations SD, MD, and WD, respectively. These three simulations have decreasing dipole field strengths.

(A color version of this figure is available in the online journal.)

where $T_{\rm ph} = T_0$ and $T_{\rm cor} = 150\,T_0$. The pre-factor $a = 1$ in Equation (11) ensures that the model convection zone is marginally stable to convective instability by setting the temperature gradient to its adiabatic value $dT/dz = (dT/dz)_{\rm ad}$ (Stix 2004). The gas density profile is then obtained by solving the hydrostatic equilibrium equation $\partial P/\partial z = -\rho g$ and using the ideal gas law and the condition that $\rho(z = 0) = \rho_0$.

The dipole field is translationally invariant along y, the tube's axial direction, and is given by $\mathbf{B} = \nabla\times\mathbf{A}$, where $\mathbf{A} = A_y\mathbf{e}_y$ and

$$A_y(x, z) = B_d\frac{z - z_d}{r_1^3}, \quad (15)$$

with $r_1 = \sqrt{x^2 + (z - z_d)^2}$ being the distance from the source. We choose z_d to be $-100\,L_0$ so that the initial sub-surface flux tube is far from the source of the dipole field. To cover various dipole strengths, we perform three simulations, each with a different value of B_d. Simulations SD (strong dipole), MD (medium dipole), and WD (weak dipole) have values $B_d = [10, 7.5, 5]\times 10^3 B_{d0}$, where $B_{d0} = B_0\,{L_0}^2 = 3.76\times 10^9\,{\rm Tm}^2$, respectively. This gives a maximum magnetic field strength at the surface ($z = 0$) of $[2.6, 1.95, 1.3]\times 10^{-3}$ T, respectively. These choices of dipole strength allow for a range in the plasma β profile, as shown in Figure 1, where $\beta = P/(|\mathbf{B}|^2/\mu_0)$. These profiles are consistent with the models of β in the solar atmosphere developed by Gary & Alexander (1999) and Gary (2001). Simulations no dipole (ND) and ND1 have no pre-existing dipole field.

A right-hand twisted magnetic flux tube is inserted at $x = 0$, $z = z_t = -12\,L_0$, aligned along the y axis, and is given by

$$B_y = B_t e^{-r^2/R^2}, \quad (16)$$

$$B_\theta = qrB_y, \quad (17)$$

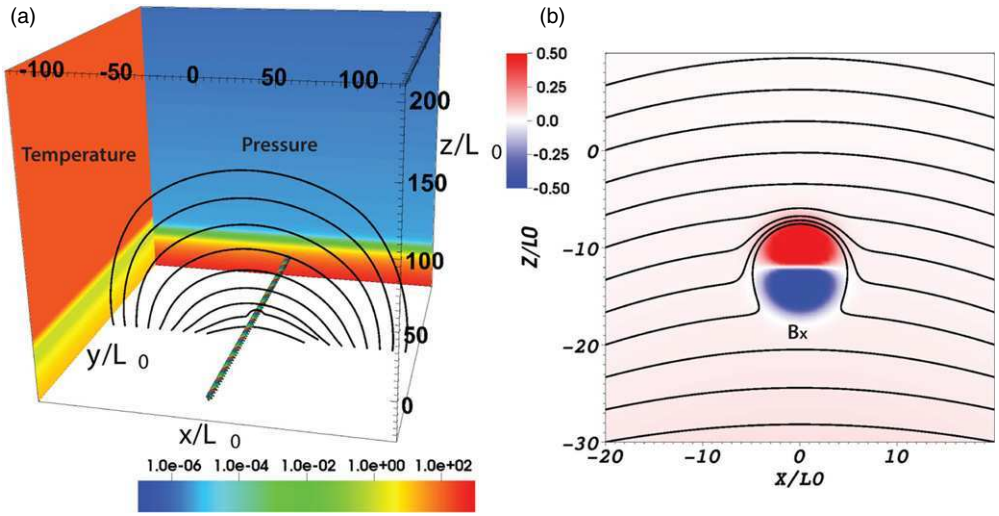

Figure 2. Initial 3D configuration for simulation SD. Panel (a) shows the initial sub-surface flux tube and the dipole field, represented by the black field lines that originate from a line along $y = 0$ on the bottom boundary. Panel (b) shows a magnified slice of the horizontal field B_x in the $y = 0$ plane as a color shading and a projection onto the $y = 0$ plane of the field lines of the dipole.

(A color version of this figure is available in the online journal.)

where $r = \sqrt{(x^2 + (z - z_t)^2)}$. The width of the tube is $R = 2.5\,L_0$ and the strength at $r = 0$ is $B_t = 5B_0$. The twist parameter is $q = 1/R$. Figure 2 shows some selected magnetic field lines from the initial configuration. The superposition of the flux tube and the dipole field is shown in Figure 2 (panel (b)). The conventional wisdom of active region formation is that large-scale Ω-shaped flux tubes, which are anchored well below the visible surface, extend through the surface and into the corona. Hence, the initial flux tube used here, which is initially horizontal and line tied at the side boundaries, is not a very realistic initial condition. However, by perturbing the density in the initial flux tube in a certain way, an Ω-shaped tube can be created. The convection zone flux tube is made buoyant at the center $y = 0$ and is neutrally buoyant at its ends at the y boundaries. This is done by perturbing the background density $\rho_0(z)$ and background specific energy density $\epsilon_0(z)$ to

$$\rho(r, z) = \rho_0(z)\left(1 + \frac{p_1(r)}{p_0(z)} e^{-\frac{y^2}{\lambda}}\right) \quad \text{and} \tag{18}$$

$$\epsilon(r, z) = \frac{(p_0(z) + p_1(r))}{\rho(\gamma - 1)}, \tag{19}$$

where $\lambda = 10\,L_0$, $p_0(z)$ is the original pressure profile, and $p_1(r)$ is determined by solving $\nabla p_1(r) = \mathbf{j} \times \mathbf{B}(r)$ for the flux tube's field. As will be shown later, this creates sub-photospheric "legs" of the emerging tube that have a significant vertical component. To optimize the confining effect of the dipole field, the direction of the dipole field is chosen so that it is aligned with the field lines in the top edge of the flux tube, i.e., $B_{x,\mathrm{dip}} > 0$.

It is worth making a point here regarding the use of the phrases "flux tube" and "flux rope." In previous studies of flux emergence, "flux tube" has been used to describe the sub-surface initial magnetic field configuration and "flux rope" has been used to describe the presence of a collection of field lines wrapped around a central field line we designate as the axis. In that sense, the original sub-surface flux tube is also a flux rope. In this paper, we adopt the previously accepted practice of calling the original sub-surface field configuration a "flux tube" and the twisted coronal structure that is formed during the emergence process a "flux rope."

3. RESULTS

3.1. Partial Emergence of a Sub-surface Flux Tube

The partial emergence of a sub-surface flux tube into the solar atmosphere has been studied and commented upon in a number of previous studies (Fan 2001; Archontis et al. 2004; Manchester et al. 2004; Murray & Hood 2008; MacTaggart & Hood 2009) and we direct the reader to those studies for a more detailed description. The salient points are these: the flux tube rises buoyantly until it reaches the convectively stable photosphere/chromosphere, where it temporarily halts and undergoes a large amount of horizontal expansion. Then, the upper portions of the deformed tube emerge via the magnetic buoyancy instability (Acheson 1979) through the photosphere/chromosphere, transition region, and into the corona.

The emergence through the surface of the rising flux tube in simulation SD is shown in Figure 3. Note that the boundary conditions employed here allow the same field lines to be tracked throughout the simulation to a good approximation by using the same seed point on the side ($y = \pm \max(y)$) boundary. Unless stated otherwise, the same field lines are drawn for each panel in a given figure. The black line in Figure 3 is the field line that intersects the side ($y = \pm \max y$) boundaries at the location of the original convection zone tube axis (note that at this early stage this is one single field line).

As shown in Figure 3, panel (a), the upper field lines of the flux tube at $t = 35\,t_0$ have penetrated the surface ($z = 0$) from below. These field lines have a high tilt relative to the axis of the tube (the y axis) and they create a bipolar structure on the surface with a neutral line parallel to the axis of the tube. As time progresses, field lines emerge with less tilt, i.e., more aligned with the axis of the flux tube. This creates an apparent shearing of the bipole, as shown in Figure 3, panels (e) and (f), and the two polarity regions drift apart. This behavior is representative of the observed evolution of emerging active regions (Luoni et al. 2011). The emerging field pushes the pre-existing dipole field both vertically and horizontally. These upper field lines of the flux tube are nearly parallel to the pre-existing dipole field and so this minimizes the amount of reconnection between the two flux systems.

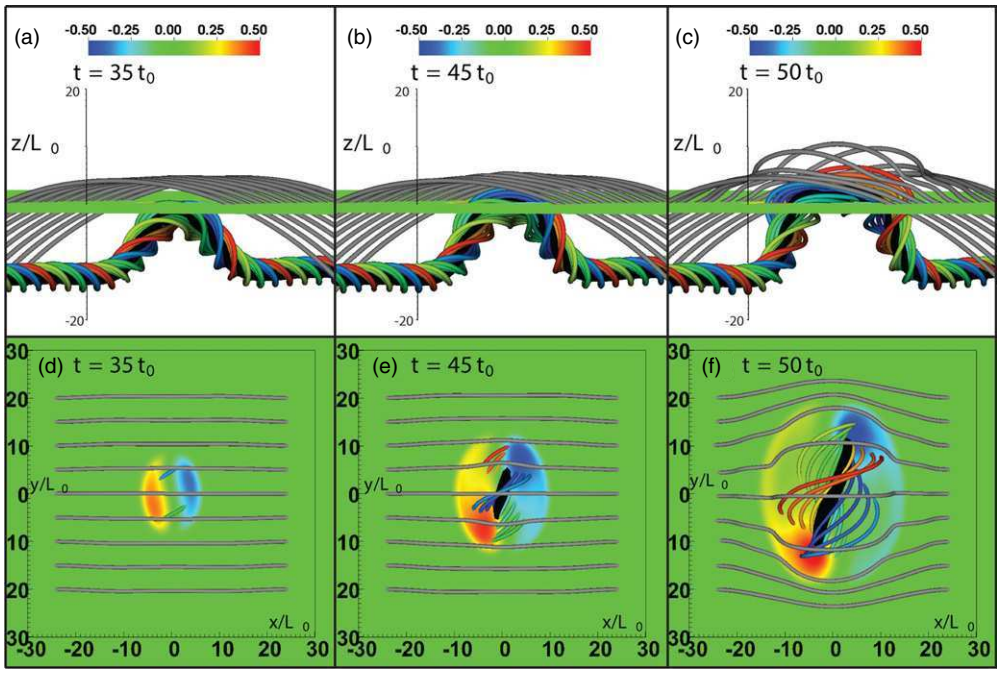

Figure 3. Early emergence of a convection zone magnetic flux tube into the solar atmosphere for simulation SD at times $35\,t_0$ (panels (a) and (d)), $45\,t_0$ (panels (b) and (e)), and $50\,t_0$ (panels (c) and (f)). The black line originates from the location of the original flux tube axis on the side ($y = \pm \max y$) boundaries. The colored lines originate from a circle on both the side boundaries centered on this axis. The gray lines originate at the lower boundary and belong to the dipole field. The color shading slice shows the vertical magnetic field B_z at the surface ($z = 0$). This figure illustrates that the apparent shearing of the bipolar structure is associated with the emergence of the flux tube's axis and the magnetic field that is more aligned with this axis.

(A color version of this figure is available in the online journal.)

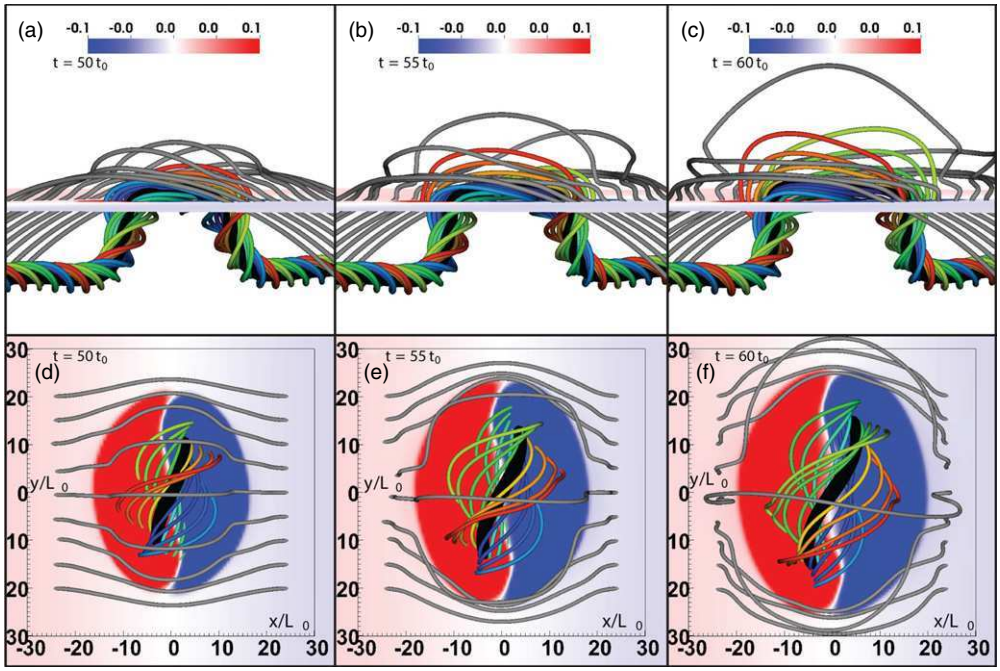

Figure 4. Partial emergence of the convection zone flux tube for simulation SD at times $50\,t_0$ (panels (a) and (d)), $55\,t_0$ (panels (b) and (e)), and $60\,t_0$ (panels (c) and (f)). The field lines shown are the same as in Figure 3. The color shading of the vertical magnetic field at the surface has been saturated to highlight the neutral line (which is located in white regions between red and blue regions). Above the flux tube axis (black line), the field lines are concave down and are able to drain mass and continue to rise. Below the axis, the field lines are concave up and are unable to drain mass and hence remain near the surface. Consequentially, only the upper part of the flux tube emerges into the corona.

(A color version of this figure is available in the online journal.)

Figure 4 shows the same field lines at later times, but with the color shading of B_z at the surface now saturated to highlight the neutral line (which appears white between red and blue). The sections of the field lines that cross above the axis of the flux tube (black line) are concave down. These sections of field lines are able to rise further as they drain mass. Beneath the emerged axis field line, the sections of the field lines are concave up. These sections carry mass that cannot be drained and are

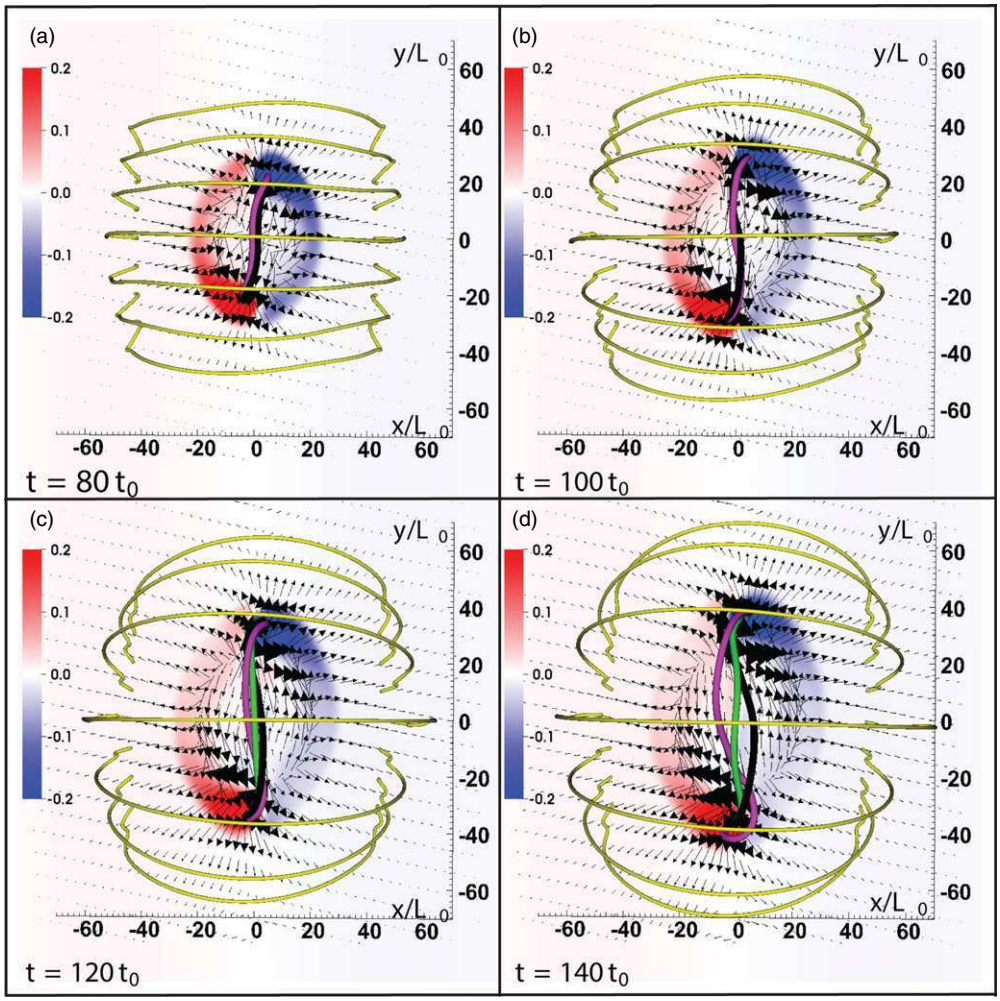

Figure 5. Rotation of sunspots and the formation of a coronal flux rope at times $t = 80$, 100, 120, and 140 t_0. The color shading shows the vertical component of the magnetic field in the $z = 0$ plane. The arrows represent horizontal velocities perpendicular to the magnetic field in the $z = 0$ plane and are scaled by magnitude. The black and purple field lines originate at $\pm \max y$, respectively, at the intersection of the original convection zone tube axis and the side boundaries. The yellow lines originate at the lower boundary and belong to the dipole field. The velocity vectors show a strong shearing component, but also suggest a rotational motion near the center of each polarity region. A new flux rope axis can be defined at the location of the O-point in the $y = 0$ plane when the black and purple field lines separate. This new axis field line is shown as the green field line.

(A color version of this figure is available in the online journal.)

therefore unable to rise further into the atmosphere, as originally found in the simulations of Fan (2001) and Manchester et al. (2004). As a result, the original flux tube emerges only partially: the sections of the field that are concave down can expand into the corona, while the sections beneath the axis that are concave up remain trapped near the surface. At $t = 60\,t_0$, the original flux tube axis has emerged to 3 L_0 above the surface and there is an O-point above the surface in the $y = 0$ plane that this axis goes through. Previous authors have reported on the location of the original flux tube axis and found that for similar flux tube parameters as those used in this paper, the flux tube axis remains close to or below the surface, typically less than 3 L_0 above the surface (Magara 2001; Murray et al. 2006; Fan 2001). However, these simulations do not explore the later evolution of the flux tube axis. As we shall show, the original axis of the convection zone flux tube splits into two new field lines and these new field lines twist around a new coronal flux rope axis.

3.2. Formation of a Coronal Flux Rope

Figures 5 and 6 show the active region for simulation SD at times [80, 100, 120, 140] t_0. The color shading shows the vertical component of the magnetic field in the $z = 0$ plane. Figure 5 also shows the horizontal velocities perpendicular to the magnetic field on the $z = 0$ plane as vectors, which excludes flows caused merely by plasma draining along field lines. Also shown in Figures 5 and 6 are selected field lines. The yellow field lines are the dipole field and originate at the lower boundary. The black and purple field lines are line tied at and originate from, the $y = \pm \max y$ boundaries, respectively, at the location of the original flux tube axis. These two field lines are coincident early in the simulation and pass through the O-point located in the $y = 0$ plane just above the surface as the original flux tube partially emerges. As can be seen in Figures 5 and 6, these two field lines, which were once the same, separate (perhaps due to magnetic diffusion) and appear to twist about each other as time progresses. They also rise higher into the corona as they do so.

It should be noted that due to a non-zero value of resistivity, the tracking of field lines cannot be exact (even with zero resistivity, there is some numerical diffusion to the scheme used to solve the induction equation). We have performed an additional simulation with ideal $\eta = 0$ and found that this splitting of the original axis field line also occurs, which suggests it may be independent of the choice of resistivity used.

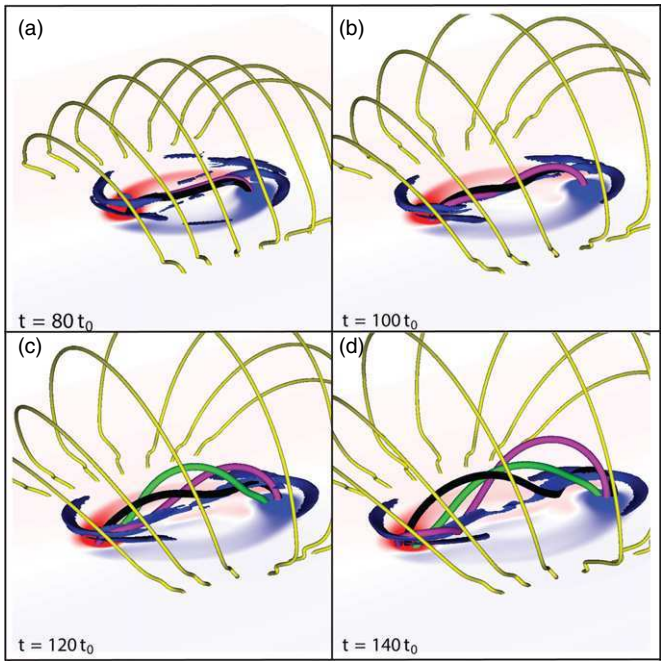

Figure 6. Same as Figure 5 but from a different viewpoint. In addition, blue iso-surfaces of $j \geqslant 0.035\, j_0$ are plotted for $z \geqslant 5\, L_0$.

(A color version of this figure is available in the online journal.)

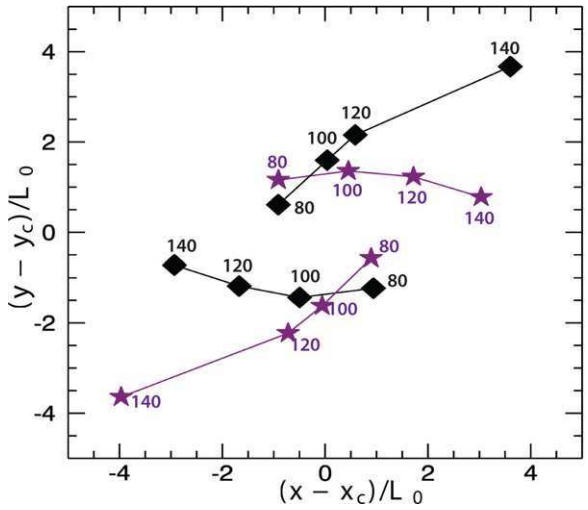

Figure 7. (x, y) locations of the intersection of the two axial field lines (black and purple field lines in Figure 5) with the surface ($z = 0$), at different times (t/t_0) in simulation SD. The black diamonds are for the black field line and the purple stars are for the purple field line. The locations are taken relative to the center of the polarity region, which is defined as the (x, y) location where the field line that goes through the central O-point in the corona (the green line in Figure 5) intersects the surface. The results from both polarity regions are superimposed to make one plot. Hence, the points in the top half ($y - y_c > 0$) are from the intersection of the black and purple field lines with the surface in the polarity region in the $y > 0$ domain and the points in the bottom half are from the polarity region in the $y < 0$ domain.

(A color version of this figure is available in the online journal.)

Figure 7 shows the (x, y) locations of the intersection of the two former axial field lines with the surface ($z = 0$) at different times in simulation SD. The black diamonds (purple stars) represent locations for the black (purple) field line in Figure 5. The locations are taken relative to the center of the polarity region, which we define as the (x, y) location where the field line that goes through the central O-point in the corona (the green line in Figure 5) intersects the surface. The results from both active regions are superimposed onto one single plot. Figure 7 shows a partial rotational motion of these locations around the center of each polarity region, with the same sign of rotation for each polarity region. A rotational motion is also suggested from the vectors of horizontal velocity perpendicular to the magnetic field in Figure 5. These motions reflect the transport of twist from the convection zone into the corona (see below). Since the green field line in Figure 5 passes through the O-point without exhibiting significant writhe, it can be considered as a good approximation of the axis of the successively forming coronal flux rope.

Previous simulations have suggested two different mechanisms for the formation of a coronal flux rope during magnetic flux emergence. Magara (2006) and Fan (2009) suggested that rotational motions, brought about by an equilibration of twist along emerging field lines, can twist up the coronal sections of field lines to create a new flux rope. On the other hand, Manchester et al. (2004), Archontis & Török (2008), and Archontis & Hood (2012) suggested that the reconnection of emerged sections of sheared field lines can create twisted field lines, resulting in a flux rope structure in the corona. We now briefly discuss these two mechanisms.

Figure 8 shows simulation SD at times $t = 50\, t_0$, $t = 100\, t_0$, and $t = 200\, t_0$. To give a sense of the local twist per unit length, the field lines are colored with the quantity $\alpha L_0 = \mu_0 L_0 \mathbf{j}\cdot\mathbf{B}/|\mathbf{B}|^2$. As the upper part of the flux tube emerges into the atmosphere, the field lines expand into the low-β atmosphere, increasing their length. As α is related to the twist per unit length and the tube expands faster than the twist propagates upward, this creates a gradient in α along the expanding field line. Such a gradient was also observed in the simulations of Fan (2009) and discussed in Longcope & Welsch (2000). A gradient in twist along a section of a flux tube will drive torsional Alfvén waves that equilibrate this twist. Figure 9 shows the quantity α at times $t = 100\, t_0$ and $t = 200\, t_0$ as a function of height along a portion of the purple field line from Figures 5 and 6 as it penetrates the surface and passes into the corona. The magnitude of the gradient of α around $z = 0$ clearly decreases with time, indicating that the twist is equilibrating along this section of the flux tube. Magara (2006) and Fan (2009) suggested that the torsional motions brought about by this process are capable of causing sunspot rotation that twists up the magnetic field in the corona. This idea is also supported by recent observations of the formation of active regions that suggest that sunspot rotation can be attributed to the emergence of twisted magnetic fields (Kumar et al. 2013).

It has also been suggested that magnetic reconnection is responsible for the formation of coronal flux ropes, by a process similar to what has been suggested based on observations of photospheric flux cancellation (van Ballegooijen & Martens 1989). In flux emergence simulations, the reconnection is driven by a combination of shearing flows, caused by Lorentz forces in the expanding field and inflows caused by pressure gradients (Manchester et al. 2004; Archontis & Török 2008; Archontis & Hood 2012). However, we see no direct evidence of magnetic reconnection, such as an X-point, outflow jets, or curved reconnecting field, underneath the flux rope axis in the simulations described in this paper. This may be due to the combined effects of (1) the limited expansion of the emerging field in the corona due to the presence of the dipole field (which may suppress the amplification of reconnection below the flux rope to a level at which it does not produce noticeable outflow

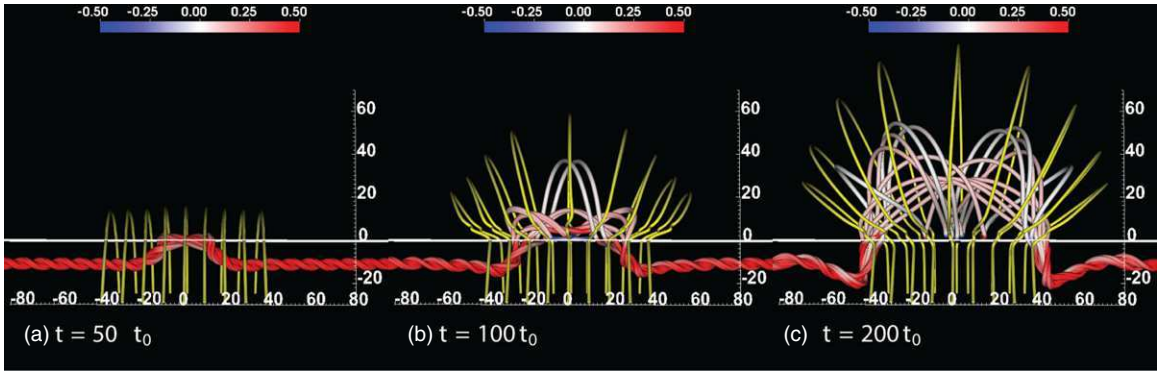

Figure 8. Twist along field lines at times $t = 50\,t_0$, $t = 100\,t_0$, and $t = 200\,t_0$ for simulation SD. Red–white–blue field lines are colored with $\alpha\,L_0 = \mu_0\,L_0\mathbf{j}\cdot\mathbf{B}/|\mathbf{B}|^2$ and originate from both side ($y = \pm \min y$) boundaries. The solid yellow field lines originate at the base of the domain and belong to the magnetic dipole field. This figure demonstrates how the emergence of field into the corona causes a gradient in twist along a field line as it goes from the convection zone into the corona.
(A color version of this figure is available in the online journal.)

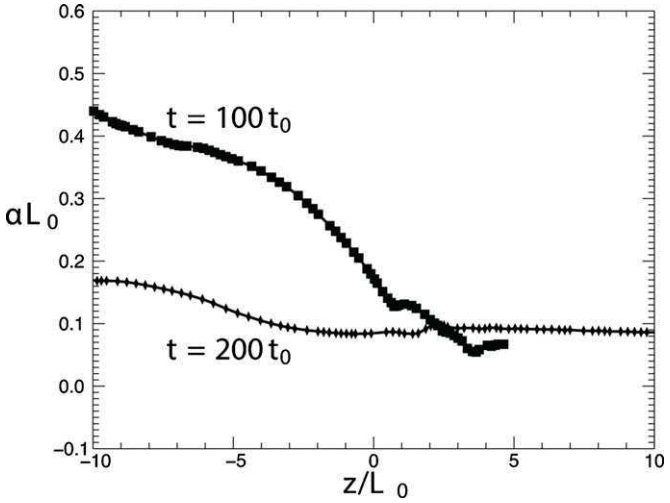

Figure 9. αL_0 as a function of z along a field line at two different times in the simulation SD, $t = 100\,t_0$ and $t = 200\,t_0$. The field line is the same for both times and originates at the location of the original convection zone flux tube axis on the $y = \min y$ boundary (the purple field line in Figures 5 and 6). After $t = 80\,t_0$, this field line splits from the axis of the flux tube and expands into the corona. A decrease in the gradient in α between $z = -5\,L_0$ and $z = 0$ can be seen from time $100\,t_0$ to $200\,t_0$. The original value of α along this field line at $t = 0$ is $0.76/L_0$.

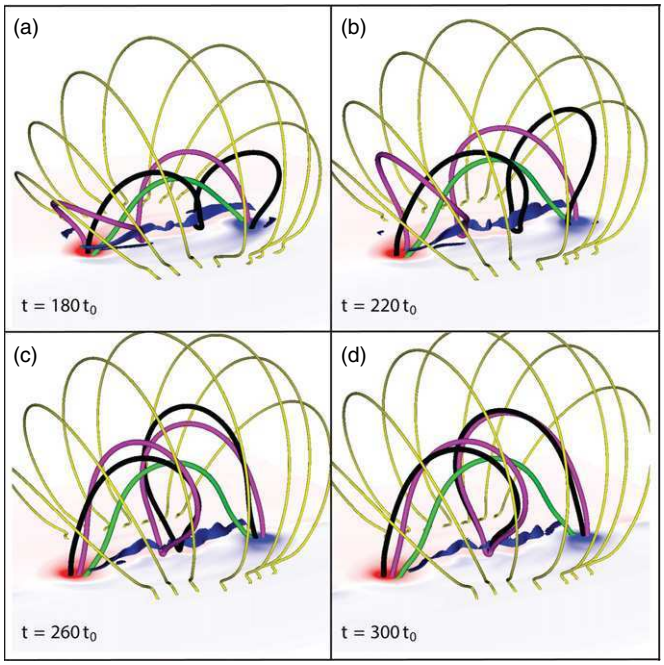

Figure 10. Same as Figure 6 but later in time.
(A color version of this figure is available in the online journal.)

velocities) and (2) the relatively high resistivity used here, which may suppress the build up of a steep current layer. We also see no direct evidence for reconnection in the simulation with $\eta = 0$, which suggests that the confinement by the dipole field in our simulations, rather than the relatively high resistivity, is the reason that magnetic reconnection beneath the flux rope axis is suppressed. We conclude that the formation process in our simulations is primarily due to the rotation of the polarity regions and the twisting of the field.

Figure 6 also shows an iso-surface of current density above $0.03\,j_0$ in the region above $z = 5\,L_0$ to highlight the current distribution below the flux rope. At $t = 80\,t_0$, the current density is larger above the two regions of concentrated opposite polarity vertical magnetic field than above the center of the bipolar region. After $t = 80\,t_0$, there is an increase in current density in the center. The predominant shape of the current sheet when viewed from above is of two distorted J-shapes that merge later to form one S-shape, a process that has been reported in previous flux emergence simulations (Fan 2009; Archontis & Hood 2012). Recent extreme ultraviolet observations of active regions have shown that high temperature (6 MK), J-shaped loops exist before the formation of coronal flux ropes (Liu et al. 2010) and that these J-structures combine to form a single S-shaped structure when the flux rope is formed (e.g., McKenzie & Canfield 2008; Aulanier et al. 2010). Such S-shaped sigmoid structures have been observed as precursors to CMEs (Sterling 2000).

Figure 10 shows the later evolution of simulation SD. The rotation of the two opposite polarity regions decreases after $t = 180\,t_0$, but there is still significant twisting of the field lines that extend into the corona. The field lines that defined the original convection zone flux tube's axis (black and purple) both wrap around the new flux rope axis in the corona. They also have a pinched U-shape at the center of the active region, which creates the strong current sheet structure.

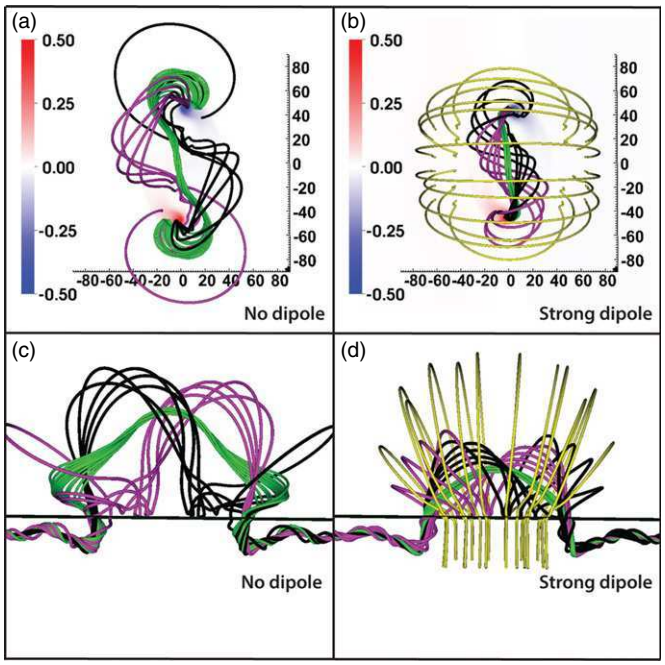

Figure 11. Comparison of flux rope evolution for simulations without an overlying dipole (simulation ND—panels (a) and (c)) and with an overlying dipole (simulation SD—panels (b) and (d)), at time $t = 360\,t_0$. The black lines originate from the $y = \max y$ boundary around the original convection zone flux tube axis and the purple lines originate from the same points on the $y = \min y$ boundary. The green lines originate close to the new coronal flux rope axis in the $y = 0$ plane. The yellow lines in panels (b) and (d) belong to the dipole field.

(A color version of this figure is available in the online journal.)

3.3. Confinement by the Overlying Field

Figure 11 compares the simulation with ND and the simulation with the strongest dipole (SD) at a late stage in the flux rope formation process ($t = 180\,t_0$) as the envelope of the flux rope expands further into the corona. In simulation SD, the dipole field, which was chosen to be aligned so as to minimize reconnection with this envelope field, constrains the expansion (both vertically and horizontally).

Figure 12 shows the height of the axis of the coronal flux rope and the height of the envelope field as a function of time. The height of the axis of the coronal flux rope is found by locating the point along the z-axis at which the horizontal field B_x is zero. This point is approximately the location of an O-point, i.e., where $\sqrt{B_x^2 + B_z^2} = 0$, and the field line that goes through this O-point appears to have very little writhe, as shown in Figure 10. The axis of the new flux rope is therefore well represented by this field line. We define the height of the envelope field by the intersection of the z-axis and the contour of $B_y = 0.1 B_y|_{\rm axis}$. Ideally, we would use the separatrix between the dipole field and the expanding flux rope field to measure the height of the envelope field, but no such separatrix exists in simulation ND. The value of $0.1 B_y|_{\rm axis}$ was chosen because the intersection of the z-axis and this contour is where the separatrix between the dipole field and the expanding flux rope field is located in simulations SD, MD, and WD for times $t > 50\,t_0$.

From $t = 200\,t_0$ to $t = 450\,t_0$, there is a slow rise of the flux rope, which appears to tend to a stable position. The vertical velocities at the envelope field fall from a typical value of $1.5 v_0$ at $t = 200\,t_0$ to $0.15 v_0$ at $t = 450\,t_0$. As can be seen in Figure 12, the height of the axis of the coronal flux rope at time $t = 450\,t_0$

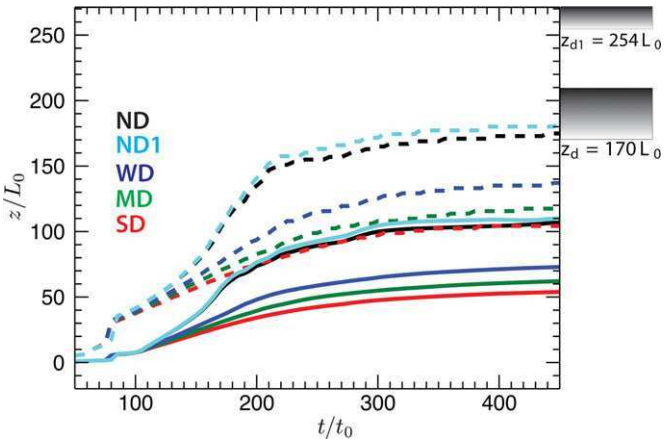

Figure 12. Height of the O-point in the $y = 0$ plane (solid lines) and the height of the envelope field (defined at the height along the $x = y = 0$ line where B_y is 0.1 times the value at the O-point; dashed lines) for five simulations (SD, MD, WD, ND, and ND1) as a function of time. The two gray shaded boxes represent the vertical extent of the two different damping regions. Simulations SD, MD, WD, and ND have damping regions that start at z_d and simulation ND1 has a damping region that starts at z_{d1}.

(A color version of this figure is available in the online journal.)

is smaller for larger dipole field strength, as expected. The simulation with no dipole, simulation ND, exhibits the strongest expansion, which continues until the envelope field of the flux rope approaches the damping region near the top boundary. From Figure 12, it appears that the flux rope in simulations SD, MD, WD, and ND are ultimately stable, but given that the envelope field is so close to the damping region in simulation ND, the effect of the boundary conditions on the stability cannot be ruled out. To investigate this, we perform an additional simulation, ND1, where the top boundary is extended further out, as is the damping region near this boundary (as described in Section 2). We find that envelope field does not extend past $\pm 80\,L_0$ in the x- or y-directions and so the side boundaries and the damping region at these side boundaries do not play a role in the stability of the flux rope. Therefore, we do not change these in simulation ND1. Figure 12 shows only a small difference in the curves between simulations ND and ND1. In both cases, the height of the envelope field appears to saturate at $180\,L_0$, which is well below the height of the top damping region for simulation ND1. We conclude that the confinement of the flux rope in the case of an initially field free corona is not a consequence of the boundary conditions, but of the self-stabilization of the flux rope by its own envelope field.

Previous simulations by Archontis & Hood (2012) with the same initial tube strength and twist as the simulations in this paper and without any pre-existing coronal field also suggest that the flux rope is ultimately stable. However, the flux rope axis in their simulations reaches a lower height of $62.3\,L_0$ above the surface compared with heights of $108\,L_0$ and $110\,L_0$ for the flux ropes in simulations ND and ND1 in this paper, respectively. This fact, together with the fact that in the simulations of Archontis & Hood (2012) the envelope of the flux rope reaches a height of $127\,L_0$ above the surface, at the boundary of the damping region between $127\,L_0$ to $130\,L_0$ above the surface, and thus very close to the top boundary at $130\,L_0$ above the surface, suggests that their boundary conditions are affecting the ultimate height of the flux rope. However, their conclusion, that the coronal flux rope is stabilized by its own envelope field, is supported by our simulations ND and ND1.

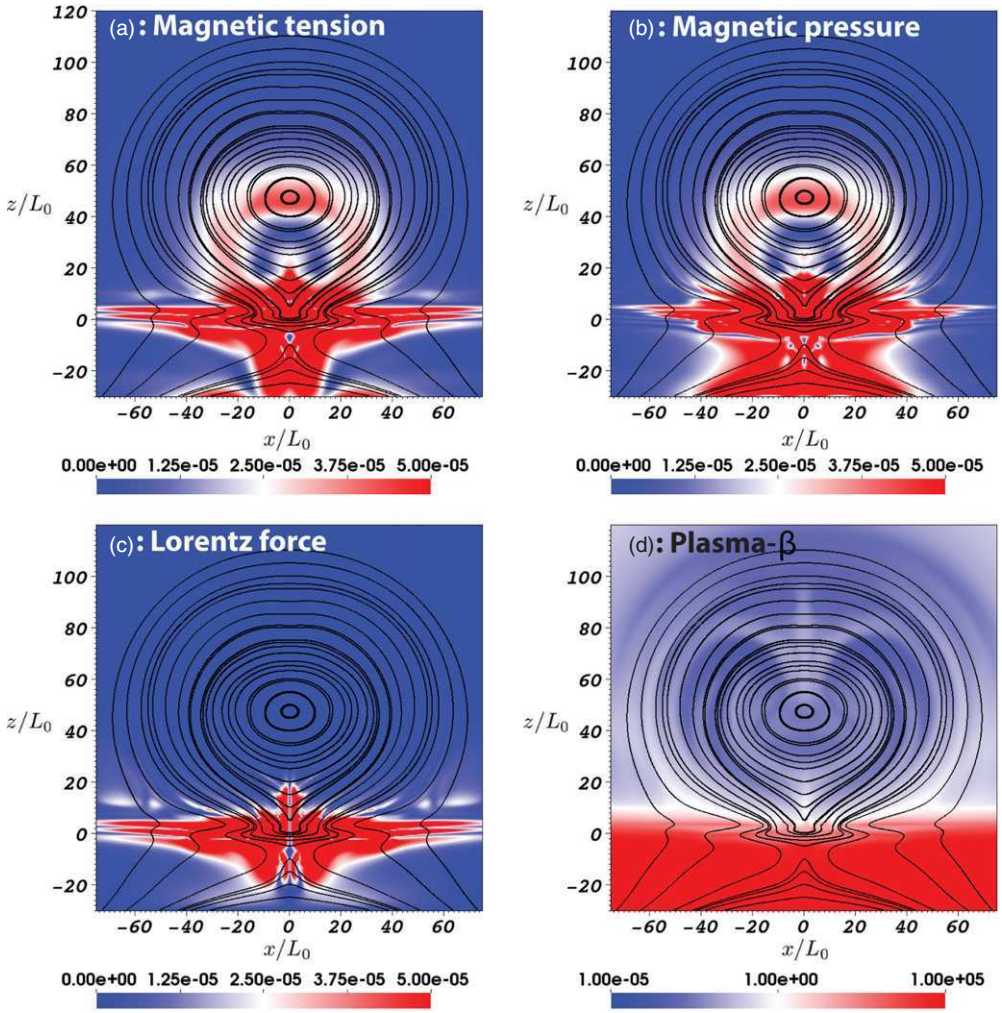

Figure 13. Magnetic forces and plasma β in the $y = 0$ plane for simulation SD at time $t = 280\,t_0$. Panel (a) shows two-dimensional (2D) field lines in the $y = 0$ plane and a color shading of the magnitude of the 2D magnetic tension vector $(\mathbf{B}\cdot\nabla B_x, \mathbf{B}\cdot\nabla B_z)\,L_0/B_0^2$ in the $y = 0$ plane. Panel (b) shows the same but for the 2D magnetic pressure vector $(\partial|\mathbf{B}|^2/\partial_x, \partial|\mathbf{B}|^2/\partial_z)\,L_0/B_0^2$. Panel (c) shows the magnitude of the 2D Lorentz force vector $((\mathbf{j}\times\mathbf{B})_x, (\mathbf{j}\times\mathbf{B})_y)\mu_0\,L_0/B_0^2$. Panel (d) shows the plasma $\beta = P/|\mathbf{B}|^2$. This figure demonstrates that in the low-β part of the corona, the magnetic tension and magnetic pressure approximately cancel out and so the coronal flux rope is in approximate Lorentz force balance.

(A color version of this figure is available in the online journal.)

In the simulations of Manchester et al. (2004), which used a slightly thinner tube ($w = 2\,L_0$ compared with $w = 2.5\,L_0$ here) and were placed initially higher in the convection zone ($z = -10\,L_0$ compared with $z = -12\,L_0$ here), the O-point of the flux rope that formed in the corona rose to a height of $50\,L_0$ by $t = 70\,t_0$ at the end of the simulation. This is higher than the flux rope reaches by $t = 70\,t_0$ in simulations ND and ND1, but the flux ropes in simulations ND and ND1 achieve heights well above $50\,L_0$ later in time, when they become stable. While the flux rope rises quickly during the initial phase presented in Manchester et al. (2004), based on the findings in this paper, it seems likely that the flux rope formed in Manchester et al. (2004) would also ultimately be confined by its own envelope field, if its evolution was followed long enough.

By including a dipole field in simulations SD, MD, and WD, we are also able to constrain the flux rope at lower heights than its own envelope field is able to hold it at. Thus, the dipole field is suppressing the rise of the coronal flux rope. The magnetic forces and plasma β in the $y = 0$ plane are shown in Figure 13 for simulation SD at time $t = 280\,t_0$. The magnitudes of the magnetic tension force and the magnetic pressure forces in the $y = 0$ plane are shown in panels (a) and (b), respectively. Above a height of $z = 10\,L_0$, the two forces approximately cancel and the magnetic field associated with the flux rope and dipole field has a small Lorentz force relative to the magnitude of the magnetic pressure and tension forces. As can be seen from panel (d), $z = 10\,L_0$ is the height at which the plasma β undergoes the transition from above unity to below unity. Above $z = 10\,L_0$, the magnetic field configuration has approximately $\mathbf{j}\times\mathbf{B} = 0$.

3.4. Distribution of Electric Currents

At present, there is much debate as to whether the electric currents in active regions are "neutralized," in the sense that, for a single sunspot or active region polarity, the direct current (current aligned parallel to the axial magnetic field of the flux tube associated with that sunspot) is surrounded by a return current (aligned anti-parallel to the axial field), which cancels this direct current out. This is important for flare and CME modeling as some models use an initial magnetic field with a net current (i.e., return currents are either absent or not large enough to neutralize the direct currents), e.g., the TD model. Although in

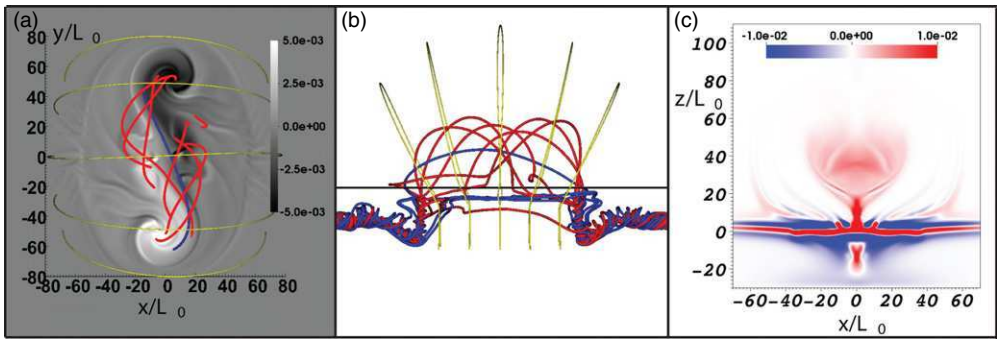

Figure 14. Distribution of currents in the corona for simulation SD due to flux emergence and subsequent formation of a coronal flux rope, at time 240 t_0. Panels (a) and (b) show red current field lines originating from regions of direct current ($j_y > 0$) on the side boundaries and blue lines originating from regions of return current ($j_y < 0$), with a grayscale slice of j_z/j_0 taken at $z = 10\,L_0$. The field lines are located at regular values of radius with the origin at the axis of the convection zone flux tube and the number of field lines at each radius is proportional to the total axial current at that radius. The yellow lines are the dipole field. Panel (c) shows j_y/j_0 in the $y = 0$ plane.

(A color version of this figure is available in the online journal.)

the simulations presented here the initial sub-surface flux tube is current neutralized, i.e., it has no net current, there is significant distortion of the magnetic field by the emergence process and so it is not clear that the resulting coronal flux rope will also be current neutralized.

To investigate this issue, we plot in Figure 14 the electric currents at time $t = 240\,t_0$ in simulation SD. Panels (a) and (b) show slices of vertical current j_z at a height of $z = 10\,L_0$, the top of the photosphere/chromosphere region in the model, where $\beta = 1$ for simulation SD. This height is chosen so as to eliminate any overshoot convective flows that distort the magnetic field. Panels (a) and (b) also show current field lines (field lines of **j**). The current field lines are colored by the sign of j_y at their location of origin on the side boundary: red for direct current ($j_y > 0$) and blue for return current ($j_y < 0$). The field lines are located at regular values of the radius, from $r = 0.4\,L_0$ to $6\,L_0$, around the axis of the convection zone flux tube on the side boundary. These radial values are $0.4\,L_0 + (0.8\,n L_0)$ for $n = 0, 7$ (j_y changes sign at the radial value $2.4\,L_0$). The number of field lines at each radial value r is proportional to the total unsigned axial current in the annulus $2\pi r dr$ centered on that radius r, where $dr = 0.8\,L_0$. The total number of field lines is 30, so each field line represents $1/30$ of the total unsigned axial current in the entire flux rope. For a given current field line there are only two routes by which it can return to a side boundary. First, it can exit through the opposite boundary. Second, it can reverse direction and return to the same boundary in a region of opposite current. Figure 14 shows that it is mostly current field lines that originate in regions of direct ($j_y > 0$) current on the side boundary that enter the corona above $z = 10\,L_0$. Figure 14, panel (c) shows that a strong central positive j_y develops above $z = 10$ in the $y = 0$ plane. As predicted by the 2.5D model of Longcope & Welsch (2000), there is a return current that flows along the interface between the sub-photosphere and corona, although the simulations in this paper show that some return current extends into the corona.

Note that a single blue line emerges into the corona in Figure 14, panels (a) and (b). This current field line originates from a region of negative j_y (but positive B_y) on the $y = \min y$ plane and so is considered return current. If this field line were to follow a simple Ω shaped path from one boundary to the other, it would intersect the $z = 10\,L_0$ plane such that the current normal to that plane j_z would be anti-parallel to the magnetic field normal to the plane B_z and it would be considered return current in the corona. However, this current field line, which is representative of many others, performs a complicated circuit, first crossing underneath the active region before passing into the corona and back into the convection zone. This loop-like circuit results in the field line having j_z parallel to the magnetic field B_z on the $z = 10\,L_0$ plane. In this sense, for the $z = 10\,L_0$ plane, the blue field line is a direct current field line, even though for its seed location on the $y = \min y$ plane it is a return current field line. This changing of currents is due to the complicated current structure underneath $z = 10\,L_0$, where the currents are far from force-free and plasma motions can dominate over magnetic forces.

These results suggest that the coronal flux rope is not neutralized, in the sense that there is not a balance of direct and return current. Of course, there may be very diffuse return currents surrounding this flux rope and further, more rigorous, analysis is required to determine whether or not the flux rope is indeed un-neutralized. An in-depth analysis of the neutralization of active region currents in an analogous simulation is presented in Török et al. (2013).

4. DISCUSSION

The aim of this paper is to use 3D visco-resistive MHD simulations to investigate whether convection zone flux tube emergence could create coronal magnetic field configurations compatible with a flux rope model such as the TD model, where a net-current coronal flux rope is tethered by an overlying potential field.

Consistent with previous simulations, we found that the initial convection zone flux tube partially emerged into the corona; only sections of field lines that were able to shed mass were able to emerge. The original flux tube axis first reached a height of 3 Mm above the surface. This is consistent with simulations by Magara (2001), Fan (2001), and Murray et al. (2006).

As a result of the transport of twist from the convection zone into the corona, torsional motions manifested themselves in corotation of the opposite-polarity regions and effectively twisted up the field in the corona, as originally shown by Fan (2009). The field line associated with the original convection zone flux tube axis separated into two field lines due to magnetic diffusion and became wrapped around a new flux rope axis in the corona. Two distinct J-shaped current layers beneath the new flux rope axis formed, which began to merge during the rotation

of the sunspots. This process of emergence and equilibration of twist supports the conclusions from observations that sunspot rotation is driven by twisted flux tube emergence and that it can cause the formation of sigmoids prior to a solar flare (e.g., Min & Chae 2009; Kumar et al. 2013).

No obvious evidence of magnetic reconnection was seen at the location of the current layer below the new coronal flux rope axis, such as the evidence presented in Manchester et al. (2004), Archontis & Török (2008), and Archontis & Hood (2012). In those simulations, there was slow, steady reconnection at the location of the current sheet during the expansion of the emerged field in the corona and this reconnection amplified as the flux rope rose to successively larger heights. Because in the simulations in this paper the emerged field was constrained by the dipole field, we did not see this reconnection stage clearly. Since, however, we did see evidence of rotational motions in sunspots, as suggested by Fan (2009), we conclude that the flux rope formation process is predominantly due to these motions in our simulations.

By varying the height of the top boundary and the upper velocity damping region and finding that the ultimate height of the flux rope axis was unchanged, we removed the effect of the top boundary conditions on the stability of the flux rope and concluded that even without a dipole field in the corona, the flux rope was constrained by its own envelope field, which support the results by Archontis & Török (2008) and Archontis & Hood (2012), which were achieved for smaller simulation boxes.

By adding a dipole field, aligned so as to minimize reconnection with the emerging field in the corona, we were able to constrain the expansion of the active region into the corona. The stronger the dipole field, the lower the height of the newly formed coronal flux rope, as expected. Such a system of a coronal current-carrying flux rope (or, alternatively, a strongly sheared arcade) stabilized by an overlying potential field is a canonical configuration believed to produce solar eruptions. We found that the relatively simple, idealized initial conditions used in our simulations, with a twisted convection zone flux tube emerging into a dipole field representing a decaying active region, is able to robustly produce such a coronal configuration.

A simple analysis of the electric currents suggests that the majority of the return currents did not emerge into the corona and so a coronal flux rope with a non-neutralized current was created. Further analysis is presented in Török et al. (2013). The preliminary results presented here suggest that coronal flux rope models that consider only direct currents, such as the TD model, are compatible with the magnetic fields created by the emergence of a twisted magnetic flux tube.

This work has been supported by the NASA Living With a Star and Solar and Heliospheric Physics programs, the ONR 6.1 Program, and by the NRL-*Hinode* analysis program. The simulations were performed under a grant of computer time from the DoD HPC program. The authors thank the anonymous referee for comments that improved the clarity and relevance of the paper.

REFERENCES

Acheson, D. J. 1979, SoPh, 62, 23
Arber, T. D., Haynes, M., & Leake, J. E. 2007, ApJ, 666, 541
Arber, T. D., Longbottom, A. W., Gerrard, C. L., & Milne, A. M. 2001, JCoPh, 171, 151
Archontis, V. 2008, JGRA, 113, 3
Archontis, V., Galsgaard, K., Moreno-Insertis, F., & Hood, A. W. 2006, ApJL, 645, L161
Archontis, V., & Hood, A. W. 2012, A&A, 537, A62
Archontis, V., Moreno-Insertis, F., Galsgaard, K., Hood, A., & O'Shea, E. 2004, A&A, 426, 1047
Archontis, V., & Török, T. 2008, A&A, 492, L35
Aulanier, G., Török, T., Démoulin, P., & DeLuca, E. E. 2010, ApJ, 708, 314
Canou, A., & Amari, T. 2010, ApJ, 715, 1566
Fan, Y. 2001, ApJL, 554, L111
Fan, Y. 2009, ApJ, 697, 1529
Fontenla, J. M., Avrett, E., Thuillier, G., & Harder, J. 2006, ApJ, 639, 441
Forbes, T. G. 2000, JGR, 105, 23153
Gary, G. A. 2001, SoPh, 203, 71
Gary, G. A., & Alexander, D. 1999, SoPh, 186, 123
Gibson, S. E., & Fan, Y. 2006, JGRA, 111, 12103
Green, L. M., & Kliem, B. 2009, ApJL, 700, L83
Green, L. M., Kliem, B., & Wallace, A. J. 2011, A&A, 526, A2
Guo, Y., Schmieder, B., Démoulin, P., et al. 2010, ApJ, 714, 343
Kumar, P., Park, S.-H., Cho, K.-S., & Bong, S.-C. 2013, SoPh, 282, 503
Leake, J. E., & Linton, M. G. 2013, ApJ, 764, 54
Liu, R., Liu, C., Wang, S., Deng, N., & Wang, H. 2010, ApJL, 725, L84
Longcope, D. W., & Welsch, B. T. 2000, ApJ, 545, 1089
Luoni, M. L., Démoulin, P., Mandrini, C. H., & van Driel-Gesztelyi, L. 2011, SoPh, 270, 45
MacTaggart, D. 2011, A&A, 531, A108
MacTaggart, D., & Hood, A. W. 2009, A&A, 507, 995
Magara, T. 2001, ApJ, 549, 608
Magara, T. 2006, ApJ, 653, 1499
Manchester IV, W., Gombosi, T., DeZeeuw, D., & Fan, Y. 2004, ApJ, 610, 588
Manchester IV, W. B., Vourlidas, A., Tóth, G., et al. 2008, ApJ, 684, 1448
McKenzie, D. E., & Canfield, R. C. 2008, A&A, 481, L65
Min, S., & Chae, J. 2009, SoPh, 258, 203
Murray, M. J., & Hood, A. W. 2008, A&A, 479, 567
Murray, M. J., Hood, A. W., Moreno-Insertis, F., Galsgaard, K., & Archontis, V. 2006, A&A, 460, 909
Parker, E. N. 1979, ApJ, 230, 905
Patsourakos, S., Vourlidas, A., & Stenborg, G. 2013, ApJ, 764, 125
Robbrecht, E., Patsourakos, S., & Vourlidas, A. 2009, ApJ, 701, 283
Roussev, I. I., Forbes, T. G., Gombosi, T. I., et al. 2003, ApJL, 588, L45
Sterling, A. C. 2000, JASTP, 62, 1427
Stix, M. 2004, in The Sun: An Introduction, ed. M. Stix (New York: Springer)
Titov, V. S., & Démoulin, P. 1999, A&A, 351, 707
Török, T., & Kliem, B. 2005, ApJL, 630, L97
Török, T., Leake, J. E., Titov, V. S., et al. 2013, ApJ, in press
van Ballegooijen, A. A., & Martens, P. C. H. 1989, ApJ, 343, 971
Vernazza, J. E., Avrett, E. H., & Loeser, R. 1981, ApJS, 45, 635
Vourlidas, A., Lynch, B. J., Howard, R. A., & Li, Y. 2013, SoPh, 284, 179
Yelles Chaouche, L., Kuckein, C., Martínez Pillet, V., & Moreno-Insertis, F. 2012, ApJ, 748, 23

The Astrophysical Journal, 777:76 (11pp), 2013 November 1 doi:10.1088/0004-637X/777/1/76

MAGNETOHYDRODYNAMIC SIMULATIONS OF INTERPLANETARY CORONAL MASS EJECTIONS

Roberto Lionello, Cooper Downs, Jon A. Linker, Tibor Török, Pete Riley, and Zoran Mikić
Predictive Science, Inc., 9990 Mesa Rim Road, Suite 170, San Diego, CA 92121-2910, USA; lionel@predsci.com, cdowns@predsci.com, linker@predsci.com, tibor@predsci.com, pete@predsci.com, mikic@predsci.com
Received 2013 July 5; accepted 2013 September 4; published 2013 October 17

ABSTRACT

We describe a new MHD model for the propagation of interplanetary coronal mass ejections (ICMEs) in the solar wind. Accurately following the propagation of ICMEs is important for determining space weather conditions. Our model solves the MHD equations in spherical coordinates from a lower boundary above the critical point to Earth and beyond. On this spherical surface, we prescribe the magnetic field, velocity, density, and temperature calculated typically directly from a coronal MHD model as time-dependent boundary conditions. However, any model that can provide such quantities either in the inertial or rotating frame of the Sun is suitable. We present two validations of the technique employed in our new model and a more realistic simulation of the propagation of an ICME from the Sun to Earth.

Key words: magnetohydrodynamics (MHD) – solar wind – Sun: coronal mass ejections (CMEs)

Online-only material: color figures

1. INTRODUCTION

Interplanetary coronal mass ejections (ICMEs) are the solar-wind counterpart of coronal mass ejections (CMEs), which are huge bursts of solar material released from the corona of the Sun (for a comprehensive review of theory and observations, see Kunow et al. 2006). After approximately one to four days after a CME eruption, an ICME may reach Earth, interact with the geomagnetic field, and cause a geomagnetic storm (Gosling 1990) if the direction of the field in the cloud is opposite (southward) with respect of that of the Earth (Burlaga et al. 1987). Therefore, knowing the structure of the magnetic field of an ICME is of fundamental importance for predicting its geoeffectiveness. CMEs are typically associated with flux ropes, but their magnetic geometry, when they arrive at Earth as ICMEs, is less clear (e.g., Vourlidas et al. 2013). Some ICMEs are observed in situ as so-called magnetic clouds, defined as regions of low proton temperature, enhanced magnetic field strength, and smooth rotation of the magnetic field vector (e.g., Burlaga et al. 1982), the latter indicating flux-rope geometry. Gosling et al. (1991) estimated that about one third of all ICMEs contain a magnetic cloud or flux rope, although this fact may vary systematically with the solar cycle (Riley et al. 2006). Some ICME ejecta have multiple magnetic clouds (i.e., a single structure with multiple subclouds distinguishable, Wang et al. 2002, 2003), the likely result of the interaction of several CMEs.

Given the importance of ICMEs for determining space weather conditions, several computational models have been developed to study their propagation in space. Although a few attempts have been made to simulate the origin of a CME on the Sun and its propagation as an ICME simultaneously (Usmanov & Dryer 1995; Wu et al. 1999; Groth et al. 2000; Manchester et al. 2006; Feng et al. 2010), this approach is very challenging for computational reasons. First, the solar corona and the heliosphere have remarkably different physical properties, resulting in a much smaller integration time step in coronal simulations compared with heliospheric simulations. Hence, a heliospheric computation costs a small fraction of a coronal calculation. Moreover, it is often the case that several coronal simulations are necessary to explore parameter space prior to modeling the full propagation. On the other hand, boundary conditions for a heliospheric model are relatively straightforward to implement beyond the critical MHD wave points. These boundary conditions can be obtained from the upper boundary of a coronal model extending just above the critical points. Therefore, a two-model integrated approach, where a coronal calculation acts as a driver for the heliospheric evolution, is more widespread. Riley et al. (2001b) integrated three-dimensional (3D) MHD models of the solar corona and heliosphere. They used a line-of-sight magnetogram as input to the coronal model and they first determined the steady-state solar wind at 30 $R_\odot$ during various solar phases of activity. Then, they used those values to drive the heliospheric model and calculate the structure of the solar wind out to 5 AU. Since the boundary conditions for this model are not time dependent, its applicability to the study of ICMEs is limited. Odstrcil et al. (2002) and Riley et al. (2003) studied the disruption of a sheared helmet streamer, which launches a CME, with a 2D MHD coronal model. Then, they used the time-dependent boundary conditions at the outer surface of the coronal solution to drive a 2D MHD heliospheric calculation of the propagation of the CME in interplanetary space. This model (Enlil) was later extended to 3D and showed how it could accept input data from empirical, observational, and numerical coronal models (Odstrcil et al. 2003, 2008). However, the present version of the model at the Community Coordinated Modeling Center[1] does not accept evolving, time-dependent boundary conditions for the magnetic field at the surface beyond the critical points. Another limitation of the Enlil model is that it does not have 4π spatial coverage (i.e., 4π steradian coverage of the spherical computational domain), an important requirement for the study of ICME propagation according to Kleimann (2012). The model of Usmanov & Goldstein (2006) combines an inner region MHD solution from 1 to 20 $R_\odot$ with a 3D outer solution, which is constructed by forward integration along the hyperbolic radial coordinate and extends from 20 $R_\odot$ to 10 AU. This model does not include the capability to evolve the boundary conditions during the simulations. Tóth et al. (2005, 2012) presented the Space Weather Modeling Framework (SWMF), an integrated suite of numerical tools that includes, among others, coupled

[1] http://ccmc.gsfc.nasa.gov

models of the solar corona and heliosphere. This framework was used, for example, by Lugaz et al. (2007) to study three CMEs originating from active region 9236 as they propagate from the Sun to the Earth. Notwithstanding the great flexibility of the SWMF, its single components are meant to be used in conjunction with one another and it requires additional software modules to be created for each additional third-party coronal model (Tóth et al. 2005, 2012). Other MHD models of ICME propagation used a steady-state ambient solar wind, which was either derived from an MHD coronal solution (Odstrcil et al. 2004) or prescribed (Odstrcil et al. 2005; Merkin et al. 2011) from the empirical Wang–Sheeley–Arge Model (WSA) model (Wang & Sheeley 1995; Arge & Pizzo 2000). The so-called cone model (Zhao et al. 2002) can be used to calculate the ICME parameters kinematically, which can be inserted into the precalculated, steady-state background. Although useful and simple to operate, the cone model does not include a flux rope and cannot provide real interplanetary magnetic field predictions for physical quantities inside the ICME. The MHD model of the solar wind presented in Hayashi (2012) does use time-dependent boundary conditions, which are determined from the solar magnetic field and interplanetary scintillation observations as input at the spherical surface beyond the critical points. Although it can also be coupled with cone models of CMEs, it does not accept the output of coronal MHD models of the initiation and early stages of propagation of CMEs as a driver at the lower boundary.

The purpose of this paper is to illustrate the details of an MHD model that provides the evolution of density, temperature, velocity, and magnetic field of ICMEs, to present validation examples of our technique; and to describe a more realistic calculation based on the interplanetary propagation of the coronal model of CME initiation by T. Török et al. (in preparation; see Section 4). Our heliospheric model is derived from the coronal model of Lionello et al. (2009), building on the work of Riley et al. (2001b). It has been designed to include capabilities that are not found together in any other single available model: (1) it is fully 3D MHD and covers the whole 4π (i.e., the polar regions are included); (2) it accepts time-dependent boundary conditions at the lower surface, making it suitable both for studies of solar-wind evolution and ejecta propagation; (3) the driver at the lower surface is flexible enough to use data obtained either from other models (coronal MHD or empirical) or from observations; these data may have been calculated either in the inertial or rotating frame of the Sun; and (4) the computation itself can be implemented either in the inertial or in the rotating frame of reference.

This paper is organized as follows. The equations and the solution technique are described in Section 2. Then, in Section 3, two validation examples are shown, one in the non-rotating frame and one in the rotating frame of reference. The description of the more realistic case is contained in Section 4, which is followed by our conclusions.

2. MODEL

Here we present the equations that are advanced numerically in our model and how the time-dependent boundary conditions are implemented in a flexible way.

2.1. MHD Equations

Our model of ICME propagation is derived from the 3D, time-dependent, MHD model of Lionello et al. (2009), the numerical details of which were presented in Lionello et al. (1998, 1999) and Mikić et al. (1999). In a computational domain extending between $r_{\min} \leqslant r \leqslant r_{\max}$, the following set of partial differential equations in spherical coordinates are solved:

$$\nabla \times \mathbf{B} = \frac{4\pi}{c}\mathbf{J}, \tag{1}$$

$$\nabla \times \mathbf{A} = \mathbf{B}, \tag{2}$$

$$\frac{\partial \mathbf{A}}{\partial t} = \mathbf{v} \times \mathbf{B} - \frac{c^2\eta}{4\pi}\nabla \times \mathbf{B}, \tag{3}$$

$$\frac{\partial \rho}{\partial t} + \nabla\cdot(\rho\mathbf{v}) = 0, \tag{4}$$

$$\frac{1}{\gamma - 1}\left(\frac{\partial T}{\partial t} + \mathbf{v}\cdot\nabla T\right) = -T\nabla\cdot\mathbf{v} + \frac{m}{k\rho}S, \tag{5}$$

$$\rho\left(\frac{\partial \mathbf{v}}{\partial t} + \mathbf{v}\cdot\nabla\mathbf{v}\right) = \frac{1}{c}\mathbf{J}\times\mathbf{B} - \nabla p + \rho\mathbf{g} + \nabla\cdot(\nu\rho\nabla\mathbf{v}) + \mathbf{F}_{\rm fict}, \tag{6}$$

where $\mathbf{B}$ is the magnetic field, $\mathbf{J}$ is the electric current density, $\mathbf{A}$ is the vector potential, ρ, $\mathbf{v}$, p, and T are the plasma mass density, velocity, pressure, and temperature, respectively, $\mathbf{g} = -g_0 R_\odot^2 \hat{\mathbf{r}}/r^2$ is the gravitational acceleration, η the resistivity, and ν is the kinematic viscosity. In the inertial frame of reference, the fictitious force term, $\mathbf{F}_{\rm fict}$, is absent. In the rotating frame of reference, we have

$$\mathbf{F}_{\rm fict} = \rho\left(2\boldsymbol{\Omega}\times\mathbf{v} + \boldsymbol{\Omega}(\times\boldsymbol{\Omega}\times\mathbf{v})\right). \tag{7}$$

Here, the first term of the right hand side is the Coriolis force, while the second term is the centrifugal force. Both depend on the angular velocity $\boldsymbol{\Omega}$. S in Equation (5) represents the energy source term. Although in future studies we plan to explore the use of the full thermodynamic treatment of Lionello et al. (2009), which includes collisionless thermal conduction, in this work we use the so-called polytropic approximation as in Linker et al. (2003), which prescribes a simple adiabatic energy equation (i.e., $S = 0$, which is appropriate in the heliosphere), and choose a suitable value for γ (generally, 1.5; Totten et al. 1996; Feldman et al. 1998).

2.2. Boundary Conditions

The method used to specify the boundary conditions in the heliospheric model is determined not only by the requirements of the heliospheric calculation itself but also by the characteristics of the coronal model that provides the data. For maximum flexibility, we allow the calculation to be either in the corotating or inertial frame of reference in either model. However, we foresee that our typical coupled calculation will be in the corotating frame for the corona and in the inertial frame for the heliosphere. Moreover, we want to be able to use coronal calculations performed in the corotating frame of reference, without including the contribution of the fictitious forces of Equation (7).

In specifying the boundary conditions in our model, we also need to ensure that the problem is well posed by examining the characteristic curves associated with the system (e.g., Jeffrey 1966, p. 122). At the lower boundary of coronal models, only some of the seven characteristic curves of MHD are outgoing (e.g., Lionello et al. 2009). Hence, there is an upper limit on

how many fields may be prescribed as boundary conditions at the lower spherical surface $r_{\rm min}$, while the rest are to be determined by solving the characteristic equations. On the contrary, in a heliospheric model, since the plasma is supersonic and super-Alfvénic, all scalar and vector fields must be specified, provided that the solenoidal property of the magnetic field, $\nabla\cdot\mathbf{B} = 0$, is preserved. To model ejecta propagation and solar wind variations, the values at $r = r_{\rm min}$ of ρ, T, $\mathbf{B}$, and $\mathbf{v}$ must be generally specified as functions of latitude, longitude, and time (θ, ϕ, t). The quantities are either extracted from a spherical shell in a coronal MHD calculation (provided it is chosen beyond the critical points), from an empirical model such as WSA, from a combination of MHD and empirical models (Riley et al. 2001b), or, in principle, from suitable observations. Transformations in coordinates with linear interpolation of all the fields in the three variables (θ, ϕ, t) are needed to account for differences in the structure of the grid and temporal sampling between our heliospheric model and the model from which the boundary values are obtained. Depending on whether the calculation providing the boundary conditions is in the same frame of reference of the heliospheric model or not, an additional interpolation in ϕ may be necessary to account for rotation:

$$f'(\theta, \phi, t) = f(\theta, \phi \pm \Omega t, t), \tag{8}$$

where f is ρ, T, or one of the components of $\mathbf{v}$ and $\mathbf{B}$ at the boundary. The minus sign is used when the boundary conditions are extracted from a corotating frame and are used in an inertial frame; the plus sign is used when the calculation is in the corotating frame and the boundary conditions are provided in an inertial frame. Finally, a frame of reference transformation is applied to v'_ϕ:

$$v_\phi^{\rm (helio)} = v'_\phi \pm \Omega r_{\rm min} \sin\theta. \tag{9}$$

However, when the boundary conditions are extracted from a corotating model that neglects the effects of fictitious forces, this transformation is applied only when calculating the electric field, as explained below.

Although the transformed ρ, T, and $\mathbf{v}$ may be directly used as time-dependent boundary conditions, the boundary condition for the induction equation, Equation (3), requires knowledge of the electric field, $\mathbf{E} = -\mathbf{v}\times\mathbf{B}$. Hence, we use the following approach, which accurately represents the interpolated $\mathbf{E}$ field on the new grid and automatically preserves the solenoidal properties of $\mathbf{B}$. The radial component of the electric field, E_r, at the boundary can be readily inserted to calculate the evolution of the radial component of the vector potential, A_r. This is not the case for the tangential components $\mathbf{E}_t = (E_\theta, E_\phi)$, because linear interpolation, when second derivatives are calculated, may introduce strong currents near the poles. To avoid this, we rewrite $\mathbf{E}_t$ as the sum of two arbitrary potentials $\Psi(\theta, \phi)$ and $\Phi(\theta, \phi)$:

$$\mathbf{E}_t = \nabla_t \times \Psi\hat{\mathbf{r}} + \nabla_t\Phi. \tag{10}$$

∇_t indicates tangential derivatives in (θ, ϕ). The potential Ψ controls the change of the radial component of the magnetic field, $B_r(\theta, \phi, t)$, and can be obtained by inverting

$$\nabla_t^2\Psi = \frac{\partial B_r}{\partial t}. \tag{11}$$

The second potential Φ controls the shearing of the magnetic field and does not change B_r. It is obtained by solving the following equation:

$$\nabla_t^2\Phi = -\nabla_t\cdot(\mathbf{v}\times\mathbf{B})_t, \tag{12}$$

where the transformation of Equation (9) is applied to the longitudinal component of $\mathbf{v}$ if the boundary conditions are extracted from a corotating model that neglects the effect of fictitious forces. Since $-\nabla^2$ is a symmetric, positive-definite operator, we discretize the operator on the (θ, ϕ) grid and invert it using a conjugate-gradient algorithm to obtain Ψ and Φ. Once we know the two potentials, we retrieve $\mathbf{E}_t$ and apply it as boundary condition for $\mathbf{A}_t$, assuming that the contribution of the resistive term in Equation (3) is negligible.

3. VALIDATION OF THE TECHNIQUE

Here, we present two validation examples of our heliospheric model, one computed for the case $\Omega = 0$ and one that accounts for solar rotation. Coronal simulations are first performed to provide the boundary conditions to drive the heliospheric model. These field values are extracted from a spherical surface within the coronal model so that there may be a partial superposition between the coronal and heliospheric computational domains. Thus, a comparison between the coronal and heliospheric calculations is possible. We simulate a CME eruption using the 3D MHD coronal model of Lionello et al. (2009) in the polytropic approximation, as it was employed by Linker et al. (2003). The computational domain extends from 1 to 50 $R_\odot$ and is discretized on a non-uniform $200\times150\times200$ mesh in (r, θ, ϕ). The radial resolution varies between 0.01 $R_\odot$ at the solar surface to 0.9 $R_\odot$ at the outer boundary. The minimum and maximum sizes of the longitudinal and latitudinal grids are $0\overset{\circ}{.}7$ and $4\overset{\circ}{.}7$, respectively, with the points concentrated in the area where the CME erupts. We have prescribed a uniform resistivity profile such that the ratio of the resistive dissipation time with the Alfvén wave propagation time is $\tau_R/\tau_A = 10^6$. A typical reference value for $\tau_A = R_\odot/V_A$ is 24 minutes, if we take an Alfvén speed $V_A = 480\,{\rm km\,s^{-1}}$ (e.g., for $|\mathbf{B}| = 2.2\,{\rm G}$ and $n_0 = 10^8\,{\rm cm^{-3}}$). This low resistivity value is prescribed to ensure that a minimum dissipation is present everywhere in the computational domain and to eliminate structures smaller than the grid resolution. In general, it is smaller than the numerical dissipation introduced by the upwinding treatment of advection, $\tau_U = 2\,R_\odot^2/(V\Delta r)$ (Lionello et al. 1999). For example, in the low corona, where $\Delta r = 0.01\,R_\odot$, we have $\tau_U \gtrsim \tau_R$ only for flows smaller than $0.1\,{\rm km\,s^{-1}}$. In the higher corona and in the heliosphere, numerical dissipation dominates over the prescribed value. Similarly, we have chosen a uniform viscosity profile such that $\tau_\nu/\tau_A = 500$. Also, this value of viscosity is necessary to dissipate unresolved scales without substantially affecting the global solution.

3.1. Non-Rotating Case

In the non-rotating case ($\Omega = 0$), we prescribe a global dipole field for $\mathbf{B}$ as the initial condition of the coronal model and a previously calculated solar wind solution for the plasma properties. Figure 1(a) shows a cut of the entire computational domain in the meridional plane showing some magnetic field lines of the initial dipole. We then relax the system for 6.7 days until we obtain a steady state. The configuration of the magnetic field after this relaxation phase is presented in Figure 1(c), where the field appears mostly radial and the current sheet in the equatorial plane is evident. Figure 2(a) shows the configuration closer to the solar surface. Open field regions are visible at the poles, while closed field lines are present at equatorial latitudes, surmounted by the typical cusp-like field lines. On top of the streamer, the current sheet is formed (Figure 2(c)), while

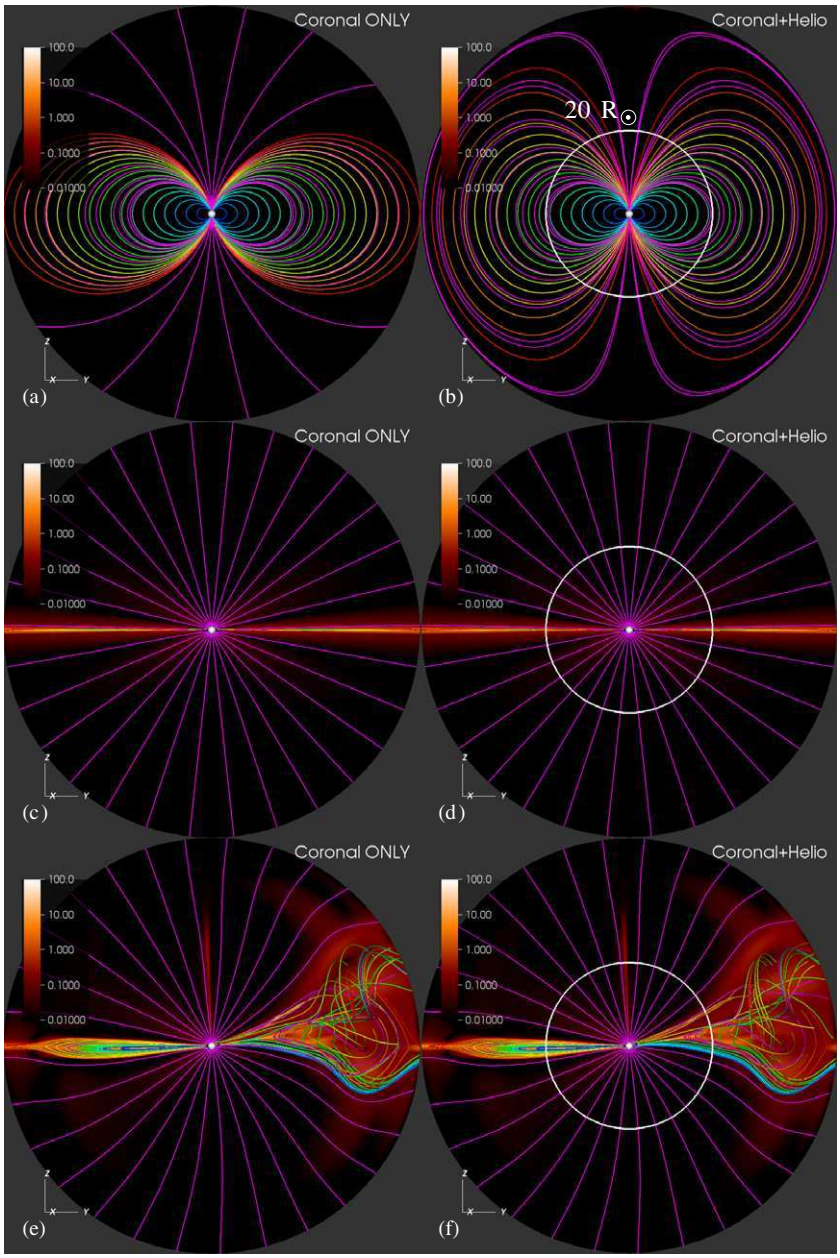

Figure 1. Magnetic field lines and J/B during the relaxation and flux rope eruption, in the coronal and heliospheric calculations without rotation, in a meridional plane (solar north is up). (a) Coronal model ($R_\odot \leqslant r \leqslant 50\,R_\odot$) at the beginning of the relaxation phase. (b) Coronal model ($R_\odot \leqslant r < 20\,R_\odot$) and the heliospheric model ($20\,R_\odot \leqslant r \leqslant 50\,R_\odot$) at the beginning of the relaxation phase. The boundary between the two models is traced in white. (c) Coronal model at the end of the relaxation phase, just before the flux rope is introduced. (d) Same as (c) for the coronal and heliospheric models combined. (e) Propagation of the flux rope in the coronal model. (f) Same as (e) for the coronal and heliospheric models combined.

(A color version of this figure is available in the online journal.)

volume currents are present in the closed-field region under the helmet streamer (Figure 2(b)). Using the technique described in Section 2.2, we extract from a spherical shell at approximately $20\,R_\odot$ the values of the fields corresponding to the initial state of the coronal model and subsequent states at every 10 hr for the entire relaxation period. As an initial condition for the magnetic field of the heliospheric model, we prescribe a potential field extrapolation of the values of B_r at $r = 20\,R_\odot$ at $t = 0$ from the coronal model. Likewise, we use the values of v_r, ρ, and T from the $r = 20\,R_\odot$ spherical surface in the coronal simulation to prescribe the initial conditions for the plasma properties. While the values of v_r and T from this surface are assigned to each internal point of corresponding latitude and longitude, the values of ρ are also scaled by a r^{-2} factor. In Figure 1(b), we show magnetic field lines of the initial state of the heliospheric solution in the region $r \geqslant 20\,R_\odot$ and of the initial state of the coronal solution for $r = 20\,R_\odot$ (the $r = 20\,R_\odot$ circle is marked in white). (It is not surprising that the $r \geqslant 20\,R_\odot$ region differs from the initial state of the coronal model shown in Figure 1(a).) Then, we relax the heliospheric model for 6.7 days, driving it with the sequence extracted from the coronal model. Our heliospheric calculation is also performed in the same inertial frame of reference as the coronal model. As Figure 1(d) shows, at the end of the relaxation phase the heliospheric solution is indistinguishable from that calculated using the coronal model.

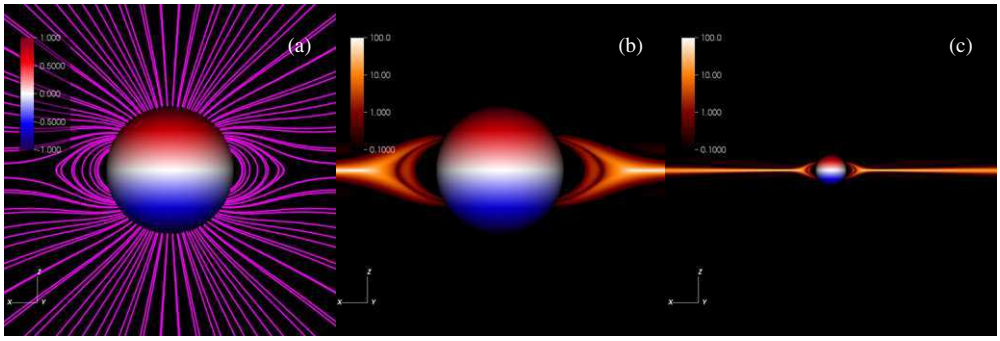

Figure 2. Relaxed state of the coronal calculation without rotation. The solar surface is colored according to the value of B_r. (a) Magnetic field lines outlining the global field structure. (b) J/B near the solar surface showing volume currents in the streamer belt. (c) J/B further out in the corona showing the equatorial current sheet.

(A color version of this figure is available in the online journal.)

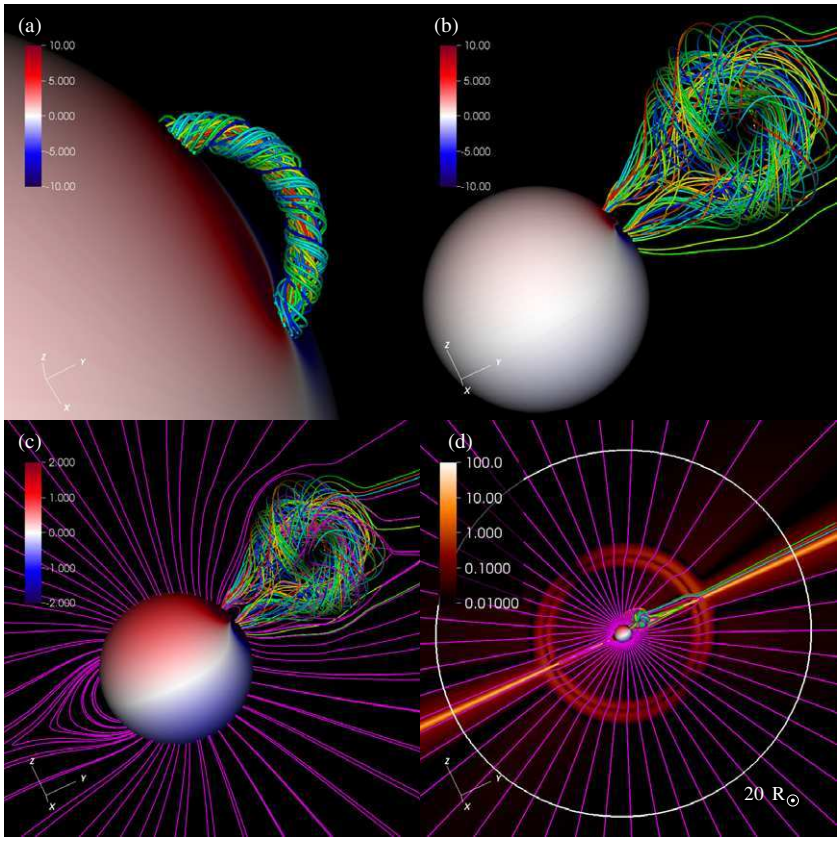

Figure 3. (a) Magnetic field lines of the out-of-equilibrium Titov-Démoulin flux rope introduced in the coronal solution after the relaxation phase. (b) The flux rope immediately erupts. (c) Interaction between the flux rope and the ambient dipole field. (d) J/B at larger heliocentric distances. We truncate the flux rope solution at $\sim 7\ R_\odot$, thus causing a disturbance that propagates outward in the solar wind.

(A color version of this figure is available in the online journal.)

Having obtained a virtually identical relaxed state for both models, we introduce a strongly out-of-equilibrium, modified version of the coronal flux rope model of Titov & Démoulin (1999, hereafter TDM) into the coronal calculation. The main difference between the original and the TDM model is that in the latter the stabilizing, analytical magnetic field is replaced with the ambient field of the CME source region into which the flux rope is inserted. Titov-Démoulin flux ropes have been used in recent simulations of observed CMEs (e.g., Tóth et al. 2007; Manchester et al. 2008; Lugaz et al. 2011) In all these cases, the flux rope was inserted out of equilibrium, causing an immediate eruption. Further details of our implementation of the TDM model will be described in a separate publication (V. S. Titov et al., in preparation), with emphasis placed on obtaining stable, pre-eruption configurations, such as the run described in Section 4. A view of some magnetic field lines of the flux rope, which is inserted at the equator into the relaxed configuration, is presented in Figure 3(a). If we simply added the flux-rope solution to the coronal field, this would instantly modify the magnetic field everywhere in the domain, including the region beyond $r = 20\ R_\odot$. This would create a discrepancy with the heliospheric model, for which the evolution for $r > 20\ R_\odot$ is solely the result of changes at the $r = 20\ R_\odot$ boundary. Therefore, when introducing the flux rope, we truncate the solution at $r = 7\ R_\odot$, which is well within the limits of the region bounded by the coronal model, but far enough from the flux rope

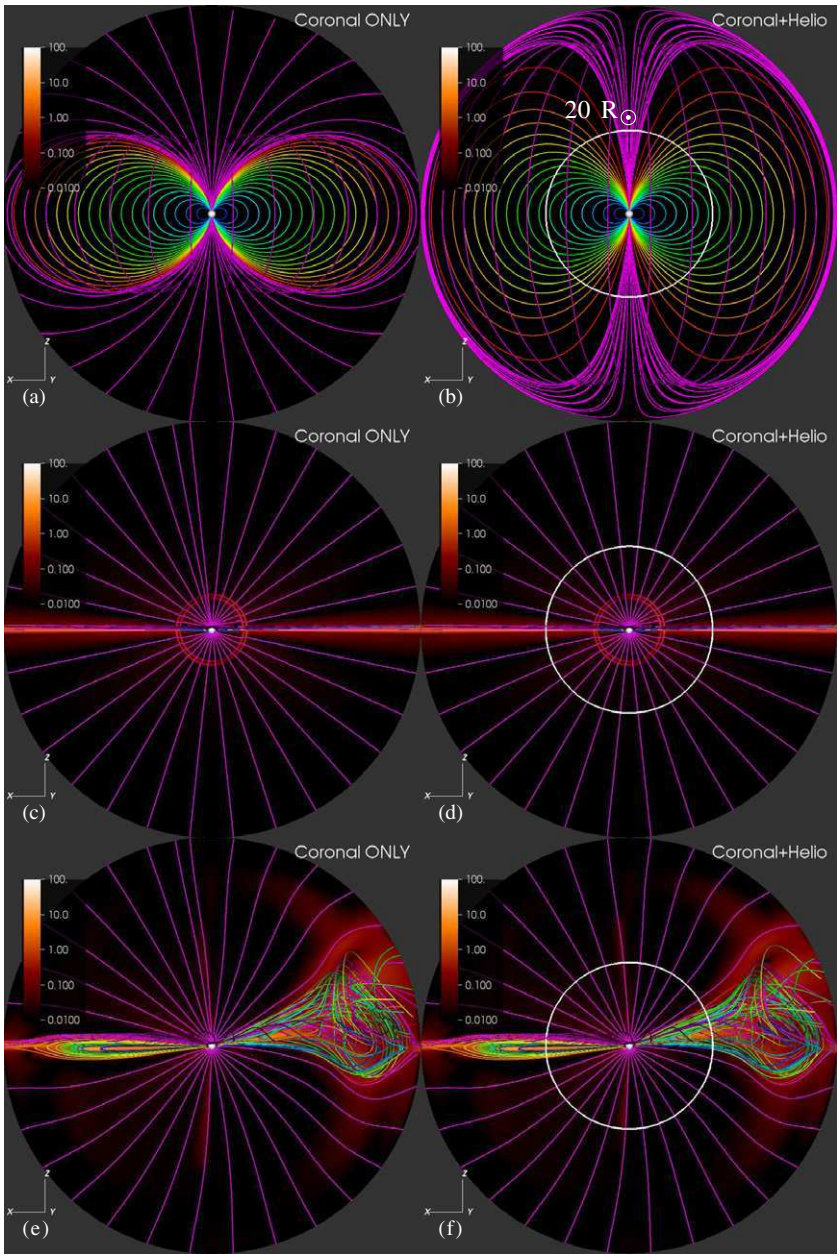

Figure 4. Magnetic field lines and J/B during the relaxation and flux rope eruption, in the coronal and heliospheric calculations with rotation in a meridional plane (solar north is up). (a) Coronal model at the beginning of the relaxation phase. (b) Coronal model and the heliospheric model at the beginning of the relaxation phase. The boundary between the two models at 20 $R_\odot$ is traced in white. (c) Coronal model at the end of the relaxation phase, just before the flux rope is introduced. (d) Same as (c) for the coronal and heliospheric models combined. (e) Propagation of the flux rope in the coronal model. (f) Same as (e) for the coronal and heliospheric models combined.

(A color version of this figure is available in the online journal.)

itself not to have significant physical consequences. However, this causes a slight deformation of the opposite streamer for $r \leqslant 7\ R_\odot$ and the formation of a small perturbation at $r = 7\ R_\odot$, which is visible in the J/B cut shown in Figure 3(d).[2] This disturbance travels out of the computational domain when we advance the calculation, further perturbing the opposite streamer as it adjusts to the presence of the inserted magnetic field. The flux rope itself, being out of equilibrium, immediately erupts, forming a CME (Figures 3(c) and (d)), which propagates and expands in the computational domain. After 20 hr, the ICME has crossed the outer boundary at 50 $R_\odot$ and we stop the calculation. Figure 1(e), which shows a cut in the meridional plane for this time, illustrates how the flux rope has expanded to an angular width of almost 30°. To model this highly dynamic phase with the heliospheric model, we extract ρ, T, $\mathbf{B}$, and $\mathbf{v}$ at $r = 20\ R_\odot$ from the coronal calculation with a higher frequency, namely a frame every 289 s. We drive the heliospheric model for 20 more hours to follow the propagation of the ICME (Figure 1(f)). The coronal and heliospheric calculations, which visually appear to be identical, are actually in agreement to within 1% for ρ, $|\mathbf{v}|$, $|\mathbf{B}|$, and T.

[2] We note that the field modification is exceptionally strong here because we have inserted a flux rope with a very intense magnetic field. If the flux rope is inserted in equilibrium with the ambient magnetic field, as in the case described in Section 4, these modifications are typically negligible outside the CME source region.

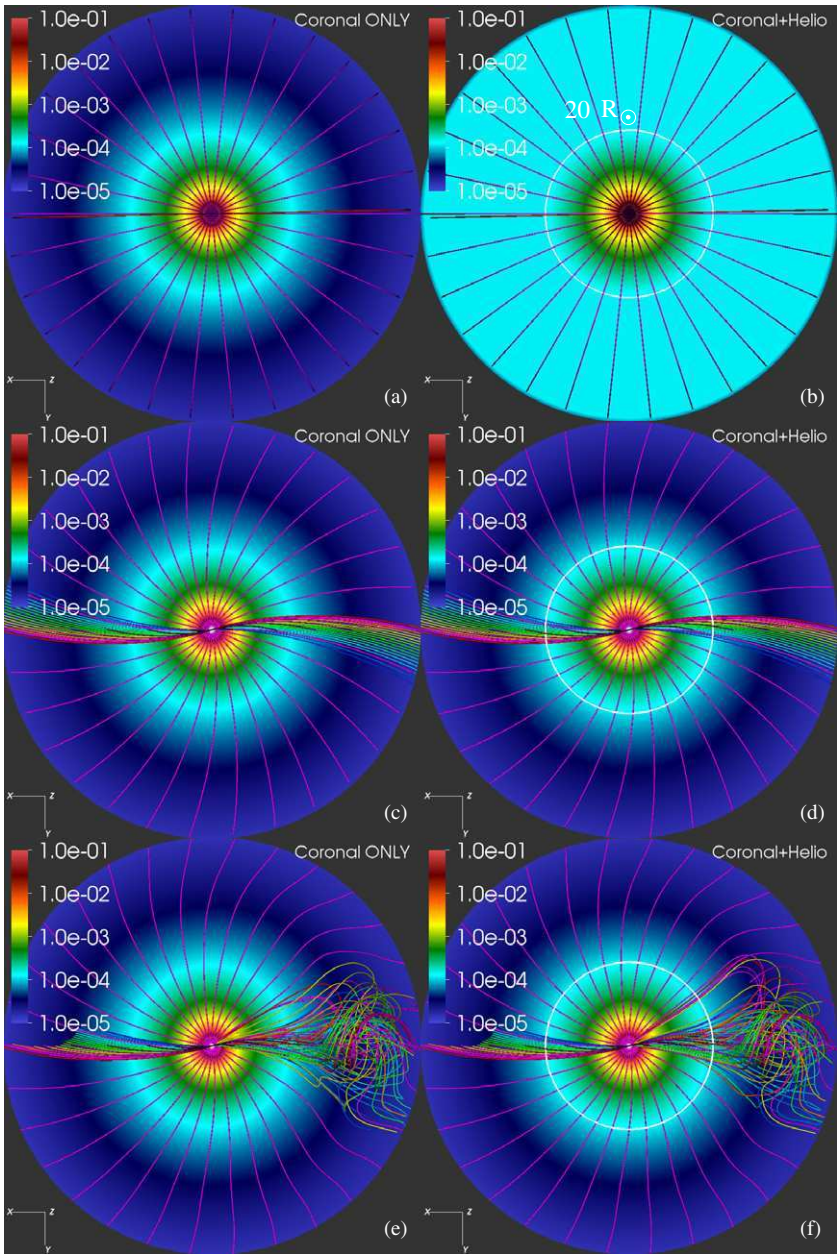

Figure 5. Magnetic field lines and scaled density (ρr^2) during the relaxation and flux rope eruption, in the coronal and heliospheric calculations with rotation in the equatorial plane (viewed from above the Sun's north pole). (a) Coronal model at the beginning of the relaxation phase. (b) Coronal model and the heliospheric model at the beginning of the relaxation phase. The boundary between the two models at 20 $R_\odot$ is traced in white. (c) Coronal model at the end of the relaxation phase, just before the flux rope is introduced. The Parker spiral is clearly visible. (d) Same as (c) for the coronal and heliospheric models combined. (e) Propagation of the flux rope in the coronal model. (f) Same as (e) for the coronal and heliospheric models combined.

(A color version of this figure is available in the online journal.)

3.2. Rotating Case

We now repeat the validation described in the previous section for a case where we account for solar rotation. We perform the calculation for the coronal model in the rotating (non-inertial) frame of reference, where Equation (6) contains a non-vanishing fictitious forces term, $\mathbf{F}_{\rm fict}$. As presented in Figure 4(a), an identical dipole state is prescribed for the initial magnetic field. At $t = 0$, the components of the magnetic field are only radial and latitudinal, as the cut in the equatorial plane of Figure 5(a) shows. Then, we relax the system by again advancing the MHD equations for 6.7 days to obtain a steady state. Figure 4(c), which displays the configuration after this time, is rather similar to the non-rotating case of Figure 1(c). However, in the present case, a longitudinal component of the magnetic field is introduced because of rotation. The effects of rotation can be appreciated in Figure 5(c), which shows, viewed from above the north pole of the Sun, how a burgeoning Parker spiral develops in the equatorial plane. From this coronal simulation, we extract a sequence of fields at the $r = 20\,R_\odot$ surface with the same frequency used in the non-rotating case and use a similar sequence of frames to drive the heliospheric model. The heliospheric calculation with rotation is performed in the inertial frame to show how our model is not tied to using the same frame of reference as the coronal simulation. Following the procedure outlined in the previous section, we

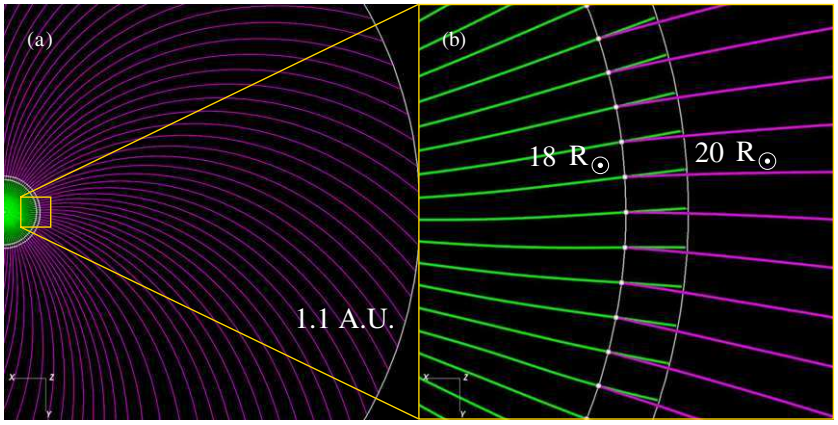

Figure 6. (a) Field lines in the equatorial plane for the combined coronal and heliospheric model of CME/ICME propagation of Section 4. All field lines are traced from 18 $R_\odot$. (b) Enlargement of a portion of (a). The coronal model (green field lines) was calculated by Török et al. (in preparation) in a non-rotating frame extending from 1 to 20 $R_\odot$. The heliospheric model (purple field lines) was calculated in an inertial frame with solar rotation included extending from 18 $R_\odot$ to 1.1 AU.
(A color version of this figure is available in the online journal.)

build the initial condition for the magnetic field through a potential field extrapolation using B_r at the lower boundary and prescribe the solar wind parameters starting from the values on the same surface. Figures 4(b) and 5(b) show magnetic field lines, in the meridional and equatorial plane, respectively. Then, we drive the heliospheric model with the series of boundary conditions extracted from the coronal model until relaxation. While the initial state of the heliospheric model is clearly different from that of the coronal model (compare Figure 4(a) with 4(b) and Figure 5(a) with 5(b)), the final states are for all purposes virtually indistinguishable (compare Figure 4(c) with Figure 4(d) and Figure 5(c) with Figure 5(d)).

Having relaxed the configuration, we insert an out-of-equilibrium TDM flux rope in the coronal model. As was the case in the non-rotating frame (see Figure 3(d)), a ring of current appears at $r \sim 7\,R_\odot$. The CME, which is formed by the expanding flux rope, propagates similarly outward. The coronal calculation is finally concluded 20 hr after triggering the eruption, resulting in the state shown in Figures 4(e) (meridional view) and 5(e) (equatorial view). As it appears in Figure 4(e), the CME occupies about 30° in the meridional plane, with current densities extending to approximately 60°. In the equatorial plane shown in Figure 5(e), the field lines of the CME appear to extend roughly over the same angle, implying a conical geometry for the whole structure. Then, using a sequence of boundary conditions extracted from the coronal model at intervals of 289 s as a driver at the $r = 20\,R_\odot$ surface, we advance the heliospheric model for 20 more hours. The injection of the flux rope and the current disturbance associated with it occur well below the $r = 20\,R_\odot$ boundary, as in the non-rotating case. The CME also propagates seamlessly through the $r = 20\,R_\odot$ boundary. The final state of the heliospheric model is shown in Figures 4(f) (meridional plane) and 5(f) (equatorial plane), which can be compared with Figures 4(e) and 5(e), respectively. As for the non-rotating case, all quantities calculated with the two models are in agreement to within 1%.

4. PROPAGATION OF A REALISTIC ICME

Having shown how the technique of coupled models successfully reproduces the results of a single domain calculation, we now present an advanced application of the heliospheric model by studying the propagation of an ICME from 18 $R_\odot$ to 1.1 AU in the inertial frame of reference. To achieve this goal, we use the results calculated by T. Török et al. (in preparation) to drive our model. Török et al. specified a more realistic plasma environment than that used in Section 3 by employing the full MHD thermodynamic model of Lionello et al. (2009). In a corotating frame of reference that neglected the effect of fictitious forces, Török et al. prescribed a potential, global dipole field together with a quadrupolar active region on the solar surface. After relaxing the configuration for about 60 hr, they inserted a TDM flux rope. Contrary to our simple and less realistic earlier approaches (Sections 3.1 and 3.2), their flux rope was inserted *in equilibrium* into the stabilizing ambient coronal field. Then, it was relaxed for another 13 hour period, during which cold and dense plasma accumulated in the flux rope, resembling the conditions observed in prominences. After that, they introduced converging flows near the polarity inversion line of the active region, which caused the field overlying the flux rope to expand quasi-statically, progressively reducing the magnetic tension. As a consequence, the flux rope rose slowly until a critical height was reached, at which point a loss of equilibrium and eruption occurred. A fast and powerful CME was formed, which rapidly accelerated to a speed of ~3,000 km s^{-1}, driven predominantly by strong reconnection below the erupting flux rope and producing a fast forward shock. The CME then rapidly slowed down to $\lesssim$1,000 km s^{-1} before it reached 3 $R_\odot$. The reasons for this significant deceleration are currently under investigation. Most likely they are related to the very strong reconnection flows ($\geqslant$10,000 km s^{-1}) that temporarily accelerated the flux rope to very large speeds. After the rapid deceleration, the CME slowed down only gradually and reached the outer coronal boundary at 20 $R_\odot$ with a speed of about 700–800 km s^{-1}. The simulation was stopped 74 hr after the insertion of the flux rope, enough for the CME to leave the coronal computational domain. Every 6 minutes, we extract from the simulation of Török et al. the magnetic field, velocity, density, and temperature on a spherical surface at 18 $R_\odot$, which is beyond the critical Alfvén and sonic points. We choose to start our simulation from 18 $R_\odot$ rather than 20 $R_\odot$ to allow overlap in the computational domains of the coronal and heliospheric model. Since the physical variables in the $18\,R_\odot \leqslant r \leqslant 20\,R_\odot$ region are directly calculated in either model, we are able to verify that no boundary effects arise in this more realistic simulation. We also estimate the importance of including rotation in the computation.

Using the first extracted set of fields at 18 $R_\odot$, we again specify a potential extrapolation as initial conditions for the magnetic field of the heliospheric model. We extrapolate radially

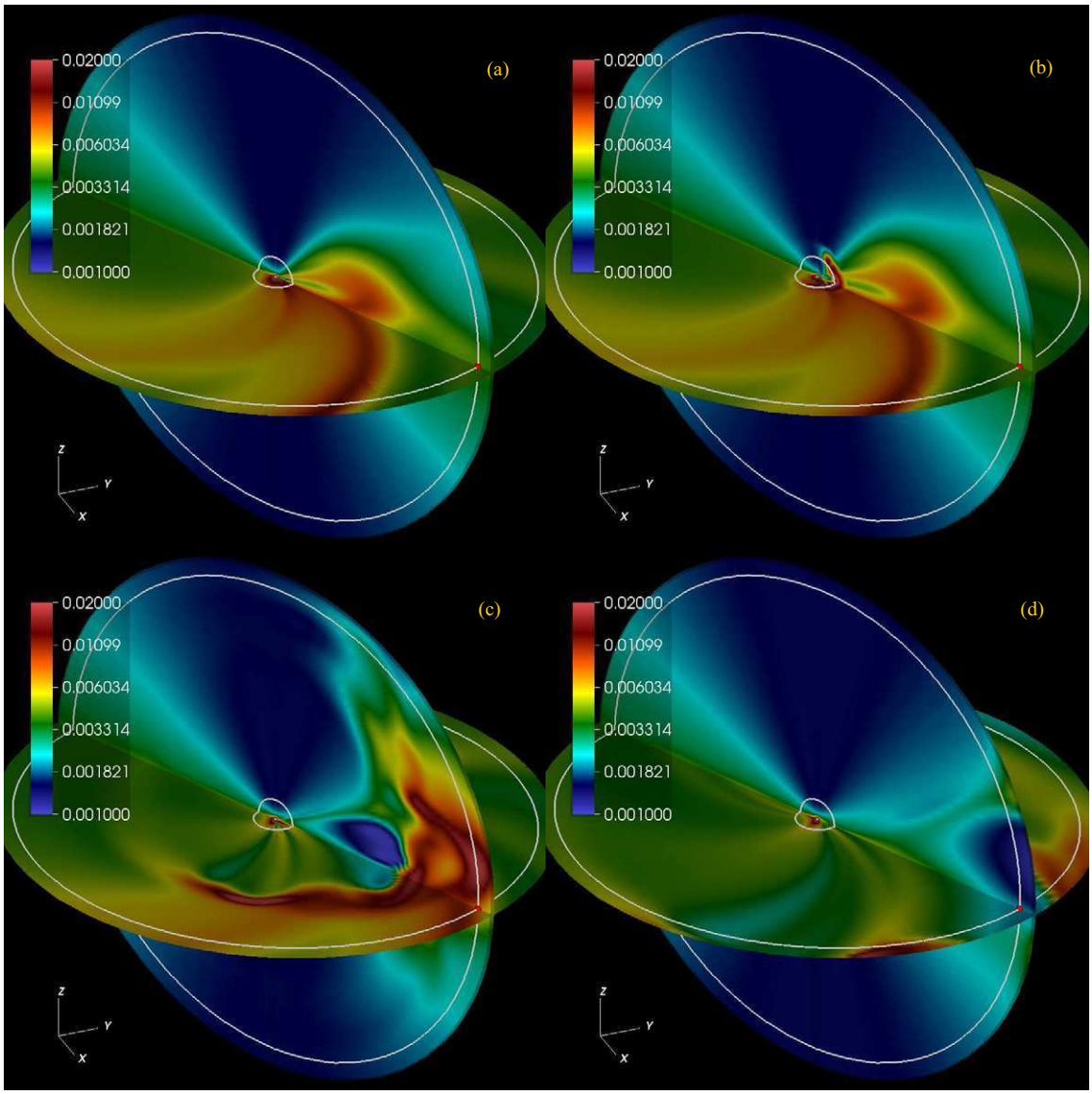

Figure 7. Evolution of the scaled density (ρr^2) in two cut-planes during the propagation of an ICME from Sun to Earth (red dot). The inner white circle lies at 20 $R_\odot$. The coronal part of the calculation is described in T. Török et al. (in preparation). (a) Configuration in steady state just before the eruption on the solar surface ($t = 402$ hr). (b) CME leaving the computational domain of the coronal model and entering the heliosphere ($t = 408$ hr). (c) ICME as it reaches Earth ($t = 458$ hr). (d) ICME leaving the computational domain of the heliospheric model. End of the calculation ($t = 502$ hr).

(A color version of this figure is available in the online journal.)

the values of v_r, ρ, and T to initialize the plasma properties, as described in the previous section. We then advance the MHD equations with fixed boundary values for 402 hr to ensure that a steady state solution is formed in the heliosphere. While in Török et al. the full thermodynamic treatment of the energy equation was employed, here we use the polytropic approximation, by setting $S = 0$ in Equation (5) and $\gamma = 1.5$ (Totten et al. 1996; Feldman et al. 1998). It has been shown that such an approximation is justified for heliospheric simulations (e.g., Riley et al. 2001a); however, in future simulations, we plan to explore the effect of including collisionless thermal conduction in the energy equation. The relaxed configuration of the magnetic field is shown in Figures 6(a) and (b). Both green (coronal) and purple (heliospheric) field lines are traced from 18 $R_\odot$. The Parker spiral is fully developed in the heliospheric calculation. Note that in the region between 18 and 20 $R_\odot$, there is a slight discrepancy between the coronal and heliospheric calculations, since the former neglects the effect of rotation.

In Figure 7(a), we show the distribution of ρr^2 in the heliosphere and corona at the end of the relaxation phase in the equatorial plane and in the meridional plane perpendicular to the Sun-Earth line. In the equatorial plane, streams characterized by higher or lower density are visible, forming the typical Parker spiral. At this point, we continue the simulation for 100 more hours, driving the lower boundary with the series of frames extracted from the simulation of Török et al. When this series is exhausted, we keep the last frame as a fixed boundary condition until $t = 502$ hr. During this second phase of the calculation, we follow the CME as it travels through the heliospheric computational domain and finally leaves through the outer boundary. At $t = 408$ hr, Figure 7(b) shows the CME as it crosses the outer boundary of the calculation of Török et al. A selection of field lines threading the CME are presented in Figure 8(b) and show the flux rope crossing into the heliospheric domain. The ICME continues to propagate in the heliosphere and at $t = 458$ hr arrives in the vicinity of

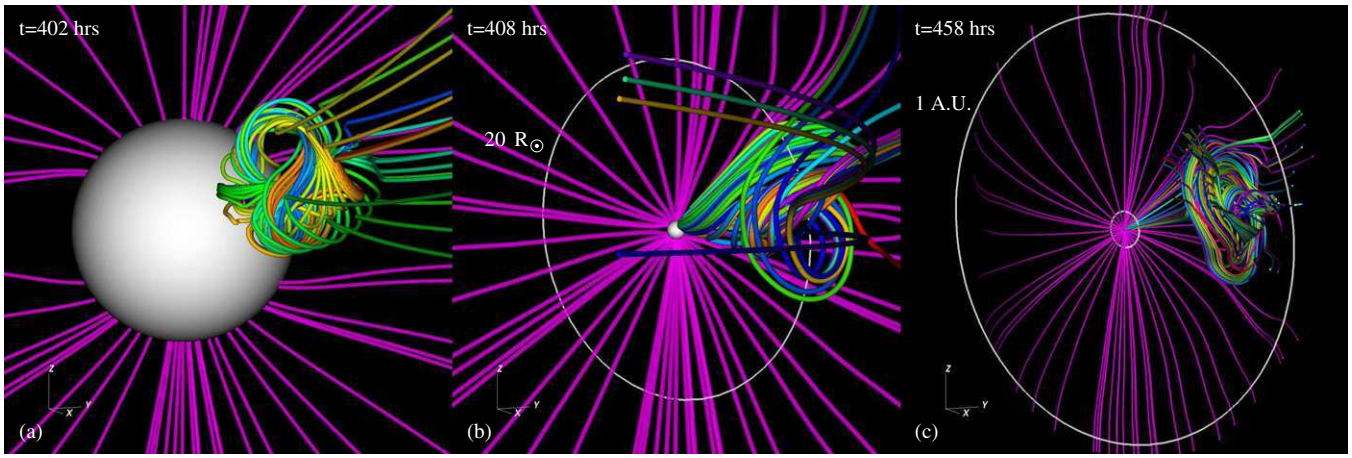

Figure 8. Magnetic field lines showing the propagation of a CME/ICME from Sun to Earth: (a) immediately after the eruption, (b) 6 hr after the eruption, the CME is crossing into the heliospheric domain, (c) 56 hr after the eruption, the ICME is about to reach Earth. The coronal part of the solution (below 20 $R_{\odot}$) was calculated by T. Török et al. (in preparation).

(A color version of this figure is available in the online journal.)

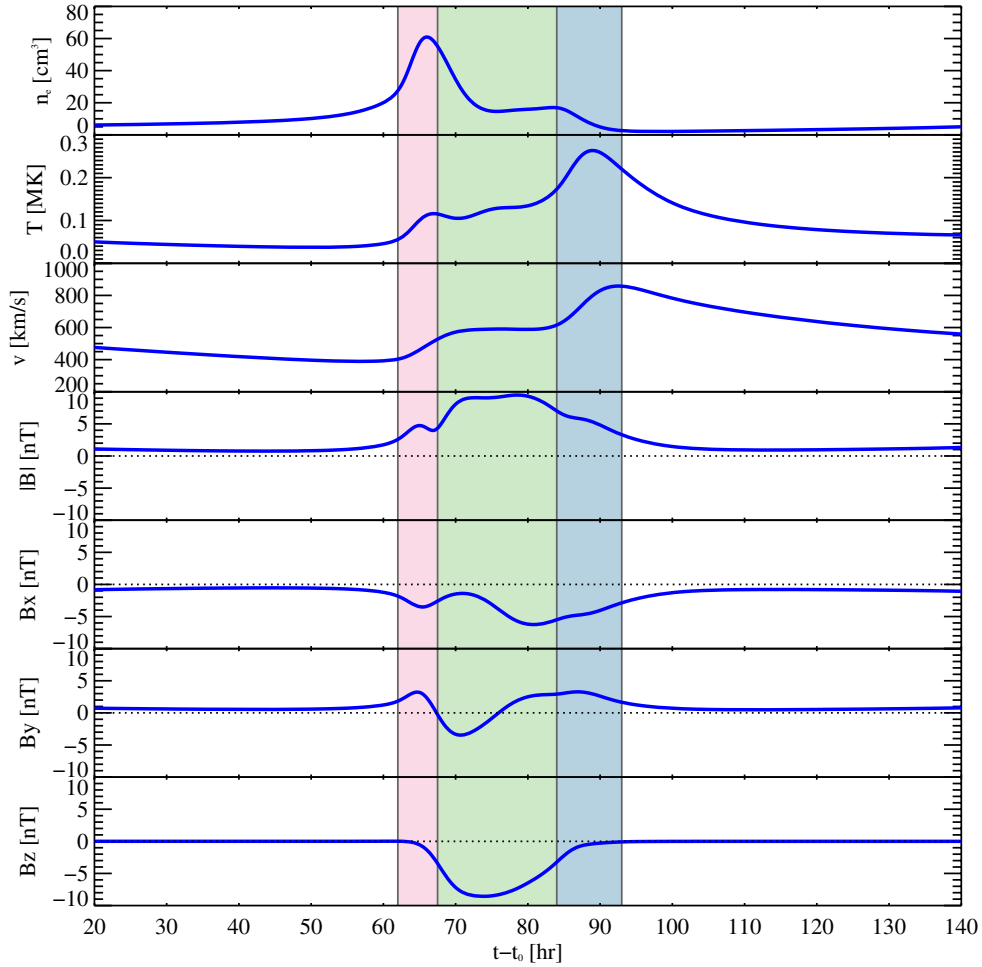

Figure 9. Time history of local plasma variables at 1AU for a point situated in the path of the ICME described in Section 4. The magnetic field vectors have been converted to GSE coordinates. The pink highlighted region indicates the compressed solar wind upstream of the ICME. The green region indicates the flux system of the ICME. The blue region indicates the trailing plasma, which was compressed by a high speed stream behind it. Time is in hours from the insertion of the CME in the calculation of T. Török et al. (in preparation; $t_0 = 402$ hr).

(A color version of this figure is available in the online journal.)

the Earth. Figure 7(c) shows the denser, enlarged structure of the ejecta followed by a depletion region, while Figure 8(c) shows the envelope of some field lines connected to the ICME. After passing by, the ICME crosses over the outer boundary and leaves the computational domain of the heliospheric model (Figure 7(d)). Since the ICME does not hit Earth directly, in Figure 9 we show the time history of the local plasma variable for an observer situated along its path. The magnetic field

components are expressed in Geocentric Solar Ecliptic (GSE) coordinates (Russell 1971). The low value of B within the ICME can be explained considering that our model active region has a field strength considerably smaller than in the source regions of the most powerful events that produce very fast CMEs ($\lesssim$1000 G versus $\gtrsim$2000 G). Thus, it is not surprising that the magnetic field at 1 AU is smaller than for typical fast events. Also, most of the interaction of the flux rope with the ambient magnetic field has already occurred in the coronal solution. Starting from 40 hr after the eruption ($t = 442$ hr), the density of the plasma begins to increase as it is swept by the ICME. The density reaches a maximum of 10 times the base value (the area shaded in pink in Figure 9). Then, the observer is overtaken by the flux system and the magnetic field exhibits a typical pattern of rotation (green area). Finally, trailing the ICME, there is region of fast solar wind that compresses the plasma (blue area). These features, which are beyond the scope of this article, are described in more detail in P. Riley et al. (in preparation).

5. CONCLUSIONS

We have shown how our computational MHD model of the heliosphere is capable of following the propagation of ICMEs from beyond the critical point to Earth. The key feature of our model is its flexibility. It can in principle accept as input at the lower boundary time-dependent results obtained from (1) MHD simulations of the solar corona, (2) Potential-Field Source-Surface (PFSS) models, (3) empirical models, (4) observations, or (5) a combination thereof. Moreover, the frame of reference from which the lower-boundary data are extracted can be either the inertial frame or the corotating frame. If the coronal model is calculated in the corotating frame, the inertial forces can either be included or neglected. The heliospheric computation itself can be either performed in the inertial or in the corotating frame. Particular care has been taken in the interpolation of the input magnetic field at the boundary to avoid the formation of spurious current layers. To demonstrate the capabilities of our model, we have presented three simulations. In the first two, we used our coronal MHD model to simulate a CME eruption from the solar surface to 50 $R_\odot$, in a fixed and a corotating frame, respectively. From these two simulations, we extracted the data at $r = 20\ R_\odot$ and used them to drive our model. In either case, the agreement between the coronal and the heliospheric models in the common portion of the computational domain was remarkable. Disturbances propagated smoothly across the lower surface and no boundary layer was formed. We also presented a third, more realistic, simulation driven by data extracted from the coronal model of a CME described by T. Török et al. (in preparation). This is a fast and powerful CME originating from a source region of approximately 3 kG. We have shown that our model is able to follow the propagation of the CME from 18 $R_\odot$ to 1.1 AU.

Our newly developed heliospheric model is not restricted to event studies of CME eruption and subsequent ICME propagation. It can also be used to model the heliosphere and the solar wind from a variety of inputs. Magnetic flux evolution models are ever more frequently used to create coronal models, either through MHD or PFSS extrapolations (for a review, see Mackay & Yeates 2012). These can be extended to study the structure of the heliosphere or, more easily, they can provide input to our heliospheric model. Computationally, it is less intense to update the boundaries of the heliospheric model when the coronal model is updated, rather than using a single model encompassing both physical regions.

This work was supported by NASA through the LWS, HTP, and SBIR programs, and by NSF through the Center for Integrated Space Weather Modeling (CISM) and Frontiers in Earth System Dynamics (FESD) program. Computational resources were provided by the NSF supported Texas Advanced computing Center (TACC) in Austin and the NASA Advanced Supercomputing Division (NAS) at Ames Research Center.

REFERENCES

Arge, C. N., & Pizzo, V. J. 2000, JGR, 105, 10465
Burlaga, L. F., Behannon, K. W., & Klein, L. W. 1987, JGR, 92, 5725
Burlaga, L. F., Klein, L., Sheeley, N. R., Jr., et al. 1982, GeoRL, 9, 1317
Feldman, W. C., Barraclough, B. L., Gosling, J. T., et al. 1998, JGR, 103, 14547
Feng, X., Yang, L., Xiang, C., et al. 2010, ApJ, 723, 300
Gosling, J. T. 1990, in Washington DC American Geophysical Union Geophysical Monograph Series, Vol. 58, Washington DC American Geophysical Union Geophysical Monograph Series, ed. C. T. Russell, E. R. Priest, & L. C. Lee (Washington, DC: AGU), 343
Gosling, J. T., McComas, D. J., Phillips, J. L., & Bame, S. J. 1991, JGR, 96, 7831
Groth, C. P. T., De Zeeuw, D. L., Gombosi, T. I., & Powell, K. G. 2000, JGR, 105, 25053
Hayashi, K. 2012, JGRA, 117, 8105
Jeffrey, A. 1966, Magnetohydrodynamics, University Mathematical Texts (Edinburgh: Oliver & Boyd)
Kleimann, J. 2012, SoPh, 281, 353
Kunow, H., Crooker, N. U., Linker, J. A., Schwenn, R., & von Steiger, R. 2006, Coronal Mass Ejections (Berlin: Springer-Verlag)
Linker, J. A., Mikić, Z., Lionello, R., et al. 2003, PhPl, 10, 1971
Lionello, R., Linker, J. A., & Mikić, Z. 2009, ApJ, 690, 902
Lionello, R., Mikić, Z., & Linker, J. A. 1999, JCoPh, 152, 346
Lionello, R., Mikić, Z., & Schnack, D. D. 1998, JCoPh, 140, 10
Lugaz, N., Downs, C., Shibata, K., et al. 2011, ApJ, 738, 127
Lugaz, N., Manchester, W. B., IV, Roussev, I. I., Tóth, G., & Gombosi, T. I. 2007, ApJ, 659, 788
Mackay, D., & Yeates, A. 2012, LRSP, 9, 6
Manchester, W. B., Ridley, A. J., Gombosi, T. I., & Dezeeuw, D. L. 2006, AdSpR, 38, 253
Manchester, W. B., IV, Vourlidas, A., Tóth, G., et al. 2008, ApJ, 684, 1448
Merkin, V. G., Lyon, J. G., McGregor, S. L., & Pahud, D. M. 2011, GeoRL, 38, 14107
Mikić, Z., Linker, J. A., Schnack, D. D., Lionello, R., & Tarditi, A. 1999, PhPl, 6, 2217
Odstrcil, D., Linker, J. A., Lionello, R., et al. 2002, JGRA, 107, 1493
Odstrcil, D., Pizzo, V. J., & Arge, C. N. 2005, JGRA, 110, 2106
Odstrcil, D., Pizzo, V. J., Arge, C. N., et al. 2008, in ASP Conf. Ser. 385, Numerical Modeling of Space Plasma Flows, ed. N. V. Pogorelov, E. Audit, & G. P. Zank (San Francisco, CA: ASP), 167
Odstrcil, D., Riley, P., Linker, J. A., et al. 2003, in ESA Special Publication, Vol. 535, Solar Variability as an Input to the Earth's Environment, ed. A. Wilson (Noordwijk: ESA), 541
Odstrcil, D., Riley, P., & Zhao, X. P. 2004, JGRA, 109, 2116
Riley, P., Gosling, J. T., & Pizzo, V. J. 2001a, JGR, 106, 8291
Riley, P., Linker, J. A., & Mikić, Z. 2001b, JGR, 106, 15889
Riley, P., Linker, J. A., Mikić, Z., et al. 2003, JGRA, 108, 1272
Riley, P., Schatzman, C., Cane, H. V., Richardson, I. G., & Gopalswamy, N. 2006, ApJ, 647, 648
Russell, C. T. 1971, CosEl, 2, 184
Titov, V. S., & Démoulin, P. 1999, A&A, 351, 707
Tóth, G., de Zeeuw, D. L., Gombosi, T. I., et al. 2007, SpWea, 5, 6003
Tóth, G., Sokolov, I. V., Gombosi, T. I., et al. 2005, JGRA, 110, 12226
Tóth, G., van der Holst, B., Sokolov, I. V., et al. 2012, JCoPh, 231, 870
Totten, T. L., Freeman, J. W., & Arya, S. 1996, JGR, 101, 15629
Usmanov, A. V., & Dryer, M. 1995, SoPh, 159, 347
Usmanov, A. V., & Goldstein, M. L. 2006, JGRA, 111, 7101
Vourlidas, A., Lynch, B. J., Howard, R. A., & Li, Y. 2013, SoPh, 284, 179
Wang, Y.-M., & Sheeley, N. R. 1995, ApJL, 447, L143
Wang, Y. M., Wang, S., & Ye, P. Z. 2002, SoPh, 211, 333
Wang, Y. M., Ye, P. Z., & Wang, S. 2003, JGRA, 108, 1370
Wu, S. T., Guo, W. P., Michels, D. J., & Burlaga, L. F. 1999, JGR, 104, 14789
Zhao, X. P., Plunkett, S. P., & Liu, W. 2002, JGRA, 107, 1223

The Astrophysical Journal, 761:25 (11pp), 2012 December 10 doi:10.1088/0004-637X/761/1/25

A MULTI-SPACECRAFT VIEW OF A GIANT FILAMENT ERUPTION DURING 2009 SEPTEMBER 26/27

Sanjay Gosain[1], Brigitte Schmieder[2], Guy Artzner[3], Sergei Bogachev[4], and Tibor Török[5]
[1] National Solar Observatory, 950 N. Cherry Avenue, Tucson, AZ 85719, USA
[2] LESIA, Observatoire de Paris, CNRS, UPMC, Université Paris Diderot, 5 Place Jules Janssen, F-92190 Meudon, France
[3] CNRS UMR 8617, Institut d'astrophysique Spatiale (IAS), F-91405 Orsay Cedex, France
[4] Lebedev Physical Institute of Russian Academy of Science, Leninskij prospekt 53, Moscow 119991, Russia
[5] Predictive Science, Inc., 9990 Mesa Rim Rd., Suite 170, San Diego, CA 92121, USA
Received 2012 June 25; accepted 2012 October 18; published 2012 November 20

ABSTRACT

We analyze multi-spacecraft observations of a giant filament eruption that occurred during 2009 September 26 and 27. The filament eruption was associated with a relatively slow coronal mass ejection. The filament consisted of a large and a small part, and both parts erupted nearly simultaneously. Here we focus on the eruption associated with the larger part of the filament. The *STEREO* satellites were separated by about 117° during this event, so we additionally used *SoHO*/EIT and CORONAS/TESIS observations as a third eye (Earth view) to aid our measurements. We measure the plane-of-sky trajectory of the filament as seen from *STEREO-A* and TESIS viewpoints. Using a simple trigonometric relation, we then use these measurements to estimate the true direction of propagation of the filament which allows us to derive the true $R/R_{\odot}$-time profile of the filament apex. Furthermore, we develop a new tomographic method that can potentially provide a more robust three-dimensional (3D) reconstruction by exploiting multiple simultaneous views. We apply this method also to investigate the 3D evolution of the top part of filament. We expect this method to be useful when *SDO* and *STEREO* observations are combined. We then analyze the kinematics of the eruptive filament during its rapid acceleration phase by fitting different functional forms to the height-time data derived from the two methods. We find that for both methods an exponential function fits the rise profile of the filament slightly better than parabolic or cubic functions. Finally, we confront these results with the predictions of theoretical eruption models.

Key words: Sun: activity – Sun: coronal mass ejections (CMEs) – Sun: filaments, prominences

Online-only material: animations, color figures

1. INTRODUCTION

Coronal mass ejections (CMEs) are huge expulsions of plasma and magnetic field from the solar corona into interplanetary space. They are often accompanied by the eruption of a filament or prominence, which becomes visible as the core of the CME in coronagraph observations, and by a flare that occurs almost simultaneously with the eruption. It is now well accepted that these three phenomena are different observational manifestations of a more general process, namely a local disruption of the coronal magnetic field (e.g., Forbes 2000). The detailed mechanisms that trigger and drive such disruptions are, however, still controversial, and a large number of theoretical models have been put forward in the past decades (for recent reviews, see Amari & Aly 2009; Aulanier et al. 2010; Forbes 2010).

Early observations indicated that there are two distinct classes of CMEs, namely fast (or impulsive) ones, originating in active regions and associated with flares, and slow (or gradual) ones, associated with large prominence eruptions outside of active regions and no, or no significant, flaring (MacQueen & Fisher 1983; Sheeley et al. 1999). Consequently, it has been suggested that different eruption mechanisms may be at work in these two types of eruptions. However, the analysis of considerably larger data sets in the *SoHO* era revealed a continuous distribution of CME velocities with a single peak (e.g., Zhang & Dere 2006), indicating that both fast and slow CMEs are driven by the same physical mechanism(s). This is supported by the considerable range of CME kinematics that could be modeled based on a single physical mechanism (Chen & Krall 2003; Török & Kliem 2007), as well as by the fact that large prominence eruptions outside active regions can produce loops and ribbons that are morphologically similar to those seen in flare-related CMEs. The majority of prominence-related CMEs are most likely not associated with flares simply because the magnetic fields in their source regions are too weak to produce significant emission in Hα and in EUV wavelengths (see, e.g., Forbes 2000).

Virtually all theoretical models describe CMEs as coronal magnetic flux ropes that are anchored in the dense photosphere (see, e.g., Gibson et al. 2006), although it is debated whether a flux rope is present in the corona prior to an eruption or is formed during the eruption process. The expulsion of a flux rope into interplanetary space as a CME has been explained by, e.g., the continuous increase of poloidal flux in the rope due to flux injection from the convection zone into the corona (e.g., Chen & Krall 2003), by ideal MHD instabilities like the helical kink instability (Fan 2005; Török & Kliem 2005) or the torus instability (Kliem & Török 2006), or by the combination of a "loss of equilibrium" of a flux rope and magnetic reconnection occurring in its wake (e.g., Forbes & Isenberg 1991). Other models invoke reconnection from the beginning of the eruption, as for example the "tether cutting" (e.g., Moore et al. 2001) and "magnetic breakout" (e.g., Antiochos et al. 1999) models.

Using observations to support or reject specific models for a particular eruption is difficult for several reasons. First, many models employ more than one physical mechanism, resulting in a partial overlap between them (see Aulanier et al. 2010). Second, several distinct mechanisms may occur almost simultaneously in an eruption, in particular in complex events, making it difficult to establish which one is the main driver of the

eruption (e.g., Williams et al. 2005). Third, the models predict a very similar evolution for the main phase of an eruption, i.e., for the evolution after the impulsive flare phase and initial rapid acceleration of the ejecta. When looking for clues for possible eruption mechanisms, one therefore often focuses on the early eruption phase, for example, on the morphology and timing of pre-flare Hα and EUV brightening (e.g., Chandra et al. 2011). For eruptions associated with large quiescent prominences, as the one studied in this paper, such signatures are, however, often not available.

Another possibility to obtain information about the mechanisms at work in an eruption is to study its kinematic properties, in particular the early rise phase (Schrijver et al. 2008). Eruptions typically start with the slow rise of a filament or prominence and/or overlying loops, at an approximately constant velocity of a few km s^{-1}, which is followed by the rapid acceleration of the ejecta to several 100 km s^{-1}. The acceleration should initially follow some functional dependence, but will then saturate and decrease afterward (see, e.g., Figure 3 in Gallagher et al. 2003). Profiles of the initial acceleration phase, if extractable from measured height-time data with sufficient coverage, can be compared with predictions of theoretical eruption models.

Observed rise profiles of the early phase of filament eruptions and CMEs have been fitted by constant-acceleration curves (e.g., Gilbert et al. 2000; Kundu et al. 2004; Chifor et al. 2006), power-law, $h(t) \propto t^m$, with $3.0 \lesssim m \lesssim 3.7$ (e.g., Alexander et al. 2002; Schrijver et al. 2008; Liu et al. 2009), and exponential functions (Gallagher et al. 2003; Williams et al. 2005). As for theoretical models, the functional dependence of eruption trajectories has not often yet been reported, and systematic investigations of its parameter dependence are quite rare so far. Still, some model predictions can be inferred from the literature. For example, an exponential early rise is naturally expected if an eruption is initially driven by an ideal MHD instability (e.g., Török et al. 2004). A power-law dependence with $m = 2.5$ has been found for the trajectory in a two-dimensional (2D) version of the loss of equilibrium model (Priest & Forbes 2002), and a parabolic rise (i.e., constant acceleration) was reported for a simulation of the breakout model (Lynch et al. 2004). Furthermore, Schrijver et al. (2008) showed that a velocity perturbation at the onset of the rapid acceleration of an eruption can change the resulting functional dependence of the trajectory (from exponential to near-cubic for the case of the torus instability they studied), given that this perturbation is sufficiently large (somewhat larger than typical velocities observed during the initial slow rise phase of an eruption). We refer to Schrijver et al. (2008) for further details.

Prominence eruptions and CMEs have been observed for a long time with various ground- and space-based instrument. For example, the LASCO coronagraphs (Brueckner et al. 1995) on board the *SoHO* spacecraft have been observing thousands of CMEs in white light. However, one of the limitations of LASCO, and of other instruments that are located at or close to Earth, is that they can only obtain 2D observations, projected onto the plane of sky (POS). Height-time data of eruptions are particularly hampered by this, since obtaining the correct radial rise velocities requires the knowledge of the true three-dimensional (3D) trajectories.

The *STEREO* mission (Kaiser et al. 2008) was launched during the solar minimum and therefore initial studies were of quiescent filament eruptions (Gosain et al. 2009; Artzner et al. 2010; Gosain & Schmieder 2010). With *STEREO* 3D reconstructions, it is, in principle, possible to derive the shape of the prominence, its twist or writhe, and its true trajectory when it erupts. These properties can be useful for comparisons with model predictions (e.g., Török et al. 2010; Kliem et al. 2012; Zuccarello et al. 2012). Other case studies of quiescent filament eruptions observed with *STEREO* are reviewed in Bemporad (2011) and Aschwanden (2011) and those of CMEs in Mierla et al. (2010).

The main difficulty in stereoscopic reconstruction arises when the separation angle between the two *STEREO* satellites is large, because then it becomes difficult to identify the same feature in both views unambiguously (Thompson et al. 2012). In such cases one has to use complementary observations from other instruments, such as *SoHO*/EIT (Delaboudinière et al. 1995), CORONAS/TESIS (Kuzin et al. 2009), and now *SDO*/AIA (Lemen et al. 2012). The addition of the Earth view to *STEREO* views makes life easier as it provides us (1) more than one stereoscopic pair, and (2) smaller separation angles. Also, in a special circumstance when a structure (filament/prominence) is not visible in one of the *STEREO* satellites (e.g., remains hidden behind the limb during initial rising phases), adding an Earth view to one of the *STEREO* satellites allows us to make stereoscopic reconstruction. Some recent examples where three views have been used are Li et al. (2011) and Feng et al. (2012).

In this paper we will present such an example. We present He II 304 Å observations of a large filament eruption that occurred during 2009 September 26–27. The observations were taken from the twin *STEREO* satellites and were combined with complementary observations from *SoHO*/EIT and CORONAS/TESIS, giving us a third view, i.e., the Earth view of the event. The filament eruption was seen as a limb event by *STEREO-A*, EIT, and TESIS, while it was seen as an on-disk event by *STEREO-B*.

Based on these multi-spacecraft data, we derive the $R/R_\odot$ or simply height-time profile of the erupting prominence by different methods. First, we independently derive the POS height-time profiles of the prominence top as viewed from *STEREO-A* and TESIS. Second, we apply a trigonometric relation to simultaneous *STEREO-A* and EIT observation of the prominence and estimate the propagation direction of the filament. Knowing the propagation direction we can derive true height-time profile of the filament top. Finally, we apply a 3D stereoscopic reconstruction method based on Marinus projections to derive the height-time profile, we call this method "tomographic method" as it can use simultaneous multiple views for reconstruction. We then fit these height-time profiles by functional forms, viz., parabolic, exponential, and cubic and compare the results.

The paper is organized as follows. Section 2 summarizes the observations. In Sections 3 and 4 we describe the trigonometric and tomographic methods, respectively, results derived from these methods. Finally, we discuss the results as well as the potential of the newly developed tomographic method.

2. OBSERVATIONS AND METHOD OF DATA ANALYSIS

2.1. He II 304 Å Filament Observations

During 2009 September 26–27 a large filament eruption was observed near the northeast solar limb. The observations were obtained in the He II 304 Å wavelength at a cadence of ten minutes by the SECCHI/EUVI instrument aboard the *STEREO-A* and *B* satellites. Figure 1 (top panel) shows on-disk observations by *STEREO-B* during the early phase of the eruption. Two filaments can be seen, a long one (LF) located

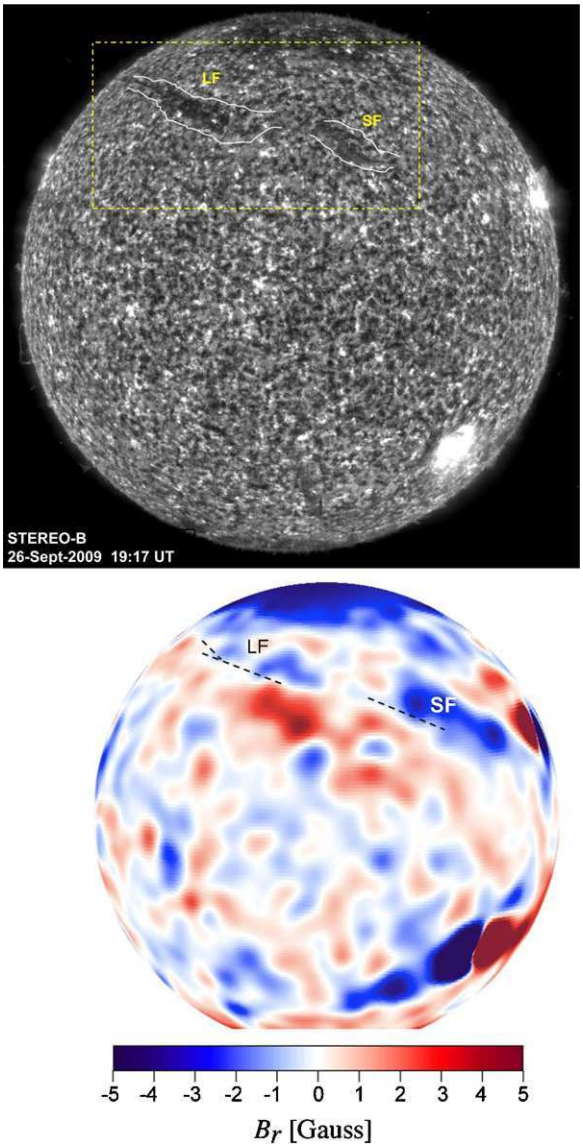

Figure 1. Top panel shows the He 304 Å filtergram observed from *STEREO-B* at 19:17 UT on 2009 September 26. LF and SF mark the large and the small filament (highlighted inside yellow rectangle, outlined by white line segments for clarity), respectively. The bottom panel shows a map of the radial magnetic field component, reconstructed from a synoptic MDI magnetogram, as *STEREO-B* would have seen it at the same time (courtesy of Z. Mikić). The dashed lines indicate the polarity inversion line above which the filaments are located.

(Animations and color version of this figure are available in the online journal.)

at 23°–34° N, and a short one (SF) located at 18°–32° N. The bottom panel shows a reconstruction of the photospheric magnetic field distribution as it would have been seen from *STEREO-B* (at 19:17 UT on 2009 September 26, using $B_0 = 5.^{\circ}54$ and CML $= 164.^{\circ}4$, where B_0 and CML are the Carrington coordinates of the disk center in the *STEREO-B* view). It can be seen that both filaments follow the same polarity inversion line (PIL), suggesting that they were both located within an extended filament channel. The magnetic field on either side of the PIL was weak (+/−3 G). In the limb view of *STEREO-A*, LF starts to rise earlier than SF (see movie 1), while both eruptions seem to occur simultaneously in the disk view of *STEREO-B* (movie 2). Since LF is much more prominent than SF, in this paper we focus on the evolution of LF and refer to Li et al. (2010) for further details on the eruption of SF. In the following, "filament" or "prominence" therefore refers only to LF.

During this event, the *STEREO* satellites were separated by about 117° and the main part of the filament was hidden behind the solar limb in the *STEREO-A* viewpoint until about 18:20 UT on 2009 September 26. A 3D stereoscopic reconstruction in combination with *STEREO-A* before 18:20 UT was therefore not possible from either *STEREO-B* or Earth view (EIT and TESIS). He II 304 Å images from *SoHO*/EIT at a cadence of 6 hr and CORONAS/TESIS images at a cadence of ten minutes provide the Earth view, which are used for 3D reconstruction with *STEREO-A* after 18:20 UT September 26 using the tomographic method described in Section 3.3. The He II 304 Å images of the filament from the four instruments are shown in Figure 2. The Earth–Sun–*STEREO-A* and Earth–Sun–*STEREO-B* angles on 2009 September 26 were 61° and 56°, respectively. The observations of the filament top from two different vantage points (TESIS and *STEREO-A*) allows us to observe the POS evolution in a piecewise continuous manner from TESIS (00:00 to 22:00 UT) and *STEREO-A* (19:10 to 23:10 UT), as shown in Figure 6 (top left panel). A simple trigonometric method, described in Section 3.2, is used to triangulate the true propagation direction of the filament apex. Knowing this angle, the POS height-time profiles are corrected to derive the true height-time profiles as shown in Figure 6 (bottom left panel).

The filament LF (as seen from *STEREO-A*; Figure 3) suggests a sheet-like morphology. The stereoscopic reconstruction by Li et al. (2010, see their Figure 2) also infers a sheet-like structure. We outline its apparent edges by dashed (red) and dotted (yellow) lines in *STEREO-A* and *B* views. A careful inspection of the legs of the prominence in *STEREO-A* images suggests a twisted morphology of the legs. However, a quantification of the twist of the filament sheet is not possible in the present case.

2.2. CME Observations

STEREO-A observed the CME associated with the filament eruption on 2009 September 26/27 with its coronagraphs, COR1 (1.4–4 $R_{\odot}$) and COR2 (2.5–15 $R_{\odot}$). The CME was not seen by *STEREO-B* since it was directed toward it and was perhaps too faint to be seen as a halo CME. The LASCO/C2 (1.5–6 $R_{\odot}$) and C3 (3.7–30 $R_{\odot}$) coronagraphs also observed the CME. The time of arrival of CME in C2 was 23:06 UT on September 26, in C3 was 14:18 UT on September 27, and in HI1 was on 21:29 UT on September 27.

The propagation angle of the CME leading edge is derived using the same procedure as described in Section 3.2 and applied to filament apex. The projection correction to the POS height-time profiles of the CME (top right panel of Figure 6) is then applied to derive the true height-time profiles (bottom right panel of Figure 6).

3. HEIGHT-TIME PROFILE OF ERUPTING FILAMENT AND CME

3.1. Plane-of-sky Measurements

We make POS measurements of the filament apex (marked by the "+" symbol in the panels of Figure 2) using TESIS and *STEREO-A* observations. The $R_{\rm POS}/R_{\odot}$ profile of the filament apex measured from the two views (from *STEREO-A* and TESIS) is plotted in the top left panel of Figure 6. Similarly, the top right panel of Figure 6 shows the $R_{\rm POS}/R_{\odot}$ profile of the leading edge of the CME measured with *STEREO-A* and LASCO coronagraph observations. The difference in the

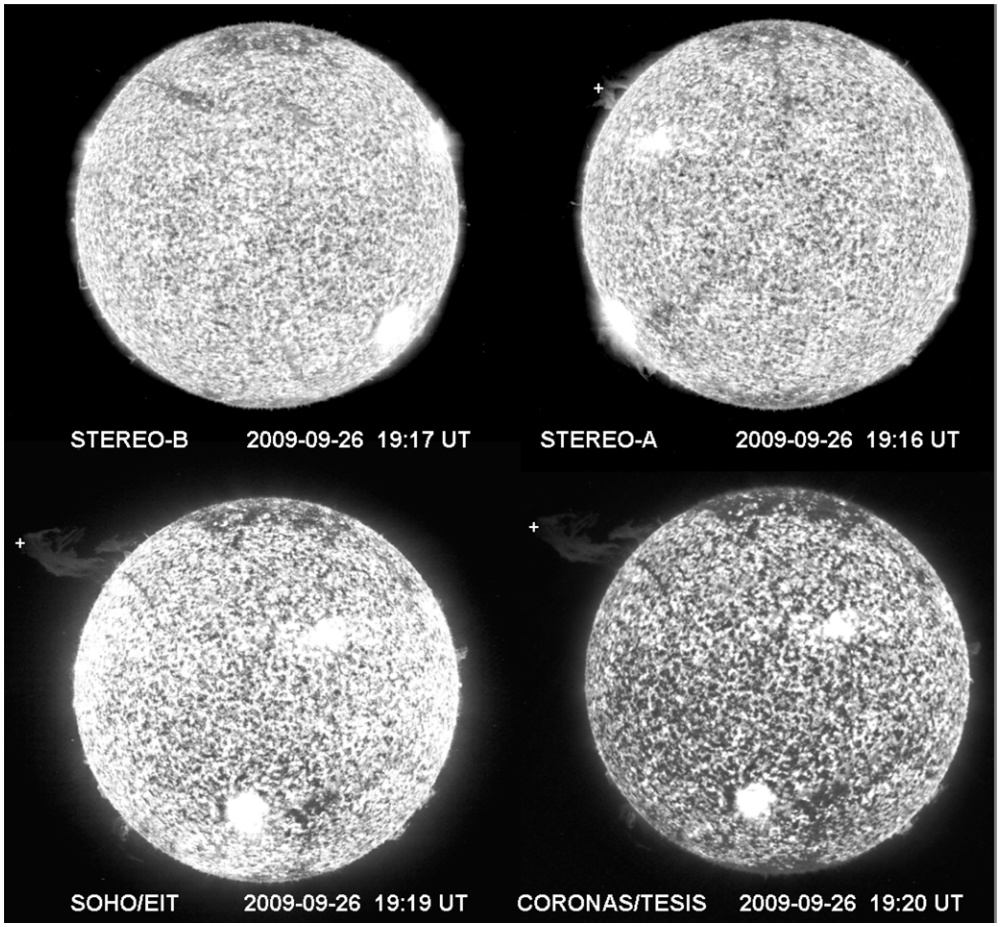

Figure 2. Four different views on the erupting filament in He II 304 Å. The top panel shows the *STEREO-Behind* (left) and *STEREO-Ahead* (right) views. The bottom panel shows the Earth views by *SoHO*/EIT (left) and CORONAS/TESIS (right).

$R_{\rm POS}/R_\odot$ profiles of the filament apex and CME leading edge as seen by different satellites is apparent, since the measurements correspond to two different vantage points.

3.2. Estimation of the True Height-time Profile using Simple Triangulation

The POS measurements, $R_{\rm POS}/R_\odot$, of the filament apex and the CME leading edge, described above, can be corrected for projection effect if we know the angle between the real trajectory of the erupting feature and the POS in the observer's frame of reference. The true $R/R_\odot$ profile is related to the $R_{\rm POS}/R_\odot$ profile, measured in the POS, by $(R/R_\odot)\cos\theta = R_{\rm POS}/R_\odot$, where θ is the angle between the real trajectory and the POS, referred to as propagation angle henceforth.

Here we apply a simple trigonometric relation, using image pairs from *STEREO-A* and TESIS/EIT (henceforth, Earth view or EV), to estimate the propagation angle. We then use this information to derive the true $R/R_\odot$ profile of the erupting filament and the CME. A simple assumption made here is that the propagation angle remains unchanged during the time of the measurements. We verified this assumption by computing the propagation angle using *STEREO-A* and TESIS pair at later times and found that the angle remains the same (see Table 1).

We explain the trigonometric procedure here briefly. The illustration in Figure 4 shows the geometric setting of the two *STEREO* satellites and the EV with respect to the filament. The projected height of the top part of the filament is h_a and h_b in the POS of *STEREO-A* and EV, respectively. S is the separation angle between *STEREO-A* and EV (61°), and α and β are the angles that the top of the filament apex (trajectory) makes with respect to the POS. We obtain the angles using the relations $S = \alpha + \beta$ and $h_a/h_b = \cos(\alpha)/\cos(S-\alpha)$. Knowing these angles, we can apply corrections to the POS heights h_a and h_b to obtain the true height $h_{\rm True} = h_a/\cos(\alpha) = h_b/\cos(\beta)$.

Figure 5 shows an example of two stereoscopic image pairs, i.e., *STEREO-A* (left panel) and EIT (right panel), observed almost simultaneously. The two images are in epipolar view. The segments h_a and h_b measure the top part of the filament as viewed from two vantage points. Knowing h_a, h_b, and S, we determine α and β to be 41°and 20°, respectively. Since only one stereoscopic pair is available between *SoHO*/EIT and

Table 1
Propagation Direction using Simple Triangulation and Marinus Method

TESIS	*STEREO-A*	$\angle\alpha$[a]	$\angle\beta$[a]	Latitude[b]	Longitude[b]
20:16 UT	20:16 UT	41°	20°	28°	148°
20:24 UT	20:26 UT	41°	20°	28°	148°
20:48 UT	20:46 UT	41°	20°	27°	149°
20:56 UT	20:56 UT	41°	20°	25°	149°
21:04 UT	21:06 UT	41°	20°	25°	149°
21:59 UT	21:56 UT	40°	21°	21°	152°
22:15 UT	22:16 UT	40°	21°	19°	152°

Notes.
[a] Angles α and β measured by simple triangulation method.
[b] Carrington latitude and longitude using Marinus method.

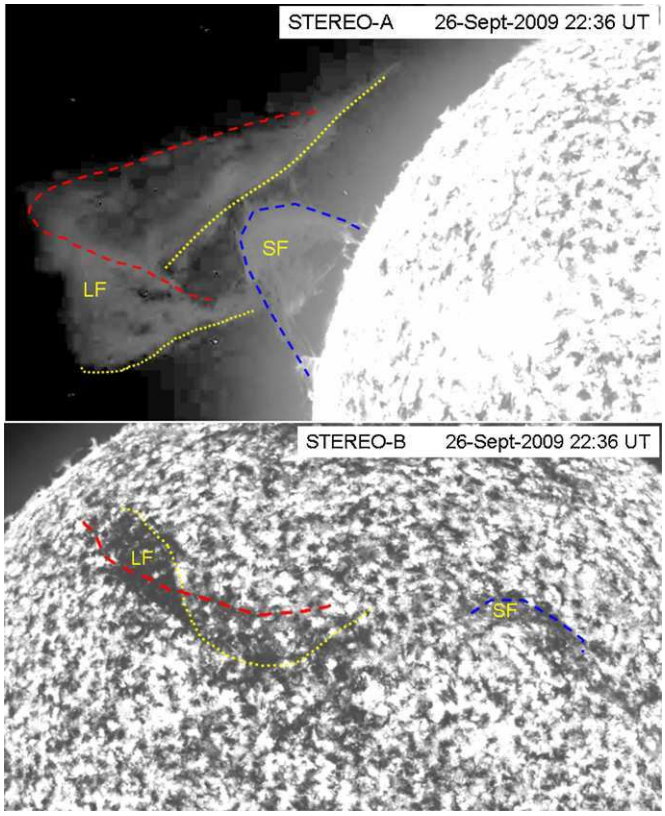

Figure 3. *STEREO-A* (top) and *B* (bottom) images of the eruptive filament (LF and SF) are shown. The edges of the filament sheet (LF) are outlined by dashed (red) and dotted (yellow) lines. The sheet appears to be twisted along its legs.
(A color version of this figure is available in the online journal.)

STEREO-A, we make use of TESIS data to make pairs with *STEREO-A*. The observations of *STEREO-A* and TESIS are not synchronized in time and both instruments follow a different time cadence (see Table 1). Assuming that the filament did not evolve significantly within the small time differences, we could make eight near-simultaneous stereoscopic pairs of TESIS and *STEREO-A*. The timings of these pairs and the value of angles α and β deduced using these pairs are given in Table 1. It may be noticed that during the observed time interval the propagation angle does not change and therefore it is possible to correct the observed POS height-time profiles for propagation angle using the single value of α and β. In Section 3.3.3 we show that these values are consistent with other 3D reconstruction methods. The corrected height-time profile of the filament apex is shown in the lower left panel of Figure 6.

Similarly, applying this method to the CME leading edge we deduce angles α and β to be 36°and 25°, respectively. The true height-time profile of CME leading edge after correcting for these angles is shown in the lower right panel of Figure 6. It is interesting to note that the direction of propagation of the filament apex and the CME leading edge differs by about 5°. The filament typically forms a core in the three part CME structure. However, since the CME leading edge is more extended, i.e., the front surface of a tear-drop shaped bubble in which filament forms a trailing part, the difference of 5°is small considering the large angular extent of the filament and the associated CME. Another interesting point about this method is that the two curves merge into one (as seen in the combined curves in lower panels) only for a unique pair of α and β angles, where the sum of the two angles ($S = \alpha + \beta$, in this case equal to separation between Earth and *STEREO-A*, i.e., 61°.5) is well constrained by the known separation angle between the two vantage points. For any other pair of these angles the two curves did not merge into one. Thus, just by knowing the separation angle between two vantage points and the respective POS height-time profiles, one can iteratively adjust the angles (in fact only one of the angles, as the two angles α and β are simply α and $S - \alpha$), until the two curves merge as one. This procedure also gives the same solution for α and β. These true height-time profiles are then used for deriving the velocity and acceleration profiles of the filament and CME, which is described in the following sections.

3.2.1. Estimating the Duration of Rapid Acceleration Phase

In this section, we use the true height-time curves, shown in the lower panels of Figure 6, to derive the velocity, acceleration, and jerk (rate of change of acceleration, following Schrijver et al. 2008) profile of the filament and CME. The latter can then be compared to the predictions of theoretical eruption models described in the Introduction. Since the acceleration and jerk are the higher order time derivative of the trajectory, errors in the measured data amplify strongly, so one is typically forced to smooth the data before calculating acceleration curves, for example, using spline smoothing (Vršnak et al. 2007). Here we will use a different approach: we first fit a fourth-order polynomial of the form $H(t) = a + bt + ct^2 + dt^3 + et^4$ to the height-time data. We then use this smooth curve to obtain the velocity, acceleration, and jerk profiles. These profiles are shown in Figure 7 for the filament and the CME leading edge in the left and right columns, respectively.

It is to be noted that the underlying physical mechanism responsible for the eruption determines the functional form of the height-time profile only initially, i.e., during the phase when acceleration is growing, but not yet saturating. Once the acceleration starts to saturate, the functional form is changing. From Figure 7 we note that the acceleration profiles as estimated from the fourth-order polynomial are quite different for the filament and the CME. While the acceleration of the CME leading edge is higher than that of the filament, the rate of change of acceleration, i.e., the value of jerk for the CME is declining, in contrast to the filament. This suggests that during the time interval of the CME data the increase of the acceleration of the leading edge is slowing down, while the growth of the acceleration of the filament is still increasing. We therefore restrict our fits of different functional forms to the filament only and not to the CME.

3.2.2. Fitting Functional Forms to the Filament Rapid Acceleration Phase

Before we fit the functional forms we make an estimation of the optimum time interval which corresponds to rapid acceleration phase of the filament. To get the first estimation, we took the start time where the acceleration starts to grow from zero and the end time as the last data point. We then fine tune our estimation of the time interval of the rapid acceleration phase by varying their start and end times and observing the resulting quality of the overall fits of all three functional forms. The interval leading to an overall best-fit quality for all functional forms is marked by vertical dashed lines in Figure 7.

Within this rapid acceleration interval we then find the best-fit functional form as described below. We fit the three different functional forms: (1) parabolic, $H(t) = a + bt + ct^2$, (2) exponential, $H(t) = ae^{bt} + c$, and (3) cubic, $H(t) = a+bt+ct^3$ to the height-time profile during the rapid acceleration

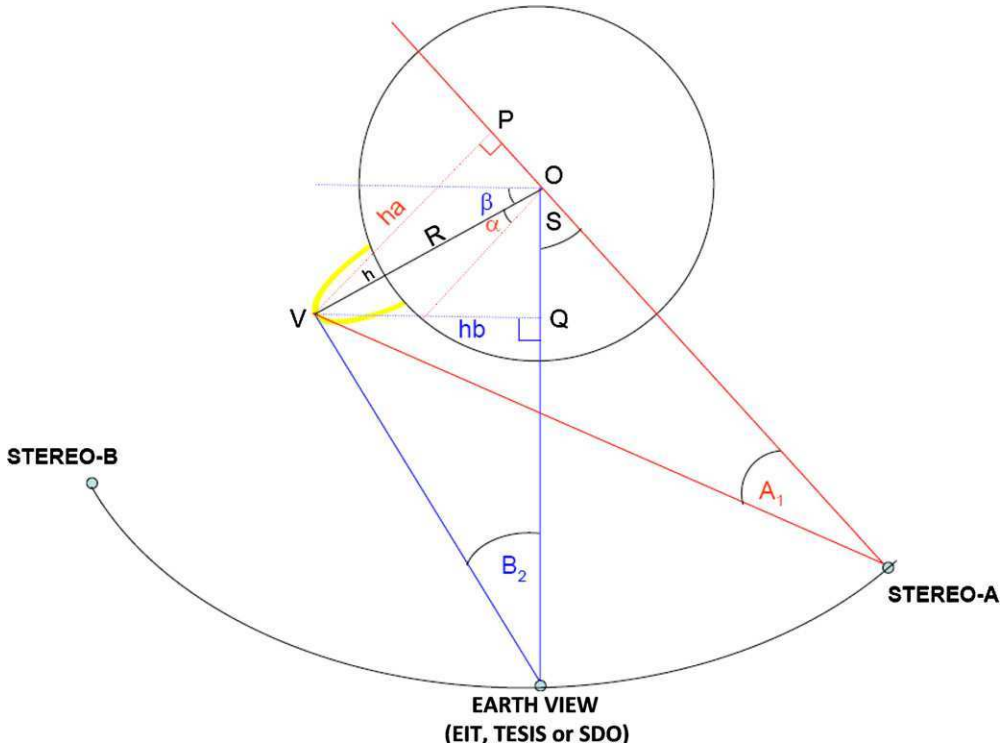

Figure 4. Illustration of the de-projection method. The coronal structure is represented by a yellow loop extending above the solar limb. The top part of this loop is at an angle α (β) to the plane of sky in the reference frame of *STEREO-A* (Earth view, EV). S is the separation angle between *STEREO-A* and EV. The segments ha and hb are the projected distances $(R+h)\cos(\beta)$ and $(R+h)\cos(\alpha)$, respectively. S is related to α and β by $S = \alpha + \beta$ (if the loop is seen in front of the limb in one view and behind the limb in the other) or by $S = |\alpha - \beta|$ (if the loop is seen on the same side of the limb, i.e., either in front of or behind the limb, in both views). If ha, hb, and S are known, α and β can be determined.

(A color version of this figure is available in the online journal.)

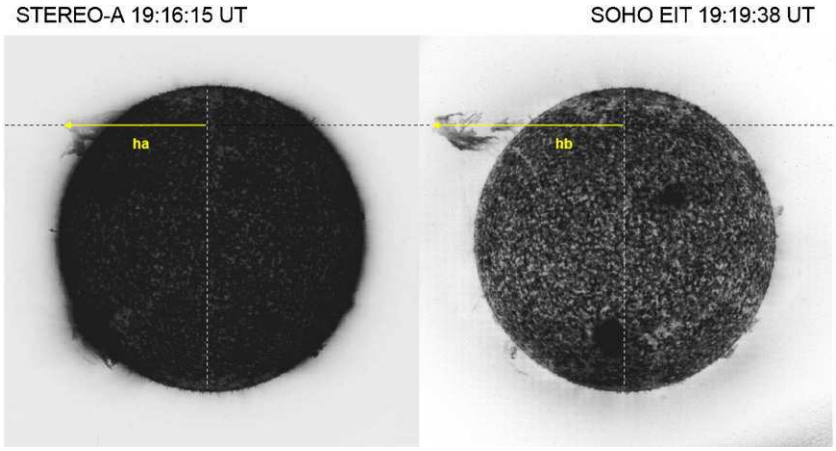

Figure 5. Near-simultaneous *STEREO-A* and *SoHO*/EIT filtergrams in epipolar geometry. The segments h_a and h_b are measured from the apex of the filament. The separation angle between Earth and *STEREO-A* is $S = \alpha + \beta = 61^\circ$.

(A color version of this figure is available in the online journal.)

phase. The left panel of Figure 9 shows these fits. The reduced χ^2 χ_ν values are shown at the top left corner of each panel. The weights that we apply to the data points for fitting are taken to be $W = 1/\sigma^2$, where σ is the standard deviation of the measurement error. We assume a Gaussian distribution for the latter. The pixel size of *STEREO*/EUVI is about 2 Mm. For the filament (or prominence), which is typically quite diffuse in He II 304 Å images, we consider 3 pixels, i.e., 6 Mm as the 1σ error. The actual errors may be somewhat different. However, while using different values of 1σ will lead to different values of χ_ν, the relative values of χ_ν between different functional forms will remain the same. The fits of the three functional forms shown in the left panels of Figure 9 clearly favor an exponential rise of the filament, with a relatively better value of χ_ν.

3.3. The 3D Reconstruction by using Marinus Projection

3.3.1. The Method

Here we describe a new tomographic method for the 3D reconstruction. We used simultaneous views of the filament from *STEREO-A* and *B* and TESIS in He II 304 Å wavelength. The essence of the method is as follows.

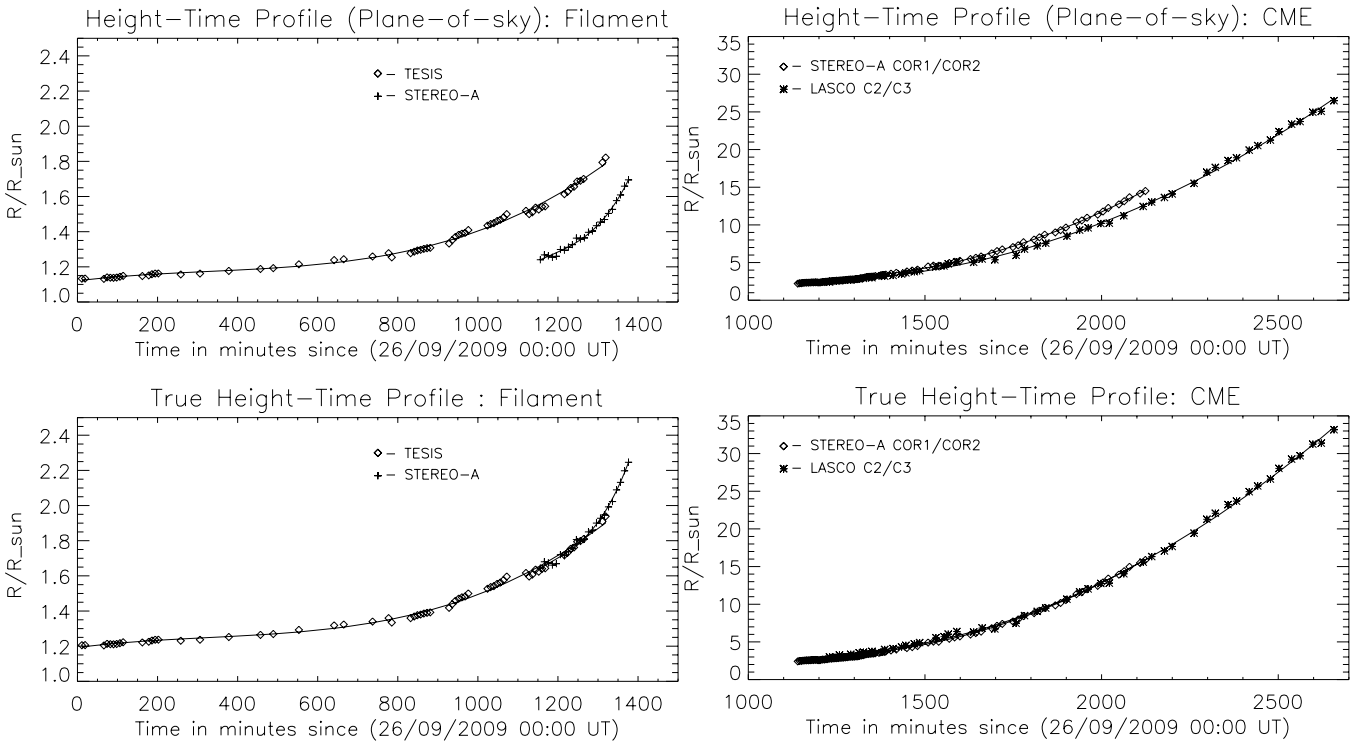

Figure 6. Top panels show the POS height-time profiles of the filament apex (left) and CME leading edge (right) as seen from different viewpoints (see the inset for the observing satellites). The lower panels show the true height-time profiles derived by using the simple trigonometric method (Section 3.2).

A continuum intensity image of the Sun, $I(x, y)$, can be easily projected into heliographic coordinates $I(l, b)$. This projection is also known as equidistant cylindrical or Marinus projection. Since the continuum intensity $I(x, y)$ corresponds to the solar photosphere, each point (x, y) on the intensity image can be associated with heliographic coordinates (l, b), assuming a spherical Sun with radius, $R = R_\odot$. A common feature on the solar disk such as a sunspot should then correspond to the same Carrington latitude–longitude, no matter what the viewing angle of the Sun is. However, for coronal images like in He II 304 Å the intensity features corresponding to filaments, spicules, etc., do not lie on the same sphere but are elevated structures in 3D. Thus, a common feature like a filament or coronal loop will correspond to location (l_1, b_1) and (l_2, b_2) in heliographic projection of the coronal images obtained from different viewing points 1 and 2, respectively (when $R = R_\odot$ is assumed). Conversely, if the heliographic projection is attempted assuming the Sun to be a sphere of radius larger than one solar radius and a correct radius of the sphere is assumed (equal to the altitude of the feature), then the we should get $l_1 = l_2$ and $b_1 = b_2$ for the common feature.

Thus, generating the generalized Carrington maps for different assumed radii of the spherical grid, using a 5 Mm step from $R = 700$ Mm to $R = 1500$ Mm, and comparing the Carrington coordinates (latitude–longitude) of a recognizable common feature, such as filament apex, in the three Carrington maps (one for each viewing angle) until they all agree gives us a solution for the 3D coordinates of the feature. We found that this step size of 5 Mm gives an optimum choice to arrive at the best agreement for the generalized coordinates of a recognizable feature. Thus the generic accuracy of the method can be assumed to be about 5 Mm.

We geometrically consider both intersections of the line of sight with the reference sphere. When the radius of the reference sphere is equal to the chromospheric radius, we take into account the single point located physically in front of the POS. When the radius of the reference sphere is greater than the chromospheric radius, we must in principle take into account both intersection points located respectively in front of and behind the POS. That is why in the top panel of Figure 8 the prominence, projected on the far side of the reference sphere, behind the POS of *STEREO-A*, appears as reversed from right to left with respect to the direct view in Figure 2. In addition, the far side of the solar disk appears as a dark, missing disk in the top panel of Figure 8.

3.3.2. Advantages and Limitations of the Method

It is well known that all stereoscopic reconstruction methods are limited by the ambiguity in recognizing a common feature in different views. Further, a common limitation that arises with any 3D stereoscopic reconstruction technique is when the apex point from two viewing angles may be different. Such situations would lead to a systematic error in the reconstructed 3D coordinates. However, we expect such errors to be less severe in our case because (1) the filament studied here has a large extension in longitude which is rising globally as a whole, so height-time profile of several neighboring points along the filament will be similar, and (2) using combination of *STEREO-A* and TESIS (separation angle 61°) as compared to *STEREO-A* and *STEREO-B* (separation angle 117°), we reduce the errors. Although such systematic errors cannot be avoided, the time derivative of measured altitude and hence the derived velocity and acceleration should not be affected severely as long as the systematic error remains similar in magnitude. Therefore, for studying the kinematic evolution of erupting prominence such reconstruction methods may still be applicable, with aforementioned limitations.

Figure 8 shows selected parts of the three generalized Carrington maps corresponding to *STEREO-A*, TESIS, and *STEREO-B* views, generated assuming radii of the spherical grid to be

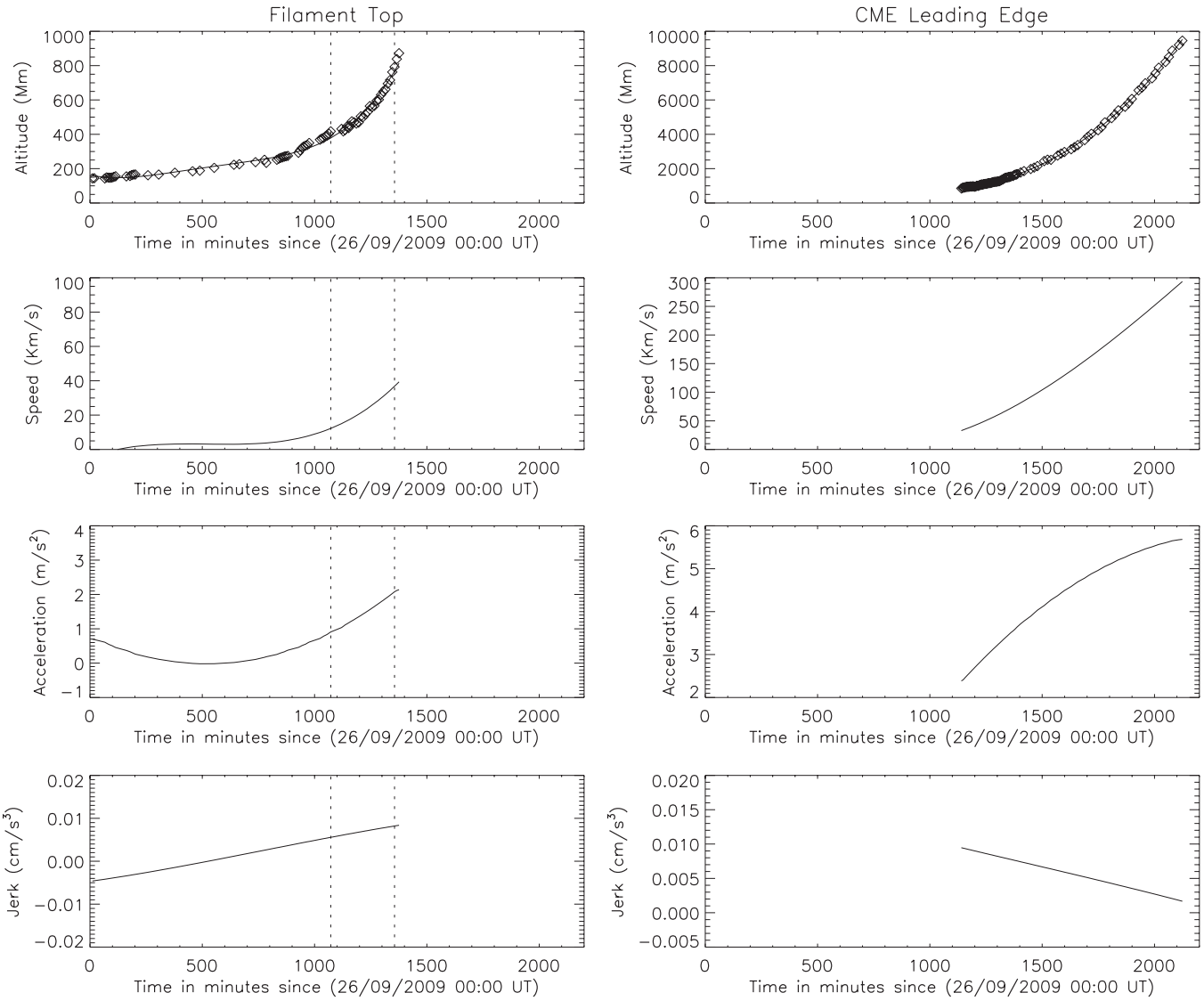

Figure 7. Left (right) panels show, from top to bottom, the height, speed, acceleration, and jerk (rate of change of acceleration) profiles of the filament apex (CME leading edge), respectively. In the top panels, the data points are shown by "+" marks and the solid line corresponds to a fourth-order polynomial fit ($H(t) = a+bt+ct^2+dt^3+et^4$) to the data. The fitted profile $H(t)$ is used to derive the speed, acceleration, and jerk curves in the subsequent panels. The two vertical dotted lines in the left panels correspond to the estimated duration of the rapid acceleration phase of the filament, which is fitted with different functional forms in Figure 9.

1245 Mm, i.e., 545 Mm above the solar surface. At the choice of this radius, the common feature, i.e., the filament apex marked by a square box, corresponds to the same Carrington latitude–longitude coordinates in the different views. In principle, two stereoscopic views are sufficient for the application of this method. However, adding more views increases redundancy (for example, in the present case more emphasis is given to TESIS and *STEREO-A* for constraining reconstruction) and therefore may add to its robustness. In the future, we plan to apply this method to the events observed simultaneously by the two *STEREO*/EUVI instruments along with the high-resolution *SDO*/AIA observations.

3.3.3. Comparison with SCC_MEASURE and Simple Triangulation Method

The 3D reconstruction of the filament studied in this paper was also carried out by Li et al. (2010) using SCC_MEASURE procedure (developed by W. Thompson). They used *STEREO-A* and *STEREO-B* pair for their reconstruction. Further, they reconstructed many (12) points along the filament body (their Figure 5). Their points 6, 7, and 8 correspond to the top of the filament and one can note that the height evolution of these points (their Figure 6(a)) is quite similar to each other (within ±6 Mm), though the points are separated spatially, this is due to the large-scale uniform evolution of the filament. For comparison, we overlay the altitude data points of location 7, as reconstructed by Li et al. (2010) in our height-time plot shown with red symbols in the top right panel of Figure 9. The reconstruction from two independent methods agrees quite well, considering the general scatter in the reconstructed coordinates.

On the other hand, a poorer match is expected between the true 3D reconstruction methods and the simple triangulation method since the latter only estimates the propagation angle and not the 3D coordinates of the filament. The height derived from simple triangulation method shows a systematic offset with respect to the true height derived from 3D reconstruction methods. Apart from the systematic offset, the profile of the derived speed and acceleration should, however, remain unaffected, as these depend upon the shape of the curve. This is evidenced in a similar fit quality of the height-time profile by both the

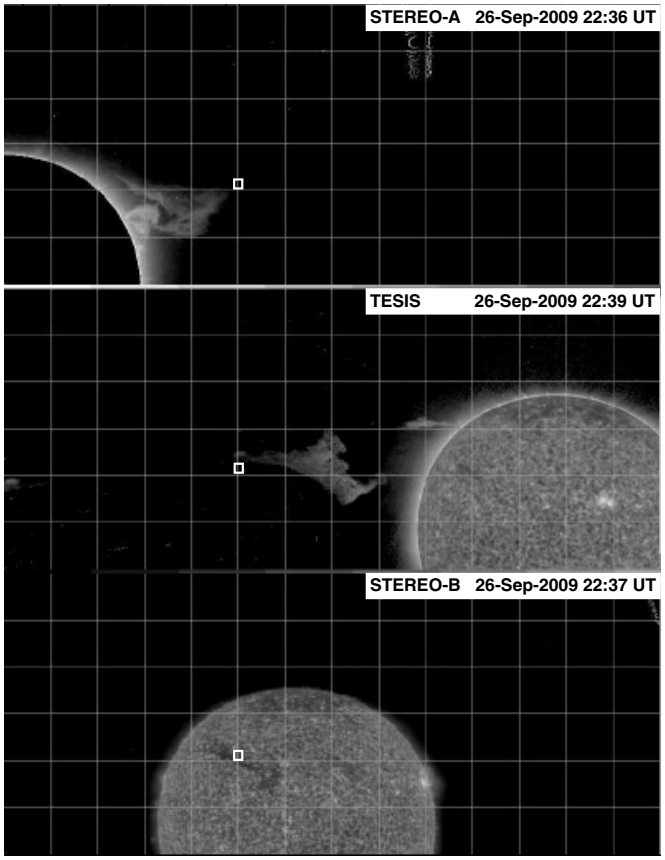

Figure 8. Top, middle, and bottom panels show the three views of the Sun from the *STEREO-A*, TESIS, and *STEREO-B*, respectively, in Marinus projection. The top part of the filament is marked by a white box in all images.

methods to different functional forms (see Section 3.3.4). Also, the method is straightforward and relies on tracking a common feature in the images taken from the same vantage point albeit at different times. The natural advantage is that it is easy to track a common feature in time if the time difference between two images is not very large.

Further, it may be noted from Table 1 that the angles α and β are not changing significantly. In the 3D reconstruction by Li et al. (2010, their Figure 4, right panels) it can be seen that a propagation angle of $\sim 20^\circ$ in front of the east solar limb is deduced and is not changing significantly. Also, the Carrington longitude of the filament apex reconstructed using Marinus method (Table 1) shows a small variation in longitude of $\sim 4^\circ$, while the mean value of the longitude, $\sim 150^\circ$, corresponds to an angle of $\sim 20^\circ$ in front of the east solar limb, in agreement with Li et al. (2010) and angle β from simple triangulation method.

3.3.4. Rapid Acceleration Phase and Its Functional Form

We use this tomographic 3D reconstruction method based on Marinus projection to obtain the 3D trajectory of the filament apex. The rise of the altitude of the filament apex is fitted for different functional forms. The time interval of the rapid acceleration phase is taken to be the same as estimated in Section 3.2.1. The height-time curve and the fitted parabolic, exponential, and cubic functions to it are shown in the right panel of Figure 9 from top to bottom, respectively. The reduced χ^2 χ_ν values are shown at the top left corner of each panel. It is found that an exponential form fits the observations relatively better as compared to the other functions. The exponential function was also found to fit the rapid acceleration phase relatively better than other functions in Section 3.2.2, where simple triangulation method was used. This is shown in the left panel of Figure 9.

4. DISCUSSION AND CONCLUSIONS

In this paper we analyzed the observations of a large erupting quiescent filament which was observed from three vantage points by *STEREO-A*, *B*, and the EV (*SoHO*/EIT and TESIS). The filament rose slowly for several hours before accelerating rapidly and erupting in two parts, a large and a small filament. We analyzed the kinematics of the large filament, whose true trajectory was derived by two methods: one simple triangulation method and another newly introduced tomography method. The new tomographic method can potentially take advantage of simultaneous observations from multiple vantage points to constrain the reconstructions better. After deriving the true trajectory by the two methods, we fitted the height-time curves with different functional forms and compared the results with predictions of theoretical eruption models.

The key points in the observational analysis can be summarized as follows.

1. The eruption involved two filaments, a large one and a small one, which were located above the same PIL, suggesting that they were embedded in the same, elongated filament channel. The photospheric magnetic field strengths at the location of the filaments were weak (up to about 3 G). The two filaments erupted almost simultaneously. In the present analysis we focused on the eruption of the more prominent large filament.
2. We used two different approaches to derive the true height-time profile of the filament. First, we used a simple triangulation method to determine the angle which the filament trajectory makes with respect to the POS and applied correction to the POS height-time profile to derive true height-time profile. Second, we used tomographic approach where we make Marinus projections of the three views of the Sun on spheres of radii larger than the solar radii so as to arrive at a common latitude–longitude position of a common feature (filament apex) in all maps. The advantage of the first method is that once we know the propagation angle with respect to POS from triangulation, we can go back and forth in time and correct the POS height-time profile obtained with even one satellite, i.e., durations when only one view is available, e.g., when in one of the stereoscopic pairs the filament is behind the limb or out of the field of view (FOV). However, the method assumes that the propagation angle of the filament with respect to POS does not change substantially over the time of observations.
3. During its early rise phase, the filament exhibits the morphology of a twisted sheet. However, its chirality could not be inferred from the images.
4. We derived the acceleration and jerk (rate of change of acceleration) profiles for the filament and the CME (Figure 7). It is believed that the initial rapid acceleration phase, when acceleration is growing, may be suggestive of the physical mechanism behind the eruption (Schrijver et al. 2008). However, the acceleration curve must be growing and not saturating or slowing down; in other words, the jerk should be increasing. By studying the jerk profiles in Figure 7 for the filament and the CME we decided to fit different functional forms to the filament observations

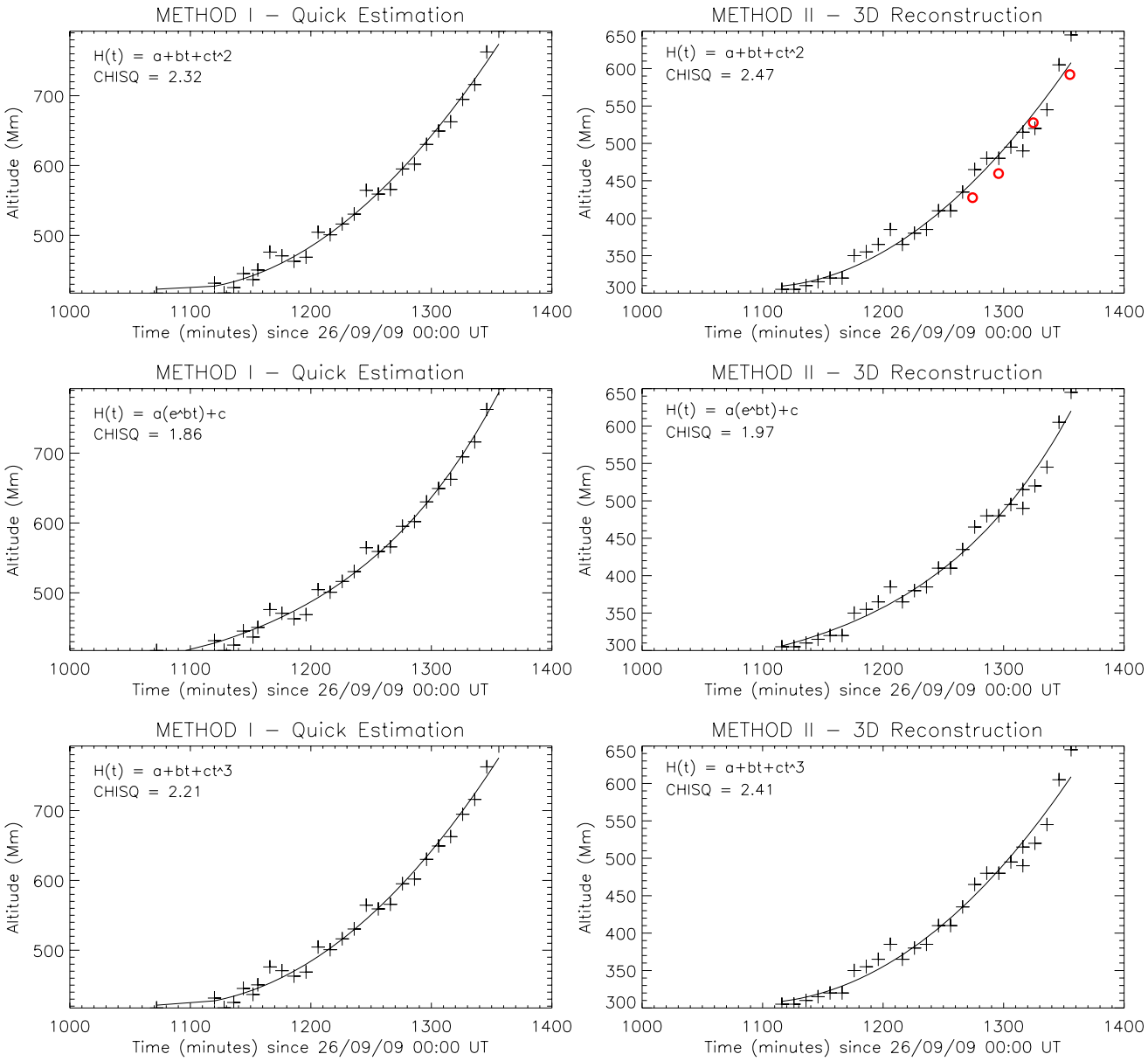

Figure 9. Panels on the left and right show the altitude-time curve for the erupting filament derived from simple triangulation method (Section 3.2) and 3D reconstruction method (Section 3.3). The four data points in red in the top right panel correspond to the altitude reconstructed by using SCC_MEASURE method. The altitude-time curve corresponds to the rapid acceleration phase of the filament eruption and is fitted for three functional forms *viz.* parabolic, exponential, and cubic (from top to bottom). The reduced χ^2 value of the fit is displayed on the top left corner of each panel.

(A color version of this figure is available in the online journal.)

only and not to the CME, because the jerk profile of the CME suggests that its acceleration is already saturating. Since the CME observations are available only when it enters the coronagraph's FOV, which is much later than the observations of the filament eruption, we missed the initial rapid acceleration phase of the CME.

5. We estimate the rapid acceleration phase of the filament between 17:50 UT and 22.33 UT, using the procedure described in Section 3.2.1. This phase is marked by two dashed lines in the left panel of Figure 7. We fit functional forms of a parabolic, exponential, and cubic function to the true height-time profile of the filament apex during the rapid acceleration phase. The fits to the true height-time curves derived from two independent reconstruction methods described in Sections 3.2 and 3.3, respectively, are shown in Figure 9.

We now compare our analysis of the eruption kinematics with the predictions of theoretical eruption models described in the Introduction. We note that the conclusions obtained from such a comparison should be read with some care and not be understood as a way to strictly confirm or rule out certain models. First, height-time data obtained with current instruments are still not accurate enough and typically do not have sufficient cadence to allow us to clearly pin down the functional forms of rise profiles, which may behave very similar over the relatively short timescales of the initial rapid acceleration in solar eruptions. Also, a clear functional dependence may not be present if several acceleration mechanisms are at work simultaneously in an eruption. Second, for many models, a proper investigation of the functional dependence of the eruption kinematics has not yet been reported, and even for most of those for which it was, there exists no parametric study, which may reveal kinematics

of a different functional dependence than reported for specific settings of the model parameters.

Our data indicate that the rapid acceleration phase already started before the eruption became visible in the coronagraph data, so we restricted our analysis of the early acceleration phase to the filament observations. Our fits suggest that the filament enters an exponential rise phase at about 17:50 UT, which then appears to saturate from around 22:33 UT. Such exponential initial acceleration is in line with many previous studies (see the Introduction) and supports the current picture that both quiescent and active region filament eruptions, and their associated CMEs, are driven by the same mechanisms. It suggests the occurrence of an ideal MHD instability, here most likely the torus instability. We did not find indications of a clear writhing motion of the filament that would suggest the additional occurrence of the helical kink instability, although the twisted appearance of the filament sheet may indicate some untwisting of the magnetic field during the early phase of the eruption.

The exponential acceleration found here is different from the cases studied by Schrijver et al. (2008), where a cubic (or near-cubic) rise was found for two active region filament eruptions. However, using numerical simulations, these authors showed that a relatively large initial velocity of the erupting structure at the onset of its rapid acceleration can change the subsequent rise behavior from exponential to cubic. The slow rise velocity of the filament (estimated from Figure 7, plateau in the filament speed curve before the first vertical dashed line) before the filament enters rapid acceleration phase is relatively small, about $\sim$2.5 km s^{-1}, however, comparable to the case described in Schrijver et al. (2008). The exponential rise also differs from the recent results by Joshi & Srivastava (2011), who found a constant acceleration for both the slow rise and rapid acceleration phases of the two 3D-reconstructed quiescent prominence eruptions. However, these authors apparently did not fit functions other than parabolic, and also the quality of their fits is not reported.

While the data we considered here support the torus instability as the mechanism responsible for the initial rapid acceleration of the filament, they do not provide reasonable clues for the cause for its preceding relatively long slow rise phase. We did not find indications of pre-flare brightening which are often used to draw conclusions. Hence, we do not find support for tether-cutting or magnetic breakout, but we cannot rule out the occurrence of these and other reconnection-related mechanisms, since the magnetic fields in the source region of the eruptions might have been simply too weak to produce detectable brightening. We therefore refrain from speculating on the exact underlying mechanism responsible in the present case. However, more studies using the methods developed in this work and encompassing larger sets of observations, including the high-resolution *SDO*/AIA observations, could provide better clues.

We thank the *SoHO*/EIT and *STEREO*/SECCHI teams for their open data policy. We thank TESIS/CORONAS team for providing the data. Financial support by the European Commission through the FP6 SOLAIRE Network (MTRN-CT-2006-035484) is gratefully acknowledged.

REFERENCES

Alexander, D., Metcalf, T. R., & Nitta, N. V. 2002, Geophys. Res.Lett., 29, 100000
Amari, T., & Aly, J. 2009, in IAU Symp. 257, Universal Heliophysical Processes, ed. N. Gopalswamy & D. F. Webb (Cambridge: Cambridge Univ. Press), 211
Antiochos, S. K., DeVore, C. R., & Klimchuk, J. A. 1999, ApJ, 510, 485
Artzner, G., Gosain, S., & Schmieder, B. 2010, Sol. Phys., 262, 437
Aschwanden, M. J. 2011, Living Rev. Sol. Phys., 8, 5
Aulanier, G., Török, T., Démoulin, P., & DeLuca, E. E. 2010, ApJ, 708, 314
Bemporad, A. 2011, J. Atmos. Solar-Terr. Phys., 73, 1117
Brueckner, G. E., Howard, R. A., Koomen, M. J., et al. 1995, Sol. Phys., 162, 357
Chandra, R., Schmieder, B., Mandrini, C. H., et al. 2011, Sol. Phys., 269, 83
Chen, J., & Krall, J. 2003, J. Geophys. Res. (Space Phys.), 108, 1410
Chifor, C., Mason, H. E., Tripathi, D., Isobe, H., & Asai, A. 2006, A&A, 458, 965
Delaboudinière, J., Artzner, G. E., Brunaud, J., et al. 1995, Sol. Phys., 162, 291
Fan, Y. 2005, ApJ, 630, 543
Feng, L., Inhester, B., Wei, Y., et al. 2012, ApJ, 751, 18
Forbes, T. 2010, in Models of Coronal Mass Ejections and Flares, ed. C. J. Schrijver & G. L. Siscoe (Cambridge: Cambridge Univ. Press), 159
Forbes, T. G. 2000, J. Geophys. Res., 105, 23153
Forbes, T. G., & Isenberg, P. A. 1991, ApJ, 373, 294
Gallagher, P. T., Lawrence, G. R., & Dennis, B. R. 2003, ApJ, 588, L53
Gibson, S. E., Fan, Y., Török, T., & Kliem, B. 2006, Space Sci. Rev., 124, 131
Gilbert, H. R., Holzer, T. E., Burkepile, J. T., & Hundhausen, A. J. 2000, ApJ, 537, 503
Gosain, S., & Schmieder, B. 2010, Ann. Geophys., 28, 149
Gosain, S., Schmieder, B., Venkatakrishnan, P., Chandra, R., & Artzner, G. 2009, Sol. Phys., 259, 13
Joshi, A. D., & Srivastava, N. 2011, ApJ, 739, 8
Kaiser, M. L., Kucera, T. A., Davila, J. M., et al. 2008, Space Sci. Rev., 136, 5
Kliem, B., & Török, T. 2006, Phys. Rev. Lett., 96, 255002
Kliem, B., Török, T., & Thompson, W. T. 2012, Sol. Phys., 281, 137
Kundu, M. R., White, S. M., Garaimov, V. I., et al. 2004, ApJ, 607, 530
Kuzin, S. V., Bogachev, S. A., Zhitnik, I. A., et al. 2009, Adv. Space Res., 43, 1001
Lemen, J. R., Title, A. M., Akin, D. J., et al. 2012, Sol. Phys., 275, 17
Li, T., Zhang, J., Zhang, Y., & Yang, S. 2011, ApJ, 739, 43
Li, T., Zhang, J., Zhao, H., & Yang, S. 2010, ApJ, 720, 144
Liu, R., Alexander, D., & Gilbert, H. R. 2009, ApJ, 691, 1079
Lynch, B. J., Antiochos, S. K., MacNeice, P. J., Zurbuchen, T. H., & Fisk, L. A. 2004, ApJ, 617, 589
MacQueen, R. M., & Fisher, R. R. 1983, Sol. Phys., 89, 89
Mierla, M., Inhester, B., Antunes, A., et al. 2010, Ann. Geophys., 28, 203
Moore, R. L., Sterling, A. C., Hudson, H. S., & Lemen, J. R. 2001, ApJ, 552, 833
Priest, E. R., & Forbes, T. G. 2002, A&AR, 10, 313
Schrijver, C. J., Elmore, C., Kliem, B., Török, T., & Title, A. M. 2008, ApJ, 674, 586
Sheeley, N. R., Walters, J. H., Wang, Y., & Howard, R. A. 1999, J. Geophys. Res., 104, 24739
Thompson, W. T., Kliem, B., & Török, T. 2012, Sol. Phys., 276, 241
Török, T., Berger, M. A., & Kliem, B. 2010, A&A, 516, A49
Török, T., & Kliem, B. 2005, ApJ, 630, L97
Török, T., & Kliem, B. 2007, Astron. Nachr., 328, 743
Török, T., Kliem, B., & Titov, V. S. 2004, A&A, 413, L27
Vršnak, B., Maričić, D., Stanger, A. L., et al. 2007, Sol. Phys., 241, 85
Williams, D. R., Török, T., Démoulin, P., van Driel-Gesztelyi, L., & Kliem, B. 2005, ApJ, 628, L163
Zhang, J., & Dere, K. P. 2006, ApJ, 649, 1100
Zuccarello, F. P., Bemporad, A., Jacobs, C., et al. 2012, ApJ, 744, 66

The Astrophysical Journal, 759:70 (17pp), 2012 November 1 doi:10.1088/0004-637X/759/1/70

2010 AUGUST 1–2 SYMPATHETIC ERUPTIONS. I. MAGNETIC TOPOLOGY OF THE SOURCE-SURFACE BACKGROUND FIELD

V. S. Titov[1], Z. Mikic[1], T. Török[1], J. A. Linker[1], and O. Panasenco[2]
[1] Predictive Science Inc., 9990 Mesa Rim Road, Suite 170, San Diego, CA 92121, USA; titovv@predsci.com
[2] Helio Research, 5212 Maryland Avenue, La Crescenta, CA 91214, USA
Received 2012 June 18; accepted 2012 September 14; published 2012 October 17

ABSTRACT

A sequence of apparently coupled eruptions was observed on 2010 August 1–2 by *Solar Dynamics Observatory* and *STEREO*. The eruptions were closely synchronized with one another, even though some of them occurred at widely separated locations. In an attempt to identify a plausible reason for such synchronization, we study the large-scale structure of the background magnetic configuration. The coronal field was computed from the photospheric magnetic field observed at the appropriate time period by using the potential field source-surface model. We investigate the resulting field structure by analyzing the so-called squashing factor calculated at the photospheric and source-surface boundaries, as well as at different coronal cross-sections. Using this information as a guide, we determine the underlying structural skeleton of the configuration, including separatrix and quasi-separatrix surfaces. Our analysis reveals, in particular, several pseudo-streamers in the regions where the eruptions occurred. Of special interest to us are the magnetic null points and separators associated with the pseudo-streamers. We propose that magnetic reconnection triggered along these separators by the first eruption likely played a key role in establishing the assumed link between the sequential eruptions. The present work substantiates our recent simplified magnetohydrodynamic model of sympathetic eruptions and provides a guide for further deeper study of these phenomena. Several important implications of our results for the S-web model of the slow solar wind are also addressed.

Key words: magnetic reconnection – solar wind – Sun: coronal mass ejections (CMEs) – Sun: flares – Sun: magnetic topology

Online-only material: color figures

1. INTRODUCTION

Coronal mass ejections (CMEs) are spectacular solar phenomena that have been intensely studied over more than 40 years. Being the main driver of space weather disturbances near the Earth, they are part of a more general eruption process, often including filament eruptions and flares. Although it is now understood that these phenomena are due to a local destabilization of the coronal magnetic field, many basic questions on the physics of CMEs are still under study (e.g., Forbes 2000, 2010). Accordingly, theoretical and numerical investigations of CME initiation and evolution have so far focused mainly on *single* eruptions.

However, there also exist *multiple* eruptions occurring within a relatively short period of time and at different, often widely separated, locations. In the largest events, the respective source regions can cover a full hemisphere (so-called global CMEs; e.g., Zhukov & Veselovsky 2007), so that such events naturally produce large heliospheric disturbances. While it has been argued whether or not the temporal correlation of multiple eruptions is coincidental (e.g., Biesecker & Thompson 2000), both statistical investigations (e.g., Moon et al. 2002; Wheatland & Craig 2006) and detailed case studies (e.g., Wang et al. 2001; Jiang et al. 2011; Yang et al. 2012; Shen et al. 2012) indicate that there are *causal connections* between them.[3] We accept this fact as a starting point of our study and will henceforth call such eruptions *sympathetic* or *linked*.

The physical mechanisms of these connections, however, have yet to be unveiled. In earlier works they have been related, for instance, to destabilization by chromospheric large-scale waves (Ramsey & Smith 1966) or large-scale properties of convective flows (Bumba & Klvana 1993). More recent research suggests that the mechanisms linking sympathetic eruptions act in the corona and involve its magnetic field structure. For example, one proposed mechanism relies on perturbations propagating along field lines between the source regions of eruptions (e.g., Jiang et al. 2008), while another appeals to changes in the background field due to reconnection (Liu et al. 2009; Zuccarello et al. 2009; Jiang et al. 2011; Shen et al. 2012). Yet such explanations were often based on qualitative and sometimes rather speculative considerations.

The high-cadence, full-disk observations by *Solar Dynamics Observatory* (*SDO*), along with studies of the large-scale coronal magnetic field, now provide us the opportunity to substantially increase our understanding of such eruptions. The event under study attracted considerable attention in the solar community and beyond. It involved an entire hemisphere of the Sun, consisted of several flares and six filament eruptions and CMEs, and triggered a geomagnetic storm on August 3 (Harrison et al. 2012). A detailed account of all eruptions and their precursors can be found in Schrijver & Title (2011). Here, we restrict ourselves to the main five eruptions, whose connections we aim to explain in the present study. Using a combination of *SDO* data and analysis of field line connectivity for the 2010 August 1–2 eruptions, Schrijver & Title (2011) found evidence that *all* involved source regions were connected by structural features such as separatrix surfaces, separators, and quasi-separatrix layers (QSLs; Priest & Démoulin 1995; Démoulin et al. 1996; Titov et al. 2002). We have recently performed a simplified magnetohydrodynamic (MHD) simulation of a subset of these eruptions (Török et al. 2011), in which two successive

[3] We do not distinguish here between sympathetic flares and sympathetic CMEs, since typically both are part of the same eruption process.

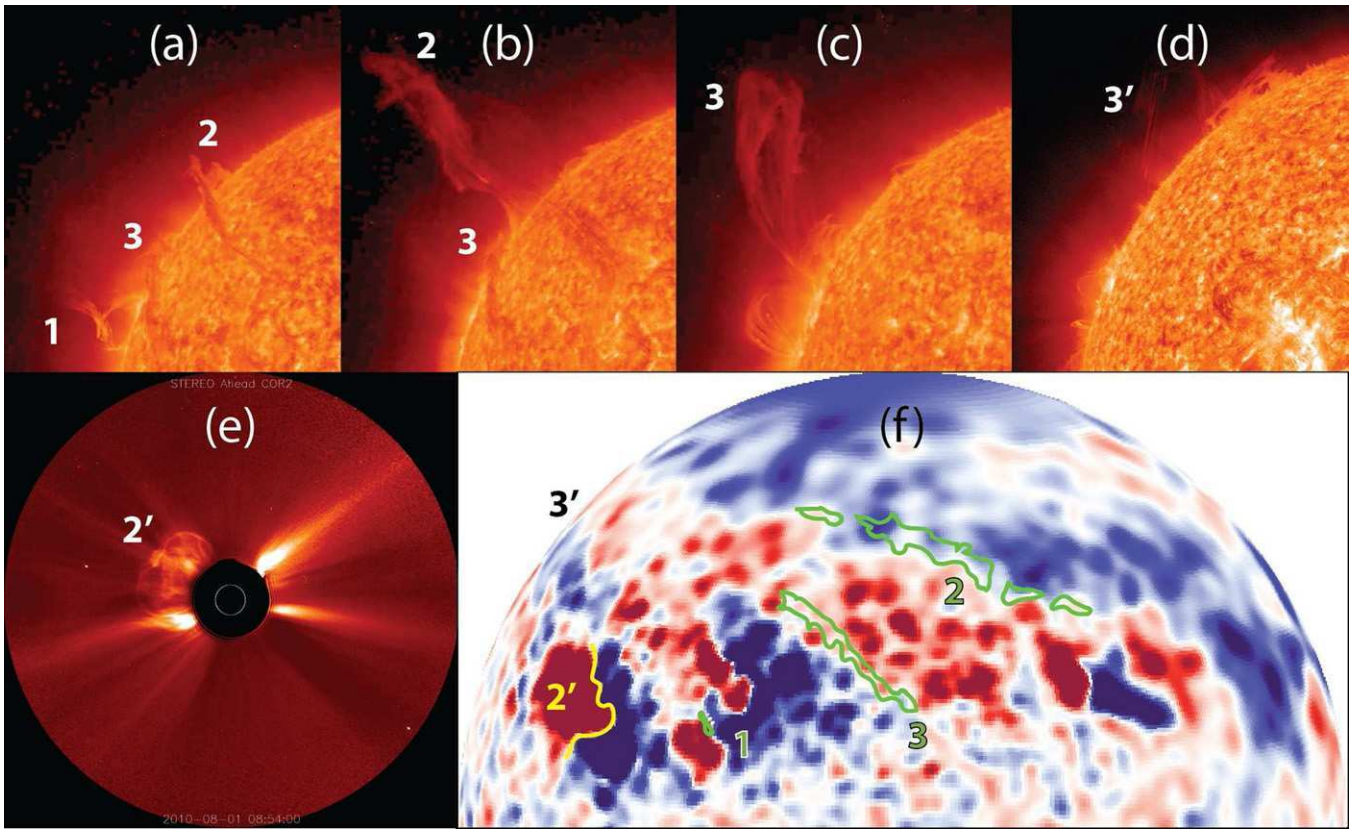

Figure 1. Sympathetic CMEs on 2010 August 1 with the main eruptions numbered in the order of their occurrence, primed numbers indicate near-simultaneous events; (a)–(c) eruptions 1, 2, and 3 as seen by *STEREO-A* 304 Å at 02:56, 09:16, and 22:06 UT (left to right); (d) eruption 3′ observed by *SDO*/AIA 304 Å at 21:30 UT; (e) eruption 2′ captured by the COR2 coronagraph on board *STEREO-A* at 08:54 UT; (f) synoptic MDI magnetogram and contours (green) of the pre-eruption filaments that were visible in Hα, the yellow line indicates the location of the active-region filament 2′ prior eruption.

(A color version of this figure is available in the online journal.)

eruptions were initiated by reconnection at a separator high in the corona. Thus, this work strongly supports the idea that the structural features can indeed play a key role in generating linked eruptions.

While these new results are very encouraging, further research is needed. First, our simulation used only a simplified magnetic configuration and addressed just a subset of the complex sequence of CMEs on 2010 August 1–2. Second, the findings by Schrijver & Title (2011), being of a general nature, did not explain the exact role of structural features in connecting individual eruptions. We show here that a comprehensive structural analysis of the magnetic environment in which such eruptions occur allows one to get deeper insights into the relationship between linked eruptions.

Figure 1 shows that the sequence of eruptions started with a CME following the eruption of the small filament 1. About 6 hr later, the large quiescent filament 2 erupted, almost simultaneously with a C-class flare and fast CME originating in active-region NOAA 11092 (whose polarity inversion line is denoted by 2′) to the east of filament 1. After another 12 hr, the large quiescent filament 3 erupted, again almost simultaneously with a large filament eruption (denoted by 3′) that was observed above the eastern limb. All of the large filament eruptions evolved into separate CMEs. Interestingly, while a filament was present along 2′, it did not erupt as part of the CME (Liu et al. 2010).

Our topological analysis of the large-scale background coronal field, which we describe in detail in Section 3, reveals that, first, all of the erupting filaments were located prior to their eruption below so-called pseudo-streamers (e.g., Hundhausen 1972; Wang et al. 2007). A pseudo-streamer is morphologically similar to a helmet streamer but, in contrast to it, divides coronal holes of the same rather than opposite polarity and contains two lobes of closed magnetic flux below its cusp to produce a $\cap$-type structure. These structures are quite common in the corona (e.g., Eselevich et al. 1999) and are often observed to harbor filaments in their lobes (Panasenco & Velli 2010). As the latter authors pointed out, an eruption in one lobe of a pseudo-streamer is often followed by an eruption in the other lobe shortly thereafter, indicating that these structures are prone to producing linked eruptions.

Second, as suggested by Török et al. (2011), the eruptions 2 and 3, which originated below one pseudo-streamer, were apparently triggered by eruption 1 that occurred outside the pseudo-streamer. Third, as also suggested in that study, the fact that filament 2 erupted before filament 3, although it was located further from eruption 1 than filament 3, can be explained by the topological properties of the pseudo-streamer.

These three conclusions are strongly supported by our analysis in Sections 3 and 4 and indicate the central role that pseudo-streamers may play in many linked eruptions. We further develop this concept and generalize it in Section 4, arguing that the order of *all* our eruptions, including those of filaments 2′ and 3′, is not coincidental but causal. It is essentially predetermined by the overall magnetic topology of the ensemble of pseudo-streamers that were involved into the eruptions. We comprehensively investigate this topology in the framework of the potential field source-surface (PFSS; Altschuler & Newkirk 1969;

Schatten et al. 1969) model (Section 2.1), using new techniques for the structural analysis of magnetic fields (Section 2.2).

Being of a general character, our findings on magnetic topology of pseudo-streamers have a broader impact than was initially anticipated for this study. In particular, they also provide important implications for the problem of the origin of the slow solar wind, which was recently addressed in the framework of the so-called S-web model (Antiochos et al. 2007; Antiochos et al. 2011; Linker et al. 2011) and whose aspects have already been discussed in a number of papers (Titov et al. 2011; Wang et al. 2012; Crooker et al. 2012). We address the implications of our new results for the S-web model in Section 5 and summarize our work in Section 6.

Although solar magnetic fields obtained from PFSS and MHD models often qualitatively match each other, at least if the latter are based only on line-of-sight magnetograms (Riley et al. 2006), it remains an open question whether the magnetic field topology, as understood in mathematical terms, is in both cases the same. Section 3.3 makes it clear that this question indeed requires a special study, which is already on the way and will be described in the part II of a series of papers. In that part, we will repeat our analysis of the magnetic structure for the global solar MHD model derived from the same magnetogram as used in the present PFSS model. We will also compare the results of our analysis for both these models and, additionally, extend the discussion of these results, which we start in Section 4, in relation to observations.

2. INVESTIGATION METHODS

2.1. PFSS Model

As a boundary condition for our PFSS model, we used the magnetic data that were derived from a *Solar and Heliospheric Observatory*/MDI synoptic map of the radial field B_r for Carrington rotation 2099 (2010 July 13–August 9) using the Level 1.8.2 calibration. We processed the synoptic map, first, by interpolating it to a uniform latitude–longitude mesh with a resolution of $0.^\circ5$. The polar magnetic field was fitted in the new map with a geometrical specification to reduce noise in the poorly observed polar regions. Second, we smoothed the resulting B_r by applying a diffusion operator such that its nonuniform diffusion coefficient was smaller in the active region and larger everywhere else. Finally, we interpolated the obtained B_r distribution from the uniform grid to a nonuniform one that has a higher and lesser resolution, respectively, inside and outside the eruptive region. This region is spread in longitude and latitude approximately from 45° to 180° and from -20° to 65°, respectively, with the resolution ranging from $0.^\circ37 \times 0.^\circ37$ in this region to $2.^\circ6 \times 1.^\circ8$ outside (see Figure 2(a)).

The spherical source surface, at which the scalar magnetic potential is set to be constant, is chosen at $r = 2.5\,R_\odot$, where $R_\odot$ is the solar radius. For such a PFSS model, we have computed the photospheric map of coronal holes on a uniform grid with an angular cell size of $0.^\circ125$, which is much smaller than the smallest grid cell for the computed field itself. The result is shown in Figure 2(b) together with the source-surface distribution of the squashing factor Q, which will be discussed below. The three coronal holes of negative polarity that are located in the eruptive region are distinctly disconnected from each other and from the negative northern polar coronal hole. As will become clear later, the presence of these coronal holes in the eruptive region is crucial for understanding both the underlying magnetic topology and the plausible casual link that this topology sets up between the erupting filaments.

2.2. Techniques for Analyzing Magnetic Structure

Magnetic configurations can generally have both *separatrix surfaces* and *QSLs*. To comprehensively analyze the structure of our configuration, it is necessary to determine all such structural features, whose complete set we call the *structural skeleton* of the configuration. We fulfill this task in two steps: first, we identify the footprints of the corresponding (quasi)-separatrix surfaces at the photosphere and source surface by calculating the distributions of the *squashing factor* Q of elemental magnetic flux tubes (Titov et al. 2002; Titov 2007); these footprints are simply high-Q lines of the calculated distributions. Second, using the found footprints as a guide, we trace a number of field lines that best represent these surfaces.

For the calculation of Q we use its definition in spherical coordinates (Titov 2007; Titov et al. 2008). By construction, the Q factor has the *same* value at the conjugate footpoints, so it can be used as a marker for field lines. In other words, despite being originally defined at the boundary surfaces only, the Q factor can be extended into the volume by simply transporting its defined values along the field lines according to the equation

$$\mathbf{B} \cdot \nabla Q = 0,$$

where $\mathbf{B}$ is a given coronal magnetic field and Q is an unknown function of space coordinates. This equation can be solved in many different ways depending on the desirable accuracy and efficiency of the computation. We will describe our methods for extending Q in the volume in a future article together with other techniques for investigating (quasi-)separatrix surfaces, while here we would like to outline a few relevant considerations.

The extension of Q in the volume makes it possible to determine the structural skeleton as a set of high-Q layers. They can intersect each other in a rather complicated way, especially low in the corona. With increasing height, however, the intersections become simpler, which particularly helps our goal of studying the large-scale structure. Determining the Q distribution at a given cut plane, similar as done before in other works (Aulanier et al. 2005; Titov et al. 2008; Pariat & Démoulin 2012; Savcheva et al. 2012a, 2012b), is also helpful for analyzing complex structures. We calculate Q distributions at cut planes, extending the method that Pariat & Démoulin (2012) described for configurations with plane boundaries to the case of spherical boundaries. The high-Q lines in such distributions visualize the cuts of the structural skeleton by those planes. As will be shown below (Figure 9), this kind of visualization becomes particularly useful if the colors corresponding to low values of Q ($\lesssim 10^2$) are chosen to be transparent.

We also find it useful to apply this transparency technique to the photospheric and source-surface Q distributions, particularly if one uses in addition a special color coding that takes into account the local sign of the normal field B_r at the boundary. The function that facilitates this color coding is called *signed log* Q or simply $\mathrm{slog}\,Q$ and defined as (Titov et al. 2011)

$$\mathrm{slog}\,Q \equiv \mathrm{sign}(B_r)\log[Q/2 + (Q^2/4 - 1)^{1/2}]. \qquad (1)$$

Using a symmetric blue–white–red palette in combination with the above transparency mask, we make visible in $\mathrm{slog}\,Q$ distributions only high-Q lines, colored either in blue or red in negative or positive polarities, respectively. The resulting maps

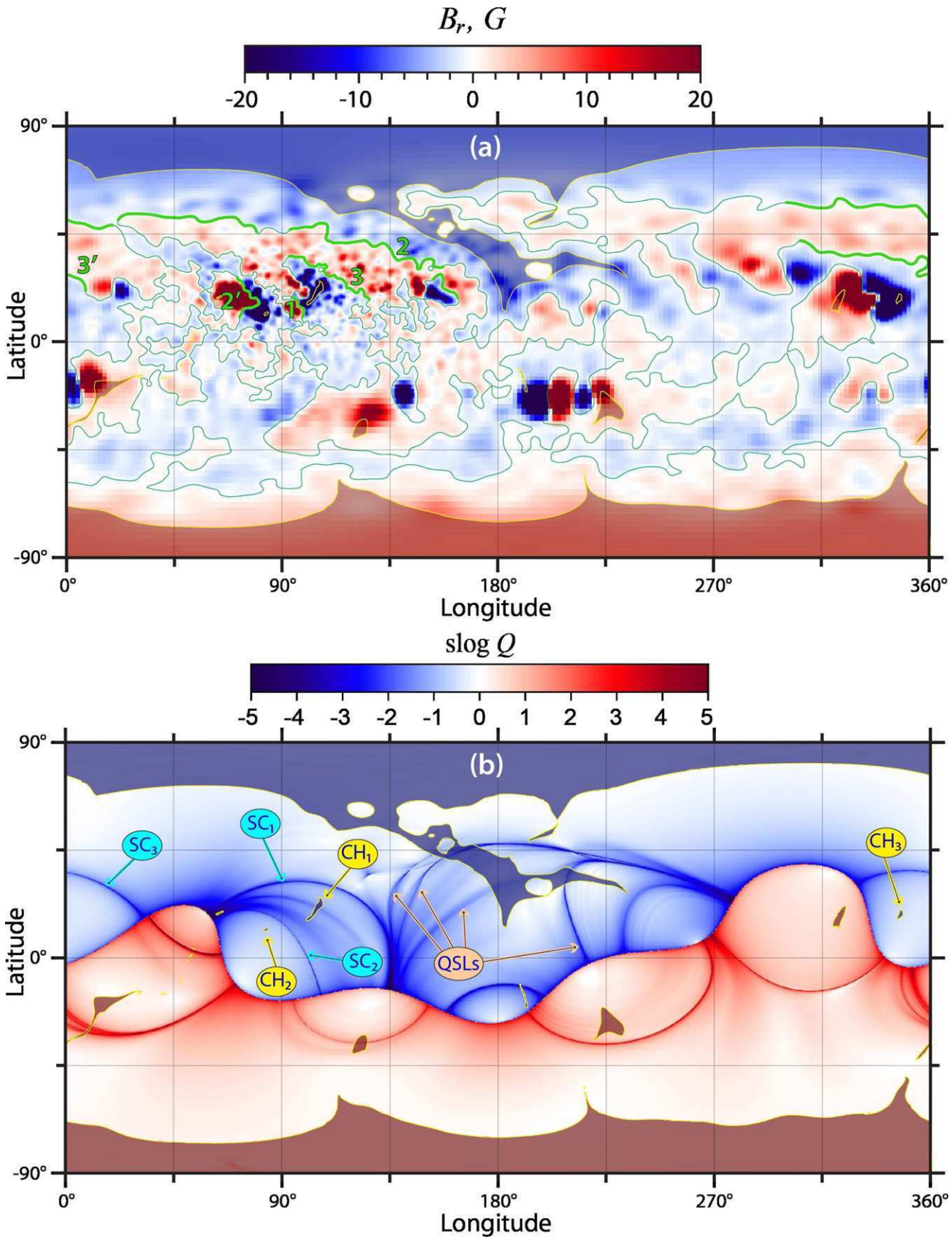

Figure 2. Map of B_r (a) used as a photospheric boundary condition for our PFSS model of the 2010 August 1–2 magnetic field and map of slog$Q$ for this model at the source surface (b) with superimposed (semi-transparent) photospheric map of coronal holes (shaded either in dark red ($B_r > 0$) or dark blue ($B_r < 0$) and outlined in yellow). Thin (green) lines represent the photospheric polarity inversion line, whose thick segments designate the location of the filaments, part of which are numbered in the order they erupted. Yellow balloons indicate the coronal holes involved in the eruptions; cyan balloons indicate source-surface footprints of the separatrix curtains of these pseudo-streamers.

(A color version of this figure is available in the online journal.)

provide a compact and powerful representation of the structural skeleton at the boundaries, as evident from our illustrations below.

Since our magnetic field is potential, Q acquires high values only in three cases: either the corresponding field lines scatter from localized inhomogeneities of the field nearby its null points or minimum points (Titov et al. 2009) or touch the so-called bald patches (BPs), which are certain segments of the photospheric polarity inversion line (Seehafer 1986; Titov et al. 1993). To make the whole analysis comprehensive, we separately determine the location of all such relevant features and then relate them to the high-Q lines at the boundaries by tracing a number of field lines that pass through these features. The pattern of high-Q lines determined at spherical surfaces of different radii provides us with estimates of the regions in which the magnetic nulls and minima can be present. Using then standard numeric algorithms (see, e.g., Press et al. 2007), both these features are found as local minima of B^2 that is defined between the grid points in these regions by cubic spline interpolation. Calculation of the matrix of magnetic field gradients $[\nabla \mathbf{B}]$ and its eigenvectors at the found nulls and minima allows us to determine the local (quasi-)separatrix structure, which is further used to initialize tracing of the respective (quasi-)separatrix field lines. For tracing generalized (quasi-)separators (see Section 3), which connect a pair of any of the above three features (i.e., nulls, minima, or BP points), we use a technique that is based on similar principles as described earlier for classical null–null separators by Close et al. (2004) and Haynes & Parnell (2010).

3. ANALYSIS OF THE MAGNETIC STRUCTURE

3.1. Coronal Holes versus High-Q Lines at the Boundaries

As mentioned in Section 2.1, the eruptive region contains three coronal holes of negative polarity that are distinctly disconnected at the photospheric level by positive parasitic polarities. With increasing height, however, these coronal holes start to expand and subsequently merge with each other and with the main body of the northern polar coronal hole. Being fully open at the source surface, the magnetic fluxes of these coronal holes still remain separated by the so-called *separatrix curtains* (SCs; Titov et al. 2011). As will become clear below, the SCs are simply vertical separatrix surfaces that originate at null points of the magnetic field low in the corona. At the source surface, their footprints appear as arcs joined at both ends to the null line of the magnetic field, so that the corresponding junction points divide the null line into several segments. Taken in different combinations, such segments and footprints of SCs form several closed contours. The contours encompass the fluxes corresponding to the coronal holes that are disconnected at the photospheric level from each other and from the like-polarity coronal holes at the poles. This fact clearly manifests itself on our source-surface $\log Q$ map that is superimposed in Figure 2(b) on top of the photospheric coronal holes' map. The figure indicates, in particular, that the high-Q line of the footprint SC_2 (SC_3) and the null-line segment to which the footprint adjoins encompass the CH_2 (CH_3) flux. Similarly, the source-surface footprints SC_1 and SC_2 and two short null-line segments to which the footprints adjoin encompass the CH_1 flux.

It should be noted, however, that some of the source-surface high-Q lines do not represent the footprints of SCs, but rather the footprints of QSLs that stem at the photosphere from narrow open-field corridors connecting spaced parts of otherwise single coronal holes. The high-Q lines of QSLs usually appear less sharp than those of SC footprints (see Figure 2(b)). The indicated QSL footprints can easily be related to certain open-field corridors in the northern polar coronal hole. If one traces down several field lines from the paths that go across these high-Q lines, the photospheric footpoints of these field lines will sweep along the respective open-field corridors, as predicted earlier by Antiochos et al. (2007). However, a similar procedure in the case of the SCs would give a very different result, which becomes clear after analyzing the magnetic topology low in the corona near the indicated coronal holes.

As a first step in this analysis, let us consider the coronal-hole maps and $\log Q$ distribution, both defined at the photospheric level and superimposed onto each other as shown in Figure 3. The pattern of high-Q lines here is more complicated than at the source surface, as expected. Nevertheless, in the region of interest, it prominently reveals three high-Q lines (red), which are identified after inspection as photospheric footprints of the above-mentioned SCs. They traverse along parasitic polarities and separate the indicated coronal holes in a similar manner as their source-surface counterparts. Note also that these footprints and nearby filaments are locally co-aligned, and at least five of these filaments were eruptive.

Figure 4 shows the described distributions of $\log Q$ and B_r in three dimensions and a few field lines that produce loop-arcade structures above the filaments. The loops of arcades are rooted with one footpoint at the positive parasitic polarities that disconnect our three coronal holes either from each other (CH_1 from CH_2) or (CH_1 and CH_3) from the northern coronal hole. Thus, these arcades form in pairs the twin magnetic field lobes of the three pseudo-streamers embedded between the indicated coronal holes. We also see here that four of the five filaments (all the numbered ones, except for 2′, in Figures 3 and 4) were initially located inside such lobes.

3.2. Separatrix Structure of Pseudo-streamers

Of particular interest to us is the question on how the pseudo-streamer lobes are bounded in our configuration by separatrix surfaces of the magnetic field. It turns out that these surfaces originate either at the null points or at the BPs, both mentioned already in Section 2.2 in connection with high-Q lines. Following Priest & Titov (1996), we will use the terms "fan surface" and "spine line" to designate, respectively, two-dimensional and one-dimensional separatrix structures that are related to a null point. They are defined through the eigenvectors of the matrix of magnetic field gradients at this point in the following way. The fan separatrix surface is woven from the field lines that start at the null point in the plane spanned on the eigenvectors, whose eigenvalues are of the same sign. The spine line is a separatrix field line that reaches the null point along the remaining third eigenvector. For a potential field, the spine line is always perpendicular to the fan surface.

In accordance with the recent analytical model of pseudo-streamers (Titov et al. 2011), the boundaries of our pseudo-streamers are composed of three types of separatrix surfaces, two of which are the fan surfaces of some coronal null points, while the third one is a BP separatrix surface. The fans of the first type have a curtain-like shape, whose field lines emanate from a null point, called henceforth basic one. We have already discussed these surfaces above as SCs in connection with boundary high-Q lines. They contain both closed and open field lines and extend from the photosphere to the source surface, as shown in Figures 5 and 6.

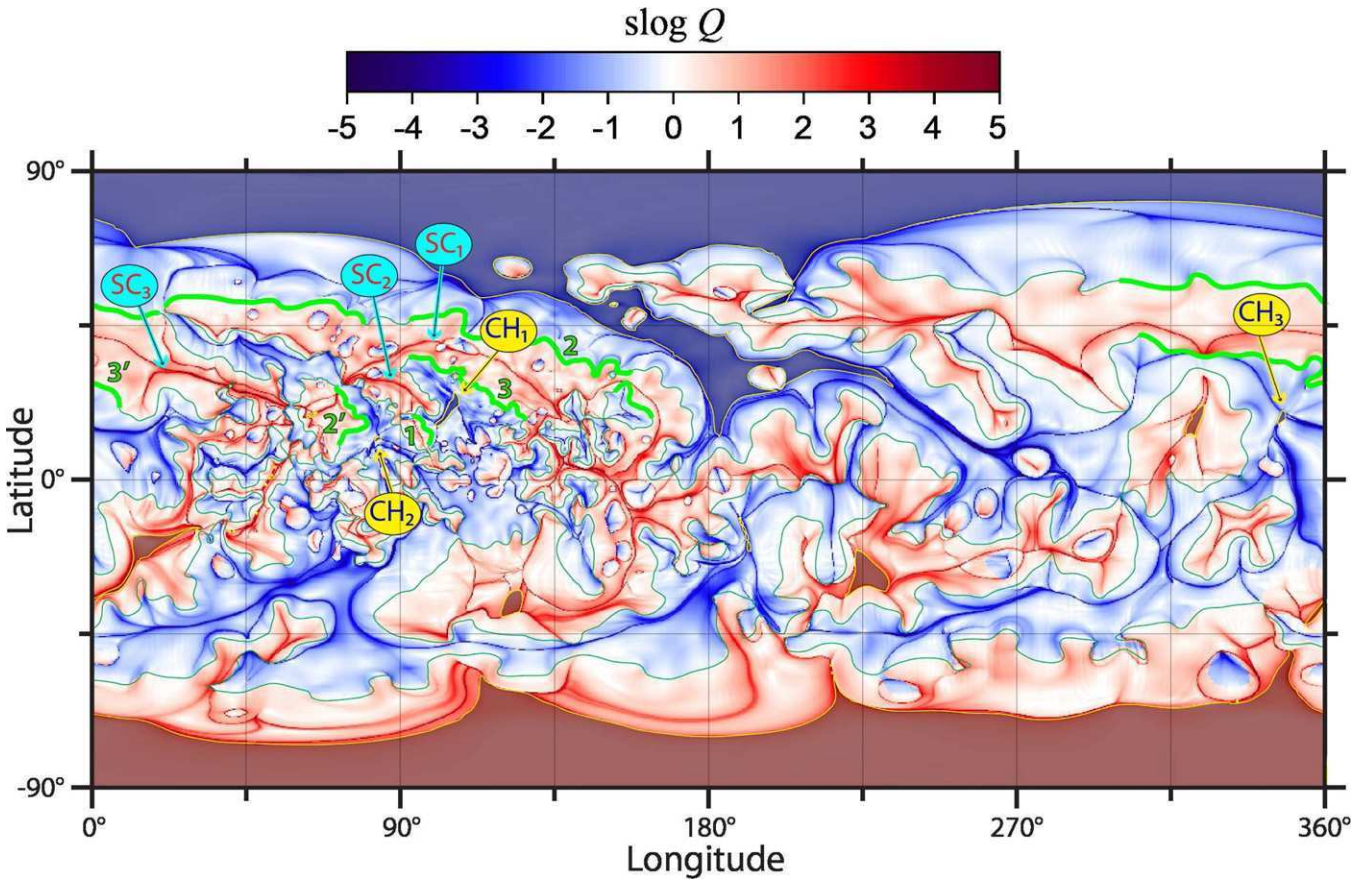

Figure 3. Map of slog Q for our PFSS model at the photosphere with superimposed (semi-transparent) photospheric map of coronal holes and the photospheric polarity inversion line, both shown in the same way as in Figure 2. Yellow balloons indicate the coronal holes of the pseudo-streamers involved in the eruptions; cyan balloons indicate photospheric footprints of the separatrix curtains of these pseudo-streamers.

(A color version of this figure is available in the online journal.)

The fans of the second type are associated with other nulls and include only closed field lines. Each of these fans bounds the closed flux of the parasitic polarity in a given pseudo-streamer only at one flank and forms a half-dome-like surface, whose edge is located in the middle of the pseudo-streamer and coincides exactly with the spine line of the basic null point (see Figure 7). The second half-dome is formed in all our three pseudo-streamers by the third type of separatrix surfaces that originate in BPs at the opposite flanks of pseudo-streamers. In fact, in our third pseudo-streamer even both separatrix half-domes are due to the presence of BPs (Figure 8).

3.3. Field Line Topology of Separatrix Curtains

Consider now in more detail the field line topology in all our three pseudo-streamers, starting from the two neighboring separatrix curtains SC_1 and SC_2 (see Figures 5 and 6). The field lines in each of these curtains fan out from its own basic null point that is located between two adjacent coronal holes of like polarity and above the respective parasitic polarity. The footprints of SCs, which are discussed in Section 3.1, can be viewed then as photospheric or source-surface images of single null points N_1 and N_2 due to their mapping along closed or open, respectively, field lines.

Within a given SC, such a mapping is continuous everywhere except for few special field lines, called *separators*, where the mapping suffers a jump. This jump takes place whenever a mapping field line hits a null point (like $N_{1\text{-}2}$ and $N_{1\text{-}3}$ in Figure 5, or a BP, like BP_1 in both Figures 5 and 6). To distinguish these separators from other field lines, we have plotted them thicker in these and further similar figures.

In addition to the mentioned closed separators, there are also two open ones for each of the curtains. These open separators connect the null N_1 (or N_2) to a pair of null points belonging to the source-surface null line. The latter is simply the helmet streamer cusp, from which the heliospheric current sheet arises. Each of these pairs of nulls also coincides with the end points of the source-surface footprints of SCs.

Note, however, that any null line of the magnetic field is a topologically unstable feature that can exist only under very special conditions. We think, therefore, that the source-surface null line is most likely an artifact inherent only in the employed PFSS model. If passing from PFSS to MHD model, such a null line must turn at radii close to 2.5 $R_\odot$ into a feature that has a substantially different magnetic topology. Thus, the indicated topological linkages have yet to be refined, using a more realistic than PFSS model of the solar corona. We will do that in our next paper II, while here we proceed the analysis, assuming that our findings on open separators are approximately correct.

3.4. Field Line Topology of Separatrix Half-domes

Consider now in more detail the topology of separatrix domes (Figure 7), starting from the pseudo-streamers that are embedded between CH_1, CH_2, and the northern polar coronal

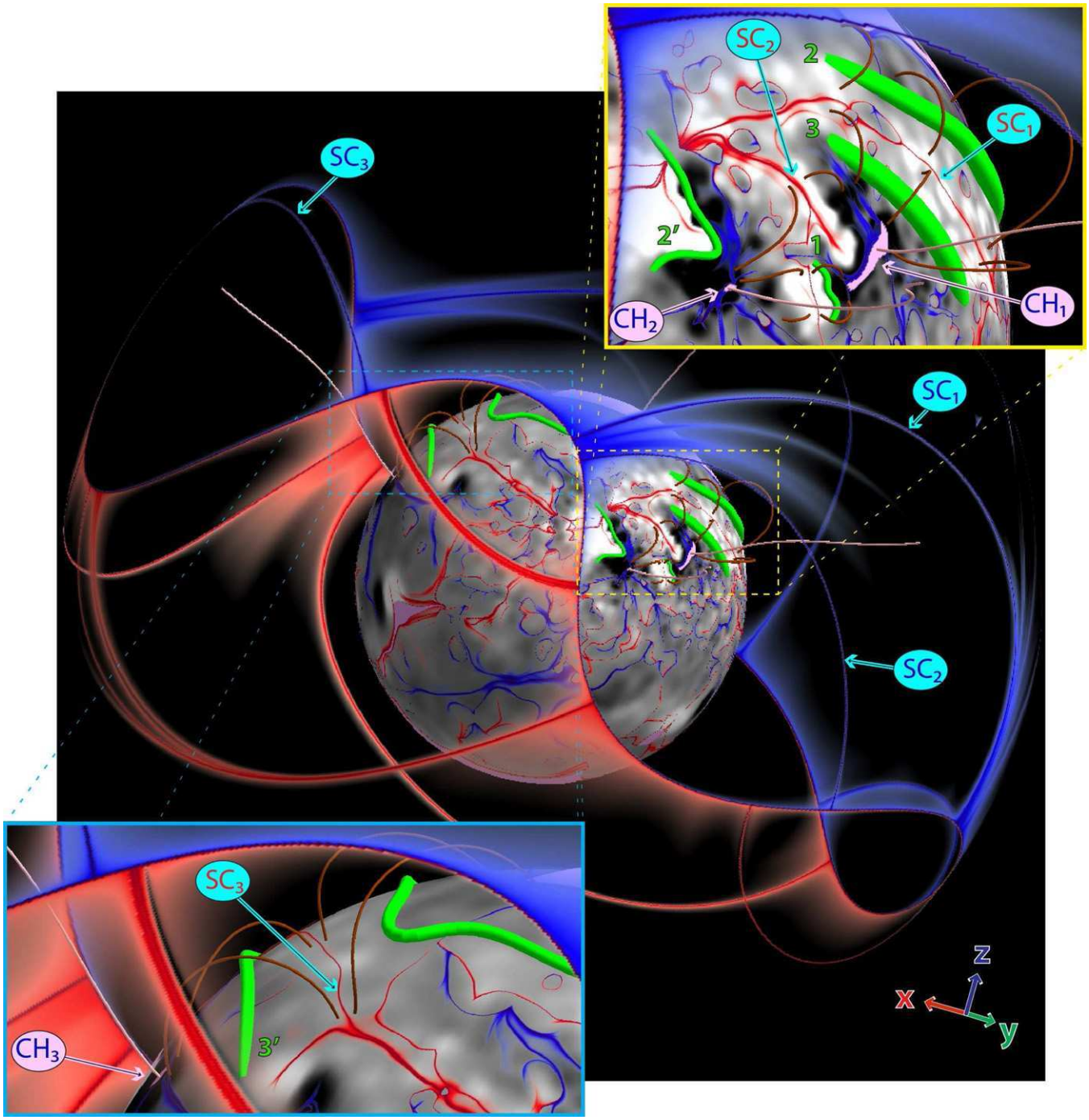

Figure 4. slog$Q$ distributions are mapped on the photospheric and source-surface globes with a varying opacity such that the low-Q areas ($Q \lesssim 300$) appear to be fully transparent. The photospheric slog$Q$ map is superimposed on the respective gray-scale B_r distribution with the coronal holes shaded in light magenta. Green tubes depict the major filaments prior to the onset of sympathetic eruptions and several field lines (brown) indicate the pseudo-streamer lobes enclosing these filaments. Open field lines (colored in pink) start in the middle of the coronal holes closest to the pseudo-streamers. The vector triad in the lower right-hand corner indicates the angle orientation of the Cartesian system that is rigidly bound to the Sun center with the z-axis directed to the north pole.

(A color version of this figure is available in the online journal.)

hole. The eastern half-domes (on the left) are combined in one simply connected surface, because they originate in one small bald patch BP_1 located at the border of an active region near the filament $2'$. Spreading out from BP_1, the field lines extremely diverge within this surface at the nulls N_1 and N_2 and hit the photosphere near the indicated coronal holes. Two of these field lines (red and thick), however, go instead straight to N_1 and N_2 and so, as discussed above, are *generalized separators* belonging to SC_1 and SC_2, respectively.

In contrast to the eastern half-domes, the western ones (on the right) do not merge with each other and have different originations. The half-dome covering filaments 2 and 3 is simply a fan surface of an extra null point $N_{1\text{-}2}$ that is located far to the west from the basic null N_1. These two nulls are connected by an ordinary separator, which belongs to both this half-dome and the curtain SC_1.

It is somewhat surprising, but the half-dome covering filament 1 appears to be a quasi-separatrix surface that originates at

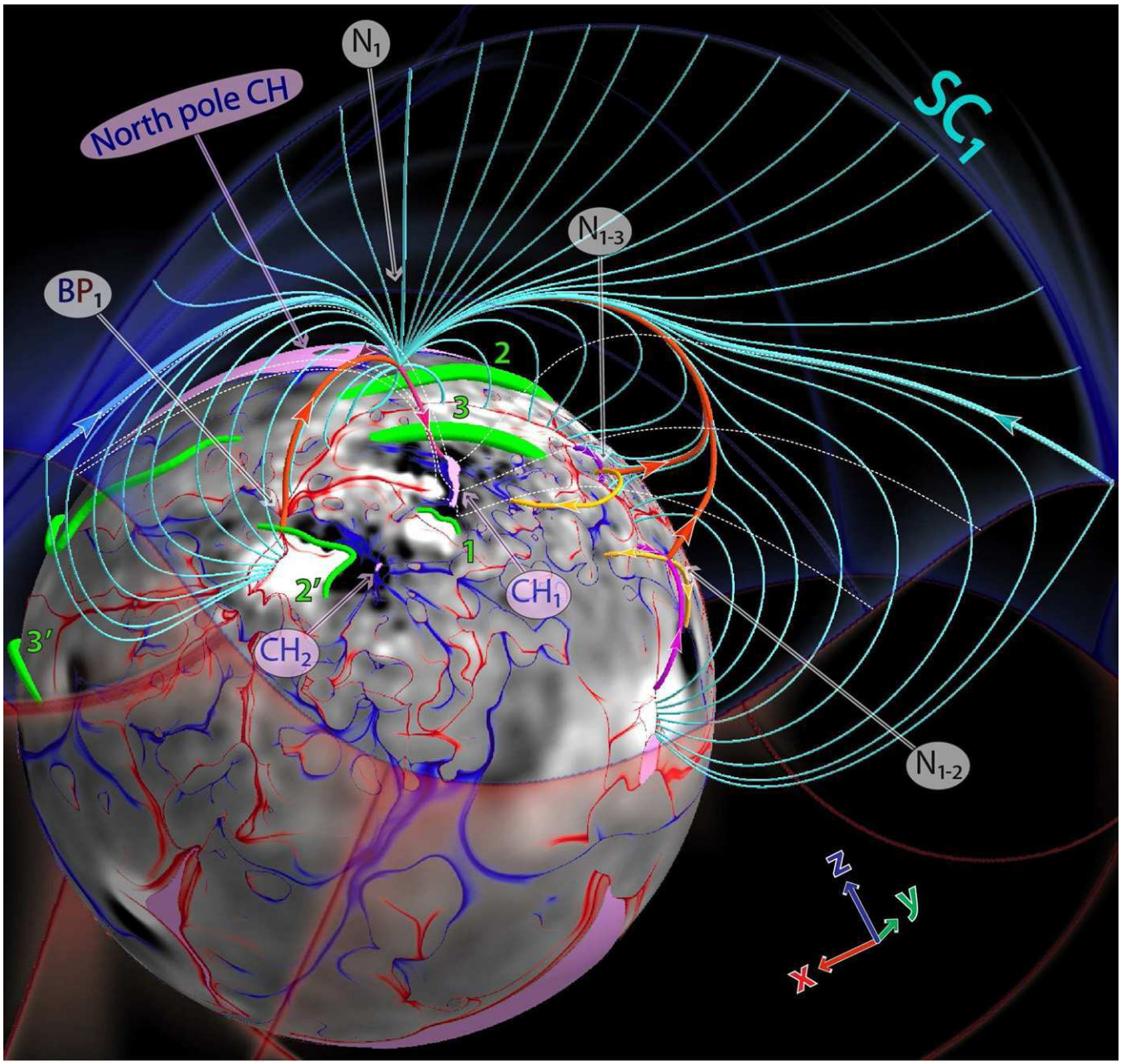

Figure 5. Field line topology of the separatrix curtain SC_1 of pseudo-streamer 1 (embedded between the northern polar coronal hole and CH_1). The thickest lines represent separators, of which the red ones are closed field lines connecting the null point N_1 either to the bald patch BP_1 or another nulls $N_{1\text{-}2}$ or $N_{1\text{-}3}$, while the cyan ones are open field lines connecting N_1 to the null line of the source surface. Magenta lines are the spine field lines of the nulls; the yellow lines are the separatrix field lines that emanate from the nulls $N_{1\text{-}2}$ and $N_{1\text{-}3}$ along the fan eigenvectors that are complementary to the separator ones; several field lines (white dashed) belonging to the boundary of CH_1 are also shown. The maps at the photosphere and source surface and their color coding are the same as in Figure 4.

(A color version of this figure is available in the online journal.)

a magnetic minimum point $M_{2\text{-}1}$ lying very close to the photosphere. The field line (red and thick) that passes through and connect $M_{2\text{-}1}$ to the basic null N_2 is a *quasi-separator*. The field direction remains unchanged after passing this line through the minimum $M_{2\text{-}1}$, as opposed to a genuine null point, where the field direction would change to the opposite. A similar behavior of the field at $M_{2\text{-}1}$ would also occur if it were a degenerate null point, whose one eigenvalue identically equals zero (Titov et al. 2011). We regard this possibility as highly unlikely here, but we cannot fully exclude it, relying only on our numerical study as an approximation of nature.

The existence of the null $N_{1\text{-}3}$ in the first of the two discussed pseudo-streamers brings an extra complexity into the structure. Figures 5 and 7 show that, similarly to $N_{1\text{-}2}$, the null $N_{1\text{-}3}$ is connected via an additional separator to the basic null N_1. This implies that the fan surface of $N_{1\text{-}3}$ is also a half-dome such that its edge coincides with the spine line of the null N_1. We did not plot this half-dome in Figure 7 to avoid cluttering the image with too many lines, but it is very similar to the plotted half-dome that originates in the null $N_{1\text{-}2}$.

The third pseudo-streamer, which is embedded between CH_3 and the northern polar coronal hole, has the topology as analogous as the one of the two others considered above (see Figure 8). The main difference is only that both half-domes originate here at bald patches BP_2 and BP_3, which are located at the opposite flanks of the pseudo-streamer. In this respect,

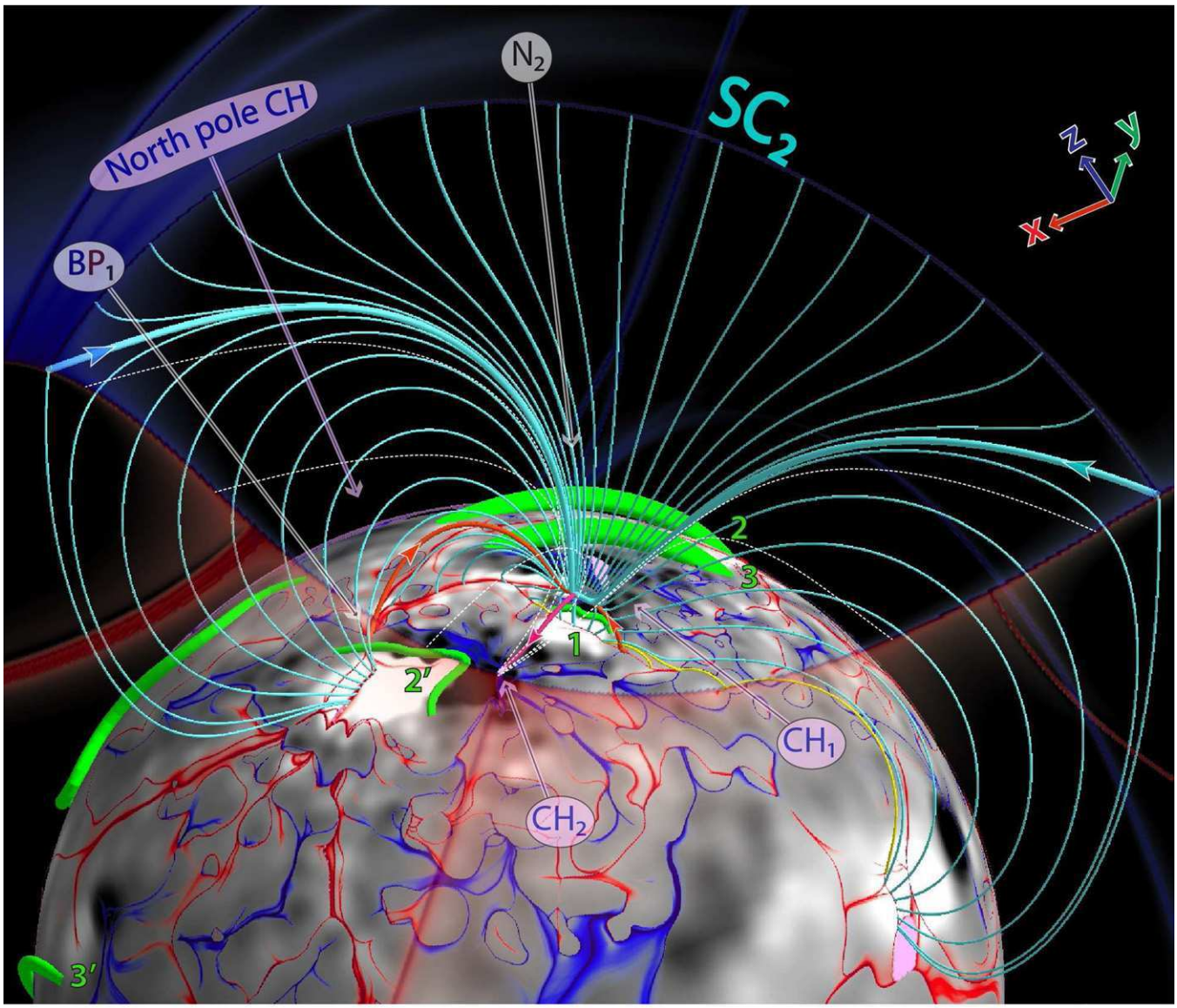

Figure 6. Field line topology of the separatrix curtain SC_2 of pseudo-streamer 2 (embedded between the coronal holes CH_1 and CH_2). The field line styles are the same as in Figure 5, except that the thin yellow lines represent separatrix field lines associated with small-scale photospheric polarity regions. The maps at the photosphere and source surface and their color coding are the same as in Figure 4.

(A color version of this figure is available in the online journal.)

the structure is the same as the one used before for initializing our MHD model of sympathetic eruptions (Török et al. 2011). It is important that these simulations have demonstrated that the generalized separators connecting such BPs and null points are physically similar to the ordinary separators. They both appear to be preferred sites for the formation of current sheets and reconnection of magnetic fluxes.

3.5. Field Line Topology versus High-Q Lines in the Cut Planes

A complementary way to study the structure of a pseudo-streamer is to consider its cross-sectional Q distributions and analyze their variation in response to changing location of the cut plane. As one can anticipate from the above analysis, the simplest pattern of high-Q lines appears to occur in the cut plane across the very middle of pseudo-streamers, where the basic null point is located. The corresponding high-Q lines form there a $\cap$-type intersection such that the vertical line and arc in the symbol $\cap$ represent, respectively, the discussed SCs and domes. The shape of separatrix domes at this place essentially follows the path of the spine line associated with the respective basic null point. Above such a dome, the SC separates the open fields of two adjacent coronal holes and observationally corresponds to the stalk of the pseudo-streamer.

However, with shifting the cut plane from the middle to the flanks of pseudo-streamers, the pattern of high-Q lines gets more complicated. In particular, the above high-Q arc can split into several lines, each of which corresponds to a separate half-dome, except for the uppermost line. The latter asymmetrically rises on one side from the curtain up to the source surface and, touching it, forms a cusp. This line determines the border between closed and open fields, since it is nothing else than an intersection line of the cut plane with the separatrix surface of the helmet streamer. Figure 9 illustrates such a structure in a particular cut plane; it also shows schematically how the cross-sectional pattern varies along the pseudo-streamer. Only three cases where the cut plane passes at the photospheric level outside CH_1 and CH_2 are shown in this figure, while the

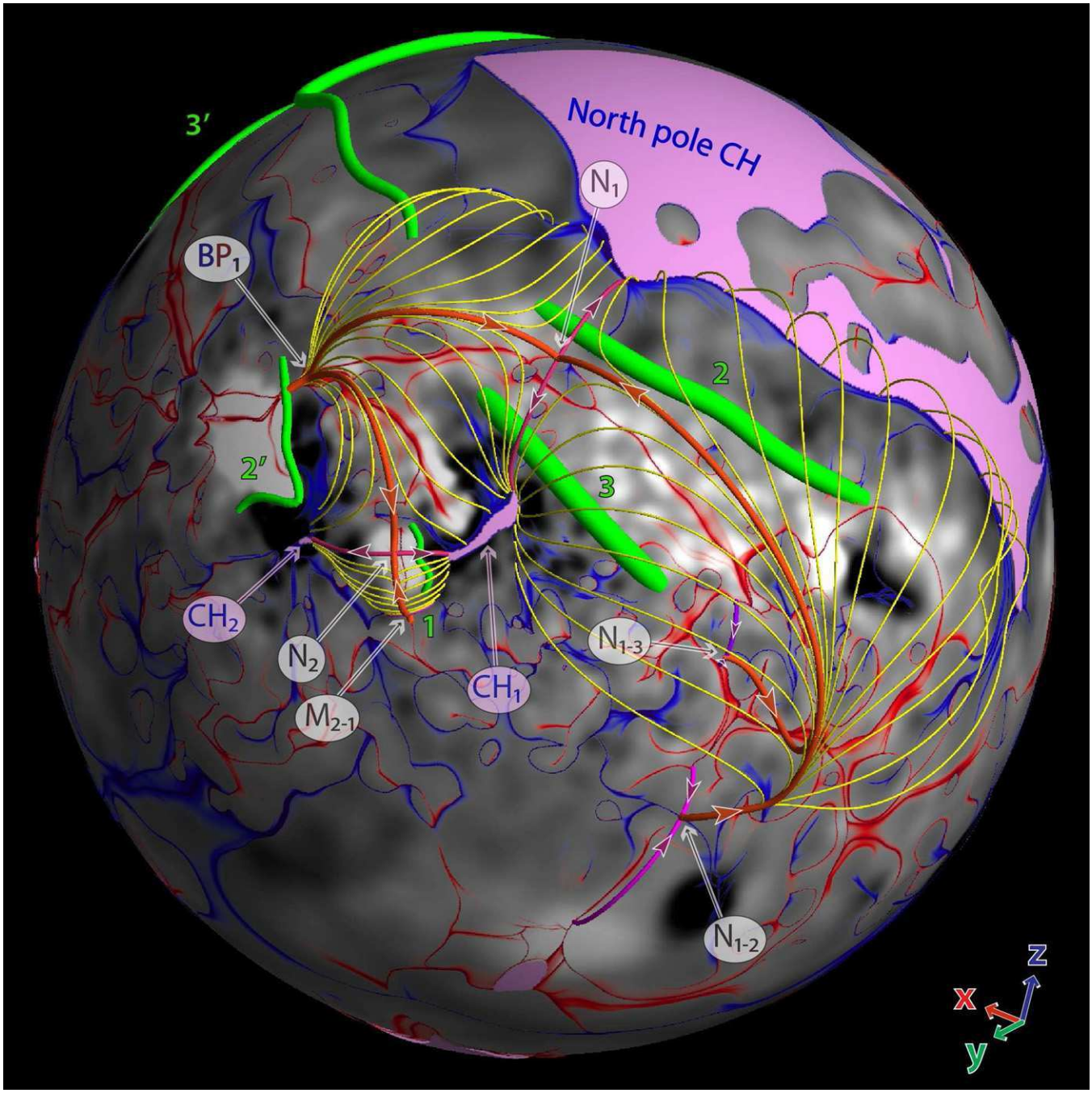

Figure 7. Field line topology of the separatrix domes of pseudo-streamers 1 and 2, one of which is embedded between the northern polar coronal hole and CH_1 and the other between the coronal holes CH_1 and CH_2. The field line styles are the same as in Figures 5 and 6, except that the thin yellow lines represent separatrix field lines starting either at the bald patch BP_1 or in the fan plane of the null point $N_{1\text{-}2}$; a similar separatrix dome associated with the null $N_{1\text{-}3}$ is not shown. The same style is used for the field lines of the quasi-separatrix surface originated at the magnetic minimum point $M_{2\text{-}1}$. The maps at the photosphere and source surface and their color coding are the same as in Figures 4–6.

(A color version of this figure is available in the online journal.)

remaining cases can be reproduced analogously from the above analysis.

3.6. Concluding Remarks

So far, we have only fully described the structural skeleton of the first pseudo-streamer, including the separatrix curtain SC_1 and respective half-domes with their separators. As concerned with the other two pseudo-streamers, we still have not touched on several separators depicted in Figures 6 and 8 with yellow and orange thin lines. These separators are due to "scattering" of the SC field lines on small photospheric flux concentrations of negative polarity. Such scattering occurs at BPs or null points to yield additional half-domes, whose edges coincide with the spine lines of the basic nulls N_2 or N_3. The existence of these features, however, can vary depending on the resolution and smoothing of the used magnetic data, so we ignore them in our study, focusing only on stable structural features that are due to large-scale properties of the configuration.

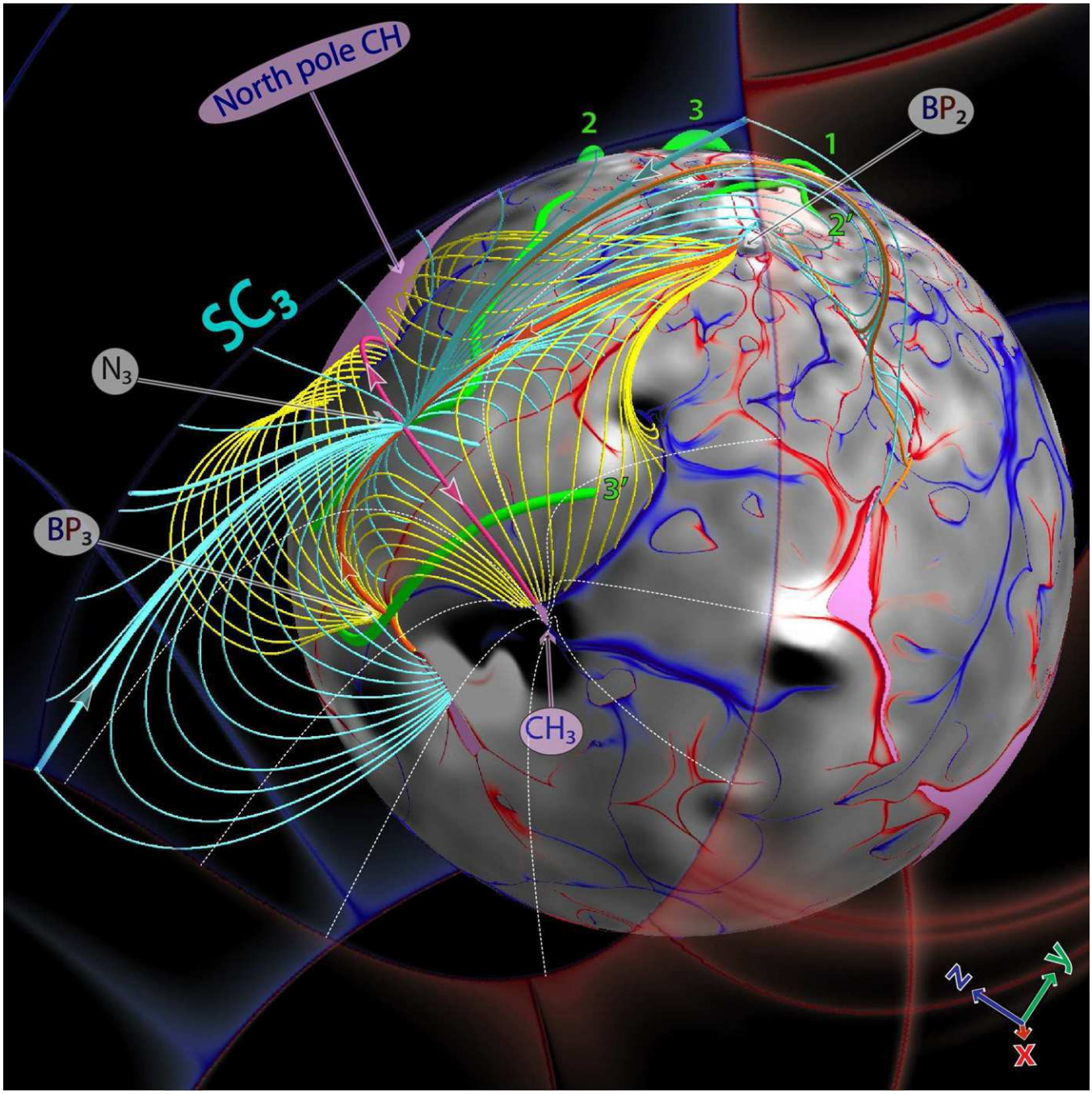

Figure 8. Field line topology of the separatrix curtain (cyan) and dome (yellow) of pseudo-streamer 3 (embedded between the northern polar CH and CH_3). The field line styles are the same as in Figures 5–7, except that the thin orange lines represent the separatrix field lines that are associated with the bald patches and null points of small-scale photospheric polarity regions. The maps at the photosphere and source surface and their color coding are the same as in Figures 4–7.

(A color version of this figure is available in the online journal.)

One also has to remember that the described structure might be distorted in reality by the field of filaments whenever they are present inside pseudo-streamer lobes. Note, however, that such filaments reside prior to eruption in the middle of the lobes along photospheric polarity inversion lines. So possible intense currents of the filaments are located relatively far from the found separatrix domes and curtains and hence the contribution of such currents to the total field must be small at these places compared to the background potential field. Therefore, we think that at large length scales our PFSS model is accurate enough to describe the structure of the real pseudo-streamers with the filaments inside the lobes.

4. MAGNETIC TOPOLOGY AS A CAUSAL LINK IN SYMPATHETIC CMEs

We have studied in Section 3 how SCs and half-domes originate in a given pseudo-streamer at magnetic null points and/or BPs and how they intersect each other along separator field lines. These results are of importance for unveiling a causal link in the sequential eruption of filaments, in which the magnetic topology and reconnection likely played a key role. Indeed, according to the present state of knowledge (Priest & Forbes 2000), a perturbation in the neighborhood of a separator line generally creates along it a current sheet, across which

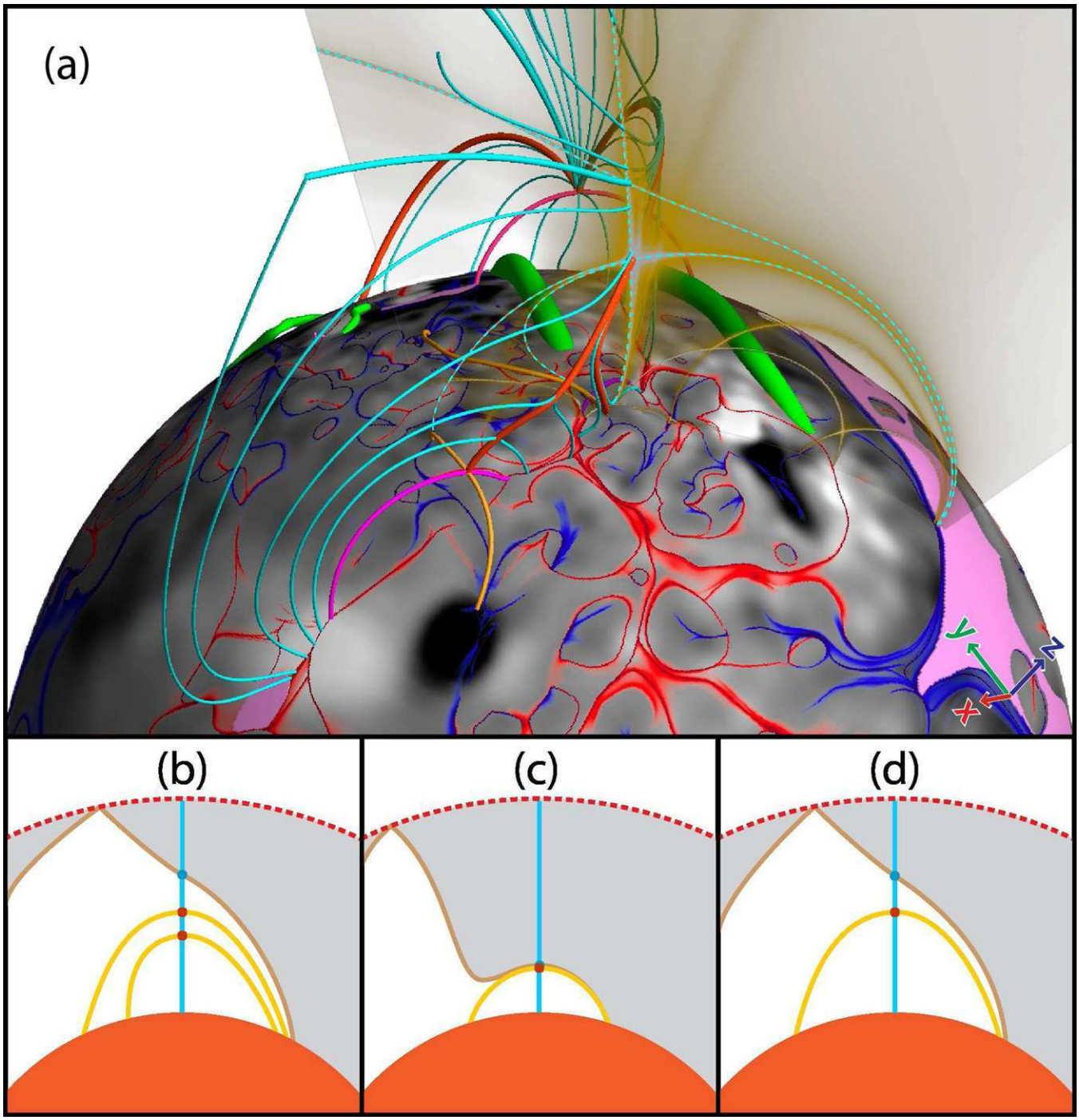

Figure 9. Field line topology of the separatrix curtain SC_1 in relation to the log Q distribution in a cut plane across the pseudo-streamer 1 (a). This distribution is plotted by using a yellow palette, whose opacity linearly decreases with log Q in the range from 2.5 to 0.3 down to a complete transparency; the maps at the photosphere, their color coding, and the field line styles are the same as in Figure 5. Dashed (cyan) curves highlight the high-Q lines that represent the intersection lines of the cut plane with SC_1, helmet-streamer separatrix surface, and two separatrix domes. Such a structure is shown also schematically for this cut and two others in panels (b)–(d), respectively, where the open-field regions are shaded in gray; the extra two cuts are made successively further eastward from the middle of the pseudo-streamer.

(A color version of this figure is available in the online journal.)

magnetic fluxes subsequently reconnect in an amount depending on the form and strength of the perturbation. As demonstrated above, each of our pseudo-streamers contains several separators, all of which are connected to a basic null point. A perturbation in its neighborhood is expected then to cause reconnection along each of these separators, resulting ultimately in a flux redistribution between adjacent topological regions.

It follows from our analysis that these regions are simply the volumes bounded by various parts of the SC, half-domes, and separatrix surface of the helmet streamer. Unfortunately, such a complex topological partition of the volume makes it difficult to foresee all the details of the response of our pseudo-streamers to different MHD perturbations. It is clear, however, that eventually such perturbations will change the magnetic fluxes in the lobes and consequently the stability conditions for the filaments within them. The latter in turn can influence the order of eruption of the filaments, which was recently demonstrated in our simple MHD model of sympathetic eruptions (Török et al. 2011).

In this model, a pseudo-streamer similar to the one that stems from the basic null N_1 played a key role in guiding the eruptions of the magnetic flux ropes, analogous to our filaments 2 and 3. Thus, our present topological analysis of the potential background field further substantiates the model.

Let us put now the results of that model into the context of our present analysis in order to explain the observed sequence of the 2010 August 1–2 CMEs. For simplicity, we restrict our consideration to the reconnection processes that occur in the vicinity of the basic nulls of the pseudo-streamers, where we expect the greatest perturbation to occur during the onset of eruptions. As shown above, all separatrix half-domes merge there and form together with the SC a simple $\pitchfork$-type intersection. Such a separatrix structure implies that, irrespective of the form of the external perturbation, the reconnection triggered there will be of the interchange type (e.g., Fisk 2005). It will exchange the fluxes between the lobes and coronal holes in such a way that the sum of the fluxes in both the two lobes and the two coronal holes remains unchanged. In other words, the diagonally opposite lobes and coronal holes form conjugate pairs, so that the flux in one pair increases by the same amount that it decreases in the other pair.

To facilitate further discussion, we label the pseudo-streamers by the numeric label of their basic null; similarly, we label the lobes by the label of their embedded filament. Note, first, that erupting filament 1 resides initially in pseudo-streamer 2, which is located south of pseudo-streamer 1 (see Figure 7). Therefore, the rise of filament 1 perturbs the southern side of pseudo-streamer 1 and eventually triggers interchange reconnection between the fluxes of coronal hole CH_1 and lobe 2. This reconnection reduces the flux in lobe 2, thereby removing the field lines that overlie and stabilize filament 2, eventually causing it to erupt (i.e., the second eruption). On the other hand, this same interchange reconnection causes the flux in lobe 3 to increase, adding field lines that overlie filament 3, thus further stabilizing it. However, later in time, after erupting filament 2 has risen to a sufficient height, a vertical current sheet forms in its wake, providing a site for interchange reconnection between the fluxes of lobe 3 and the northern polar coronal hole. This second reconnection eventually reduces the flux in lobe 3, removing field lines that overlie and stabilize filament 3, eventually causing filament 3 to erupt (i.e., the third eruption).

This scenario is consistent with that proposed for the sequential eruption of filaments 1–3 in our idealized model (Török et al. 2011). There is one difference though: our present PFSS model reveals that filament 1 was also located inside a pseudo-streamer, which is pseudo-streamer 2 in our notation. The presence of this pseudo-streamer, however, merely facilitates the eruption of filament 1, because its overlying field becomes open at a very low height. So this new feature fits nicely with our earlier proposed mechanism.

The present analysis suggests possible explanations also for the eruptions 2′ and 3′. According to Figures 5–7, filament 2′ passes above bald patch BP_1, which is connected by two separators to the basic null points N_1 and N_2. As discussed above, the rise of filaments 1 and 2 is expected to activate these separators, forming current sheets along them, and subsequently triggering reconnection. Around the location of BP_1, this reconnection may have been of the tether-cutting type (Moore et al. 2001), reducing the confinement of the active-region core field and eventually unleashing its eruption. This explanation is in agreement with the fact that *SDO*/AIA observed several brightenings in the active region before the CME occurred. There was a particularly strong brightening at ∼06:36 UT below and above filament 2′, very close to the bald patch BP_1 (see the inset in Figure 10). This brightening occurred after filament 2 had already started to rise, implying the above activation of the separator and subsequent reconnection in the vicinity of bald patch BP_1. We note that Liu et al. (2010) also associated the pre-eruption brightening at ∼06:36 UT to tether-cutting reconnection, triggered, however, by photospheric converging flows rather than separator activation. It appears indeed possible that both processes played a role. We will make a more detailed comparison of our topological analysis with observations in Paper II.

The location of pseudo-streamers 1 and 3 indicates that the eruptions 2 and 2′ should produce a significant perturbation of the northern side of pseudo-streamer 3. This should lead to interchange reconnection between lobe 3′ and the northern polar coronal hole, reducing the magnetic flux in this lobe and eventually causing filament 3′ to erupt, in a similar way as described for filament 2. Note also that filament 3′ rises above bald patch BP_3, which is connected by a separator to the basic null N_3 (see Figure 8). As discussed above for eruption 2′, resulting tether-cutting reconnection may trigger the destabilization of filament 3′, in tandem with the indicated flux reduction in the lobe 3′ caused by interchange reconnection.

This concludes the extended scenario for the sympathetic eruptions under study. Figure 10 summarizes it, presenting all the topological features that are relevant for this scenario. In particular, it depicts the closed separators (red thick lines) that form a long chain that traverses through all three pseudo-streamers. As described above, such a separator chain likely sets up a global coupling between eruptions occurring at widely separated locations. Figuratively speaking, this separator chain plays the role of a "safety fuse" in which a single eruption at one end of the chain triggers along it a sequence of the observed electromagnetic explosions.

Additional global coupling between pseudo-streamers and eruptions might also be provided by the open separators (thick cyan lines in Figure 10), which connect the basic nulls of the pseudo-streamers to the cusp of the helmet streamer. This coupling, however, has yet to be verified. It requires a more advanced model than the PFSS model used in the present study. We plan to use an MHD model for this purpose in the next step of our study.

The proposed explanation of the assumed causal link in the observed sympathetic eruptions is of substantial heuristic value. It is particularly useful as a guide for setting up and analyzing further numerical studies of these eruptions. In combination with our structural analysis, more detailed numerical simulations of CMEs in this configuration are needed to prove the existence of such a link and to deepen its understanding.

5. IMPLICATIONS FOR THE S-WEB MODEL

The structural analysis of pseudo-streamers that we have described has important implications not only for sympathetic CMEs but also for the slow solar wind. The recent S-web model (Antiochos et al. 2011; Linker et al. 2011) has sparked substantial interest in the community (Crooker et al. 2012; Wang et al. 2012). Unfortunately, several important issues related to this model are not well understood. Since the results obtained above relate to the S-web model, we will use this opportunity to clarify these issues.

The first issue relates to the concept of coronal-hole connectivity. Some confusion has arisen because the connectivity

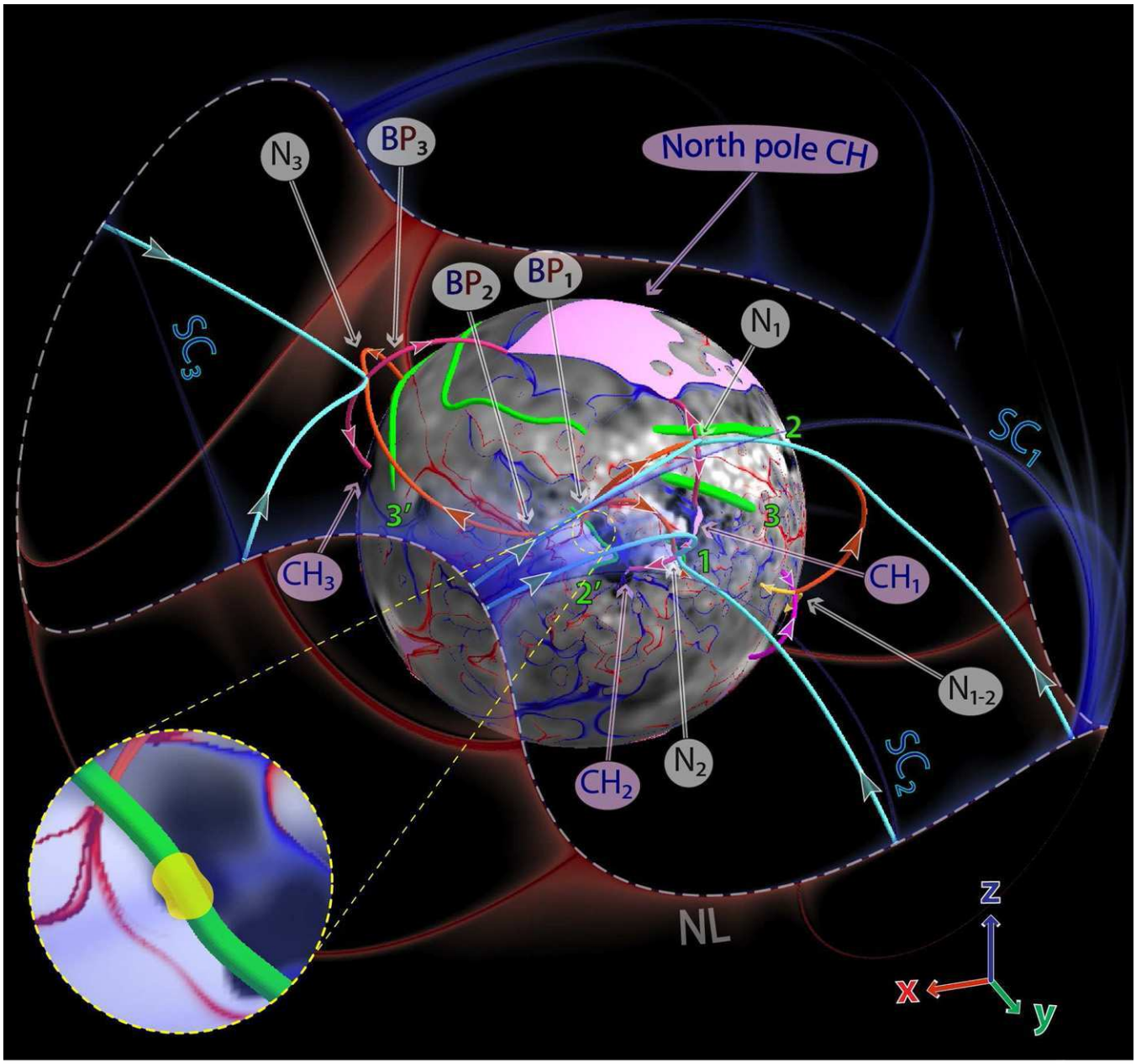

Figure 10. Chain of separators and spine lines in all three pseudo-streamers that were involved in the 2010 August 1–2 sympathetic CMEs. The white dashed line is the null magnetic field line of the source surface—together with the open separator field lines (cyan), it provides a global coupling between all three null points of the pseudo-streamer separatrix curtains. The inset shows a zoomed region near BP_1, where a strong pre-flare brightening (indicated by yellow blob) was observed by *SDO*/AIA at ~06:36 UT shortly after which eruption 2′ started.

(A color version of this figure is available in the online journal.)

of coronal holes has been interpreted in two different senses. We can consider coronal holes either as two-dimensional regions at the photosphere or as three-dimensional regions in the corona. Though coronal holes of like polarity are always connected when considered as three-dimensional regions, it is important to note that they *can be disconnected* in the photosphere when considered as two-dimensional regions (Titov et al. 2011). In this case, they merge at some height in the corona via a field line separatrix structure that observationally manifests itself as a pseudo-streamer.

The pseudo-streamers we described above (see Figures 5–8) illustrate this fact conclusively. All these cases were characterized by disconnected coronal holes CH_1, CH_2, and CH_3 (Figure 2), each of which merges with an adjacent coronal hole at the height of the basic null point of the corresponding pseudo-streamer. At heights where the magnetic field becomes completely open, the corresponding separatrix curtains SC_1, SC_2, and SC_3 serve as interfaces between the holes. Note also that their footprints appear at the source surface as very sharp high-Q lines, whose ends are joined to the null line of the magnetic field (Section 3.1).

Of course, this does not exclude the possibility for different parts of photospheric open-field regions to be connected with each other through narrow corridors. Several examples of such corridors are also seen in our northern polar coronal hole (Figure 2). They imply the appearance of QSLs in the open field, as proposed first by Antiochos et al. (2007), and whose transformation into SCs and back to QSLs has been described

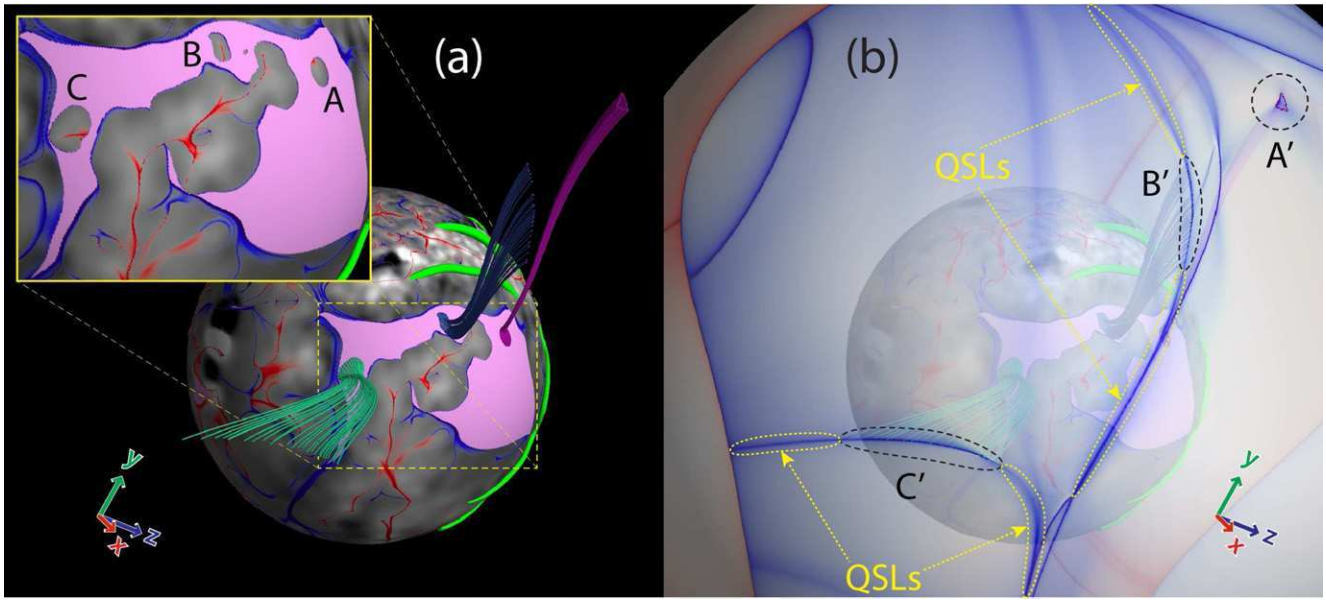

Figure 11. Structure of magnetic field lines near parasitic polarity regions A, B, and C embedded into the northern coronal hole (a) and location of their footprints A′, B′, and C′ at the source surface (b), where a (semi-transparent) slog$Q$ distribution is also displayed. The high-Q lines encircled by dashed (yellow) lines correspond to the footprints of QSLs that originate in the photospheric open-field corridors adjacent to these polarities.

(A color version of this figure is available in the online journal.)

at length by Titov et al. (2011). As already pointed out in Section 3.1, such QSLs appear at the source surface as high-Q lines with a smooth distribution of Q across their widths (Figure 2(b)). Just as in the case of SCs, these high-Q lines are joined at both ends to the null line of the magnetic field.

Thus, in both the case of truly disconnected and connected coronal holes, interpreted as two-dimensional photospheric regions, their mapping to the source surface connects to the null line of the helmet streamer. This is in contrast to the interpretation of Crooker et al. (2012), who regarded this property of the field line mapping as evidence of the connectivity of coronal holes at the photospheric level. Moreover, we think that the V-shaped coronal hole they interpreted as connected in the photosphere is actually disconnected, as our earlier study of the same case indicates in the framework of the global MHD model (Titov et al. 2011). This particular example shows that when coronal holes are connected in three dimensions it does not necessarily imply that they are connected in the photosphere too.

It remains to be studied how numerous the above open-field QSLs are, compared to SCs, in magnetic configurations with a realistically high resolution. Note that by definition they both belong to the S-web. In the slog$Q$-distribution at the source surface, the S-web appears as a network of high-Q arcs connected to the null line of the helmet streamer (Figure 2(b)). The width in latitude of the S-web at this surface is a well-defined quantity, because its value is uniquely related to the open photospheric flux that is (nearly) disconnected from the main bodies of the polar coronal holes. It is unlikely that this flux, and hence the width of the corresponding S-web, will significantly change if one further increases the resolution of the input magnetic data and the corresponding PFSS model.

This conclusion is in contrast with the statement of Wang et al. (2012) that the S-web will extend to the polar region if one resolves its small parasitic polarities. Each such polarity will, indeed, bring additional (quasi-)separatrix structures into the open-field regions. However, in contrast to the SCs of pseudo-streamers, these structures will, first, have a much smaller angular size and, second, will not criss-cross the S-web, but rather stay mostly isolated from it. Since the quasi-separatrix structures arising from parasitic polarities in polar coronal holes have different geometrical sizes and structural properties, their physical properties are also likely to be different. Therefore, they have not been included into the definition of the S-web (Antiochos et al. 2011), regardless of the fact that the polar plumes associated with these parasitic polarities might appear similar to pseudo-streamers observationally.

To clearly make this point, Figure 11 shows what happens around three small parasitic polarities (A, B, and C) embedded into the northern coronal hole. Panel (a) depicts three sets of open field lines that start very close to the oval high-Q lines bordering the closed magnetic flux of these polarities. Panel (b) shows their source-surface footpoints A′, B′, and C′, indicating that such field lines hit the boundary far away from the null line. Thus, their behavior indeed differs from that of the field lines belonging to the SCs we described previously.

In particular, as stated above, for polarities that are far from the main border of their surrounding coronal hole, such as A, their signature at the source surface A′ is completely isolated from the S-web. Polarities B and C, however, are much closer to the coronal-hole border; they are detached from it by only a relatively narrow open-field corridor. As expected, the field lines starting in these corridors form QSLs whose footprints at the source surface adjoin on each side of their respective footprints B′ and C′ (as shown in Figure 2(b)). The high-Q lines resulting from these merged QSLs would appear, at first sight, to form arcs whose ends join the null line of the helmet streamer. However, we would argue that these "arcs" do not genuinely belong to the S-web because these segments have rather low values of log Q ($\lesssim 1.5$). In summary, we have argued that the addition of small parasitic polarities in polar coronal holes would not contribute to the S-web significantly, if at all. We intend to test this conjecture in future work by explicitly calculating the contribution of parasitic polarities in high-resolution PFSS models.

These considerations help us to predict how our S-web will change with increasing resolution of the input magnetic data

and the corresponding PFSS model. First, increased resolution will cause additional fragmentation of the disconnected coronal holes, while leaving their total magnetic flux approximately unchanged. Our analysis suggests that this will increase the number of cells and high-Q lines in the S-web, but will not substantially increase its width in latitude at the source surface.

Depending on the strength of the parasitic polarities introduced when going to higher resolution, and their positions in coronal holes, the separatrix structure enclosing these polarities can be of two types. First, it can be just a single BP separatrix surface, as in our examples shown in Figure 11. This structure contains no null points in the corona, but nevertheless it completely separates the closed flux of the parasitic polarity from the surrounding magnetic field (Bungey et al. 1996; Müller & Antiochos 2008). Second, it can also be a more familiar structure with a dome-like fan surface and spine line across both coming out from a single null point and surrounded by QSLs (Masson et al. 2009).

These two types of separatrix structures are similar in that their (quasi)-separatrix field lines do not fan out in the open-field region as much as they do in pseudo-streamers. The perturbation of such a structure due to local flux emergence or photospheric motion causes formation of a current sheet and reconnection, both localized in a small region near the corresponding BPs or null points. This process can be considered as a mechanism for producing coronal plumes or "anemone" jets in polar coronal holes (Moreno-Insertis et al. 2008; Müller & Antiochos 2008; Pariat et al. 2010).

The pseudo-streamers are structurally very different. As shown above, they contain several separators, two of which are open, while the others are closed. An emergence, submergence, and/or displacement of photospheric flux concentrations in the lobes of pseudo-streamers, and in their surrounding, must lead to the formation of current sheets along the separators closest to the source of the perturbations. Since current sheets form along the entire length of separators, the related reconnection processes proceed similarly (Parnell et al. 2010). This indicates that reconnection in pseudo-streamers and coronal plumes might have quite different characteristics, which additionally substantiates the original definition of the S-web.

The open separators are lines at which the open and closed magnetic fields become in contact with each other. They appear to be the longest separators in the pseudo-streamers, so most of the interchange reconnection must occur along them. How does it proceed in the presence of multiple closed separators, all connected together with the basic nulls of the pseudo-streamers? This question is of particular importance for understanding the physics of pseudo-streamers and has never been investigated before, because their topological structure was unknown. The answer to this fundamental question is crucial to determine if the S-web model can explain the origin of the slow solar wind. Therefore, it ought to be the focus of the future studies, with special emphasis on the processes that occur both at open separators and the QSLs associated with open-field corridors.

The plasma sheets of pseudo-streamers, as observed in the white-light corona, are composed of fine ray-like structures that are presumed to be formed by interchange reconnection at the streamer cusp (Wang et al. 2012). Such an explanation is consistent with our discussion of open separators, except that in our scenario reconnection occurs along the entire length of these separators rather than just at the mentioned cusp points (which are the footpoints of our open separators at the source surface). In light of our present analysis, the observed ray-like structures are likely a part of the S-web. For structural features (like separators) to be visible, they have to not only be present, but also perturbed sufficiently (e.g., by waves or photospheric motions). Therefore, at any moment in time, only a small fraction of the S-web might be visible in white light.

It should also be emphasized that the S-web model does not assume a priori that reconnection in pseudo-streamers generates the slow wind in the form of plasma blobs, as it does in helmet streamers (Wang et al. 2012). In fact, we expect that this process must be so different here that it will directly affect the observational properties of the pseudo-streamers. Indeed, in contrast to the helmet streamers, the reconnection in the pseudo-streamers has to occur not in the plasma sheet itself but rather at its edges, where the above open separators are located. Consequently, the pseudo-streamer material must be replenished, at least in part, by the plasma that flows out from those edges. This process has likely to occur in a sporadic fashion, namely, each time when the interchange reconnection takes place between open and closed fields. As a result, the respective reconnection outflows have to be modulated accordingly to produce in the pseudo-streamers the mentioned above ray-like rather than blob-like structures. This consideration shows that, irrespective of its relevance to the problem of the origin of the slow solar wind, the question on how the interchange reconnection modifies the properties of the wind flow in the pseudo-streamers deserves very close attention in the future studies.

6. SUMMARY

We have studied the large-scale topology of the coronal magnetic field determined in the framework of a PFSS model for the time period 2010 August 1–2, when a sequence of sympathetic CMEs occurred. First, this model was computed from the observed data of the photospheric magnetic field. Second, we have calculated high-resolution distributions of the squashing factor Q at the photospheric and source-surface boundaries and at several cut planes across the regions where the CMEs started. Third, we have developed a special technique for tracing (quasi-)separatrix field lines that pass through the high-Q lines of such distributions. These tools allowed us to fulfill a comprehensive analysis of the magnetic field structure.

Of particular interest to us were large-scale separatrix surfaces that divide the coronal volume into topologically distinct regions in which the erupting filaments originated. We have found that four of these five filaments were initially located in the lobes of three pseudo-streamers. Such lobes are obtained as a result of intersection of curtain-like and dome-like separatrix surfaces of the coronal magnetic field. The SC is a fan separatrix surface associated with a null point that is called basic one and located at a certain height in the corona between two adjacent coronal holes of like polarity. Such a curtain is formed by open and closed field lines fanning out from the basic null point. The dome separatrix surfaces are made of two half-domes joined with each other along the spine line of this null point. The half-domes are formed by the field lines that also fan out either from a BP or another null point, which both are located at the flanks of the pseudo-streamer.

In the middle cross-section passing through the basic null of a pseudo-streamer, these separatrix surfaces intersect to produce a $\cap$-type shape in which the vertical line and arc represent the SC and adjoint half-domes, respectively. Above the half-domes in this cross-section, the curtain separates adjacent coronal holes of like polarity and observationally corresponds to the stalk of

pseudo-streamers. At heights below the basic null of the pseudo-streamer, the coronal holes become disconnected by closed magnetic fields rooted in parasitic polarities and separated by the distance equal to the local width of the separatrix half-domes.

The separatrix surfaces of the pseudo-streamers in the August 1–2 events are located relatively far from the pre-eruption positions of the filaments, so that their contributions to the total field and hence their influence on these surfaces must be small. Therefore, our source-surface model should be sufficiently accurate to reproduce the large-scale structure of real pseudo-streamers with filaments inside.

The indicated SCs intersect half-domes along closed separator field lines, or simply separators, that pass through the null points or BPs at the flanks of the pseudo-streamers. In addition, these curtains intersect the helmet-streamer separatrix surface twice along open separator field lines, which connect the basic nulls of the pseudo-streamers to streamer-cusp points. Invoking our recent MHD model of sympathetic eruptions (Török et al. 2011), we argue that magnetic reconnection at both these types of separators is likely a key process in sympathetic eruptions, because it controls how magnetic fluxes are redistributed between the lobes of pseudo-streamers during eruptions. It has been demonstrated here that the configuration which harbored the first three erupting filaments had a similar magnetic topology as was assumed in that model. Thus, the present topological analysis of the PFSS background field substantiates the previous assumptions on the initial configuration in Török et al. (2011).

Here, we proceeded with a generalization of this earlier proposed scenario, by noticing, first, that the indicated separators in our configuration form a huge chain that traverses through all three pseudo-streamers involved in the eruptions. We have qualitatively explained how a single eruption at one end of such a separator chain can trigger a whole sequence of eruptions.

We have also discussed the implications of our obtained results for the S-web model of the slow solar wind by emphasizing those issues that have not been well understood so far. First, we have demonstrated how the pseudo-streamer structure accommodates disconnection and merging of two coronal holes, respectively, below and above the basic nulls of the pseudo-streamers. Second, we have explained the differences in magnetic topology between pseudo-streamers and separatrix structures enclosing small parasitic polarities in the polar coronal holes and discussed why such structures were not included in the original definition of the S-web. Third, we have emphasized that the sources of the slow solar wind most likely reside both at the separators of pseudo-streamers and QSLs originated in narrow photospheric corridors of the open magnetic field.

The contribution of V.S.T., Z.M., T.T., and J.A.L. was supported by NASA's HTP, LWS, and SR&T programs, SHINE under NSF Grant AGS-1156119, CISM (an NSF Science and Technology Center), and a contract from Lockheed-Martin to Predictive Science, Inc.; O.P. was supported by NSF Grant ATM-0837519 and NASA Grant NNX09AG27G.

REFERENCES

Altschuler, M. D., & Newkirk, G. 1969, Sol. Phys., 9, 131
Antiochos, S. K., DeVore, C. R., Karpen, J. T., & Mikić, Z. 2007, ApJ, 671, 936
Antiochos, S. K., Mikić, Z., Titov, V. S., Lionello, R., & Linker, J. A. 2011, ApJ, 731, 112
Aulanier, G., Pariat, E., & Démoulin, P. 2005, A&A, 444, 961
Biesecker, D. A., & Thompson, B. J. 2000, J. Atmos. Sol.–Terr. Phys., 62, 1449
Bumba, V., & Klvana, M. 1993, Ap&SS, 199, 45
Bungey, T. N., Titov, V. S., & Priest, E. R. 1996, A&A, 308, 233
Close, R. M., Parnell, C. E., & Priest, E. R. 2004, Sol. Phys., 225, 21
Crooker, N. U., Antiochos, S. K., Zhao, X., & Neugebauer, M. 2012, J. Geophys. Res., 117, 4104
Démoulin, P., Henoux, J. C., Priest, E. R., & Mandrini, C. H. 1996, A&A, 308, 643
Eselevich, V. G., Fainshtein, V. G., & Rudenko, G. V. 1999, Sol. Phys., 188, 277
Fisk, L. A. 2005, ApJ, 626, 563
Forbes, T. 2010, in Models of Coronal Mass Ejections and Flares, ed. C. J. Schrijver & G. L. Siscoe (Cambridge: Cambridge Univ. Press), 159
Forbes, T. G. 2000, J. Geophys. Res., 105, 23153
Harrison, R. A., Davies, J. A., Möstl, C., et al. 2012, ApJ, 750, 45
Haynes, A. L., & Parnell, C. E. 2010, Phys. Plasmas, 17, 092903
Hundhausen, A. J. (ed.) 1972, Coronal Expansion and Solar Wind (Berlin: Springer)
Jiang, Y., Shen, Y., Yi, B., Yang, J., & Wang, J. 2008, ApJ, 677, 699
Jiang, Y., Yang, J., Hong, J., Bi, Y., & Zheng, R. 2011, ApJ, 738, 179
Linker, J. A., Lionello, R., Mikić, Z., Titov, V. S., & Antiochos, S. K. 2011, ApJ, 731, 110
Liu, C., Lee, J., Karlický, M., et al. 2009, ApJ, 703, 757
Liu, R., Liu, C., Wang, S., Deng, N., & Wang, H. 2010, ApJ, 725, L84
Masson, S., Pariat, E., Aulanier, G., & Schrijver, C. J. 2009, ApJ, 700, 559
Moon, Y.-J., Choe, G. S., Park, Y. D., et al. 2002, ApJ, 574, 434
Moore, R. L., Sterling, A. C., Hudson, H. S., & Lemen, J. R. 2001, ApJ, 552, 833
Moreno-Insertis, F., Galsgaard, K., & Ugarte-Urra, I. 2008, ApJ, 673, L211
Müller, D. A. N., & Antiochos, S. K. 2008, Ann. Geophys., 26, 2967
Panasenco, O., & Velli, M. M. 2010, Magnetic Structure of Twin Filaments Inside Pseudostreamers, AGU Fall Meeting Abstracts, A1663
Pariat, E., Antiochos, S. K., & DeVore, C. R. 2010, ApJ, 714, 1762
Pariat, E., & Démoulin, P. 2012, A&A, 541, A78
Parnell, C. E., Haynes, A. L., & Galsgaard, K. 2010, J. Geophys. Res., 115, A02102
Press, W. H., Teukolsky, S. A., Vetterling, W. T., & Flannery, B. P. 2007, Numerical Recipes: The Art of Scientific Computing (3rd ed.; Cambridge, NY: Cambridge Univ. Press)
Priest, E. R., & Démoulin, P. 1995, J. Geophys. Res., 100, 23443
Priest, E. R., & Forbes, T. G. 2000, Magnetic Reconnection: MHD Theory and Applications (Cambridge: Cambridge Univ. Press), 612
Priest, E. R., & Titov, V. S. 1996, Phil. Trans. R. Soc. A, 354, 2951
Ramsey, H. E., & Smith, S. F. 1966, AJ, 71, 197
Riley, P., Linker, J. A., Mikić, Z., et al. 2006, ApJ, 653, 1510
Savcheva, A., Pariat, E., van Ballegooijen, A., Aulanier, G., & DeLuca, E. 2012a, ApJ, 750, 15
Savcheva, A. S., van Ballegooijen, A. A., & DeLuca, E. E. 2012b, ApJ, 744, 78
Schatten, K. H., Wilcox, J. M., & Ness, N. F. 1969, Sol. Phys., 6, 442
Schrijver, C. J., & Title, A. M. 2011, J. Geophys. Res., 116, A04108
Seehafer, N. 1986, Sol. Phys., 105, 223
Shen, Y., Liu, Y., & Su, J. 2012, ApJ, 750, 12
Titov, V. S. 2007, ApJ, 660, 863
Titov, V. S., Forbes, T. G., Priest, E. R., Mikic, Z., & Linker, J. A. 2009, ApJ, 693, 1029
Titov, V. S., Hornig, G., & Démoulin, P. 2002, J. Geophys. Res., 107, 1164
Titov, V. S., Mikić, Z., Linker, J. A., & Lionello, R. 2008, ApJ, 675, 1614
Titov, V. S., Mikić, Z., Linker, J. A., Lionello, R., & Antiochos, S. K. 2011, ApJ, 731, 111
Titov, V. S., Priest, E. R., & Démoulin, P. 1993, A&A, 276, 564
Török, T., Panasenco, O., Titov, V. S., et al. 2011, ApJ, 739, L63
Wang, H., Chae, J., Yurchyshyn, V., et al. 2001, ApJ, 559, 1171
Wang, Y.-M., Grappin, R., Robbrecht, E., & Sheeley, N. R., Jr. 2012, ApJ, 749, 182
Wang, Y.-M., Sheeley, N. R., Jr., & Rich, N. B. 2007, ApJ, 658, 1340
Wheatland, M. S., & Craig, I. J. D. 2006, Sol. Phys., 238, 73
Yang, J., Jiang, Y., Zheng, R., et al. 2012, ApJ, 745, 9
Zhukov, A. N., & Veselovsky, I. S. 2007, ApJ, 664, L131
Zuccarello, F., Romano, P., Farnik, F., et al. 2009, A&A, 493, 629

The Astrophysical Journal, 757:150 (12pp), 2012 October 1 doi:10.1088/0004-637X/757/2/150

CONTRACTING AND ERUPTING COMPONENTS OF SIGMOIDAL ACTIVE REGIONS

Rui Liu[1,2], Chang Liu[2], Tibor Török[3], Yuming Wang[1], and Haimin Wang[2]
[1] CAS Key Lab of Geospace Environment, Department of Geophysics & Planetary Sciences, University of Science & Technology of China, Hefei 230026, China; rliu@ustc.edu.cn
[2] Space Weather Research Laboratory, Center for Solar-Terrestrial Research, NJIT, Newark, NJ 07102, USA
[3] Predictive Science Inc., 9990 Mesa Rim Road, Suite 170, San Diego, CA 92121, USA
Received 2011 December 29; accepted 2012 August 2; published 2012 September 12

ABSTRACT

It has recently been noted that solar eruptions can be associated with the contraction of coronal loops that are not involved in magnetic reconnection processes. In this paper, we investigate five coronal eruptions originating from four sigmoidal active regions, using high-cadence, high-resolution narrowband EUV images obtained by the *Solar Dynamic Observatory* (*SDO*). The magnitudes of the flares associated with the eruptions range from *GOES* class B to class X. Owing to the high-sensitivity and broad temperature coverage of the Atmospheric Imaging Assembly (AIA) on board *SDO*, we are able to identify both the contracting and erupting components of the eruptions: the former is observed in cold AIA channels as the contracting coronal loops overlying the elbows of the sigmoid, and the latter is preferentially observed in warm/hot AIA channels as an expanding bubble originating from the center of the sigmoid. The initiation of eruption always precedes the contraction, and in the energetically mild events (B- and C-flares), it also precedes the increase in *GOES* soft X-ray fluxes. In the more energetic events, the eruption is simultaneous with the impulsive phase of the nonthermal hard X-ray emission. These observations confirm that loop contraction is an integrated process in eruptions with partially opened arcades. The consequence of contraction is a new equilibrium with reduced magnetic energy, as the contracting loops never regain their original positions. The contracting process is a direct consequence of flare energy release, as evidenced by the strong correlation of the maximal contracting speed, and strong anti-correlation of the time delay of contraction relative to expansion, with the peak soft X-ray flux. This is also implied by the relationship between contraction and expansion, i.e., their timing and speed.

Key words: Sun: coronal mass ejections (CMEs) – Sun: flares

Online-only material: animation, color figures

1. INTRODUCTION

It is generally regarded that solar eruptions are due to a disruption of the force balance between the upward magnetic pressure force and the downward magnetic tension force. Since the eruption can only derive its energy from the free energy stored in the coronal magnetic field (Forbes 2000), "the coronal field lines must contract in such a way as to reduce the magnetic energy $\int_{\mathcal{V}} B^2/8\pi$" (Hudson 2000, p. L75). The contraction must be associated with the reduction of the magnetic tension force for each individual loop-like field line undergoing contraction, as its footpoints are effectively anchored in the photosphere. Eventually, a new force balance would be achieved between the magnetic pressure and tension force after the energy release. From an alternative viewpoint, the average magnetic pressure $B^2/8\pi$ must decrease over the relevant volume $\mathcal{V}$ across the time duration of the eruption. $\mathcal{V}$ can be roughly regarded as the flaring region, primarily in which magnetic energy is converted into other forms of energies. The contraction process, termed "magnetic implosion" by Hudson (2000), is very similar to the shrinkage of post-flare loops (Forbes & Acton 1996), except that loop shrinkage is driven by temporarily enhanced magnetic tension force at the cusp of the newly reconnected field lines, whereas loop contraction is driven by reduced magnetic pressure in the flaring region. Additionally, with newly reconnected loops piling up above older ones, the post-flare arcade as a whole often expands, rather than shrinks, with time.

Hudson (2000, p. L75) concluded that "a magnetic implosion must occur simultaneously with the energy release," based on no assumption about the energy release process itself. However, the detailed timing and location of loop contraction might provide diagnostic information on the eruption mechanism. For example, when the reconnection-favorable flux emerges inside a filament channel (Figure 1(a); adapted from Chen & Shibata 2000), it cancels the small magnetic loops below the flux rope, which results in a decrease of the local magnetic pressure. The whole dipolar magnetic structure must contract correspondingly. Meanwhile, plasmas on both sides of the polarity-inversion line (PIL) would move inward to form a current sheet below the flux rope and the subsequent evolution could follow the paradigm of the standard flare model (e.g., Kopp & Pneuman 1976). In that case, overlying coronal loops could be observed to initially contract and then erupt. In a different scenario, a twisted flux rope confined by potential-like magnetic fields is found to be energetically favorable to "rupture" through the overlying arcade via ideal-MHD processes (Figure 1(b); adapted from Sturrock et al. 2001). This is clearly demonstrated in MHD simulations by Gibson & Fan (2006) and Rachmeler et al. (2009), in which overlying loops can be seen to be pushed upward and aside as the flux rope kinks and expands, and after the rope ruptures through the arcade, overlying loops on both sides quickly contract toward the core region, due to the reduction of the magnetic pressure in the core field with the escape of the flux rope. In particular for this scenario (Figure 1(b)), one would expect to see both the expanding flux rope and the contracting overlying loops during the eruption as long as the arcade is only partially opened. Although both scenarios involve a pre-existing flux rope, they can supposedly

Table 1
List of Events

Date	AR	Location	Hale	*GOES*	v_c^{max} (km s^{-1})[a]	v_e^{max} (km s^{-1})[b]	Δt (min)[c]
2010 Aug 1	11092	N13E21	α/β	C3.2	−51	83	9.0
2010 Sep 3	11105	N19W23	$\beta/-$	B2.8	−12	94	34.6
2011 Feb 13	11158	S19W03	β/β	M6.6	−195	538	1.8
2011 Feb 15	11158	S21W21	$\beta\gamma/\beta\gamma$	X2.2	−320	401	2.4
2011 Jun 21	11236	N17W19	$\beta\gamma/\beta\gamma$	C7.7	−57	90	12.4

Notes.
[a] Maximum contracting speed.
[b] Maximum expanding speed.
[c] Time delay of contraction relative to expansion.

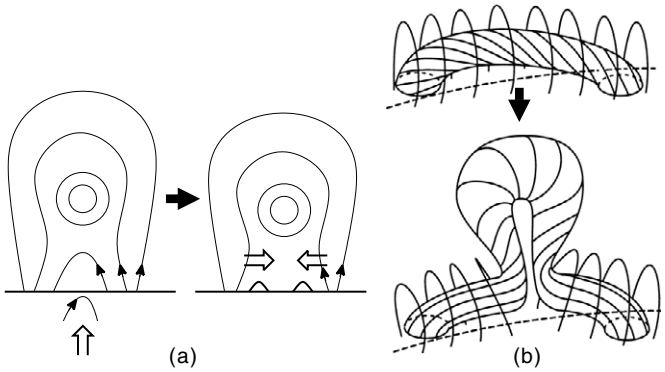

Figure 1. CME models relevant to magnetic implosion. (a) Schematic diagram of the emerging flux triggering mechanism for CMEs (adapted from Chen & Shibata 2000). The emerging flux inside the filament channel cancels the pre-existing loops, which results in the in situ decrease of the magnetic pressure. Magnetized plasmas are driven inward to form a current sheet beneath the flux rope. (b) Schematic sketch showing that in the three-dimensional space a twisted flux rope can rupture the overlying magnetic arcade and erupt by pushing the magnetic arcade aside (adapted from Sturrock et al. 2001). With the escape of the flux rope, the arcade field undergoes contraction due to the decreased magnetic pressure in the core field.

also accommodate those models in which the flux rope forms immediately prior to (e.g., Moore et al. 2001), or during the course of (e.g., Antiochos et al. 1999), the eruption.

Corresponding to the aforementioned models (Figure 1), our previous observational studies also suggest two different scenarios, i.e., (1) the bunch of coronal loops undergoing contraction later becomes the front of the eruptive structure (Liu et al. 2009b) and (2) the contracting loops are distinct from the eruptive structure (Liu & Wang 2009, 2010). The role of contraction in the eruption, however, has been unclear in both scenarios. For Scenario 1, the event reported by Liu et al. (2009b) remains unique in the literature; as for Scenario 2, the eruptive structure is not easy to detect before its appearance as a coronal mass ejection (CME) in the coronagraph, unless there is dense filament material serving as the tracer (Liu & Wang 2009). In some cases, its slow ascension and expansion during the early stage might manifest as the gradual inflation of overlying coronal loops (Liu et al. 2010b). Only with the advent of the *Solar Dynamic Observatory* (*SDO*; Pesnell et al. 2012), which provides a continuous and wide temperature coverage, is the eruptive structure itself more frequently identified beneath the coronagraph height as a hot, diffuse plasmoid (e.g., Liu et al. 2010c; Cheng et al. 2011).

Here in a further investigation of Scenario 2, we identify both the erupting and contracting components using *SDO* data, and hence for the first time we are able to study in detail their relationship as well as the implication for the eruption mechanism and the associated energy release process. In the rest of this paper, we present in Section 2 the results of our investigation on five flares (Table 1) observed by the Atmospheric Imaging Assembly (AIA; Lemen et al. 2012) on board *SDO*, and we make concluding statements in Section 3.

2. OBSERVATION

2.1. Overview

In addition to the symbiosis of the erupting and contracting components, the five flares studied here all occurred in sigmoidal active regions (Figure 2), which had a sinusoidal shape in the warm AIA channels such as 211 Å (dominated by Fe XIV, $\log T = 6.3$) and 335 Å (dominated by Fe XVII, $\log T = 6.4$) or hot channels like 94 Å (dominated by Fe XVIII, $\log T = 6.8$). Upon close inspection, one can see that two groups of J-shaped loops, which are oppositely oriented with respect to each other, collectively have a sinusoidal appearance (Figure 2). In cold channels such as 171 Å (dominated by Fe IX and Fe X, $\log T = 5.8$) and 193 Å (dominated by Fe XII, $\log T = 6.1$), these regions were dominated by large-scale loops arched over the elbows of the hot sigmoid, suggesting that the highly sheared core field is restrained by the potential-like overlying field. Since nonpotential (sheared or twisted) fields are reservoirs of magnetic free energy, it is not surprising that sigmoidal regions are significantly more likely to be eruptive than non-sigmoidal regions (Hudson et al. 1998; Canfield et al. 1999; Glover et al. 2000), and are deemed to be one of the most important precursor structures for solar eruptions.

Of the five flares, both the M6.6 flare on 2011 February 13 and the X2.2 flare two days later on February 15 occurred in the same AR 11158. One can see that on February 13, when it was still classified as a β-region, AR 11158 was only a "rudimentary" sigmoid compared with its status on February 15. The hot loops in AIA 94 Å in the center of the active region, however, were already highly sheared, taking the similar east–west orientation as the major PIL along which the two bipolar regions interacted and major flares took place (see Beauregard et al. 2012 for details).

Utilizing the newly released vector magnetograms with the 0.″5 pixel size for AR 11158 (Hoeksema et al. 2012) obtained by the Helioseismic and Magnetic Imager (HMI; Scherrer et al. 2012) on board *SDO*, we constructed the non-linear force-free field (NLFFF) model using the "weighted optimization" method (Wiegelmann 2004) after preprocessing the photospheric boundary to best suit the force-free condition (Wiegelmann et al. 2006). NLFFF extrapolation using the vector magnetogram at about 16:00 UT on 2011 February 13

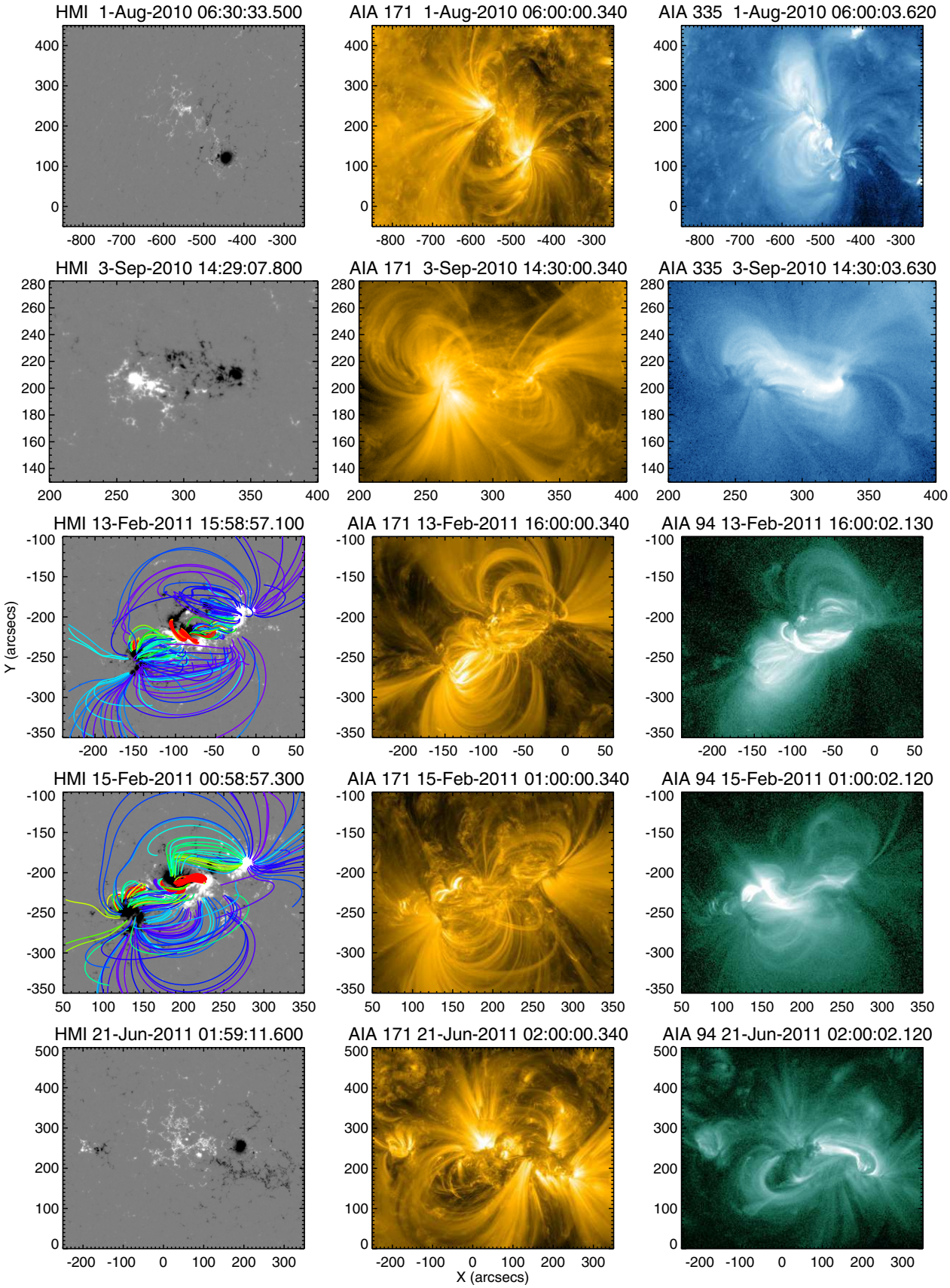

Figure 2. Pre-flare configuration for the five flares studied. Left column: line-of-sight magnetograms obtained by the Helioseismic and Magnetic Imager (HMI) on board *SDO*. Middle and right columns: corresponding EUV images in the cold and warm/hot AIA channels, respectively, showing the sigmoidal morphology and structure. For AR 11158 (third and fourth rows), we use HMI vector magnetograms to construct nonlinear force-free field (NLFFF; see the text for details). The extrapolated field lines are color coded according to the intensity of vertical currents on the surface.

(A color version of this figure is available in the online journal.)

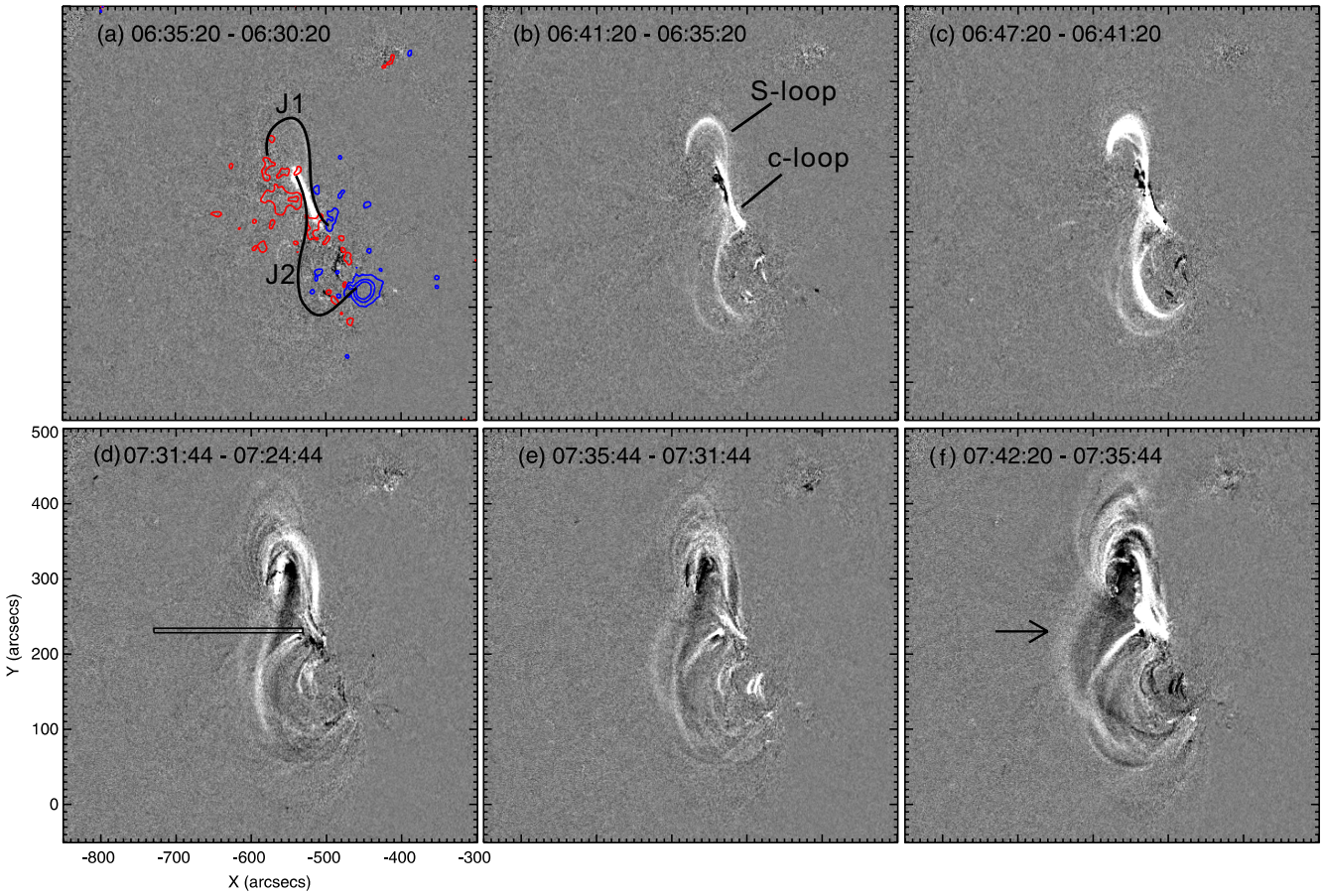

Figure 3. AIA 94 Å difference images, displaying the formation of an S-shaped loop via tether-cutting from two J-shaped loops and its subsequent transformation into a blowing-out bubble marked by an arrow in panel (f). Panel (d) shows the slit through which the space–time diagram in Figure 5(c) is obtained.

(A color version of this figure is available in the online journal.)

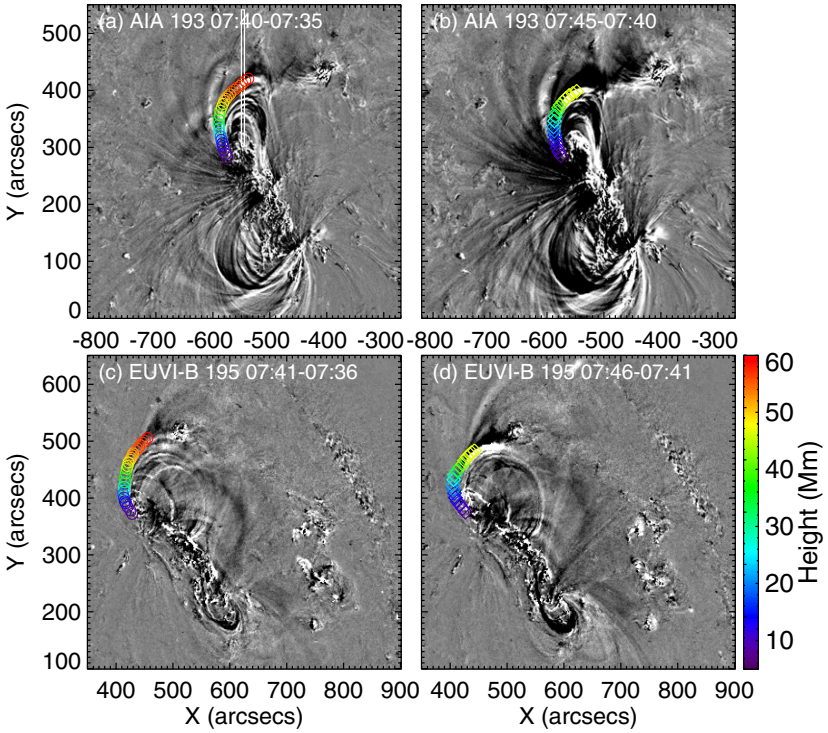

Figure 4. Stereoscopic reconstruction of the contracting loop overlying the northern elbow of the sigmoid. The height information of the loop, which is color coded, is obtained by pairing AIA 193 Å and EUVI-B 195 Å images. Panel (a) shows the slit through which the space–time diagram in Figure 5(b) is obtained. The expanding bubble is also visible in both view points, associated with coronal dimming in AIA 193 Å.

(A color version of this figure is available in the online journal.)

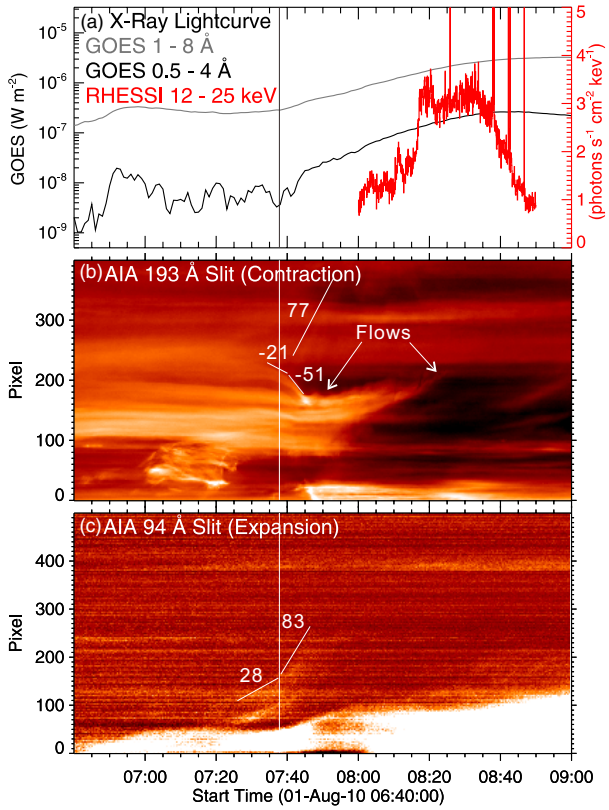

Figure 5. Temporal evolution of the contracting loop and the expanding bubble seen through the slits, in relation to the X-ray emission. Numbers indicate speeds of various features in km s^{-1}. The vertical line marks the transition of the exploding bubble from a slow- to a fast-rise phase.

(A color version of this figure is available in the online journal.)

indeed shows highly sheared field lines near the flaring PIL and potential-like field lines overlying it, similar in morphology to the hot and cold coronal loops, respectively (Figure 2). NLFFF extrapolation using the vector magnetogram at about 01:00 UT on February 15 gives a similar result. The extrapolated field lines are color coded according to the intensity of vertical currents on the surface. Field lines whose footpoints are associated with strong current densities (>0.02 A m^{-2}) are in red. The footpoints of these red field lines are cospatial with the four footpoint-like flare brightenings in AIA 94 Å images (Liu et al. 2012; Wang et al. 2012).

2.2. 2010 August 1 Event

The eruption in the sigmoidal region NOAA AR 11093 on 2010 August 1 conformed to the classical "sigmoid-to-arcade" transformation (e.g., Moore et al. 2001), i.e., prior to the eruption, the sigmoidal structure consisted of two opposite bundles of J-shaped loops, and after the eruption, it appeared as a conventional post-flare arcade. The evolution in between the two states was revealed in detail for the first time by AIA observations (Liu et al. 2010c). In the AIA 94 Å difference images (Figure 3), one can see that an S-shaped loop started to glow at about 06:40 UT, about 1 hr before the flare onset. As its glowing was preceded by a heating episode in the core region (Figure 3(a)), the topological reconfiguration resulting in the formation of the continuous S-shaped loop was very likely due to the tether-cutting reconnection (Moore et al. 2001). The S-shaped loop remained in quasi-equilibrium in the lower corona for about 50 minutes, with the central dipped portion rising quasi-statically. During this interval, there was a weak enhancement in *GOES* soft X-rays (SXRs), whose source, however, was located at the southeast limb according

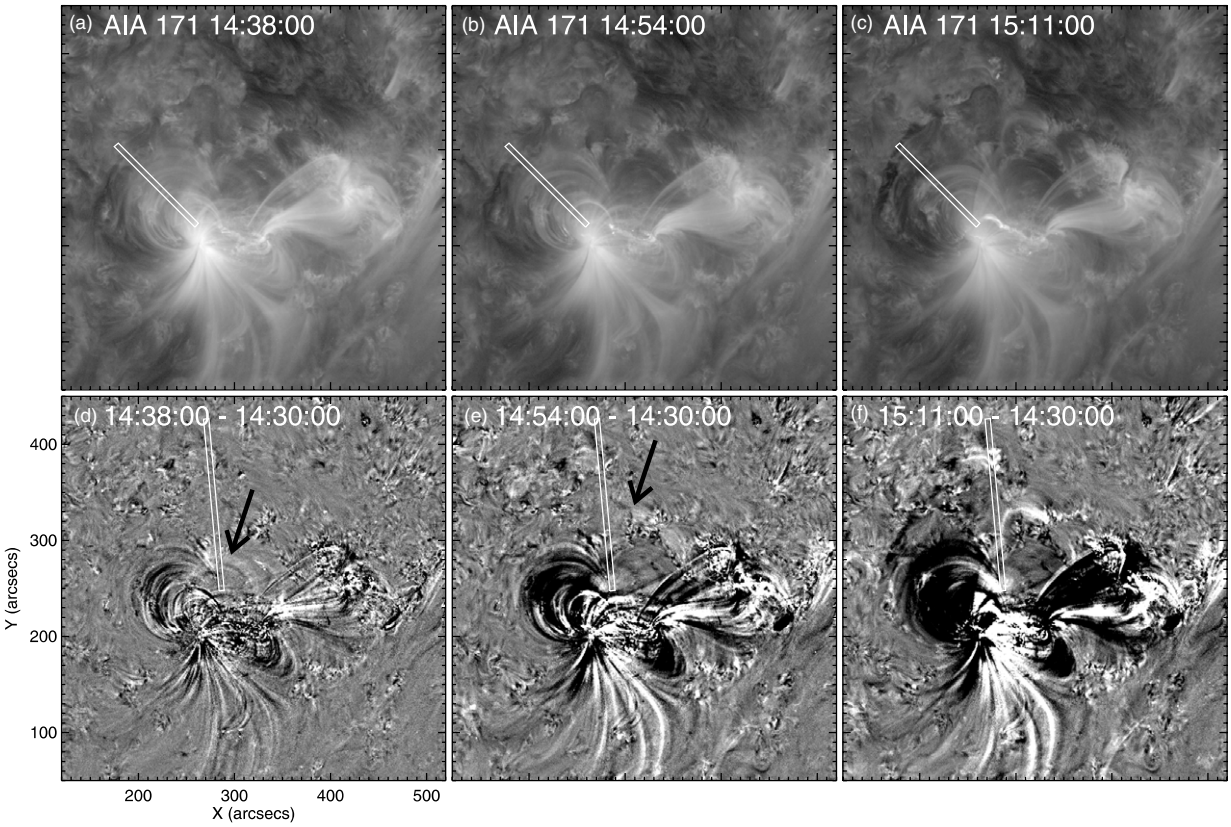

Figure 6. AIA observation of the 2010 September 3 B-flare. Top panels show original 171 Å images and bottom panels show the corresponding difference images. The expanding bubble is indicated by arrows.

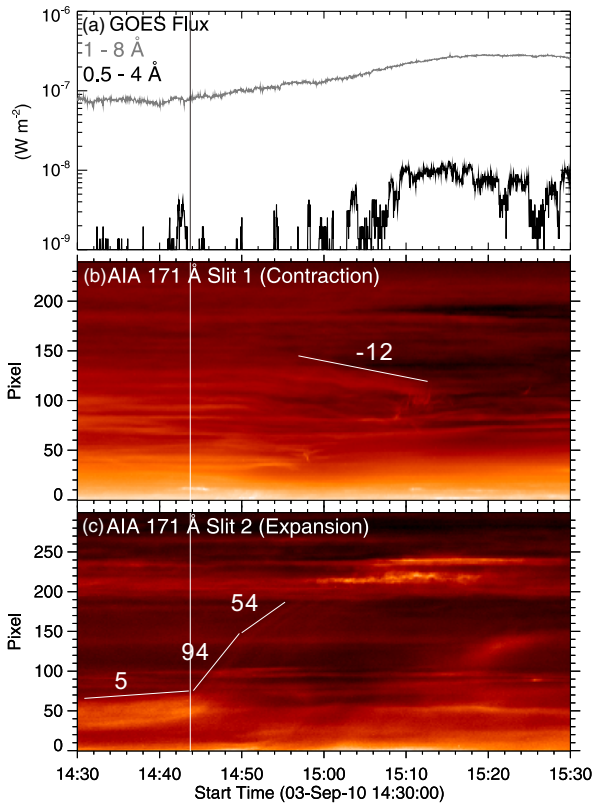

Figure 7. Temporal evolution of the contracting loop and the expanding bubble in relation to the X-ray emission. The space–time diagrams are obtained by stacking image slices cut by the slits shown in Figure 6. The vertical line marks the transition of the exploding bubble from a slow- to a fast-rise phase.

(A color version of this figure is available in the online journal.)

to *RHESSI* observations (see Figure 3 in Liu et al. 2010c). At about 07:30 UT, about 10 minutes prior to the onset of the C3.2 flare, the speed increased to tens of kilometers per second, as the S-shaped loop sped up its transformation into an arch-shaped loop, which eventually led to a CME.

During the eruption, a group of coronal loops overlying the northern elbow of the sigmoid was observed to contract in cold AIA channels such as 171 and 193 Å. The contraction was also visible in EUV images taken by the Extreme-UltraViolet Imager (EUVI; Wuelser et al. 2004) on board the "Behind" satellite of the *Solar Terrestrial Relations Observatory* (*STEREO-B*). The viewing angle was separated by about 70° between *SDO* and *STEREO-B*. By pairing EUVI with AIA images, we are able to derive the three-dimensional location of the loop undergoing contraction via a triangulation technique called *tie point* (Inhester 2006), which is implemented in an SSW routine, `SCC_MEASURE`, by W. Thompson. From the difference images (Figure 4) one can see both the contracting loop, whose height is color coded, and the expanding bubble, which is associated with coronal dimming in AIA 193 Å. With stereoscopic views, it becomes clear that the contraction is not simply a projection effect due to the loops being pushed aside by the expanding bubble.

We place slits across both the contracting loops (Figure 4(a)) and the expanding bubble (Figure 3(d)). By stacking the resultant image cut over time, we obtain space–time diagrams for a series of AIA 193 and 94 Å images at 12 s cadence (Figures 5(b) and (c)). Note that to increase the signal-to-noise ratio, we integrate over the width of the slit (10 pixels), and that to reveal the diffuse, expanding bubble, we carry out base differencing to make the 94 Å space–time diagram, whereas original 193 Å images are used for the contracting loops which are more clearly

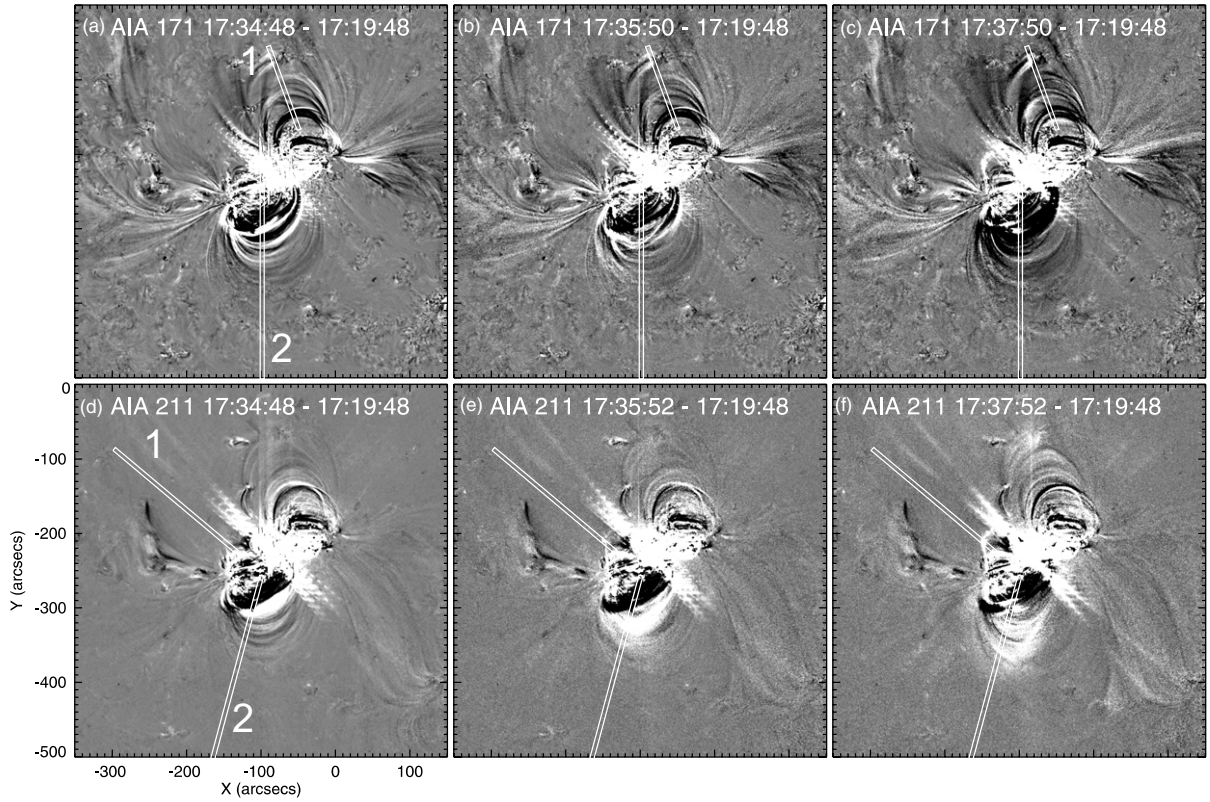

Figure 8. AIA observation of the 2011 February 13 M flare. Top panels show 171 Å difference images and bottom panels 211 Å difference images. An animation of 211 Å images as well as corresponding difference images is available in the online version of the journal.

(Animation of this figure is available in the online journal.)

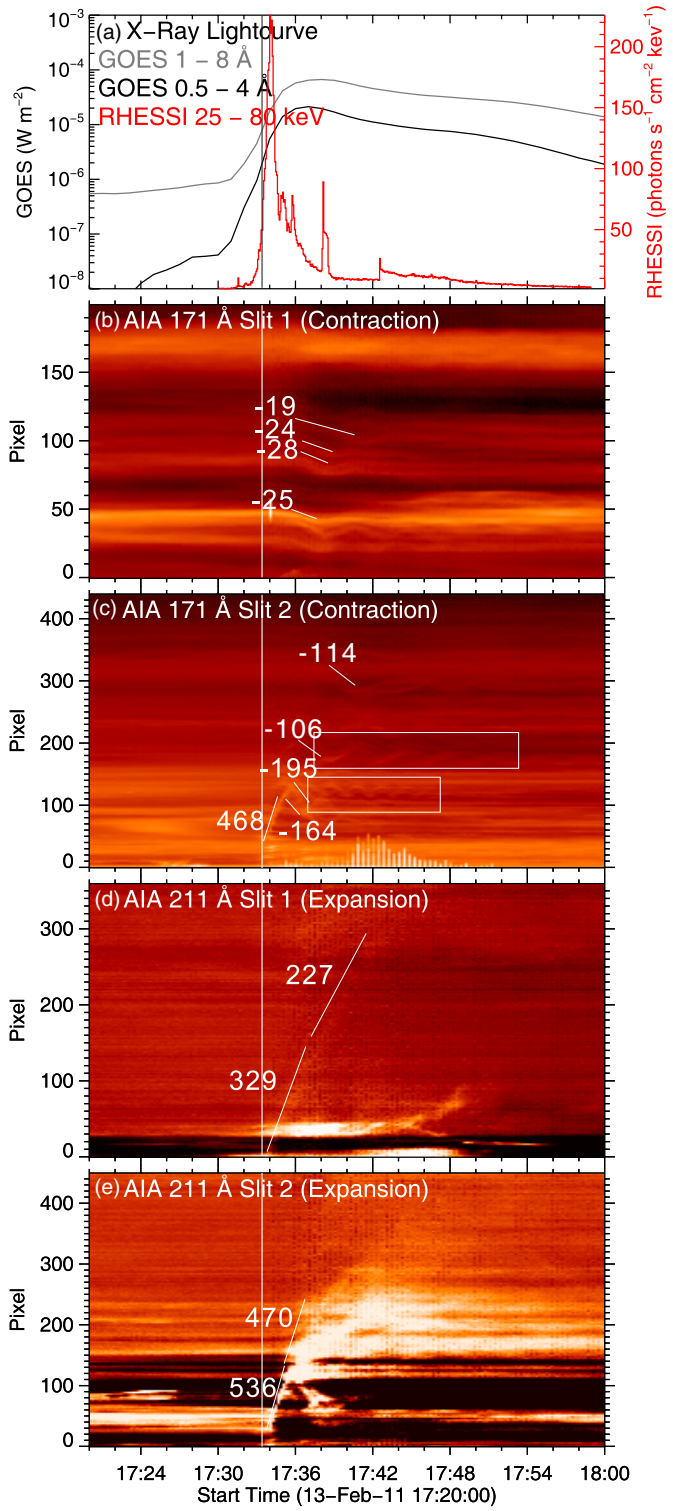

Figure 9. Temporal evolution of the contracting loop and the expanding bubble in relation to the X-ray emission. The space–time diagrams are obtained by stacking image slices cut by the slits as shown in Figure 8. The vertical line marks the beginning of the explosion.

(A color version of this figure is available in the online journal.)

defined in EUV. From Figure 5(c), one can see that the bubble initially rose slowly by ~30 km s^{-1}, and then transitioned into a phase of fast rise by ~80 km s^{-1} at about 07:38 UT. The height–time profile is piecewise-linear fitted although the transition is smooth and there seems to be continuous acceleration. The transition time is approximately coincident with the flare onset in terms of the *GOES* 1–8 Å flux. A very diffuse erupting feature can also be marginally seen in the 193 Å space–time diagram, whose speed is similar to the bubble in 94 Å. The contraction of the overlying loops slightly lagged behind the rising of the bubble, and there was a similar transition from slow to fast contraction, slightly lagging behind the speed transition of the bubble by less than three minutes. It is worth noting that the apparently upward-moving feature in the wake of contraction was due to flows along the northern elbow of the sigmoid, not to the recovery of the contracting loops.

2.3. 2010 September 3 Event

In the 2010 September 3 event, both the contracting loops and expanding bubble were visible in the 171 Å channel. But the diffuse bubble can only be seen in the difference images (bottom panels in Figure 6, marked by arrows). The contracting loops were located to the east of the bubble, overlying the eastern elbow of the sigmoid (top panels in Figure 6). Similar to the 2010 August 1 event, in the wake of the bubble erupting, obvious coronal dimming can be seen in the cold AIA channels such as 171 and 193 Å. The dynamics of the bubble can also be characterized by a slow-rise followed by a fast-rise phase, the transition of which coincided with the gradual increase of the *GOES* 1–8 Å flux (Figure 7). The bubble shows a deceleration signature after 14:48 UT. The loop contraction lagged behind the transition time at about 14:44 UT by about 10 minutes.

2.4. 2011 February 13 Event

The 2011 February 13 M6.6 flare was associated with irreversible changes in the photospheric magnetic field (Liu et al. 2012). Using high-resolution and high-precision *Hinode* vector magnetograms and line-of-sight HMI magnetograms, Liu et al. (2012) found that the field change mainly took place in a compact region lying in the center of the sigmoid, where the strength of the horizontal field increased significantly across the time duration of the flare. Moreover, the near-surface field became more stressed and inclined toward the surface while the coronal field became more potential. An intriguing observation is that the current system derived from the extrapolated coronal field above the region with an enhanced horizontal field underwent an apparent downward collapse in the wake of the sigmoid eruption. Liu et al. (2012) concluded that these results are a superimposed effect of both the tether-cutting reconnection producing the flare and the magnetic implosion resulting from the energy release.

Coronal EUV observations agree with the above conclusion drawn from photospheric field measurements regarding magnetic implosion. At the onset of the impulsive phase, two arch-shaped loops originating from the center of the sigmoid were observed to expand outward in 211 Å in different directions (bottom panels of Figure 8) but at similar projected speeds (Figures 9(d) and (e)), while coronal loops overlying both elbows of the sigmoid were observed to contract (top panels of Figure 8), with the loops overlying the eastern elbow contracting much faster (Figures 9(b) and (c)). For this relatively energetic event, the eruption only preceded the contraction by tens of seconds, and the contracting speed becomes as fast as 200 km s^{-1}. In the wake of the contraction, loops overlying the eastern elbow underwent oscillation for several cycles (marked by rectangles in Figure 9), similar to the events studied by Liu & Wang (2010), Gosain (2012), and Kallunki & Pohjolainen (2012). Beyond the

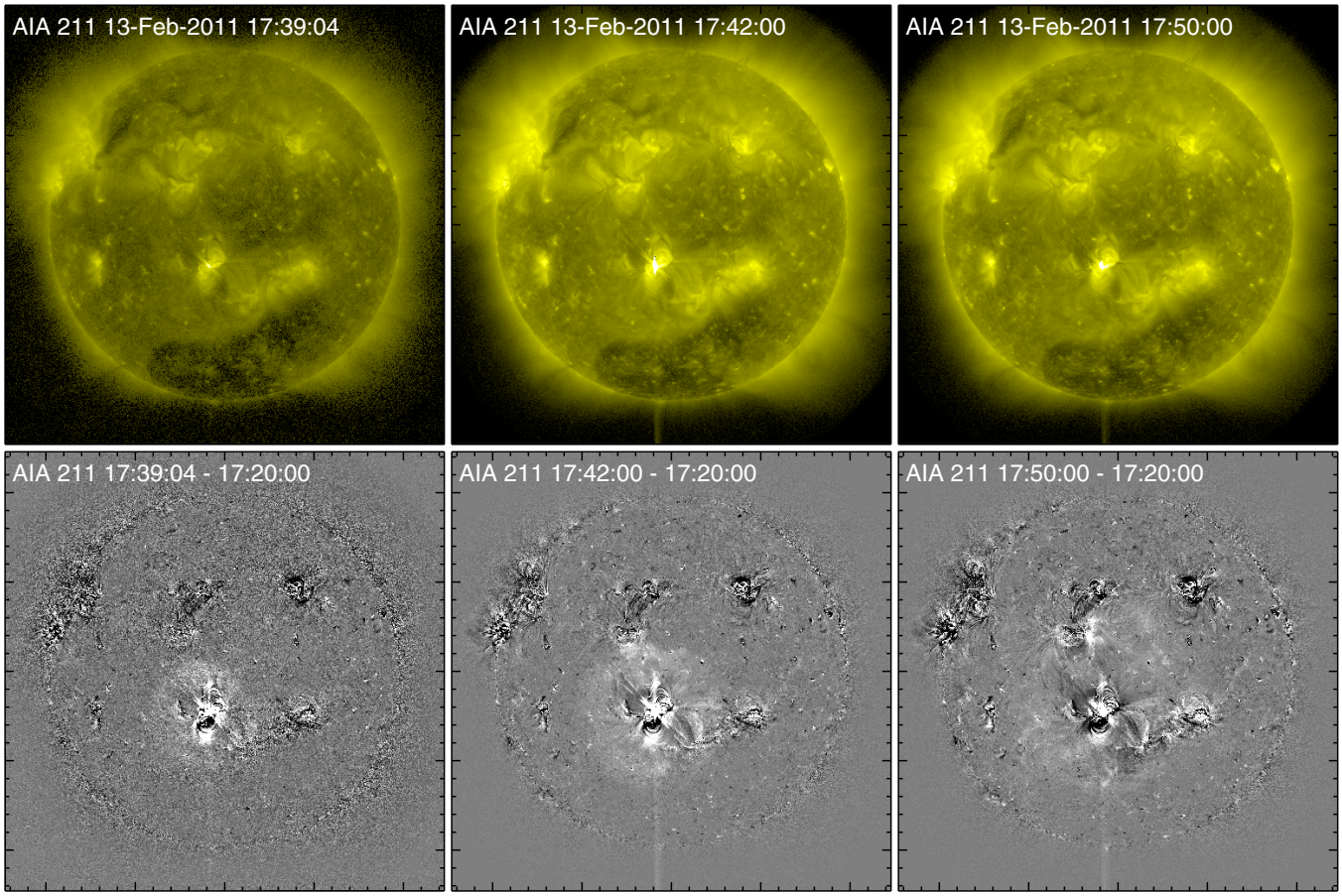

Figure 10. Snapshots of the full-disk AIA 211 Å images (top panels) and the corresponding difference images (bottom panels). In the difference images, a diffuse front can be seen propagating outward from the active region of interest.

(A color version of this figure is available in the online journal.)

expanding loops, one can also see in the animation of the AIA 211 Å difference images (accompanying Figure 8) a diffuse oval front with enhanced intensity propagating outward, well separated from the expanding loops. This oval structure has been identified in MHD simulations as a shell of return currents surrounding the flux rope (Aulanier et al. 2010; Schrijver et al. 2011). From Figure 10 one can see that the front was propagating anisotropically, apparently restrained by nearby active regions and the coronal hole in the southern polar region.

2.5. 2011 February 15 Event

The 2011 February 15 X2.2 flare in AR 11158 is the first X-class flare of the current solar cycle, hence it has generated a lot of interests and has been intensively studied. Kosovichev (2011) reported that the flare produced a powerful "Sunquake" event due to its impact on the photosphere. Wang et al. (2012) reported a rapid, irreversible change of the photospheric magnetic field associated with the flare. Beauregard et al. (2012) studied the shear flows along the PIL as well as the white-light flare emission. Schrijver et al. (2011) investigated the coronal transients associated with the flare. In particular, Schrijver et al. (2011, p. 167) observed "expanding loops from a flux-rope-like structure over the shearing PIL between the central δ-spot groups of AR 11158, developing a propagating coronal front ("EIT wave"), and eventually forming the CME moving into the inner heliosphere." Here the expanding loops are identified as the erupting component.

The active region as seen in the AIA 171 Å channel was dominated by two groups of potential-like loops overlying the elbows of the forward S-shaped sigmoid as seen in the hot AIA channels (Figure 2). Both groups of potential-like loops were observed to contract during the X2.2 flare. In each group, loops underwent contraction successively with those located at lower altitudes starting to contract first, presumably due to the limited propagation speed of the Alfvén wave (see also Liu & Wang 2010; Gosain 2012), whereas loops at higher altitudes had a faster contraction speed (Figures 12(b) and (c)). These contracting/collapsing features were also independently noted by Schrijver et al. (2011), Gosain (2012), and Sun et al. (2012) using different approaches but with similar interpretation, in agreement with Liu & Wang (2009).

Immediately prior to the loop contraction, a bubble (marked by red arcs in the middle panels of Figure 11) can be best seen to originate from the core of the sigmoid and to expand northeastward in the 211 Å channel and southwestward in the 94 Å channel (bottom panels of Figure 11; marked by red arcs). A transition from a slow- to fast-rise phase can still be marginally seen in the 211 Å channel. But the duration of the slow-rise phase was very short, lasting for only about two minutes. The transition time at about 01:50 UT still preceded the loop contraction by about three minutes. The commencement of the bubble expansion at about 01:48 UT was concurrent with the onset of the nonthermal hard X-ray (HXR) emission at 35–100 keV. This expanding bubble was also closely associated with "an expanding intensity front propagating away from the

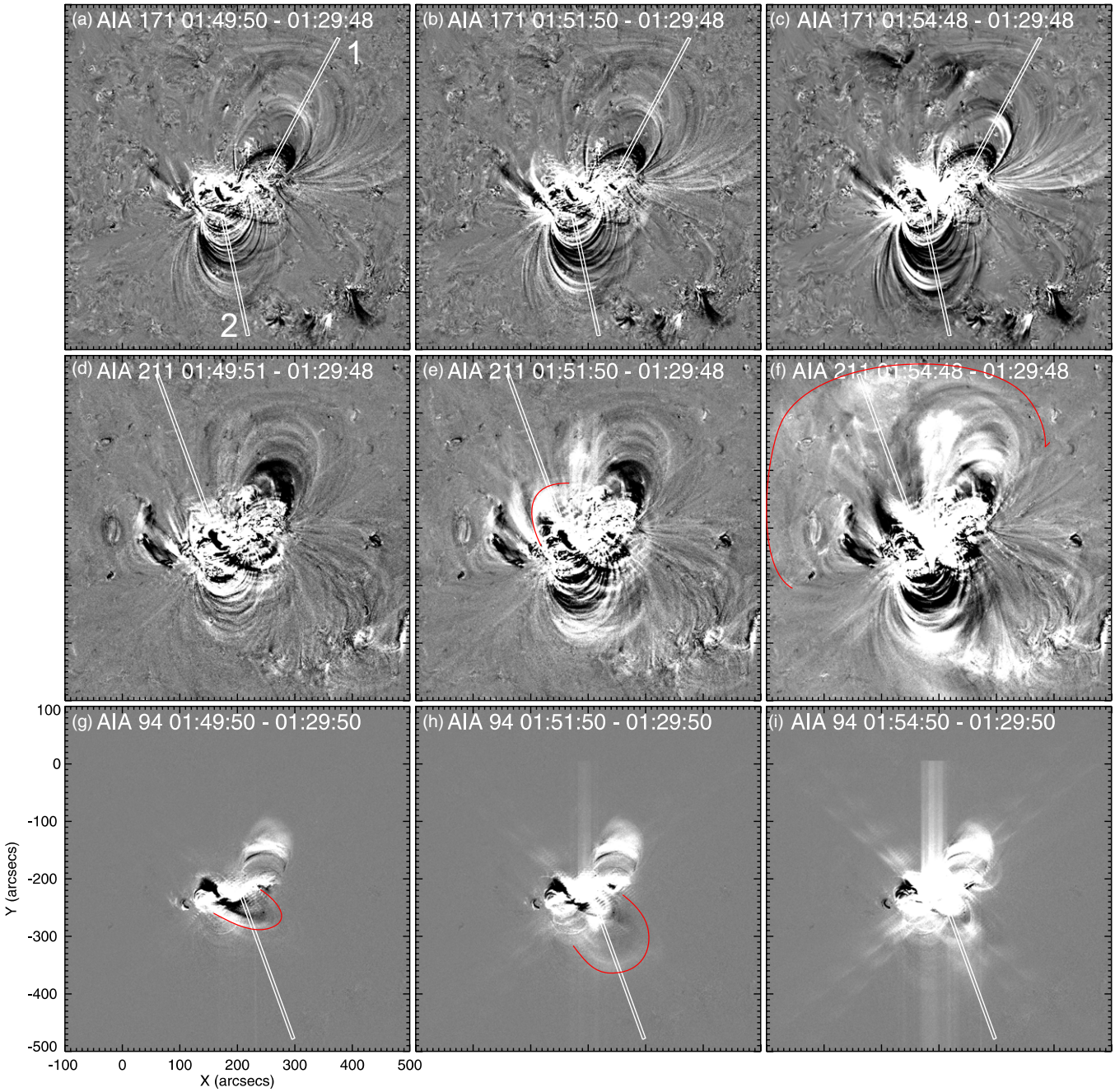

Figure 11. AIA observation of the 2011 February 15 X-flare. From the top, middle, to bottom panels, we show the 171, 211, and 94 difference images, respectively. The expanding bubble is highlighted by red arcs.

(A color version of this figure is available in the online journal.)

flaring region seen on the disk, and the leading edge of the intensity signature of the CME propagating outward from the Sun into the heliosphere," as identified by Schrijver et al. (2011, p. 181). These three distinct features are suggested to be different observational aspects of the eruption of a flux rope (Schrijver et al. 2011). Similar to the February 13 event, in the wake of the contraction, loops overlying both elbows underwent oscillation (see Figure 12, also see Liu & Wang 2010; Gosain 2012; Kallunki & Pohjolainen 2012).

2.6. 2011 June 21 Event

In the 2011 June 21 event, the group of coronal loops overlying the eastern elbow of the sigmoid was observed to contract in the 171 Å channel (top panels in Figure 13). At the same time, a bubble originating from the center of the sigmoid was observed to expand eastward in the 94 Å channel (bottom panels in Figure 13). Both the contraction and the expansion occurred prior to the C7.7 flare. The transition time of the bubble from a relatively slow- to a fast-rise phase was roughly coincident with the onset of the flare (Figure 14).

3. DISCUSSION AND CONCLUSION

We have investigated four sigmoidal active regions, in which five eruptions with signatures of magnetic implosion occurred. The magnitudes of the flares associated with the eruptions span almost the whole flare "spectrum," from *GOES* class B

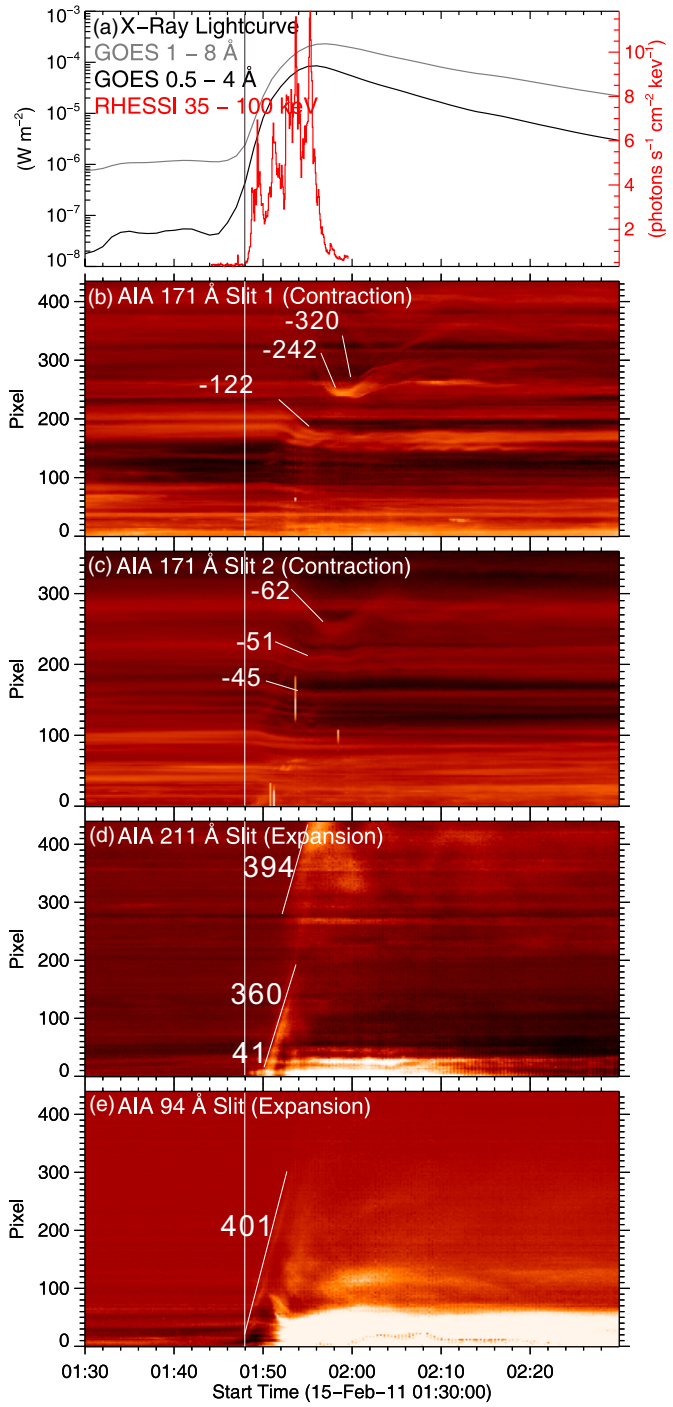

Figure 12. Temporal evolution of the contracting loop and the expanding bubble in relation to the X-ray emission. The space–time diagrams are obtained by stacking image slices cut by the slits as shown in Figure 11. The vertical line marks the beginning of the explosion.

(A color version of this figure is available in the online journal.)

to X. In all of the flares studied, there are both contracting and erupting components: the former is only observed in cold EUV channels and the latter is preferentially visible in warm/hot EUV channels. This is because the contracting component is composed of large-scale, potential-like coronal loops overlying the elbows of the sigmoid, while the erupting component is associated with newly reconnected flux tubes originating from the center of the sigmoid (cf. Liu et al. 2010c; Aulanier et al. 2010; Schrijver et al. 2011). Several important aspects of these observations are discussed as follows.

1. *Consequence of loop contraction*. The overlying loops undergoing contraction never regain their pre-flare positions, which implies a new equilibrium with reduced magnetic energy as the eruption is powered by magnetic energy. One may argue that the apparent contraction of coronal loops could be a projection effect, i.e., the loop plane tilts due to the flare impulse. But in that case, one would expect the restoration of the loops once the flare impulse has passed away. In observations, however, the contracting loops may oscillate about a lower height (e.g., Figure 9; see also Liu & Wang 2010), but never reach the original heights after the eruption. Thus, the contraction within the loop plane must make a significant contribution.
2. *Correlation between contraction and eruption*. The contraction speed seems to depend on the intensity/magnitude of the eruption. From Figure 15, one can see that despite this very small sample size, the peak *GOES* SXR flux as a proxy of the flare magnitude is linearly correlated very well with the measured maximal contraction speed in the log–log plot, although not so well with the maximal erupting speed. Unlike contracting loops which are clearly defined, however, the measurement of the erupting speed involves larger uncertainties as the front of the expanding bubble tends to get more and more diluted and eventually overwhelmed by the background during propagation, thereby leading to underestimation of its speed. One more caveat to keep in mind is that these speeds are not necessarily measured at the time of the peak SXR flux.
3. *Timing*. The eruption precedes the contraction in all of the flares studied, thus establishing loop contraction as a consequence of eruption. There is also a trend that the more energetic the eruption, the smaller the time delay of the loop contraction relative to the onset of the expansion of the erupting component, which is demonstrated in Figure 15 as a strong anti-correlation between the time delay and the peak *GOES* SXR flux in the log–log plot. This time delay is presumably determined by the expansion speed of the erupting component. In addition, in the relatively weak B- and C-flares, the initiation of the erupting component precedes the increase in *GOES* SXR fluxes, but in the stronger M- and X-flares, it is concurrent with the increase in nonthermal HXR fluxes. This may lend support to Lin (2004), who concluded that CMEs are better correlated with flares if there is more free energy available to drive the eruption. However, since the CME progenitor, i.e., the expanding bubble, forms before the flare onset as the weak events clearly demonstrate, the CME must be independent of the conventionally defined flare, or, the flare is only a byproduct of the CME, unless the eruption mechanism for the weak events is different from that for the energetic ones.
4. *Asymmetry of contraction*. The two groups of coronal loops overlying the elbows of the sigmoid often contract asymmetrically, i.e., not only do they contract at different speeds but either group could show little sign of contraction, which depends on the detailed interaction between the core field and the arcade field, including, presumably, their relative strength and the spatial distribution of the decay index of the restraining field (Kliem & Török 2006; Liu et al. 2009a, 2010a). For the 2010 August 1 event in particular, Liu et al. (2010c) concluded that the majority of the flare loops were formed by the reconnection of the stretched legs of the less sheared loops overlying the southern elbow and the center of the sigmoid, based on the reconnection rate

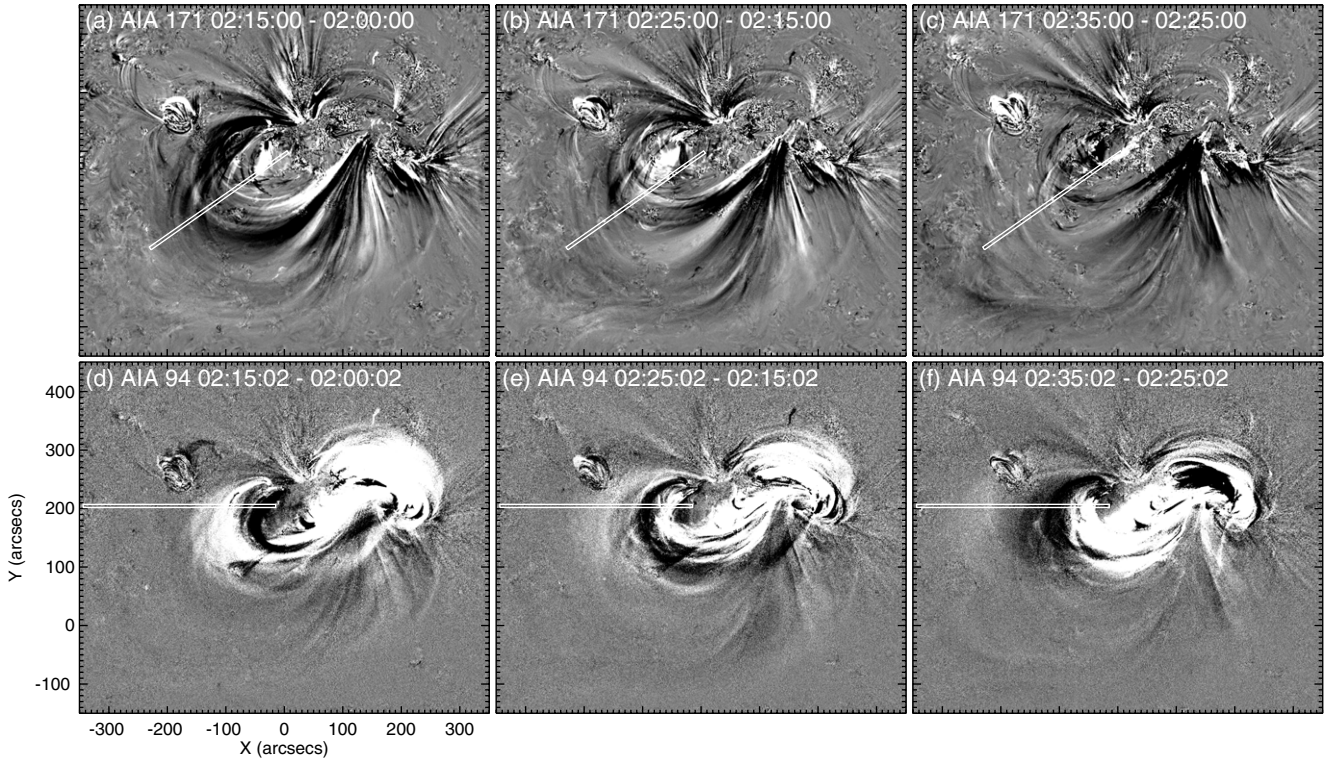

Figure 13. AIA observation of the 2011 June 21 C-flare. The top panels show the 171 Å difference images and the bottom panels the 94 Å difference images.

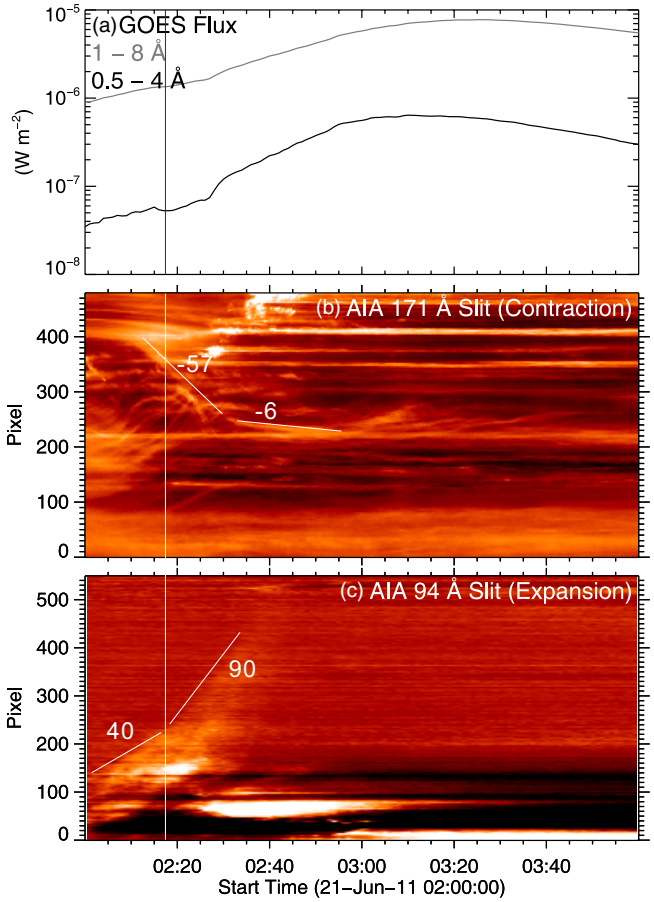

Figure 14. Temporal evolution of the contracting loops and the expanding bubble in relation to the X-ray emission. The space–time diagrams are obtained by stacking image slices cut by the slits as shown in Figure 13. The vertical line marks the transition of the exploding bubble from a slow- to a fast-rise phase.

(A color version of this figure is available in the online journal.)

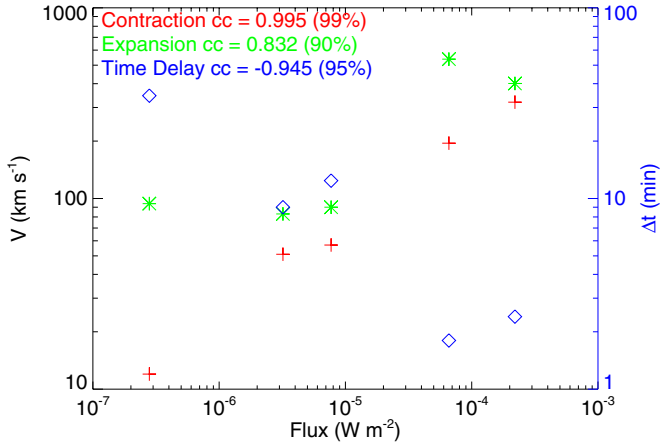

Figure 15. Correlation of the maximal contraction/expansion speed, V, and the time delay of contraction relative to expansion, Δt, with the flare magnitude in terms of the peak *GOES* 1–8 Å flux. The confidence level of the linear correlation coefficient, cc, of $\log(V)$ and $\log\Delta t$ with $\log(F)$ is given in the brackets.

(A color version of this figure is available in the online journal.)

inferred from the Hα ribbon motion. The eruption therefore left most loops overlying the northern elbow unopened. This explains why only these loops underwent obvious contraction. The intensity/magnitude of the eruption could be another relevant factor as among the events studied only those greater than M class show contraction of loops overlying both elbows of the sigmoid.

5. *Implication for eruption mechanism*. As the contracting component is distinct from the erupting component, we conclude that these eruptions conform to the "rupture model" in which the arcade field is partially opened (Sturrock et al. 2001; Figure 1(b)). We can further exclude the breakout model because the coronal loops undergoing

contraction are arched over, rather than located to the side of, the sheared core field. The loop contraction in the latter occasion results from reconnection at the magnetic null above the central lobe in the breakout model.

In conclusion, these observations substantiate that loop contraction is an integrated process in eruptions of sigmoidal active regions in which the restraining arcade field is only partially opened, consistent with theoretical expectations. The consequence of loop contraction is a new equilibrium of the coronal field with reduced magnetic energy, and the process itself is a result of the flare energy release, as evidenced by the strong correlation of the maximal contracting speed, and strong anti-correlation of the time delay of contraction relative to expansion, with the peak SXR flux.

The authors are grateful to the *SDO*, *STEREO*, and *RHESSI* teams for the free access to the data and the development of the data analysis software. R.L. acknowledges the Thousand Young Talents Program of China. R.L. and Y.W. were supported by grants from NSFC 41131065 and 41121003, 973 key project 2011CB811403, CAS Key Research Program KZZD-EW-01-4, and the fundamental research funds for the central universities WK2080000031. R.L., C.L., and H.W. were supported by NSF grants ATM-0849453 and ATM-0819662. The contribution of T.T. was supported by CISM (an NSF Science and Technology Center).

REFERENCES

Antiochos, S. K., DeVore, C. R., & Klimchuk, J. A. 1999, ApJ, 510, 485
Aulanier, G., Török, T., Démoulin, P., & DeLuca, E. E. 2010, ApJ, 708, 314
Beauregard, L., Verma, M., & Denker, C. 2012, Astron. Nachr., 333, 125
Canfield, R. C., Hudson, H. S., & McKenzie, D. E. 1999, Geophys. Res. Lett., 26, 627
Cheng, X., Zhang, J., Liu, Y., & Ding, M. D. 2011, ApJ, 732, L25
Chen, P. F., & Shibata, K. 2000, ApJ, 545, 524
Forbes, T. G. 2000, J. Geophys. Res., 105, 23153
Forbes, T. G., & Acton, L. W. 1996, ApJ, 459, 330
Gibson, S. E., & Fan, Y. 2006, ApJ, 637, L65
Glover, A., Ranns, N. D. R., Harra, L. K., & Culhane, J. L. 2000, Geophys. Res. Lett., 27, 2161
Gosain, S. 2012, ApJ, 749, 85
Hoeksema, et al. 2012, Sol. Phys., to be submitted
Hudson, H. S. 2000, ApJ, 531, L75
Hudson, H. S., Lemen, J. R., St. Cyr, O. C., Sterling, A. C., & Webb, D. F. 1998, Geophys. Res. Lett., 25, 2481
Inhester, B. 2006, arXiv:astro-ph/0612649
Kallunki, J., & Pohjolainen, S. 2012, Sol. Phys., 122
Kliem, B., & Török, T. 2006, Phys. Rev. Lett., 96, 255002
Kopp, R. A., & Pneuman, G. W. 1976, Sol. Phys., 50, 85
Kosovichev, A. G. 2011, ApJ, 734, L15
Lemen, J. R., Title, A. M., Akin, D. J., et al. 2012, Sol. Phys., 275, 17
Lin, J. 2004, Sol. Phys., 219, 169
Liu, C., Deng, N., Liu, R., et al. 2012, ApJ, 745, L4
Liu, C., Lee, J., Jing, J., et al. 2010a, ApJ, 721, L193
Liu, R., Alexander, D., & Gilbert, H. R. 2009a, ApJ, 691, 1079
Liu, R., Liu, C., Park, S.-H., & Wang, H. 2010b, ApJ, 723, 229
Liu, R., Liu, C., Wang, S., Deng, N., & Wang, H. 2010c, ApJ, 725, L84
Liu, R., & Wang, H. 2009, ApJ, 703, L23
Liu, R., & Wang, H. 2010, ApJ, 714, L41
Liu, R., Wang, H., & Alexander, D. 2009b, ApJ, 696, 121
Moore, R. L., Sterling, A. C., Hudson, H. S., & Lemen, J. R. 2001, ApJ, 552, 833
Pesnell, W. D., Thompson, B. J., & Chamberlin, P. C. 2012, Sol. Phys., 275, 3
Rachmeler, L. A., DeForest, C. E., & Kankelborg, C. C. 2009, ApJ, 693, 1431
Scherrer, P. H., Schou, J., Bush, R. I., et al. 2012, Sol. Phys., 275, 207
Schrijver, C. J., Aulanier, G., Title, A. M., Pariat, E., & Delannée, C. 2011, ApJ, 738, 167
Sturrock, P. A., Weber, M., Wheatland, M. S., & Wolfson, R. 2001, ApJ, 548, 492
Sun, X., Hoeksema, J. T., Liu, Y., et al. 2012, ApJ, 748, 77
Wang, S., Liu, C., Liu, R., et al. 2012, ApJ, 745, L17
Wiegelmann, T. 2004, Sol. Phys., 219, 87
Wiegelmann, T., Inhester, B., & Sakurai, T. 2006, Sol. Phys., 233, 215
Wuelser, J.-P., Lemen, J. R., Tarbell, T. D., et al. 2004, Proc. SPIE, 5171, 111

The Astrophysical Journal, 756:59 (14pp), 2012 September 1 doi:10.1088/0004-637X/756/1/59

SLOW RISE AND PARTIAL ERUPTION OF A DOUBLE-DECKER FILAMENT. I. OBSERVATIONS AND INTERPRETATION

Rui Liu[1,2], Bernhard Kliem[3,4], Tibor Török[5], Chang Liu[2], Viacheslav S. Titov[5], Roberto Lionello[5], Jon A. Linker[5], and Haimin Wang[2,6]
[1] CAS Key Laboratory of Geospace Environment, Department of Geophysics & Planetary Sciences, University of Science & Technology of China, Hefei 230026, China; rui.liu@njit.edu
[2] Space Weather Research Laboratory, Center for Solar-Terrestrial Research, NJIT, Newark, NJ 07102, USA
[3] Institute of Physics and Astronomy, University of Potsdam, D-14476 Potsdam, Germany
[4] Mullard Space Science Laboratory, University College London, Holmbury St. Mary, Dorking, Surrey RH5 6NT, UK
[5] Predictive Science Inc., 9990 Mesa Rim Road, Suite 170, San Diego, CA 92121, USA
[6] Key Laboratory of Solar Activity, National Astronomical Observatories, Beijing, China
Received 2012 May 14; accepted 2012 July 5; published 2012 August 14

ABSTRACT

We study an active-region dextral filament that was composed of two branches separated in height by about 13 Mm, as inferred from three-dimensional reconstruction by combining *SDO* and *STEREO-B* observations. This "double-decker" configuration sustained for days before the upper branch erupted with a *GOES*-class M1.0 flare on 2010 August 7. Analyzing this evolution, we obtain the following main results. (1) During the hours before the eruption, filament threads within the lower branch were observed to intermittently brighten up, lift upward, and then merge with the upper branch. The merging process contributed magnetic flux and current to the upper branch, resulting in its quasi-static ascent. (2) This transfer might serve as the key mechanism for the upper branch to lose equilibrium by reaching the limiting flux that can be stably held down by the overlying field or by reaching the threshold of the torus instability. (3) The erupting branch first straightened from a reverse S shape that followed the polarity inversion line and then writhed into a forward S shape. This shows a transfer of left-handed helicity in a sequence of writhe–twist–writhe. The fact that the initial writhe is converted into the twist of the flux rope excludes the helical kink instability as the trigger process of the eruption, but supports the occurrence of the instability in the main phase, which is indeed indicated by the very strong writhing motion. (4) A hard X-ray sigmoid, likely of coronal origin, formed in the gap between the two original filament branches in the impulsive phase of the associated flare. This supports a model of transient sigmoids forming in the vertical flare current sheet. (5) Left-handed magnetic helicity is inferred for both branches of the dextral filament. (6) Two types of force-free magnetic configurations are compatible with the data, a double flux rope equilibrium and a single flux rope situated above a loop arcade.

Key words: Sun: coronal mass ejections (CMEs) – Sun: filaments, prominences – Sun: flares

Online-only material: animations, color figures

1. INTRODUCTION

It is generally accepted that the magnetic field plays a crucial role for dense and cold filaments to be suspended in and thermally isolated from the surrounding hot, tenuous coronal plasma. Filaments are always formed along a polarity inversion line (PIL) of the photospheric field. Studies utilizing Zeeman and Hanle effects demonstrated that the flux threading the filament is largely horizontal and mainly directed along the filament axis (Leroy 1989; Bommier et al. 1994). This is also manifested in the chromospheric fibril pattern (Martin 1998 and references therein): fibrils near the filament are nearly parallel to the filament axis, but away from the filament they tend to be perpendicular to the filament axis. This pattern implies the presence of two types of *filament chirality*: for an observer viewing the filament from the positive-polarity side, the axial field in a *dextral* (*sinistral*) filament always points to the right (left). Independent of the solar cycle, dextral (sinistral) filaments are predominant in the northern (southern) hemisphere (Martin et al. 1994; Zirker et al. 1997; Pevtsov et al. 2003).

Most quiescent filaments have what is known as *inverse polarity* configuration, i.e., the magnetic field component perpendicular to the axis traverses the filament from the region of negative polarity to the region of positive polarity in the photosphere, opposite to what would be expected from a potential field. *Normal polarity* configuration is mainly found in active-region filaments, i.e., the field lines pass through the filament from the region of positive polarity to the region of negative polarity (Leroy 1989). Magnetic configurations with either a dipped field or a helically coiled field have been invoked to explain the equilibrium and stability of filaments, which leads to three basic filament models as reviewed by Gilbert et al. (2001): the normal polarity dip model (e.g., Kippenhahn & Schlüter 1957), the normal polarity flux rope model (e.g., Hirayama 1985; Leroy 1989), and the inverse polarity flux rope model (e.g., Kuperus & Raadu 1974; Pneuman 1983; Anzer 1989; Low & Hundhausen 1995). In addition, by transporting the core flux into regions of increasingly weak field via shear flows, Antiochos et al. (1994) were able to produce a dipped, inverse-polarity configuration of sheared field lines. By applying greater shear, DeVore & Antiochos (2000) find that magnetic reconnection produces helical field lines threading the filament. In all these models, the magnetic tension force pointing upward provides mechanical support for the filament material against gravity. Alternatively, Karpen et al. (2001) found that cool plasma can be supported in a dynamic state on flat-topped arcade field lines and argued that magnetic dips are not necessary for the formation and suspension of filaments.

The correspondence between the filament chirality and the helicity sign has been controversial due to different opinions on how the filament is magnetically structured. Rust (1994) conjectured that sinistral (dextral) filaments are threaded by

right-handed (left-handed) helical fields, considering that barbs, which are lateral extensions veering away from the filament spine, should rest at the bottom of the helix. Martin & Echols (1994), on the other hand, noticed that the ends of barbs are fixed at patches of parasitic polarities (also termed minority polarities), which are opposite in polarity to the network elements of majority polarity, and suggested that dextral filaments are right helical. Chae et al. (2005), however, reported that the barbs terminate over the minority PIL. This lends support to the suggestion that the barb material is suspended in field line dips which form due to the existence of parasitic polarities. The latter scenario is consistent with force-free field models (Aulanier & Démoulin 1998; Aulanier et al. 1998), in which the filament spine, the barbs, and the surrounding fibrils are all modeled as the dipped portions of the field lines. With projection effects, a continuous pattern of dipped field lines could give the illusion that barbs are made of vertical fields joining the spine to the photosphere. Projection effects also contribute to the confusion about the chirality-helicity correspondence of the sigmoidal structures in the corona: the projection of a single twisted field line includes both forward and inverse S shapes (Gibson et al. 2006). Furthermore, a left-handed flux rope can take either forward or reverse S shapes depending on whether it kinks upward or downward (Kliem et al. 2004; Török et al. 2010).

Considerable attention has been given to the eruption of filaments, with the dense filament material tracing the otherwise invisible progenitor of the coronal mass ejection (CME). Relevant models can be roughly classified into two categories: those that rely on magnetic reconnections to remove the tethering field so that the filament can escape (Moore et al. 2001; Antiochos et al. 1999) and those in which the eruption occurs when a flux rope loses equilibrium, due to a catastrophe (e.g., van Tend & Kuperus 1978; Forbes & Priest 1995) or due to ideal MHD instabilities (e.g., Hood & Priest 1979; Kliem & Török 2006). While the torus instability almost certainly plays a role (Liu 2008; Aulanier et al. 2010; Fan 2010), the occurrence of the helical kink mode has recently been quite controversial. It is motivated by observations of writhed eruptive structures (e.g., Rust & Kumar 1994, 1996; Ji et al. 2003; Romano et al. 2003; Rust & LaBonte 2005; Alexander et al. 2006; Liu et al. 2007c; Liu & Alexander 2009; Cho et al. 2009; Karlický & Kliem 2010), most of which are filaments. It is also supported by successful MHD numerical modeling of key properties of eruptions, e.g., writhe, rise profile, and sigmoidal features, and of specific eruptive events (e.g., Fan & Gibson 2004; Fan 2005, 2010; Gibson & Fan 2006b; Török et al. 2004; Török & Kliem 2005; Kliem et al. 2010). On the other hand, signatures of the required amount of twist prior to the eruption remain difficult to detect (e.g., Chae 2000; Su et al. 2011). Eruptions driven by the kink instability also provide an opportunity to determine the helicity sign of the filament. Due to helicity conservation, an unstable flux rope only writhes into a kink of the same handedness, which can be inferred from the writhing motion of the filament axis (e.g., Green et al. 2007), especially if stereoscopic observations are available.

In this paper, we address these issues in analyzing the observations of an eruptive filament which showed strong writhing motions preceded by unwrithing motions. The filament had a special "double-decker" configuration and formed a hard X-ray (HXR) sigmoidal source of coronal origin between the rapidly rising upper branch and the stable lower branch, which provides some unique insight into the physics of solar filaments and their eruption. The observations and data analysis are presented in Section 2. Interpretations are discussed in Section 3. Section 4 summarizes the main results.

In Paper II (Kliem et al. 2012b) we consider the existence, stability, and instability of equilibria containing two vertically arranged force-free flux ropes in bipolar external field, which further corroborates our interpretations based on the present data analysis and suggests new models for partial eruptions.

2. OBSERVATIONS AND DATA ANALYSIS

2.1. Instruments and Data Sets

The key data sources in this study include the EUV imaging instruments on board the *Solar Dynamic Observatory* (*SDO*), the *Solar Terrestrial Relations Observatory* (*STEREO*; Kaiser et al. 2008), and the *Reuven Ramaty High Energy Solar Spectroscopic Imager* (*RHESSI*; Lin et al. 2002).

The Atmospheric Imaging Assembly (AIA; Lemen et al. 2012) on board *SDO* takes EUV/UV images at multiple wavelengths with a resolution of $\sim 1\farcs2$ and a cadence of 12 s for each individual wavelength, covering an unprecedentedly wide and nearly continuous temperature range. AIA Level-1 data are further processed using the standard SSW procedure `AIA_PREP` to perform image registration.

The Extreme-Ultraviolet Imager (EUVI; Wuelser et al. 2004) of the Sun Earth Connection Coronal and Heliospheric Investigation (Howard et al. 2008) imaging package on board both *STEREO* satellites provides three passbands, namely, 171 Å (Fe IX), 195 Å (Fe XII), and 304 Å (He II). The top panel of Figure 1 shows the positions of the *STEREO* "Ahead" and "Behind" satellites (hereafter referred to as *STEREO-A* and *STEREO-B*, respectively) in the X–Y plane of the Heliocentric Earth Ecliptic (HEE) coordinate system. In the bottom panel, the red and blue arcs mark the corresponding limb positions of the *STEREO* satellites in the AIA image obtained at 18:11 UT on 2010 August 7. The active region of interest, NOAA Active Region 11093, was located at N12E31, connecting with AR 11095 (S19E20) in the southern hemisphere through a group of transequatorial loops as indicated by an arrow.

2.2. Pre-eruption Configuration

The filament located in AR 11093 was composed of two branches, hereafter referred to as the *lower branch* and the *upper branch*. As shown in Figure 2, the lower branch was aligned along the PIL as filaments usually do, while the upper branch was projected onto the region of positive polarities, owing to the fact that it was located high in the corona (Section 2.3). The southern ends of both branches were apparently rooted in the penumbra of the sunspot that was of negative polarity. (Note that due to the projection effect the field in the eastern periphery of the penumbra possessed a positive component along the line of sight. This is clearly demonstrated in the line-of-sight magnetogram taken two days later (bottom panel of Figure 2), in which the sunspot was close to the disk center and the positive patch to the east of the sunspot has disappeared.) Hence, the field direction along the filament axis must be pointing southward, spiraling counterclockwise into the sunspot. Therefore, both branches of the filament were dextral, according to the definition of the filament chirality (Martin 1998). This is consistent with the empirical hemispheric chirality rule of filaments.

2.3. 3D Reconstruction and Analysis

By using a pair of EUV images taken from different perspectives, the three-dimensional location of the filament under

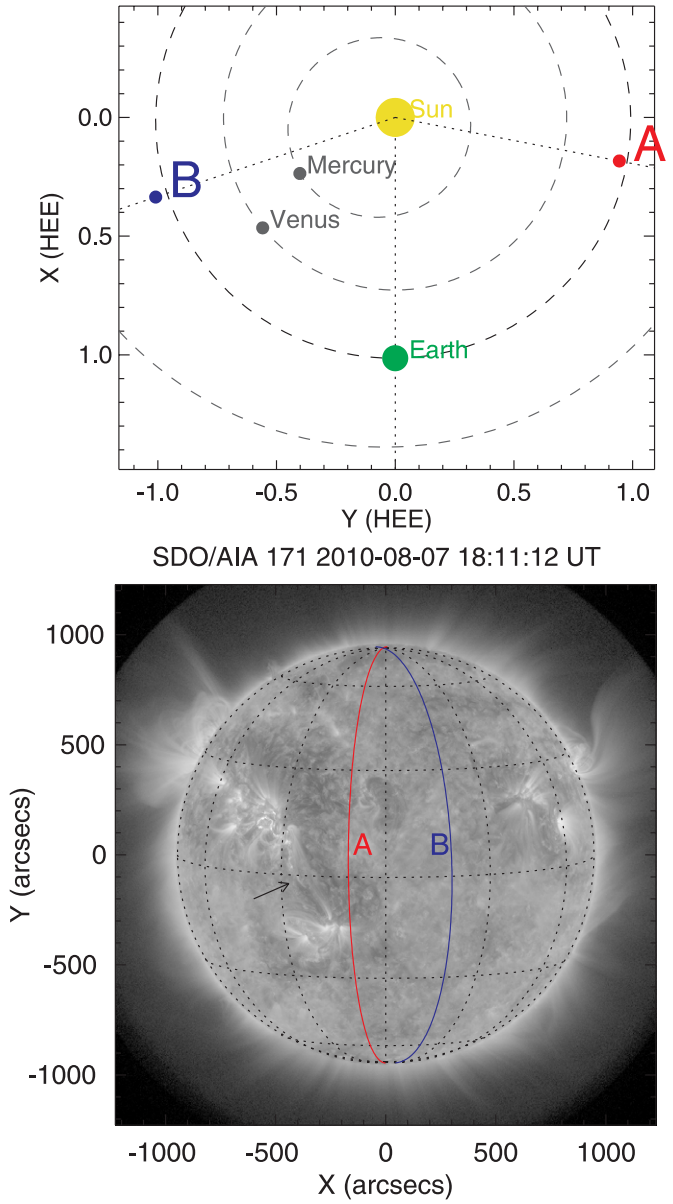

Figure 1. Top: positions of the pair of *STEREO* satellites in the Heliocentric Earth Ecliptic (HEE) coordinate system at about 18:00 UT on 2010 August 7; bottom: red and blue curves indicate the limb positions of the *STEREO* "Ahead" and "Behind" satellites, respectively, on an *SDO* image taken near the onset of the eruption. The arrow marks a group of transequatorial loops connecting AR 11093 in the northern hemisphere, where a sigmoid is visible, and AR 11095 in the south.

(A color version of this figure is available in the online journal.)

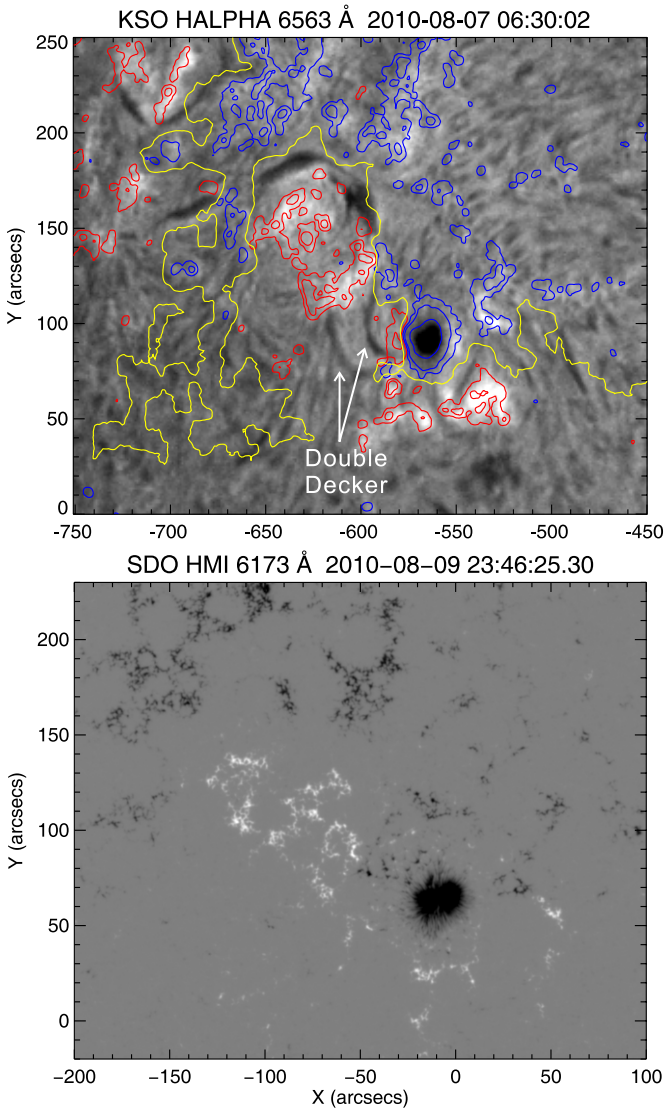

Figure 2. Hα image taken by Kanzelhöhe Solar Observatory (KSO; top panel), overlaid by an HMI line-of-sight magnetogram taken at the same time. Contour levels indicate the magnitude of magnetic flux density at 50, 200, and 800 G for positive (red) and negative (blue) polarities. Yellow contours indicate the major PIL of the active region. The bottom panel shows a line-of-sight magnetogram taken two days later when the sunspot was close to the disk center.

(A color version of this figure is available in the online journal.)

investigation can be derived by a triangulation technique called *tie point* (Inhester 2006). This is implemented in an SSW routine, `SCC_MEASURE`, by W. Thompson and has been utilized to obtain the three-dimensional shape and height of filaments observed by *STEREO* (e.g., Li et al. 2010; Xu et al. 2010; Seaton et al. 2011; Bemporad et al. 2011; Thompson et al. 2012). In our case, *STEREO-B* images are to be paired with Earth-view images provided by *SDO*, as the filament was occulted from the *STEREO-A* view (Figure 1). In EUVI images, the filament is more clearly defined with better contrast in 171 Å than in 195 Å or 304 Å, but 171 Å images are often not available, suffering from much lower cadence (2 hr) than the other two channels (usually 5–10 minutes).

The two observers, *SDO* and *STEREO-B*, and the point in the solar corona to be triangulated define a plane called the epipolar plane. For each observer, the epipolar plane intersects with the image plane in the epipolar line. The basis for triangulation is known as the epipolar constraint (Inhester 2006), i.e., a point identified on a certain epipolar line in one image must be situated on the corresponding epipolar line in the other image. Matching features that appear on a pair of epipolar lines therefore establishes a correspondence between pixels in each image, and the reconstruction is achieved by tracking back the lines of sight for each pixel, whose intersection in the same epipolar plane defines a unique location in three-dimensional space.

Figure 3 shows two pairs of EUV images from AIA on board *SDO* and from EUVI on board *STEREO-B* taken on 2010 August 5 and 7. On August 5, both branches of the filament can be clearly seen in the AIA image (Figure 3(b)),

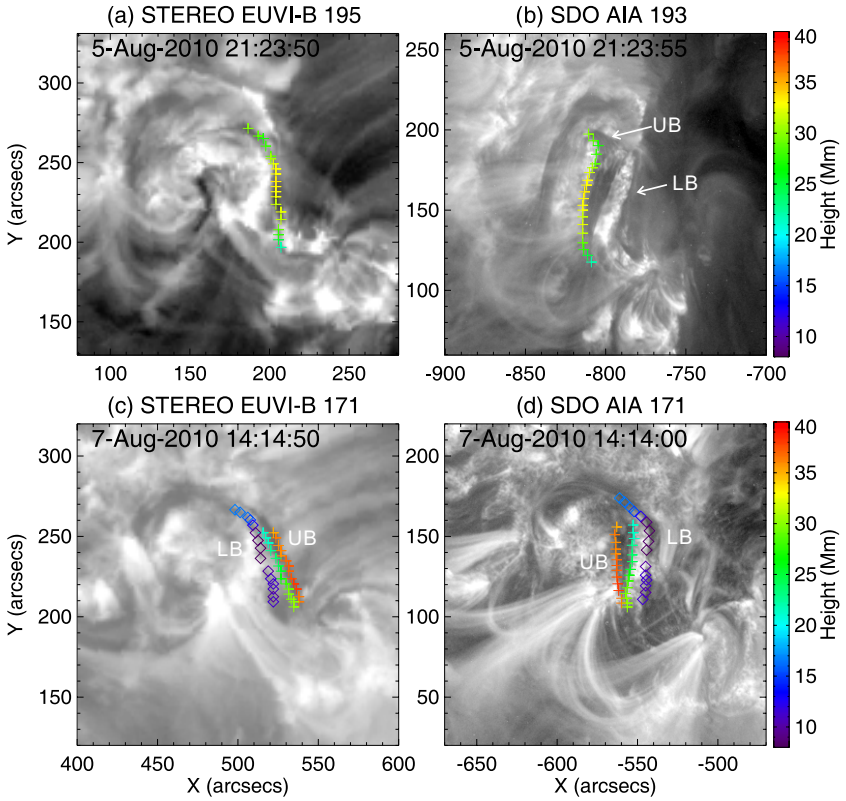

Figure 3. Three-dimensional reconstruction of the filament height using the tie-point method. Points on the upper branch (UB) are indicated by crosses and those on the lower branch (LB) by diamonds. The heights of these points above the solar surface in Mm are color coded as indicated by the color bar on the right.
(A color version of this figure is available in the online journal.)

while only a single thread-like structure of reverse S shape was displayed by the corresponding *STEREO-B* image (Figure 3(a)). For *STEREO-B* the filament was located close to the disk center, suggesting that the upper branch was located right above the lower branch. Hence, we will refer to the configuration as a "double-decker filament." By triangulation, we obtain the height of the upper branch, which was at about 30 ± 3 Mm above the solar surface. The reconstruction error is $\sim w/\sin\alpha \simeq 2.6$ Mm, where $w \simeq 2.5$ Mm is the width of the observed filament thread in the *STEREO-B* image and $\alpha \simeq 71^\circ$ is the separation angle between *STEREO-B* and *SDO* on August 5.

On August 7, the two branches were visible in both the *STEREO-B* and *SDO* views (Figures 3(c) and (d)). About 4 hr later, the upper branch in the *SDO* view moved eastward and then erupted, while in the *STEREO-B* images, one can see that the branch in the west moved westward and then erupted. Hence, we are able to match the two branches unambiguously in the image pair (Figures 3(c) and (d)). For the upper branch, the triangulation results show that its upper rim was located at about 36 ± 2 Mm above the surface, 6 Mm higher than it was on August 5, corresponding to an average rising speed of about 0.1 km s^{-1}. Its lower rim was 25 ± 3 Mm high, hence the vertical extent of the upper branch was about 11 ± 4 Mm. For the lower branch, its upper rim had a height of about 12 ± 3 Mm, which was separated from the lower rim of the upper branch by a distance similar to the vertical extension of the upper branch.

2.4. Filament Rise and Eruption

The evolution of the active region's photospheric field in the course of the one to two days during which it was well visible before the eruption was mainly characterized by the moat flow around the sunspot and ongoing gradual dispersion of the positive polarity flux in the northern hook of the filament. Episodes of significant new flux emergence, shearing, or cancellation were not observed. Weak-flux cancellation proceeded at the north–south-directed section of the PIL under the middle of the filament. The two filament branches did not show strong changes in position either. However, there were quite dramatic signs of interaction between them, which appeared to be the most significant changes associated with the filament system, in addition to the weak-flux cancellation under its middle part. Episodes repeatedly occurred in which a dark thread within the lower branch was heated, brightened, lifted upward, and merged with the upper branch, apparently cooling down again. To show this evolution, we place a virtual "slit" across the center of the double-decker filament in the AIA 304 Å images and generate a stack plot from these data. The slit is taken to be 260 by 10 pixels spanning from $-719\farcs7$ to $-564\farcs3$ in the east–west direction and from $119\farcs1$ to $124\farcs5$ in the north–south direction (see the animation accompanying Figure 4). The intensities are summed in vertical direction, and the solar rotation and differential rotation are removed. The resulting space–time diagram is plotted in Figure 4 in the range of 07:00:10 to 19:59:10 UT. Three exemplary mergers occurring within 10 hr prior to the eruption are visible. Each merger corresponds to a small bump in the light curve of the AIA 304 Å channel (top panel of Figure 4), which is obtained by integrating over a region enclosing the filament (Figure 5(a), green box). The bumps manifest the heating of the filament, due to the reconnection associated with flux transfer from the lower to the upper branch. Assuming dominantly horizontal field direction in the filament, the mass transfer implies a corresponding flux transfer.

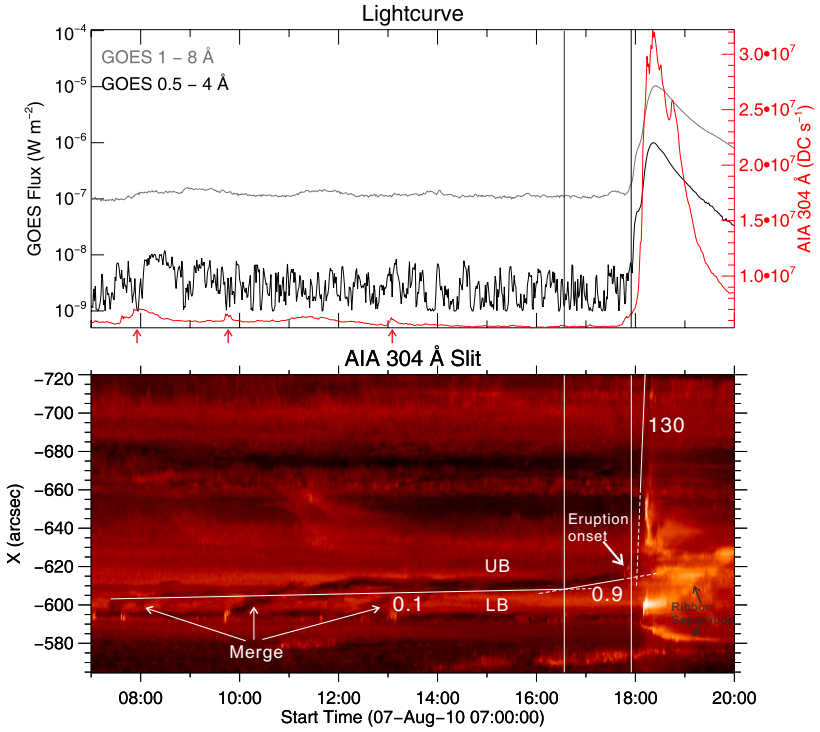

Figure 4. Intermittent merging process observed in AIA 304 Å. Top panel: *GOES* and AIA light curves. The AIA light curve (red) is obtained by integrating over the green box in Figure 5(a). Three bumps in the light curve corresponding to the heating at the start of each merging process are marked by arrows in the bottom. Bottom panel: a space–time diagram (stack plot) obtained from the slit displayed in the accompanying animation of AIA 304 Å images for the same time interval, with all images being registered with the first image at 07:00:10 UT. The intensities in the space–time diagram are displayed in logarithmic scale. The first two sloping lines are adjusted to the western edge of the upper branch, which is better defined than its eastern edge, and the third sloping line follows the eruptive feature, which briefly swept across the slit from 18:07 to 18:17 UT. Dashed lines are simply extensions of the solid lines which outlines the corresponding features. The implied velocities are quoted in km s^{-1}. The two vertical lines mark the crossing of the first two sloping lines and the onset of the *GOES* flare, respectively.

(An animation and a color version of this figure are available in the online journal.)

The merging episodes cannot be associated with significant changes in the position of the branches, but they occurred in a long-lasting phase of very gradual displacement (likely gradual rise) of the upper branch, as indicated by the first of the three sloping lines in Figure 4. The slope of the line represents a velocity of 0.1 km s^{-1} in the plane of the sky, consistent with the average rise velocity since August 5 ($\sim$0.1 km s^{-1}) estimated from the three-dimensional reconstruction in Section 2.3. Both the transfer of flux into the upper branch and the weakening of the overlying field by the gradual cancellation are plausible causes of the indicated very gradual rise of the branch.

Following the mergers, the upper branch appeared thicker and darker, presumably due to the mass loading effect. A few other factors could also affect the observed absorption, such as Doppler shift, change in perspective, shift of the filament structure, and condensation of coronal plasma. It is difficult to evaluate how these effects impact on filament darkness and thickness in relation to the mass loading, which is the most obvious factor.

About 1.5 hr prior to the eruption, the displacement of the upper branch accelerated slightly to reach more typical velocities of a slow-rise phase; the slope of the second line in Figure 4 corresponds to about 0.9 km s^{-1}. Whether this change occurred abruptly at the crossing time (16:34 UT) of the lines or gradually, and whether it was due to external influences or changing conditions in the filament, cannot be determined from the available data. No significant external influence on the filament can be discerned near this time.

Threads in the upper branch lightened up in the EUV from about 17:42 UT. The resulting mix of dark and bright structures strongly increased the visibility of the internal motions in both branches (see the animation accompanying Figure 5). At earlier times, motions directed toward the sunspot could be seen throughout the lower branch and in the southwest half of the upper branch. With the onset of the brightening, the motions in the upper branch intensified, becoming faster in the southwest half. Additionally, motions toward the other end of the branch became very visible in the northeast half (this may be a true enhancement or be due to the improved perception). The motions toward the ends of the upper branch continued into the onset phase of the eruption.

The eruption of the upper filament branch commenced in relatively close temporal association with the soft X-ray (SXR) flare. It can be seen from Figure 4 that the brightening and acceleration of the upper branch (marked by an arrow) started slightly earlier (about 10 minutes) than the onset of the *GOES*-class M1.0 flare at about 17:55 UT. Due to the acceleration, the crossing time of the second and third sloping lines slightly lagged (about seven minutes) behind the onset of flare. Within about two minutes, also a flare spray was ejected from the vicinity of the sunspot, but into a different direction (Figure 5). The flare spray propagated along the transequatorial loops connecting with AR 11095 in the southern hemisphere (see also Figure 1). The lower branch of the filament, on the other hand, obviously remained stable at its original location, flanked by a pair of conjugate flare ribbons in 304 Å separating from each other (Figure 5; see also Vemareddy et al. 2012 for a study of the ribbon separation in relation to the filament eruption). The eruption evolved into a fast CME detected by the *SOHO*/LASCO and *STEREO*/COR coronagraphs.

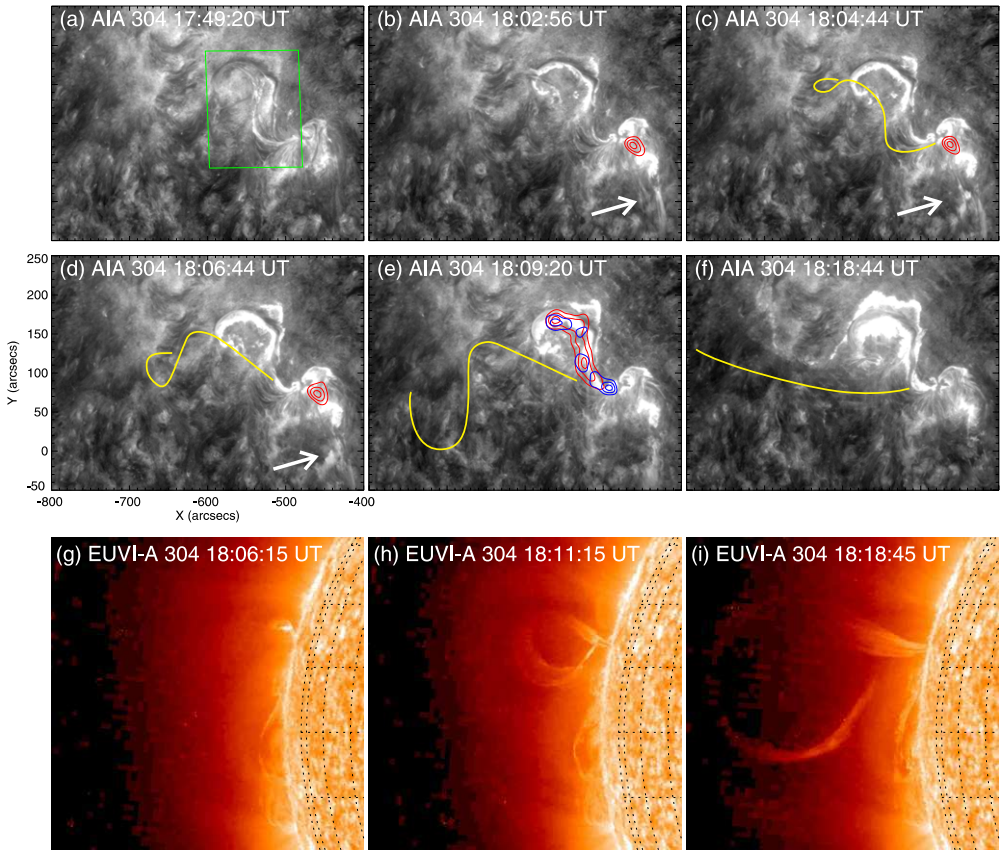

Figure 5. Filament eruption observed in He II 304 Å in two different viewpoints. Panels (a)–(f): snapshots of AIA 304 Å images, overlaid by contours indicating *RHESSI* emission at 3–9 keV (red) and 15–40 keV (blue), respectively. Contour levels are set at 50%, 70%, and 90% of the maximum brightness of each individual image. Yellow curves highlight the upper branch of the filament which was too diffuse to be seen in static images but visible in the animation accompanying the figure; in the animation, the left panel shows an original AIA 304 Å image and the right panel shows the same image enhanced with a wavelet technique. White arrows mark the flare spay propagating along the transequatorial loops connecting to AR 11095 in the southern hemisphere. Panels (g)–(i): 304 Å images obtained by the Ahead satellite of *STEREO*. The green box in panel (a) marks the integration area to obtain the AIA 304 Å light curve in Figure 4. It is slightly slanted due to differential rotation, as the box is defined in the image at 07:00:08 UT.

(An animation and a color version of this figure are available in the online journal.)

The upper filament branch experienced a dramatic change of shape in the course of its eruption. Originally, it had a strong reverse S shape following the PIL (Figures 3 and 5). The AIA images in Figure 5 first indicate a straightening of the branch (panel (c)), followed by a strong writhing into a forward S shape (panels (d)–(e)). With yellow curves, we highlight the shape of the branch, which was too diffuse to be clearly seen in static images, but is visible in the animation of these images accompanying in Figure 5. Both the reverse S shape of the low-lying filament branches and the forward S shape of the erupted, high arching upper branch are signatures of left-handed writhe (Török et al. 2010), indicating left-handed chirality for this dextral filament.

These considerations are supported by the *STEREO* data. In the *STEREO-A* 304 Å images in which the upper branch of the filament was above the east limb from 18:06 UT, a leg-crossing loop configuration developed (Figures 5(g)–(i)), indicative of strong writhing. By examining the animation of AIA 304 Å images, one can see that the filament leg that was fixed at the sunspot penumbra was more perceptible than the other leg, which became too tenuous to be seen by 18:05 UT. Assuming a similar visibility for the corresponding *STEREO-A* images in the same wavelength, we identify the filament leg that was apparently attached to the surface in the *STEREO-A* view (Figures 5(h)–(i)) with the leg fixed at the sunspot penumbra in the Earth view (Figures 5(a)–(f)). Since this footpoint is closer to the observer, the filament traces a left-handed helical curve, consistent with the left-handed writhe inferred from the counterclockwise rotation of the filament's upper section in the AIA images (Figures 5(c)–(e)).

2.5. Associated Flare

X-ray flaring activity associated with the eruption commenced as a microflare at 17:30 UT, detected by *RHESSI* in the energy range ≈ 3–9 keV (Figure 6(b)). In the *GOES* SXR flux, the signal was very weak, barely above the background noise (Figure 6(a)). *RHESSI* images at 3–9 keV show a compact source located to the west of the sunspot. The source location and morphology was almost identical to the early phase of the *GOES*-class M1.0 flare starting at about 17:56 UT (Figures 5(b)–(d)), suggesting that the magnetic configuration stayed largely unchanged in this interval. No specific change in the filament can be associated with the microflare. It appears that this tiny event did not play any significant role in the evolution toward the eruption.

The spatial and spectral evolution of the M1 flare is shown in Figures 7 and 8, respectively. Throughout the flare interval, the spatially integrated spectra can be well fitted by an isothermal, exponential component below about 10 keV (red line) and a nonthermal, power-law component above about 15 keV (blue line) plus a narrow Gaussian component emulating the iron-line complex at 6.7 keV (green line). Toward the flare peak,

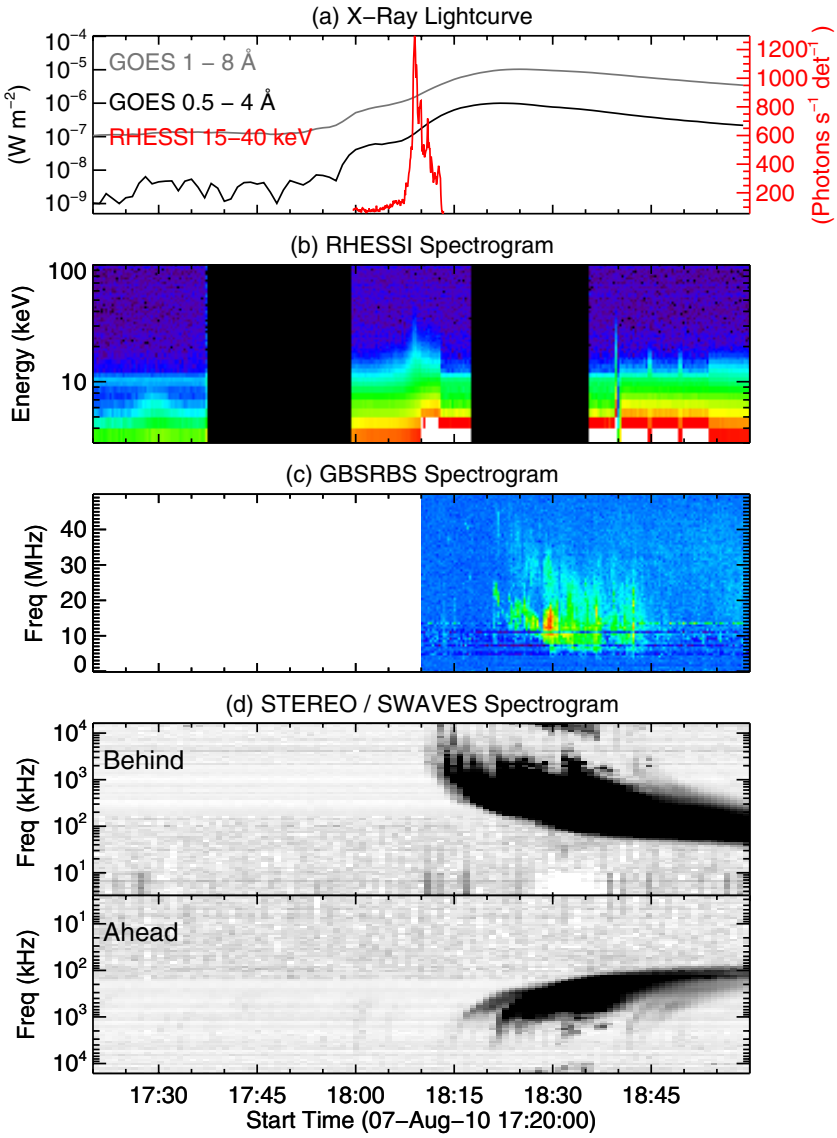

Figure 6. Time evolution of the filament eruption in X-rays and radio.
(A color version of this figure is available in the online journal.)

the power-law section hardened significantly, and the flare morphology underwent a drastic change as the upper branch of the filament rose and writhed. Until 18:08 UT, the compact source to the west of the sunspot was still visible, but new emission began to develop to the east of the sunspot from 18:06 UT, whose shape roughly followed the curved filament. At the peak of the nonthermal emission at about 18:09 UT (Figure 6(a)), a sigmoidal HXR source was fully developed (Figures 7(h) and (i)), outshining the compact source to the west of the sunspot.

In the dynamic spectrograms obtained by the Green Bank Solar Radio Burst Spectrometer[7] on the ground (Figure 6(c)) and the WAVES instrument on board *STEREO* (Bougeret et al. 2008) (Figure 6(d)), one can see a fast-drift burst (type III) starting at about 08:12 UT near 35 MHz, indicating the escape of some nonthermal electrons along open field lines, presumably due to the interaction of the filament field with the surrounding field. One can also see a slow-drift (type II) burst commencing at about 18:20 UT near 50 MHz, which reveals the formation of a large-scale coronal shock by the fast CME.

2.6. Coronal HXR Sigmoid

The HXR nonthermal emission at 15–40 keV was composed of four kernels, $K1$–$K4$ (Figure 9(a)), at the flare peak. Overall it took a reverse S shape, and $K1$–$K3$ were cospatial with the thermal source (3–9 keV) that possessed a continuous, reverse S shape passing over the PIL. This thermal sigmoidal source was roughly projected to the gap between the two filament branches in the AIA 304 Å image (Figure 9(a)), and was cospatial with a hot ridge in the temperature map (Figure 9(b)) which is obtained with the differential emission measure (DEM) method utilizing the six AIA coronal wavelengths (131, 171, 193, 211, 335, and 94 Å; Aschwanden & Boerner 2011). The temperature of this hot ridge is consistent with the isothermal temperature of the SXR emission derived from spectral fitting (~12 MK; Figure 8), confirming that the flaring plasma was observed by both *RHESSI* and AIA. Thermal sources are usually coronal sources, not footpoint sources. The continuous structure, passing over the

[7] http://gbsrbs.nrao.edu/

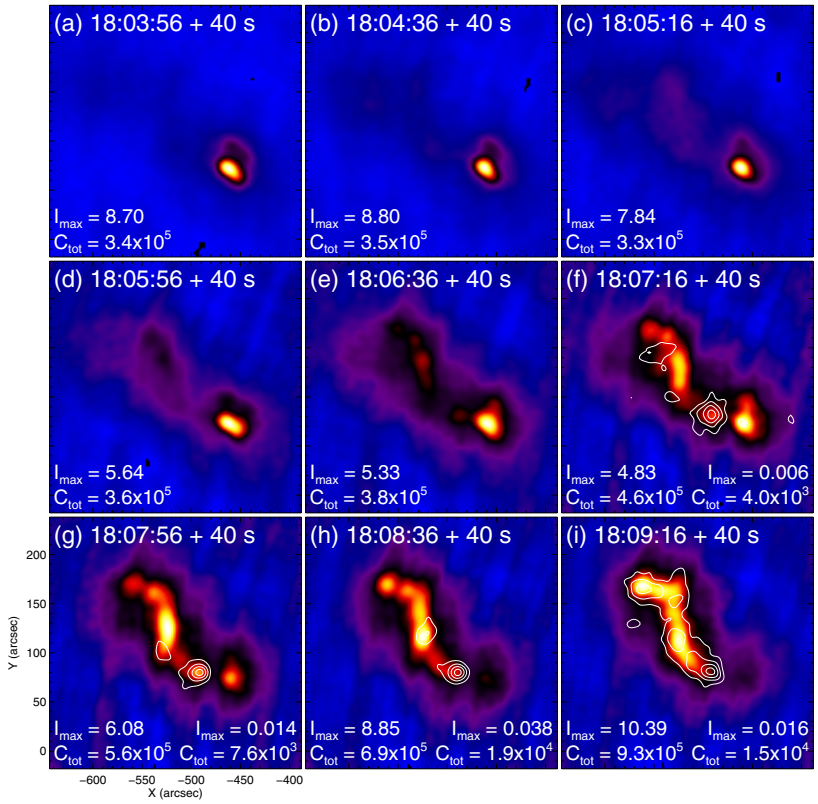

Figure 7. Evolution of flare morphology in HXRs. The figure shows a series of *RHESSI* CLEAN images at 3–9 keV, overlaid by contours at 50%, 70%, and 90% of the maximum brightness, $I_{\max}$ (photons cm^{-2} s^{-1} arcsec^{-2}) of each image obtained for the same time interval at 15–40 keV. $I_{\max}$ is given in the bottom left (right) of each panel for the 3–9 (15–40) keV energy ranges; also quoted is $C_{\rm tot}$, the total counts accumulated by Detectors 3–8.

(A color version of this figure is available in the online journal.)

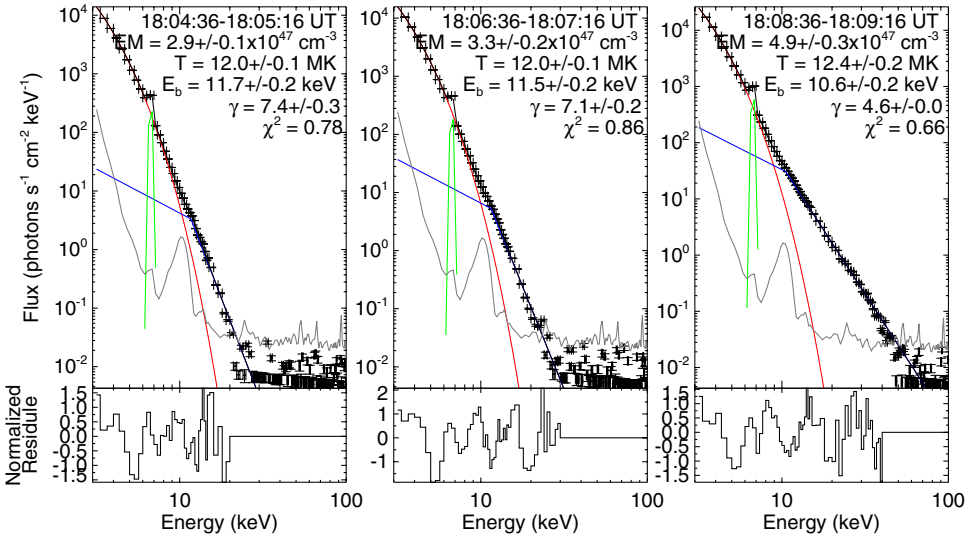

Figure 8. *RHESSI* spatially integrated, background-subtracted spectra and the corresponding spectral fits. The three time intervals correspond to the three panels in the middle column of Figure 7. The red line indicates an optically thin thermal bremsstrahlung radiation function, the blue line a broken power-law function, the green line a Gaussian function, and the gray line the background. The fitting parameters are shown in each panel, including emission measure (EM), temperature (T), break energy of the broken power-law function (E_b), spectral index (γ) above the break energy, and χ^2 of each fitting, assuming a system uncertainty of 5%. The spectral index below the break energy is fixed at 1.5. The maximum energy to fit is chosen automatically by the software based on the spectral values with respect to the background. Fitting residuals normalized to the 1σ uncertainty of the measured flux are shown at the bottom. Detectors 1, 4, and 6 are used.

(A color version of this figure is available in the online journal.)

PIL, clearly favors a coronal source in the present event as well. The hot ridge must show plasma in the flare current sheet above the arcade of flare loops or the tops of the flare loops, which are known to often have the highest brightness in the arcade.

From the above observations, we conclude that the sigmoid featured by SXR emission was of coronal origin. But were the nonthermal kernels, $K1$–$K4$, coronal or footpoint sources? First of all, we believe that these kernels are unlikely "ghost" images

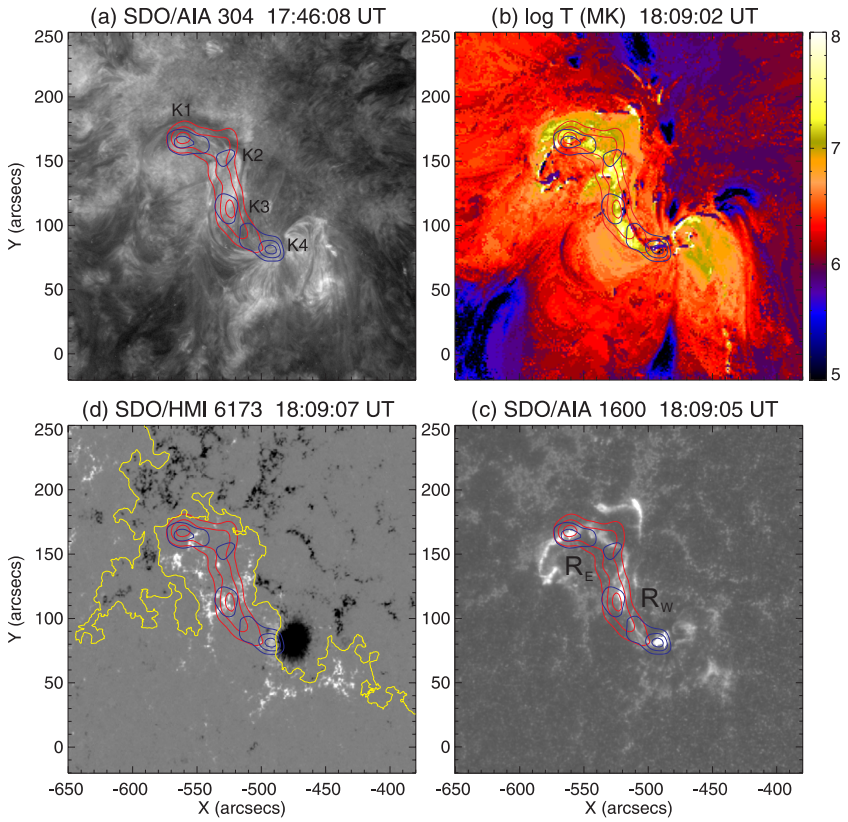

Figure 9. Sigmoidal HXR source in relation to (a) the double-decker filament, (b) flaring loops in the corona, (c) flare ribbons in the chromosphere, and (d) photospheric line-of-sight magnetic field. Panel (b) is a temperature map obtained with the DEM method using six AIA coronal channels. Red and blue contours show the 3–9 and 15–40 keV emission, respectively, integrated over 18:09:16–18:09:56 UT.

(A color version of this figure is available in the online journal.)

due to the pulse pileup effect (Smith et al. 2002; Hurford et al. 2002), as the fractional live time is relatively high (87.96% at the peak of the nothermal emission) and the count rate is relatively low (the peak count rate at 12–25 keV is $\sim$200 s^{-1} det^{-1} with no attenuators in front of the detectors). The spatially resolved spectra of $K3$ and $K4$ (Figure 11) were significantly harder than the other two kernels, making these the strongest candidates for footpoint sources. The source $K4$ coincided with the southern end of the western, negative-polarity ribbon R_W (Figures 9(c) and 10), and it was spatially distinct with both the SXR source and the EUV hot ridge (Figure 9(b)); hence it was very likely a footpoint source. The sources $K1$–$K3$ had projected locations on the positive-polarity side of the PIL. While the stronger source K1 fell on the eastern, positive-polarity ribbon R_E, the centroids of $K2$ and $K3$ were clearly displaced from the ribbon. (Note that R_E was shorter, ending near $K3$, while R_W ended at $K4$.) Moreover, both UV ribbons were formed as early as 18:04 UT, before the HXR sigmoid appeared (Figure 10). This is in contrast to previously reported cases, in which UV-bright kernels tended to be both cospatial and co-temporal with HXR footpoints (e.g., Warren & Warshall 2001; Liu et al. 2007a; Qiu et al. 2010), although the latter are often more compact. This timing, the spatial association of $K2$ and $K3$ with the SXR source, and their displacement from the UV ribbon are all naturally explained if $K2$ and $K3$ were coronal sources. The nature of kernel $K1$ is less clear: its location is consistent with a footpoint source (although not inconsistent with a coronal source falling on the ribbon only in projection), while its soft spectrum, similar to $K2$ (Figure 11), indicates a coronal source. Overall, the HXR sigmoid observed here is at least partly of coronal origin, different from that reported by Ji et al. (2008), which appeared in a typical flare morphology with two conjugate footpoints and a looptop source.

3. INTERPRETATION

3.1. Filament Chirality and Magnetic Configuration

The writhing motion and the consequent formation of the left-handed kink clearly indicate that the upper branch of the filament was embedded in a left-handed flux rope. Thus, the inverse polarity configuration is indicated for this branch. The helicity sign of the lower branch can be inferred from its magnetic connections at the ends, which were the same as for the upper branch, and from its interaction with the upper branch. The MHD simulations by Linton et al. (2001) showed that two parallel flux tubes with the same sign of helicity tend to merge while those with the opposite sign of helicity tend to bounce off each other. Thus, left-handed helicity is indicated for the lower branch as well.

However, the lower branch could be either embedded in a flux rope with the inverse polarity configuration (Figure 12(a)) or in a sheared arcade (Figure 12(b)) with the normal polarity configuration. The latter case simply corresponds to a flux rope configuration bounded below by an X-type structure, i.e., in general a hyperbolic flux tube (HFT; e.g., Titov et al. 2002). It is well known that this configuration admits both stable and unstable states for the flux rope (while the arcade below does not erupt): the helical kink mode and the torus instability have been demonstrated to occur if the flux rope's twist or height exceeds a threshold (e.g., Török et al. 2004; Török & Kliem 2007).

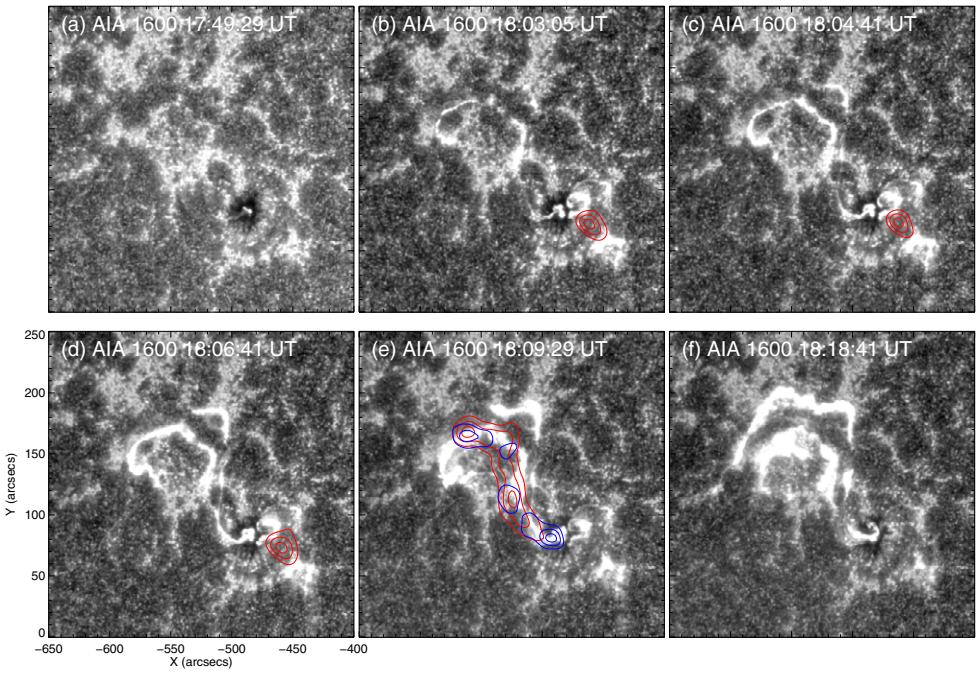

Figure 10. UV flare ribbons in relation to HXR emission represented by contours (same as in Figure 5).
(A color version of this figure is available in the online journal.)

The consideration of the former case in Paper II shows that it likewise admits of both stable and unstable states for the upper flux rope, with the lower flux rope being stable (in addition to states with both ropes being unstable). Consequently, both configurations sketched in Figure 12 represent plausible models for the observed double-decker filament.

3.2. Formation Mechanism

A question naturally arises as to how a double-decker configuration containing two flux ropes in equilibrium can form. We provide two possible scenarios as follows.

1. The lower branch emerges from below the photosphere after the upper branch has formed above the PIL. This is motivated by the recent *Hinode* observation which suggests that a flux rope can emerge under a pre-existing filament (Okamoto et al. 2008). In this particular observation, the upper and lower flux systems appeared to merge within a couple of hours right after the emergence of the lower flux system (Okamoto et al. 2009). Such merging may be delayed or inhibited if the upper flux system is elevated to substantial heights or if the ambient field between the flux systems is very strong (see Paper II for the latter case).
2. Both branches originally belong to a single flux rope or flux bundle and are separated later. This is motivated by the "partial eruption" scenario proposed by Gilbert et al. (2001), in which the reconnection within a stretched flux rope splits it into two ropes with the same handedness. However, it is unclear whether the two ropes can remain in equilibrium for an extended period of time (a few days), since in previous simulations (e.g., Gibson & Fan 2006b) and observations (e.g., Gilbert et al. 2001, 2007; Liu et al. 2007c; Tripathi et al. 2009; Régnier et al. 2011) the splitting often occurs during the eruption or, in some cases, shortly before the eruption (e.g., Contarino et al. 2003; Guo et al. 2010). See Paper II for a new simulation addressing this problem.

We suggest that a double-decker configuration is not a unique occurrence, since it is possible for either branch to be void of filament material so that only a single-branch filament is visible. In particular, it is sometimes observed that a filament survives the eruption directly above it (e.g., Pevtsov 2002; Liu et al. 2007b, 2007c, 2010). This could be similar to the eruption studied here except that the upper branch is not traced by filament material. As the upper branch rises, reconnection occurs between the oppositely directed legs of the overlying field which recloses between the two branches, so that the lower branch is confined by the newly reconnected field (similar to the middle panel of Figure 3 in Gilbert et al. 2001).

3.3. Flux Transfer

The transfer of material from the lower to the upper filament branch implies a corresponding transfer of flux if the field in the filament has a dominantly horizontal direction, which is the standard configuration at least for active-region filaments. Such transfer of flux through the HFT between the filament branches is different from a conventional reconnection process at the HFT (e.g., tether-cutting reconnection), which would exchange flux in both branches with the ambient flux. Thus, it must be due to upward Lorentz forces of the current-carrying flux in the lower branch which enforce part of this flux to rise even through the HFT. Such a process is conceivable if part of the flux in the lower branch is particularly stressed (sheared or twisted) by appropriate photospheric changes in its footpoint areas. It is also natural to expect that such flux rearrangement is accompanied by reconnection between the flux of the lower branch and that of the upper branch. We conclude that the transfer of flux as indicated by the observed mass transfer must involve a transfer of current from the lower to the upper filament branch. This will be further considered in the modeling of the partial eruption in Paper II.

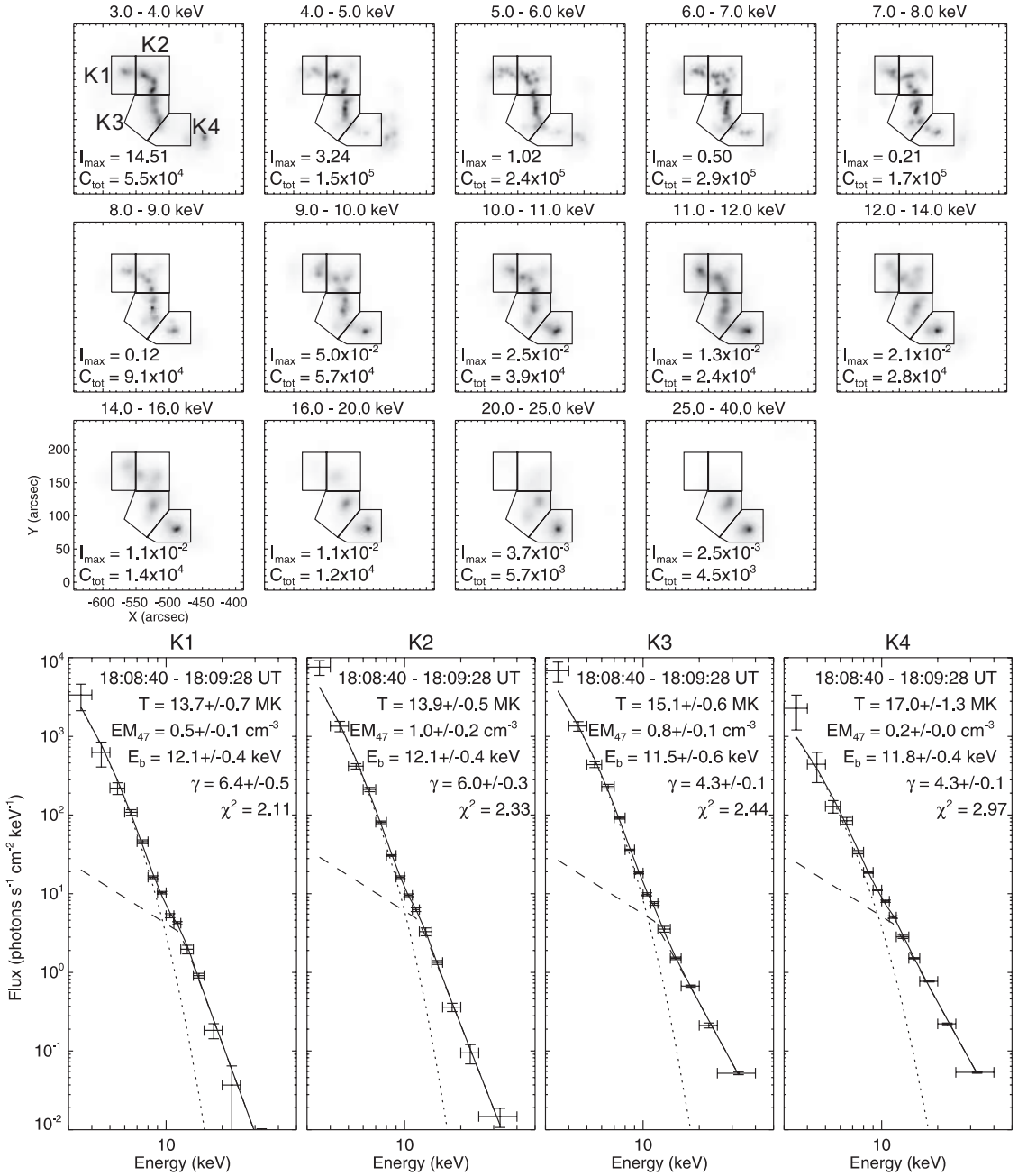

Figure 11. Imaging spectroscopy for a 48 s interval at the peak of the HXR burst at about 18:09 UT on 2010 August 7. Pixon images are made with detectors 2–8 in 14 energy bins from 3 to 40 keV. Indicated in the bottom left corner of each image are the maximum brightness, I_{max} (photons cm^{-2} s^{-1} arcsec^{-2}), of each individual Pixon map, and the total counts accumulated by the detectors used, C_{tot}. The spatially resolved spectrum for each region as marked by polygons is fitted with an isothermal function (dotted line) plus a broken power-law function (dashed line) with the spectral index below the break energy being fixed at 1.5. Resultant fitting parameters, as in Figure 8, are given for each spectrum. Emission measures given as EM_{47} are to be multiplied by 10^{47}.

3.4. Eruption Mechanism

3.4.1. Role of the Helical Kink Instability

The pronounced writhing of the upper filament branch into a projected forward S shape in the course of its rise is an indication for the occurrence of the helical kink instability. However, since the filament had a low-lying, reverse S shape prior to the eruption, it must have temporarily straightened out during the initial rise before it could adopt the high-arching, forward S shape. Both a low-lying reverse S-shaped structure and a high-arching forward S-shaped structure have negative (left-handed) writhe, while a straight loop (lying in a plane) has no writhe (Török et al. 2010). Therefore, the straightening implies a reduction of writhe, excluding the helical kink instability as the trigger of the eruption. This is because the helical kink which transforms twist into writhe is supposed to increase the writhe. The only exception is an opposite sign of the initial twist and writhe, which would be a very unusual case and is in no way supported by the data of the considered event, which all indicate left-handed helicity.

As has also been noted in Török et al. (2010), the initial increase of the flux rope twist by the transformation of writhe helicity supports the occurrence of the helical kink in the further evolution. Part of the acquired twist would thus be transformed

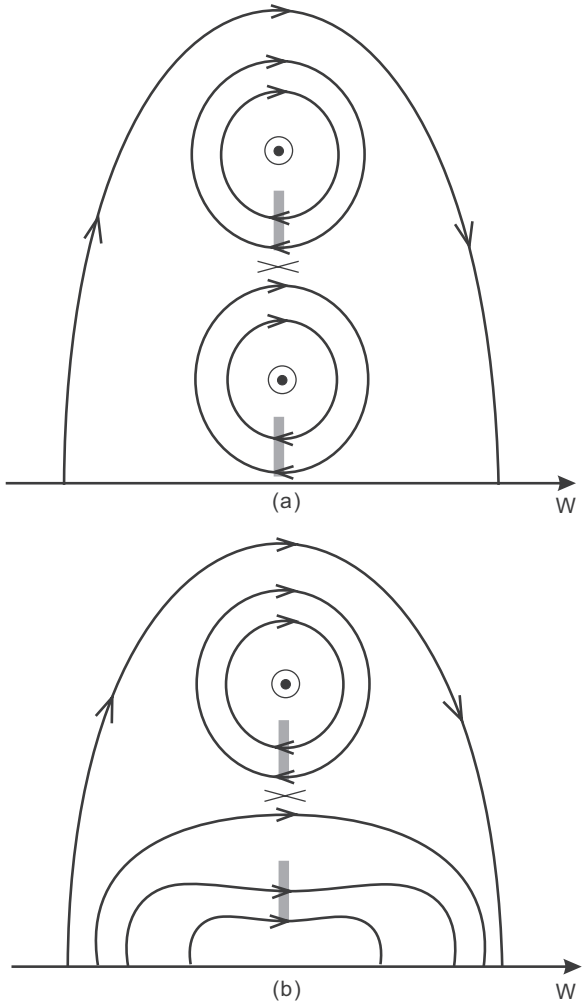

Figure 12. Schematic illustrating the cross section of the two suggested double-decker filament configurations as viewed from the south. The axial field of both filament branches points out of the plane. Regions to the east (west) of the filament are associated with positive (negative) polarity. Slabs of gray color indicate the filament body.

back into left-handed writhe. Inferring the occurrence of the instability from an observed writhing (helical kinking) alone is often not conclusive, however, since a writhing of the same sign is given to a rising flux rope by the shear component of the ambient field (Isenberg & Forbes 2007). This component is usually present and acts quite efficiently (Kliem et al. 2012a). In AR 11093, it must have been rather strong because the main polarities were situated near the ends of the filament. In order to infer the helical kink unambiguously, one needs to find a super-critical amount of twist (through observation of highly twisted substructure, magnetic field extrapolation, or a parametric study as in Kliem et al. 2012a) or features incompatible with a writhing driven (nearly) exclusively by the shear field. The latter—approaching flux rope legs, apex rotation considerably exceeding 90°, or more than one helical turn—were justified in Kliem et al. (2012a).

In the present case, we find an indication against a purely shear-field-driven writhing from the filament shape in the *SDO* images in Figures 5(d) and (e). The filament exhibits two strong and localized bends in this phase, which, at the given oblique perspective, indicate an apex rotation exceeding 90° (with respect to the line connecting the footpoints) by a considerable amount. Projection effects can easily produce such a bend on one side of a gently writhed loop with $\lesssim$90° apex rotation. However, the other leg would then appear quite straight. Two strong and localized bends are seen from many perspectives if the apex rotation clearly exceeds 90°. Such a strong rotation is not expected to result from the shear field mechanism alone because the shear field causes the flux rope legs to lean to the side in opposite direction perpendicular to its own direction. If there were no further effect, the resulting rotation would always stay below 90°. In fact, there is an additional contribution to the rotation from the relaxation of the twist in a rising force-free flux rope even if the twist is insufficient to trigger the helical kink. Kliem et al. (2012a) have found that this contribution is about 40° if the shear field is very small, and it should be smaller for larger shear field because the shear-field-driven rotation then has a share in reducing the twist. Hence, a total rotation of $\approx$130° or more represents an indication for the occurrence of the helical kink instability. The two strong bends in Figures 5(d) and (e) are consistent with a rotation of this magnitude. The alignment of the filament section between the bends with the solar-*y*-axis in Figure 5(e) is suggestive of a rotation beyond the meridional plane, since the height of the structure is initially still increasing if one goes southward from the northern bend (compare the *STEREO* image in Figure 5(h)). If this section of the filament were lying in the meridional plane, then it would run slightly southeastward in the plane of the sky for *SDO*. This suggests a rotation even slightly exceeding 135° with respect to the diagonal line between the footpoints of the filament, which is an indication that the helical kink instability did occur in the main phase of the eruption.

3.4.2. Flux Imbalance and Torus Instability

Which other mechanism could have triggered this event? We suggest that it was a loss of equilibrium caused by flux imbalance or by the torus instability. Both mechanisms, which may actually be closely related, are supported by the main characteristics of the gradual evolution prior to the event's onset: the transfer of flux from the lower to the upper filament branch and the slow rise of the upper branch (Figure 4).

Through parametric study of flux ropes in numerical models of erupting active regions, it has been found that the amount of axial flux in the rope, relative to the total amount of flux in the region, possesses a limiting value for the existence of stable equilibria (Bobra et al. 2008; Savcheva & van Ballegooijen 2009; Su et al. 2011). The limiting value appears to be rather small, in the ~(10%–20%) range (although compare Green et al. 2011, who presented support for a higher value for a flux rope still in the process of formation). The conjectured flux rope in the present event was lying rather high, thus likely well developed, so that the given small limiting value appears to be relevant and a rather modest amount of flux transfer to the upper branch may have led it to a point where no neighboring equilibrium was available.

The torus instability (Kliem & Török 2006; Török & Kliem 2007) sets in if a flux rope rises to a critical height at which the overlying field declines with height at a sufficiently steep rate (Liu 2008; Aulanier et al. 2010; Olmedo & Zhang 2010; Fan 2010). Thus, the observed slow rise of the upper filament branch makes this instability a potential trigger mechanism.

3.4.3. Mass (Un-)Loading

The observations in Section 2.4 show that mass is transferred from the lower to the upper branch of the filament. Mass "loading" in some form may often play a role in the final

evolution of filaments toward an eruption, since their darkness and thickness often increase in this phase (e.g., Kilper et al. 2009; Guo et al. 2010). Since this darkening is not yet fully understood, other effects, listed in Section 2.4, may be relevant in addition, or alternatively. Mass loading is very suggestive as a mechanism that helps holding down current-carrying flux, thus raising the amount of free magnetic energy that can be stored in the configuration (Low et al. 2003). A destabilizing influence of "mass unloading" may also be conjectured from the observation that the internal motions in filaments tend to amplify prior to eruption, which happened also in the event analyzed here. Moreover, these motions were systematically directed from the middle toward the ends of the upper branch for an extended period of time, at least ≈15 minutes prior to the onset of the fast rise (Section 2.4). However, a consideration of the typical gravitational and magnetic energy densities in active regions leaves mass unloading at most the role of a "final drop" in an equilibrium sequence approaching the point where the equilibrium is lost. Forbes (2000) estimates that the magnetic energy of an average active region ($B \sim 100$ G) exceeds the gravitational energy by three orders of magnitude, based on a typical coronal density of 10^9 cm^{-3}. For the denser filament material, the measured values of the electron density vary greatly, ranging from 10^9 to 10^{11} cm^{-3} (Labrosse et al. 2010), due to differences among the techniques that have been used, as well as to an unknown filling factor, but the temperature is often better constrained ($T \leqslant 10^4$ K). Thus, to maintain a local pressure balance, filaments must be about 100 times denser than their typical coronal surroundings ($T \simeq 10^6$ K, $n \simeq 10^9$ cm^{-3}). Still, the energy density of the gravitation is at least one order of magnitude smaller than that of the magnetic field. This renders gravity largely irrelevant for the energy storage in active regions. Thus, while mass unloading of the upper filament branch may have played a minor role in the evolution toward the eruption, a role in the actual driving process can almost certainly be excluded.

3.5. Transient HXR Sigmoid

An important structure associated with the dynamic evolution of a twisted flux rope is a sigmoidal current sheet under the rope, as revealed in various MHD simulations. The current sheet may form at a bald-patch separatrix surface (e.g., Titov & Démoulin 1999; Magara & Longcope 2001; Gibson & Fan 2006a; Archontis et al. 2009; Fan 2010), at an HFT (e.g., Titov et al. 2003; Galsgaard et al. 2003; Kliem et al. 2004), or simply in a layer of highly sheared field (Török & Kliem 2003; Aulanier et al. 2005). In each of these cases, a reverse S-shaped current sheet is associated with a left-handed flux rope whose axis writhes into a forward S shape when the rope rises (Gibson & Fan 2006a; Kliem et al. 2004). The dissipation process in this current sheet and the resultant heating of plasma are suggested to be responsible for transient sigmoidal structures that brighten in SXRs prior to or during coronal eruptions. Our observation of the reverse S-shaped HXR sigmoid underlying the left-handed kink is also consistent with these simulations.

As demonstrated in Figure 5, the coronal HXR sigmoid only formed after the upper branch of the filament had risen to relatively high altitudes above the surface. As the X-ray sigmoid is largely of coronal origin (between ∼12 and 25 Mm; recall Section 2.3 and see also Figure 9(a)), it is likely associated with the flare current sheet formed at the HFT. We therefore suggest that accelerated electrons trapped in this current sheet produced the HXR sigmoid.

4. SUMMARY

We investigate the pre-eruptive evolution and the partial eruption of a filament which is composed of two branches separated in height, combining *SDO*, *STEREO*, and *RHESSI* data. This is complemented by MHD modeling in Paper II. To our knowledge, such a double-decker configuration is analyzed in detail for the first time. We summarize the major results as follows.

1. With stereoscopic observations from *SDO* and *STEREO-B*, we obtain the three-dimensional height information of the two filament branches. They are separated in height by about 13 Mm, and the vertical extension of the upper branch is about 10 Mm.
2. The strong writhing of the upper branch into a left-handed helical kink, unambiguously determined by combining *SDO* and *STEREO-A* observations, clearly indicates the structure of a left-handed flux rope for this branch. Since the lower branch has the same magnetic connections at its ends and transfers some of its flux into the upper branch in the course of the pre-eruptive evolution, left-handed helicity is indicated also for the lower branch, and hence for the dextral filament as a whole.
3. This structure is compatible with two model configurations, a flux rope above a sheared magnetic arcade with dips and a double flux rope equilibrium. In either case, the filament material in each branch can be supported against gravity by upward concave field lines, and an HFT separates the branches. The first configuration is well known to possess stable and unstable states of the flux rope, with the arcade remaining stable (Titov & Démoulin 1999). Equilibria of the second type are analytically and numerically constructed in Paper II. MHD simulations demonstrate that they possess stable as well as unstable states with only the upper flux rope erupting (and also unstable states that lead to the ejection of both flux ropes).
4. The pre-eruptive evolution of the filament is characterized by a slow rise of the upper branch most likely driven by the transfer of current-carrying flux from the lower to the upper branch in a sequence of partial merging episodes. Weak-flux cancellation may also have contributed to the rise. These properties suggest that the eruption was triggered by reaching a point of flux imbalance between the upper branch and the ambient field (e.g., Su et al. 2011) or the threshold of the torus instability.
5. The initial straightening of the erupting upper filament branch from its original reverse S shape excludes the helical kink instability as trigger of the eruption, but it supports the occurrence of the instability in the main phase of the eruption, which is indeed indicated by the strong forward S shape acquired in this phase.
6. The main acceleration of the erupting branch commences very close in time with the impulsive phase of the associated M1-class flare. The eruption results in a reverse S-shaped HXR sigmoid which is at least partly located in the gap between the two branches from about 12 Mm to 25 Mm above the surface. To our knowledge, this is the first time that a coronal sigmoid is clearly observed in HXRs. We suggest that electrons accelerated in the vertical (flare) current sheet under the rising filament branch produced the coronal HXR emission, in agreement with a previous model for transient sigmoids (Kliem et al. 2004).

The authors are grateful to the *SDO*, *STEREO,* and *RHESSI* teams for the free access to the data and the development of the data analysis software. KSO Hα data are provided through the Global H-alpha Network operated by NJIT. R. Liu acknowledges the Thousand Young Talents Program of China, NSFC grants 41131065 and 41121003, 973 key project 2011CB811403, CAS Key Research Program KZZD-EW-01-4, and the fundamental research funds for the central universities WK2080000031. R. Liu, C.L., and H.W. were supported by NASA grants NNX08-AJ23G and NNX08-AQ90G, and by NSF grants ATM-0849453 and ATM-0819662. B.K. acknowledges support by the DFG and the STFC. The contributions of T.T., V.S.T., R. Lionello, and J.A.L. were supported by NASA's HTP, LWS, and SR&T programs, and by CISM (an NSF Science and Technology Center). Computational resources were provided by NSF TACC in Austin and by NASA NAS at Ames Research Center. H.W. acknowledges travel support by Key Laboratory of Solar Activity, National Astronomical Observatories of Chinese Academy of Sciences, under grant KLSA201201.

REFERENCES

Alexander, D., Liu, R., & Gilbert, H. R. 2006, ApJ, 653, 719
Antiochos, S. K., Dahlburg, R. B., & Klimchuk, J. A. 1994, ApJ, 420, L41
Antiochos, S. K., DeVore, C. R., & Klimchuk, J. A. 1999, ApJ, 510, 485
Anzer, U. 1989, in Dynamics and Structure of Quiescent Solar Prominences, ed. E. R. Priest (Astrophysics and Space Science Library, Vol. 150; Dordrecht: Kluwer), 143
Archontis, V., Hood, A. W., Savcheva, A., Golub, L., & Deluca, E. 2009, ApJ, 691, 1276
Aschwanden, M. J., & Boerner, P. 2011, ApJ, 732, 81
Aulanier, G., & Démoulin, P. 1998, A&A, 329, 1125
Aulanier, G., Demoulin, P., van Driel-Gesztelyi, L., Mein, P., & Deforest, C. 1998, A&A, 335, 309
Aulanier, G., Pariat, E., & Démoulin, P. 2005, A&A, 444, 961
Aulanier, G., Török, T., Démoulin, P., & DeLuca, E. E. 2010, ApJ, 708, 314
Bemporad, A., Mierla, M., & Tripathi, D. 2011, A&A, 531, A147
Bobra, M. G., van Ballegooijen, A. A., & DeLuca, E. E. 2008, ApJ, 672, 1209
Bommier, V., Landi Degl'Innocenti, E., Leroy, J.-L., & Sahal-Brechot, S. 1994, Sol. Phys., 154, 231
Bougeret, J. L., Goetz, K., Kaiser, M. L., et al. 2008, Space Sci. Rev., 136, 487
Chae, J. 2000, ApJ, 540, L115
Chae, J., Moon, Y.-J., & Park, Y.-D. 2005, ApJ, 626, 574
Cho, K.-S., Lee, J., Bong, S.-C., et al. 2009, ApJ, 703, 1
Contarino, L., Romano, P., Yurchyshyn, V. B., & Zuccarello, F. 2003, Sol. Phys., 216, 173
DeVore, C. R., & Antiochos, S. K. 2000, ApJ, 539, 954
Fan, Y. 2005, ApJ, 630, 543
Fan, Y. 2010, ApJ, 719, 728
Fan, Y., & Gibson, S. E. 2004, ApJ, 609, 1123
Forbes, T. G. 2000, J. Geophys. Res., 105, 23153
Forbes, T. G., & Priest, E. R. 1995, ApJ, 446, 377
Galsgaard, K., Titov, V. S., & Neukirch, T. 2003, ApJ, 595, 506
Gibson, S. E., & Fan, Y. 2006a, J. Geophys. Res., 111, A12103
Gibson, S. E., & Fan, Y. 2006b, ApJ, 637, L65
Gibson, S. E., Fan, Y., Török, T., & Kliem, B. 2006, Space Sci. Rev., 124, 131
Gilbert, H. R., Alexander, D., & Liu, R. 2007, Sol. Phys., 245, 287
Gilbert, H. R., Holzer, T. E., & Burkepile, J. T. 2001, ApJ, 549, 1221
Green, L. M., Kliem, B., Török, T., van Driel-Gesztelyi, L., & Attrill, G. D. R. 2007, Sol. Phys., 246, 365
Green, L. M., Kliem, B., & Wallace, A. J. 2011, A&A, 526, A2
Guo, J., Liu, Y., Zhang, H., et al. 2010, ApJ, 711, 1057
Hirayama, T. 1985, Sol. Phys., 100, 415
Hood, A. W., & Priest, E. R. 1979, Sol. Phys., 64, 303
Howard, R. A., Moses, J. D., Vourlidas, A., et al. 2008, Space Sci. Rev., 136, 67
Hurford, G. J., Schmahl, E. J., Schwartz, R. A., et al. 2002, Sol. Phys., 210, 61
Inhester, B. 2006, arXiv:astro-ph/0612649
Isenberg, P. A., & Forbes, T. G. 2007, ApJ, 670, 1453
Ji, H., Wang, H., Liu, C., & Dennis, B. R. 2008, ApJ, 680, 734
Ji, H., Wang, H., Schmahl, E. J., Moon, Y.-J., & Jiang, Y. 2003, ApJ, 595, L135
Kaiser, M. L., Kucera, T. A., Davila, J. M., et al. 2008, Space Sci. Rev., 136, 5
Karlický, M., & Kliem, B. 2010, Sol. Phys., 266, 71
Karpen, J. T., Antiochos, S. K., Hohensee, M., Klimchuk, J. A., & MacNeice, P. J. 2001, ApJ, 553, L85
Kilper, G., Gilbert, H., & Alexander, D. 2009, ApJ, 704, 522
Kippenhahn, R., & Schlüter, A. 1957, Z. Astrophys., 43, 36
Kliem, B., Linton, M. G., Török, T., & Karlický, M. 2010, Sol. Phys., 266, 91
Kliem, B., Titov, V. S., & Török, T. 2004, A&A, 413, L23
Kliem, B., & Török, T. 2006, Phys. Rev. Lett., 96, 255002
Kliem, B., Török, T., & Thompson, W. T. 2012a, Sol. Phys.
Kliem, B., Török, T., Titov, V. S., et al. 2012b, ApJ, submitted (Paper II)
Kuperus, M., & Raadu, M. A. 1974, A&A, 31, 189
Labrosse, N., Heinzel, P., Vial, J.-C., et al. 2010, Space Sci. Rev., 151, 243
Lemen, J. R., Title, A. M., Akin, D. J., et al. 2012, Sol. Phys., 275, 17
Leroy, J. L. 1989, in Dynamics and Structure of Quiescent Solar Prominences, ed. E. R. Priest (Astrophysics and Space Science Library, Vol. 150; Dordrecht: Kluwer), 77
Li, T., Zhang, J., Zhao, H., & Yang, S. 2010, ApJ, 720, 144
Lin, R. P., Dennis, B. R., Hurford, G. J., et al. 2002, Sol. Phys., 210, 3
Linton, M. G., Dahlburg, R. B., & Antiochos, S. K. 2001, ApJ, 553, 905
Liu, C., Lee, J., Gary, D. E., & Wang, H. 2007a, ApJ, 658, L127
Liu, C., Lee, J., Yurchyshyn, V., et al. 2007b, ApJ, 669, 1372
Liu, R., & Alexander, D. 2009, ApJ, 697, 999
Liu, R., Alexander, D., & Gilbert, H. R. 2007c, ApJ, 661, 1260
Liu, R., Liu, C., Wang, S., Deng, N., & Wang, H. 2010, ApJ, 725, L84
Liu, Y. 2008, ApJ, 679, L151
Low, B. C., Fong, B., & Fan, Y. 2003, ApJ, 594, 1060
Low, B. C., & Hundhausen, J. R. 1995, ApJ, 443, 818
Magara, T., & Longcope, D. W. 2001, ApJ, 559, L55
Martin, S. F. 1998, Sol. Phys., 182, 107
Martin, S. F., Bilimoria, R., & Tracadas, P. W. 1994, in Proc. NATO Adv. Res. Workshop, Solar Surface Magnetism, ed. R. J. Rutten & C. J. Schrijver (NATO Sci. Ser. C, Vol. 433; Dordrecht: Kluwer), 303
Martin, S. F., & Echols, C. R. 1994, in Solar Surface Magnetism, ed. R. J. Rutten & C. J. Schrijver (NATO Sci. Ser. C, Vol. 433; Dordrecht: Kluwer), 339
Moore, R. L., Sterling, A. C., Hudson, H. S., & Lemen, J. R. 2001, ApJ, 552, 833
Okamoto, T. J., Tsuneta, S., Lites, B. W., et al. 2008, ApJ, 673, L215
Okamoto, T. J., Tsuneta, S., Lites, B. W., et al. 2009, ApJ, 697, 913
Olmedo, O., & Zhang, J. 2010, ApJ, 718, 433
Pevtsov, A. A. 2002, Sol. Phys., 207, 111
Pevtsov, A. A., Balasubramaniam, K. S., & Rogers, J. W. 2003, ApJ, 595, 500
Pneuman, G. W. 1983, Sol. Phys., 88, 219
Qiu, J., Liu, W., Hill, N., & Kazachenko, M. 2010, ApJ, 725, 319
Régnier, S., Walsh, R. W., & Alexander, C. E. 2011, A&A, 533, L1
Romano, P., Contarino, L., & Zuccarello, F. 2003, Sol. Phys., 214, 313
Rust, D. M. 1994, Geophys. Res. Lett., 21, 241
Rust, D. M., & Kumar, A. 1994, Sol. Phys., 155, 69
Rust, D. M., & Kumar, A. 1996, ApJ, 464, L199
Rust, D. M., & LaBonte, B. J. 2005, ApJ, 622, L69
Savcheva, A., & van Ballegooijen, A. 2009, ApJ, 703, 1766
Seaton, D. B., Mierla, M., Berghmans, D., Zhukov, A. N., & Dolla, L. 2011, ApJ, 727, L10
Smith, D. M., Lin, R. P., Turin, P., et al. 2002, Sol. Phys., 210, 33
Su, Y., Surges, V., van Ballegooijen, A., DeLuca, E., & Golub, L. 2011, ApJ, 734, 53
Thompson, W., Kliem, B., & Trk, T. 2012, Sol. Phys., 276, 241
Titov, V. S., & Démoulin, P. 1999, A&A, 351, 707
Titov, V. S., Galsgaard, K., & Neukirch, T. 2003, ApJ, 582, 1172
Titov, V. S., Hornig, G., & Démoulin, P. 2002, J. Geophys. Res. (Space Phys.), 107, 1164
Török, T., Berger, M. A., & Kliem, B. 2010, A&A, 516, A49
Török, T., & Kliem, B. 2003, A&A, 406, 1043
Török, T., & Kliem, B. 2005, ApJ, 630, L97
Török, T., & Kliem, B. 2007, Astron. Nachr., 328, 743
Török, T., Kliem, B., & Titov, V. S. 2004, A&A, 413, L27
Tripathi, D., Kliem, B., Mason, H. E., Young, P. R., & Green, L. M. 2009, ApJ, 698, L27
van Tend, W., & Kuperus, M. 1978, Sol. Phys., 59, 115
Vemareddy, P., Maurya, R. A., & Ambastha, A. 2012, Sol. Phys., 277, 337
Warren, H. P., & Warshall, A. D. 2001, ApJ, 560, L87
Wuelser, J.-P., Lemen, J. R., Tarbell, T. D., et al. 2004, Proc. SPIE, 5171, 111
Xu, Y., Jing, J., & Wang, H. 2010, Sol. Phys., 264, 81
Zirker, J. B., Martin, S. F., Harvey, K., & Gaizauskas, V. 1997, Sol. Phys., 175, 27

The Challenge in Making Models of Fast CMEs

Zoran Mikić, Tibor Török, Viacheslav Titov, Jon A. Linker, Roberto Lionello, Cooper Downs and Pete Riley

Predictive Science, Inc., 9990 Mesa Rim Road, San Diego, CA 92121

Abstract. It has been a challenge to explain theoretically how fast CMEs (exceeding $\sim 1{,}000\,\mathrm{km/s}$) occur. Our numerical models suggest that it is not easy to release enough magnetic energy impulsively from an active region. We have been studying CME models that are constrained by observed magnetic fields, with realistic coronal plasma density and temperature profiles, as derived from thermodynamic models of the corona. We find that to get fast CMEs, the important parameters are the magnetic energy density, the magnetic field drop-off index, and the Alfvén speed profile in active regions. We describe how we energize active regions, and how we subsequently initiate CMEs via flux cancellation. We contrast CMEs from idealized zero-beta models with more sophisticated models based on thermodynamic solutions.

Keywords: Coronal Mass Ejections, Solar Corona, Magnetohydrodynamics (MHD)
PACS: 96.60.P-, 96.60.ph, 96.60.qf, 95.30.Qd

INTRODUCTION

It has been difficult to develop successful models of fast coronal mass ejections (CMEs). By fast CMEs we mean those whose speed significantly exceeds the ambient solar wind speed (i.e., exceeding $\sim 1{,}000\,\mathrm{km/s}$). In order to explain fast CMEs, we need to demonstrate that a significant fraction of the magnetic energy in an active region can be converted into kinetic energy to accelerate the CME, produce a shock wave low in the corona, open overlying closed magnetic field lines, and accelerate energetic particles. Our numerical models suggest that it is not easy to release enough magnetic energy impulsively for these purposes. This has to be done using realistic parameters (magnetic field strength, coronal density, active region size, solar wind, and global field model). It is desirable to use self-consistent CME initiation mechanisms (e.g., photospheric shearing flows, flux cancellation, flux emergence), rather than starting from configurations that are initially out of equilibrium.

To understand CMEs theoretically it is helpful to idealize the problem to the simplest possible configuration that retains the essential characteristics of CMEs. This is a difficult task, since this simplification might compromise the very goal of getting a fast CME. The photospheric magnetic field that is used in models is typically smoothed because simulations with large Alfvén speed and high-resolution meshes are computationally challenging. This smoothing tends to reduce the size of the photospheric field. In our experience, models with overly smoothed fields do not tend to produce fast CMEs. The smoothing process reduces the magnetic energy density in the active region and the magnitude of the Alfvén speed in the corona, and it is likely that these reductions may lower the speed of CMEs.

The plasma density can also affect the speed of CMEs (presumably via the Alfvén speed). Therefore, the models need to have a realistic density profile, requiring an accurate energy equation in the model, and a reasonable coronal heating model. With a sophisticated energy equation [1], we are able to model the cold, dense prominences that frequently erupt together with the CME. As we describe below, the mass trapped in the prominence may affect the speed of the CME, requiring an accurate model of the lower corona and chromosphere.

Finally, the magnetic field overlying the active region may affect how the CME is confined and the nature of the eruption. Since this field arises from distant magnetic field sources, a global model whose scale is much larger than the source active region may be required to properly model the CME.

It is apparent that all these aforementioned considerations make the modeling of fast CMEs difficult. This may be the reason that models have generally not been able to produce fast CMEs.

AN IDEALIZED MODEL

We illustrate our methodology by developing an idealized model of a CME that was observed on 12 May 1997. We have studied this event for many years. Even though this CME occurred in the SOHO era, it is still relevant today, simply because it is not very well understood yet. The halo CME originated in a "simple" small bipolar active region (AR 8038) at N21°W08°, and was accompanied by a C1.3 flare at 04:42 UT. The projected CME speed was $\sim 250\,\mathrm{km/s}$; the estimated actual CME speed was $\sim 600\,\mathrm{km/s}$. This CME has been described by Plunkett et al. [2] (LASCO); Thompson et al. [3] (EIT waves); Webb et al. [4] (interplanetary magnetic cloud);

Solar Wind 13
AIP Conf. Proc. 1539, 42-45 (2013); doi: 10.1063/1.4810985

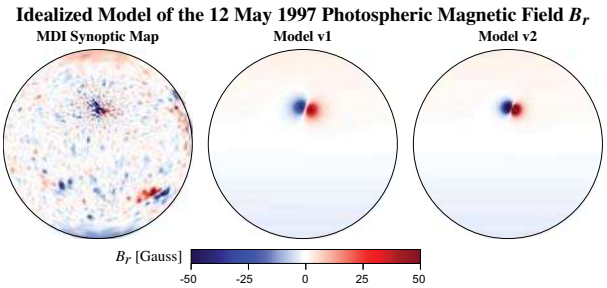

FIGURE 1. The two idealized models of the 12 May 1997 photospheric magnetic field, compared to the SOHO/MDI magnetogram.

Ambastha and Mathew [5] (flux cancellation); Gopalswamy and Kaiser [6] (Type II radio); Attrill et al. [7] (coronal dimmings); and Crooker and Webb [8] (interchange reconnection).

Despite the fact that this was not a fast CME, it is an excellent case to study for the following reason. Our simulations of the pre-eruption corona with a thermodynamic model reproduce several characteristics of the observations, including signatures in EUV and X-ray emission (coronal hole morphology, quiet Sun and active region emission, sigmoid). Furthermore, our simulated eruptions also match the observations, including prominence formation, dimming regions in EUV and X-rays, post-flare loops, and EIT waves. Nevertheless, all our attempts to simulate this CME produce an eruption that is less energetic than the observed CME.

A procedure for developing a simplified model using a global sun-centered dipole and a sub-surface bipole to represent the active region (AR) was described by Titov et al. [9]. We adopt a similar procedure, matching the observed AR flux ($\sim 5\times10^{21}$ Mx) and the total global flux ($\sim 4.3\times10^{22}$ Mx). The resulting global dipole has $B_r = 2.8$ G at the poles.

We are studying two versions of the model: v1 has a smoother version of the magnetogram with $B_r(\max) = 50$ G in the AR; v2 has less smoothing with $B_r(\max) = 180$ G. The idea is to determine if the reduction of photospheric magnetic field by smoothing reduces the speed of the CME. Both models match the observed AR magnetic flux. Figure 1 shows the models compared to the photospheric field observed with the SOHO/MDI magnetogram.

The simulations are performed with our spherical 3D resistive MHD code, using a semi-implicit technique to overcome the time step limit imposed by the Alfvén speed, and a fully implicit scheme to advance the resistive, viscous, and thermal conduction terms [10, 11]. In the transverse direction, the smallest cells (in the AR) have a size of 2,300 km (690 km) for a medium (high) resolution mesh. In the vertical direction, for the thermodynamic model, the smallest cells have a size of 220 km (60 km) for a medium (high) resolution mesh. The resistivity is chosen to be uniform, with a Lundquist number $S = 10^6$.

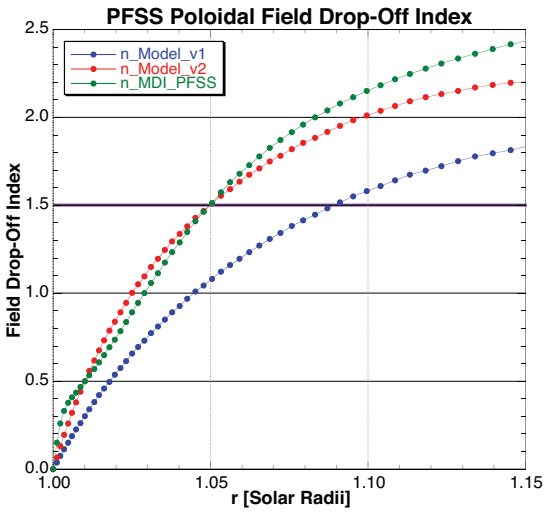

FIGURE 2. The field drop-off index (vertically above the neutral line) for the high-resolution MDI data and for Models v1 and v2.

Kliem and Török [12] have described how the drop-off of the poloidal component of the potential field that confines a flux rope affects its stability. Assuming that locally $B_{\rm pol} = B_0(h/h_0)^{-n}$, where $h = r - R_\odot$ is the height above the photosphere, the local drop-off index is $n = -d(\ln B_{\rm pol})/d(\ln h)$. A heuristic condition for stability is: when $n \gtrsim 1.5$ above the flux rope, the rope erupts more easily; when $n \lesssim 1.5$, the rope tends to be stable [12]. Démoulin and Aulanier [13] consider the critical value to be closer to 1.1–1.3. Török and Kliem [14] have investigated the effect of n on the speed of CMEs. Fields that fall off rapidly with height (larger n) are easier to disrupt, and may produce faster CMEs. An example is a quadrupolar configuration, as exemplified by the Breakout Model [15]. Figure 2 compares n for the high-resolution MDI magnetogram, and for Models v1 and v2 (using a PFSS model). It can be seen that Model v2 matches n of the high-resolution data, whereas Model v1 has a lower n. This is an indication that Model v1 may have been smoothed too much and may have difficulty producing fast CMEs, consistent with our preliminary results. Full confirmation will require a detailed comparison of models v1 and v2 (work in progress).

ACTIVE REGION ENERGIZATION AND CME TRIGGERING

We briefly describe how we typically energize the active region in our model, and how we trigger the eruption. We start with a potential field, and energize the AR by emerging transverse magnetic field along the polarity inversion line (PIL), specified via a boundary condition at $r = R_\odot$ on the transverse electric field, $\mathbf{E}_t = \nabla_t\Phi$.

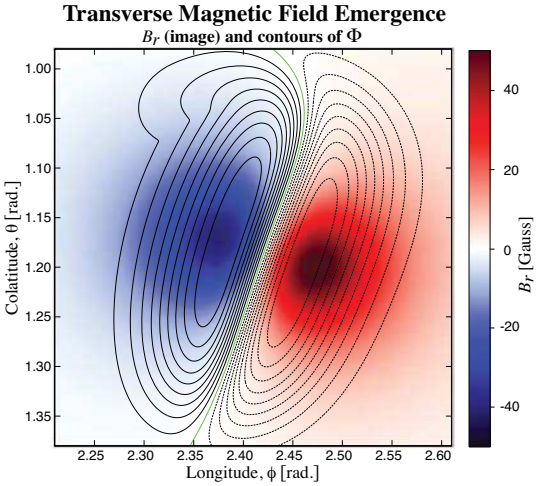

FIGURE 3. The potential Φ used to energize the AR by emerging transverse magnetic field along the PIL (green).

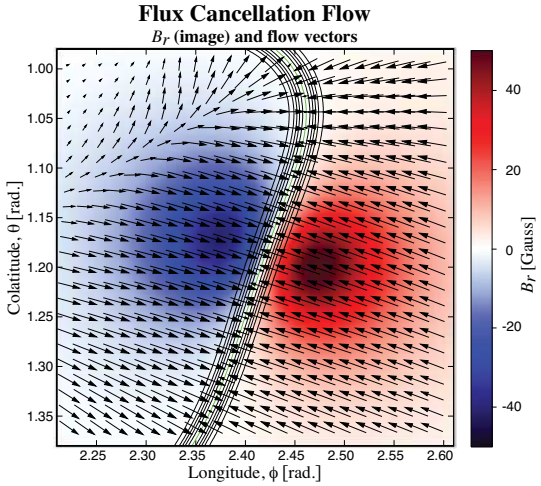

FIGURE 4. Flow applied at $r = R_\odot$ that converges towards the PIL (green), resulting in cancellation of flux. This frequently triggers the initiation of a CME. The contours show the photospheric resistivity.

The potential Φ is chosen to change sign across the PIL; see Fig. 3. Since $\mathbf{E}_t$ is the gradient of a scalar, this electric field does not change B_r in the photosphere. We find that the transverse magnetic field emerged by this process introduces shear at the neutral line. The magnetic energy in the active region is raised significantly above the potential field energy.

After the energization is complete, the eruption is triggered by applying flux cancellation at the PIL. There is evidence that flux cancellation preceded the 12 May 1997 CME [5], and may have been its trigger. MDI magnetograms show clear evidence of cancellation of flux at the PIL. This flux cancellation is specified by imposing converging flows at $r = R_\odot$, together with photospheric diffusion [e.g., 16, 17, 18]. Figure 4 shows a typical example of the flow used. In its early stages, flux cancellation converts the highly sheared field along the PIL into a filament. We have found these techniques to be a very flexible way to energize and trigger CMEs.

ZERO BETA AND THERMODYNAMIC MODELS

The full thermodynamic model with an improved energy equation is very costly to run, since it requires high-resolution meshes and small time steps. A "zero-beta" model, in which gravity and pressure forces are neglected, is a useful approximation. In this model, the energy equation is not solved (since $p = 0$). The zero-beta model is numerically more efficient, and is frequently used for the rapid investigation of stability. It is important to note that the coronal density profile $\rho(\mathbf{x})$ can be chosen freely in this model. This choice affects the Alfvén speed profile. In general, it is difficult to choose a realistic ρ profile, especially when the magnetic field varies over a large range (as is the case for global simulations with high resolution in active regions). That is a primary reason to use a thermodynamic model in which ρ is determined self-consistently. We have found that the choice of $\rho(\mathbf{x})$ can dramatically influence the assessment of a fast CME model.

We studied the energization and eruption of Model v1 using the zero-beta and thermodynamic models. We found that when an arbitrary, though reasonable, density profile was specified in the zero-beta model, the CME reached a certain speed. When we repeated this case using a density profile that was derived from the thermodynamic model (which is more realistic), the CME speed was significantly different. The case with the "fake" density profile was appreciably more energetic. (It turned out to have a higher coronal Alfvén speed.) This ought to be a cautionary tale for users of zero-beta models.

Furthermore, we noticed that the thermodynamic model generally gave less energetic eruptions for the same conditions (energization and flux cancellation), as illustrated in Fig. 5. The thermodynamic model has a smaller burst of kinetic energy, and a correspondingly more gradual release of magnetic energy, than the zero-beta model. (In this case the zero-beta model used the ρ profile from the thermodynamic model to make the comparison as similar as possible.) In the thermodynamic model, the lower field lines in the erupting filament appear to be trapped by the dense plasma in the chromosphere/low corona, in contrast to the zero-beta model, as seen in Figure 6. The thermodynamic model shows the self-consistent formation of a prominence (cool, dense material) in the filament channel, an exciting development in its own right. Since the physics in the thermodynamic model is more accurate, conclusions about the speed of CMEs based on the zero-beta model need to be

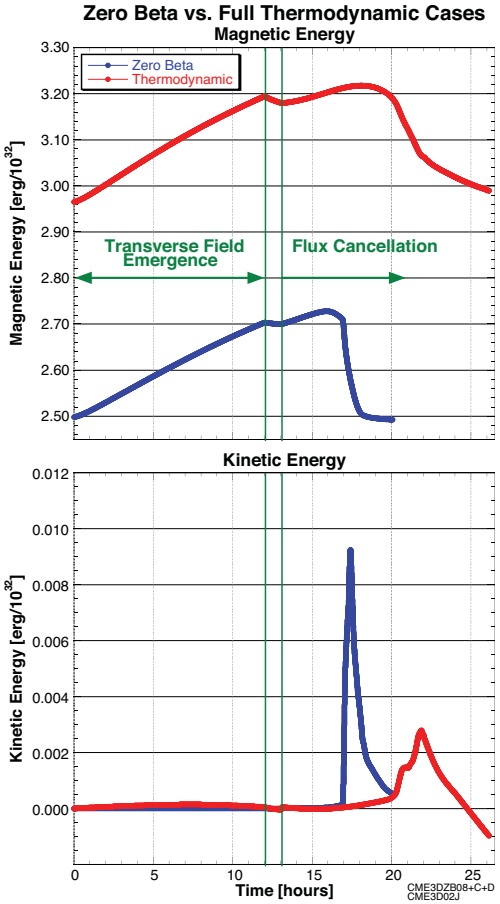

FIGURE 5. The magnetic and kinetic energy for zero-beta and a full thermodynamic simulations. The kinetic energy for the thermodynamic case is that above the initial value.

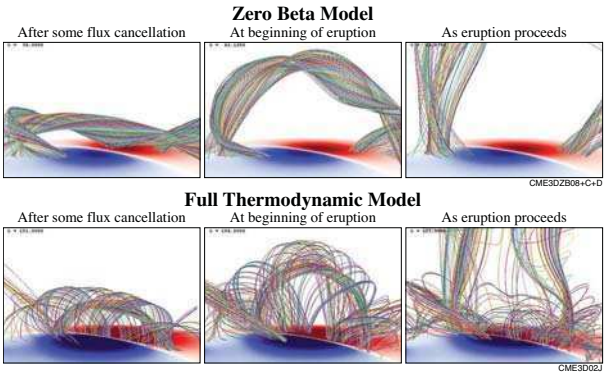

FIGURE 6. The evolution of selected field lines for zero-beta and full thermodynamic simulations.

made carefully.

CONCLUSIONS

It is apparent that models of fast CMEs do not come easily. Although our analysis is not complete, there are strong indications that magnetograms of active regions used in models must not be smoothed too much, to maximize the chances of getting a fast CME. It appears to be necessary for the models to maintain high Alfvén speeds. The presence of a large field drop-off index low in the corona also helps. Zero-beta models are very useful, but need to be used carefully when making conclusions about the speed of CMEs. Full thermodynamic models offer promise to model the formation of prominences and their eruption within CMEs.

ACKNOWLEDGMENTS

This work was supported by NASA's LWS & Heliophysics Theory Programs, by a subcontract from Lockheed Martin (NASA prime contract NNG04EA00C in support of SDO/AIA), and by NSF via the CISM and FESD Centers.

REFERENCES

1. R. Lionello, J. A. Linker, and Z. Mikić, ApJ **690**, 902–912 (2009).
2. S. P. Plunkett, B. J. Thompson, R. A. Howard, D. J. Michels, O. C. St. Cyr, S. J. Tappin, R. Schwenn, and P. L. Lamy, Geophys. Res. Lett. **25**, 2477–2480 (1998).
3. B. J. Thompson, S. P. Plunkett, J. B. Gurman, J. S. Newmark, O. C. St. Cyr, and D. J. Michels, Geophys. Res. Lett. **25**, 2465–2468 (1998).
4. D. F. Webb, R. P. Lepping, L. F. Burlaga, C. E. DeForest, D. E. Larson, S. F. Martin, S. P. Plunkett, and D. M. Rust, J. Geophys. Res. **105**, 27251–27260 (2000).
5. A. Ambastha, and S. K. Mathew, in *Advanced Solar Polarimetry*, edited by M. Sigwarth, 2001, vol. 236 of *ASP Conf. Series*, p. 313.
6. N. Gopalswamy, and M. L. Kaiser, *Adv. Sp. Res.* **29**, 307–312 (2002).
7. G. Attrill, M. S. Nakwacki, L. K. Harra, L. van Driel-Gesztelyi, C. H. Mandrini, S. Dasso, and J. Wang, Sol. Phys. **238**, 117–139 (2006).
8. N. U. Crooker, and D. F. Webb, *J. Geophys. Res. (Space Physics)* **111**, 8108 (2006).
9. V. S. Titov, Z. Mikić, J. A. Linker, and R. Lionello, ApJ **675**, 1614–1628 (2008).
10. Z. Mikić, D. C. Barnes, and D. D. Schnack, ApJ **328**, 830–847 (1988).
11. Z. Mikić, J. A. Linker, D. D. Schnack, R. Lionello, and A. Tarditi, *Physics of Plasmas* **6**, 2217–2224 (1999).
12. B. Kliem, and T. Török, *Phys. Rev. Lett.* **96**, 255002 (2006).
13. P. Démoulin, and G. Aulanier, ApJ **718**, 1388–1399 (2010).
14. T. Török, and B. Kliem, *Astron. Nachr.* **328**, 743 (2007).
15. S. K. Antiochos, C. R. DeVore, and J. A. Klimchuk, ApJ **510**, 485–493 (1999).
16. T. Amari, J. F. Luciani, J. J. Aly, Z. Mikić, and J. Linker, ApJ **585**, 1073–1086 (2003).
17. T. Amari, J.-J. Aly, Z. Mikić, and J. Linker, ApJ **717**, L26–L30 (2010).
18. T. Amari, J.-J. Aly, J.-F. Luciani, Z. Mikić, and J. Linker, ApJ **742**, L27 (2011).